Nanoscale Materials

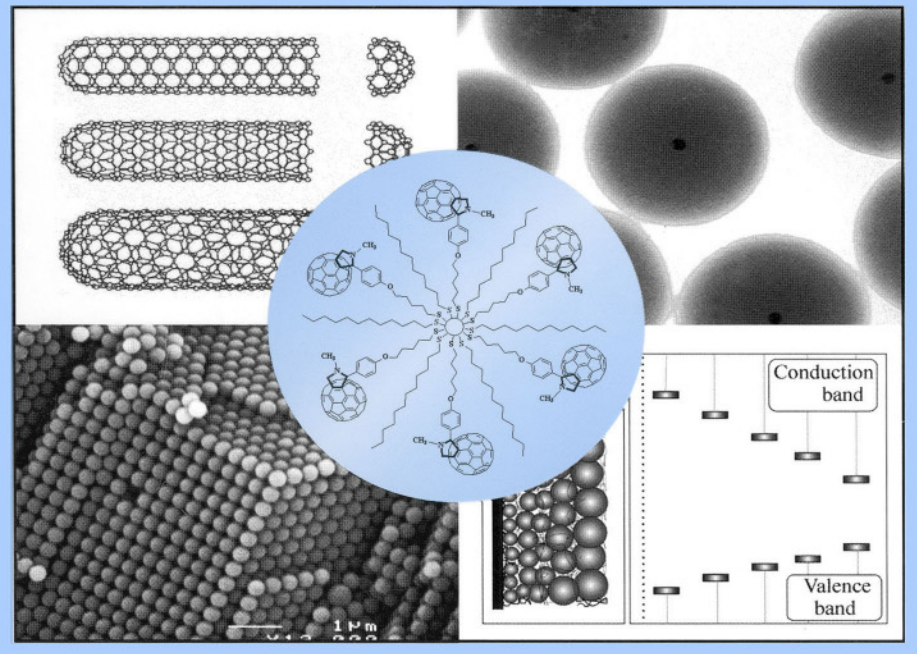

Edited by
Luis M. Liz-Marzán and Prashant V. Kamat

Kluwer Academic Publishers

NANOSCALE MATERIALS

This page intentionally left blank

NANOSCALE MATERIALS

edited by

Luis M. Liz-Marzán
Universidade de Vigo
Spain

Prashant V. Kamat
University of Notre Dame
U.S.A.

KLUWER ACADEMIC PUBLISHERS
NEW YORK, BOSTON, DORDRECHT, LONDON, MOSCOW

eBook ISBN: 0-306-48108-1
Print ISBN: 1-4020-7366-6

Created in the United States of America

Visit Kluwer Online at: http://kluweronline.com
and Kluwer's eBookstore at: http://ebooks.kluweronline.com

To Neha, Neeta, Pedro and Sofía

This page intentionally left blank

CONTENTS

This page intentionally left blank

PREFACE

The unique electronic and chemical properties of nanoparticles have drawn the attention of chemists, physicists, biologists and engineers who wish to use them for the development of next generation nanodevices. Organized nanoassemblies of inorganic nanoparticles and organic molecules are building blocks of nanodevices, whether they are designed to perform molecular level computing, sense the environment or improve the catalytic properties of a material. The key to creation of these hybrid nanostructures lies in understanding the chemistry at a fundamental level. This book serves as a reference book for advanced graduate students and active researchers by providing fundamental understanding of many nanoscopic materials. Scientists and engineers who wish to diversify their research into nanoscience and nanotechnology will find this book extremely useful.

The rapidly evolving field of nanoscience has come out of its infancy and is paving its way into novel technological applications. The topics chosen for this book provide a global perspective into the status of an extremely active research field. Constantly evolving methodologies and techniques provide new dimensions to this field every year. Though many issues are still being debated, the general interest in nanoscience will continue to grow during the coming decade.

Luis M. Liz-Marzán

Prashant V. Kamat

This page intentionally left blank

ACKNOWLEDGMENTS

We thank all the contributors to this book for their extra effort in presenting state-of-art developments in their areas of expertise. This book would have not been possible without them. Additionally, we need to acknowledge the patience of our families, specially our wives (Charo and Shobha), which allowed us to spend time on the preparation of the book at the cost of not being with them.

This page intentionally left blank

1
NANOSCALE MATERIALS

Luis M. Liz-Marzán and Prashant V. Kamat*

Nanoscale materials can be defined as those whose characteristic length scale lies within the nanometric range, i.e. in the range between one and several hundreds of nanometers. Within this length scale, the properties of matter are sufficiently different from individual atoms or molecules and from bulk materials, that their study has been recently recognized as a new area of science, which is generally termed *Nanoscience.* Even more popular than Nanoscience has become the term *Nanotechnology,* which relates to the ability to build functional devices based in the controlled assembly of nanoscale objects, for specific technological applications. The importance of both nanoscience and nanotechnology has been confirmed by a number of national and international initiatives to promote their study. Funding agencies in the USA, Europe, Australia and Japan are spending a significant part of their funds for the development of this relatively new area of study. Likewise, the number of groups working in nanoscience or nanotechnology has dramatically increased during the past two decades, which also means that the amount of information available is becoming larger and larger, so large that it is basically impossible to follow in sufficient detail.

A key to designing organized nanoassemblies for next generation nanodevices is to understand their electronic, structural, and chemical properties, and the manner in which their components contribute to these properties. Such fundamental information is generally lacking. We have attempted to provide this missing link by selecting a broad range of topics that include micro and mesoporous structures, semiconductor and metal nanoparticles, as well as sol-gel and core-shell materials. The spectroscopy and theoretical topics chosen for this book will provide the basic knowledge of dynamics and charge transfer processes of photoactive nanomaterials.

Although it is basically impossible to cover all the areas where nanoscale materials are involved, we have made a choice of topics for this book that will provide the reader not only with a broad overview of current hot topics in materials chemistry, but also with specific examples of the special properties of these materials and some particular applications of interest.

Chapters 2-4 are concerned with metal nanoparticles, one of the most extensively investigated nanoscale materials since the origins of this area. Firstly, Katz, Shipway, and

* Luis M. Liz-Marzán, Departamento de Química Física, Universidade de Vigo, 36200, Vigo, Spain. Prashant V. Kamat, Radiation Laboratory, University of Notre Dame, Notre Dame, Indiana, 46556.

Willner extensively review the large amount of work that has been devoted to the synthesis, properties and applications of surface functionalized metal nanoparticles. Then, Toshima focuses in the third chapter on the catalytic activity of metallic and bimetallic nanoparticles, describing the role of the nanoparticle structure on activity. Finally, Hu and Hartland describe the electron dynamics within spherical and rod-like metal nanoparticles upon expoure to an electromagnetic radiation. Meisel also covers the interaction of electromagnetic radiation with nanoparticles, but in this case high-energy radiation is considered, and the nanoparticle nature is not necessarily metallic. The chapter by López-Quintela and co-workers is devoted to a particular method for nanoparticle synthesis, namely chemical reactions in microemulsions. The authors have tried to describe the mechanisms involved in this method using Monte-Carlo simulations, comparing their results with experimental observation. Two chapters on semiconductor quantum dots follow. Trindade describes basic concepts on the nature of this very special state of matter, and reviews various synthetic methods often used in the literature. The chapter by Guyot-Sionnest focuses on the manipulation of quantum dot optics by means of charge injection. The following two chapters deal with polymeric, nanoscale materials. Schaertl describes the behavior of nanoparticles of which the surface has been modified through the adsorption of polymer molecules, as well as their potential use as fillers within bulk polymers with tailored properties. On the other hand, Hellweg describes hydrogels, which display very interesting properties due to their very high and temperature-dependent porosity. In this chapter we also find a clear explanation of the basics of scattering methods for the characterization of nanoscale materials.

The following block of chapters (11-18) is mainly concerned with the organization of nanoscale building blocks for the preparation of nanostructured materials with interesting properties. Liz-Marzán tackles the coating approach to tailor interparticle separation within nanostructures. The particular system chosen here comprises gold nanoparticles homogeneously coated with silica shells, so that upon assembly the optical properties can be modulated in various ways. Tamil-Selvan also deals with the incorporation of nanoparticles within nanostructures, covering both metal and semiconductor nanoparticles. The chapter by Kotov and Liz-Marzán focuses on the now well-established layer-by-layer assembly method, which has proven very effective for the construction of uniform thin films using nanoparticles of various nature as building blocks. Another standard thin film construction technique is the Langmuir-Blodgett method, which provides an unrivaled degree of order within thin films. This method, as well as novel applications are described by Prieto, Martín and Camacho in chapter 14. Three chapters follow on different approaches to magnetic thin films. Hilgendorff and Giersig review the synthesis of magnetic colloids, and describe several ways to assemble them as thin films with novel properties. The approach presented by Perez et al. is also based on small magnetic nanoparticles, but they are created in the gas phase, which comprises a very different problem, and yields quite different materials. Finally, Farle describes continuous (rather than particulate), nanoscale thin films and carefully approaches the effect of several parameters on their optical properties. The final assembly chapter within this block is that by Imhof, dealing with another hot topic, namely photonic crystals. Since there are a number of approaches to construct these novel materials used to modulate the flow of light, which would be impossible to cover in a single chapter, Imhof reviews here properties and techniques for photonic crystals based only on colloid assembly.

The subsequent two chapters are related to nanoscale materials that are based in carbon. In chapter 19, Subramoney reviews the fundamental properties of carbon

nanotubes, several procedures for their synthesis, and selected applications that are currently on the way to the market. The chapter by Thomas and Kamat deals with fullerenes, and more specifically with their assembly to create novel nanostructured carbon systems.

Design and development of nanoscale materials is not just another step towards miniaturization. The physical, chemical, electrical and optical properties of these materials are size and shape dependent. They often exhibit important differences from the bulk properties that are not fully explained by current theories. The major challenge for the future is to exploit these unique properties and develop next generation nanodevices. The selected topics of nanoscale materials covered in this book should assist future scientists and engineers to achieve this goal.

This page intentionally left blank

2

CHEMICALLY FUNCTIONALIZED METAL NANOPARTICLES

Synthesis, Properties and Applications

Eugenii Katz, Andrew N. Shipway and Itamar Willner *

1. INTRODUCTION

Nanoparticles (particles of 1-100 nm in diameter) exhibit unique electronic, optical, photonic and catalytic properties[1-3] and are an ideal size for use as nanotechnological building blocks.[4] They may be composed of any substance, including metals,[5,6] semiconductors,[7,8] core-shell composite architectures,[9-11] and organic polymers.[12, 13] These particles often display properties intermediate between quantum and bulk materials because of their intermediate size[14,15] and large surface area-to-volume ratios.[16] Nanoparticles of different sizes and shapes exhibit different absorbance and fluorescence features and reveal polarization effects.[6,17,18] Microscopy techniques including high-resolution TEM, SEM, and scanning microscopy methods such as AFM, STM and NSOM can be employed to characterize their size, shape, crystal morphology and energy band gaps.[19-25] Ingenious methods for the preparation of nanoparticles have been reported during the last years. Nanoparticles represent metastable clusters exhibiting the fundamental property to aggregate. Thus, the stabilization of the nanoparticles against aggregation is a fundamental pre-requisite in nanoparticle science and technology. The stabilization of nanoparticles may be accomplished by the capping of the nanoparticles with weakly, electrostatically-bound ions (e.g. citrate stabilized Au or Ag particles),[5,26,27] by molecular ligands,[28,29] and the protection of the nanoparticles in polymer matrices,[30,31] or micellar assemblies.[32,33]

The association of ligands to growing nanoparticles can control the dimensions[34] and shapes of nanocrystals.[35] Nanoengineering of nanoparticle surfaces, eg. layer-by-layer deposition of organic modifiers, allows fine control of the shell size and structure.[36] The linkage of ligands to cation-rich nanocrystals may yield surface-states that could, for example, act as surface traps for excited electrons generated in the nanocrystal.[37,38] Such surface functionalities may then be used to link particles to surfaces or to inter-connect particles into extended nanoscale architectures and functional systems.[39-41] Specifically,

* Eugenii Katz, Andrew N. Shipway, Itamar Willner, Institute of Chemistry, The Hebrew University of Jerusalem, Jerusalem 91904, Israel.

the integration of chemical units of predesigned chemical functions such as recognition sites, redox groups, or chromophore units, may yield hybrid systems combining the unique features of nanoparticles with the tailored properties of the molecular or macromolecular coatings. Such integrated hybrid systems may yield new sensoric, photonic, and electronic devices.[42]

Tremendous scientific progress has been made in the past few years in the synthesis, characterization and functional design of chemically modified nanoparticles. This article will limit itself to the synthesis, characterization and application of chemically-functionalized metal nanoparticles. It will exclude recent advances in the synthesis and characterization of other nanoparticle materials (e.g. semiconductors or nanostructured polymers). Even in the area of functionalized metal nanoparticles, we are forced to exclude significant advances that include biomaterial-functionalized nanoparticles (e.g. DNA- or protein-modified metal nanoparticles), but this subject has been reviewed recently.[43,44]

2. SYNTHESIS AND PROPERTIES OF MONOLAYER CAPPED METAL NANOPARTICLES

Thiolate monolayers were assembled on different bulk surfaces such as Au, Ag or Pt.[45,46] The thiol monolayers are covalently linked to the surfaces by the reaction of the metal surfaces with the respective thiols and for some metals by the reaction with disulfides. For gold surfaces, two different mechanisms for the formation of the monolayers were experimentally supported,[45,46] as outlined in Eq. (1) and Eq. (2). As the upper gold surface includes an oxide sublayer, its reduction by the thiol was suggested as a path for the formation of the Au-thiolate bond, Eq. (1). Alternatively, hydrogen evolution by the Au-mediated reduction of the thiol protons could lead to the Au-thiolate bond, Eq. (2). The formation of the Au-thiolate bond in the presence of the disulfide is a redox process where the gold surface is oxidized by the disulfide and the disulfide bond is splitted, Eq. (3). The self-assembly and the organization of monolayers on flat surfaces has been studied in detail.[45,46]

$$Au_n\text{-}Au_2O + 2RSH \rightarrow Au_n(Au\text{-}SR)_2 + H_2O. \quad (1)$$

$$Au_n\text{-}Au_2 + 2RSH \rightarrow Au_n(Au\text{-}SR)_2 + H_2 \quad (2)$$

$$Au_n\text{-}(Au)_2 + R\text{-}S\text{-}S\text{-}R \rightarrow Au_n(Au\text{-}SR)_2 \quad (3)$$

It was found that the primary formation of the Au-thiolate monolayer is accompanied by the release of 40-45 $kcal \cdot mol^{-1}$. Subsequently, the monolayer reorganizes to a dense packing stabilized by van der Waals or π-interactions. For monolayers that include terminal groups capable of forming intermolecules, interaction of the monolayer is further reorganized to reach a minimum energy configuration. Different methods such as ellipsometry, surface plasmon resonance (SPR), microgravimetric quartz crystal microbalance, contact angle, XPS, FTIR, different scanning microscopy techniques, and electrochemical methods were applied to characterize these monolayers.[45,46]

Not surprisingly, thiols and disulfides were employed as capping reagents for the stabilization of different metal nanoparticles and for the surface derivatization of metal nanoparticles with molecular functionalities.

2.1. Functionalized Metal Nanoparticles in Organic Phases

The synthesis of metal nanoparticles covered with a hydrophobic monolayer of alkanethiols is usually performed in a two-phase system composed of aqueous and non-aqueous solutions. This method was introduced by Faraday, who reduced an aqueous gold salt with phosphorus in carbon disulfide, and obtained a ruby colored aqueous solution of dispersed gold particles.[5,47] Combining this two-phase approach with the modern techniques of ion extraction[48] and monolayer self-assembly with alkanethiols,[45,46] a one-step method for the preparation of monolayer-functionalized nanoparticles was developed by Schiffrin et al.[49,50] According to this method, $AuCl_4^-$ ions are transferred from an aqueous to a toluene solution using tetraoctylammonium bromide as the phase-transfer reagent. The gold is reduced with an aqueous solution of borohydride in the presence of dodecanethiol as a capping reagent, Eq. (4) and Eq.(5).

$$AuCl_{4\,(aq)}^- + N(C_8H_{17})_{4\,(toluene)}^+ \rightarrow N(C_8H_{17})_4^+AuCl_{4\,(toluene)}^- \quad (4)$$

$$mAuCl_{4\,(toluene)}^- + nC_{12}H_{25}SH_{(toluene)} + 3me^-_{(from\ aq.\ reductand)} \rightarrow 4mCl^-_{(aq.)} + (Au_m)(C_{12}H_{25}SH)_{n(toluene)} \quad (5)$$

Upon the addition of the reducing agent ($NaBH_4$) to the aqueous phase, the organic phase changes color from orange to deep brown within a few seconds. This color change indicates the formation of Au nanoparticles protected with a self-assembled thiol monolayer. High resolution Transmission Electron Microscopy (TEM) photographs of the nanoparticles (Figure 1) show that they have diameters in the range 1-3 nm and a maximum size distribution of 2.0-2.5 nm. Examination of the specimens at high resolution reveals a mixture of particle shapes with a preponderance of cuboctahedral and icosahedral structures.[51,52] In contrast with some other preparations of colloidal gold, twinned particles are rare. It is proposed that this could result from the conditions of growth employed, where the formation of a self-assembled thiol layer on the growing nuclei inhibits twinning. Alkanethiolate monolayer-functionalized Au-nanoparticles obtained by this method differ from conventional colloids[5] and nanoparticles prepared by other routes (micelle[34] and polymer stabilization,[32] gas-phase cluster formation,[53] stabilization with small organic ligands[26,28]) in that they can be repeatedly isolated from and redissolved in common organic solvents without irreversible aggregation or decomposition. This property, together with their the air stability, is difficult to overemphasize, since it allows for their handling and derivatization by standard synthetic methods, and gives considerable flexibility in their characterization. The method has the following advantages: (i) It leads to a simple way for the direct synthesis of surface-functionalized nanoparticles. (ii) Since the kinetics of the cluster growth is determined by the surface coverage, cluster size can be controlled by the reaction conditions and not by the metal ion reduction kinetics, as is usually the case in condensed-phase colloidal metal preparations. (iii) These new hydrophobic metal clusters are of intrinsic interest since in some respects, they behave like simple chemical compounds; they can be precipitated, redissolved and chromatographed without any apparent change in properties.

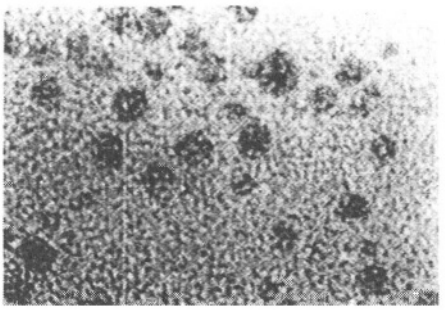

Figure 1. Transmission Electron Microscograph (TEM) of dodecanethiol-derivatized Au-nanoparticles.

Alkanethiols with various chain lengths (C_3 – C_{24})[54] and perfluorinated thiols[55-57] have been used in this procedure, yielding a variety of organic-phase soluble thiolate-capped metal nanoparticles. The perfluorinated alkane-functionalized Au nanoparticles were only soluble in fluorocarbon media.[56] Differential scanning calorimetry (DSC),[58,59] FTIR-spectroscopy,[54,59,60,62] small-angle X-ray scattering (SAXS),[58] and ^{3}H- and ^{13}C-NMR-spectroscopy[59-62] have been used to characterize structure and properties of thiolate-capping monolayers. Smaller chain lengths (C_3 – C_5) are relatively disordered, with large amounts of gauche defects present. The longer length alkanethiolates are predominantly in the all-trans zigzag configuration. However, even the long alkyl chains with a high degree of conformational order are not rigid, but instead undergo a dynamic process involving large-amplitude motion about the chain axes.[61] Molecular mobility increases towards the unbound ends, where there is a higher population of gauche conformers. Equilibrium structures and thermodynamic properties of dodecanethiol self-assembled monolayers on small (Au_{140}) and larger (Au_{1289}) gold nanocrystallites were investigated with the use of molecular dynamics simulations.[63] Compact passivating monolayers were theoretically predicted on the (111) and (100) facets of the nanocrystallites with adsorption site geometry differing from those found on extended flat Au(111) and Au(100) surfaces, as well as with higher packing densities.

Simple alkanethiol capping molecules provide good protecting properties for the metal cores, and allow reasonable solubility in non-polar organic solvents.[50] Although most studies have been performed with Au-capped nanoparticles, other nanoparticles (e.g. Pd, Pt, Ag) can also be prepared by the same method.[62,64,65] In addition, considerable modifications in regard to the protecting ligands are tolerated.[49] Arenethiol-protected Au nanoparticles have been prepared by Shiffrin's method using phenethyl mercaptan, benzylthiol, thiophenol, 4-thiocresol, and 2-naphthalenethiol.[66] The resulting arenethiol-functionalized Au nanoparticles have small cores of 2-3 nm less polydisperse than in the case of the usual alkanethiolate-shell. In order to introduce unique electronic properties, a thiol derivative containing a chromophore unit with a large dipole moment, $C_{22}H_{45}$-SO_2-C_6H_4-O-C_4H_8-SH, was applied for capping of Au nanoparticles.[67]

Although most studies were performed using thiol-derivatives for the functionalization of metal nanoparticles, disulfides offer several attractive properties.[68,69] First, the use of unsymmetrical disulfides having two distinct functional groups at the molecular termini (X-R-SS-R-Y) offers the possibility of generating mixed self-assembled monolayers possessing a homogeneous distribution of functional groups.

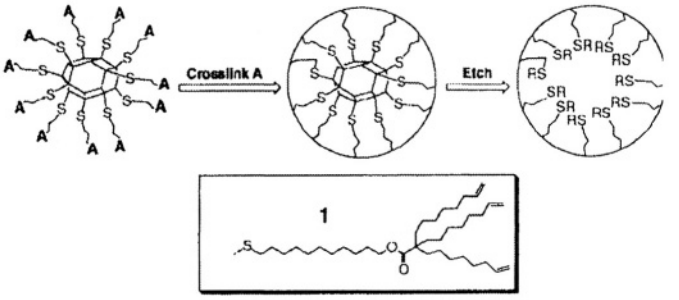

Figure 2. The production of polymer shells by the use of nanoparticle templates.

Studies of nanoparticles that have these multicomponent interfaces might, for example, permit the modeling of complex biological systems (e.g., cell-cell interactions). Second, the use of unsymmetrical disulfides possessing two distinct chain lengths (X-R-SS-R'-X) offers the possibility of generating nanoparticles designed with molecular "roughness". This might prove useful in manipulating the interactions between nanoparticles by controlling the degree of interdigitation of the molecular tail groups. Third, disulfides can be used to generate functionalized nanoparticles with terminal groups that are incompatible with thiol anchor groups. Thus, Shiffrin's method was extended to disulfides using n-octadecyl disulfide for the preparation of functionalized Au and Ag nanoparticles.[68] The resulting metal nanoparticles exhibited solubilities and size distributions that were comparable to those prepared by the adsorption of alkanethiols. Raman spectroscopy showed that the self-assembled monolayer is formed by the covalent attachment of the sulfur atoms of the disulfide to the surface of gold.[68] ^{13}C-NMR shows that the anchor group exists in the form of thiolate, R-S$^-$, and not of disulfide R-SS-R.[70] FTIR-spectra suggests that the alkyl chains are highly ordered in the region near the sulfur anchor-group.[68] The application of disulfide capping molecules with polymerizable moieties (**1**) allows the formation of polymer shells around Au nanoparticles upon intraparticle polymerization.[71] Further etching of the Au cores results in the formation of nanosize polymer capsules with small size dispersion, Figure 2.

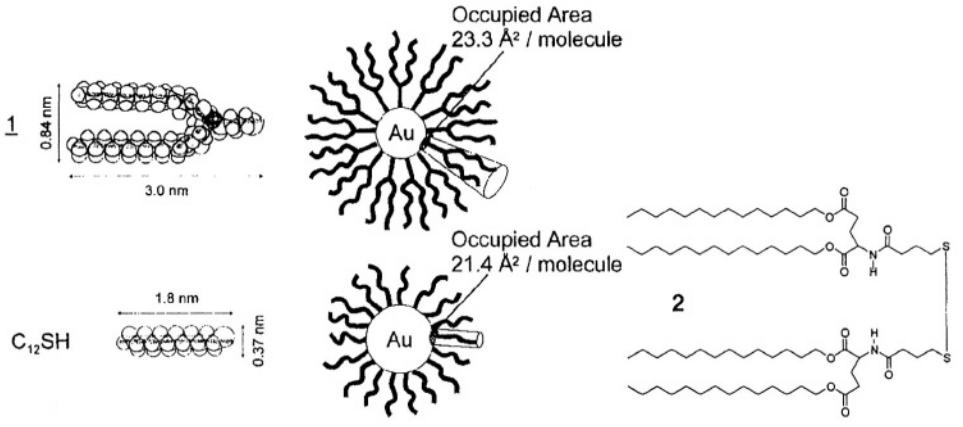

Figure 3. Schematic illustration of stabilizing structure of **2**- and $C_{12}SH$-stabilzied gold nanoparticles.

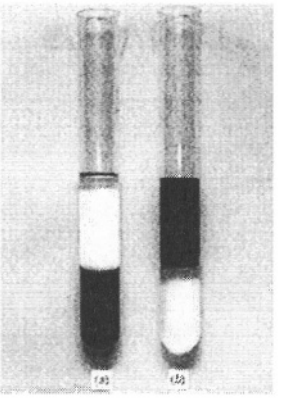

Figure 4. Immiscible layers of (a) the gold hydrosol (at the bottom) and the clean toluene solution containing the thiol (on top). (b) Thiol-derivatized Au sol in toluene (on top) and the clean acidified aqueous solution at the bottom.

Size control of Au nanoparticles by tuning the molecular cross section of capping disulfides was also attempted.[69] The use of a four-chained disulfide ligand (**2**) resulted in smaller and monodispersed gold nanoparticles compared to Au nanoparticles capped with a conventional single chain alkanethiol, Figure 3.

A different approach to the formation of thiol-derivatized nanoparticles of Au, Pt and Ag (diameter 1-10 nm) included the acid-facilitated transfer of hydrosol particles to a toluene layer containing a thiol.[65] The nanoparticles were produced by chemical reduction of the respective salts and stabilized in the aqueous solution at a high pH value. When an organic layer containing a capping thiol was added and the aqueous solution was acidified, the nanoparticles were destabilized in the aqueous solution and moved to the organic layer, yielding thiolate-functionalized metal nanoparticles in the organic phase, Figure 4.

Au nanoparticles have also been functionalized with chalcogenide (Se, Te) alkane derivatives.[72] Alkaneselenide and alkanetelluride functionalized Au nanoparticles can be prepared by methods similar to those used for preparation of alkanethiolate-functionalized Au nanoparticles. However, the electron orbitals are extended on Se and Te relative to S, thus it should lead to a significant change in electronic coupling between the ligand and the gold core. Likewise, the change in binding energy will lead to differences between Se, Te, and Au, both with regard to exchange reactions and ligand shell mobility, allowing increased tuneability of the system for particular purposes.

2.2. Functionalized Metal Nanoparticles in Aqueous Systems

While alkanethiolate self-assembled monolayers are nonpolar and the metal nanoparticles capped with them are usually produced in two-phase immiscible liquid-liquid systems, highly polar ligands can yield water-soluble metal nanoparticles that can be obtained directly in an aqueous phase.[73] An aqueous solution of a metal salt (e.g. $AuCl_4^-$ in case of formation of Au nanoparticles) was reacted with a reductant (e.g. $NaBH_4$) in the presence of a water-soluble bifunctional thiol yielding thiolate-capped Au nanoparticles directly in the aqueous solution, Eq. (6). Thiol-capping molecules used in this procedure have a polar functional group providing their solubility in an aqueous

solution (hydroxyl,[55,73-75] carboxylic,[55,74,76,77] amino,[74,78] sulfonic,[79] boronic acid,[55] phosphonic acid,[55] thioheterocycles[80]). Multifunctional molecules (i.e. tiopronin[81,82]) including bioorganic compounds such as cysteine,[83] glutathione,[84,85] and coenzyme A[81] were also used in this procedure as the water-soluble capping material.

$$mAuCl_4^- + nX\text{-}R\text{-}SH + 3me^-_{(\text{from reductand})} \rightarrow 4mCl^- + (Au_m)(X\text{-}R\text{-}SH)_n \quad (6)$$

where R is an aliphatic or aromatic spacer and X is a polar group, i.e. OH, NH_2, CO_2H, SO_3H, PO_3H_2, BO_2H_2.

The presence of the ligand and its attachment to the Au nanoparticles via the formation of a thiolate bond was established using FTIR spectroscopy.[74] Sulfur-containing heterocycles could demonstrate various molecular orientations on the surfaces of different metal nanoparticles. For example, surface-enhanced Raman spectroscopy (SERS) showed that the capping molecules of 2-mercaptobenzothiazole adsorb with their molecular plane flat on Ag and perpendicular on Au nanoparticles.[80] The process could include the *in situ* formation of the thiol-anchor group upon reduction of thiosulfate salt (Bunte salt),[79] Figure 5. Stability of the functionalized-metal nanoparticles in a water solution, provided by hydrophilic moieties at the capping layer, strongly depends on the extent of their hydrophilicity and the charge state of the functional groups. Charging properties of the functionalized metal nanoparticles were characterized by measuring their ξ-potentials (–45.3 mV for carboxylic-derivatized Au nanoparticles).[76]

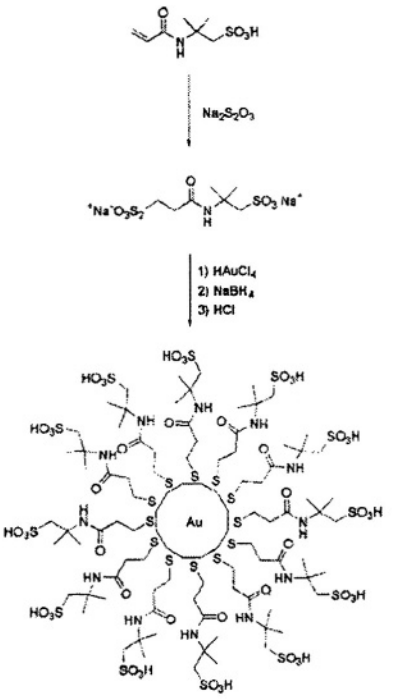

Figure 5. Synthesis of water-soluble Au nanoparticles using Bunte salt of 2-acrylamido-2-methyl-1-propanesulfonic acid.

The charge of the dissociated head groups is pH dependent, allowing control on the solubility of the nanoparticles. For example, nanoparticles functionalized with amino groups are soluble in acidic solutions, whereas carboxylic units provide solubility in basic solutions. When pH change results in neutralization of the functional groups of the shell layer, the nanoparticles loose the solubility and start to coagulate, precipitate or adsorb at solid supports.[86] Nanoparticles functionalized with sulfonic acid units are well soluble in a broad pH range. Dissociation of the functional groups at the nanoparticle surfaces is quite similar to that in planar self-assembled monolayers,[87,88] however, hydrogen bonding between the nearest groups was found to be less efficient for the functionalized nanoparticles than for planar monolayers, probably because of longer distances between them at curved surfaces.[75] The dissociation of the functionalized metal nanoparticles was studied by measurements of the contact angle at a solid support covered with the nanoparticles,[75] Figure 6(A). The increase of pH value results in dissociation of the carboxylic groups at the particle surfaces ($pK \approx 6.8$), thus resulting in the increase of the surface hydrophilicity, and therefore the decrease of the advancing contact angle for a drop of water. Nanoparticles functionalized with CO_2H and NH_2 units demonstrate a propensity for H-bond formation, leading to particle-particle, particle-solvent, and particle-water vapor interactions,[76,89] Figure 7. These interactions result in significant aggregation and 3-D growth.[74] The interparticle H-bonding and their aggregation also show pH dependent character. Titration of carboxylate-functionalized Au nanoparticles with NaOH produced an increase ($pK \approx 8.1$) in the intensity of the plasmon band at 550 nm, Figure 6(B). This behavior was attributed to the conversion of CO_2H groups, that provide effective H-bonding and aggregation, to $CO_2^-Na^+$ groups that provide repulsion and dissociation of the particle aggregates. The values of pK corresponding to the transitions in the titration curves, Figures 6(A) and 6(B), are significantly higher than the pK value of benzoic acid in solution ($pK_{benzoic\ acid} = 4.8$), however, this pK shift is typical for polyelectrolytes and it has already been observed for carboxylic acid-derivatized planar self-assembled monolayers.[90] Intrashell-hydrogen bonding could result in the increased particle stability, including the metal core stability against chemical etching.[91]

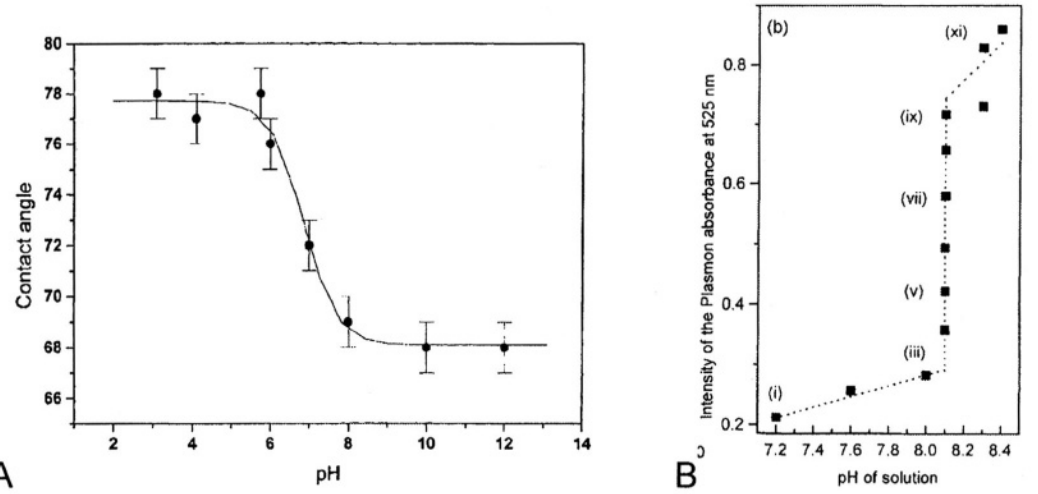

Figure 6. (A) Dependence of advancing contact angles on water drop pH for 4-carboxythiophenol-functionalized Au nanoparticles on a Au support. (B) Variation of the plasmon absorbance at $\lambda = 525$ nm.

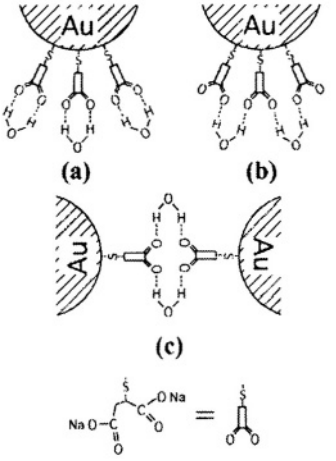

Figure 7. Interparticle and particle-solvent interactions in carboxylic acid-functionalized nanoparticles.

Amphoteric capping molecules that have basic NH_2/NH_3^+ groups and acidic CO_2H/CO_2^- groups in addition to the thiol anchor groups (e.g. cysteine) provide very efficient aggregation of the functional nanoparticles due to H-bonding and electrostatic attraction,[83] Figure 8(A). This aggregation process is temperature-dependent and the particles can dissociate upon increase of the temperature resulting in the absorbance decrease at 550 nm, Figure 8(B). However, this process is reversible and a temperature decrease results in re-association of the functionalized nanoparticles.

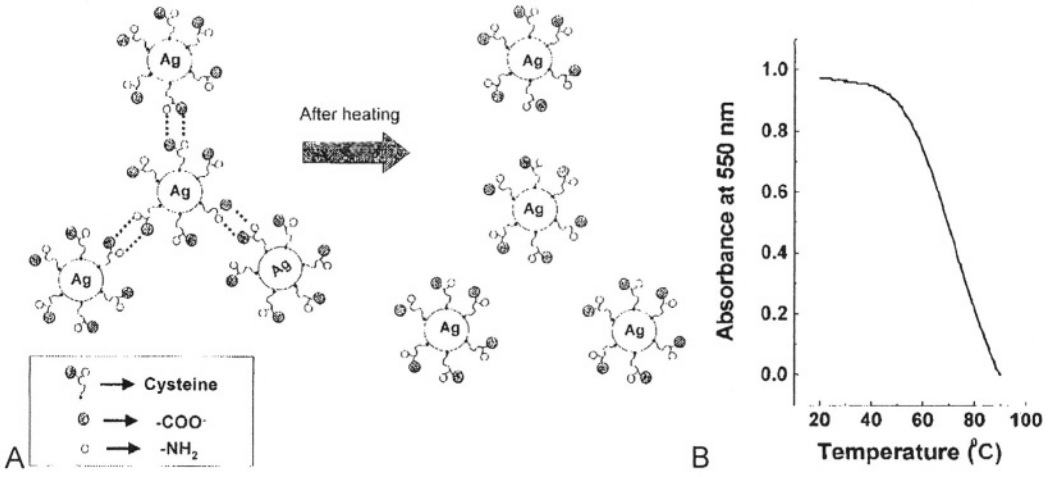

Figure 8. (A) Schematic diagram showing interparticle aggregation and its loss at heating. (B) Absorbance of a solution of cysteine-capped silver colloidal solution at 550 nm as a function of temperature.

2.3. Chemical Reactivities of Functionalized Metal Nanoparticles and their Stepwise Modifications

Understanding chemical reactivities of functionalized metallic nanoparticles and developing efficient strategies to functionalize them is key to their application in areas such as catalysis and chemical sensing. Towards this aim, ligand place-exchange,[92-94] nucleophilic substitutions[95] and ester and amide couplings[73,96,97] were studied.

It has been shown that thiol-monolayers self-assembled on bulk Au electrodes can be exchanged with other thiols.[98-100] This reaction can also be performed at metal nanoparticle surfaces, thus resulting in the formation of a capping layer that cannot be directly formed upon formation of the nanoparticles,[92] Eq. (7). Partial substitution of the primary capping molecules leads to a mixed monolayer shell structure.

$$nR'SH + Au(RS^-)_n \rightarrow nRSH + Au(R'S^-)_n \quad (7)$$

The reactions were characterized by ^{1}H-NMR and IR spectroscopy, and the dispersity of place-exchange reaction products was inspected by chromatography.[92] The results of these experiments show that ligand exchange is an associative reaction and that the displaced thiolate is found in solution. Disulfides and oxidized sulfer species are not involved in the reaction.

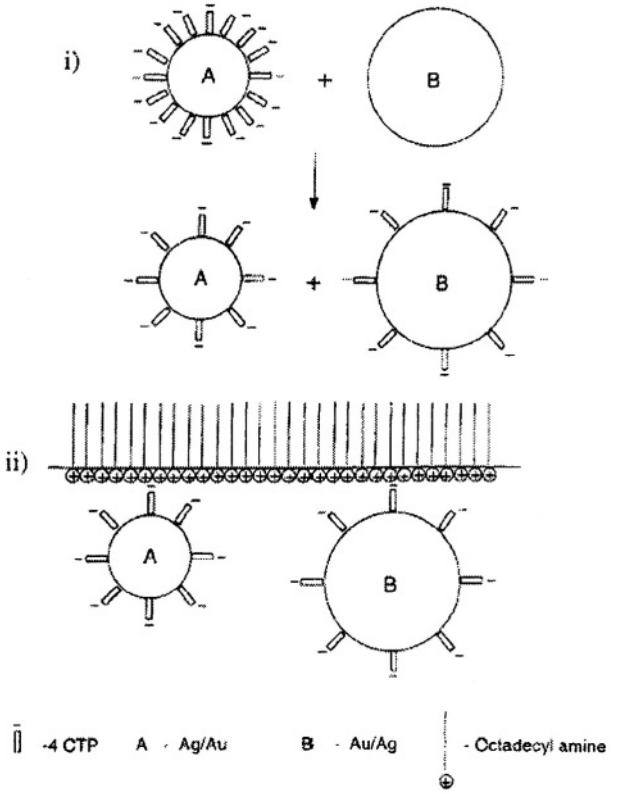

Figure 9. (i) The transfer of 4-CTP between nanoparticles by mixing (ii) The electrostatic complexation of nanoparticles A and B with a Langmuir-Blodgett film of octadecylamine as a consequence of 4-CTP transfer.

Nanoparticle-bound thiolate ligands differ widely in susceptibility to place-exchange, presumably owing to differences in binding sites. Au core edge and vertex sites are presumably more reactive than terrace sites. The rate of place-exchange decreases as the chain length and/or steric bulk of the initial protecting ligand shell is increased. Positive charges electrochemically placed on the thiolate-functionalized Au nanoparticles make the bounding of the sulfur-anchor group weaker, and thus enhance exchange reactions.[101] Thiolate-capping molecules can move from one metallic nanoparticle to another one that has a bare unprotected surface.[102] This was shown by mixing negatively charged 4-carboxythiophenol (4-CTP)-functionalized Au nanoparticles with bare Ag nanoparticles. After the interparticle thiolate-transfer reaction, both particles were functionalized with the same, but diluted capping monolayer that has been demonstrated by their electrostatic attraction to positively charged Langmuir-Blodgett monolayer, Figure 9. Transfer from the functionalized Ag nanoparticles to bare Au nanoparticles was also possible. Functional groups on the outermost portion of the monolayer-functionalized nanoparticles can undergo many synthetic transformations. Covalent binding of a secondary modifier to functional groups of the primary capping molecules is a powerful technique that allows the synthesis of very complex structures. For example, p-mercaptophenol-capped Au nanoparticles were esterificated using propionic anhydride,[73,97] Figure 10(A). Even more complex structures were obtained when Au nanoparticles functionalized with tiopronin capping molecules were covalently modified with *N*-methyl-*N*'-ethylamine-4,4'-bipyridinium by the amide bond formation between the carboxylic group of tiopronin and the amino group of the secondary modifier.[82] Steric effects in the reactivity of mixed functionalized Au nanoparticles with S_N2 reactions were studied.[95] Nanoparticles functionalized with monolayers terminated with a Br-atom were reacted with amines, Figure 10(B). The rate of the S_N2 reactions were found to be dependent on the steric bulk of the incoming nucleophile (rates of n-propylamine > isopropylamine > tert-butylamine) and on the relative chain lengths of ω-bromoalkanethiolate and surrounding alkanethiolate chains (rates of $C_{12}/C_{12}Br$ > C_{12}/C_8Br > C_{12}/C_3Br). It is surprising that even in the system C_{12}/C_3Br where the active Br-atom is deeply screened by the surrounding C_{12}-alkanethiolate chains, the reaction proceeds with an observable rate. This dramatically differs from a 2D-self-assembled monolayer at a planar Au support, where the similar reaction is fully blocked. The higher chemical activity of the monolayer at the nanoparticle surface originates from the curved surface, which allows flexibility of the chains and allows access to the active sites of the ligands.

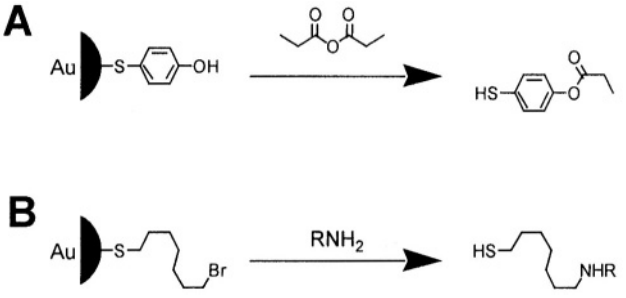

Figure 10. Some reactions of monolayer-protected nanoparticles.

3. SYNTHESIS AND PROPERTIES OF POLYMER-CAPPED METAL NANOPARTICLES

Polymers are often used as stabilizing matrices for nanoparticles and the nanoparticle-polymer composite materials have been extensively reviewed.[103-105] Most polymers are easily processable and a transparent, permeable, or conductive material can be chosen, as required for specific applications. Numerous methods for preparation of nanoparticle-polymer composites have been developed. Polymer-metal nanoparticle composites have been synthesized by the condensation of metal vapors into liquid monomers, followed later by polymerization,[106,107] by reduction of metal complexes in solution where the solvent also acts as a polymerizable ligand,[108] by emulsion polymerization in the presence of nanoparticles,[109] and by electrosynthesis at liquid-liquid interfaces.[110] Supercritical CO_2 solutions have also been used to load bulk polymer films with metal salts and to reduce these salts to metal nanoclusters by chemical post-treatment.[111] Au nanoparticles were produced inside growing polyaniline using H_2O_2 as a reducing agent for $AuCl_4^-$ and an oxidizing agent for aniline.[112] Insoluble crosslinked polymers (resins) are often used as matrices for metallic nanoparticles used as catalysts.[113] In the frame of the present review we will discuss chemical methods based on complex formation between a polymer shell and a metallic core.

Functional groups of a capping polymer molecule can provide strong interaction with metallic cores included into the polymer matrix. For example, poly(vinylpyrrolidone)[114] and poly(dithiafulvene)[115] are polymers capable of complexing and stabilizing metal nanoparticles. A more general method for the synthesis of different metal nanoparticles (Ag, Au, Cu, Ni, Pb, Pd and Pt) using diblock copolymers has also been developed.[104, 116] Diblock copolymers, owing to their ability to form microdomains and to associate in solution in the form of micelles, can provide small compartments inside which particles of a finite size can be generated and stabilized. Metal ions or complexes are coordinated to carboxylic acid groups within the hydrophilic blocks of a diblock copolymer by immersion of the polymer in an aqueous metal salt solution. The metal ions or complexes are subsequently reduced by exposure to hydrogen at elevated temperatures or by immersion in an aqueous sodium borohydride solution. This approach leads to uniformly sized nanoclusters homogeneously dispersed within the water-soluble domains of the diblock copolymers, and the length of the hydrophilic domains controls the size of the resulting nanoparticles.[117-120] Additional conductive polymeric shells capping the metal cores could be introduced inside the diblock copolymer matrices. For example, polypyrrole-coated Au nanoparticles were synthesized within the microdomains of a diblock copolymer, providing an excellent means for the formation of such dispersions.[121,122] Polystyrene-*block*-poly(2-vinylpyridine) (PS-b-P2VP), taken in toluene solution (0.5% w/w) was treated with $HAuCl_4$ (0.5 to 2VP units) which got selectively bound within the P2VP cores of the micelles. This solution was treated with pyrrole so that it diffused into the core of the micelles where polymerization was readily effected by $HAuCl_4$, with the simultaneous generation of Au nanoparticles and an *in situ* formation of polypyrrole-Au nanocomposite. The diblock supplied the core within which the composite was formed and stabilization could thereby take place. Au nanoparticles (7-9 nm), surrounded by the shell of polypyrrole (24 nm) within the core of micelle of the PS-b-P2VP copolymer were finally obtained.

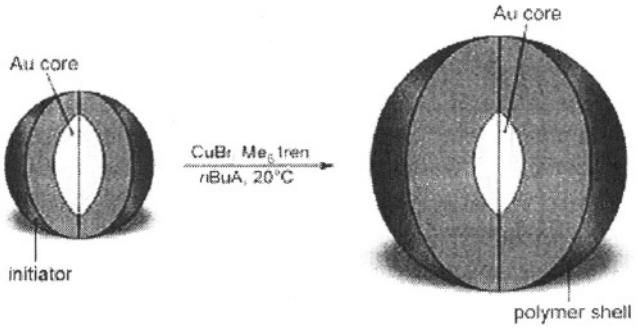

Figure 11. The construction of a polymer shell around an Au-nanoparticle (nBuA=n-butylacrylate).

Thiol anchor groups have been applied in several different approaches to provide efficient binding of polymeric shells to metallic nanoparticles. The methods include nanoparticle capping with polymers containing thiol groups, or primary formation of a thiol-monolayer functionalized nanoparticles followed by stepwise assembly of a secondary polymer shell bound to the primary thiol via covalent or non-covalent (e.g. electrostatic) modes. For example, a preformed polymer containing thiol anchor groups, α-methoxy-ω-mercapto-poly(ethylene glycol), was employed to enhance the binding of a polymeric shell layer to a Au core surface.[123] A thiolated polymer layer bound to a Au core could be further covalently modified by reactiong its other functional groups with bifunctional linkers.[124] Au nanoparticles capped with a thiol with α-bromoester moiety capable of initiating atom transfer radical polymerization were used to enlarge the primary thiol shell by the formation of a polymeric layer.[125,126] The functionalized Au nanoparticles were reacted with n-butylacrylamide in the presence of $Cu^{I}Br/Me_6tren$ (Me_6tren = tris(2-dimethylaminoethyl)amine) catalyst, yielding a growing polymeric shell covalently bound to the primary thiol with a diameter depending on the monomer concentration and polymerization time, Figure 11. Very small, uniform Au nanoparticles (diameter less than 5 nm) capped with a functionalized siloxane shell were obtained by reduction of $AuCl_4^-$ with $NaBH_4$ in ethanolic solution containing (γ-mercaptopropyl) trimethoxysilane (MPS), followed by reaction with (γ-aminopropyl)trimethoxysilane and crosslinking of the silane layer,[127] Figure 12. A cage-like silane structure is formed around the Au core and functional amine groups are put at the nanoparticle shell periphery. Finally, the silane molecules forming the shell structure are crosslinked, resulting in a rigid siloxane layer with amine functional groups at the surface.

A versatile method based on the non-covalent binding of the primay thiolate shell and secondary polymer shell includes the primary adsorption of thiols functionalized with a charged head group (e.g. 10-mercaptodecanesulfonate) at a Au core surface followed by layer-by-layer deposition of polyelectrolytes holding opposite charges (e.g. poly(diallyldimethylammonium chloride and poly(styrenesulfonate)),[128] Figure 13. The multilayer shell diameter depends on the number of the polymer layers and the last polymeric layer exposed to the liquid phase determines the charge of the nanoparticle. Thus, the method allows tuning of the shell size and controlling its charge by simple variation of the building steps.

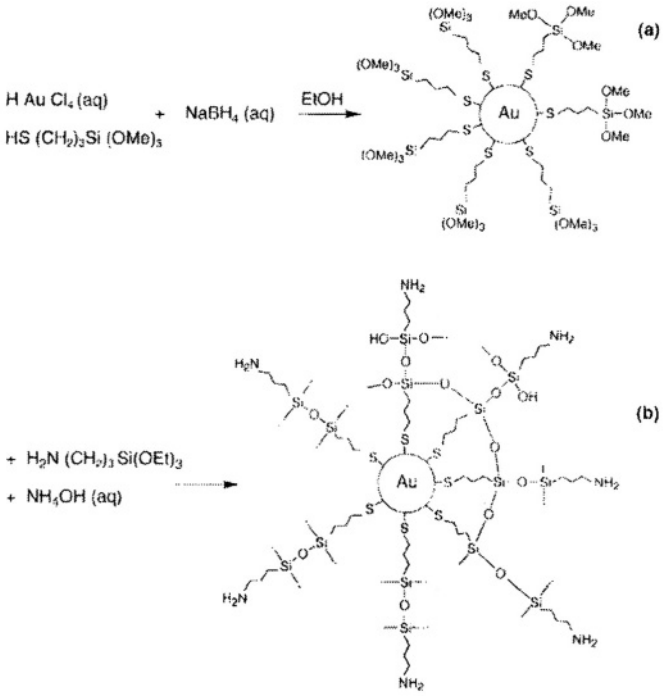

Figure 12. (a) Formation of MPS-stabilized gold nanoparticles by the reduction of $HAuCl_4$-MPS (b) The formation of a silane shell around the nanoparticles

Several noble metal nanoparticles have been prepared in the presence of dendrimers in aqueous solution or organic solvents.[129-142] When metal ions are chemically reduced in the presence of dendrimers, individual metal nanoparticles are surrounded by small dendrimers, or alternatively, several metal nanoparticles can be encapsulated by large size dendrimers, Figure 14.

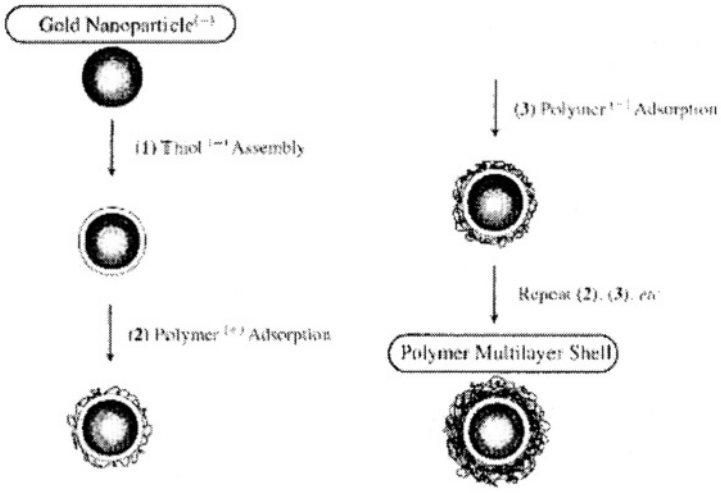

Figure 13. Schematic diagram of layer-by-layer polymer deposition on Au-nanoparticles.

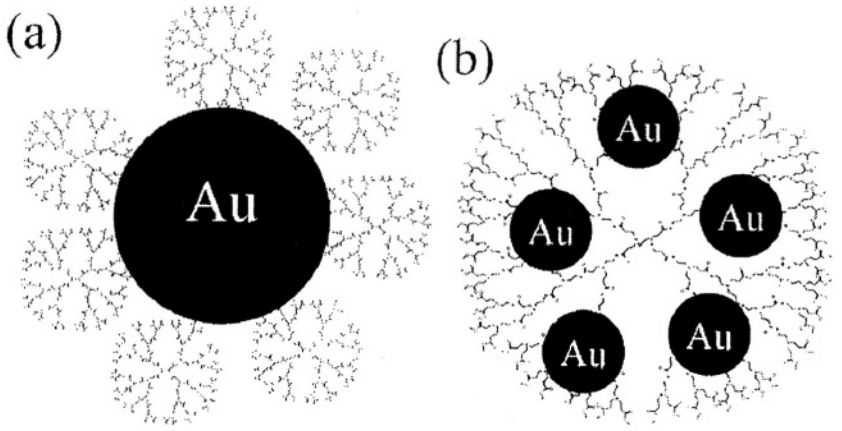

Figure 14. Nanoparticle-dendrimer nanocomposite structures: (a) a gold nanoparticle surrounded by a low generation of dendrimer; (b) dendrimer-encapsulated gold nanoparticles.

Whether a dendrimer functions as a capping material or allows encapsulation of nanoparticles inside its volume depends on the size of the dendrimer and on the interactions between metal ions and functional groups of the dendrimer. For example, in aqueous solutions poly(amidoamine) (PAMAM) dendrimers with surface hydroxyl groups provide dendrimer-encapsulated noble metal nanoparticles,[132,133,135] while PAMAM dendrimers with surface amino groups act as stabilizers by capping the surface of noble metal nanoparticles.[130, 137] When the surface functional groups of the dendrimer do not provide efficient binding to the metallic surface, the nanoparticles grow inside the dendrimer's structure if its size is sufficient. In order to provide bulk polymeric support for the dendrimer-encapsulated metallic nanoparticles, positively charged poly-(amidoamine) dendrimers were electrostatically entrapped into a negatively charged poly(2-hydroxyethyl methacrylate) network.[141] Then the dendrimer units were saturated with metal ions that were further chemically reduced to yield metal nanoparticles inside the dendrimer molecules distributed within the polymeric network.

4. CONTROLLING THE SIZE AND COMPOSITION OF THE METALLIC CORES OF NANOPARTICLES

The ability to selectively synthesize metal nanoparticles of any desired size or shape would generate significant opportunities in chemistry, because catalytic, optical, magnetic, and electronic activities are dimensionally sensitive.[143-146] Very small clusters (< 50 metal atoms) act like large molecules, whereas large ones (> 300 metal atoms) exhibit characteristics of bulk samples of those atoms. Between these extremes lie materials with intermediate chemical and physical properties that are unique, but largely unknown. As an example, the optical properties of a metal cluster, including the intensity and energy of its surface plasmon bands, strongly correlate to its size.[147-150] Schiffrin's method allowed preparation of Au nanoparticles of variable size (average diameter from 1.5 nm to 5.2 nm),[151] thus providing a unique opportunity to synthesize nanoparticles with tailored properties.

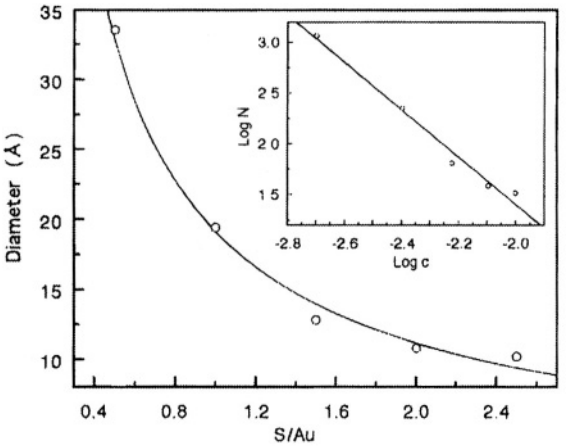

Figure 15. Relationship between nanoparticle diameter and the initial S/Au molar ratios during Au nanoparticle preparation. The inset shows a double-logarithmic plot of the number of atoms in a Au particle vs. the concentration of mercaptosuccinic acid.

The ratio between the capping thiol molecules and metal nanoparticles controls the size of the resulting functionalized nanoparticles.[62,64,76,152] Figure 15 exemplifies the relationship between the diameter of carboxylic-functionalized Au nanoparticles and the molar ration between mercaptosuccinic acid and Au precursor salt. The increase of this ratio results in the inhibition of the particle growth and thus results in their smaller diameter. The sizes of the thiol monolayer-functionalized Au nanoparticles were measured, with generally good agreement, by scanning tunneling microscopy (STM),[58] atomic force microscopy (AFM),[58] transmission electron microscopy (TEM),[49,151,153] small-angle X-ray scattering (SAXS),[58,151] laser desorption-ionization mass spectrometry (LDI-MS)[153] and X-ray diffraction (XRD).[151,154]

Knowing and controlling the dispersity of core size is also important. Figure 16 illustrates the use of LDI-MS[153] to track the solubility-fractionation of core sizes of dodecanethiolate-functionalized Au nanoparticles, conducted in concert with theoretical modeling to predict the core size and shape of isolated fractions. The number of atoms per nanoparticle tends toward closed shell structures ("magic numbers") with an equilibrium truncated octahedral shape. However, since the synthesis of the thiol-functionalized nanoparticles (Eqs. (4)-(5)) is based on competing core growth-passivation kinetics, the occurrence of non-equilibrium core shapes cannot be discounted. The size of polymer-capped metallic nanoparticles could also be controlled by changing relative concentration of the polymer, its molecular weight, and the metal reduction conditions.[155,156] For example, the preparation of Pd nanoparticles capped with polyvinylpyrrolidone (PVP) with sizes varying from 1.5 to 15 nm with relative standard deviation of < 0.5 depending on synthetic procedure was reported.[155]

Various shapes of functionalized-metal nanoparticles (e.g. triangular, hexagonal, pentagonal, square and rhombohedral nanocrystals of polymer-capped Pd[157]) as well as the extent of their aggregation resulting in different particle assemblies[158] have also been achieved by controlling the metal atom/capping molecules ratio during the reductive particles formation.

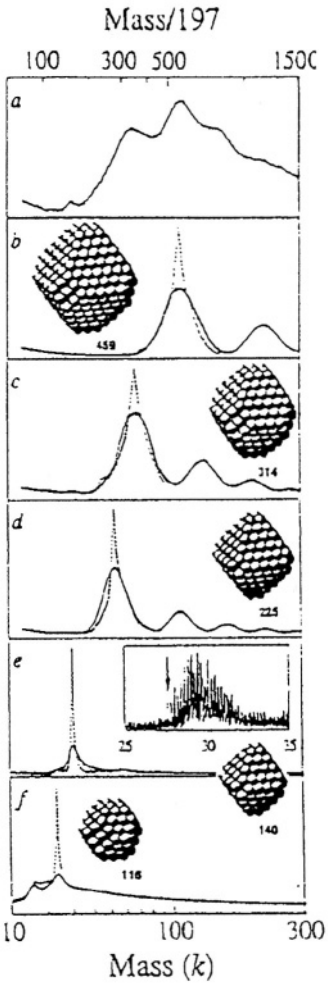

Figure 16. Laser desorption-ionization (LDI) mass spectra of: (a) Dodecanethiolate-functionalized Au nanoparticle mixture. (b-e) Au nanoparticle fractions. (f) A mixture of the two lightest fractions. Inset: high-resolution mass spectrum (arrow marks the first peak at 27,609±2 amu).

The rate of the reductive formation of the functionalized metallic nanoparticles, controlled by the reductant chemical properties, can affect the resulting shape of the obtained capped nanocrystals. For example, a slow reduction of $PtCl_6^{2-}$ by H_2 in the presence of capping polyacrylic acid results in the formation of tetrahedral Pt nanoparticles, whereas its fast reduction by methanol mainly results in truncated octahedral Pt nanoparticles.[159]

Metals different from gold, such as Ag, Pt, pd[62,64,65,160] and various alloys (Au/Ag, Au/Cu, Au/Ag/Cu, Au/Pt, Au/Pd, and Au/Ag/Cu/Pd[161]) have been applied successfully for the synthesis of monolayer-covered nanoparticles. Alloy nanoparticles can provide particularly broad applications because they exhibit electronic,[162-164] optical,[165-171] and catalytic[172,173] properties that are controllable by the alloy composition. For example, Figure 17 shows spectral properties of the thiol monolayer-functionalized alloy nanoparticles dependent on the ratio of the metallic components.[161] Small variation of the (Au:Ag) ratio as well as addition of Cu results in changes in the spectrum.

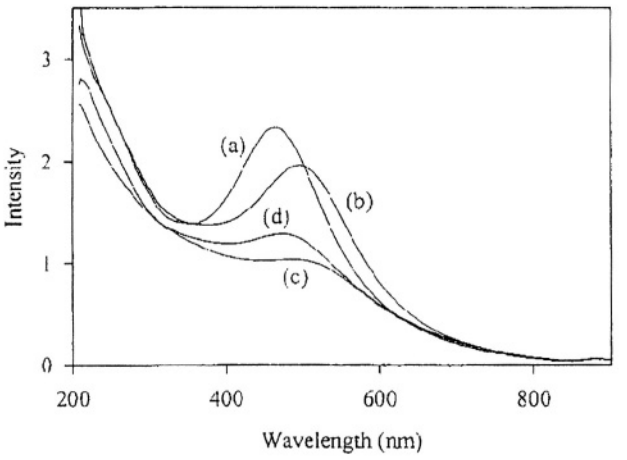

Figure 17. UV/Vis spectra of dodecanethiolate-functionalized alloy nanoparticles: (a) $AuAg_{2.5}$ (468 nm), (b) $AuAg_{1.4}$ (504 nm), (c) $AuAg_{0.4}$ (518 nm), (d) $AuAg_{0.9}Cu_{0.4}$ (488 nm).

TEM showed that Au/Pd cores are small and relatively monodisperse (1.7 nm average, ca. 20% dispersion), while most Au/Ag cores are larger (3.2 nm). Other alloy cores were of intermediate size. Elemental and XPS analyses showed that overall thiol-functionalized alloy core nanoparticles have metal ratios dependent on but different to the original salt composition, and that incorporation of the more noble metal into the core is favored. Galvanic effects may be in part responsible for the differential incorporation; for example, in Ag/Cu mixtures the Cu core content could be depressed by Cu^0 acting as an ancillary reductant of Ag^+, which leaches Cu^0 from the nascent core.

Dielectric core – metallic shell composite nanoparticles (e.g. silica core and Au or Ag shell) have been prepared and capped with self-assembled monolayers or polymers.[174,175] The resulting composite nanoparticles show unique optical and photophysical properties. A main characteristic of dielectric spheres with continuous metallic coatings is that their optical plasmon absorption consists of several modes, generally dipole and quadrupole, with peak positions dependant on the dielectric core diameter to metallic shell thickness ratio. Further organic capping layers provide solubility and stability.

5. CATALYTIC, ELECTROCHEMICAL AND PHOTOCHEMICAL PROPERTIES OF FUNCTIONALIZED METAL NANOPARTICLES

The controlled sizes and shapes of chemically-modified metal nanoparticles are anticipated to yield unique catalytic, electrochemical and photochemical functionalities as a result of the hybrid structures of the nanoassemblies. The high surface-area of nanoparticles and the control of the edge-step ratio by the particle morphology, is expected to yield effective heterogeneous catalysts differing from bulk heterogeneous metal catalysts. Furthermore, the molecular functionalization of the nanoparticles, e.g. with chiral molecules, might generate unique nanoenvironments for stereoselective synthesis. The electrochemical properties of monolayer-functionalized metal nanoparticles are expected to be controlled by the particle sizes. As the capacitance of

nanoparticles is controlled by their sizes, charging effects dominated by the particle dimensions are expected to lead to intermolecular interactions of redox species and to electron transfer properties that differ from the electrochemistry in solution. The discrete electronic levels existing in metal nanoparticlels, and the control of the energy levels of this electronic state by the particle dimensions, may lead to important photochemical functionalities of chromophore-capped metal nanoparticles. Photoinduced electron transfer in chromophore-functionalized metallic nanoparticles is envisaged to proceed in analogy to molecular dyads, and the intra-hybrid quenching rate constants should be controlled by the nanoparticle dimensions and the distance separating the chromophore and the metal particle.

5.1. Catalytic Properties of Functionalized Metal Nanoparticles

Catalytic properties of metallic nanoparticles have been known for decades, and they have been reviewed, particularly for nanoparticles included into vesicles of surfactants and water-soluble polymers,[1] and nanoparticles included into insoluble polymers, resins.[2] The long list of reactions catalyzed by functionalized metallic nanoparticles (mainly Rh, Pd, Pt, Ir, Os, Au) includes isomerizations, reductions of multiple bonds (C=C, C=O, N=O), hydroformylation, Fischer-Tropsch synthesis, cleavage of carboxylic acid ester groups,[176] and the reduction of O_2 and NO_3^-.[1, 2] The unique catalytic properties of nanosized materials and their differences from the catalytic properties of the bulk materials are acknowledged.[177] For example, although gold is a poor catalyst in the bulk form, the high catalytic activity of Au nanoparticles has led to inspiration for exploring nanoscale gold catalysis.[178] A typical example is CO oxidation. The achievement of highly active catalysts for this reaction has been shown to require Au nanoparticles less than 5 nm, and a fortunate combination of factors and conditions.[179] However, most of the studied systems deal with catalytic nanoparticles included into polymer matrices and then immobilized on solid supports.[180,181] New methods for the incorporation of catalytic nanoparticles into polymeric matrices have been developed. Self-assembly of thiol-functionalized metal nanoparticles at a polymer-template due to electrostatic interactions allows formation of stable catalytic aggregates of desired size and shape.[182] Alternating adsorption of polyethyleneimine-metal ions, Ag^+ or Pt^{2+}, complexes and polyanions (e.g. polyacrylic acid) results in the formation of multilayered polyelectrolyte films.[183] Postdeposition reduction of the metal ions by heating or exposure to $NaBH_4$ then yields composite films containing catalytically active Ag or Pt nanoparticles. More versatile electrochemical reduction of metal ions included into a polyelectrolyte layer at an electrode surface yields metallic species of various sizes and properties.[184] Less attention was paid to homogeneous catalysis provided by soluble polymer-protected nanoparticles[185] and dendrimer-encapsulated nanoparticles,[186] polymer-microcapsules-entrapped nanoparticles,[187] including those that operate under extreme conditions, e.g. in supercritical fluids.[188]

Novel monolayer-functionalized metal nanoparticles could provide a unique opportunity for highly efficient catalyses with precisely tunable activity and selectivity. Weak temporary association of selected species with functionalized nanoparticles could provide their increased local concentration and thus enhanced reactivity at the particle surfaces. This effect could be used to develop nanosized catalytic centers with selective activity. The shell-structure of the functionalized nanoparticles could also provide a favorable environment for a specific chemical route, resulting in selectivity.

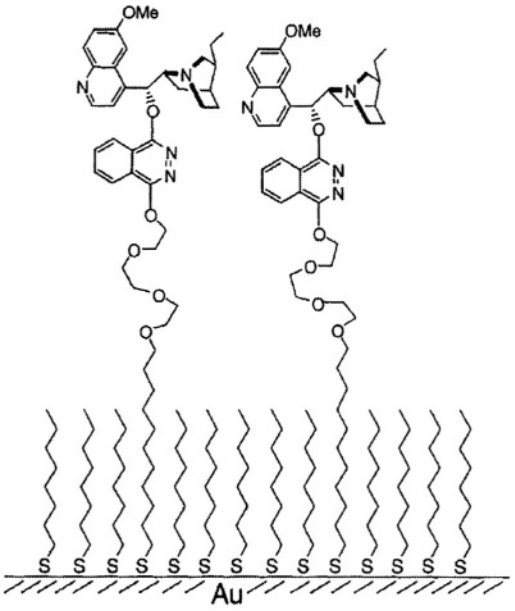

Figure 18. Representation of the structure of a mixed monolayer incorporating dihydroquinidine ligands and methyl groups on a surface of a Au nanoparticle.

Metal nanoparticles capped with chiral molecules can lead to a new type of enantioselective catalyst combining good selectivity control and extraordinarily high activity and simple extraction. For example, AU nanoparticles (2.5 nm) functionalized with alkanethiols that have dihydroquinidine head groups, Figure 18, were used to catalyze the asymmetric dihydroxylation of olefins.[189] Dihydroxylation reactions were performed at room temperature in *t*-butylalcohol/water with the functionalized nanoparticles in the presence of OsO_4 and $K_3[Fe(CN)_6]$ as oxidizers. The dihydroxylation of trans-β-methylstyrene proceeded in 80% yield and gave diol with an enantiomeric excess of 90%, Eq. (8).

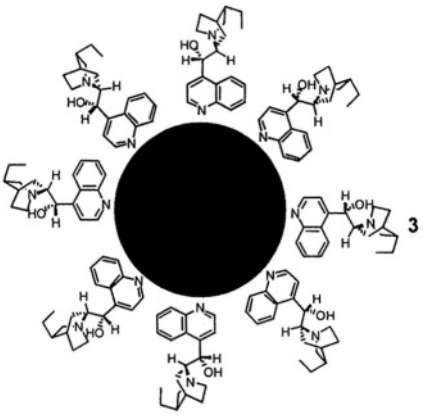

Figure 19. Cinchona-stabilized Pt nanoparticles.

Another example of an enantioselective nano-sized catalyst includes Pt nanoparticles (size from 1.5 nm to 4 nm depending on the Pt/capping molecules ratio) capped with alkaloid dihydrocinchonidine (**3**),[190,191] Figure 19. The (**3**)-functionalized Pt nanoparticles catalyzed enantioselective hydrogenation of ethyl pyruvate, Eq. (9).

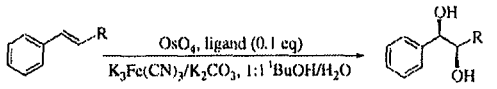

(8)

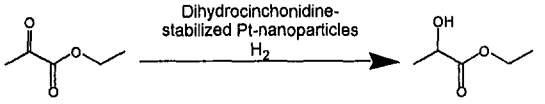

(9)

Highly specific and effective catalysts based on functionalized metal nanoparticles will find broad applications not only for synthetic purposes, but also for the decomposition of waste materials and environmental cleaning, and for the development of chemical sensors and fuel cells.[27]

5.2. Electrochemical Properties of Functionalized Metal Nanoparticles

The electrochemical properties of nanoparticles could be significantly different from those of the same bulk metal. For example, bulk Au electrodes are not electrocatalytically active for CO oxidation, unlike alkanethiolate-functionalized Au nanoparticles deposited onto a bulk Au conductive support.[192] The overpotential for electrochemical dioxygen reduction is significantly decreased at electrode surfaces modified with Au or Pt nanoparticles, thus indicating the electrocatalytic process.[193,194] The electrocatalytic activity of electrodes modified with metallic nanoparticles depends on the size of the nanoparticles, and it is similar to the increase of an electrode catalytic activity upon roughening of an electrode surface.[195]

Double-layer capacitances of individual functionalized metal nanoparticles in electrolyte solutions are small (sub-attoFarad, aF). This results in the potential change of the metal core by >0.1 V increments for single-electron transfers at the electrode/electrolyte interface. This allows the electrochemical observation of quantized capacitance charging (Coulomb staircase) behavior.[62,152,196] For example, a differential pulse voltammogram obtained for a solution of thiolate-capped Au nanoparticles clearly shows peaks for a multi-step single-electron charging process,[62] Figure 20.

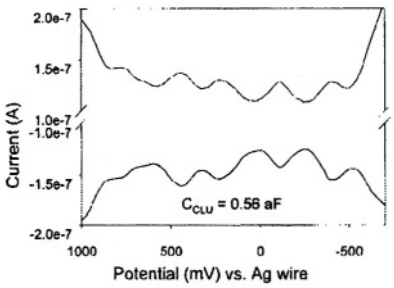

Figure 20. Differential pulse voltammetry (DPV) traces of Au thiol-capped Au-nanoparticles.

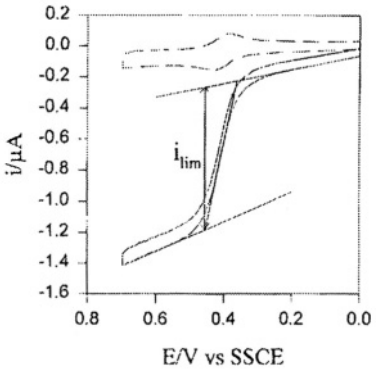

Figure 21. Cyclic voltammograms at 5 mV/s for a 1 M ferrocene-capped nanoparticle solution in 0.1 Bu_4NClO_4/CH_2Cl_2 at 0.15 cm^2 stationary (- -) and rotated (-, 1600 rpm) glassy carbon disk electrode.

The electrochemical properties of redox unit-functionalized nanoparticles are unusual in comparison with free redox-molecules because they transfer many redox-equivalents under diffbsional control to the electrode/solution interface. The few known precedents of poly-electron transfer reactions include soluble redox polymers[197,198] and redox-labeled dendrimers.[199] Monolayer-capped nanoparticles with different metallic cores, such as Au, Ag, Pd, were poly-redox-functionalized with ferrocene (≤ 25 redox sites per particle),[62,93,94,200-205] anthraquinone (≤ 25 redox sites per particle),[206-209] phenothiazine (≤ 7 redox sites per particle),[96] viologen (≤ 36 redox sites per particle),[82] and fullerene (≤ 7 redox sites per particle).[210-212]

Electrochemical studies of redox-functionalized metal nanoparticles reveal that all redox-units bound to the metal core are electrically contacted and participate in the electrochemical process that can originate from internal electrical conductivity of the metallic core and fast rotation of the functionalized nanoparticles at the electrode surface. Thus, the redox-functionalized nanoparticles can be considered as nanoelectrodes with a modified surface. Cyclic voltammetry and rotating disk electrode (RDE) measurements demonstrated that diffusionally limited electrochemistry could be achieved for the redox-units bound to the soluble nanoparticles.[93,94,200,201] Effective sizes of the functionalized metal nanoparticles were derived from their diffusional coefficients.[213] Figure 21 shows typical cyclic voltammograms at a stationary electrode (curve a), and a RDE (curve b), in the presence of ferrocene-functionalized Au nanoparticles.[93] However, even in those systems that show diffusional type of electrochemistry, "prewaves" and "postwaves" in the cyclic voltammograms[201] are sometimes observed as evidence of complications in the redox processes possibly originating from the adsorption phenomena.

Octylthiolate-covered Pd nanoparticles (3.8±0.8 nm) were prepared by reduction of $PdCl_2(CH_3CN)_2$ salt with $LiBEt_3H$ in tetrahydrofuran (THF) solution and capped *in situ* with $C_8H_{17}SH$ monolayer.[203] The functionalization of the Pd nanoparticles with biferrocene units was performed by an exchange reaction of the biferrocene thiol derivative (**4**) with the octylthiolate-capping monolayer in CH_2Cl_2 solution. Cyclic voltammograms of the biferrocene-functionalized Pd nanoparticles were recorded on indium-tin oxide (ITO) electrodes in CH_2Cl_2 solution, Figure 22(A). The first cyclic voltamograms showed two-step one-electron waves at $E^{o\prime}$ = 0.175 and 0.577 V (vs. Ag/Ag^+) corresponding to the reversible oxidation of both ferrocene units bound to the

solubilized Pd nanoparticles. However, the peak currents were linearly dependent on the applied potential scan rate, characteristic of electrochemistry of redox-species adsorbed at the electrode surface. Consecutive potential scans exhibited a gradual increase in the peak current and the voltammogram slowly changed its shape to display one new redox wave between the two original waves. After the electrode was washed and immersed into a background solution, the cyclic voltammogram still showed the same redox process. This behavior is similar to the electropolymerization processes and can originate from an electrochemically induced intra-molecular reaction of ferrocene units resulting in their binding to the electrode surface. The electrochemical deposition of ferrocene-functionalized Pd nanoparticles yields a Pd layer with the thickness controlled by the time of the electrochemical process and the electrochemical properties quite different from the original ones, Figure 22(A). The spectral measurements performed upon the electrodeposition process also show the increase of the Pd film thickness when the process progressed, Figure 22(B)). Similar oxidative electrodeposition processes were achieved for biferrocene-functionalized Au nanoparticles[205] and reductive electro-deposition was reported for anthraquinone-functionalized Au nanoparticles.[208,209]

The adsorption of redox-functionalized metal nanoparticles could be reversibly controlled by their electrochemical reaction. For example, *N*-methyl-*N*'-ethylamino-4,4'-bipyridinium (amino-viologen) was covalently linked to the carboxylic groups of tiopronin-functionalized Au nanoparticles by amide bond formation.[82] Since the viologen units carry two charges, the resulting functionalized Au nanoparticles are soluble in water and can be studied in aqueous solution. Figure 23(A) shows cyclic voltammograms of functionalized Au nanoparticles (curve a), and of a solution of free amino-viologen with the same concentration of the viologen units (curve b). It can be seen that the vilogen units bound to the Au nanoparticles show slightly positive-shifted redox potentials as a result of the association that is typical for vilogen monolayers,[214] and a low peak current that originates from the smaller diffusion coefficient of the nanoparticles.

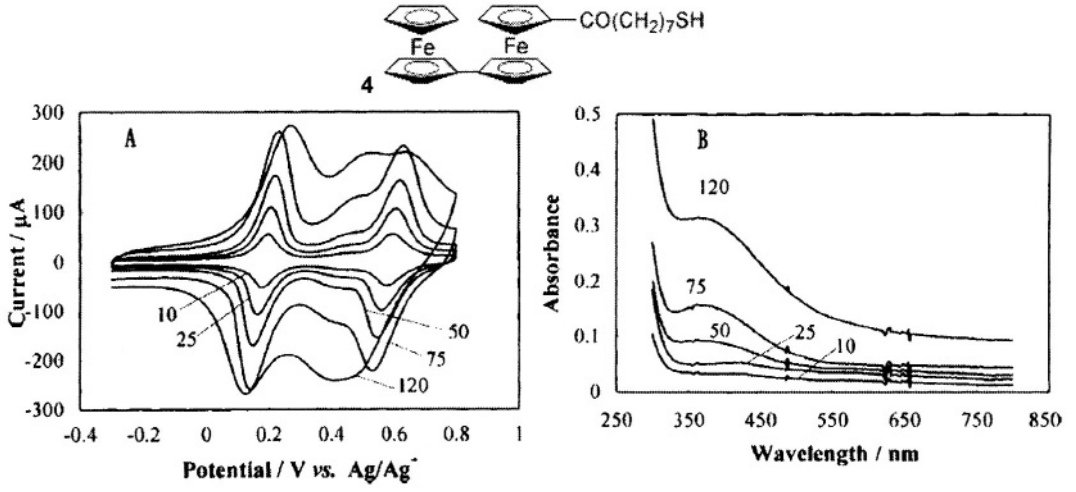

Figure 22. (A) Cyclic voltammograms and (B) UV-Vis spectra of electrodeposited Pd nanoparticle film prepared by consecutive potential scans between –0.3 V and 0.9 V (vs. Ag/Ag^+) in a solution of (**4**)-functionalized Pd nanoparticles (1.9×10^{-6} M) in 0.1 M Bu_4NClO_4/CH_2Cl_2 at an ITO electrode at 100 mV s^{-1}. Numbers in the figure refer to those of the cyclic scans.

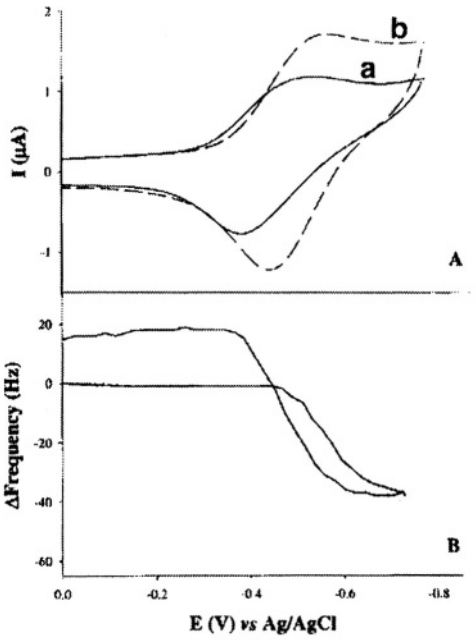

Figure 23. (A) Cyclic voltammetry of amino-viologen (- - -) and 1 mM (in amino-viologen) of cluster poly-functionalized with amino-viologen (36/cluster, -). (B) EQCM crystal frequency change vs potential at 10 mV/s (···) and 100 mV/s (-) in 2 mM (in $MEAV^{+2}(NO_3^-)$) cluster poly-functionalized with amino-viologen (36/cluster).

Electrochemical *in situ* quartz crystal microbalance (EQCM) measurements, Figure 23(B), show the frequency decrease upon the viologen units electrochemical reduction and the frequency increase upon its oxidation. This originates from the reversible adsorption/desorption of the functionalized nanoparticles to and from the electrode when the viologen units are reversibly reduced and oxidized, respectively.

Electrochemistry of the redox-functionalized metal nanoparticles can be studied after their association with a solid conductive support. For example, C_{60}-functionalized Au nanoparticles were synthesized by the exchange reaction of octanethiol-derivatized Au nanoparticles (2.9±0.9 nm) with C_{60}-thiol (**5**) in $CHCl_3$ solution.[211] The C_{60}-functionalized Au nanoparticles were spontaneously adsorbed on a flat Au electrode by simple dipping of the electrode into the nanoparticle solution in CH_2Cl_2. The adsorbed C_{60}-functionalized Au nanoparticles demonstrate well resolved reversible redox waves with $E^{\circ\prime} = -0.94$ V and –1.29 V (vs. Ag/Ag^+, in CH_2Cl_2) corresponding to $C_{60}/C_{60}^{\cdot-}$ and $C_{60}^{\cdot-}/C_{60}^{2-}$ redox transformations of the fullerene units, Figure 24, curve (a). For comparison, the **5** was directly chemisorbed onto a flat Au electrode yielding a C_{60}-monolayer electrode. However, this C_{60}-functionalized electrode showed a poorly resolved cyclic voltammogram with the peak potentials different from those of the C_{60}-Au nanoparticle adsorbed at the Au electrode, Figure 24, curve (b). The electrochemical properties of redox-functionalized metal nanoparticles can be affected by their association with ions or molecules. This suggests the application of redox-functionalized metal nanoparticles for electrochemical sensing. For example, alkylthiolate-functionalized Au nanoparticles[49] were reacted with a dendritic ferrocene thiol derivative to yield ferrocene-functionalized Au nanoparticles by thiol exchange.[202]

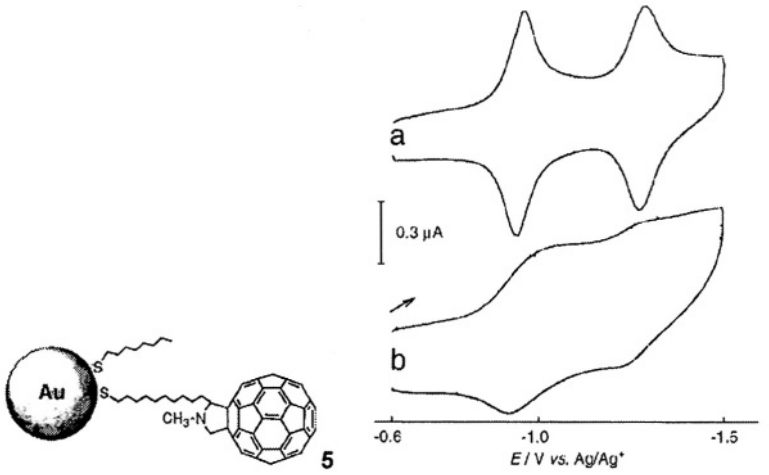

Figure 24. Cyclic voltammogram of (a) a C_{60}-functionalized-Au nanoparticle film adsorbed onto a gold electrode, and (b) self-assembled monolayer of **5** on a Au electrode in 0.1 M Bu_4NClO_4-CH_2Cl_2.

A cyclic voltammogram of the ferrocene-functionalized Au nanoparticles solubilized in CH_2Cl_2 shows reversible electrochemistry for the ferrocene units. This redox wave is decreased and finally disappeared upon titration of the particle solution with $H_2PO_4^-$, while a new redox wave of the ferrocene/$H_2PO_4^-$ complex appears at a potential less positive by 210 mV, Figure 25. An apparent association constant for the ferrocene derivative and $H_2PO_4^-$ of 5200±1000 was derived from the titration curves. Another kind of amidoferrocenylalkylthiol ligands bound to Au nanoparticles allowed specific sensing of $H_2PO_4^-$ and HSO_4^- ions due to a potential shift originating from the complex formation between the ions and the ferrocene redox units.[215] The redox potential of the amidoferrocenyl group is sufficiently perturbed by the synergy between the hydrogen bonding, electrostatic interaction and topology in the alkylthiol-Au nanoparticles containing amidoferrocenyl ligands. Redox-functionalized metal nanoparticles can behave as nanoelectrodes and can also be used for transporting reduced or oxidized multi-electron equivalents. This allows their application for electrocatalysis. For example, anthraquinone-functionalized Au nanoparticles were used for the electrocatalytic reduction of 1, 1-dinitrocyclohexane,[206,207]

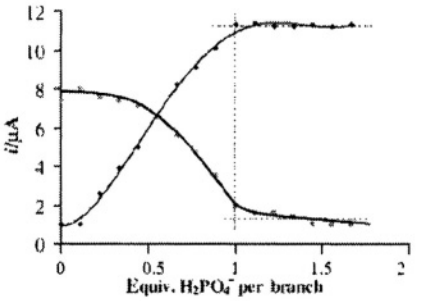

Figure 25. Titration of the dendritic ferrocene-functionalized Au nanoparticle (1×10^{-6} M in CH_2Cl_2) with [n-Bu_4N][H_2PO_4] (1×10^{-2} M in CH_2Cl_2) monitored by cyclic voltammetry.

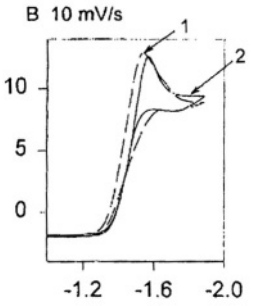

Figure 26. Cyclic voltammograms for the electrocatalytic reduction of 1,1-dinitrocyclohexane in the presence of anthraquinone and anthraqinone-functionalized nanoparticles.

Comparison of cyclic voltammograms corresponding to the electrocatalytic process in the presence of the anthraquinone-functionalized Au nanoparticles and molecular solution of the anthraquinone, Figure 26, curves (1) and (2), respectively, show comparable efficiencies of the electron transfer. Similar electron transfer rate constants for the electrocatalytic process of both systems were derived from rotating disk electrode (RDE) experiments. This opens the way for the use of redox-functionalized metal nanoparticles also as multi-electron carriers in bioelectrocatalytic reactions.

5.3. Photochemical Properties of Functionalized Metal Nanoparticles

Photochemical properties of chromophore-functionalized metal nanoparticles have been extensively studied and reviewed.[216] For this purpose metal nanoparticles functionalized with pyrene,[217,218] fluorescein,[82] stilbene,[219] porphyrin,[220,221] azobenzene,[222] and fullerene[210,212] were synthesized, Figure 27. It has been shown that various chromophore-functionalized metal nanoparticles can demonstrate efficient quenching of the photoexcited chromophore states with or without the formation of photoseparated charges, but in some cases they show long a lifetime of the photoexcited state.

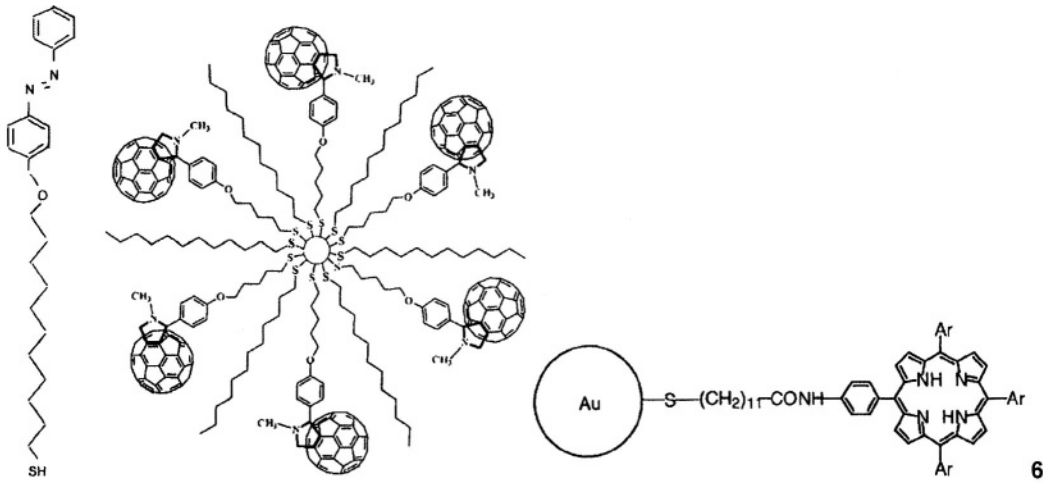

Figure 27. Some representative photoactive nanoparticle functionalities.

Interestingly, that fullerene thiol emission is totally quenched when it is anchored on the Au nanoparticles.[212,216] This observation shows that the decay of singlet fullerene moieties is affected by its binding to the particle. Time-resolved spectroscopy has shown that energy transfer from the photoexcited singlet state of the fullerene to the Au core is responsible for the efficient quenching of the fluorescence, Eq. (10), whereas the photoinduced electron transfer mechanism does not contribute significantly.[212,216]

$$\text{Au-C}_{60} + h\nu \rightarrow \text{Au-}^{1}\text{C}_{60}^{*} \rightarrow \text{Au}^{*}\text{-C}_{60} \tag{10}$$

Another nanosized photochemical system involving pyrene (Py)-functionalized nanoparticles was studied by time-resolved spectroscopy.[216,223] It was seen that electron transfer resulting in the formation of a photooxidized pyrene cation radical and charged Au core, Eq. (11), is mainly responsible for the fluorescence quenching.

$$\text{Au-Py} + h\nu \rightarrow \text{Au-}^{1}\text{Py}^{*} \rightarrow \text{Au}(e^{-}) + \text{Py}^{+\cdot} \tag{11}$$

Thiolate-capped Au nanoparticles are capable of holding charge in a quantized fashion.[6,196,224,225] This photoinduced charge separation between the Au nanocore and the pyrene ligand is sustained for several microseconds before undergoing the recombination. The ability of functionalized Au nanoparticles to participate in photoinduced electron transfer reactions, and the long lifetime of the photoseparated charges, suggests that such systems could be used as nanosized photoreactive centers.[216] Such application of photoactive functionalized metal nanoparticles has been demonstrated with photoinduced hydrogen evolution.[226] The fact that metallic nanocores can be charged in quantized mode allows control over their ability to quench bound fluorophores.[216] For example, a pyrene amino derivative yields very low fluorescence in solution because of self-quenching of the pyrene by the electron donating amine group.[217] However, binding of this material to Au nanoparticles results in high fluorescence due to coupling of the electron donating amino group with the Au metallic core,[216,217] Figure 28. Recent studies on some other fluorescent ligands bound to gold nanoparticles have shown suppression of their quenching by the Au cores.[82,217,219] In this context, porphyrin-functionalized Au nanoparticles were studied in detail. Au nanoparticles (2.4±0.6 nm) were synthesized in toluene by reduction of $AuCl_4^-$ with $NaBH_4$ in the presence of the porphyrin disulfide derivative **6**, yielding porphyrin-functionalized Au nanoparticles,[220,21] Figure 27. The resulting derivatized Au nanoparticles were characterized by ^{1}H-NMR, UV-visible,and fluorescence spectroscopies, electrochemistry, elemental analysis, and transmission electron microscopy (TEM). It was concluded that the Au nanoparticle coverage with the porphyrin units (109 porphyrin molecules per particle) corresponds to 56% ratio between the porphyrin molecules and Au atoms at the particle surface — almost one order of magnitude higher than that of a 2D-monolayer of the porphyrin. Electrochemical and spectral properties of the porphyrin molecules bound to the Au nanoparticles are not significantly different from those of the free porphyrin molecules in solution. The most surprising and important result is that the lifetime of the excited porphirin bound to the Au nanoparticle is similar to that of free porphyrin molecules. Thus, there is no significant quenching of the porphyrin excited state by the nanoparticle, whereas a bulk Au electrode effectively quenches the fluorescence of a 2D-monolayer of the porphyrin self-assembled at a Au surface.

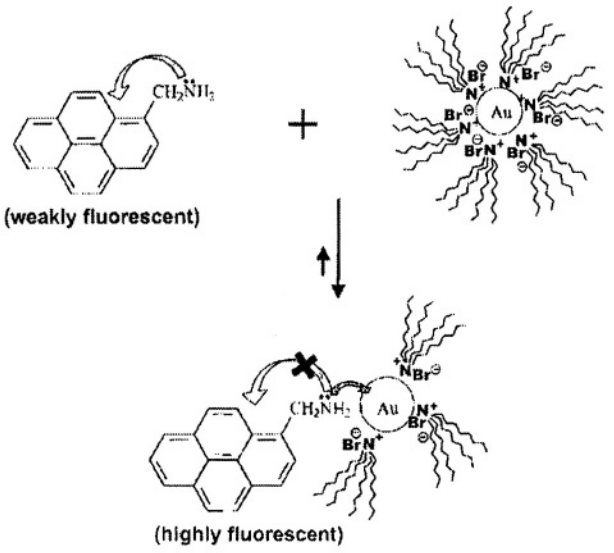

Figure 28. The charging of a Au nanoparticle with the donation of lone-pair electrons results in the stabilization of the excited state.

Taking into account the high loading of the porphyrin at Au nanoparticles and its long-life fluorescence, one could conclude that such a system is promising for light harvesting in photoelectrochemical devices.

Photoisomerizable molecules have been used extensively in photoswitchabe systems in solutions and at interfaces.[227,228] Au nanoparticles were functionalized with an azobenzene thiol derivative (**7**), Figure 27, in order to study their photoizomerizable features in solution.[222] Photoswitching was not observed in a single-component monolayer of the azobenzene bound to Au nanoparticles, however, by increasing the free volume available per azo unit by monolayer dilution with alkanethiol, reversible photoisomerization between the *cis*- and *trans*-states was observed.

5.4. Recognition, Specific Association, and Sensoric Operation of Functionalized Metal Nanoparticles

Metallic nanoparticles functionalized with specific recognition sites have been suggested for the controlled binding of low molecular components and controlled aggregation. For example, non-covalent multivalent hydrogen bonding between flavin-guest molecules and diacyldiaminopyridine-functionalized Au nanoparticles provides an efficient host-guest complex formation.[229] Such a system is different from molecular host-guest complexes because a single functionalized Au nanoparticle carries many binding sites that accommodate many guest molecules. The diacyldiaminopyridine-host sites have different affinities to the oxidized and reduced states of flavin-guest, and the binding of flavin increases more than 20-fold upon its reduction. This provides a direct electrochemical switch for the control of complex formation at the surface of the functionalized nanoparticles. Specific host-guest interactions between the flavin and diacyldiaminopyridine units were enhanced when pyrene aromatic stacking elements were introduced into the shell layer.[230]

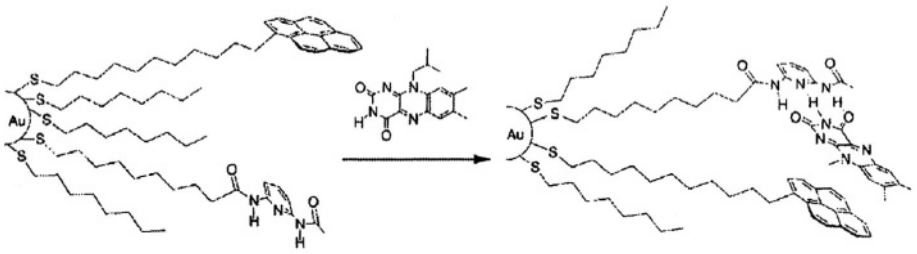

Figure 29. Binding of flavin by the multifunctional nanoparticles.

While the diacyldiaminopyridine units bind flavin via triple hydrogen bonds, the pyrene aromatic units provide an additional π-π interaction with the flavin aromatic system, Figure 29. It has been shown that this multivalent interaction results in an association constant of $323 \pm 20\ M^{-1}$ — nearly double that provided by the H-bonding only in the absence of pyrene units ($193 \pm 8\ M^{-1}$). It is interesting to note that multivalent complex formation between the flavine-guest molecule and two binding sites of the shell requires lateral movement of the binding units in order to meet the guest molecule and form the complex. The stability of the resulting complex depends on the spacer length between the Au core and the binding sites.[231] When the spacer is shorter (so the flavin molecule is closer to the metallic core), the recognition was enhanced ca. 3-fold due to increased preorganization of the shell structure. The effect of preorganization is reversed upon reduction of flavin, where the functionalized Au nanoparticles with longer side chains bind the reduced flavin ca. 7-fold stronger than the short chain counterpart due to unfavorable dipolar interactions between the electron-rich aromatic stacking pyrene units of the host and the anionic flavin guest.

Formation of host-guest complexes between a molecular guest and two host units that belong to different nanoparticles would result in the nanoparticle crosslinking and therefore aggregation. In order to build up such a system, intraparticle host-guest complex formation should be excluded. For example, γ-cyclodextrin-functionalized Au nanoparticles were interacted with C_{60} guest component resulting in the crosslinked Au nanoparticle aggregate originating from γ-cyclodextrin/C_{60} host-guest complex formation.[232] The size of the C_{60} guest molecule prohibits intraparticle complex formation, but allows the interparticle binding, thus resulting in their crosslinking. Bioorganic capping molecules can also provide complexation sites. For example, Au-nanoparticles capped with glutathione tripeptide molecules could be used for the binding of glutathione S-transferase, the enzyme having special affinity to glutathione substrate,[84] whereas Au nanoparticles functionalized with coenzyme A molecules could be used for affinity binding of the coenzyme A-dependent enzymes.[81] Au-nanoparticles functionalized with receptor units can bind to enzyme molecules competing with natural substrate molecules, thus resulting in the inhibition of enzymatic activity.[233] Nanoparticle-biomolecule hybrid systems have been extensively studied and reviewed,[44] thus we will not discuss them in the present paper.

Non-covalent bonding between functionalized metal nanoparticles and complementary polymeric templates could result in the formation of controlled aggregates. As an example, complementarity between functionalized metal nanoparticles and a polymer template was achieved using the diaminotriazine-thymine three-point

hydrogen bonding interaction,[234,235] Figure 30. For the polymer component, diaminotriazine-functionalized polystyrene (**8**) was employed. The required thymine-functionalized Au nanoparticles were synthesized starting with ca. 2 nm Au nanoparticles capped with an octanethiolate monolayer. Thiol place-exchange with a thymine-functionalized alkanethiol then provided the thymine-derivatized Au nanoparticles.

The temperature-controlled association of the thymine-functionalized Au nanoparticles with the complementary diaminotriazine-functionalized polymer resulted in the formation of spherical aggregates of size 97±17 nm at 23 °C, Figure 31(A)), spherical assemblies of size $0.5 - 1\ \mu m$ with ca. $(5\text{-}40)\times10^5$ individual subunits at –20 °C, Figure 31(B). In addition to controlling the size of the aggregates, temperature strongly affects the morphology of the resulting assemblies. At 10 °C, networks of ca. 50 nm subunits were formed, Figure 31(C), as opposed to the discrete structures observed at higher and lower temperatures. This suggests that network formation is an intermediate process in the formation of the giant assemblies at –20 °C. The individual assemblies within these networks remained spherical, although their sizes are more highly dispersed. Further control of the aggregate size could be achieved by controlling the length of the template polymer and by introducing binding and non-binding domains into the polymer structure.[236] Mixed aggregates composed of negatively-charged functionalized Au and functionalized silica nanoparticles associated with a positively charged polymer were prepared by a similar approach.[237]

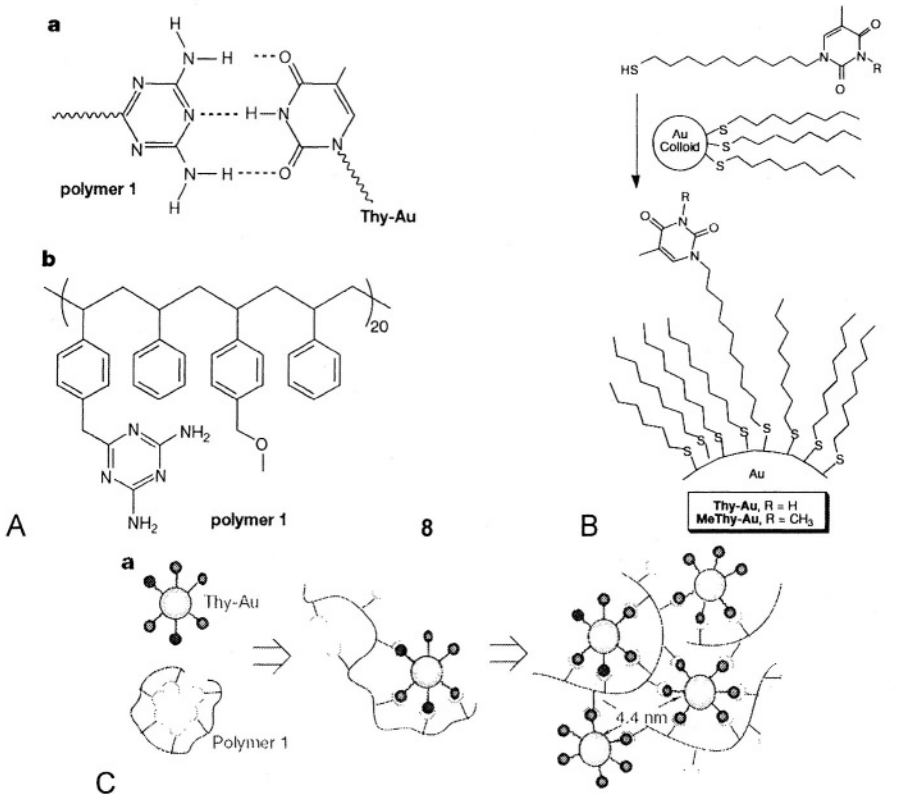

Figure 30. (A) Recognition motif: (a) Diaminotriazine-thymine recognition; (b) triazine-functionalized random copolymer. (B) Preparation of Thy-Au and MeThy-Au. (C) Proposed mechanism for aggregation.

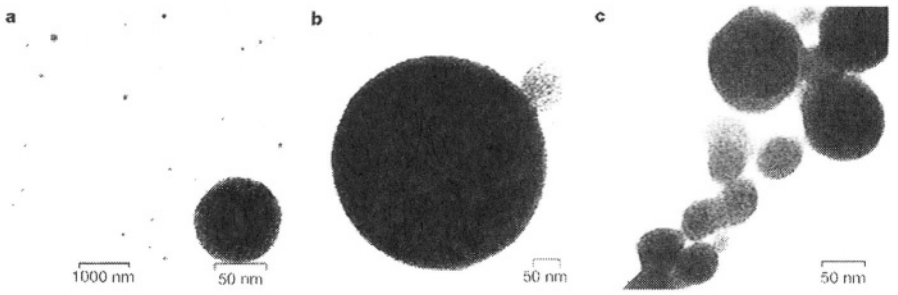

Figure 31. TEM images of polymer **8**-Thy-Au aggregates formed at (a) 23 °C, (b) −20 °C, and (c)10 °C.

The degree of ordering and the control of particle material, size and shape, coupled with the inherent modularity of the 'bricks and mortar' nanoparticle-polymer self-assembly process, represent a powerful and general strategy for creation of highly structured multifunctional materials.[234,235]

Metallic nanoparticles capped with molecules providing recognition sites for host-guest interactions could be used for the development of specific sensors and selective catalysts. Au nanoparticles (18 nm) were functionalized with alkylthiol with a 15-crown-5 head group.[238] The 15-crown-5 units form different kinds of complexes with Na^+ and K^+ ions, Figure 32(A). While in the presence of Na^+ ions the 15-crown-5 units bind one Na^+ guest ion per the host crown-unit providing charging of the functionalized Au nanoparticles and resulting in their dispersion in an aqueous environment with a red color, Figure 32(B), each K^+ ion is bound with two crown-units resulting in sandwich-type complexes. There are two possible binding schemes for the sandwich complexation, in which the two 15-crown-5 are either from neighboring chains or from different nanoparticles. In the former case, the exterior of sandwich crown ethers and thus the entire nanoparticles become hydrophobic. The polar aqueous medium enhances interparticle attractions (such as van der Waal's attraction) among less polar nanoparticles, resulting in the formation of aggregates. In the later case, nanoparticles are networked via sandwich complexes. Because there are multiple binding sites on the nanoparticles, the aggregates are developed in a hexagonally close-packed structure, Figure 32(C). The aggregation of Au nanoparticles in the presence of K^+ ions results in the change of their dispersion from red to blue color, Figure 32(D), and finally to the precipitation of the particles aggregates. The system demonstrates an analytical application of metal nanoparticles functionalized with recognition units. Another example of the spectroscopic detection of metal ions includes interaction of multi-charged metal ions (e.g. Pd^{2+}, Cd^{2+}, Hg^{2+}) with carboxylic derivatized thiolate-capped Au nanoparticles.[239] Interparticle chelation of the metal ions by the negatively charged shell molecules results in the aggregation of the functionalized Au nanoparticles, thus resulting in a change in the spectrum. Another example of recognition elements bound to the thiolate-shell of Au nanoparticles includes aminophenylboronic acid, which provides specific binding of vicinal-glycols.[240] The aminophenylboronic acid-functionalized Au nanoparticles show affinity properties for binding of glycol-containing molecules, particularly sugars and glyco-proteins, thus allowing their specific assembly and sensing.

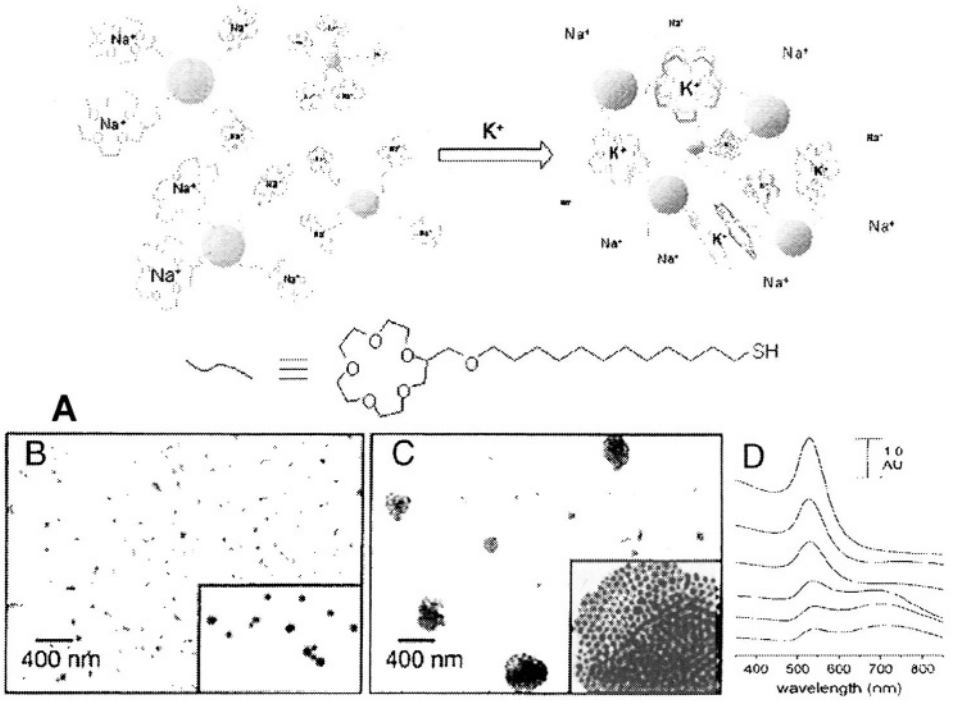

Figure 32. (A) K^+-Induced aggregation of crown-thiol molecules in a sodium-containing solution. TEM micrographs of crown-functionalized gold nanoparticles (B) before and (C) after addition of 0.1 mM K^+. (D) UV-visible spectra of solutions of colloidal gold responding to various concentrations of K^+.

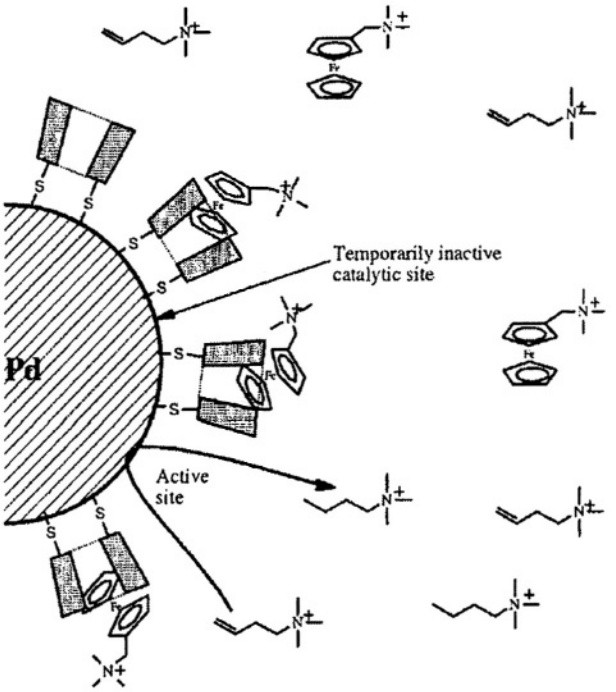

Figure 33. The deactivation of catalytic sites by the binding of ferrocene to CD hosts on the Pd-nanoparticles.

Specific binding sites organized as a "shell" monolayer on functionalized metallic nanoparticles could provide substrate, promoter or inhibitor binding, thus resulting in the activation, enhancement or inhibition of catalytic reactions, respectively. For example, cyclodextrin-functionalized Pd nanoparticles have demonstrated catalytic activity for the hydrogenation of olefins.[241] Specific binding of a ferrocene derivative to the cyclodextrin units of the shell results in the inhibition of the catalytic process, since it partially blocks the catalytically active surface of the Pd nanoparticles, Figure 33. Thus, the host-guest binding allows tuning the nanoparticles' catalytic activity.

6. FUNCTIONALIZED METAL NANOPARTICLE ARRAYS ON SURFACES

The construction of nanoparticle architectures on surfaces attracts substantial interest because of the degree of control that can be exercised over the size, shape and functions of the nanoparticle blocks and by their integration with bulk solid surfaces. The integration of functionalized metal nanoparticles with bulk conductive supports may lead to the electrical contacting of the nanoparticles and to the assembly of devices demonstrating single electron transfer charging devices or triggered electron transfer devices.[4,242] The assembly of metal nanoparticles functionalized with recognition sites on electronic transducers such as electrodes or field-effect transistors may lead to new selective sensoric devices.[243,244] Similarly, the assembly of nanoparticles on transparent surfaces or conductive transparent supports, may lead to controllable optical[245] and electrochromic[246] functionalities. For all of these functional systems the development of methods for the assembly and characterization of the nanoparticles on surfaces is essential. Several recent reviews have addressed this topic.[6,7,42] The present section will briefly discuss the concepts for immobilization of metal nanoparticles on surfaces, and will exemplify the scientific methodologies of transforming the organized nanostructures into functional sensoric, electronic and photonic devices.

6.1. Preparation of Functionalized Metal Nanoparticles Arrays on Surfaces

Monolayer deposition of functionalized nanoparticles onto a solid support surface is the first step for further multilayer functional assembly. Organized lattices, 2D- and 3D-ordered assemblies demonstrating sensoric, catalytic, electrochemical and photoelectrochemical properties have been obtained. Nanosized electronic circuits were organized upon assembling of conductive metal nanoparticles on non-conductive solid supports. There are numerous methods to generate polymeric matrices with non-ordered, randomly distributed metal nanoparticles. These include absorption of metal ions by polymer matrices (usually negatively charged polymers such as polyacrylic acid are used) and their chemical or electrochemical reduction to yield nanoparticles[247] or entrapment of stabilized nanoparticles by growing polymer layers upon their formation (e.g. upon electropolymerization step).[248] Metal nanoparticles could be also entrapped into the polymeric matrix upon its swelling-shrinking in the presence of nanoparticles.[249] The polymer-nanoparticles composite materials demonstrate interesting features, for example their conductive and optical properties could be reversibly switched by temperature,[250] solvent,[249] or potential change.[184] However, these non-ordered composite materials are mainly out of the frame of the present review.

6.1.1. Adsorption of Nanoparticles at Modified Surfaces

Nanoparticles have been assembled on a wide variety of substrates, sometimes by highly ingenious means, but true nanoengineering requires nanoscale control, i.e. control over the nanoparticle packing morphology on the surface. This is becoming a reality with new research into the ordering of adsorbed particles, bringing new applications to light, such as the use of nanoparticles as nanoscale "masks" for lithography of surfaces.[251-253] It should be noted that one should expect some nonideality even from networks of nanoparticles with a very narrow size distribution (variation less than 10%). Theoretical consideration of nanoparticle lattices using Hamiltonian based on a Hückel-type tight binding like approximation results in the conclusion that they have a configurational disorder and are never identical.[254]

Various functionalized solid supports such as glass (including conductive glasses) and metallic electrodes have been used for the adsorption of nanoparticles. The most usual way for chemical derivatization of glass substrates is silanization.[255,256] The silanized glass surface bears chemical groups that are capable of binding a colloid particle either covalently (e.g. thiol to bind Au nanoparticles, Figure 34(A)) or through electrostatic interactions (e.g. amine to bind anionic nanoparticles, Figure 34(B)). The formation of a colloid monolayer is achieved by placing the surface-functionalized glass substrate in a solution of the nanoparticle, which binds to the surface, assembling into a saturated monolayer over a period of time. The monolayer density is dependent on factors such as the particle size and charge as well as the attachment method and the substrate.[257] In a study of citrate-stabilized gold nanoparticles assembled on amine- and thiol-functionalized ITO glass surfaces, it was found that 80 nm particles formed layers over 20 times less dense than 15 nm particles (ca. 2×10^{9} particles·cm^{-2} as opposed to ca. 4.5×10^{10} particles·cm^{-2}).[258] Amine-functionalized substrates are found to bind the particles at a slightly higher density than thiol-functionalized substrates. The dynamics of monolayer assembly has been followed directly by quartz crystal microgravimetry (QCM),[259,260] and spectroscopy,[261] and in the case of citrate-capped Au-particles occurs over a period of a few hours. It should be noted that electrostatic adsorption of negatively charged Au nanoparticles on amino-functionalized solid supports is pH-dependent.[262] The electrostatic attraction of the oppositely charged nanoparticles and the amino-functionalized surface is effective only when the amino groups are protonated at pH smaller than the pK-value of the surface bound amino groups.

The assembly of nanoparticles on gold substrates often follows a similar procedure to that for glass substrates, i.e. surface modification of the substrate followed by the adsorption of colloid particles. The modification of the gold surface is achieved by use of a thiol,[45,46] which forms a covalent link to the Au-surface. This thiol also bears a group capable of binding a nanoparticle, for instance another thiol for Au or Pt nanoparticles,[263] or an amine for Au nanoparticles.[264,265] Aluminium surfaces are easily functionalized by carboxylic acids, Figure 34(C), and thus nanoparticles may be immobilized on them either by the use of carboxylic acid-functionalized nanoparticles or by functionalizing the surface with carboxylic acids attached to a colloid-binding group (such as a thiol for gold nanoparticles).[266] It is interesting to note that a bifunctional linker containing a carboxylic group and a thiol group (e.g. 4-carboxythiophenol) is capable to adsorb differently on Al and Au surfaces, via the carboxylic and thiol groups, respectively, thus exposing to the solution the opposite functional group and providing additional synthetic possibilities including the possibility of patterning.[267]

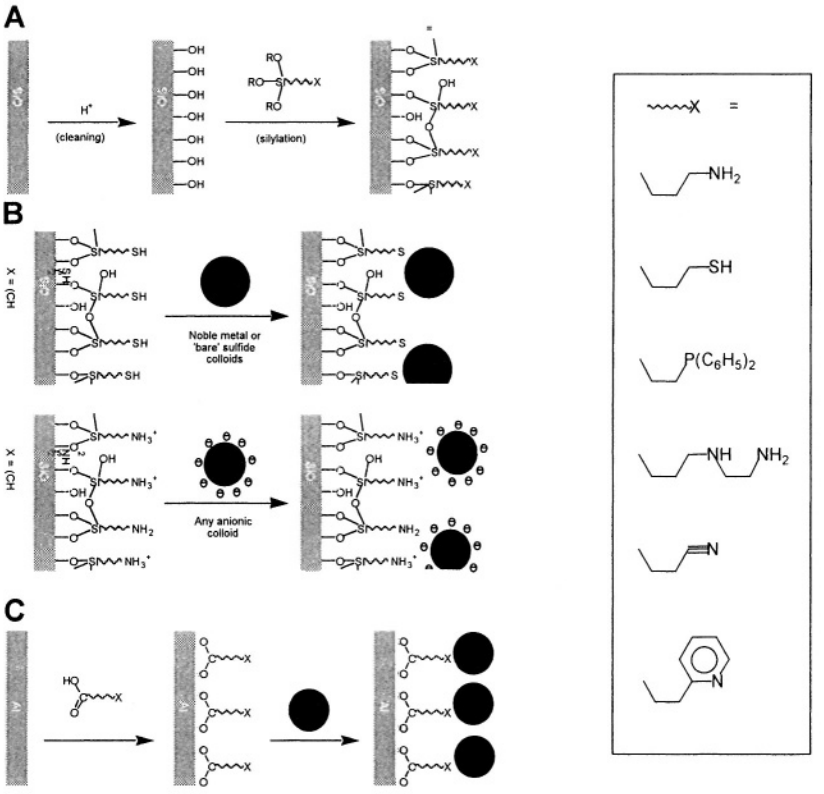

Figure 34. The construction of Au-nanoparticle monolayers on various substrates.

Studies on the adsorption of Au nanoparticles functionalized with thiols (e.g. $CH_3(CH_2)_{11}SH$, or $HO(OCH_2CH_2)_6(CH_2)_6SH$) at planar gold electrode surfaces modified with the same thiols[268] show that the strongest adsorption is achieved when hydrophobic-functionalized Au nanoparticles interact with a hydrophobic electrode surface, whereas interactions between hydrophilic/hydrophobic surfaces are much weaker.

Conductive substrates also allow the possibility for particle adsorption by electrophoretic means.[269-272] In this procedure, the Au nanoparticle surface is first reacted with alkanethiols in order to lower the surface charge. The particles are then deposited on anodic surfaces under relatively low potentials, and are subsequently desorbed if the electrode polarity is reversed. The monolayers formed have extremely regular structures, but the particles are not truly bound to the substrate so the structures exhibit low stabilities. Real electrocatalyzed adsorption can be accomplished by the use of functionalized nanoparticles. Reduced viologen is known to adsorb strongly to gold electrodes, and thus viologen-functionalized Au-colloids can be electrochemically activated to form a monolayer on a QCM surface.[82] When the viologen units are subsequently oxidized, the nanoparticles are released from the electrode surface.

The electrochemical deposition of metal nanocrystals on carbon electrodes has been the subject of a large number of investigations[273-276] as this type of interface is of great importance to electrocatalysis and as a model system for electroplating. The focus of many of these studies has been on the early stages of electrochemical deposition in an

effort to elucidate the nucleation and growth mechanism of the metal phase on the substrate (usually a glassy carbon electrode).[275] The electrochemically-assisted deposition of metal nanoparticles includes the electrochemical reduction of the respective salt (e.g. $AuCl_4^-$ for Au-deposition), primary formation of ad-atoms and the further growth of nanocrystals on the carbon electrode. The overall surface area of gold as well as the nanocrystal size, density, and surface texture, can be controlled by the variation of deposition conditions (the bulk concentration of the salt and the overpotential applied).[274]

Significant results have been accomplished for the assembly of negatively charged nanoparticle layers on adsorbed polycationic polymer films such as poly(ethyleneimine) or poly(diallyldimethylammonium chloride). This methodology is very general, yielding successful results for various metal nanoparticles.[277,278] Techniques for the construction of thin polymer films are very well known, and allow the construction of nanoparticle arrays almost irrespective of the substrate material. Similarly, nanoparticles have been assembled on PAMAM dendrimer films.[279,280] Surfaces have also been prepared for nanoparticle organization by the formation of Langmuir-Blodgett films.[281] This methodology gives access to very thin, dense sublayers, but is not suitable for large-scale production or shaped substrates. The Langmuir-Blodgett technique and a similar "surface-tension-driven" method[282] have also been used for the direct assembly of nanoparticle layers. The nanoparticles can be immobilized at the air-water interface either within a 'carrier' monolayer (for instance, negatively-charged silver colloids have been immobilized in positively-charged fatty amine monolayers[283,284]) or by virtue of their own properties.[283-285] Langmuir-Blodgett films allow for a very high degree of control over the nanoparticle density and ordering since the monolayer can be manipulated prior to its assembly on the substrate,[286] but their formation has neither the generality nor the ease of the self-assembly method.

We have already seen that monolayers formed by electrophoresis can have very regular, close-packed structures. Similar results can be obtained from the evaporation of colloid solutions on substrate surfaces under carefully-controlled conditions,[287,288] but other methods of monolayer formation tend to give less organized films of lower coverages. The particle density of electrostatically-produced monolayers is dependent on factors such as the particle size[258] and surface charge — the particles in these films are usually well spaced as their charges do not allow them to come into close contact with each other. Citrate-stabilized Au-nanoparticles normally give adsorption coverages of around 30% for 12 nm particles,[261,289] but closer packing can be achieved by the neutralization of their surface charge, Figure 35. If a thiol-bound monolayer of citrate-stabilized colloids is exposed to a solution of an alkanethiol, then the alkanethiol displaces the citrate, neutralizing the particle's charge, Figure 35(A). After this procedure, additional nanoparticles can be adsorbed in the spaces between those in the original layer as electrostatic repulsion no longer inhibits their approach.[261] Continued cycles of neutralization and nanoparticle adsorption lead to a dense monolayer with interparticle spacings controlled by the choice of the alkanethiol.[277] A similar procedure on an amine-functionalized substrate can even coax the nanoparticles into reorganizing themselves, Figure 35(B).[290] In this case, when the citrate layer is removed from the nanoparticles, their electrostatic bond to the substrate is substantially weakened. The freed nanoparticles can then self-assemble into highly regular hexagonally-packed structures on the surface, and further neutralization and adsorption cycles give rise to highly ordered surfaces. These monolayers suffer from low stabilities however, as a consequence of the loss of binding between the particles and the surface. Other studies

have generated crystallized monolayers by applying carefully optimized conditions for colloid deposition,[291] and very dense but uneven layers by the aggregation of the colloid solution prior to its adsorption onto the substrate.[289] A two-dimensional (2D) assembly of Au nanoparticles with regular controlled distances (ca. 2 nm) between metallic cores was produced using tetrapyridylporphine molecules as spacers between the nanoparticles.[292] The system represents a 2D regular network composed of Au nanoparticles forming hexagonally packed array. Similarly, metallic nanoparticles (e.g. Ag, Pd) functionalized with hydrophobic long-chain thiols were organized in 2D arrays with the core-to-core distaces controlled by the length of the thiol chains.[293,294] A 2D-nanoparticle assembly with a gradient of its density was prepared by deposition of Au nanoparticles on a solid support with the gradient of the surface concentration of amino groups responsible for the nanoparticle binding.[295]

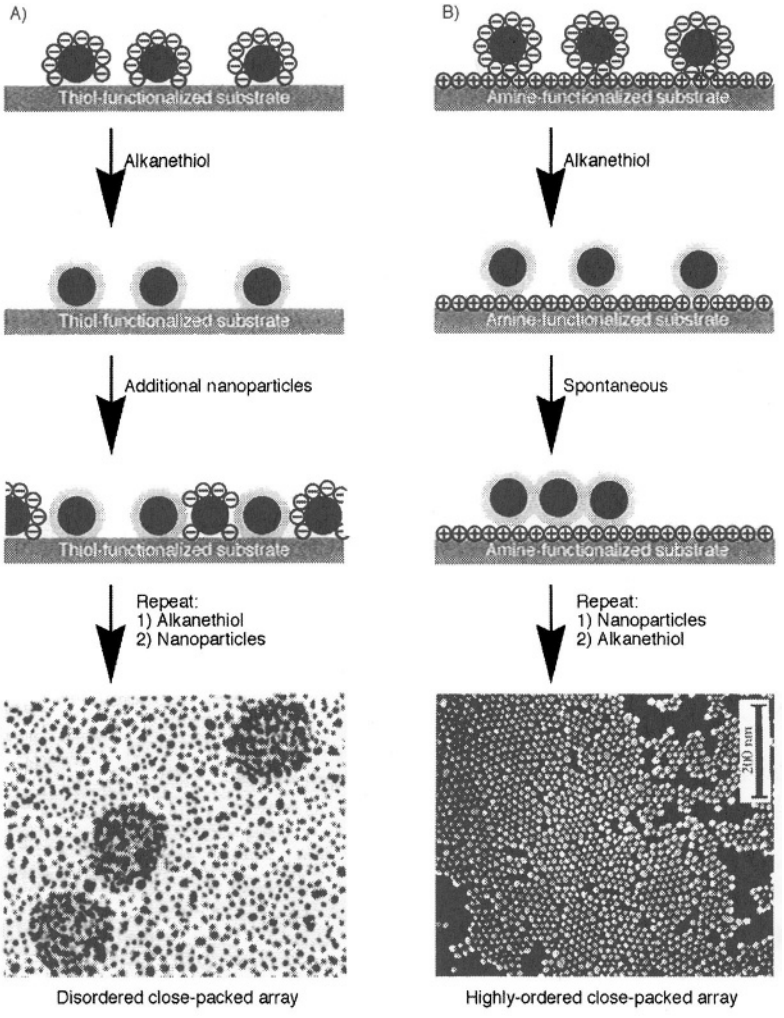

Figure 35. Controlling interparticle spacing and packing. (A) Assembly of a high-density monolayer by the neutralization of nanoparticle surface charge. (B) Assembly of a "crystallized" monolayer by loosening the nanoparticle-substrate bond, allowing particle reorganization.

6.1.2. Layer-by-Layer Assembly of Functionalized Metal Nanoparticles Crosslinked by Charged Molecules

In order to assemble nanoparticle multilayers, a monolayer must be primed in some way for the adsorption of the second (and subsequent) particle layers. This "priming" may be little more than a modification of the surface layer, or it may involve functionalization with another significant component. The forces used to hold such structures together are either covalent or ionic. Architectures may be much more complicated than simple alternating layers — constructions may contain different layers consisting of different types of nanoparticle[263,296] or crosslinker,[297,298] leading to designed functional materials.

The assembly of electrostatically-linked nanoparticle arrays is a general method which has been shown to be effective up to the micron-scale using charged polymers or small molecules as linkers.[299] Nanoparticle arrays can be constructed from any charged nanoparticle and an oppositely multicharged "crosslinker".[39,40,42] Metal nanoparticles stabilized with weakly bound ionic species (e.g. citrate ions), as well as charged thiolate-functionalized nanoparticles have been used in this kind of layered assemblies. For example, negatively charged 11-mercaptoundecanoic acid functionalized gold nanoparticles were self-assembled in a multilayer configuration using positively charged poly(allylamine hydrochloride) as a linker,[300] Figure 36(A). The charge on anionic Au nanoparticles allows them to be adsorbed onto the cationic polymer and *vice versa,* allowing a three-dimensional structure to be built up in a stepwise fashion. On the other hand, positively charged 4-mercaptophenylamine-functionalized Au nanoparticles were crosslinked with negatively charged poly(sodium 4-styrene sulfonate) yielding a similar structure,[300] Figure 36(B). In another example Au nanoparticles capped with positively charged poly(amidoamine) dendrimers were crosslinked by negatively charged poly(sodium 4-styrene sulfonate) to yield a multilayer assembly.[301] Application of dendrimers with different numbers of generations allowed precise control of the interparticle distances. Strong interaction between charged thiolate-functionalized Au nanoparticles and the oppositely charged polymer molecules involves multiple hydrogen bond formation between them.[302] Figure 36(C) shows how a polymer-nanoparticle multilayer composite can be constructed by the exploitation of electrostatic interactions. If the base nanoparticle layer has a net negative charge, it facilitates the assembly of a thin film of a polycationic polymer. In turn, the polymer layer leaves a surface positive charge, on which a second negatively charged nanoparticle layer is assembled, and subsequent layers are built likewise. Polymers that have been used include positively charged poly(diallyldimethyl ammonium chloride),[303,286] negatively charged poly(sodium 4-styrene sulfonate)[300] and others,[278,297,304] and a wide range of metal nanoparticles such as Au,[278,297] Ag[303] have been utilized. Another synthetic route includes the electrostatic deposition of metal ions between oppositely charged polymer layers and their further reduction to yield metallic nanoparticles entrapped in the layered polymeric matrix.[183,305,306] This approach allows control of metal nanoparticle concentration in the polymeric matrix as well as their size. For example, $PdCl_4^-$ ions were self-assembled with a polycationic poly(4-vinylpyridine) linker in a multilayer configuration on a conductive support and then they were electrochemically reduced resulting in Pd nanoparticles (3-7 nm) sandwiched between the polyelectrolyte layers.[305]

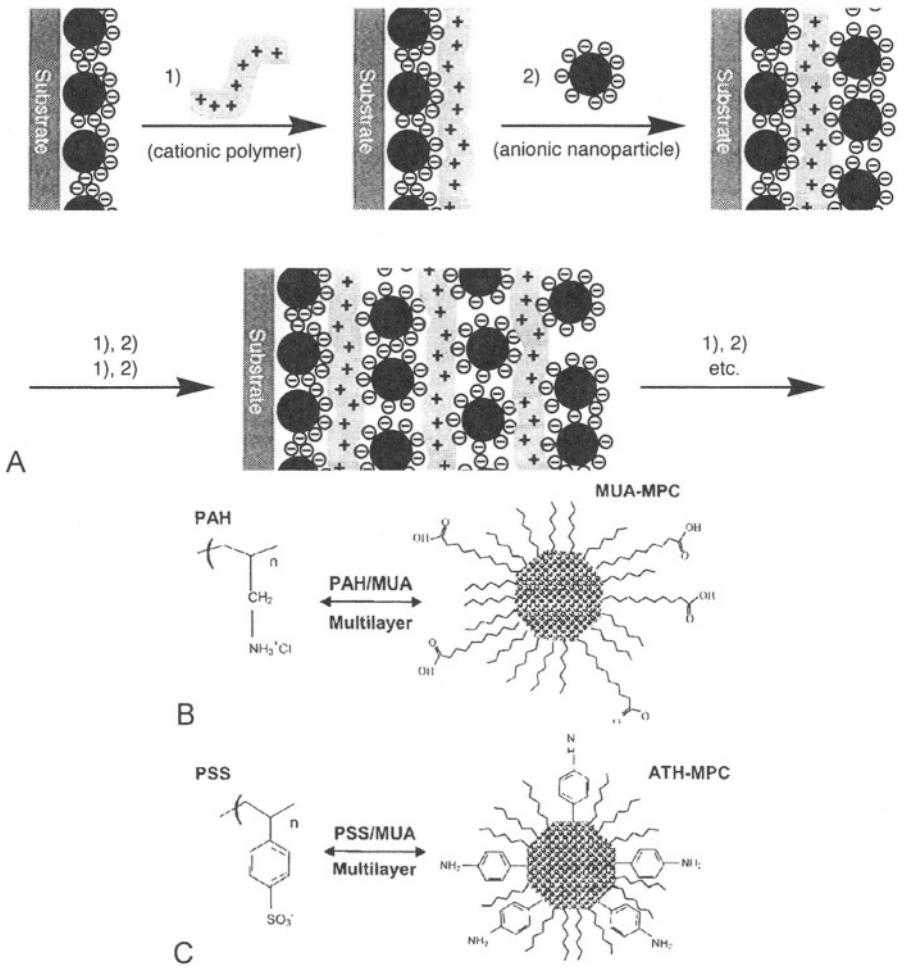

Figure 36. (A) The construction of molecular oligocation — anionic colloid multilayers by the exploitation of electrostatic interactions. (B) The use of poly(allyamine hydrochloride) (PAH) and poly(sodium 4-styrene sulfonate) (PSS) MPCs, and the exchange ligands mercaptoundecanoic acid (MUA) and 4-Mercaptophenylamine (ATH), in building MPC/polymer multilayers.

Similarly Ag^+ ions were complexed with polyethyleneimine and then layer-by-layer deposited on an electrode support using polyacrylic acid as a negatively charged polymeric linker.[183] Post-deposition reduction of the Ag^+ ions yielded Ag nanoparticles in the multilayered polymeric assembly. The "crosslinker" may be not only a charged polymer, but also a small molecule or even another functionalized-nanoparticle.[307,308] For example, sequential layer-by-layer deposition of oppositely charged amino-derivatized Au and carboxylic-derivatized Ag nanoparticles was performed on a glass support.[78] The electrostatic crosslinker must bear multiple charges so it can interact with the colloid layers both above and below it simultaneously. Singly-charged species such as tetrabutylammonium chloride are able to partially neutralize the colloid's charge so that greater coverages can be realized, but they cannot be used to assemble true multilayer structures.[307] In fact, not even all oligocations are successful. Those that bind the nanoparticle more strongly than the underlying substrate may destroy the superstructure,

and those with a low charge density may not be effective. The oligocationic molecule can be assembled in a variety of solvents, but to achieve efficient coverage, a fairly concentrated nanoparticle solution (ca. 10 mM) is usually required for a period of at least 30 minutes. It is very important that the sample is washed very thoroughly before every colloid treatment as any weakly-bound crosslinker can diffuse into the bulk solution, causing aggregation of the nanoparticles.

Like in the construction of polymer-linked structures, the treatment of a nanoparticle monolayer with an oppositely-charged species results in a surface ready for the assembly of a second nanoparticle layer. In this case however, the much smaller "crosslinker" means the nanoparticle layers are much closer — even interleaved — such that there can be electrical communication throughout the entire structure.[309] The use of *N,N'*-diaminoethyl-4,4'-bipyridine as a crosslinker has been used to demonstrate the versatility of the method — gold and silver colloids offer the same assembly characteristics, allowing composite structures to be built.[296] Great success has been realized by the use of 4,4'-bipyridinium-based cyclic crosslinkers,[41,296,298,309-311] which also exhibit electrochemical activity as well as sensoric functions (to be discussed in Section 6.3). Complexation of carboxylic-thiolate-functionalized metal nanoparticles with multiply-charged cations (e.g. Zn^{2+}, Cu^{2+}) was used to build up multilayered assemblies.[312,313] These assemblies were also used for the deposition of continuous metallic layers on solid supports.[313] For this purpose, several layers of carboxylic-functionalized Au nanoparticles were deposited onto a glass support using Cu^{2+} ions as bridging units. Further heating of the nanoparticle covered surfaces resulted in the formation of continuous metallic films of controllable thickness.

Although the charged nanoparticles-crosslinker architectures are only stabilized by ionic interactions, they tend to be highly stable in almost any solvent, requiring physical scratching or chemical reaction to damage them. Further stabilization of nanoparticle-polymer assemblies can be achieved if the multilayers are covalently linked. For example, the use of a positively charged diazo-functionalized polymer between negatively charged sulfonate-thiol-functionalized Au nanoparticles allowed photochemical transformation of the electrostatic interactions to covalent bonds.[314] In another example, a single step deposition of Au nanoparticles complexed with a diblock copolymer, polystyrene-*block*-poly(4-vinylpyridine), onto a solid support yielded a multilayered assembly of alternating pure polymeric lamellae and Au nanoparticle-containing lamellae, both in a nanometer thickness.[315] It should be noted that all the polymeric layers are covalently linked and belong to a single diblock polymer. The spontaneous separation of the Au nanoparticle-containing diblock polymer in well-defined layers originates from minimization of the interfacial energies. Covalently-linked colloid superstructures can be built in an analogous way to electrostatically-linked architectures. This has been accomplished by using bisthiol crosslinkers for Au[259,316-319] and other[263] nanoparticles, Figure 37, and has been verified by QCM and other techniques. If a Au-colloid monolayer is exposed to a solution of a bisthiol, then the crosslinker assembles on the Au-surface, leaving thiol moieties at the nanostructure-solution interface. The assembly of a second colloid layer is then possible, and construction can be continued in the same way. This methodology allows some control over interparticle spacing by the use of bisthiols with spacers of various lengths,[316] and in turn, the interparticle spacing affects lattice properties such as conductivity.[320]

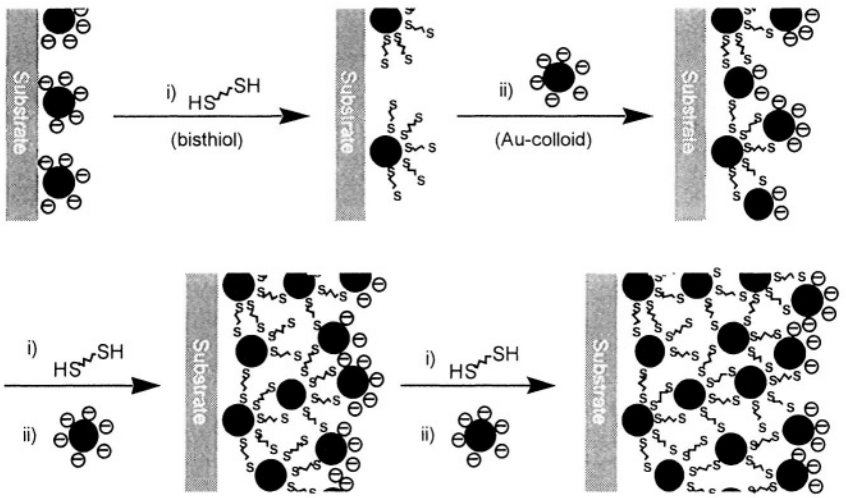

Figure 37. The construction of thiol-crosslinked multilayers of Au-nanoparticles.

The conditions required for assembly are very similar to those of electrostatic assembly, but this methodology has not yet been extended to the use of functionally interesting crosslinkers. It should be noted that reaction of the Au-surface with a thiol displaces the negatively charged citrate ions, leaving the thiolate-functionalized nanoparticle interface uncharged. As is seen in Figure 37 however, the charge remains at the colloid-solution interface, leaving a path open for the construction of composite covalent-ionic structures. 2-Mercaptoethylamine has been used as an interparticle crosslinker.[321] A novel strategy to prepare Au nanoparticles multilayers using 3-(mercaptopropyl)-trimethoxysilane as a linker molecule was demonstrated.[322] The nanostructure consists of alternative layers of ultrathin thiol-functionalized silica films and Au nanoparticles, Figure 38. A stepwise surface sol-gel process was used to prepare the thiol-functionalized silica matrix with included Au nanoparticle layers.

The characteristics of nanoparticle layers can be controlled by the conditions at which they are adsorbed. Polymer layers or molecular spacers between the nanoparticles can be of controllable thickness, isolating colloid layers from each other by whatever distance is required, and may also be conducting, semiconducting or insulating. Layered nanoparticle assemblies hold great promise for the construction of nanoscale electronic devices. Novel electrical and optical properties have been observed for metallic nanoparticles self-assembled in polymer-layered matrices. For example, a thin film electrostatically assembled by layer-by-layer deposition of negatively charged polyacrylic acid-capped Ag nanoparticles and positively charged poly(diallyldimethylammonium chloride) linker showed electroconductive properties and a reversible blue shift in the position of the surface plasmon resonance upon application of a negative potential of–1 V.[323] This shift originates from excess electrons. Strong inter-particle interactions could result in the formation of a new plasmon band whereas increase of the interparticle distances due to excessive amount of the polymer-linker results in gradual decrease of this band intensity and restoration of the spectrum typical for the non-aggregated nanoparticles.[324]

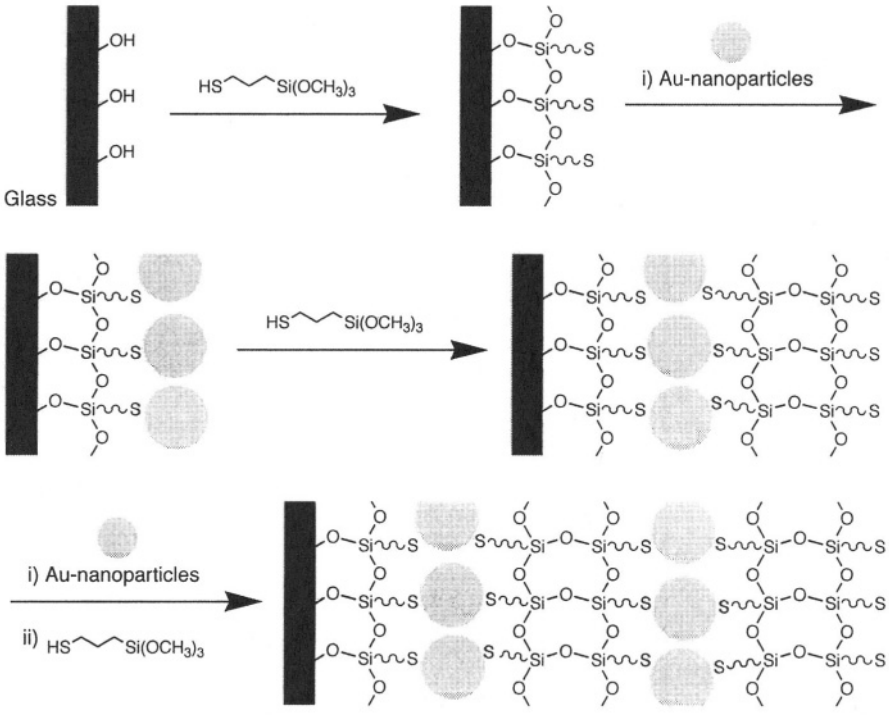

Figure 38. Method for the preparation of an alternate-layer silica and Au-nanoparticle nanostructure.

Thus, application of various metallic nanoparticles separated by controllable distances allows design of tunable optical filters. C_{60}-Mediated aggregation of Au-nanoparticles can be used for the C_{60}/Au-multilayer construction with unusual optical and electronic properties.[325] The origin of the binding interaction between gold particles and fullerene molecules is still unclear, but it has been suggested that it involves an electron transfer process between the organic and inorganic components of the array.

6.2. Patterning of Functionalized Metal Nanoparticles Arrays

The patterning of nanoparticle arrays is of paramount importance if these structures are to be used in nanoelectronic applications or to tailor addressable sensing domains. In recognition of this fact, methods for the patterning of nanoparticle-functionalized surfaces have been developed, which can broadly be categorized into three paradigms: lithography, microcontact printing and physical engineering.[42] The direct engineering of surfaces by scanning microscopic tools such as STM and AFM tips is intriguing but is far from a cheap industrial or general laboratory process. Nanoparticles have been electrodeposited,[326,327] "swept"[328-330] and even etched by CN^- at the touch of a scanning microscopy tip.[331] Au nanoparticles have been selectively deposited on a self-assembled monolayer surface, which had been already patterned with AFM electrochemical engraving lithography.[332,333] Even so, the construction of large devices is unfeasible, and even the manipulation of a single particle is currently seen as quite an achievement.

The pattern engineering of the nanoparticle monolayer after its formation has not been studied in any depth. This route would involve the construction of a nanoparticle monolayer and its subsequent patterning, for instance by scanning nanocapillaries filled with an "etching ink". In one example, a thin film of surfactant-covered Pd nanoparticles was patterned by an electron beam. In the exposed areas, the surfactant coating was removed from the particles, allowing them to agglomerate into solid metal. The remaining (unexposed) separate nanoparticles were then washed away to leave the metal pattern.[334]

Lithography provides a well-known route to patterned substrates, and a number of examples concerning nanoparticle systems are known. The most trivial of these relies on standard lithographic techniques to produce a PMMA pattern on a silica substrate.[335] The "windows" in the pattern can then be silanated and a nanoparticle layer assembled by the standard procedure, Figure 39(A). In other methods, substrates are functionalized so that they may adsorb colloids depending on their exposure to the lithographic medium. Figure 40(A) shows the photolithographic patterning of a thiol-surfaced substrate.[336,337] Irradiation at 254 nm under air oxidizes the exposed thiol moieties to sulfonates, which are unable to bind Au-nanoparticles. Subsequently, treatment of the photolithographed surface with an Au-nanoparticle solution results in colloids being immobilized only in the areas that have not been irradiated (as seen in Figure 39(B)). The system outlined in Figure 40(B) behaves in the opposite fashion.[338] An amine monolayer is protected with the photolabile nitroveratryloxycarbonyl (NVOC) group. Upon UV irradiation, the neutral NVOC-amines are photodeprotected, exposing the positively-charged amines. The nanoparticle pattern is generated by immersing the pattern-irradiated substrate in a solution of negatively-charged Au-nanoparticles, which adsorb only to the amine. This pattern of Au-nanoparticles can also be intensified by the construction of further layers of nanoparticles crosslinked by bisthiol molecules (the final pattern is shown in Figure 39(C)). Electron beam lithography on Langmuir-Blodgett films of alkanethiol-capped Au nanoparticles was shown to be a viable strategy to define nanoscale structures of such particles.[339] Sub-50 nm wide "nanowires", the thickness of which is controlled at the single particle level, were created with e-beam doses in the 0.8-6.0 $mC \cdot cm^{-2}$ range. It was shown that the patterns are formed by radiation-induced cross-linking of the alkyl chains.

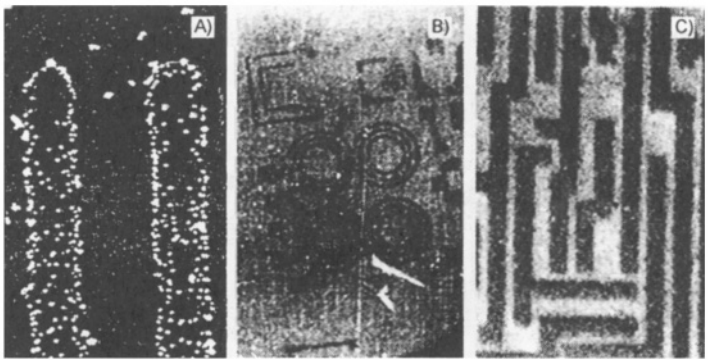

Figure 39. (A) A pattern of 20 nm Au-nanoparticles selectively adsorbed on amine-functionalized regions of the substrate. (B) SEM image of an Au-nanoparticle pattern assembled on non-irradiated areas of a thiol-functionalized substrate. (C) Optical microscope image of an Au-nanoparticle pattern assembled on the photodeprotected regions of a protected amine-functionalized substrate.

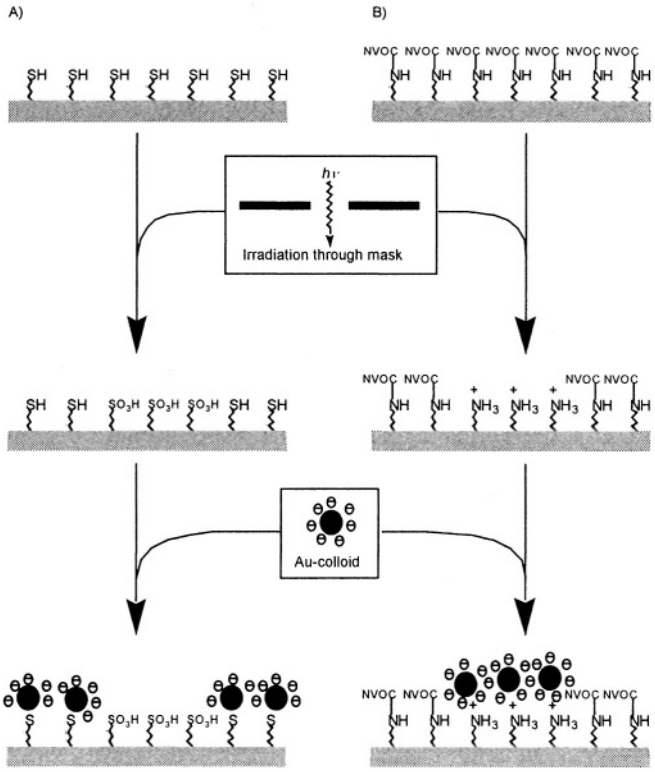

Figure 40. The construction of Au-nanoparticle patterns by irradiative patterning methods. (A) Nanoparticles only assemble on the non-irradiated parts of a thiol-surfaced substrate. (B) Nanoparticles only assemble on the irradiated parts of a NVOC-amine-surfaced substrate.

In another example an e-beam resulted in the crosslinking of a Langmuir-Blodgett organic matrix where metallic nanoparticles were dispersed,[340] thus resulting in the insolubility of the hydrocarbon matrix in organic solvents and in the impossibility of nanoparticle aggregation in the exposed regions. After immersion of the film into an organic solvent, the exposed areas remain insulating while conductive nanoparticle layers are formed in the nontreated zones due to removal of the matrix and particle aggregation. Ag nanoparticles were covered with a photosensitizing dye to stimulate their growth and aggregation upon irradiation with a laser or electron-beam.[341] This system allowed one-step "writing" on the surface yielding one-dimensional (1D), 2D, and 3D patterns of the aggregated Ag nanoparticles. Other lithographic methods have been used similarly, and the final nanoparticle pattern has been used for the deposition of other metals to create continuous metal patterns.[342-344]

Nanoparticle patterns have also been achieved by the process of microcontact printing, often as a means to construct other architectures.[345,346] This technique uses a microstructured "stamp" to form the nanoparticle pattern by one of two general routes, Figure 41. In one of the these routes, the stamp is used to introduce a pattern of functionality onto the substrate, which may be either specifically chosen or of the well-known hydrophobic/hydrophilic type, Figure 41 (A). Self-assembly of nanoparticles on the functionalized surface yields the colloid pattern.

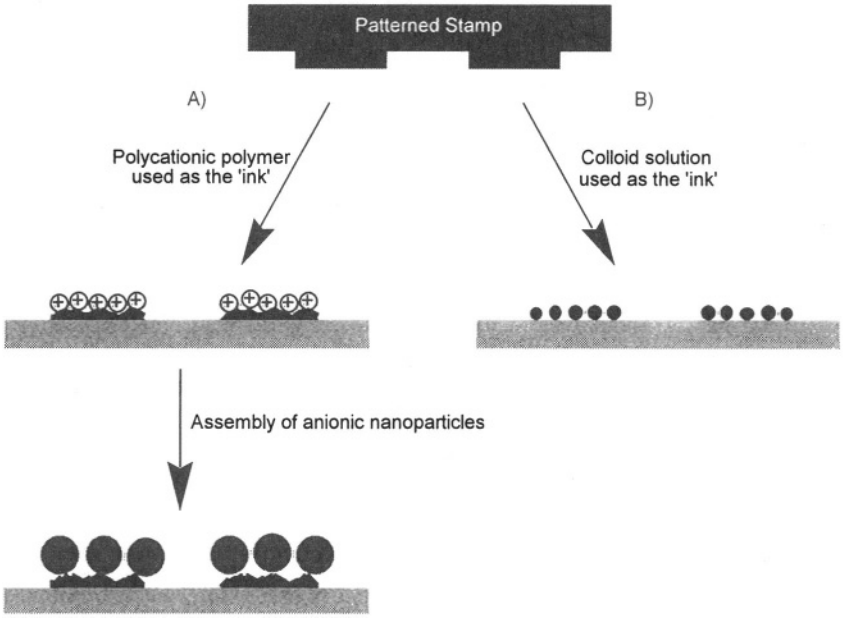

Figure 41. The construction of nanoparticle patterns by microcontact printing methods.

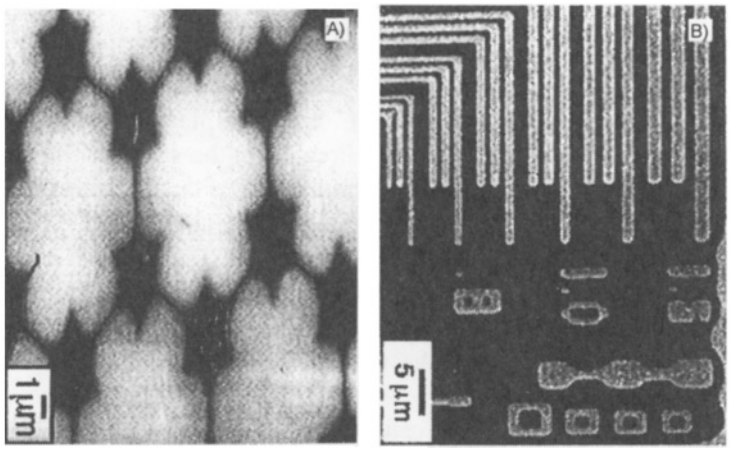

Figure 42. (A) A pattern of magnetite (dark areas) made by selective deposition on hydrophilic areas patterned by microcontact printing. (B) Microstructure generated on a glass substrate by microcontact printing with Pd-colloids, followed by the electroless deposition of copper.

Figure 42(A) shows a pattern generated by the evaporation of a nanoparticle solution which had selectively adsorbed to 2-mercaptoethanesulfonic acid-functionalized areas, leaving hexadecanethiol-functionalized areas bare.[346] This method was further modified by *in situ* formation of nanoparticles at the microprinted domains.[347] A silicon wafer was primarily microprinted with $C_{16}H_{33}SiCl_3$, resulting in the formation of a protecting hydrophobic layer with bare domains used to adsorb dendrimers that provide binding sites for Pd^{2+} ions, Figure 43.

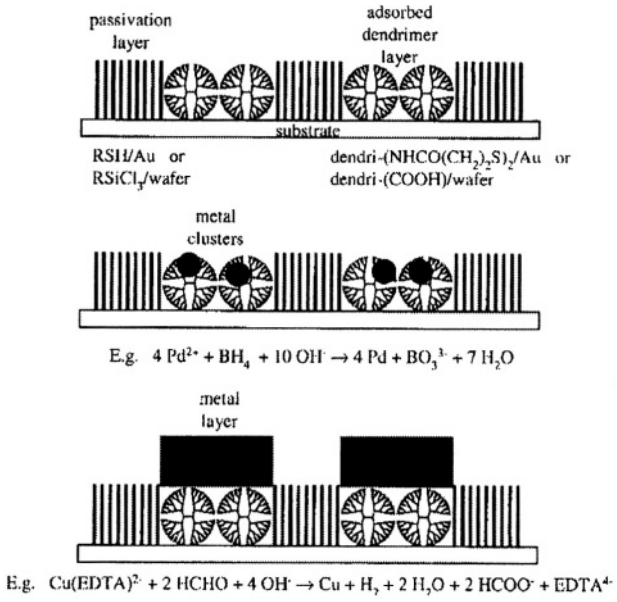

Figure 43. Creation of a pattern by means of microcontct printing of dendrimers and subsequent metallization.

Chemical reduction of the Pd^{2+} ions with BH_4^- yields Pd nanoparticles associated with dendrimer-covered domains of the surface. Catalytically-active Pd nanoparticles were further used for electroless deposition of copper as a continuous metal layer that follows the primary microprinted pattern. The other, simpler method is to use the stamp to introduce a nanoparticle-containing "ink" directly on the surface, Figure 41(B). In one such example, a pattern of palladium nanoparticles was deposited on a siloxane-functionalized substrate by means of a poly(dimethylsiloxane) (PDMS) stamp.[345] The nanoparticle domains were used to catalyze the electroless deposition of copper, forming a submicron-scale conductive pattern on the surface, which is shown in Figure 42(B). Similar direct microprinting of Ag nanoparticles onto a cystamine-functionalized gold support was also carried out.[348] The adhesion of the negatively charged citrate-stabilized Ag nanoparticles originates from their electrostatic attraction to the positively charged protonated cystamine monolayer. The resulting pattern was imaged by surface-enhanced Raman scattering (SERS) spectroscopy.

6.3. Sensoric Applications of Functionalized Metal Nanoparticles Arrays

The use of metal nanoparticle superstructures for the creation of electrochemical sensing devices is an extremely promising prospect. Multilayers of conductive nanoparticles give rise to a porous, high surface-area electrode, where the local microenvironment of the metallic nanoparticles can be controlled by the crosslinking elements and may lead to specific and selective interactions with substrates.[39,40,42]

6.3.1. Vapor Sensors

Chemiresistors are simple solid-state devices whose electrical resistance is changed by the presence of chemical species. The resistance of nanoparticle arrays depends on the colloid size, interparticle distance and dielectric properties of the interparticle material. An array consisting of Au nanoparticles stabilized with hydrophobic long-alkyl thiols is a medium that can accommodate organic materials such as hydrocarbons or halogen-hydrocarbons between the particles. Incorporation of the additional material can increase the interparticle distance and lower the medium dielectric permittivity, resulting in a decrease of the electrical resistance of the array. This approach was recently applied for the detection of toluene and tetrachloroethylene vapors, providing a detection threshold of ca. 1 ppm (v/v).[349] The device demonstrated high sensitivity to these low polarity materials being almost insensitive to materials with higher polarity (e.g. 1-propanol and water) at the same vapor pressure.

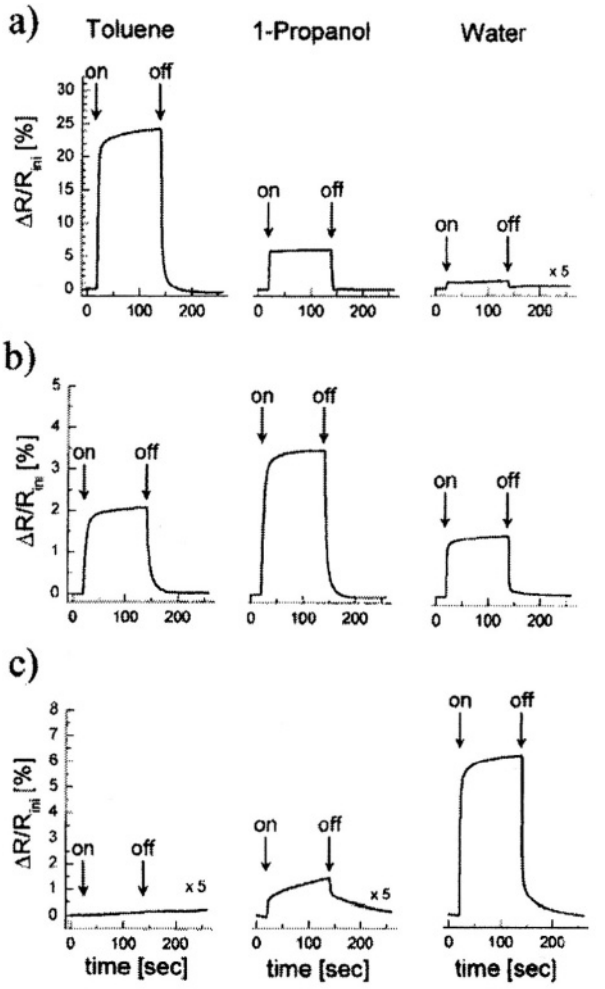

Figure 44. Responses of Au/dendrimer films to toluene, 1-propanol, and water: (a) Au/PPh; (b) Au/PPI; (c) Au/PAMAM (vapor concentration 5000 ppm_v).

The application of different kinds of metallic nanoparticles within various organic matrices, providing interactions with different vapors, allows the development of chemiresistors selectively sensitive to specific analyte molecules.[350,351] For example, Pd nanoparticles incorporated into a poly(*p*-xylylene) film demonstrated sensoric capability for NH_3 vapor.[352] Precise control of hydrophobicity/hydrophilicity of the matrix as well as control of the sizes of pores between the matrix chains would allow tuning of the chemiresistor selectivity.[353,354] This aim was achieved using Au-nanoparticles self-assembled with various dendrimer molecules.[355,356] Vapor-sensitive thin-film resistors comprising Au-nanoparticles and different types of organic dendrimers (polyphenylene, poly(propylene imine), and PAMAM) were prepared by layer-by-layer self-assembly. While the Au nanoparticles were utilized to provide the film material with electric conductivity, the dendrimers served to crosslink the nanoparticles and to provide sites for the selective absorption of analyte molecules. The dendrimers (with differing hydrophobicity/hydrophilicity) allowed the specific sensing of different analyte molecules, Figure 44. While the less polar polyphenylene dendrimers were more sensitive to toluene molecules, the most polar PAMAM dendrimers were more affected by water vapor.

Although chemiresistors are usually used for direct current measurements, the application of impedance spectroscopy could result in a better understanding of the physical mechanisms of the sensing phenomenon, i.e. finding which component of the resistance — faradaic or non-faradaic is mainly responsible for the resistance change.

6.3.2. Sensing by a Receptor-Crosslinked Array

A series of electrochemical sensors were built by the electrostatic crosslinking of Au nanoparticles with the bipyridinium cyclophanes **9** or **11**, or the oligocationic Pd(II)-ethylenediamine bipyridine square-type complex **12**,[41,298,309,311] Figure 45. The bipyridinium cyclophanes act as receptors for the association of π-donor substrates in their cavities and the 3D-conductivity of the Au nanoparticle array permits the electrochemical sensing of π-donor substrates associated with the cyclophane units. The formation of π-donor-acceptor complexes between the host-receptor and the π-donor analyte enables the preconcentration of the analyte at the conductive surface. Furthermore, control of the number of Au nanoparticle layers associated with the ITO electrode allows tuning of the sensor sensitivity. Figure 46(A) shows the electrochemical sensing of *p*-hydroquinone (**13**) at a bulk concentration corresponding to 1×10^{-5} M, by **9**-crosslinked Au-nanoparticle-functionalized electrodes consisting of different numbers of particle layers. The electrical responses of both the cyclophane (E°= –0.450 V vs. SCE) and the analyte increase with the number of layers, implying that the array must be porous. Figure 46(B) shows the calibration curve for the response of the 5-layer electrode to **13**. The electrochemical response of the electrode as indicated by the calibration curve is approximately linear within the concentration range examined, showing that the sensor is not easily saturated. The electrochemical sensing of the hydroquinone is possible at concentrations as low as 1×10^{-6} M. In contrast, within the concentration range of 10^{-5} – 10^{-6} M, it is electrochemically undetectable by a Au nanoparticle array crosslinked by the acyclic crosslinker *N,N'*-diaminoethyl-4,4'-bipyridinium (**10**).

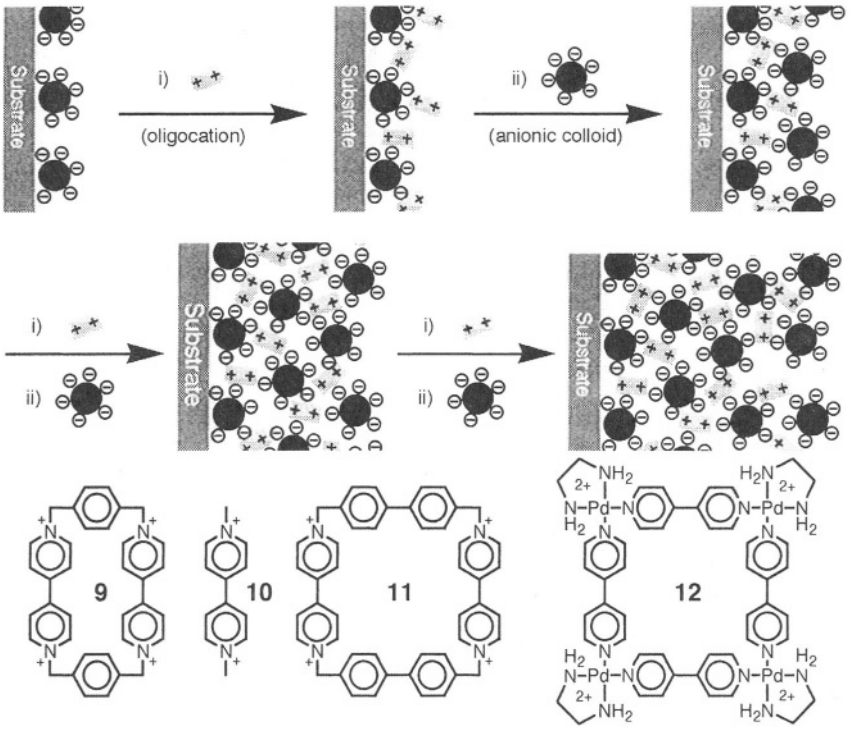

Figure 45. The construction of molecular oligocation — anionic colloid multilayers by the exploitation of electrostatic interactions and examples of some bipyridinium-based oligocations.

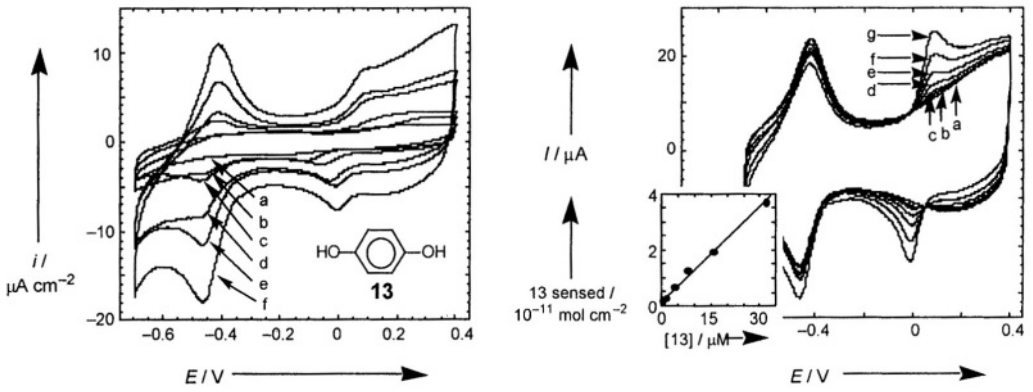

Figure 46. (A) Cyclic voltammograms of 1-5 layer **9**-Au-colloid arrays in the presence of hydroquinone (**13**) 1×10^{-5} M. (B) Cyclic voltammograms of the five layer electrode in various concentrations of **13**. Inset: Calibration curve corresponding to the electrochemical sensing of (**13**).

These observations clearly reveal that the successful sensing of **13** by the **9**-crosslinked superstructure originates from a specific host-guest interaction rather than from the fabrication of a roughened Au nanoparticle interface. In addition to the enhanced sensitivity in the analysis of **13** upon the growth of the layers, the electron transfer kinetics of the guest is vastly improved upon the build-up of the layers, as evidenced by the decrease in its peak-to-peak separation.

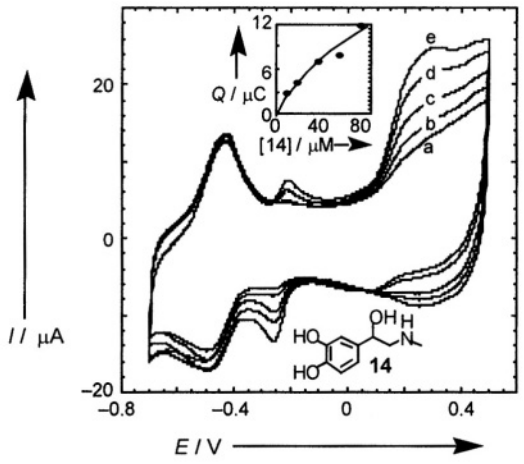

Figure 47. Cyclic voltammograms of a **9**-Au-colloid electrode in various concentrations of **14**. Inset: Calibration curve corresponding to the electrochemical sensing of **14**.

Other π-donor substrates such as dihydroxyphenyl acetic acid and the neurotransmitters adrenaline (**14**) and dopamine (**15**) can also be sensed by the **9**-crosslinked Au nanoparticle electrode.[41] These substrates contain π-donor *o*-hydroquinone units, but in addition include β-aminoalkyl substituents on the aromatic ring. Oxidation of the *ortho*-hydroquinone residue to the respective quinone is only partly reversible since the amine substituent induces a Michael-type ring-closure, bringing about a species that exhibits quasi-reversible electrochemical properties. Figure 47 shows the electrochemical sensing of different concentrations of adrenaline by an electrode consisting of five layers of **9**-crosslinked Au nanoparticles.[41] In addition to the cyclophane redox-wave, an irreversible oxidation wave for adrenaline is observed (0.3 V vs. SCE) as well as a quasi-reversible redox-wave at $E^{\circ} = -0.28$ V vs. SCE, corresponding to the electrochemically-induced cyclization product generated from the primary oxidized species. Coulometric assay of the quasi-reversible redox wave of the electrogenerated product enables the extraction of the respective calibration curve.

The selectivity of these Au-nanoparticle electrodes is controlled by the structure of the crosslinking receptor units. Application of the enlarged cyclophane **12** as crosslinker for the Au nanoparticles enables the electrochemical sensing of *bis*-dihydroxymethylferrocene (**15**), Figure 48(A), but not of **13**, due to its large cavity dimensions.[298] Likewise, the **11**-crosslinked Au-nanoparticle superstructure fails to sense **13** because of the small receptor dimensions that preclude the accommodation of the larger guest, Figure 48(B).

The Pd(II)-octacationic complex **12** enables the electrochemical sensing of both substrates since its cavity is large enough for the former, and the letter can associate with it in a diagonal orientation.[311] Lastly, the sensoric features of the cyclophane-colloid electrodes are affected by the lattice morphology. A Au-superstructure consisting of three layers of **9** crosslinked Au nanoparticles followed by three layers of **11**-crosslinked nanoparticles (the outer layers) enables the electrochemical sensing of both *p*-hydroquinone and *bis*-dihydroxymethylferrocene.

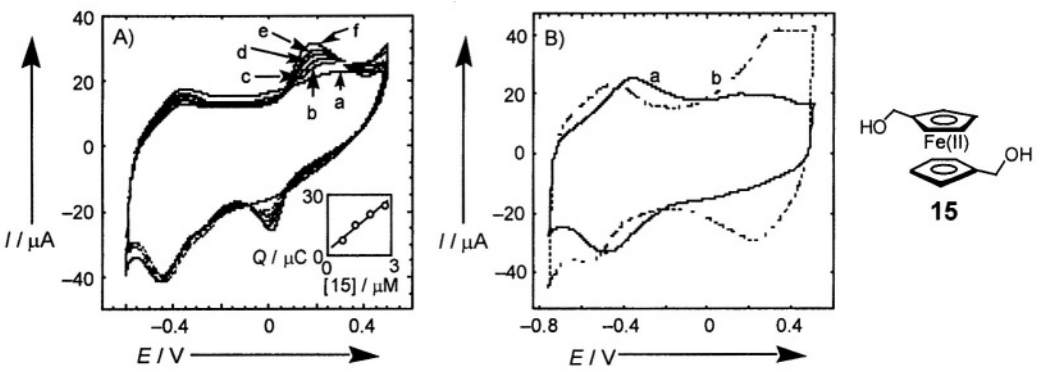

Figure 48. (A) Cyclic voltammograms of a **11**-crosslinked electrode in various concentrations of **15**. Inset: Calibration curve corresponding to the amperometric reponses of the electrode at different concentrations of **15**. (B) Cyclic voltammograms of electrodes crosslinked by **9** and **11** in the presence of **15** (1×10^{-6} M).

Conversely, an Au-nanoparticle composite electrode consisting of **11**-crosslinked Au nanoparticles followed by **9**-crosslinked Au nanoparticles, enables the electrochemical sensing of hydroquinone only.[298] This phenomenon has been attributed to the porosity control of the Au nanoparticle array by the receptor crosslinking units — the superstructure consisting of **11**-crosslinked Au nanoparticles is porous to **9**, but is impervious to the larger molecule **15**.

The receptor-based sensors described above are efficient in the concentration of the analyte at the substrate surface, but since the sensing is fundamentally electrochemical, the technique is limited to redox-active analytes. The same sensing principle can be used with a different sensing methodology however, allowing the analysis of non redox-active compounds. Ion-Sensitive Field-Effect Transistors (ISFETs) provide a means to detect charged species in close proximity to a gate surface. A charged species at the sensing interface of such a device causes a change in the polarization of the underlying SiO_2/Si interface (a thin layer of a non-conductive material on the sensing interface, e.g. GaAs, Al_2O_3, is often used to ensure insulation), Figure 49(A). The conductance of electrons from the source electrode to the drain electrode through the semiconductor is highly sensitive to this gate polarization (which has the effect of either attracting or repelling charge carriers). By measuring either (a) the source-drain current at a given gate-source potential (V_{gs}) or (b) the gate-source potential required for a given source-drain voltage (V_{sd}) and source-drain current (I_{sd}), it is possible to determine the polarization of the sensing interface.

An ISFET-based sensor for small π-donors was made by the fabrication of a Au nanoparticle-**9** assembly at the Al_2O_3 sensing interface of an ISFET,[243,244] Figure 49(A). This assembly was built up by the stepwise deposition of polyethyleneimine, Au nanoparticles and **9** on the sensing interface. The resulting sensor is able to detect any charged molecule that complexes the receptor, including those that are not electrochemically active, such as serotonin. Figure 49(B and C) shows the results from a study of adrenaline. Reliable data can be obtained over six orders of magnitude of concentration, and Benesi-Hildebrand analysis allows the calculation of a binding constant between **9** and adrenaline of $200\pm30\ M^{-1}$.

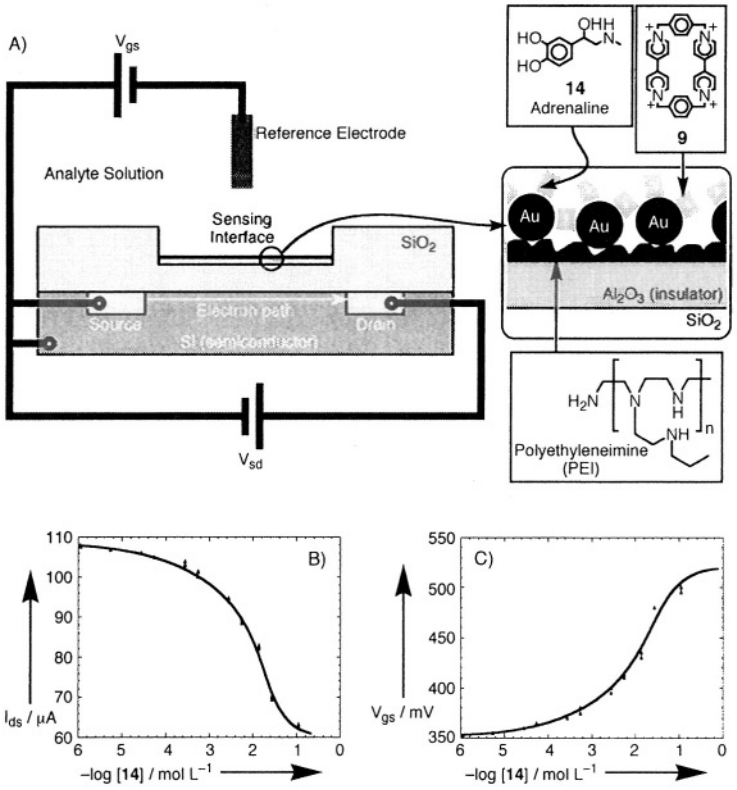

Figure 49. (A) Schematic diagram of an Au-nanoparticle/**9**-based ISFET sensor. (B) Results for the sensing of adrenaline (**14**) by the ISFET.

6.4. Photoelectrochemical Applications of Functionalized Metal Nanoparticles Arrays

The high surface area, porosity, and conductive properties of Au nanoparticle arrays can be exploited for the construction of photoelectrochemically active superstructures. Au-nanoparticles were functionalized with a mixed monolayer composed of a fullerene thiol derivative and dodecanethiol, Figure 27. The resulting C_{60}-functionalized Au-nanoparticles were self-assembled onto a Au electrode covered with SnO_2 nanoparticles, Figure 50(A). Figure 50(B), curve (a), shows the absorbance spectrum of the obtained photoelectrode, demonstrating significant absorption in the visible region with spectral features similar to those observed for the nanoparticle suspension in toluene. The modified electrode was irradiated in the presence of I_3^-/I redox couple dissolved in acetonitrile, generating a photoanodic current, Figure 50(B), curve (b). The system showed a steady photovoltage (ca. 150 mV) and short circuit photocurrent (130 $\mu A \cdot cm^{-2}$), that were reversibly switched on and off, Figure 50(B), inset. The observed photocurrent density was more than 2 orders of magnitude greater than that obtained from a fullerene self-assembled monolayer film on a plane Au surface.[357] The robust coverage and high surface area of the nanostructured C_{60}-Au assembly are the major factors that make the high photocurrent generation possible in the photoelectrochemical cell.

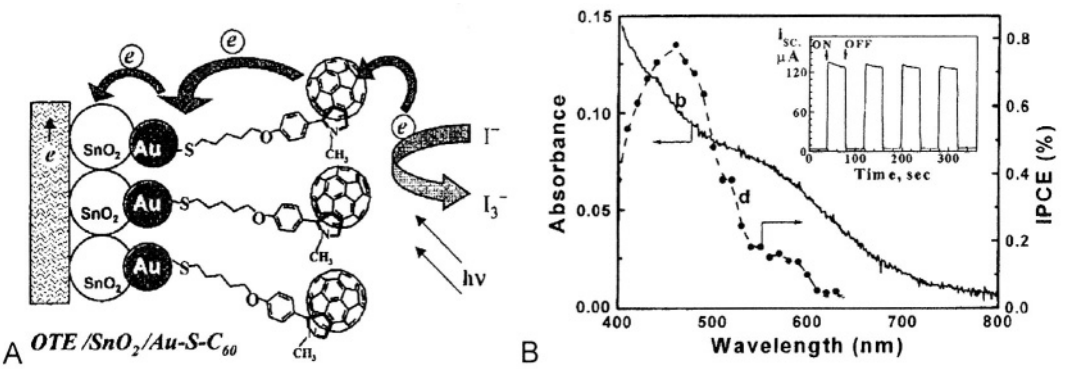

Figure 50. (A) Mechanism of photocurrent generation at a OTE/SnO_2/Au-S-C_{60} electrode. (B) Photocurrent action spectra of (b) OTE/SnO_2 and (d) OTE/SnO_2/Au-S-C_{60} electrodes The inset shows the photocurrent response to ON-OFF cycles of illumination (> 400 nm).

More sophisticated multi-component systems including chromophores and electron relays aligned in nanostructured aggregates can be envisaged.[358] Another photoelectrochemically active array was assembled by layer-by-layer deposition of Au nanoparticles crosslinked by chromophore-electron relay units.[39,40,359] Figure 51 (A and B) shows absorbance spectra and cyclic voltammograms of a gold nanoparticle multilayer architecture crosslinked by the hexacationic catenane **16**. This catenane consists of non-covalently bound ruthenium tris(bipyridine) (photosensitizer) and bipyridinium (electron acceptor) groups. The absorbance spectra show similar features to those of other molecule-crosslinked gold nanoparticle arrays, as well as an additional absorbance at 425 nm that is attributed to the ruthenium tris(bipyridinium) chromophore. Coulometric assay of the cyclic voltammograms corresponding to the bipyridinium crosslinking units reveals an almost linear increase in the surface coverage of the crosslinking units upon the build-up of the layers. The derived surface coverage of **16** per layer is 3.6×10^{-12} $mol\cdot cm^{-2}$, and it was estimated that on average ca. 45 units of the photosensitizer/electron acceptor crosslinker are associated with each Au nanoparticle.

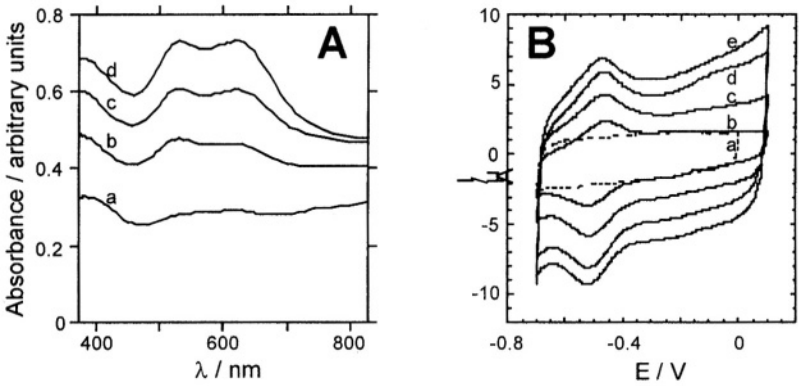

Figure 51. (A) Absorbance spectra of (a–d) 1–4 layer Au-nanoparticle superstructures crosslinked by the catenane **16**. (B) Cyclic voltammograms of (a–e) 0,1,3,4 and 5-layer **16**-crosslinked Au-nanoparticle arrays.

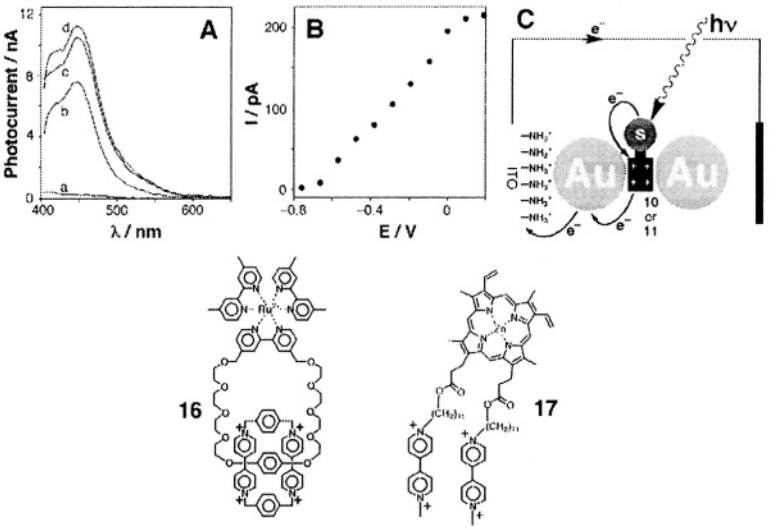

Figure 52. (A) Photocurrent action spectra (a–d) obtained from 0-, 1-, 3- and 4-layer **16**-crosslinked Au-nanoparticle arrays. (B) Dependance of the photocurrent on the electrode potential. (C) Mechanism for the generation of the photocurrent.

Irradiation of the nanoparticle multilayer array results in the photocurrent action spectra shown in Figure 52(A), which follow the absorbance features of the Ru(II)-tris(bipyridinium) chromophore. The photocurrent increases upon the build-up of the array and is reversibly cycled between "on" and "off" states upon switching the light on and off. Figure 52(B) shows the dependence of the photocurrent intensity on an applied potential. The photocurrent decreases as the potential is negatively shifted and it is blocked at a potential where the bipyridinium units are reduced to the radical cation. This observation led to the conclusion that the photocurrent originates from primary electron transfer quenching of the excited $Ru(II)^*$-tris(bipyridine) chromophore by the bipyridinium electron acceptor. The reduced acceptor acts as an electron mediator for charge injection into the electrode, Figure 52(C). Upon the electrochemical reduction of the bipyridinium units, intramolecular electron transfer quenching is inhibited and photocurrent generation is blocked. The nanoengineered electrode operated at a quantum efficiency of 1×10^{-4} in the generation of the photocurrent. A related electrode for photocurrent generation using Zn(II)-protoporphyrin IX-bis(bipyridinium) dyad (**17**) as a crosslinker was also developed.[310]

6.5. Functional Devices Based on Electronic Properties of Metal Nanoparticles Arrays

If metallic particles with a size of a few nanometers are arranged within ca. 1 nm of each other, they build tunnel junctions with electrical capacitances down to ca. 10^{-19} F.[4] This allows controlled charge transport between the particles by single electron tunneling (SET) events at room temperature, which has been recognized to be a fundamental requirement for the development of quantum electronics.[242] Charging energy (E_c) as well as capacitance depends on the size of the metallic nanoparticles and the distances

between them. The charging energy (i.e. the energy barrier that has to be overcome to transfer a single electron from an initially neutral cluster to a neutral nearest neighboring cluster) is dependent of the inter-particle capacitance C, as follows from Eq. (12), where *e* is the charge of electron.

$$E_c = \frac{e^2}{2C} \tag{12}$$

The use of interparticle spacers can be valuable in controlling capacitance. For instance, while the close packing of the $Pd_{561}phen_{36}O_{200}$ clusters gives a capacitance of 4.0×10^{-18} F, the insertion of 4,4'-diamino-1,2-diphenylethane spacers decreases it down to 1.6×10^{-18} F.[360] The electrical conductivity and capacitance of nanostructured materials have been studied using direct current (DC) measurements[4,360] and impedance spectroscopy.[361] Cyclic voltammetry performed at a single Au-nanoparticle contacted with an STM-tip has also been used to study single electron transfer processes.[362]

SET devices range from a single conductive nanoparticle located between two micro-electrodes[363-365] or contacted with an STM-tip[362,366] to 2D and 3D arrays.[201,366,367] Scanning tip-microscopy techniques can be used to observe SET-events and even to build-up the respective devices. For example, scanning tunneling spectroscopy (STS) has been applied for the observation of SET effects on nanoparticle monolayers of $Au_{55}(Ph_2C_6H_4SO_3H)Cl_6$ contacted with a tip, demonstrating "Coulomb staircase" behavior up to room temperature, where the capacitance of the cluster/substrate junction was calculated to be 3.9×10^{-19} F.[368] Similar results were obtained applying STS to self-assembled 1.8 nm-gold nanoparticles on a dithiol-modified Au surface.[366,369] A single-particle device was fabricated by AFM-assisted manipulation of a 20-nm sized Au nanoparticle between two metallic leads.[370] Two-dimensional lattices for SET devices can be prepared by self-assembly techniques.[371-373] Layer-by-layer assembly has been used for the construction of metal-insulator-nanoparticle-insulator-metal (MINIM) capacitors which demonstrate single electron transfer steps in the *i-V* curve (Coulomb staircase).[297]

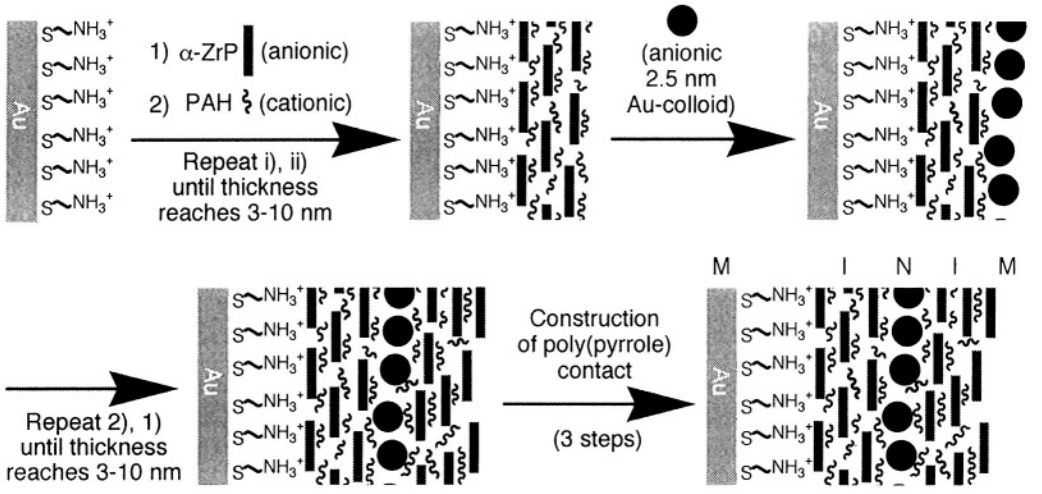

Figure 53. The stepwise construction of a 'MINIM' device.

These devices were made, Figure 53, by first priming the surface of a gold substrate with cysteamine. Insulating layers of α-$Zr(HPO_4)_2 \cdot H_2O$ (α-ZrP) and polyallylamine (PAH) hydrochloride were adsorbed (terminating in cationic substance) until the desired thickness was obtained (typically 30-100 Å) as measured by ellipsometry. Subsequently, citrate-stabilized gold particles (ca. 2.5 nm) were immobilized on top of the insulating layer. The remaining half of the double junction was constructed by simply reversing the adsorption sequence described. For a junction thickness of 80 Å and a particle radius of 1.25 nm, the capacitance of a double tunnel junction device calculated from Eq (13) (where μ_0 is the vacuum permittivity constant, μ is the dielectric constant of the insulator, r is the particle radius, and L is the junction thickness[374]) is 4.5 10^{-19} F. A Coulomb gap, e/C = 360 mV, should be observed at room temperature since it is substantially higher than kT.

$$C = 4\,\mu_0\mu_r\left[1 + \left(\frac{r}{2L}\right)\right] \tag{13}$$

A typical *i-V* curve for such a MINIM-structure is shown in Figure 54(A). The high impedance region is observed on both sides of 0 V and represents the average charging potential (± e/2 C) of each particle at the double junction array by a single electron. When enough energy is supplied to charge particles, electrons tunnel through the junction, resulting in the square-law dependence of the current rise on either side of the gap. Figure 54(B) shows the *i-V* behavior of a device of similar thickness in the absence of the gold particles. The linear curve typical for ohmic resistance is observed. In the next generation of single-electron devices,[375] "switchable" quantum dots and quantum channels with correlated electrons will provide us with components orders of magnitude smaller than classical electronic switches or semiconductor memory. This could result in a new generation of computers,[376] supersensitive electrometers, near-infrared receivers and very simple miniature lasers.[242]

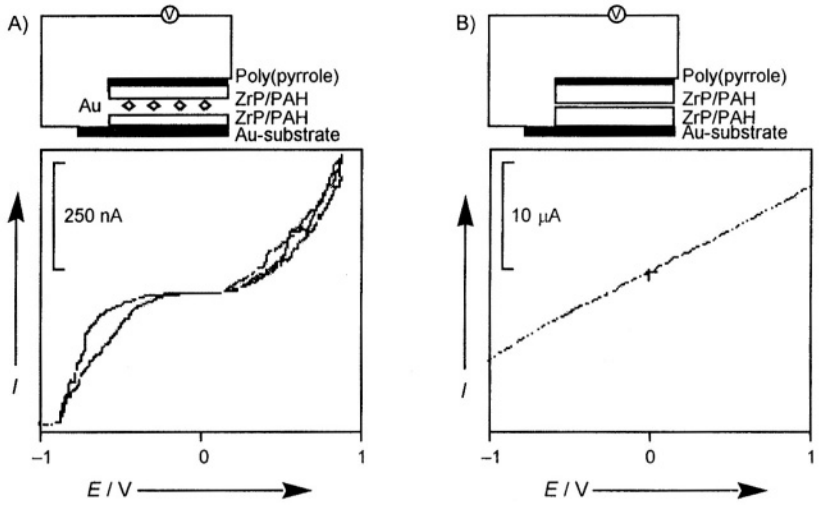

Figure 54. Current/voltage curves for the 'MINIM' device shown in Scheme 11. (A) *i-v* curve for the properly constructed 'MINIM' device. (B) *i-v* curve for a device without the nanoparticle layer.

Recently a single electron transistor was constructed using alkanedithiol-stabilized gold nanoparticles as tunnel junctions.[363,364] Three Au-colloidal particles (10 nm) were linked *via* 1,6-hexanedithiol, producing an Au-colloid-chain. The particle chain was formed on a SiO_2 substrate with source, drain and gate electrodes defined by electron beam lithography, Figure 55. The Au-colloid-chain bridged a 30 nm-gap between the source and drain, forming a single electron transistor with a multi-tunnel junction in the particle chain. Electron conduction through the chain exhibited a clear Coulomb staircase and the periodic conductance oscillation as a function of gate voltage. Gold nanoparticles capped with dissociating modifier molecules (Au/galvinol) provided pH-adjustable resistance for single electron transfer processes, even at only ca. 10 modifier molecules per Au-nanoparticle.[377] A redox-switchable electron tunneling device was produced by covalent attachment of a Au nanoparticle to a conductive support using *N,N'*-bipyridinium (18) as redox-active bridging units, Figure 56.[378] The nanoarchitecture embedded in an electrochemical cell allows the reduction of the bipyridinium units to the respective cation-radical by means of the bulk conductive support, and the reversible electrochemical oxidation of the cation-radical to the original *N,N'*-bipyridinium. The oxidized bipyridinium bridge was found to act as a barrier for electron tunneling from an STM tip to the electrode surface. Reduction of the bipyridinium units results in the occupation of the LUMO energy level and the formation of a hybrid electronic wave extending over the Au nanoparticle and the molecular bridging unit. This reduces the tunneling barrier and a high tunneling current is observed. Thus, by the cyclic reduction and oxidation of the redox units a gated tunneling current switched between "ON" and "OFF" states is generated, respectively. While single electron computing continues to be the ultimate goal of SET technology, its most advanced practical application is currently the construction of a super-sensitive electrometer. FET devices with nanoparticles in the gate have so far provided a charge sensitivity of 600 pA per gate electron.[242] This electrometer could be used as an extremely sensitive tool for the detection of the redox-state of a single molecule linked to the nanoparticle, thus allowing determination of single molecule chemical reactions.

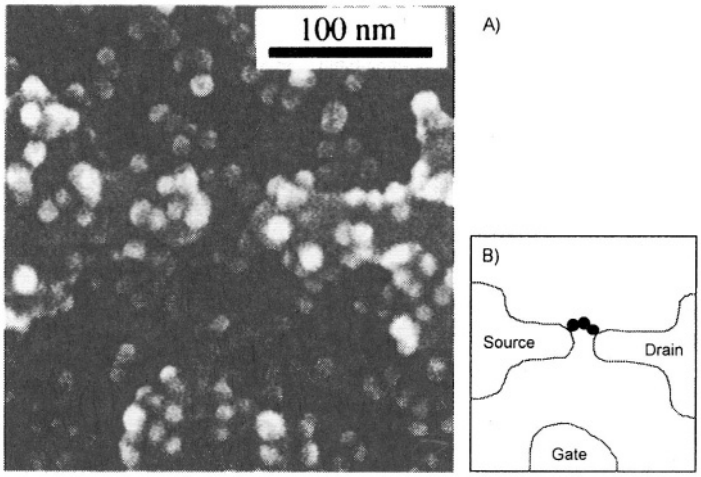

Figure 55. (A) An electron micrograph and (B) Schematic clarification of a three-nanoparticle bridge constructed between two electodes. The gate electrode is seen in the lower part of the mircograph.

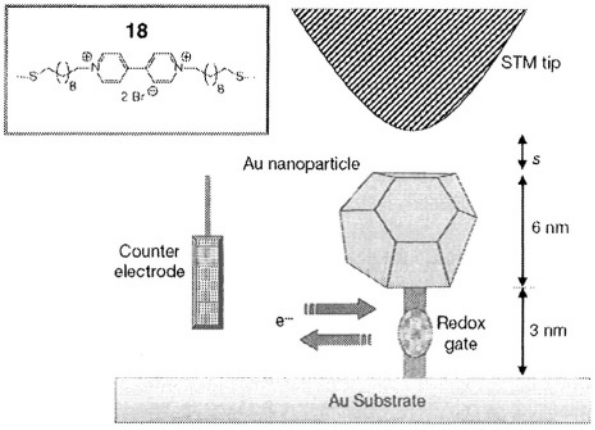

Figure 56. A switchable device based on a redox-molecule and a nanoparticle.

Combining many SET elements together for the development of computing devices remains challenging. It may not be an impossible task to make electrical connections to a single nano-transistor, but fabricating the billion-transistor network that is required for computing is currently a far-off dream, Two independent approaches to contact many SET-units have been suggested recently. The first approach involves the simple combination of SET-units with well-developed FET-devices, where a multi-gate FET-device is used and each gate is associated with a single SET-unit.

The second, more novel approach is to forgo the wires altogether.[379,380] This scheme, named quantum cellular automata (QCA), is based on the electrostatic interactions present between cells of connecting clusters.

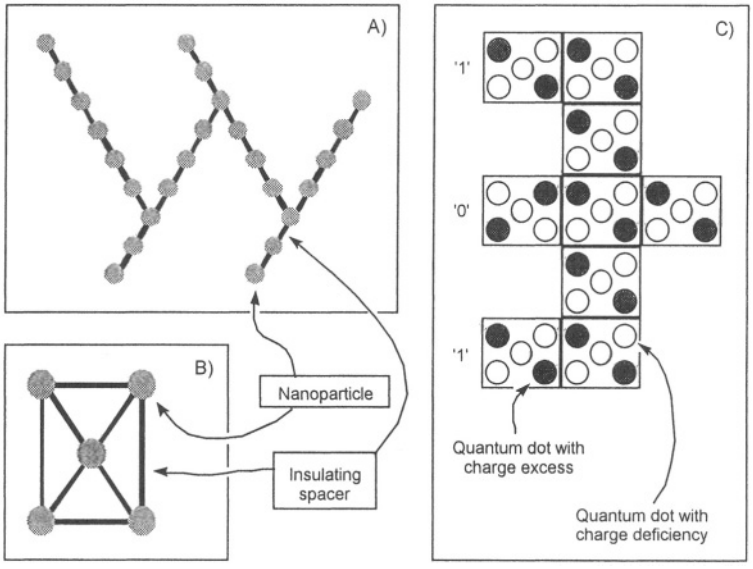

Figure 57. Schematic representations of proposed "wireless" computation devices based on nanoparticle assemblies.

In one possible design, the basic cell is a line of nanoclusters connected by insulating material, Figure 57(A). An electric field polarizes the string to give a "1" or "0" state, depending on the field direction. A similar design is produced from square cells of nanoclusters carrying the polarization states, Figure 57(B). Again, two states are possible depending upon the direction of the applied field. In either design the cells can be connected in various configurations to make more complex logic circuits. Figure 57(C) illustrates how the cells can be connected to form a logic gate. The dark and open circles correspond to one-electron rich and one-electron deficient clusters, respectively. The signals in QCA are rapidly transferred between interconnecting cells *via* electrostatic interactions at the speed of light. Fast inter-cell interactions and the small size of each cell (as low as ca. 2.5 nm^2) make the prospects of ultra-high density data storage and processing excellent from this kind of device.

7. CONCLUSIONS AND PERSPECTIVES

We have reviewed recent advances in the synthesis and applications of chemically-modified metal nanoparticle hybrid systems. Diverse synthetic methods are available to synthesize and functionalize metal nanoparticles of controlled sizes and shapes. The functional nanoparticles have enabled the preparation of organized two-dimensional and three-dimensional structures on surfaces. These architectures are generated by covalent bonds or supramolecular binding interactions between the functionalized particles and the respective surfaces or by interparticle linkage of particles that contain complementary functionalities. The functional nanoparticle hybrid systems reveal unique optical, electronic, catalytic, photonic and sensoric functions in solutions and upon their integration with electronic transducers.

The future perspectives of chemically-modified metal nanoparticles certainly lie in the area of functional nanodevices. The size-controlled capacitance properties of metal nanoparticles, the single-electron charging features of nanoparticles, the tunneling barriers introduced by chemical modification layers, and the ability to switch the electronic wave functions of capped metal nanoparticles by redox processes or photochemical reactions, yield new building units to nanoengineer functional smart devices. Numerous applications of such nanodevices in information storage and processing are envisaged. Different scanning microscopy techniques to manipulate and assemble nano-structures on surfaces exist. These include, for example, the lateral movement and positioning of nano-objects on surfaces by an AFM tip,[333] the chemical patterning of surfaces with nanoparticles using dip-pen lithography methods[332] and the nano-capillary delivery of chemical structures on surfaces. These provide invaluable tools for the future fabrication of nanodevices. To reach these goals, however, the development of means to connect and electronically communicate nanostructures is essential. Thus, the development of methods for interparticle circuitry and wiring is important. Preliminary studies have been reported on the generation of nanoparticle wires and circuits.[381, 382] Other approaches to wire nanostructures could involve the use of nanotubes of different compositions. The subject of developing nanodevices based on functional nanoparticles is at its infancy. It opens, however, challenging interdisciplinary problems where chemists, physicists and materials scientists will find exciting opportunities in the near future.

8. ACKNOWLEDGMENT

The support of our research on functional nanoparticle structures by the Israel Science Foundation and The U.S.-Israel Binational Science Foundation is gratefully acknowledged.

9. REFERENCES

1. L. N. Lewis, Chemical catalysis by colloids and clusters, *Chem. Rev.* **93**, 2693-2730 (1993).
2. M. Králik and A. Biffis, Catalysis by metal nanoparticles supported on functional organic polymers, *J. Mol. Catal. A* **177**, 113-138 (2001).
3. A. P. Alivisatos, Semiconductor clusters, nanocrystals, and quantum dots, *Science* **271**, 933-937 (1996).
4. D. L. Feldheim and C. D. Keating, Self-assembly of single electron transistors and related devices, *Chem. Soc. Rev.* **27**, 1-12(1998).
5. *Colloidal Gold: Principles, Methods, and Applications,* edited by M.A. Hayat (Academic Press, New York, 1989).
6. W. P. McConnell, J. P. Nowak, L. C. Brousseau, III, R. R. Fuierer, R. C. Tenent, and D. L. Feldheim, Electronic and optical properties of chemically modified metal nanoparticles and molecular bridged nanoparticle arrays, *J. Phys. Chem. B* **104**, 8925-8930 (2000).
7. T. Trindade, P. O'Brien, and N. L. Pickett, Nanocrystalline semiconductors: Synthesis, properties, and perspectives, *Chem. Mater.* **13**, 3843-3858 (2001).
8. K. Grieve, P. Mulvaney, and F. Grieser, Synthesis and electronic properties of semiconductor nanoparticles/quantum dots, *Curr. Opin. Colloid Inter. Sci.* **5**, 168-172 (2000).
9. J. M. Nedeljkovic, Nanoengineering of inorganic and hybrid composites, *Trends Adv. Mater. Processes Mater. Sci. Forum* **352**, 79-85 (2000).
10. S. C. Farmer and T. E. Patten, Photoluminescent polymer/quantum dot composite nanoparticles, *Chem. Mater.* **13**, 3920-3926(2001).
11. J. H. Hodak, A. Henglein, and G. V. Hartland, Tuning the spectral and temporal response in Pt/Au core-shell nanoparticles, *J. Chem. Phys.* **114**, 2760-2765 (2001).
12. M. P. Hughes, Dielectrophoretic behavior of latex nanospheres: Low-frequency dispersion, *J. Colloid Interface Sci.* **250**, 291-294 (2002).
13. X. J. Xu, P. Y. Chow, and L. M. Gan, Nanoparticles of latexes from commercial polystyrene, *J. Nanoscience Nanotechnol.* **2**, 61-65 (2002).
14. A. Henglein, Small-particle research – Physicochemical properties of exteremely small colloidal metal and semiconductor particles, *Chem. Rev.* **89**, 1861-1873 (1989).
15. G. D. Stucky and J. E. MacDougall, Quantum confinement and host guest chemistry – Probing a new dimension, *Science* **247**, 669-678 (1990).
16. G. C. Bond, The origins of particle size effects in heterogeneous catalysis, *Surf. Sci.* **156**, 966-981 (1985).
17. M. Brust and C. J. Kiely, Some recent advances in nanostructure preparation from gold and silver particles: a short topical review, *Colloid Surf. A* **202**, 175-186 (2002).
18. J. T. Lue, A review of characterization and physical property studies of metallic nanoparticles, *J. Phys. Chem. Solids* **62**, 1599-1612 (2001).
19, M. J. J. Jak, C. Konstapel, A. van Kreuningen, J. Verhoeven, R. van Gastel, and J. W. M. Frenken, Automated detection of particles, clusters and islands in scanning probe microscopy images, *Surf. Sci.* **494**, 43-52(2001).
20. H. Osman, J. Schmidt, K. Svensson, R. E. Palmer, Y. Shigeta, and J. P. Wilcoxon, STM studies of passivated Au nanocrystals immobilised on a passivated Au(111) surface: ordered arrays and single electron tunnelling, *Chem. Phys. Lett.* **330**, 1-6 (2000).
21. T. Tsirlin, J. Zhu, J. Grunes, and G. A. Somorjai, AFM and TEM studies of Pt nanoparticle arrays supported on alumina model catalyst prepared by electron beam lithography, *Topics Catal.* **19**, 165-170 (2002).
22. P. Mesquida and A. Stemmer, Guiding self-assembly with the tip of an atomic force microscope, *Scanning* **24**, 117-120(2002).
23. S. Takahashi, S. Machida, and K. Horie, Photochemistry in small domains and single polymer nanoparticles, *Macromol. Symp.* **175**, 299-308 (2001).

24. K. V. Sarathy, K. S. Narayan, J. Kim, and J. O. White, Novel fluorescence and morphological structures in gold nanoparticle-polyoctylthiophene based thin films, *Chem. Phys. Lett.* **318**, 543-548 (2000).
25. M. Jose-Yacaman, M. Marin-Almazo, J. A. Ascencio, High resolution TEM studies on palladium nanoparticles, *J. Mol. Catal. A* **173**, 61-74 (2001).
26. *Clusters and Colloids,* edited by G. Schmid (VCH, Weinheim, 1994).
27. H. Bönnemann and R. M. Richards, Nanoscopic metal particles – Synthetic methods and potential applications, *Eur. J. Inorg. Chem.,* 2455-2480 (2001).
28. G. Schmid, B. Morun, and J.-O. Malm, $Pt_{309}Phen_{36}{}^{*}O_{30\pm10}$, a four-shell platinum cluster, *Angew. Chem. Int. Ed. Engl.* **28**, 778-780 (1989).
29. M. Green and P. O'Brien, A simple one phase preparation of organically capped gold nanocrystals, *Chem. Commun.,* 183-184 (2000).
30. S. V. Manorama, K. M. Reddy, C. V. G. Reddy, S. Narayanan, P. R. Raja, and P. R. Chatterji, Photostabilization of dye on anatase titania nanoparticles by polymer capping, *J. Phys. Chem. Solids* **63**, 135-143 (2002).
31. Y. Zhou, H. Itoh, T. Uemura, K. Naka, and Y. Chujo, Preparation, optical spectroscopy, and electrochemical studies of novel π-conjugated polymer-protected stable PbS colloidal nanoparticles in a nonaqueous solution, *Langmuir* **18**, 5287-5292 (2002).
32. D. H. Cole, K. R. Shull, P. Baldo, and L. Rehn, Dynamic properties of a model polymer/metal nanocomposite: Gold particles in poly(tert-butyl acrylate), *Macromolecules* **32**, 771-777 (1999).
33. B. K. Paul and S. P. Moulik, Microemulsions: An overview, *J. Disper. Sci. Technol.* **18**, 301-367 (1997).
34. M. P. Pileni, J. Tanori, A. Filankembo, J. C. Dedieu, and T. Gulik-Krzywicki, Template design of microreactors with colloidal assemblies: Control the growth of copper metal rods, *Langmuir* **14**, 7359-7363 (1998).
35. M. J. Yacaman, J. A. Ascencio, H. B. Liu, and J. Gardea-Torresdey, Structure, shape and stability of nanometric sized particles, *J. Vac. Sci. Technol. B.* **19**, 1091-1103 (2001).
36. F. Caruso, Nanoengineering of particle surfaces, *Adv. Mater.* **13**, 11-22 (2001).
37. T. X. Wang, D. Q. Zhang, W. Xu, J. L. Yang, R. Han, and D. B. Zhu, reparation, characterization, and photophysical properties of alkanethiols with pyrene units-capped gold nanoparticles: Unusual fluorescence enhancement for the aged solutions of these gold nanoparticles, *Langmuir* **18**, 1840-1848 (2002).
38. A. Eychmuller, Structure and photophysics of semiconductor nanocrystals, *J. Phys. Chem. B* **104**, 6514-6528 (2000).
39. A. N. Shipway and I. Willner, Nanoparticles as structural and functional units in surface-confined architectures, *Chem. Commun.,* 2035-2045 (2001).
40. A. N. Shipway, M. Lahav, and I. Willner, Nanostructured gold colloid electrodes, *Adv. Mater.* **12**, 993-998 (2000).
41. M. Lahav, A. N. Shipway, and I. Willner, Au-nanoparticle-bis-bipyridinium cyclophane superstructures: assembly, characterization and sensoric applications, *J. Chem. Soc., Perkin Trans. 2,* 1925-1931 (1999).
42. A. N. Shipway, E. Katz, and I. Willner, Nanoparticle arrays on surfaces for electronic optical, and sensoric applications, *Chem. Phys. Chem.* **1**, 18-52 (2000).
43. C. M. Niemeyer, Nanoparticles, proteins, and nucleic acids: Biotechnology meets materials science, *Angew. Chem.* **40**, 4128-4158 (2001).
44. E. Katz, A. N. Shipway, and I. Willner, Biomaterial-nanoparticle hybrid systems: Synthesis, properties and applications, in: *Nanoparticles - From Theory to Applications,* edited by G. Schmid (Wiley-VCH, Weinheim), in press.
45. H. O. Finklea, Electrochemistry of organized monolayers of thiols and related molecules on electrodes, in: *Electroanalytical Chemistry,* edited by A. J. Bard and I. Rubinstein (Marcel Dekker, New York, 1996), Vol. 19, pp. 109-335.
46. J. Xu and H.-L. Li, The chemistry of self-assembled long-chain alkanethiol monolayers on gold, *J. Colloid Interface Sci.* **176**, 138-149 (1995).
47. M. Faraday, The Bakerian Lecture. - Experimental relations of gold (ans other metals) to light, *Philos. Trans. R. Soc. London* **147**, 145-181 (1857).
48. G. W. Stevens, J. M. Perera, and F. Grieser, Interfacial aspects of metal ion extraction in liquid-liquid systems, *Rev. Chem. Eng.* **17**, 87-110 (2001).
49. M. Brust, M. Walker, D. Bethell, D. J. Schiffrin, and R. Whyman, Synthesis of thiol-derivatised gold nanoparticles in a two-phase liquid-liquid system, *J. Chem. Soc. Chem. Commun.,* 801-802 (1994).
50. A. C. Templeton, W. P. Wuelfing, and R. W. Murray, Monolayer-Protected Cluster Molecules, *Acc. Chem. Res.* **33**, 27-36 (2000).

51. D. G. Duff, A. C. Curtis, P. P. Edwards, D. A. Jefferson, B. F. G. Johnson, A. I. Kirkland, and D. E. Logan, The morphology and microstructure of colloidal silver and gold, *Angew. Chem. Int. Ed. Engl.* **26**, 676-678 (1987).
52. J.-O. Bovin and J.-O. Malm, Atomic resolution electron-microscopy of small metal-clasters, *Z. Phys. D* **19**, 293-298 (1991).
53. R. C. Bell, K. A. Zemski, and A. W. Castleman, Gas-phase chemistry of vanadium oxide cluster cations. 3. Reactions with CCl_4, Jr., *J. Phys. Chem. A* **103**, 1585-1591 (1999).
54. M. J. Hostetler, J. J. Stokes, and R. W. Murray, Infrared spectroscopy of three-dimensional self-assembled monolayers: *N*-Alkanethiolate monolayers on gold cluster compounds, *Langmuir* **12**, 3604-3612 (1996).
55. C. S. Weisbecker, M. V. Merritt, and G. M. Whitesides, Molecular self-assembly of aliphatic thiols on gold colloids, *Langmuir* **12**, 3763-3772 (1996).
56. T. Yonezawa, S. Onoue, and N. Kimizuka, Formation of uniform fluorinated gold nanoparticles and their highly ordered hexagonally packed monolayer, *Langmuir* **17**, 2291-2293 (2001).
57. M. Moreno-Mañas, R. Pieixats, and S. Villarroya, Palladium nanoparticles stabilizd by polyfluorinated chains, *Chem. Commun.,* 60-61 (2002).
58. R. H. Terrill, T. A. Postiethwaite, C.-H. Chen, C.-D. Poon, A. Terzis, A. Chen, J. E. Hutchison, M. R. Clark, G. Wignall, J. D. Londono, R. Superfine, M. Falvo, C. S. Johnson, Jr., E. T. Samulski, and R. W. Murray, Monolayers in three dimensions: NMR, SAXS, thermal, and electron hopping studies of alkanethiol stabilized gold clusters, *J. Am. Chem. Soc.* **117**, 12537-12548 (1995).
59. A. Badia, L. Cuccia, L. Demers, F. Morin, and R. B. Lennox, Structure and dynamics in alkanethiolate monolayers self-assembled on gold nanoparticles: A DSC, FT-IR, and deuterium NMR study, *J. Am. Chem. Soc.* **119**, 2682-2692 (1997).
60. A. Badia, S. Singh, L. Demers, L. Cuccia, G. R. Brown, and R. B. Lennox, Self-assembled monolayers on gold nanoparticles, *Chem. Eur. J.* **2**, 359-363 (1996).
61. A. Badia, W. Gao, S. Singh, L. Demers, L. Cuccia, and L. Reven, Structure and chain dynamics of alkanethiol-capped gold colloids, *Langmuir* **12**, 1262-1269 (1996).
62. F. P. Zamborini, S. M. Gross, and R. W. Murray, Synthesis, characterization, reactivity, and electrochemistry of palladium monolayer protected clusters, *Langmuir* **17**, 481-488 (2001).
63. W. D. Luedtke and U. Landman, Structure and thermodynamics of self-assembled monolayers on gold nanocrystallites, *J. Phys. Chem. B* **102**, 6566-6572 (1998).
64. I. Quiros, M. Yamada, K. Kubo, J. Mitzutani, M. Kurihara, and H. Nishihara, Preparetion of alkanethiolate-protected palladium nanoparticles and their size dependence on synthetic conditions, *Langmuir* **18**, 1413-1418 (2002).
65. K. V. Sarathy, G. U. Kulkarni, and C. N. R. Rao, A novel method of preparing thiol-derivatised nanoparticles of gold, platinum and silver forming superstructures, *Chem. Commun.,* 537-538 (1997).
66. S. Chen and R. W. Murray, Arenethiolate monolayer-protected gold clusters, *Langmuir* **15**, 682-689 (1999).
67. S. R. Johnson, S. D. Evans, S. W. Mahon, and A. Ulman, Alkanethiol molecules containing an aromatic moiety self-assembled onto gold clusters, *Langmuir* **13**, 51-57 (1997).
68. L. A. Porter, Jr., D. Ji, S. L. Westcott, M. Graupe, R. S. Czernuszewcz, N. J. Halas, and T. R. Lee, Gold and silver nanoparticles functionalized by the adsorption of dialkyl disulfides, *Langmuir* **14**, 7378-7386 (1998).
69. T. Yonezawa, K. Yasui, and N. Kimizuka, Controlled formation of smaller gold nanoparticles by the use of four-chained disulfide stabilizer, *Langmuir* **17**, 271-273 (2001).
70. A. Badia, L. Demers, L. Dickinson, F. G. Morin, R. B. Lennox, and L. Reven, Gold-sulfur interactions in alkylthiol self-assembled monolayers formed on gold nanoparticles studied by solid-state NMR, *J. Am. Chem. Soc.* **119**, 11104-11105 (1997).
71. M. Wu, S. A. O'Neill, L. C. Brousseau, W. P. McConnell, D. A. Shultz, R. J. Linderman, and D. L. Feldheim, Synthesis of nanometer-sized hollow polymer capsules from alkanethiol-coated gold particles, *Chem. Commun.,* 775-776 (2000).
72. M. Brust, N. Stuhr-Hansen, K. Nørgaard, J. B. Christensen, L. K. Nielsen, and T. Bjørnholm, Langmuir-Blodgett films of alkane chalcogenide (S, Se, Te) stabilized gold nanoparticles, *Nano Lett.* **1**, 189-191 (2001).
73. M. Brust, J. Fink, D. Bethell, D. J. Schiffrin, and C. Kiely, Synthesis and reactions of functionalized gold nanoparticles, *J. Chem. Soc. Chem. Commun.,* 1655-1666 (1995).
74. S. R. Johnson, S. D. Evans, and R. Brydson, Influence of a terminal functionality on the physical properties of surfactant-stabilized gold nanoparticles, *Langmuir* **14**, 6639-6647 (1998).
75. K. S. Mayya, V. Patil, and M. Sastry, On the stability of carboxylic acid derivatized gold colloidal particles: The role of colloidal solution pH studied by optical absorption spectroscopy, *Langmuir* **13**, 3944-3947 (1997).

76. S. Chen and K. Kimura, Synthesis and characterization of carboxylate-modified gold nanoparticle powders dispersible in water, *Langmuir* **15**, 1075-1082 (1999).
77. M. Sastry, K. S. Mayya, and K. Bandyopadhyay, pH Dependent changes in the optical properties of carboxylic acid derivatized silver colloidal particles, *Colloids Surf. A* **127**, 221-228 (1997).
78. A. Kumar, A. B. Mandale, and M. Sastry, Sequential electrostatic assembly of amine-derivatized silver colloidal particles on glass substrates, *Langmuir* **16**, 6921-6926 (2000).
79. Y.-S. Shon, W. P. Wuelfing, and R. W. Murray, Water-soluble, sulfonic acid-functionalized, monolayer-protected nanoparticles and an ionically conductive molten salt containing them, *Langmuir* **17**, 1255-1261 (2001).
80. N. Sandhyarani and T. Pradeep, 2-Mercaptobenzothiazole protected Au and Ag clusters, *J. Mater. Chem.* **10**, 981-986 (2000).
81. A. C. Templeton, S. Chen, S. M. Gross, and R. W. Murray, Water-soluble, isolable gold clusters protected by tiopronin and coenzyme A monolayers, *Langmuir* **15**, 66-76 (1999).
82. A. C. Templeton, D. E. Cliffel, and R. W. Murray, Redox and fluorophore functionalization of water-soluble, tiopronin-protected gold clusters, *J. Am. Chem. Soc.* **121**, 7081-7089 (1999).
83. S. Mandal, A. Gole, N. Lala, R. Gonnade, V. Ganvir, and M. Sastry, Studies on the reversible aggregation of cysteine-capped colloidal silver particles interconnected via hydrogen bonds, *Langmuir* **17**, 6262-6268 (2001).
84. T. G. Schaaff, G. Knight, M. N. Shafigullin, R. F. Borkman, and R. L. Whetten, Isolation and selected properties of a 10.4 kDa gold-glutathione cluster compound, *J. Phys. Chem. B* **102**, 10643-10646 (1998).
85. S. Link, A. Beeby, S. Fritz-Gerald, M. A. El-Sayed, T. G. Schaaff, and R. L. Whetten, Visible to infrared luminescence from a 28-atom gold cluster, *J. Phys. Chem. B* **106**, 3410-3415 (2002).
86. J. Simard, C. Briggs, A. K. Boal, and V. M. Rotello, Formation and pH-controlled assembly of amphiphilic gold nanoparticles, *Chem. Commun.,* 1943-1944 (2000).
87. M. A. Bryant and R. M. Crooks, Determination of surface pK_a values of surface-confined molecules derivatized with pH-sensitive pendant groups, *Langmuir* **9**, 385-387 (1993).
88. J. Zhao, L. Luo, X. Yang, E. Wang, and S. Dong, Determination of surface pK_a of SAM using an electrochemical titration method, *Electroanalysis* **11**, 1108-1111 (1999).
89. A. K. Boal and V. M. Rotello, Intra- and Intermonolayer hydrogen bonding in amide-functionalized alkanethiol self-assembled monolayers on gold nanoparticles, *Langmuir* **16**, 9527-9532 (2000).
90. S. E. Creager and J. Clarke, Contact-angle titrations of mixed ω-mercaptoalkanoic acid/alkanethiol monolayers on gold. Reactive vs. nonreactive spreading, and chain length effects on surface pK_a values, *Langmuir* **10**, 3675-3683 (1994).
91. R. Paulini, B. L. Frankamp, and V. M. Rotello, Effects of branched ligands on the structure and stability of monolayers on gold nanoparticles, *Langmuir* **18**, 2368-2373 (2002).
92. M. J. Hostetler, A. C. Templeton, and R. W. Murray, Dynamics of place-exchange reactions on monolayer-protected gold cluster molecules, *Langmuir* **15**, 3782-3789 (1999).
93. M. J. Hostetler, S. J. Green, J. J. Stokes, and R. W. Murray, Monolayers in three dimensions: Synthesis and electrochemislry of ω-functionalized alkanethiolate-stabilized gold cluster compounds, *J. Am. Chem. Soc.* **118**, 4212-4213(1996).
94. R. S. Ingram, M. J. Hostetler, and R. W. Murray, Poly-hetero-ω-functionalized alkanethiolate-stabilized gold cluster compounds, *J. Am. Chem. Soc.* **119**, 9175-9178 (1997).
95. A. C. Templeton, M. J. Hostetler, C. T. Kraft, and R. W. Murray, Reactivity of monolayer-protected gold cluster molecules: Steric effects, *J. Am. Chem. Soc.* **120**, 1906-1911 (1998).
96. A. C. Templeton, M.J. Hostetler, E.K. Warmoth, S. Chen, C. M. Hartshorn, V. M. Krishnamurthy, M. D. E. Forbes, and R. W. Murray, Gateway reactions to diverse, polyfunctional monolayer-protected gold clusters, *J. Am. Chem. Soc.* **120**, 4845-4849 (1998).
97. D. Bethell, M. Schiffrin, D. J. Schiffrin, and C. Kiely, From monolayers to nanostructured materials: An organic chemist's view of self-assembly, *J. Electroanal. Chem.* **409**, 137-143 (1996).
98. D. M. Collard and M. A. Fox, Use of electroactive thiols to study the formation and exchange of alkanethiol monolayers on gold, *Langmuir* **7**, 1192-1197 (1991).
99. C. E. D. Chidsey, C. R. Bertozzi, T. M. Putvinski, and A. M. Mujsce, Coadsorption of ferrocene-terminated and unsubstituted alkanethiols on gold: electroactive self-assembled monolayers, *J. Am. Chem. Soc.* **112**, 4301-4306(1990).
100. E. Katz and A. A. Solov'ev, Chemical modification of platinum and gold electrodes by naphthoquinones using amines containing sulfhydryl or disulfide groups, *J. Electroanal. Chem.* **291**, 171-186 (1990).
101. Y. Song and R. W. Murray, Dynamics and extent of ligand exchange depend on electronic charge of metal nanoparticles, *J. Am. Chem. Soc.* **124**, 7096-7102 (2002).
102. K. S. Mayya and M. Sastry, Intercolloidal particle monolayer transfer in mixed metal colloids, *Langmuir* **14**, 6344-6346 (1998).

103. N. Herron and D. L. Thorn, Nanoparticles: uses and relationships to molecular cluster compounds, *Adv. Mater.* **10**, 1173-1184 (1998).
104. J. F. Ciebien, R. T. Clay, B. H. Sohn, and R. E. Cohen, Brief review of metal nanoclusters in block copolymer films, New J. Chem. **22**, 685-691 (1998).
105. R. Gangopadhyay and A. De, Conducting polymer nanocomposites: A brief overview, *Chem. Mater.* **12**, 608-622 (2000).
106. K. J. Klabunde, J. Habdas and G. Cadenas-Trivino, Colloidal metal particles dispersed in monomeric and polymeric styrene and methyl methacrylate, *Chem. Mater.* **1**, 481-483 (1989).
107. M. S. El-Shall and W. Slack, Ultrafine metal particles in polymers and the formation of periodic polymer stripes, *Macromolecules* **28**, 8456-8458 (1995).
108. J. H. Golden, H. Deng, F. J. DiSalvo, J. M. J. Frechet, and P. M. Thompson, Monodisperse metal-clusters 10-Angstroms in diameter in a polymeric host – the monomer-as-solvent approach, *Science* **268**, 1463-1466(1995).
109. L. Quaroni and G. Chumanov, Preparation of polymer-coated functionalized silver nanoparticles, *J. Am. Chem. Soc,* **121**, 10642-10643 (1999).
110. C. Johans, J. Clohessy, S. Fantini, K. Kontturi, and V.J. Cunnane, Electrosynthesis of polyphenylpyrrole coated silver particles at a liquid-liquid interface, *Electrochem. Commun.* **4**, 227-230 (2002).
111. J. J. Watkins and T. J. McCarthy, Polymer/metal nanocomposite synthesis in supercritical CO_2, *Chem. Mater.* **7**, 1991-1994(1995).
112. T. K. Sarma, D. Chowdhury, A. Paul, and A. Chattopadhyay, Synthesis of Au nanoparticle-conductive polyaniline composite using H_2O_2 as oxidizing as well as reducing agent, *Chem. Commun.,* 1048-1049 (2002).
113. B. Corain and M. Kralik, Generating palladium nanoclusters inside functional cross-linked polymer frameworks, *J. Molec. Catal. A* **173**, 99-115 (2001).
114. I. Pastoriza-Santos and L. M. Liz-Marzán, Formation of PVP-protected metal nanoparticles in DMF, *Langmuir* **18**, 2888-2894 (2002).
115. Y. Zhou, H. Itoh, T. Uemura, K. Naka, and Y. Chujo, Preparation of π-conjugated polymer-protected gold nanoparticles in stable colloidal form, *Chem. Commun.,* 613-614 (2001).
116. R. T. Clay and R. E. Cohen, Synthesis of metal nanoclusters within microphase-separated diblock copolymers: ICP-AES analysis of metal ion uptake, *Supramol. Sci.* **4**, 113-119 (1997).
117. Y. N. C. Chan, R. R. Schrock, and R. E. Cohen, Synthesis of silver and gold nanoclusters within microphase-separated diblock copolymers, *Chem. Mater.* **4**, 24-27 (1992).
118. Y. N. C. Chan, R. R. Schrock, and R. E. Cohen, Synthesis of single silver nanoclusters within spherical microdomains in block copolymer films, *J. Am. Chem. Soc.* **114**, 7295-7296 (1992).
119. M. Moffitt and A. Eisenberg, Scaling relations and size control of block ionomer microreactors containing different metal ions, *Macromolecules* **30**, 4363-4373 (1997).
120. Y. N. C. Chan, G. S. W. Craig, R. R. Schrock, and R. E. Cohen, Synthesis of palladium and platinum nanoclusters within microphase-separated diblock copolymers, *Chem. Mater.* **4**, 885-894 (1992).
121. S. T. Selvan, Novel nanostructures of gold-polypyrrole composites, *Chem. Commun.,* 351-352 (1998).
122. S. T. Selvan, J. P. Spatz, H. A. Klok, and M. Moller, Gold-polypyrrole core-shell particles in diblock copolymer micelles, *Adv. Mater.* **10**, 132-134(1998).
123. W. P. Wuelfing, S. M. Gross, D. T. Miles, and R. W. Murray, Nanometer gold clusters protected by surface-bound monolayers of thiolated poly(ethylene glycol) polymer electrolyte, *J. Am. Chem. Soc.* **120**, 12696-12697(1998).
124. C. Mangeney, F. Ferrage, I. Aujard, V. Marchi-Artzner, L. Jullien, O. Ouari, E. D. Rékai, A. Laschewsky, I. Vikholm, and J.W. Sadowski, Synthesis and properties of water-soluble gold colloids covalently derivatized with neutral polymer monolayers, *J. Am. Chem. Soc.* **124**, 5811-5821 (2002).
125. S. Nuß, H. Böttcher, H. Wurm, and M. L. Hallensleben, Gold nanoparticles with covalently attached polymer chains, *Angew. Chem. Int. Ed.* **40**, 4016-4018 (2001).
126. T. K. Mandal, M. S. Fleming, and D. R. Walt, Preparation of polymer coated gold nanoparticles by surface-confined living radical polymerization at ambient temperature, *Nano Lett.* **2**, 3-7 (2002).
127. P. A. Buining, B. M. Humbel, A. P. Philipse, and A. J. Verkleij, Preparation of functional silane-stabilized gold colloids in the (sub)nanometer size range, *Langmuir* **13**, 3921-3926 (1997).
128. D. I. Gittins and F. Caruso, Tailoring the polyelectrolyte coating of metal nanoparticles, *J. Phys. Chem. B* **105**, 6846-6852 (2001).
129. K. Esumi, A. Kameo, A. Suzuki, and K. Torigoe, Preparation of gold nanoparticles in formamide and N,N-dimethylformamide in the presence of poly(amidoamine) dendrimers with surface methyl ester groups. *Colloids Surf. A* **189**, 155-161 (2001).
130. E. Esumi, A. Suzuki, N. Aihara, K, Usui, and K. Torigoe, Preparation of gold colloids with UV irradiation using dendrimers as stabilizer, *Langmuir* **14**, 3157-3159 (1998).

131. M. E. Garcia, L. A. Baker, and R. M. Crooks, Preparation and characterization of dendrimer-gold colloid nanocomposites, *Anal. Chem.* **71**, 256-258 (1999).
132. M. Zhao and R. M. Crooks, Homogeneous hydrogenation catalysis with monodisperse, dendrimer-encapsulated Pd and Pt nanoparticles, *Angew. Chem. Int. Ed.* **38**, 364-366 (1999).
133. M. Zhao and R. M. Crooks, Dendrimer-encapsulated Pt nanoparticles: Synthesis, characterization, and applications to catalysis, *Adv. Mater.* **11**, 217-220 (1999).
134. V. Chechik, M. Zhao and R. M. Crooks, Self-assembled inverted micelles prepared from a dendrimer template: Phase transfer of encapsulated guests, *J. Am. Chem. Soc.* **121**, 4910-4911 (1999).
135. M. Zhao and R. M. Crooks, Intradendrimer exchange of metal nanoparticles, *Chem. Mater.* **11**, 3379-3385 (1999).
136. K. Esumi, T. Hosoya, A. Suzuki, and K. Torigoe, Spontaneous formation of gold nanoparticles in aqueous solution of sugar-persubstituted poly(amidoamine) dendrimers, *Langmuir* **16**, 2978-2980 (2000).
137. K. Esumi, A. Suzuki, A. Yamahira, and K. Torigoe, Role of poly(amidoamine) dendrimers for preparing nanoparticles of gold, platinum, and silver, *Langmuir* **16**, 2604-2608 (2000).
138. K. Esumi, R. Nakamura, A. Suzuki, and K. Torigoe, Preparation of platinum nanoparticles in ethyl acetate in the presence of poly(amidoamine) dendrimers with a methyl ester terminal group, *Langmuir* **16**, 7842-7846 (2000).
139. K. Esumi, T. Hosoya, A. Suzuki, and K. Torigoe, Formation of gold and silver nanoparticles in aqueous solution of sugar-persubstituted poly(amidoamine) dendrimers, *J. Colloid Interface Sci.* **226**, 346-352 (2000).
140. K. Esumi, T. Hosoya, A. Suzuki, and K. Torigoe, Preparation of hydrophobically modified poly(amidoamine) dendrimer-encapsulated gold nanoparticles in organic solvents, *J. Colloid Interface Sci.* **229**, 303-306 (2000).
141. F. Gröhn, G. Kim, B. J. Bauer, and E. J. Amis, Nanoparticle formation within dendrimer-containing polymer networks: Route to new organic-inorganic hybrid materials, *Macromolecules* **34**, 2179-2185 (2001).
142. O. Rossell, M. Seco, A. M. Caminade, and J. P. Majoral, Gold-containing dendrimers: A new class of macromolecules, *Gold Bulletin* **34**, 88-94 (2001).
143. E. Matijevic, Controlled colloid formation, *Curr. Opin. Coll. Interface. Sci.* **1**, 176-183 (1996).
144. J. Belloni, Metal nanocolloids, *Curr. Opin. Coll. Interface. Sci.* **1**, 184-196 (1996).
145. K. J. Klabunde, J. Stark, O. Koper, C. Mohs, D. G. Park, S. Decker, Y. Jiang, I. Lagadic, and D. Zhang, Nanocrystals as stoichiometric reagents with unique surface chemistry, *J. Phys. Chem.* **100**, 12142-12153 (1996).
146. *Clusters ofAtoms and Molecules,* edited by H. Haberland (Springer-Verlag, New York, 1994).
147. *Optical Properties of Metal Clasters,* edited by U. Kreibig and M. Vollmer (Springer-Verlag, New York, 1995).
148. S. Underwood and P. Mulvaney, Effect of the solution refractive-index on the color of gold colloids, *Langmuir* **10**, 3427-3430 (1994).
149. P. Mulvaney, Surface plasmon spectroscopy of nanosized metal particles, *Langmuir* **12**, 788-800 (1996).
150. U. Kreibig, K. Fouth, M. Quinten, and D. Schönauer, Many-cluster-systems – models of inhomogeneous matter, *Z. Phys. D* **12**, 505-514 (1989).
151. M. J. Hostetler, J. E. Wingate, C.-J. Zhong, J. E. Harris, R. W. Vachet, M. R. Clark, J. D. Londono, S. J. Green, J. J. Stokes, G. D. Wignall, G. L. Glish, M. D. Porter, N. D. Evans, and R. W. Murray, Alkanethiolate gold cluster molecules with core diameters from 1.5 to 5.2 nm: Core and monolayer properties as a function of core size, *Langmuir* **14**, 17-30 (1998).
152. S. Chen, A. C. Templeton, and R. W. Murray, Monolayer-protected cluster growth dynamics, *Langmuir* **16**, 3543-3548 (2000).
153. R. L. Whetten, J. T. Khoury, M. M. Alvarez, S. Murthy, I. Vezmar, Z. L. Wang, P. W. Stephen, C. L. Cleveland, W. D. Luedtke, and U. Landman, Nanocrystal gold molecules, *Adv. Mater.* **8**, 428-433 (1996).
154. D. V. Leff, P. C. O'Hara, J. R. Heath, W. M. Gelbart, Thermodynamic control of gold nanocrystal size - experiment and theory, *J. Phys. Chem.* **99**, 7036-7041 (1995).
155. H. P. Choo, K. Y. Liew, and H. Liu, Factors affecting the size of polymer stabilized Pd nanoparticles, *J. Mater. Chem.* **12**, 934-937 (2002).
156. X. Yan, H. Liu, and K. Y. Liew, Size control of polymer-stabilized ruthenium nanoparticles by polyol reduction, *J. Mater. Chem.* **11**, 3387-3391 (2001).
157. H. P. Choo, K. Y. Liew, W. A. K. Mahmood, and H. Liu, Morphology and crystalline structure of polymer stabilized Pd nanoparticles, *J. Mater. Chem.* **11**, 2906-2908 (2001).
158. Q. F. Zhou, J. C. Bao, and Z. Xu, Shape-controlled synthesis of nanostructured gold by a protection-reduction technique, *J. Mater. Chem.* **12**, 384-387 (2002).

159. T. Teranishi, R. Kurita, and M. Miyake, Shape control of Pt nanoparticles, *J. Inorg. Organometal. Polym.* **10**, 145-156 (2000).
160. C. P. Collier, R. J. Saykally, J. J. Shiang, S. E. Henrichs, and J. R. Heath, Reversible tuning of silver quantum dot monolayers through the metal-insulator transition, *Science* **277**, 1978-1981 (1997).
161. M. J. Hostetler, C.-J. Zhong, B. K. H. Yen, J. Anderegg, S. M. Gross, N. D. Evans, M. Porter, and R. W. Murray, Stable, monolayer-protected metal alloy clusters, *J. Am. Chem. Soc.* **120**, 9396-9397 (1998).
162. K. R. Harikumar, S. Ghosh, and C. N. R. Rao, X-Ray photoelectron spectroscopic investigations of Cu-Ni, Au-Ag, Ni-Pd, and Cu-Pd bimetallic clusters, *J. Phys. Chem. B* **101**, 536-540 (1997).
163. T. J. Schmidt, M. Noeske, H. A. Gasteiger, R. J. Behm, P. Britz, W. Brijoux, and H. Bönnemann, Electrocatalytic activity of Pt/Ru alloy colloids for CO and CO/H_2 electrooxidation: Stripping voltammetry and rotating disk measurements, *Langmuir* **13**, 2591-2595 (1997).
164. C. Sangregorio, M. Galeotti, U. Bardi, and P. Baglioni, Synthesis of Cu_3Au nanocluster alloy in reverse micelles, *Langmuir* **12**, 5800-5802 (1996).
165. J. Sinzig, U. Radtke, M. Quinten, and U. Kreibig, Binary clusters – homogeneous alloys and nucleus-shell structures, Z. *Phys. D* **26**, 242-245 (1993).
166. N. Toshima, M. Harada, Y. Yamazaki, and K. Asakura, Catalytic activity and structural analysis of polymer protected Au/Pd bemetallic clusters prepared by the simultaneous reduction of $HauCl_4$ and $PdCl_2$, *J. Phys. Chem.* **96**, 9927-9933 (1992).
167. M. Michaelis, A. Henglein, and P. Mulvaney, Composite Pd-Ag particles in aqueous solution, *J. Phys. Chem.* **98**, 6212-6215 (1994).
168. A. Henglein and C. Brancewicz, Absorption spectra and reactions of colloidal bimetallic nanoparticles containing mercury, *Chem. Mater.* **9**, 2164-2167 (1997).
169. S. Remita, M. Mostafavi, and M. 0. Delcourt, Bimetallic Ag-Pt and Au-Pt aggregates synthesized by radiolysis, *Radial Phys. Chem.* **47**, 275-279 (1996).
170. L. M. Liz-Marzán and A. P. Philipse, Stable hydrosols of metallic and bimetallic nanoparticles immobilized on imogolite fibers, *J. Phys. Chem.* **99**, 15120-15128 (1995).
171. H. Remita, J. Khatouri, M. Treguer, J. Amblard, and J. Belloni, Silver-palladium alloyed clusters synthesized by radiolysis, *Z. Phys. D* **40**, 127-130 (1997).
172. G. Schmid, H. West, H. Mehles, and A. Lehnert, Hydrosilation reactions catalyzed by supported bimetallic colloids, *Inorg. Chem.* **36**, 891-895 (1997),
173. M. S. Nashner, A. I. Frenkel, D. L. Adler, J. R. Shapley, and R. G. Nuzzo, Structural characterization of carbon-supported platinum-ruthenium nanoparticles from the molecular cluster precursor $PtRu_5C(CO)_{16}$, *J. Am. Chem. Soc.* **119**, 7760-7771 (1997).
174. T. Pham, J. B. Jackson, N. J. Halas, and T. R. Lee, Preparation and characterization of gold nanoshells coated with self-aasembled monolayers, *Langmuir* **18**, 4915-4920 (2002).
175. T. Cassagneau and F. Caruso, Contiguous silver nanoparticle coatings on dielectric spheres, *Adv. Mater.* **14**, 732-736 (2002).
176. L. Pasquato, F. Rancan, P. Scrimin, F. Mancin, and C. Frigeri, *N*-Methylimidazole-functionalized gold nanoparticles as catalysts for cleavage of a carboxylic acid ester, *Chem. Commun.,* 2253-2254 (2000).
177. G. A. Somorjai and Y. G. Borodko, Research in nanosciences – Great opportunity for catalysis science, *Catal. Lett.* **76**, 1-5 (2001).
178. M. Haruta and M. Daté, Advances in the catalysis of Au nanoparticles, *Appl. Catal. A* **222**, 427-437 (2001).
179. C.-J. Zhong and M. M. Maye, Core-shell assembled nanoparticles as catalysts, *Adv. Mater.* **13**, 1507-1511 (2001).
180. R. Brayner, G. Viau, and F. Bozon-Verduraz, Liquid-phase hydrogenation of hexadienes on metallic colloidal nanoparticles immobilized on supports via coordination capture by bifunctional organic molecules, *J. Mol. Catal. A* **182-183**, 227-238 (2002).
181. N. Toshima, Y. Shiraishi, and T. Teranishi, Effect of additional metal ions on catalyses of polymer-stabilized metal nanoclusters, *J. Mol. Catal. A* **177**, 139-147 (2001).
182. T. H, Galow, U. Drechsler, J. A. Hanson, and V. M. Rotello, Highly reactive heterogeneous Heck and hydrogenation catalysts constructed through 'bottom-up' nanoparticle self-assembly, *Chem. Commun.,* 1076-1077 (2001).
183. J. Dai and M. L. Bruening, Catalytic nanoparticles formed by reduction of metal ions in multilayered polyelectrolyte films, *Nano Lett.* **2**, 497-501 (2002).
184. V. Chegel, O. A. Rahman, O. Lioubashevski, Y. Shirshov, E. Katz, and I. Willner, Redox-switching of electrorefractive, electrochromic and conducting functions of Cu^{2+}/polyacrylic acid films associated with electrodes, *Adv. Mater,* in press.
185. A. Borsla, A. M. Wilhelm, and H. Delmas, Hydrogenation of olefins in aqueous phase, catalyzed by polymer-protected rhodium colloids: kinetic study, *Catal. Today* **66**, 389-395 (2001).

186. Y. H. Niu, L. K. Yeung, and R. M. Crooks, Size-selective hydrogenation of olefins by dendrimer-encapsulated palladium nanoparticles, *J. Amer. Chem. Soc.* **123**, 6840-6846 (2001).
187. C. Ramarao, S. V. Ley, S. C. Smith, I. M. Shirley, and N. DeAlmeida, Encapsulation of palladium in polyurea microcapsules, *Chem. Commun.,* 1132-1133 (2002).
188. H. G. Niessen, A. Eichhorn, K. Woelk, and J. Bargon, Homogeneous hydrogenation in supercritical fluids mediated by colloidal catalysts, *J. Mol. Catal. A* **182-183**, 463-470 (2002).
189. H. Li, Y.-Y. Luk, and M. Mrksich, Catalytic asymmetric dihydroxylation by gold colloids functionalized with self-assembled monolayers, *Langmuir* **15**, 4957-4959 (1999).
190. H. Bönnemann and G. A. Braun, Enantioselective hydrogenations on platinum colloids, *Angew. Chem. Int. Ed. Engl.* **35**, 1992-1995 (1996).
191. H. Bönnemann and G. A. Braun, Enantioselectivity control with metal colloids as catalysts, *Chem. Eur. J.* **3**, 1200-1202 (1997).
192. M. M. Maye, Y. Lou, and C.-J. Zhong, Core-shell gold nanoparticle assembly as novel electrocatalyst of CO oxidation, *Langmuir* **16**, 7520-7523 (2000).
193. M. S. El-Deab and T. Ohsaka, An extraordinary electrocatalytic reduction of oxygen on gold nanoparticles-electrodeposited electrodes, *Electrochem. Commun.* **4**, 288-292 (2002).
194. O. Antoine, Y. Bultel, and R. Durand, Oxygen reduction kinetics and mechanism on platinum nanoparticles inside Nafion, *J. Electroanal. Chem.* **499**, 85-94 (2001).
195. R. Woods, Specific activity of platinum for the electrocatalytic oxidation of acetate, *Electrochim. Acta* **13**, 1967-1972 (1968).
196. J. F. Hicks, A. C. Templeton, S. Chen, K. M. Sheran, R. Jasti, and R. W. Murray, The monolayer thickness dependence of quantized double-layer capacitances of monolayer-protected gold clusters, *Anal. Chem.* **71**, 3703-3711 (1999).
197. J. B, Flanagan, S. Margel, A. J. Bard, and F. C. Anson, Electron transfer to and from molecules containing multiple, noninteracting redox centers. Electrochemical oxidation of poly(vinylferrocene), *J. Am. Chem. Soc.* **100**, 4248-4253 (1978).
198. L. D. Margerum, R. W. Murray, and T. J. Meyer, Transient storage of photochemically produced oxidative and reductive equivalents in soluble redox polymers, *J. Phys. Chem.* **90**, 728-730 (1986).
199. G. R. Newkome, C. N. Moorefield, and F. Vogtie, *Dendritic Molecules – Concepts, Synthesis, Properties* (VCH, New York, 1996).
200. S. J. Green, J. J. Pietron, J. J. Stokes, M. J. Hostetler, H. Vu, W. P. Wuelfing, and R. W. Murray, Three-dimensional monolayers: Voltammetry of alkanethiolate-stabilized gold cluster molecules, *Langmuir* **14**, 5612-5619 (1998).
201. S. J. Green, J. J. Stokes, M. J. Hostetler, J. Pietron, and R. W. Murray, Three-dimension monolayers: Nanometer-sized electrodes of alkanethiolate-stabilized gold cluster molecules, *J. Phys. Chem. B* **101**, 2663-2668 (1997).
202. M.-C. Daniel, J. Ruiz, S. Nlate, J. Palumbo, J.-C. Blais, and D. Astruc, Gold nanoparticles containing redox-active supramolecular dendrons that recognize $H_2PO_4^-$, *Chem. Commun.,* 2000-2001 (2001).
203. M. Yamada, I. Quiros, J. Mizutani, K. Kubo, and H. Nishihara, Preparetion of palladium nanoparticles functionalized with biferrocene thiol derivatives and their electro-oxidative deposition, *Phys. Chem. Chem. Phys.* **3**, 3377-3381 (2001).
204. W.-J. Lee, M. J. Hostetler, R. W. Murray, and M. Majda, Electron hopping and eleclronic conductivity in monolayers of alkanethiol-stabilized gold nano-clusters at the air/water interface, *Isr. J. Chem.* **37**, 213-223 (1997).
205. T. Horikoshi, M. Itoh, M. Kurihara, K. Kubo, and H. Nishihara, Synthesis, redox behavior and electrodeposition of biferrocene-modified gold clusters *J. Electroanal. Chem.* **473**, 113-116 (1999).
206. R. S. Ingram and R. W. Murray, Electroactive three-dimensional monolayers. Anthraquinone ω-functionalized alkanethiolate-stabilized gold clusters, *Langmuir* **14**, 4115-4121 (1998).
207. J. J. Pietron and R. W. Murray, Mediated electrocatalysis with polyanthraquinone-functionalized monolayer-protected clusters, *J. Phys. Chem. B* **103**, 4440-4446 (1999).
208. M. Yamada, K. Kubo and H. Nishihara, Electroreductive deposilion of Au clusters modified with an anthraquinone derivative, *Chem. Lett.,* 1335-1336 (1999).
209. M. Yamada, T. Tadera, K. Kubo, and H. Nishihara, Electroreductive deposition of anthraquinone derivative attached Au clusters: Optical properties and scanning tunneling microscopy observation of the electrodeposited cluster film, *Langmuir* **17**, 2363-2370 (2001).
210. N. Sun, Y. Wang, Y. Song, Z. Quo, L. Dai, and D. Zhu, Novel [60]fullerene-silver nanocomposile with large optical limiting effect, *Chem. Phys. Lett.* **344**, 277-282 (2001).
211. H. Fujihara and H. Nakai, Fullerenethiolate-functionalized gold nanoparticles: A new class of surface-confined metal-C_{60} nanocomposites, *Langmuir* **17**, 6393-6395 (2001).

212. P. K. Sudeep, B. O. Ipe, K. G. Thomas, M.V. George, S. Barazzouk, S. Hotchandani, and P. V. Kamat, Fullerene-functionalized gold nanoparticles. A self-assembled photoactive antenna-metal nanocore assembly, *Nano Lett.* **2**, 29-35 (2002).
213. W. P. Wuelfing, A. C. Templeton, J. F. Hicks, and R. W. Murray, Taylor dispersion measurements of monolayer protected clusters: A physicochemical determination of nanoparticie size, *Anal. Chem.* **71**, 4069-4074 (1999).
214. E. Katz, N. Itzhak, and I. Willner, Electron transfer in self-assembled monolayers of *N*-methyl-*N*'-carboxyalkyl-4,4'-bipyridinium linked to gold electrodes, *Langmuir* **9**, 1392-1396 (1993).
215. A. Labande and D. Astruc, Colloids as redox sensors: recognition of $H_2PO_4^-$ and HSO_4^- by amidoferrocenylalkylthiol-gold nanoparticles, *Chem. Commun.,* 1007-1008 (2000).
216. P. V. Kamat, Photophysical, photochemical and photacatalytic aspects of metal nanoparticles, *J. Phys. Chem. B* **106**, 7729-7744 (2002).
217. K. G. Thomas and P. V. Kamat, Making gold nanoparticles glow: Enhanced emission from a surface-bound fluoroprobe, *J. Am. Chem. Soc.* **122**, 2655-2656 (2000).
218. M. M. Y. Chen and A. Katz, Steady-state fluorescence-based investigation of the interaction between protected thiols and gold nanoparticles, *Langmuir* **18**, 2413-2420 (2002).
219. J. Hu, J. Zhang, F. Liu, K. Kittredge, J. K. Whitesell, and M. A. Fox, Competitive photochemical reactivity in a self-assembled monolayer on a colloidal gold cluster, *J. Am. Chem. Soc.* **123**, 1464-1470 (2001).
220. H. Imahori and S. Fukuzumi, Porphyrin monolayer-modified gold clusters as photoactive materials, *Adv. Mater.* **13**, 1197-1199 (2001).
221. H. Imahori, M. Arimura, T. Hanada, Y. Nishimura, I. Yamazaki, Y. Sakata, and S. Fukuzumi, Photoactive three-dimensional monolayers: Porphyrin-alkanethiolate-stabilized gold clusters, *J. Am. Chem. Soc.* **123**, 335-336 (2001).
222. S. D. Evans, S. R. Johnson, H. Ringsdorf, L. M. Williams, and H. Wolf, Photoswitching of azobenzene derivatives formed on planar and colloidal surfaces, *Langmuir* **14**, 6436-6440 (1998).
223. B. I. Ipe, K. G. Thomas, S. Barazzouk, S. Hotchandani, and P. V. Kamat, Photoinduced charge separation in a fluorophone-gold nanoassembly, *J. Phys. Chem. B* **106**, 18-21 (2002).
224. S. Chen and R. W. Murray, Electrochemical quantized capacitance charging of surface ensembles of gold nanoparticles, *J. Phys. Chem. B* **103**, 9996-1000 (1999).
225. J. Li, Y. Yamada, K. Murakoshi, and Y. Nakatoa, Sustainable metal nano-contacts showing quntized conductance prepared at a gap of thin metal wires in solution, *Chem. Commun.,* 2170-2171 (2001).
226. A. Henglein, B. Lindig, and J. Westerhausen, Photochemical electron storage on colloidal metals and hydrogen formation by free radicals, *J. Phys. Chem.* **85**, 1627-1628 (1981).
227. G. M. Tsivgoulis and J.-M. Lehn, Photoswitched and functionalized oligothiophenes: synthesis and photochemical and electrochemical properties, *Chem. Eur. J.* **2**, 1399-1406 (1996).
228. A. N. Shipway, E. Katz, and I. Willner, Molecular memory and processing devices in solution and on surfaces, in: *Structure and Bonding,* edited by J.-P. Sauvage (Springer-Verlag, Berlin, 2001), Vol. 99, pp. 237-281.
229. A. K. Boal and V. M. Rotello, Redox-modulated recognition of flavin by functionalized gold nanoparticles, *J. Am. Chem. Soc.* **121**, 4914-4915 (1999).
230. A. K. Boal and V. M. Rotello, Fabrication and self-optimization of multivalent receptors on nanoparticie scaffolds, *J. Am. Chem. Soc.* **122**, 734-735 (2000).
231. A. K. Boal and V. M. Rotello, Radial control of recognition and redox processes with multivalent nanoparticie hosts, *J. Am. Chem. Soc.* **124**, 5019-5024 (2002).
232. J. Liu, J. Alvarez, W. Ong, and A. E. Kaifer, Network aggregates formed by C_{60} and gold nanoparticles capped with γ-cyclodextrin hosts, *Nano Lett.* **1**, 57-60 (2001).
233. N. O. Fischer, C. M. McIntosh, J. M. Simard, and V. M. Rotello, Inhibition of chymotrypsin through surface binding using nanoparticle-based receptors, *Proc. Natl. Acad. Sci. USA* **99**, 5018-5023 (2002).
234. A. K. Boal, F. Ilhan, J. E. DeRouchey, T. Thurn-Albrecht, T. P. Russell, and V. M. Rotello, Self-assembly of nanoparticles into structured spherical and network aggregates, *Nature* **404**, 746-748 (2000).
235. A. K. Boal, M. Gray, F. Ilhan, G. M. Clavier, L. Kapitzky, and V. M. Rotello, Bricks and mortar self-assembly of nanoparticles, *Tetrahedron* **58**, 765-770 (2002).
236. B. L. Frankamp, O. Uzun, F. Ilhan, A. K. Boal, and V. M. Rotello, Recognition-mediated assembly of nanoparticles into micellar structures with diblock copolymers, *J. Am. Chem. Soc.* **124**, 892-893 (2002).
237. A. K. Boal, T. H. Galow, F. Ilhan, and V. M. Rotello, Binary and ternary polymer-mediated 'bricks and mortar' self-assembly of gold and silica nanoparticles, *Adv. Funct. Mater.* **11**, 461-465 (2001).
238. S.-Y. Lin, S.-W. Liu, C.-M. Lin, and C.-I. Chen, Recognition of potassium ion in water by 15-crown-5 functionalized gold nanoparticles, *Anal. Chem.* **74**, 330-335 (2002).

239. Y. Kim, R. C. Johnson, and J. T. Hupp, Gold nanoparticle-based sensing of "spectroscopically silent" heavy metal ions, *Nano Lett.* **1**, 165-167 (2001).
240. M. Valina-Saba, G. Bauer, N. Stich, F. Pittner, and T. Schalkhammer, A self assembled shell of 11-mercaptoundecanoic aminophenylboronic acids on gold nanoclusters, *Mater. Sci. Eng. C* **8-9**, 205-209 (1999).
241. J. Liu, J. Alvarez, W. Ong, E. Roman, and A. E. Kaifer, Tuning the catalytic activity of cyclodextrin-modified palladium nanoparticles through host-guest binding interactions, *Langmuir* **17**, 6762-6764 (2001).
242. *Single Charge Tunneling and Coulomb Blockade Phenomena in Nanostructures,* edited by M. H. Devoret and H. Grabert (NATO ASI Series, Plenum Press, New York, 1992) Vol. 294.
243. A. B. Kharitonov, A. N. Shipway, and I. Willner, An Au nanoparticle/bisbipyridinium cyclophane-functionalized ion-sensitive field-effect transistor for the sensing of adrenaline, *Anal. Chem.* **71**, 5441-5443 (1999).
244. A. B. Kharitonov, A. N. Shipway, E. Katz, and I. Willner, Gold-nanoparticle/bis-bipyridinium cyclophane-functionalized ion-sensitive field-effect transistors: Novel assemblies for the sensing of neurotransmitters, *Rev. Anal. Chem.* **18**, 255-260 (1999).
245. E. Cattaruzza, G. Battaglin, F. Gonella, R. Polloni, G. Mattei, C. Maurizio, P. Mazzoldi, C. Sada, M. Montagna, C. Tosello, and M. Ferrari, On the optical absorption and nonlinearity of silica films containing metal nanoparticles, *Philos. Mag. B* **82**, 735-744 (2002)
246. U. Bach, D. Corr, D. Lupo, F. Pichot, and M. Ryan, Nanomaterials-based electrochromics for paper-quality displays, *Adv. Mater.* **14**, 845-848 (2002).
247. O. Antoine and R. Durand, *In situ* electrochemical deposition of Pt nanoparticles on carbon and inside Nafion, *Electrochem. Solid State Lett.* **4**, A55-A58 (2001).
248. Z. Peng, E. Wang, and S. Dong, Incorporation of surface-derivatized gold nanoparticles into electrochemically generated polymer films, *Electrochem. Commun.* **4**, 210-213 (2002).
249. V. Pardo-Yissar, R. Gabai, A.N. Shipway, T. Bourenko, and I. Willner, Gold nanoparticle/hydrogel composites with solvent-switchable electronic properties, *Adv. Mater.* **13**, 1320-1323 (2001).
250. L. Sheeney-Haj-Ichia, G. Sharabi, and I. Willner, Control of the electronic properties of thermosensitive poly(N-isopropykacrylamide) and Au-nanoparticle/poly(N-isopropylacrylamide composite hydrogels upon phase transition, *Adv. Funct. Mater.* **12,** 27-32 (2002).
251. F. Burmeister, C. Schafle, B. Keilhofer, C. Bechinger, J. Boneberg, and P. Liederer, From mesoscopic to nanoscopic surface structures: Lithography with colloid monolayers, *Adv. Mater.* **10**, 495-497 (1998).
252. F. Burmeister, W. Badowsky, T. Braun, S. Wieprich, J. Boneberg, and P. Liederer, Colloid monolayer lithography - A flexible approach for nanostructuring of surfaces, *Appl. Surf. Sci.* **144-145,** 461-466 (1999).
253. F. Burmeister, C. Schäfler, T. Matthes, M. Böhmisch, J. Boneberg, P. Leiderer, Colloid monolayers as versatile lithographic masks, *Langmuir* **13**, 2983-2987 (1997).
254. F. Remacle, C.P. Collier, G. Markovich, J. R. Heath, U. Banin, and R. D. Levine, Networks of quantum nanodots: The role of disorder in modifying electronic and optical properties, *J. Phys. Chem. B* **102**, 7727-7734 (1998).
255. R. W. Murray, Chemically modified electrodes, *Acc. Chem. Res.* **13**, 135-141 (1980).
256. R. W. Murray, Chemically modified electrodes, in: *Electroanalytical Chemistry,* edited by A.J. Bard (Marcel Dekker, New York, 1984), Vol. 13, pp. 191-368.
257. J. Schmitt, P. Mächtle, D. Eck, H. Möhwald, and C. A. Helm, Preparation and optical properties of colloidal gold monolayers, *Langmuir* **15**, 3256-3266 (1999).
258. A. Doron, E. Katz, and I. Willner, Organization of Au colloids as monolayer films onto ITO glass surfaces – Application of the metal colloid films as base interfaces to construct redox-active monolayers, *Langmuir* **11**, 1313-1317 (1995).
259. M. Brust, R. Etchenique, E. J. Calvo, and G. J. Gordillo, The self-assembly of gold and SCd nanoparticle multilayer structures studied by quartz crystal microgravimetry, *Chem. Commun.,* 1949-1950 (1996).
260. T. Yonezawa, S. Onoue, and T. Kunitake, Growth of closely packed layers of gold nanoparticles on an aligned ammonium surface, *Adv. Mater.* **10**, 414-416 (1998).
261. K. C. Grabar, P, C. Smith, M. D. Musick, J. A. Davis, D. G. Walter, M. A. Jackson, A. P. Guthrie, and M. J. Natan, Kinetic control of interparticle spacing in Au colloid-based surfaces: Rational nanometer-scale architecture, *J. Am. Chem. Soc.* **118**, 1148-1153 (1996).
262. T. Zhu, X. Fu, T. Mu, J. Wang, and Z. Liu, pH-Dependent adsorption of gold nanoparticles on *p*-aminothiophenol-modified gold substrates, *Langmuir* **15**, 5197-5199 (1999).
263. K. V. Sarathy, P. J. Thomas, G. U. Kulkarni, and C. N. R. Rao, Superlattices of metal and metal-semiconductor quantum dots obtained by layer-by-layer deposition of nanoparticle arrays, *J. Phys. Chem. B* **103**, 399-401 (1999).

264. T. Zhu, X. Zhang, J. Wang, X. Fu, and Z. Liu, Assembling colloidal Au nanoparticles with functionalized self-assembled monolayers, *Thin Solid Films* **327-329**, 595-598 (1998).
265. T. Sagara, N. Kato, and N. Nakashima, Electroreflectance study of gold nanoparticles immobilized on an aminoalkanethiol monolayer coated on a polycrystalline gold electrode surface, *J. Phys. Chem. B* **106**, 1205-1212 (2002).
266. K. Bandyopadhyay, V. Patil, K. Vijayamohanan, and M. Sastry, Adsorption of silver colloidal particles through covalent linkage to self-assembled monolayers, *Langmuir* **13**, 5244-5248 (1997).
267. K. Bandyopadhyay, V. P. K. Vijayamohanan, and M. Sastry, Adsorption of silver colloidal particles through covalent linkage to self-assembled monolayers, *Langmuir* **13**, 5244-5248 (1997).
268. H. Fan and G. P. López, Adsorption of surface-modified colloidal gold particles onto self-assembled monolayers: a model system for the study of interactions of colloidal particles and organic surfaces, *Langmuir* **13**, 119-121 (1997).
269. T. Teranishi, M. Hosoe, T. Tanaka, and M. Miyake, Size control of monodispersed Pt nanoparticles and their 2D organization by electrophoretic deposition, *J. Phys. Chem.* **103**, 3818-3827 (1999).
270. T. Teranishi, M. Hosoe, and M. Miyake, Formation of monodispersed ultrafine platinum particles and their electrophoretic deposition on electrodes, *Adv. Mater.* **9**, 65-67 (1997).
271. M. Giersig and P. Mulvaney, Preparation of ordered colloid monolayers by electrophoretic deposition, *Langmuir* **9**, 3408-3413 (1993).
272. M. Giersig and P. Mulvaney, Formation of ordered 2-dimensional gold colloid lattices by electrophoretic deposition, *J. Phys. Chem.* **97**, 6334-6336 (1993).
273. J. V. Zoval, J. Lee, S. Gorer, and R. M. Penner, Electrochemical preparation of platinum nanocrystallites with size selectivity on basal plane oriented graphite surfaces, *J. Phys. Chem. B* **102**, 1166-1175 (1998)
274. M. O. Finot, G. D. Braybrook, and M. T. McDermott, Characterization of electrochemically deposited gold nanocrystals on glassy carbon electrodes, *J. Electroanal. Chem.* **466**, 234-241 (1999).
275. K. H. Ng and R. M. Penner, Electrodeposition of silver-copper bimetallic particles having two archetypes by facilitated nucleation, *J. Electroanal. Chem.* **522**, 86-94 (2002).
276. D. Lu, K. Domen, and K. Tanaka, Electrodeposited Au-Fe, Au-Ni, and Au-Co alloy nanoparticles from aqueous electrolytes, *Langmuir* **18**, 3226-3232 (2002).
277. S. Peschel and G. Schmid, First steps towards ordered monolayers of ligand-stabilized gold clusters, *Angew. Chem. Int. Ed. Engl.* **34**, 1442-1443 (1995).
278. J. Schmitt, G. Decher, W. J. Dressick, S. L. Brandow, R. E. Geer, R. Shashidhar, and J. M. Calvert, Metal nanoparticle/polymer superlattice films: Fabrication and control of layer structure. *Adv. Mater.* **9**, 61-65 (1997).
279. S. Rubin, G. Bar, T. N. Taylor, R. W. Cutts, and T. A. Zawodzinski, Jr., Novel approach for the preparation of metal colloid monolayers on modified surfaces, *J. Vac. Sci. Technol. A* **14**, 1870-1877 (1996).
280. G. Bar, S. Rubin, R. W. Cutts, T. N. Taylor, and T. A. Zawodzinski, Dendrimer-modified silicon oxide surfaces as platforms for the deposition of gold and silver colloid monolayers: Preparation method, characterization, and correlation between microstructure and optical properties, *Langmuir* **12**, 1172-1179 (1996).
281. M. Gao, X. Zhang, B. Yang, and J. Shen, A monolayer of PbI_2 nanoparticles adsorbed on MD-LB film, *J. Chem. Soc., Chem. Commun.,* 2229-2230 (1994).
282. K. S. Mayya and M. Sastry, A new technique for the spontaneous growth of colloidal nanoparticle superlattices, *Langmuir* **15**, 1902-1904 (1999).
283. M. Sastry, K. S. Mayya, V. Patil, D. V. Paranjape, and S. G. Hegde, Langmuir-Blodgett films of carboxylic acid derivatized silver colloidal particles: Role of subphase pH on degree of cluster incorporation, *J. Phys. Chem. B* **101**, 4954-4958 (1997).
284. V. Patil and M. Sastry, Surface derivatization of colloidal silver particles using interdigitated bilayers: A novel strategy for electrostatic immobilization of colloidal particles in thermally evaporated fatty acid fatty amine films, *Langmuir* **14**, 2707-2711 (1998).
285. M. Sastry, K. S. Mayya, and V. Patil, Facile surface modification of colloidal particles using bilayer surfactant assemblies: A new strategy for electrostatic complexation in Langmuir-Blodgett films, *Langmuir* **14**, 5921-5928 (1998).
286. J. H. Fendler, Self-assembled nanostructured materials, *Chem. Mater.* **8**, 1616-1624 (1996).
287. L. Motte, F. Billoudet, E. Lacaze, J. Douin, and M.P. Pilena, Self-organization into 2D and 3D superlattices of nanosized particles differing by their size, *J. Phys. Chem. B* **101**, 138-144 (1997).
288. M. T. Reetz, M. Winter, and B. Tesch, Self-assembly of tetraalkylammonium salt-stabilized giant palladium clusters on surfaces, *Chem. Commun.,* 147-148 (1997).

289. K. C. Grabar, K. J. Allison, B. E. Baker, R. M. Bright, K. R. Brown, R. G. Freeman, A. P. Fox, C. D. Keating, M. D. Musick, and M. J. Natan, Two-dimensional arrays of colloidal gold particles: A flexible approach to macroscopic metal surfaces, *Langmuir* **12**, 2353-2361 (1996).
290. T. Sato, D. Brown, and B. F. G. Johnson, Nucleation and growth of nano-gold colloidal lattices, *Chem. Commun.,* 1007-1008 (1997).
291. G. Schmid, M. Bäumle, and N. Beyer, Ordered two-dimensional monolayers of Au_{55} clusters, *Angew. Chem. Int. Ed.* **39**, 181-183 (2000).
292. I. Sloufová-Srnová and B. Vlckova, Two-dimensional assembling of Au nanoparticles mediated by tetrapyridylporphine molecules, *Nano Lett.* **2**, 121-125 (2002).
293. S. He, J. Yao, S. Xie, H. Gao, and S. Pang, Superlattices of silver nanoparticles passivated by mercaptan, *J. Phys. D* **34**, 3425-3429 (2001).
294. P. J. Thomas, G. U. Kulkarni, and C. N. R. Rao, An investigation of two-dimensional arrays of thiolized Pd nanocrystals, *J. Phys. Chem. B* **104**, 8138-8144, (2000).
295. R. R. Bhat, D. A. Fischer, and J. Genzer, Fabricating planar nanoparticle assemblies with number density gradients, *Langmuir* **18**, 5640-5643 (2002).
296. R. Blonder, L. Sheeney, and I. Willner, Three-dimensional redox-active layered composites of Au-Au, Ag-Ag and Au-Ag colloids, *Chem. Commun.,* 1393-1394 (1998).
297. D. L. Feldheim, K. C. Grabar, M. J. Natan, and T. E. Mallouk, Electron transfer in self-assembled inorganic polyelectrolyte/metal nanoparticle heterostructures, *J. Am. Chem. Soc.* **118**, 7640-7641 (1996).
298. M. Lahav, A. N. Shipway, I. Willner, M. B. Nielsen, and J. F. Stoddart, An enlarged bis-bipyridinium cyclophane-Au nanoparticle superstructure for selective electrochemical sensing applications, *J. Electroanal. Chem.* **482**, 217-221 (2000).
299. J. Tien, A. Terfort, and G. M. Whitesides, Microfabrication through electrostatic self-assembly, *Langmuir* **13**, 5349-5355 (1997)
300. J. F. Hicks, Y. Seok-Shon, and R. W. Murray, Layer-by-layer growth of polymer/nanoparticle films containing monolayer-protected gold clusters, *Langmuir* **18**, 2288-2294 (2002).
301. J.-A. He, R. Valluzzi, K. Yang, T. Dolukhanyan, C. Sung, J. Kumar, and S. K. Tripathy, Electrostatic multilayer deposition of a gold-dendrimer nanocomposite, *Chem. Mater.* **11**, 3268-3274 (1999).
302. E. Hao and T. Lian, Buildup of polymer/Au nanoparticle multilayer thin films based on hydrogen bonding, *Chem. Mater.* **12**, 3392-3396 (2000).
303. T. Cassagneau and J. H. Fendler, Preparation and layer-by-layer self-assembly of silver nanoparticles capped by graphite oxide nanosheets, *J. Phys. Chem. B,* **103**, 1789-1793 (1999).
304. S. Malynych, I. Luzinov, and G. Chumanov, Poly(vinyl pyridine) as a universal surface modifier for immobilization of nanoparticles, *J. Phys. Chem B* **106**, 1280-1285 (2002).
305. J. Liu, L. Cheng, Y. Song, B. Liu, and S. Dong, Simple preparation method of multilayer polymer films containing Pd nanoparticles, *Langmuir* **17**, 6747-6750 (2001).
306. T. C. Wang, M. F. Rubner, and R. E. Cohen, Polyelectrolyte multilayer nanoreactors for preparing silver nanoparticle composites: controlling metal concentration and nanoparticle size, *Langmuir* **18**, 3370-3375 (2002).
307. A. N. Shipway, M. Lahav, R. Gabai and I. Willner, Investigations into the Electrostatically-Induced Aggregation of Au-Nanoparticles, *Langmuir* **16**, 8789-8795 (2000).
308. T. H. Galow, A. K. Boal, and V. M. Rotello, A "building block" approach to mixed-colloid systems through electrostatic self-organization, *Adv. Mater.* **12**, 576-579 (2000).
309. A. N. Shipway, M. Lahav, R. Blonder, and I. Willner, Bis-bipyridinium cyclophane receptor-Au nanoparticle superstructures for electrochemical sensing applications, *Chem. Mater.* **11**, 13-15 (1999).
310. M. Lahav, T. Gabriel, A. N. Shipway, and I. Willner, Assembly of a Zn(II)-porphyrin-bipyridinium dyad and Au-nanoparticle superstructures on conductive surfaces, *J. Am. Chem. Soc.* **121**, 258-259 (1999).
311. M. Lahav, R. Gabai, A. N. Shipway, and I. Willner, Au-colloid-'molecular square' superstructures: novel electrochemical sensing interfaces, *Chem. Comm.,* 1937-1938 (1999).
312. J. F. Hicks, F. P. Zamborini, A. J. Osisek, and R. W. Murray, The dynamics of electron self-exchange between nanoparticles, *J. Am. Chem. Soc.* **123**, 7048-7053 (2001).
313. W. P. Wuelfing, F. P. Zamborini, A. C. Templeton, X. Wen, H. Yoon, and R. W. Murray, Monolayer-protected clusters: Molecular precursors to metal films, *Chem. Mater.* **13**, 87-95 (2001).
314. Y. Fu, H. Xu, S. Bai, D. Qiu, J. Sun, Z. Wang, and X. Zhang, Fabrication of a stable polyelectrolyte/Au nanoparticles multilayer film, *Macromol. Rapid Commun.* **23**, 256-259 (2002).
315. B. H. Sohn and B. H. Seo, Fabrication of the multilayered nanostructure of alternating polymers and gold nanoparticles with thin films of self-assembling diblock copolymers, *Chem. Mater.* **13**, 1752-1757 (2001).
316. M. D. Musick, C. D. Keating, M. H. Keefe, and M. J. Natan, Stepwise construction of conductive Au colloid multilayers from solution, *Chem. Mater.* **9**, 1499-1501 (1997).

317. T. Baum, D. Bethell, M. Brust, and D. J. Schiffrin, Electrochemical charge injection into immobilized nanosized gold particle ensembles: Potential modulated transmission and reflectance spectroscopy, *Langmuir* **15**, 866-871 (1999).
318. M. Brust, D. Bethell, C. J. Kiely, and D. J. Schiffrin, Self-assembled gold nanoparticle thin films with nonmetallic optical and electronic properties, *Langmuir* **14**, 5425-5429 (1998).
319. M. Lu, X. H. Li, B. Z. Yu, and H. L. Li, Electrochemical behavior of Au colloidal electrode through layer-by-layer self-assembly, *J. Colloid Interface Sci.* **248**, 376-382 (2002).
320. N. Fishelson, I. Shkrob, O. Lev, J. Gun, and A. D. Modestov, Studies on charge transport in self-assembled gold-dithiol films: conductivity, photoconductivity, and photoelectrochemical measurements, *Langmuir* **17**, 403-412 (2001).
321. M. D. Musick, D. J. Peña, S. L. Botsko, T. M. McEvoy, J. N Richardson, and M. J. Natan, Electrochemical properties of colloidal Au-based surfaces: Multilayer assemblies and seeded colloid films, *Langmuir* **15**, 844-850 (1999).
322. J.-Y. Tseng, M.-H. Lin, and L.-K. Chau, Preparation of colloidal gold multilayers with 3-(mercaptopropyl)-trimethoxysilane as a linker molecule, *Colloids Surf. A* **182**, 239-245 (2001).
323. R. Chapman and P. Mulvaney, Electro-optical shifts in silver nanoparticle films, *Chem. Phys. Lett.* **349**, 358-362 (2001).
324. N. Malikova, I. Pastoriza-Santos, M. Schierhorn, N. A. Kotov, and L. M. Liz-Marzán, Layer-by-layer assembled mixed spherical and planar gold nanoparticles: control of interparticle interactions, *Langmuir* **18**, 3694-3697 (2002).
325. M. Brust, C. J. Kiely, D. Bethell, and D. J. Schiffrin, C_{60} mediated aggregation of gold nanoparticles, *J. Am. Chem. Soc.* **120**, 12367-12368 (1998).
326. F. P. Zamborini and R. M. Crooks, Nanometer-scale patterning of metals by electrodeposition from an STM tip in air, *J. Am. Chem. Soc.* **120**, 9700-9701 (1998).
327. P. Mesquida and A. Stemmer, Maskless nanofabrication using the electrostatic attachment of gold particles to electrically patterned surfaces, *Microelectron. Eng.* **61-62**, 671-674 (2002).
328. R. Resch, C, Baur, A. Bugacov, B.E. Koel, A. Madhukar, A. A. G. Requicha, and P. Will, Building and manipulating three-dimensional and linked two-dimensional structures of nanoparticles using scanning force microscopy, *Langmuir* **14**, 6613-6616 (1998).
329. S. L. Brandow, W. J. Dressick, C. S. Dulcey, T. S. Koloski, L. M. Shirey, J. Schmidt, and J. M. Calvert, Nanolithography by displacement of catalytic metal clusters using an atomic force microscope tip, *J. Vac. Sci. Technol. B* **15**, 1818-1824 (1997).
330. W. Yang, M. Chen, W. Knoll, and H. Deng, Synthesis of hexanedithiolate/decanethiolate mixed monolayer protected gold clusters and scanning tunneling microscope tip induced patterning on the clusters/Au(l 11) surfaces, *Langmuir* **18**, 4124-4130 (2002).
331. A. Doron, E. Joselevich, A. Schlittner, and I. Willner, AFM characterization of the structure of Au-colloid monolayers and their chemical etching, *Thin Solid Films,* **340**, 183-188 (1999).
332. Y. M. Jung, S. J. Ahn, E. R. Kim, and H. Lee, Gold nanoparticle assemblies on a functionalized surface patterned by AFM lithography, *J. Korean Phys. Soc.* **40**, 712-715 (2002).
333. Y. M. Jung, S. J. Ahn, H. J. Chae, H. Lee, E. R. Kim, and H. Lee, The fabrication of gold nanoparticle assemblies on the functionalized surface patterned by AFM lithography, *Molec. Cryst. Liquid Cryst.* **370**, 231-234 (2001).
334. M. T. Reetz and M. Winter, Fabrication of metallic and bimetallic nanostructures by electron beam induced metallization of surfactant stabilized Pd and Pd/Pt clusters, *J. Am. Chem. Soc.* **119**, 4539-4540 (1997).
335. T. Sato, D. G. Hasko, and H. Ahmed, Nanoscale colloidal particles: Monolayer organization and patterning, *J. Vac. Sci. Technol. B* **15**, 45-48 (1997).
336. J. Liu, L. Zhang, P. Mao, D. Chen, N. Gu, J. Ren, Y. Wu, and Z. Lu, Controlled assembly of patterned gold thin films using photolithographed self-assembled monolayers as templates, *Chem. Lett.,* 1147-1148 (1997).
337. J.-F. Liu, L.-G. Zhang, J.-Y. Ren, Y.-P. Wu, Z.-H. Lu, P.-S. Mao, D.-Y. Chen, Fabrication of colloidal gold micro-patterns using photolithographed self-assembled monolayers as templates, *Thin Solid Films* **327-329**, 176-179(1998).
338. T. Vossmeyer, E. DeIonno, and J. R. Heath, Light-directed assembly of nanoparticles, *Angew. Chem. Int. Ed Engl.* **36**, 1080-1083 (1997).
339. M. H. V. Werts, M. Lambert, J.-P. Bourgoin, and M. Brust, Nanometer scale patterning of langmuir-Blodgett films of gold nanoparticles by electron beam lithography, *Nano Lett.* **2**, 43-47 (2002).
340. V. Erokhin, V. Troitsky, S. Erokhina,, G. Mascetti, and C. Nicolini, In-plane patterning of aggregated nanoparticle layers, *Langmuir* **18**, 3185-3190 (2002).

341. F. Stellacci, C. A. Bauer, T. Meyer-Friedrichsen, W. Wensellers, V. Alain, S. M. Kuebler, S. J. K. Pond, Y. Zhang, S. R. Marder, and J. W. Perry, Laser and electron-beam induced growth of nanoparticles for 2D and 3D patterning, *Adv. Mater.* **14**, 194-198 (2002).
342. W. J. Dressick, C. S. Dulcey, S. L. Brandow, H. Witschi, and P. F. Neeley, Proximity x-ray lithography of siloxane and polymer films containing benzyl chloride functional groups, *J. Vac. Sci. Technol. A* **17**, 1432-1440 (1999).
343. S. L. Brandow, M.-S. Chen, R. Aggarwal, C. S. Dulcey, J. M. Calvert, and W. J. Dressick, Fabrication of patterned amine reactivity templates using 4-chloromethylphenylsiloxane self-assembled monolayer films, *Langmuir* **15**, 5429-5432 (1999).
344. B. E. Baker, N. J. Kline, P. J. Treado, and M. J. Natan, Solution-based assembly of metal surfaces by combinatorial methods, *J. Am. Chem. Soc.* **118**, 8721-8722 (1996).
345. P. C. Hidber, W. Helbig, E. Kim, and G. M. Whitesides, Microcontact printing of palladium colloids: Micron-scale patterning by electroless deposition of copper, *Langmuir* **12**, 1375-1380 (1996).
346. S. Palacin, P. C. Hildber, J.-P. Bourgoin, C. Miramond, C. Fermon, and G. M. Whitesides, Patterning with magnetic materials at the micron scale, *Chem. Mater.* **8**, 1316-1325 (1996).
347. A. M. Bittner, X. C. Wu, and K. Kern, Electroless metallization of dendrimer-coated micropatterns, *Adv. Funct. Mater.* **12**, 432-436 (2002).
348. H. S. Shin, H. J. Yang, Y. M. Jung, and S. B. Kim, Direct patterning of silver colloids by microcontact printing: possibility as SERS substrate array, *Vibrational Spectr.* **29**, 79-82 (2002).
349. H. Wohltjen and A.W. Snow, Colloidal metal-insulator-metal ensemble chemiresistor sensor, *Anal. Chem.* **70**, 2856-2859 (1998).
350. S. D. Evans, S. R. Johnson, Y. L. Cheng, and T. Shen, Vapour sensing using hybrid organic-inorganic nanostructured materials, *J. Mater. Chem.* **10**, 183-188 (2000).
351. N. Cioffi, I. Farella, L. Torsi, A. Valentini, and A. Tafuri, Correlation between surface chemical composition and vapor sensing properties of gold-fluorocarbon nanocomposites, *Sens. Actual. B* **84**, 49-54 (2002).
352. V. E. Bochenkov, N. Stephan, L. Brehmer, V. V. Zagorskii, and G. B. Sergeev, Sensor activity of thin polymer films containing lead nanoparticles, *Colloids Surf. A* **198-200**, 911-915 (2002).
353. E. E. Foos, A. W. Snow, M. E. Twigg, and M. G. Ancona, Thiol-terminated di-, tri-, and tetraethylene oxide functionalized gold nanoparticles: A water-soluble, charge-neutral cluster, *Chem. Mater.* **14**, 2401-2408 (2002).
354. F. P. Zamborini, M. C. Leopold, J. F. Hicks, P. J. Kulesza, M. A. Malik, and R. W. Murray, Electron hopping conductivity and vapor sensing properties of flexible network polymer films of metal nanoparticles, *J. Am. Chem. Soc.* **124**, 8958-8964 (2002).
355. N. Krasteva, I. Besnard, B. Guse, R. E. Bauer, K. Müllen, A. Yasuda, and T. Vossmeyer, Self-assembled gold nanoparticle/dendrimer composite films for vapor sensing applications, *Nano Lett.* **2**, 551-555 (2002).
356. T. Vossmeyer, B. Guse, I. Besnard, R. E. Bauer, K. Müllen, and A. Yasuda, Gold nanoparticle/polyphenylene dendrimer composite films: preparation and vapor-sensing properties, *Adv. Mater.* **14**, 238-242 (2002).
357. H. Imahori, T. Azuma, A. Ajavakom, H. Norieda, H. Yamada, and Y. Sakata, An investigation of photocurrent generation by gold electrodes modified with self-assembled monolayers of C_{60}, *J. Phys. Chem. B* **103**, 7233-7237 (1999).
358. S. N. Rao and D. Fitzmaurice, Heterosupramolecular chemistry: Synthetic strategies for the covalent and noncovalent assembly and organization of nanocrystals and molecules, *Helv. Chim. Acta* **81**, 902-915 (1998).
359. M. Lahav, V. Heleg-Shabtai, J. Wasserman, E. Katz, I. Willner, H. Dürr, Y.-Z. Hu, and S. H. Bossmann, Photoelectrochemistry with integrated photosensitizer-electron acceptor and Au-nanoparticle arrays, *J. Am. Chem. Soc.* **122**, 11480-11487 (2000).
360. U. Simon, R. Flesch, H. Wiggers, G. Schön, and G. Schmid, Chemical tailoring of the charging energy in metal cluster arrangements by use of bifunctional spacer molecules, *J. Mater. Chem.* **8**, 517-518 (1998).
361. U. Simon, G. Schön, and G. Schmid, The application of Au_{55} clusters as quantum dots, *Angew. Chem. Int. Ed. Engl.* **32**, 250-254 (1993).
362. R. S. Ingram, M. J. Hostetler, R. W. Murray, T. G. Schaff, J. T. Khoury, R. L. Whetten, T. P. Bigioni, D. K. Guthrie, and P. N. First, 28 kDa Alkanethiolate-protected Au clusters give analogous solution electrochemistry and STM Coulomb staircases, *J. Am. Chem. Soc.* **119**, 9279-9280 (1997).
363. T. Sato, H. Ahmed, D. Brown, and B. F. G. Johnson, Single electron transistor using a molecularly linked gold colloidal particle chain, *J. Appl. Phys.* **82**, 696-701 (1997).
364. T. Sato and H. Ahmed, Observation of a Coulomb staircase in electron transport through a molecularly linked chain of gold colloidal particles, *Appl. Phys. Lett.* **70**, 2759-2761 (1997).

365. D. L. Klein, P. L. McEuen, J. E. B. Katari, R. Roth, and A. P. Alivisatos, An approach to electrical studies of single nanocrystals, *Appl. Phys. Lett.* **68,** 2574-2576 (1996).
366. R. P. Andres, T. Bein, M. Dorogi, S. Feng, J. I. Henderson, C. P. Kubiak, W. Mahoney, R. G. Osifchin, and R. Reifenberger, "Coulomb staircase" at room temperature in a self-assembled molecular nanostructure, *Science* **272**, 1323-1325 (1996).
367. J. R. Petta, D. G. Salinas, and D. C. Raloh, Measurements of discrete electronic states in a gold nanoparticle using tunnel junctions formed from self-assembled monolayers, *Appl. Phys. Lett.* **77**, 4419-4421 (2000).
368. L. F. Chi, M. Hartig, T. Drechsler, T. Schaak, C. Seidel, H. Fuchs, and G. Schmid, Single-electron tunneling in Au_{55} cluster monolayers, *Appl. Phys. Lett.* **66,** S187-S190 (1998).
369. U. Simon, Charge transport in nanoparticle arrangements, *Adv. Mater.* **10,** 1487-1492 (1998).
370. G. S. McCarty and P. S. Weiss, Scanning probe studies of single nanostructures, *Chem. Rev.* **99,** 1983-1990 (1999).
371. R. P. Andres, J. D. Bielefeld, J. I. Henderson, D. B. Janes, V. R. Kolagunta, C. P. Kubiak, W.J. Mahoney, and R. G. Osifchin, Self-assembly of a two-dimensional superlattice of molecularly linked metal clusters, *Science* **273**, 1690-1693 (1996).
372. J. R. Tucker, Complementary digital logic based on the Coulomb blockade, *J. Appl. Phys.* **72**, 4399-4413 (1992).
373. A. N. Korotkov, R. H. Chen, and K. Likharev, Possible performance of capacitively coupled single-electron transistors in digital circuits, *J. Appl. Phys.* **78**, 2520-2530 (1995).
374. J. B. Barner and S. T. Ruggerio, Observation of the incremental charging of Ag particles by single electrons, *Phys. Rev. Lett.* **59**, 807-810 (1987).
375. K. K. Likharev and T. Claeson, Single electronics, *Sci. Am.* **266**, 80-85 (1992).
376. R. F. Service, Making single electrons compute, *Science* **275**, 303-304 (1997).
377. L. C. Brousseau III, Q. Zhao, D. A. Shultz, and D. L. Feldheim, pH-Gated single-electron tunneling in chemically modified gold nanoclusters, *J. Am. Chem. Soc.* **120**, 7645-7646 (1998).
378. D. I. Gittins, D. Bethell, D. J. Schiffrin, and R. J. Nichols, A nanometre-scale electronic switch consisting of a metal cluster and redox-addressable groups, *Nature* **408**, 67-69 (2000).
379. M. S. Montemerlo, J. C. Love, G. J. Opiteck, D. Goldhaber-Gordon, and J. C. Ellenbogen, *Technologies and Designs for Electronic Nanocomputers* (Mitre Corp., McLean, VA, 1996).
380. A. O. Orlov, I. Amlani, G. H. Berstein, C. S. Lent, and G. L. Snider, Realization of a functional cell for quantum-dot cellular automata, *Science* **277**, 928-930 (1997).
381. J. Schmelzer, S. A. Brown, A. Wurl, M. Hyslop, and R. J. Blaikie, Finite-size effects in the conductivity of cluster assembled nanostructures, *Phys. Rev. Lett.* **88**, 226802-1-226802-4 (2002).
382. F. Patolsky, Y. Weizmann, O. Lioubashevski, and I. Willner, DNA and polylysine templated Au-nanoparticle nano-wires, *Angew. Chem. Int. Ed* **41,** 2323-2327 (2002).

3
METAL NANOPARTICLES FOR CATALYSIS

Naoki Toshima*

1. INTRODUCTION

Metal nanoparticles have attracted a great interest in scientific research and industrial applications, owing to their unique large surface-to-volume ratios and quantum-size effects.[1-3] Since industrial catalysts usually work on the surface of metals, the metal nanoparticles, which possess much larger surface area per unit volume or weight of metal than the bulk metal, have been considered as promising materials for catalysis.

Industrial catalysts are usually composed of inorganic supports and metals on the supports. They are often prepared by heat treatment of metal ions on the support at high temperature sometimes under hydrogen. They have very complex structures. For example, they are the mixtures of metal particles with various sizes and shapes. Metal particles often strongly interact with the inorganic supports, thus resulting in the structure of half balls, for example.

In contrast, colloid chemistry has provided the colloidal dispersion of metal fine particles in water.[4] In the 1950's colloidal dispersions of metal fine particles were already prepared and applied to catalysis. Although they contained metal nanoparticles, the size of nanoparticles was not sufficiently monodispersed. In addition they were not stable enough when used in solution. Thus, there still remain many problems in the reproducibility of the preparation and catalysis of metal nanoparticles. In 1976, we prepared colloidal dispersions of rhodium nanoparticles protected by water-soluble polymers by reduction of rhodium(III) ions under mild conditions, i.e., reduction with refluxing alcohol in the presence of water-soluble polymers.[5] These nanoparticles were applied as catalysts for hydrogenation of olefins. In 1989, we have developed colloidal dispersions of Pd/Pt bimetallic nanoparticles by simultaneous reduction of Pd and Pt ions in the presence of poly(*N*-vinyl-2-pyrrolidone) (PVP).[6] These bimetallic nanoparticles display much higher catalytic activity than the corresponding monometallic nanoparticles, especially at particular molecular ratios of both elements. In this chapter, the preparation and catalytic properties of colloidal dispersions of metal nanoparticles will be discussed.

* Naoki Toshima, Tokyo University of Science, Yamaguchi [The former Science University of Tokyo in Yamaguchi], Onoda-shi, Yamaguchi, Japan 756-0884

Although there are many reports[7,8] on the preparation of monodispersed metal nanoparticle catalysts supported on inorganic supports by physical methods, we have chosen not to include them in this chapter.

2. METALS AS CATALYSTS

Catalysts play a very important role not only in industrial chemical processes but also in chemical reactions (enzymatic reactions) in the human body. Industries usually use heterogeneous catalysts supported on inorganic supports at high temperature, and sometimes use homogenous catalysts at lower temperature. The former catalysts are much superior than the latter from the viewpoint of recycling of catalysts. In a human body or any living being, in contrast to industries, enzymes are used as catalysts in reactions at low temperature around 40 °C. They are very active and selective, and rather homogenous.

Both in industries and living beings, acid or base is used as the most popular catalyst for simple reactions, and metals work as active sites of the catalysts for rather complex reactions. Transition metals have often been used in the form of metal particles dispersed onto inorganic supports such as silica gel, alumina and activated charcoal. Dispersed particles on an inorganic support have advantages over metal powders in that:

(a) the particles can be readily dispersed through the use of the support;
(b) the resulting dispersed particles exhibit a much larger total surface area per unit weight than the bulk metal, thus allowing more effective utilization of the expensive transition metal as a result of dispersion;
(c) the active sites of the metal catalyst can be brought into a homogeneous condition by dispersion; and
(d) the small particles resulting from dispersion may exhibit new catalytic properties.

Colloidal dispersions of metal nanoparticles usually work at rather low temperature as homogeneous catalysts. In this point, metal nanoparticles are similar to enzymes and are often regarded as artificial enzymes.[9] From the viewpoint of green chemistry (less energy, less byproduct, more efficiency, more selectivity, etc.), enzymes could be a model of industrial catalysts. Thus, metal nanoparticles could provide a step forward for industrial catalysts to step up from the present practical heterogeneous catalysts to more ideal and enzyme-like ones.

A polymer-protected metal nanoparticle catalyst has not only the similar advantages to dispersed particles on an inorganic support but also new benefits in that:

(a) colloidal dispersions can form “homogeneous” solutions;
(b) the protecting polymer can shield a nanoparticle catalyst from deactivation by catalytic poisons or air;
(c) the protecting polymer can interact attractively or repulsively with substrates, which results in high selectivity and/or sometimes high activity; and
(d) colloidal dispersions of metal nanoparticles transmit light more readily than powders.

As a result of this last benefit, colloidal dispersions of metal nanoparticles have frequently been used as catalysts in recent photochemical investigations.

3. PREPARATION OF METAL NANOPARTICLES

Preparation of metal nanoparticles can be classified into two categories: physical and chemical methods. The physical methods are based on subdivision of bulk metals, including mechanical crushing or pulverization of bulk metal, arc discharge between metal electrodes, and so on. Metal nanoparticles thus produced are usually large in size and have wide size distribution. The chemical methods are based on the reduction of metal ions or decomposition of precursors to form atoms, followed by aggregation of the atoms (c.f. Figure 1). Nanoparticles prepared by chemical methods have usually a narrow size distribution.[10]

The formation of metal nanoparticles by chemical methods can be carried out by reduction of metal ions with chemical reductants or decomposition of metal precursors with extra-energy. The chemical reductants involve molecular hydrogen, alcohol, hydrazine, $NaBH_4$, $LiAlH_4$, citrate, and so on. Energy provided from the outside involves photo-energy (ultra-violet and visible light), γ-ray, electricity, thermal energy (heat), sonochemical energy, and so on. In order to produce metal nanoparticles with a narrow size distribution, stabilizers are important. Without stabilizers it is difficult to obtain stable colloidal dispersions of metal nanoparticles with a narrow size distribution.

Many kinds of materials have been used as stabilizers for metal nanoparticles. In the traditional colloidal dispersions of metal, electric charges could be used as the stabilizer. Electric repulsion between the metal particles prevents them from the aggregation. The electric charges may be attributed to anions adsorbed on the metal surface. Another method to stabilize the dispersion of metal particles is steric repulsion between the stabilizers adsorbed on the metal particles. Water-soluble polymers are often used for this purpose. Even small organic molecules can work as the stabilizer. In this case many organic molecules strongly bind to the surface of metal particles as ligands of the metal. The polymeric stabilizers do not necessarily make a strong bond at one site, but can interact with the metal particle at many sites (cf. Figure 2 (a)).

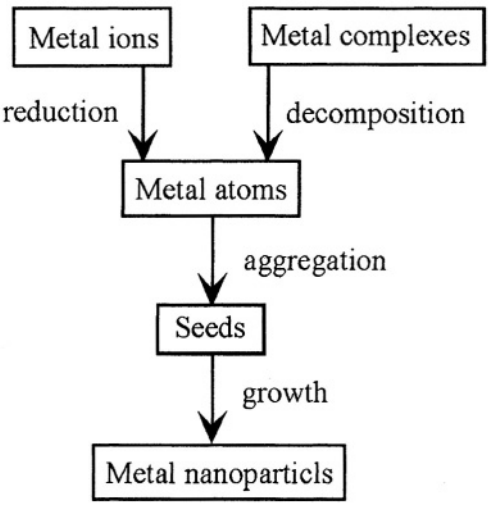

Figure 1. Preparation of metal nanoparticles in homogeneous solution by chemical methods.

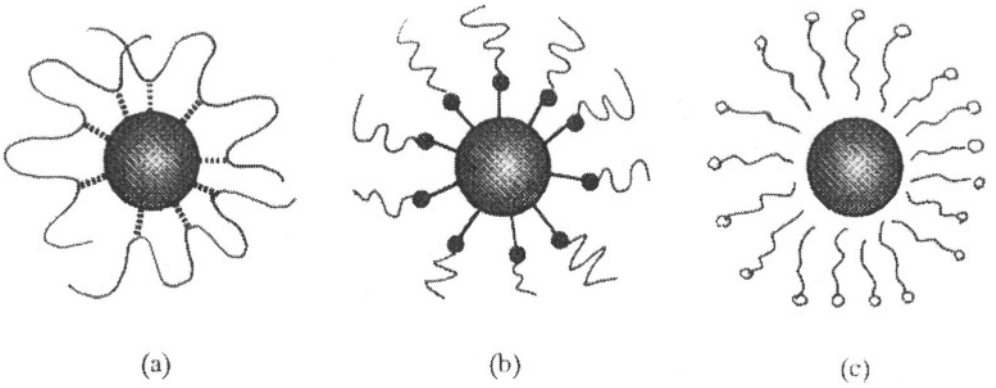

Figure 2. Metal nanoparticles stabilized by polymers (a), ligand molecules with low molecular weight (b), and micelles (c).

The multi-interaction results in totally strong adsorption of the polymer molecule onto the metal particle. In the case of molecules with low molecular weight, in contrast, the bond between the molecule and the metal particle must be strong (cf. Figure 2 (b)). Otherwise, the stabilizer can be detached from the surface of metal nanoparticles, which results in aggregation of the nanoparticles.

Each weak interaction between a coordinating site of the stabilizing polymer molecule and the surface of a metal nanoparticle seems insufficient to stabilize the colloidal dispersion of metal nanoparticles. But this is not true. Weak but multiple coordination of the polymer molecules can sufficiently stabilize the metal nanoparticles. Polymer-stabilized metal nanoparticles, on the contrary, can work as the most effective catalysts. If the interaction between the polymer and the metal at each site is strong, there remains no vacant site on the surface of the metal nanoparticle. This means that, when substrate molecules are going to attack the surface of metal particles, they cannot reach the surface of metal because of the absence of a vacant site, i.e., no catalytic reaction occurs on the surface of metal nanoparticles. If the interaction is weak, then the substrate molecule can replace a coordinating site of the polymer molecule and attack the surface of metal, which results in the prompt catalytic reaction. This process is illustrated in Figure 3.

If the molecules with low molecular weight strongly interact with the metal surface as stabilizers, the substrate cannot attack the surface and no reaction can be catalyzed by the metal nanoparticles surface. However, the metal nanoparticles can work as catalysts when the interaction between the stabilizing organic molecules and the metal particles is not strong enough to inhibit the attack by the substrates. This is the case when the metal nanoparticles are stabilized by micelles (cf. Figure 2 (c)). In this case the substrate molecules can attack the surface of metal nanoparticles. After being attacked by substrates, the metal particles can be still stabilized by the micelles. Another example is the metal nanoparticles which are partially stabilized by strongly coordinating ligands and partially covered by weakly coordinating ligands providing vacant sites. The giant cluster $Pd_{561}phen_{60}(OAc)_{180}$ is one of such examples, where phen (phenanthlorine) works as the strong ligand to stabilize the nanoparticles. It catalyzes the oxidation of benzylalcohol under oxygen for example.[11]

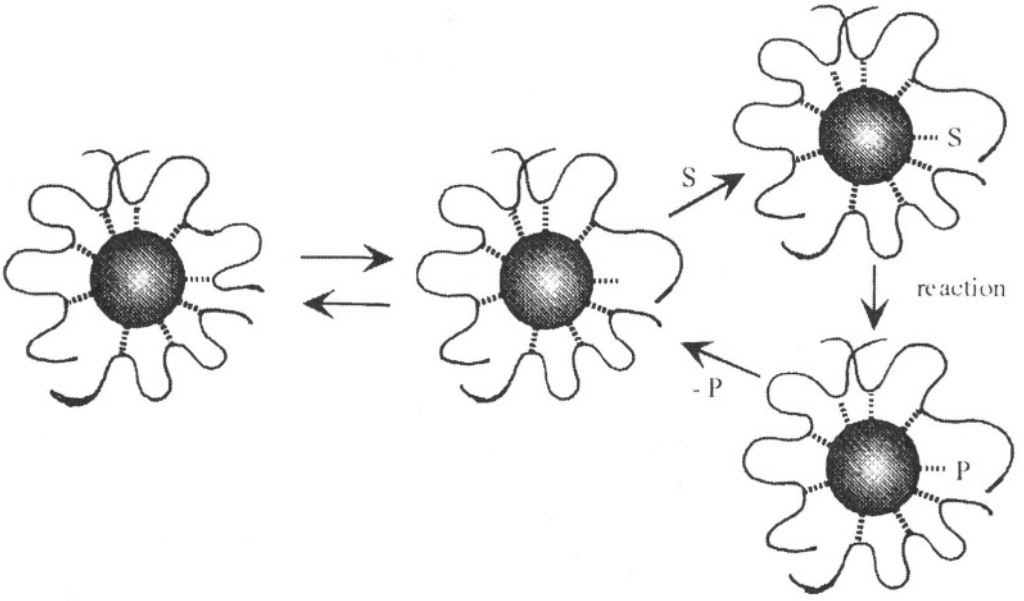

Figure 3. Schematic illustration of the reaction processes on the metal nanoparticle catalyst. S: Substrate, P: Product.

A typical method to prepare the colloidal dispersions of metal nanoparticles stabilized by water-soluble polymers is alcohol-reduction of metal ions in the presence of the polymers.[5] In this case, easily oxidized solvents such as ethanol can be used both as a reductant and a dispersing medium of colloidal dispersions of metal nanoparticles. The alcohol reduction method has the following advantages:

(a) The procedure is very simple.
(b) The colloidal dispersions prepared by this method are usually very stable and reproducible.
(c) The particle sizes of metal nanoparticles are rather small and their distribution is rather narrow.
(d) The size and shape of metal nanoparticles can be controlled by preparative conditions, for example, the concentration and the kind of metal precursors or metal ions, the kind of reductants used, the quantity and the variety of polymers, the quantity and the quality of additives, etc.

Reduction of metal ions with alcohol can form metal atoms and aldehyde. Thus, the reduction of palladium chloride with ethanol, for example, can proceed as follows:

$$PdCl_2 + CH_3CH_2OH \rightarrow Pd(0) + CH_3CHO + 2HCl \quad (1)$$

Acetaldehyde produced does not reduce another palladium chloride to palladium(0). Any alcohol with α-hydrogen can be used for this purpose. The details of other preparation methods can be found in the various articles.[2-4, 12, 13]

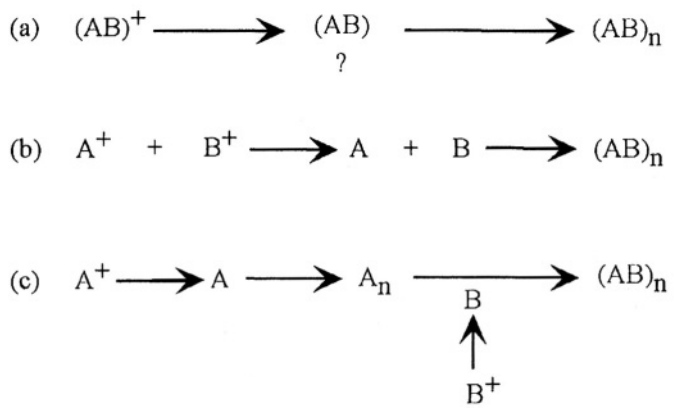

Figure 4. Schematic representation of three procedures for the preparation of bimetallic nanoparticles $(AB)_n$.

Metal nanoparticles composed of two (or more) different metal elements are of great interest as catalysts. For the preparation of the colloidal dispersions of bimetallic nanoparticles by chemical methods[2,14] three typical procedures have been reported as follows, which are schematically shown in Figure 4 as well.

(a) *Preparation from bimetallic precursors.* The bimetallic complexes composed of two different metal elements are used as the precursor. Reduction or decomposition of the precursors in the presence of stabilizers may produce bimetallic clusters, the aggregation of which can result in the formation of colloidal dispersions of bimetallic nanoparticles. Metal-metal bond(s) may be kept during the reactions.

(b) *Simultaneous reactions of mixtures of the precursors of two different metal elements.* The simultaneous reactions may produce atoms of two different metal elements. If they aggregate together and the sizes of aggregates are controlled by the stabilizers, then colloidal dispersions of bimetallic nanoparticles can be produced. For this purpose a kind of interaction between the two different metal atoms is required. Otherwise, the mixtures of two different atoms will just result in the formation of the mixtures of two kinds of monometallic nanoparticles. Sometimes the simultaneous procedure does not result in the simultaneous reactions but practically successive reactions.

(c) *Successive reactions.* After the formation of colloidal dispersions of monometallic nanoparticles A_n, the precursors of another meal B^+ are added into the colloidal dispersions. Then, the monometallic nanoparticles A_n may work as a seed and atoms of another metal may deposit on the former nanoparticles producing bimetallic nanoparticles. This kind of ideal reactions do not always proceed.

In 1989 we succeeded to prepare the colloidal dispersions of Pd/Pt bimetallic nanoparticles with a core/shell structure by simultaneous reduction of $PdCl_2$ and H_2PtCl_6 in refluxing ethanol/water in the presence of poly(*N*-vinyl-2-pyrrolidone).[6,15] After that, several reports have appeared on the formation of the core/shell-structured bimetallic nanoparticles by simultaneous reactions.[2,16-18]

4. CHARACTERIZATION OF METAL NANOPARTICLE CATALYSTS

The complete characterization of colloidal dispersions of metal nanoparticles is not so easy. Difficulties arise from not only their smallness but also their complexity. The complete characterization requires clarifying the following kinds of structures;

(a) dispersion structure,
(b) structure of stabilizers, and
(c) structure of metallic parts.

Many methods are used in order to clarify these structures. References can be referred to for the detailed discussions.[2,12,14] Table 1 summarizes these methods.

The structures of colloidal dispersion of metal nanoparticles can be schematically illustrated as Figure 5. The size of superstructures can be measured by small angle X-ray scattering analysis. The size of whole nanoparticles including stabilizers can be measured by light scattering or a Taylor dispersion method.[19] Scanning tunneling microscopes (STM) can measure the similar size in a dry state.[20] Transmission electron microscopy (TEM) is the best method to evaluate the size and size distribution of metal parts of nanoparticles. However, sizes evaluated by TEM often contain the aggregated size of metal nanoparticles. Extended X-ray absorption fine structure (EXAFS) analysis can give the size of elementary metal clusters which can not be seen by other methods like TEM.[21] EXAFS is also the best method to analyze the bimetallic structure.[15, 16, 21]

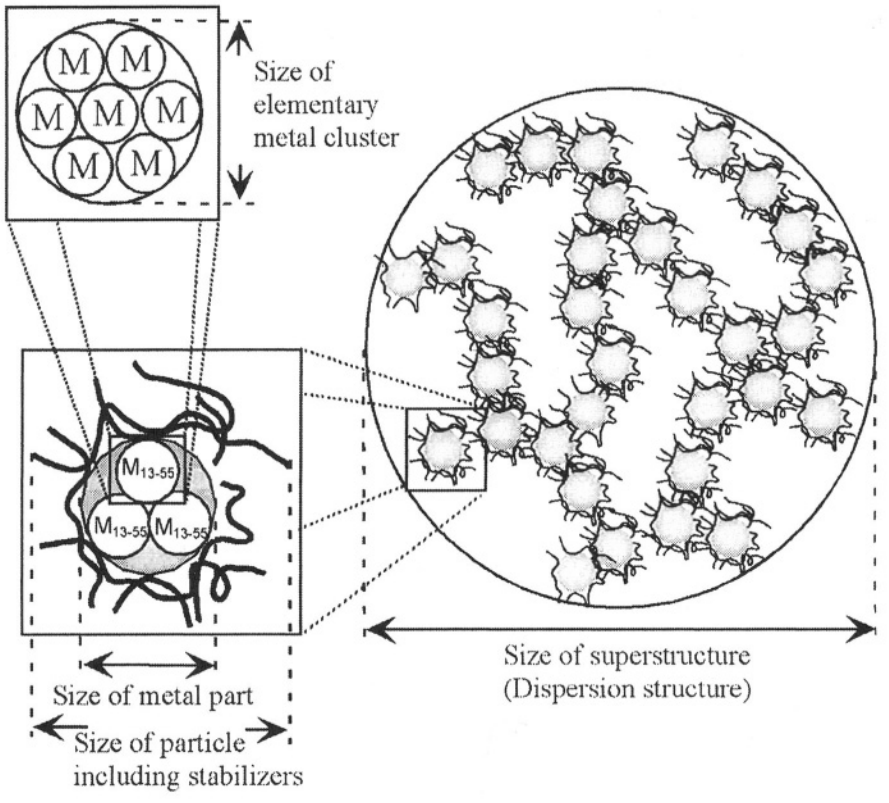

Figure 5. Schematic illustration of the structures of colloidal dispersions of metal nanoparticles.

Table 1. Analytical methods and items characterizing three kinds of structures of colloidal dispersions of metal nanoparticles.

Method	Dispersion st.	Stabilizer st.	Metal st.
Light scattering	(Size)	Size	-------
Small angle X-ray scattering	Superstructure	-------	-------
IR spectrum	-------	Coordination structure	(Surface structure)
UV-Vis spectrum	Dispersing	Charge transfer band	Plasmon band
NMR	-------	Coordination structure	Metal structure
X-ray diffraction	-------	(Alignment)	Crystal structure
XPS	-------	(Coordination)	Metal state, Structure
EXAFS	-------	(Coordination)	Bimetallic structure
TEM	-------	(Size)	Size, Morphology
SEM	-------	(Size)	Size, Morphology
EPMA, EDX	-------	-------	Element, Distribution
STM, AFM	-------	Size	(Size, Structure)

5. EFFECT OF STRUCTURES ON CATALYSIS OF METAL NANOPARTICLES

5.1. Size of Metal Nanoparticles

The size of the metal parts is one of the most important factors that affect the catalytic properties of metal nanoparticles. The total surface area per unit amount of metal particles increases in proportion to the square of the diameter (d^2) of the particles. Thus, the surface-to-volume ratio increases with decreasing particle size (see Figure 6). If the fcc (face-centered-cubic) structure is assumed, for example, a platinum nanoparticle with 1.4 nm in diameter is composed of 44 Pt atoms, and 32 of those 44 atoms (about 80% of the total amount of atoms) are located in the surface layer of the nanoparticles.

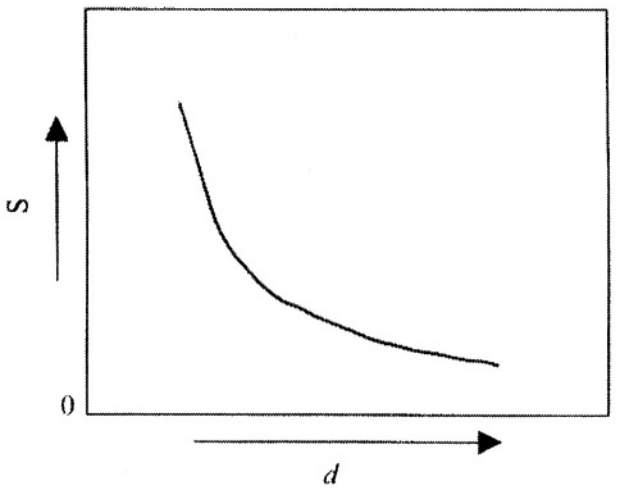

Figure 6. Dependence of total surface area of metal nanoparticles composed of unit amount of metal atoms (S) upon the nanoparticle diameter (d).

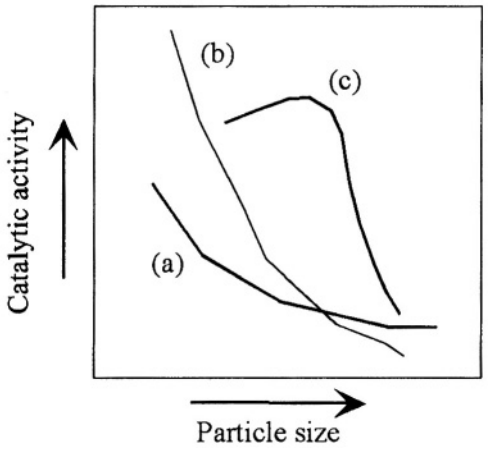

Figure 7. Schematic illustration of the dependence of the catalytic activity on the size of metal nanoparticles. See text for details.

Since the catalytic reactions occur only on the surface of the metal nanoparticles, the small size can provide a large ratio of surface atoms, which results in the high catalytic activity per unit amount of metal.

In addition, the small size may provide a completely different structure, which may in turn result in different catalytic activity. This way of thinking has not completely been proved yet, but is going to be important when considering specific catalytic properties of metal nanoparticles. In fact shape-selective preparation of metal nanoparticles has been achieved in reverse micelles[22] and in the presence of oxalate.[23]

There are many reports showing the size effect of metal nanoparticles on the catalytic activity. For example, the hydrogenation rate of olefins over Rh nanoparticles increases rapidly with decreasing size (cf. Figure 7 a and b atoms).[24] However, the increment is not proportional to that of the total surface area. The rate of hydrogenation of internal olefins increases slowly with decreasing size (Figure 7a), while that of external olefins increases rapidly (Figure 7b). This is probably due to the steric effect and/or the surface structure effect.

Sometimes, the catalytic activity increases with decreasing size until a certain size, but after the certain size the activity does not increase with decreasing size. Thus the most prompt size is observed for some reactions (cf. Figure 7c). In photochemical hydrogen generation catalyzed by platinum, for example, the Pt nanoparticles with about 3 nm were observed to be most active as the catalyst.[25] This is probably due to the mechanism of catalysis. For hydrogen generation two-electron reduction is required for the platinum nanoparticles. Thus, a certain size is necessary to maintain enough numbers of electrons in a Pt nanoparticle.

The size of metal nanoparticles can also affect the selectivity of the catalyst. For example, the selectivity of monoene formation in the partial hydrogenation of cyclopentadiene catalyzed by PVP-protected Pd nanoparticles increases with decreasing size below about 2 nm.[26] This is probably due to the steric effect and/or the surface structure effect of nanoparticle catalysts.

5.2. Bimetallic Structure

The catalytic activity of one metal is usually improved through the addition of another metal. Thus, the catalytic activity of bimetallic nanoparticles changes with their composition. Figure 8 shows the three types of changes of the catalytic activity of bimetallic nanoparticles depending on the composition of the metal elements. Curve (a) shows the case where the additive B can increase the catalytic activity of the metal A even though the additive B itself has a low or no catalytic activity. Curve (b) is the case where there is no interaction between metal A and metal B. Thus, the catalytic activity of bimetallic nanoparticles is just the average of those of metal A and B. Curve (c) shows the case that the additive B can decrease the catalytic activity of the metal A. This is reverse to the case (a).

The effect of the additive on the catalytic activity can be attributed to two kinds of effects. One is a ligand effect (an electronic effect) and the other is an ensemble effect (a steric effect). Let us consider the case where the metal A works as the catalyst and provides a catalytic site(s). If the additive metal B has the former effect on the catalysis of metal A, metal B can influence the electronic density and/or electronic structure of the metal A. In this case the metal B must be located near the metal A. Since the catalytic site is located on the metal A, it is not necessary that metal B is located on the surface, but must be located near the metal A. If the metal B is adjacent to the metal A, the effect could be most effective. In the case of an ensemble effect, on the other hand, both metals A and B must be located on the surface of the metal particles, since the catalytic sites of metal A are located on the surface and the metal B must attack the substrate together with the metal A. The metal B does not need to be adjacent to the metal A. However, it could be better for the metal B to be adjacent to the metal A, because then metal A and metal B can easily attack the substrate at the same time. These two effects are illustrated in Figure 9.

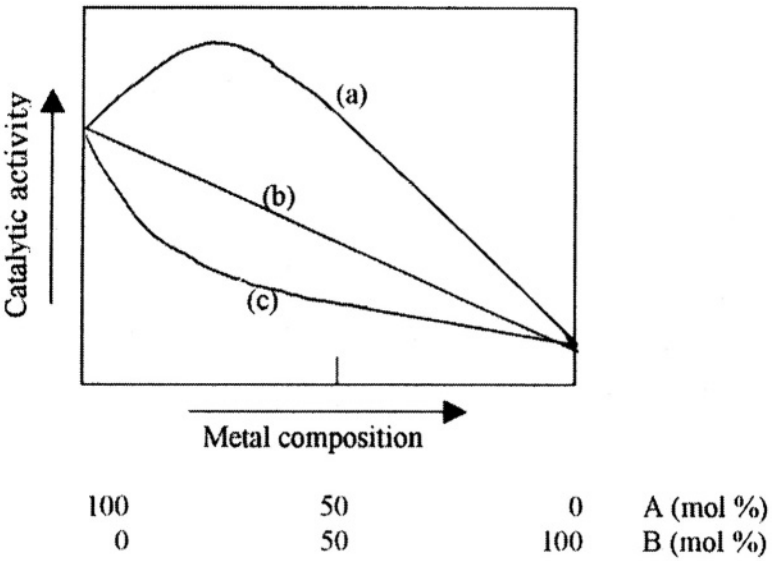

Figure 8. Dependence of catalytic activity of bimetallic nanoparticles upon the composition of metals A and B.

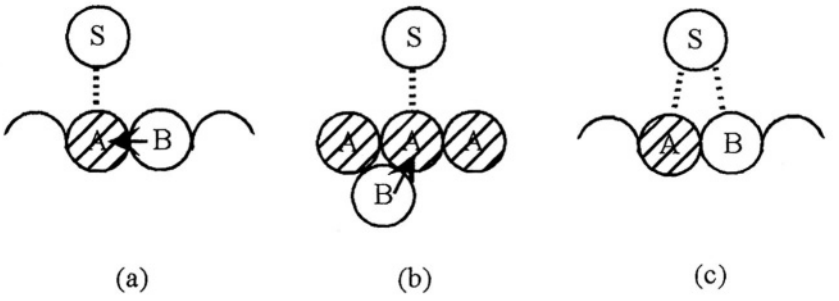

Figure 9. Schematic illustration of a ligand effect (a and b) and an ensemble effect (c).

When the metal A and the metal B form a bimetallic particle composed of the two elements, there are a variety of possible bimetallic structures. The most common structure could be a random alloy structure, where metals A and B are located completely at random. The cross section of the model structure for 55-atom clusters with A:B=1:1 is illustrated in Figure 10, in which Figure 10 (a) shows the random model.

The reversed structure to the random model could be a "cluster-in-cluster" strcuture. "Cluster-in-cluster" means that small metal clusters are located in a large cluster. Figure 10 (b) shows the case where a half-sphere cluster of metal A and another half-sphere cluster of metal B are combined to form a 55-atom cluster. This is one of the typical cluster-in-cluster structures.

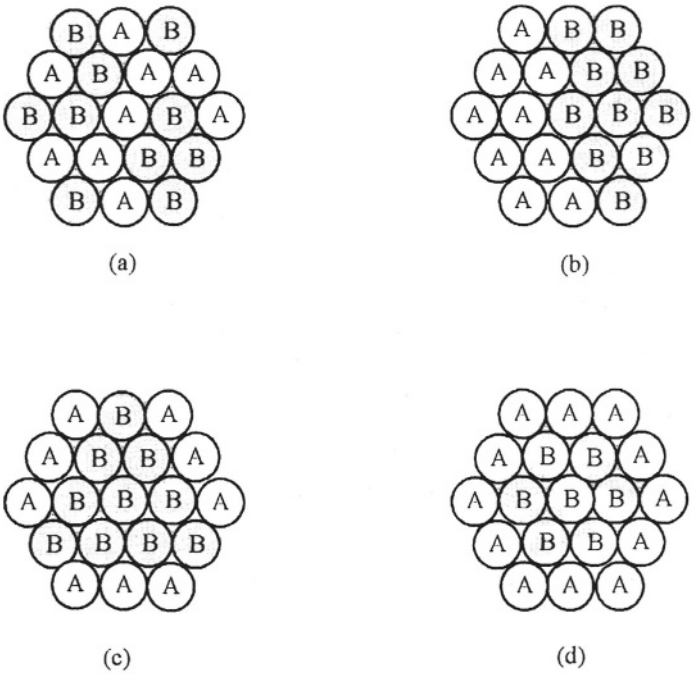

Figure 10. Schematic illustration of various structures of bimetallic nanoparticles. (a) random structure (A/B=1/1); (b) cluster-in-cluster structure (A/B=1/1); (c) core-shell structure (A/B=1/1); and (d) core-shell structure (A/B=4/1).

The other most interesting one will be a core-shell structure, where one metal forms a core and the other metal surrounds the core to form a shell. Figure 10 (c) shows the case where metal B forms a core and metal A surrounds the core. In this case some atoms of the core metal B are not located in the core but in the surface layer because the atomic ratio of metal A and B equals 1:1.

In the case of a 55-atom cluster with an fcc structure, 42 atoms are necessary to cover the core. Thus, the A-B bimetallic cluster with the atomic ratio of metal A and B of 4:1 can provide a completely covered core-shell structure as shown in Figure 10 (d). This kind of perfect core-shell structured bimetallic nanoparticles have been produced by simultaneous alcohol-reduction of Pd and Pt ions in the presence of poly(*N*-vinyl-2-pyrrolidone) (PVP). The structure shown in Figure10 (d) (A=Pd, B=Pt) was proved by EXAFS analysis.[15] Similar structures are produced in the combinations of two kinds of noble metal.[16,21,27] The mechanism for the formation of this kind of interesting structure by the simultaneous reaction has also been proposed.[28] Two factors are concerned with the formation of the core-shell structure. The first factor is redox potential. The metal easily reduced can form the core. The other factor is a coordination ability of the ligand polymer (PVP in this case) upon the metal. The metal strongly coordinated by the ligand polymer can form the shell.

The core-shell structure is interesting from the viewpoint of not only the structure itself, but also the catalysis. When the Pd-Pt bimetallic nanoparticles with various Pd/Pt ratios were produced in the presence of PVP, they have a similar size to each other, but display a quite different catalytic activity for selective partial hydrogenation of 1,3-cyclooctadiene to cyclooctene. The highest catalytic activity was achieved by the bimetallic nanoparticles with Pd/Pt=4/1. This is the nanoparticle with the perfect core-shell structure. The catalytic activity decreases with decreasing the Pd/Pt ratio, in other words, with decreasing number of Pd atoms. If the total catalytic activity is divided by the number of Pd atoms in a bimetallic nanoparticle, the catalytic activity of the Pd atoms nearly equals to each other. This means that all Pd atoms are located in the surface layer of the Pd-Pt bimetallic nanoparticles. In addition, the Pd atom in the bimetallic nanoparticles has much higher catalytic activity than the surface Pd atom in Pd monometallic nanoparticles. This fact demonstrates that the Pt atom, located in the core of bimetallic nanoparticles and adjacent to the surface Pd atom, affects the catalytic activity of the surface Pd atoms. This cannot be an ensemble effect but should be a ligand effect. The inner Pt atom should change the electronic density and/or structure of the surface Pd atoms, resulting in the higher catalytic activity of Pd-Pt bimetallic nanoparticles than Pd monometallic ones.

Now let's consider why and how these bimetallic structures are constructed. Thermodynamically stable structures should principally be favored. Sometimes, however, the structure can be controlled by kinetics. A kinetically controlled and thermodynamically non-equilibrium structure may be produced. Even if the thermodynamically stable structures are concerned, there are many factors to affect the stability. Not only the interactions between the metals, but also the interactions involving ligands, solvents and so on must be considered.

In order to simplify the discussion, only the interactions between metals will be considered now. In the A-B bimetallic nanoparticles, there are three kinds of bond, i.e., bonds A-A, B-B, and A-B. In relation to the strength of these three bonds, four kinds of structures are considered, namely: (a) core-shell, (b) inverted core-shell, (c) dispersed, and (d) cluster-in-cluster structures.

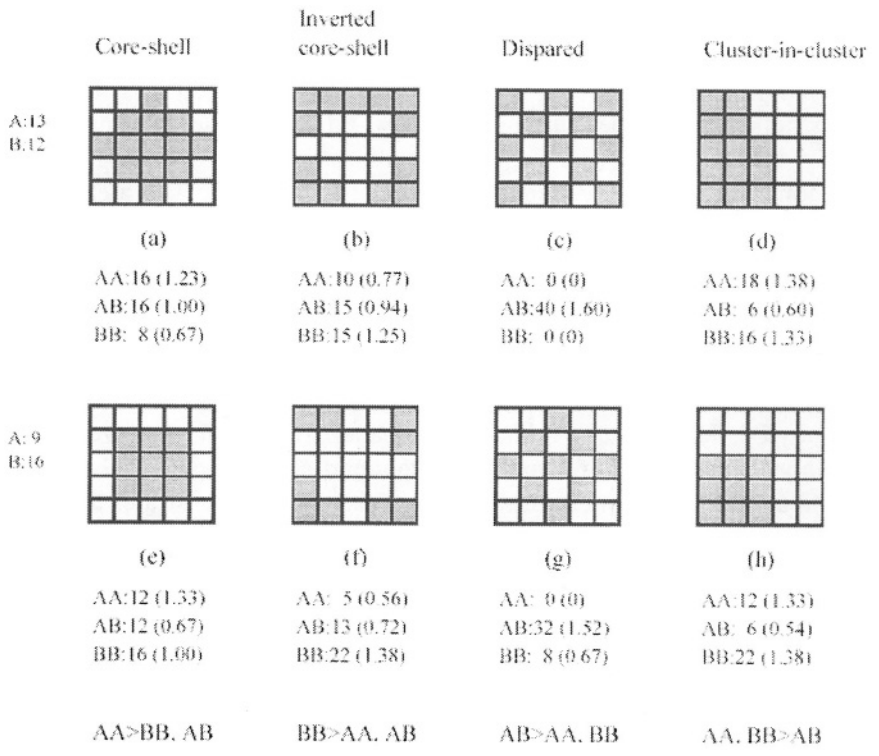

Figure 11. Two-dimensional illustration of various structures of bimetallic nanoparticles composed of A and B in relation with homobond (A-A and B-B) and heteromond (A-B)-philicity. 25-atom clusters composed of 13 A's and 12 B's (a~d) and 9 A's and 16 B's (e~h).

They are illustrated in a two-dimensional way in Figure 11. A hatched box shows atom A and an open box shows atom B. In the upper series (Figure 11 a - d), the clusters are composed of 13 atoms of metal A and 12 atoms of metal B. In the core-shell structure (Figure 11a), there exist 16 A-A bonds and each atom concerned with the bond has 1.23 A-A bonds in average (shown in brackets in Figure 11a). In the lower series (Figure 11 e - h), the bimetallic nanoparticles are composed of 9 atoms of metal A and 16 atoms of metal B. The number of bonds and the average number of bonds per atom concerned with the bond are shown in Figure 11 as well.

In the cases of core-shell structure (Figure 11 a and e), the average number of bonds per atom for the A-A bond is larger than those of B-B bond and A-B bond. This is shown in the last row in Figure 11. In the inverted core-shell structure (Figure 11 b and f), the average number of B-B bonds is larger than those of A-A and A-B bonds. In these cases the homo-bond (A-A or B-B bonds) is preferred to the hetero-bond (A-B bond). In other words, they are a homobond-philic structure, but there still remains the difference in homobond strength between A-A and B-B bonds.

In contrast, the heterobond (bond A-B) is preferred to the homobond (A-A and B-B bonds) in the dispersed structures (Figure 11 c and g). This is a heterobond-philic structure. Sometimes, this structure is referred to as a completely random structure. But this is not correct because “complete random” should allow any atom to be located adjacent to atom A. Then homobond A-A could be formed.

In the case of Figure 11c neither A-A nor B-B bonds are formed. Opposite to the

dispersed structure, "cluster-in-cluster" (Figure 11 d and h) is a homobond-philic structure, where bond A-A and bond B-B are equally favored. The concept of heterobond and homobond-philicity could be very important for understanding the structure of bimetallic nanoparticles. The structures of Cu-Pd bimetallic nanoparticles can be understood by this concept.[29] The Cu-Pd bimetallic nanoparticles were first prepared by thermal decomposition of a bimetallic acetate precursor.[30] Later, well-defined PVP-protected Cu-Pd bimetallic nanoparticles were prepared by reduction of $CuSO_4$ and $Pd(CH_3COO)_2$ in refluxing glycol/dioxane at $pH \approx 0$ in the presence of PVP.[31] These nanoparticles are very important from a viewpoint of catalysis, because they have high catalytic activity for two completely different reactions, i.e., hydration of acrylonitrile to acrylamide and selective partial hydrogenation of 1,3-cyclooctadiene to cycooctene. The former hydration of acrylonitrile is usually catalyzed by Cu and the latter hydrogenation of octadiene, by Pd. The same Cu-Pd bimetallic nanoparticles can catalyze both reactions, and the catalytic activities of bimetallic nanoparticles are much higher than the corresponding monometallic ones, respectively. This result demonstrates that both Cu and Pd atoms are located in the surface layer of bimetallic nanoparticles. In fact the ensemble effect of Pd is proposed for the hydration of acrylonitrile catalyzed by Cu-Pd bimetallic nanoparticles.[32]

Now let us consider the core-shell and inverted core-shell structures shown in Figure 11. The core-shell structure and the inverted core-shell structure are based on the very same concept. The difference is just which homobond, A-A or B-B, is favored. If A-A bond is preferred to B-B bond but the inverted core-shell structure is still constructed, then this inverted core-shell structure should be thermodynamically unstable and of great interest. This has been successfully achieved by using the so-called "sacrificial hydrogen strategy".[32] In the case of Pd-Pt bimetallic nanoparticles, Pd-cores were first prepared. After the Pd-cores were covered by hydride by contact with molecular hydrogen, Pt ions were added to be reduced by hydride adsorbed on the surface of Pd-cores, which resulted in bimetallic nanoparticles with the inverted core-shell structure of Pd-core and Pt-shell. Without the sacrificial hydrogen strategy the successive reduction cannot give rise to the inverted core-shell structure but rather to the cluster-in-cluster structure usually. The thermodynamical instability of the present inverted core-shell structure has been confirmed by the change of the catalytic activity of nanoparticles with inverted core-shell structure with heat treatment.[33]

6. EFFECT OF POLYMER FIELD ON CATALYSIS OF METAL NANOPARTICLES

As described in the last section, the polymers surrounding the metal nanoparticle play an important role to stabilize nanoparticles and control the structure. The stability of metal nanoparticles, especially under catalytic reaction conditions, is very important. To understand the effect of the polymer on this stability is still a target of researchers.[34,35] In addition, some polymers and organic stabilizers are used for modifying the metal nanoparticles to be stabilized in not only aqueous but also nonaqueous solutions. The palladium nanoparticles were stabilized by polystyrene-*b*-poly-4-vinylpyridine micelles in toluene and used as a catalyst for the coupling reaction of styrene and 4-bromoacetophenone (Heck reaction).[36] Palladium nanoparticles embedded in inverse microemulsions were prepared by reduction of palladium acetate by ethanol in systems

containing tetrahydrofuran (THF) as dispersion medium and tetradodecylammonium bromide surfactant as stabilizer.[37] Cobalt nanoparticles, synthesized by decomposition of biscobalt octacarbonyl in dioctyl ether in the presence of oleic acid and trioctylphosphine, were used in THF as catalysts for cycloaddition of alkynes with alkenes and carbon monoxide to cyclopentenones (Pauson-Khand reaction).[38]

On the other hand, the polymers or stabilizers play an important role to improve the catalytic activity and selectivity of metal nanoparticles, which is similar to the case of protein surrounding the active site of metal enzymes.[9] The polymers usually have interactions with substrate molecules, which can increase the rate of reaction with the substrates and/or increase the selectivity by choosing the particular substrate (cf. Figure 12). For example, acidic or basic polymers can construct the acidic or basic reaction field. The acidic polymers can concentrate basic substrates into the acidic polymer field near the metal nanoparticles. This concentration of basic substrates can increase the reaction rate of the basic substrates. In contrast, the polymers involving basic functional groups like amino groups can increase the reaction of acidic substrates.[39]

Acidic polymers such as poly(acrylic acid) can interact with not only basic substrates but also metal ions. These metal ions, which can be located near the metal nanoparticle catalysts by the interactions with acidic polymer surrounding the nanoparticles, can play a role of the promoter for the metal nanoparticle catalyst.

For example, the lanthanide ions located near Pd and Ag nanoparticles by this method can promote the hydrogenation of oxygen-containing olefins and epoxidation of ethylene with oxygen, respectively.[40] The other examples of the effect of coexisting metal ions on the catalytic activity of metal nanoparticles were reported for enantioselective hydrogenation of methyl pyruvate over PVP-protected Pt nanoparticle catalysts[41] and hydrogenation of o-chloronitrobenzene over PVP-protected Ru nanoparticle catalysts.[42].

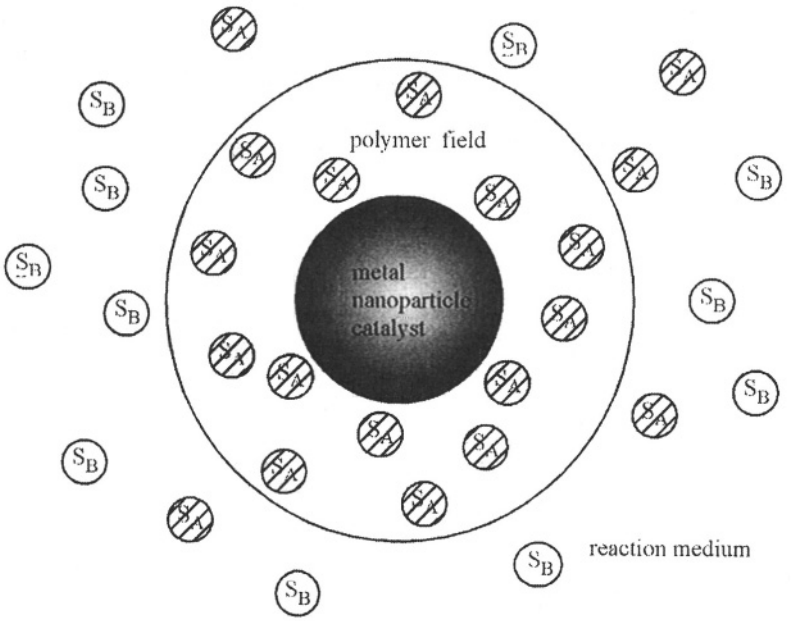

Figure 12. Schematic illustration of the effect of polymer field upon the concentration of favorite substrates S_A from mixtures of substrates S_A and S_B in a reaction medium.

Cyclodextrins are known to play a role of molecular recognition. This property can be used for improvement of catalytic properties of metal nanoparticles. Metal nanoparticles surrounded by polycyclodextrin were prepared and applied to the catalysis. Reactions of the substrates which can be easily included into the cavity of cyclodextrin were accelerated by the presence of polycyclodextrins surrounding metal nanoparticle catalysts.[43] Coordination of optical active ligands to the metal nanoparticle catalysts can promote the enatioselective reactions.[41,44]

Hydrophobic fields surrounding metal nanoparticle catalysts can play another role to improve the catalytic activity. The micelles surrounding metal nanoparticles are one of the most interesting examples. For example, the hydrophobic field can accelerate the charge separation in photochemical hydrogen generation (artificial photosynthesis) by favorite interactions with cation radicals of viologen rather than those with dications.[45] The micelles surrounding the nanoparticles can also provide the aligned field, which can align the substrate molecules. This alignment can provide a suitable regioselectivity in the catalytic reactions.[46]

7. CONCLUDING REMARKS AND FUTURE ASPECTS

Recent developments in chemistry including chemistry of macromolecular complexes makes it easy to construct the metal nanoparticles with the desired size and structure. Design of not only size and structure of metal parts of the nanoparticles but also properties and alignment of polymer field surrounding the nanoparticles is important to develop tailor-made catalysts. This is now in hand for chemists. Recent research targets on metal nanoparticles for catalysis are:

(a) control of structures of metal parts,[47] especially those of bimetallic and multimetallic nanoparticles,[48]
(b) control of the structures and properties of the surroundings of metal naoparticles, especially for stabilization of catalysts and improvement of selective reactions, and
(c) application of metal nanoparticles to practical catalysts, for example by supporting on inorganic supports.[49-52]

Metal nanoparticle catalysts can now be applied to a lot of reactions. Hydrogenation and hydrosilation of olefins or dienes are one of the most popular reactions. Other kinds of reductions and C-C coupling reactions like Heck reaction and Suzuki reaction are the other target. Oxidation reactions have been less reported because the organic stabilizers are usually less stable for oxidation than for reduction. However, this limitation is now removed by using more stable stabilizers.

Real tailor-made catalysts for industrial purposes will be expected to be developed on the basis of the basic research results on metal nanoparticles in the near future.

8. REFERENCES

1. G. Schmid (Ed.): *Clusters and Colloids. From theory to Applications* (VCH, Wienheim, 1994).
2. N. Toshima and T. Yonezawa, Bimetallic nanoparticles—novel materials for chemical and physical applications, *New J. Chem.* **22**, 1179-1201 (1998).

3. N. Toshima and Y. Shiraishi, Catalysis by metallic colloids. In: *Encyclopedia of Surface and Colloid Science,* edited by A. T. Hubbard (Marcel Dekker, New York, 2002), pp. 879-886.
4. H. Hirai and N. Toshima, Polymer-attached catalysis. In: *Tailored Metal Catalysts,* edited by Y. Iwasawa (D. Reidel Pub. Co., Dordrecht, 1985), pp. 87-140.
5. H. Hirai, Y. Nakao, N. Toshima, and K. Adachi, Colloidal rhodium in polyvinyl alcohol as hydrogenation catalyst of olefins, *Chem. Lett.,* 905 (1976).
6. N. Toshima, K. Kushihashi, T. Yonezawa, and H. Hirai, Colloidal dispersions of palladium-platinum bimetallic clusters protected by polymers. Preparation and application to catalysis, *Chem. Lett.,* 1769-1772 (1989).
7. A. S. Eppler, G. Rupprechter, E. A. Anderson, and G. A. Somorjai, Thermal and chemical stability and adhesion strength of Pt nanoparticle arrays supported on silica studied by transmission electron microscopy and atomic force microscopy, *J. Phys. Chem. B* **104**, 7286-7292 (2000).
8. A. S. Eppler, J. Shu, E. A. Anderson, and G. A. Somorjai, Model catalysts fabricated by electron beam lithography: AFM and TPD surface studies and hydrogenation/dehydrogenation of cyclohexene/H_2 on a Pt nanoparticle array supported by silica, *Topics in Catal.* **13**, 33-41 (2000).
9. N. Toshima, Nanostructured metal clusters in polymeric field as a model of artificial enzyme, *Supramol. Sci.* **5**, 395-398 (1998).
10. N. Toshima, Reactions in homogeneous solutions. In: *Fine Particle. Synthesis, Characterization, and Mechanism of Growth,* edited by T. Sugimoto (Marcel Dekker, New York, 2000), pp. 430-459.
11. S. S. Hladyi, M. K. Starchevsky, Y. A. Pazdersky, M. N. Vargaftik, and I. I. Moiseev, Oxidative and anaerobic reactions of benzyl alcohol catalysed by a Pd-561 giant cluster, *Mendeleev Commun.,* 45-46 (2002).
12. J. S. Bradley, The chemistry of transition metal colloids. In: *Clusters and Colloids. From Theory to Application,* edited by G. Schmid (VCH, Wienhiem, 1994), pp. 459-544.
13. H. Bönneman and W. Brijoux, Surfactant-stabilized nanosized colloidal metals and alloys as catalyst precursors. In: *Advanced Catalysts and Nanostructured Materials,* edited by W. R. Moser (Academic Press, San Diego, 1996), pp. 165-196.
14. T. Teranishi and N. Toshima, Preparation, characterization and properties of bimetallic nanoparticles. In: Catalysis and Electrocatalysis at Nanoparticle Surfaces, edited by E. R. Savinova, et al. (Marcel Dekker, New York, 2002) in press.
15. N. Toshima, M. Harada, T. Yonezawa, K. Kushihashi, and K. Asakura, Structural analysis of polymer-protected Pd-Pt bimetallic clusters as dispersed catalysts by using extended X-ray absorption fine structure spectroscopy, *J. Phys. Chem.* **95**, 7448-7453 (1991).
16. N. Toshima, M. Harada, Y. Yamazaki, and K. Asakura, Catalytic activity and structural analysis of polymer-protected Au-Pd bimetallic clusters prepared by the simultaneous reduction of $HAuCl_4$ and $PdCl_2$, *J. Phys. Chem.* **96**, 9927-9933 (1992).
17. Y. Mizukoshi, T. Fujimoto, Y. Nagata, R. Oshima, and Y. Maeda, Characterization and catalytic activity of core-shell structured gold/palladium bimetallic nanoparticles synthesized by the sonochemical method, *J. Phys. Chem. B* **104**, 6028-6032 (2000).
18. M.-L. Wu, D.-H. Chen, and T.-C. Huang, Synthesis of Au/Pd bimetallic nanoparticles in reverse micelles, *Langmuir* **17**, 3877-3883 (2001).
19. T. Yonezawa, T. Tominaga, and N. Toshima, Novel Characterization of the structure of surfactants on nanoscopic metal clusters by a physico-chemical method, *Langmuir* **11**, 4601-4604 (1995).
20. M. T. Reetz, W. Helbig, S. A. Quaiser, U. Stimming, N. Breuer, and R. Vogel, Visualization of surfactants on nanostructured palladium clusters by a combination of STM and high-resolution TEM, *Science* **267**, 367-369 (1995).
21. M. Harada, K. Asakura, and N. Toshima, Structural analysis of polymer-protected platinum/rhodium bimetallic clusters using extended X-ray absorption fine structure spectroscopy. Importance of microclusters for the formation of bimetallic clusters, *J. Phys. Chem.* **98**, 2653-2662 (1994).
22. M. P. Pileni, Nanosized particles made in colloidal assemblies, *Langmuir* **13**, 3266-3276 (1997).
23. X. Fu, Y. Wang, N. Wu, L. Gui, and Y. Tang, Shape-selective preparation and properties of oxalate-stabilized Pt colloid, *Langmuir* **18**, 4619-4624 (2002).
24. H. Hirai, Y. Nakao, and N. Toshima, Colloidal rhodium in poly(vinylpyrrolidone) as hydrogenation catalyst for internal olefins, *Chem. Lett.,* 545 (1978).
25. N. Toshima, M. Kuriyama, Y. Yamada, and H. Hirai, Colloidal platinum catalyst for light-induced hydrogen evolution from water. A particle size effect, *Chem. Lett.,* 793-796 (1981).
26. H. Hirai, H. Chawanya, and N. Toshima, Colloidal palladium protected with poly(N-vinyl-2-pyrrolidone) for selective hydrogenation of cyclopentadiene, *Reactive Polym.* **3**, 127-141 (1985).
27. N. Toshima and K. Hirakawa, Polmer-protected bimetallic nanocluster catalysts having core/shell structure for accelerated electron transfer in visible-light-induced hydrogen generation,*Polym. J.* **31**, 1127-1132 (1999).

28. T. Yonezawa and N. Toshima, Mechanistic consideration of formation of polymer-protected nanoscopic bimetallic clusters, *J. Chem. Soc., Faraday Trans.* **91**, 4111-4119 (1995).
29. C.-R. Bian, S. Suzuki, K. Asakura, L. Ping, and N. Toshima, EXAFS studies on the structure of the PVP-stabilized Cu/Pd nanoclusters colloidally dispersed in solution, *J. Phys. Chem. B,* in press (2002).
30. K. Esumi, T. Tano, K. Torigoe, K. Meguro, Preparation and characterization of bimetallic palladium-copper colloids by thermal decomposition of their acetate compounds in organic solvents, *Chem. Mater.* **2**, 564-567(1990).
31. N. Toshima and Y. Wang, Preparation and catalysis of novel colloidal dispersions of copper/noble metal bimetallic clusters, *Langmuir* **10**, 4574-4580 (1994).
32. Y. Wang and N. Toshima, Preparation of Pd-Pt bimetallic colloids with controllable core/shell structures, *J. Phys. Chem. B* **101**, 5301-5306 (1997).
33. N. Toshima, Y. Shiraishi, A. Shiotsuki, D. Ikenaga, and Y. Wang, Novel synthesis, structure and catalysis of inverted core/shell structured Pd/Pt bimetallic nanoclusters, *Eur. Phys. J. D* **16**, 209-212 (2001).
34. M. T. Reetz and G. Lohmer, Propylene carbonate stabilized nanostructured palladium clusters as catalysts in Heck reactions, *Chem. Commun.,* 1921-1922 (1996).
35. Y. Li and M. A. El-Sayed, The effect of stabilizers on the catalytic activity and stability of Pd colloidal nanoparticles in the Suzuki reactions in aqueous solution, *J. Phys. Chem. B* **105**, 8938-8943 (2001).
36. S. Klingelhöfer, W. Heitz, A. Greiner, S. Oestreich, S. Förster, and M. Antonietti, Preparation of palladium colloids in block copolymer micelles and their use for the catalysis of the Heck reaction, *J. Am. Chem. Soc.* **119**, 10116-10120(1997).
37. S. Papp and I. Dékány, Structural properties of palladium nanoparticles embedded in inverse microemulsions, *Colloid Polym. Sci.* **279**, 449-458 (2001).
38. S.-W. Kim, S. U. Son, S. S. Lee, T. Hyeon, and Y. K. Chung, Colloidal cobalt nanoparticles: a highly active and reusable Pauson-Khand catalyst, *Chem. Commun.,* 2212-2213 (2001).
39. M. Ohtake, M. Komiyama, H. Hirai, and N. Toshima, Effects of polymer support on substrate selectivity of covalently immobilized ultrafine rhodium particles as catalyst for olefin hydrogenation, *Macromolecules* **24**, 5567-5572 (1991).
40. N. Toshima, Y. Shiraishi, and T. Teranishi, Effect of additional metal ions on the catalysis of polymer-stabilized metal nanoclusters, *J. Mol. Catal. A, Chem.* **177**, 139-147 (2001).
41. X. Yan, H. Liu, and J. Zhao, Improvement in the enantioselective hydrogenation of mehyl pyruvate over platinum clusters by addition of rare earth cations, *Catal. Lett.* **74**, 81-83 (2001).
42. X. Yan, M. Liu, H. Liu, K. Y. Liew, and N. Zhao, Metal complex effect on the hydrogenation of o-chloronitrobenzene over polymer-stabilized colloidal ruthenium clusters, *J. Mol. Catal. A. Chem.* **170**, 201-208(2001).
43. Y. Shiraishi, M. Hayashi, and N. Toshima, Preparation and catalysis of poly(β-cyclodextrin)-stabilized palladium nanoclusters, *Abstracts of 9 Int'l. Symp. Macromol.-Metal Complexes,* August 2001, New York, Poster Abstract No. 49.
44. H. Bönnemann and G. A. Braun, Enantioselective hydrogenations on platinum colloids, *Angew. Chem. Int. Ed. Engl.* **35**, 1992-1995 (1996).
45. N. Toshima, T. Takahashi, and H. Hirai, Polymerized micelle-protected platinum clusters. Preparation and application to catalyst for visible light-induced hydrogen generation, *J. Macromol. Sci. Cham.* **A25**, 669-686 (1988).
46. N. Toshima and T. Takahashi, Colloidal dispersion of platinum and palladium cluster embedded in micelles. Preparation and application to catalysis for hydrogenation of olefins, *Bull. Chem. Soc. Jpn.* **65**, 400-409 (1992).
47. S.-W. Kim, M. Kim, W. Y. Lee, and T. Hyeon, Fabrication of hollow palladium spheres and their successful application to the recyclable heterogeneous catalyst for Suzuki coupling reactions, *J. Am. Chem. Soc.* **124**, 7642-7643 (2002).
48. S. Hermans, R. Raja, J. M. Thomas, B. F. G. Johson, G. Sankar, and D. Gleeson, Solvent-free, low-temperature, selctive hydrgenation of polyenes using a bimetallic nanoparticle Ru-Sn catalyst, *Angew. Chem. Int. Ed. Engl.* **40**, 1211-1215 (2001).
49. H. Bönnemann, W. Brijoux, A. S. Tilling, and K. Siepen, Application of heterogeneous colloid catalysts for the preparation of fine chemicals, *Topics in Catalysis* **4**, 217-227 (1997).
50. H. Bönnemann, U. Endruschat, B. Tesche, A. Rufínska, C. W. Lehmann, F. E. Wagner, G. Filoti, V. Pârulescu, and V. I. Pârulescu, An SiO_2-embedded nanoscopic Pd/Au alloy colloid, *Eur. J. Inorg. Chem.* 819-822 (2000).
51. J. P. M. Niederer, A. B. J. Arnold, W. F. Hölderich, B. Spliethof, B. Tesche, M. Reetz, and H. Bönnemann, Noble metal nanoparticles incorporated in mesoporous hosts, *Topics in Catalysis* **18**, 265-269 (2002).
52. H. Bönnemann and N. Waldöfner, Preparation and characterization of three-dimensional Pt nanoparticle networks, *Chem. Mater.* **14**, 1115-1120 (2002).

4

ULTRAFAST DYNAMICS OF METAL NANOSPHERES AND NANORODS

Min Hu and Gregory V. Hartland *

1. INTRODUCTION

The optical properties of metal nanoparticles have played a key role in the development of physical chemistry and nanotechnology.[1] The existence of metal particles in solution was first recognized by Faraday in 1857,[2] and a quantitative explanation of their colour was given by Mie in 1908.[3] Mie's theory allows the extinction spectra of spherical particles to be calculated from the dielectric constants of the metal and the surrounding medium. These calculations show that the distinctive colours of metal particle solutions arise from a collective dipolar oscillation of the conduction electrons, which is called the surface plasmon band.[1] The position of the plasmon band depends on the identity of the metal and the surroundings and is also sensitive to the distance between particles. For example, the characteristic purple colour of flocculated Au sols arises from dipolar coupling between the plasmon oscillations of neighbouring particles. For Au, Ag and Cu the plasmon band falls in the visible region of the spectrum, and is responsible for the brilliant colours of solutions of these particles. For most other metals the plasmon band occurs in the UV, yielding solutions with a drab grey or brown colour.[1] Mie's theory is extremely successful, so much so that deviations from it are automatically assigned to changes in the dielectric constant of the material. For example, the broadening of the plasmon band for small Au or Ag particles is attributed to electronic scattering at the particle surface, which becomes significant when the particle diameter is less than the mean free path of the electrons in the metal.[4-7]

Recent optical experiments with metal nanoparticles have concentrated on using time-resolved techniques to study the electron dynamics. The majority of these experiments (ours included) have been performed with ca. 100 fs laser pulses, which provide sufficient time resolution to study coupling between the excited electron distribution and the phonon modes of the particles.[8-15] Our view of the photophysics of these materials is that the ultrafast laser pulse excites single electrons, that rapidly redistribute their energy over the entire electron distribution, causing an increase in the electronic temperature.[16,17] This broadens the plasmon band,[18,19] causing a strong

* Min Hu and Gregory V. Hartland. Department of Chemistry and Biochemistry, University of Notre Dame, Notre Dame, IN 46556-5670, USA

bleaching at the band maximum.[17] The initial temperature of the electrons can be calculated from the electronic heat capacity and the number of photons absorbed by the particle.[20] Because metal particles can absorb many photons (their absorption transitions do not bleach in the same way that molecules do) and electrons have a very small heat capacity, the initial temperature rise can be very large, thousands of Kelvin.[16,17,20] The hot electron distribution then equilibrates with the phonon modes via electron-phonon (*e-ph*) coupling. This process can be described using the Two-Temperature Model (TTM).[21-24]

In the TTM the electron and phonon sub-systems are characterised by two separate temperatures, T_E and T_L, and they exchange energy in a way that depends on the difference in temperature. Specifically,

$$C_E \frac{dT_E}{dt} = -g(T_E - T_L) \tag{1a}$$

and

$$C_L \frac{dT_L}{dt} = g(T_E - T_L) \tag{1b}$$

where C_E and C_L are the electronic and lattice heat capacities, and g is the electron-phonon (*e-ph*) coupling constant.[21-24] The electronic and lattice heat capacities play off each other in an interesting way. The lattice heat capacity is over two orders of magnitude larger than the electronic heat capacity,[25] which means that the overall change in the lattice temperature (once the electrons and phonons have reached equilibrium) is much less than the initial electronic temperature. However, inspection of Eq. (1a) shows that the time scale for coupling between the electrons and phonons is controlled by C_E/g.[26] Thus, the overall temperature rise is determined by C_L, but the time scale for heating is determined by C_E. Given that the electronic heat capacity is known, time resolved measurements for metal particles (or for bulk metals) yield g — the *e-ph* coupling constant. For particles larger than a few nanometres the size dependence of g is moderate,[26-30] and can be explained by classical theories that consider how the electrons couple to the surface phonon modes of the particles.[31] For Au particles (which have been the main topic of our studies) the value for the *e-ph* coupling constant is the same as bulk Au for particles as small as 2 nm.[28]

Current topics of interest in this field are to perform measurements on very fast time scales (< ps) to examine the dynamics before the electrons have equilibrated amongst themselves,[32,33] or (conversely) to look at slower time scales to investigate heat dissipation to the environment.[34-37] The last point has been neglected by the ultrafast community, but it is an important issue for nanoparticle applications. For example, heat dissipation from bio-functionalized Au particles has been used to selectively kill cells and study denaturation of proteins.[38] Heat dissipation is also an important consideration in laser-induced annealing, and size and shape transformation of metal particles,[39-47] as well as for laser-induced alloying of multi-component particles.[48] The time scale for heat dissipation will be one of the points discussed in this article.

Another topic that will be examined in detail is lattice expansion. The heat deposited into the lattice causes the particles to expand. For Au particles larger than ca. 6 nm, the time scale for heating (C_E/g) is faster than the period of the phonon mode that corresponds to the expansion co-ordinate — which is the symmetric breathing mode for spherical particles.[49-52] This means that this mode can be impulsively excited. The

coherently excited vibrational motion shows up as a modulation in the transient absorption traces because it changes the electron density and, therefore, the position of the plasmon resonance of the particles.[50,52,53] The observed period depends on the size and shape of the particles, and their elastic properties.[1,50-52,54-57]

The vibrational modes of spherical particles have been analysed using continuum mechanics. The result for the symmetric breathing mode is[54,55]

$$\tau = \frac{2\pi R}{\eta c_l} \tag{2}$$

where R is the radius of the particle, c_l is the longitudinal speed of sound, and η is an eigenvalue that depends on the transverse and longitudinal speeds of sound. The value of η can be determined by solving the boundary condition equation: $\eta\cot\eta = 1 - \eta^2/4\delta^2$ where $\delta = c_t/c_l$ and c_t is the transverse speed of sound.[54-57] This result assumes that the particles are isotropic, i.e., polycrystalline. Calculations using Eq. (2) and values of c_l and c_t for bulk Au are in excellent agreement with our experimental data for Au particles with diameters between 8 nm and 120 nm.[52] This means that the elastic constants of 8 nm diameter particles (~16,000 atoms) are the same as those for bulk Au. Unfortunately, simple expressions for the period are not available for the vibrational modes of non-spherical particles, or for particles that are single crystals.

The aim of this chapter is to review our recent work on heat dissipation and coherent vibrational motion in nanospheres and nanorods. The topics that will be examined are: (i) The mechanism for coherent excitation of vibrational motion (lattice expansion versus hot electron pressure). (ii) How the time scale for heat dissipation depends on the size of the particles and the intensity of the excitation source (i.e., the initial temperature rise). (iii) Mode softening in spherical particles at high temperatures. (iv) How the measured period depends on the shape of the particles, especially the differences between spheres and rods. As a whole these experiments demonstrate a unique capability of transient absorption studies of nanoparticles — they can provide information about the elastic constants of nanometer sized objects. Specifically, our measurements provide information about the transverse and longitudinal speeds of sound, which are related to the bulk (K) and shear (G) moduli by:[58]

$$c_l = \sqrt{\frac{K + 4/3\,G}{\rho}} \qquad \text{and} \qquad c_t = \sqrt{\frac{G}{\rho}} \tag{3}$$

where ρ is the density. It is important to note that this information cannot be obtained by conventional (or even non-conventional) techniques, due to the difficulty in making mechanical contact with the samples. The work discussed in this chapter is a combination of recently published and unpublished results and, as such, represents a review of work that we feel is extremely topical and exciting. Of course, this means that some of the statements in this chapter are a little speculative, and may be modified as our understanding of these systems improves!

2. EXPERIMENTAL TECHNIQUES

The experiments described in this paper were performed with a regeneratively amplified Ti:Sapphire laser (Clark-MXR, CPA-1000) pumped by a Spectra Physics Millenia Vs solid-state diode pumped Nd:YAG laser. The output of the regenerative amplifier (λ = 780 nm; 0.5 mJ/pulse; 120 fs fwhm $sech^2$ deconvolution; 1 kHz repetition rate) is split by a 90:10 beamsplitter. The 90% portion is frequency doubled in a 1 mm BBO crystal to generate 390 nm pump pulses. The intensity of these pulses is controlled with a $\lambda/2$-waveplate/polarizer combination. The 10% portion is used to generate a white light continuum in a 3 mm sapphire window, which was used as the probe. The pump and probe are cross-overlapped at the sample by focussing with a 10 cm lens, and the polarizations are typically set to parallel. The relative polarization of the pump and probe beams is not crucial for spherical metal particles. Specific probe wavelengths are selected using a Jobin-Yvon Spex H-10 monochromator (10 nm spectral resolution) placed after the sample. Fluctuations in the probe laser intensity are normalized by splitting-off and monitoring a small portion of the probe beam before the sample.[17] The timing between the pump and probe pulses was controlled by a stepper motor driven translation stage (Newport UTM150PP.1). The length of the translation stage and the geometry of our experiment allow us to collect transient absorption data over an ca. 500 ps delay range. The pump laser intensity at the sample was measured by a Molectron J3-02 Energy Detector, and the pump laser spot size was ~ $6x10^{-4}$ cm^2 for the experiments described below. The spot size was measured using both standard laser burn paper or by observing the laser-induced colour change in a thin film of Au particles deposited on a glass slide. These measurements gave equivalent results, but the images of the beam are much clearer from the thin Au particle films.

Au particles with a 15 nm diameter were prepared using the standard citrate reduction recipe.[59] Smaller 4 nm diameter Au particles were made using $NaBH_4$ as the reductant rather than citrate.[60] Larger diameter particles were made by depositing Au onto the surface of the 15 nm particles using radiation chemistry.[61,62] In this technique the excess citrate is removed by ion exchange with Cl^- and a Au salt is added to the solution. The Au salt is then reduced onto the existing particles by γ-irradiating under an atmosphere of nitrous oxide with ~0.3 M methanol added to the solution. The particle sizes were measured either by TEM, or by observing quantum beats due to the symmetric breathing mode of the particles in transient absorption experiments. Although it is not strictly relevant to the experiments discussed in this paper, radiation chemistry is an extremely flexible technique for synthesizing metal nanoparticles. For example, core-shell bimetallic particles can be simply produced by adding a salt of a different metal to a solution of "seed" particles. This technique has been used to produce bimetallic particles with a core of Au, Ag, Pd or Pt, and shells of Au, Ag, Pt, Cd, Hg or Tl.[61-69] Tri-metallic particles have even been produced by successive radiation treatments.[70]

Samples of Au nanorods were obtained from Prof. Paul Mulvaney of the University of Melbourne. The rods were synthesized using the electrochemical technique first described by Wang and co-workers.[42,71-73] The nanorod samples used in our experiments had average aspect ratios between 2 and 5.5, and widths between 12 and 28 nm. Despite extensive purification, these samples are polydisperse, i.e., each sample contains a wide distribution of different length rods. The UV-vis absorption spectra of the samples show the characteristic longitudinal and transverse plasmon resonances, that correspond to

oscillation of the conduction electrons along the length or width of the rod.[42,71-73] The transverse plasmon band appears at ca. 520 nm for all the samples, whereas, the longitudinal resonance appears between 600 nm and 840 nm, depending on the aspect ratio. It is important to note that the absorbance at the pump laser wavelength (400 nm) does not strongly depend on aspect ratio, i.e., in our experiments all the rods in the sample are equally excited by the pump laser pulses. The samples were held in 2 mm cuvettes for the transient absorption experiments, and the data was collected without flowing or stirring. However, the relatively low pump laser powers and repetition rates used in these experiments mean that thermal effects — which arise from heat accumulation in the solvent — are not a problem.

3. RESULTS AND DISCUSSION

3.1. Coherent Vibrational Motion in Nanospheres: Observations and Excitation Mechanism

Figure 1 shows results from transient absorption experiments with ca. 50 nm diameter Au particles performed with a series of probe wavelengths. Modulations due to the symmetric breathing mode can be clearly seen in the data. The maximum in the modulations occurs at ca. 550 nm, which is 25 nm red-shifted from the maximum of the plasmon band for these samples. Careful inspection of the transient absorption data shows that the modulations for probe wavelengths on the red and blue sides of the plasmon band are 180° out-of-phase. This implies that this signal arises from a periodic change in the position of the plasmon band.

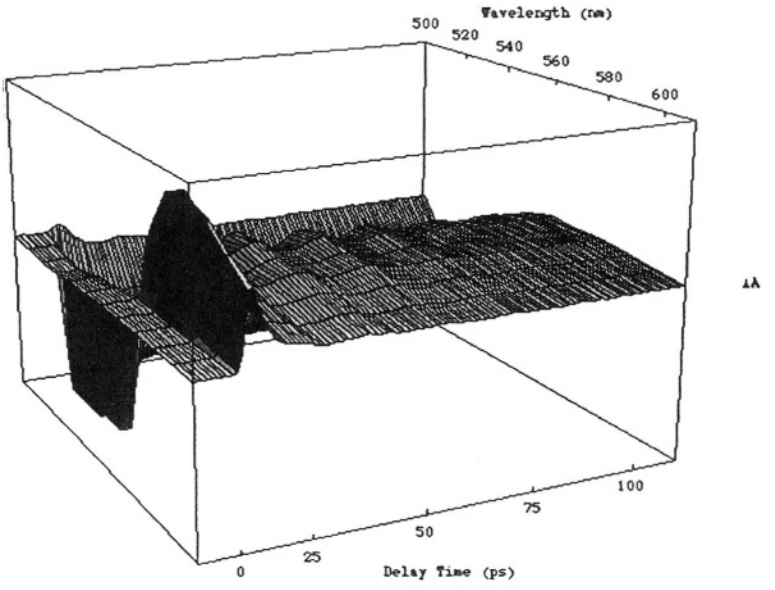

Figure 1. Transient absorption data for ca. 50 nm diameter Au particles in aqueous solution, recorded with different probe laser wavelengths. Note that the strong bleach signal in the 520 nm to 560 nm region has been cut-off to better illustrate the modulated portion of the data.

The transient absorption data in Figure 1 can be use to determine how the position of the plasmon band (ω_{max}) changes with time. The peak position versus time data, in turn, allows us to estimate how the size of the particles changes with time.[74] Assuming that the dielectric function of the metal is dominated by free electron contributions,[25] it can be shown that the maximum of the plasmon band occurs at:[1]

$$\omega_{max}^2 = \frac{\omega_p^2}{(1+2\varepsilon_m)}, \tag{4}$$

where ε_m is the dielectric constant of the medium and ω_p is the plasma frequency. The plasma frequency is given by $\omega_p^2 = ne^2 / \varepsilon_o m_e$ where n is the electron density, m_e is the effective mass of the electrons, and ε_o and e have their usual meanings.[25] Calculations using Eq. (4) to convert the ω_{max} data to radius versus time are shown in Figure 2.[74] The important points to note are that: (i) laser excitation produces an overall increase in the radius of the particles of ~0.4%, just after the electrons and phonons have reached equilibrium. (ii) The oscillations in the radius are ~50% of the overall increase in size.

A simple way to understand how this beat signal is generated is as follows. The pump laser deposits energy in the electronic degrees of freedom, which subsequently flows into the phonon modes on a picosecond time scale. This increases the lattice temperature, and causes the particles to expand. Because lattice heating is faster than the phonon mode that correlates with the expansion coordinate, the nuclei cannot respond instantaneously. Thus, following excitation the nuclei start to move along the expansion coordinate (the symmetric breathing mode) and pick-up momentum. When they reach the equilibrium radius of the hot particles their inertia will cause them to overshoot.

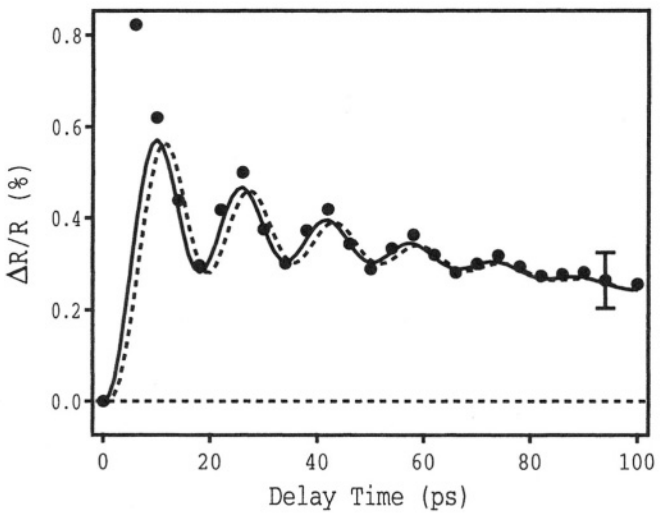

Figure 2. Change in radius versus time for the Au particles in Figure 1. (•) Experimental data; (—) calculated using Eqs. (5) and (6); (---) calculations that ignore hot-electron pressure effects in the coefficient for thermal expansion.

The elastic properties of the particle then provide a restoring force that makes the nuclei stop, and reverse their motions. The competition between the impulsive kick from the rapid laser induced heating, and the restoring force from the elastic response of the particles, cause the nuclei to "ring" around the equilibrium radius of the hot particles.

The response of the nuclei to the rapid laser induced heating can be modelled by treating the symmetric breathing mode as a harmonic oscillator:[51,52,74-76]

$$\frac{d^2R}{dt^2} + 2\Gamma\frac{dR}{dt} + \left(\frac{2\pi}{\tau}\right)^2 \left[R - \left\{R_0 + \Delta R_0(T)\right\}\right] = 0 \tag{5}$$

In this equation τ is the period of the vibrational motion, $\Delta R_0(T)$ is the increase in the radius of the particles due to heating, and Γ is a phenomenological damping constant. ΔR_0 can be simply calculated from the coefficient for thermal expansion (α) by $\Delta R_0/R_0=(\alpha/3)\Delta T$, where ΔT is the temperature increase.[52,74] It is important to note that the coefficient for thermal expansion contains contributions from the lattice and the electronic degrees of freedom. This can be seen by writing α in terms of the heat capacities:[25]

$$\alpha = \frac{1}{K}\left(\gamma_L C_L + \frac{2}{3} C_E(T_E)\right) \tag{6}$$

where K is the bulk modulus, γ_L is the Grüneisen parameter for the lattice,[25] and the temperature dependence of C_E has been explicitly noted. For metals $C_E << C_L$ when the electrons and lattice are in thermal equilibrium, which means that the anharmonicity in the potential energy surface for the ions dominates expansion. However, in ultrafast experiments $T_E >> T_L$ at early times, which makes the electronic and lattice contributions to expansion approximately equal. The effect of the electronic degrees of freedom on α is known as hot-electron pressure.[75-78]

The hot-electron pressure and nuclear contributions to expansion are shown schematically in Figure 3. The force due to the hot electrons decays rapidly as the electrons equilibrate with the phonons. On the other hand, the contribution to expansion from the nuclei reaches a maximum when the electrons and phonons reach thermal equilibrium, and decays slowly as energy is transferred from the particle to the environment. Thus, the nuclear heating contribution to expansion is a step function like perturbation, whereas, the electronic contribution is a delta-function like perturbation. In the harmonic oscillator model these two driving forces produce modulations that have a different phase.[74-76]

Calculations using the harmonic oscillator model with Eq. (6) for α are included in Figure 2 as the solid line. The time dependent temperatures for the electrons and the lattice were calculated using Eqs. (1a) and (1b), and the initial temperature rise was determined from the pump laser intensity and spot size, and the absorbance of the sample at 400 nm.[74]

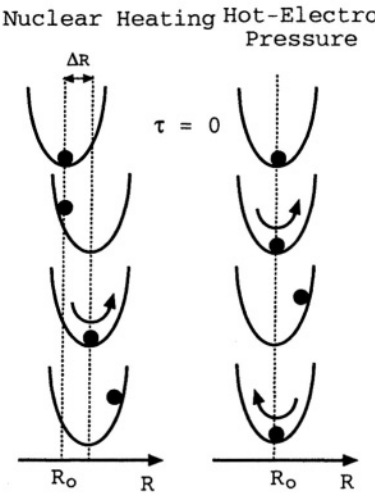

Figure 3. Cartoon of the coherent vibrational motion induced by nuclear heating (left) and hot-electron pressure (right).

The harmonic oscillator model does a good job of reproducing the magnitude and the phase of the oscillations. Importantly, calculations that do not include the contribution from hot-electron pressure (shown as the dashed line in Figure 2) do not correctly reproduce the phase of the modulations. The difference in phase between the two calculations is ~ 45°. This analysis provides strong evidence for the existence of hot electron pressure effects in ultrafast experiments with metal nanoparticles. Our conclusions are in excellent agreement with recent work on spherical and ellipsoidal Ag particles in a glass matrix.[75,76] It is important to note that the instantaneous force due to hot electron pressure may make it possible to coherently excite vibrational motion in very small metal particles, where the period of the symmetric breathing mode is comparable to or faster than the time-scale for lattice heating. Experiments are currently being conducted to probe particles in the < 4 nm diameter range, to see if the elastic constants for these objects (< 2000 atoms) differ from that of bulk gold.

3.2. Heat Dissipation for Gold Particles in Aqueous Solution

Once the electrons and phonons have reached equilibrium the temperature of the particles decays though heat transfer to the environment. Typical time scales quoted in the literature for energy dissipation from metal particles are several hundred picoseconds.[34-36] However, it is not clear how this process depends on factors such as the size and surface properties of the particles. In recent studies El-Sayed and co-workers examined how the time scale for energy dissipation from ~15 nm Au particles depended on the environment.[35,36] Their results showed that the surroundings do influence relaxation, specifically, liquids with higher thermal conductivities give faster relaxation times. Au particles supported on a solid substrate ($MgSO_4$ powder) were also examined, again they found that the relaxation time depends on the environment of the particles. In a recent paper we examined different sized Au particles in aqueous solution. The aim of these experiments was to determine how size affects the rate of heat dissipation.[37]

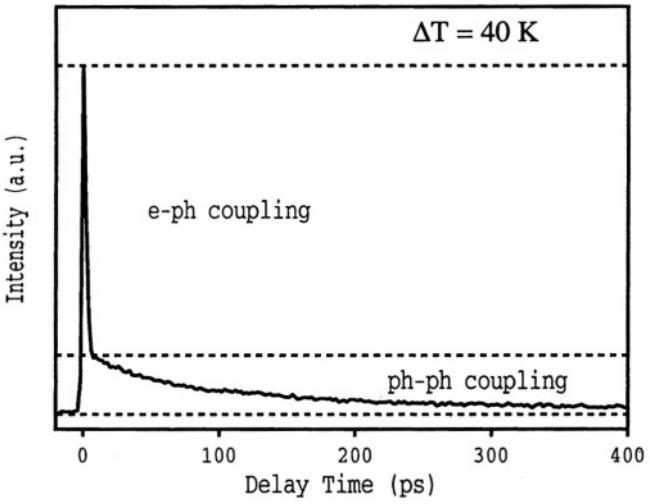

Figure 4. Transient bleach data for 15 nm diameter Au particles recorded with a pump laser power of 0.2 μJ/pulse. The calculated temperature rise of the lattice is given in the figure.

Figure 4 shows transient bleach data for 15 nm diameter Au particles recorded with 530 nm probe pulses, i.e., with the probe laser tuned to the peak of the plasmon band. This probe laser wavelength was chosen for two reasons (i) the signal from the coherently excited phonon modes (which is a distraction in these experiments) is minimized at the plasmon band maximum, and (ii) the magnitude of the transient bleach signal at 530 nm is roughly proportional to the electronic temperature.[17] The data shows two distinct regions. First, a fast initial decay due to coupling between the hot electrons created by the pump laser and the phonon modes (labelled as *e-ph* coupling in Figure 4). Second, a slow decay due to heat dissipation from the particle to the environment (labelled as *ph-ph* coupling). When the time scale for *ph-ph* coupling is much longer than the time scale for *e-ph* coupling, the break in the transient absorption trace represents the point where the electrons and phonons have reached equilibrium. At this point the temperature of the particles can be simply calculated from the number of photons absorbed and the heat capacity of the metal.

Transient bleach data for different sized Au particles (15, 26, 40 or 50 nm diameter) are presented in Figure 5(a). The pump laser power used in these experiments was 0.2 μJ per pulse. The data have been normalized by the break point between the *e-ph* and *ph-ph* coupling regions of the decay. Note that in general the magnitude of the bleach signal depends on the sample concentration, the particle size (through the intensity of the plasmon band), and the electronic temperature. Normalizing by the break point in the transient bleach decay allows us remove the effects of the sample size and concentration from the signal, and simply examine how the temperature varies for the different sized particles. Also shown in Figure 5(a) are fits to the transient bleach data using a stretched exponential function: $\exp[-(t / \tau_d)^{\beta}]$. Figure 5(b) shows the characteristic time constant for energy dissipation (τ_d) obtained from these fits versus the diameter of the particles. The value of the stretching parameter (β) obtained from the data is $\beta = 0.7 \pm 0.1$.

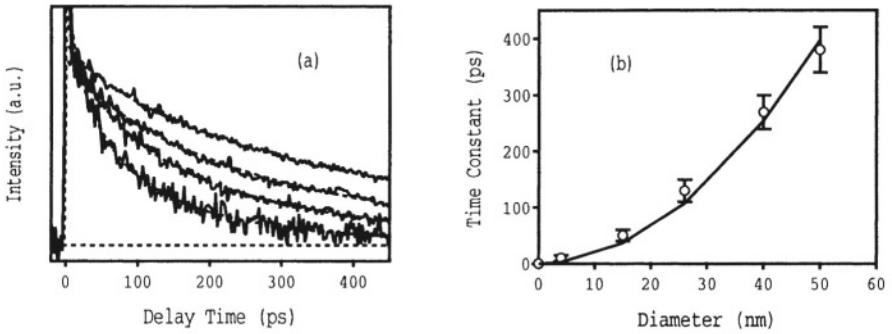

Figure 5. (a) Transient bleach data for different sized Au particles recorded with 0.2 μJ pump laser pulses (ΔT = 40°C). The different traces correspond (top-to-bottom) to particles with diameters of 50 nm, 40 nm, 26 nm or 15 nm. (b) Time constant for heat dissipation obtained by fitting the data to a stretched exponential function.

These results show that the time constant for heat dissipation is proportional to the (diameter)^2, i.e., to the surface area of the particles. The solid line in Fig. 5(b) is a fit to the experimental time constants assuming that $\tau_d \propto R^2$. We find a proportionality constant of 0.64 ± 0.01 for τ_d in ps and R in nm. Experiments performed with pump laser pulse energies up to 2 μJ gave identical results. This shows that in this excitation region (<200°C increase in lattice temperature) the heat dissipation time is independent of the initial temperature. This somewhat surprising result is confirmed by analysis of classical theories for heat transfer derived for a sphere in infinite fluid medium.[79,80] Taken together, these results mean that the temperature in the particles at any time t can be estimated by:

$$\frac{T(t)-T_o}{T_i-T_o} = Exp\left\{-\left(t/0.64\times R^2\right)^{0.7}\right\} \tag{7}$$

where T_i is the initial temperature, T_o is the temperature of the surroundings and t and R are expressed in ps and nm, respectively. For 4 nm diameter particles the time scale for heat dissipation (~10 ps) is comparable to the time scale for electron-phonon coupling (several ps). This implies that for very small particles significant energy transfer to the environment can occur before the electrons and phonons have reached equilibrium. Thus, for these particles the solvent molecules may interact with non-thermal electrons.

3.3. Mode Softening at High Temperature

The harmonic oscillator description of vibrational motion (section 3.1) is an approximation that works extremely well at low excitation levels.[81,82] However, at high vibrational levels anharmonicity effects need to be accounted for. For stretching vibrations in molecules anharmonicity decreases the vibrational frequency.[81] In our experiments higher levels of vibrational excitation can be probed by simply increasing the pump laser power. An example is shown in Figure 6, where data for ca. 100 nm diameter Au particles is presented. Large particles were chosen for these experiments for two reasons. First, the time scale for heat dissipation is very long, so that the temperature

changes during the experiments are minimized. Second, the size distributions are much sharper for large particles,[61,62] which allows us to measure the vibrational periods more accurately.

The two traces in Figure 6 have been normalized for better comparison of the modulations. The vibrational period from these measurements is plotted versus pump laser power in Figure 7 (a). The period increases as the pump laser power increases and, therefore, the temperature of the system increases. This "mode softening" is consistent with the concept of anharmonicity; that is, the attractions between atoms become weaker at high levels of vibrational excitation.[81]

The way the period of the symmetric breathing mode changes with laser intensity can be quantitatively calculated by considering the temperature dependence of the elastic constants and the density of Au (see Eq. (3)).[83] A plot of the calculated period versus temperature is presented in Figure 7(b). Note that for liquid metal particles, the frequency of the symmetric breathing mode is given by[84]

$$\tau = \frac{2R}{c_l} \tag{8}$$

where c_l is the speed of sound in the molten metal. The speed of sound in liquid Au is $c_l = 2560 - 0.55 \times \Delta T$ m/s, where ΔT is the temperature above the melting point.[85] This is significantly different to the speed of sound in solid Au near the melting point, which we estimate to be ca. 3040 m/s,[83] and produces the break in the calculated period versus temperature at the melting point of Au (1336 K).

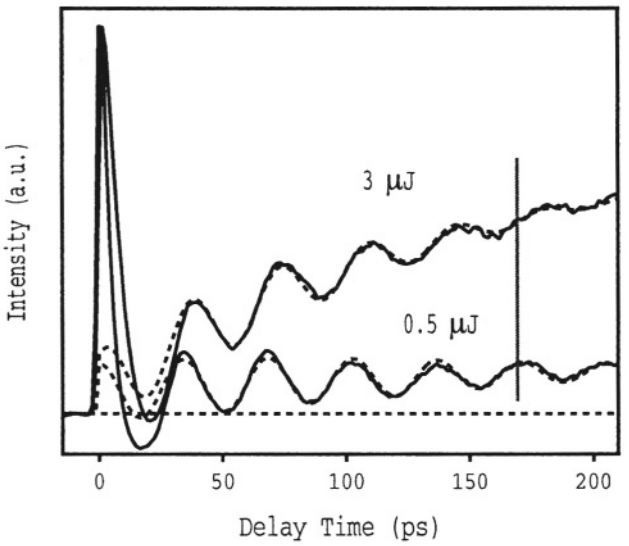

Figure 6. Transient absorption data for ~100 nm diameter Au particles recorded with different intensity pump laser pulses. The period of the modulations is clearly different for the two traces, as indicated by the vertical line. The dashed lines are fits to the data using damped cosine functions.

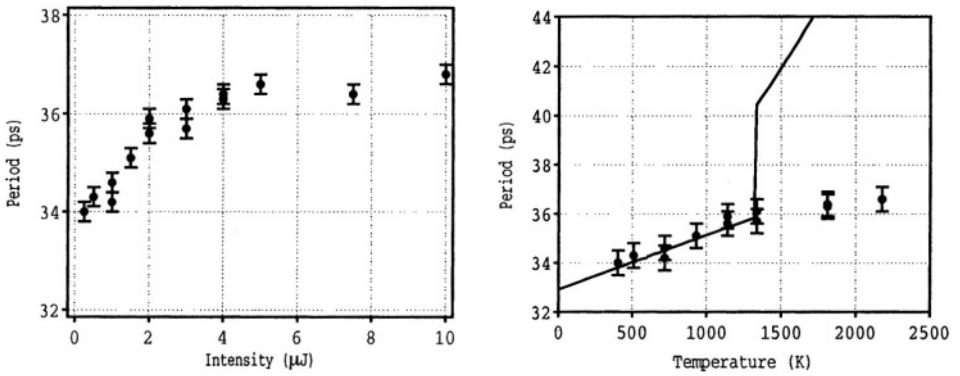

Figure 7. Left: (a) Period versus pump laser power for the ~100 nm diameter Au particles in Figure 6. The period increases as the intensity increases due to softening of the elastic properties of the particles. Right: (b) Period versus temperature (—) calculated from the temperature dependent elastic constants of Au.

The points in Figure 7(b) are the experimental data from Figure 7(a). The temperatures in the experiments were estimated from the pump laser power and spot size at the sample, the absorbance of the Au particles at the pump laser wavelength, and the heat capacity and enthalpy of fusion for Au. Note that the sample absorbance was corrected for scattering in this calculation, which is significant for particles larger than ca. 50 nm diameter.[86] The calculated and experimental periods are in reasonable agreement for temperatures below the melting point of Au. This shows that the estimated temperatures are quite reliable for pump laser powers less than ca. 3 μJ per pulse. At higher pump powers the calculated and experimental data deviate quite dramatically. Specifically, Eq. (8) predicts that the vibrational period for ~100 nm diameter liquid Au particles should be greater than 40 ps, whereas, the experimental values flatten off to $\tau \approx 37$ ps at high power. This indicates that the particles do not completely melt in our experiments.

There are several points to note about the estimated temperatures presented in Figure 7(b). First, we have not considered energy transfer to the environment, which means that the actual temperatures in our experiments are lower than the calculated temperatures. Calculations using Eq. (7) indicate that the temperature of the particles decreases by ca. 50% during the experiments. However, Eq. (7) may not be valid at very high powers, where the temperature of the solution surrounding the particles could exceed the boiling point of water. The rate of heat dissipation from the particles depends on the thermal conductivity of the surroundings,[79,80] and the thermal conductivity of water vapour is significantly less than liquid water. This means that Eq. (7) probably overestimates the rate of heat dissipation in our experiments for high pump laser powers. Thus, the temperatures in the experiments are lower than those indicated in Figure 7(b) due to heat dissipation, but it is not clear how much lower. Second, measurements of the transmission of the pump laser beam through the sample as a function of power show that the transmission is independent of power at low excitation levels (< 3 μJ), i.e., the extinction of the pump follows Beer's Law. However, at pump laser powers > 3 μJ there are significant nonlinear effects (self-focussing and white light generation) in our samples. These effects reduce the pumping efficiency (they compete with linear absorption), with the result that the effective temperatures in the particles are less than

that calculated using Beer's Law. The transmission of high-power, short-pulse width laser beams through nanoparticle samples is not well understood, and we are currently performing experiments to try and understand how the relative contributions from scattering and absorption change as a function of laser power. These effects are responsible for the optical limitation properties of metal nanoparticles,[87,88] which is a potential commercial use for these materials.

From the above considerations and the data in Figure 7, it appears reasonable to state that we can use ultrafast laser excitation to increase the temperature of the particles up to the melting point of Au. However, we cannot make completely liquid Au particles. Metal particles at or near their melting point consist of a solid core and a liquid shell.[89-93] The thickness of the liquid shell depends on the amount of heat added to the system. Thus, it is very possible that at high pump laser powers we have $\text{solid}_{\text{core}}\text{-liquid}_{\text{shell}}$ particles. The period of the breathing mode for these core-shell particles will be different to that for completely solid or completely liquid particles. Continuum elastic theory calculations for the breathing mode of core-shell nanoparticles have recently been published by Sader et al..[57] Using these results, and the speeds of sound for liquid and solid Au at the melting point, shows that the vibrational period for $\text{solid}_{\text{core}}\text{-liquid}_{\text{shell}}$ Au particles will be < 38 ps for a shell thickness up to approximately 20% of the total diameter of the particles. On the other hand, the vibrational period will be essentially the same as pure liquid Au particles for shell thickness greater than 75% of the total diameter. The maximum period observed in our experiments is 37 ps, which indicates that the thickness of the liquid shell (if present) remains much less than 20% of the particle diameter. (A period of 37 ps corresponds to a liquid shell thickness of 13% in the continuum elastic calculations.)

The last point to note from the intensity dependent measurements is that the damping times at high powers are significantly faster than those at low power. We have previously shown that at low excitation levels (< μJ) the dephasing of the signal in our experiments is dominated by polydispersity in the samples.[52,74] Specifically, different sized particles have different modulation frequencies, and the sum of the contributions from all the particles in the sample leads to an inhomogeneous decay in the beat signal. Assuming that the sample distribution is reasonably narrow, and can be described by a Gaussian distribution, the signal in our experiments can be written as:[74]

$$S(t) \approx Cos\left(\frac{2\pi}{\bar{\tau}}t + \phi\right) \times e^{-(\gamma t)^2} \tag{9}$$

where $\bar{\tau} = 2\pi\bar{R}/\eta c_l$ is the period corresponding to the average radius of the sample, and $1/\gamma = \bar{R}\bar{T}/\sqrt{2}\pi\sigma_R$ is the inhomogeneous damping time due to polydispersity in the sample. The width of the sample distribution is characterized by the standard deviation σ_R. Fits to the experimental data for the 100 nm particles at low power indicates a sample polydispersity of ~ 5% (assuming that there are no contributions from homogeneous damping to the decay). At high power the decay rate increases, but the sample polydispersity does not change (we believe that fragmentation of the particles does not occur in these experiments). We attribute the increased damping to an additional homogeneous contribution to the dynamics. Assuming that the homogeneous contribution can be described by a simple single exponential function, analysis of the experimental

data at high pump powers yields a homogeneous damping time of 600 ± 100 ps. At present we do not know the mechanism for this decay. Two possibilities are energy transfer to the environment, or visco-elastic damping due to the formation of a liquid Au shell at high power. The 550 ps homogeneous decay time is close to the energy dissipation time predicted by $0.16 \times R^2$ (~ 400 ps). However, energy transfer should produce a change in the modulation frequency rather than a dephasing of the modulations, since it results in a decrease in the temperature of the system. Thus, these experiments may allow us to examine visco-elastic damping in $solid_{core}$-$liquid_{shell}$ particles, which is an exciting opportunity. We plan to further investigate these effects by performing experiments with much greater temperature control, i.e., by placing the particles in a solid matrix which can be precisely heated in an oven.

3.4. Vibrational Modes of Nanorods

The continuum mechanics calculations described above are explicitly derived for spherical, elastically isotropic (i.e., polycrystalline) particles. An interesting question is to consider what happens for particles that have different shapes and/or are single crystals. Synthetically it is difficult to control the shape of metal or semiconductor nanoparticles, although there has been considerable progress in recent years. For example, cubic Pt nanoparticles can be synthesized by H_2 reduction of $PtCl_6^{2-}$,[94] triangular Ag particles have been produced by aging a citrate stabilized Ag sol in light,[95] and elliptical metal particles can be made by deformation of spherical particles embedded in a glass.[96] However, the most significant progress has been made in synthesizing rod-shaped particles. Rods of different widths and almost any length can be made by electrochemical deposition in a template, such as the pores of a membrane.[97-100] This method has the advantage that a variety of different metals can be deposited, however, significant post-synthesis processing has to be performed to remove the rods from the template.

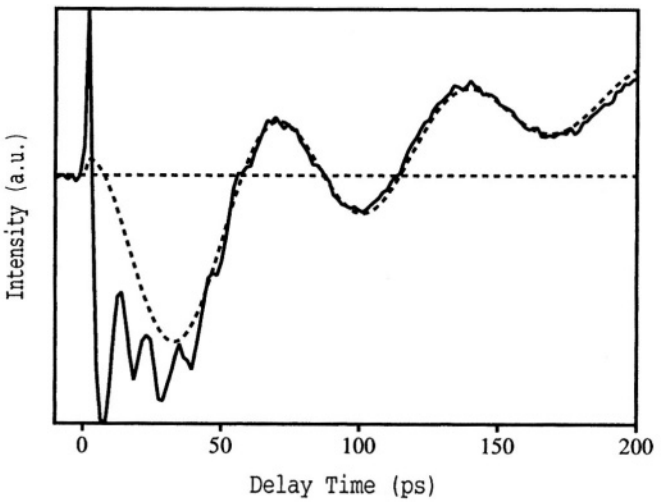

Figure 8. Transient absorption data for Au nanorods with an average aspect ratio of ~2. The pump and probe wavelengths were 400 and 640 nm, respectively. The dashed line shows a fit to the slow modulation in the data.

A more straightforward technique is to use a micelle solution to direct the growth of the rods in combination with either chemical or electrochemical reduction of a metal salt.[42,71-73,101-103] This technique can be used to make Au or Ag rods, with aspect ratios up to ~20.[101-103] Nanorods are of particular interest because of their unusual optical properties. Specifically, rod-shaped particles show two plasmon bands corresponding to electron oscillations along the long or the short axis of the rod.[1,71,73] For Au, the transverse plasmon band occurs at ~520 nm (which is close to the plasmon resonance for spherical Au particles), and the longitudinal band falls in the visible to near-IR spectral region. The position of the longitudinal resonance makes these materials potentially useful as polarizing filters or as labels for biological molecules, and the optical properties of Au nanorods have attracted considerable attention.

Figure 8 shows representative transient absorption data for a Au nanorod sample with an average aspect ratio of ~2. The rods were synthesized in Paul Mulvaney's group at the University of Melbourne, using the electrochemical technique first described by Wang and co-workers.[42,71] Detailed TEM analysis has shown that the rods produced by this technique are single crystals, and that they grow along the [001] direction.[104,105] The transient absorption experiments were performed with 400 nm pump laser pulses and a probe laser wavelength of 640 nm, which is resonant to the longitudinal plasmon band of the sample. Note that the rod samples also contain spherical particles, however, the vibrational modes of spheres cannot be observed at probe wavelengths greater than ~600 nm, as shown in Figure 1. Two types of modulations can be observed in our data: a fast modulation with a period of ca. 11 ps and a slower (more pronounced) modulation with a period of ca. 70 ps. The period of the faster modulation is approximately equal to $2L/c_l$, which is the value expected for a vibrational motion that corresponds to expansion and compression along the long axis of the rod. In contrast, the period of the slower modulation is closer to $2L/c_t$. Perner et al. have also observed modulations due to coherently excited vibrational motion in their transient absorption measurements with ellipsoidal Ag particles.[76] In these experiments the vibrational period was found to be close to $2L/c_l$.

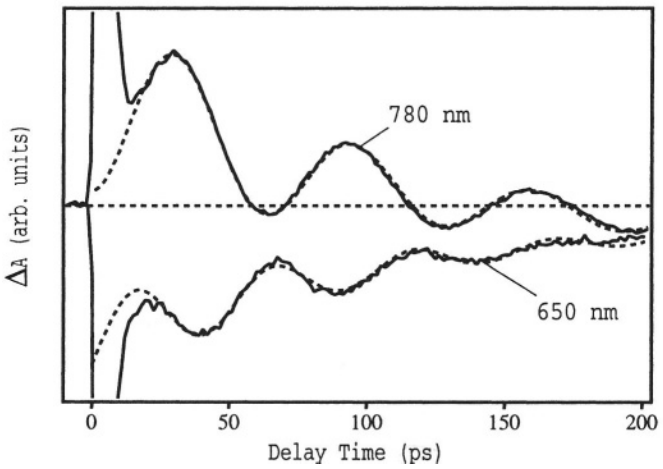

Figure 9. Transient absorption data recorded with 400 nm pump pulses and probe wavelengths of 650 nm and 780 nm for a nanorod sample with an average aspect ratio of 3.5. The dashed lines are fits to the data using a damped cosine function.

We have performed extensive measurements on rod samples with different aspect ratios, and have observed that for a given sample the exact value of the period depends on the probe wavelength. On the other hand, for spherical particles the measured periods are independent of wavelength to within the accuracy of our measurements. An example of the probe wavelength dependence is shown in Figure 9, where results for a Au nanorod sample with an average aspect ratio of 3.5 are presented.[106] The two probe wavelengths used in these experiments lie on either side of the longitudinal plasmon band of the sample. There are several points to note. First, both the frequency and the phase are different for these two probe wavelengths. Second, the fast modulations are not present, i.e., only the slower vibrational motion is observed in these experiments. Indeed, we have only observed the fast modulation, which corresponds to the expected compressional wave, in a few experiments.

The way the period of the vibrational motion changes with probe wavelength is shown in Figure 10. This figure presents data collected from five different samples with a variety of probe laser wavelengths. The average aspect ratios for the samples are given in the figure caption. The increase in the period with increasing probe laser wavelength can be qualitatively explained as follows. The nanorod samples are polydisperse, i.e., each sample contains rods with a variety of different lengths.

The different length rods have different longitudinal plasmon resonances, with longer rods (larger aspect ratio) absorbing further into the near-IR: for Au nanorods in aqueous solution $\lambda_{max} \approx 86 \times \xi + 419$, where the aspect ratio ξ = length/width.[42,71,73] As the probe laser is tuned from the blue to the red, it probes (on average) longer rods in the sample. Because the vibrational period is proportional to the length of the rod, longer vibrational periods are obtained for longer probe laser wavelengths. The period versus probe wavelength results appear to fall onto two curves: the rods with an average aspect ratio of $\xi = 2.1$ are on one curve, and the rods with aspect ratios of 2.7, 3.0, 3.5 and 5.5 are on another. This is because the rods in the sample with $\xi = 2.1$ are approximately 2× wider than the rods in the other samples.

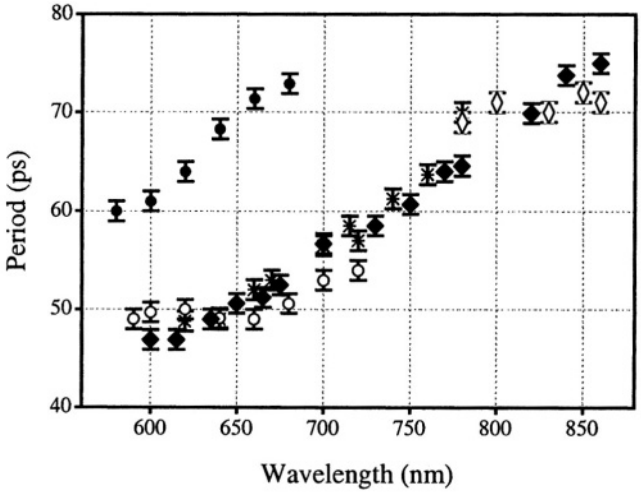

Figure 10. Period versus probe wavelength for Au nanorod samples with aspect ratios of 2.1 (•), 2.7 (o), 3.0 (*), 3.5 (♦) and 5.5 (◊).

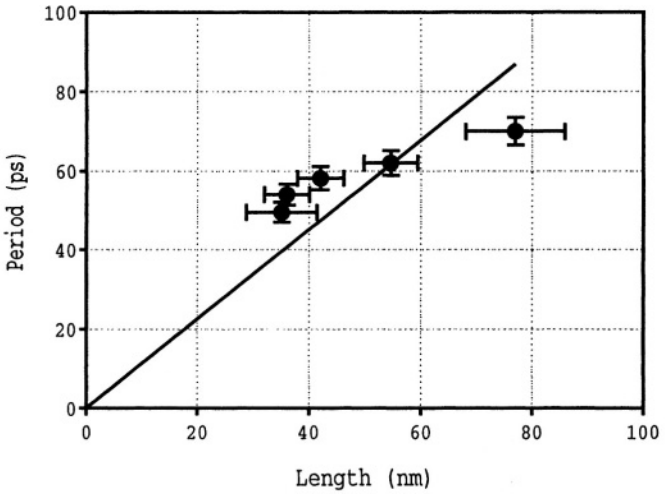

Figure 11. Period versus length for the Au nanorods examined in this work. The straight line is a fit to the data assuming that the period is linearly proportional to the length of the rod. The horizontal error bars reflect the polydispersity in the samples.

A given probe wavelength interrogates rods with a certain aspect ratio, but the actual length probed depends on their width (w). Specifically, $L = \xi \times w \approx (\lambda - 419) \times w / 86$, using the relationship between ξ and λ given above.[106]

Note that the period versus wavelength data for a given sample is not a straight line — the period "flattens off" at high and low probe wavelength. This occurs because of the finite size distributions of the samples. The exact way the vibrational period changes with probe wavelength depends on the bandwidth of the probe laser, the size distribution of the sample, and the transient absorption spectrum of a single rod.[106] Our initial report on coherently excited vibrational modes in nanorods presented an analysis of the period versus probe wavelength data using Gaussian functions for the distribution of lengths, and the spectra of the rods and the laser. These simulations showed that at probe laser wavelengths near the plasmon band maximum the effect of the sample polydispersity is minimized, i.e., the measured periods are close to the values expected from the average length of the rods. Thus, to compare different samples, the probe laser should be tuned as close to the maximum of the longitudinal plasmon band as possible. Figure 11 shows results for different rod samples, where the period of the acoustic vibrational mode was determined from experiments with $\lambda_p \approx \lambda_{max}$. The straight line is a fit to the data assuming that the period is linearly proportional to the length of the rod, i.e., $T = 2L/\alpha$. The value of α obtained is $1800\ \mathrm{ms}^{-1}$, which is in between the values for the transverse and longitudinal speeds of sound in Au: $1200\ \mathrm{ms}^{-1}$ and $3200\ \mathrm{ms}^{-1}$, respectively.[83,107]

At this point it is not clear why our Au nanorod samples give a different period compared to the ellipsoidal Ag particles. Two possibilities are, first, the vibrational modes excited in the Au nanorods are fundamentally different to those for the Ag ellipses (i.e., we are exciting a motion that is much more complicated than simple stretching and compression along a single axis). Second, use of material properties for bulk (polycrystalline) gold is not appropriate for these small crystalline nanorods. In comparison, the Ag ellipses of ref. 76 are polycrystalline and show good agreement with

bulk data. The elastic properties of the single crystal nanorods may be different to those of polycrystalline rods. Further experiments and continuum mechanics calculations are currently being performed to elucidate the vibrational dynamics of these systems.

4. SUMMARY AND CONCLUSIONS

Excitation of metal nanoparticles with an ultrafast laser pulse causes a rapid increase in the electronic temperature. The hot-electrons subsequently equilibrate with the phonon modes on a several picosecond time scale. These rapid heating processes can impulsively excite the phonon mode that correlates with the expansion co-ordinate. For spherical particles the symmetric breathing mode is excited. For particles with diameters between 8 nm and 120 nm the frequency of this mode can be exactly calculated using continuum mechanics.[52,57] For nanorod samples the period of the coherently excited phonon mode depends on the length of the rod, but the values obtained do not match those previously observed for Ag ellipses. It is not clear whether this difference is due to differences in the symmetry of the particles (cylindrical compared to ellipsoidal), or their material properties (the gold nanorods in our experiments are single crystals, whereas, the Ag particles in ref. 76 are polycrystalline).

By performing wavelength dependent transient absorption measurements for a ca. 50 nm diameter Au particle sample we have been able to calculate how the radius changes with time. These results can be directly compared to model calculations where the expansion co-ordinate (the symmetric breathing mode) is treated as a harmonic oscillator. A careful analysis of the phase of the modulations shows that both hot-electron pressure and lattice heating contribute to the impulsive excitation process. The force due to the hot electrons is only significant at early times, when the electronic temperature is much greater than the lattice temperature. The overall expansion of the particles, and the magnitude of the oscillations in the particle radius, are controlled by the lattice heating contribution. The rate of energy dissipation from Au nanoparticles to their surroundings was also examined by time-resolved spectroscopy. These experiments were performed for particles suspended in aqueous solution, with average sizes ranging from 4 nm to 50 nm diameter. The results show that energy relaxation is a very non-exponential process. The relaxation times were found to be proportional to the square of the radius, but do not depend on the initial temperature of the particles (i.e., the pump laser power) at low excitation levels. For very small particles the time scale for energy dissipation is comparable to the time scale for electron-phonon coupling, which implies that significant energy loss occurs before the electrons and phonons reach equilibrium within the particle.

Finally, at very high pump laser power our transient absorption experiments reveal a "softening" of the coherently excited vibrational mode. This can be qualitatively explained by considering how the elastic properties of gold change with temperature. Analysis of the way the period depends on the pump laser intensity indicates that we can approach the melting point of Au in these experiments, however, we do not create completely liquid particles. This raises the possibility that the particles have a liquid-shell/solid-core structure. The data at high power shows an increased damping compared to the low power experiments, which may be due to visco-elastic damping effects from the liquid shell.

5. ACKNOWLEDGEMENTS

The work described in this paper was supported by the National Science Foundation by Grant No. CHE98-16164. The authors would like to thank Dr. Jose Hodak, and Profs. Arnim Henglein, Paul Mulvaney and John Sader for their contributions during the course of these experiments.

6. REFERENCES

1. U. Kreibig and M. Vollmer, *Optical Properties Of Metal Clusters* (Springer, Berlin, 1995).
2. M. Faraday, Experimental relations of gold (and other metals) to light, *Philos. Trans. Roy. Soc. Lon.* **147**, 145-181 (1857).
3. G. Mie, Beiträge zur optik trüber medien, speziell kolloidaler metallösungen, *Ann. Physik* **25,** 377-445 (1908).
4. R. H. Doremus, Optical properties of small silver particles, *J. Chem. Phys.* **42**, 414-417 (1965).
5. W.A. Kraus and G. C. Schatz, Plasmon resonance broadening in small metal particles, *J. Chem. Phys.* **79**, 6130-6139 (1983).
6. H. Hovel, S. Fritz, A. Hilger, U. Kreibig, and M. Vollmer, Width of cluster plasmon resonances: bulk dielectric functions and chemical interface damping, *Phys. Rev. B* **48**, 18178-18188 (1993).
7. T. Jensen, L. Kelly, A. Lazarides, and G. C. Schatz, Electrodynamics of noble metal nanoparticles and nanoparticle clusters, *J. Cluster Sci.* **10**, 295-317 (1999)
8. J. Z. Zhang, Ultrafast studies of electron dynamics in semiconductor and metal colloidal nanoparticles: effects of size and surface, *Acc. Chem. Res.* **30**, 423-429 (1997).
9. S. Link and M. A. El-Sayed, Spectral properties and relaxation dynamics of surface plasmon electronic oscillations in gold and silver nanodots and nanorods, *J. Phys. Chem. B* **103**, 8410-8426 (1999).
10. J. H. Hodak, A. Henglein, and G. V. Hartland, Photophysics of nanometer sized metal particles: electron-phonon coupling and coherent excitation of breathing vibrational modes, *J. Phys. Chem. B* **104**, 9954-9965 (2000).
11. J. Y. Bigot, V. Halte, J. C. Merle, and A. Daunois, Electron dynamics in metallic nanoparticles, *Chem. Phys.* **251**, 181-203 (2000).
12. N. Del Fatti, F. Vallee, C. Flytzanis, Y. Hamanaka and A. Nakamura, Electron dynamics and surface plasmon resonance nonlinearities in metal nanoparticles, *Chem. Phys.* **251**, 215-226 (2000).
13. S. Stagira, M. Nisoli, S. De Silvestri, A. Stella, P. Tognini, P. Cheyssac and R. Kofman, Ultrafast optical relaxation dynamics in metallic nanoparticles: from bulk-like toward spatial confinement regime, *Chem. Phys.* **251**, 259-267 (2000).
14. C. Voisin, N. Del Fatti, D. Christofilos, and F. Vallee, Ultrafast electron dynamics and optical nonlinearities in metal nanoparticles, *J. Phys. Chem. B* **105**, 2264-2280 (2001).
15. M. A. El-Sayed, Some interesting properties of metals confined in time and nanometer space of different shapes, *Acc. Chem. Res.* **34**, 257-264 (2001).
16. S. L. Logunov, T. S. Ahmadi, M. A. El-Sayed, J. T. Khoury, and R. L. Whetten, Electron dynamics of passivated gold nanocrystals probed by subpicosecond transient absorption spectroscopy, *J. Phys. Chem. B* **101**, 713-3719 (1997).
17. J. H. Hodak, I. B. Martini, and G. V. Hartland, Spectroscopy and dynamics of nanometer-sized noble metal particles, *J. Phys. Chem. B* **102**, 6958-6967 (1998).
18. L. M. Liz-Marzán and P. Mulvaney, $Au@SiO_2$ colloids: effect of temperature on the surface plasmon absorption, *New J. Chem.* **22**, 1285-1288 (1998).
19. S. Link and M. A. El-Sayed, Size and temperature dependence of the plasmon absorption of colloidal gold nanoparticles, *J. Phys. Chem. B* **103**, 4212-4217 (1999).
20. N. Del Fatti, C. Voisin, D. Christofilos, F. Vallee, and C. Flytzanis, Acoustic vibration of metal films and nanoparticles, *J. Phys. Chem. A* **104**, 4321-4326 (2000).
21. H. E. Elsayed-Ali, T. B. Norris, M. A. Pessot, and G. A. Mourou, Time-resolved observation of electron-phonon relaxation in copper, *Phys. Rev. Lett.* **58**, 1212-1215 (1987).
22. R. W. Schoenlein, W. Z. Lin, J. G. Fujimoto, and G. L. Eesley, Femtosecond studies of nonequilibrium electronic processes in metals, *Phys. Rev. Lett.* **58**, 1680-1683 (1987).
23. C. K. Sun, F. Vallee, L. H. Acioli, E. P. Ippen, and J. G. Fujimoto, Femtosecond-tunable measurement of electron thermalization in gold, *Phys. Rev. B* **50**, 15337-15348 (1994).

24. J. Hohlfeld, S. S. Wellershoff, J. Gudde, U. Conrad, V. Jahnke, and E. Matthias, Electron and lattice dynamics following optical excitation of metals, *Chem. Phys.* **251**, 237-258 (2000).
25. N. W. Ashcroft and N. D. Mermin, *Solid State Physics* (Harcourt Brace, Orlando, 1976).
26. J. H. Hodak, I. B. Martini, and G. V. Hartland, Ultrafast study of electron-phonon coupling in colloidal gold particles, *Chem. Phys. Lett.* **284**, 135-141 (1998).
27. M. Nisoli, S. Stagira,S. De Silvestri, A. Stella, P. Tognini, P. Cheyssac, and R. Kofman, Ultrafast electronic dynamics in solid and liquid gallium nanoparticles, *Phys. Rev. Lett.* **78**, 3575-3578 (1997).
28. J. H. Hodak, A. Henglein, and G. V. Hartland, Electron-phonon coupling dynamics in very small (between 2 and 8 nm diameter) Au nanoparticles, *J. Chem. Phys.* **112**, 5942-5947 (2000).
29. S. Link, C. Burda, M. B. Mohamed, B. Nikoobakht, and M. A. El-Sayed, Femtosecond transient-absorption dynamics of colloidal gold nanorods: shape independence of the electron-phonon relaxation time, *Phys. Rev. B* **61**, 6086-6090 (2000).
30. C. Voisin, N. Del Fatti, D. Christofilos, and F. Vallee, Ultrafast electron dynamics and optical nonlinearities in metal nanoparticles, *J. Phys. Chem. B* **105**, 2264-2280 (2001).
31. E. D. Belotskii and P. M. Tomchuk, Surface electron phonon energy exchange in small metallic particles, *Int. J. Electron.* **73**, 955-957 (1992).
32. N. Del Fatti, R. Bouffanais, F. Vallee, and C. Flytzanis, Nonequilibrium electron interactions in metal films, *Phys. Rev. Lett.* **81**, 922-925 (1998).
33. S. Link, C. Burda, Z. L. Wang, and M. A. El-Sayed, Electron dynamics in gold and gold-silver alloy nanoparticles: the influence of a nonequilibrium electron distribution and the size dependence of the electron-phonon relaxation, *J. Chem. Phys.* **111**, 1255-1264 (1999).
34. T. W. Roberti, B. A. Smith, and J. Z. Zhang, Ultrafast electron dynamics at the liquid-metal interface - femtosecond studies using surface-plasmons in aqueous silver colloid, *J. Chem. Phys.* **102**, 3860-3866 (1995).
35. M. B. Mohamed, T. S. Ahmadi, S. Link, M. Braun, and M. A. El-Sayed, Hot electron and phonon dynamics of gold nanoparticles embedded in a gel matrix, *Chem. Phys. Lett.* **343**, 55-63 (2001).
36. S. Link, A. Furube, M. B. Mohamed, T. Asahi, M. Masuhara, and M. A. El-Sayed, Hot electron relaxation dynamics of gold nanoparticles embedded in $MgSO_4$ powder compared to solution: the effect of the surrounding medium, *J. Phys. Chem. B* **106**, 945-955 (2002).
37. M Hu and G. V. Hartland, Heat dissipation for Au particles in aqueous solution: relaxation time versus size, *J. Phys. Chem. B,* **106**, 7029-7033 (2002).
38. G. Huttmann and R. Birngruber, On the possibility of high-precision photothermal microeffects and the measurement of fast thermal denaturation of proteins, *IEEE J. Select. Top. Quant. Electron.* **5,** 954-962 (1999).
39. H. Kurita, A. Takami, and S. Koda, Size reduction of gold particles in aqueous solution by pulsed laser irradiation, *App. Phys. Lett.* **72**, 789-791 (1998).
40. P. V. Kamat, M. Flumiani, and G. V. Hartland, Picosecond dynamics of silver nanoclusters. photoejection of electrons and fragmentation, *J. Phys. Chem. B* **102**, 3123-3128 (1998).
41. A. Takami, H. Kurita, and S. Koda, Laser-induced size reduction of noble metal particles, *J. Phys. Chem. B* **103**, 1226-1232 (1999).
42. S. S. Chang, C. W. Shih, C. D. Chen, W. C. Lai, and C. R. C. Wang, The shape transition of gold nanorods, *Langmuir* **15,** 701-709 (1999).
43. H. Fujiwara, S. Yanagida, and P. V. Kamat, Visible laser induced fusion and fragmentation of thionicotinamide-capped gold nanoparticles, *J. Phys. Chem. B* **103**, 2589-2591 (1999).
44. S. Link, C. Burda, B. Nikoobakht, and M. A. El-Sayed, Laser-induced shape changes of colloidal gold nanorods using femtosecond and nanosecond laser pulses, *J. Phys. Chem. B* **104**, 6152-6163 (2000).
45. C. S. Ah, H. S. Han, K. Kim, and D. J. Jang, Photofragmentation dynamics of n-dodecanethiol-derivatized silver nanoparticles in cyclohexane, *J. Phys. Chem. B* **104**, 8153-8159 (2000).
46. S. Link and M. A. El-Sayed, Spectroscopic determination of the melting energy of a gold nanorod, *J. Chem. Phys.* **114**, 2362-2368 (2001).
47. A. Dawson and P. V. Kamat, Semiconductor-metal nanocomposites. Photoinduced fusion and photocatalysis of gold-capped TiO_2 (TiO_2/gold) nanoparticles, *J. Phys. Chem. B* **105**, 960-966 (2001).
48. J. H. Hodak, A. Henglein, M. Giersig, and G. V. Hartland, Laser-induced inter-diffusion in Au-Ag core-shell nanoparticles, *J. Phys. Chem. B* **104**, 11708-11718 (2000).
49. M. Nisoli, S. De Silvestri, A. Cavalleri, A. M. Malvezzi, A. Stella, G. Lanzani, P. Cheyssac, and R. Kofman, Coherent acoustic oscillations in metallic nanoparticles generated with femtosecond optical pulses, *Phys. Rev. B* **55**, 13424-13427 (1997).
50. J. H. Hodak, I. B. Martini, and G. V. Hartland, Observation of acoustic quantum beats in nanometer sized Au particles, *J. Chem. Phys.* **108**, 9210-9213 (1998)

51. N. Del Fatti, C. Voisin, F. Chevy, F. Vallee, and C. Flytzanis, Coherent acoustic mode oscillation and damping in silver nanoparticles *J. Chem. Phys* **110**, 11484-11487 (1999).
52. J. H. Hodak, A. Henglein, and G. V. Hartland, Size dependent properties of Au particles: coherent excitation and dephasing of acoustic vibrational modes, *J. Chem. Phys.* **111**, 8613-8621 (1999).
53. P. Mulvaney, Surface Plasmon spectroscopy of nanosized metal particles, *Langmuir* **12**, 788-800 (1996).
54. H. Lamb, On the vibrations of an elastic sphere, *Proc. London Math. Soc.* **13**, 189-212 (1882).
55. V. A. Dubrovskiy and V. S. Morochnik, Natural vibrations of a spherical inhomogeneity in an elastic medium, *Izv. Earth Phys.* **17**, 494-504 (1981).
56. K. E. Bullen and B. A. Bolt, *An Introduction to Seismology,* 4th Edition, (Cambridge University Press, Cambridge, 1985).
57. J. E. Sader, G. V. Hartland, and P. Mulvaney, Theory of acoustic breathing modes of core-shell nanoparticles. *J. Phys. Chem. B,* **106**, 1399-1402 (2002).
58. H. F. Pollard, *Sound Waves In Solids* (Pion, London, 1977).
59. B. V. Enüstün and J. Turkevich, Coagulation of colloidal gold, *J. Am. Chem. Soc.* **85**, 3317-3328 (1963).
60. V. V. Vukovic and J. M. Nedeljkovic, Surface modification of nanometer-scale silver particles by imidazole, *Langmuir* **9**, 980-983 (1993).
61. A. Henglein and D. Meisel, Radiolytic control of the size of colloidal gold nanoparticles, *Langmuir* **14**, 7392-7396 (1998).
62. A. Henglein, Radiolytic preparation of ultrafine colloidal gold particles in aqueous solution: optical spectrum, controlled growth, and some chemical reactions, *Langmuir,* **15**, 6738-6744 (1999).
63. P. Mulvaney, M. Giersig, and A. Henglein, Surface-chemistry of colloidal gold - deposition of lead and accompanying optical effects, *J. Phys. Chem.* **96**, 10419-10424 (1992).
64. M. Michaelis, A. Henglein, and P. Mulvaney, Composite Pd-Ag particles in aqueous-solution, *J. Phys. Chem.* **98**, 6212-6215 (1994).
65. F. Henglein, A. Henglein, and P. Mulvaney, Surface-chemistry of colloidal gold - deposition and reoxidation of Pb, Cd, And Tl, *Ber. Bunsen-Gesellschaft-Phys. Chem. Chem. Phys.* **98**, 180-189 (1994).
66. A. Henglein and M. Giersig, Optical and chemical observations on gold-mercury nanoparticles in aqueous solution, *J. Phys. Chem. B* **104**, 5056-5060 (2000).
67. A. Henglein, Preparation and optical aborption spectra of Au_{core}-Pt_{shell} And Pt_{core}-Au_{shell} colloidal nanoparticles in aqueous solution, *J. Phys. Chem. B* **104**, 2201-2203 (2000).
68. J. Belloni, M. Mostafavi, H. Remita, J. L. Marignier, and M. O. Delcourt, Radiation-induced synthesis of mono- and multi-metallic clusters and nanocolloids, *New J. Chem.* **22**, 1239-1255 (1998).
69. J. Belloni, Metal Nanocolloids, *Current Opinion Coll. Int. Sci.* **1**, 184-196 (1996).
70. A. Henglein, Colloidal Palladium nanoparticles: reduction of Pd(II) by H_2; Pd_{core}-Au_{shell}-Ag_{shell} particles, *J. Phys. Chem. B,* **104**, 6683-6685 (2000).
71. Y. Y. Yu, S. S. Chang, C. L. Lee, and C. R. C. Wang, Gold nanorods: electrochemical synthesis and optical properties, *J. Phys. Chem. B,* **101**, 6661-6664 (1997).
72. M. B. Mohamed, K. Z. Ismail, S. Link, and M. A. El-Sayed, Thermal reshaping of gold nanorods in micelles, *J. Phys. Chem. B* **102**, 9370-9374 (1998).
73. S. Link, M. B. Mohamed, and M. A. El-Sayed, Simulation of the optical absorption spectra of gold nanorods as a function of their aspect ratio and the effect of the medium dielectric constant, *J. Phys. Chem. B* **103,** 3073-3077 (1999).
74. G. V. Hartland, Coherent vibrational motion in metal particles: determination of the vibrational amplitude and excitation mechanism, *J. Chem. Phys.* **116**, 8048-8055 (2002).
75. C. Voisin, N. Del Fatti, D. Christofilos and F. Vallee, Time-resolved investigation of the vibrational dynamics of metal nanoparticles, *App. Surf. Sci.* **164**, 131-139 (2000).
76. M. Perner, S. Gresillon, J. Marz, G. Von Plessen, J. Feldmann, J. Porstendorfer, K. J. Berg, and G. Berg, Observation of hot-electron pressure in the vibration dynamics of metal nanoparticles, *Phys. Rev. Lett.* **85**, 792-795 (2000).
77. G.Tas and H. J. Mans, Electron-diffusion in metals studied by picosecond ultrasonics, *Phys. Rev. B* **49**, 15046-15054 (1994).
78. V. E. Gusev, On the duration of acoustic pulses excited by subpicosecond laser action on metals, *Opt. Comm.* **94**, 76-78 (1992).
79. F. Cooper, Heat transfer from a sphere to an infinite medium, *Int. J. Heat Mass Transfer* 991-993 (1977).
80. S. Kanac and Y. Yenev, *Heat Conduction* (Taylor And Francis, Washington, 1993).
81. G. Herzberg, *Molecular Spectra and Molecular Structure, II Infrared and Raman Spectra of Polyatomic Molecules* (Van Nostrand Reinhold Co., New York, 1945).
82. E. B. Wilson, J. C. Decius, and P. C. Cross, *Molecular Vibrations, The Theory of Infrared and Raman Vibration Spectra* (Dover Publications, New York, 1980).

83. G. Simmons and H. Wang, *Single Crystal Elastic Constants and Calculated Aggregate Properties: A Handbook* (The MIT Press, Cambridge, 1971).
84. J. E. Sader, personal communication.
85. T Iida and R. I. L. Guthrie, *The Physical Properties of Liquid Metals* (Clarendon Press, Oxford, 1988).
86. H. C. van der Hulst, *Light Scattering by Small Particles* (Dover Publications, New York, 1981).
87. L. Francois, M. Mostafavi, J. Belloni, J. F. Delouis, J. Delaire, and P. Feneyrou, Optical limitation induced by gold clusters. 1. size effect, *J. Phys. Chem. B* **104**, 6133-6137 (2000).
88. G. Battaglin, P. Calvelli, E. Cattaruzza, R. Polloni, E. Borsella, T. Cesca, F. Gonella, and P. Mazzoldi, Laser-irradiation effects during Z-scan measurement on metal nanocluster composite glasses, *J. Opt. Soc. Am. B* ***17*****,** 213-218 (2000).
89. K. F. Peters, J. B. Cohen, and Y. W. Chung, Melting of Pb Nanocrystals, *Phys. Rev. B* **57**, 13430-13438 (1998).
90. Z. L. Wang, J. M. Petroski, T. C. Green, and M. A. El-Sayed, Shape transformation and surface melting of cubic and tetrahedral platinum nanocrystals, *J. Phys. Chem. B* **102**, 6145-6151 (1998).
91. C. L. Cleveland, W. D. Luedtke, and U. Landman, Melting of gold clusters, *Phys. Rev. B* **60**, 5065-5077 (1999).
92. Y. Lereah, R. Kofman, J. M. Penisson, G. Deutscher, P. Cheyssac, T. Ben David, and A. Bourret, Time-resolved electron microscopy studies of the structure of nanoparticles and their melting, *Philos. Magazine B* **81,** 1801-1819 (2001).
93. Y. G. Chushak and L. S. Bartell, Melting and freezing of gold nanoclusters, *J. Phys. Chem. B* **105**, 11605-11614(2001).
94. T. S. Ahmadi, Z. L. Wang, T. C. Green, A. Henglein, and M. A. El-Sayed, Shape-controlled synthesis of colloidal Pt nanoparticles, *Science* **272**, 1924-1926 (1996).
95. R.C. Jin, Y. W. Cao, C. A. Mirkin, K. L. Kelly, G. C. Schatz, and J. G. Zheng, Photoinduced conversion of silver nanospheres to nanoprisms, *Science* **294**, 1901-1903 (2001)
96. R. Borek, K. J. Berg, and G. Berg, Low-temperature tensile deformation of flat glass containing metal particles to generate dichroism, *Glastech. Berichte-Glass Sci. Tech.* **71**, 352-359 (1998).
97. B. R. Martin, D. J. Dermody, B. D. Reiss, M. M. Fang, L. A. Lyon, M. J. Natan, and T. E. Mallouk, Orthogonal self-assembly on colloidal gold-platinum nanorods, *Adv. Mater.* **11**, 1021-1025 (1999).
98. J. S. Yu, J. Y. Kim, S. Lee, J. K. N. Mbindyo, B. R. Martin, and T. E. Mallouk, Template synthesis of polymer-insulated colloidal gold nanowires with reactive ends, *Chem Comm.* (24), 2445-2446 (2000).
99. S. R. Nicewarner-Pena, R. G. Freeman, B. D. Reiss, L. He, D. J. Pena, I. D. Walton, R. Cromer, C. D. Keating, and M. J. Natan, Submicrometer metallic barcodes, *Science* **294**, 137-141 (2001).
100. Z. T. Zhang, S. Dai, D. A. Blom, and J. Shen, Synthesis of ordered metallic nanowires inside ordered mesoporous materials through electroless deposition, *Chem. Mater.* **14**, 965 (2002).
101. S. O. Obare, N. R. Jana, and C. J. Murphy, Preparation of polystyrene- and silica-coated gold nanorods and their use as templates for the synthesis of hollow nanotubes, *Nano Lett.* **1**, 601-603 (2001).
102. N. R. Jana, L. Gearheart, and C. J. Murphy, Wet chemical synthesis of high aspect ratio cylindrical gold nanorods, *J. Phys. Chem. B* **105**, 4065-4067 (2001).
103. C. S. Ah, S. Do Hong, and D. J. Jang, Preparation of Au core Ag shell nanorods and characterization of their surface plasmon resonances, *J. Phys. Chem. B* **105**, 7871-7873 (2001).
104. Z. L. Wang, M.B. Mohamed, S. Link, and M. A. El-Sayed, Crystallographic facets and shapes of gold nanorods of different aspect ratios, *Surf. Sci.* **440**, L809-L814 (1999).
105. Z. L. Wang, R. P. Gao, B. Nikoobakht, and M. A. El-Sayed, Surface reconstruction of the unstable {110} surface in gold nanorods, *J. Phys. Chem. B* **104**, 5417-5420 (2000).
106. G. V. Hartland, M. Hu, O. Wilson, P. Mulvaney, and J. E. Sader, Coherent excitation of vibrational modes in gold nanorods, *J. Phys. Chem. B* **106**, 743-747 (2002).
107. *CRC Handbook of Chemistry and Physics, 80th ed.* (CRC Press, Boca Raton, 1999).

5
RADIATION EFFECTS IN NANOPARTICLE SUSPENSIONS

Dan Meisel*

1. INTRODUCTION

Several directions may be identified is studies of the effects of ionizing radiation on particles in suspension. The first one is simply to understand the consequences of irradiating a multi-phase system.[1,2] Would the energy be confined into one phase or the other? How much energy or charge is transferred across the interface and what fraction remains arrested in each of the phases? Does the interface, its composition and the surface charge alter the outcome of the chemistry? In another direction ionizing radiation is used as a synthetic tool to prepare particle suspensions. Many metallic particles and a few semiconductors as well, were prepared using this approach.[3-6] The advantage of using radiolytic approach over wet chemical methods is the ability to control the size and size distribution by controlling the dose-rate delivered to the precursors solution. A third direction focuses on mechanistic studies conducted on suspensions of nanoparticles. The suspensions allow time domain optical measurements, which are common in radiation research, and therefore are often utilized to study mechanisms of short-lived intermediates generated in the suspensions. In this report we survey mostly recent observations from the first area of activity: transfer of energy or charge initially generated by ionizing radiation in one phase into the other.

Interfacial processes induced by ionizing radiation are of interest as a fundamental scientific question, as well as a technologically relevant concern. When high-energy particles travel through a multiphase system, ionization and excitations occur at each of the phases. When the weight percentage of each phase is significant, these events occur in both phases and both phases contribute to the degradation of the original material. Often the consequences of the radiation in each of the phases is reasonably well understood but when the two phases coexist, in particular when the dimensions of one of the phases are small, interfacial charge or energy transfer can occur. The various possible pathways that the carriers can undergo are illustrated in Scheme 1. The electron or the hole can lose its excess energy and thermalize, it can localize in a trap state within the particle, and the two carriers can recombine. While these processes occur the carriers may also cross into

* Dan Meisel, Radiation Laboratory and Department of Chemistry and Biochemistry, University of Notre Dame, Notre Dame, IN 46556.

the other phase (large arrows in Scheme 1). This is the process of interest in the present discussion. The technologically relevant issue is the potential for radiolytic processes to occur preferentially in one of the phases. In the case of particles suspended in water, the potential for enhanced water radiolysis products, e.g., molecular hydrogen generation, is a very practical concern.[7] On the other hand, strategies to remedy contaminated soils may benefit from enhanced radiolytic yields in the aqueous phase of such heterogeneous systems.[8] Transfer of radiolytically generated charge carriers across the solid-liquid interface is of great technological significance to the vitrification of radioactive waste.[9] Escape of charges from irradiated particles has important consequences for stored high-level-liquid waste, which invariably is heavily loaded with solid particles.[10] Various molecules adsorbed onto metal oxide particles or porous bulk materials have been shown to form radical anions, radical cations, or to decompose under the action of ionizing radiation due to charge migration to the interface.[2] Although the underlying mechanisms are not entirely clear, the adsorbates are believed to interact with surface-trapped charge carriers. As a result, possible applications of ionizing radiation to the degradation of adsorbed environmental pollutants are being explored.[11,22]

Early studies demonstrated catalytic conversion of all the reducing equivalents (and sometimes the oxidizing equivalents as well) that are produced by radiolysis of water into molecular hydrogen in the presence of metallic particles.[13-15] Detailed mechanisms were developed to delineate the pathways that lead radical reactions, commonly one-electron redox entities, to participate in multi-electron redox reactions via the catalytic particles.[16,17] However, in these studies essentially no energy was deposited in the solid particles; rather the aqueous phase alone absorbed the energy. Radicals were generated in the water but their chemical fate was determined by the catalytic surface of the nanoparticles. Below we focus on the reverse processes, transfer of charges from the solid to the water.

Several groups recently studied irradiation of wet oxide surfaces.[18-20] Often these studies concentrate on the first few monolayers in intimate contact with the solid.

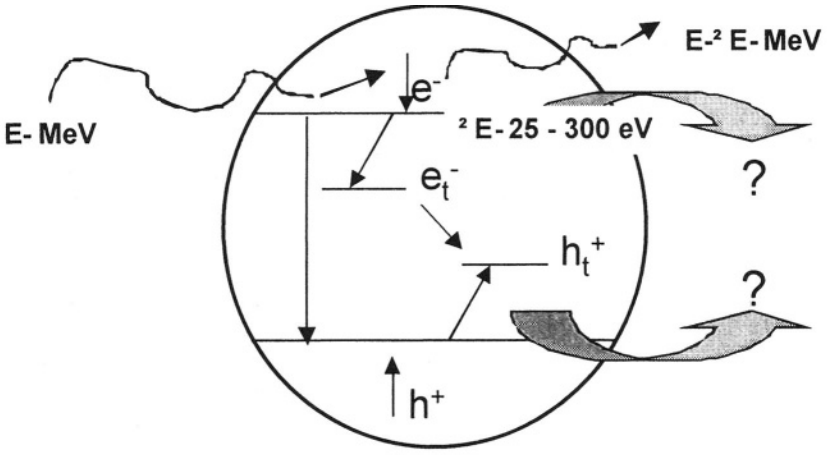

Scheme 1. Ionizing radiation in a nanoparticle in suspension. A high-energy particle (≈MeV) generates an electron-hole pair (≈ tens of eV). Both carriers can thermalize, localize in traps, recombine or cross the interface into the surrounding medium.

In several instances it was shown that yields of stable water radiolysis products, e.g., H_2, from water layers on several oxides, such as ZrO_2 or CeO_2, are unusually high.[21,22] This high yield necessitates energy transfer from the solid material to the aqueous layers. Furthermore, this yield and the correlation between the yield and the oxide bandgap led Petrik and coworkers to suggest transfer of excitons across the interface. Zhang et al.[18] reported redox processes at silica powders and slurries surfaces, where siloxane groups are abundant, which lead to efficient H_2 production upon irradiation, following release of H atom from surface –SiO-H moieties. The holes in that system are trapped at acceptor sites, such as pyrene molecules, generating the radical cation. The structure of the water under such circumstances is significantly different from bulk water and the behavior of the few water layers under the field of radiation may then differ from that of bulk water.

In our own studies we focus on radiolytic products from bulk water that is in the vicinity of the suspended particles. It was shown recently, by directly following the hydrated electrons, that their yield does not decrease upon addition of SiO_2 nanoparticles up to loading of 50% by weight to the suspensions.[23] On the other hand it was found that holes remain trapped in the silica particle even at the smallest size available.[24] The observation that the production of OH radicals decreases upon loading the suspension with silica particles suggests that the trapped holes cannot oxidize water at the interface. However, the energy level at which they are trapped has not been determined. Furthermore, it is evident that charge separation occurs across the silica nanoparticle/ aqueous solution interface. These observations are summarized in the following sections.

2. ENERGY DEPOSITION IN PARTICLE SUSPENSIONS

High-energy electrons, in the range of a few MeV, lose their kinetic energy mostly via interactions with the electrons of the medium. The cross section for absorption of ionizing radiation can be estimated by the Bethe formula, in which the energy loss is directly proportional to the electron density of the irradiated material.[25] For all practical purposes the electron density of the material can be considered equal to its density. As the high-energy electrons pass through the aqueous colloidal suspension of particles, energy is lost via electronic interactions in both the liquid and solid phases in a ratio determined by their relative electron densities and concentration. Thus, as the percentage of solid material increases, so does the fraction of energy deposited in the solid phase. Since it is common to conduct radiolytic experiments at constant volume (to ensure constant geometry relative to the radiation source) the dose absorbed in the sample increases with the increase of total density of the sample. This is shown in Figure 1 as the upper solid curve.

If the energy originally deposited in the particles remains in the solid, the total number of hydrated electrons observed in a given volume of sample must decrease upon increasing the weight % of the solid proportionately with the decrease in the volume fraction of water. If no electrons are transferred from the particles to the water, the concentration of e^-_{aq} will decrease. The lower solid curve in Figure 1 describes this decrease for SiO_2 in water suspensions. This description also assumes that the probability of capture of electrons from water by silica particles is small.

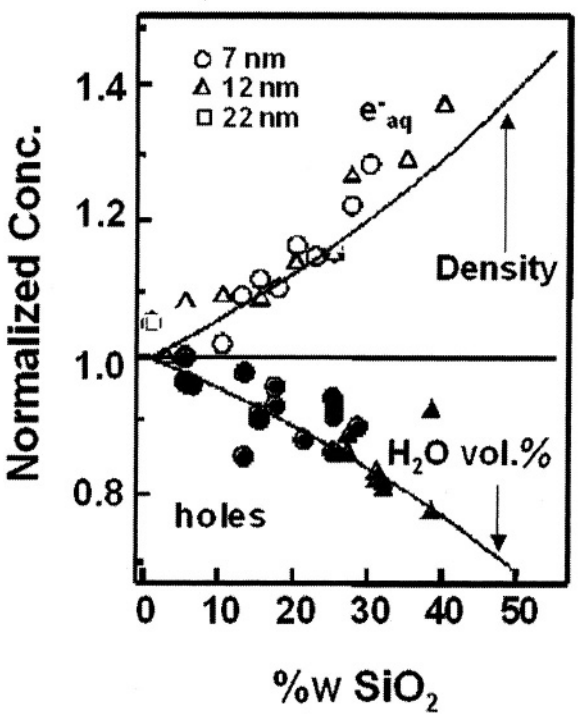

Figure 1. Normalized observed concentrations of e^-_{aq} (upper half) and OH radicals (scavenged by SCN^-, lower half) vs. loading of several size silica particles. The upper and lower solid curves are the increase in density and decrease of water volume with SiO_2 loading, respectively. Results taken from References 23 and 24.

There is little doubt that when the particles are large enough this lower-limit curve will be followed, unless some chemical process intervenes. When the particles are small, a fraction of the charge carriers may escape into the water.

Energetic considerations may affect the fate of charge carriers in either phase. At the very early physical stage of the generation of an electron in the material its energy may be very high, tens of eV. At these energies the identity of the material makes little impact. It may appear in either phase. As the energy degrades and the charge carrier thermalizes the identity of the medium and its energy levels become increasingly important.

Figure 2 shows the energies of the conduction and valence bands of silica and zirconia. It also shows the redox level of e^-_{aq}. A thermal electron in the conduction band of SiO_2 can generate a hydrated electron but the latter cannot return into the conduction band. The order of the levels is reversed in ZrO_2. Therefore, one expects in ZrO_2 suspensions a facile reaction of e^-_{aq} with the particles. In practical terms this means that direct determination of the yield of hydrated electrons in the latter suspensions is essentially impossible. High concentrations of scavengers of redox potential more positive than the conduction band of ZrO_2 are needed. Because of the very negative redox potential of the hydrated electron, most oxides can serve as its acceptors.[26] On the other hand, the valence band of many oxides, including those in Figure 2, allows oxidation of water to hydroxyl radicals. Experimentally, however, it is very difficult to observe directly the hydroxyl radical and scavengers required to follow its formation.

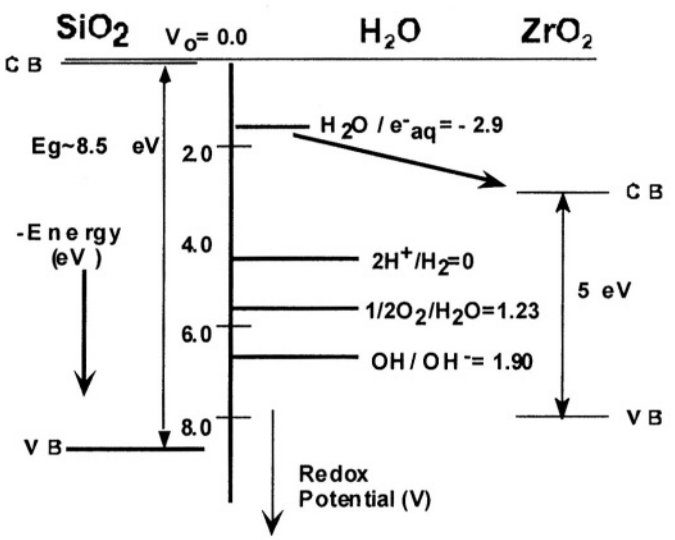

Figure 2. Energy levels for SiO_2 (left) and ZrO_2 (right) and a few redox potentials for water species. An electron in SiO_2 conduction band can convert to e^-_{aq} but not in ZrO_2.

3. EXPERIMENTAL PROCEDURES

Short-lived intermediates were determined using pulse-radiolysis of aqueous colloidal suspensions of silica or zirconia particles. The pulse radiolysis experiments were performed using 2-3 ns pulses of 8 MeV electrons from the Notre Dame linear electron accelerator. Early studies utilized the Argonne National Laboratory linac with pulses of 30 ps and time resolution of 0.1 ns. The doses used generated $(1\text{-}10)\times10^{-6}$ M of solvated electrons. Spectrophotometric detection of the radicals was used in these experiments. Several principles guided the choice of particles. The colloidal solutions allow convenient Spectrophotometric detection. Silica and zirconia, in addition to being a common material in many nuclear applications, are also transparent across the near UV-visible range allowing convenient detection of the radicals. No interference from trapped species in the particles could be observed in any of the suspensions. All experiments involving silica were performed in the basic pH range, where silica is negatively charged and thus the scavengers remain in the water phase, removed from the interface. Silica particles were DuPont Ludox products ranging in size from 7 to 22 nm in diameter. High concentrations of silica particles are easy to obtain and the energy levels are conveniently posed relative to the redox levels of water. Zirconia suspensions were studied at pH 3-4 in the presence of high acetate concentrations to stabilize the suspensions. Whereas the particles at this pH are usually positively charged we believe that ion-pairing and specific surface adsorption at the high concentrations used modified significantly the surface.

For yields of molecular hydrogen a ^{60}Co irradiator was used at a dose rate of 0.2-0.3 kGy/min. The production of H_2 was measured with an in-line gas chromatograph using 5A molecular sieve columns, Ar carrier gas, and a thermal conductivity detector. Dosimetry was done with the standard Fricke dosimeter. No corrections were made for changes in the dose absorbed by the suspensions due to changes in their density in the steady state, as well as in the pulse radiolysis experiments.

4. ESCAPE OF ELECTRONS INTO THE AQUEOUS PHASE

Attempts to determine the yield of charge carriers that escape from the particles to the water phase are scarce. For SiO_2, detailed studies were reported and for ZrO_2 some information is available. The experimental data in Figure 1 shows the concentration of hydrated electrons in silica suspensions as a function of the concentration of particles. These concentrations are normalized to the concentration of e^-_{aq} in neat water. They were measured as close as possible to the time of generation of the hydrated electrons, 10^{-10} – 10^{-9} sec following the electron pulse before significant recombination occurred. As can be seen in the figure, e^-_{aq} concentration increases upon increasing the concentration of the particles. It is also clear that the size of the particles has little effect if any on the yield up to 22 nm particles. Taking the radius as the average distance traveled by the escaping electron, one may compare it with results obtained from electron microscopy studies of metal oxide thin films.[27,28] The most probable escape depth observed in these studies is ~25 nm. Thus, only upon increasing the particle size to about twice the largest size studied, might a significant fraction remain (recombine or get trapped) in the particle.

As discussed in the preceding section, the dose deposited in the sample increases as well (upper curve in Figure 1). The close similarity between the increase in the absorbed dose and the concentration of hydrated electrons indicates the yield (number of species generated per unit absorbed energy) of electrons in water remains unchanged even when 50% of the water have been replaced by silica. Clearly, electrons that are generated initially in the particles escape to the water. Furthermore, assuming that the initial yield of electron-hole pairs that are generated in silica is not very different from water, the majority of them escape. Indeed, even though the band gap in silica is ~9 eV, the lowest energy required for the generation of an electron-hole pair is ~20 eV.[29] Alig et al[30] suggested a correlation between the bandgap of the material, E_g, and the average energy required to produce an electron-hole pair, E_p: $E_p \approx 2.73E_g + 0.5$. This leads to $E_p \approx 24$ eV for silica, and 14 eV for zirconia. From this correlation one expects similar yields (G~4-5 electrons per 100 eV) in silica and water. The yield, however, should increase in zirconia suspensions (expected G≈7 electrons/100 eV).

Zirconia particles are difficult to maintain in transparent suspensions. Acetate stabilized (1.5 mole/mole ZrO_2) 5-10 nm particles, up to 20% weight were used in these studies.[31] All experiments were conducted at pH 3.4 in solutions containing 2.76 M acetic acid. Under these conditions the majority of electrons are converted to hydrogen atoms. Electrophoresis of diluted suspensions show that the surface charge of the particles is positive and the point-of-zero-charge (pzc) was ≈7. Methyl Viologen, labeled MV^{2+}, was used to scavenge the reducing equivalents and all yields were compared to the same solutions containing no ZrO_2. At the MV^{2+} concentration used (10 mM) complete scavenging occurs to generate the reduced radical, MV^+. Figure 3 shows the concentration of MV^+, normalized to the yield in the absence of ZrO_2. The increase in MV^+ concentration upon increasing ZrO_2 loading far exceeds the absorbed dose and thus, the yield (in terms of the number of equivalents per unit of absorbed energy, i.e., $G(MV^+)$) increases as well. At the highest ZrO_2 concentration shown in Figure 3 the yield increased by 50%, from 4.2 radicals/100 eV in the absence of the particles to 6.3 radicals/100 eV at 20% weight. Thus, one concludes that thermalization, recombination and trapping of charge carriers in the small ZrO_2 particles are significantly less efficient than they are in water.

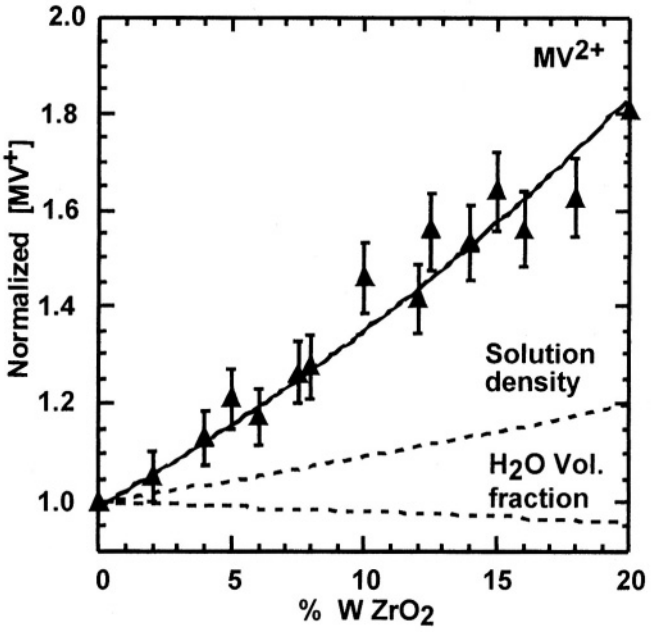

Figure 3. Normalized concentration of MV^+ as a function of % weight ZrO_2. Also shown is the increased dose absorbed by the sample (density) and the decrease in absorbed dose by the aqueous phase (volume fraction of H_2O). The increase beyond the increase of the density indicates large increase in yield.

Quantitatively, it can be shown that this high total yield of reducing equivalents requires a yield of approximately 10 electrons per 100 eV that escape from the particles, somewhat higher than the yield of 7 electrons/100 eV predicted above. One possible explanation to that increased yield is partial conversion of holes to reducing radicals (e.g., from acetate). Another possibility is increased capture of electrons by surface adsorbed species as described below in Section 6.

5. ESCAPE OF HOLES INTO THE AQUEOUS PHASE

The mobility of hot holes in silica is much slower than that of electrons. Furthermore, many trapping sites for holes have been identified in silica. Thus, one may expect more efficient trapping of holes relative to electrons and consequently less escape into the aqueous phase. To test this expectation the yields of OH radicals in the aqueous phase following radiolysis of suspensions of silica colloidal particles were measured. The yield of two OH scavengers was determined $Fe(CN)_6^{3-}$ and $(SCN)_2^-$ (from $Fe(CN)_6^{2-}$ and SCN^-, respectively). These negatively charged scavengers are expected to reside exclusively in the aqueous phase, removed from the particle surface. The result from suspensions of particles of 7 and 12 nm in diameter, are shown in Figure 1 (lower half of the figure). Upon increasing the loading the relative yield of OH radicals decreases. These results seem to follow the solid lower curve in Figure 1, which describes the fraction of energy absorbed by the aqueous phase. Thus, the only observed OH radicals seem to be those that were generated from radiolysis of the aqueous phase and no holes cross the interface even from the smallest particles available.

The consequences of charge separation across the interface, electrons in the aqueous phase and holes in the particles, were alluded to earlier. Mechanisms to relieve this electrostatic asymmetry must intervene since electrons cannot indefinitely escape the continuously increasing attractive potential. Charge compensation by migration of ions from the solution towards the surface will undoubtedly occur and will relief some of the electrostatic stress. The solution pH often determines the surface-potential for oxides. Therefore, protons or hydroxide ions are the most common ions to migrate to the surface of oxides. Release of protons from the surface can reduce the electrostatic potential but such a process still leaves trapped holes in the solid. An increase in the yield of oxidation equivalents in the water upon loading the suspensions with ZrO_2 particles was observed. However, electrostatic imbalance is observed in these suspensions as well.[31]

The fate of the holes that are generated in ZrO_2 particle suspensions was determined using a similar approach to that described above for electrons, except that SCN^- ions were used to scavenge the escaping holes. At sufficiently high concentrations (1 M) it captures most of the OH radicals before their reaction with the acetic acid. The valence band edge of ZrO_2 is at 4,0 V vs. NHE at pH = 0 (Figure 2), and therefore, the holes can thermodynamically oxidize water to OH radicals. Nonetheless, both direct capture of holes by SCN^- and oxidation of water to OH, were proposed to generate the oxidized $(SCN)_2^-$ radicals. In the absence of zirconia the yield of OH in these solutions is assumed to be equal to the yield of reducing species, 4.2 radicals/100 eV. The normalized yield of $(SCN)_2^-$ as a function of the % weight of ZrO_2 increases upon addition of particles but is only 35% higher in 20% weight zirconia than in the absence of the particles. For comparison, the yield of electrons in Figure 3 is 80% higher. When corrected for the increase in dose absorbed upon increasing ZrO_2 loading, the yield at 20% is only 4.9 molecules/100 eV. The imbalance between the yield of electrons and holes captured indicates that the escape into the solution competes mostly with thermalization and trapping processes and not with recombination. Similar to the results in silica, it also leads to the conclusion that positive charges accumulate in the solid particle. Alternatively, if as suggested above the holes are partially converted to reducing radicals before they are captured by the thiocyanide ions, then the imbalance may be due to this competing process.

6. INTERFACIAL CAPTURE

It is of interest to test the effect of the interface on the yields discussed above. At least two parameters of the interface can be externally modified: the surface potential and the chemical identity of species at the interface. If these parameters can modify the yield, then the yields may be controlled externally. These possibilities were studied in silica suspensions.[32] To change the surface potential of the silica particles, Mg^{2+} ions (up to 25 mM) were added to the suspensions. Above the pzc of silica these ions strongly adsorb at the surface thus neutralizing much of the surface charges. The yields of e^-_{aq} were measured with and without these ions with essentially the same results. We concluded that a significant reduction in the negative charge density at the surface has little effect on the yield of e^-_{aq}.

Similar experiments to those described in Figure 1 for the yields of hydrated electrons from silica suspensions were repeated with MV^{2+} added. All of the MV^{2+}

acceptors were adsorbed on the silica particles at the conditions of these experiments as was evident from the reduction of the rate of e^-_{aq} reaction with MV^{2+}. Furthermore, from the ionic strength dependence of the rate constant for this reaction, it was shown that the hydrated electrons react against a negative potential (rather than positive if MV^{2+} has been free in solution). Hydrated electrons that originate from direct ionization of water in the same suspensions were scavenged by NO_3^- ions in the bulk of the aqueous phase. The yield of electrons captured by MV^{2+} was found to track the fraction of dose absorbed by the silica particles. Since this is also the contribution of silica to the total generation of solvated electrons, one concludes that the acceptors at the surface can capture all the electrons that cross the interface. Yet, the possibility that the presence of acceptors at the interface affects competing processes within the particle, such as recombination, trapping, and escape, cannot be precluded. A slight increase in the yield, beyond the increase in absorbed dose, may result from such an effect. The results described above serve to further illustrate the difficulties of determining the yields of charge carriers when the energy levels of the solid are within the gap allowed by water (Figure 2). Once scavengers are required in order to measure the yield of charge carriers, the effect of the scavenger needs to be examined.

7. HYDROGEN YIELDS

Generation of molecular hydrogen during irradiation of particle suspensions is often of much concern, especially in technological applications. Therefore, some effort was taken to determine the yield of H_2 from irradiated oxide suspensions. Hydrogen yields from wet oxide surfaces are sometimes very high[21] and some correlation between that yield and the oxide bandgap has been suggested.[22,23] Yet, the mechanism for hydrogen evolution from irradiated water is reasonably well understood. There is ample evidence to suggest that much, if not all, of the H_2 produced in neat water comes from reactions of hydrated electrons and/or their precursors, the "dry" but thermalized electrons.[34,35] One may expect then a similar mechanism in the suspensions as well.

As described above, an increase in the concentration of solvated electrons is observed in both, SiO_2 and ZrO_2, which may lead to enhanced H_2 production. Such a "trivial" effect is not the focus of our studies and efforts were made to scavenge most radicals that are formed in the bulk aqueous phase. However, since the energy of the escaping electrons is not known, it is conceivable that different mechanisms may contribute to the final generation of hydrogen. Furthermore, because the surface of most oxides is covered with Si-OH groups in water, new pathways may become available in the presence of oxide particles.[18] The yield of H_2 in silica suspensions at high SiO_2 loading was therefore measured.[36]

Figure 4 shows the dependence of hydrogen yield, $G(H_2)$ in molecules per 100 eV, on the weight percentage of SiO_2 for three particle sizes. The solution contained 1 mM of each ferricyanide and ferrocyanide. Neither ion is expected to adsorb on the negatively charged silica surface. However, the mixture of $Fe(CN)_6^{3-/4-}$ efficiently reacts with all three radicals, e^-_{aq}, OH, and H in the aqueous phase. Thus, no contribution is observed from homogeneous reactions in the bulk to the production or destruction of hydrogen.

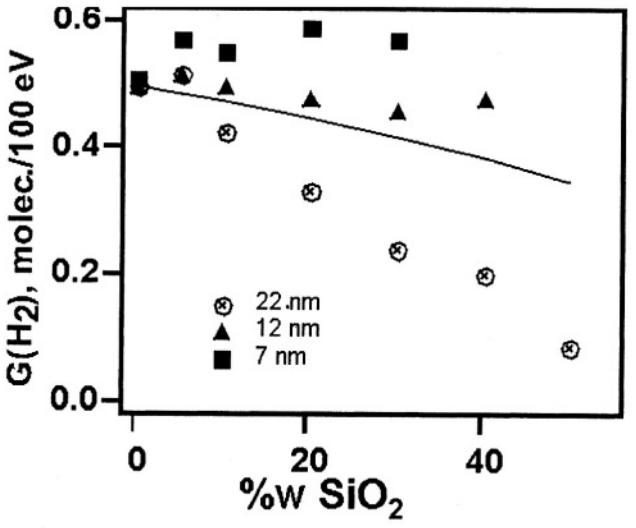

Figure 4. Dependence of $G(H_2)$ on wt % of SiO_2 particles of the sizes shown in the figure. Solutions contained 1 mM of each $Fe(CN)_6^{4-}$ and $Fe(CN)_6^{3-}$. The solid line presents the calculated curve of $G(H_2)$ assuming no interaction between the two phases.

The solid curve in Figure 4 shows the effect of the excluded volume due to the particles. If no energy is transferred in either direction, the decrease should follow the excluded volume of silica in the suspension. Surprisingly, the yield depends on particle size. It is slightly higher than expected from the water volume-fraction effect for the smaller sizes and significantly lower for the larger size.

The observations of Figure 4 are independent of the scavengers used, provided they do not adsorb onto the particles. Similar results were obtained using nitrite instead of the combination of $Fe(CN)_6^{3-/4-}$. The slight increase in $G(H_2)$ above the yield in the absence of silica, noticeable in particular for the smaller particles in Figure 4, is attributed to the escape of electrons from the particles as described in Section 4. Apparently, a small fraction of these are not scavenged by ferricyanide and recombine to produce molecular hydrogen. The decrease in $G(H_2)$ beyond the predicted excluded-volume effect is attributed to a back reaction between H_2 and the trapped holes in the solid particles. From the results described in Section 5 it is clear that the holes in silica do not oxidize water. They do not oxidize 2-propanol either,[24] even though the valence band in silica is at ~4 to 4.5 V vs. NHE. However, the energy of the trapped holes is presently unknown and two-electron oxidation of H_2 may be thermodynamically feasible. Indeed it is now well established that H_2 can react with trapped holes in amorphous silica. The H atom that is produced from that reaction certainly can react with the trapped holes.[20,37-41]

This back reaction of holes with H_2 can also rationalize the dependence of the yield on size seen in Figure 4. As the size of the particles increases their concentration decreases, for a given weight percentage of silica. Therefore, the probability that a given particle contains a trapped hole following a given dose of irradiation increases. The probability that an H_2 molecule or some of its precursors, from the water will encounter a hole-containing particle is larger for the bigger particles. The probability that a single particle will contain two holes, required for oxidation of hydrogen to protons, is even more dependent on particle size. For the smallest particles shown in Figure 4, the number

of holes per particle at the dose delivered in these experiments ≈0.4, is assuming every hole that is generated in the particles remains trapped in the solid. Under the same conditions ~5 holes are trapped at the largest particles of Figure 4. Note that under these assumptions the number of holes trapped in a particle is independent of the concentration of the particles. As the concentration of particles increases the dose absorbed by the particles increases proportionately to their concentration. If this hypothesis is correct then elimination of the trapped holes before they can back react with molecular hydrogen should remove the size dependence. Several experiments were devised to demonstrate that this is indeed the case. For example, when suspensions of SiO_2 were irradiated in the presence of 1mM of $Ru(NH_3)_6^{2+}$, (and 10 mM KNO_2 to eliminate radical reactions in the bulk) the size dependence disappeared (Figure 5).

The redox potential of the $Ru(NH_3)_6^{2/3+}$ couple in water is 0.2 V vs. NHE but in contrast to the ferri/ferrocyanide couple used in the experiments of Figure 4, the ruthenium hexamine cations adsorb at the surface of the particles. The divalent state is, therefore, expected to react with the trapped holes in the solid, similar to hydrogen. As can be seen in Figure 5, all the suspensions produce a similar yield of H_2 independent of particle size. Furthermore, the yield also closely tracks the expected decrease resulting from the drop in volume fraction of water.

To conclude, no excess of molecular hydrogen can be observed from the irradiated silica suspensions, and similar results were obtained from zirconia. Any effect of the first few water monolayers is too small to be observed in the suspensions.[18,21,22] On the other hand, the presence of trapped holes may significantly affect the measured hydrogen yields because of the intervention of back reactions with trapped holes.

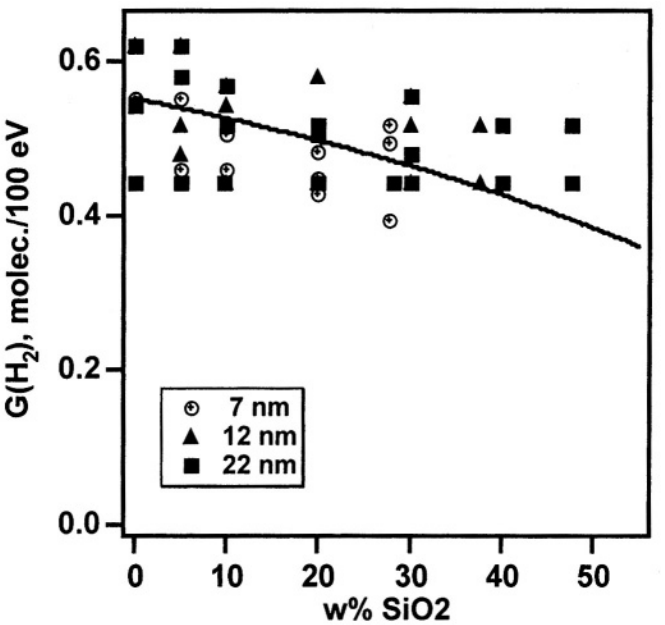

Figure 5. Dependence of $G(H_2)$ on wt % of SiO_2 for the particle sizes shown in the figure. All solutions contained 10 mM KNO_2 and 1 mM of $Ru(NH_3)_6^{2+}$.

8. RADIOLYSIS AS A SYNTHETIC TOOL

Numerous reports describe the use of radiolysis in the synthesis of metallic nanoparticles and a few extend this approach to the synthesis of semiconductor particles. A comprehensive description of these studies is beyond the scope of the present report. Henglein and coworkers[42-44] and Belloni and coworkers[5,45,46] describe the radiolytic reduction of many metal ions either of a single metal or in combination of a variety of metals to generate metallic or bimetallic mixtures as well as core-shell structures. To obtain metallic particles from their parent ions one only needs to ensure reductive conditions during the irradiation. Naturally, both oxidizing as well as reducing radicals are generated by the radiolysis of water. The oxidizing equivalents, OH radicals, can conveniently be converted to reducing radicals by the addition of organic scavengers (e.g., alcohols, formate ions) that will produce reducing radicals. The radiolytic approach may offer some advantages because of the fine control over the rate of generation of the growing species afforded by the control over the dose rate delivered to the sample. Furthermore, the mechanism of nucleation and growth can be delineated[5,46] and properties, such as absorption spectra or redox potentials, of the growing clusters can be determined.[47-49] By judicious selection of the parent metal ion or complex narrow size distribution of the particles at predetermined sizes can be achieved.[3] To generate core-shell structures one would rely on the large difference in redox potentials between the reduction of the parent ion to a single atom and its reduction to the bulk metal (Scheme 2). The presence of core seed particles of the first metal will then serve as the "bulk" for the shell metal. Using this strategy only few new seeds are generated and most of the reduction occurs on top of the existing seeds. When the same metal (but a different parent complex so the redox potential allows only reduction on "seeds") is deposited on existing seeds the synthesis leads merely to increase in the particle sizes. However, because the rate of growth is inversely proportional to the square of the size, whereas the rate of reduction is directly proportional to the size, the net rate of size increase is inversely proportional to the size. This results in narrowing of the size distribution as the particles grow. The smaller particles grow faster than the larger ones.

The strategies described above lead to well defined structures, often to core-shell materials of high quality. This allows detailed studies of the properties of the core-shell particles.[50,51] However, recent results indicate that the core-shell structures may not last for very long periods of time. Core-shell, silver on gold particles were observed to spontaneously alloy at ambient temperature and in suspension.[52] This spontaneous mixing of the two metals is a size-dependent process, which is accelerated when the sizes reach a few nm. A possible explanation for the size dependent alloying is the strong depression of the melting temperature of the metals when the particle size drops into this size regime.[53,54] The depression of the melting point leads to increased diffusion coefficients at ambient temperature of the solid metals in one another, and therefore might enhance their inter-mixing. Quantitative estimations of the rate of mixing from the estimated diffusion coefficients, however, indicate that this effect is still too slow to rationalize the observed rate of alloying. Molecular dynamics calculations suggest that defects at the bimetallic interface in the core-shell particles might explain the fast alloying.[55]

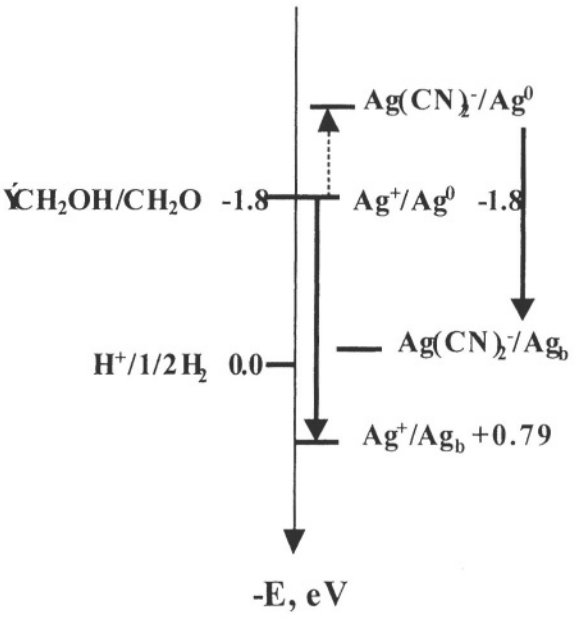

Scheme 2. Redox levels for enlargement, or deposition of shells, on existing seeds. Reduction of the cyanide complex to a single atom by the methanol radical is impossible but reduction on existing "bulk" is feasible.

To initiate radiolytic growth of semiconductors, one component of the material, e.g., Ag^+ or Cd^{2+} is added to the solution. An organic precursor that contains the counter ion, RX, where X^- is a halide or chalcogenide, is also added. The reaction of the precursor with e^-_{aq} releases the counter ion, X^-, and the growth of the nanoparticles can be followed.[56,57] The main reason to use radiolytic techniques to initiate the production of the particles is to study the mechanism of their growth and the properties of the various intermediates. Using this approach the absorption spectrum of the single molecule (e.g., AgX, CdS) could be measured and the equilibrium constant between the molecule and its component ions can be determined. As might be expected, these studies reveal that the single molecule dissociates into its component ions to a much larger extent than the bulk material. The solubility is size dependent, and therefore, the stability of the nanoparticles to dissolution in polar solvents is significantly lower than that of the bulk.

9. CONCLUSIONS

This report summarizes the effects of ionizing radiation on nanoparticles suspensions in aqueous media. Radiolytic methodologies to synthesize nanoparticles of metals and semiconductors in suspension were developed and the use of radiolytic techniques to outline mechanisms of a large number of processes at the surface of the particles has been reported. However, the focus of the present report is on radiolytic yields and on interfacial exchange of charge carriers among the solid particle and the aqueous phase. It is clear that the interface does not offer a barrier to exchange of carriers. On the contrary, the presence of the solid phase often enhances products from the fragmentation of water molecules. This has practical implications in technological application where ionizing

radiation and radioactivity are present. Absorption of radiation by the surfaces of pipelines in nuclear reactors can contribute to radiolytic water dissociation and thus to the generation oxidizing intermediates, hydroxyl radicals or hydrogen peroxide. These are the major sources of corrosion processes in the cooling system lines of the reactor. Similarly, nuclear materials stored as powders in sealed cylinders can accumulate water from humid environments. The irradiated water then can generate high quantities of gases not merely from direct irradiation of the water but from the radiation energy absorbed by the solid material. Nuclear waste stored in tanks as heterogeneous suspensions waiting permanent disposition can lead to water products, including flammable gas mixtures, from absorption of dose in both phases. On the other hand, the deep penetration of ionizing radiation together with the exchange of carriers among the phases might be utilized to increase the efficiency of radiolytic processes. For example, electron-beam sterilization of foods or hardware in general, as well as, decontamination of polluted environments may benefit from this exchange.

10. ACKNOWLEDGEMENT

The contribution of my colleagues to the work described above is much appreciated. Part of this work was supported by the US-Department of Energy, Office of Basic Energy Sciences, by the Environmental Management Science Program and by the Nuclear Energy Initiative. This is contribution NDRL No. 4383 from the Notre Dame Radiation Laboratory.

11. REFERENCES

1. G. Zhang, X. Liu, and J. K. Thomas, Radiation Induced Physical and Chemical Processes in Zeolite Materials, *Radiat. Phys. Chem.* **51**, 135-152 (1998).
2. J. K. Thomas, Physical Aspects of Photochemistry and Radiation-Chemistry of Molecules Adsorbed on SiO_2, Gamma-Al_2O_3, Zeolites, and Clays, *Chem. Rev.* **93**, 301-320 (1993).
3. A. Henglein and D. Meisel, Radiolytic control of the size of colloidal gold nanoparticles, *Langmuir* **14**, 7392-7396(1998).
4. A. Henglein, Nanoclusters of Semiconductors and Metals. Colloidal Nanoparticles of Semiconductors and Metals. Electronic structure and Processes, *Ber. Bunsenges., Phys. Chem.* **101**, 1562--1572 (1997).
5. J. Khatouri, M. Mostafavi, J. Ridard, J. Amblard, and J. Belloni, Kinetics of Cluster Growth by Aggregation, *Z. Phys. D* **34**, 47-56 (1995).
6. E. Gachard, H. Remita, J. Khatouri, B. Keita, L. Nadjo, and J. Belloni, Radiation-Induced and Chemical Formation of Gold Clusters, *New J. Chem.* **22**, 12571265 (1998).
7. T. Orlando and D. Meisel, Radiation-Induced Processes in Aqueous Suspensions of Nanoparticles and Nanoscale Water Films: Relevance to H_2 Production in Mixed Waste and Spent Nuclear Fuel, in *Nuclear Site Remediation;* G. Eller and W. R. Heineman, Eds.; ACS Symposium Series, **2001**; Vol. 778, pp. 284-296.
8. G. A. Zacheis, K. A. Gray, and P. V. Kamat, Radiation-Induced Catalysis on Oxide Surfaces: Degradation of Hexachlorobenzeneon □-Irradiated Alumina Nanoparticles, *J. Phys. Chem. B* **103**, 2142-2150(1999).
9. M. Antonini, A. Manara, and P. Lensi, *The Physics of SiO_2 and Its Interfaces;* Pergamon Press: New York, 1978.
10. A. Lawler, *Researchers Vie for Role in Nuclear- Waste Cleanup, Science* **275**, 1730(1997).
11. U. Stafford, K. A. Gray, and P. V. Kamat, Radiolytic and TiO_2-assisted photocatalytic degradation of 4-chlorophenol. A comparative study, *J. Phys. Chem.* **98**, 6343-6351 (1994).
12. R. J. Hilarides, K. A. Gray, J. Guzzetta, N. Cortellucci, and C. Sommer, Radiolytic degradation of 2,3,7,8-TCDD in artificially contaminated soils, *Environ. Sci. & Technol.* **28**, 2249-2258 (1994).

13. A. Henglein, Reactions of organic free radicals at colloidal silver in aqueous solution. Electron pool effect and water decomposition, *J. Phys. Chem.* **83**, 2209-2216 (1979).
14. A. Henglein, The reactivity of silver atoms in aqueous solutions (A γ-radiolysis study), *Ber. Bunsenges. Phys. Chem.* **81**, 556-561 (1977).
15. D. Meisel, Catalysis of H_2 production in irradiated aqueous solutions by Au sols, *J. Am. Chem. Soc.* **101**, 6133-6135 (1979).
16. A. Henglein and J. Lilie, Storage of electrons in aqueous solution: the rates of chemical charging and discharging of the colloidal Ag microelectrode, *J. Am. Chem. Soc.* **103**, 1059-1066 (1981).
17. A. Henglein, Physicochemical properties of small metal particles in solution: "Microelectrode" reactions, chemisorption, composite metal particles, and the atom-to-metal transition, *J. Phys. Chem.* **97**, 5457-5471 (1993).
18. G. Zhang, Y. Mao, and J. K. Thomas, Surface chemistry induced by high energy radiation in silica of small particle structures, *J. Phys. Chem. B* **101**, 7100-7013 (1997).
19. I. A. Shkrob and A. D. Trifunac, Time-resolved EPR of spin-polarized mobile H atoms in amorphous silica: the involvement of small polarons, *Phys. Rev. B* **54**, 15073-15078 (1996).
20. I. A. Shkrob, B. M. Tadjikov, S. D. Chemerisov, and A. D. Trifunac, Electron trapping and H atoms in oxide glasses, J. *Chem. Phys. B* **111**, 5124-5140 (1999).
21 J. A. LaVerne and L. Tandon, H_2 production in the radiolysis of water on CeO_2 and ZrO_2, *J. Phys. Chem. B* **105**, 9316-9322(2001).
22. N. G. Petrik, A. B. Alexandrov, A. I. Vall, Interfacial energy transfer during gamma radiolysis of water on the surface of ZrO_2 and some other oxides, *J. Phys. Chem. B* **105**, 5935-5944 (2001).
23. T. Schatz, A. R. Cook, and D. Meisel, Charge carrier transfer across the silica nanoparticle/water interface, *J. Phys. Chem.* **102**, 7225-7230 (1998).
24. N. M. Dimitrijevic, A. Henglein, and D. Meisel, Charge separation across the silica nanoparticle/water interface, *J. Phys. Chem. B,* **103**, 7073-7076 (1999).
25. E. I. Grigoriev and L. I. Trakhtenberg, *Radiation Chemical Processes in Solid Phase. Theory and Application";* CRC Press: Boca Raton, 1996.
26. P. Mulvaney, F. Grieser, and D. Meisel, Redox reactions on colloidal metals and metal oxides, in *Kinetics and Catalysis in Microheterogeneous Systems;* M. Graetzel and K. Kalyanasundaram, Eds.; Marcel Dekker: New York, **1991**; pp. 303-373.
27. H. Seiler, Secondary electron emission in the scanning electron microscope, *J. Appl. Phys.* **54**, R1-R18 (1983).
28. K. Kanaya, S. Ono, and F. Ishigaki, Secondary electron emission from insulators, *J. Phys. D: Appl. Phys.* **11**, 2425-2437 (1978).
29. I. Petr, Production of electron-hole pairs in SiO_2 films, *J. Radioanal. Nucl. Chem., Letters* **95**, 195-200 (1985).
30. R. C. Alig, S. Bloom, and C. W. Struck, Scattering by ionization and phonon emission in semiconductors, *Phys. Rev. B* **22**, 5565-5582 (1980).
31. Treguer, M.; D. Meisel, *To be published.*
32. T. Schatz, A. Cook, and D. Meisel, Capture of charge carriers at the silica nanoparticle - water interface, *J. Phys. Chem. B* **103**, 10209-10213 (1999).
33. A. B. Aleksandrov, A. Yu Bychkov, A. I. Vall, N. G. Petrik, and V. M. Sedov, Radiolysis of adsorbed substances on oxide surfaces, *Zhurnal Fischeskoi Khirnii (English Trans.)* **65**, 1604-1608 (1991).
34. J. A. LaVerne and S. M. Pimblott, New mechanism for H_2 formation in water, *J. Phys. Chem. A* **104**, 9820-9822 (2000).
35. B. Pastina, J. A. LaVerne, and S. M. Pimblott, Dependence of molecular hydrogen formation in water on scavengers of the precursor to the hydrated electron, *J. Phys. Chem. A* **103**, 5841-5846 (1999).
36. H. Miyoshi, T. Schatz, and D. Meisel, *To be published.*
37. L. Scuja, Optically active oxygen-deficiency-related centers in amorphous silicon dioxide, *J. Non-Cryst. Solids* **239**, 16-48(1998).
38. R. E. Stahlbush, A. H. Edwards, D. L. Griscom, and B. J. Marstik, Post-irradiation cracking of H_2 and formation of interface states in irradiated metal-oxide-semiconductor field-effect transistors, *J. Appl. Phys.* **73**, 658-667(1993).
39. D. L. Griscom, Diffusion of radiolytic molecular hydrogen as a mechanism for the post-irradiation buildup of interface states in SiO_2-On-Si structures, *J. Appl. Phys.* **58**, 2524-2533 (1985).
40. D. L. Griscom and E. J. Friebele, Fundamental radiation-induced defect centers in synthetic fused silicas - atomic chlorine, delocalized e' centers, and a triplet-state, *Phys. Rev. B* **34**, 7524-7533 (1986).
41. A. H. Edwards, J. A. Pickard, and R. E. Stahlbush, Interaction of hydrogen with defects in A-SiO_2, *J. Non-Cryst. Solids* **179**, 148-161 (1994).

42. A. Henglein, Electronics of colloidal nanometer particles, *Ber. Bunsenges. Phys. Chem.* **99**, 903-913 (1995).
43. A. Henglein, Mechanism of reactions on colloidal microelectrodes and size quantization effects, *Top. Curr. Chem.* **143**, 113-180 (1998).
44. M. Gutierrez and A. Henglein, Nanometer-sized Bi particles in aqueous solution: absorption spectrum and some chemical properties, *J. Phys. Chem.* **100**, 7656-7661 (1996).
45. J. L. Marignier, J. Belloni, M. 0. Delcourt, and J. P. Chevalier, Microaggregates of non-noble metals and bimetallic alloys prepared by radiation-induced reduction, *Nature* **317**, 344-345 (1985).
46. J. Khatouri, J. Ridard, M. Mostafavi, J. Amblard, and J. Belloni, Kinetics of cluster aggregation in competition with a chemical growth reaction, *Z. Phys. D* **34**, 57-64 (1995).
47. A. Henglein, Remarks on the electrochemical potential of small silver clusters in aqueous solution, *Ber. Bunsenges. Phys. Chem.* **94**, 600-603 (1990).
48. M. Mostafavi, J. L. Marignier, J. Amblard, and J. Belloni, Size-dependent thermodynamic properties of silver aggregates. Simulation of the photographic development process, *Z. Phys. D* **12**, 31-35 (1989).
49. J. Khatouri, M. Mostafavi, J. Amblard, and J. Belloni, lonization potential of clusters in liquid, *Z Phys. D* **26** (Suppl.), 82-86 (1993).
50. J. H. Hodak, A. Henglein, and G. V. Hartland, Photophysics and spectroscopy of metal particles, *Pure Appl. Chem.* **72**, 189-197 (2000).
51. J. H. Hodak, A. Henglein, M. Giersig, and G. V. Hartland, Laser-induced inter-diffusion in Au-Ag core-shell nanoparticles, *J. Phys. Chem. B* **104**, 11708-11718 (2000).
52. T. Shibata, H. Tostmann, B. Bunker, A. Henglein, D. Meisel, S. Cheong, and M. Boyanov, EXAFS studies of gold and silver-gold clusters in aqueous solutions, *J. Synch. Rad.* **8**, 545-547 (2001).
53. P. Buffat and J.-P. Borel, Size effect on the melting temperature of gold particles, *Phys. Rev. A* **13**, 2287-2297 (1976).
54. K. Dick, T. Dhanasekaran, Z. Zhang, and D, Meisel, Size dependent melting of silica - encapsulated gold nano-particles, *J. Am. Chem. Soc.* **124**, 2312-2317 (2002).
55. T. Shibata, B. Bunker, Z. Zhang, D. Meisel, C. Vardeman, and D. Gezelter, *submitted for publication.*
56. K. H. Schmidt, R. Patel, and D. Meisel, Growth of silver halides from the molecule to the crystal. A pulse radiolysis study, *J. Am. Chem. Soc.* **1110**, 4882-4884 (1998).
57. D. Hayes, O.I. Micic, M. T. Nenadovic, V. Swayambunathan, and D. Meisel, Radiolytic production and properties of ultrasmall CdS particles, *J. Phys. Chem.* **93**, 4603-4608 (1989).

6
SYNTHESIS OF NANOPARTICLES IN MICROEMULSIONS

M.A. López-Quintela, J.Rivas, M.C. Blanco and C. Tojo*

1. INTRODUCTION

The technique of chemical reactions in microemulsions to produce nanoparticles has already 20 years of history behind[1], but the mechanisms to control the final size and the size distribution are still not well known. The knowledge of the mechanism is a crucial step in order to extend the potential applications of this technique. Nowadays there is a great interest in nanotechnologies and the developing of simple and reproducible methods to synthesize nanomaterials has attracted the interest of many researchers. The microemulsion method is a good candidate for this purpose. Microemulsions are thermodynamically stable systems composed of two inmiscible liquids (usually, water and oil) and a surfactant. Droplets of water-in-oil (W/O) or oil-in-water (O/W) are stabilized by surfactants when small amounts of water or oil are used, respectively. The size of the droplets can be controlled very precisely just by changing the ratio R = [water or oil] / [surfactant] in the nanometer range. These nanodroplets can be used as nanoreactors to carry out chemical reactions. It was initially assumed that these nanodroplets could be used as templates to control the final size of the particles, however, the research carried out in the last years has shown that besides the droplet size, several other parameters play an important role in the final size distribution.

The purpose of this review is not to summarize all the results obtained in microemulsions, for which other reviews are available,[2] but to provide a general picture of the different mechanisms involved. The influence of different parameters, such as exchange rate constant, film flexibility, reactant concentration, etc, on the final particle size will be discussed on the basis of Monte Carlo simulation results. Although this study is more focussed on reactions carried out in W/O microemulsions the general conclusions could be also applied to O/W microemulsions.

---

* M.A. López-Quintela and M.C. Blanco, Dept. of Physical Chemistry, University of Santiago de Compostela, E-15782 Santiago de Compostela, Spain. J. Rivas, Dept. of Applied Physics, University of Santiago de Compostela, E-15782 Santiago de Compostela, Spain. C. Tojo, Dept. of Physical Chemistry, University of Vigo, E-36200 Vigo, Spain.

2. MECHANISM OF FORMATION OF PARTICLES IN MICROEMULSIONS

The main idea behind the microemulsion technique is very simple: two reactants (A and B) are introduced in two identical microemulsions. After mixing both microemulsions, droplets collide and interchange the reactants. Then the reaction can take place inside the nanoreactors (see Figure 1A). Different variations of this procedure have been employed. For example, one of the reactants can be introduced in solution into a microemulsion carrying the other reactant; or can be added directly to the microemulsions as a solid, liquid or gas (see Figure 1B). The most commonly used method of synthesis is the use of two similar microemulsions containing the reactants. In this case, the different steps of the mechanim are shown in Figure 2.

Because the different parameters involved in the mechanism are crucial for the final particle size distribution, we discuss each one separately.

2.1. Intermicellar material exchange

In order to discuss this influence we have to distinguish two cases depending on the ratio of the intermicellar exchange rate, k_{ex}, to the reaction rate, k_r:

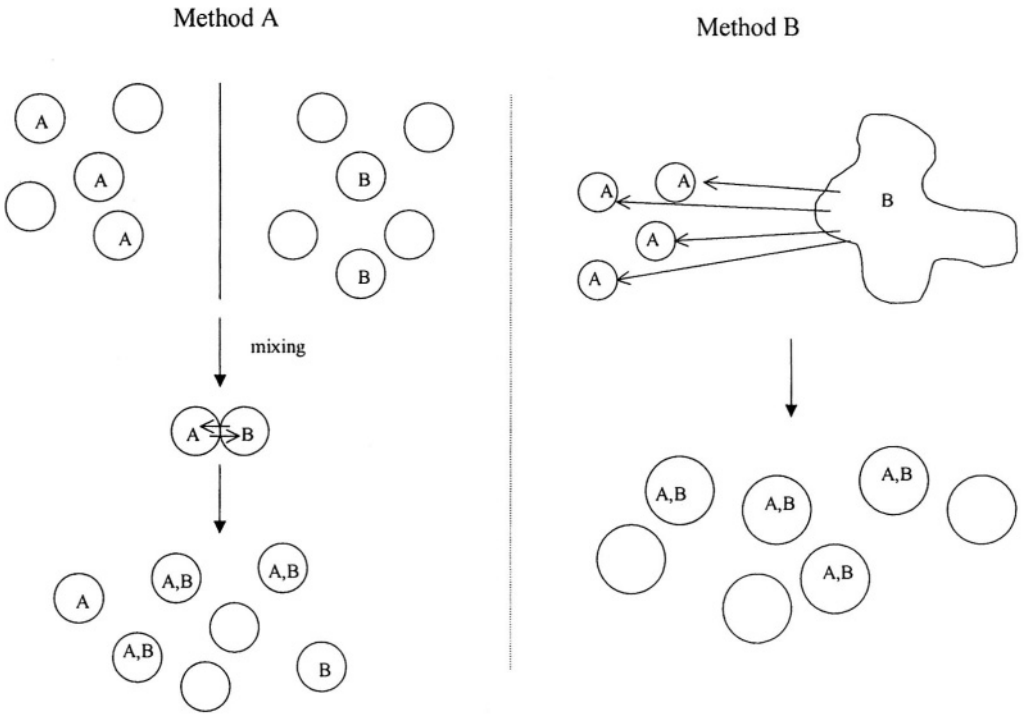

Figure 1. Microemulsion techniques: A) Mixing two microemulsions containing the reactants. B) Adding one of the reactants into a microemulsion containing the other reactant.

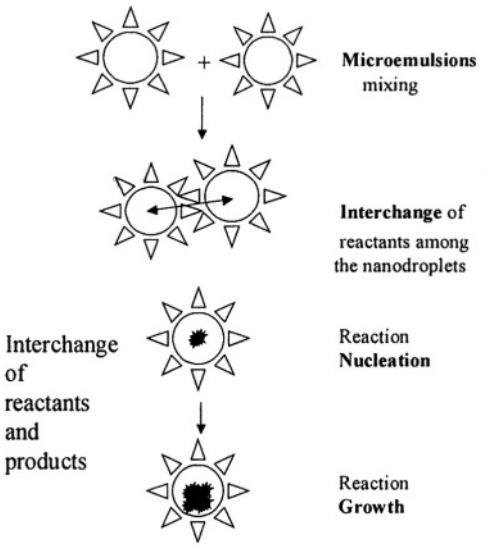

Figure 2. Mechanism of formation of nanoparticles in microemulsions.

a) $k_{ex}/k_r >> 1$

In this case each droplet behaves as a small piece of a bulk reaction because all reactants are statistically distributed inside the droplets from the beginning. Then, the reaction proceeds similarly as it does in the bulk. To obtain small and monodisperse particles it is necessary that the nucleation and growth processes be well-separated to produce a bursting of nuclei. In this case the material exchange does not play an important role on the particle formation and the same parameters which control the reaction in bulk should be considered.

b) $k_{ex}/k_r << 1$

In this case the intermicellar material exchange is the determinant step in particle formation. According to Fletcher *et al.*[3] the material exchange takes place following the mechanism shown in Figure 3. Microemulsion droplets collide and form transient dimers (encounter pairs) being this a diffusion-controlled process, For uncharged droplets of radius r and diffusion coefficient D, the encounter rate constant, k_{en} (see Figure 3), can be estimated by the Smolochowski equation, $k_{en} = 16\pi\, NDr = 8000RT/3\eta$, being N Avogadro's number, R the gas constant, T the absolute temperature, and η the viscosity of the medium. As an example, for microemulsion droplets at 25°C moving in a typical oil, like n-heptane, $k_{en} \approx 10^{10}\,M^{-1}\,s^{-1}$. The transient dimer has a lifetime given by[4] $\tau_{en} = k_{-en}^{-1} = 4r^2/6D = 4\pi N\eta r^3/RT$. For droplets of radius r = 5 nm in the same conditions $\tau_{en} \approx 0.15\mu s$. Therefore, the equilibrium constant of this process is given by[5] $K^o_{en} = k_{en}/k_{-en} = (32/3)\pi Nr^3$. For the same case considered above, $K^o_{en} = 1.5x10^3\ M^{-1}$. If the droplets are charged the Coulomb interaction between the droplets has to be taken into account. In this case the equilibrium constant is given by Fuoss equation[6]: $K_{en} = K^o_{en} \exp(-z^2e^2/2\varepsilon rkT)$, where z is the droplet charge, e the elementary charge, ε the dielectric constant of the medium, and k the Boltzmann constant.

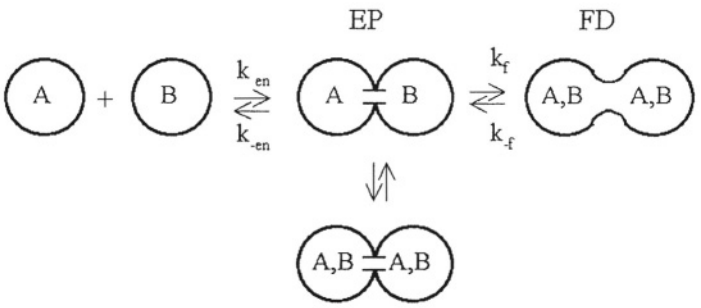

Figure 3. Material exchange mechanism. EP=encounter pair, FD= fused dimer.

It is interesting to note that the value of K_{en} can be much lower than K^{o}_{en} (by various orders of magnitude!) if the droplets are charged. The formation of the encounter-pair can be followed by another process in which the droplets fuse together. This is a slow process because it needs the opening of the micellar walls and the inversion of the surfactant film curvature. Therefore it will depend on the film flexibility (*f*) and, until now, there is no theory from which this rate constant can be estimated. The overall rate constant, k_o, is then given by: $k_o = K_{en}\, k_f$. The material exchange can take place either during the encounter pair or in the fused dimer. In the first case the material interchange is only possible if a channel is opened through the surfactant bilayer which is created between both droplets (see Figure 4). The channel would be created only if the surfactant film is distorted by the presence of species which are dissolved into the palisade layer (cosurfactants, etc). The permeation rate through the channel would be highly material dependent: a voluminous and highly charged ion will hardly cross the channel whereas a small and neutral molecule will cross more easily. Both factors can be taken into account introducing in the encounter rate a factor γ(film distortion, material) which would depend on the kind of exchanged material and film distortion: $k_{ex} = \gamma(\text{film distortion, material})k_{en}$. Moreover the encounter lifetime, $\tau_{en} = 1/k_{-en}$, has to be large enough to allow the material exchange.

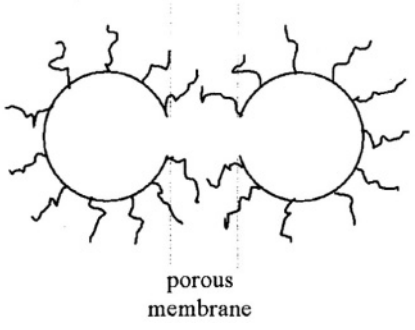

Figure 4. Channel through the surfactant bilayer in a encounter pair.

Taking into account the previous estimation of $\tau_{en} = 0.15$ μs, one can calculate the approximate distance travelled by a species during this time: $d = (2\ D\ \tau_{en})^{1/2} \approx 15$ nm (for this calculation we have taken a diffusion coefficient $D = 10^{-9}$ m^2 s^{-1}). Then, for small droplets the encounter lifetime should not have much influence on the exchange rate. However for big droplets the exchange rate would decrease as the droplet size increases. In the case that the material exchange occurs in the fused dimer, the intermicellar material exchange rate is given by the overall rate constant, k_o, and can be expressed as: $k_{ex} = K_{en}\ k_f(f)$, in which we have explicitly introduced the idea that k_f mainly depends on the film flexibility. It can be seen that the micellar exchange rate increases with increasing the dimer stability.

The interchange mechanism involved in a particular synthesis in microemulsions can be deduced from the rate of exchange and from the dependence of this rate on the exchanging species. When the exchange rate is near the diffusion-encounter rate limit and this exchange rate depends on the kind of interchanging species, the involved exchange mechanism goes through the encounter-pair. In the opposite case, the exchange takes place in the fused dimer. As an example, in AOT microemulsions, for some species like H^+, Zn^{2+}, electron-transfer reagents (negatively charged), Cu^{2+}, and Fremy's salt, $k_{ex} = 10^7\ M^{-1}s^{-1}$ (i.e., far from the diffusion-controlled limit) regardless of the species. The low value of k_{ex} (aprox. 1000 times lower than k_{en}) and its species independence clearly show that the exchange mechanism occurs through a fused dimer, which was first pointed out by Fletcher *et al*[3]. However, much higher exchange rates which could be associated with an exchange through the encounter pair have been reported. For example, Gebicki *et al.*[7] have shown that $(SCN)_2^-$ radical anions show a high exchange rate ($0.2\text{-}0.9 \times 10^9\ M^{-1}s^{-1}$) depending on the droplet size. Also Atik *et al.*[8] have found a value of $k_{ex} = 0.3 \times 10^9\ M^{-1}\ s^{-1}$ by adding benzyl alcohol to an AOT/heptane microemulsion. The high values of the exchange rates would be an indication that the exchange takes place through the encounter-pair. It is interesting to note that k_{ex} is smaller than k_{en} by a factor γ(film distorsion,material) $\approx 0.02 - 0.1$, that is, only 1 of each 10–50 collisions are effective. Compare this value with that of the fusion mechanism where only one of each about 1000 collisions are effective.

2.2. Droplet Volume Fraction (ϕ)

When the droplet volume fraction increases the interaction between droplets becomes more and more important. Depending on the flexibility of the surfactant film, droplet clusters (in rigid films, like AOT) or bicontinuous structures can be formed due to attractive interactions between droplets. When droplet clusters are formed and the reactant concentration is low, the intercluster material interchange is slower than the interchange between individual droplets, because both the average distance between reactants and the number of walls to be crossed by the reactants increase.

The reduction of the exchange rate constant is approximately given by the number of walls to be overcome, as has been found by Gebicki *et al.*[7] For a fractal cluster with a radius of gyration, R_g, the number of walls is given by: $R_g / d_{droplet} \approx N^{1/D_f}$, where $d_{droplet}$ is the droplet diameter, N the number of droplets in the cluster and D_f the fractal dimension of the cluster. Figure 5 shows how the number of droplets changes on approaching the percolation point in AOT microemulsions with different droplet volume fractions, obtained by DLS.

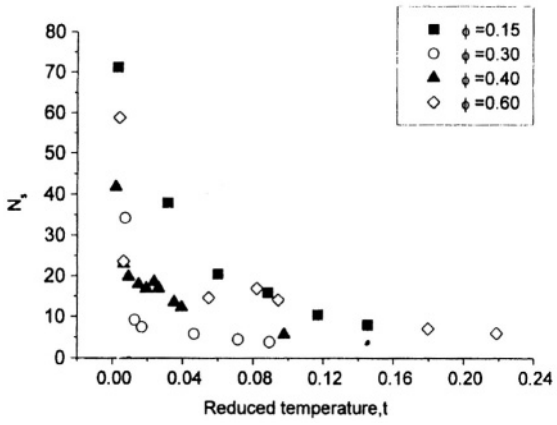

Figure 5. Number of droplets vs reduced temperature at different values of droplet volume fractions in water in oil microemulsions. $t = |T-T_p|/T_p$; T=absolute temperature, T_p= percolation temperature.

Figure 6 shows how the fractal dimension of the clusters changes on approaching the percolation point.[9] From N and D_f one can estimate the reduction in k_{ex}. As an example, for microemulsions far away from the percolation point, the average number of droplets per cluster is about 10, independent of ϕ. Then, a reduction of a factor about 3 is expected in k_{ex}, as has been found by Gebincki *et al.*[7] This factor increases on approaching the percolation point.

2.3. Film Flexibility

The film flexibility depends on the type of surfactant, cosurfactant and oil used as well as on the droplet size. From a thermodynamic point of view, the film flexibility increases on approaching the upper boundary of the microemulsions due to the increase of the difference between the natural curvature and actual curvature of the surfactant film.[10,11]

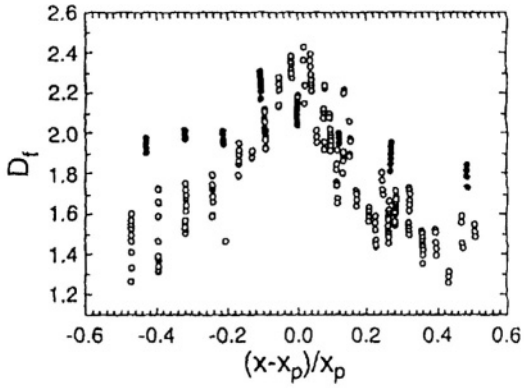

Figure 6. Fractal dimension of the clusters for acrylamide-facilitated (full circles) and temperature facilitated (open circles) percolation. x=distance to the percolation point (T or ϕ). Reproduced from ref. 9 with permission.

In Figure 7 the one-phase microemulsion stability region is shown for AOT microemulsions in two solvents with different number of carbon atoms (n=5 and 9). The continuous lines indicate the low and high temperature phase boundaries. Near the low temperature phase boundary the film curvature is highly negative corresponding to a W/O micromulsion. In this region the actual curvature (=1/droplet size) is equal to the natural curvature. By increasing the temperature the negative film curvature gradually decreases until the phase inversion temperature (PIT) (indicated in Figure 7 by the discontinuous line for the oil with n=5). At the PIT the film has a zero natural curvature, and corresponds to the temperature at which the maximum amount of water is solubilized. At higher temperatures the positive curvature increases being maximum near the upper boundary region in which an inverse O/W microemulsion is formed. Near this region the discrepancy between the natural and the actual curvature (proportional to the film flexibility) is maximum, because the radius of the droplets does not appreciably change with temperature. The upper boundary in AOT microemulsions (that is, high flexible films) can be reached by increasing the temperature, the chain length of the oil or the droplet radius. The influence of the chain length of the oil has been explained assuming that, when solvent molecules penetrate between the surfactant tails produce an increase of the curvature and a decrease of the flexibility.[11,12] The longer the chain length, the more difficult is to penetrate into the surfactant layer because the extent of interaction between the surfactant tail and the solvent chain decreases.

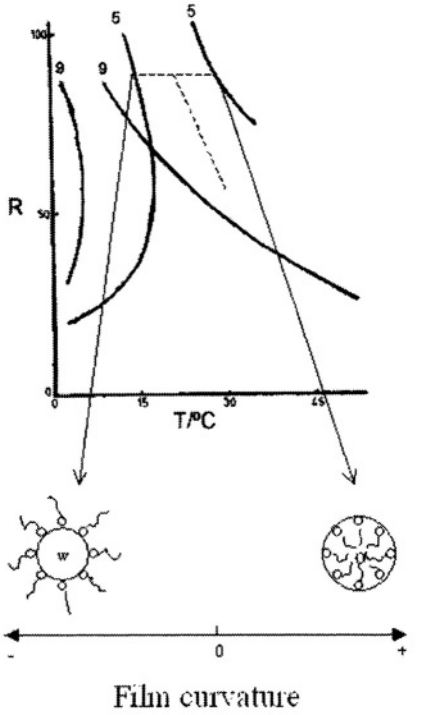

Figure 7. One-phase microemulsion stability maps for 0.1 mol dm^3 AOT in two solvents of different number of carbon atoms (n = 5 and 9). R = [water]/ [AOT]. Reproduced from ref. 3 with permission of the Royal Society of Chemistry.

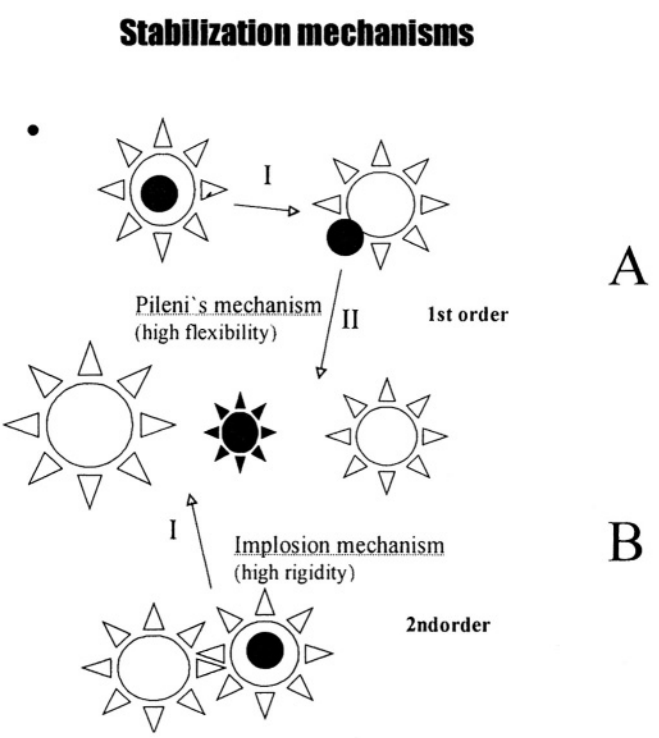

Figure 8. Nanoparticle stabilization mechanisms.

The film flexibility plays two important roles in the mechanism controlling the particle size: first, it is related with the material exchange mechanism as it has been pointed out above (section 2.1b). Second, it is related to the mechanism of particle stabilization. Once the particle has been formed inside a droplet two different stabilization mechanisms are possible depending on the film flexibility. For highly flexible surfactant films the mechanism shown in Figure 8A has been proposed by Pileni *et al.*[13] Firstly the particle approaches to the droplet interface and part of the surfactant molecules are adsorbed onto the particle leaving the droplet. This first order process requires an inversion of the film curvature and, therefore, is favored at high flexibilities. For rigid films another mechanism activated by droplet collisions has been proposed by Rivadulla *et al.*[14], as it is shown in Figure 8B. In this case the whole surfactant droplet film can be adsorbed onto the particle by a second order "implosion" mechanism, when a collision with an empty droplet takes place.

This mechanism is favored when particle size and droplet size are similar and can be clearly distinguished from the other one because the adsorption of surfactant onto the particles is higher.[14] When the film is very flexible the surfactant film is able to adjust to the particle size during the growth. Consequently, in this case, particles much bigger than the droplet size are obtained.[15]

2.4. Nucleation and Growth Processes

As it has been pointed out above, the role of microemulsions is to compartmentalize reactants. From a mechanistic point of view, the reactants confinement within the water

pools modifies both nucleation and growth with respect to the same processes in bulk. Nucleation and growth processes involved in particle formation in homogeneous media are well-known.[3,10,16,17] According to the classical crystallization theory, the final particle size depends mainly on the ratio of nucleation to growth rates. A slow nucleation leads to a low number of nuclei which can grow and reach large polydisperse sizes. On the contrary, if nucleation is quick, a large number of nuclei are formed, so that the final particle size will be small and monodisperse. There is a critical number of atoms forming a stable nuclei, for which growth is favored against redisolution. Although this critical number has been determined for many reactions in bulk, there are no data for reactions in microemulsions. Particle formation in compartmentalized media is different, because interdroplet material exchange plays an important role in the mechanism as it will be shown below (see section 3.5).

2.5. Ripening

Many studies have been reported for different growing, aging, or ripening mechanisms in bulk.[18,19] A particular coarsening process which has to be considered in microemulsions is the Ostwald ripening. The particle size changes by solubilization and condensation of the material. The ripening theory assumes that the largest particles will grow by condensation of material, coming from the smallest particles that solubilize more than the larger ones. In microemulsions this growth can only take place through the fused dimer mechanism because of the great size of the material exchanged (Figure 9). The flexibility of the surfactant film around the droplets governs both the ease to form colliding droplet communicating channels and the size (l) of these channels. Therefore, a small nanoparticle formed inside a droplet, can be transferred or not to another one carrying a bigger particle, depending on the size ratio (d_1/l) between the small particle and the interdroplet channel. Therefore, the surfactant film flexibility plays a fundamental role in the ripening contribution to the growth process.

2.6. Autocatalysis

The reaction inside the microemulsion droplet can be catalyzed by the surface of an existing aggregate. A large aggregate has a greater probability of acting as a catalyst because of its big surface. Therefore, if the reaction is autocatalytic, the growth process will be quicker on bigger nanoparticles.

Both ways of growth, ripening and autocatalysis, favor the growth of the biggest nanoparticles. It is interesting to point out that there is an important difference between both mechanisms: the autocatalysis depends on the reactant interdroplet exchange, whereas ripening depends on the product interdroplet exchange. This autocatalytic mechanism can be successfully applied for the production of multilayer nanoparticles, as it will be shown later on.

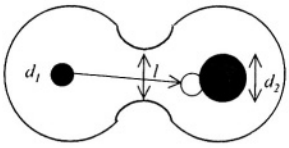

Figure 9. Ripening mechanism in a fused dimer.

2.7. Concentration

It has been observed both experimentally[20-23] and by simulation[24-25] that concentration (absolute reactant concentrations as well as relative reactant concentrations) has a large influence on the final particle size distribution. Until now most of the explanations were based on the idea that high concentrations imply fast reaction rates (nucleation). However, concentration can also have a large influence on the growth mechanisms, autocatalysis and ripening. Therefore, it is difficult to predict how the concentration affects the final particle size.

2.8. Droplet Size

When the microemulsion technique was introduced, it was believed that with this technique the particle size could be controlled just by controlling the droplet size. But in the mean time different behaviors have been observed when the droplet size increases: increasing of particle size[20-22,26-32], constant particle size, bimodal distributions[31,33], and even almost no control by droplet size.[15] Although water droplets are no real templates, the combination of the droplet size with all previous discussed parameters can be used to have a very precise control of the final particle size, as it will be discussed in the next section.

3. MONTE CARLO SIMULATION

The final nanoparticle size and its monodispersity depend on the particular combination of all previously described parameters. From an experimental point of view is difficult to fix all parameters in order to study the influence of a given parameter on the final particle size. To gain more insight into this problem, different computer simulations on the formation of nanoparticles in microemulsions have recently been performed which elucidate some concrete aspects of the problem. In particular, the nanoparticle size distribution and the effects of intermicellar exchange have been successfully studied by simulation.[34,35] We discuss in this chapter only the main results obtained by the Monte Carlo simulation program developed in our laboratory.[36-40] This simulation procedure allows to analyze the influence of droplet size (q), concentration (c), excess of one of the reactants (x), film flexibility (f), and reactant exchange constant (k), as well as the phenomena of ripening and autocatalysis. We will briefly describe the main results and show the comparison of simulation and experimental results for different systems.[24,25,31] The simulation details can be seen in references 36,37,40.

3.1. Study of Nucleation and Growth Processes

The simulation procedure allows to follow the time evolution of a particular particle size. In this way, the nucleation and growth processes can be clearly distinguished. Figures 10A and B show the time evolution of small clusters (a) and particles (b) for high and low concentrations, respectively. Curves (a) show a quick increase in the number of nuclei followed by a further decrease due to the growth, because the nuclei are disappearing during the growth process. Curves (b) show mainly the growth process.

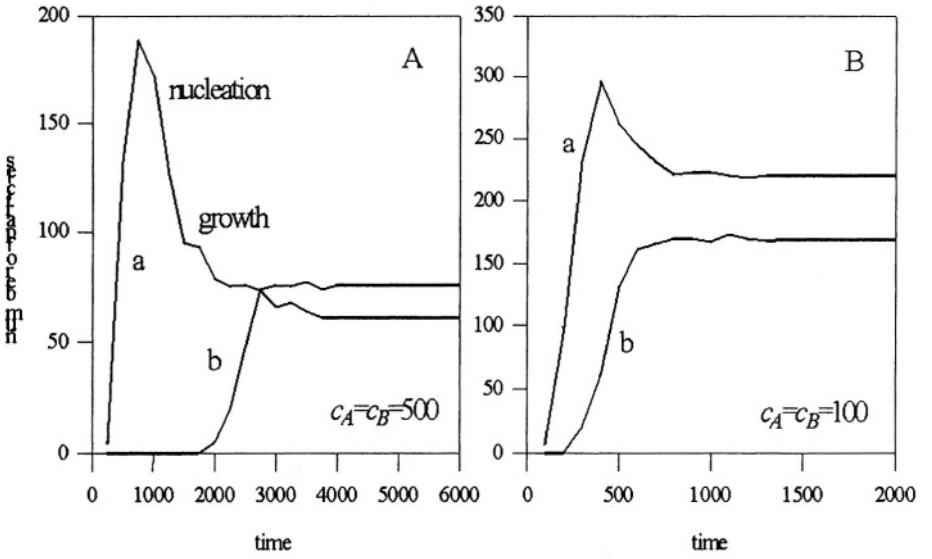

Figure 10. Time evolution of droplets carrying particles. A (c_A=c_B = 500): Curve *a* represents the number of droplets containing particles of sizes between 100 and 150 *P* units. Curve *b* plots the number of droplets containing the biggest particles (sizes between 500 and 550 *P* units). B (c_A=c_B =100): Curve *a* represents the number of droplets containing particles with sizes between 50 and 100 *P* units. Curve *b* plots the number of droplets containing the biggest particles (sizes between 100 and 150 *P* units). In both figures a surfactant film flexibility f = 5 (nuclei of less than 5 units can be interchanged) is used and a large value of droplet size (q = 5000).

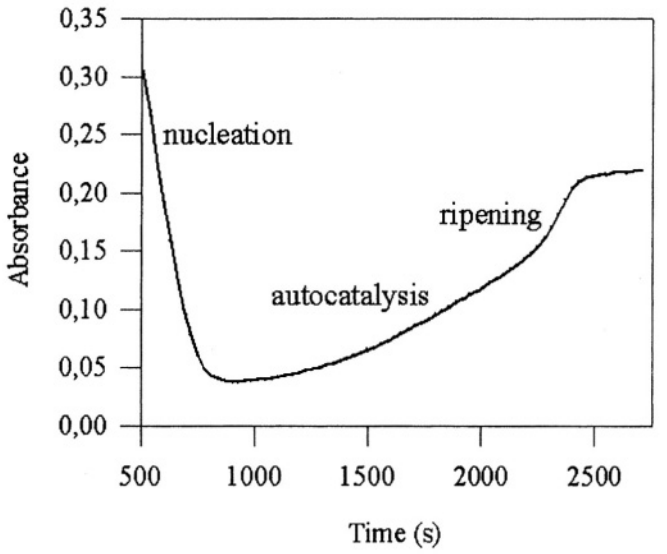

Figure 11. Time course of absorbance at λ = 260 nm during the formation of Pt particles in microemulsions. Microemulsion: 16.54%Brij30/2.47%(PtIV)ac, R=3.01, [PtIV]=0.01M, [Hydrazine]=0.05M.

At high reactant concentrations, the nuclei are rapidly generated, and a large number of seed nuclei appear (Figure 10A). Thereafter, particle growth starts. At low concentrations the reaction is slower and some particles may grow whereas the reaction is still taking place. Therefore the nucleation and growth can take place on a different time scale only when the concentration is high (Figure 10A).

This is in agreement with experimental results obtained for the formation of different kinds of particles in microemulsions. As an example, Figure 11 shows the evolution of the absorbance during the formation of Pt particles in Brij30 microemulsions.[14] The nucleation can be observed as a decrease in the absorbance (reactant disappearence). After nucleation, the absorbance increase due to the scattering of the growing particles is observed. Autocatalysis and ripening can be clearly distinguished in this figure by comparison with simulation results.[36]

3.2. Influence of the Concentration

The influence of the reactants concentration on the mechanism of particle formation has important consequences on the final particle size distribution. It has been experimentally found that increasing the concentration the distribution changes from unimodal to bimodal. Figure 12A shows experimental results obtained for AgBr particles prepared in AOT microemulsions.[33] Figure 12B shows simulation results obtained using a rigid film (f=5, see below). A good agreement between experimental and simulation results can be seen. The influence of the concentration depends on the film flexibility[24]: the bimodality disappears when a flexible surfactant film is used. Furthermore, low concentrations give rise to unimodal distributions being broader as the film flexibility increases.[24,41] These results are contrary to what is expected for a reaction in bulk since at low concentrations the nucleation and growth processes overlap, whereas at high concentrations both processes are well-separated (see Figures 10A,B).

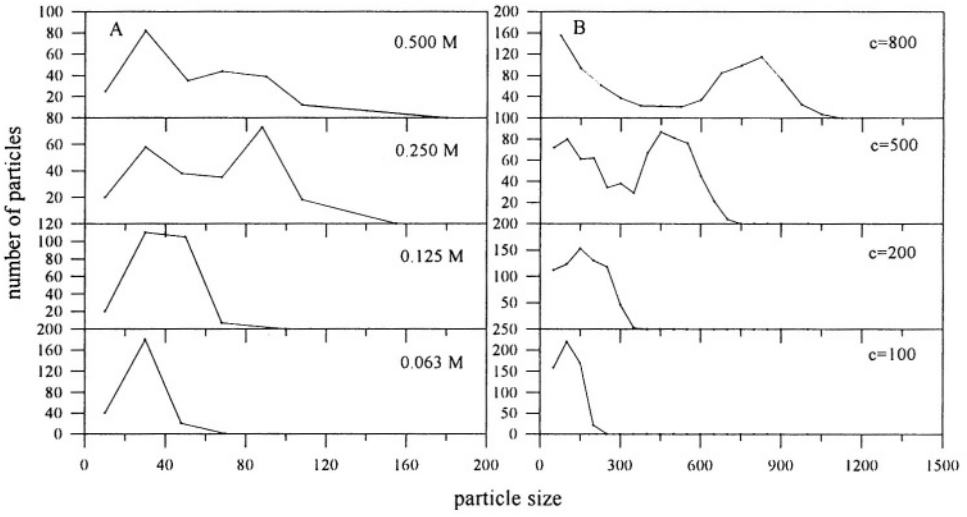

Figure 12. (A) Size distributions (number of particles vs diameter of particles (Å) of the AgBr particles (data obtained from reference 33). (B) Size distributions obtained from simulation for a fixed value of film flexibility (f=5), fixed droplet size (q=500) and different values of concentration (c_A=c_B).

Therefore, at high concentrations a narrow size distribution of particles would be expected and the contrary at low concentrations. The reason for this different behavior can be attributed to the rigidity of the film which does not allow the interchange of big particles. This size restriction has two implications depending on the reactant concentration. At low concentrations, the autocatalysis is the main growth mechanism (see below) and this limits the growth. Therefore, small monodisperse particles are obtained. At high concentrations the main growth mechanism is by ripening (see below). The interchange size restriction of the rapidly formed bursting nuclei gives rise to small particles being present all the time. They cannot grow by autocatalysis because the reactants are almost exhausted after the nuclei formation. However, the growth by ripening is always possible giving rise to a second population of particles which grow faster creating a final bimodal distribution. This process can be nicely seen in Figure 13 which shows simulation results of the temporal evolution of the bimodal distribution obtained at high concentrations for a rigid film.

3.3. Influence of the Film Flexibility

Surfactant film flexibility places a limit on the size of the particles traversing the droplet-droplet channels. The film flexibility is introduced in the simulation by varying a flexibility parameter (f) specifying a maximum particle size for transfer between droplets: particles with more than f units (number of P atoms forming a cluster) are not allowed to pass from one droplet to another. In this way, a highly flexible film will allow the interchange of larger aggregates than a rigid film.

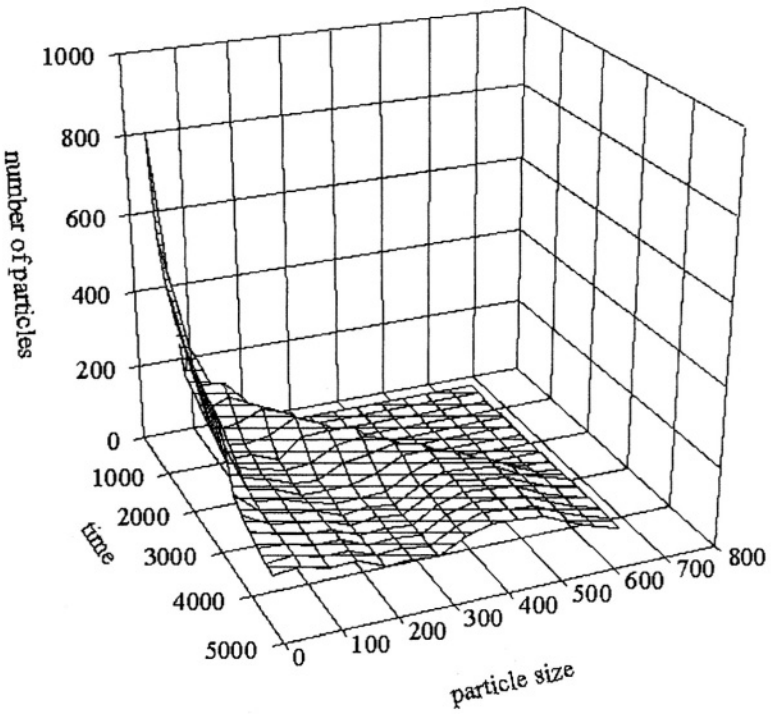

Figure 13. Time evolution of the number of droplets carrying different size particles (f=5, c_A= c_B=500, q=5000).

Figure 14 illustrates both, simulation (Figure 14A) and experimental results (Figure 14B) of the flexibility influence on the final nanoparticle size distribution. Low concentrations are used in order to avoid bimodal distributions. The best values of the film flexibility to reproduce the experimental results are $f = 15$ (cyclohexane) and $f = 30$ (isooctane). Taking into account that the parameter $f \approx \kappa^{-3/2}$, being κ the curvature elastic modulus,[11,42] it can be deduced that the curvature elastic modulus for the AOT surfactant film in isooctane is approximately half than in cyclohexane. This result agrees with the exchange rate constant obtained for both oils:[3] k_{ex} (cyclohexane, T=15°C) = 0.8×10^6 $M^{-1}s^{-1}$ and k_{ex} (isooctane, T=15°C) = 6.6×10^6 $M^{-1}s^{-1}$ if one considers that the activation energy for the droplet exchange is proportional to the curvature elastic modulus and to the change of the area when the dimer is formed.[42] Both experimental and simulation results show that bigger sizes with a wider size distribution are obtained for the film with the highest flexibility.

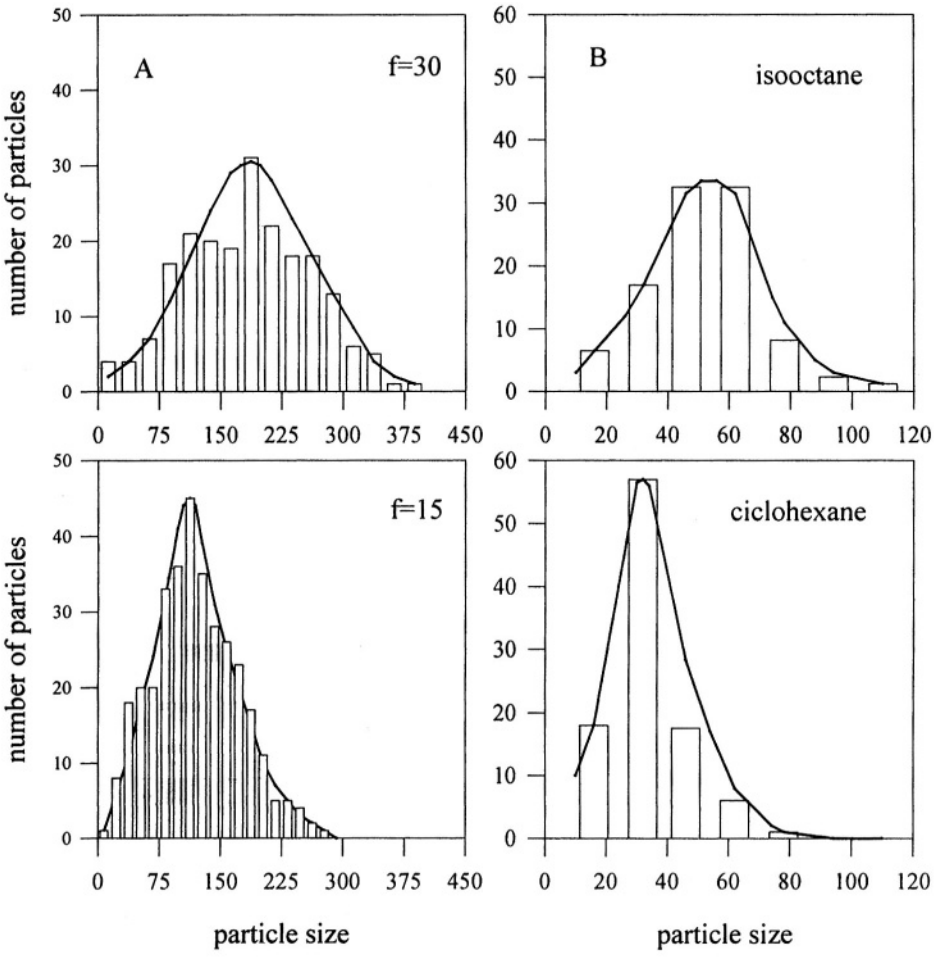

Figure 14. (A) Simulation results for low concentrations (c_A=c_B=100) and different values of f. (B) Size distribution of silver particles synthetized in isooctane and cyclohexane. Lines are guides to the eye. Reproduced with permission from ref. 41. Copyright (1993) American Chemical Society

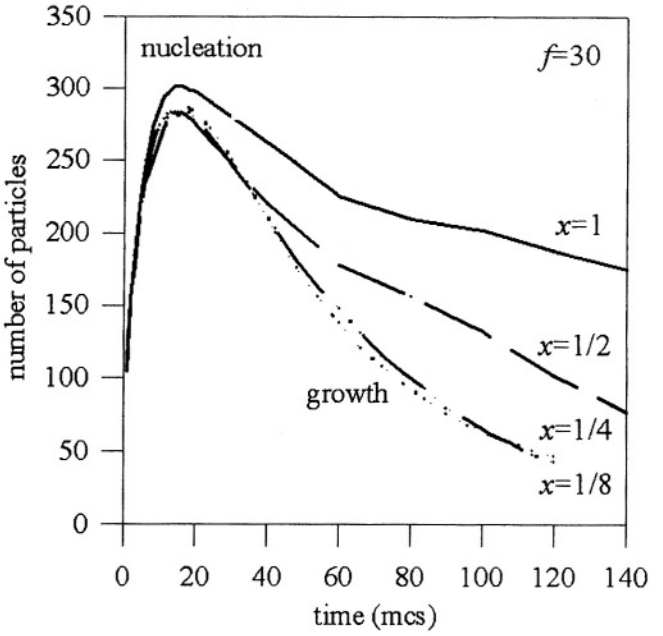

Figure 15. Time evolution of droplets carrying particles smaller than 10 *P* units for different values of *x* ($x=c_B/c_A$). All curves were simulated for $f=30$ and $x=1$ ($c_B=c_A$).

3.4. Influence of the Reactant Excess

The influence of the excess of one of the reactants $(x=c_A/c_B)$ has been investigated for different systems.[20,21,39,43] It is observed that the particle size decreases as *x* increases. Similar qualitative behaviors are obtained for any film flexibility. These results have been explained, as in bulk, assuming that an increase of the reactant excess produces a faster nucleation.

However, simulation results (Figure 15) show that, contrary to the behavior expected in bulk, the *x* parameter hardly influences the nucleation process, although it has a great influence on the growth mechanism. The growth rate of the aggregates is higher when one of the reactants is in excess, being this effect less important as *x* increases.

This result can be explained taking into account that for $x=1$ two possible mechanisms, autocatalysis and ripening, contribute to the growth as it has been said above. However, for $x>1$ growth is mainly due to ripening because growth by autocatalysis is not possible when one of the reactants is exhausted. Growth by ripening is limited by the channel size (*f*), whereas growth by autocatalysis is only limited by the reactant concentration. For a fixed film flexibility, when $x\approx1$, particles can grow larger than the channel size through the autocatalysis mechanim. As *x* increases the size is reduced because the contribution of autocatalysis is smaller. Because ripening is faster than autocatalysis the whole process is faster at higher reactant excess, but the simulation results clearly show that the different rates are not responsible for the final particle size.

3.5. Influence of the Interdroplet Material Exchange

As we said above, the interdroplet material exchange can take place in two situations: in the fused dimer or in the encounter pair. The fused dimer formation is determined by the surfactant film flexibility: when the film flexibility increases the inversion of the curvature needed to form a fused dimer is easier. In the simulation procedure the f parameter is related to the channel size:[40] a value f=30 would imply a "permeation channel" (the minimum section inside the fused dimer) of aproximately 6-10 Å in diameter, assuming that 30 P units are aggregated in a spherical shape. For f=5 one can obtain a permeation channel of about 1-2 Å. A smaller value *of* f would imply that interchange would occur only through the encounter pair.

The interdroplet material exchange includes different species: reactants and products. When a chemical reaction gives rise to clusters or particles the interchange of these species can only be possible through the fused dimer. Contrary to these species, reactants could be interchanged in both encounter pair and fused dimer, as was described in section 2.1.b). The interchange mechanism of reactants depends on the exchange rate k_{ex}, being through the encounter pair when the exchange rate is fast ($k_{ex} \approx 10^8$-10^9 $M^{-1}s^{-1}$), and through the fused dimer when it is slow ($k_{ex} \approx 10^6$-10^7 $M^{-1}s^{-1}$). In order to take into account both possibilities it has been introduced in the simulation a variable which controls the rate of reactant exchange, k.[40] The reactant exchange parameter k determines how many units of reactant could be interchanged in each collision. Until now, the effective collisions were referred to collisions which lead to the fused dimer (k=1), and the experimental results have been successfully interpreted using flexibility parameters in the range $5 \leq f \leq 30$. However, because k and f are not independent when the reactant interchange mechanism goes through the fused dimmer, the range of f values to explain the experimental results is more restricted. As we said above (see Section 2.1.b) the interchange rate in the encounter pair is, at least, approximately 20 times larger than the interchange rate in the fused dimer. Therefore, for the reactants exchange, the transition from the fused dimer to the encounter pair mechanism can be simulated introducing a value $k \geq 20$. Consequently, k should vary in the range $1<k<3$ corresponding to $5 \leq f \leq 15$ in the fused dimmer mechanism; $k>20$ in the encounter pair region, and $5<k<20$ in the transition region in which both mechanisms contribute to the reactants interchange. The different interchange possibilities will influence the final particle size. Figure 16 shows the change of the nanoparticle size with k obtained by simulation for x=1. In the fused dimer region the particle size increases with k, i.e., with the exchange rate, as it has been experimentally observed.[12,44] As we have said above, growth by ripening is favored at high flexibilities. Besides, an increase of the exchange rate implies a larger contribution of the growth by autocatalysis, because more reactants are interchanged per unit time. The simultaneous increase of both parameters, f and k, in the fused dimer region gives rise to a large increase of the final particle size. At high k values reactants could be interchanged through the encounter pair. In this case the growth is mainly by autocatalysis, and the film flexibility has a minor influence on the final size, but still an increase in the final size with k_{ex} is observed. The transition region from the fused dimer to encounter pair interchange mechanism is accompanied by a decrease in the final particle size as it can be seen in Figure 16. Table 1 shows the experimental results obtained by Bagwe *et al.*[12] for silver chloride and silver particles obtained in AOT microemulsions.

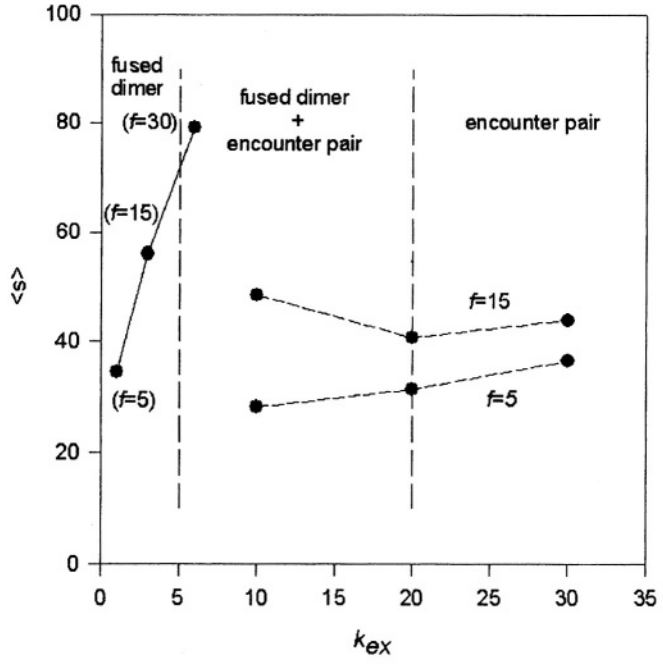

Figure 16. Particle size versus reactant exchange constant obtained by simulation for different values of the film flexibility (f). Reactant exchange mechanism: FD fused dimer, EP encounter pair.

It can be observed the increase in the particle size with k_{ex} in both mechanisms as well as the decrease in size corresponding to the transition of reactants exchange mechanism. A change in the mechanism can be induced by changing either the film flexibility for a particular reaction (as it is shown in Table 1) or the reactants for a particular film flexibility. It has to be pointed out that most of the results reported in the literature assume exchange through the fused dimer, and there are only few reports about exchange through the encounter pair.[7,8] In fact the exchange through the encounter pair should be difficult unless the surfactant film is disrupted, as it is the case of some cosurfactants like benzylalcohol.[8] This exchange mechanism through the membrane formed in the encounter pair (see Figure 4) is somehow similar to the porous-facilitated transport in membranes.

Table 1. Summary of the k_{ex} values and the corresponding particle sizes (d_p) obtained for AgCl and Ag particles synthesized in AOT microemulsions. FD= fused dimer. EP = encounter pair.

system	k_{ex}	ClAg d_p, nm	Ag d_p, nm	Reactant exchange mechanism
AOT/cyclohexane	10^6 (ref.3)	7,6	5,4	FD
AOT/heptane	10^7 (ref.3)	10,1	22,0	FD
AOT/decane	5.10^7 (ref.3)	4,4	6,0	FD + EP
AOT/heptane and benzylalcohol	3.10^8 (ref.8)	9,9	--	EP

Figure 17. Antiferromagnetic coupling observed in Fe@Cu@Fe multilayer nanoparticles. Size of the successive layers: 8 nm, 10 nm and 11.4 nm, respectively.

4. EXAMPLES

By choosing the appropriate conditions one can obtain particles smaller than the droplet size of the employed microemulsions. The particle size can then be increased by adding new reactants to the microemulsion containing the particles, as has been previously described.[45]

By successive additions of reactants, Fe nanoparticles of 4 nm in size were grown to 5 nm after a first addition and further up to 6 nm after a second addition. The size increase being only limited by the used reactant concentration. By a similar procedure multilayer "onion-like" particles can be obtained just by changing the employed reactants in the successive additions. As an example, we will show here how antiferromagnetic coupled Fe@Cu@Fe nanoparticles can be obtained. By reducing Fe^{2+} (0.1M) with $NaBH_4$ (0.2M) in AOT-water-n-heptane microemulsions Fe particles of 8 nm in size are obtained. Adding Cu^{2+} (0.1M) and $NaBH_4$ (0.2M) a Cu covering layer with a thickness of 1 nm is obtained. Finally, a third reaction similar to the first one produces a third Fe layer of 0.7 nm. In Table 2 it is shown the fundamental parameters of the hysteresis loops (H_c=coercive field, M_s=magnetization) measured for the different samples (Fe, Fe@Cu and Fe@Cu@Fe) at a maximum magnetic field of 10 kOe and room temperature. In the same table the calculated magnetization, at 10 kOe, is also shown. Taking as reference the value of the magnetization obtained for the Fe particles, it can be seen that the calculated and experimental values of the magnetization agree for the Fe@Cu particles. In the case of Fe@Cu@Fe particles two magnetic couplings are possible, but only an antiferromagnetic coupling agrees with the experimental data[46] (see Figure 17). It is interesting to note that this result surprisingly agrees with that found in flat sputtered Fe-Cr multilayers,[47] offering now the possibility to study the change in the type of magnetic coupling in spherical geometries just by changing the thickness of the non-magnetic layer. This will be a very promising route in order to understand the magnetic interactions at the nanoscopic level, which is of crucial importance in the development of new magnetic nanotechnologies.

Table 2. Experimental and calculated magnetic properties of onion-like multilayers.

Particles	H_c(Oe)	M_s (emu/g)	$M_s^{calculated}$ (emu/g)
Fe	105	51	--
Fe@Cu	340	24	26
Fe@Cu@Fe	70	1.6	1.2*
			33.7**

* Antiferromagnetic coupling. ** Ferromagnetic coupling

5. CONCLUSIONS AND FUTURE PERSPECTIVES

Microemulsions are not real templates but they constitute an elegant technique which can provide a good control on the final particle size. The reason for that is a complex interplay between different parameters, mainly film flexibility, reactant concentration and reactant exchange rate. By adequately choosing these parameters one can obtain a homogeneous distribution of particle sizes. The high precision in the particle size control allows the preparation of multilayer onion-like particles with a thickness precision of few Ångstrøms.

The preparation of spherical multilayers having a great number of layers is very important in order to obtain not only magnetic materials with new properties, but also particles having gradual variation of the refraction index which could be of great interest in nonlinear optics. From a more fundamental point of view this technique could provide an useful tool to compare the physicochemical properties of flat and spherical multilayers.

Finally the arrangement of these multilayer particles in one, two and three dimensional structures could provide nano-composite materials having tailor-made properties.

6. ACKNOWLEDGEMENTS

M.A.L.Q., J.R. and M.C.B. acknowledge partial financial support by the Ministerio de Ciencia y Tecnología, Spain, Project FEDER MAT 2001-3749.

7. REFERENCES

1. see e.g., *Handbook of Microemulsion Science and Technolgy,* edited by P. Kumar and K. L. Mittal (Marcel Dekker, New York, 1999) Part III, 457-742; *Reactions and Synthesis in Surfactant Systems,* edited by J. Texter (Surfactant Science Series, Vol.100, Marcel Dekker, 2001) Part IV, 577-665; and references therein..
2. M. Boutonnet, J. Kizling, P. Stenius, and G. Maire, The preparation of monodisperse colloidal metal particles from microemulsions, *Colloids Surf.* **5**, 209-225 (1982).
3. P.D.I. Fletcher, A.M. Howe, and B.H. Robinson, The Kinetics of Solubilisate Exchange between water droplets of a water–in-oil microemulsion, *J. Chem. Soc., Faraday Trans. 1* **83**, 985-1006 (1987).
4. M. A. López-Quintela, J. Samios, and W. Knoche, Steric hindrance of diffusion-controlled reactions, *J. Mol. Liq.* **29**, 243-261(1984).
5. A. M. North, *The Collision Theory of Chemical Reactions in Liquids* (Methuen, London, 1964).
6. R. M. Fuoss, Ionic association III. The equilibrium between ion pairs and free ions, *J. Am. Chem. Soc.* **80**, 5059-5061 (1958).
7. J. L. Gebicki and L. Gebicka, Intermicellar material exchange and droplet clustering in AOT reverse micellar systems. A pulse radiolysis study of $(SCN)_2$ radical anion spectra and decay, *J. Phys. Chem.* **101**, 10828-10832(1997).
8. S. S. Atik and J. K. Thomas, Transport of photoreduced ions in water in oil microemulsions: movement of ions from one water pool to another, *J. Am. Chem. Soc.* **103**, 3543-3550 (1981).
9. Y. Alexandrov, N. Kozlovich, and Y. Feldman, Dielectric spectroscopy of cosurfactant facilitated percolation in reverse microemulsions, *J. Chem. Phys.* **111**, 7023-7028 (1999).
10. T. F. Towey, A. N. Khan-Lodhi, and B. H. Robinson, Kinetics and mechanism of formation of quantum-sized cadmium sulphide particles in water-aerosol-OT-microemulsions, *J. Chem. Soc., Faraday Trans.* **86**, 3757-3762(1990).
11. D. Langevin and J. Meunier, in: *Physicochemical Hydrodynamics. Interfacial Phenomena,* edited by M. G. Velarde (NATO ASI Series, series B, Physics Vol.174, Plenum Press, New York, 1988) pp. 147-162.

12. R. P. Bagwe and K. C. Khilar, Effects of the intermicellar exchange rate and cations on the size of silver chloride nanoparticles formed in reverse micelles of AOT, *Langmuir* **13,** 6432-6438 (1997).
13. M. P. Pileni, Water in oil colloidal droplets used as microreactors, *Adv. Colloid Interface Sci.* **46,** 139-163 (1993).
14. J. F. Rivadulla, M. C. Vergara, M. C. Blanco, M. A. López-Quintela, and J. Rivas, Optical properties of platinum particles synthesized in microemulsions, *J. Phys. Chem. B* **101**, 8997-9004 (1997).
15. V. Chhabra, M. Lal, A. N Maitra, and P. Ayyub, Preparation of ultrafine high density gamma ferric oxide using aerosol OT microemulsions and its characterization, *Colloid Polym. Sci.* **273**, 939-946 (1995).
16. M. A. López-Quintela and J. Rivas, Chemical reactions in microemulsions: a powerful method to obtain ultrafine particles, *J. Colloid Interface Sci.* **158**, 446-451 (1993).
17. C. Petit, P. Lixon, and M. P. Pileni, Synthesis of cadmium sulfide in situ reverse micelles. 2. Influence of the interface on the growth of the particles, *J. Phys. Chem.* **94**, 1598-1603 (1990).
18. Y. De Smet, L. Deriemaecker, and R. Finsy, A Simple computer simulation of Ostwald ripening, *Langmuir* **13,** 6884-6888 (1997).
19. L. Taisne and B. Cabane, Emulsification and ripening following a temperature quench, *Langmuir,* **14**, 4744-4752(1998).
20. M. P. Pileni, I. Lisiecki, L. Motte, C. Petit, J. Cizeron, N. Moumen, and P. Lixon, Synthesis "in situ" of nanopartciles in reverse micelles, *Progr. Colloid Polym. Sci.* **93**, 1-9 (1993).
21. M. Wu, D. Chen and T. Huang, Preparation of Pd/Pt bimetallic nanoparticles in water/AOT/isooctane microemulsions, *J. Colloid Interface Sci.* **243**, 102-108 (2001).
22. S. Qiu, J. Dong and G. Chen, Preparation of Cu nanoparticles from water-in-oil microemulsions, *J. Colloid Interface Sci.* **216**, 230-234 (1999).
23. D. Chen and S. Wu, Synthesis of nickel nanoparticles in water-in-oil microemulsions, *Chem. Mater.* **12**, 1354-1360(2000).
24. C. Tojo, M. C. Blanco, and M. A. López-Quintela, Preparation of nanoparticles in microemulsions: a Monte Carlo study of the influence of the synthesis variables, *Langmuir* **13**, 4527-4537 (1997).
25. C. Tojo, M. C. Blanco, and M. A. López-Quintela, Microemulsions as microreactors: a Monte Carlo simulation on the synthsis of particles, *J. Non-Cryst. Solids* **235-237**, 688-691 (1998).
26. M. Kotlarchyk, S. H. Chen, J. S. Huang, and M. W. Kim, Structure of three component microemulsions in the critical region determined by small-angle neutron scattering, *Phys. Rev. A* **29**, 2054-2069 (1984).
27. G. X. Cheng, F. Shen, L. F. Yang, L. R. Ma, Y. Tang, K. D. Yao, and P. C. Sun, On properties and structure of the AOT-water-isooctane reverse micellar microreactor for nanoparticles, *Mater. Chem. Phys.* **56**, 97-101 (1998).
28. J. Tanori, and M. P. Pileni, Control of the shape of copper metallic particles by using a colloidal system as template, *Langmuir* **13**, 639-646 (1997).
29. A. Khan-Lodhi, B. H. Robinson, T. Towey, C. Hermann, W. Knoche, and U. Thesing, in: *The Structure, Dynamics and Equilibrium Properties of Colloidal Systems,* edited by D. M. Bloor and E. Wyn-Jones (NATO ASI Series C, Kluwer Academic Publishers, Dordrecht, 1990) vol.324, pp. 373-383.
30. G. D. Rees, R. Evans-Gowing, S. J. Hammond, and B. H. Robinson, Formation and morphology of calcium sulfate nanoparticles and nanowires in water-in-oil microemulsions, *Langmuir* **15**, 1993-2002 (1999).
31. C. Tojo, M. C. Blanco, and M. A. López-Quintela, in: *Non-Crystalline and Nanoscale Materials,* edited by J. Rivas and M.A. López-Quintela (World Scientific Publisher, Singapore, 1998), pp. 451-456.
32. S. Santra, R. Tapec, N. Theodoropoulou, J. Dobson, A. Hebard, and W. Tan, Synthesis and characterization of silica-coated iron oxide nanoparticles in microemulsion: the effect of nonionic surfactants, *Langmuir* **17**, 2900-2906 (2001).
33. Ph. Monnoyer, A. Fonseca, and J. B. Nagy, Preparation of colloidal AgBr particles from microemulsions, *Colloids Surf.* **100**, 233-243 (1995).
34. Y. Li, and C.-W. Park, Particle size distribution in the synthesis of nanoparticles using microemulsions, *Langmuir* **15**, 952-956 (1999).
35. U. Natarajan, K. Handique, A. Mehra, J. R. Bellare, and K. C. Khilar, Ultrafine metal particle formation in reverse micellar systems: effects of intermicellar exchange on the formation of particles, *Langmuir* **12**, 2670-2678 (1996).
36. C. Tojo, F. Rivadulla, M. C. Blanco, and M. A. López-Quintela, Kinetics of the formation of particles in microemulsions, *Langmuir* **13**, 1970-1977 (1997).
37. C. Tojo, M. C. Blanco, and M. A. López-Quintela, A computer simulation on the synthesis of nanoparticles in microemulsions, *Curr. Topics in Coll. & Inter. Sci.* **4**, 103-112 (2001).
38. C. Tojo, M. C. Blanco, and M. A. López-Quintela, Synthesis of nanoparticles in microemulsions: a simulation study, *Recent Res. Devel. Non-Cryst. Solids* **2**, in press (2002).

39. C. Tojo, M. C. Blanco, and M. A. López-Quintela, The influence of reactant excess and film flexibility on the mechanism of nanoparticle formation in microemulsions: a Monte Carlo simulation, *Langmuir* **14**, 6835-6839 (1998).
40. S. Quintillán, C. Tojo, M. C. Blanco, and M. A. López-Quintela, Effects of the intermicellar exchange on the size control of nanoparticles synthesized in microemulsions, *Langmuir* **17**, 7251-7254 (2001).
41. C. Petit, P. Lixon, and M. P. Pileni, In situ synthesis of silver nanoclusters in AOT reverse micelles, *J. Phys. Chem.* **97,** 12974-12983 (1993).
42. C. Tojo, M. C. Blanco, and M. A. López-Quintela, in preparation.
43. I. Lisiecki and M. P. Pileni, Copper metallic particles synthesized "in situ" in reverse micelles: influence of various parameters on the size of the particles, *J. Phys. Chem.* **99**, 5077-5082 (1995).
44. R. P. Bagwe and K. C. Khilar, Effects on the intermicellar exchange rate on the formation of silver nanoparticles in reverse microemulsions of AOT, *Langmuir* **16**, 905-910 (2000).
45. L. Liz, M. A. López-Quintela, J. Mira, and J. Rivas, Preparation of colloidal Fe_3O_4 ultrafine particles in microemulsions, *J Mater. Sci.* **29**, 3797-3801 (1994).
46. M. A. López-Quintela and J. Rivas, in preparation.
47. S. S. P. Parkin, A. Mansour, and G. P. Felcher, Antiferromagnetic interlayer exchange coupling in sputtered iron/chromium multilayers: dependence on number of iron layers, *Appl. Phys. Lett.* **58,** 1473-1475 (1991).

This page intentionally left blank

7
CHEMICAL ASPECTS OF SEMICONDUCTOR NANOCRYSTALS

Tito Trindade*

1. INTRODUCTION

The last two decades have seen an increasing progress in the synthesis and characterization of inorganic nanocrystals. These materials are of great interest because they show unique properties related to their small size and large surface-to-volume ratio. Whether or not a finely divided crystalline material is considered as formed by nanocrystals is a matter of some discussion. Nanocrystals have intermediate dimensions between the molecules and the sub-micrometric crystallites. Therefore, a definition based solely on the particles dimension does not take into account the type of material considered and the property to be evaluated. One possible definition is based on the scaling of a property of a material with nanometric dimensions, which varies with the particles dimensions and which is intrinsically different from both the macrocrystalline analogues and molecules. For most semiconductor materials this has been observed for particles within the 1-20 nm size range, i.e. when the semiconductor nanocrystals have dimensions less than the Bohr radius of the exciton of the corresponding macrocrystalline material.

The foundations of the chemistry and physics of inorganic nanocrystals are becoming well established. A wealth of information can be found in several reviews in this field.[1-6] Here the main focus will be on recent developments in the application of chemical methods to the synthesis and chemical manipulation of semiconductor nanocrystals. This branch of chemistry, sometimes simply referred to as nanochemistry, deals with a sort of engineering of quasi-molecular objects at a mesoscopic level. From colloidal science to solid-state chemistry, nanochemistry gathers methodologies from diverse scientific areas and has acquired the status of a chemical discipline on its own. To understand this tendency one has to realize that there are specific methodologies to develop nanomaterials that will show specific properties related to their size and surface characteristics. Therefore this review starts with a brief summary of some fundamental properties of semiconductor nanocrystals, followed by the discussion of some important synthetic routes. Finally, examples of surface derivatization methods and of the

* Tito Trindade, Department of Chemistry, University of Aveiro, 3810-193 Aveiro, Portugal.

fabrication of functional materials from the assembly of inorganic nanocrystals will be addressed.

2. STRUCTURAL, ELECTRONIC AND OPTICAL PROPERTIES

A semiconductor nanocrystal is a crystalline arrangement of hundreds to thousands of atoms, with a bulk structure similar to the macrocrystalline compound. Starting from the macrocrystalline semiconductor, as the particle size is reduced to the nanosize regime, there is an increase in the ratio between the number of surface atoms and the total number of atoms. This increase in the surface area originates an increasing number of disrupted chemical bonds at the surface, therefore creating an excess of energy when compared to the bulk structure. This increase in the surface energy is thermodynamically unfavorable, in fact the nanocrystals form a metastable phase in which surface reconstruction has to occur leading to chemical and structural environments distinct from those of the bulk. Unless the nanocrystals are properly stabilized, with time they will grow to yield the stable macrocrystalline phase, although the kinetics involved may be rather slow. From a chemical perspective, inorganic nanocrystals are small crystalline fragments with an internal structure similar to the bulk lattice, which have been stabilized, usually using a capping agent. This means that considering a semiconductor compound, the surface in the nanocrystals is different from the macroscopic material surface. As it will be clear below, this definition takes into account the fact that nanochemistry has much to do with surface chemistry phenomena, in the sense that surface derivatized nanocrystals can be manipulated in solution as larger inorganic macromolecules. It is important to note that in this discussion, the main focus will be on semiconductor nanocrystals in which the internal crystalline structure is similar to the macrocrystalline lattice but show distinct electronic properties. This is not the case for particle sizes approaching the molecular level, nanoclusters, in which quantum mechanical effects are important in determining the type of the internal structure. Besides, in nanocrystals the stable crystalline structure (polymorph) is largely conditioned by their surface energy, hence by their surface characteristics and particle size. In fact, highly monodispersed nanocrystals are suitable models to investigate the fundamentals of phase transformations in crystalline solids because they behave as single structural domains. This has been elegantly demonstrated in a key-note paper by Tolbert and Alivisatos on the structural transformations occurring in CdSe nanocrystals under high-pressure.[7] At high pressures, the hexagonal based structure of CdSe nanocrystals is transformed in a denser cubic close-packed structure (NaCl-type).

A macrocrystalline semiconductor is composed of a large number of atoms covalently bound. The energy levels diagram consists of sets of molecular orbitals very closely spaced in energy, each set forming effectively a continuum. At 0 K the levels of lower energy are filled with electrons, the valence band; the levels at higher energy are unoccupied, the conduction band. These two bands are separated by an energy gap (*Eg*), the magnitude of which is characteristic of the macrocrystalline semiconductor at a specific temperature. Due to thermal activation or light absorption, electrons in the valence band may receive enough energy (> Eg) to be excited across the band gap to the conduction band. An excited electron in the conduction band and the resulting hole in the valence band form an electron-hole pair.

The charge carriers in a semiconductor, conduction-band electron and valence-band hole, can form a bound state when they approach each other. This bounded electron-hole pair (Wannier exciton) is delocalised within the crystal lattice and experiences a screened Coulomb interaction. The Bohr radius (a_B) of the bulk exciton is given by

$$a_B = \frac{\hbar^2 \varepsilon}{e^2}\left[\frac{1}{m^*_e} + \frac{1}{m^*_h}\right] \quad (1)$$

(ε is the bulk optical dielectric coefficient, e the elementary charge, m_e^* and m_h^* represent the effective mass of the electron and hole, respectively).

As stated above, semiconductor nanocrystals have intermediate dimensions between the molecular state and sub-micrometric crystallites. In a first approximation, one can consider that strong quantum size effects are observed for semiconductor nanocrystals in the size range defined by[8]:

$$l << R \approx a_B \quad (2)$$

(l is the characteristic length of the semiconductor lattice, R is the particle radius and a_B is the bulk-exciton Bohr radius of the semiconductor). At this size range, the electronic and optical properties of semiconductor nanocrystals, often referred to as quantum dots, are very sensitive to:

i) particle size (comparable to the De Broglie wavelength of electrons or holes in the semiconductor);
ii) surface characteristics and interface phenomena (due to large surface-to-volume ratios).

Quantum confinement of the electron-hole pairs (excitons) occurs in nanocrystals with dimensions comparable to the bulk-exciton Bohr radius of the semiconductor (2). In this case, due to the small dimensions of the lattice, the Coulomb interaction between electron and hole cannot be neglected and they have higher kinetic energy than in the bulk solid. The *valence band* and the *conduction band* in nanocrystalline materials are formed by sets of discrete electronic levels. In relation to the macrocrystalline material, the exciton binding energy increases and the charge carriers in the lattice are no longer described using infinitely delocalized wave functions. A quantum description based on the particle-in-a-box model gives the approximate size-dependent energy of the first electronic transition of the exciton[9-11] (i.e. the semiconductor nanocrystalline band gap):

$$\Delta E \cong \frac{\hbar^2 \pi^2}{2R^2}\left[\frac{1}{m^*_e} + \frac{1}{m^*_h}\right] - \frac{1.786e^2}{\varepsilon R} \quad (3)$$

In Brus equation (3) the first term is the kinetic energy of both the electron and the hole ($1/R^2$ dependence). The second term represents the Coulomb energy ($1/R$ dependence). For semiconductors with small dielectric constants, the spatial correlation between the charge carriers can be significant, hence a third term corresponding to the effective Rydberg energy (E_{Ry}) has to be taken in account[12,13]:

$$a_B = \frac{\hbar^2 \varepsilon}{e^2}\left[\frac{1}{m^*_e} + \frac{1}{m^*_h}\right] \quad (1)$$

This size-independent term is given by:

$$E_{Ry} = \frac{e^4}{2\varepsilon^2 \hbar^2}\left[\frac{1}{m^*_e} + \frac{1}{m^*_h}\right]^{-1} \quad (5)$$

Eqs. (3) and (4) show that for a nanocrystalline semiconductor there is a size-dependent band gap due to a quantum localization term with a $1/R^2$ dependence and to the electron-hole Coulomb attraction with a $1/R$ dependence. As a result the band gap increases in energy as the particle size decreases (Figure 1). Using a molecular terminology, this means that in the energy-level diagram the difference between the HOMO and LUMO increases with decreasing particle dimensions. This prediction has been confirmed experimentally for a wide range of semiconductor nanocrystals; a blue shift is observed for the optical band edge (or excitonic peak) in the optical spectrum. For some nanocrystalline semiconductors (e.g. CdSe) there are perceptible dramatic color changes during the synthesis due to these quantum size effects (Figure 1). A large number of semiconductors have band gaps and localized electronic states in the visible or near-infrared region of the electromagnetic spectrum, therefore optical spectroscopy is a powerful characterization technique to evaluate the quantum confinement behavior. For example, Eq. (3) is particularly useful for the experimental chemist as the dependent size energy shift can be easily estimated during a synthetic task, allowing size tuning from the optical properties. As the particle size approaches the molecular level, Eqs. (3) and (4) are no longer valid and other calculation methods have been reported using distinct theoretical approaches.[13-16]

The surface characteristics of semiconductor nanocrystals have a strong influence on important properties for device fabrication, including luminescence,[17-21] optical non-linearity,[13,22,23] and redox chemistry.[4,24,25] Here, only a brief reference to the luminescence of semiconductor nanocrystals will be made. Photoluminescence and electro-luminescence in semiconductor nanocrystals depend strongly on the chemical nature and defects at the particles surface. In order to fabricate photoluminescent devices such as lasers[26,27] and bio-probes,[28,29] charge separation upon photoexcitation is required. Size tuning luminescence over a wide energy range has been observed for nanocrystalline semiconductors; CdSe and CdS nanocrystals have been particularly investigated.[2-6] Surface capped semiconductor nanocrystals of these compounds emit at wavelengths close to the respective optical band gap, originating sharp emission bands. This emission is due to electron-hole pair recombination processes with short lifetimes and has been designated as (near) band edge or excitonic emission. Crystalline defects in nanocrystals are mainly located at their surfaces, due to unbalanced surface sites. Recombination of the charge carriers at such surface defects is a competitive emission process with longer luminescence lifetimes, originating broad emission bands at energies greater than the corresponding band gap.

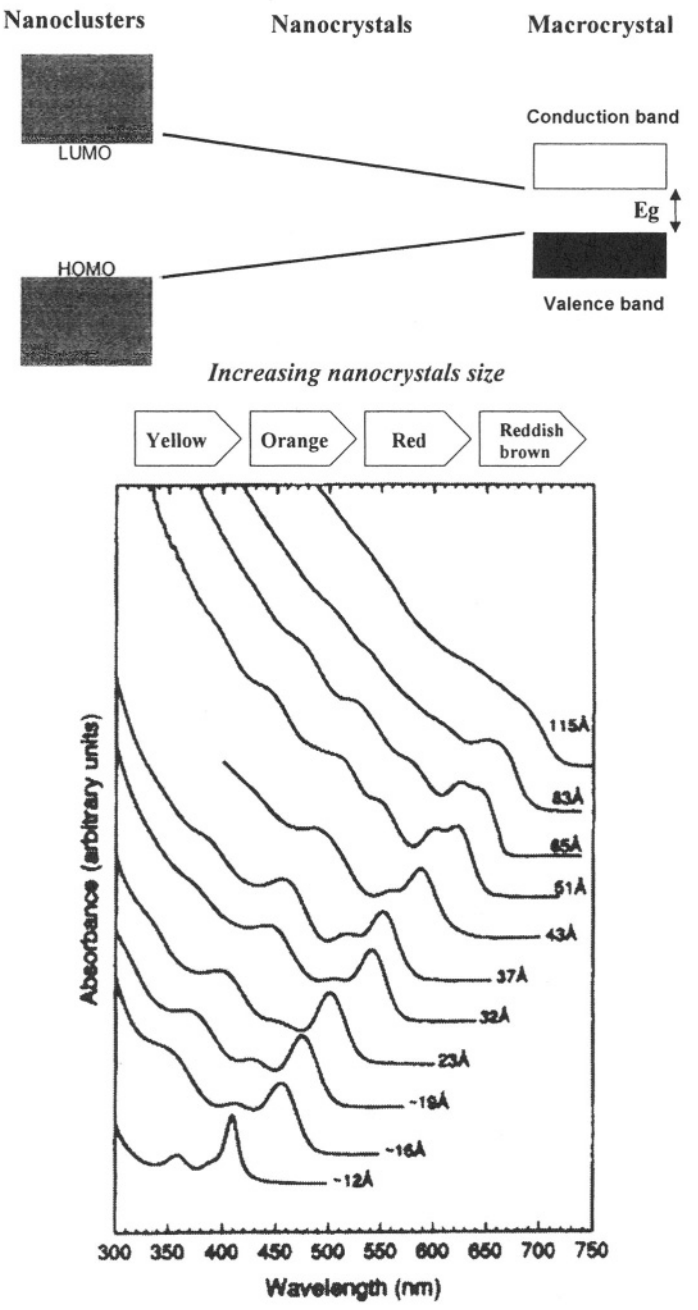

Figure 1. Evolution of a semiconductor band gap from a quasi-molecular to the macrocrystalline state. The intermediate region is exemplified with synthetic CdSe showing color variations depending on the nanocrystals size. Reproduced in part with permission from ref. 45. Copyright 1993, American Chemical Society.

These considerations have been confirmed in many experiments which have shown a remarkable enhancement of the near band gap luminescence on semiconductor nanocrystals mediated by surface modification.[17-21] Two main approaches have been delineated, (1) the growth of a wide-gap semiconductor coating the surface of

semiconductor nanocrystals, or (2) the surface derivatization with organic ligands which may subsequently be exchanged for another ligand. In this case, the surface defects are filled with electron-donors or –acceptors, precluding trapping of the semiconductor charge carriers. The exact mechanisms involved and the electron-hole recombination dynamics are strongly dependent on the nanocrystals characteristics in particular on their surface nature.[30-32] This is a topic in which photophysic studies associated to surface modification methods will necessarily bring some light to the luminescence of semiconductor nanocrystals.

3. CHEMICAL SYNTHESIS OF SEMICONDUCTOR NANOCRYSTALS

3.1. General Concepts

The chemical synthesis of semiconductor nanostructures has been a very active area of research.[6] For CdS, in particular, a wide range of chemical methods have been reported in the literature. Table 1 gives examples of chemical methods for the preparation of nanocrystals of CdS. In some way, this semiconductor has been used as a prototypical material in semiconductor nanocrystals synthesis. Some of the methods mentioned in Table 1 have also been adapted to other semiconducting materials.[6] It has become clear that among the variety of synthetic methods developed over the last two decades, just a few are reliable paths to produce high-quality nanomaterials for technological applications. Nowadays, the development of novel synthetic methods to produce high quality semiconducting nanostructures is still a challenge for the materials chemist.

Table 1. Chemical methods for the preparation of CdS nanocrystals (adapted from ref.6).

Synthetic method	particles size range/nm	references
Controlled precipitation in confined spaces		
Arrested precipitation within amphiphilic systems	2-6	33
Growth inside zeolite cavities	<1.3	34
Growth inside porous silica-pillared layered metal (IV) phosphates	2.5	35
Formation within polymer matrices using ionomers	1.5-2.3	36
Treatment of a xerogel matrix (polysilsesquioxane) with Cd^{2+} and S^{2-}	6-9	37
Arrested precipitation in aqueous and methanolic media	3	38
$Cd(SO_4)$+$(NH_4)_2S$ in aqueous/acetonitrile and copolymers as stabilizers	2.1-7.5	39
Arrested precipitation in aqueous solution within surfactant vesicles	2.2-5	40
Formation at air-water interface in a Langmuir film balance	2.7-3.4	41
Synthesis using phosphatidylcholine vesicles	2-6	42
Arrested precipitation in the presence of 1-thioglycerol	1.3-3.9	43
Molecular precursors route		
Hydrolysis of P_2S_5 in an ethanol solution of Cd^{2+}	<6	44
$CdMe_2$ + $[(Me_3Si)_2S$ in hot TOPO	2-3	45
Thermalysis of $[Cd(S_2CNRR')_2]_2$ in hot TOPO	3-7	46
$CdCl_2$ + TOPS in hot TOPO	4.5	47
Methatesis of $Cd[N(Me_3Si)_2]_2$+SCNR in TOPO	1.5-2	48
Solventothermal reaction of CdC_2O_4 + S	20-60x200-4800 (rods)	49
Cluster building-up approach		
Thermalysis of $(NMe_4)_4Cd_{10}S_4SPh_{16}$	1.5 (core)	50
Superlattice built up of $Cd_{17}S_4(SCH_2CH_2OH)_{26}$		51
Oxidation of $[Cd_{10}S_4SPh_{16}]^{4-}$ by I_2		52

The choice of a particular synthetic method to produce semiconductor nanocrystals depends on several factors, including the envisaged applications and scale production. Relevant considerations common to traditional synthetic chemical methods also apply in developing a synthetic route towards nanomaterials, including the possibility to scale-up, reaction yield, safety hazards and environmental implications. In order to take advantage of the unique properties of semiconductor quantum dots there are specific characteristics required for these materials. Among the principal aims of semiconducting nanochemistry are the preparation and the assembly of ideal nanocrystals with the following characteristics:

i) size monodispersity and controlled shape;
ii) ability for surface derivatization;
iii) high degree of crystalinity;
iv) chemical purity and homogeneity;
v) defects free.

Recently, a tentative broad classification for the most common and well-established solution chemical methods for the preparation of semiconductor nanocrystals has been proposed (Table 1).[53] In brief, the following three main categories have been considered:

i) controlled precipitation in confined spaces;
ii) molecular precursors route;
iii) cluster building-up approach.

The outline in this section will follow this classification although it should be clear that in such classification, the borderlines within those chemical routes are diffuse. Herein the term "controlled precipitation" include the methods based in traditional exchange reactions, involving the formation of a stable sol from the mixture of the chemical components of the semiconductor in the form of the respective ionic sources. The stability of this sol is attained either by using the presence of stabilizers in solution (e.g. polymers, surfactants, Lewis basis) or by the electric double-layer repulsion. The formation of nanoparticles either using sol-gel methods or inside confined spaces of matrices is also included in this category. The term "controlled precipitation" has its origin in some commonly used synthetic colloidal techniques. The molecular precursors approach, includes the methods involving the preparation of nanocrystals using a thermal, chemical or mechanical treatment applied to a reacting solution containing the molecular precursor species, which may consist in metal complexes or other molecular compounds. The cluster-building-up approach involves the preparation of nanocrystals or superlattices by phase transformation or assembling of inorganic nanoclusters. The latter have a definite chemical composition and dimensions smaller than the final nanostructure.

There is still a lack of understanding on the fundamental mechanisms of nucleation and growth of a solid. In the classical nucleation theory, a solid forms from critical nuclei which result of random collisions from small structural units (ions, atoms or molecules). In certain experimental conditions some of these nuclei are stable enough to grow into larger particles without loosing mass. The classical nucleation theory assumes that the critical nuclei are in fact very small fragments of the bulk crystalline lattice, having structural features in common. Quantum mechanical effects are neglected in the classical nucleation theory, although they are important in determining the properties of particulates approaching the molecular scale. A thorough explanation of these considerations is beyond the scope of this text but alternative theoretical framework has

been investigated. For the purposes of this chapter, two main ideas should be retained from the above considerations:

i) The dimensions of the critical nuclei can be considered to be in the nanosize regime, this means that there is an interesting interplay between the understanding of the mechanisms of solid formation, and of the nanocrystals properties,

ii) The critical nuclei formed are thermodynamically unstable; the nuclei grow into larger particles decreasing the total surface energy.

3.2. Controlled Precipitation in Confined Spaces

In a large number of methods for the chemical synthesis of nanocrystals, experimental conditions are set up in order that the growth process is terminated abruptly and a stable sol is formed in solution. The stability of the small particles against agglomeration can be attained using chemical protective agents. This general idea is behind many synthetic methods in which polymers, surfactants or Lewis bases have been used to surface cap the small particles formed (nanocrystals). An elucidative example of this concept is the controlled precipitation of a metal sulfide in confined spaces such as reverse micelles (water-in-oil microemulsions). The formation of the semiconducting phase occurs inside a nanoreactor which in this case is the water droplet confined by the surfactant molecules dispersed in a hydrocarbon solvent (Figure 2). Knowing the phase diagram for an amphiphilic system, the controlled precipitation can occur in the cavities of more complex nanostructures, for example by preparing lipid bi-layers or liquid crystals. The chemical reaction occurring inside the nanoreactors (Figure 2) is typically a controlled precipitation at room temperature, using the corresponding metal salts as the chemical sources. However, provided that the experimental conditions are compatible with the presence of a stable microemulsion, other soluble starting chemicals can be employed to yield nanocrystalline semiconductors. Nanocrystalline metal chalcogenides have been prepared in reverse micelar solutions by reacting organometallic species such as silylorganochalcogenides with metal alkyls or simple metal salts.[54,55]

$$CdCl_2 + Se(SiMe_3)_2 \xrightarrow[-2Me_3SiCl]{} CdSe \tag{6}$$

$$ZnEt_2 + Se(SiMe_3)_2 \xrightarrow[-2SiEtMe_3]{} ZnSe \tag{7}$$

Typically, microemulsions containing the metal ions were prepared and a silylchalcogenide reagent was added (Eqs. (6) and (7)). The nanocrystals surface was then tailored using either organic ligands or a second inorganic phase to replace the surfactant molecules. This is a clear example that the borderlines in the classification proposed above are not rigid, in fact this synthetic approach is a controlled precipitation in confined spaces using molecular precursors. The synthesis in reverse micelles also addresses two major requirements for nanocrystals preparation:

i) size-tuning: by varying the relative amount of water/surfactant, distinct particle size distributions are obtained;

ii) surface modification: the surfactant molecules at the nanocrystals surface can be replaced by other chemical capping agents, such as thiols or amines.

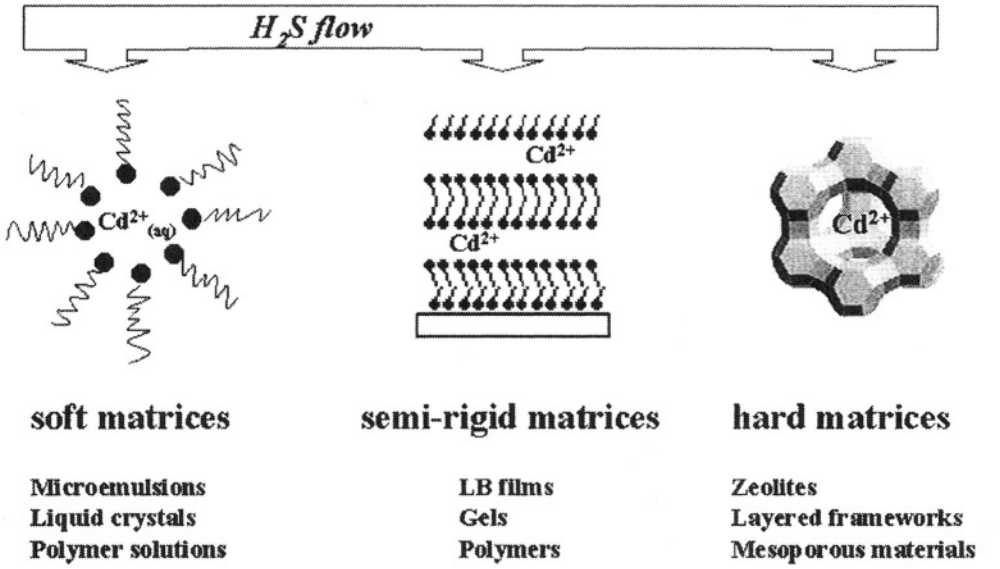

Figure 2. Scheme of general chemical routes to prepare CdS nanocrystals in confined spaces using distinct matrices.

Capped nanocrystals can be isolated as powders and re-dispersed in solvents for further chemical or physical treatments. For example, although semiconductor nanocrystals prepared at room temperature have a fair crystallinity, this can be improved by annealing the nanocrystals in a high boiling point solvent. This means that the nanocrystals surface has to be efficiently capped to avoid the coalescence into the bulk material or the substitution of the capping molecules by the solvent. An efficient annealing can considerably improve the nanocrystals properties, therefore the choice of the high boiling point solvent is important. Both coordinating solvents (e.g. 4-ethylpyridine) and non-coordinating solvents (e.g. p-xylene) should be tested in order to get the best crystalline samples.

It is easily recognized that there is a plethora of synthetic strategies to prepare nanocrystals by extending the concept of precipitation within a confined space to other types of nanoreactors (Figure 2). Examples of other commonly used host matrices for the preparation of semiconductor nanocrystals include: zeolites,[34] layered solids,[35] mesoporous materials,[56] gels[37,57], polymers[36,58] and Langmuir-Blodgett monolayers.[41,59,60] In using these nanoreactors, there is a template-assisted effect determining the morphology of the nanocrystals and there is also a chemical-assisted effect, which defines the chemical nature of the particles surface. Zeolites and porous inorganic frameworks are rigid templates and are examples of hard matrices. In these matrices the nanocrystals diameter is limited by the pore size existing within the inorganic framework; typically nanocrystals smaller than 20 Å are obtained. Although the chemical manipulation of the nanocrystals, once they have been removed from the host matrix, is not feasible, in the right conditions this method leads to very low particle size dispersions. For example the preparation of CdS in zeolite Y cages[34] involved a pre-step in which the sodium form was ion-exchanged to the cadmium cation form by treatment with aqueous Cd(II) at pH 5. Hydrogen sulfide gas was then flowed over the sample.

Depending on the loading level of Cd(II) inside the zeolite, different sizes for the CdS clusters were obtained. A low loading (1:1 metal/sulfide ratio) led to isolated CdS clusters with an average size of less than 13 Å, showing an absorption peak at around 280 nm in the optical spectrum. When an excess of cadmium was used, a higher loading level, the individual clusters aggregated into an extended structure, modulated by the internal cavities of the zeolite. The optical spectrum shows an excitonic shoulder near 350 nm corresponding to CdS clusters of about 28 Å in diameter. In the synthesis of nanocrystalline semiconductors using more flexible confined spaces, such as polymers or organic Lewis bases, to avoid large particle size dispersions, strict experimental conditions are required, as compared to the use of solid matrices. On the other hand, these matrices offer the possibility of surface modification and interface chemical reactivity in order to fabricate hybrid materials.

Many other solution methods have been described for the synthesis of nanocrystalline semiconductors in which confined growth and surface passivation are not so obvious. Although somewhat different, the fact is that the basic concept still applies to other common synthetic methods. Provided the chemical feedstock is not depleted, following nucleation of the solid, the as formed nuclei will grow into the bulk phase unless particle growth is terminated in an intermediate stage by physical or chemical means. Hence, simple arrested precipitation techniques have been applied to prepare colloidal nanocrystals. The colloidal stability of these nanocrystals has been achieved by electrostatic double-layer repulsion or by using stabilizers such as hexametaphosphates.[38,61]

3.3. Molecular Precursors Routes

A protective effect, similar to that mentioned in the previous section, occurs when the particles are generated in a coordinating solvent chemical and thermally stable at certain reacting conditions. If the reactants, metal and non-metal sources, are introduced into the reaction vessel containing the coordinating solvent at a high temperature, a burst of nuclei will form and tend to grow. Experimental parameters such as reaction temperature and time can be adjusted to allow steady growth of the particles formed. The solvent molecules will coordinate to the particles surface, avoiding further growth and the coalescence of the colloidal nanocrystals to the bulk phase of the semiconductor. For most of the purposes, the presence of the solvent molecules at the particles surface is not a limitation. By the contrary, as discussed before, it is now well established that optical properties such as photoluminescence are strongly enhanced due to surface passivation effects by the solvent.

The use of molecular precursors is commonly associated, although not exclusively, to the preparation of semiconductor nanocrystals in coordinating solvents. Generally, the molecular precursors are decomposed in a coordinating solvent at relatively high temperatures, hence promoting the crystallinity and allowing the nanocrystals surface passivation. This is the case of the chemical synthesis of nanocrystals using tri-octylphosphine oxide (TOPO) as the solvent. Taking into account the properties of TOPO, one may consider this compound as a prototypical solvent for nanocrystal synthesis:

i) it has high chemical and thermal stability;

ii) coordinates to metal sites at the inorganic surfaces, but can be displaced by other coordinating molecules when these are used as the new solvent;

iii) allows size-tuning (via Ostwald ripening) during the synthetic process by adjusting the time and temperature of synthesis,

iv) the long octyl chains confer hydrophobic character to the nanocrystals, which can be isolated and manipulated using traditional solution chemistry.

Since the landmark work[45] of Murray, Norris and Bawendi, describing the synthesis of cadmium chalcogenides in TOPO, a wide range of nanocrystalline semiconductors has been prepared by diverse molecular precursor methods which have in common the use of that solvent as the reacting medium (Table 2). In the conventional TOPO method, a non-metal source (e.g TOPSe) and the metal source (e.g $Cd(CH_3)_2$) are injected separately into hot TOPO to produce TOPO capped CdSe quantum dots. A major limitation of this method is the use of toxic and highly pyrophoric compounds at high temperatures, this is a especial concern if scale-up procedures are envisaged.

Table 2. Molecular precursors used in the preparation of semiconductor nanocrystals in TOPO/TOP (adapted from 6).

Compound	Synthetic method	Particles size range/nm	references
II/VI semiconductors			
ZnS	thermalysis of $[Zn(S_2CNRR')_2]_2$	5	62
ZnSe	thermalysis of $[Zn(Se_2CNRR')_2]_2$	5	62
CdS	$CdMe_2$ + $[(Me_3Si)_2S$	2-3	45
	thermalysis of $[Cd(S_2CNRR')_2]_2$	3-7	46
	$CdCl_2$ + TOPS	4.5	47
	methatesis of $Cd[N(Me_3Si)_2]_2$+SCNR	1.5-2	48
CdSe	$CdMe_2$ + TOPSe	1.2-11.5	45
	thermalysis of $[R(Cd(Se_2CNEt_2)]$	3-8	46
	thermalysis of $[Cd(Se_2CNRR')_2]_2$	5	62
	methatesis of $Cd[N(Me_3S)_2]_2$+SCNR	1.5-2	48
CdTe	$CdMe_2$ + (TOP)Te	2-3	45
ZnSe/CdSe	$CdMe_2$+TOPSe then CVD using H_2Se+$ZnEt_2$	4-6.8	63
III/V semiconductors			
GaP	thermalysis of $[Cl_2GaP(SiMe_3)_2]_2$	2-6.5	64
InP	$InCl_3$+$P[Si(CH_3)_3]_3$	2-5	65
	thermalysis of a chloroindium oxalate complex + $P(SiMe_3)_3$	2-6.5	64
InAs	$InCl_3$+$As[Si(CH_3)_3]_3$	2.5-6	66
$GaInP_2$	chlorogallium oxalate+chloroindium oxalate +$P(SiMe_3)_3$	2.5	64
III/V semiconductors			
Cd_3P_2	thermalysis of $[MeCdPtBu_2]_3$	3	67
IV/VI semiconductors			
PbS	thermalysis of $Pb(S_2CNRR')_2$	6.3-20	68
PbSe	thermalysis of $Pb(Se_2CNRR')_2$	16	69
	lead oleate + TOPSe in diphenylether	3-9	70

To overcome these limitations and to extend the TOPO method to a wider range of semiconductors, a single source approach was developed.[46] In this method, single molecule precursors, i.e. compounds which contain both elements of the final semiconductor within a single molecule, are injected into TOPO yielding surface capped quantum dots. Hence, the thermalysis of simple cadmium dithiocarbamates, such as $Cd(S_2CNEt_2)_2$, in TOPO yielded high quality TOPO capped CdS quantum dots. In similar reacting conditions, but using the analogous cadmium diselenocarbamato complex, a mixture of elemental selenium and hexagonal CdSe was obtained. Working out the molecular precursors chemistry, the method was proven to be successful also for CdSe quantum dots. Instead of $Cd(Se_2CNEt_2)$, the alkyl derivatives $([RCd(SeCNEt_2)]$, R=Me, Np) were used[46] or, since these compounds are air-sensitive, unsymmetrical and air-stable complexes type $Cd(S_2CNMeHex)_2$ are an alternative.[62] Metal dithiocarbamates and metal diselenocarbamates have been extensively used as precursors for numerous metal chalcogenides (Table 2). However, there is still a rich molecular precursor chemistry associated to the simplicity of this approach which has yet to be fully developed. The use of single-molecule precursors in other high-boiling point solvents has also been investigated. For example, well-defined Bi_2S_3 nanofibers have been synthesised using the thermalysis of bismuth (III) dithiocarbamates in ethyleneglycol.[71]

In the TOPO methods described above, nearly spherical nanocrystals (a prolate shape has been described as more realistic) are generally obtained. In fact the description of nanocrystals as having a spheroidal or prolate shape is a crude description which derives from what is observed in conventional TEM images. As expected, these nanocrystals have faceted surfaces leading to more complex morphologies at the atomic scale.[5] Recently Alivisatos *et al.* have prepared CdSe nanocrystals of diverse morphologies by using a binary surfactant mixture of HPA (hexylphosphonic acid)/TOPO.[72] The precise control of the synthesis parameters, such as HPA/TOPO ratio, volume and number of injections in the surfactant mixture, resulted in nanoparticles with rod-, arrow-, teardrop- and tetrapod-shapes. Spheroidal shapes are obtained at slow particle growth rates whereas nanorods are favored at higher growth rates by unidirectional growth of selected faces of the nanocrystallites. CdSe nanorods with different aspect ratios were thus obtained by careful control on the synthetic conditions and also nanorods were formed by the stacking of both polymorphs of the semiconductor (wurtzite and blenda lattices).

3.4. Cluster Building-Up Approach

There is a prominent perspective concerning the synthesis of truly monodisperse semiconductor nanocrystals by the chemical synthesis of inorganic nanoclusters.[50-52] These nanoclusters can be regarded themselves as structural-like units of a semiconductor, although the bulk structure has not yet been achieved, with dimensions generally smaller than those of the nanocrystals mentioned in the previous sections. This approach is more related to molecular chemistry than the other chemical methods reported above, in the sense that clusters with a well-defined chemical composition and crystal structures are envisaged. In some particular cases, X-ray crystal structures have been reported showing structural features common to macrocrystalline solids.[50,51] This type of knowledge associated to quantum mechanical calculations on metal chalcogenide clusters, can provide some understanding on the structural development of clusters of atoms into the corresponding macrocrystalline lattice.[73]

In terms of synthesis, the concept is the development of larger nanostructures using a cluster build-up approach. For example, the synthetic clusters can be used as the starting materials to produce a semiconductor nanostructure by phase transformation. An example is the preparation of 15 Å diameter clusters of $[Cd_{32}S_{14}(SC_6H_5)_{36}.DMF_4]$, using $Cd_{10}S_4(SC_6H_5)_{12}$ clusters as the starting materials.[50] The $Cd_{10}S_4(SC_6H_5)_{12}$ clusters have been prepared in the process of the gradual conversion of a discrete molecular solid $[(NMe_4)_4Cd_{10}S_4(SC_6H_5)_{16}]$ into bulk crystalline CdS, on a controlled thermal decomposition. In a first step at 250°C, the tetramethylammonium cations and four thiophenolate ligands are removed, yielding $Cd_{10}S_4(SC_6H_5)_{12}$ as the product. The phenyl groups are then eliminated at 500°C originating bulk crystalline CdS. The cluster $[Cd_{32}S_{14}(SC_6H_5)_{36}.DMF_4]$ was obtained by recrystallization from a pyridine solution containing the solid $Cd_{10}S_4(SC_6H_5)_{12}$ and to which N,N-dimethylformamide was added. X-ray analysis and ^{113}Cd NMR spectra, show that the structure of this quantum dot is an 82-atom CdS core with a cubic spharelite lattice (~12 Å), with four corners capped by hexagonal wurtzite-like CdS units (~15 Å in whole). The absorption spectra of the cluster is blue-shifted from the bulk (358 nm), and the peak position is insensitive to the effect of the solvent (THF) polarity, which means that the ground state of the corresponding excited state has a vanishing small dipole moment.

A major breakthrough in this field is the fabrication of more complex networks using the clusters as the building-blocks.[51] In this cluster build-up approach, the clusters retain their chemical individuality although conferring unique properties to the final nanostructures due to their collective behavior. The processes in which these clusters will be assembled into larger nanostructures have much in common with the chemistry involved on the assembly of nanoparticles into superlattices or nanostructured films. Although considerably less investigated, the surface chemistry of these nano-objects will play a major role on the fabrication of functional nanomaterials. In the next section some of the results in this area are summarized.

4. SURFACE CHEMISTRY AND ASSEMBLY METHODS

4.1. Nanocrystals Surface Modification

The ability to control the chemical surface in nanocrystalline semiconductors is essential to the fabrication of nanodevices. However, compared to the study of their bulk properties, the chemistry of the surfaces of semiconductor nanocrystals is still at a primitive stage. Two main issues arise in the fabrication of a nanostructured material by manipulation of nanocrystals with derivatized surfaces:

i) the chemical reactivity at the interface between the nanocrystals and a distinct material, usually an organic matrix;

ii) assembly methods to produce organized nanostructures using passivated nanocrystals as the building blocks.

Obviously both approaches require derivatization techniques at the particles surface which do not disturb the integrity of the semiconductor core. The nanocrystals surface can be derivatized either by an inorganic layer, an organic layer or both. Associated to the ability to chemically manipulate the nanocrystals, surface derivatization also improves the physical properties of semiconductor nanocrystals. It is now well established that the surface passivation of cadmium chalcogenide nanocrystals with an organic cap (e.g.

TOPO, amines, thiolates) promotes the near band-edge photoluminescence of the semiconductor.[45,46,74] For CdSe nanocrystals prepared in TOPO, the replacement of the solvent molecules by a cap of a wide-gap semiconductor, increases considerably the luminescence quantum yield. As discussed earlier, the increase on the near-band edge photoluminescence quantum yield has been explained by attenuation of the broad emission due to charge carriers recombination at defects mainly located at the nanocrystals surface.[26,74] There are restraints on the growth of such composite particles in solution, which include the relative solubility of the solids and the mismatch in the lattice constants of the solid phases. The growth of a crystalline phase on the surface of semiconductor nanocrystals, immediately remits to the need to develop hetero-epitaxial growth techniques for nanocrystalline semiconductors. In these heterostructures, among other properties, there is need to control conduction type, charge carriers concentration and lattice mismatch.

The semiconductor nanocrystals can also be coated with an inorganic amorphous layer such as silica. The SiO_2 encapsulation of semiconductors and metal nanocrystals has been recently reviewed.[75] A possible route involves the controlled hydrolysis of sodium metasilicate in the presence of inorganic nanocrystals which were previously surface treated with a silane coupling agent (e.g. aminopropyltrimethoxysilane $(NH_2C_3H_7Si(OCH_3)_3)$ or mercaptopropyltrimethoxysilane $(HS(C_3H_7)Si(OCH_3))$.[75] In these compounds, the electron donor atoms (nitrogen or sulfur) coordinate to metal sites at the particle surface, with the siloxy group directed outwards from the particle surface, hence rendering the surface vitreophilic. The SiO_2 coated inorganic nanocrystals obtained in this way can be further derivatized using typical solution chemistry. There is a wealth of information on the organic functionalization of amorphous SiO_2 and the silica functionalization of commercial polymers.[76,77] For example, Bourgeat-Lami *et al.* have used this approach to prepare inorganic-organic hybrid colloids, in which a SiO_2 shell was grown on the core of SiOH-functionalized polymer beads (Figure 3).[76] This type of chemistry associated to the preparation of coated semiconductor nanocrystals will provide the means to fabricate new hybrid products with novel properties. In fact, the importance of silica encapsulation of inorganic particles associated to the dispersion in polymer matrices, has been long recognized for example in the fabrication of composites or in the paints and pigments industries. Some inorganic pigments require a stabilization step, consisting of the coating of the pigment using a robust chemical material such as SiO_2 or Al_2O_3. Similarly to the coated pigment particles, in silica coated semiconductor nanocrystals, the core is chemically protected and the thermal stability is improved. In the particular case of nanocrystalline CdS, the photochemical stability is enhanced because the CdS sulfur layer is not available for photo-oxidation of sulfur to sulfate by molecular oxygen.[78] Moreover, as stated above, the optical properties of the semiconducting phase can be improved because surface defects at the disordered surface of the semiconductor become passivated by an amorphous phase.

It may be of interest to produce a nanocrystalline phase at the surface of particulate materials or porous matrices, for example to develop novel substrates for electrochemical cells or heterogeneous catalysts. The synthesis of inorganic nanocrystals inside zeolitic cavities, as mentioned above, is an example of the later process.[34] Recently, a novel method to synthesize metal sulfide nanocrystals at the surface of sub-micrometric SiO_2 particles has been described.[79] This mild temperature deposition method involves the decomposition of metal dithiocarbamato complexes in the presence of ethylenediamine and a SiO_2 colloid, yielding SiO_2 particles coated with the respective metal sulfide.

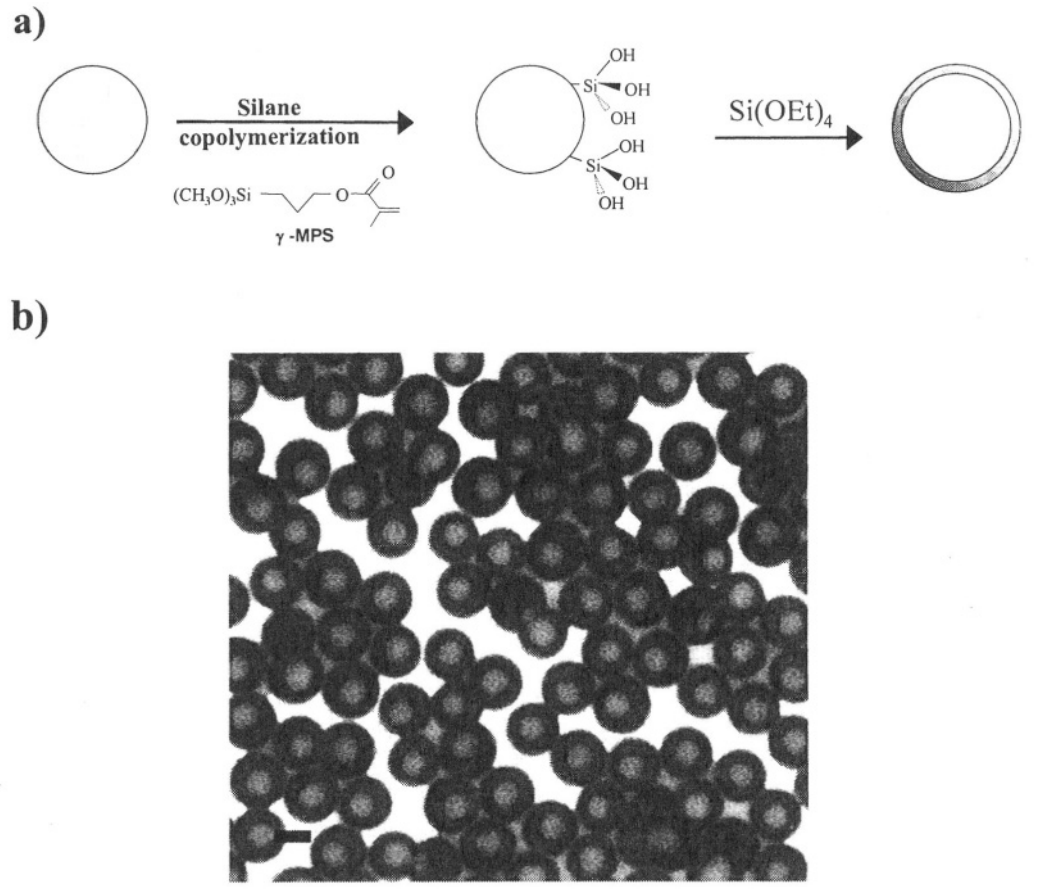

Figure 3. (a) A chemical route for the silica functionalization of latex particles; (b) TEM image (bar=100 nm) of core-shell latex/SiO_2 particles. Reproduced with permission from ref. 76. Copyright 2001, ACS.

Varying the metal dithiocarbamato complexes, a variety of nanocrystalline semiconductors at the surface of SiO_2 substrates can be prepared in a single-step synthesis. Since mild temperatures are used in this process, typically 60°C, the chemical and morphological integrity of the core is maintained. In these nanocomposites the outer semiconducting layer is formed by islands of smaller nanocrystallites leading to quantum size effects in the diffuse reflectance spectra of the powdered solid.[79] The nanocomposite particles can be further coated with a protective SiO_2 layer using reported SiO_2 coating processes.[75]

The preparation of nanostructures termed quantum-dot-quantum-well systems, such as CdS/HgS/CdS, has also been reported.[80] In this nanostructure, a core of CdS, and a well of 1-3 monolayers of HgS, are capped by 1-5 monolayers of CdS, the outer shell. The synthesis involved the growth of cubic-type HgS on cubic-type CdS (52 Å diameter) by ion replacement when adding aqueous $Hg(ClO_4)_2$ to the CdS colloid. The solubility products of CdS and HgS are respectively 5×10^{-8} and 1.6×10^{-52}, therefore the substitution of Cd^{2+} for Hg^{2+} in $(CdS)_n$ is thermodynamically favored. There is a good match between the lattice constants of cubic CdS (5.818 Å) and cubic HgS (5.851 Å)

which also favors the formation of CdS@HgS core shell nanocomposites. The capping of these nanocomposites with a CdS outer shell has been performed by re-precipitation of displaced Cd^{2+}, on the CdS/HgS particle surface, followed by the dropwise addition of a dilute solution of H_2S. The final particle diameter was estimated as 77 Å ± 12 Å. The authors[80] reported fluorescence measurements in which the band-edge emission for CdS/HgS/CdS (1-3 monolayers of HgS between CdS) is shifted to lower energy as the HgS monolayer becomes thicker.

The organic functionalization of semiconductor nanocrystals provides the means to use these materials as building blocks to fabricate hybrid nanostructures. A possible approach involves the use of (macro)molecules carrying specific functional groups to coordinate to the particles surface and which further react to form more complex nanostructures. Ideally the resulting dots should have surfaces bearing chemically active sites and improved molecular moieties such as cromophores or redox centers. Pietro *et al.* reported the preparation of CdS nanocrystals by the controlled mixing of a solution containing Na_2S and cadmium acetate at room temperature, in the presence of 4-mercaptoaniline.[81] Following purification, stabilized 4-mercaptoaniline surface passivated CdS nanocrystals were obtained. The organic coating provides a platform for linking chemically active functionalities. In this case the thiol derivatized nanocrystals were subjected to different coupling procedures,[82] promoting the reaction between the aniline nitrogen at the particles surface, with molecules containing a carboxylic acid, amide or chloride terminal, and an alternative group (R) that should provide special characteristics to the surface. The electronic absorption spectra of derivatized CdS nanocrystals showed confinement effects, affording a band gap energy of 3.27 eV (2.53 eV for bulk CdS), and 2.1 nm in diameter. The absorption spectra of the CdS nanocrystals do not change significantly after derivatization, suggesting that the inorganic core was maintained intact. The same authors showed that the thiolate-capped CdS nanocrystals (3 nm) photo-decompose to yield bulk CdS and a single organic product, the symmetric disulfide corresponding to the thiolate cap. Furthermore, they report that the decomposition rate is enhanced by both electron donors and acceptors in the 4-position of the thiolate capping agent, and is strongly correlated with the fluorescence quenching efficiency of the substituted cap. These results drove the investigators to the conclusion that there is a facile electronic contact between the core of the semiconductor and the remote substitutes, which is an important criterion for the realization of activity in novel electronic and optical devices. The state of the art on the fabrication of functional inorganic-organic nanostructures from nano-building blocks has been recently reviewed.[83]

4.2. Nanocrystals Assemblies

There has been an increasing interest on the use of chemical synthesis accomplished with assembly methods to build nanoelectronic components. It is believed that the electronic devices for the next generation will consist of integrated circuits of nanoscale and molecular units. Although important in this context, supramolecular devices are beyond the scope of this chapter and will not be discussed here. At the nanoscale, single electron tunneling and quantum size effects are noticeable and can be used at room temperature. Recent advances have been reported such as single electron-transistors[84] or the use of carbon nanotubes as electron field emitters.[85] To take advantage of the unique properties of nanocrystals in nanodevices, it is crucial the formation of superstructures

with long-range order. Some assembly chemical methods have been investigated, including:

i) Colloidal crystallization,
ii) Langmuir-Blodgett (LB) manipulation
iii) Layer-by-Layer (LbL) deposition.

The use of scanning probe techniques to organize nanoscale patterns will not be considered here. There are some fundamental requirements in order to assemble inorganic nanocrystals using chemical methods. These include the availability of nanocrystals with a high degree of monodispersity, an efficient surface functionalization and chemical stability. When the appropriate conditions are found, such high quality nanocrystals can assemble into well-ordered superstructures by simple techniques. An interesting example is the formation of colloidal crystals obtained by the selective crystallization of capped CdSe/TOPO dispersed in organic solvents.[86] The highly monodispersed CdSe nanocrystals (< 5%) pack into a hexagonal pattern forming three dimensional ordered structures. The optical properties of the superlattice retain the main characteristics of the starting CdSe nanocrystals, including size tuned photoluminescence behavior; small red-shifts in the emission spectra were assigned to inter-nanocrystal coupling. Underlying the mechanism of this self-assembly process are nanocrystal-specific interactions not yet fully elucidated. Fitzmaurice *et al.* have anticipated some possible explanations related to the formation of thiol capped Ag nanocrystal superlattices.[87] The capped inorganic nanocrystals behave as soft balls, the organic ligands filling the voids between the Ag cores, hence determining the interparticle spacing. Entropy effects at high particle volume fractions drive the proper positioning of the capped Ag nanocrystals into an extended face centered cubic structure. Since these two studies refer to distinct nanocrystal systems, a semiconductor (TOPO capped CdSe) and a metal (thiol capped Ag), some caution should be present in drawing conclusions about a possible common assembly mechanism. Undoubtedly this is an area requiring further investigation at a fundamental level.

Langmuir-Blodgett (LB) techniques have seen a renewed interest associated to nanodevice fabrication. Typically, LB thin films are prepared by the layer-by-layer deposition of amphiphilic molecules onto a substrate, using a Langmuir trough. The films consist of arrays of monolayers showing a high degree of organization. Compared to other deposition techniques, the LB manipulation allows a high degree of order over large areas and high control over packing. However, in order to prepare reliable nanodevices using conventional LB techniques there are also some limitations to overcome, including: photodegradation, slow disorganization of the monolayers with time and the high number of deposition cycles required to get an appropriate thickness for the film. The LB technique as a possible route to prepare nanostructures may be approached by two main strategies:

i) the *in situ* preparation of nanocrystals within deposited monolayers;
ii) the assembly of as prepared organically capped nanocrystals into LB monolayers.

In the first method, the synthetic and assembly processes are performed concomitantly. As discussed before, this methodology relies on the concept of nanocrystal synthesis in confined spaces.[87] The second method has been less investigated to produce monolayers of well-defined nanocrystals.[88-90] Compared to conventional LB

monolayers, there are advantages in using such an approach to build nanostructured films. The films are formed by robust units (passivated nanocrystals) and hence display enhanced photo and chemical stability. Moreover, the film thickness and state of organization of the films can be controlled by size fractionation and surface passivation of the starting nanocrystals. Cadmium chalcogenide nanocrystals capped with TOPO molecules have been deposited on glass substrates using the LB technique.[88,89] CdSe monolayers obtained by this process have been characterized[88] showing a hexagonal packing array as observed for the CdSe nanocrystals superlattices mentioned previously.[86]

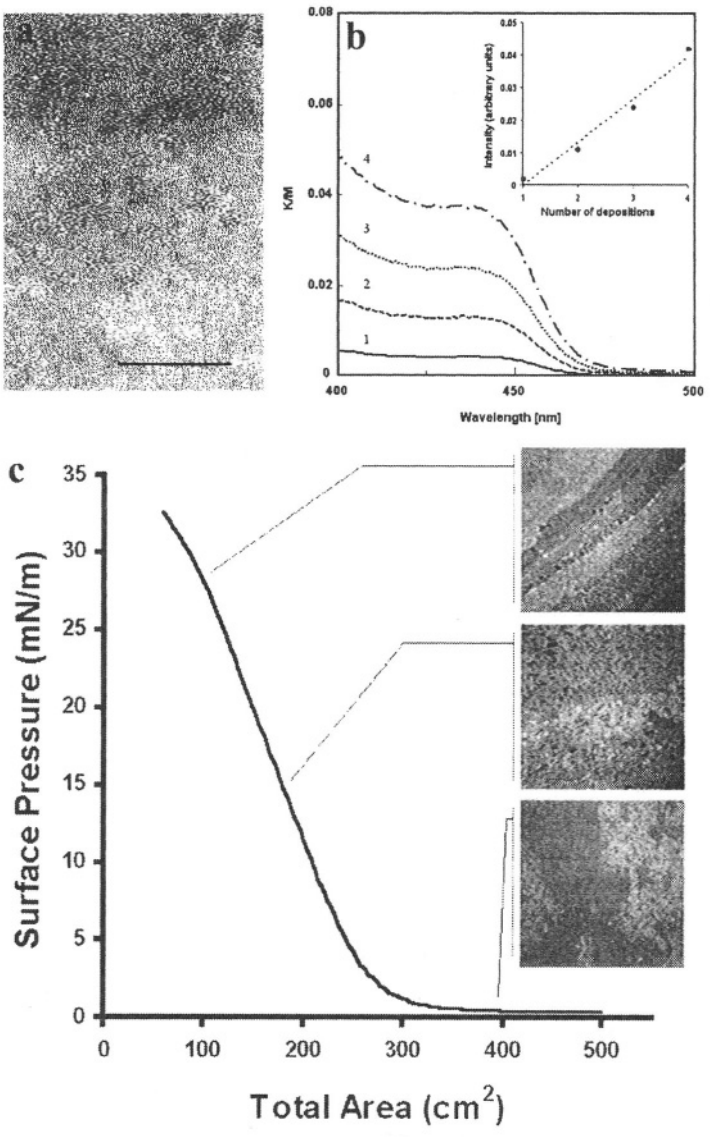

Figure 4. Langmuir-Blodgett manipulation of TOPO capped CdS nanocrystals: (a) TEM image of the starting material (bar=20 nm); (b) Kubelka-Munk spectra of deposited monolayers on polymer treated glass substrates; (c) Langmuir isotherm and Brewster angle measurements. Reproduced with permission from ref. 90. Copyright 2001, Elsevier.

The LB manipulation studies of TOPO capped CdS nanocrystals prepared by a single source method,[90] including Langmuir isotherms and Brewster angle measurements, suggest that the nanocrystals do not form true monolayers, in the sense usually applied to amphiphilic molecules (Figure 4). Using this technique, the CdS nanocrystals have been deposited on neat glass as well as in polymer coated glass substrates. Comparative photoluminescence studies performed on the CdS nanostructured films and the starting nanocrystals, suggest that the main optical features of the starting nanocrystals were maintained in the final nanostructure.

Finally a brief mention to the LbL deposition method using polyelectrolytes.[91,92] This assembly method is technically simple although requiring the strict control of deposition parameters. The high quality of the final assemblies associated to the simplicity and wide applicability of LbL, makes this approach a very interesting process to obtain ordered assemblies of inorganic nanocrystals for industrial production. The LbL assembly of inorganic nanocrystals is based on the alternate dip coating of a substrate, using a solution containing high molecular weigh chemical species (polyelectrolyte) and a dispersion of the nanocrystals. Distinct substrates can be used and they are normally homogeneously coated with a polyelectrolyte with numerous charged chemical sites available. Obviously the type of polyelectrolytes chosen depends on the nanocrystals surface properties. The polyelectrolytes and the nanocrystals form a hybrid layered superstructure stabilized by electrostatic forces and van der Walls interactions. The film thickness, ranging from the nanometer to sub-micron range, can be controlled by the number of dip-coating steps in a cyclic process. Provided the substrate is optically transparent, the deposition process can be monitored by measuring the absorbance as a function of the number of deposited layers, at a characteristic wavelength. This assembly method has been applied successfully to a variety of semiconductor nanocrystals, as well as to other inorganic systems such as polyoxometalates, metal oxides and lamellar materials.

5. CONCLUSIONS AND OUTLOOK

Much progress has been achieved during the last decade in understanding fundamental phenomena related to semiconductor nanocrystals. This fundamental research has been dependent on the availability of synthetic methods to produce high quality nanocrystals. Although this has been achieved for a number of nanocrystalline semiconductors, there is still a need of reliable synthetic processes for other types of nanostructures. The preparation of semiconductor nanocrystals with controlled doping and the preparation of epitaxial hetero-nanostructures are just two examples. Unsurprisingly the assembly of semiconductor nanocrystals into superstructures with long-range order has been less investigated, since to date semiconductor nanochemistry has developed mainly the control on the particle sizes and the nanocrystals characterization. The unprecedented progress observed in semiconductors nanochemistry teaches us that the foresight of research directions in this area is a daring exercise. Nevertheless, the fabrication of functional nanodevices using assembly methods associated to surface modification strategies will be a major breakthrough in Chemistry.

6. REFERENCES

1. A. Henglein, Small-particle research-physicochemical properties of extremely small colloidal metal and semiconducting particles, *Chem. Rev.* **89**, 1861-1873 (1989).
2. M. G. Bawendi, M. L. Steigerwald, and L. E. Brus, The quantum mechanics of larger semiconductor clusters ("quantum dots"), *Ann. Rev. Mater. Sci.* **41**, 477-496 (1989).
3. H. Weller, Quantized semiconductor particles: a novel state of matter for materials science, *Adv. Mater. 5,* 88-95(1993).
4. A. Hagfeldt and M. Grätzel, Light-induced redox reactions in nanocrystalline systems, *Chem. Rev.* 95, 49-68 (1995).
5. A. P. Alivisatos, Perspectives on the physical chemistry of semiconductor nanocrystals, *J. Phys. Chem.* **100**, 13226-13239 (1996).
6. T. Trindade and P. O'Brien, Nanocrystalline semiconductors: synthesis, properties and perspectives, *Chem. Mater.* **13,** 3843-3858 (2001).
7. S. H. Tolbert and A. P. Alivisatos, The wurtzite to rock-salt structural transformation in CdSe nanocrystals under high pressure, *J. Chem. Phys.* **102**, 4642-4656 (1995).
8. H. Haug and S. W. Koch, Quantum theory of the optical and electronic properties of semiconductors, World Scientific Publishing Co. Pte. Ltd: London, 1990, p.333.
9. L. E. Brus, A simple model for the ionization potential, electron affinity, and aqueous redox potentials of small semiconductor crystallites, *J. Chem. Phys.* **79**, 5566-5571 (1983).
10. L. E. Brus, Electron-electron and electron-hole interactions in small semiconductor crystallites: the size dependence of the lowest excited electronic state, *J. Chem. Phys.* **80**, 4403-4409 (1984).
11. L. E. Brus, Electron wave functions in semiconductor clusters: experiment and theory, *J. Phys. Chem* **90**, 2555-2560(1986).
12. Y. Kayanuma, Wannier exciton in microcrystals, *Solid State Commun.* **59**, 405-408 (1986).
13. Y. Wang and N. Herron, Nanometer-sized semiconductor clusters: materials synthesis, quantum size effects, and photophysical properties, J. *Phys.Chem.* 95, 525-532 (1991).
14. P. E. Lippens and M. Lannoo, Calculation of the band gap for small CdS and ZnS crystallites, *Phys. Rev. B* **39**, 10935-10942 (1989).
15. Y. Nosaka, Finite depth spherical well model for excited states of ultrasmall semiconductor particles. An application, *j. Phys.Chem* **95**, 5054-5058 (1991).
16. M. V. Rama Krishna and R. A Friesner, Quantum confinement effects in semiconductor clusters, *J. Chem. Phys.* **95**, 8309-8322 (1991).
17. L. Spanhel, M. Haase, H. Weller, and A. Henglein, Photochemistry of colloidal semiconductors. 20. Surface modification and stability of strong luminescing CdS particles, *J. Am. Chem. Soc.* **109**, 5649-5655 (1987).
18. S. A. Majetich and A. C. Carter, Surface effects on the optical properties of cadmium selenide quantum dots, *J. Phys.Chem* **97**, 8727-8731 (1993).
19. H. S. Zhou, H. Sasahara, I. Honna, H. Komiyama, and *J.* W. Haus, Coated semiconductor nanoparticles: the CdS/PbS system's photoluminescence properties, *Chem. Mater.* **6**, 1534-1541 (1994).
20. M. Nirmal, B. O. Dabbousi, M. G. Bawendi, J. J. Macklin, J. K. Trautman, T. D. Harris, and L. E. Brus, Fluorescence intermittency in single cadmium selenide nanocrystals. *Nature* **383**, 802-804 (1996).
21. M. Gao, S. Kirstein, H. Möhwald, A. L. Rogach, A. Kornowski, A. Eychmüller, and H. Weller, Strongly photoluminescence CdTe nanocrystals by proper surface modification, *J. Phys.Chem* **102**, 8360-8363 (1998).
22. Y. Wang, N. Herron, W. Mahler, and A. Suna, Linear and nonlinear-optical properties of semiconductor clusters, *J. Opt. Soc. Am. B* **6**, 808-813 (1989).
23. Y. Wang, Nonlinear optical properties of nanometer-sized semiconductor clusters, *Acc. Chem. Res.* **24**, 133-139 (1991).
24. S. Hotchandani and P. V. Kamat, Charge-transfer processes in coupled semiconductor systems. Photochemistry and photoelectrochemistry of the colloidal CdS-ZnO system, *J. Phys.Chem* **96**, 6834-6839 (1992).
25. J. M. Nedeljkovic, M. T. Nenadovic, O. I. Micjic, and A. J. Nozik, Enhanced photoredox chemistry in quantized semiconductor colloids, *J. Phys.Chem* **90**, 12-13 (1996).
26. M. G. Bawendi, Optical gain and stimulated emission in nanocrystal quantum dots, *Science* **290**, 314-317 (2000).
27. V. I. Klimov and M. G. Bawendi, Ultrafast carrier dynamics, optical, amplification, and lasing in nanocrystal quantum dots, *MRS Bulletin* **26**, 998-1004 (2001).

28. M. Bruchez, M. Moronne, P. Gin, S. Weiss, and A. P. Alivisatos, Semiconductor nanocrystals as fluorescent biological labels, *Science* **281**, 2013-2016 (1998).
29. W. C. W. Chan and S. Nie, Quantum dot bioconjugates for ultrasensitive nonisotopic detection, *Science* **281**, 2016-2018 (1998).
30. N. Chestnoy, T. D. Harris, R. Hull, and L. E. Brus, Luminescence and photophysics of CdS semiconductor clusters: the nature of the emitting electronic state, *J. Phys. Chem.* 90, 3393-3399 (1986).
31. M. O'Neil, J. Marohn, and G. McLendon, Dynamics of electron –hole pair recombination in semiconductor clusters, *J. Phys. Chem.* 94, 4356-4363 (1990).
32. K. Sooklal, B. S. Cullum, S. M. Angel, and C. J. Murphy, Photophysical properties of ZnS nanoclusters with spatially localized Mn^{2+}, *J. Phys. Chem.* **100**, 4551-4555 (1996).
33. T. F. Towey, A. Khan-Lodi, and B. H. Robinson, Kinetics and mechanism of formation of quantum-sized cadmium sulphide particles in water-aerosol-OT-oil microemulsions, *J. Chem. Soc. Faraday Trans.* 86, 3757-3762 (1990).
34. Y. Wang and N. Herron, Optical properties of CdS and PbS clusters encapsulated in zeolites, *J. Phys. Chem.* **91**, 257-260 (1987).
35. T. Cassagneau, G. B. Hix, D. J. Jones, P. Maireles-Torres, M. Rhomari, and J. Roziere, Nano/nanocomposites systems: in situ growth of particles and clusters of semiconductor metal sulfides in porous silica-pillared layered phosphates, *J. Mater. Chem.* **4**, 189-195 (1994).
36. M. Moffitt and A. Eisenberg, Size-control of nanoparticles in semiconductor-polymer composites. 1. Control via multiplet aggregation numbers in styrene-based random ionomers, *Chem. Mater.* **7**, 1178-1184 (1995).
37. K. M. Choi and K. J. Shea, Amorphous polysilsesquioxanes as a confinement matrix for quantum-sized particle growth. Size analysis and quantum size effect of CdS particles grown in porous polysilsesquioxanes, *J. Phys. Chem.* **98**, 3207-3214 (1994).
38. R. Rossetti, R. Hull, J. M. Gibson, and L. E. Brus, Excited electronic states and optical spectra of ZnS and CdS crystallites in the almost-equal-to-15 to 50 A size range-evolution from molecular to bulk semiconducting properties, *J. Chem. Phys.* **82**, 552-559 (1985).
39. R. Rossetti, J. L. Ellison, J. M. Gibson, and L. E. Brus, Size effects in the excited electronic states of small colloidal CdS crystallites, *J. Chem. Phys.* **80**, 4464-4469 (1984).
40. H. J. Watzke and J. H. Fendler, Quantum size effects in situ generated colloidal CdS particles in dioctadecyldimethylammonium chloride surfactant vesicles, *J. Phys. Chem.* **91**, 854-861 (1987).
41. N. A. Kotov, F. C. Meldrun, C. Wu, and J. Fendler, Monoparticulate layer and Langmuir-Blodgett-type multiparticulate layers of size-quantized cadmium sulfide clusters: a colloidal chemical approach to superlattice construction, *J. Phys. Chem.* **98**, 2735-2738 (1994).
42. B. A. Korgel and H. G. Monbouquette, Synthesis of size-monodispersed CdS nanocrystals using phosphatidylcholine vesicles, *J. Phys. Chem.* **100**, 346-351 (1996).
43. T. Vossmeyer, L. Katsikas, M. Giersig, I. G. Popovic, K. Diesner, A. Chemseddine, A. Eychmüller, and H. Weller, CdS nanoclusters: synthesis, characterization, size dependent oscillator strength, temperature shift of the excitonic transition energy, and reversible absorbance shift, *J. Phys. Chem.* **98**, 7665-7673 (1994).
44. M. Ohtaki, K. Oda, K. Eguchi, and H. Arai, Preparation of nanosized CdS particles using decomposition of P_2S_5 in a non-aqueous solvent, *Chem. Commun.* 1209-1210 (1996).
45. C. B. Murray, D. J. Norris, and M. G. Bawendi, Synthesis and characterization of nearly monodisperse CdE (E=S,Se,Te) semiconductor nanocrystallites, *J. Am. Chem. Soc.* **115**, 8706-8715 (1993).
46. T. Trindade, P. O'Brien, and X. Zhang, Synthesis of CdS and CdSe nanocrystallites using a novel single-molecule precursors approach, *Chem. Mater,* **9**, 523-530 (1997).
47. M. Lazell and P. O'Brien, Synthesis of CdS nanocrystals using cadmium dichloride and trioctylphosphine sulfide, *J. Mater. Chem.* **9**, 1381-1382 (1999).
48. J. R. Babcock, R. W. Zehner, and L. R. Sita, A heterocumulene metathesis route to $Cd[ESiMe_3]_2$ and passivated CdE (E= S and Se) nanocrystals, *Chem. Mater.* **10**, 2027-2029 (1998).
49. S. Yu, Y. Wu, J. Yang, Z. Han, Y. Xie, Y. Qian, and X. Liu, A novel solventothermal synthetic route to nanocrystalline CdE (E= S, Se, Te) and morphological control, *Chem. Mater.* **10**, 2309-2312 (1998).
50. N. Herron, J. C. Calabrese, W. E. Farneth, and Y. Wang, Crystal structure and optical properties of $Cd_{32}S_{14}(SC_6H_5)_{36}$. DMF, a cluster with a 15 Angstrong core, *Science* **259**, 1426-1428 (1998).
51. T. Vossmeyer, G. Reck, L. Katsikas, E. T. K. Haupt, B. Schulz, and H. Weller, A "double-diamond superlattice" built up of $Cd_{17}S_4(SCH_2CH_2OH)_{26}$ clusters, *Science* **267**, 1476-1479 (1995).
52. T. Lover, G. A. Bowmaker, J. M. Seakins, R. P. Cooney, and W. Henderson, Preparation of a novel CdS material from a thiophenolate-capped CdS cluster by chemical removal of SPh- ligands, *J. Mater. Chem.* **7**, 647-651 (1997).

53. A. C. C. Esteves and T. Trindade, Synthetic studies on II/VI semiconductor quantum dots, *Curr. Opin. Solid State Mater. Sci.,* in press.
54. M. L. Steigerwald, A. P. Alivisatos, J. M. Gibson, T. D. Harris, A. R. Kortan, A. J. Muller, A. M. Thayer, T. M. Duncan, D. C. Douglass, and L. E. Brus,Surface derivatization and isolation of semiconductor cluster molecules, *J. Am. Chem. Soc.* **110**, 3046-3050 (1988).
55. A. R. Kortan, R. Hull, R. L. Opila, M. G. Bawendi, M. L. Steigerwald, P. J. Carroll, and L. E. Brus, Nucleation and growth of CdSe on ZnS quantum crystallite seeds, and vice versa, in inverse micelle media, *J. Am. Chem. Soc.* **112**, 1327-1332 (1990).
56. J. R, Agger, M. W. Anderson, M. E. Pemble, O. Terasaki, and Y. Nozue, Growth of quantum-confined indium phosphide inside MCM-41, *J. Phys. Chem. B* **101**, 3345-3353 (1998).
57. J. P. Carpenter, C. M. Lukehart, D. O. Henderson, R. Mu, B. D. Jones, R. Glosser, S. R. Stock, J. E. Wittig, and J. G. Zhu, Formation of crystalline germanium nanoclusters in a silica xerogel matrix from an organogermanium precursor, *Chem. Mater.* **8**, 1268-1274 (1996).
58. Y. Wang, A. Suna, W. Mahler, and R. Kasowski, PbS in polymers. From molecules to bulk solids, *J. Chem. Phys.* **87**, 7315-7321 (1987).
59. Y. Tian, C. Wu, N. A. Kotov, and J. H. Fendler, Morphology-dependent spectroelectrochemical behavior of PbS nanoparticulate films grown under surfactant monolayers, *Adv. Mater.* **6**, 959-962 (1994).
60. R. S. Urquhart, D. N. Furlong, T. Gengenbach, N. J. Geddes, and F. Grieser, Studies of the formation and growth of Q-state cadmium selenide particles in cadmium arachidate Langmuir-Blodgett films, *Langmuir* **11**, 1127-1133(1995).
61. L. Spanhel, H. Weller, A. Fojtik, and A. Henglein, Photochemistry of semiconductor colloids. 17. Strong luminescing CdS and CdS-Ag_2S particles, *Ber. Bunsenges. Phys. Chem.* **91**, 88-94 (1987).
62. B. Ludolph, M. A. Malik, P. O'Brien, and N. Revaprasadu, Novel single molecule precursor routes for the direct synthesis of highly monodispersed quantum dots of cadmium and zinc sulfide or selenide, *Chem. Commun.* 1849-1850(1998).
63. M. Danek, K. F. Jansen, C. B. Murray, and M. G. Bawendi, Synthesis of luminescent thin-film CdSe/ZnSe quantum dot composites using CdSe quantum dots passivated with an overlayer of ZnSe, *Chem. Mater.* **8**, 173-180 (1996).
64. O. I. Micic, J. R. Sprague, C. J. Curtis, K. M. Jones, J. L. Machol, A. J. Nozic, H. Giessen, B. Fluegel, G. Mohs, and N. Peyghambarian, Synthesis and characterization of InP, GaP, and $GaInP_2$ quantum dots, *J. Phys. Chem.* **99**, 7754-7759 (1995).
65. A. A. Guzelian, J. E. B. Katari, A. V. Kadavanich, U. Banin, K. Hamad, E. Juban, A. P. Alivisatos, R. H. Wolters, C. C. Arnold, and J. R. Heath, Synthesis of size-selected, surface-passivated InP nanocrystals, *J. Phys. Chem.* **100**, 7212-7219 (1996).
66. A. A. Guzelian, U. Banin, A. V. Kadavanich, X. Peng, and A. P. Alivisatos, Colloidal chemical synthesis and characterization of InAs nanocrystal quantum dots, *Appl. Phys. Lett.* **69**, 1432-1434 (1996).
67. M. Green and P. O'Brien, A novel synthesis of cadmium phosphide nanoparticles using the single-source precursor $[MeCdPtBu_2]_3$, *Adv. Mater.* **10**, 527-528 (1998).
68. T. Trindade, P. O'Brien, X. Zhang, and M. Motevalli, Synthesis of PbS nanocrystallites using a novel single molecule precursors approach: X-ray single-crystal structure of $Pb(S_2CNEtPr^i)_2$, *J. Mater. Chem.***7**, 1011-1016 (1997).
69. T. Trindade, O. C. Monteiro, P. O'Brien, and M. Motevalli, Synthesis of PbSe nanocrystallites using a single-source method. The X-ray crystal structure of lead (II) diethyldiselenocarbamate, *Polyhedron* **18**, 1171-1175 (1999).
70. C. B. Murray, S. Sun, W. Gaschler, H. Doyle, T. A. Betley, and C. R. Kagan, Colloidal synthesis of nanocrystals and nanocrystal superlattices, *IBM J. Res. Dev.* **45**, 47-56 (2001).
71. O. C. Monteiro, H. I. S. Nogueira, T. Trindade, and M. Motevalli, Use of dialkyldithiocarbamato complexes of bismuth (III) for the preparation of nano- and micro-sized Bi_2S_3 particles and the X-ray crystal structures of $[Bi\{S_2CN(CH_3)(C_6H_{13})\}_3]$ and $[Bi\{S_2CN(CH_3)(C_6H_{13})\}_3(C_{12}H_8N_2)]$, *Chem. Mater.* **13**, 2103-2111 (2001).
72. L. Manna, E. C. Scher, and A. P. Alivisatos, Synthesis of soluble and processable rod-, arrow-, teardrop, and tetrapod-shaped CdSe nanocrystals, *J. Am. Chem. Soc.* **122**, 12700-12706 (2000).
73. V. S. Gurin, A variety of metal chalcogenide clusters: MOLCAO calculations and interplay between quantum-sized semiconductors and multinuclear complexes, *Colloids Surf. A* **202**, 215-222 (2002).
74. J. Rodriguez Viejo, F. V. Mikulec, J. R. Heine, H. Mattossi, R. Ober, K. F. Jensen, and M. G. Bawendi, (CdSe)ZnS core-shell quantum-dots: synthesis and characterization of a size series of highly luminescent nanocrystallites, *J. Phys. Chem. B* **101**, 9463-9475 (1997).
75. P. Mulvaney, L. M. Liz-Marzán, M. Giersig, and T. Ung, Silica encapsulation of quantum dots and metal clusters, J. *Mater. Chem.* **10**, 1259-1270 (2000).

76. I. Tissot, C. Novat, F. Lefebvre, and E. Bourgeat-Lami, Hybrid latex particles coated with silica, *Macromolecules* **34**, 5737-5739 (2001).
77. A. Sayari and S. Hamoudi, Periodic mesoporous silica-based organic-inorganic nanocomposite materials, *Chem. Mater.* **13**, 3151-3168 (2001).
78. M. A. Correa-Duarte, M. Giersig, and L. M. Liz-Marzán, Stabilization of CdS semiconductor nanoparticles against photodegradation by a silica coating procedure, *Chem. Phys. Lett.* **286**, 497-501 (1998).
79. O. C. Monteiro, A. C. C. Esteves, and T. Trindade, The synthesis of SiO_2@CdS nanocomposites using single-molecule precursors, *Chem. Mater.* **14**, 2900-2904 (2002).
80. A. Mews, A, Eychmüller, M. Giersig, D. Schloss, and H. Weller, Preparation, characterization and photophysics of the quantum dot quantum well system CdS/HgS/CdS, *J. Phys. Chem.* **98**, 934-940 (1994).
81. W. J. Pietro, J. G. C. Veinot, J. Galloro, L. Pugliese, V. Bell, and R. Pestrin, Surface functionalization of CdS quantum-confined nanoclusters: 4. Formation and reactivity of an aniline surface quantum dot, *Can. J. Chem.* 76, 1530-1539 (1998).
82. J. G. C. Veinot, J. Galloro, L. Pugliese, R. Pestrin, and W. J. Pietro, Surface functionalization of CdS quantum confined nanoclusters: evidence of facile surface-core electronic communication in the photodecomposition mechanism of functionalised quantum dots, *Chem. Mater.* **11**, 642-648 (1999).
83. C. Sanchez, G. J. de A. A. Soler-Illia, F. Ribot, T. Lalot, C. R. Mayer, and V. Cabuil, Designed hybrid organic-inorganic nanocomposites from functional nanobuilding blocks, *Chem. Mater.* **13**, 3061-3083 (2001).
84. D. L. Klein, R. Roth, A. K. L. Lim, A. P. Alivisatos, and P. L. McEuen, A single electron transistor made from a cadmium selenide nanocrystals, *Nature* **389**, 699-701 (1997).
85. W. A. Der Heer, J. M. Bonard, K. Fouth, A. Chatelain, L. Forro, and D. Ugarte, Electron field emitter based on carbon nanotube films, *Adv. Mater.* **9**, 87 (1997).
86. C. B. Murray, C. R. Kagan, and M. G. Bawendi, Self-organization of CdSe nanocrystallites into three-dimensional quantum dot superlattices, *Science* **270**, 1335-1338 (1995).
87. P. Facci, V. Erokhin, A. Tronin, and C. Nicolini, Formation of ultrathin semiconductor films by CdS nanostructured aggregation, *J. Phys. Chem.* **98**, 13323-13327 (1994).
88. B. O. Dabbousi, C. B. Murray, M. F. Rubner, and M. G. Bawendi, Langmuir-Blodgett manipulation of size-selected CdSe nanocrystallites, *Chem. Mater.* 6, 216-219 (1994).
89. S. R. Cordero, P. J. Carson, R. A. Estabrook, G. F. Strouse, and S. K. Buratto, Photo-activated luminescence of CdSe quantum dot monolayers, *J. Phys. Chem. B* **104**, 12137-12142 (2000).
90. P. M. S. Ferreira, A. B. Timmons, M. C. Neves, P. Dynarowicz, and T. Trindade, Langmuir-Blodgett manipulation of capped cadmium sulfide quantum dots, *Thin Solid Films* **389**, 272-277 (2001).
91. G. Decher, Fuzzy nanoassemblies: toward layered polymeric multifcomposites, *Science* **277**, 1232-1237 (1997).
92. N. A. Kotov, Ordered layered assemblies of nanoparticles, *MRS Bull.* **26**, 992-997 (2001).

This page intentionally left blank

8

INFRARED AND VISIBLE ELECTROCHROMIC SEMICONDUCTOR COLLOID QUANTUM DOTS

Philippe Guyot-Sionnest*

1. INTRODUCTION

Colloidal semiconductor nanostructures are most interesting because they conveniently associate the flexibility of chemical synthesis along with the predictable optical properties of semiconductor materials. The field of quantum confined semiconductor nanocrystals probably originates back to 1980 with the discoveries of Ekimov[1] and Efros.[2] Its extension into colloid chemistry was actively pursued in the 80's, largely under the leadership of Brus,[3] Henglein,[4] and Nozik.[5] By 1993, the monodispersity of the materials was greatly improved with the use of high-temperature solvent and organometallic reagents introduced by C. B. Murray et al.[6] To date, the absorption edge of colloid quantum dots covers the whole spectrum from the UV to the mid-infrared with II-VI, III-V and IV-VI materials, along with high monodispersity and fluorescence efficiency. A typical example is shown by PbSe nanocrystals in Figure 1. In many groups, the processing of the colloid materials is evolving towards core-shell heterostructures, and more complex shapes. Furthermore, self-assembly and directed assembly of colloids is also being investigated with the hope that new functions may arise from the interactions. The stable and high-quality materials have spawned a number of potential applications such as photovoltaic materials, light-emitting diodes and lasers, electrochromic materials and fluorescent markers for biological microscopy.

Various levels of theoretical modelling, have been developed, from the multiband effective mass theories that have been extremely useful and effective[7] to more elaborate atomistic methods[8-10] that promise to provide finer details. From a basic point of view, several physical concepts take on an increased significance in the strongly confined colloid quantum dots. These are exchange interaction,[11-13] Auger effects,[14,15] phonon bottleneck,[16] boundary conditions[17] and charging.[18,19]

There have also been unexpected observations, such as the blinking of the fluorescence,[20] the presence of large dipole moments,[21] a strong Stark effect,[22,23] and spectral diffusion upon photoexcitation.[24,25] To date, these effects have been tentatively assigned to charging and surface charges.

* Philippe Guyot-Sionnest, James Franck Institute, The University of Chicago, Chicago IL 60637.

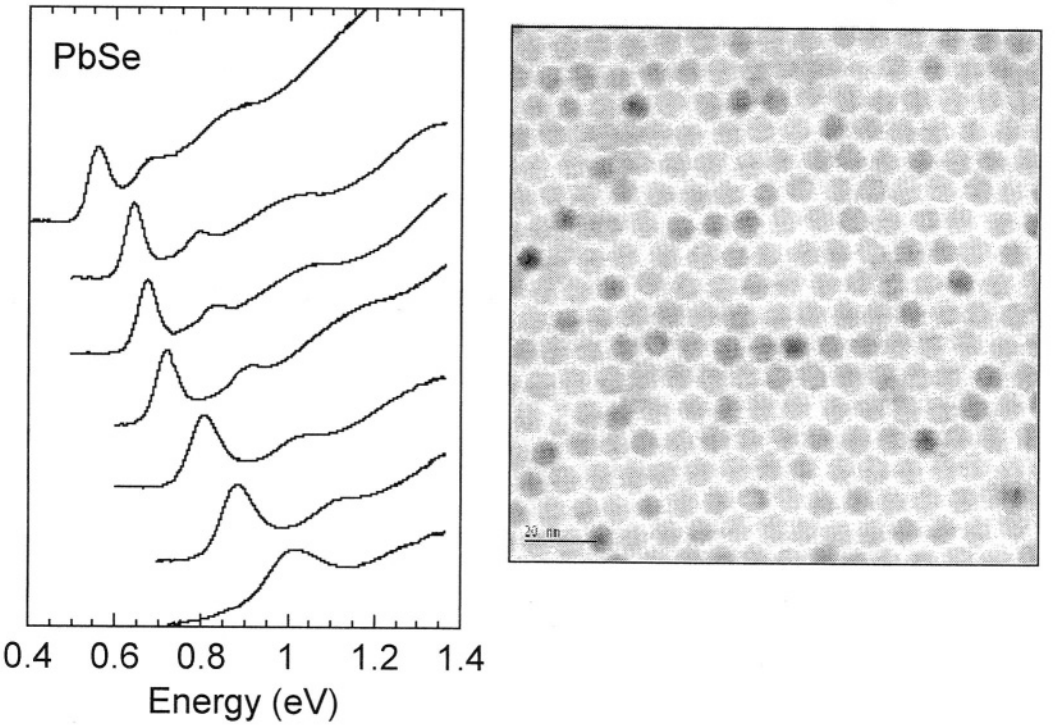

Figure 1. Size dependent linear absorption of monodispersed PbSe nanocrystal colloid solutions. The sizes range from 5 to 10 nm diameter. TEM image of an ordered array of PbSe nanocrystals, the line bar is 20 nm.[26]

Yet, it is in fact unknown whether charging is truly the cause, where the charges are and their exact role. As a consequence, charging is one of the most unknown aspects in the colloid quantum dots.

2. CHARGING AND SEMICONDUTOR QUANTUM DOTS

The combined effects of the sparse density of state and the increasingly large Coulomb energy at small sizes lead to the significant effects of charging. In an ideal quantum dot, charging by occupation of conduction band states (reduction) or extraction from valence band states (oxidation) is expected and observed to lead to bleach of previously allowed interband exciton transitions and appearance of intraband transitions with "giant" oscillator strength in the infared.[27] The interaction between charges is also stronger as the nanocrystal radius becomes smaller, largely exceeding thermal energies at room temperature for small dots.

The controlled charge injection gives a great flexibility in determining the optical and electronic properties of nanocrystals. In the infrared, the presence of a charge in the delocalized quantum states of the "artificial atoms" opens up the intraband transitions with well-defined, strong and easily tunable absorption band. Organic materials are notably lacking these qualities in the infrared, and therefore semiconductor colloids may

provide great opportunities for solution processing of infrared specialty coating and electrooptic materials.

The controlled charging can also tune the electronic transport within nanocrystal close packed films, therefore semiconductor colloids may also someday be used as thin film electronic materials.[28]

In addition to occupying the quantum confined interior states, charging can also arise from the occupation of localized "dark" surface states. Such surface charges have not yet been detected but it is widely understood that they could have a significant effect on the photophysical properties of nanocrystals. One may in fact speculate that one or a few charges could be used to control the quantum dot brightness with potential applications as displays or in the detection of oxidizing or reducing species.

Electrical techniques have been applied to the colloid quantum dots to detect charges and transport through the quantum dots. In the most direct effort to detect charging, Brus and Krauss developed a capacitive AFM technique to monitor charging events in individual surface supported quantum dots.[19,29] The technique showed very interesting results of fluctuating charges under optical excitation but there is not yet an established correlation between the fluorescence characteristics and the charging events. High quality data on transport through individual semiconductor colloid quantum dots have been obtained by Millo, Banin and coworkers with low-temperature STM.[30,31] The data have revealed charging energies associated with the quantum confined states occupation and energy differences that are consistent with the spectroscopic data. The charging energies are in fair agreement with simple expectation, as well as with more elaborate estimates using pesudopotential approaches.[32] To further understand the effect of charging on transport, one should use a gate electrode. This provides the possibility to tune the system right through all surface states and then monitoring the small changes in the transport. This approach has been demonstrated on single nanocrystals using nanolithography techniques by McEuen, Alivisatos and coworkers,[33,34] however the results on nanocrystals have not yet been illuminating. One possible drawback is the practical difficulty to obtain a wide statistics of behaviour. Furthermore, the nanocrystal colloids that are prepared in solution and capped by organic ligands must be transferred to a vacuum environment for the low temperature measurements. This affects the chemical nature of surface and immediate environment of the nanocrystals in unknown ways.

3. SPECTROELECTROCHEMISTRY OF COLLOID QUANTUM DOTS

Electrochemistry is an alternative method to measure charging processes with the solution acting as a gate electrode. In the realm of nanoparticles, the electrochemistry of metallic clusters has been studied for some years. The smallest systems, molecular-like clusters of a few metal atoms, can exhibit very clear and multiple reduction steps.[35] For larger metal nanoparticles, differential pulse voltammetry is a derivative technique that allows small amplitude redox process to be discerned from a larger current background. It was used by R.W. Murray et al. to detect the charging energy of metal nanocrystal colloids of rather high monodispersity.[36] The technique is being recently applied to semiconductor colloids.[37,39] The electrochemistry of semiconductor nanocrystals is little explored and there is still much to be gained by measuring the currents in ensembles of nanocrystals to obtain quantitative information on the charges passed through. For most

semiconductor nanoparticles, voltammetric studies are better performed in non-aqueous electrolytes to limit anodic and cathodic dissolutions.[37-39] Challenges are to reduce or account for the parasitic currents and care must be taken to eliminate water and oxygen from the dried and distilled electrolyte.

With semiconductor colloid for which the optical spectra are a-priori so sensitive to charges, it is particularly advantageous to combine optical spectroscopy with voltammetric methods. As such, spectroelectrochemistry of thin films of quantum confined colloids was first used by Hoyer and Weller.[40,41] At the time, the spectroscopy of the ZnO colloids used in these experiments was not well understood, and the conclusions remained uncertain as to the nature of the mechanism underlying the electrochromic effects.

More recently, we have applied this approach to high quality semiconductor nanocrystals of various materials. We have also extended the optical measurements to the infrared spectral range in order to strengthen the evidence for electron injection. This line of research started when Moonsub Shim first showed that biphenyl radicals could be used to inject electrons in the nanocrystals and the electrochemistry was subsequently developed by Congjun Wang and Moonsub Shim.[27,42,43]

In small monodispersed quantum dots the transitions between quantum states are clearly resolved. Thus, changes in state occupation leads directly to strong electrochromic effects. Figure 2 shows the electrochromic response in visible and infrared spectral ranges upon reducing a thin film of nanocrystals.[27,43,44] The visible spectra show clear bleach of the first exciton transition. In fact, a shoulder can be identified to the high energy side of the first bleach resonance and another transition is clearly bleached about 0.4 eV above. These three features can be assigned to the $1S_e$-$1S_{h3/2}$, $1S_e/2S_{h3/2}$ and $1S_e$-$1S_{h1/2}$ electron-hole excitons. With proper care in the film preparation, the electron occupation of the $1P_e$ state can also be observed providing effectively a voltage controlled chromatic shift.

The infrared provides the most definite evidence of quantum state occupation. The size-tunable IR absorption is due to the intraband transition and can be directly compared to similar infrared absorption observed upon photoexcitation. In the case of CdSe, the IR transition is between the lowest $1S_e$ state of the conduction and the $1P_e$ state manifold as shown in the inset of Figure 2. The strength of the IR transition is also of practical interest. As expected in semiconductor quantum dots, the oscillator strength of the bleached exciton is mostly transferred to the intraband transition, leading to oscillator strength of the order of 5 to 10. This is a large value totally unheard of for any other soluble molecular material, in this mid-infared spectral range. Further spectroscopy experiments have also shown that the homogeneous linewidth of this transition can be much smaller than the overall observed inhomogeneous linewidth,[45] promising further improvement in spectral definition.

With the IR spectra convincingly proving that the electron injection takes place in the quantum state, one may then identify the visible spectral changes with more confidence. Difference spectra of electrochemically reduced nanocrystal films show the bleaches of several transitions. Based on the intraband spectra and the known occupation of the $1S_e$ state, the bleach features can be attributed to excitonic transitions from hole states to $1S_e$ and this agrees reasonably well with the assignments by Norris and Bawendi.

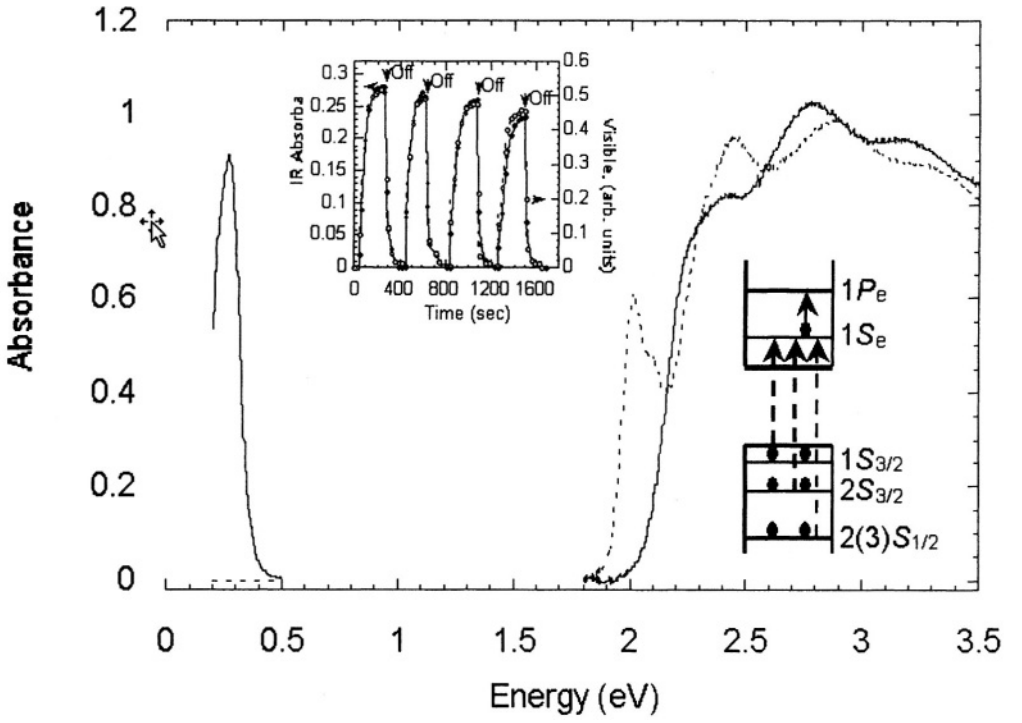

Figure 2. Spectroelectrochemical changes of a thin film of CdSe/TOPO nanocrystals on a Pt electrode in acetonitrile/tetrabutyl ammonium perchlorate electrolyte. Solid line at –1.2 V/ pseudo Ag electrode, and dotted line at 0V. The inset shows the reversibility and the very close relation between the visible bleach and the infrared absorbance. This shows that the bleach is indeed due to the occupation of the $1S_e$ conduction ba quantum state. After ref. 42.

Nevertheless, induced weak absorption features are observed in both colloid solutions and thin films, and probably reflect that is not appropriate to simply assign all features to the $1S_e$ state occupation, neglecting Stark effect or Coulomb interactions which can shift and broaden ensemble transitions.[46] The spectral changes provide also an accurate monitoring of the electron injection potential and using electrochemistry and a reference electrode, Wang et al. measured the reduction potential of CdSe nanocrystals as a function of size,[42,44] For CdSe nanocrystals of sizes between 7 nm and 3 nm, the reduction potential varies from ~ –0.8 V to ~ –1.6 V/SHE, corresponding to rather reducing potentials, that preclude the possibility of these experiments in hydrous conditions.

The stability of the electron injection is strongly function of the dryness and cleanliness of the solutions and the kinetics of charge injection and recovery are strongly affected by the film preparation. In Figure 2, the inset shows the switching kinetics for a film obtained by drop casting CdSe/TOPO nanocrystals. Using a more careful procedure for the film preparation, switching times of less that 100 ms are obtained. Voltammetry data also show the quantitative injection and retrieval of charges from not only the $1S_e$ state but even the $1P_e$ state.[47] An example of the data is shown in Figure 3. Video rates of the electrochromic changes seem to be well within reach.

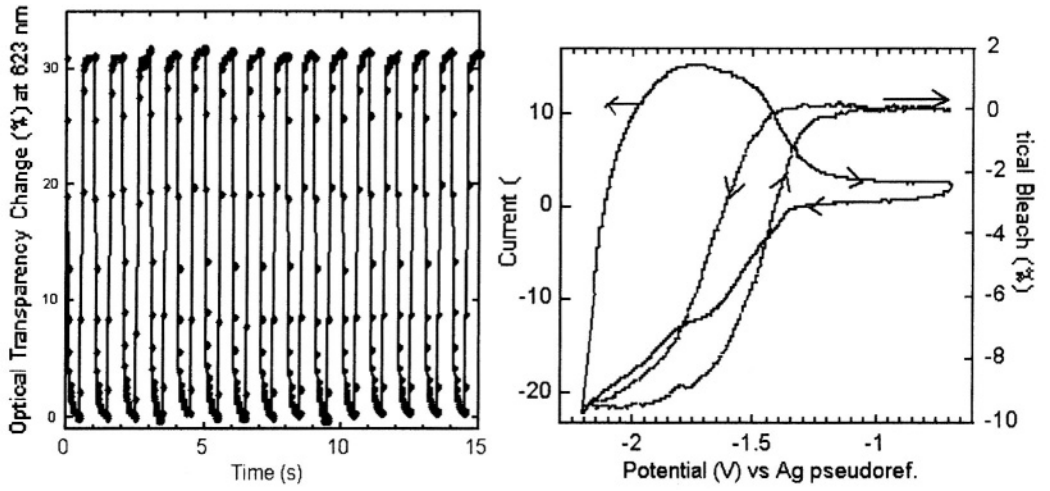

Figure 3. Left: repeated electrochromic switching of the CdSe thin film on ITO electrode at room temperature. Data points are taken every 20 ms. On the right: current (solid line) and bleach (dotted line) for a cyclic voltammogram at 85 mV/s. The electrolyte is dimethyl formamide/0.1M tetrabutyl ammonium perchlorate and the temperature is −50°C

In addition to the spectral changes in absorption, the reduction leads to quenching of the fluorescence. Reduction with biphenyl radicals in solution can lead to a quenching in excess of 10^3 that is fully recoverable after some time.[43] Electrochemistry of thin films of nanocrystals showed also a large quench although not as extensive.[42] A common feature is that while the absorption electrochromic changes are reversibly and directly tied to the occupation of the quantum confined state, the fluorescence quenching appears synchronous to charge injection but the fluorescence recovery is much slower. This is true for both solution and thin film electrochemistry. This suggests that the electron injection readily modifies the nanocrystal, via a low barrier process while the recovery of the nanocrystal is hindered by a higher barrier. The first barrier is supported by the temperature-dependent stability of the electron in the 1Se state, from minutes to hours at room temperature and indefinitely at 10K.

The question remains then as to what is the nature of the mechanism underlying the fluorescence quenching: i) it may be due to charges in the quantum-confined states or at surfaces states, or ii) it is the result of surface chemistry induced by the strongly reducing electrons.

i) Charge induced quenching: a mechanism first developed by Chepic et al for fluorescence quenching of nanocrystals is the Auger process.[14] In the Auger process, the Coulomb interaction between a charge and an exciton can lead to nonradiative recombination of the exciton, at the same time exciting the charge to a higher state. With an electron already in the $1S_e$ state, Auger electron-exciton relaxation leads to a nonradiative recombination rate of order 100 ps, in approximate agreement with bulk CdSe Auger recombination rates. Compared to the triplet state lifetime (> 100 ns) or the singlet lifetime (~ a few ns) this would be sufficient to explain some fluorescence quenching, although probably not 3 orders of magnitude. Furthermore, since the fluorescence is still quenched after the electron is removed from the $1S_e$ state, the Auger process cannot be the sole mechanism. Electrons in surface states could also lead to a

similar interaction, however the possibly smaller density of state and increased physical separation should make it even less efficient. On the other hand, electrons in surface states can be efficient hole traps and ps hole trapping time scales are reasonable.

ii) The surface modification mechanism can only generically be described. One plausible scenario would involve reduction of the surface metal ions to metal, with possibly bond rearrangement. The recovery could then involve the oxidation and removal of the exposed chalcogen surface. This is consistent with the small diameter reduction of about 0.2 nm observed after one complete solution reduction experiment.

At present, the two distinct possibilities have not been experimentally distinguished. In both cases, surface modifications are expected to lead to stability improvement and difference in quenching behavior. For example ZnS capped CdSe nanocrystal are relatively easier to completely reduce (e.g. two electrons in the $1S_e$ state) by exposure to biphenyl, but the fluorescence quenching is not as complete as for TOPO capped CdSe.

Determining the exact mechanism of charge induced fluorescence quenching will be useful in helping stabilizing the reduced nanocrystals. The resolution of the problem may be related to understanding the blinking behavior observed in nanocrystals where the current belief involves tunneling charges. It will also be of practical interest to be able to turn on and off the fluorescence with single electron injection.

4 CONCLUSIONS

Charging of semiconductor nanoparticles is a basic issue that may be behind many unexplained effects including blinking, Stark effects and dipole moments. Spectroelectrochemistry has provided a deep insight into the possibility of redox processes involving the quantum states of nanocrystals. It is now possible to inject electrons in the conduction band of several quantum dot materials leading to switchable and reversible electrochromic changes in the visible and in the mid-IR spectral ranges. There remains still to explain the mechanism underlying the fluorescence quenching observed during charging.

As it is now possible to control charging and the strong effects that it has on the optical properties, new prospects may emerge for applications of colloid quantum dots as electrochromic absorber and fluorophores, in the visible and infared, for example the sensitivity of the fluorescence to charges may lead to sensors of local potential or ionic concentration, or as components of energy efficient fluorescent displays. As electrochromic materials, the colloid quantum dots have unusual properties such as the spectrally narrow and potential-controlled optical bleach and most dramatically the unique infrared response.

5. ACKNOWLEDGMENTS

The recent group activity in part described here is primarily based on the research of most recent group members, Moonsub Shim, Congjun Wang and Brian Wehrenberg, but would not have been possible without the contributions of all other previous members Sean Blanton, Margaret Hines, Mark Schmidt. Over the last few years, funding was provided by the US National Science Foundation, Division of Material Research, as well as a grant from Motorola.

6. REFERENCES

1. A. I. Ekimov, and A. A. Onushchenko, Quantum size-effect in 3-dimensional microscopic semiconductor crystals, *JETP Lett.* **34**, 345-349, (1981); and Quantum size effects in the optical spectra of semiconductor micro-crystals, *Soviet Physics Semicond. -USSR* **16**, 775-778 (1982).
2. Al. Efros and A. L. Efros, Interband absorption of light in a semiconductor sphere, *Soviet Physics Semicond.-USSR* **16**, 772-775 (1982).
3. M. L. Steigerwald and L. E. Brus, Synthesis, stabilization, and electronic structure of quantum semiconductor nanoclusters, *Ann. Rev. Mater. Sci.* **19**, 471-495 (1989).
4. A. Henglein, Small-particle research-physicochemical properties of extremely small colloidal metal and semiconducting particles, *Chem. Rev.* **89**, 1861-1873 (1989).
5. A. J. Nozik, F. Williams, M. T. Nenadovic, T. Rahj, O. I. Micic, Size-quantization in small semiconductor particles, *J. Phys. Chem.* **89**, 397-399 (1985),
6. C. B. Murray, D. J. Norris, and M. G. Bawendi, Synthesis and characterization of nearly monodisperse CdE (E=S,Se,Te) semiconductor nanocrystallites, *J. Am. Chem. Soc.* **115**, 8706-8715 (1993).
7. A. L. Efros and M. Rosen, The electronic structure of semiconductor nanocrystals, *Ann. Rev. Mater. Sci.* **30**, 475-521 (2000).
8. L. W. Wang and A. Zunger, Pseudopotential calculations of nanoscale CdSe quantum dots, *Phys. Rev. B* **53**, 9579-9582 (1996).
9. S. V. Nair, L. M. Ramaniah, and K. C. Rustagi, Electron states in a quantum dot in an effective bond-orbital model, *Phys. Rev. B* **45**, 5969-5979, (1992).
10. K. Leung, S. Pokrant, and K. B. Whaley, Exciton fine structure in CdSe nanoclusters, *Phys. Rev. B* **57**, 12291-12301 (1998).
11. S. Nomura, Y. Segawa, and T. Kobayashi, Confined excitons in a semiconductor quantum dot in a magnetic field, *Phys. Rev. B,* **49**, 13571-13582 (1994).
12. M. Chamarro, C. Gourdon, P. Lavallard, and A. I. Ekimov, Enhancement of exciton exchange interaction by quantum confinement in CdSe nanocrystals, *Jpn. J. Appl. Phys.* **34**, Suppl. 34-1,12-14 (1995).
13. M. Nirmal, D. J. Norris, M. Kuno, M. G. Bawendi, A. L. Efros, and M. Rosen, Observation of the dark exciton in CdSe quantum dots, *Phys. Rev. Lett.* **75**, 3728-3731 (1995).
14. D. I. Chepik, A. L. Efros, A. I. Ekimov, M. G. Vanov, V. A. Kharchenko, I. A. Kudriavtsev, and T. V. Yazeva, Auger ionization of semiconductor quantum dots in a glass matrix, *J. Lumin. 47,* 113-127 (1990).
15. Efros Al.L. Kharchenko V.A., Rosen M., Breaking the phonon bottleneck in nanometer quantum dots-role of Auger-like process, *Solid State. Commun.* **93**, 281-284 (1995).
16. U. Bockelmann and G. Bastard, Phonon scattering and energy relaxtion in 2-dimensional, one-dimensional and zero-dimensional electron gases, *Phys. Rev. B* **42**, 8947-8951 (1990); H. Benisty, C. M. Sotomayor-Torres, and C. Weisbuch, Intrinsic mechanism for the poor luminescence properties of quantum box systems, *Phys. Rev. B* **44**, 10945-10951 (1991).
17. P. C. Sercel, Al. L. Efros, and M. Rosen, Intrinsic gap states in semiconductor nanocrystals, *Phys. Rev. Lett.* **83**, 2394-2397 (1999).
18. L. E. Brus, A simple model for the ionization-potential, electron affinity, and aqueous redox potentials of small semiconducotr crystallites, *J. Chem. Phys.* **79**, 5566-5571 (1983).
19. T. D. Krauss and L. E. Brus, Charge, polarizability, and photoionization of single semiconductor nanocrystals, *Phys. Rev. Lett.* **83**, 4840-4843 (1999).
20. M. Nirmal, B. O. Dabbousi, M. G. Bawendi, J. J. Macklin, J. K. Trautman, T. D. Harris, L. E. Brus,, Fluorescence intermittency in single cadmium selenide nanocrystals, *Nature* **383**, 802-804 (1996).
21. M. Shim and P. Guyot-Sionnest, Permanent dipole moment and charges in colloidal semiconductor quantum dots, *J. Chem. Phys.* **111**, 6955-6964 (1999).
22. V. I. Colvin, K. I. Cunningham, and A. P. Alivisatos, Electric filed modulation studies of optical absorption in CdSe nanocrystals-dipolar character of the excited state, *J. Chem. Phys.* **101**, 7122-7128 (1994).
23. S. Empedocles and M. G. Bawendi, Influence of spectral diffusion on the line shapes of single CdSe nanocrystallite quantum dots, *J. Phys. Chem.* **103**, 1826-1830 (1999).
24. S. Empedocles and M. G. Bawendi, Quantum-confined stark effect in single CdSe nanocrystallite quantum dots, *Science* **278**, 2114-2117 (1997).
25. S. A. Blanton, M. A. Hines, and P. Guyot-Sionnest, Photoluminescence wandering in single CdSe nanocrystals, *Appl. Phys. Lett.* **69**, 3905-3907 (1996).
26. B. L. Wehrenberg, C. Wang, and P. Guyot-Sionnest, to be published.

27. M. Shim and P. Guyot-Sionnest, N-type colloidal semiconductor nanocrystals, *Nature* **407**, 981-983 (2000).
28. A. L. Roest, J. J. Kelly, D. Vanmaekelbergh, and E. A. Meulenkamp, Staircase in the electron mobility of a ZnO quantum dot assembly due to shell filling, *Phys. Rev. Lett.* **89**, 036801/1-036801/4 (2002)
29. T. D. Krauss, S. O'Brien, L. E. Brus, Charge and photoionization properties of single semiconductor nanocrystals, *J.Phys. Chem. B* **105**, 1725-1733 (2001).
30. O. Millo, D. Katz, Y. W. Cao, and U. Banin, Imaging and spectroscopy of artificial-atom states in core/shell nanocrystal quantum dots, *Phys. Rev. Lett.* **86**, 5751-5754 (2001).
31. D. Katz, O. Millo, S. H. Kan, and U. Banin, Control of charging in resonant tunneling through InAs nanocrystal quantum dots, *Appl. Phys. Lett.* **79**, 117-119 (2001).
32. J. Shumway, A. Franceschetti, and A. Zunger, Correlation versus mean-field contributions to excitons, multiexcitons, and charging energies in semiconductor quantum dots, *Phys. Rev. B* **63**, 155316/1-155316/13, (2001).
33. D. L. Klein, P. L. McEuen, J. E. B. Katari, R. Roth, and A. P. Alivisatos, An approach to electrical studies of single nanocrystals, *Appl. Phys. Lett.* **68**, 2574-2576 (1996).
34. D. L. Klein, R. Roth, A. K. L. Lim, A. P. Alivisatos, and P. L. McEuen, A single-electron transistor made from a cadmium selenide nanocrystal, *Nature* **389**, 699-701 (1997).
35. M. J. Weaver and X. P. Gao, Molecular capacitance-sequential electron-transfer energetics for solution-phase metallic clusters in relation to gas-phase clusters and analogous interfaces, *J. Phys. Chem.* **97,** 332-338 (1993).
36. A. C. Templeton, M. P. Wuelfing, and R. W. Murray, Monolayer protected cluster molecules, *Acc. Chem. Res.* **33**, 27-36 (2000).
37. S. Chen and J. M. Sommers, Alkanethiolate protected PbS nanoclusters:synthesis, spectroscopic and electrochemical studies, *J. Phys. Chem. B* **105**, 8816-8820 (2001).
38. S. K. Haram, B. M. Quinn, A. J. Bard, Electrochemistry of CdS nanoparticles: A correlation between optical and electrochemical band gaps, *J. Am. Chem. Soc.* **123**, 8860-8861 (2001).
39. Z. Ding, B. M. Quinn, S. K. Haram, L. E. Pell, B. A. Korgel, and A. J. Bard, Electrochemistry and electrogenerated chemiluminescence from silicon nanocrystal quantum dots, *Science* **296**, 1293-1297 (2002).
40. P. Hoyer and H. Weller, Size-dependent redox potentials of quantized Zinc Oxide measured with an optically transparent thin layer electrode, *Chem. Phys. Lett.* **221**, 379-384 (1994).
41. P. Hoyer and H. Weller, Potential-dependent electron injection in nanoporous colloidal ZnO films, *J. Phys. Chem.* **99**, 14096-14100 (1995).
42. C. Wang, M. Shim, and P. Guyot-Sionnest, Electrochromic semiconductor nanocrystal films, *Appl. Phys. Lett.* **80**, 4-6 (2002).
43. M. Shim, C. Wang, and P. Guyot-Sionnest, Charge-tunable optical properties in colloidal semiconductor nanocrystals, *J. Phys. Chem. B* **105**, 2369-2373 (2001).
44. C. Wang, M. Shim, and P. Guyot-Sionnest, Electrochromic nanocrystal quantum dots, *Science* **291**, 2390-2392(2001).
45. M. Shim and P. Guyot-Sionnest, Intraband hole burning of colloidal quantum dots, *Phys. Rev. B* **64**, 245342/1-245342/4 (2001).
46. A. Franceschetti and A. Zunger, Optical transitions in charged CdSe quantum dots, *Phys. Rev. B*, **62**, R16287-R16290, (2000).
47. P. Guyot-Sionnest and C. Wang, to be published.

This page intentionally left blank

9

NANOPARTICLES WITH POLYMERIC SURFACES

Fillers and Models for Ultrasoft Colloids

Wolfgang Schaertl*

1. INTRODUCTION

Blending colloidal nanoparticles with linear polymer chains is a well-known strategy to improve the quality of plastic or elastic polymeric materials. One of the most famous examples is carbon black blended into tire rubber to enhance the mechanical properties. In general, colloidal additives may cause a variety of effects within the colloid-polymer blend, concerning, for example, mechanical stability, scratch resistance, optical and magnetic properties. The efficiency of the colloidal filler depends on its miscibility with the polymer chains: the more homogeneous the distribution of the colloidal particles within the matrix, the lower the amount of colloidal additives necessary to achieve the desired effect. However, ordinary colloidal particles with smooth surfaces are incompatible with linear chains for entropic reasons. Phase separation based on the so-called depletion mechanism[1,2] is found. This effect may be overcome by adequate compatibilization strategies: one possibility is to modify the surface of the colloidal particles to achieve an enthalpic compatibility with the polymer host.[3] For example, it is possible to mix colloidal particles coated with polyvinylmethylether (PVME) homogeneously with polystyrene (PS) chains[4] because of the enthalpic compatibility of the two polymers PVME and PS. Here, we will present a way of suppressing depletion demixing which is only based on entropic effects. The advantage of this approach is that the surface modification in our case is chemically identical with the polymer host: polymer chains of the same type as the polymer matrix are grafted onto the colloidal particle surface. Consequently, this coating of the particles should have no unforeseen effects on the desired blend properties based on specific colloid-polymer interactions, as is to be expected for particles modified according to achieve enthalpic compatibility. On the other hand, as will be shown, entropic compatibilization is less effective than enthalpic compatibilization, and is limited basically to comparatively short-chain polymer hosts.

* Wolfgang Schaertl, Institut für Physikalische Chemie, Universität Mainz, Welderweg 11, 55099 Mainz, Germany, E-Mail: schaertl@mail.uni-mainz.de.

Interestingly, our entropically compatibilized colloidal nanoparticles within a matrix of linear polymer chains provide an excellent model for ultrasoft colloids. The effective particle size, interaction pair potential and particle deformability can be adjusted in a very simple way by the particle topology, that is grafting density of the polymer coating and length of the graft chains in respect to the matrix chains. Such soft particles provide an even more important model than the famous hard spheres studied during the last decades due to the fact that they more closely resemble systems of practical use (coatings etc.).

This chapter is organized as follows: first, potential strategies to synthesize model colloidal spherical nanoparticles with surfaces of linear polymer chains are presented and discussed. Note that in the subsequent text the colloidal particle itself will be named *core,* the polymeric coating *hairs,* and the whole particle spherical *polymer brush.* In the second part of this chapter, the compatibility of such spherical brushes with linear polymer chains, in comparison with simple colloidal particles, will be discussed. Finally, using copolymer micelles in a matrix of homopolymer chains as a model spherical brush system blended with linear polymer chains, properties of ultrasoft colloids will be presented. Here, we will focus on the increase of the viscosity with increasing particle concentration which provides a quantitative measure of effective particle size and particle interaction potential.

2. SYNTHESIS OF MODEL PARTICLES

In principle, colloidal particles with surfaces of linear polymer hairs may be synthesized by three different approaches as sketched in Figure 1:

1. Grafting-onto:[5] Colloidal particles and polymeric chains are prepared separately. During this synthesis, certain chemical functionalities have to be introduced on the colloidal surface (SiH-groups) and the chain end (vinylic double bonds), respectively. These functionalities are used later on, to couple the chains with the particle surface by hydrosilylation, that is coupling of SiH and C=C upon platinum catalysis. Advantages of this approach are: well defined core size and hair length, simple characterization due to separate access to both components, simple adjustment of hair number and hair length. The major disadvantage is: for steric reasons, it is not possible to graft a large number of long hairs onto the colloidal surface.

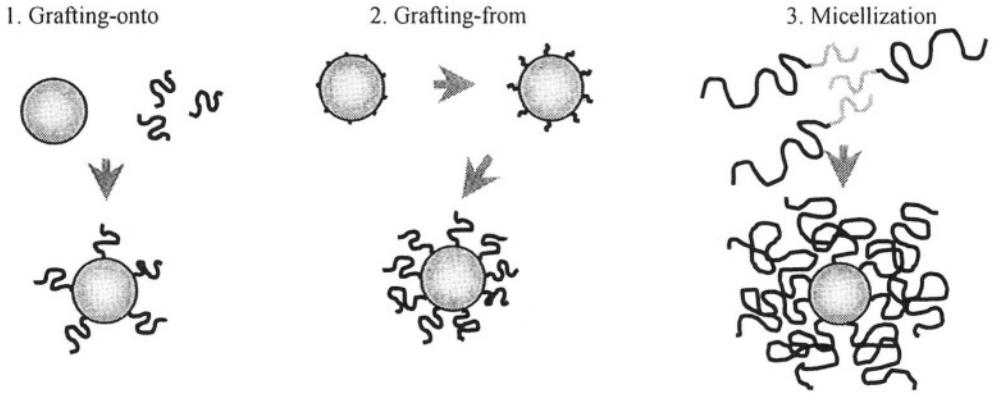

Figure 1. Scheme of the three different synthetic approaches to polymer-modified colloidal particles.

2. Grafting-from: Colloidal particles with polymerization initiator functionalities at the particle surface are prepared. After adding the monomer and starting a living polymerization reaction, for example atom transfer radical polymerization (ATRP), the hairs are growing simultaneously from the colloidal surface. Here, particle characterization is much more complicated (no separate access to core and hairs, besides the hairs could be cleaved from the particle surface after the reaction. In this case, however, the hairy particles could exhibit insufficient stability for further applications.). Since the steric problems encountered during grafting-onto are avoided, grafting-from may yield densely grafted spherical brushes even with very long hairs. An additional disadvantage besides the difficult particle characterization, however, is the larger polydispersity in hair length compared to the grafting-onto procedure.

3. Micellization:[6,7] A method which combines the advantages of both grafting techniques 1 and 2 is the use of asymmetric copolymer chains with two thermodynamically incompatible polymer blocks: these copolymers, being dissolved together with homopolymer chains chemically identical to the longer copolymer block in a solvent for this longer block (and a non-solvent for the shorter block), form spherical micelles in a self-organization process upon evaporation of the solvent. If the shorter block polymer, which forms the core of the micelles, has a much higher glass transition temperature than the corona block polymer, so-called frozen micelles, that is micelles with a solid glassy core embedded in a matrix of molten polymer which is comprised both of the corona and the (chemically identical) homopolymer chains, can be obtained. One disadvantage of the micellization approach is the impossibility to control core size and grafting density exactly, since both depend on the copolymer composition in a complicated way. A second disadvantage is the limitation to copolymer concentrations well above the critical micelle concentration and below the concentration of potential microphase transitions, e.g. from spherical micellar to bicontinuous at very high copolymer concentration. On the other hand, copolymer micelles provide access to spherical brushes containing dye labels within their core simply by using a copolymer chain containing one dye molecule at the chain end of the shorter block. Such particles have been employed successfully as optical tracers to study the diffusional mobility of a spherical brush within a colloid-polymer blend.[8,9]

So far, each of these three approaches has been performed successfully in our group. Details of the synthesis may be found in the references cited above. Here, just a summary of the characteristics of the particles treated in this chapter is given (see Table 1).

The problem of steric hindrance encountered during grafting-onto of long hairs is demonstrated by the fact that, using identical core particles of radius 8 nm, the maximum hair number achievable drops from about 300 to only 150 if the hair molecular weight is increased from 4200 to 16800 g/mol. On the other hand, micellization allows the preparation of very dense spherical brushes even for hairs with molecular weight much larger than 20000 g/mol.

Table 1. Characteristics of spherical colloidal nanoparticles with polymeric surfaces synthesized by different approaches.

sample	synthesized by	core, radius	hairs, molar mass, number[c]
gr1	grafting-onto	POS[a], R = 8 nm	PS, M = 4200 g/mol, 295
gr2	grafting-onto	POS[a], R = 8 nm	PS, M = 9900 g/mol, 330
gr3	grafting-onto	POS[a], R = 8 nm	PS, M = 16800 g/mol, 150
mic1	micellization	PS[b], R = 10.5 nm	PI[b], M = 54000 g/mol, 250
mic2	micellization	PS, R = 10 nm	PB[b], M = 80000 g/mol, 250

[a] polyorganosiloxane-nanogel (polycondensate of $CH_3Si(OCH_3)_3$)
[b] PS:polystyrene, PI:polyisoprene, PB:polybutadiene
[c] hairs per particle

3. COMPATIBILITY OF COLLOIDAL PARTICLES AND LINEAR CHAINS

Compatibility studies have been performed using standard polyorganosiloxane nanogel particles of radius 10 nm without polymeric surfaces and samples gr1, gr2 and gr3 (see Table 1), blended with a matrix of linear polystyrene chains of varying molecular weight by solution casting from toluene.[5]

If even a very small amount (1 wt%) of the standard colloidal particles is blended with linear chains, an optically turbid highly brittle polymer film is obtained. The turbidity is caused by the presence of large clusters of aggregated colloidal particles, as seen in the transmission electron micrograph of a thin slice cut from the as-cast film by using a microtome (Figure 2). As mentioned already in the introduction, the colloidal particles are immiscible with the linear polymer chains for purely entropic reasons. This so-called depletion effect shall be explained in a little more detail using the sketch of Figure 3.

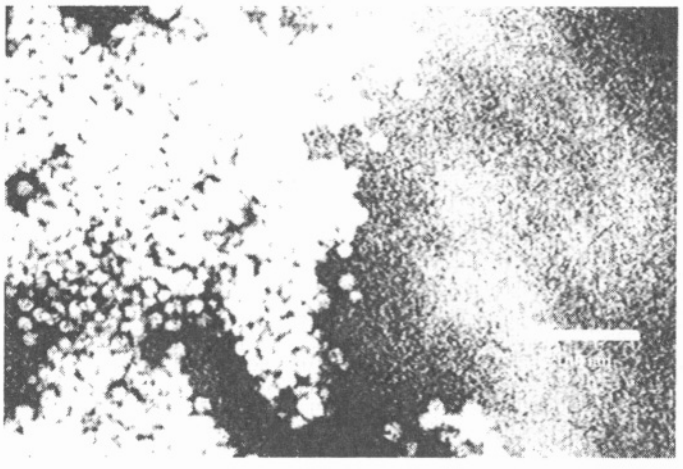

Figure 2. TEM of a thin slice cut from the as-cast blend of standard nanogels with PS chains (M = 4200 g/mol), colloidal particle content 1 wt%. The white bar indicates 100 nm.. Reproduced with permission from ref. 5. Copyright 2000, American Chemical Society.

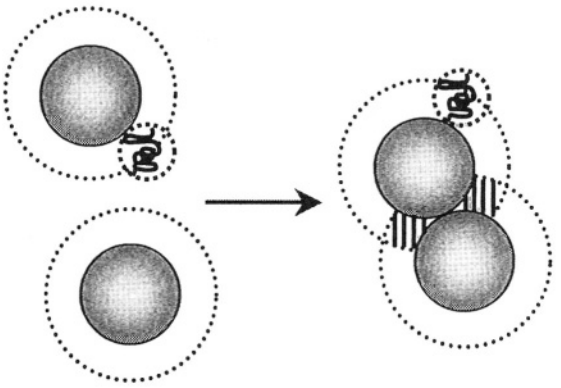

Figure 3. Sketch showing the entropic origin of depletion demixing found in blends of simple colloidal particles with linear polymer chains.

In Figure 3, the dotted circles around the colloidal particles show the excluded volume zone into which the center of mass of the polymeric chains cannot penetrate, being repelled by the smooth surface of the colloidal particles. In case two colloidal particles aggregate, their excluded volume zones overlap as shown by the striped pattern on the right hand side of Figure 3. This leads to an increase in accessible volume for the polymeric chains, which therefore gain in entropy. Since this gain in entropy due to the large number of polymer chains present in the colloid-polymer blend (in respect to the much smaller number of the large colloidal particles) largely compensates the loss in entropy caused by the aggregation of the colloidal particles, the total blend system favors a demixed state.

This depletion mechanism can successfully be suppressed by using colloidal particles modified with polymeric surfaces, as is shown by the TEM picture in Figure 4. By this approach, homogeneous and optically transparent films are obtained even for a very high colloidal particle content, as can be seen from Figure 4. The entropic mechanism by which depletion may successfully be suppressed in blends of spherical brushes and linear chains can be explained according to the scheme shown in Figure 5.

The main difference between Figures 3 and 5 is that, in case of the spherical brushes shown in Figure 5, no excluded volume zone can be defined. Due to the polymeric surface of the colloidal particles, which is rough and deformable, the centers of mass of the linear matrix chains can interpenetrate the colloidal particles beyond their effective radius (which is shown by the dotted circle). Therefore, particle aggregation does not lead to any gain in free volume for the single polymer chains, but only causes a loss in entropy for the colloids. The system in this case favors entropically a homogeneous mixture of colloidal particles and polymer chains.

However, the interested reader already might have recognized that this line of argumentation only holds for comparatively small polymer chains, which may penetrate far into the polymer coating of the spherical brushes. In case of very long (in respect to the polymer hairs) polymer chains, however, the interpenetration depth is expected to be much smaller than the chain radius, and in analogy to simple colloidal particles with smooth surfaces (Figure 3) an excluded volume zone around the spherical brushes for the chains can be defined again (see Figure 6).

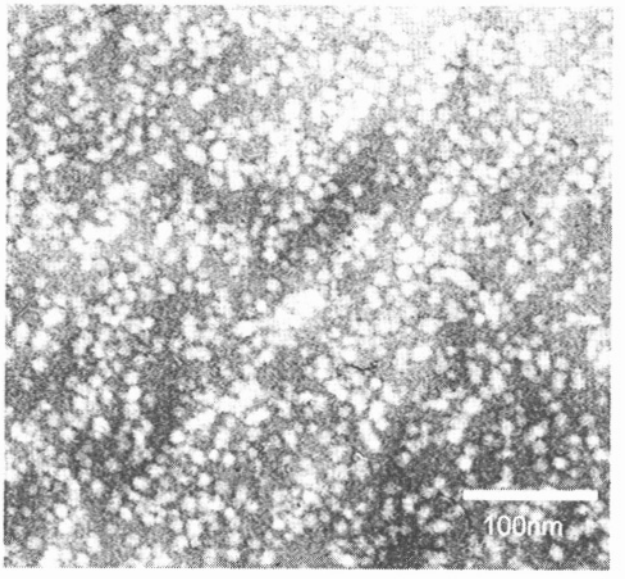

Figure 4. TEM of a thin slice cut from the as-cast blend of spherical brushes gr2 (hair molecular weight 9900 g/mol) with PS chains (M = 4200 g/mol), colloidal particle content 30 wt%. The white bar indicates 100 nm. Reproduced with permission from ref. 5. Copyright 2000, American Chemical Society.

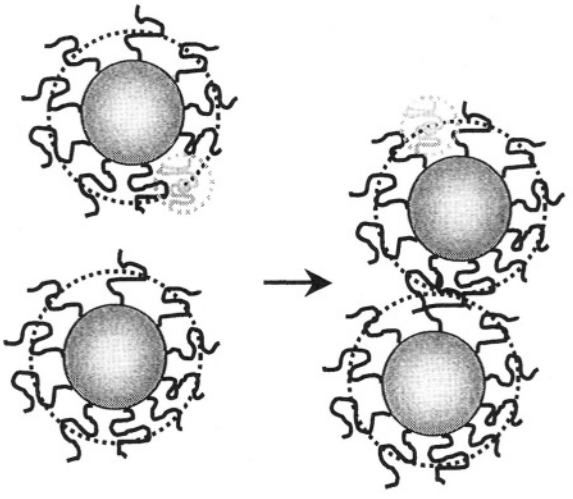

Figure 5. Sketch showing how depletion demixing is suppressed in a blend of colloidal particles with polymer-modified surfaces and linear chains.

As shown in Figure 6, in case of long matrix chains the depletion mechanism should not be suppressed, which consequently leads to an entropically driven demixed state. That indeed spherical brushes, especially those with short hairs, are incompatible with comparatively long linear chains is exemplified by the TEM picture shown in Figure 7.

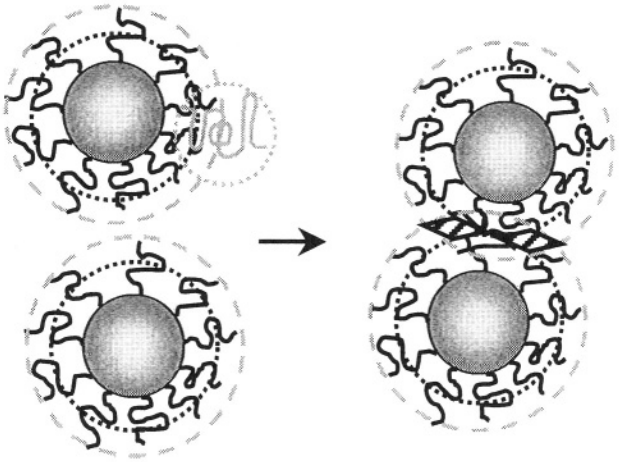

Figure 6. Sketch showing how depletion demixing may also be found for spherical brushes in case the linear polymer chains are longer than the polymer hairs. Dotted circle = effective particle radius, gray dashed circle = excluded volume zone.

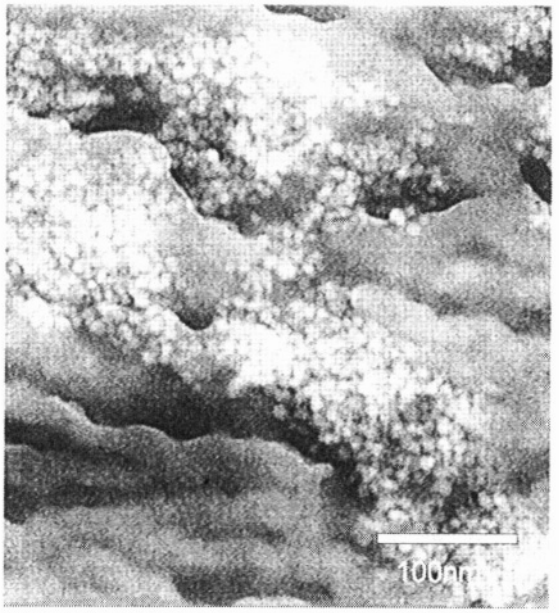

Figure 7. TEM of a thin slice cut from the as-cast blend of spherical brushes gr1 (hair molecular weight 4200 g/mol) with PS chains (M = 16800 g/mol), colloidal particle content 15 wt%. The white bar indicates 100 nm. Reproduced with permission from ref. 5. Copyright 2000, American Chemical Society.

From a series of investigations of colloid-polymer blends analogous to the few examples shown above we deduced the following rule-of-thumb: depletion demixing is completely suppressed and homogeneous colloid-polymer blends are obtained for spherical brushes if the length of the hairs of the particles exceeds that of the linear matrix chains. Although we have only studied particles with a very small core size of

about 10 nm, this rule should hold even for larger particles as long as the surface has a definite curvature, that is up to a radius of about 200 nm. This statement is supported by earlier studies of the compatibility of large thermally crosslinked polybutadiene (PB) spheres grafted with poly(acrylonitrile-co-styrene) (AS) with linear AS chains.[10]

Before closing this section, one final remark is necessary: results presented so far only hold for densely grafted spherical brushes (about 150– 300 hairs/800 nm^2). The compatibilization effect of polymeric surfaces is expected to depend not only on hair length but also on grafting density. This aspect, which already has been studied for the larger PB-spheres where an optimum grafting density for compatibilization has been found,[10] has not yet been investigated in case of very small nano-sized particles.

4. ULTRASOFT COLLOIDS IN COLLOID-POLYMER-BLENDS

4.1. Spherical Micellar Brushes with Colloidal Particle Character

Whereas hard sphere colloids by now have been thoroughly explored in experiment,[11-14] simulation,[15-17] and theory,[18,19] and their structural and dynamical behavior is fairly well understood, soft spherical particles due to their more complex interaction potential and their inherent instability of size and shape still provide a major challenge. Investigation of such systems, however, is very important due to their practical importance, e.g. as polymer fillers, coatings etc.. Here, the hairy particles already presented above provide a nice model system which allows adjustment of the interaction potential via the particle topology, that is size of the rigid core, hair length and hair density. In the following, we will only consider blends of copolymer micelles with homopolymer chains (mic1, mic2, see Table 1). The grafted nanogel spheres in a homopolymer matrix behave correspondingly as swollen soft colloidal particles. Further, we will not discuss here the single particle mobility extensively studied by the holographic grating technique of Forced Rayleigh Scattering[20,21] but restrict ourselves to rheological studies only, since these can easily be applied to all kinds of model spherical brush colloids without any additional optical labeling.

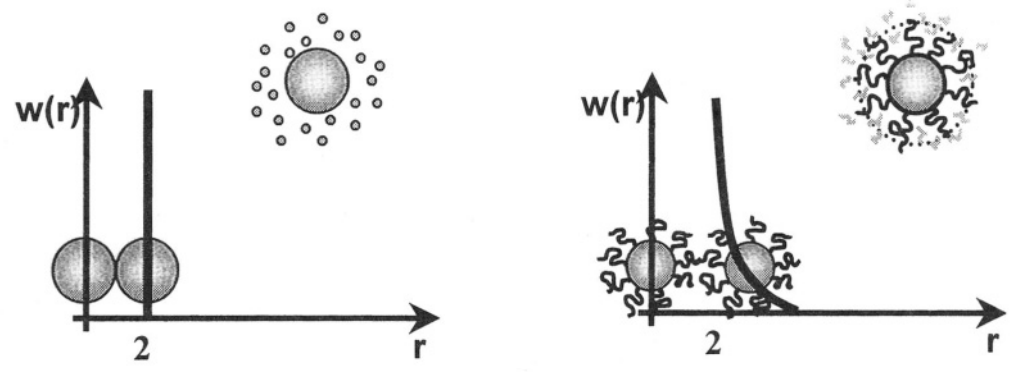

Figure 8. Sketch of the interaction pair potential w(r) of hard sphere colloidal dispersions (left) in comparison to spherical brushes in a polymer chain matrix (soft particles, right).

To investigate the interparticle interactions between spherical brushes in a homopolymer matrix in a semiquantitative way, we consider a hard sphere reference system of simple rigid colloidal particles with a smooth surface dispersed in a simple molecular solvent, as sketched in Figure 8.

Whereas hard spheres show an infinitely steep repulsive interaction at particle touching distance, spherical brushes should show a softer repulsive interaction: its range should depend on the effective particle size while the softness should depend on particle compressibility and/or deformability. To get a quantitative measure of these two parameters, we consider the dependence of the structural relaxation of the system on particle concentration. A very simple model based on free volume theory yields:

$$\frac{\eta_0}{\eta} = \exp\left(-\frac{\kappa}{\varphi^{-1} - \varphi_{cp}^{-1}}\right) \tag{1}$$

Eq. (1) is the so-called Doolittle-equation,[22] with η_0 the zero-shear viscosity of the pure polymer chain matrix and η the zero-shear viscosity of a blend of spherical micelles and homopolymer chains, with copolymer volume fraction φ. Effective particle size and softness are quantified by the two fitting parameters in the following way: κ is a measure for the steepness of the slowing down of sample dynamics with increasing particle volume fraction and thereby provides a semi-quantitative approach to the particle compressibility and/or deformability, whereas φ_{cp} is the particle volume fraction at the liquid-solid transition where the viscosity becomes infinite. For a hard sphere model system with suppressed crystallization, which usually is the case for particles of size polydispersity larger than 10% like our spherical brushes, these parameters are κ= 1.4 and φ_{cp} = 0.64,[23] the later corresponding to the glassy state of random closed packed spheres.

To investigate the structural relaxation of our micellar system for a detailed data analysis according to Eq. (1), we have performed mechanical spectroscopic measurements with an oscillatory shear rheometer type Rheometrics RMS 800. The experimental setup and typical signals for mixtures of spherical micellar brushes and linear chains are shown in Figures 9 and 10.

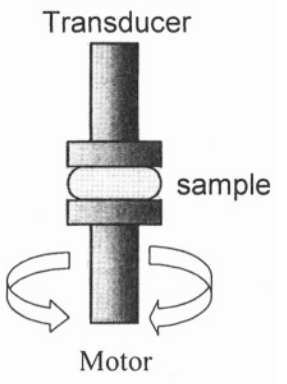

Figure 9. Sketch of an oscillatory shear rheometer. The sample is fixed in between a motor-driven plate, which implies an oscillatory strain, and a transducer plate, which measures the stress transferred through the sample at the given strain.

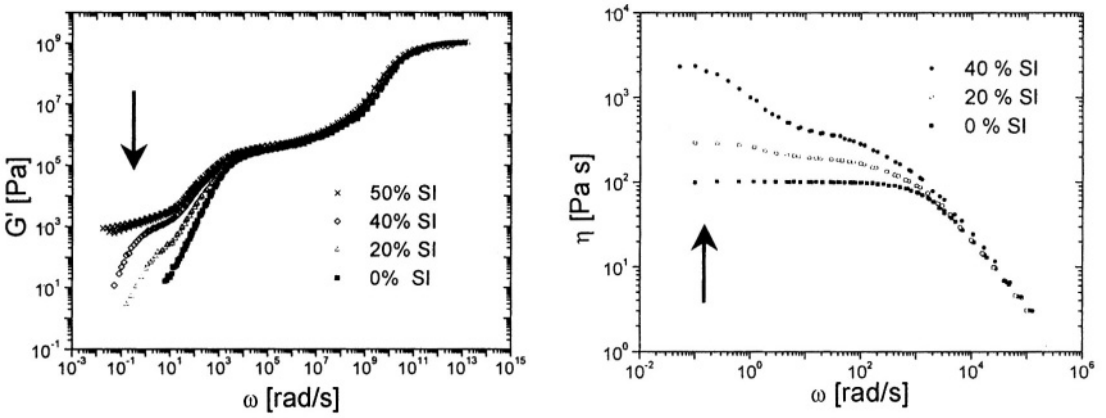

Figure 10. Typical quantities measured in an oscillatory shear experiment on micelle/homopolymer mixtures: elastic modulus G' and viscosity η as a function of shear frequency ω and micelle concentration (% SI). The structural relaxation depending on the micellar motion itself is the slowest relaxation process of the system and therefore shows up at very low frequency (see arrows).

As shown in Figure 10, at very low shear frequencies the elastic shear modulus and the viscosity of the blend strongly increase with increasing micelle concentration. This signal behavior corresponds to a slowing down of the structural relaxation of the blend, which itself is based directly on the translational mobility of individual micelles, with increasing particle interactions. Here, it should be noted than at very high micelle concentration (50 % SI), the elastic modulus approaches a plateau value as shown in the figure. Correspondingly, the viscosity should become infinite in this regime. Let us have a closer look on the concentration dependence of the zero-shear viscosity:

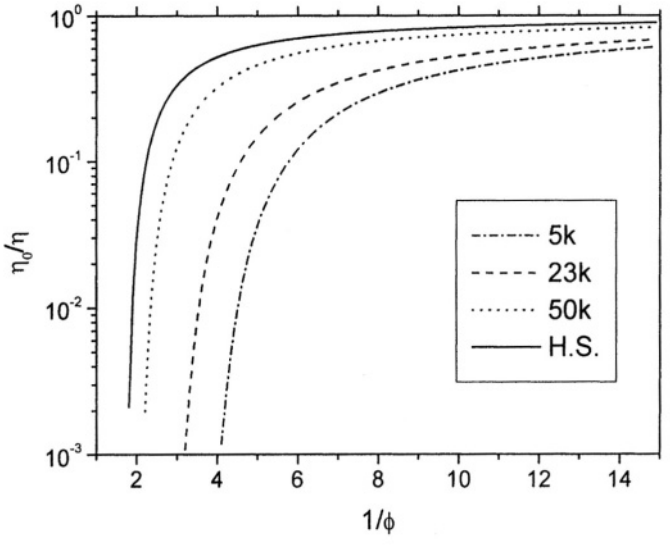

Figure 11. Doolittle-fits of the inverse normalized zero-shear viscosity versus inverse copolymer volume fraction for spherical micelles mic1 (see Table 1) in three different homopolymer matrices (M = 5000 (5k), 23000 (23k) and 50000 (50k) g/mol) and for the hard sphere reference system (H.S.).

In Figure 11, the best fits to the experimental data according to Eq. (1) for three different micellar systems and the hard sphere reference are presented. The data for the shortest matrix (5k) have been determined from diffusion coefficients of spherical micelles published in ref. 9, which have been recalculated to yield sample viscosities using a generalized Stokes-Einstein equation, i.e. $D(\phi) \sim 1/\eta(\phi)$. All systems show the typical signature of a colloidal particle dispersion, that is occurrence of a liquid-solid transition by divergence of the viscosity at particle volume fractions well below 1.

Obviously, the strong slowing-down of the particle mobility, that is the increase of the zero-shear viscosity, occurs at lower micelle concentration with decreasing molecular weight of the matrix homopolymer. This signifies that the effective particle size and, at a given copolymer concentration, the effective particle volume fraction, of the micelles is larger in a low molecular weight matrix than in a high molecular weight matrix. Here, the reader should note that the liquid-solid transition for all three micellar systems occurs at micellar volume fractions well below the transition of a hard-sphere system, that is $\varphi_{cp}^{-1} = 1.6$. Therefore, the micelles either possess long-range repulsive interactions, or the particle size itself is increased by matrix polymer interpenetrating the hairy corona (swollen spherical brushes). Since the system consists of non-polar materials and particles should therefore only interact if their surfaces are touching each other, the later is more probable. Here, it has to be taken into account that corona and matrix are chemically identical.

Therefore, the driving force for the matrix chains to migrate into the corona is of purely entropic origin: by entering the corona, the chains gain in free volume. On the other hand, this leads to a stretching of the corona chains and correspondingly to a loss in configurational chain entropy. The overall degree of swelling will be determined by a delicate balance of these two contributions, that is gain in free volume of homopolymers interpenetrating the corona, and loss in configurational entropy by subsequent stretching of corona hairs. In this context, the effect of molecular weight of the matrix homopolymer on the effective size of the micelles may be described as follows: for short chains, the gain in free volume upon corona interpenetration in respect to the homopolymer size is considerable, whereas stretching of the corona hairs is insignificant.

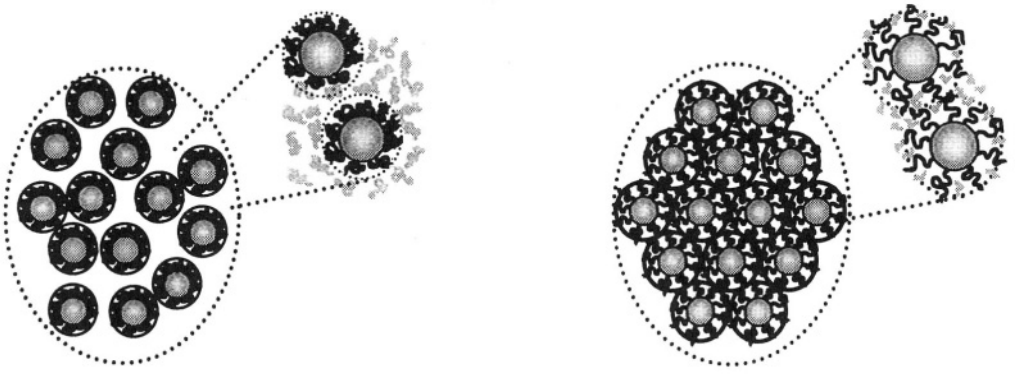

Figure 12. Sketch of non-swollen dry-brush micelles (left) and strongly swollen wet-brush micelles (right) at identical copolymer concentration. The larger effective volume fraction in the wet-brush case causes stronger interparticle interactions and, as a consequence, a higher viscosity at a given concentration, or, respectively, a shift of the liquid-solid-transition.

Table 2. Doolittle fit parameters (see Eq. (1)) for all curves shown in Figure 11.

sample	φ_{cp}	κ
5k (wet-brush)	0.31	5.80
23k (med.-brush)	0.40	4.80
50k (dry-brush)	0.56	2.50
H.S.	0.65	1.60

Practically speaking, short homopolymer chains behave like a good solvent, and the micellar corona is strongly swollen (wet brush). On the other hand, the corona stretching necessary for a significant increase in free volume for interpenetrating long chains is considerable. Therefore, long homopolymer chains scarcely interpenetrate the micellar corona and behave like a bad solvent, causing only slight swelling of the micelles (dry brush). This explains why, at identical micelle concentration, the system with the lower molecular weight matrix has an effectively higher particle volume fraction and therefore shows the higher viscosity, as sketched in Figure 12.

Whereas the dry-brush system shown in Figure 12 still is in a liquid state, the wet-brush system already shows a close particle packing, which causes a complete jamming of the structural relaxation dynamics of the blend.

Finally, let us have a closer look at the parameters corresponding to the Doolittle fits shown in Figure 11. Table 2 summarizes these parameters for all curves shown.

As already discussed, the liquid-solid transition (φ_{cp}) is shifted towards smaller micelle concentration with decreasing length of the matrix homopolymer because of the more pronounced increase in effective particle size, which itself is caused by the strong corona swelling found in a wet-brush system. On the other hand, the wet-brush sample shows a much larger κ than the hard sphere reference, whereas the κ-value of the dry-brush sample is fairly close to the hard sphere value of $\kappa = 1.4$. This is also obvious from Figure 11, where the dry-brush Doolittle fit looks very similar to the hard sphere case, but the wet-brush shows a less abrupt slowing down of particle dynamics although shifted to much lower concentrations. Simply speaking, our findings indicate that the more strongly swollen wet-brush micelle also shows the higher compressibility and deformability, that is the effective particle size is more strongly decreasing with particle concentration than in the dry-brush case. This behavior and the significance of the difference in κ can be analyzed in more detail if one uses Eq. (1) to determine the increase in particle size, in respect to the original size of a non-swollen micelle, in dependence of micellar concentration as follows:

$$\frac{\eta_0}{\eta} = \exp\left(-\frac{\kappa}{\varphi_{SI}^{-1} - \varphi_{cp}^{-1}}\right) = \exp\left(-\frac{1.60}{\varphi_{H.S.}^{-1} - 0.65^{-1}}\right) \tag{2}$$

By mapping the mobility of a given micellar sample onto the hard sphere reference, we assume that identical normalized zero-shear viscosities correspond to identical effective hard sphere volume fractions $\varphi_{H.S.}$. Correspondingly, any micelle volume fraction φ_{SI} (non-swollen micelle) corresponds to an effective particle volume fraction $\varphi_{H.S.}$ (swollen micelle), and the degree of particle swelling is simply given by the ratio $\varphi_{H.S.}/\varphi_{SI}$.

Table 3. Effective particle swelling as calculated by Eq. (2).

$\phi_{H.S.}$ =	0.10	0.20	0.30	0.40	0.50	0.60
50k: $\phi_{H.S.}/\phi_{SI}$ =	1.50	1.44	1.38	1.32	1.25	1.19
23k: $\phi_{H.S.}/\phi_{SI}$ =	2.69	2.57	2.34	2.14	1.94	1.71
5k: $\phi_{H.S.}/\phi_{SI}$ =	3.42	3.18	2.91	2.70	2.45	2.20

Note, however, that this simplified approach treats also strongly swollen wet-brush micelles, at a given concentration, as if they would effectively interact via a hard sphere potential. By this simple approach, particle softness, that is compressibility and/or deformability of the particles, is indirectly considered by the fact that it causes a decrease of the effective hard sphere radius with increasing micelle concentration. A physically more realistic approach based on a soft-interaction pair potential is currently under investigation. Following the simple approach described by Eq. (2) yields for the effective particle swelling versus micelle concentration for the three different micellar systems the results summarized in Table 3.

For the wet-brush micellar system (5 k),[9] from dilute ($\varphi_{H.S.} = 0.10$) up to close to the liquid-solid transition ($\varphi_{H.S.} = 0.60$) the swelling ratio and therefore the effective particle size decreases by about 50%, whereas the volume of the dry-brush micelle (50k) in the same effective concentration regime only decreases by about 20 %. This underlines that wet-brush micelles indeed are more compressible and/or deformable than dry-brush micelles, and consequently also show a softer interaction potential. From the decrease in particle size with increasing concentration, one also gets a rough estimate of the range of the soft potential: the size of a non-swollen spherical micelle of type mic1 (see Table1) according to the polymer densities of PI and PS should be about 18.4 nm. Using the volume swelling ratios given in Table 3, it is straight forward to calculate the effective particle radius of the swollen micelles, which are given in Table 4. The dry-brush micelle (50k), with an effective particle radius of about 21 – 21.5 nm in comparison to 18.4 nm for a strictly non-swollen micelle, still seems to be slightly swollen. The range of the soft interaction potential as deduced from the shrinking of the micellar size from dilute to highly concentrated systems is in the order of 2 nm. The intermediate brush micelle (23k) is more strongly swollen up to R = 26 nm, the range of the compressibility or soft potential in this case is about 4 nm. The wet-brush (5k), on the other hand, with R about 28.5 nm, exhibits the strongest swelling whereas the compressibility range, with about 4 – 4.5 nm, is comparable to that of the intermediate system. These results concerning the respective particle compressibility can also be seen from the similarity in κ (4.80 for 23k, 5.80 for 5k). Here, we would like to note that the micellar radii given in Table 4 for dilute samples agree very well with hydrodynamic radii calculated from rotational and translational diffusion coefficients measured by Forced Rayleigh Scattering.

Table 4. Effective radius of swollen micelles vs. effective particle concentration.

$\phi_{H.S.}$ =	0.10	0.20	0.30	0.40	0.50	0.60
50k: R [nm]	21.1	20.8	20.5	20.2	19.8	19.5
23k: R [nm]	25.6	25.2	24.4	23.7	22.9	22.0
5k: R [nm]	27.7	27.1	26.3	25.6	24.8	23.9

Figure 13. Sketch of the interpretation of swollen spherical micelles in terms of sterically stabilized colloidal particles, where both effective hard-core particle size (solid circle) and thickness of the stabilization layer (dashed circle) depend on the matrix molecular weight. High molecular weight matrix: dry-brush, smaller effective particle size, comparatively thin steric stabilization layer (right). Low molecular weight matrix: wet-brush, larger effective particle size, comparatively thick steric stabilization layer (right).

As can be seen, the range of the soft interaction potential as deduced from the maximum particle compression is comparatively small in respect to the overall particle size. In this respect, it might as well be possible to regard the swollen micelles, in analogy to colloidal particles with stabilizing surface layers of linear chains studied by other groups,[11,14] as sterically stabilized particles, that is rigid and compact colloidal particles covered by a thin layer of hydrocarbon chains. Importantly, in our case the thickness of this stabilizing layer cannot be neglected in respect to the particle core size. Also, for our swollen spherical brushes the effective layer thickness depends on the molecular weight of the matrix chains: for a wet-brush micelle, this stabilizing layer, which is expected to be highly compressible, seems to extend much further than for the less-swollen dry-brush micelles (Figure 13).

Here, it should be stressed that the effective particle size at the liquid-solid transition, which in Figure 13 is identified with an effective hard-core particle size (solid circle), is still much larger than the size of the glassy PS core (10.5 nm) for all micellar systems considered so far. Therefore, the major part of the corona contributes to a compact colloidal particle, and only a small part of it to an outer hairy stabilization layer and therefore to the particle softness. This contribution of the hairy corona to the colloidal particle character, however, strongly depends on the ratio of corona hair length vs. rigid core size, as will be discussed in the last part of this chapter.

4.2. Spherical Micellar Brushes Behaving Like Hyperbranched Polymers

The micellar systems discussed in section 4.1 all show a liquid-solid transition as typical for dispersions of colloidal particles. What, however, happens if the corona thickness is huge in respect to the size of the rigid PS core of the micelle? Figure 14 shows rheological measurements for a corresponding copolymer wet-brush micelle with rigid PS core and PB corona in a matrix of low molecular weight polybutadiene (mic2, see Table 1), which should exhibit strong swelling. For comparison, the rheological data for the wet-brush system of the former SI micelles (mic1) are also presented:

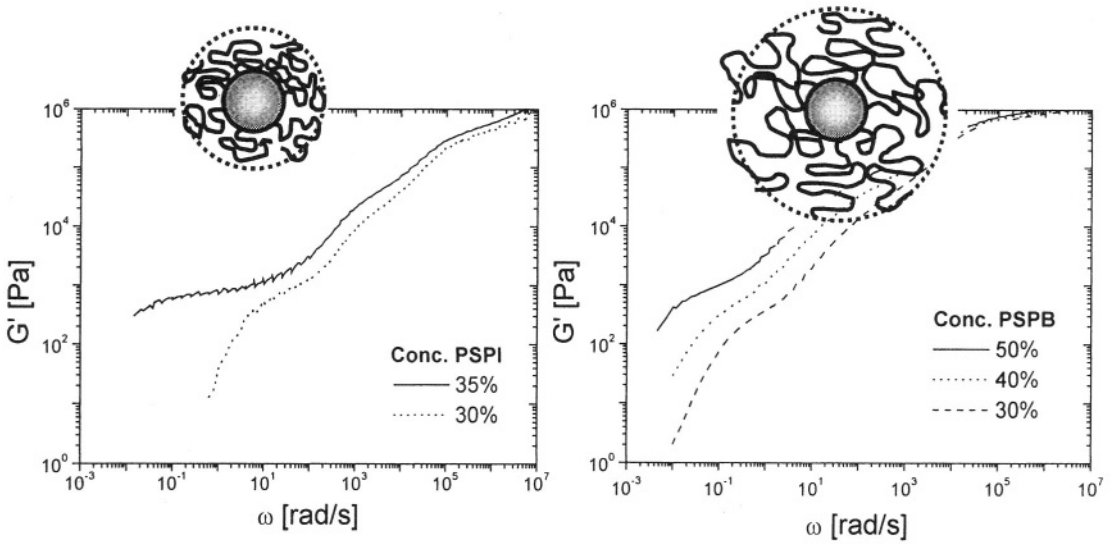

Figure 14. Elastic moduli for two different wet-brush micelles (M_{PI} = 23000 g/mol, M_{PB} = 20000 g/mol) at various micellar concentrations. Left: mic1 (Table 1), core-radius 10.5 nm, corona volume ca. 80 vol% of non-swollen micelle. Right: mic2 (Table 1), core-radius 10 nm, corona volume ca. 90 vol% of non-swollen micelle.

Whereas the system with the smaller corona clearly shows an elastic plateau and thereby the signature of a liquid-solid transition at a micelle concentration of 35 %, the modulus of the micelle with the larger corona shows the signature of a polymer melt up to micelle concentrations as high as 50 %. Also, it was not possible to analyze the concentration dependence of the zero-shear viscosity of this second micellar system with the Doolittle model. Therefore, one may conclude that if the size of the hairy corona in respect to the size of the rigid particle core exceeds a certain limit, a spherical brush behaves not like a swollen colloidal particle but like a flexible, although highly branched, polymer. In this case, highly concentrated samples or even a sample which purely consists of the micelles themselves rheologically behave like a melt.

These findings can be explained as follows: although the corona is coupled onto a rigid core with high grafting density, the size of this core is insufficient to create an effective colloidal particle, and therefore most of the corona retains its original polymer flexibility. In addition, if the corona is not to a large extent participating in the particle character of the micelle as found for the first system (mic1), even for the pure micellar system the particle volume fraction of just the rigid cores (even including a very small part of the corona in direct vicinity of the rigid core surface) is far too low to reach the liquid-solid transition regime (effective hard sphere volume fraction $\varphi = 0.64$).

Therefore, although spherical polymer brushes in a melt of homopolymer chains may exhibit the behavior of soft compressible colloidal particles, sometimes the corona brush may dominate the behavior of the system and the particle character is lost in favor of a polymer melt of hyperbranched chains, where the rigid colloidal core of the brush simply acts as a branching point.

5. CONCLUDING REMARKS

In this chapter, we have discussed the compatibility of densely grafted nano-sized spherical brushes with linear polymer chains, and, in case of homogeneous particle-polymer blends, their behavior as soft colloidal particles. Although we could not yet present an exact interaction pair potential for these spherical brush systems, a simple analysis of the viscosity versus particle concentration following a free volume approach (Doolittle equation) provided much important information, like the effective particle size and particle swelling by the matrix homopolymer chains, or the softness/compressibility of the system. Although there exist some theoretical predictions in literature concerning the interaction potential of such swollen polymer brushes,[24-27] so far we have not been able to find any suitable interaction pair potential for our given micellar system. Whereas our simple approach allowed us to gain some insight in the complex behavior of spherical brushes in a polymer melt, there still remains a lot of work to be done. One aspect not treated here is a systematic variation of grafting density, which should effect both compatibility and soft particle character. Another important point is the significance of the core size in respect to the polymer brush surface.

6. ACKNOWLEDGEMENTS

The author wishes to express his sincere gratitude to Dr. G.Lindenblatt for preparing the graft-onto microgels and her compatibility investigations, Dr. K. Tsutsumi and Prof. A.H.E. Milller for providing the copolymer and homopolymer samples, and Ms. Kerstin Gohr for the rheological investigations presented in this chapter. Our work has been financially supported by the Deutsche Forschungsgemeinschaft via grants SFB 262/D23 and Scha620/2-l,2.

7. REFERENCES

1. S. Asakura and F. Oosawa, On interaction between two bodies immersed in a solution of macromolecules, *J. Chem. Phys.* ***22,*** 1255-1256 (1954).
2. A. Vrij, Polymers at interfaces and the interactions in colloidal dispersions, *Pure Appl. Chem.* **48**, 471-483 (1976).
3. I. Borukhov and L. Leibler, Stabilizing grafted colloids in a polymer melt: Favorable enthalpic interactions, *Phys. Rev. E* ***62,*** R41-R44 (2000).
4. J. Won, C. Onyenemezu, W.G. Miller, and T.P. Lodge, Diffusion of spheres in entangled polymer solutions: a return to Stokes-Einstein behavior, *Macromolecules* **27**, 7389-7396 (1994).
5. G. Lindenblatt, W. Schärtl, T. Pakula, and M Schmidt, Synthesis of polystyrene-grafted polyorganosiloxane microgels and their compatibility with linear polystyrene chains, *Macromolecules* **33**, 9340-9347 (2000).
6. W. Schärtl, Structure and dynamics of block copolymer micelles, *Macromol .Chem. Phys.* **200**, 481-500 (1999).
7. H. Watanabe, Rheology of diblock copolymer micellar systems, *Acta Polymer.* **48**, 215-233 (1997).
8. W. Schärtl, K. Tsutsumi, K. Kimishima, and T. Hashimoto, FRS study of diffusional processes in block copolymer/homopolymer blends containing glassy spherical micelles, *Macromolecules* **29**, 5297-5305 (1996).
9. H. Watanabe, T. Sato, K. Osaki, M.W. Hamersky, B.R. Chapman, and T.P. Lodge, Diffusion and viscoelasticity of copolymer micelles in a homopolymer matrix, *Macromolecules* **31**, 3740-3742 (1998).
10. R. Hasegawa, Y. Aoki, and M. Doi, Optimum graft density for dispersing particles in polymer melts, *Macromolecules* **29**, 6656-6662 (1996).

11. P.N. Pusey, W. van Megen, S.M. Underwood, P. Bartlett, and R.H. Ottewill, Colloidal fluids, crystals and glasses, *J. Phys.: Condens. Matter* **2**, SA373-SA377 (1990).
12. E. Bartsch, V. Frenz, J. Baschnagel, W. Schärtl, and H. Sillescu, The glass transition dynamics of polymer micronetwork colloids - a mode coupling analysis, *J. Chem. Phys.* **106**, 3743-3756 (1996).
13. E. Bartsch, Diffusion in concentrated colloidal suspensions and glasses, *Current Opinion in Coll. Interface Sci.* **3**, 577-585 (1998).
14. W. van Megen, T.C. Mortensen, S.R. Williams, and J. Müller, Measurement of the self-intermediate scattering function of suspensions of hard spherical particles near the glass transition, *Phys. Rev. E* **58**, 6073-6085(1998).
15. D.A. Young and B.J. Alder, Studies in molecular dynamics. XIII. Singlet and pair distribution functions for hard-disk and hard-sphere solids, *J. Chem. Phys.* **60**, 1254-1267 (1974).
16. B. Cichocki and K. Hinsen, Dynamic computer simulation of concentrated hard sphere suspensions. Part I: Simulation technique and mean-square displacement data, *Physica A* **166**, 473-478 (1990).
17. W. Schaertl, Brownian Dynamics of Colloidal Hard Spheres - 3.Extended Studies in the Phase Transition Regime, *J. Stat. Phys.* **79**, 299-312 (1995).
18. W. Götze and L. Sjögren, Relaxation processes in supercooled liquids, *Rep. Prog. Phys.* **55**, 241 (1995).
19. M. Tokuyama and I. Oppenheim, On the theory of concentrated hard-sphere suspensions, *Physica A* **216**, 85-119(1995).
20. K. Gohr, T. Pakula, K. Tsutsumi, and W. Schärtl, Dynamics of copolymer micelles in an entangled homopolymer matrix, *Macromolecules* **32**, 7156-7165 (1999).
21. K. Gohr and W. Schärtl, Dynamics of copolymer micelles in a homopolymer melt: influence of the matrix molecular weight, *Macromolecules* **33**, 2129-2135 (2000).
22. A. K. Doolittle, Newtonian flow II. The dependence of the viscosity of liquids on free space, *J. Appl. Phys.* **22**, 1471-1475(1951).
23. C. Graf, W. Schärtl, M. Maskos, and M. Schmidt, Tracer diffusion of polyorganosiloxane nanoparticles in solution - Effects of tracer topology and particle concentration, *J. Chem. Phys.* **112**, 3031-3039 (2000).
24. L. Leibler and P.A. Pincus, Ordering transition of copolymer micelles, *Macromolecules* **17**, 2922-2924 (1984).
25. A. N. Semenov, D. Vlassopoulos, G. Fytas, G. Vlachos, G. Fleischer, and J. Roovers, Dynamic structure of interacting spherical polymer brushes, *Langmuir* **15,** 358-368 (1999).
26. A. Jusufi, M. Watzlawek, and H. Löwen, Effective interaction between star polymers, *Macromolecules* **32**, 4470-4473 (1999).
27. C. N. Likos, H. Löwen, M. Watzlawek, B. Abbas, O. Jucknischke, J. Allgaier, and D. Richter, Star polymers viewed as ultrasoft colloidal particles, *Phys. Rev. Lett.* **80**, 4450-4453 (1998).

This page intentionally left blank

10

PROPERTIES OF NIPAM-BASED INTELLIGENT MICROGEL PARTICLES

Investigated using scattering methods

Thomas Hellweg*

1. INTRODUCTION

Hydrogels can be seen as intermediates between solids and liquids, exhibiting a rather complex mixture of properties of these two limiting states.[1] Moreover, hydrogels are of great importance in living systems (e.g. the cytoskeleton is a hydrogel) and are of broad interest for a large variety of industrial products (e.g. as storage and separation media).

In recent years a large number of works[2-6] and also reviews[7,8] on the subject of so called intelligent macroscopic hydrogels were published. This class of hydrogels is of special interest, due to the volume phase transition encountered in these systems i.e. the collapse of the gel when a certain temperature (low critical solution temperature (LCST))[6,9-11] or ionic strength[12] is reached. Most of these intelligent gels are made of N-isopropyl acrylamide (NIPAM). In addition to the already mentioned applications NIPAM based gels exhibit bio-adhesive properties. This may allow for applications as drug delivery systems.

Copolymerisation with charged[9] and uncharged co-monomers[13] can be used to tune the transition temperature and other properties of these network materials.

However, the major disadvantage of these macroscopic gels is their rather slow response to the change of an external parameter. It may take several days until the equilibrium is reached.[2,3] Therefore, since the pioneering works of Pelton and Chibante[14] there is growing interest in NIPAM based so-called microgel particles. Microgels are colloidal particles (diameter typically ranging from 100 nm to 1 μm), which internally have the same gel structure as their macroscopic homologues. They react nearly instantaneously on changes of external parameters e.g. temperature and are therefore well suited to study the volume phase transition. Consequently, a growing number of publications can be found in the literature investigating these systems using differential scanning calorimetry (DSC),[15] dynamic light scattering[16-19] and neutron scattering

* T. Hellweg, TU Berlin, Stranski-Laboratorium, Strasse des 17 Juni 112, D-10623 Berlin, Germany.
E-mail: thomas.hellweg@tu-berlin.de

techniques.[20-23] In addition to the gel properties, microgels exhibit the typical behavior of colloids e.g. crystallization.[24-26] Besides the homo-polymer particles, also colloidal microgels can be prepared using copolymerisation of N-isopropyl acrylamide with charged monomers e.g. acrylic acid[19] or dimethylaminoethyl methacrylate.[27] Similar effects as induced by charged co-monomers can be found in PNIPAM complexes with anionic surfactants.[28] Also core-shell structures with thermo-sensitive PNIPAM shells were prepared and investigated using small angle scattering techniques.[29-31] For additional references we recommend a rather recent review by Pelton.[32]

In this contribution we present and discuss the possibilities to investigate microgels by means of elastic and quasi-elastic scattering methods. However, these techniques are of course also useful for the study of other mesoscopically structured systems. In addition, some results obtained by real space imaging techniques will be shown. This text is organized as follows. The next section gives a general description of the preparation of microgels. The first subsection of section 3 provides a general introduction to scattering experiments and then in the following subsections the different methods, which can be used for the characterization of microgels are introduced.

2. MICROGEL PREPARATION

2.1. Synthesis of PNIPAM Microgels

PNIPAM microgels are prepared using the method of surfactant-free emulsion polymerization. N-isopropylacrylamide (NIPAM), N,N'-methylene bis-acrylamide (BIS), and potassium persulfate (KPS) were obtained commercially from Sigma-Aldrich. All chemicals were reagent grade and used without further purification. The microgel preparation is based on the procedure described by Pelton et al.[14] For the synthesis of the particles used here we employed a conventional stirring technique as described elsewhere.[33] 1.25 g (10.05 mmol) NIPAM and the desired amounts of BIS were dissolved in 100 ml triple distilled, degassed water. In case of copolymer microgels (e.g. with acrylic acid) the desired mole fraction of the co-monomer has also to be added to the reaction mixture. The synthesis was performed under a nitrogen atmosphere. After heating the solution to 343 K (two phase region of the binary mixture water/NIPAM), 3.6 μmol of potassium persulfate were added to start the polymerization. The mixture became turbid and the reaction proceeded for 4 h at constant temperature. Then the microgel suspension was cooled for twelve hours under continued stirring. The final step of the preparation involves extensive dialysis for 20 days against double distilled water in order to remove unreacted monomers and other low molecular weight impurities.

2.2. Sample Preparation for Scattering Experiments

For light scattering experiments, very dilute solutions of microgels in dust-free solvents and sample cells are used. To generate contrast in neutron scattering experiments usually D_2O serves as solvent. Heavy water has different scattering length density compared to the hydrogen containing polymer particles. Also mixtures of water and D_2O can be used in some cases, especially when investigating partly deuterated microgels. The scattering length density of the solvent can be adjusted this way to exactly match the scattering length density of parts of polymer network in the microgel.

3. SCATTERING METHODS

In elastic and quasi-elastic scattering experiments the most important quantity is the magnitude of the so called scattering vector given by

$$q = 4\pi/\lambda \sin \theta/2, \quad (1)$$

with λ being the wavelength of the used radiation (e.g. neutrons or light) and θ the scattering angle, q has the dimension of a reciprocal length and is a measure for the spatial resolution of a scattering experiment.

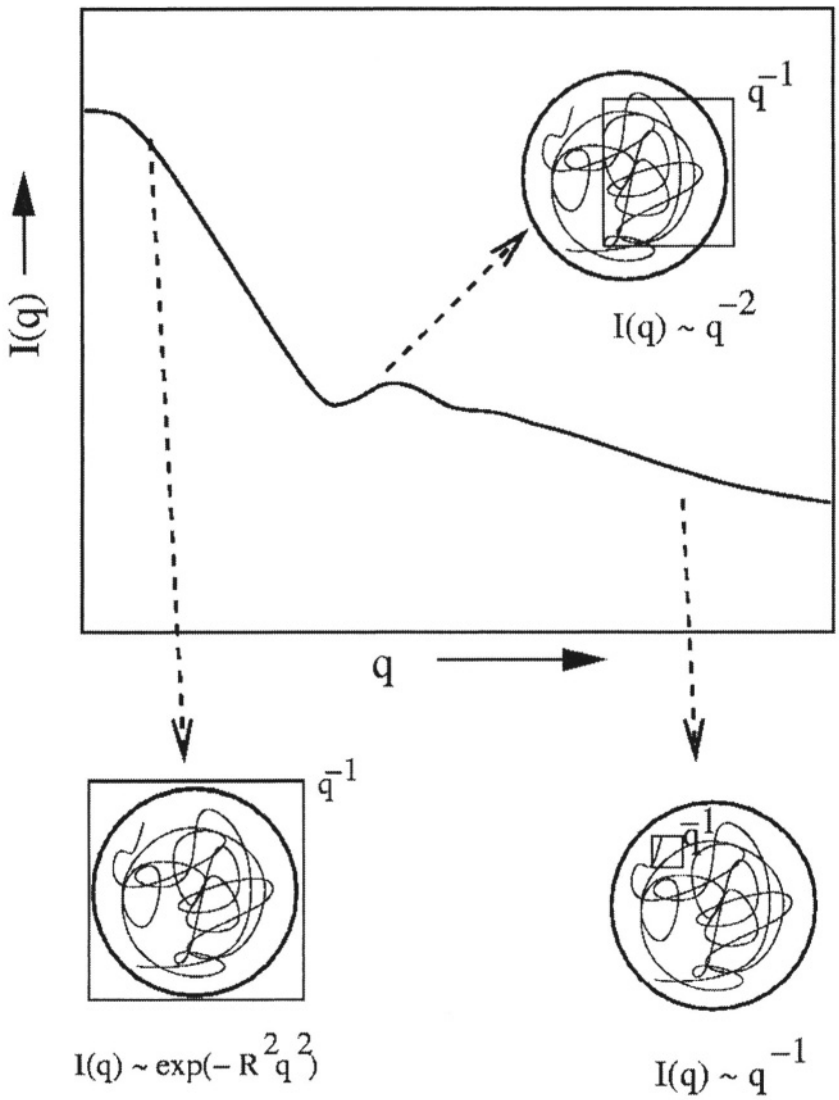

Figure 1. Schematic elastic scattering curve of a colloidal microgel particle in solution. At low q-values the overall size of the particles can be monitored (typically by static and dynamic light scattering). At high q the internal structure of the particles i.e. the polymer network is resolved (e.g. by small angle scattering and neutron spin-echo spectroscopy).

This is schematically shown in Figure 1. In this figure the squares indicate the spatial resolution in the respective q-range. At low values of q the overall size and shape of the microgels is seen. At high q the internal structure of the particles can be resolved. The choice of the appropriate scattering method, which has to be used to probe a specific property of the microgels depends on the relationship between length-scale and q-range. Static (SLS) and especially dynamic light scattering (DLS) are e.g. well suited to study the overall size of the particles. In small angle neutron scattering experiments (SANS) the accessible q-range is usually 0.007-0.4 $Å^{-1}$. This is two orders of magnitude smaller compared to light scattering experiments. Therefore, SANS and also neutron spin-echo spectroscopy (NSE) are well suited to study local (internal) structures and movements in microgels. SLS and SANS are elastic scattering methods (also called static) because they monitor the time averaged scattering intensity (see Figure 1). Photon correlation spectroscopy (DLS) and NSE are inelastic (or better quasi-elastic) scattering techniques. These methods scrutinize the energy transfer between the sample and the used radiation. As can be seen in Figure 2, the initial wavelength distribution (e.g from a laser or a neutron source) is broadened by energy transfer with the sample (Doppler broadening) or in other words the dynamic structure factor $S(q,\omega)$ can be monitored this way. DLS and NSE both directly measure the Fourier transform of $S(q,\omega)$, the intermediate scattering function $S(q,t)$ (see Figure 2).

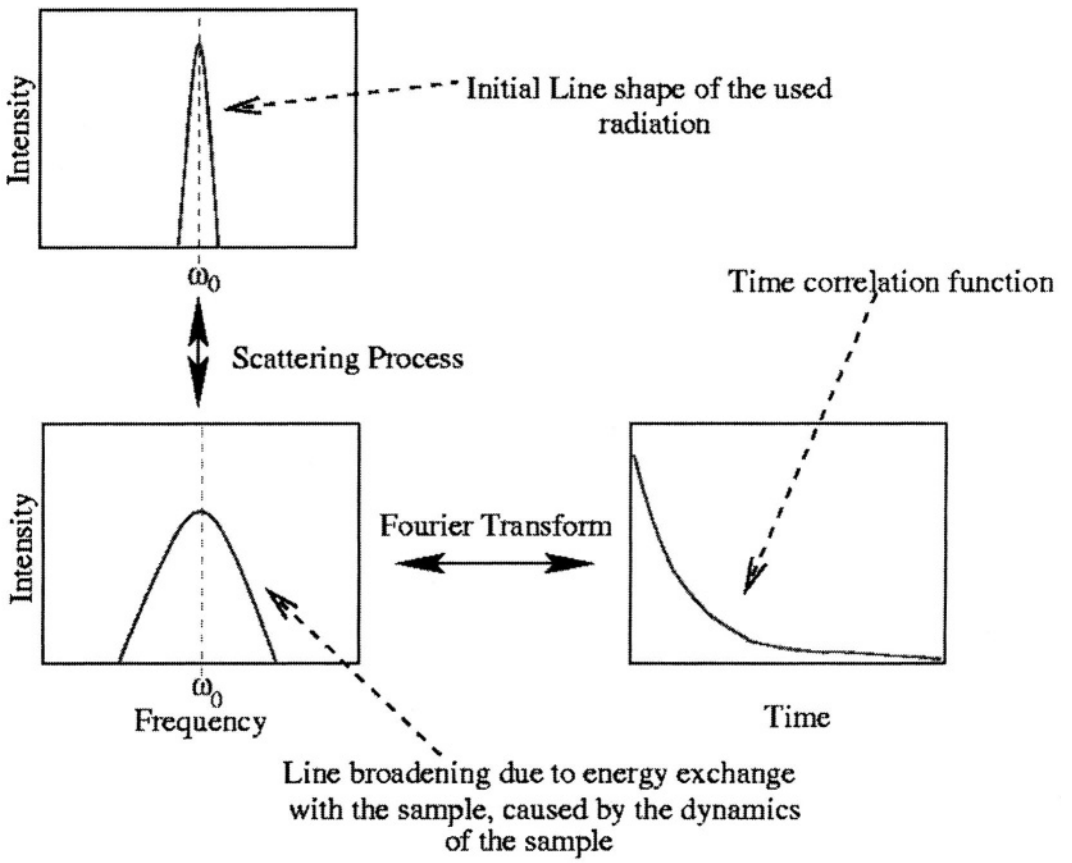

Figure 2. Scheme of the important processes and relationships in quasielastic scattering experiments.

At lot of books and reviews concerned with scattering techniques have been published[34-43] and for a detailed description of the different method the reader is referred to these publications. However, in the following these methods will be briefly discussed. In addition, in all sections examples with respect to the characterization of microgels will be given.

3.1. Dynamic Light Scattering

When light interacts with matter, the electrical field of the initial beam generates an oscillating polarization in the molecules of the illuminated volume. These molecules then emit secondary waves (they scatter). The polarization direction, the angular dispersion and the energy shift of the scattered light depend on properties of the scattering medium (e.g. the shape and movements of the scatterer).

A static light scattering experiment simply measures the time averaged scattered intensity $\langle I \rangle_t$, which is proportional to the square of the scattered electric field $\langle E^2 \rangle_t$. However, on short time scales I is a fluctuating quantity. These fluctuations of I can be analyzed in terms of correlation functions.[44] The normalized electric field autocorrelation function contains the information about the dynamics of the scattering system, in this case of the microgel suspension.

$$g^1(\tau) = \frac{\langle E_s^*(t) E_s(t+\tau) \rangle}{\langle I \rangle} \tag{2}$$

In a so called *heterodyne*-experiment the above function can directly be measured. This is achieved by mixing unscattered laser light with the scattered light coming from the sample. Much easier to perform is the *homodyne*-experiment. Currently, this is the preferred way to perform DLS experiments and leads to the intensity time correlation function $g^2(\tau)$.

$$g^2(\tau) = \frac{\langle E_S^*(t) E_S(t) E_S^*(t+\tau) E_S(t+\tau) \rangle}{\langle I \rangle^2} \tag{3}$$

These two functions are connected by the *SIEGERT*-relation:

$$g^2(\tau) = \left[1 + \left| g^1(\tau) \right|^2 \right] B \tag{4}$$

B is a baseline parameter. In the case of a monodisperse ideal sample $g^1(\tau)$ is represented by a single exponential:

$$g^1(\tau) = \exp(-\Gamma \tau) \tag{5}$$

with $\Gamma = D^T q^2$, D^T being the translational diffusion coefficient and q the scattering vector.[34]

Normally samples are polydisperse and the decay of the correlation function must be described by a weighted sum of exponentials

$$g^1(\tau) = \int_0^{+\infty} G(\Gamma) \exp(-\Gamma\tau)\, d\Gamma\,, \tag{6}$$

where $G(\Gamma)$ is the distribution function of the relaxation rates.

The analysis of this distribution of relaxation rates can be performed with different methods. The ones most frequently used are the method of cumulants[45] and the analysis by an inverse LAPLACE transformation of Eq. (6) by the use of the FORTRAN program CONTIN.[46,47] Another possibility is to apply ORT by O. Glatter.[48,49] In Figure 3 an example for an obtained correlation function is shown. This function was measured for a sample made of deuterated NIPAM cross-linked with 5% hydrogenated BIS. The shown data were measured at a temperature of 302.2 K in D_2O. The solid line in the left part of the figure is the fit obtained using a second order cumulant function.[45] The data are perfectly described by this function and the calculation leads to a z-averaged relaxation rate $\bar{\Gamma}$ of 70 s^{-1}. The found polydispersity is ca. 3%. The right-hand side of the figure shows the relaxation rate distribution function $G(\Gamma)$ as obtained by inverse Laplace transformation of the data using CONTIN.[46,47] Also this distribution reveals the low polydispersity of the prepared microgel particles. The z-averaged relaxation rate obtained using CONTIN is 68 s^{-1}.

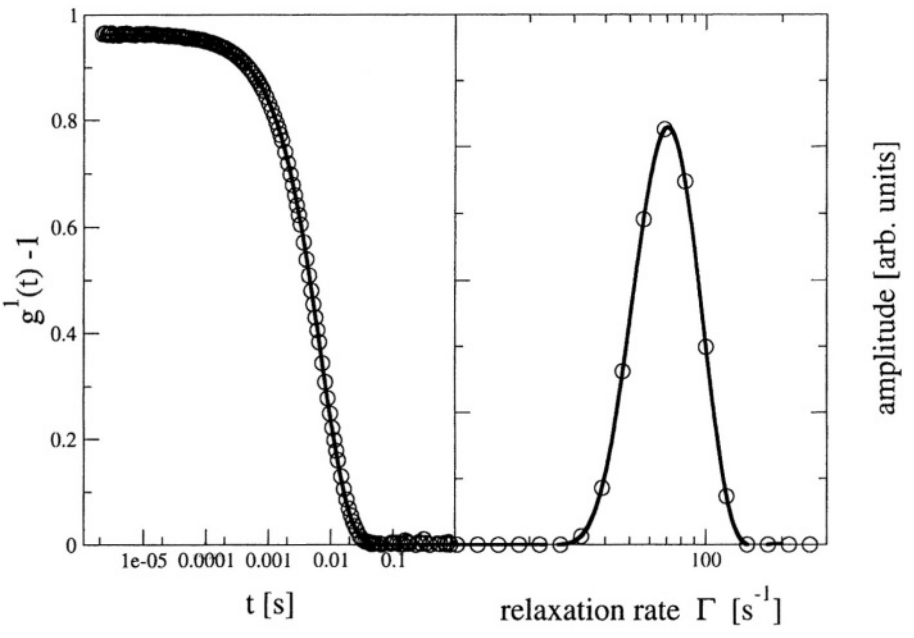

Figure 3. Experimental correlation function for a microgel made of deuterated NIPAM containing 5% hydrogenated cross-linker (BIS) (left part of the figure). The solid line is the fitting result with a second order cumulant function.[45] The right hand side of the figure shows the respective inverse Laplace transform obtained using CONTIN.[46,47]

From the mean value $\bar{\Gamma}$ one can obtain D^T:

$$\bar{\Gamma} = D^T q^2 \tag{7}$$

Knowing D^T it is easy to calculate the STOKES-radius R_S making use of the STOKES-EINSTEIN-equation.

$$D^T = kT/6\pi\eta R_S \tag{8}$$

with: η being the viscosity, k the BOLTZMANN-constant. The STOKES-radius is the radius of a sphere, behaving hydrodynamically equivalent to the sample. This rather easy determination of a characteristic length scale in the sample makes dynamic light scattering an ideal tool to monitor the swelling and de-swelling of microgels. The swelling ratio of a colloidal microgel particle can be defined by

$$\alpha = V_{\text{collapsed}}/V_{\text{swollen}} = [R_S^{\text{collapsed}}/R_S^{\text{swollen}}]^3 \tag{9}$$

In Figure 4 an example for a swelling curve of a typical microgel is shown. The presented data were obtained for the same microgel as described above (see Figure 3). Partly deuterated microgels are prepared for neutron scattering experiments. The deuteration allows to easily change the scattering contrast and in the present case e.g. to investigate only the scattering from the cross-linker. Compared to microgel particles made with the hydrogenated compounds,[50] the volume transition is shifted to higher temperature by 2.5 K. The swelling ratio α is found to be 0.125 for these particles. This is in agreement with swelling ratios found for the hydrogenated particles at comparable cross-linker concentration.[21,24,50]

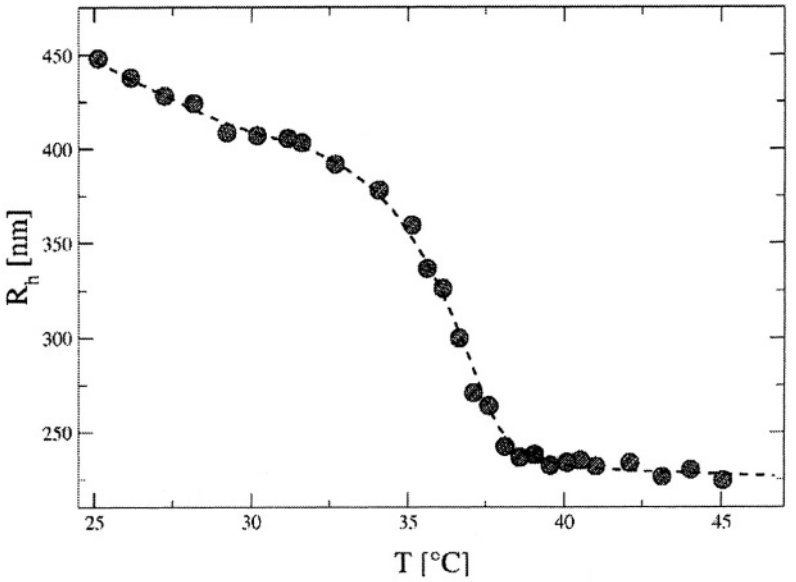

Figure 4. Swelling curve of a PNIPAM microgel containing 5% cross-linker (BIS). The microgel was prepared with deuterated NIPAM. The solvent is heavy water (dashed line = guide to the eye).

3.2. Small Angle Neutron Scattering

In general SANS curves obtained from solutions of particles exhibiting a low polydispersity can be described by

$$I(q) = N\,S(q)P(q) + I_{\text{incoherent}}, \tag{10}$$

where $S(q)$ is the inter-particle structure factor, N is the particle concentration, and $P(q)$ is the particle form factor. The scattering vector q is given by Eq. (1). $I_{\text{incoherent}}$ is the so-called incoherent background arising from the q independent scattering from hydrogen. For low concentration and intermediate or large values of q the inter-particle structure factor $S(q) \approx 1$ and therefore the analysis of the experiments has mainly to deal with the particle form factor.[51,52]

For the rather large microgel particles the scattering at low q-values is dominated by the Porod part[53] of the particle form factor (leads to $I(q) \propto q^{-4}$).

At high q-values the internal network structure of the microgels is contributing significantly to the scattered intensity.[21,22,31,50] This contribution can be described by an ORNSTEIN-ZERNICKE function and the scattered intensity can be written as

$$I(q) = N\frac{A}{V}\frac{1}{q^4} + \frac{I(0)_{OZ}}{1+\xi^2 q^2} + I_{incoherent}\,. \tag{11}$$

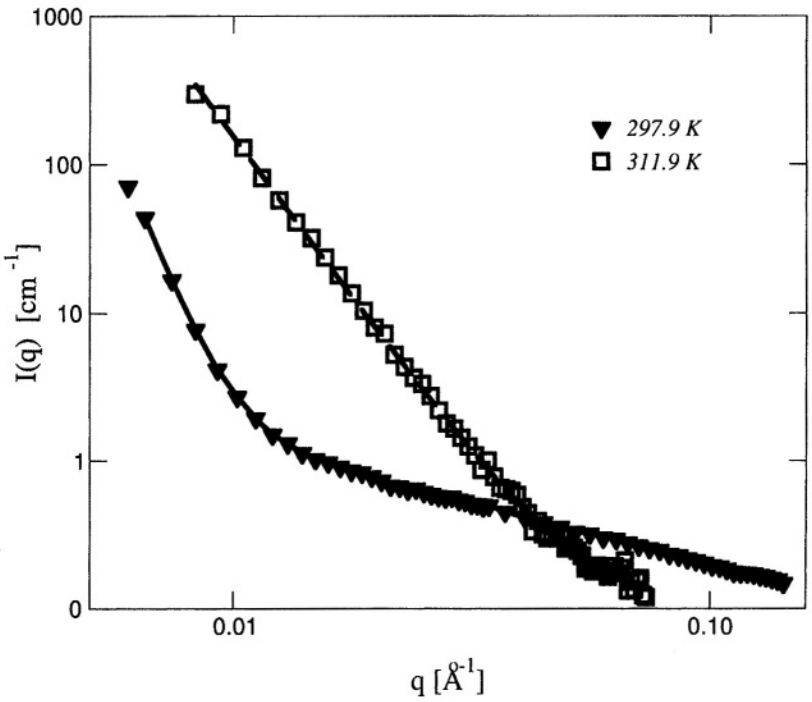

Figure 5. Typical small angle scattering curves as obtained from a microgel (NIPAM, 7% BIS) in the swollen (triangles) and in the shrunken state (circles). The solid line indicates a fit to Eq. (11). The dashed line which is used to describe the collapsed microgel is a simple fit to Porod law.

Here, $I(0)_{OZ}$ denotes the scattering intensity of the ORNSTEIN-ZERNICKE part at $q = 0$. In this equation A is the interfacial area in the scattering volume and V the scattering volume. The contribution from the cross-links, which can be resolved in macroscopic gels[6,54-56] is omitted in this description. In microgels this contribution is negligible compared to the form factor contribution and can therefore not be resolved. In Figure 5 an example for the small angle scattering curves as obtained from a typical suspension of microgels is shown. At low temperature the experimental data (triangles) can be described by Eq. (11). This leads to a correlation length ξ of the network of 2.4 nm.[50] At high temperatures the network is collapsed and only the Porod contribution remains (circles). For large particles it is however difficult to obtain information about the form factor (and therefore the size, shape and the polydispersity) of the microgels. This is due to their rather large diameter. Because of the different q-range static light scattering is well suited for this purpose and will be discussed in the next section.

3.3. Static Light Scattering

In principle for large particles a static light scattering experiment is simply performed by measuring the $I(q)$ as a function of q. An example for a typical experimental result is shown in Figure 6.

The solid line in Figure 6 is a fit using an analytical solution of the following integral

$$P_{\sigma,R_0}(q) = \frac{1}{\sqrt{\pi\sigma^2 q^6}} \int_0^\infty [\sin(qR) - qR\cos(qR)]^2 \exp\left(\frac{(R-R_0)^2}{2\sigma^2}\right) dR \,. \tag{12}$$

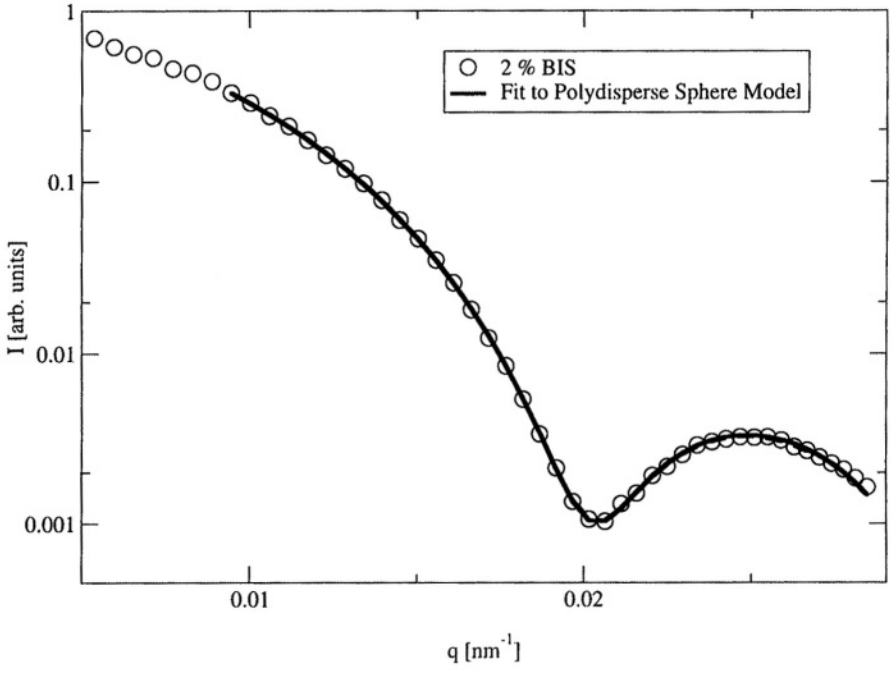

Figure 6. Static light scattering intensity as a function of q for a BIS (2%) cross-linked PNIPAM microgel.

In this description the polydispersity of the particles is modeled assuming a Gaussian particle size distribution. The argument has to be integrated over the interval $-\infty$ to ∞ to find an analytical solution. This leads to a negligible error, when the polydispersity is low (error $\leq$ 1%). The obtained fit is represented by the solid line in Figure 6 and leads to the following parameters characterizing the investigated particles (i.e. PNIPAM microgels cross-linked with 2% BIS).

The radius of gyration R_g is found to be 221 nm and the polydispersity is 5%. This value is not corrected for the instrumental resolution. The same form factor can also be used to analyze SANS data obtained for smaller particles or SANS data measured in a comparable q-range. On some SANS machines it is possible to nearly reach the q-range of SLS (e.g. the D11 machine at the ILL in Grenoble) and currently several ultra small angle neutron scattering (USANS) machines are under development. In Figure 7 SLS and SANS experiments on the same microgel particles are compared.

The form factor minima are found at approximately the same position. However, the SANS curve shows a much stronger smearing of the form factor.[38,57] This is due to the different collimation and the broader initial wavelength distribution in SANS experiments compared to SLS. Another aspect is that SLS experiments can and have to be performed on extremely dilute solutions. The SANS samples contain 10 vol% of polymer. Therefore, also structure factor influences are present, at least at low q-values.

From the data shown in Figure 7 the radius of gyration, R_g, is found to be (338 ±30) nm (SLS) and (276 ±35) nm (SANS), respectively.

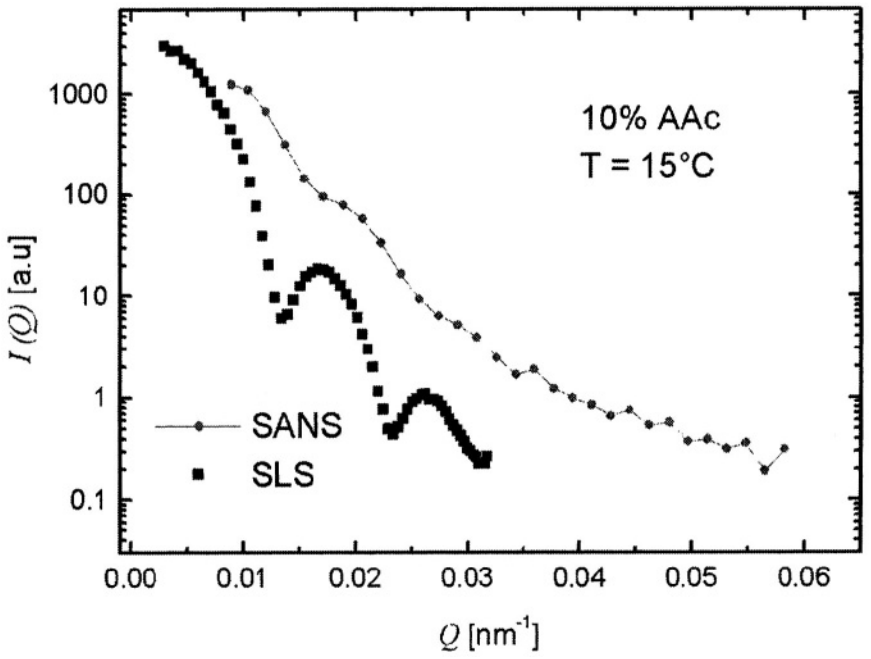

Figure 7. Comparison of SLS and SANS data measured for the same PNIPAM-co-acrylic acid microgel. The particles were cross-linked using 3% BIS.

3.4. Characterization of Microgel Based Colloidal Crystals

As other colloidal particles, microgels can form colloidal crystals. The phase diagram for this crystallization process was studied by Senff and Richtering.[24] However, compared to "classical" colloids (e.g. PMMA spheres) microgels offer an interesting additional feature, because of their temperature sensitivity. Microgel crystals can be molten by increasing the temperature slightly above the LCST.[26] This can be used to reduce the number of grain boundaries in the obtained crystals. With respect to crystal formation copolymer particles with styrene as co-monomer are especially interesting. They exhibit very low polydispersities. In Figure 8 a scanning electron micrograph of a crystal of these PNIPAM-co-PS particles is shown.

Scattering methods can be employed to get information about the crystal structure in colloidal systems.[26,58,59] In SANS experiments one would measure a dilute solution of the particles to determine the form factor $P(q)$. Then the structure factor can be obtained by dividing an experimental curve from a crystallized sample by this form factor following

$$I(q) \propto S(q)\, P(q). \tag{13}$$

From the peak positions in the structure factor the crystal structure can then be derived. This is e.g. shown in ref. 26.

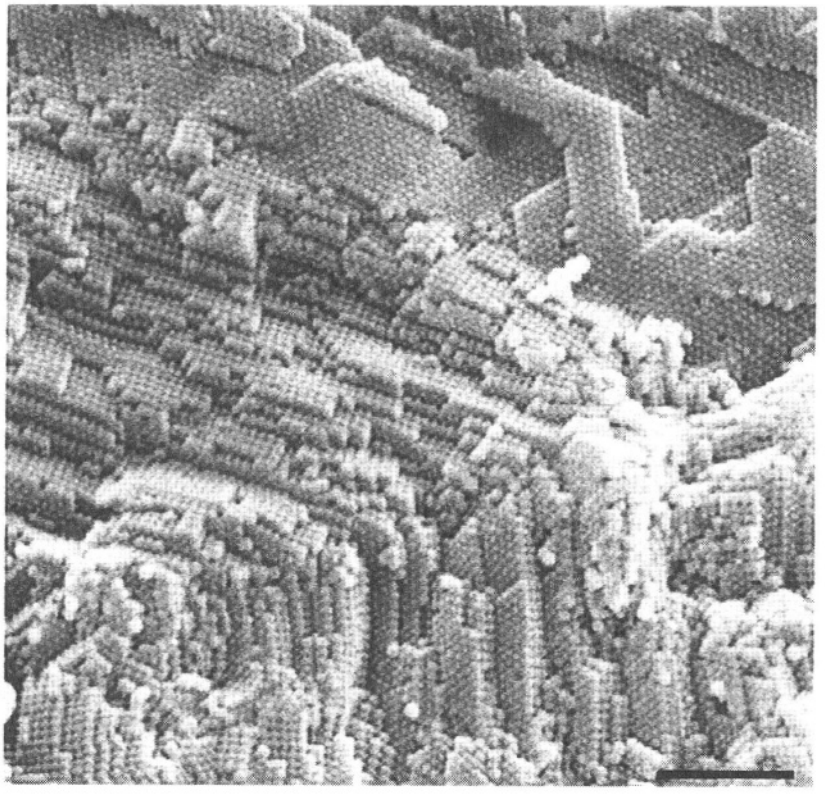

Figure 8. Crystallized PNIPAM-co-PS particles with styrene content of 75% (the solid line indicates 3 μm).

3.5. Internal Dynamics of Microgels Studied by Neutron Spin-Echo Spectroscopy

It is not an easy task to investigate the network dynamics of a gel. Most of the studies of dynamics in gels used DLS experiments. DLS measurements on gels have to cope with two major difficulties. Firstly, gels are non-ergodic media.[60,61] Secondly, at higher cross-linker concentration the systems are opaque. Additionally, investigating microgels with respect to internal movements is complicated by the center of mass diffusion of the particles, which is the major contribution to the intermediate scattering function (intensity correlation function ISF).[62] An experimental technique, which can be used to access the network breathing modes is the neutron spin-echo technique, which was invented by Mezei.[63] This type of experiment overcomes some of the disadvantages of DLS when investigating gels (e.g. NSE yields directly the ensemble average and can also be used for highly cross-linked systems) and was already successfully applied to microgels.[23] The first NSE spectrometer was realized at the ILL in Grenoble (IN 11 machine), but only very recently several new machines became available, making the method accessible for a larger public.[64-70] However, the experiments presented here were carried out on the IN 11 machine.

The spin-echo method is based on the fact that the neutron has a magnetic moment. It can therefore be spin-polarized using magnetic super-mirrors.[71] The spin is then used as a kind of hand of a watch which is attached to each neutron. This allows to measure the speed of each neutron separately, and therefore also changes in speed due to quasi-elastic scattering caused by the dynamics in the sample under investigation. The experiment has lot of similarities with nuclear magnetic resonance self-diffusion measurements.[72,73] The energy exchange with the sample leads simply to a loss of polarization of the re-focused neutrons compared to an elastically scattering standard sample (e.g. graphite).[74-77] The spin-echo polarization P is defined by

$$P = (N_{up} - N_{down})/(N_{up} + N_{down}) \tag{14}$$

where $N_{up/down}$ indicates the number of neutrons oriented spin-up and spin-down after the precession coils. These two numbers are measured using the change of the current in the last $\pi/2$-flipper and P can then be calculated.

The probability for a scattering process with an energy transfer ω is described by the dynamic structure factor $S(q,\omega)$. Averaging $\cos(\Delta\psi)$ with $S(q,\omega)$ leads to

$$\langle P_S \rangle_E = \langle \cos(\Delta\psi) \rangle_E = \frac{\int S(q,\omega)\cos(t\Delta\omega)\,\mathrm{d}\omega}{\int S(q,\omega)\,\mathrm{d}\omega}, \tag{15}$$

with $\Delta\psi = t\,\Delta\omega$.

This Fourier transform in time can be rewritten as

$$\langle P_S(q,t) \rangle_E = \frac{\langle I(q,t) \rangle_E}{\langle I(q,0) \rangle_E}. \tag{16}$$

$\langle ... \rangle_E$ indicates the ensemble average, which is obtained in an NSE experiment due to the relationship between beam and sample dimension.

The Fourier time is given by

$$t = [(\gamma\, l_0\, H_0\, m^2) / (2\pi\, h^2)]\, \lambda^3. \quad (17)$$

Here, λ is the wavelength of the neutrons, γ the gyro-magnetic ratio and $l_0 H_0$ the integral of the magnetic field along the neutrons path.[74,75,78] Each Fourier time corresponds to one point of the intermediate scattering function, and the intermediate scattering function (or correlation function) describing the dynamics in the sample is obtained by variation of the current in the precession coils. By changing the wavelength the probed time window can be extended.

The first approach describing the network dynamics in a gel was published by Tanaka and co-workers[1] and predicts a simple single exponential decay for the intermediate scattering function.

$$\langle ISF(q,t)\rangle_E \propto \exp(-\Gamma t) \quad (18)$$

However, as already mentioned DLS experiments on gels are always perturbed by the non-ergodicity of the network. In NSE experiments due to the short neutron wavelength the condition $q^2\langle\xi^2\rangle \to \infty$ is approximately fulfilled.[60] This should allow us to obtain quasi-ergodic scattering behavior or in other words the simple behavior as predicted by Eq. (18) should be recovered. In Figure 9 experimental $\langle ISF(q,t)\rangle_E$ curves are shown for a PNIPAM microgel cross-linked with the cross-linker EGDMA (15 mol%).[22]

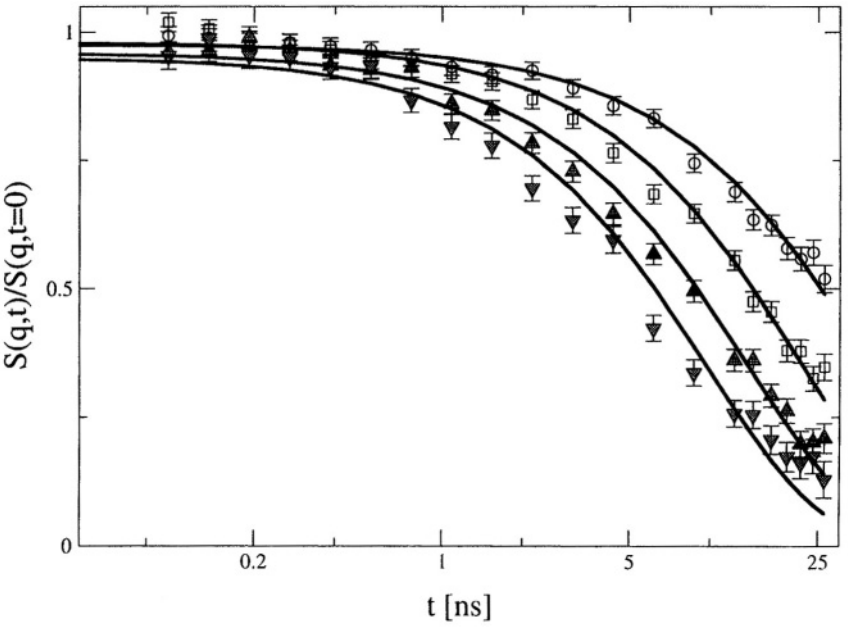

Figure 9. Experimental intermediate scattering functions for immobilized PNIPAM microgels cross-linked with 15 Mol\% EGDMA at four different q-values. Solid lines are single exponential fits (two adjustable parameters).

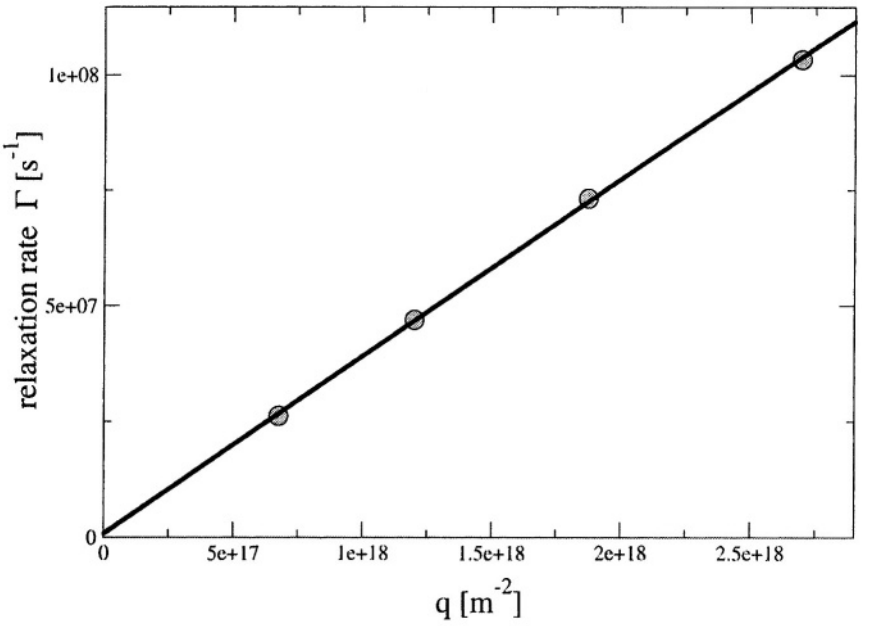

Figure 10. Plot of the relaxation rates for the EGDMA cross-linked microgels. The linear q^2-dependence reveals the diffusional character of the obtained dynamics.

The particle volume fraction in these experiments was close to 1 (→ particles immobilized; no center of mass diffusion). The shown data were obtained at four different scattering angles (6°, 8°, 10°, 12°) and using neutrons with a wavelength of 8Å. The solid lines in Figure 9 represent fits to Eq. (18).

In Figure 10 the obtained relaxation rates describing the decay of the single exponential fits are plotted as a function of q^2. As predicted for network breathing modes (breathing modes have the same dispersion relation as diffusional movements; see Eq. (7)) a nice linear dependence is found. The diffusion coefficient associated with the breathing mode is calculated to be 3.8262×10^{-11} m^2s^{-1}. This quantity can now be related to mechanical properties of the network[79] and to the correlation length of the breathing mode.

4. SUMMARY AND OUTLOOK

This chapter can of course not be complete, but we hope we have demonstrated that colloidal PNIPAM microgels are interesting particles, which offer a lot of possibilities with respect to applications due to the combination of colloidal properties with those of the network. Scattering methods are well suited to characterize these particles and ordered assemblies formed by them.

For future work it will be of great importance to vary the properties (e.g. LCST) by copolymerization with different comonomers. This strategy can also be used to prepare particles with enhanced bio-compatibility. A second interesting route for further experiments is the investigation of the formed mesoscopic crystals of these materials, which may be useful as templates for the preparation of mesoporous inorganic materials.

5. ACKNOWLEDGMENTS

The author would like to thank K. Kratz and W. Eimer for the fruitful cooperation. The author is grateful to the Laboratoire Léon Brillouin (Laboratoire comun CEA/CNRS) and the Institut Laue Langevin for providing beam-time. Also financial support from the European Union within the HIPRI program is gratefully acknowledged.

6. REFERENCES

1. T. Tanaka, L. O. Hocker, and G. B. Benedek, Spectrum of light scattered from a viscoelastic gel, *J. Chem. Phys.* **59**, 5151-5159 (1973).
2. T. Tanaka and D. J. Fillmore, Kinetics of swelling of gels, *J. Chem. Phys.* **70**, 1214-1218 (1979).
3. T. Tanaka, D. Fillmore, S.-T. Sun, I. Nishio, G. Swislow, and A. Shah, Phase transitions in ionic gels, *Phys. Rev. Lett.* **45,** 1636-1639 (1980).
4. Y. Hirokawa and T. Tanaka, Volume phase transition in a nonionic gel, *J. Chem. Phys.* **81**, 6379-6380 (1984).
5. M. Shibayama, Spatial inhomogeneity and dynamic fluctuations of polymer gels, *Macromol. Chem. Phys.* **199**, 1-30(1998).
6. M. Shibayama, T. Tanaka, and C. C. Han, Small angle neutron scattering study on poly(N-isopropyl acrylamide) gels near their volume-phase transition, *J. Chem. Phys.* **97**, 6829-6841 (1992).
7. K. Dusek, *Responsive Gels: Volume Transitions I,* volume 109 of *Advances in Polymer Science,* Springer Verlag, Berlin, 1st edition, 1993.
8. K. Dusek, *Responsive Gels: Volume Transitions II,* volume 110 of *Advances in Polymer Science,* Springer Verlag, Berlin, 1st edition, 1993.
9. M. Shibayama, T. Tanaka, and C. C. Han, Small-angle neutron scattering study on weakly charged temperature sensitive polymer gels, *J. Chem. Phys.* **97**, 6842-6854 (1992).
10. M. Shibayama and T. Tanaka, Small-angle neutron scattering study on weakly charged poly(N-isopropyl acrylamide-co-acrylic acid) copolymer solutions, *J. Chem. Phys.* **102**, 9392-9400 (1995).
11. M. Shibayama, S. Takata, and T. Norisuye, Static inhomogeneities and dynamic fluctuations of temperature sensitive polymer gels, *Physica A* **249**, 245-252 (1998).
12. M. Shibayama, F. Ikkai, S. Inamoto, S. Nomura, and C. C. Han, pH and salt concentration dependence of the microstructure of poly(N-isopropylacrylamide-co-acrylic acid) gels, *J. Chem. Phys.* **105**, 4358-4366 (1996).
13. V. S. Shinde, M. V. Badiger, A. K. Lele, and R. A. Mashelkar, Core-shell morphology in poly(N-isopropyl acrylamide) copolymer gels induced by restricted diffusion of surfactant, *Langmuir* **17**, 2585-2588, 2001.
14. R. H. Pelton and P. Chibante, Preparation of aqueous latices with N-isopropylacrylamide, *Colloid Surf.* **20**, 247(1986).
15. M. J. Snowden, B. Z. Chowdhry, B. Vincent, and G. E. Morris, Colloidal copolymer microgels of N-isopropylacrylamide and acrylic acid: pH, ionic strength and temperature effects, *J. Chem. Soc., Faraday Trans.* **92**, 5013-5016(1996).
16. H. M. Crowther and B. Vincent, Swelling behavior of poly(N-isopropylacrylamide) microgel particles in alcoholic solutions, *Colloid Polym. Sci.* **276**, 46-51 (1998).
17. P. Bouillot and B. Vincent, A comparison of the swelling behaviour of copolymer and interpenetrating network microgel particles, *Colloid Polym. Sci.* **278**, 74-79 (2000).
18. J. R. Weeeks, J. S. van Duijneveldt, and B. Vincent, Formation and collapse of gels of sterically stabilized colloidal particles, *J. Phys.: Condens. Matter.* **12**, 9599-9606 (2000).
19. K. Kratz, T. Hellweg, and W. Eimer, Influence of charge density on the swelling of colloidal poly(N-isopropylacrylamide-co-acrylic acid) microgels, *Colloid Surf. A* **170**, 137-149 (2000).
20. K. Kratz, T. Hellweg, and W. Eimer, Effect of connectivity and charge density on the swelling and local structural properties of colloidal PNIPA microgels, *Ber. Bunsenges. Phys. Chem.* **102**, 1603-1608 (1998).
21. H. M. Crowther, B. R. Saunders, S. J. Mears, T. Cosgrove, B. Vincent, S. M. King, and G.-E. Yu, Poly(NIPAM) microgel particle de-swelling: a light scattering and small-angle neutron scattering study, *Colloid Surf. A* **152**, 327-333 (1999).
22. K. Kratz, A. Lapp, W. Eimer, and T. Hellweg, Volume phase transition and structure of TREGDMA, EGDMA, and BIS cross-linked PNIPAM microgels: A small angle neutron and dynamic light scattering study, *Colloid Surf. A* **197**, 55-67 (2002).

23. T. Hellweg, K. Kratz, S. Pouget, and W. Eimer, Internal dynamics in colloidal PNIPAM microgel particles immobilised in a mesoscopic crystal, *Colloid Surf. A* **202**, 223-232 (2002).
24. H. Senff and W. Richtering, Influence of cross-link density on rheological properties of temperature-sensitive microgel suspensions, *Colloid Polym. Sci.* **278**, 830-840 (2000).
25. F. M. Horn, W. Richtering, J. Bergenholtz, N. Willenbacher, and N. J. Wagner, Hydrodynamic and colloidal interactions in concentrated charge-stabilized polymer dispersions, *J. Colloid Interface Sci.* **225**, 166-178(2000).
26. T. Hellweg, C. D. Dewhurst, E. Brückner, K. Kratz, and W. Eimer, Colloidal crystals made of PNIPA-microgel particles, *Colloid Polym. Sci.* **278**, 972-978 (2000).
27. L. Zha, J. Hu, C. Wang, S. Fu, A. Elaissari, and Y. Zhang, Preparation and characterization of poly(N-isopropylacrylamicde-co-dimethylaminoethy methacrylate) microgel latexes, *Colloid Polym. Sci.* **280**, 1-6 (2002).
28. T. Gilanyi, I. Varga, R. Meszaros, G. Filipcsei, and M. Zrinyi, Interaction of monodisperse poly(N-isopropylacrylamide) microgel particles with sodium dodecyl sulfate in aqueous solution, *Langmuir* **17**, 4764-4769(2001).
29. N. Dingenouts, C. Nordhausen, and M. Ballauff, The volume transition in thermosensitive micronetworks as observed by small-angle X-ray scattering, *Ber. Bunsenges. Phys. Chem.* **102**, 1594-1596 (1998).
30. N. Dingenouts, C. Nordhausen, and M. Ballauff, Observation of the volume transition in thermosensitive core-shell latex particles by small-angle-X-ray scattering, *Macromolecules* **31**, 8912-8917 (1998).
31. N. Dingenouts, S. Seelenmeyer, I. Deike, S. Rosenfeldt, M. Ballauff, P. Lindner, and T. Narayanan, Analysis of thermosensitive core-shell colloids by small-angle neutron scattering including contrast variation, *Phys. Chem. Chem. Phys.* **3,** 1169-1174 (2001).
32. R. Pelton, Temperature-sensitive aqueous microgels, *Adv. Colloid Interface Sci.,* **85**, 1-33 (2000).
33. K. Kratz and W. Eimer, Swelling properties of colloidal poly(N-isopropylacrylamide) microgels in solution, *Ber. Bunsenges. Phys. Chem.* **102**, 848-854 (1998).
34. B. J. Berne and R. Pecora, *Dynamic Light Scattering,* John Wiley & sons, Inc., New York, 1976.
35. J. S. Higgins and R. S. Stein, Recent developments in polymer applications of small-angle neutron, X-ray and light scattering, *J. Appl. Cryst.* **11**, 346-375 (1978).
36. A. Maconnachie and R. W. Richards, Neutron scattering and amorphous polymers, *Polymer* **19**, 739-762 (1978).
37. H. Eisenberg, Forward scattering of light, X-rays and neutrons, *Quarterly Rev. Biophys.* **14**, 141-172 (1981).
38. O. Glatter and O. Kratky, *Small Angle X-ray Scattering,* Academic Press, London, 1982.
39. K. S. Schmitz, *An Introduction to Dynamic Light Scattering by Macromolecules,* Academic Press, Inc., New York, 1990.
40. W. Brown, *Dynamic Light Scattering,* Clarendon Press, Oxford, 1993.
41. J. Baruchel, J.-L. Hodeau, M. S. Lehmann, J.-R. Regnard, and C. Schlenker, editors, *Dynamics and Diffusion in Macromelcules, Colloids and Microemulsions,* Springer Verlag, Berlin, 1994.
42. J. S. Higgins and H. C. Benoit, *Polymers and Neutron Scattering,* Clarendon Press, Oxford, 2 edition, 1996.
43. M. Ballauff, SAXS and SANS studies of polymer colloids, *Current Opinion in Colloid & Interface Sci.* **6**, 132-139(2001).
44. R. Zwanzig, Time-correlation functions and transport coefficients in statistical mechanics, *Ann. Rev. Phys. Chem.* **16,** 67-102 (1965).
45. D. E. Koppel, Analysis of macromolecular polydispersity in intensity correlation spectroscopy: The method of cumulants, *J. Chem. Phys.* **57**, 4814-4820 (1972).
46. S. W. Provencher, A constrained regularization method for inverting data represented by linear algebraic or integral equations, *Computer Physics Com.* **27**, 213-217 (1982).
47. S. W. Provencher, Contin: a general purpose constrained regularization program for inverting noisy linear algebraic and integral equations, *Computer Physics Com.* **27**, 229-242 (1982).
48. O. Glatter, Data evaluation in small angle scattering: Calculation of the radial electron density distribution by means of indirect fourier transformation, *Acta Physica Austriaca* **47**, 83-102 (1977).
49. O. Glatter, A new method for the evaluation of small-angle scattering data, *J. Appl. Cryst.* **10**, 415-421 (1977).
50. K. Kratz, T. Hellweg, and W. Eimer, Structural changes in PNIPA microgel particles as seen by SANS, DLS, and EM techniques, *Polymer* **42**, 6531-6539 (2001).
51. T. Hellweg and D. Langevin, The dynamics in dodecane/$C_{10}E_5$/water microemulsions determined by time resolved scattering techniques, *Physica A* **264**, 370-387 (1999).

52. M. Gradzielski, D. Langevin, and B. Farago, Experimental investigation of the structure of nonionic microemulsions and their relation to the bending elasticity of the amphiphilic film, *Phys. Rev. E* **53**, 3900-3919 (1996).
53. L. Auvray and P. Auroy, *Scattering by Interfaces: Variations on Porod's Law,* pp. 199-221, Elsevier Science Publishers B.V., 1991.
54. A.-M. Hecht, R. Duplessix, and E. Geissler, Structural inhomogeneities in the range 2.5-2500 Å in polyacrylamide gels, *Macromolecules* **18**, 2167-2173 (1985).
55. S. Mallam, F. Horkay, A.-M. Hecht, A. R. Rennie, and E. Geissler, Microscopic and macroscopic thermodynamic observations in swollen poly(dimethylsiloxane) networks, *Macromolecules* **24**, 543-548 (1991).
56. F. Horkay, A.-R. Hecht, S. Mallam, E. Geissler, and A. R. Rennie, Macroscopic and microscopic thermodynamic observations in swollen poly(vinyl acetate) networks, *Macromolecules* **24**, 2896-2902 (1991).
57. N. Dingenouts and M. Ballauff, Structural investigation of latexes by small-angle X-ray scattering in slit collimation: Measurements and evaluation of data, *Acta Polymer.* **49**, 178-183 (1998).
58. A. Heymann, A. Stipp, C. Sinn, and T. Palberg, Observations of oriented close-packed lattice planes in polycrystalline hard-sphere solids, *J. Colloid Interface Sci.* **207**, 119-127 (1998).
59. Th. Palberg, Crystallization kinetics of repulsive colloidal spheres, *J. Phys.: Condens. Matter.* **11,** R323-R360 (1999).
60. P. N. Pusey and W. van Megen, Dynamic light scattering by non-ergodic media, *Physica A* **157**, 705-741 (1989).
61. J. G. H. Joosten, E. T. F. Gelade, and P. N. Pusey, Dynamic light scattering by nonergodic media: Brownian particles trapped in polyacrylamide gels, *Phys. Rev. A* **42**, 2161-2175 (1990).
62. C. Wu and S. Zhou, Internal motions of both poly(N-isopropylacrylamide) linear chains and spherical microgel particles in water, *Macromolecules* **29**, 1574-1578 (1996).
63. F. Mezei, Neutron spin echo: A new concept in polarized thermal neutron techniques, *Z. Phys.* **255**, 146-160 (1972).
64. T. Takeda, S. Komura, H. Seto, M. Nagai, H. Kobayashi, E. Yokoi, T. Ebisawa, S. Tasaki, C. M. E. Zeyen, Y. Ito, S. Takahashi, and H. Yosshizawa, Neutron spin-echo spectrometer at jrr-3m, *Physica B* **213**, 863-865 (1995).
65. M. Köppe, P. Hank, J. Wuttke, W. Petry, R. Gähler, and R. Kahn, Performance and future of a neutron resonance spinecho spectrometer, *J. Neutron Res.* **4**, 261-273 (1996).
66. M. Monkenbusch, The Jülich neutron spin echo spectrometer, *Neutron News* **8**(1), 25 (1997).
67. M. Monkenbusch, R. Schatzler, and D. Richter, The Jülich neutron spin-echo spectrometer - design and performance, *Nuclear Instruments & Methods in Physics Research Section A* **399**, 301-323 (1997).
68. C. Pappas, G. Kali, P. Boni, R. Kischnik, L. A. Mertens, P. Granz, and F. Mezei, Performance of the multidetector nse spectrometer span at bensc, *Physica B* **268**, 285-288 (1999).
69. M. Köppe, M. Bleuel, R. Gähler, R. Golub, P. Hank, T. Keller, S. Longeville, U. Rauch, and J. Wuttke, Prospects of resonance spin-echo, *Physica B* **266**, 75-86 (1999).
70. S. Longeville, La spectroscopie neutronique a echo de spin a champ nul ou par resonance, *J. Phsys. IV France* **10**, Prl-59-Prl-75 (2000).
71. P. Boni, D. Clemens, M. S. Kumar, and C. Pappas, Applications of remanent supermirror polarizers, *Physica B* **268**, 320-327 (1999).
72. P. T. Callaghan, Pulsed field gradient nuclear magnetic resonance as a probe of liquid state molecular organization, *Aust. J. Phys.* **37**, 359-87 (1984).
73. M. Nyden, O. Söderman, and P. Hansson, Microemulsions in the didodecyldimethylammonium sulfate (bromide)/hydrocarbon/water system. Microstructure and specific counterion effects, *Langmuir* **17**, 6794-6803 (2001).
74. F. Mezei, editor, *Neutron Spin Echo,* volume 124 *of Lecture Notes in Physics,* Springer Verlag, Berlin, 1980. Prodeedings from Spin-echo meeting in Grenoble 1979.
75. J. B. Hayter, In S.-H. Chen, B. Chu, and R.~Nossal, editors, *Scattering Techniques Applied To Supramolecular And Nonequilibrium Systems,* pp. 3-33, Plenum Press, New York, 1981.
76. R. Pynn, Neutron spin-echo and three-axis spectrometers, *J. Phys. E: Sci Instrum.* **11**, 1133-1140, 1978.
77. R. Papoular, La spectromètre par Echos de Spin de Neutron. Application a l'ètude de la dynamique des polymers en solution, PhD thesis, Universitè de Paris-Sud, 1992.
78. B. Farago. In J. Baruchel, J.-L. Hodeau, M. S. Lehmann, J. R. Regnard, and C. Schlenker, editors, *HERCULES: Neutron and Synchrotron Radiation for Condensed Matter Studies. Vol. 3: Applications to Soft Condensed Matter and Biology,* chapter 7, pp. 93-116. Springer Verlag, Berlin, 1994.
79. A. M. Hecht and E. Geissler, Dynamic light scattering from polyacrylamide-water gels, *J. Phys.* **39**, 631-638(1978).

This page intentionally left blank

11
DESIGN OF NANOSCALE MATERIALS USING SILICA-COATED METAL NANOCOLLOIDS

Luis M. Liz-Marzán *

1. INTRODUCTION

This chapter deals with the synthesis and properties of nanostructures based on the assembly of composite nanoparticles with core-shell morphology. The interest of such nanosystems relies mostly on the combination of the properties of the two (or more) materials involved, with the important feature that one of the materials (the shell) will determine the surface properties of the particles, while another (the core) is completely encapsulated by the shell, so that it does not contribute to surface properties at all but can be mainly responsible for other (optical, catalytic, magnetic, etc.) properties of the system. Apart from this extremely important feature, it is also essential to take into account the possible interactions between the core and the shell, which may in certain cases determine the potential applications of the material.

Due to the unique combination of properties achieved by using the core-shell geometry, there has been an increasing interest in creating nanomaterials and nanostructures with unique, complex properties. The properties of interest are mainly optical, electronic or magnetic, involving metal, oxide or semiconductor nanoparticles. Encapsulated particles have been known since the 1920's. However, it was only in 1951, that the first theoretical studies were reported by Aden and Kerker,[1] who extended Mie theory for the optical properties of spherical particles to include the interaction of plane electromagnetic waves with a sphere coated with a concentric spherical shell, with the view to applying it to certain problems in radar meteorology. The first experiments on core-shell metal particles only appeared later in 1964 when Morriss and Collins[2] applied the theory of Aden and Kerker to silver coated gold sols. As metal nanoparticles gained increasing attention, more detailed investigations began in the late 1980's, encompassing various types and aspects of coated particles. In the case of semiconductor nanoparticles, or quantum dots, the core-shell strategy has been often used to enhance the luminescence efficiency, while magnetic particles have been coated to improve their colloidal and chemical stability and to create thin films with improved properties for data storage. Thorough descriptions of the different kinds of core-shell particles that have been studied, as well as their properties can be found in recent reviews.[3,4] The focus of this

* Luis M. Liz-Marzán, Departamento de Química Física, Universidade de Vigo, Vigo, Spain, 36200.

chapter will be on the description of different techniques that can be used for the construction of nanoscale materials, using core-shell nanoparticles as building blocks. It will be shown how the use of particles comprising two different materials can lead to materials with novel properties, that can therefore be utilized in practice to improve the efficiency of real devices. Although several different properties can be exploited, we shall concentrate here on optical properties, and specifically those related to the use of metal nanoparticles. In order to understand the discussion below, it will be necessary to have a basic knowledge about the interaction between electromagnetic radiation and metal nanoparticles. Both detailed[5] and simplified[6] accounts of such phenomena can be found in several recent publications. However, with the aim to facilitate the further reading of this chapter, provided in the following section is a short description of the phenomenon and how it can be modeled.

Then, various assemblies of gold nanoparticles coated with silica (which will be denoted $Au@SiO_2$), as well as their optical properties will be described. The main benefits from using such nanoparticles, rather than "bare" nanoparticles, stem from: (1) a greatly enhanced colloidal stability, especially in aqueous media; and (2) the possibility to tune the separation between the metal nanoparticles through the thickness of the silica shell. Stable dispersions are a requirement for the assembly of close-packed films and ordered, crystalline assemblies, while a precise control of interparticle separation will be essential for a suitable control of interparticle interactions.

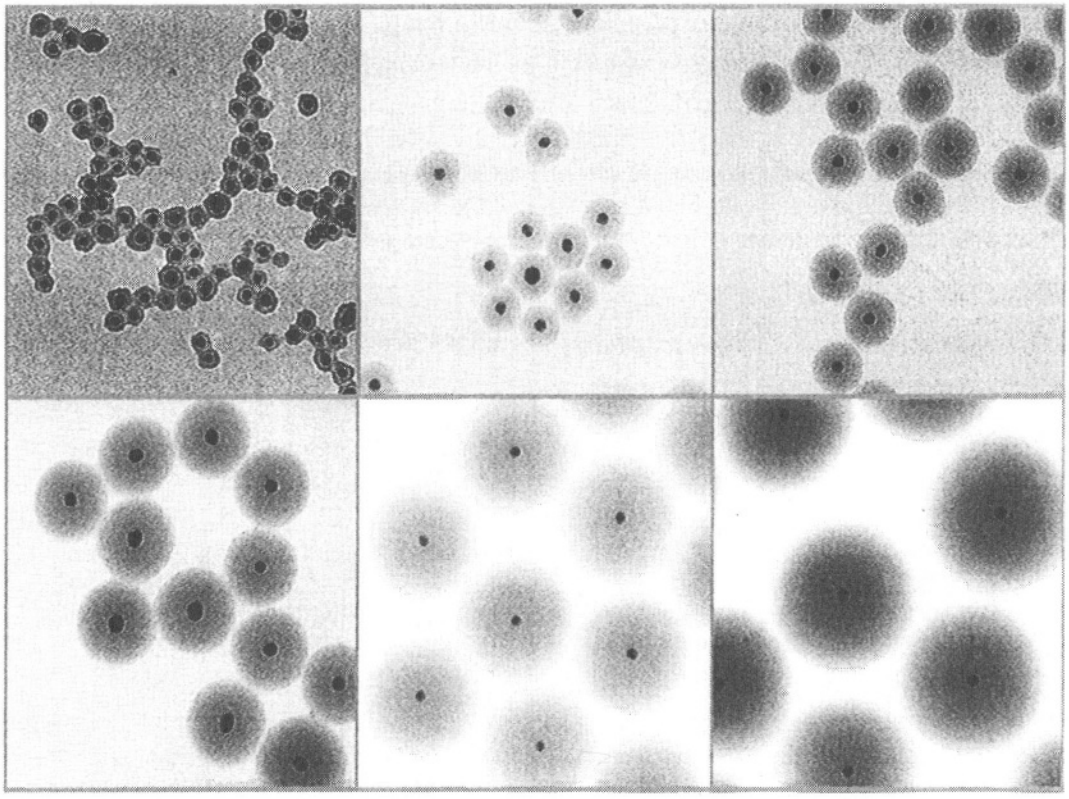

Figure 1. Transmission electron micrographs of $Au@SiO_2$ nanoparticles with cores of the same size (15 nm) and increasingly thick silica shells.

Several accounts have been published on the coating of colloid particles with silica, mainly based on either the polymerization of silicate moieties from aqueous solution,[7] or on the hydrolysis and condensation of alkoxysilanes in an alcohol[8] or in microemulsion.[9] However, the coating of citrate-stabilized gold[10] or silver[11] nanoparticles with uniform silica shells required a preliminary surface modification with a silane coupling agent, so as to facilitate the deposition of thin shells from sodium silicate solution, which allows a fine tuning of the shell thickness through the time of mutual contact with such solution. Thicker shells can then be grown in ethanol through the base-catalyzed hydrolysis and condensation of an alkoxysilane. This method has proven extremely efficient to deposit silica shells with uniform thickness all the way from 1.5 up to several hundreds of nanometers, so that the Au cores are always placed precisely at the center of the sphere. Some examples of silica coated gold nanoparticles with a constant core diameter of ca. 15 nm and varying shell thickness are shown in Figure 1.

2. MODELLING OF OPTICAL PROPERTIES

The optical properties of small metal nanoparticles are dominated by the collective oscillation of conduction electrons due to the interaction with an electromagnetic radiation. Among the different metals, these properties are mainly observed in gold, silver and copper, because of the presence of free conduction electrons. The electric field of the incoming radiation induces the formation of a dipole in the nanoparticle, and there is a restoring force that tries to compensate it, so that a unique resonance wavelength matches this electron oscillation within the nanoparticle.[12] Such a wavelength depends on quite a few factors, among which particle size and shape, as well as the nature of the surrounding medium, are probably the most important ones.[5] The description is restricted here to small spherical particles, but the interested reader can find further information on other shapes in refs. 13 and 14, as well as references therein. Even after setting a restriction to spheres, we need to distinguish two different kinds of systems, based on nanoparticle concentration, because the interactions between neighboring nanoparticles when they are close enough to each other do not allow us to use the same models we use for isolated particles. The properties of dilute dispersions will be discussed first, on the basis of Mie theory and Drude model, while a simple effective medium theory (Maxwell-Garnett) will be described next to account for the behavior of more concentrated systems, such as close-packed thin films.

2.1. Dilute Dispersions

The optical properties of dispersions of spherical particles can be predicted by Mie theory.[15] Mie derived expressions for the extinction cross section of spherical particles with a frequency dependent, complex dielectric function $\varepsilon = \varepsilon' + i\varepsilon''$, embedded in a medium of dielectric function ε_m, which, for very small particles can be expressed as[10,16]

$$C_{ext} = \frac{24\pi^2 R^3 \varepsilon_m^{3/2}}{\lambda} \frac{\varepsilon''}{(\varepsilon' + 2\varepsilon_m)^2 + \varepsilon''^2} \quad (1)$$

In the case of many metals, the region of absorption up to the bulk plasma frequency (in the UV) is dominated by the free electron behavior, and the dielectric response is well described by the simple Drude model. According to this theory,[17] the real and imaginary parts of the dielectric function may be written as,

$$\varepsilon' = \varepsilon^{\infty} - \omega_p^2/(\omega^2 + \omega_d^2) \tag{2}$$

$$\varepsilon'' = \omega_p^2\, \omega_d / \omega(\omega^2 + \omega_d^2), \tag{3}$$

where ε^{∞} is the high frequency dielectric constant due to interband and core transitions and ω_p is the bulk plasma frequency,

$$\omega_p^2 = Ne^2/m\varepsilon_0\,. \tag{4}$$

in terms of N, the concentration of free electrons in the metal, and m, the effective mass of the electron. ω_d is the relaxation or damping frequency, which is related to the mean free path of the conduction electrons, R_{bulk}, and the velocity of electrons at the Fermi energy, v_f, by

$$\omega_d = v_f/R_{bulk.} \tag{5}$$

When the particle radius, R, is smaller than the mean free path in the bulk metal, conduction electrons are additionally scattered by the surface, and the mean free path, R_{eff}, becomes size dependent as

$$1/R_{eff} = 1/R + 1/R_{bulk.} \tag{6}$$

The advantage of the Drude model is that it allows changes in the absorption spectrum to be interpreted directly in terms of the material properties of the metal. The origin of the strong color changes displayed by small particles lies in the denominator of Eq. (1), which predicts the existence of an absorption peak when

$$\varepsilon' = -2\varepsilon_m. \tag{7}$$

From Eq. (2) it can be seen that over the whole frequency regime below the bulk plasma frequency of the metal, ε' is negative, which is due to the electrons oscillating out of phase with the electric field vector of the light wave. This is why metal particles display absorption spectra which are strong functions of the size parameter kR. In a small metal particle the dipole created by the electric field of the light wave sets up a surface polarization charge, which effectively acts as a restoring force for the free electrons. The net result is that, when condition (7) is fulfilled, the long wavelength absorption by the bulk metal is condensed into a single surface plasmon band.

Eq. (1) provides the extinction cross section for spherical particles in a dielectric medium. When the particles are coated by a surface layer, the optical properties of both the core and shell materials must be considered. The extinction cross section of a concentric core-shell sphere is given by,[11]

$$C_{ext} = 4\pi R^2 k * \times$$
$$\mathrm{Im}\left\{\frac{(\varepsilon_{shell}-\varepsilon_m)(\varepsilon_{core}-2\varepsilon_{shell})+(1-g)(\varepsilon_{core}-\varepsilon_{shell})(\varepsilon_m+2\varepsilon_{shell})}{(\varepsilon_{shell}+2\varepsilon_m)(\varepsilon_{core}+2\varepsilon_{shell})+(1-g)(\varepsilon_{shell}-2\varepsilon_m)(\varepsilon_{core}-\varepsilon_{shell})}\right\} \quad (8)$$

where ε_{core} is the complex dielectric function of the core material, ε_{shell} is that of the shell, ε_m is the real dielectric function of the surrounding medium, g is the volume fraction of the shell layer, and R is the radius of the coated particle. As expected, when g=0, Eq. (8) reduces to Eq. (1) for an uncoated sphere, and for g=l, Eq. (8) yields the extinction cross section for a sphere of the shell material.

2.2. Thin Films

When the metal nanoparticle volume fraction is high, the above equations are not valid any longer, since dipole-dipole interactions between neighboring nanoparticles are then present, i.e., the oscillating dipoles of neighboring particles influence the frequency of a central particle. Under these conditions, effective medium theories are the simplest way to describe the optical response of the system. These theories provide us with expressions to calculate the effective dielectric constant of the composite material, which can then be used to determine the corresponding absorption and reflection coefficients.

Among the several effective medium theories available, it was found,[18] that the one by Maxwell-Garnett[19] better describes the dipole-dipole interactions, and thus will be used in this context. Through the average polarization of the nanoparticles and the surrounding medium, the average dielectric function ($\varepsilon_{av} = (n_{av} + ik_{av})^2$) is calculated as:

$$\varepsilon_{av} = \varepsilon_m \frac{\varepsilon(1+2\phi)+2\varepsilon_m(1-\phi)}{\varepsilon(1-\phi)+\varepsilon_m(2+\phi)} \quad (9)$$

where ϕ is the metal volume fraction, ε_m is the dielectric function of the surrounding medium, and ε is the complex dielectric function of the nanoparticles. The transmittance of radiation with a frequency ω through the film can be then calculated as,

$$T_{film} = \frac{(1-R)^2 + 4R\sin^2\psi}{R^2\exp(-\alpha h)+\exp(\alpha h)-2R\cos(\zeta+2\psi)} \quad (10)$$

where h is the film thickness, R is the reflectance at normal incidence,

$$R = \frac{(n_{av}-1)^2+k_{av}^2}{(n_{av}-1)^2+k_{av}^2} \quad (11)$$

and α is the absorption coefficient, which can be calculated as $\omega\mathrm{Im}(\varepsilon_{av})/cn_{av}$. Finally,we define the parameters $\zeta = 4\pi n_{av}h/\lambda$, and $\psi = \tan^{-1}(2k_{av}/(n_{av}^2 + k_{av}^2 - 1)$.

Note that the expression for the transmittance takes into account not only the absorption by the metal centers, but also the reflection losses. Therefore, we can say that it can be considered as the extinction coefficient of the film.

3. THIN FILMS THROUGH LAYER-BY-LAYER ASSEMBLY

The use of polyelectrolytes for the assembly of nanoparticles was developed only recently,[20] but has experienced a tremendous advance during the last decade (see the chapter 13 in this volume). The basis of this, so-called layer-by-layer (LBL), technique is the electrostatic attraction between oppositely charged species.[21] Briefly, a substrate (typically with negative surface charge) is immersed within a solution of a positively charged polyelectrolyte, so that the surface charge is reversed, which is known as overcompensation effect. A subsequent immersion in a solution of negatively charged nanoparticles leads to the deposition of a homogeneous, compact nanoparticle monolayer on the surface. Since the surface has now a global negative charge, the process can be repeated to deposit successive monolayers and build up a more complex film. If we compare it to traditional deposition techniques, such as sputtering and vacuum evaporation, layer-by-layer deposition possesses features that make it specially valuable for the formation of complex nanostructures. Firstly, LBL deposition can be performed at ambient conditions and does not require subsequent annealing of the deposited film, so that a wide variety of substrates can be used. Furthermore, the shape and size of the constituting nanoparticles can be selected prior to assembly. This makes possible a careful design of the properties of the film by means of the proper choice of the parent colloid. With respect to other standard film formation techniques, such as Langmuir-Blodgett deposition (see chapter 14), the LBL assembly is much simpler to carry out and does not require special equipment such as Langmuir troughs. However, it is also true that Langmuir-Blodgett films show a higher in-plane order.

All these features make LBL an ideal technique for the assembly of core-shell nanoparticles. The nanoparticle synthesis can be performed completely prior to the assembly process, and the desired properties can be designed in the first synthetic stage. Although several kinds of core-shell nanoparticles with various properties have been assembled into thin films using this method,[22-24] we only discuss here thin films made of monodisperse gold nanoparticles coated with uniform, thin shells of amorphous silica.

The interest of the assembly of silica-coated gold nanoparticles relies on the possibility of controlling the particle volume fraction by means of the variation of the silica shell thickness, provided that the assembled films are close-packed. In close-packing conditions, the separation between metal cores is just twice the thickness of the coating shell, which can be controlled during the synthesis of the colloids. This system has been recently studied in detail by Ung et al.,[25,26] and described here are the main results on the influence of metal nanoparticles volume fraction (through interparticle interactions) on the optical properties of the films. For the calculation of the spectra, Eqs. (10) and (11) have been used for transmittance and reflectance, respectively, assuming that the films are constituted by a silica matrix, where the gold nanoparticles are uniformly distributed.

In Figure 2, the experimental and calculated absorbance spectra are shown for thin films with different metal contents. It can be clearly observed that, as the gold volume fraction increases (the separation between nanoparticles decreases), there is a red-shift of the plasmon resonance, as well as a broadening of the band. This effect originates in the dipole-dipole interactions between neighboring nanoparticles, and we can see here that a separation of just 15 nm is sufficient to screen such interactions, so that the thin films display basically the same properties as a dilute dispersion of the same nanoparticles in water.

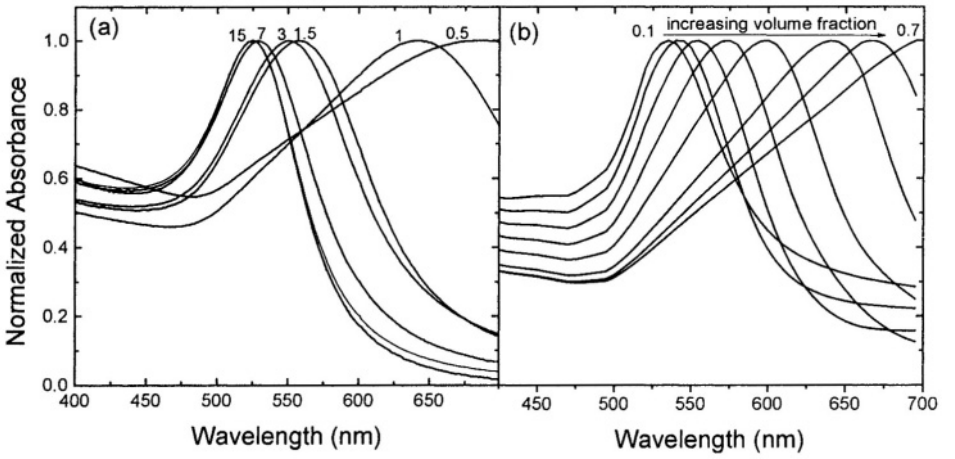

Figure 2. a) Experimental spectra as a function of the particle spacing (nm), as indicated. (b) Calculated and normalized extinction spectra of the 13.2 nm particles as a function of the metal volume fraction using Eq. (10). Film thickness used was 100 nm. Refractive index of silica used was 1.46. The dielectric response of particles was corrected for surface scattering.

The agreement between the experimental results and the calculated spectra demonstrates that Maxwell-Garnett effective medium theory effectively accounts for such dipole-dipole interactions.

Similarly, the reflectance properties of the films are also affected by the interparticle spacing. This can be observed in Figure 3, where the specular reflectance for films with different interparticle separation are compared to the spectra calculated by means of Eq. (11). Again, as the particles approach each other, the reflected spectrum red-shifts and broadens. The effect is not so dramatic as we have seen for absorption, but it is clear that the film becomes golden as more of the higher wavelengths are reflected, while for larger separations also red light is reflected, so that a different color is observed, and the reflected intensity is noticeably lower.

Thus, both the transmission and reflection properties of thin gold films can be easily controlled by means of an adjustment of the thickness of the silica shell surrounding each nanoparticle, so that dipole-dipole interparticle interactions are effectively screened. Detailed studies using different metal core sizes have not been carried out yet, but it is expected that the distance at which interactions are effectively screened will scale up with particle size, being of the order of one particle diameter.

It should be mentioned here that a similar effect was observed on the magnetic properties of thin films of silica-coated magnetite nanoparticles,[22] which means that the use of core-shell nanoparticles can be seen as a general tool for the design of nanostructured thin films with tailored properties.

Screening of interparticle interactions using LBL has also been performed by depositing inert monolayers between each two consecutive metal[27] or magnetic[28] nanoparticle layers. In such methods, only interlayer interactions are screened, but that can be sufficient in certain cases.

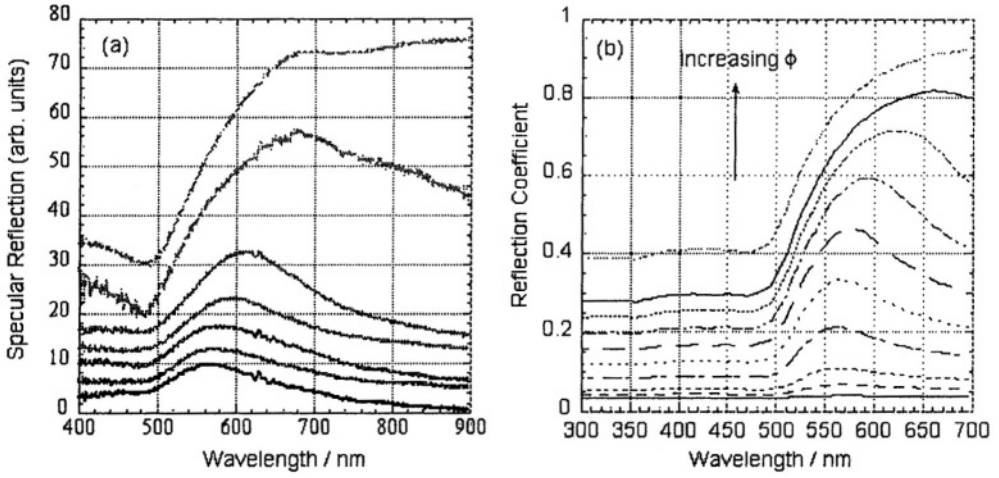

Figure 3. (a) Experimentally measured specular reflectance spectra for a series of $Au@SiO_2$ films as a function of the metal volume fraction. (b) Calculated reflectance spectra for gold colloid films of different volume fractions, using Eq. (11).

4. NANOPARTICLE ASSEMBLY ON COLLOID SPHERES

The LBL method described above can also be used for the assembly of nanoparticles on suitable colloid particles. This procedure was recently developed by Caruso et al.[29,30] and has found application in a great variety of materials, which have been recently reviewed.[31] We focus here on the assembly of $Au@SiO_2$ nanoparticles on spherical polystyrene latex colloids. This is an alternative way to build up nanostructures using core-shell nanoparticles as building blocks. The main difference with the materials described in the previous section is that the optical effects observed for the macroscopic thin films are now obtained for colloidal particles, which possess themselves a core-shell geometry as well, so that they can be used in turn for the construction of more complex, nanoscale materials. It should be remarked that the choice of silica coated nanoparticles was also motivated by their noticeably higher performance with respect to the formation of close-packed monolayers, as compared to other techniques for the assembly of metal particles on colloid spheres.[32] The resulting spheres are also essentially different to continuous metal shells grown on colloid templates, which have been reported lately.[33-35] Such continuous shells display optical properties associated to resonances along the whole shell, and are therefore extremely sensitive to both core size and shell thickness, while in the system presented here the optical properties only depend on the nature and dimensions of the constituting units.

The assembly was initially performed for $Au@SiO_2$ with very thin shells (ca. 2 nm) on 640 nm polystyrene spheres,[36] and later extended for latex cores of various sizes and gold nanoparticles coated with thicker shells.[37] Examples of nanostructured colloids formed by assembly of $Au@SiO_2$ with identical cores but silica shells with various thickness are shown in Figure 4. It is clear that, although the surface of the particles is rough, the obtained coating layers are very compact and uniform, so that, again, the interparticle separation will be determined by the corresponding thickness of the silica shell.

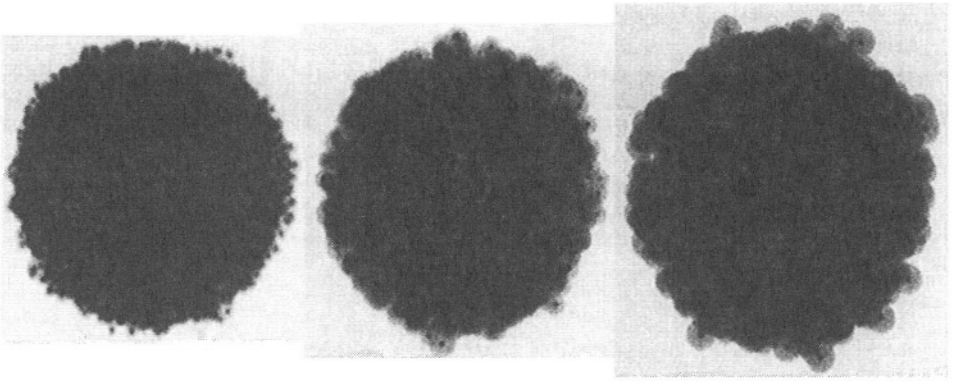

Figure 4. Typical transmission electron micrographs of 640 nm polystyrene spheres on which one monolayer of $Au@SiO_2$ nanoparticles has been assembled. The size of the Au cores is 15 nm in all cases. From left to right, the silica shell thicknesses are 8, 18, and 28 nm.

The UV-visible spectra of 640 nm polystyrene colloids coated with five monolayers of $Au@SiO_2$ nanoparticles of various shell thickness are shown in Figure 5. Again, as the separation between gold nanoparticles increases, the plasmon resonance blue-shifts toward that characteristic of isolated Au nanoparticles. As opposite to assemblies of the same coated nanoparticles on flat substrates, it has also been observed in the present case that the low-wavelength tail of the spectra dramatically rises as the size of the deposited nanoparticles increases, which is due to a larger effect on light scattering by the larger, composite spheres. These scattering effects also slightly affect the actual position of the plasmon band, as demonstrated by a larger shift as the size of the polystyrene cores is increased.[37]

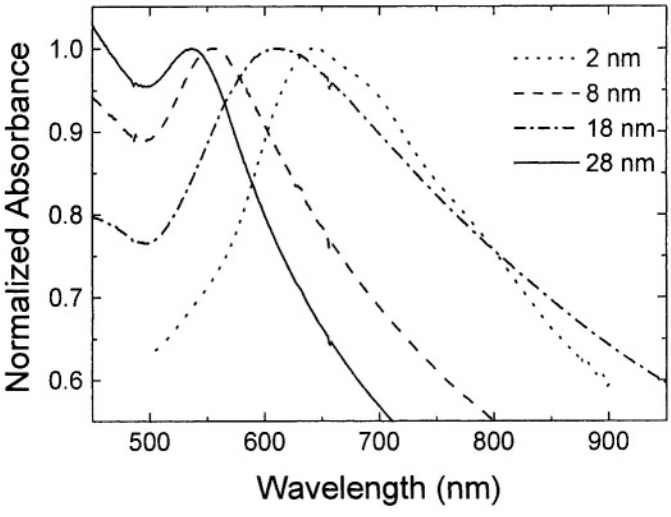

Figure 5. Normalized UV-visible spectra of dilute dispersions of 640 nm latex spheres coated with five monolayers of $Au@SiO_2$ nanoparticles. The thickness of the corresponding silica shells is indicated.

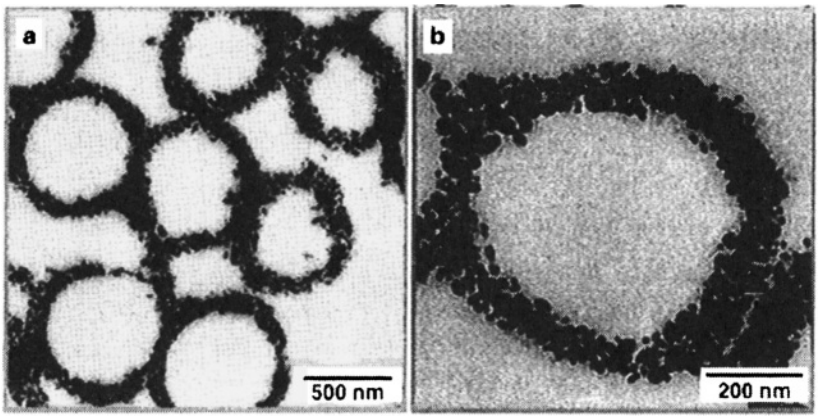

Figure 6. Transmission electron micrographs of cross-sections of hollow Au-SiO_2 spheres, prepared by calcination of 640 nm latex coated with five monolayers of Au@SiO_2 nanoparticles (core size 15 nm, shell thickness 2 nm). Reproduced with permission from ref. 36. Copyright 2001, Wiley-VCH.

The versatility of this system is clearly higher than that of the thin films on flat substrates, since the composite colloid spheres can still be further modified for the synthesis of complex nanostructures. An example of further modification can be found in Figure 6, showing transversal sections of calcined coated spheres. Calcination leads to sintering of the silica shells, so that they become more stable, but also leads to the combustion of the polystyrene spheres, so that hollow Au-SiO_2 shells are finally obtained. Such hollow spheres are extremely interesting for the construction of photonic materials with a large dielectric contrast (see below and chapter 18 in this volume). Additionally, it is also possible to remove the insulating silica shells by gentle dissolution with hydrofluoric acid, so that shells made of closely packed gold nanoparticles are obtained.[37]

5. DOPED GLASS FROM COATED NANOPARTICLES

The use of glass doped with metal nanoparticles for the construction of materials with nonlinear optical properties has been implemented long ago. Most of the methods used for the doping of glasses comprise the reduction of infiltrated metal salts within the wet or dry gel. Although successful in most cases, such methods fail from controlling adequately the particle size and shape, and of course are unable to allow for the modification of nanoparticle composition to, for instance, vary the optical properties by using alloys of different metals.[38] These difficulties from the *in-situ* preparation methods can be overcome if pre-made nanoparticles are used for incorporation into the glass matrix.

It was recently demonstrated[39,40] that silica-coated nanoparticles are ideal candidates for the fabrication of silica gels and glasses homogeneously doped with different kinds of nanoparticles. The reason for this is that the silica shell provides the core-shell nanoparticles with precisely the same surface properties as those of the silica units that are assembled during the sol-gel process, so that they do not have any preferred tendency to mutual coagulation and thus will be randomly placed within the final nanostructure.

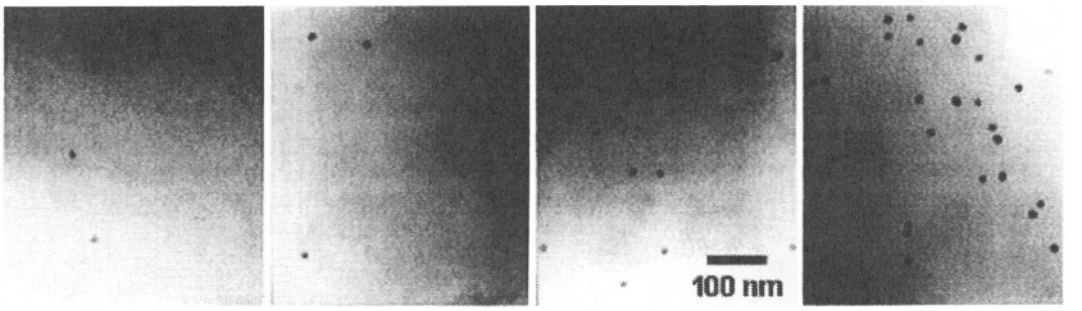

Figure 7. Transmission electron micrographs of silica gels doped with $Au@SiO_2$ nanoparticles. From left to right, the weight percentages of Au in the gels are 0.06, 0.14, 0.29 and 0.61. Reproduced with permission from ref. 39. Copyright 2001, American Chemical Society.

Since silica coating has been demonstrated for a number of nanoparticles with different composition, size and shape, the use of silica-coated nanoparticles offers an almost unlimited range of possibilities for the synthesis of doped gels and glasses with various properties.

The doped silica gels can be prepared by simple addition of sodium silicate and neutralization.[41] However, this leads to the formation of relatively large pores, so that light gets scattered within the material, which is therefore less transparent. Nicer materials for optical applications can be prepared by performing the sol-gel process through the controlled hydrolysis of alkoxysilanes.[42] Examples are shown in Figure 7, of 15 nm Au nanoparticles coated with 10 nm thick silica shells, which are homogeneously distributed within silica gels prepared by citrate acid catalyzed hydrolysis of tetramethoxysilane in water/metnanol mixtures, in the presence of the $Au@SiO_2$ nanoparticles. The concentration of the nanoparticles within the gels was varied by simple adjustment of the concentration of the colloid prior to the sol-gel process.

The advantage of such a homogeneous distribution, apart from a high uniformity in particle size (which can be controlled prior to the sol-gel processing) is once again that the (linear) optical properties of the material can be predicted before the material is prepared, since there is no coupling between the plasmon resonances of the gold nanoparticles (see above). This is exemplified in Figure 8, in which the spectra of thin xerogels corresponding to the micrographs in Figure 7 have been plotted. It is remarkable that the plasmon band is centered precisely at the same position, regardless of concentration. It has also been shown[39] that for larger gold cores the optical properties are equally preserved during the sol-gel transition.

The third-order non-linear optical properties of such gels have been measured[43] by degenerate four-wave mixing, which yields values for the third-order susceptibility, $|\chi^{(3)}|$, from the following equation,

$$\chi^{(3)} = (n^2 c\lambda/32\pi^3)\,[\alpha/(1-T)T^{0.5}]\,(\eta^{0.5}/I_0) \qquad (12)$$

where λ is the wavelength of incident light, α the absorption coefficient, T the transmissivity, η the diffraction efficiency, n the refractive index, and c the light velocity, η is defined by the intensity ratio of the signal beam I_s to the incident beam I_0.

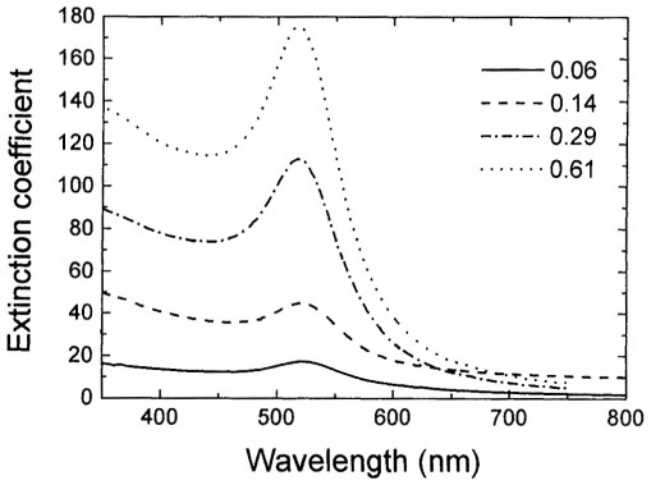

Figure 8. UV-visible spectra of xerogels doped with Au@SiO_2 nanoparticles (15 nm core, 10 nm shell). The Au content is indicated in the labels as w/w%.

The value of $|\chi^{(3)}|$ is obtained from the measurement of the intensities of incident, transmitted, and signal beams, at a wavelength close to the maximum of the surface plasmon band. For a thin xerogel containing 0.14 wt% Au the measured value was of 2.3×10^{-10} esu, while after sintering at 600 °C to convert it into a glass, the $|\chi^{(3)}|$ value was 4.6×10^{-10} esu. These values are over 10 times larger than those of Au particles in glasses prepared by the conventional melt-quenching method,[44] which demonstrates the validity of this very simple synthetic procedure for the fabrication of materials with interesting and useful optical properties.

6. ORDERED THREE-DIMENSIONAL ASSEMBLIES

The study of ordered colloidal assemblies is anotner extremely not topic in materials science. A full chapter is dedicated to photonic crystals in this volume, where A. Imhof describes the properties and several construction procedures of the so-called photonic crystals. In this section, we restrict ourselves to colloid crystals and opals prepared through the assembly of core-shell nanoparticles. In particular, ordered nanostructures made from silica-coated metal nanoparticles are described in some detail. The interest of such nanostructures stems again from the optical properties of gold nanoparticles, which display a well-defined plasmon absorption band in the visible, that can in principle, either interact with the Bragg diffraction peak characteristic of the ordered assembly, or just add up to it, thereby providing the material with a second optical feature, which can be independently tuned.

6.1. "Wet" Colloidal Crystals

We define "wet" colloidal crystals as ordered dispersions of colloid particles in solution. The study of colloidal crystals was initiated in the context of the determination of phase diagrams for colloids, as a means to model phase behavior in molecular

systems.[45] Extensive literature is available on the dynamics of colloidal crystal formation, as a function of several parameters, such as the nature of the solvent, surface charge, particle size and concentration, etc.. The results described here refer to the formation of colloidal crystals from dispersions of silica-coated gold nanoparticles in ethanol, after silica surface functionalization with 3-(trimethoxysilyl)propyl methacrylate (TPM). Earlier studies by Philipse and Vrij[46] showed that TPM adsorption leads to a reduction in surface charge, so that the particles are stable in organic solvents with low polarity, such as ethanol, toluene or DMF. This means that the particles behavior is intermediate between hard and soft spheres and thus the crystallization concentration is also intermediate. Dhont et al.[47] showed that for silica spheres coated with TPM, crystallization takes place around 20 vol%. Since the colloid chemistry of our $Au@SiO_2$ particles is governed by the silica surface (the Au volume fraction in each particle is small enough to consider that it hardly affects the Hamaker constant), we expect crystallization to occur at similar concentration values.

It was actually found[48] that the precise concentration range in which crystallization occurs depends on particle size, with higher concentrations being necessary to crystallize larger particles. Examples of this are crystallization at 16 vol% for a total diameter of 150 nm, while not below 24 vol% for a total diameter of 185 nm. Results are shown in Figure 9 for 150 nm coated particles, with a particle volume fraction close to 16%. This choice is motivated by the similarity in the Au content (0.31 w%) with respect to that of the gels described above. The optical characterization was performed through specular reflectance measurements, so that the spectra in Figure 9 for different incident angles show the crystalliniry of the sample, through intense Bragg reflection peaks. The peak positions for different incident angles have been fitted using the following equation for Bragg law:

$$\lambda = 2d_{111}\,(\langle n^2\rangle - \sin^2\theta)^{1/2} \tag{13}$$

where $\langle n^2\rangle$ is the effective dielectric constant of the sample, which can just be calculated as a simple average,

$$\langle n^2 \rangle = n_1^2\phi + n_2^2(1-\phi) \tag{14}$$

n_1 and n_2 being the refractive indices of silica and ethanol, respectively. d_{111} is the lattice parameter for an fcc structure, calculated as $0.739\phi^{-1/3}d$, d being the particle diameter. The Au cores have not been included in the calculation, since they only occupy about 0.1% of each particle, and therefore their contribution to diffraction should be negligible. However, there is still a contribution from absorption, as will be shown below.

It is interesting to note here that Asher and co-workers have recently reported[49] on the formation of colloidal crystals made from silica particles doped with a random distribution of Ag nanoparticles. These authors found that the plasmon band of the Ag nanoparticles varied during the transition from a disordered to an ordered state, which suggests the existence of some sort of coupling between the two optical responses of the system. However, it is not clear how the coupling between silver clusters within each silica sphere affects the optical properties of the whole system.

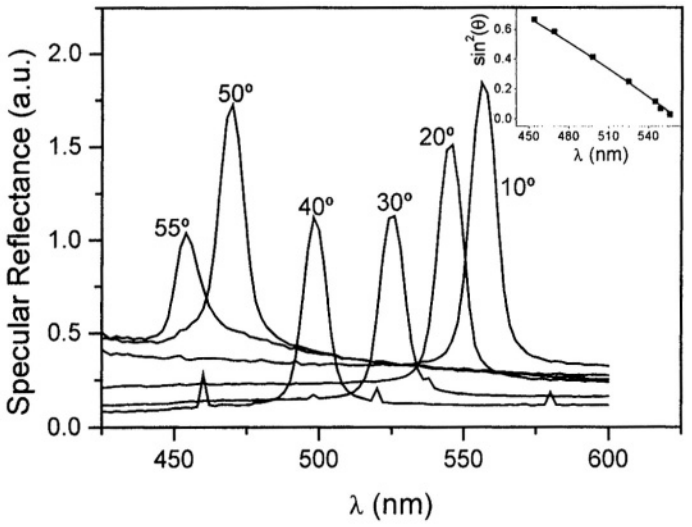

Figure 9. Specular reflectance spectra at different incident angles for a colloidal crystal made of TPM-modified $Au@SiO_2$ particles with 15 nm core diameter and 150 nm total diameter. The particle volume fraction in this sample was 15.8 vol%, corresponding to 0.31 wt% Au content. The inset shows the fit of the experimental Bragg peak positions with Eq. (13).

6.2. Solid "Opals"

Despite the simplicity of the formation of colloidal crystals in solution, which is a spontaneous process at the right concentration and temperature conditions, such systems suffer from a number of problems for their use as photonic crystals. One of the major drawbacks of colloidal crystals is their large polycrystallinity, i.e., small crystallites form in solution, rather than a large, well-ordered single crystal, which strongly limits their efficiency for the final goal of obtaining a full photonic band-gap.[50] Therefore, a number of methods have been developed during the last decade (see chapter 18) for the assembly of colloid particles in the form of solid crystalline compacts, with the largest possible ordered domains. One simple way that leads to opal formation consists of a slow sedimentation of the colloid particles in a suitable solvent, so that the interparticle interactions during deposition result in ordered structures with a face-centered-cubic (fcc) crystal lattice.[51] The same method can be used for the formation of opals using $Au@SiO_2$ particles as constituting units, since the nature of the surface is identical.[52] Oppositely to Asher's report (see previous section), the optical characterization of such opals suggests that plasmon resonance and Bragg diffraction are independent phenomena in this case. A clear evidence for this is shown in Figure 10, where optical extinction spectra have been plotted for a single $Au@SiO_2$ opal, but with different materials filling the interstices between the spheres. While the position of the Bragg peak is red-shifted and its intensity reduced as the refractive index of the medium is increased, the plasmon band position remains basically unchanged, since the silica shell around the Au cores is thick enough so that they do not "see" the outer medium any longer.[10] A reduction of the plasmon band intensity is also observed because of the global reduction of light scattering as the contrast is reduced.

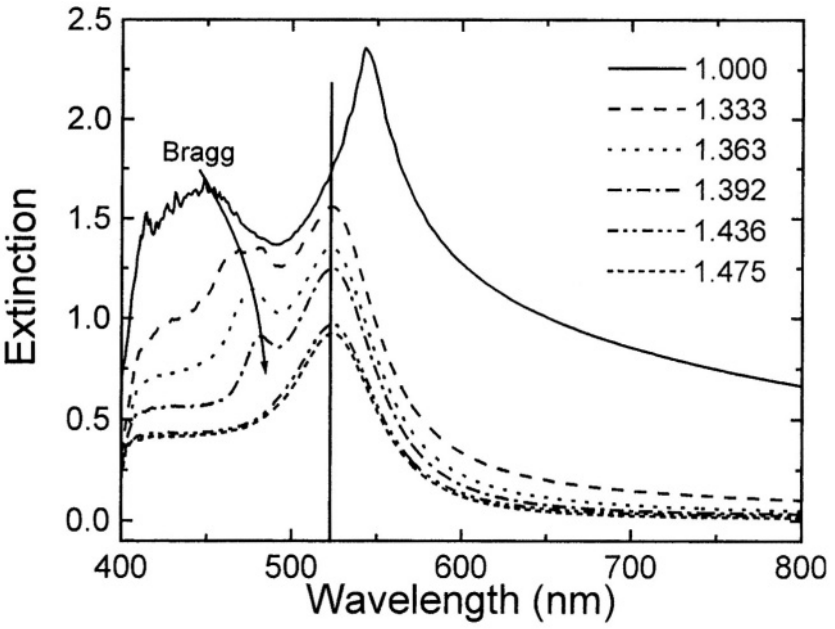

Figure 10. Extinction spectra in different media (air, water and water-glycerol mixtures) for sintered opals made of Au@SiO_2 particles with 15 nm core diameter and 225 nm total diameter. The corresponding refractive indices are indicated.

The main difference between this system and crystals formed from silica spheres loaded with a large amount of silver nanocrystals is the amount of metal within the particles, as well as the relative separation between metal particles, which, as expected, preserves the optical response of the individual nanoparticles within the ordered, nanostructured material. This result renders the material very interesting, since, as was mentioned previously, the nature and morphology of the core material (and in turn its optical properties) can be designed prior to opal formation, which allows for an endless number of possible combinations, including the tuning of plasmon resonance and Bragg diffraction to the same wavelength.

6.3. Inverse Opals from Au@SiO_2 Particles

One final example of nanostructures created from the assembly of silica-coated nanoparticles is the formation of ordered macroporous solids, also known as inverse opals. These structures are similar to opals, in the sense that they comprise solids with an ordered structure whose lattice constant lies in the optical wavelength range. The only difference relies in the nature of the crystal centers and the embedding medium. While "direct" opals are constituted by solid (or liquid) particles typically embedded in air, "inverse" opals comprise air bubbles embedded in a solid material. One of the most extended pathways toward the fabrication of inverse opals is the infiltration of the interstices of direct opals with the desired material, followed by removal of the colloid templates.[53]

Theoretical modeling shows that this configuration is more favorable for the achievement of a full photonic band-gap, provided that a sufficient dielectric contrast of

at least 2.8 is present.[54] This requirement is hard to achieve, and it has only been reported for silicon[55] and germanium[56] inverse opals. An alternative can be the use of metals with a Drude-like behavior of the dielectric function:

$$\varepsilon(\omega) = 1 - \omega_p^2/\omega^2 \tag{15}$$

where $\varepsilon(\omega)$ is the dielectric constant of the material, ω_p is the plasma frequency, and ω is the frequency of light. When $\omega \approx \omega_p$, the dielectric contrast of the photonic crystal becomes extremely large, which favors opening of a complete photonic bandgap, even in a simple face-centered cubic (fcc) structure.[57] It is therefore desirable to use metals with a well-defined plasmon frequency, which is the case for metal nanoparticles. Thus, one suitable approach is the infiltration of preformed opals with the previously described $Au@SiO_2$ nanoparticles,[58] so that the optical features of single nanoparticles are preserved in the final, inverse opal. Upon removal of the template, rigid and mechanically stable nanostructures can be easily obtained through sintering of the silica shells, while retaining the individuality of the gold nanoparticles.

An example of Au/SiO_2 inverse opals prepared by infiltration of polystyrene latex opals and template removal by calcination, is shown in Figure 11. The figure contains low and high resolution scanning electron micrographs of an inverse opal formed by $Au@SiO_2$ nanoparticles with 15 nm Au cores surrounded by 28 nm thick silica shells. The spherical particles can still be recognized within the nanostructured system. The optical characterization of these inverse opals shows again that the position of both the plasmon band and Bragg peak can be modulated independently, so that a gate is open to search for the coupling needed to achieve a full photonic bandgap. However, in this case, since the relative amount of gold nanoparticles is larger, the resulting high dielectric constant is expected to affect the diffraction properties of the system.

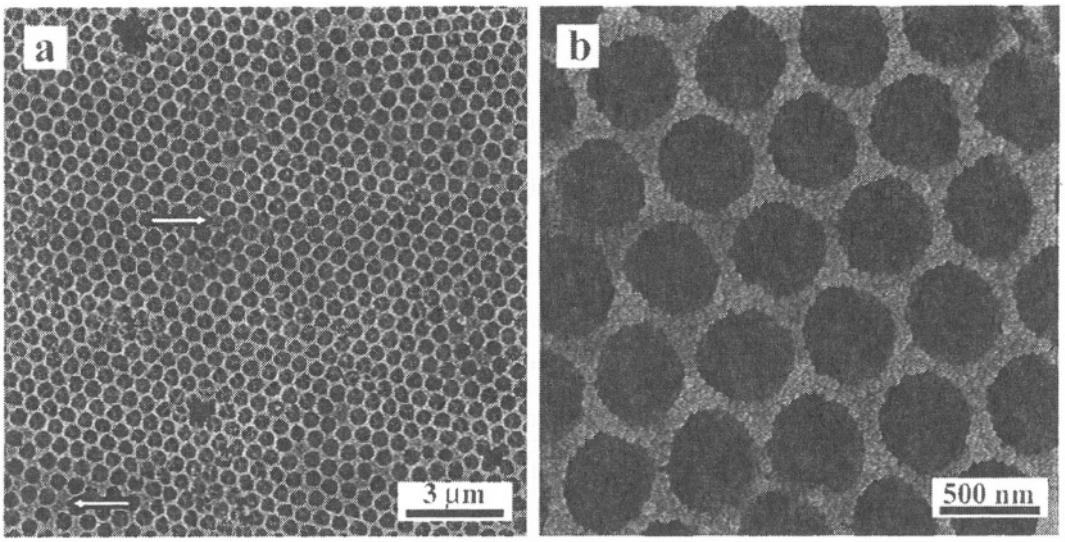

Figure 11. Scanning electron micrographs of gold-silica inverse opals formed by infiltrating colloidal crystals made of polystyrene spheres (diameter 640 nm) with $Au@SiO_2$ nanoparticles (core 15 nm; shell 28 nm). Arrows show point defects within the crystalline structure.

Inverse opals of a different nature, but also synthesized through the assembly of $Au@SiO_2$ core-shell spheres, have been recently reported.[59] In this case, opals made from silica-coated gold nanoparticles (exactly as described in section 6.2, with a total diameter of 225 nm) were infiltrated with a curable epoxy resin. Upon curing of the resin at 70 °C and subsequent etching of the silica shells with hydrofluoric acid, an ordered macroporous polymer is obtained, within which Au nanoparticles were homogeneously distributed. Note that complete dissolution of the silica shells is only possible because of the contact between neighboring spheres, which is ensured through the sintering of the opal. Electron microscopy images showing the morphology of the system during the subsequent synthetic steps, are shown in Figure 12. It is clear that the ordered nature of the sacrificial opal is retained in the inverse structure, but although the metal nanoparticles are homogeneously distributed within the porous material, they do loose their crystalline arrangement since, as the silica shells are dissolved, they randomly stick to the closest wall available.

The applications of such systems are not only restricted to the area of photonic materials, but can be also found in catalysis.[60] Due to the connecting windows between neighboring air bubbles, the metal nanoparticles can be easily accessed when the porous solid is placed within the medium where the reaction to be catalyzed is to take place. Various modifications of this process can also be envisaged for the fabrication of materials with different and interesting properties.

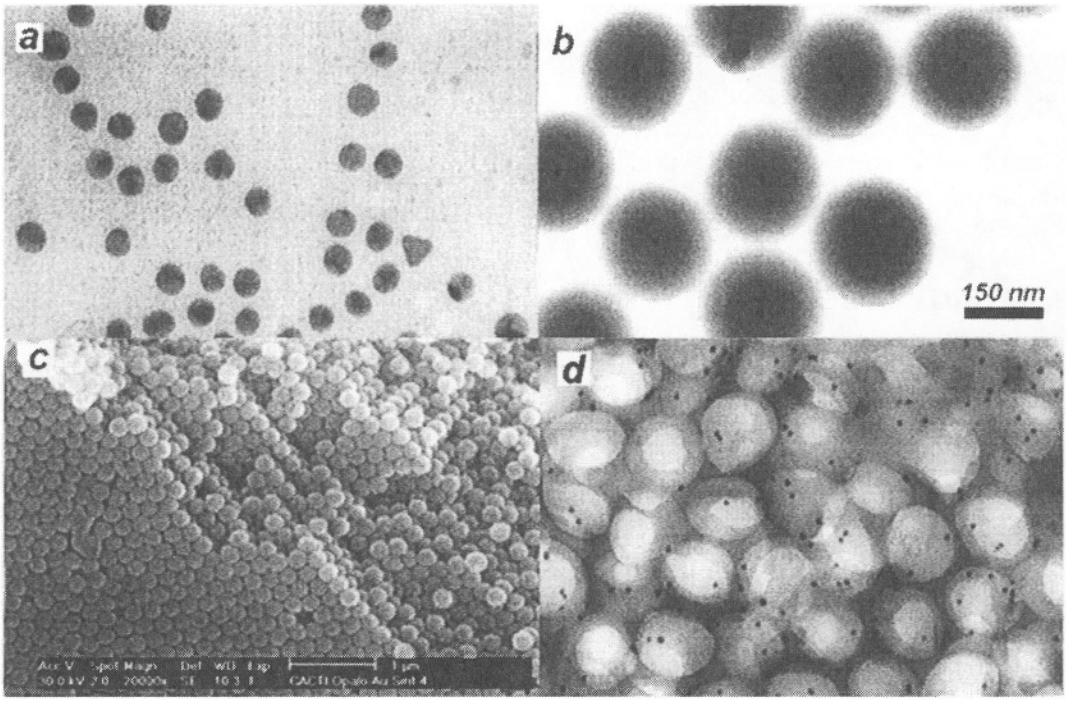

Figure 12. Electron micrographs showing the subsequent steps during the formation of an ordered macroporous polymer containing gold nanoparticles. (a) citrate stabilized gold nanoparticles (15 nm); (b) the same Au particles coated with silica (total diameter: 225 nm); (c) sintered opal from $Au@SiO_2$ spheres; (d) detail of epoxy resin inverse opal with incorporated Au nanoparticles. Reproduced with permission from ref. 59. Copyright 2002, American Chemical Society.

7. CONCLUSIONS AND OUTLOOK

In this chapter, we have described the use of core-shell nanoparticles for the construction of functional, nanostructured materials. All of the examples discussed in detail are based on the assembly of silica-coated gold nanoparticles, due to the special optical properties of the metal cores, which are extremely sensitive to the dispersed nature of the system. It was shown that a careful control of the thickness of the insulating shell leads to a sensitive tuning of the global response of the system toward incoming light. Furthermore, it was shown that gold nanoparticles can be randomly incorporated within silica gels, through sol-gel processing of the silica-coated nanoparticles, and finally, the formation of three-dimensional, ordered arrangements of the coated metal particles was discussed, which sets a starting point for a more detailed study of the coupling between surface plasmon resonance and Bragg diffraction.

For any of these examples, it is to be expected a further study of the influence of the different parameters that control single particle plasmon resonance, such as particle size and shape, composition and nature of the environment.

The construction of nanostructures using core-shell nanoparticles comprising semiconductor materials has not been discussed here, but constitutes a broad and promising area by itself, that is already starting to be explored. Such coated particles exhibit enhanced luminescence and chemical stability, so that they constitute ideal candidates for the design of novel lasers and light-emitting displays, among a range of other practical devices.

Because of space limitations, we have also left out of the scope of the chapter organic and hybrid organic-inorganic core-shells, but such particles are also extremely interesting from several points of view.

The next step to be expected is the fabrication of actual devices, which can be incorporated within commercial products, such as selective optical filters, optoelectronic devices, sensors or biocompatible materials.

8. ACKNOWLEDGMENTS

I would like to thank all the students and co-workers who have contributed to the results presented in this chapter, for their enthusiasm, hard work and extensive discussions. Financial support from the Spanish Ministerio de Ciencia y Tecnologia and Xunta de Galicia, through several research grants is also greatly appreciated.

9. REFERENCES

1. A. L. Aden and M. Kerker, Colours in metal glasses and in metallic films, *J. Appl. Phys.* **22**, 1242-1246 (1951).
2. R. H. Morriss and L. F. Collins, Optical properties of multilayer colloids, *J. Chem. Phys.* **41**, 3357-3363 (1964).
3. L. M. Liz-Marzán, M. A. Correa-Duarte, I. Pastoriza-Santos, P. Mulvaney, T. Ung, M. Giersig, and N. A. Kotov, in: *Handbook of Surfaces and Interfaces of Materials,* edited by H. N. Nalwa (Academic Press, New York, 2001), vol. 3, pp. 189-232.
4. F. Caruso, Nanoengineering of particle surfaces, *Adv. Mater.* **13**, 11-22 (2001).
5. P. Mulvaney, Surface plasmon spectroscopy of nanosized metal particles, *Langmuir* **12**, 788-800 (1996).

6. P. Mulvaney, in: *Nanoscale Materials in Chemistry,* edited by K. Klabunde (Wiley, New York, 2001), pp. 121-167.
7. R. K. Iler, Product comprising a skin of dense, hydrated amorphous silica bound upon a core of another solid material and process of making same, *US Patent #* 2,885,366 (1959).
8. W. Stöber, A. Fink, and E Bonn, Controlled growth of monodisperse silica spheres in the micron size range, *J. Colloid Interface Sci.* **26**, 62-69 (1968).
9. S. Chang, L. Liu, and S. A. Asher, Preparation and properties of tailored morphology, monodisperse colloidal silica-cadmiun sulfide nanocomposites, *J. Am. Chem. Soc.* **116**, 6739-6744 (1994).
10. L. M. Liz-Marzán, M. Giersig, and P. Mulvaney, Synthesis of nanosized gold-silica core-shell particles, *Langmuir* **12,** 4329-4335 (1996).
11. T. Ung, L. M. Liz-Marzán, and P. Mulvaney, Controlled method for silica-coating of silver colloids. Influence of coating on the rate of chemical reactions, *Langmuir* **14**, 3740-3748 (1998).
12. A. Henglein, Physicochemical properties of small metal particles in solution: "microelectrode" reactions, chemisorption, composite metal particles, and the atom-to-metal transition, *J. Phys. Chem,* **97**, 5457-5471 (1993).
13. B. M. I. van der Zande, M. R. Böhmer, L. G. Fokkink, and C. Schöneberger, Colloidal dispersions of gold rods: synthesis and optical properties, *Langmuir* **16**, 451-458 (2000).
14. R. Jin, Y. W. Cao, C. A. Mirkin, K. L. Kelly, G. C. Schatz, J. G. Zheng, Photoinduced conversion of silver nanospheres to nanoprisms, *Science* **294**, 1901-1903 (2001).
15. M. Kerker, *The Scattering of Light and Other Electromagnetic Radiation,* (Academic Press, New York, 1969).
16. C. F. Bohren and D. F. Huffman, *Absorption and Scattering of Light by Small Particles* (Wiley, New York, 1983).
17. C. Kittel, *Introduction to Solid State Physics* (Wiley, New York, 1956).
18. P. Mulvaney, T. Ung, M. Giersig, and L. M. Liz-Marzán, Silica encapsulation of quantum dots and metal clusters, *J. Mater. Chem.* **10**, 1259-1269(2000).
19. J. C. Maxwell-Garnett, Scattering of electromagnetic waves from two concentric spheres, *Phil. Trans. Roy. Soc*. **203**, 385-430 (1904).
20. N. A. Kotov, 1. Dekàny, and J. H. Fendler, Layer-by-layer self-assembly of polyelectrolyte-semiconductor nanoparticle composite films, *J. Phys. Chem.* **99**, 13065-13069 (1995).
21. G. Decher, Fuzzy nanoassemblies: toward layered polymeric multicomposites, *Science* **277***,* 1232-1237 (1997).
22. F. Aliev, M. A. Correa-Duarte, A. Mamedov, J. Ostrander, M. Giersig, L. M. Liz-Marzán, and N. A. Kotov, Layer-by-layer assembly of core-shell magnetite nanoparticles: effect of silica coating on interparticle interactions and magnetic properties, *Adv. Mater.* **11**, 1006-1010 (1999).
23. I. Pastoriza-Santos, D. S. Koktysh. A. A. Mamedov, M. Giersig, N. A. Kotov, and L. M. Liz-Marzán, One-pot synthesis of $Ag@TiO_2$ core-shell nanoparticles and their layer-by-layer assembly, *Langmuir* **16**, 2731-2735 (2000).
24. D. Koktysh, X. Liang, B.-G. Yun, I. Pastoriza-Santos, R. L. Matts, M. Giersig, C. Serra-Rodriguez, L. M. Liz-Marzán, and N. A. Kotov, Biomaterials by design: layer-by-layer assembled ion-selective and biocompatible films of TiO_2 nanoshells for neurochemical monitoring, *Adv. Funct. Mater.* **12**, 255-265 (2002).
25. T. Ung, L. M. Liz-Marzán, and P. Mulvaney, Optical properties of thin films of $Au@SiO_2$ particles, *J. Phys. Chem. B* **105**, 3441-3452 (2001).
26. T. Ung, L. M. Liz-Marzán, and P. Mulvaney, Gold nanoparticle thin films, *Colloid Surf. A* **202**, 119-126 (2002).
27. N. Malikova, I. Pastoriza-Santos, M. Schierhorn, N. A. Kotov, and L. M. Liz-Marzán, Layer-by-layer assembled mixed spherical and planar gold nanoparticles: control of interparticle interactions, *Langmuir* **18**, 3694-3697 (2002).
28. A. Mamedov, J. W. Ostrander, F. Aliev, and N. A. Kotov, Stratified assemblies of magnetite nanoparticles and montmorillonite prepared by the layer-by-layer assembly, *Langmuir* **16,** 3941-3949 (2000).
29. F. Caruso, R. A. Caruso, and H. Möhwald, Nanoengineering of inorganic and hybrid hollow spheres by colloidal templating, *Science* **282**, 1111-1114 (1998).
30. F. Caruso, R. A. Caruso, and H. Möhwald, Production of hollow microspheres from nanostructured composite particles, *Chem. Mater.* **11**, 3309-3314 (1999).
31. F. Caruso, Hollow capsule processing through colloidal templating and self-assembly, *Chem. Eur. J.* **6**, 413-419(2000).
32. A. Dokoutchaev, J. T. James, S. C. Koene, S. Pathak, G. K. S. Prakash, and M. E. Thompson, Colloidal metal deposition onto functionalized polystyrene microspheres, *Chem. Mater.* **11**, 2389-2399 (1999).

33. S. J. Oldenburg, R. D. Averitt, S. L. Westcott, and N. J. Halas, Nanoengineering of optical resonances, *Chem. Phys. Lett.* **288**, 243-247 (1998).
34. J. B. Jackson and N. J. Halas, Silver nanoshells: variations in morphologies and optical properties, *J. Phys. Chem. B* **105**, 2743-2746 (2001).
35. C. Graf and A. Van Blaaderen, Metallodielectric colloidal core-shell particles for photonic applications, *Langmuir* **18**, 524-534 (2002).
36. F. Caruso, M. Spasova, V. Salgueiriño-Maceira, and L.M. Liz-Marzán, Multilayer assemblies of silica-encapsulated gold nanoparticles on decomposable colloid templates, *Adv. Mater.* **13**, 1090-1095 (2001).
37. V. Salgueiriño-Maceira, F. Caruso, and L.M. Liz-Marzán, in preparation, 2002.
38. S. Link, Z. L. Wang, and M. A. El-Sayed, Alloy formation of gold-silver nanoparticles and the dependence of the plasmon absorption on their composition, *J. Phys. Chem. B* **103**, 3529-3533 (1999).
39. Y. Kobayashi, M. A. Correa-Duarte, and L. M, Liz-Marzán, Sol-gel processing of silica-coated gold nanoparticles, *Langmuir* **17**, 6375-6379 (2001).
40. M. A. Correa-Duarte, Y. Kobayashi, and L. M. Liz-Marzán, Photodegradation of SiO_2-coated CdS nanoparticles within silica gels, *J. Nanosci. Nanotechnol.* **1**, 95-100 (2001).
41. R. K. Iler, *The Chemistry of Silica* (John Wiley & Sons, New York, 1979).
42. C. J. Brinker and G. W. Scherer, *Sol-Gel Science* (Academic Press, San Diego, 1990).
43. S. Tamil Selvan, T. Hayakawa, M. Nogami, Y. Kobayashi, L. M. Liz-Marzán, Y. Hamanaka, and A. Nakamura, Sol-gel derived gold nanoclusters in silica glass possessing large optical nonlinearities, *J. Phys. Chem. B* **106**, 10157-10162 (2002).
44. F. Hache, D. Ricard, C. Flytzanis, and U. Kreibig, The optical Kerr effect in small metal particles and metal colloids: the case of gold, *Appl. Phys. A* **47**, 347-357 (1988).
45. A. K. Arora and B. V. R. Tata (Editors), *Ordering and Phase Transitions in charged Colloids* (VCH, New York, 1996).
46. A. P. Philipse and A. Vrij, Determination of static and dynamic interactions between monodisperse, charged silica spheres in an optically matching, organic solvent, *J. Chem. Phys.* **88**, 6459-6470 (1989).
47. J. K. G. Dhont, C. Smits, and H. N. W. Lekkerkerker, A time resolved static light scattering study on nucleation and crystallization in a colloidal system, *J. Colloid Interface Sci.* **152**, 386-401 (1991).
48. L. M. Liz-Marzán, V. Salgueiriño-Maceira, Y. Kobayashi, F. García-Santamaría, and C. López, Three-dimensional assemblies of silica-coated metal nanoparticles, IPAP Conf. Ser. **3,** 84-87 (2001).
49. W. Wang and S. A. Asher, Photochemical incorporation of silver quantum dots in monodisperse silica colloids for photonic crystal applications, *J. Am. Chem. Soc.* **123**, 12528-12535 (2001).
50. J. D. Joannopoulos, R. D. Meade, and J. N. Winn, *Photonic Crystals* (Princeton University Press, Princeton, 1995).
51. H. Míguez, F. Meseguer, C. López, A. Mifsud, J. S. Moya, and L. Vázquez, Evidence of fcc crystallization of SiO_2 nanospheres, *Langmuir* **13,** 6009-6011 (1997).
52. F. García-Santamaría, V. Salgueiriño-Maceira, C. López, and L. M. Liz-Marzán, Synthetic opals based on silica-coated gold nanoparticles, *Langmuir,* **18**, 4519-4522 (2002).
53. Special issue on Photonic Crystals, *Adv. Mater.* **13**(6) (2001).
54. D. J. Norris and Y. A. Vlasov, Chemical approaches to three-dimensional semiconductor photonic crystals, *Adv. Mater.* **13**, 371-376(2001).
55. A. Blanco, E. Chomski, S. Grabtchak, M. Ibisate, S. John, S. W. Leonard, C. Lopez, F. Meseguer, H. Miguez, J. P. Mondia, G. A. Ozin, O. Toader, and H. M. van Driel, Large-scale synthesis of a silicon photonic crystal with a complete three-dimensional bandgap near 1.5 micrometres, *Nature* 405, 437-440 (2000).
56. H. Míguez, E. Chomski, F. García-Santamaría, M. Ibisate, S. John, C. Lopez, F. Meseguer, J. P. Mondia, G. A. Ozin, O. Toader, and H. M. van Driel, *Adv. Mater.* **13,** 1634 (2001).
57. A. Moroz, Photonic crystals of coated metallic spheres, *Europhys. Lett.* **50**, 466-472 (2000).
58. D. Wang, V. Salgueiriño-Maceira, L. M. Liz-Marzán, and F. Caruso, Gold-silica inverse opals by colloidal crystal templating, *Adv. Mater.* **14**, 908-912 (2002).
59. B. Rodríguez-González, V. Salgueiriño-Maceira, F. García-Santamaría, and L. M. Liz-Marzán, Fully Accessible Gold Nanoparticles Within Ordered Macroporous Solids, *Nano Lett.,* **2** (2002) 471-473.
60. M. P. Andrews and G. A. Ozin, Liquid-phase agglomeration of Ag atoms in olefinic media: electrocatalytic application. 2, *J. Phys. Chem.* **90**, 2929-2938 (1986).

12
FABRICATION OF INORGANIC NANOCOMPOSITES USING SELF-ASSEMBLY AND SOL-GEL PROCESSING

S. Tamil Selvan [*]

1. INTRODUCTION

Nanocomposites comprise one of the rapidly growing and emerging areas in nanomaterials science. The possibility of mixing both organic and inorganic components at the nanometer scale level allows for the fabrication of multi-functional materials with improved optical, electrical, catalytic and mechanical properties as compared to their bulk counterparts.

The field of nanocomposites has recently exploded with the birth of soft inorganic processes in solution or sol-gel media, exploiting the use of self-assembly processes, controlled polymeric reactions in solution or directed assembly of nanobuilding blocks, which could be used as templates for new materials and devices. Nanocomposites can broadly be classified into four types: inorganic-organic (e.g. metal or semiconductor nanoclusters dispersed in a polymer matrix such as poly methyl methacrylate and block copolymers), organic-inorganic (e.g. organic dyes or biopolymers dispersed in an inorganic matrix such as silica, titania or alumina), inorganic-inorganic (e.g. Au@Silica) and organic-organic (e.g. organic dyes in poly methyl methacrylate) composites.

This chapter is directed toward the design, synthesis, and functional properties of various nanomaterials prepared in our laboratory using either self assembly of block copolymers or sol-gel processing. The main focus will be placed on the optical properties of noble metal (Au) nanoparticles embedded within a polymer matrix, and rare-earth ions and/or semiconductor nanoparticles embedded within a silica matrix, prepared by a sol-gel method, which have been well studied in our laboratory. The chapter is organized in the following manner: a) Metal-conducting polymer (gold-polypyrrole) nanocomposites through self-assembly of block copolymers; b) Gold-doped silica glasses and their non-linear optical properties; c) Rare-earth doped silica gels and their luminescence characteristics; d) Semiconductor quantum dots (QDs) and their photo-physical behavior; e) Highly luminescent, tunable QD-glasses and f) Silica-coated QDs.

[*] Chemistry School, University of Melbourne, Parkville, Victoria 3010, Australia.

1.1. Quantum Size Effects in Nanocrystals

Nanoscale materials composed of either metal[1-21] or semiconductor particles[22-42] are playing an increasingly important role as novel building blocks in solid state chemistry, physics, materials science, and also in biology. Many fundamental properties of nanocrystals (e.g., ionization potential, melting point, band gap, saturation magnetization) depend upon the high quality of the solid being periodic over a particular length scale, typically in the nanometer regime. Because of the high surface to volume ratio of nanoparticles, the surface properties have significant effects on their structural and optical properties. Quantum confinement of both electrons and holes in all three dimensions leads to an increase in the effective band gap of the material with decreasing particle size. Consequently, both the optical absorption and emission of QDs shift to the lower wavelength (higher energies) as the size of the dots gets smaller.

Therefore, by precisely controlling the size and surface of a nanocrystal, its properties can be tuned. Solution-phase chemistry has proven to be an important bottom-up approach for the creation of nanocrystals as building blocks for new materials and devices.[23-42] Modification of QD surfaces with various organic and inorganic species is currently being carried out to remove the surface defects and influence their optical properties. Organic capping of QDs with surfactants would give rise to a barrier against aggregation and electronic passivation of the crystallites. Typically, CdSe QDs with trioctylphosphine oxide (TOPO) already have a quantum yield of ~10% at room temperature. Over-coating the nanocrystallites with higher band gap inorganic materials has been shown to improve the photoluminescence quantum yields by passivating surface non-radiative recombination sites. QDs passivated with inorganic shell structures are more robust than organically passivated dots and have greater tolerance to processing conditions necessary for incorporation into solid state structures.

1.2. Polymer Nanocomposites

A variety of metal, semiconductor and magnetic nanoparticles can be encapsulated within polymer matrices in order to provide enhanced stability and functional properties.[43-54] By virtue of self-assembly, block copolymers can form ordered micro-domains wherein the particles can be stabilized. Block copolymer micelles can exhibit well defined colloidal dispersions, by which the particles of a finite size can be formed. Another advantage is the tunability of both size and inter-particle distance by varying the block lengths of the polymer.[13-20]

Recently, colloidal polymer templating has attracted a great deal of interest in several groups[55-59] for the creation of core-shell structures of metal, semiconductor and magnetic particles onto polystyrene core particles, exploiting the use of electrostatic attraction between the particles and polyelectrolytes using layer-by-layer (LBL) coating. These materials are of interest in the area of novel photonic bandgap materials (See the chapter by Liz-Marzán).

1.3. Sol-gel Processing

There is a need to increase materials' chemical, thermal and mechanical stability durability, lifetime and bio-compatability for different applications. Toward this end, available are numerous coating procedures such as chemical vapor deposition (CVD),

plasma-assisted techniques, pulsed laser deposition, mechanical milling, magnetron sputtering, self-assembly, layer-by-layer coating, dip coating, and electrochemical deposition. Most of these techniques are used to coat planar substrates. However, when more complex shapes require coating without loss of the integrity on the nanometer to micrometer scale, many of these methods have serious drawbacks. In this case the sol-gel process, which can be carried out in solution, is very attractive.[60-63] In addition, the sol-gel process is cost effective.

Furthermore, the sol-gel process offers unique opportunities to synthesize nano-materials in the form of thin films, fibers, fine powders and even monoliths. It provides a versatile way to make gels, glasses, and organic-inorganic hybrid materials through the hydrolysis and condensation of metal alkoxides.[64] The homogeneous mixing of several components at a molecular level makes it possible to vary the chemical nature of optical materials over a wide range of compositions to tailor their optical properties. Inorganic nanoparticles, organic dyes, lanthanide ions, and even biological species can be embedded in sol-gel matrices, which have been extensively used in the development of new materials for applications in optics, catalysis, chemical sensors, chemical analysis, chromatography, membrane design, bioanalysis and solid state electrochemistry.[65-74]

By combining methods of amphiphilic block copolymer self-assembly, emulsion/ latex sphere templating, and/or sol-gel chemistry and soft lithography, new classes of ordered nanoporous-macroporous materials[75] and patterned structures[76-80] can be developed.

1.4. Photonic Glasses

Glasses are ideal systems for photonic switching and photonic data storage.[81,82] The success of photonic switching depends on materials and devices that are capable of processing light signals without converting them to electronic forms. They are based on the non-linear optical properties of the materials, that is, changes of the refractive index caused by an intense optical beam or by an applied electric field. Glasses are promising materials for these all-optical devices because of their fast-responding non-linearities and low absorption. The future opportunities in photonic switching and information processing will depend critically on the development of improved photonic materials.

Metal or semiconductor nanoclusters dispersed in a transparent matrix such as glass have high resonant-type third-order non-linear optical susceptibility, $\chi^{(3)}$. Nanoparticle-glass composites exhibit not only a large third-order nonlinear response, but also picosecond switching and relaxation times, thermal and chemical stability, high laser damage threshold, low photon absorption, and tunability.[83-95]

Glass melting is a well known method in which the particles are nucleated in the molten glass and subsequent nascent growth occurs after annealing cycles. Although QD -glasses prepared by melting exhibit fast responding non-linearities and low absorption, they suffer from several limiting factors. There is no control over the cluster surfaces to modulate or influence the surface traps or non-radiative recombination of charge carriers. Furthermore, it is hard to prepare core-shell structures or other complex structures within glass as particles are nucleated in molten condition. Limitations are also due to large size distribution, trap states such as vacancies, defects and dangling bonds and also due to photo-darkening effects. Alternatively, the sol-gel method is attractive since it can be carried out in solution at room temperature, and fine control over the cluster surface is possible prior to incorporation into gels. Therefore, by combining both solution phase

synthesis and sol-gel processing novel QD-glasses can be easily fabricated.

We have recently demonstrated a protocol for the preparation of highly luminescent and tunable QD-silica composites.[31] The surface of QD largely determines the quantum yield and emission life-time. The surrounding medium can have a profound effect on the cluster properties. Cluster surfaces can act as electron and/or hole traps upon optical excitation. The presence of these trapped electrons and holes can, in turn, modify the optical properties of the clusters – a nonlinear optical effect. Metal and semiconductor QD-doped glasses have emerged as potential candidates for nonlinear optical devices.[83-95]

Peyghambarian, Mackenzie and coworkers reported room temperature optical gain in sol-gel derived CdS QDs embedded in a sodium borosilicate glass matrix.[91-95] The gain originated from the quantum confined states, specifically from the biexciton to exciton states. However, the gain was spectrally broad and the crossing between absorption and gain was well above the bulk absorption band energy, since the nanocrystals were in the intermediate quantum confinement regime. The gain had a long tail extending to the low energy side of the absorption edge. This tail was shown theoretically to originate from the multiple excited states involved in the recombination between two and one electron-hole pairs.

The feasibility of QD lasers has been demonstrated recently by Klimov et al.,[29] who observed large optical gain and stimulated emission at the wavelength of the emitting transition for close-packed solids of CdSe QDs. The narrow band emission and high volume fraction are main prerequisites to observe amplified stimulated emission in semiconductor QDs.

1.5. Silica Particles

Silica allows easily for the introduction of a specific surface functionality, which can be obtained by modifying the surface hydroxyls on the silica surface with amines, thiols, carboxyl and methacrylate groups, among others. This modification can facilitate the incorporation into non-polar solvents, glasses and polymeric matrices. Colloidal Stöber[96] silica dispersions have been surface modified by organosilanes to prepare core-shell particles comprised of either dye molecules or magnetic particles.[97,98] Liz-Marzán, Mulvaney and coworkers[5,99,100] reported an elegant method for silica coating of gold, silver and CdS nanoparticles, consisting of a slow deposition of a thin silica shell from a silicate solution followed by transfer into ethanol to grow thicker shells (See the chapter by Liz-Marzán),

Since the pioneering work of Yablonovitch,[101] photonic crystals with a three dimensional ordered structure (with a periodically modulated dielectric constant) have attracted a huge amount of interest on colloidal silica suspensions and silica-coated metal and semiconductor core-shell structures, which have been proven to be model systems for the photonic band gap (PEG) applications.[102-110]

Alternatively, microemulsions[111-113] can also be used as nanoreactors for a variety of nanocomposite systems ranging from metal[109] and semiconductor QDs[114-117] to polymers.[118-122] Using inverse microemulsions, monodisperse silica particles can be synthesized.[113] By providing an inert barrier to the influence of an external environment, encapsulation of the nanoparticles within silica leads to an enhancement in chemical and photostabilities. This has been realized in a heterostructure system, viz., ZnS (core)-two photon dye-silica (shell) particles. The dye encapsulated within silica shell showed enhanced luminescence and life-time.[115] All these microemulsion methods have utilized

for the formation of metal or semiconductor particles in the water pools. Whereas the highly luminescent CdSe QDs, synthesized through organometallic route using trioctylphosphine oxide (TOPO) as the surfactant, are soluble only in nonpolar solvents,[23-26] these QDs need to be soluble in water, especially for biological applications. We have developed a simple strategy in order to transfer the QDs into water by silica coating through a novel inverse microemulsion method. The silica coated QDs exhibited both colloidal stability and photostabilty.[117]

2. GOLD-POLYPYRROLE CORE-SHELL NANOCOMPOSITES THROUGH SELF-ASSEMBLY OF BLOCK COPOLYMERS

The formation of polymer nanocomposites is one versatile approach to stabilize nanoclusters of various nature.[12-20] We have used block copolymers as a template to synthesize monodisperse Au nanoparticles[14-15] as well as novel Au-polypyrrole core-shell composites.[16-18] Spatz et al have studied the mineralization of Au nanoparticles in block copolymer micelles.[13,14] Uniform, monodisperse Au particles were obtained when anhydrous hydrazine was used as the reducing agent. Gold-polypyrrole inorganic-organic nanocomposites were fabricated by a similar approach, replacing hydrazine by the monomer, pyrrole. A micellar solution of a block copolymer, polystyrene-block-poly (2-vinylpyridine) in toluene was treated with $HAuCl_4$, which became selectively bound within the P2VP cores of the micelles. When this solution was treated with pyrrole, polymerization occurred, yielding polypyrrole under concurrent formation of Au nanoparticles (Scheme 1), as supported by FTIR and UV-visible spectroscopy. The protonation of the pyridine groups is evident at 325 nm (Figure 1; traces a-c). This absorption band disappears and a new band arises at 450 nm when [Pyrrole]/[$HAuCl_4$] > 0.2. The broad absorption maximum at around 450 nm indicates the formation of ultrasmall Au particles (traces d-f). The sizes of the tiny Au particles are estimated from the width of the absorption band to be close to 2 nm. The fitted results of surface plasmon peaks by the Mie-Drude theory are included in Figure 1.

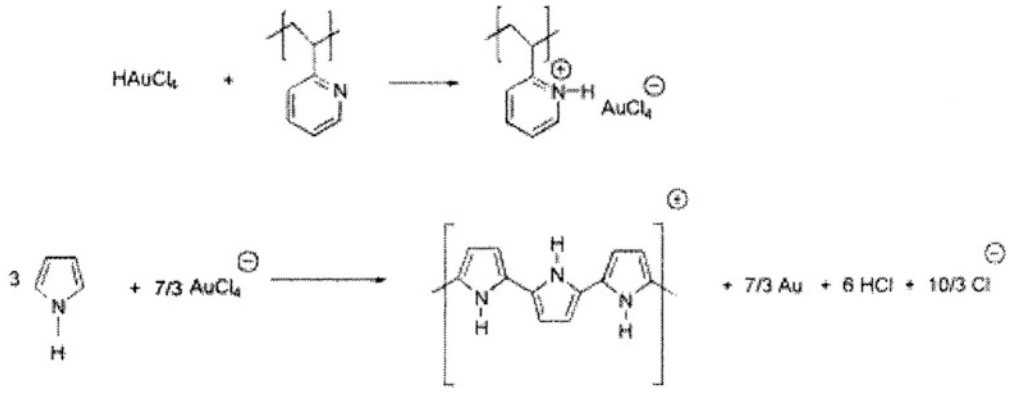

Scheme 1. The protonation of poly (2-vinylpyridine) cores of the block-copolymer micelles by $HAuCl_4$. The second step involves the reduction of $AuCl_4^-$ ions by pyrrole, forming colloidal Au and polypyrrole.

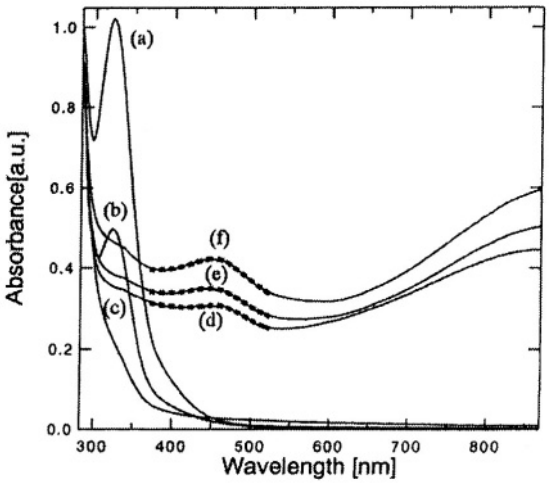

Figure 1. UV-visible spectra of colloidal polymer solutions. Traces (a) – (f) are for [Pyrrole]/[$HAuCl_4$] = 0, 0.02, 0.2, 1.0, 4.0 and 10.0, respectively. The broad absorption maximum at around 450 nm reveals the formation of tiny Au nanoparticles. Note that traces (d)-(f) indicate both experimental results (solid lines) and analysis from Mie-Drude theory (dotted squares). Reprinted with permission from ref. [18].

These tiny Au particles formed larger clusters, with a diameter of 7 nm, upon annealing the film at 130 °C (above the glass transition temperature of the block copolymer) for ca. 2h. Apparently, polypyrrole slowed down the crystallization of Au considerably, allowing the fabrication of novel core-shell particles. We have also produced different shapes of Au nanoclusters by allowing the particles to crystallize severely under ambient conditions with vigorous stirring for several weeks. It is obvious that an ordered aggregation produces uniform particles, since a disordered aggregation would result in polydisperse particles of variable morphology.

We have also demonstrated the variation in particle size of monodisperse Au (7-13 nm) by changing the length of the block copolymers. Importantly, using this block copolymer approach we have synthesized monodisperse hexagonally packed Au nanoclusters and also gold-polypyrrole composites with core-shell morphology (Figure 2). Our interest in these novel composites stems from three intriguing perspectives. First, the preparative strategy could lead to a simple way for the direct synthesis of conducting polymer/metal nanocomposites. Second, the block copolymer architecture is useful for commercial applications of a processable form of polypyrrole by providing colloidal stability to the suspension of polypyrrole. Third, different (spheroids, cuboids) Au nanoparticles may have important implications in the field of catalysis. We have also observed dendritic nanostructures of gold-polypyrrole through vapor phase polymerization of pyrrole.[17,18]

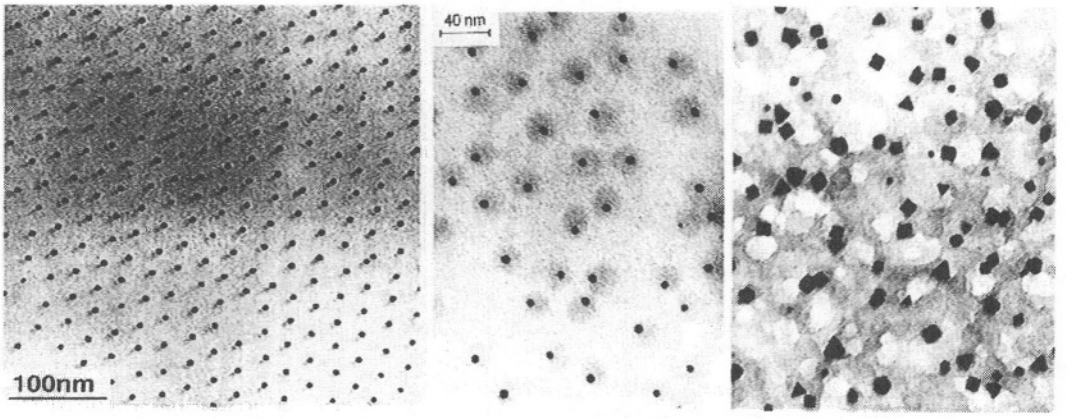

Figure 2. A gallery of TEM micrographs showing a hexagonal arrangement of Au nanoclusters (left); gold-polypyrrole core-shell particles (middle) and different (tetrahedral and octahedral) shapes of Au particles (right). Scale bar is common for the middle and right micrographs. PS-b-P2VP block copolymer micelles were employed as the template. Reprinted with permission from refs. 14 and 18.

3. NONLINEAR OPTICAL PROPERTIES OF AU/SiO_2 COMPOSITES

$|\chi^{(3)}|$ is expressed by the following equation using the third-order nonlinear susceptibility of a metal particle itself, $\chi_m^{(3)}$, and the local field factor $f_l(\omega)$,[123]

$$|\chi^{(3)}| = p f_l(\omega)^2 \mid f_l(\omega) \mid^2 \chi_m^{(3)}, \tag{1}$$

where $f_l(\omega)$ is given by

$$f_l(\omega) = 3\,\varepsilon_d / [\varepsilon_m(\omega) + 2\,\varepsilon_d], \tag{2}$$

ε_m and ε_d are the dielectric constants of the metal particle and matrix, respectively. At the plasmon resonance ($\omega \approx \omega_s$), the following equation holds:

$$\varepsilon_m'(\omega_s) + 2\,\varepsilon_d(\omega_s) = 0 \tag{3}$$

$f_l(\omega_s)$ is then simply expressed by the following equation:

$$f_l(\omega_s) = 3\,\varepsilon_d / \varepsilon_m''(\omega_s) \tag{4}$$

In Figure 3, the absorption spectra of Au-doped (0.1 to 1 wt%) silica gels and glasses and a representative TEM image for gels with a 0.5 wt% Au are shown. The absorption coefficient in the vicinity of the surface plasmon resonance is given by

$$\alpha = p\,(\omega / n\,c) f_l(\omega)^2\,\varepsilon_m'', \tag{5}$$

where n is the refractive index of the matrix, c the light velocity, and p the volume fraction of particles.

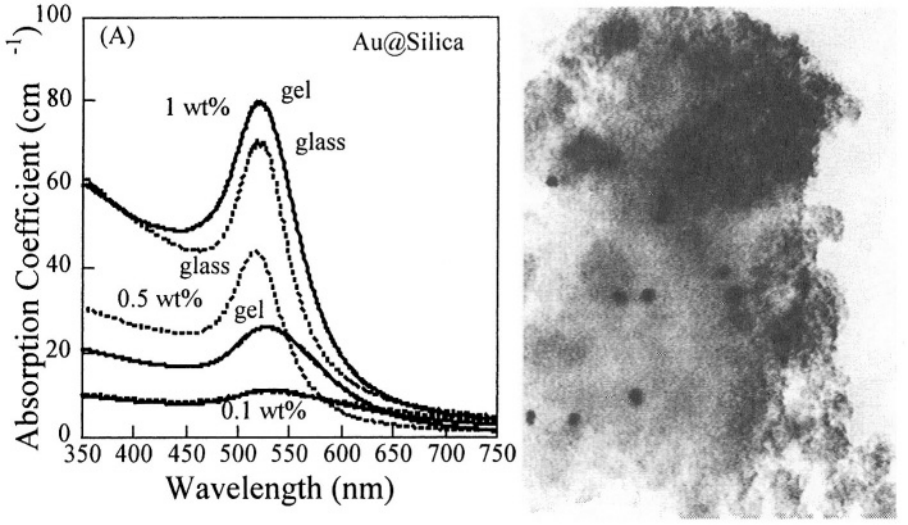

Figure 3. (Left) UV-visible spectra of Au-doped silica gels and glasses prepared by a facile sol-gel method. Au composition is given in weight percentage. The surface plasmon resonance for Au ranges from 520 to 526 nm. The increase in particle size at higher concentration of Au is characterized by sharper peaks. (Right) Transmission electron micrograph of Au-doped silica gel (0.5 wt% Au). The mean particle diameter is 18 nm. Reprinted with permission from ref. [87].

Accordingly, the following expression is obtained for $\chi^{(3)}/\alpha$:

$$\chi^{(3)} / \alpha = p\,(n\,c / \omega) f_l\,(\omega)^2\ \chi_m^{(3)} / \varepsilon_m''\,(\omega) \qquad (6)$$

Assuming that $\chi_m^{(3)}$ is independent of particle size, $\chi^{(3)}/\alpha$ must be proportional to $f_l\,(\omega)^2/\varepsilon_m''\,(\omega)$. The value of $\varepsilon_m''\,(\omega)$ can be easily obtained from the optical absorption spectra by using the analysis described above,[124] and $f_l(\omega)$ is calculated using the value of $\varepsilon_m''(\omega)$, through Eq. (4). The size-dependent behavior of $f_l(\omega)^2/\varepsilon_m''(\omega)$ reasonably agreed with the measured $\chi^{(3)}/\alpha$. This suggested that the enhancement of the local field inside the particle gives rise to the size dependence of $\chi^{(3)}/\alpha$.[123] In our case, the value of $\chi_m^{(3)}$ was estimated to be 6.6×10^{-8} esu from Eq. (1). This value of $\chi_m^{(3)}$ is in reasonable agreement with the experimental values of $\chi_m^{(3)} = 4 \times 10^{-8} - 1 \times 10^{-7}$ esu.[124] The size-dependent enhancement of $\chi^{(3)}$ in Au particles with the mean diameter of 11.0-37.0 nm has also been investigated. The value of $\chi^{(3)}/\alpha$ for the films increased with an increase of the mean diameter of Au particles. This is interpreted in terms of the size dependence of the local-field factor and the imaginary part of the dielectric constant of the metal particles. This size dependence effect has also been observed for Cu particles by Uchida et al.[125]

The third order optical non-linearity $|\chi^{(3)}|$ by the degenerate four-wave mixing method (DWFM) for gel samples with 0.1 wt% Au and 0.14 wt% Au showed values of 4.6×10^{-11} and 2.3×10^{-10} esu, respectively.[89] These values are about two orders of magnitude larger than those of the silica gels doped with Au, reported by Yazawa et al. by a similar sol-gel method.[126] At higher Au concentrations, $\chi^{(3)}$ increases further, revealing that a larger size induces a larger effect.

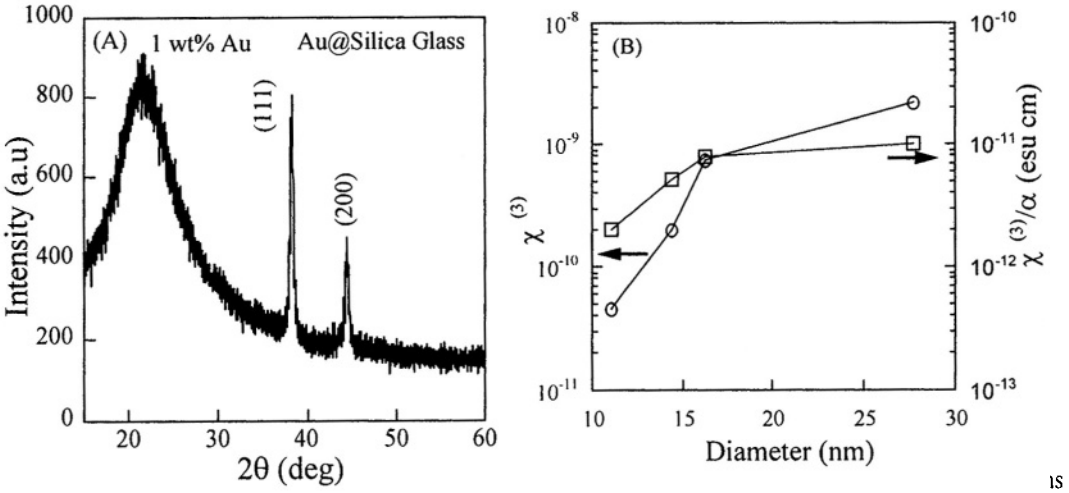

is from SiO_2. The characteristic (111) and (200) planes of cubic Au are noted. (B) Dependence of $\chi^{(3)}$ and $\chi^{(3)}/\alpha$ on Au particle size. Both values increase dramatically with particle diameter up to 16 nm and then saturate.[72]

The powder X-ray diffraction (XRD) pattern for a glass sample is shown in Figure 4A. The broad halo pattern at around $2\theta = 23°$ confirms the formation of amorphous silica. Sharp crystalline peaks are noticed at ca. $2\theta = 38°$ and 44°. These reflections are assigned, respectively, to (111) and (200) planes of cubic Au. The Au particle size was estimated using the Scherrer's equation and found to be ~26 nm from the diffraction band at $2\theta = 38°$. Thus the XRD pattern indicates that a cubic Au-silica nanocomposites can be readily formed by a facile sol-gel method.

A glass sample with 0.5 wt% Au exhibits a higher value of 2.2×10^{-9} esu.[89] This value is two orders of magnitude larger than those of Au particles in glasses prepared by the conventional melt-quenching method.[127] This is because the concentration of Au in the films is two orders of magnitude larger than that of the conventional glasses containing Au particles. The third-order nonlinear susceptibility of Au/SiO_2 thin films prepared by a sputtering method, exhibited a peak at the wavelength of the absorption peak and the maximum value of $\chi^{(3)}$ obtained was 2.0×10^{-7} esu.[123] When the particle size increases, so does $\chi^{(3)}$. In Figure 4B, we show the dependence of $\chi^{(3)}$ and $\chi^{(3)}/\alpha$ on the mean particle diameter of Au particles. Although the sputtering method produced high $\chi^{(3)}$,[123] the method presented here offers a greater $\chi^{(3)}/\alpha$, a figure of merit, which should be compared with regard to different preparative strategies. Compared to sputtering[123] and sol-gel dip coating,[128] our sol-gel method offers about five times greater $\chi^{(3)}/\alpha$ values.[89]

4. LUMINESCENCE OF Eu^{3+}-DOPED SILICA COMPOSITES

Rare-earth ion doped gels and glasses are another important class of materials of considerable technological interest. The optical properties play a crucial role in such applications and sensitized luminescence can particularly serve as the basis for

applications of rare-earth ions in photonic devices and color displays.[129] Among rare earth ions, Eu^{3+} has a simple energy level structure, which allows the absorption and emission spectroscopy in the visible range. We have recently developed a simple methodology to enable a greater enhancement of luminescence from Eu^{3+}-doped silica gels containing adsorbed silver islands.[130] The procedure involves the preparation of Eu^{3+}-doped silica gels by a sol-gel method and then immersion in a silver sol for ca. 48 h to allow the adsorption of Ag particles on the pore surfaces of silica gels. The absorption and emission spectra of Eu^{3+}-doped silica gels are shown in Figure 5. We have also studied the effect of Ag particles in silica glass. The enhancement of fluorescence is originated from the local field enhancement around Eu^{3+} ions, owing to the surface plasmon resonance of small Ag particles in glass.[131,132]

We have also observed enhanced photoluminescence from Eu^{3+}-doped silica gels containing cadmium sulfide (CdS) QDs.[133-135] The method is essentially a two step process. First Eu^{3+} -doped silica gels were prepared by a typical sol-gel route described elsewhere.[130] Then CdS nanoparticles were allowed to adsorb onto the pore surface of the gels by immersing them in CdS sol for different periods of time. Figure 6 shows the absorption and excitation spectra of the samples before and after immersion. In the absorption spectra, a broad peak at 325 nm for a sample immersed for 1 day in 50 mL of CdS sol (Figure 6c) shows a size quantization effect (~3 nm), as compared to samples that have been immersed for longer periods of time in CdS sol. Figures 6b and 6d show the photoluminescence excitation spectra for samples before and after immersion. The intensity of emission at 618 nm was measured as a function of the excitation wavelength. The excitation spectrum (Figure 6b) is typical of Eu^{3+} doped silica gels. Figure 6d shows a different behavior. As the wavelength of the incident radiation decreases below 450 nm, CdS nanoclusters begin to absorb light in addition to the overlapping of Eu^{3+} absorption, and a corresponding increase in the intensity of Eu^{3+} emission results in a sharp peak at 618 nm (see Figure 7b). In the excitation spectrum, a broad peak at around 325 nm (Fig. 6d) is identical to the absorption spectrum (Figure 6c) of the CdS– adsorbed gels. From the perfect coincidence of the excitation with the absorption spectrum, we infer that the enhanced luminescence arises from the CdS energy transfer to the Eu^{3+} ions, evidencing the location of Eu^{3+} ions close to the surface of CdS.

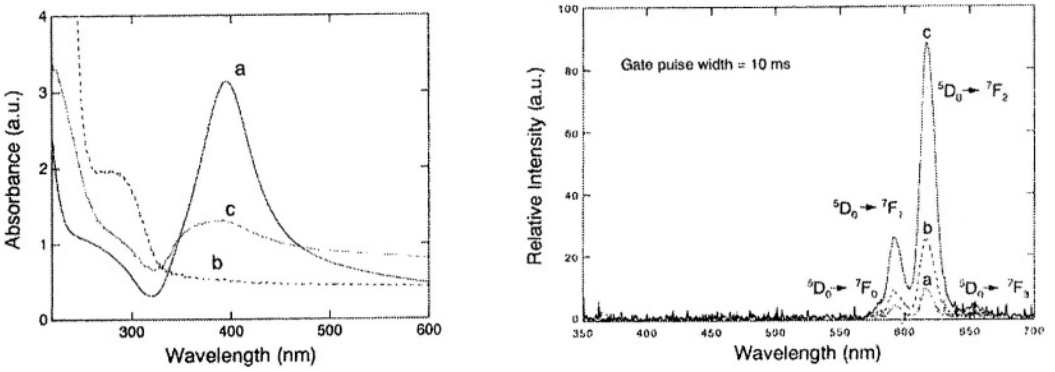

Figure 5. (Left) Absorption spectra of (a) Ag sol, (b) Eu^{3+}/SiO_2 gel without Ag and (c) Ag adsorbed Eu^{3+}/SiO_2 gel. (Right) Fluorescence spectra of Eu^{3+}-doped silica gels without Ag (a) and with Ag (b and c) with different concentrations of Ag colloid. The enhancement of fluorescence in trace (c) is ca. 8 times greater than that in trace (a). Reprinted with permission from ref. [130].

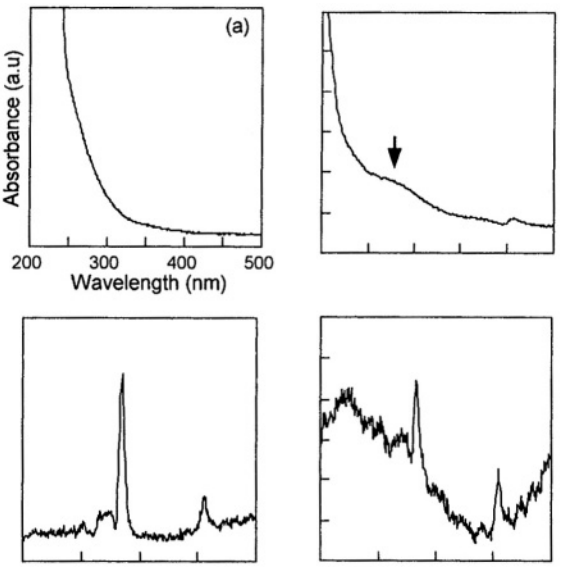

Figure 6. Absorption and excitation spectra of Eu^{3+}-doped SiO_2 gels without CdS (traces a, b: Eu/SiO_2), and with CdS –1 day immersed gels in 50 mL of CdS sol (traces c, d). The increase in excitation intensity from 400 nm and a broad peak at 325 nm (trace d), in consonance with the absorption spectrum (trace c), confirms the formation of CdS nanoclusters and their energy transfer to the Eu^{3+} -ions. Reprinted with permission from ref. [133].

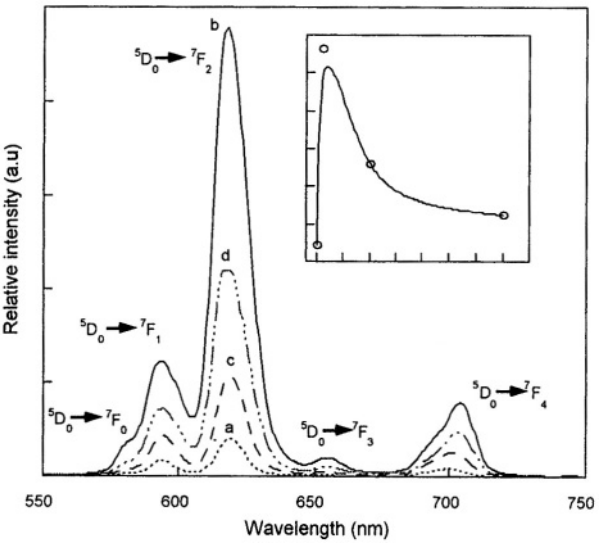

Figure 7. Fluorescence spectra of Eu^{3+}-doped silica gels without CdS (trace a: control, Eu/SiO_2) and with CdS (trace b: Eu/SiO_2 –CdS1, trace c: Eu/SiO_2 –CdS10 and trace d: Eu/SiO_2 –CdS35. The numbers indicate the immersion time in days in CdS colloids). The remarkable influence of CdS on the significant enhancement of fluorescence (trace b) is noticed. Inset shows that the enhancement of fluorescence for $^5D_0 \rightarrow {}^7F_2$ emission (618 nm) in trace (b) is *ca.* one order of magnitude greater than that in trace (a). Reprinted with permission from ref. [133].

An increase in fluorescence is noted for CdS adsorbed silica gels (traces b-d in Figure 7). At a lower immersion time of 1 day (trace b), the increase in fluorescence for the emission $^5D_0 \rightarrow {}^7F_2$ (618 nm) is ca. one order of magnitude greater than that of the control sample (trace a). The luminescence intensity is found to be greater for 1 day immersed sample than those of other samples immersed for a longer duration (inset of Figure 7). Apparently, a decrease in CdS particle size (~2.8 nm) resulting from 1 day immersion causes an enhancement of fluorescence because of the quantum size effect, in comparison with a sample immersed for 10 days (~6.5 nm).

Compared to Ag adsorbed Eu^{3+}-doped SiO_2 gels,[130] CdS adsorbed similar gels produced a greater enhancement of fluorescence.[133-135] In the former, the fluorescence was originated from the local field enhancement around Eu^{3+} ions, caused by the electronic plasmon resonance of the Ag islands. Despite the enhancement of factor 12, the CdS particles did not influence the Eu^{3+} fluorescence decay curves, which were almost exponential and the lifetime of Eu^{3+} was found to be ca. 100 μs. As the particle size of CdS decreases (≤ 3 nm), there is a possibility of energy transfer from the nanocrystals to the Eu^{3+} ions, owing to the electron or hole trapped surface levels. The photogenerated electron is first trapped in the surface levels of CdS particles and then interacts with Eu^{3+} ions located close to the CdS surface. Secondly, the electron in the surface trap recombines with a valence band free hole and the energy is nonradiatively transferred to the Eu^{3+} ions. The fluorescence excitation spectrum shown in Figure 6d confirms the energy transfer from CdS nanoparticles to the Eu^{3+} ions. Since the lifetime of CdS nanoparticles is extremely low (~10^{-10} s) in comparison with that of Eu^{3+} (10^{-4} s) the CdS fluorescence is not seen in the spectra. Importantly, the studies presented here serve to illustrate the usefulness of semiconductor colloids in assessing the optical properties of lanthanide ion-doped silica gels.

5. PHOTOPHYSICS OF QUANTUM DOTS

CdSe (@ZnS)–TOPO quantum dots provide efficient surface passivation in the mother solution, butanol or nonpolar solvents such as hexane. However, the QDs exhibit slow degradation and photo-dissolution upon exposure to ambient light. Oxygen present in the solvent deteriorates the QD luminescence.

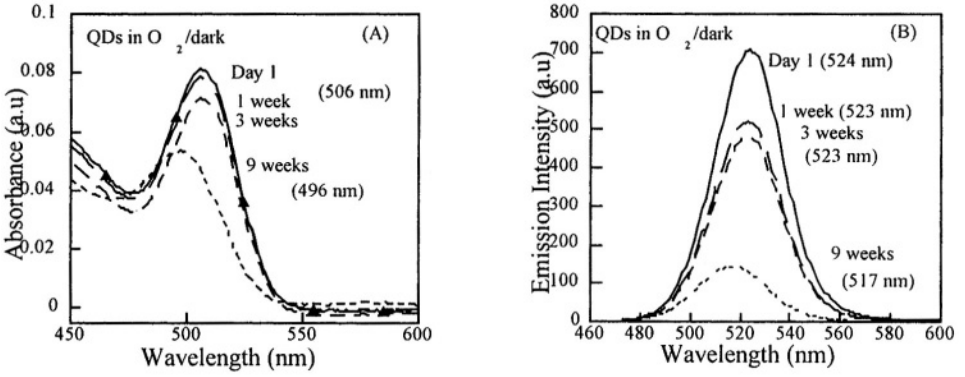

Figure 8. Absorption and emission spectra of QDs stored in oxygen and dark over several periods of time.[136]

We have analyzed the effect of oxygen in dark and in ambient light.[136] We have found that the QDs exposed to oxygen but stored in the dark exhibit photo-dissolution but weaker than those stored in ambient light. Figure 8 shows the absorption and emission spectra for QDs stored in oxygen and in the dark. There is no change in absorption maximum at 506 nm up to 3 weeks. After 9 weeks of storage a 10 nm "blue shift" indicates that the particles dissolve despite being stored in dark. This dissolution might be attributed to a combination of photo-darkening and dissolution effects. The emission wavelength at 524 nm slowly shifts to 517 nm over 9 weeks, in addition to a decreased quantum yield (QY), which again indicates photo-darkening and dissolution effects, in consonance with the absorption spectra.

The absorption and emission spectra for QDs stored in oxygen and ambient light are shown in Figure 9. Over 9 weeks of storage, the absorption and emission peaks are noted at 467 and 500 nm respectively. The photo-dissolution effects are worsened in the case of light plus oxygen, with respect to the samples stored in the dark and with oxygen.

Bawendi and co-workers have studied the tunneling mechanism for the blinking *on* and *off* (emitting to nonemitting, i.e. bright to dark) process for CdSe QDs.[137] These QDs need to be encapsulated within a rigid matrix in order to prevent the photo-darkening and blinking effects. What guidelines do actually exist for achieving this goal? QD-silica composites fabricated through sol-gel processing have been shown to exhibit remarkable photostability against photo-degradation.[31]

6. HIGHLY LUMINESCENT QD-GLASSES

Readily prepared via colloid methods, luminescent CdSe QDs can be made in a range of colors by carefully controlling the particle size.[23] Their photoluminescence (PL) spectra are blue-shifted with respect to the bulk PL due to strong quantum confinement effects. Recent success in the surface passivation of these QDs with higher band gap semiconductors (e.g. ZnS) have yielded highly luminescent core -shell QDs.[25,26] The size and shape dependent optical properties of semiconductor nanocrystals render them attractive candidates as tunable light absorbers and emitters in optoelectronic devices[36,37] and as fluorescent probes of biological systems.[32-35,38,39]

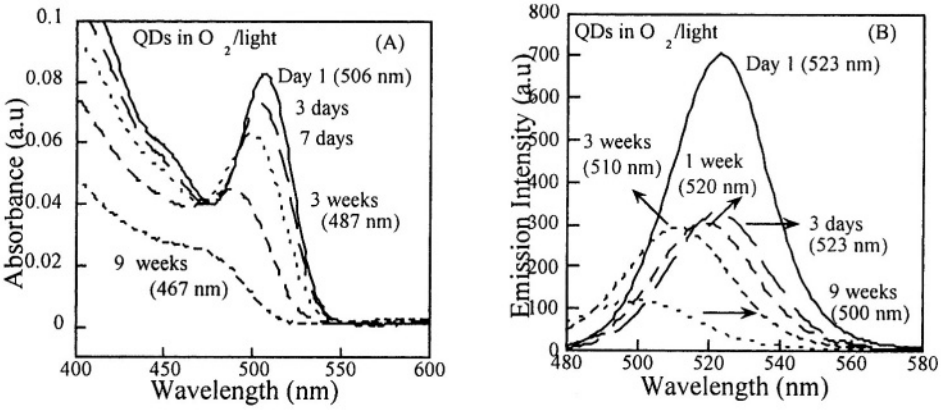

Figure 9. Absorption and emission spectra of QDs stored in oxygen and light for several periods of time.[136]

Whilst such capped and coated QDs display vastly improved photostability in the solvent of preparation, changes to the solvent polarity can cause solvation, which results in slow quenching of the luminescence. Consequently, the transfer of these materials into glasses through sol-gel processing has not been straightforward. Recently, we reported a facile synthesis of tunable, highly luminescent QD-silica composites through sol-gel processing.[31]

Full color emission has been observed from CdSe/ZnS QD-silica monoliths at 365 nm excitation. The QY was estimated to be 0.15 for red gels by comparison to rhodamine dye (QY=0.92). Octylamine was used as surface passivator and sol-gel catalyst. Orange emission was created by mixing red and green emitting QDs. CdSe QDs capped with ZnS remained luminescent over several months. The pH dependence of the sol-gel transition time is often used as a measure of the overall condensation kinetics for sol-gel systems. The overall condensation rate is maximized at intermediate pH values. Above pH 4, surface silanol groups are deprotonated and hence are negatively charged, as indicated below:

$$\equiv Si\text{-}OH + OH^- \Leftrightarrow Si\text{-}O^- + H_2O$$
$$\equiv Si\text{-}OH + Si\text{-}O^- \Leftrightarrow \equiv Si\text{-}O\text{-}Si + OH^-$$

As the number of siloxane bonds increases, the individual molecules are bridged and jointly aggregate in the sol. When the sol particles aggregate or inter-knit into a network, a gel is formed. Upon drying, trapped volatiles, (alcohol, water etc) are driven off and the network shrinks as further condensation can occur.

Generally, the gelation time, t_{gel} is decreased by factors that increase the condensation rate. For gels made from silicon alkoxides, gelation is much faster in the presence of a base. Increase in the ratio of water to alkoxide, temperature and a decrease in the size of the alkoxy group all decrease t_{gel}. Figure 10 shows the absorption and emission spectra from a CdSe @ ZnS QDs during sol to gel transition.

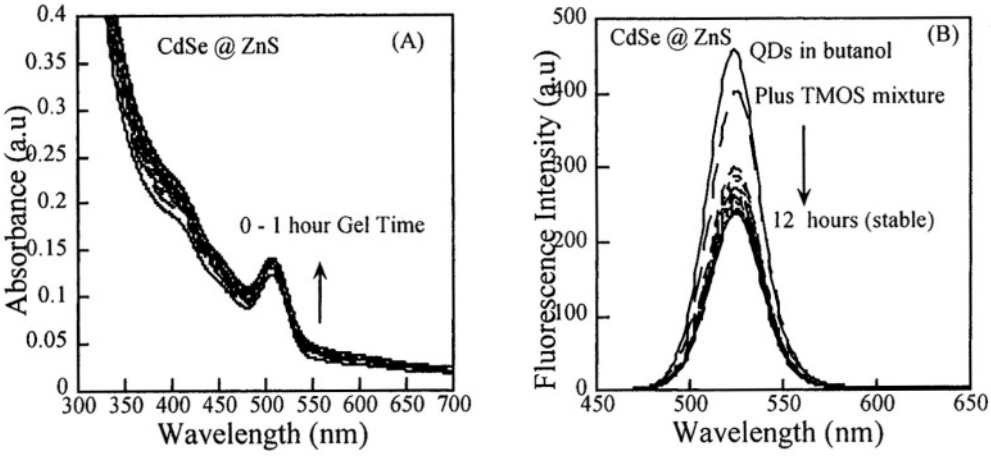

Figure 10. (A) UV-visible absorption spectra of CdSe @ ZnS QDs recorded continuously for 1 h during sol-gel transition. The gelation time is about 10 min after the addition of QDs in butanol with octyl amine (1 mM) to TMOS (0.4 mL to 2.0 mL of QDs). (B) Fluorescence spectra of the same sample as a function of time. The emission decreases over some 12 h and then stabilizes. Reprinted with permission from ref. [31].

It is clear that the position of the exciton absorption band remains unchanged during the sol-gel transition, with the only difference being a slow, steady increase in scattering arising from the porous structure of the silica gel. Emission spectra (Figure 10B) indicate that the luminescence decreases over 12 hours upon TMOS addition, and then stabilizes. This decrease is attributed to changes to the surface chemistry of QD sols despite the amine capping agent. However, loss in band gap luminescence is not accompanied by a peak blue-shift, and the final QDs in gels have about 60% of the original QY of the same particles in butanol. In Figures 11 and 12, time resolved luminescence decay curves are shown for both CdSe and for CdSe@ZnS QDs in butanol prior to sol-gel processing and after formation of the monolith. Both the QY and luminescence lifetime are relatively unchanged for the core-shell QDs over the first hour, but the CdSe particles show a noticeable loss in band gap luminescence as soon as processing starts. These CdSe QDs display roughly biexponential decays, with τ =30 ns, τ =100 ns. For the core-shells, a single exponential decay of τ = 55 ns was observed for the first 15 min, but after this initial gelation, the QY slowly decreased to the levels shown in Figure 10.

Although we have developed a strategy to prepare highly luminescent QD-glasses, we currently have these materials at volume fractions up to 0.1%, homogeneously distributed and exhibiting QYs of only 5-10%. It seems likely that with further optimization of the QD surface chemistry, cheap, photostable QD glasses with high volume fraction and QY will be readily attainable.

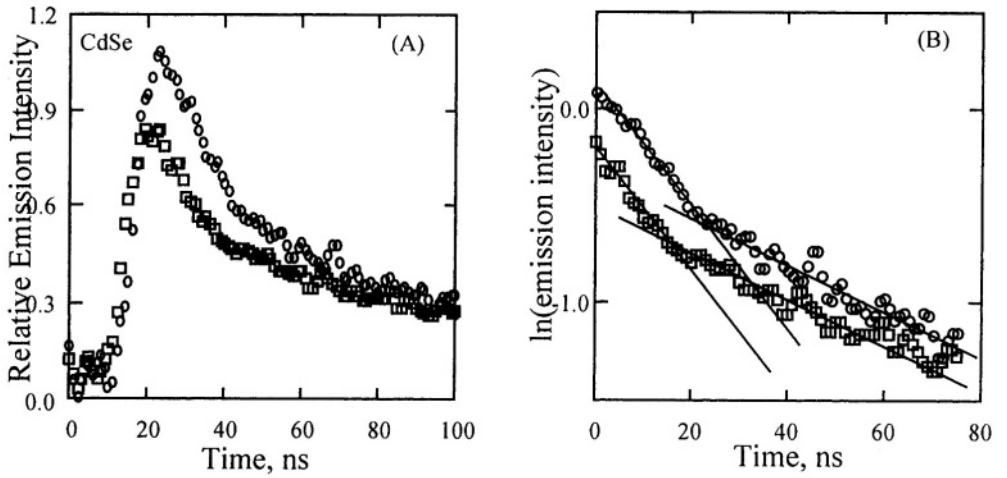

Figure 11. (A) Band gap luminescence decay for CdSe before (O) and after (□) sol-gel processing. The CdSe band gap luminescence decreases during gelation by some 20% and continues to decrease after gelation until it is almost gone. (B) The decay kinetics are complex, but do not seem to change with loss of luminescence. Reprinted with permission from ref. [31].

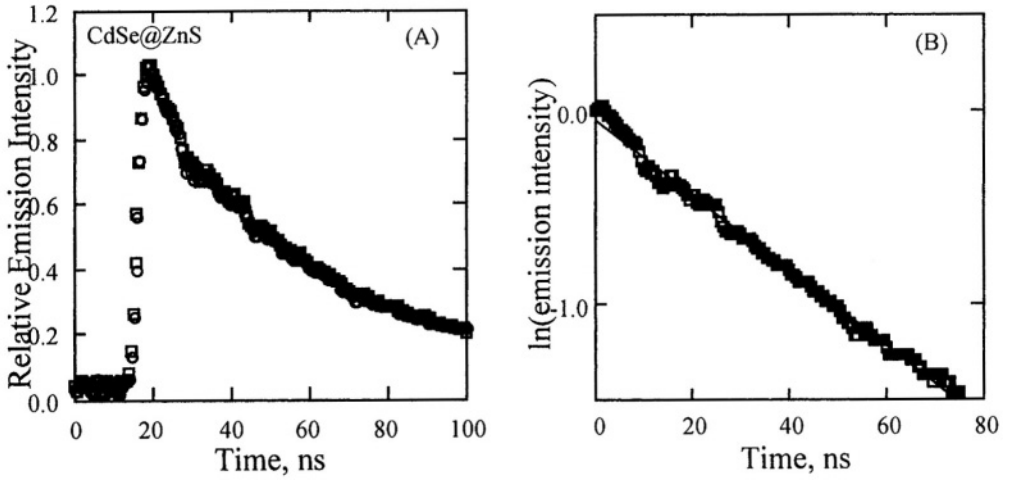

Figure 12. Normalized band gap luminescence decay of CdSe@ZnS QDs before (○)and after the first 15 min (□) of gelation. The decay is first order and does not change during sol-gel processing, though the QY decreases slowly for the first 12 h before stabilizing. Pump source: 337 nm N_2 laser. Pulse width: 2 ns. Reprinted with permission from ref. [31].

7. SILICA COATED QUANTUM DOTS

A fundamental drawback is that the particles remain both highly luminescent and photostable only in non-polar media, in which both ligand desorption and lattice dissolution can be neglected. For biological applications in particular, transfer of these luminescent materials into water is a pre-requisite and one potential method is to synthesize a QD with an impermeable coating that impedes material exchange between the lumophore and its environment. Silica capped core-shell quantum dots could fulfill this need, since such surfaces are biocompatible, and easily functionalized for bioconjugation purposes. The silica shell also minimizes fluorescence quenching by surface adsorbates or redox active molecules. Furthermore photodegradation can be minimized.

Until now, only a few transfer protocols from non-polar to polar media have been reported and these involve numerous purification steps for silica coating[32,39] or lead to photochemically unstable nanocrystals capped with organic ligands in aqueous solution.[38] The organically capped QDs are usually degraded in these polar media before coating can be effected. Consequently, a method is needed for encapsulating nanocrystals of luminescent semiconductors (or other materials) that are only soluble in non-polar media. Very recently, we have demonstrated a straight-forward approach for the preparation of photostable, highly luminescent, water-soluble core–shell CdSe@ZnS@SiO_2 nanocrystals, starting with TOPO–capped nanocrystals.[117]

CdSe@ZnS QDs with excess TOPO without any surface modification were prepared according to literature procedures.[23,26] The particles had luminescence quantum yields of 10-25% and emission at 625nm (FWHM=30nm). The particles were precipitated once from methanol to remove excess TOPO and TOP. Inverse micelles were prepared using Igepal CO-520 (polyoxyethylene nonylphenylether) and cyclohexane as solvent.[113,114]

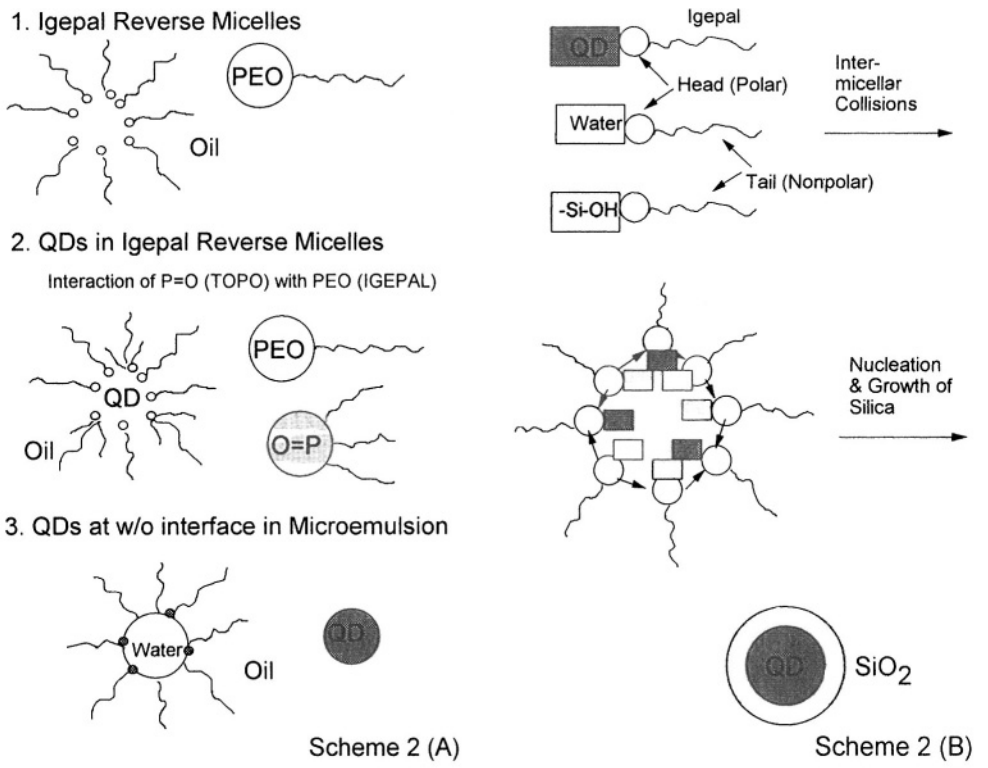

Scheme 2. (A) Step 1: Formation of Igepal micelles; Step 2: Interaction of hydrophiles of both TOPO and Igepal surfactants. QD surface is capped with Igepal, becoming hydrophilic. Step 3: QDs move to water/oil interface. (B) Addition of NH_4OH and TEOS forms silica. Inter-micellar collisions and nucleation and growth of silica form core-shell particles.

Typically, TOPO QDs (OD=1.35/cm at 610 nm) dissolved either in butanol or n-hexane (0.1mL) were injected into the inverse micelles (4mL), followed by the addition of TEOS (2μL) and allowed to stir for 1h. Addition of ammonia (40μL) resulted in a stable water-in-oil microemulsion. The resulting solution was stirred for 24h, which resulted in homogeneous silica deposition. Due to the large excess of Igepal, the TOPO ligand is exchanged for Igepal in cyclohexane and the QDs become more hydrophilic. They then become solubilized by water through exchange of the Igepal capped QDs with Igepal capped water pools.

UV-visible (Figure 13A) and photoluminescence spectra (Figure 13B) show the evolution of silica coating over 24 h in a microemulsion medium. The luminescence intensity increased after the addition of ammonia, due to the removal of electron trapping sites following the formation of a dative bond between the amine lone pair and surface cadmium ions. A 7 nm red shift accompanied this increase (Figure 13B).

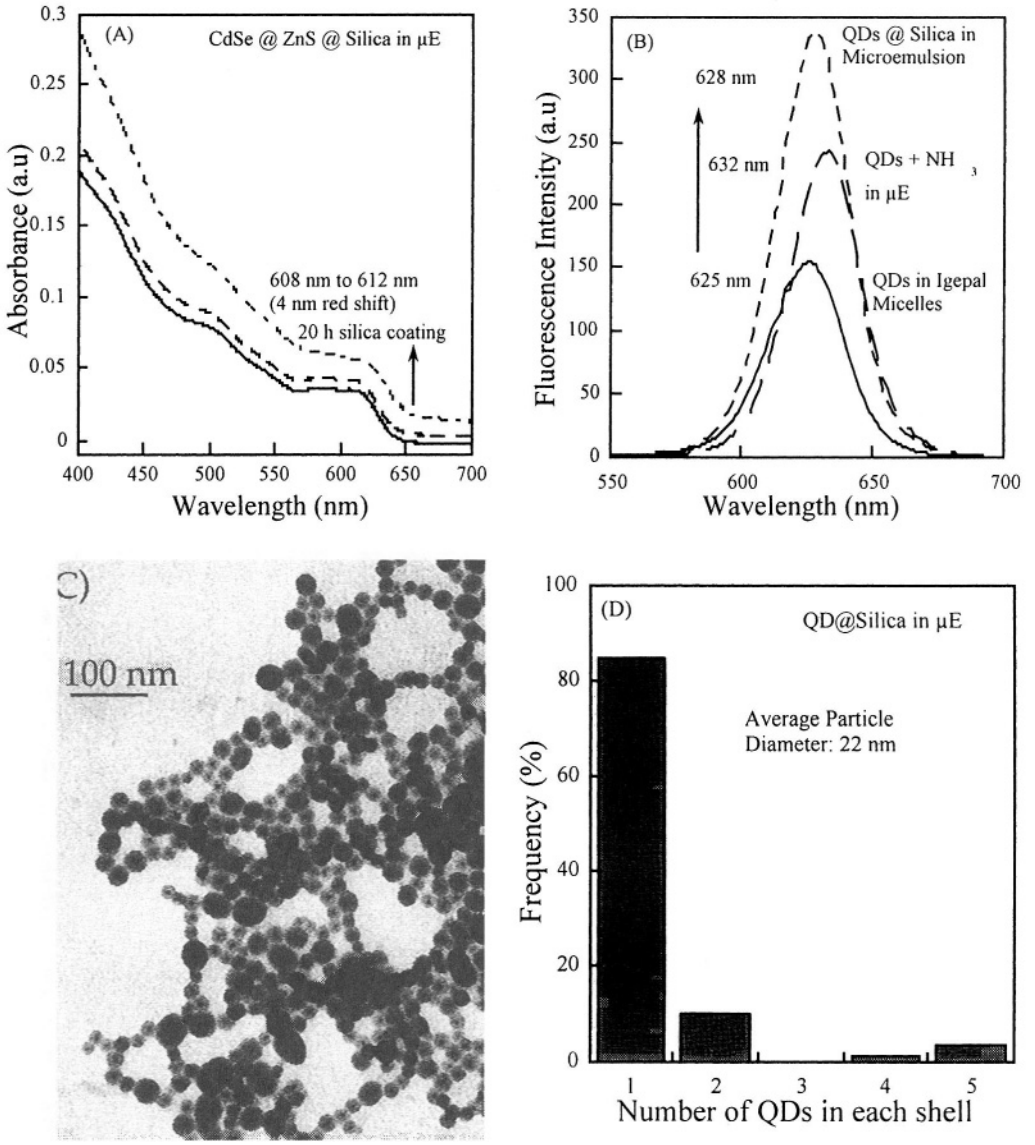

Figure 13. Absorption (A) and luminescence (B) spectra of CdSe@ZnS QDs in microemulsion during silica coating. Solid lines (bottom traces) correspond to QDs in Igepal micelles. Dotted lines (middle traces) after ammonia addition. Top traces correspond to QD@ZnS@SiO_2. (C) Transmission electron micrograph of 5nm CdSe@ZnS QDs encapsulated within 22 nm silica. (D) Histogram showing the majority of single QDs encapsulated within a single silica shell. [117]

The luminescence remained constant for about a week, but thereafter the quantum yield decreased slowly. This is due to slow loss of ammonia from the QD surface. Electron microscopy revealed that the majority (>90%) of QDs are encapsulated as single particles within a silica shell (Figure 13C). The average total diameter of QD@Silica is ~ 22 nm under the above conditions (Figure 1D). The silica shell thickness can be increased or decreased by varying the TEOS concentration. Varying the amount of water and ammonia in the microemulsion also affects the shell thickness, since this alters the water

pool size. The diameter of CdSe@ZnS particles was 5 nm. the silica shell is not clear in the images when the total diameter is down to 10 nm, for lower concentration of TEOS, 0.45 μM. Conversely, homogeneously coated particles are seen at a TEOS concentration of 9 μM (Figure 13C) and above. Centrifugation at 15,000 rpm for about 2 h precipitated out QD@Silica particles from the microemulsion. The precipitate was washed with cyclohexane and sonicated to repeptize the colloid. This process was repeated twice and the fluorescent precipitate was then dried under nitrogen. Finally, the colloid was sonicated to disperse it in alkaline solution (NaOH, pH 9) and subjected to centrifugation at 3000 rpm to yield a homogeneous, fluorescent solution.

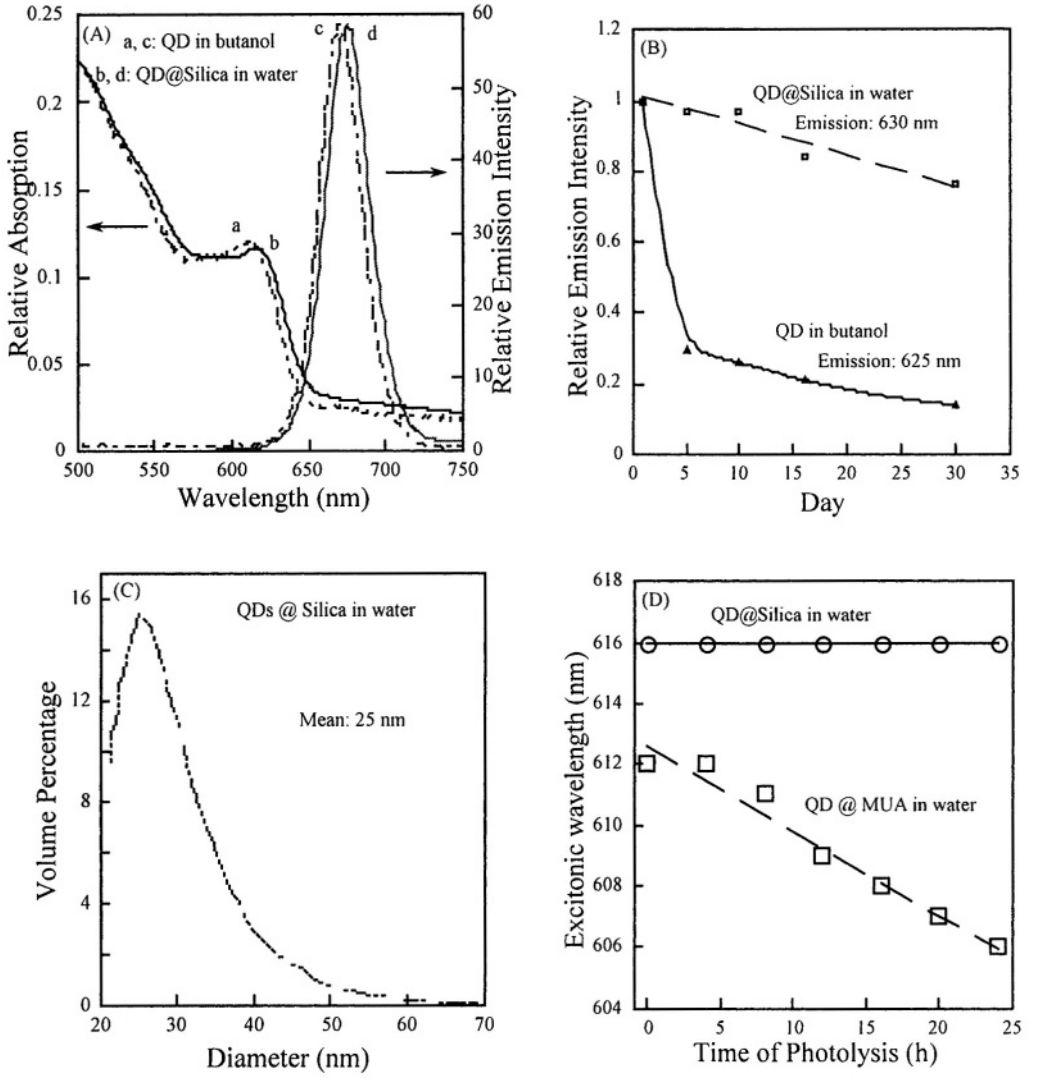

Figure 14. Absorption and emission spectra of CdSe@ZnS@SiO_2 QDs in water. The solid lines correspond to silica coated QDs in water. The dotted lines are for QDs in butanol. (B) Stability of silica-coated QDs over time. QD in butanol is shown for comparison. (C) Dynamic light scattering (DLS) of QD@Silica in water. The mean diameter is 25nm. (D) Exciton absorption peak of QD@Silica in water, and QD@MUA in water, as a function of photolysis time with a 100W Xe lamp (335nm cut-off filter).[117]

UV-visible (Figure 14A) and photoluminescence spectra (Figure 14B) show that there is a 5 nm red-shift for QD@Silica in water, in comparison to the QDs in the parent solution, butanol. Silica-coated QDs in water show remarkable colloidal stability, as shown in Figure 14C. The final quantum yield (QY) for silica-coated QDs in water is about half that of the parent nanocrystal solution. The losses occur primarily prior to the deposition process and relate to loss as the TOPO desorbs from the surface and is replaced by Igepal. The mean diameter of silica coated QDs in water prepared according to the above protocol was measured by DLS to be 25 nm (Figure 14C). In Figure 14D, we demonstrate that these materials exhibit remarkable photostability. The core-shell particles have been exposed to UV irradiation (335 nm cut-off filter) in water and in butanol, both polar solvents. About 85% of the QY is retained for QD@Silica in water, where as the parent QD solution virtually lost all luminescence (not shown). We also compared the results with those dots in water capped by mercaptoundecanoic acid (MUA). MUA-QDs in water exhibited initial photo-brightening and then photo-dissolution over a period of 24h. The exciton absorption peak position is plotted against time of photolysis in Figure 14D. The peak position remains constant at 616 nm for silica coated QDs indicating the fact that the dots are photostable over extended periods of photolysis time. On the contrary, the QDs capped with MUA show photodissolution as exemplified by blue-shifts in exciton position over photolysis time of 24h (Figure 14D).

8. SUMMARY AND OUTLOOK

Inorganic nanocomposites fabricated in our laboratory using either self-assembly of block copolymers or through a sol-gel method have shown interesting optical properties which are expected to find applications in areas ranging from tunable lasers and photonic crystals to biology. Fluorescent labeling using QDs is one of the key areas in nano-biotechnology because miniaturization reduces the size of the fluorescent signal causing detection problems. This could do drug screening at a much higher level compared to conventional organic dyes. QDs coated with silica particles could impart functional properties with respect to the above in labeling technologies. For example, magnetic QD particles can isolate biological target materials, such as DNA or RNA. Unlike polymer based magnetic particles, silica-coated particles can be easily dispersed in organic and aqueous solutions. QD-glasses could be used as ideal candidate systems for applications in LEDs, solar-concentrators, waveguides and solid-state lasers. Nanotechnology has acquired enormous learning to create designed functional nanostructures using bottom up strategies such as self assembly. It will be important to develop strategies to organize these nanostructures over various length scales to create advanced systems and materials.

9. ACKNOWLEDGEMENTS

I would like to thank all my co-workers who have contributed to the work cited in this chapter. I would also like to thank the Alexander von Humboldt (AvH) foundation, Bonn, Germany and the Japan Society for the Promotion of Science (JSPS), Tokyo, Japan for the award of research fellowships, and Quantum Dot Corporation, California, U.S.A for supporting my stay in Melbourne. I wish to thank Prof. Paul Mulvaney and Prof. Luis Liz-Marzán for their stimulating discussions and critical reading of the manuscript .

10. REFERENCES

1. U. Kreibig, and M. Vollmer, *Optical Properties of Metal Clusters,* Springer, Berlin (1995).
2. G. Schmid, *Clusters and Colloids,* VCH, Weinheim (1994).
3. S. E. Henrichs, J. L. Sample, J. J. Shiang, J. R. Heath, C. P. Collier, and R. J. Saykally, Positive and negative contrast lithography on silver quantum dot monolayers, *J. Phys. Chem. B* **103**, 3524-3528 (1999).
4. P. Mulvaney, Surface plasmon spectroscopy of nanosized metal particles, *Langmuir* **12**, 788-800 (1996).
5. L. M. Liz-Marzán, M. Giersig, and P. Mulvaney, Synthesis of nanosized gold-silica core-shell particles, *Langmuir* **12**, 4329-4335 (1996).
6. M. Schierhorn and L. M. Liz-Marzán, Synthesis of bimetallic colloids with tailored intermetallic separation, *Nano Lett.* **2,** 13-16 (2002).
7. T. Yonezawa, S. Onoue, and N. Kimizuka, Self-organized superstructures of fluorocarbon-stabilized silver nanoparticles, *Adv. Mater.* **13**, 140-144 (2001).
8. S. T. Ahmadi, Z. L. Wang, T. C. Green, A. Henglein, and M. A. El-Sayed, Shape-controlled synthesis of colloidal platinum nanoparticles, *Science* **272**,1924-1926 (1996).
9. J. H. Hodak, A. Henglein, and G. V. Hartland, Photophysics of nanometer sized metal particles: electron-phonon coupling and coherent excitation of breathing vibrational modes, *J. Phys. Chem. B* **104**, 9954-9965 (2000).
10. K. G. Thomas, J. Zajicek, and P. V. Kamat, Surface binding properties of tetraoctylammonium bromide-capped gold nanoparticles, *Langmuir* **18**, 3722-3727 (2002).
11. P. V. Kamat, M. Flumiani, and A. Dawson, Metal-metal and metal-semiconductor composite nanoclusters, *Colloid Surf. A* **202**, 269-279 (2002).
12. M. Antonietti, E. Wenz, L. Bronstein, and M. Seregina, Synthesis and characterization of noble metal colloids in block copolymer micelles. *Adv. Mater.* **7**, 1000-1005 (1995).
13. J. P. Spatz, A. Roescher, and M. Moeller, Gold nanoparticles in micellar poly(styrene)-b-poly(ethylene oxide) films. Size and interparticle distance control in monoparticulate films, *Adv. Mater.* **8**, 337-340 (1996).
14. J. P. Spatz, S. Mäßmer, and M. Möller, Mineralization of gold nanoparticles in a block copolymer microemulsion, *Chem. Eur. J.* **2**, 1552-1555 (1996).
15. M. Möller, J. P. Spatz, A. Roescher, S. Mößmer, S. T. Selvan, and H.-A. Kick, Mineralization of gold in block copolymer micelles, *Macromol. Symp.* **117**, 207-218 (1997).
16. S. T. Selvan, J.P. Spatz, H.A. Klok, and M. Möller, Gold-polypyrrole core-shell particles in diblock copolymer micelles, *Adv. Mater.* **10**, 132-13(1998).
17. S. T. Selvan, Novel nanostructures of gold-polypyrrole composites, *J. Chem. Soc. Chem. Commun.* 351-352(1998).
18. S. T. Selvan, T. Hayakawa, M. Nogami, and M. Möller, Block copolymer mediated synthesis of gold quantum dots and novel gold-polypyrrole nanocomposites, *J. Phys. Chem. B* **103**, 7441-7448 (1999).
19. B. H. Sohn and R. E. Cohen, Electrical properties of block copolymer containing silver nanoclusters within oriented lamellar microdomains, *J. Appl. Polym. Sci.* **65**, 723-729 (1997).
20. Y. N. C. Chan, R. R. Schrock, and R. E. Cohen, Synthesis of single silver nanoclusters within spherical microdomains in block copolymer films, *J. Am. Chem. Soc.* **114**, 7295-7296 (1992).
21. E. Shevchenko, D. Talapin, A. Kornowski, F. Wiekhorst, J. Kotzler, M. Haase, A. Rogach, and H. Weller, Colloidal crystals of monodisperse FePt nanoparticles grown by a three-layer technique of controlled oversaturation, *Adv. Mater.* **14**, 287-290 (2002).
22. A. P. Alivisatos, Perspectives on the physical chemistry of semiconductor nanocrystals, *J. Phys. Chem.* **100**, 13226-13239(1996).
23. C. B. Murray, D. J. Norris, and M. G. Bawendi, Synthesis and characterization of nearly monodisperse CdE (E = S, Se, Te) semiconductor nanocrystallites, *J. Am. Chem. Soc.* **115**, 8706-8715 (1993).
24. C. B. Murray, C. R. Kagan, and M. G. Bawendi, Self-organization of CdSe nanocrystallites into three-dimensional quantum dot superlattices, *Science* **270**, 1335-1338 (1995).
25. B. O. Dabbousi, J. R.-Viejo, F. V. Mikulec, J. R. Heine, H. Mattoussi, R. Ober, K. F. Jensen, and M. G. Bawendi, (CdSe)ZnS core-shell quantum dots - synthesis and characterization of a size series of highly luminescent nanocrystallites, *J. Phys.Chem. B* **101**, 9463-9475 (1997).
26. M. A. Hines and P. Guyot-Sionnest, Synthesis and characterization of strongly luminescing ZnS-capped CdSe nanocrystals, *J. Phys. Chem.* **100**, 468-471 (1996).
27. M. A. Hines and P. Guyot-Sionnest, Bright UV-blue luminescent colloidal ZnSe nanocrystals, *J. Phys. Chem. B* **102**, 3655-3657 (1998).
28. M. Shim and P. Guyot-Sionnest, n-Type colloidal semiconductor nanocrystals, Nature **407**, 981-983 (2000).

29. V. I. Klimov, A. A. Mikhailovsky, S. Xu, A. Malko, J. A. Hollingsworth, C. A. Leatherdale, H.-J. Eisler, and M. G. Bawendi, Optical gain and stimulated emission in nanocrystal quantum dots, *Science* **290**, 314-317(2000).
30. J. Lee, V. C. Sundar, J. R. Heine M. G. Bawendi, and K. F. Jensen, Full color emission from 11-VI semiconductor quantum dot-polymer composites, *Adv. Mater.* **12**, 1102-1105 (2000).
31. S. T. Selvan, C. Bullen, M. Ashokkumar, and P. Mulvaney, Synthesis of tunable, highly luminescent QD-glasses through sol-gel processing, *Adv. Mat.* **13**, 985-988(2001).
32. M. J. Bruchez, M. Moronne, P. Gin, S. Weiss, and A. P. Alivisatos, Semiconductor nanocrystals as fluorescent biological labels, *Science* **281**, 2013-2016 (1998).
33. W. C. Chan and S. Nie, Quantum dot bioconjugates for ultrasensitive nonisotopic detection, *Science* **281**, 2016-2018(1998).
34. M. Taylor, M. Fang, and S. Nie, Probing specific sequences on single DNA molecules with bioconjugated fluorescent nanoparticles, *Anal. Chem.* **72**, 1979-1986 (2000).
35. M. Han, X. Gao, J. Z. Su, and S. Nie, Quantum-dot-tagged microbeads for multiplexed optical coding of biomolecules, *Nature Biotechnology,* **19**, 631-635 (2001).
36. X. Peng, L. Manna, W. Yang, J. Wickham, E. Scher, A. Kadavanich, and A.P. Alivisatos, Shape control of CdSe nanocrystals, *Nature* **404**, 59-61 (2000).
37. D. L. Klein, R. Roth, A. K. L. Lim, A. P. Alivisatos, and P. L. McEuen, A single-electron transistor made from a cadmium selenide nanocrystal, *Nature* **389**, 699-701 (1997).
38. H. Mattoussi, J. M. Mauro, E. R. Goldman, G. P. Anderson, V. C. Sundar, F. V. Mikulec, and M. G. Bawendi, Self-assembly of CdSe-ZnS quantum dot bioconjugates using an engineered recombinant protein, *J. Am. Chem. Soc.* **122**, 12142-12150 (2000).
39. D. Gerion, F. Pinaud, S.C. Williams, W.J. Parak, D. Zanchet, S, Weiss, A.P. Alivisatos, Synthesis and properties of biocompatible water-soluble silica-coated CdSe/ZnS semiconductor quantum dots, *J. Phys. Chem.* **105**, 8861-8871 (2001).
40. C. Pacholski, A. Kornowski, and H. Weller, Self-assembly of ZnO: from nanodots to nanorods, *Angew. Chemie, Int. Ed.* **41**, 1188-1191 (2002).
41. D. V. Talapin, A. L. Rogach, E. V. Shevchenko, A. Kornowski, M. Haase, and H. Weller, Dynamic distribution of growth rates within the ensembles of colloidal Il-VI and III-V semiconductor nanocrystals as a factor governing their photoluminescence efficiency, *J. Am. Chem. Soc.* **124**, 5782-5790 (2002).
42. Z. A. Peng and X. Peng, Nearly monodisperse and shape-controlled CdSe nanocrystals via alternative routes: nucleation and growth, *J. Am. Chem. Soc.* **124**, 3343-3353 (2002).
43. J. P. Spatz, S. Moessmer, C. Hartmann, M. Moeller, T. Herzog, M. Krieger, H.-G. Boyen, P. Ziemann, and B. Kabius, Ordered deposition of inorganic clusters from micellar block copolymer films, *Langmuir* **16**, 407-415(2000).
44. J. P. Spatz, S. Moessmer, M. Moeller, M. Kocher, D. Neher, and G. Wegner, Controlled mineralization and assembly of hydrolysis-based nanoparticles in organic solvents combining polymer micelles and microwave techniques, *Adv. Mater.* **10**, 473-475 (1998).
45. M. Moeller, H. Kuenstle, and M. Kunz, Inorganic nanoclusters in organic glasses - novel materials for electro-optical applications, *Synth. Met.* **41**, 1159-1162 (1991).
46. R. E. Cohen, Block copolymers as templates for functional materials, *Current Opinion in Solid State & Materials Science* **4**, 587-590 (2000).
47. R. S. Kane, R. E. Cohen, and R. Silbey, Synthesis of doped ZnS nanoclusters within block copolymer nanoreactors, *Chem. Mater.* **11**, 90-93 (1999).
48. B. H. Sohn, R. E. Cohen, and G. C. Papaefthymiou, Magnetic properties of iron oxide nanoclusters within microdomains of block copolymers, *J. Magn. Magn. Mater.* **182**, 216-224 (1998).
49. M. Moffitt and A. Eisenberg, Size control of nanoparticles in semiconductor-polymer composites. 1. Control via multiplet aggregation numbers in styrene-based random ionomers, *Chem. Mater.* **7**, 1178-84 (1995).
50. M. Moffitt, L. McMahon, V. Pessel, and A. Eisenberg, Size control of nanoparticles in semiconductor-polymer composites. 2. Control via sizes of spherical ionic microdomains in styrene-based diblock ionomers, *Chem. Mater.* **7**, 1185-92 (1995).
51. L. Qi, H. Coelfen, and M. Antonietti, Synthesis and characterization of CdS nanoparticles stabilized by double-hydrophilic block copolymers, *Nano Lett.* **1**, 61-65 (2001).
52. M. Breulmann, S. A. Davis, S. Mann, H.-P. Hentze, and M. Antonietti, Polymer-gel templating of porous inorganic macro-structures using nanoparticle building blocks, *Adv. Mater.* **12**, 502-507 (2000).
53. S. Klingelhoefer, W. Heitz, A. Greiner, S. Oestreich, S. Foerster, and M. Antonietti, Preparation of palladium colloids in block copolymer micelles and their use for the catalysis of the Heck reaction, *J. Am. Chem. Soc.* **119**, 10116-10120 (1997).

54. M. Antonietti, S. Forster, and S. Oestreich, Micellization of amphiphilic block copolymers and use of their micelles as nanosized reaction vessels, *Macromol. Symp.* **121**, 75-88 (1997).
55. F. Caruso, Nanoengineering of particle surfaces, *Adv. Mater.* 13, 11-22 (2001).
56. F. Caruso, M. Spasova, V. Salgueiriño-Maceira, and L.M. Liz-Marzán, Multilayer Assemblies of Silica-Encapsulated Gold Nanoparticles on Decomposable Colloid Templates, *Adv. Mater.* **13**, 1090-1095 (2001).
57. F. Aliev, M. A. Correa-Duarte, A. Mamedov, J. Ostrander, M. Giersig, L. M. Liz-Marzán, and N. A. Kotov, Layer-by-layer assembly of core-shell magnetite nanoparticles: Effect of silica coating on interparticle interactions and magnetic properties, *Adv. Mater.* **11**, 1006-1010 (1999).
58. I. Pastoriza-Santos, D. S. Koktysh, A. A. Mamedov, M. Giersig, N. A. Kotov, and L. M. Liz Marzán, One-Pot Synthesis of Ag@TiO_2 Core-Shell Nanoparticles and Their Layer-by-Layer Assembly, *Langmuir,* **16**, 2731-2735(2000).
59. I. L. Radtchenko, G. B. Sukhorukov, N. Gaponik, A. Kornowski, A. L. Rogach, and H. Mohwald, Core-shell structures formed by the solvent-controlled precipitation of luminescent CdTe nanocrystals on latex spheres, *Adv. Mater.* **13,** 1684-1687(2001).
60. B. Smarsly, S. Polarz, and M. Antonietti, Preparation of porous silica materials via sol- gel nanocasting of nonionic surfactants: a mechanistic study on the self-aggregation of amphiphiles for the precise prediction of the mesopore size, *J. Phys. Chem. B* **105**, 10473-10483 (2001).
61. R. A. Caruso, M. Antonietti, Sol-gel nanocoating: an approach to the preparation of structured materials, *Chem. Mater.* **13**, 3272-3282 (2001).
63. L. M. Bronstein, S. Polarz, B. Smarsly, and M. Antonietti, Sub-nanometer noble-metal particle host synthesis in porous silica monoliths. *Adv. Mater.* **13**, 1333-1336 (2001).
64. C. J. Brinker and G. W. Scherer, "Sol-Gel Science", Academic Press, New York, 1990.
65. H. B.- Levy and D. Avnir, Entrapment of organic molecules within metals: dyes in silver, *Chem. Mater.* **14**, 1736-1741 (2002).
66. C. Rottman, G. Grader, Y. D. Hazan, S. Melchior, and D. Avnir, Surfactant-induced modification of dopants reactivity in sol-gel matrixes, *J. Am. Chem. Soc.* **121**, 8533-8543 (1999).
67. D. Avnir, Organic chemistry within ceramic matrixes: doped sol-gel materials, *Ace. Chem. Res.* **28**, 328-334(1995).
68. R. Hernandez, A.-C. Franville, P. Minoofar, B. Dunn, and J. I. Zink, Controlled placement of luminescent molecules and polymers in mesostructured sol-gel thin films, *J. Am. Chem. Soc.* **123**, 1248-1249 (2001).
69. R. Reisfeld, Prospects of sol-gel technology towards luminescent materials, *Opt. Mater.* **16**, 1-7 (2001).
70. M. Nogami, K. Nagasaka, and M. Takata, CdS microcrystal-doped silica glass prepared by the sol-gel process, *J. Non-Cryst. Solids* **122**, 101-106 (1990).
71. L. Spanhel, E. Arpac, and H. Schmidt, Semiconductor clusters in the sol-gel process: synthesis and properties of CdS nanocomposites, *J. Non-Cryst. Solids* **147&148**, 657-662 (1992).
72. M. Nogami, S. T. Selvan, and H. Song, in *Handbook of Advanced Electronic and Photonic Materials and Devices,* H. S. Nalwa (Editor), Academic Press, New York, **Vol. 5**, Chapter 5, pp. 141-162 (2001).
73. M. M. Collinson, in *Handbook of Advanced Electronic and Photonic Materials and Devices,* H. S. Nalwa (Editor), New York, **Vol. 5**, Chapter 6, pp. 163-194 (2001).
74. V. C. Costa, Y. Shen, A. M. M. Santos, and K. L. Bray, Luminescence measurements on Sm^{2+}-doped sol-gel glasses, *J. Non-Cryst. Solids* **304**, 238-243 (2002).
75. A. Imhof and D. J. Pine, Ordered macroporous materials by emulsion templating, *Nature* **389**, 948-951 (1997).
76. M. Su, X. Liu, S.-Y. Li, V. P. Dravid, and C. A. Mirkin, Moving beyond molecules: patterning solid-features via dip-pen nanolithography with sol-based inks, *J. Am. Chem. Soc.* **124**, 1560-1561 (2002).
77. J. P. Spatz, T. Herzog, S. Moessmer, P. Ziemann, and M. Moeller, Micellar inorganic-polymer hybrid systems. A tool for nanolithography, *Adv. Mater.* **11**, 149-153 (1999).
78. J. P. Spatz, P. Eibeck, S. Moessmer, M. Moeller, T. Herzog, and P. Ziemann, Ultrathin diblock copolymer/titanium laminates. A tool for nanolithography, *Adv. Mater.* **10**, 849-852 (1998).
79. R. A. Caruso and M, Antonietti, Silica films with bimodal pore structure prepared by using membranes as templates and amphiphiles as porogens, *Adv. Func. Mater.* **12**, 307-312 (2002).
80. H.-P. Hentze and M. Antonietti, Porous polymers and resins for biotechnological and biomedical applications, *Reviews in Molecular Biotechnology* **90**, 27-53 (2002).
81. M. Yamane and Y. Asahara, *Glasses for Photonics,* Cambridge University Press, Cambridge (2000).
82. D. R. Uhlmann and H. Yinnon, *Glass Science and Technology,* **Vol. 1**, Academic Press, San Diego, CA (1983).
83. T. Fujii, Y. Hisakawa, E. J. Winder, and A. B. Ellis, Effect of heat and gases on the photoluminescence of CdS quantum dots confined in silicate glasses prepared by the sol-gel method, *Bull. Chem. Soc. Jpn.* **68**, 1559-1564(1995).

84. R. Reisfeld and H. Minti, Nonlinear properties of semiconductor quantum dots in glasses prepared by the sol-gel method, *J. Sol-gel Sci. Technol.* **2**, 641-645 (1994).
85. R. Reisfeld, H. Minti, M. Eyal, and V. Chernyak, Nonlinear properties of semiconductor quantum dots and organic molecules in glasses prepared by the sol-gel method, *Mol. Cryst. Liq. Cryst. Sci. Technol. Sect. B* **5**, 339-360(1993).
86. K.V. Yumashev, V.S. Gurin, P.V. Prokoshin, V.B. Prokopenko, and A.A. Alexeenko, Nonlinear optical properties and laser applications of copper chalcogenide quantum dots, *Physica Status Solidi B: Basic Research* **224**, 815-818 (2001),
87. S. T. Selvan, M. Nogami, A. Nakamura, and Y. Hamanaka, A facile sol-gel method for the encapsulation of gold nanoclusters in silica gels and their optical properties, *J. Non-Cryst. Solids* **255**, 254-258 (1999).
88. S. T. Selvan, Y. Ono, and M. Nogami, Polymer-protected gold clusters in silica glass, *Mater. Lett.* **37**, 156-161 (1998).
89. S. T. Selvan, T. Hayakawa, M. Nogami, Y. Kobayashi, L. M. Liz-Marzán, Y. Hamanaka, and A. Nakamura, Sol-gel derived gold nanoclusters in silica glass possessing large optical nonlinearities, *J. Phys. Chem. B* **106**, 10157-10162 (2002).
90. Y. Kobayashi, M. A. Correa-Duarte, and L. M. Liz-Marzán, Sol-gel processing of silica-coated gold nanoparticles, *Langmuir,* **17**, 6375-6379 (2001).
91. J. Butty, N. Peyghambarian, Y. H. Kao, and J. D. Mackenzie, Room temperature optical gain in sol-gel derived CdS quantum dots, *Appl. Phys. Lett.* **69**, 3224-3226 (1996).
92. J. Butty, Y. Z. Hu, N. Peyghambarian, Y. H. Kao, and J. D. Mackenzie, Quasicontinuos gain in sol-gel derived CdS quantum dots, *Appl. Phys. Lett.* **67**, 2672-2674 (1995).
93. N. Peyghambarian, Semiconductor quantum dots in glass: open problems and challenges, *Glass Sci. Technol.* **70C**, 313-320 (1997).
94. K. Kang, A. D. Kepner, Y. Z. Hu, S. W. Koch, N. Peyghambarian, C.-Y. Li, T. Takada, Y. Kao, and J. D. Mackenzie, Room temperature spectral hole burning and elimination of photodarkening in sol-gel derived CdS quantum dots, *Appl. Phys. Lett.* **64**, 1487-1489 (1994).
95. C. Chia, Y. H. Kao, Y. Xu, and J. D. Mackenzie, Cadmium telluride quantum dot-doped glass by the sol-gel technique, *Proc. SPIE-Int. Soc. Opt. Eng.* **3136** (Sol-gel Optics IV), 337-347 (1997).
96. W. Stöber, A. Fink, and E. Bonn, Controlled growth of monodisperse silica spheres in the micron size range, *J. Colloid Interface Sci.* **26**, 62-69 (1968).
97. N. A. M. Verhaegh and A. van Blaaderen, Dispersions of rhodamine-labeled silica spheres: synthesis, characterization, and fluorescence confocal scanning laser microscopy, *Langmuir* **10**, 1427-1438 (1994).
98. C. Pathmamanoharan P. Wijkens, D. M. Grove, and A. P. Philipse, Paramagnetic silica particles: synthesis and grafting of a silane coupling agent containing nickel ions onto colloidal silica particles, *Langmuir,* **12**, 4372-4377(1996).
99. M. Giersig, T. Ung, L. M. Liz-Marzán, and P. Mulvaney, Direct observation of chemical reactions in silica-coated gold and silver nanoparticles, *Adv. Mater.* **9**, 570-575 (1997).
100. M. A. Correa-Duarte, M. Giersig, and L. M. Liz-Marzán, Stabilization of CdS semiconductor nanoparticles against photodegradation by a silica coating procedure, *Chem. Phys. Lett.* **286**, 497-501 (1998).
101. E. Yablonovitch, Inhibited spontaneous emission in solid-state physics and electronics, *Phys. Rev. Lett.* **58**, 2059-2062(1987).
102. A. Moroz, Three-dimensional complete photonic-band-gap structures in the visible, *Phys. Rev. Lett.* **83**, 5274-5277(1999).
103. K. Yoshino, Y. Shimoda, Y. Kawagishi, K. Nakayama, and M. Ozaki, *Appl. Phys. Lett.* **75**, 932-934 (1999).
104. C. Graf and A. van Blaaderen, Metallodielectric colloidal core-shell particles for photonic applications, *Langmuir* 18, 524-534 (2002).
105. K. P. Velikov and A. van Blaaderen, Synthesis and characterization of monodisperse core-shell colloidal spheres of zinc sulfide and silica, *Langmuir* **17**, 4779-4786 (2001).
106. A.L. Rogach, D. Nagesha, J.W. Ostrander, M. Giersig, and N.A. Kotov, Raisin bun -type composite spheres of silica and semiconductor nanocrystals, *Chem. Mater.* **12**, 2676-2685 (2000).
107. F. García-Santamaría, V. Salgueiriño-Maceira, C. López, and L. M. Liz-Marzán, Synthetic opals based on silica-coated gold nanoparticles, *Langmuir,* **18**, 4519-4522 (2002).
108. Special issue on Photonic Crystals, *Adv. Mater.* **13**, 6 (2001).
109. W. Wang and S. A. Asher, Photochemical incorporation of silver quantum dots in monodisperse silica colloids for photonic crystal applications, *J. Am. Chem. Soc.* **123**, 12528-12535(2001).
110. Y. Xia, B. Gates, Y. Yin, and Y. Lu, Monodisperse colloidal spheres: Old materials with new applications, *Adv. Mater.* **12**, 693-713 (2000).

111. V. Pillai and D. O. Shah, *Industrial Applications of Microemulsions,* (C. Solans and H. Kunieda, Eds), Surfactant Science Series, Marcel Dekker, New York, **vol. 66**, (1997).
112. M. Bourrel and R. S. Schechter, (Eds), *Microemulsions and Related Systems,* Surfactant Science Series, Marcel Dekker: New York, **vol. 30**, (1988).
113. F. J. Arriagada and K. Osseo-Asare, Synthesis of nanosize silica in a nonionic water-in-oil microemulsion: effects of the water/surfactant molar ratio and ammonia concentration, *J. Colloid and Int. Sci,* **211**, 210-220(1999).
114. S. Chang, L. Liu, and S.A. Asher, Preparation and properties of tailored morphology, monodisperse colloidal silica-cadmium sulfide nanocomposites, *J. Am. Chem. Soc.* **116**, 6739-6744 (1994).
115. M. Lal, L. Levy, K. S. Kim, G. S. He, X. Wang, Y. H. Min, S. Pakatchi, and P. N. Prasad, Silica nanobubbles containing an organic dye in a multilayered organic/inorganic heterostructure with enhanced luminescence, *Chem. Mater.* **12**, 2632-2639 (2000).
116. S. C. Farmer and T. E. Patten, Photoluminescent polymer/quantum dot composite nanoparticles *Chem. Mater.* **13**, 3920-3926 (2001).
117. S. T. Selvan, C. Bullen, D. Dunstan, and P. Mulvaney, Highly-luminescent, water-soluble, silica coated CdSe @ ZnS quantum dots through a facile inverse microemulsion approach, *Angew. Chemie.* Submitted (2002).
118. S. T. Selvan, A. Mani, S. Pitchumani, and K.L.N. Phani, Synthesis of polyparaphenylene by electropolymerization in microemulsion medium: morphology and crystalline character, *J. Electroanal. Chem.* **384**, 183-186(1995).
119. A. Mani, S. T. Selvan, K, L. N. Phani, and S. Pitchumani, Studies on the generation of polyaniline microstructures using microemulsion polymerisation, *J. Mater. Sci. Lett.* **17**, 385-387 (1998).
120. A. Mani, S. T. Selvan, and K. L. N. Phani, Solid state structural aspects of electrochemically prepared poly(p-phenylene) thin films - crystalline order and spherulite morphology, *J. Solid State Electrochem,* **2**, 242-246(1998).
121. S. T. Selvan, A, Mani, K. Athinarayanasamy, K. L. N. Phani,and S. Pitchumani, Synthesis of crystalline polyaniline, *Mater. Res. Bull.* **30**, 699-705 (1995).
122. K. L. N. Phani, S. Pitchumani, S. Ravichandran, S. T. Selvan, and S. Bharathey, Microemulsion based electrosynthesis of polyparaphenylene, *J. Chem. Soc. Chem. Commun.* 179-181 (1993).
123. I. Tanahashi, Y. Manabe, T. Tohda, S. Sasaki, and A. Nakamura, Optical nonlinearities of Au/SiO_2 composite thin films prepared by a sputtering method, *J. Appl. Phys.* 79, 1244-1249 (1996).
124. M. J. Bloemer, J. W. Haus, and P. R. Ashley, Degenerate four-wave mixing in colloidal gold as a function of particle size, *J. Opt. Soc. Am. B* 7, 790-795 (1990).
125. K. Uchida, K. Kaneko, S. Omi, C. Hata, H. Tanji, Y. Asahara, A. J. Ikushima, T. Tokizaki, and A. Nakamura, Optical nonlinearities of a high concentration of small metal particles dispersed in glass: copper and silver particles, *J. Opt. Soc. Am. B* **11**, 1236-1243 (1994).
126. T. Yazawa, K. Kadono, H. Tanaka, T. Sakaguchi, S. Tsubota, K. Kuraoka, M. Miya, and D. Wang, Preparation and optical property of monolithic silica gel uniformly dispersed with gold colloid from aqueous solution, *J. Non-Cryst. Solids* **170**, 105-108 (1994).
127. F. Hache, D. Ricard, C. Flytzanis, and U. Kreibig, The optical Kerr effect in small metal particles and metal colloids: the case of gold, *Appl. Phys. A* **47**, 347-357 (1988).
128. J. Matsuoka, R. Mizutani, S. Kaneko, H. Nasu, K. Kamiya, K. Kadano, T. Sakaguchi, and M. Miya, Sol-gel processing and optical nonlinearity of gold colloid-doped silica glass, *J. Ceram. Soc. Jpn.* **101**, 53-58 (1993).
129. K. L. Frindell, M. H. Bartl, A. Popitsch, and G. D. Stucky, Sensitized luminescence of trivalent europium by three-dimensionally arranged anatase nanocrystals in mesostructured titania thin films, *Angew. Chem. Int. Ed.* **41**, 960-962 (2002).
130. S. T. Selvan, T. Hayakawa, and M. Nogami, Remarkable influence of silver islands on the enhancement of fluorescence from Eu^{3+} ion-doped silica gels, *J. Phys. Chem. B* **103**, 7064-7067 (1999).
131. T. Hayakawa, S. T. Selvan, and M. Nogami, Field enhancement effect of small Ag particles on the fluorescence from Eu^{3+} -doped SiO_2 glass, *Appl. Phys. Lett.* **74**, 1513-1515 (1999).
132. T. Hayakawa, S. T. Selvan, and M. Nogami, Enhanced fluorescence from Eu^{3+} owing to surface plasma oscillation of silver particles in glass, *J. Non-Cryst. Solids* **259**, 16-22 (1999).
133. S. T. Selvan, T. Hayakawa, and M. Nogami, Enhanced fluorescence from Eu^{3+} -doped silica gels by adsorbed CdS nanoparticles, *J. Non-Cryst. Solids* **291**, 137-141 (2001).
134. T. Hayakawa, S. T. Selvan, and M. Nogami, Influence of adsorbed CdS nanoparticles on $^5D_o \rightarrow {}^7F_J$ emissions in Eu^{3+} -doped silica gel, *J. Luminescence,* **87-89**, 532-534 (2000).
135. T. Hayakawa, S. T. Selvan, and M. Nogami, Energy transfer between Eu^{3+} ion and CdS quantum dot in sol-gel derived $CdS/SiO_2:Eu^{3+}$ gel, *J. Sol-Gel Sci. Tec.* **19**, 779-783 (2000).
136. S. T. Selvan, C. Bullen, and P. Mulvaney, Unpublished.

137. K. T. Shimizu, R. G. Neuhauser, C. A. Leatherdale, S. A. Empedocles, W. K. Woo, and M. G. Bawendi, Blinking statistics in single semiconductor nanocrystal quantum dots, *Phys. Rev. B* **63**, 205316-1-5 (2001).

13

ORGANIZATION OF LAYER-BY-LAYER ASSEMBLED NANOCOMPOSITES

Functional effects in photonics and biomaterials

Nicholas A. Kotov and Luis M. Liz-Marzán*

1. INTRODUCTION

The studies on materials properties of nanoparticles (nanocrystals, quantum dots) represent one of the most dynamic areas of today's science. Charge carrier confinement leads to a variety of unique phenomena in optics, magnetism and chemical reactivity. Considering the technological utilization of these qualities, spatial organization of nanoparticles becomes one of the most challenging problems in nanoscience. The production of ordered nanoparticle structures is pivotal both for the design of nanoelectronic devices and for bulk quantum dot composites. This review is focused on the organization of nanoparticle layers by means of a technique, which is most often referred to as layer-by-layer assembly (LBL) also known as electrostatic self-assembly (ESA) and polyelectrolyte multilayers (PEM). The feature of this method is the opportunity to create virtually any sequences of nanoparticle monolayers with materials properties determined by the layer's order. It is particularly convenient for the spatial organization of nanocolloids in bulk materials. The principal questions that we shall try to answer here are the following: "What are the limits of the spatial organization by LBL?" and "What are the materials and practical applications that can benefit from this technique?"

2. LAYER-BY-LAYER ASSEMBLY

The layer-by-layer assembly (LBL) is a relatively new method of thin film deposition, which became popular after being applied to oppositely charged polyelectrolytes.[1] The exceptional ease of preparation of thin films of polyelectrolytes as opposed to more complex Langmuir-Blodgett deposition attracted a lot of attention to it. It can also be utilized for nanoparticles as described in the many original works of the groups of H. Möhwald, T. Mallouk, G. Decher, M. Rubner, N. Kotov, L. Liz-Marzan, Y.

* Nicholas A. Kotov, Department of Chemistry, Oklahoma State University, Stillwater, OK, USA.
Luis M. Liz-Marzán, Departamento de Química Física, Universidade de Vigo, Vigo, Spain, 36200.

Lvov, F. Caruso, J. Shen, A. Laschewski, J. Schlenoff, T. Kunitake, Zhang Xi, G. Sukhorukov, R. Claus, L. Halaoui and many others. In most general terms, the layer-by-layer assembly can be described as the sequential adsorption of positively and negatively charged species, say *A* and *B,* by dipping a substrate alternatively into their solutions. Rinsing with solvent (most often water) between the adsorption steps removes the excess of the previous solution and leaves a thin layer of charged species on the surface, thereby preparing the surface for the next adsorption step.

Three major advantages of LBL should be pointed out:

- simplicity;
- universality;
- nanometer scale thickness control.

The LBL process does not require sophisticated hardware or high purity of the components. Considering this feature the quality of coatings is very high.[1,2] Universality implies that for virtually any aqueous dispersion of a relatively high molecular weight species (i.e. polymers, nanoparticles, colloids, oligomers, proteins, etc.) one can find an LBL pair with a steady film build-up.[3] Since in each adsorption step a monolayer or a submonolayer of the species is deposited, the overall thickness of the stack can be controlled with similar precision.[3-5]

An LBL film obtained after *n* deposition cycles can be generically referred to as $(A/B)_n$, and this notation will be used throughout this work. It is important to note that the $(A/B)_n$ abbreviation describes primarily the *deposition procedure,* rather than the actual sequence of the multilayers obtained as a result of it. The presence of strong interpenetration of PE chains[6-8] blurring the border between the adjacent layers needs to be pointed out. For some research tasks related to organized layered superstructures this can be a problem, in particular when one wants to replicate the organization of the Langmuir-Blodgett layers, but for others this feature can be beneficial and can be used for imparting truly unique materials properties.The LBL process for nanoparticles and nanocolloids is similar to that used for the other systems.[3,9,10] Their layer-by-layer assembly is typically monitored by the increase of the UV-visible absorbance, when the particles are deposited on a transparent substrate, which is often linear,[1,11,17] but may also level up as a plateau, be zig-zag like, or even exponential.[18] The superposition of all these deposition patterns may, of course, result in an irregular buil-up curve, which happens with nanoparticles under unfavorable conditions.[3] The linearity of absorbance *vs. n* shows the equality of the amounts of the material transferred on the substrate in every deposition cycle. For nanoparticles, the linear growth of the multilayers on planar substrates similar to that in Figure 1 was demonstrated by many authors. The nanocrystalline materials used in such multilayers are very diverse. In 1995 it started from simple CdS nanoparticles[9,19-21] and then was quickly extended to CdSe,[22-24] CdTe,[19,25] ZnS,[26] PbS,[27] TiO_2,[9,20,21,24,27-29] ZrO_2,[30] Ag,[5,31] Au,[32-35] SiO_2,[36-38] MoO_2,[39] polyoxometallates,[12,40] HgTe,[10] Fe_3O_4,[2,41] etc.

The thickness of the coating calculated from ellipsometric or quartz crystal microbalance measurements followed the linear behavior of the absorbance *vs. n* plots. The thickness increment added in one deposition cycle often approached that of a monolayer of polyelectrolyte or nanoparticles.[38,42,43] Sometimes it exceeded the average nanoparticle diameter; for instance, HgTe nanoparticles formed 2-3 monolayers in each deposition cycle.[10]

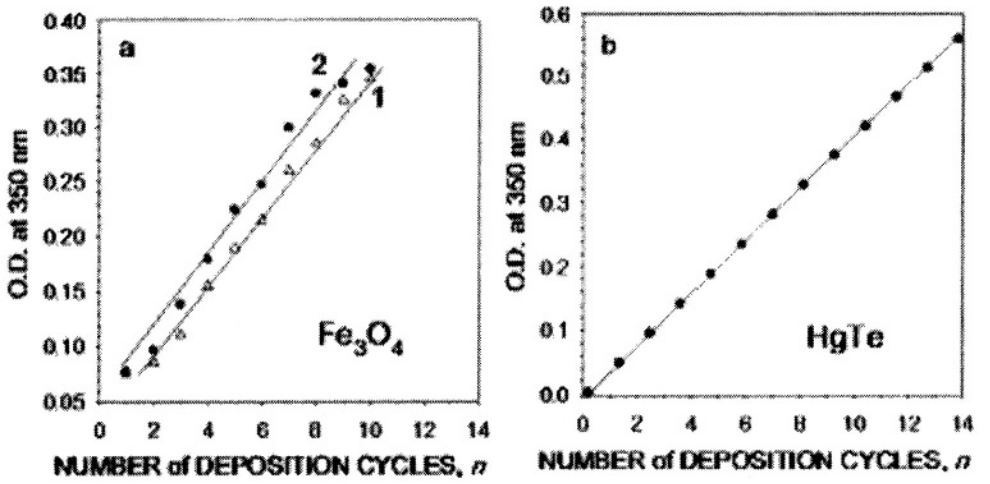

Figure 1. Linear growth of the layer-by-layer assembled films of nanoparticles.

In some cases, such as *ca.* 32 nm yittrium iron garnet (YIG), as well as for some other relatively big hydrophilic nanoparticles made from oxides, the obtained thickness was noted to be significantly lower than its average value expected for densely packed layers of nanoparticles of this diameter. The thickness increment, which was added to the coating by a single PDDA/YIG layer, was 3.5 nm. This thickness corresponded to the average surface density of YIG of one particle per 32,300 nm^2. Significantly less-than-a-monolayer thicknesses were also observed for citrate-stabilized CdSe.[44] Such a small thickness of adsorption layer and a low density of particles combined with the steady linear growth of nanoparticle multilayers implies that the LBL process does not require the formation of *complete* monolayers for total charge switching. Thus, despite the simplicity of the procedure, one needs to admit that there are essential fundamental aspects of this technique, that we do not currently understand.

3. ORDERING OF THE LBL ASSEMBLED NANOMATERIALS

Over the past ten years, several aspects of ordering with LBL have been considered. The most apparent as well as probably the most powerful approach to the nanoparticle ordering is to make ordered stacks of multilayers. The thickness of each strata and their sequence can be tailored to a particular application. Several examples of such assemblies have already been reported.[2,45-49] Besides that, one should also consider the possibility and the necessity of ordering in each adsorption layer. Our efforts to respond to these challenges are described below.

3.1. Sequence Effects in Nanoparticle Multilayers

3.1.1. Stratified multilayers from different materials

The generic nature of the electrostatic and van der Waals interactions affords combining nanocolloids of different types in the polyelectrolyte multilayers and

investigate their interactions. The optical properties of metal nanoparticles have been intensively studied for the last few decades, because of strong catalytic properties, intense surface plasmon resonances, and strong surface enhanced and nonlinear optical properties. Surface plasmon effects arising from the coupling of surface electrons with incident electromagnetic waves,[50,51] are especially relevant in noble metals such as gold and silver, and the plasmon-related phenomena have been studied for them for a large number of scattering conditions at the nanoparticle interface.[52-54] Dipole-dipole interactions play an important role in optics of metal nanoparticles as well, and especially so for closely spaced nanoparticle films. In these systems, the interparticle separation determines the plasmon oscillation frequency. The dependence of the surface plasmon wavelength on the interparticle interactions can be the most significant parameter to consider. Thus, the search for the methods of control over the optical properties of noble metal nanoparticle materials is the subject of significant importance. The strength of nanoparticle-nanoparticle through-space coupling can be tuned by the variation of the spacing between the nanoparticle layers, which was recently demonstrated for spherical and triangular gold nanoparticles by the collaborative effort of the groups of Drs. Kotov and Liz-Marzan.[55]

A representative TEM image of gold nanoparticles used in this project is shown in Figure 2. Gold nanoparticles with several different shapes are formed, including large polygons (mainly triangles and hexagons), as well as smaller, polydisperse spheres. The lower contrast observed for the polygons suggests that they are flat, unlike the spherical nanoparticles around them. Also, at some places (see arrows) two planar particles overlap, yielding a darker region. The electron diffraction analysis confirmed the hexagonal structure of a single triangle lying flat on the TEM grid. Such a flat geometry imposes strong restrictions for the oscillation frequency of the free conduction electrons, which is directly reflected on the optical properties of the dispersion.

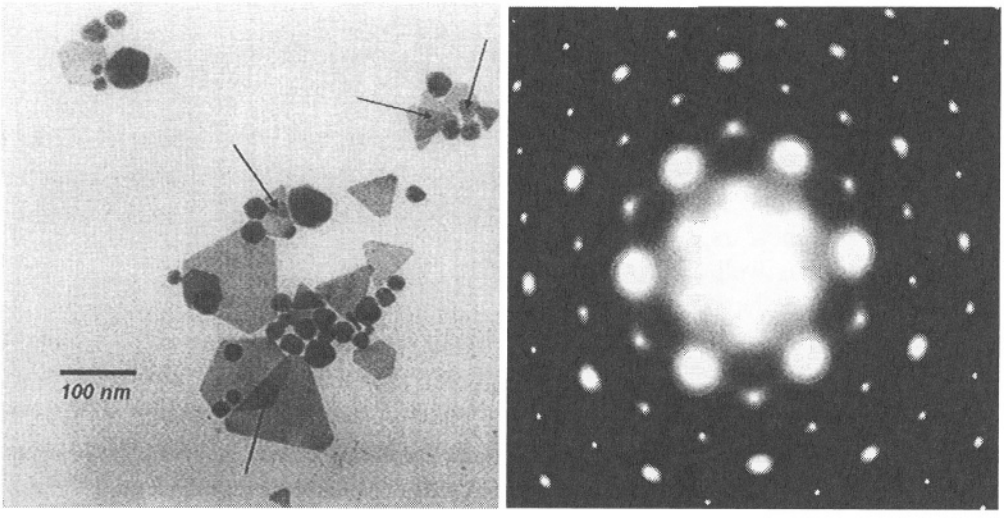

Figure 2. (a) Representative TEM image of gold nanoparticles formed by reduction with salicylic acid. Both spheres and polygons are clearly visible. Arrows point some places where two flat particles overlap. (b) Electron diffraction pattern from a single Au triangle with the electron beam perpendicular to the [111] plane. The spot array indicates a hexagonal structure. Reproduced with permission from ref. 55. Copyright 2002, American Chemical Society.

The UV-visible spectrum shown in Figure 3 was measured from the gold dispersion in water. The spectrum shows two distinct plasmon absorption bands centered at 540 and 860 nm. The band at higher energy is located at typical values for Au spheres, with a certain distortion with respect to the spherical shape. However, the band at 860 nm could only correspond to a resonance over much larger distances (observed for the longitudinal resonance in nanorods or for nanoshells) or to tight aggregates formed by smaller nanoparticles. The last possibility is discarded because of the long-term stability of the colloid, and because only separate nanoparticles were found under TEM observation. The band is broad because of the relatively high polydispersity, both in size and shape, which implies quite a broad range of possible resonance frequencies. Therefore, the 860 nm band is attributed to the surface plasmon band in flat gold particles of triangular and related shapes seen in Figure 2. The anisotropic morphology and specific shape of the particles makes possible the plasmon transition over the long distances. Although three well-differentiated bands are expected for these systems,[56] because of the relatively low concentration of polygons, the absorption by the spheres screens the out-of-plane quadrupole resonance (located at lower wavelengths).

The control of nanoparticle-nanoparticle coupling with this technique was previously attempted for magnetic nanoparticles,[2,57] however little change in magnetic properties has been observed. The electron interactions between the gold nanoparticles are of much shorter range than magnetic dipole interactions and result in a strong shift in the frequency of the surface plasmon resonance. The later can be easily observed by UV-visible absorption spectroscopy, which can be utilized to monitor the strength of the particle interactions in adjacent layers.

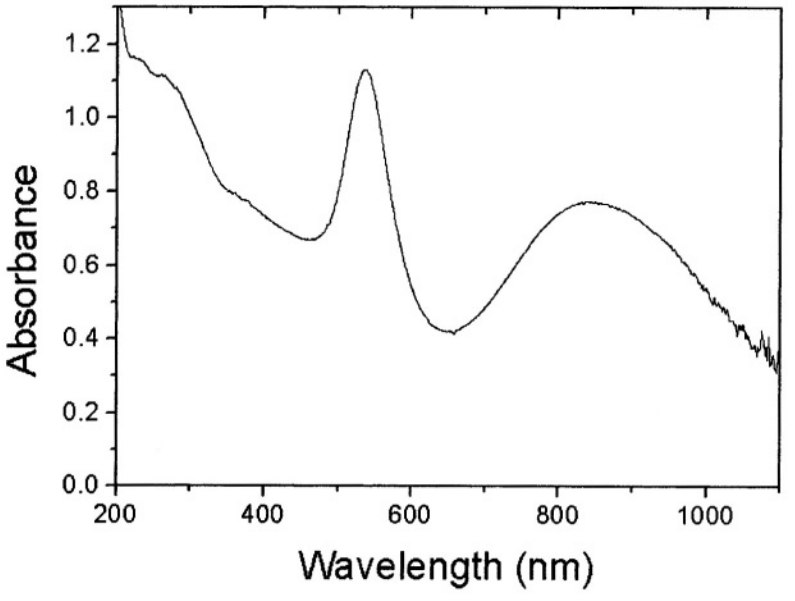

Figure 3. UV-visible spectrum measured from a dilute sol containing the particles shown in Figure 2. Reproduced with permission from ref. 55. Copyright 2002, American Chemical Society.

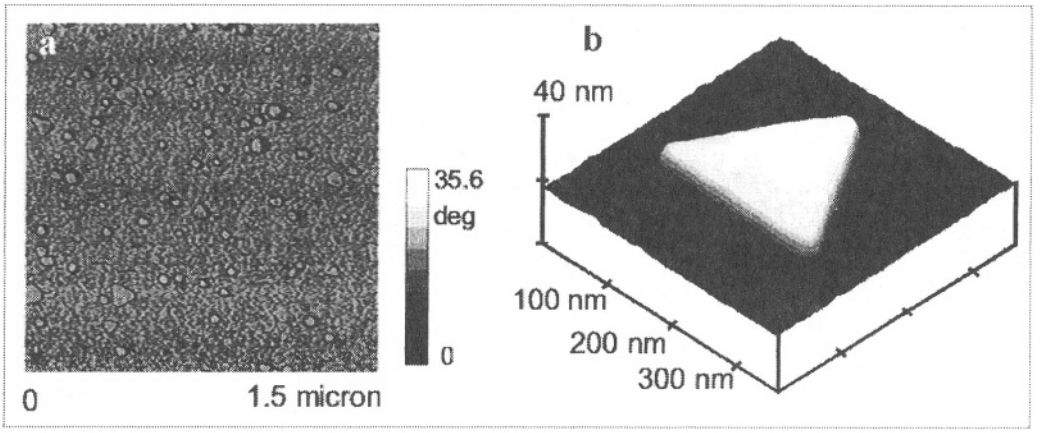

Figure 4. Atomic force microscopy of a PDDA/Au bilayers deposited on a Si wafer: (a) large area phase contrast image; (b) closer topographic view of a triangular particle. Adapted with permission from ref. 55 Copyright 2002, American Chemical Society.

The gold nanoparticles are negatively charged owing to the stabilizing layer of salicylic acid, and therefore, a positively charged polyelectrolyte was chosen as an LBL partner macromolecule for them. The morphology of the deposited monolayers was studied by AFM. A typical image is shown in Figure 4a, where it can be observed that the proportion of polygons is relatively low, as compared to spheres, which form a compact monolayer on the background. It is also interesting to note that AFM measurements confirm the TEM observation that the triangular and hexagonal particles are flat (Figure 4b), with lateral dimensions much larger than their height. It can also be clearly seen that the flat particles are deposited in parallel to the substrate similarly to montmorillonite sheets studied previously.[58,59]

The high density of adsorbed nanoparticles translated at the macroscale into a high optical uniformity of the coatings over the entire area of the samples prepared. UV-visible absorption spectra acquired for sequentially deposited PDDA/Au bilayers, *i.e.* for coatings $(PDDA/Au)_n$, where n is the number of the deposition cycles, show that the absorbance gradually increases with every new bilayer (Figure 5) similarly to the previously described cases of other oxide and semiconductor nanoparticles (Figure 1). It can also be seen in the inset that the first (PDDA/Au) bilayer displays absorption bands at 525 nm and 790 nm, which are very similar to those of the starting nanoparticle dispersion. The slight shift of both peaks can be related to the change in environment after the deposition, since at least one side is surrounded by air.

The intensity of the absorption band for triangular nanoparticles significantly increases in respect to the band for spherical nanoparticles (Figure 5a *vs.* Figure 3). This can be rationalized as the result of stronger PDDA-nanoparticle attraction forces involving anisotropic flat triangular nanoparticles than those with spherical ones resulting in the preferential adsorption of the flat nanoparticles. In the assessment of the absorption preference, the UV-visible data are more representative than AFM images because they provide cumulative information about a large area of the sample. Additionally, smaller spherical nanoparticles can be easily adsorbed on top of the triangles,[55] thereby masking them both in topography and phase scans.

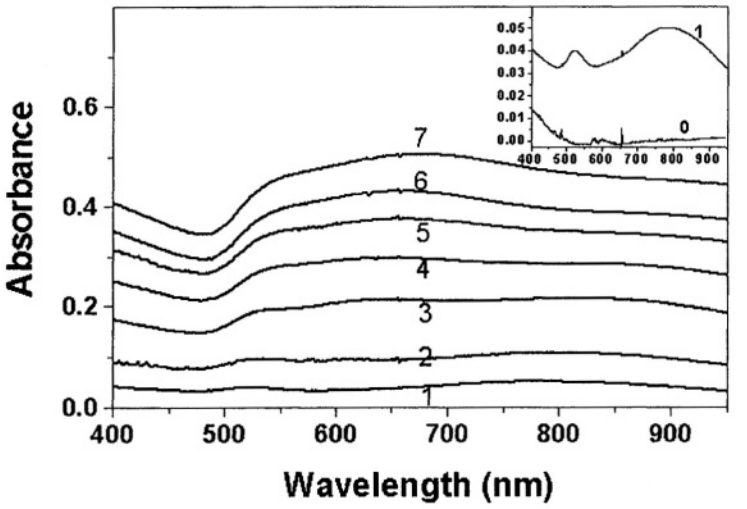

Figure 5. UV-visible spectra of successive LBL assembled $(PDDA/Au)_n$ bilayers (the number of the deposition cycles n is given as the trace number). The inset shows the background absorption of the substrate and the first $(PDDA/Au)_1$ bilayer. Reproduced with permission from ref. 55. Copyright 2002, American Chemical Society.

It can also be seen in the inset that the first (PDDA/Au) bilayer displays absorption bands at 525 nm and 790 nm, which are very similar to those of the starting nanoparticle dispersion. The slight shift of both peaks can be related to the change in environment after the deposition, since at least one side is surrounded by air.

Importantly, a new optical feature develops as the number of layers increases. An intense band is formed between the two previous ones becoming clearly visible in the fourth layer and becoming dominant by the seventh bilayer (Figure 5). This new band at 650 nm is attributed to the interparticle interactions between neighboring monolayers, which can be supported by the extensive literature on the dependence of surface plasmon band on interparticle separation.[50,51,60]

Since the nanoparticle-nanoparticle coupling typically results in the red shift of the surface plasmon bands, we believe that the parent transition for the new band is that in the spherical nanoparticles at 525 nm. In the multilayer assembly, they interact both with similar spherical nanoparticles and triangular ones. In the latter case, the coupling strength should be higher than in former because of the geometry of sphere on a plane results in greater integral electrostatic attraction than that between two spheres. The variety of different geometrical arrangements causes band broadening, which can be seen in Figure 5. Note that the transversal modes of the flat nanoparticles can also contribute to this new band. However, their contribution is expected to be quite small, since all such flat nanoparticles lie parallel to the substrate. At the same time, the longitudinal modes of flat nanoparticles should also be red-shifted and show up in the range of 800-900 nm partially overlapping with the new band at 650 nm. In order to confirm the origin of this new band, further LBL experiments were performed by taking advantage of the structural control afforded by the LBL technique and different insulting layers, which can be used to separate the Au NPs bilayers. This was accomplished by depositing a polyelectrolyte (PDDA/PAA) bilayer between PDDA/Au strata as a nanoscale spacer (Figure 6a).

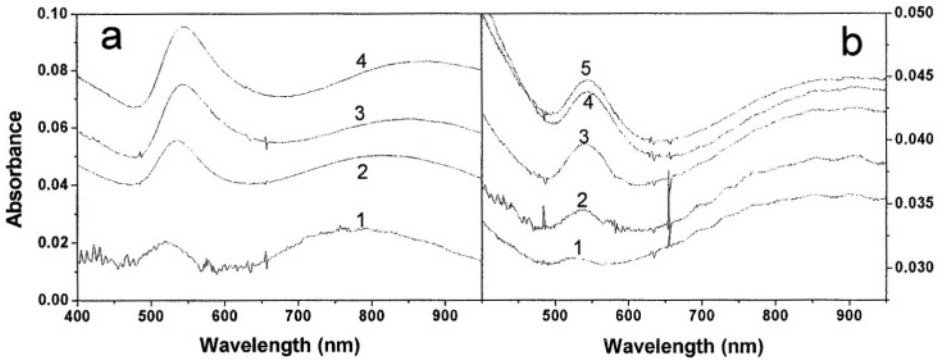

Figure 6. UV-visible spectra of sequentially deposited (PDDA/Au/PDDA/PAA)$_n$, n=1-4 (a); and (PDDA/Au/PDDA/clay)$_n$, n = 1-5 films (b). Adapted with permission from ref. 55. Copyright 2002, ACS.

It is clear that by placing an additional polymeric region in between the nanoparticle bilayers reduces the interactions of the adjacent Au nanoparticles layers and the band at 650 nm does not develop. However, there is a noticeable red shift of both plasmon bands as the number of layers increases, showing that there is still a certain electronic communication between neighboring layers. Flat nanoparticles are deposited parallel to the substrate as evidenced by atomic force microscopy. This implies that the interparticle interactions between adjacent layers are strong, which can be seen by the appearance of a new absorption band. The interaction between the layers can be controlled by depositing insulating layers of clay and/or polyelectrolytes between the gold nanoparticle layers.

Therefore, further experiments were carried out to obtain virtually electronically independent surface plasmon oscillations in each Au nanoparticles layer. To achieve that, the separation layers were made from montmorillonite clay platelets that are (1) better electrical insulators than polyelectrolytes and (2) reduce interdigitation of the adjacent layers due to their sheet-like morphology.[59,61] Thus, the layered stacks with a repeat unit of (PDDA/Au/PDDA/clay)$_n$ were made and their optical spectra are shown in Figure 6b. As expected, the improved insulation and better separation of the adjacent gold nanoparticles bilayers lead to the constant position of both plasmon absorption bands in every deposition cycle. It should be noted that there is still a slight red-shift of the maxima in comparison to the UV-visible spectrum of the dispersion because of the refractive index increase after the deposition of the montmorillonite sheets.

Summarizing the factual material in this section, the sequence of the deposited LBL layers can be utilized for the gradual control of interparticle interactions, when the thickness of the layers is comparable with the characteristic length of the interactions. The demonstrated structural control over the optical properties of the nanoparticle assemblies can be applied for the design of thin film sensors with a transduction mechanism based on the variations of spacing between the Au layers.

3.1.2. Stratified multilayers from nanoparticles of the same parent material

Layer-by-layer assembly (LBL) enables effective processing of semiconductor, metal, or metal oxide nanoparticle dispersions into functional advanced materials, which retain distinctive optical, magnetic and electrical qualities of size-quantized state of matter.[22,33,44,62-66]

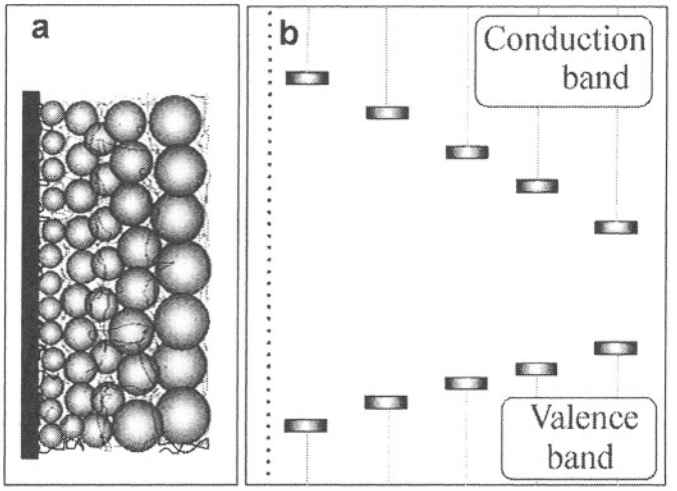

Figure 7. Schematic representation of (a) cross-section and (b) band energies in the graded semiconducting material from nanoparticles.

In an optimized LBL deposition, when the UV-visible absorption density linearly increases with the number of deposition cycles, the packing and thickness of nanoparticles is reproduced from layer to layer. After coating with polyelectrolyte, the nanoparticles become virtually immobile in the densely packed multilayer stack, which prevents phase separation of the nanoparticle/polymer mixture even at the nanoscale. This leads to materials with much better homogeneity (especially for high nanoparticle loadings) than spin-coated or painted nanoparticle/polymer mixtures, which is important for many optical and electronic devices.[22,25,33] Besides that, tight packing of nanoparticles also makes possible the design of materials with intentional inhomogeneity by depositing LBL bilayers in a certain sequence.[2,45-49] It would be interesting to demonstrate the possibility of the LBL production of one-dimensionally graded semiconducting materials. The latter have unique capabilities as photodetectors, bipolar transistors, waveguides, light-emitting, non-linear optical, magnetooptical, and high-speed devices.[67-70] This type of materials also reveals new phenomena in charge injection, charge carrier dynamics, and light trapping.[71-77]

However, graded semiconductors are difficult to make, and typically high capital investment techniques such as molecular beam epitaxy and plasma enhanced chemical vapor deposition are required for their preparation. By using the LBL assembly of nanoparticles we built a graded semiconducting material by laying nanoparticles on a substrate in a sequence from smaller to bigger ones, which can be done even in high school chemical laboratory.[78] Because of the strong size dependence of the nanoparticle conduction and valence band energies, their arrangement by particle diameters results in a gradual change of the band gap as pictured in Figure 7, and therefore, creates an intrinsic ramp of hole and electron potential. Having said that, one also need to mention that the inherently granular nature of the nanocomposites resulting from LBL deposition of colloidal particles introduces its own challenges related to facilitation of charge transport in the film.

The model graded films were prepared from highly luminescent CdTe nanoparticles (quantum yield 15-20%) stabilized by thioglycolic acid. CdTe nanocrystals of different

diameters were synthesized according to a published procedure. The graded nanoparticle films were assembled by using four different CdTe dispersions with luminescence maxima at 495-505, 530-545, 570-585, and 605-620 nm which display respectively green, yellow, orange and red luminescence (Figure 8a) and which will be referred to accordingly. Layer-by-layer assembly was carried out on glass and plastic substrates and typically 5-10 CdTe nanoparticle bilayers of each of the four luminescent colors were deposited. It is necessary to point out that high luminescence quantum yield is not a rigid requirement for further studies of graded semiconductors from nanoparticles, however it is a useful property that enables convenient probing of the film structure.

The assembly started from the smallest nanoparticles ("green") and proceeded to the biggest ones ("red") according to the visible light spectral sequence. With addition of the layers of increasing diameter, the luminescence of the assembly shifted toward the red part of the spectrum while also becoming broader (Figure 8b). Finally, the luminescence spectrum of the stack of all four nanoparticle diameters had a plateau appearance reflecting almost equal emission intensity in a wide range of wavelengths. As compared to the original spectra of CdTe nanoparticle, some prevalence of the red emission (red shift) should be attributed to the excitation energy transfer from smaller nanoparticles to bigger ones.[79]

To evaluate the internal structure of the gradient CdTe film, it was assembled on a flexible cellulose acetate substrate as described in reference 80. A cross-sectional slice of the nanoparticle stack was analyzed by transmission electron microscopy (TEM).

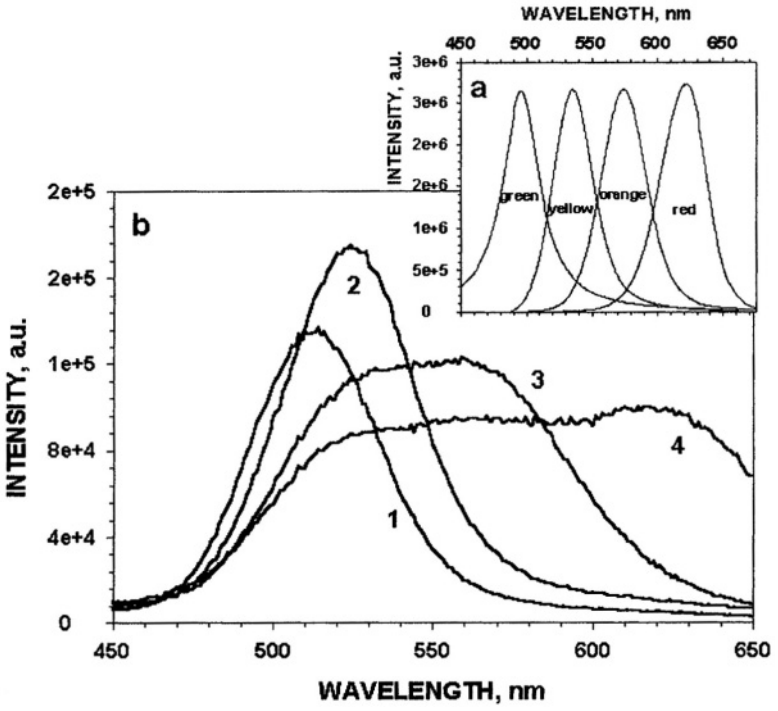

Figure 8. Luminescence spectra of (a) exemplary CdTe nanoparticles used in this work and (b) thin films obtained after the sequential deposition of 5 bilayers of (1) "green", (2) "yellow" (3) "orange", and (4) "red" CdTe. Reproduced with permission from ref. 78. Copyright 2001, American Chemical Society.

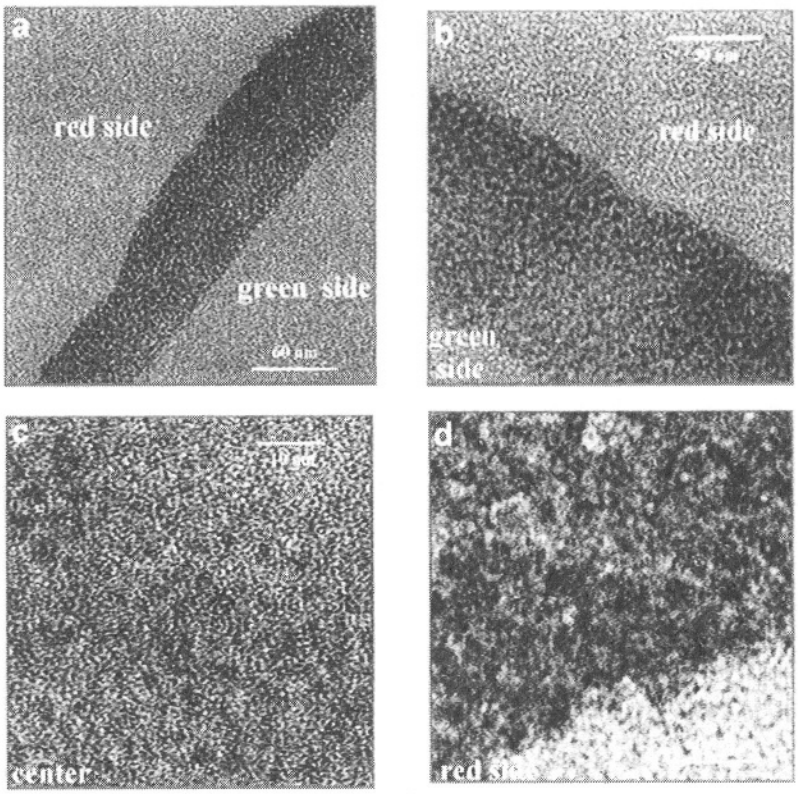

Figure 9. Transmission electron microscopy images of the graded film cross-sections made from 5 bilayers of "green", "yellow", and "red (total 15): nanoparticles. (a) and (b) are survey images; (c) and (d) are close-up images of the center section and "red" side of the nanoparticle film. Reproduced with permission from ref. 78. *Copyright 2001, American Chemical Society.*

The asymmetry of the film can be seen in the difference of electron diffracting power of the "red" and "green" sides of the assembly (Figure 9a,b). The layers of bigger nanoparticles appear noticeably darker in the TEM image due to the greater percentage of heavier elements on this side of the multiplayer stack (Figure 9a,b). Although it was quite difficult to obtain the images of single nanoparticles in the network of the polyelectrolyte matrix, the areas of crystallinity, that could be identified with the diameter of the particles, were observed to be different in the corresponding parts of the gradient film being 2-3 nm in the "green" and "yellow" parts and 5-6 nm on the "red" side of the assembly, which correlates well with the particle size expected from the emission wavelength (Figure 8a).[81]

The gradient nature of the prepared nanoparticle film was also unequivocally established by confocal optical microscopy. The sample was assembled as described above on a glass slide and the series of luminescence images were obtained at a different focus depth inside the assembly. Cross-sectional images without physical sectioning of the film were obtained clearly showing the gradual change of the luminescence emission wavelength from green in the bottom to red on the top of the stack.[57] This also indicates

the concomitant increase of the nanoparticle diameters, and therefore, confirms the arrangement of the valence and conduction band energies as described in Figure 7.

Looking at the perspectives of the graded semiconductor films made of nanoparticles, one can expect significant interest toward this type of materials for use in photonic devices. The combination of size quantization and gradient nature of the material opens a possibility for new optical and electrical effects as well as for the optimization of existing applications of nanoparticle thin films based on charge transfer from particle to particle as well as from particle to electrode. For the latter, the benefits of the graded media can be demonstrated by the markedly better light emitting performance when the homogeneous media in polymer light-emitting diodes is replaced with a graded one.[46] Additionally, the nanoparticle layers can be organized on a scale smaller than the wavelength of visible light, and therefore, one can engineer polarizability, refractive index and other parameters on the molecular level in such assemblies, so that the overall interaction of electromagnetic waves with the film will be significantly different than in the traditional optically uniform material.

We want to point out that the layer sequence has been used here as a parameter controlling the properties of the LBL assemblies. Although being simple in concept, one-dimensional ordering of nanoparticle assemblies, which produce a gradual, abrupt or any other programmed change in properties, can be a powerful tool for optimizing diverse functional properties of nanostructured materials from biological, such as designing artificial leaves,[45] to electronic. With this task in mind, it would be important to engineer the charge transport between the nanoparticles within the assembly, which should be addressed in future research.

4. LATERAL ORDERING IN LBL FILMS

Control of ordering of the layers in the LBL assemblies is a powerful tool for the design of materials. However, it implicitly assumes that the individual adsorption layers are closely packed, which quite often is not the case. This necessitates us to consider how the organization of particles and other species depends on and can be directed by experimental parameters.

4.1. Improvement of Packing Density of Nanoparticles in the Adsorption Layer by Surface Modification

As was noted above, YIG nanoparticles do not form a densely packed layer when adsorbed on PDDA.[3] The SEM images of $(YIG/PDDA)_n$ multilayers revealed that the repetition of adsorption cycles resulted not in the sandwich-like layering of organic and inorganic strata,[2,5,10,30,32,33,37,38,41,80,82] but rather in the growth of fairly isolated YIG islands (Figure 10). In layer 1, the film consisted of YIG domains of 0.5-1.5 micron in diameter (Figure l0a), which increased to 1-3 micron in deposition cycle 2 (Figure 10b), and 3-4 micron in deposition cycle 3 (Figure 10c). The domains were laterally expanding along the substrate surface, which was also accompanied by the increase of their average height. In the close-up image, one could see that the YIG islands were 3D agglomerates of YIG nanoparticles (Figure 10d), growing in size with increasing *n*.

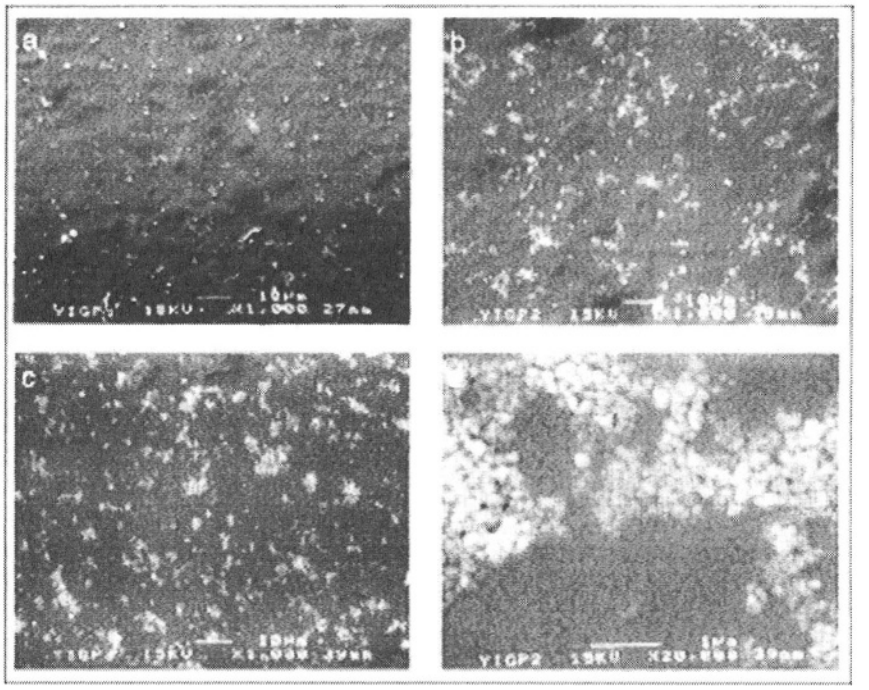

Figure 10. Scanning electron microscopy images of $(PDDA/YIG)_n$ films with (a) $n = 1$, (b) and (d) $n = 2$, and (c) $n = 3$ assembled on a precursor layer $(PDDA/PAA)_5PDDA$.

This demonstrated that the particles deposited in the LBL deposition cycles adhered predominantly to the existing domains rather than to the bare PDDA-covered surface, although the total number of domains may also increase. The lateral structure of the adsorption YIG film remains similar to that in Figure 10 in a wide range of pH and ionic strengths. One of the most effective means to control the surface packing density of the particles is surface modification. The native surface of YIG is very hydrophilic and negatively charged. As for many oxide surfaces, alkylsiloxanes can be grafted to YIG. Hence, 3-aminopropyl siloxane was used, which rendered the nanoparticles positively charged in acidic media due to the exposed $-NH_3$ group. The LBL assembly for 3-aminopropyl-siloxane-modified YIG nanoparticles was performed with negatively charged polyelectrolytes, such as poly(styrenesulfonate), PSS, and poly(acrylic acid), PAA. AFM revealed a great improvement of the film structure: the nanoparticles were densely packed after just one deposition cycle (Figure 11).

The change in the film morphology can be understood considering the new forces introduced by the surface modification. When YIG was modified with 3-aminopropyl siloxane, both the electrostatic and van der Waals components of nanoparticle-polyelectrolyte interactions were changed and, in addition to that, the native and modified YIG had a different electrical charge. The increase in surface density of the nanoparticles for modified YIG is primarily attributed to the attractive interactions between hydrocarbon groups or the organic modifier and the polyelectrolyte chains adsorbed to the substrate, *i.e.* hydrophobic interactions. Their amplification increased the attraction of the nanoparticles *both* to the polyelectrolyte *and* to each other.

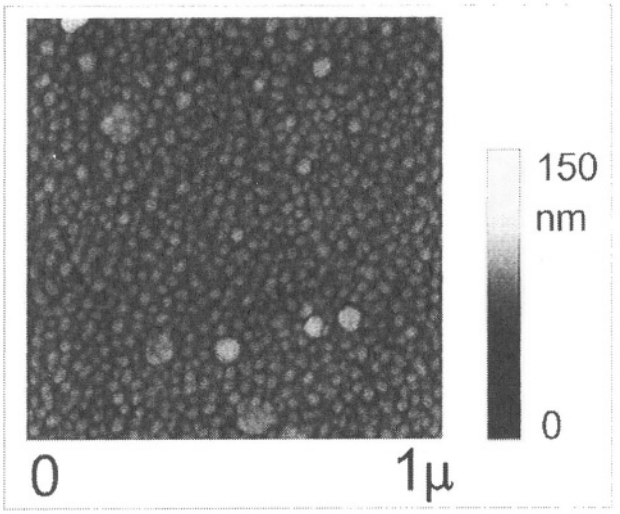

Figure 11. AFM image of YIG nanoparticles surface- modified with 3-aminopropyl-siloxane adsorbed on PAA.

4.2. Improvement of Packing Density by Assembly Conditions

The nanoparticles-polyelectrolyte and nanoparticle-nanoparticle interactions determining the packing density of the adsorption layers are strongly dependent on the pH and ionic strength conditions during the assembly. For particles with free energy of adsorption on the polyelectrolyte layer such as YIG, the effect of these parameters is obscured, but for most other nanoparticles it is as strong as for LBL assembly of polyelectrolyte pairs.[1,83,84] A convenient example of such dependence is the assembly of TiO_2-on-Ag core-shell nanoparticles also denoted as Ag@TiO_2.[5]

4.2.1. Synthesis of Ag@TiO_2

The preparation of these core-shell nanoparticles can be considered as a combination of two processes that occur sequentially in a single reaction mixture - the formation of the silver core and the coating. The ability of N,N-dimethylformamide (DMF) to reduce silver ions and yield stable silver colloids, in the presence of a stabilizer was recently reported.[85] On the other hand, controlled hydrolysis and condensation of $Ti(OC_4H_9)_4$ (TOB) can be accomplished by refluxing in the presence of a chelating agent, such as acetylacetone, to slow down the hydrolysis. As a result, titania colloids with different particle sizes can be obtained. In this study, we attempted to combine these two processes in one single procedure, comprising the high temperature reduction of Ag^+ by a DMF/ethanol mixture in the presence of TOB and acetylacetone. The prepared nanoparticles were characterized by high resolution transmission electron microscopy. Two different populations were found on the carbon-coated copper grids, as shown in Figure 12. There is a population of larger silver particles, with an average diameter of ca. 20 nm, which are homogeneously coated with a thin shell of amorphous TiO_2 as identified by EDAX. Additionally, smaller silver particles are also present on the grid, with an average particle size of some 4 nm. For them, the low contrast of the image does not allow for the visualization of a shell.

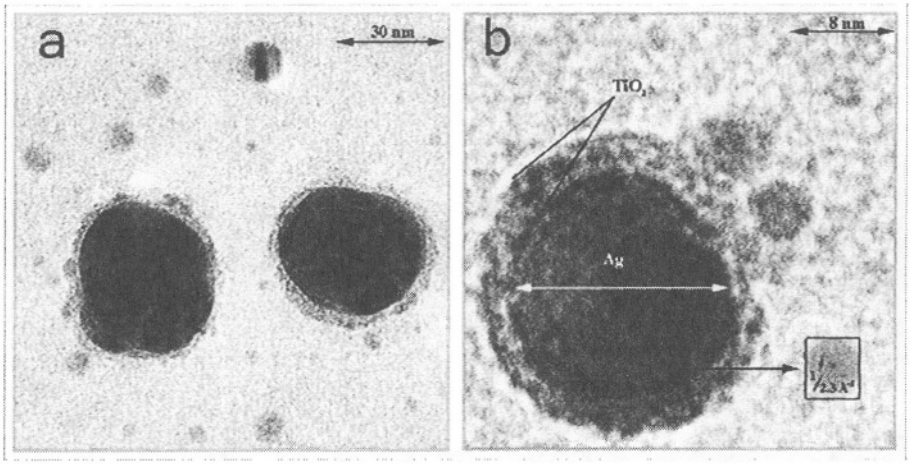

Figure 12. (a) TEM micrograph of Ag @TiO_2 nanoparticles. Two different populations exist in the sample; the titania shell around the larger particles can be clearly seen in the images. (b) HRTEM showing the crystalline nature of the metallic core and the amorphous nature of the shell of Ag@TiO_2. Reproduced with permission from ref. 5. Copyright 2000, American Chemical Society.

However, the stability of these dispersions at pH > 2, when standard naked silver colloids flocculate, suggests that their surface is also modified by TOB. UV-visible spectroscopy of the dilute aqueous sol of the core-shell nanoparticles shows a large red-shift of the silver plasmon band from 400 nm, which is typical for uncoated silver nanoparticles, to 435 nm, as well as largely enhanced absorbance at lower wavelengths. Both of these spectral features are related to the high refractive index of TiO_2 being in contact with the silver surface. The electronic nature if this spectral shift is similar to the one observed for interacting multilayers of gold triangles shown in Figures 5 and 6. A relatively hydrophobic environment of the DMF-ethanol mixture of the original dispersion and low surface charge of nanoparticles makes the LBL from the as prepared dispersions problematic. Therefore, the first step for the film preparation is the 1:15 dilution of the original dispersion (in DMF/ethanol) with water at pH < 3.5. Under these conditions, the titania coated particles become positively charged, while the large amount of dilution water activates the hydrophobic attraction to the polyelectrolyte strands. For positively charged Ag@TiO_2 nanoparticles, negatively charged poly(acrylic acid), Mw = 100,000 (PAA) is used as a partner polyelectrolyte for LBL.

The AFM images revealed that the surface density of nanoparticles can be varied by changing the pH of the nanoparticle dispersions (Figure 13). The highest particle density is obtained at pH = 2.5 (Figure 13c), while the best ordering is observed at pH = 2.0, when the nanoparticles form closely packed films (Figure 13d). A deviation in pH in both directions from the optimal range pH = 2.0 - 2.5 yields a decrease in particle density. At low pH ≈ 2.0, the adsorption of protons on the TiO_2 shells results in a high surface charge of nanoparticles (IEP of TiO_2 is pH = 6.55). Consequently, strong repulsion between them dominates over other intermolecular forces. Additionally, the degree of PAA ionization is decreased, too. Both factors make adsorption thermodynamically less favorable and rarified layers of individual nanoparticles are produced (Figure 13e,f). At pH = 2.0, the surface charge of nanoparticles is decreased and so is the interparticle repulsion.

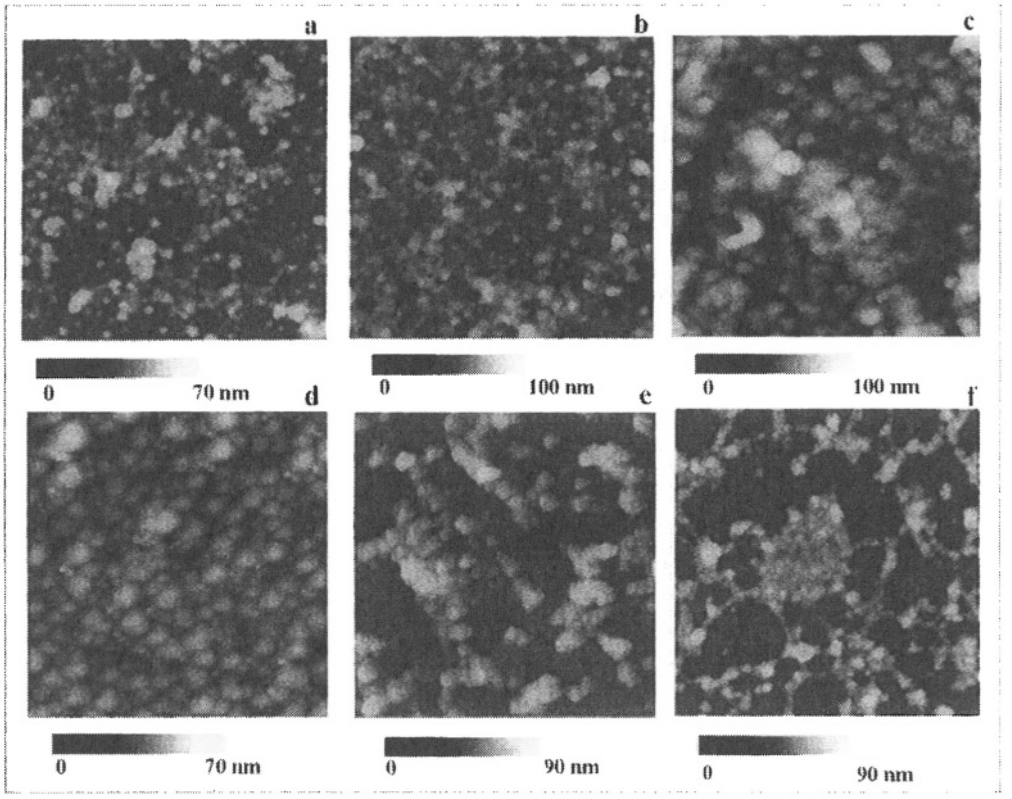

Figure 13. AFM 1μ × 1μ AFM images of monolayers of the nanoparticles shown in Figure 12 assembled from dispersion at pH = 3.5 (a), 3.0 (b), 2.5 (c), 2.0 (d), 1.5 (e), and 1.0 (f). Reproduced with permission from ref. 5. Copyright 2000, American Chemical Society.

The relative contribution of the electrostatic and hydrophobic attraction to the PAA-coated surface increases, which results in the alteration of film structure and increase of particle density. The situation when the repulsion and attraction both remain strong, while balancing each other, promotes well-ordered closely packed structures as can be seen in Figure 13d. Further increase of pH to 2.5 leads to shift of the balance toward nonspecific attractive interactions due to the charge independent hydrophobic interactions of nanoparticles with each other and with PAA macromolecules. In response to that, the films become thicker and less organized with fairly large aggregates distributed all over the surface (Figure 13c). At relatively high pH. 3.0, the kinetics of adsorption become very slow due to smaller charge on TiO_2 and the corresponding weakness of the long-range electrostatic attraction of nanoparticles to the substrate, which results in rarified films consisting from 3D clusters of many particles (Figure 13a,b). The agglomeration was found to be stimulated by loose segments of polyelectrolyte chains protruding into the solution.[4]

This process of multilayer build-up on glass slides can be monitored by UV-visible spectroscopy (Figure 14a,b). Similarly to other nanoparticle systems (Figure 1), the consecutively acquired spectra display a virtually linear increase of absorbance in every deposition cycle (*i.e.* with each $PAA/Ag@TiO_2$ bilayer) (Figure 14a).

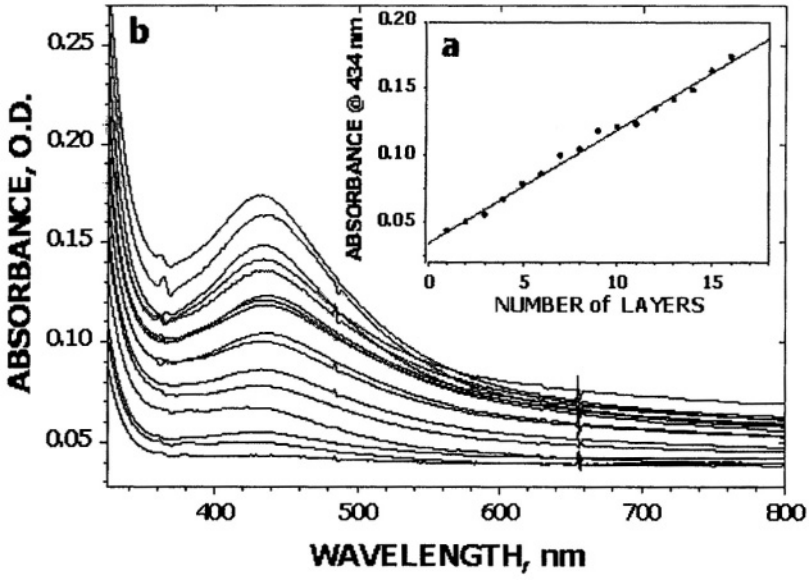

Figure 14. Monitoring of the LBL buildup of $Ag@TiO_2$ core-shell NPs assembled with PAA: (a) Dependence of adsorption at 434 nm vs. the number of deposition cycles. (b) UV-vis spectra of sequentially deposited layers. Reproduced with permission from ref. 5. Copyright 2000, American Chemical Society.

Note that the position of the surface plasmon band of silver (Figure 14b) remains identical for any number of layers, which indicates that, while being in close contact with each other, the nanoparticles remain electrically insulated. This feature distinguishes the proposed films from LBL assemblies of gold triangles discussed above (Figures 5,6). The constancy of the absorption band should be attributed to the presence of an insulating (probably amorphous) shell of titania around the metal cores. It reduces the strength of dipole-dipole interaction between them manifesting in the red-shifted plasmon peak.

4.3. Effect of Lateral Ordering on the Materials Functions

The lateral ordering of nanoparticles in the multilayers can affect the functional properties to a great extent. This idea can be exemplified by the ion-selective properties of TiO_2 nanoshell films, which can be produced from the $Ag@TiO_2$ nanoparticles. In combination with biocompatibility, such properties can be utilized for selective detection of neurotransmitters.[86]

In order to make nanoshells, the silver core is removed by adding a concentrated solution of ammonia. NH_3 molecules form coordinate compounds with Ag surface atoms, which reduces the redox potential of Ag/Ag^+ pair and results in the oxidation of silver metal by oxygen from the environment. The oxidation products, *i.e.* silver ion complexes, diffuse out from the interior of the $Ag@TiO_2$ nanoparticles into the solution through pores in the titania shell. Upon complete extraction of the silver core, ammonia treatment yields hollow porous spheres of TiO_2 with a shell thickness of 3-5 nm as evidenced by TEM.[86]

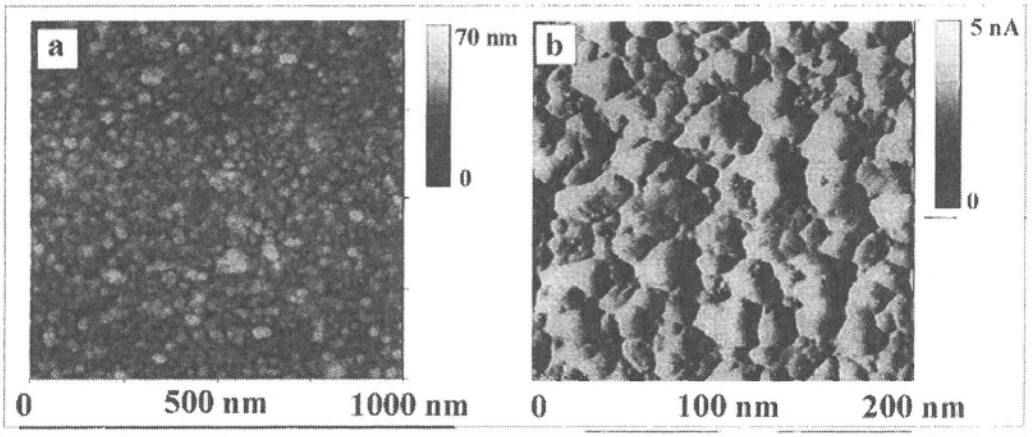

Figure 15. (a) AFM and (b) STM images of monolayer of TiO_2 nanoparticles assembled on gold surface. Reproduced with permission from ref. 86. Copyright 2002, Wiley-VCH.

TiO_2 nanoshells form stable dispersions at acidic pH, when they are positively charged (point of zero charge (pzc) of TiO_2 is *ca.* pH 6). At pH 2, the zeta potential of the nanoshell dispersion was determined to be +30 mV. Similarly to the parent $Ag@TiO_2$ nanoparticles, a negatively charged polyelectrolyte, such as PAA, could be employed to prepare LBL films from the composite core-shell nanoparticles as was previously demonstrated.[5] The sequential adsorption of PAA and TiO_2 nanoshell layers results in a gradual build-up of a composite film analogously to the layers of $Ag@TiO_2$ described above. The film build-up occurred in a fairly wide range of conditions. In this study, we typically used the films obtained at pH 2.5, which display dense packing of the composite $Ag@TiO_2$ nanoparticles (Figure 13), which were subsequently converted into nanoshells. AFM and STM images show the in-plane structure of the assembled nanoshell layers (Figure 15). STM images, which typically allow for better resolution than AFM, demonstrate the closely packed structure of the film (Figure 15b), while the AFM image taken over the greater surface area shows the uniformity of the packing (Figure 15a). Dense and uniform packing of the nanoparticle film is critical for attaining selective ion transport. No difference in particle packing and image features was observed before and after removal of the silver core.

4.3.1. Ion-sieving properties

The existence of pores in TiO_2 nanoshells sufficient for Ag^+ ions to escape gave us a reason to expect sufficient ion permeability in the LBL films made from them. The hollow sphere geometry of the nanoshells with thin walls provides both high surface area and nanoscale porosity. All these structural features are indicative of ion-sieving capabilities of the nanomaterial. Therefore, we investigated the ion-permeable properties of the nanoshell films using the standard electrochemical method of cyclic voltammetry with potassium ferricyanide $Fe(CN)_6^{3-}$ as a probe molecule. This probe was selected on the basis of its formal redox potential, which must be within the stability limits of the films. Figure 16a,c shows voltammograms obtained on an LBL coated glass carbon (GC) electrode *with* and *without* Ag cores, while Figure 17 displays the dependence of the peak

current on the sweep rate. Both of these sets of data are necessary to evaluate the mechanism of ion transport through the nanoshell LBL film.

Ion permeability of the LBL nanoshell films strongly depends on pH and ionic strength (Figures 16,17). The flow of $Fe(CN)_6^{3-}$ from solution to the electrode is almost completely blocked at low ionic strength at pH 11 (Figure 16a, trace 2 and Figure 16b). At the same time, ionic strength has little effect when the nanoshell film is at pH 2 (Figure 16c, traces 2, 3 and Figure 16d). The change of pH from 11 to 2 results in a drastic increase of transparency of the nanoshell film for the probe molecule as indicated by the increase of the peak current in the voltammograms (Figures 16,17).

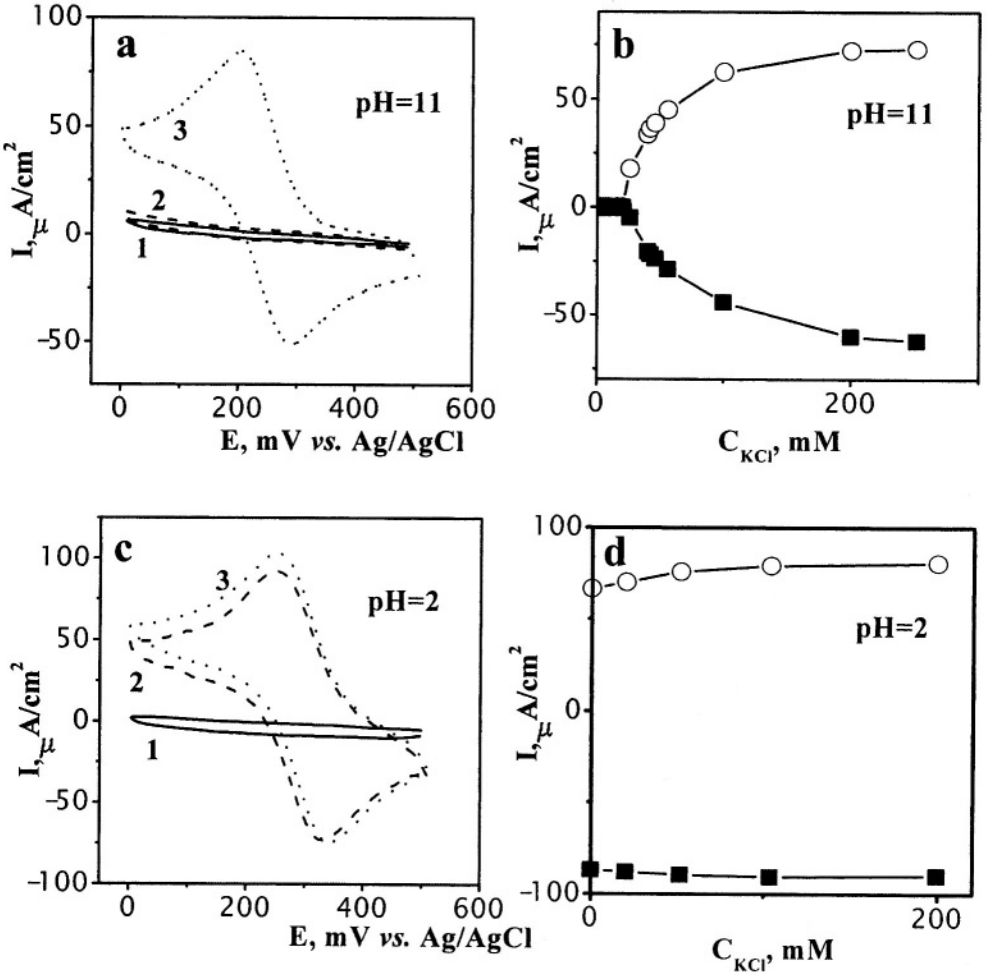

Figure 16. Cyclic voltammetry data in 2mM $K_3Fe(CN)_6$ on a glassy carbon electrode coated with $PDDA(PAA/TiO_2)_{20}$ film. The data were taken (a), (b) at pH11 and (c),(d) at pH2. On (a) and (c), individual traces correspond to (1) electrodes coated with Ag/TiO_2 core-shell particles, and to nanoshell-modified glassy carbon electrode in (2) 0.02 M KCl and (3) 0.5 M KCl. Graphs (b) and (d) show the plots of cathodic (closed squares) and anodic (open circles) maximum cyclic voltammetry peak currents *vs.* the concentration of supporting electrolyte. Scan rate 5 mV/s. Reproduced with permission from ref. 86. Copyright 2002, Wiley-VCH.

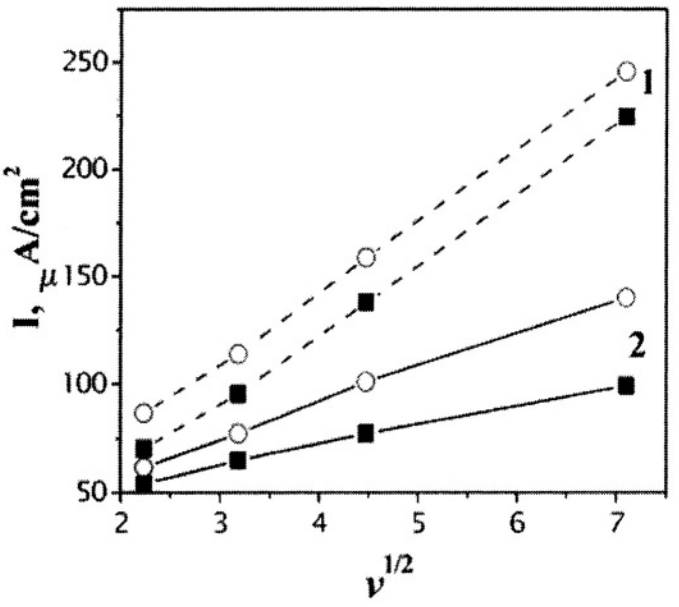

Figure 17. Scan rate dependence of the cathodic (closed squares) and anodic (open circles) peaks currents vs. v1/2 for electrode modified with PDDA(PAA/TiO2)20 film in 2mM K3Fe(CN)6/0.5M KCl solution at different pH: (1) pH 11 and (2) pH 2. Reproduced with permission from ref. 86. Copyright 2002, Wiley-VCH

The magnitude of the voltammetric redox currents – both cathodic and anodic – reflects the barrier properties of the coatings. Despite the conductive nature of the silver core, the voltammograms obtained using the electrode covered by Ag-core/TiO_2-shell nanoparticles indicate that the multilayer film from the precursor nanoparticle *with* silver core effectively passivates the electrode surface and blocks the oxidation and reduction of the probe at any pH and at any ionic strength (Figures 16a,c, traces 1). Conversely, when the silver cores are removed, the strong current from the redox reactions of $Fe(CN)_6^{3-}$ is observed (Figures 16a,c, traces 4). Linear dependence of I-$\nu^{1/2}$ for a wide range of pH (Figure 17) proves that the observed electrochemical processes are diffusion-controlled, which is commensurate with the through-pore mass transfer mechanism of $Fe(CN)_6^{3-}$ typical for many membranes. The permeability of these layers without the silver core shows that the penetration of ions occurs predominantly through the shell rather than through the possible gaps between the TiO_2 hollow spheres or defects in the coating. For poorly packed films, a substantial background current was observed before and after the core removal. The prevention of the defect currents necessitated maximization of the packing density of the nanoshells in the film and pH optimization.

The obtained structural information about the films and nanoparticles helps in understanding the mechanism of the ionic selectivity and transport. Importantly, the ion permeability curves for PAA/TiO_2 and PAA/PDDA films are very similar.[86] As well, there is also no effect of the nature of the terminal layer – positive or negative – on the voltamogramms. These observations give evidence that the Donnan equilibrium, which was considered to be the primary source of ion selectivity in other polyelectrolyte layer-by-layer assembled systems[87,88] is not the reason for ionic sieving in this system. The observed on/off behavior of the ion diffusion (Figure 16) in response to the changes in

pH and ionic strength is related to the distribution/organization of charges in the *bulk* of the assembled film, *i.e.* is based on the electrostatic (and possibly chemical) interactions with the film matrix. The molecular mechanism of the pH/ionic strength dependence of ion permeability can be understood considering the model of ions/double layer interaction inside ultra narrow pores as suggested by C. R. Martin[89-91] and further developed by R. Crooks and M. Bruening[87,92,93] For channels with a diameter comparable to the thickness of a diffuse part of electrical double layer, *i.e.* 0.3-30 run, the Hemholtz layers on pore walls may overlap.

When this happens, the ions of one sign tend to dominate in the channel, while their counterions are virtually expelled from it. This results in exclusive transport of the ions with the dominant charge and stoppage of the minority charge carriers. The selectivity of the membrane improves with lowering of ionic strength when the diffuse layers are becoming thicker, and worsens for the opposite trend. Changing pH may reverse the charge of the electrical double layer, and thus, the roles of counterions and their relative selectivity.[87,90-94]

The behavior of the TiO_2 nanoshell films can be adequately described by this model. The variation of the surface potential of TiO_2 with ionic strength and pH is well known.[95,96] For the LBL films of nanoshells at pH 11, the diffuse part of the electrical double layer is formed predominantly by positively charged ions of the supporting electrolyte (K^+) (Figure 16c,d). Negatively charged $Fe(CN)_6^{3-}$ ions are mostly excluded from the network of voids and channels formed by nanoshells, and therefore, the redox current is virtually zero in 0.02 M KCl (Figure 16a,b). When ionic strength increases to 0.5 M KCl, the diffuse part of the double layer shrinks opening the space for diffusion of the negatively charged ions, and the current increases (Figure 16b). At low pH, the electrical double layer is always formed from the negatively charged ions of $Fe(CN)_6^{3-}$ and Cl^-, and therefore, their diffusion through the film is quite efficient for any ionic strength (Figure 16c,d).

The complete closing of the nanoshell film occurs for [KCl] = 0.02 M. The characteristic thickness of the electrical double layer according to the Gouy-Chapman theory under these conditions is 2-2.5 nm,[97,98] which indicates that the upper limit of the pore diameter is 4-5 nm. The existence of pores in this size range in the nanoshells can be seen in AFM images obtained with high aspect ratio AFM probes (Figure 18a). Similar openings in the shells can also be seen in the TEM images (Figure 18b).

One needs to emphasize the significance of the nanoshell morphology of the particles for obtaining pronounced ion-selective properties in the LBL film. The shells provide the rigid pores with oxide walls comparable in dimensions with the thickness of the electrical double layer, which is absent in solid particles. Simultaneously, the 10-30 nm scale particles form layers with little amount of defects above that limit, which would be difficult to achieve with particles in, for instance, 100 nm range. The defects of these dimensions will create a significant background current masking ion conductance through the pores. This also underscores the importance of fine-tuning the deposition conditions of the nanoshells maximizing the particle density of the surface. We also noticed that only freshly prepared nanoshells display the described ion-selective behavior, while the colloid assembled after 3 month aging period under exactly the same conditions showed significantly worse performance presumably because of unoptimized nanoshell packing, which no longer corresponds to the altered balance of attractive/repulsive forces caused by the change of charge distribution on the nanoshell surface.

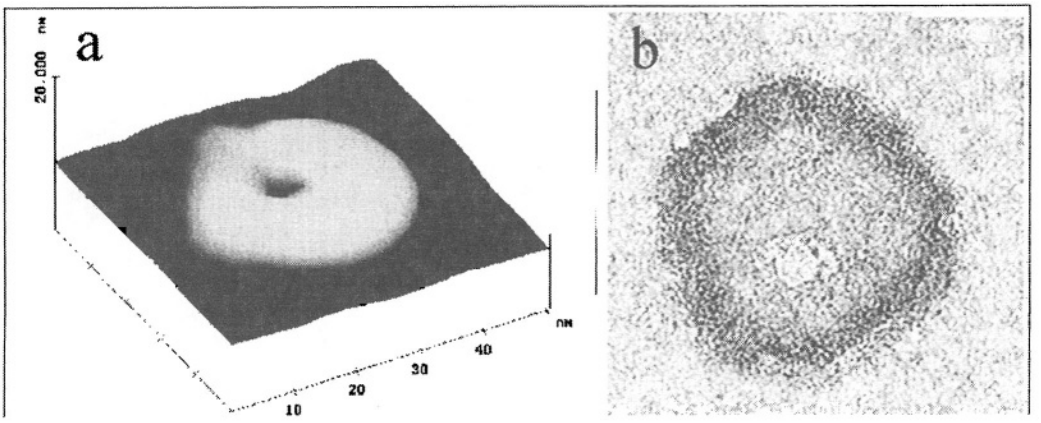

Figure 18. Images of nanoshells with pores: (a) AFM image and (b) TEM image. Reproduced with permission from ref. 86. Copyright 2002, Wiley-VCH.

4.3.2. Separation of dopamine

Small thickness on the order of hundreds of nanometers and high density of pores per unit volume characteristic for TiO_2 nanoshell LBL films, as well as some polyelectrolyte LBL multilayers,[99] resembles the quality of biomembranes and tissues produced by biomineralization.[100] Similarly to the polyelectrolyte/TiO_2 film, they also combine organic and inorganic components.[101,102] This resemblance prompted us to seek biological functionalities of the nanoparticle LBL films and the observed ion selective properties.

In recent years, there has been considerable interest in developing detection methods for the secretion of small molecules, known as neurotransmitters, from cells deep inside the brain.[103,104] Understanding the mechanism of their secretion and metabolism holds the key to curing many neurological disorders such as Parkinson's disease as well as drug addictions. Among them, dopamine (Figure 19) is one of the most important chemicals in the nervous system controlling movement, emotional response, and ability to experience pleasure and pain. It can be easily detected electrochemically with carbon fiber electrode.[105] However, the major problem is the interference of ascorbic acid, which is often present with dopamine in the tissue and has virtually identical electrochemical behavior.[93,106-108]

The blocking of the permeation of negatively charged $Fe(CN)_6^{3-}$ ions (Figure 16) suggests the possibility of imparting the selectivity for dopamine over ascorbic acid, which forms negatively charged ions. Although these substances are both electroactive and have similar size, the film structure and the conditions may be chosen so that the permeation of ascorbic acid is blocked. In order to test this hypothesis, the electrochemical response of LBL-modified electrodes to dopamine and ascorbic acid was compared to those for uncoated electrodes. For this, we used differential pulse voltammetry for monitoring electrode reactions, which is the primary method of dopamine detection in neurochemistry.

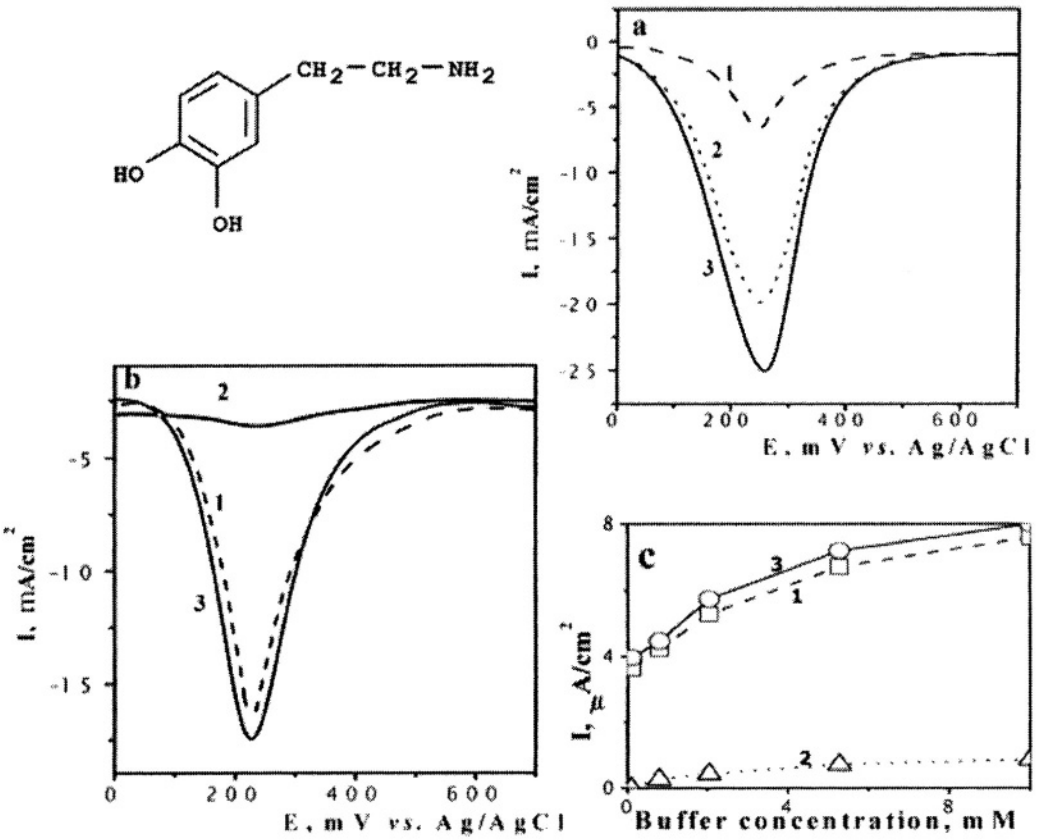

Figure 19. *Differential pulse voltammograms for (1) 1mM dopamine, (2) 1mM ascorbic acid, and (3) the mixture of 1mM dopamine + 1mM ascorbic acid in 0.1M phosphate buffer for (a) nascent and (b) coated by* $PDDA(PAA/TiO_2)_{20}$ *electrode. (c) The dependence of peak currents of differential pulse voltammograms for (1) 1mM dopamine, (2) 1mM ascorbic acid, and (3) dopamine/ascorbic acid mixture on the concentration of phosphate buffer. Reproduced with permission from ref. 86. Copyright 2002, Wiley-VCH*

As one can see, the LBL coating with nanoshells makes a drastic difference in the magnitude of electrochemical signal of ascorbic acid and dopamine (Figure 19). Without this modification, 1 mM ascorbic acid produces a peak (Figure 19a, trace 2), which is 3 times stronger than that for the equal 1 mM concentration of dopamine (Figure 19a, trace 1). The peak from the 1:1 molar mixture of dopamine and ascorbic acid is approximately equal to the superposition of those obtained separately (Figure 19a, trace 3), with the dominant contribution of ascorbic acid. When the electrode was coated with 20 LBL layers of TiO_2 nanoshells, the peak from ascorbic acid becomes hardly visible (Figure 19b, trace 2), while that of dopamine significantly increases as compared to the bare electrode (Figure 19b, trace 1).

Considering the predominantly electrostatic nature of the ion-sieving effects in the porous LBL films, one can take advantage of the difference in the ionization state and the characteristic charge of the permeating ions, for instance dopamine and ascorbic acid. Provided a sufficient space charge exists inside the nanoparticle channels, an electrode with the LBL layer of nanoshells may behave as if it is simultaneously in the "open" state for dopamine and in the "closed" state for ascorbic acid. This makes possible the

selective enhancement of the permeation of positively charged dopamine and retardation of the transport of negatively charged ascorbic acid.

All the measurements were made at pH 7. At these conditions, TiO_2 nanoshells are negatively charged, and therefore, the diffuse part of the double layer is made primarily from cations as required for the separation of positively charged dopamine and negatively charged ascorbic acid. The ratio between the dopamine and ascorbic acid signals changes from 1:3 for native GC surface to 9:1 for nanoshell-modified electrode, which gives an overall 27-fold enhancement of the selectivity between these substances. The signal from the mixture of ascorbic acid and dopamine is virtually equal to that from neat 1 mM dopamine (Figure 19b, trace 3). Importantly, the overall current from dopamine on coated and uncoated electrodes is virtually identical, *i.e.* the LBL coating does not decrease the detection limit of dopamine. The examination of the performance of the electrode at different ionic strengths demonstrates that the separation effect remains strong even at fairly high buffer concentration of 10 mM (Figure 19c) improving slightly with the decrease of ionic strength, as expected. It is important to note that, the excellent performance of the coating for physiological pH 7 and for different ionic strengths within the typical parameters of living organisms, makes possible the utilization of the nanoshell films in neurochemistry for *in vivo* monitoring of neurotransmitters.

Thus, a new type of composite material was prepared from TiO_2 nanoshells by using the layer-by-layer deposition procedure. As a result of their closely-packed morphology and nanoscale dimensions of the pores inside the nanoshells, TiO_2/PAA films display strong ion-selectivity. This quality can be further optimized and tailored to various systems of interest by the size control and surface modification of nanoparticles owing to exceptional versatility of the LBL deposition. An important aspect of this study is that it presents a new example of biomedical applications of nanoparticles. Considering that biocompatibility of the LBL films can be easily attained with appropriate film sequence, extension of presented technique to other nanoparticle/polyelectrolyte films will enable preparation of a large variety of biomaterials with different functionalities on this basis. *In-vivo* neurochemical monitoring is just one of a few possible areas, where such films can be successfully utilized.

5. CONCLUSIONS

Layer-by-layer assembly research experienced high-speed growth for the last decade, which was initially aimed at the expansion of the number of coatings and other nanostructured objects that can be obtained by this technique. The multilayers reached substantial structural sophistication. The lateral packing of the nanoparticles in the adsorption layers can be controlled in a wide range of packing densities by varying the assembly conditions and particle surface morphology. The limits of the layer organization originate from the use of polyelectrolyte macromolecules, which, on one hand, enables the LBL deposition by dipping, but on the other hand, its chaotic conformation introduces a certain degree of disorder in the films.[4] We believe that it will be more advantageous to embrace this degree of disorder and utilize it for the benefit of the material rather than to force the polyelectrolyte in a more regular structure. The initial implementation of this idea is described in a recent work from the Kotov's group.[108] We also intend to elaborate on this issue in upcoming publications.

The large variety of the components available for LBL led to an exceptional functional versatility. Therefore, the answer to the second question raised in the introduction to this review about possible technological limits of LBL assembled materials should probably be the following. In our opinion, any application considering the use of an organic-inorganic composite can find functional reasons for the use of LBL, which improves the performance of the material. Stratification of LBL can also make such composite multifunctional.

The inherent hydrophilicity of the films, the polyelectrolyte nature of many biomolecules, and the characteristic distances of spatial control all point to the direction of numerous biomedical applications of planar LBL films in the future, which we are beginning to see now. The incorporation of photonic materials in multilayers (such as luminescent nanoparticles) will enable the design of a new type of biocomposites, which possess the functionalities of the nano-sized state of matter.

6. REFERENCES

1. G. Decher, Fuzzy nanoassemblies toward layered polymeric multicomposites, *Science* **277**, 1232-1237 (1997).
2. A. Mamedov, J. Ostrander, F. Aliev, and N. A. Kotov, Stratified assemblies of magnetite nanoparticles and montmorillonite prepared by the layer-by-layer assembly, *Langmuir* **16**, 3941-3949 (2000).
3. J. W. Ostrander, A. A. Mamedov, and N. A. Kotov, Two modes of linear layer-by-layer growth of nanoparticle-polyelectrolyte multilayers and different interactions in the layer-by-layer deposition, *J. Am. Chem. Soc.* **123**, 1101-1110 (2001).
4. M. A. Correa-Duarte, M. Giersig, N. A. Kotov, and L. M. Liz-Marzán, Control of packing order of self-assembled monolayers of magnetite nanoparticles with and without SiO_2 coating by microwave irradiation, *Langmuir* **14**, 6430-6435 (1998).
5. I. Pastoriza-Santos, D. S. Koktysh, A. A. Mamedov, M. Giersig, N. A. Kotov, and L. M. Liz-Marzán, One-pot synthesis of $Ag@TiO_2$ core-shell nanoparticles and their layer-by-layer assembly, *Langmuir* **16**, 2731-2735 (2000).
6. G. Decher, Y. Lvov, and J. Schmitt, Proof of multilayer structural organization in self assembled polycation polyanion molecular films, *Thin. Solid. Films.* **244**, 772-777 (1994).
7. Y. Lvov, G. Decher, and H. Möhwald, Assembly, structural characterization, and thermal behavior of layer-by-layer deposited ultrathin films of poly(vinyl sulfate) and poly(allylamine), *Langmuir* **9**, 481-486 (1993).
8. Y. Lvov, G. Decher, H. Haas, H. Mohwald, and A. Kalachev, X-Ray analysis of ultrathin polymer films self assembled onto substrates, *Physica B* **198**, 89-91 (1994).
9. N. A. Kotov, I. Dekany, and J. H. Fendler, Layer by layer self assembly of polyelectrolyte semiconductor nanoparticle composite films, *J. Phys. Chem.* **99**, 13065-13069(1995).
10. A. L. Rogach, D. S. Koktysh, M. Harrison, and N. A. Kotov, Layer-by-layer assembled films of HgTe nanocrystals with strong infrared emission, *Chem. Mater.* **12**, 1526-1528 (2000).
11. Y. Lvov, *Electrostatic layer-by-layer assembly of proteins and polyions,* Marcel Dekker Inc., New York (2000).
12. F. Caruso, D. G. Kurth, D. Volkmer, M. J. Koop, and A. Mueller, Ultrathin molybdenum polyoxometalate- polyelectrolyte multilayer films, *Langmuir* **14**, 3462-3465 (1998).
13. J. Q. Sun, Y. P. Sun, S. Zou, Z. Xi, C. Q. Sun, Y. Wang, and J. C. Shen, Layer-by-layer assemblies of polycation bearing Os complex with electroactive and electroinactive polyanions and their electrocatalytic reduction of nitrite, *Macromol. Chem. Phys.* **200**, 840-844 (1999).
14. M. Schutte, D. G. Kurth, M. R. Linford, H. Colfen, and H. Möhwald, Metallosupramolecular thin polyelectrolyte films, *Angew. Chem., Int. Ed* **37**, 2891-2893 (1998).
15. K. Ariga, Y. Lvov, and T. Kunitake, Assembling alternate due-polyion molecular films by electrostatic layer-by-layer adsorption, J. *Am. Chem. Soc.* **119**, 2224-2231 (1997).
16. M. Ferreira and M. F. Rubner, Molecular level processing of conjugated polymers. 1. Layer by layer manipulation of conjugated polyions, *Macromolecules* **28**, 7107-7114 (1995).

17. G. J. Kellogg, A. M. Mayes, W. B. Stockton, M. Ferreira, M. F. Rubner, and S. K. Satija, Neutron reflectivity investigations of self assembled conjugated polyion multilayers, *Langmuir* **12**, 5109-5113 (1996).
18. P. Lavalle, C. Gergely, F. J. G. Cuisinier, G. Decher, P. Schaaf, J. C. Voegel, and C. Picart, Comparison of the structure of polyelectrolyte multilayer films exhibiting a linear and an exponential growth regime: an in situ atomic force microscopy study, *Macromolecules* **35**, 4458-4465 (2002).
19. C. Lesser, M. Gao, and S. Kirstein, Highly luminescent thin films from alternating deposition of CdTe nanoparticles and polycations, *Mater. Sci. Eng., C* **C8-C9**, 159-162 (1999).
20. E. Hao, B. Yang, H. Ren, X. Qian, T. Xie, J. Shen, and D. Li, Fabrication of composite film comprising TiO_2/CdS and polyelectrolytes based on ionic attraction, *Mater. Sci. Eng., C* **C10**, 119-122 (1999).
21. E. Hao, X. Qian, B. Yang, D. Wang, and J. Shen, Assembly and photoelectrochemical studies of TiO_2/CdS nanocomposite film, *Mol. Cryst. Liq. Cryst. Sci. Technol., Sect. A* **337**, 181-184 (1999).
22. M. Y. Gao, B. Richter, S. Kirstein, and H. Möhwald, Electroluminescence studies on self assembled films of PPV and CdSe nanoparticles, *J. Phys. Chem. B* **102**, 4096-4103 (1998).
23. T. Cassagneau, T. E. Mallouk, and J. H. Fendler, Layer by layer assembly of thin film Zener diodes from conducting polymers and CdSe nanoparticles, *J. Am. Chem. Soc.* **120**, 7848-7859 (1998).
24. E. Hao and T. Lian, Layer-by-layer assembly of CdSe nanoparticles based on hydrogen bonding, *Langmuir* **16**, 7879-7881 (2000).
25. M. Gao, C. Lesser, S. Kirstein, H. Mohwald, A. L. Rogach, and H. Weller, Electroluminescence of different colors from polycation/CdTe nanocrystal self-assembled films, *J. Appl. Phys.* **87**, 2297-2302 (2000).
26. J. Sun, E. Hao, Y. Sun, H. Zhang, B. Yang, S. Zou, J. Shen, and S. Wang, Multilayer assemblies of colloidal ZnS doped with silver and polyelectrolytes based on electrostatic interaction, *Thin Solid Films* **327-329**, 528-531(1998).
27. Y. Sun, E. Hao, X. Zhang, B. Yang, J. Shen, L. Chi, and H. Fuchs, Buildup of composite films containing TiO_2/PbS nanoparticles and polyelectrolytes based on electrostatic interaction, *Langmuir* **13**, 5168-5174 (1997).
28. Y. J. Liu, A. B. Wang, and R. Claus, Molecular self assembly of TiO_2/polymer nanocomposite Films., *J. Phys. Chem. B* **101**, 1385-1388 (1997).
29. E. Hao, B. Yang, J. Zhang, X. Zhang, J. Sun, and J. Shen, Assembly of alternating TiO_2 and CdS nanoparticle composite films, *J. Mater. Chem.* **8**, 1327-1328 (1998).
30. A. Rosidian, Y. J. Liu, and R. O. Claus, Ionic self assembly of ultrahard ZrO2/polymer nanocomposite thin films. *Adv. Mater.* **10**, 1087 (1998).
31. T. Cassagneau and J. H. Fendler, Preparation and layer-by-layer self-assembly of silver nanoparticles capped by graphite oxide nanosheets, *J. Phys. Chem. B* **103**, 1789-1793 (1999).
32. Y. Liu, Y. Wang, and R. O. Claus, Layer-by-layer ionic self-assembly of Au colloids into multilayer thin-films with bulk metal conductivity, *Chem. Phys. Lett.* **298**, 315-319 (1998).
33. W. Schrof, S. Rozouvan, E. Van Keuren, D. Horn, J. Schmitt, and G. Decher, Nonlinear optical properties of polyelectrolyte thin films containing gold nanoparticles investigated by wavelength dispersive femtosecond degenerate 4 wave mixing (dfwm). *Adv. Mater.* **10**, 338-341 (1998).
34. J. A. He, R Valluzzi, K. Yang, T. Dolukhanyan, C. Sung, J. Kumar, S. K. Tripathy, L. Samuelson, L. Balogh, and D. A. Tomalia, Electrostatic multilayer deposition of a gold-dendrimer nanocomposite, *Chem. Mater.* **11**, 3268-3274(1999).
35. E. Hao and T. Lian, Buildup of polymer/Au nanoparticle multilayer thin films based on hydrogen bonding. *Chem. Mater.* **12**, 3392-3396 (2000).
36. K. Ariga, Y. Lvov, I. Ichinose, and T. Kunitake, Ultrathin films of inorganic materials (SiO_2 nanoparticle, montmorillonite microplate, and molybdenum oxide) prepared by alternate layer-by-layer assembly with organic polyions, *Appl. Clay Sci.* **15**, 137-152(1999).
37. Y. Lvov, K. Ariga, M. Onda, I. Ichinose, and T. Kunitake, Alternate assembly of ordered multilayers of SiO_2 and other nanoparticles and polyions, *Langmuir* **13**, 6195-6203 (1997).
38. Y. M. Lvov, Rusling, James F.; Thomsen, D. Laurence; Papadimitrakopoulos, Fotios; Kawakami, Takeshi; Kunitake, Toyoki., High speed multilayer film assembly by alternate adsorption of silica nanoparticles and linear polycation. *Chem. Commun,* 1229-1230(1998).
39. I. Ichinose, H. Tagawa, S. Mizuki, Y. Lvov, and T. Kunitake, Formation process of ultrathin multilayer films of molybdenum oxide by alternate adsorption of octamolybdate and linear polycations, *Langmuir* **14**, 187-192(1998).
40. I. Moriguchi and J. H. Fendler, Characterization and electrochromic properties of ultrathin films self assembled from poly(diallyldimethylammonium) chloride and sodium decatungstate, *Chem. Mater.* **10**, 2205-2211 (1998).

41. Y. J. Liu, A. B. Wang, A. B., and Claus, R. O., Layer by layer electrostatic self assembly of nanoscale Fe_3O_4 particles and polyimide precursor on silicon and silica surfaces, *Appl. Phys. Lett.* **71**, 2265-2267 (1997).
42. M. Fang, C. H. Kim, G. B. Saupe, H.-N. Kim, C. C. Waraksa, T. Miwa, A. Fujishima, and T. E. Mallouk, Layer-by-layer growth and condensation reactions of niobate and titanoniobate thin films, *Chem. Mater.* **11**, 1526-1532(1999).
43. C. Tedeschi, H. Möhwald, and S. Kirstein, Polarity of layer-by-layer deposited polyelectrolyte films as determined by pyrene fluorescence, *J. Am. Chem. Soc.* **123**, 954-960 (2001).
44. Z. Tang, Y. Wang, and N. A. Kotov, Semiconductor nanoparticles on solid substrates: film structure, intermolecular interactions and polyelectrolyte effects, *Langmuir* in press, (2002).
45. D. M. Kaschak, J. T. Lean, C. C. Waraksa, G. B. Saupe, H. Usami, and T. E. Mallouk, Photoinduced energy and electron transfer reactions in lamellar polyanion/polycation thin films: Toward an inorganic "leaf", *J. Am. Chem. Soc.* **121**, 3435-3445 (1999).
46. P. K. H. Ho, J. S. Kim, J. Burroughes, H. Becker, F. Y. L. Sam, T. M. Brown, F. Cacialli, and R. H. Friend, Molecular-scale interface engineering for polymer light-emitting diodes, *Nature* **404**, 481-484 (2000).
47. M. Onda, Y. Lvov, K. Ariga, and T. Kunitake, Sequential reaction and product separation on molecular films of glucoamylase and glucose oxidase assembled on an ultrafilter, *J. Ferment. Bioeng.* **82**, 502-506 (1996).
48. G. B. Sukhorukov, Donath, Edwin; Davis, Sean; Lichtenfeld, Heinz; Caruso, Frank; Popov, Victor I.; Mohwald, Helmuth, Stepwise polyelectrolyte assembly on particle surfaces. A novel approach to colloid design, *Polym Adv. Technol.* **9**, 759-767 (1998).
49. J. Dai and M. L. Bruening, Catalytic nanoparticles formed by reduction of metal ions in multilayered polyelectrolyte films, *Nano Lett.* **2**, 497-501 (2002).
50. A. Henglein, Physicochemical properties of small metal particles in solution: "microelectrode" reactions, chemisorption, composite metal particles, and the atom-to-metal transition, *J. Phys. Chem.* **97**, 5457-5471 (1993).
51. P. Mulvaney, Surface plasmon spectroscopy of nanosized metal particles, *Langmuir* **12**, 788-800 (1996).
52. B. M. I. van der Zande, M. R. Böhmer, L. G. Fokkink, and C. Schöneberger, Colloidal dispersions of gold rods: synthesis and optical properties, *Langmuir* **16**, 451-458 (2000).
53. S. J. Oldenburg, R. D. Averitt, S. L. Westcott, and N. J. Halas, Nanoengineering of optical resonances, *Chem. Phys, Lett.* **288**, 243-247 (1998).
54. S. Link, and M. A. El-Sayed, Spectral Properties and Relaxation Dynamics of Surface Plasmon Electronic Oscillations in Gold and Silver Nanodots and Nanorods, *J. Phys. Chem. B* **103**, 8410-8426(1999).
55. N. Malikova, I. Pastoriza-Santos, M. Schierhorn, N. A. Kotov, and L. M. Liz-Marzán, Layer-by-layer assembled mixed spherical and planar gold nanoparticles: control of interparticle interactions, *Langmuir* **18**, 3694-3697 (2002).
56. T. Ung, L. M. Liz-Marzán, and P. Mulvaney, Optical properties of thin films of $Au@SiO_2$ particles, *J. Phys. Chem. B* **105**, 3441-3452 (2001).
57. N. A. Kotov, Ordered layered assemblies of nanoparticles, *MRS Bull.* **26**, 992 (2001).
58. N. A. Kotov, S. Magonov and E. Tropsha, Layer-by-layer self-assembly of alumosilicate-polyelectrolyte composites: mechanism of deposition, crack resistance, and perspectives for novel membrane materials, *Chem. Mater.* **10**, 886-895 (1998).
59. N. A. Kotov, T. Haraszti, L. Turi, G. Zavala, R. E. Geer, I. Dékány, and J. H. Fendler, Mechanism of and defect formation in the self assembly of polymeric polycation montmorillonite ultrathin films, *J. Am. Chem. Soc.* **119**, 6821-6832 (1997).
60. F. Caruso, M. Spasova, V. Salgueiriño-Maceira, and L.M. Liz-Marzán, Multilayer assemblies of silica-encapsulated gold nanoparticles on decomposable colloid templates, *Adv. Mater.* **13**, 1090-1095 (2001).
61. E. R. Kleinfeld and G. S. Ferguson, Stepwise formation of multilayered nanostructural films from macromolecular precursors, *Science* **265**, 370-373 (1994).
62. J. H. Fendler, N. A. Kotov, and I. Dekany, in: *Fine Particles Science and Technology,* Pelizzetti,E. (ed.), pp. 557-577 (Kluwer Academic Publ, Dordrecht, 1996).
63. N. A. Kotov, I. Dekany, and J. H. Fendler, Ultrathin graphite oxide polyelectrolyte composites prepared by self assembly transition between conductive and nonconductive states. *Adv. Mater.* **8**, 637 (1996).
64. F. Aliev, M. A. Correa-Duarte, A. Mamedov, J. Ostrander, M. Giersig, L. M. Liz-Marzán, and N. A. Kotov, Layer-by-layer assembly of core-shell magnetite nanoparticles: effect of silica coating on interparticle interactions and magnetic properties, *Adv. Mater.* **11**, 1006-1010 (1999).
65. F. Caruso, A. S. Susha, M. Giersig, and H. Möhwald, Magnetic core-shell particles. Preparation of magnetite multilayers on polymer latex microspheres, *Adv. Mater.* **11**, 950-953 (1999).

66. H. Mohwald, H. Lichtenfeld, S. Moya, A. Voigt, H. Baumler, G. Sukhorukov, F. Caruso, and E. Donath, From polymeric films to nanoreactors, *Macromol. Symp.* **145**, 75-81 (1999).
67. A. Newman and J. M. Liu, Physical characteristics of band-gap engineered, photovoltaic detectors, *J. Appl. Phys.* **82**, 4637-4646 (1997).
68. J. H. Lee, S. S. Li, M. Z. Tidrow, W. K. Liu, and K. Bacher, Quantum-well infrared photodetectors with digital graded superlattice barrier for long-wavelength and broadband detection, *Appl. Phys. Lett.* **75**, 3207-3209 (1999).
69. F. Capasso, New graded band gap and superlattice structures and their applications to photodetectors, bipolar transistors and high-speed devices. *NATO ASI Ser. B* **180**, 659-682 (1988).
70. L. Aigouy, V. Mathet, F. Liaci, B. Gil, O. Briot, N. Briot, T. Cloitre, M. Averous, and R. L. Aulombard, R. L., Optical spectroscopy in (Zn,Cd)Se-ZnSe graded-index separate-confinement heterostructures, *Phys. Rev. B* **53**, 4708-4721 (1996).
71. S. Vlaev, V. R. Velasco, and F. Garcia-Moliner, Electronic states in graded-composition heterostructures. *Phys. Rev. B* **49**, 11222-11229 (1994).
72. R. Tomasiunas, *I.* Pelant, B. Honerlage, R. Levy, T. Cloitre, and R. L. Aulombard, Stimulated emission and optical gain in a single MOVPE-grown ZnxCdl-xSe-ZnSe quantum well. *Phys. Rev. B* **57**, 13077-13085 (1998).
73. B. S. Sokolovskii, Multilayer structures based on doped graded-band-gap semiconductors. Features of energy band diagram, *Phys. Status Solidi A* **163**, 425-432 (1997).
74. M. R. Geller, Dynamics of electrons in graded semiconductors, *Phys. Rev. Lett.* **78**, 110-113 (1997).
75. H. Fujiwara, J. Koh, C. R. Wronski, R. W. Collins, and J. S. Burnham, Optical depth profiling of band gap engineered interfaces in amorphous silicon solar cells at monolayer resolution, *Appl. Phys. Lett.* **72**, 2993-2995 (1998).
76. S. K. Chattopadhyaya and V. K. Mathur, Photomagnetoelectric effect in graded band-gap semiconductors, *Phys. Rev. B* **3**, 3390-3399 (1971).
77. G. Aichmayr, M. D. Martin, H. van der Meulen, C. Pascual, L. Vina, J. M. Calleja, F. Schafer, J. P. Reithmaier, and A. Forchel, Carrier and light trapping in graded quantum-well laser structures, *Appl. Phys. Lett.* **76**, 3540-3542 (2000).
78. A. A. Mamedov, A. Belov, M. Giersig, N. Mamedova, and N. A. Kotov, Nanorainbows: graded semiconductor thin films from quantum dots, *J. Am. Chem. Soc.* **123**, 7738-7739 (2001)
79. C. R. Kagan, C. B. Murray, and M. G. Bawendi, Long-range resonance transfer of electronic excitations in close-packed CdSe quantum-dot solids, *Phys. Rev. B* **54**, 8633-8643 (1996).
80. A. A. Mamedov and N. A. Kotov, Free-standing layer-by-layer assembled films of magnetite nanoparticles, *Langmuir* **16**, 5530-5533 (2000).
81. A. L. Rogach, L. Katsikas, A. Kornowski, D. Su, A. Eychmuller, and H. Weller, Synthesis, morphology, and optical properties of thiol-stabilized CdTe nanoclusters in aqueous solution, *Ber. Bunsen-Ges. Phys. Chem.* **101**, 1668-1670 (1997).
82. M. Gao, X. Zhang, B. Yang, F. Li, and J. Shen, Assembly of modified CdS particles/cationic polymer Based on Electrostatic Interactions. *Thin Solid Films* **284-285**, 242-245 (1996).
83. J. H. Cheung, A. F. Fou, and M. F. Rubner, Molecular self assembly of conducting polymers, *Thin Solid Films* **244**, 985-989 (1994).
84. S. S. Shiratori and M. F. Rubner, pH-dependent thickness behavior of sequentially adsorbed layers of weak polyelectrolytes, *Macromolecules* **33**, 4213-4219 (2000).
85. I. Pastoriza-Santos and L. M. Liz-Marzán, Formation and Stabilization of Silver Nanoparticles through Reduction by N,N-dimethylformamide, *Langmuir* **15**, 948-951 (1999).
86. D. Koktysh, X. Liang, B.-G. Yun, I. Pastoriza-Santos, R. L. Matts, M. Giersig, C. Serra-Rodríguez, L. M. Liz-Marzán, and N. A. Kotov, Biomaterials by design: layer-by-layer assembled ion-selective and biocompatible films of TiO_2 nanoshells for neurochemical monitoring, *Adv. Funct. Mater.* **12**, 255-265 (2002).
87. J. J. Harris, J. L. Stair, and M. L. Bruening, Layered Polyelectrolyte Films as Selective, Ultrathin Barriers for Anion Transport, *Chem. Mater.* **12**, 1941-1946 (2000).
88. L. Krasemann and B. Tieke, Selective ion transport across self-assembled alternating multilayers of cationic and anionic polyelectrolytes, *Langmuir* **16**, 287-290 (2000).
89. V. P. Menon and C. R. Martin, Fabrication and evaluation of nanoelectrode ensembles, *Anal. Chem.* **67**, 1920-1928 (1995).
90. K. B. Jirage, J. C. Hulteen, and C. R. Martin, Nanotubule-based molecular-filtration membranes, *Science* **278**, 655-658 (1997).
91. M. Nishizava, V. P. Menon, and C. R. Martin, Metal nanotubule membranes with electrochemically switchable ion-transport selectivity, *Science* **268**, 700-702 (1995).

92. O. Chailapakul and R. M. Crooks, Interactions between Organized, Surface-Confined Monolayers and Liquid-Phase Probe Molecules. 4. Synthesis and Characterization of Nanoporous Molecular Assemblies: Mechanism of Probe Penetration, *Langmuir* **11**, 1329-1328 (1995).
93. L. Sun, B. Johnson, T. Wade, and R. M. Crooks, Selective electrostatic binding of ions by monolayers of mercaptan derivatives adsorbed to gold substrates, *J. Phys. Chem.* **94**, 8869-8871 (1990).
94. Y. Liu, W. Zhao, Y. X. Wang, and R. O. Claus, Functionally-tailored nanoparticle-based ionically self-assembled multi-layer thin-films. *Proc. SPIE-Int. Soc. Opt. Eng.* **3324**, 45-48 (1998).
95. M. Kosmulski, S. Durand-Vidal, J. Gustafsson, and J. B. Rosenholm, Charge interactions in semi-concentrated titania suspensions at very high ionic strengths, *Colloids Surf.* **157**, 245-259 (1999).
96. J. L. Look and C. F. Zukoski, Colloidal stability and titania precipitate morphology: influence of short-range repulsions, *J. Am. Ceram. Soc.* **78**, 21-32 (1995).
97. A. W. Adamson and A. P. Gast, *Physical Chemistry of Surfaces,* 6th ed.., pp. 171-175 (John Wiley&Sons, New York, 1997).
98. P. J. Kemery, J. K. Steehler, and P. W. Bohn, Electric field mediated transport in nanometer diameter channels, *Langmuir* **14**, 2884-2889 (1998).
99. J. D. Mendelsohn, C. J. Barrett, V. V. Chan, A. J. Pal, A. M. Mayes, and M. F. Rubner., Fabrication of microporous thin films from polyelectrolyte multilayers, *Langmuir* **16**, 5017-5023 (2000).
100. S. Mann and G. Ozin, Synthesis of inorganic materials with complex form, *Nature* **382**, 313-318 (1996).
101. S. L. Burkett, S. D. Sims, and S. Mann, Synthesis of hybrid inorganic-organic mesoporous silica by co-condensation of siloxane and organosiloxane precursors, *Chem. Commun.* 1367-1368 (1996).
102. K. K. W. Wong and S. Mann, Small-scale structures in biomineralization and biomimetic materials chemistry. *Curr. Opinion. Colloid Interface Sci.* **3**, 63-68 (1998).
103. J. Smythies, Redox mechanisms at the glutamate synapse and their significance: a review, *Eur. J. Pharmacol.* **1999**, *1-7,* 370. *Europ. J. of Pharmacology* **370**, 1-7 (1999).
104. J. A. Stamford and J. B. Justice, Jr., Probing brain chemistry. Voltammetry comes of age, *Anal. Chem.* 359A-363A (1996).
105. F. L. Leibowitz, W. Zheng, M. M. Maye, and C. J. Zhong, Structures and Properties of Nanoparticle Thin Films Formed via a One-Step Exchange-Cross-Linking-Precipitation Route, *Anal. Chem.* **71**, 5076-5083 (1999).
106. A. Dalmia, C. C. Liu, and R. F. Savinell, Electrochemical behavior of gold electrodes modified with self-assembled monolayers with an acidic end group for selective detection of dopamine, *J. Electroanal. Chem.* **430**, 205-214 (1997).
107. A. J. Downard, A. D. Roddick, and A. M. Bond, Covalent modification of carbon electrodes for voltammetric differentiation of dopamine and ascorbic acid, *Anal. Chim. Acta* **317**, 303-310 (1995).
108. L. Qingwen, W. Yiming, and L. Guoan, Voltammetric separation of dopamine and ascorbic acid with graphite electrodes modified with ultrafine TiO_2, *Mater. Sci. Engineer. C* **11**, 71-74 (2000).
109. S. Westenhoff, and N. A.Kotov, Quantum Dot On A Rope, *J. Am. Chem. Soc.* **124**, 2448-2449 (2002).

This page intentionally left blank

14
NEW APPLICATIONS AND PROPERTIES OF LANGMUIR-BLODGETT FILMS

Inmaculada Prieto, María Teresa Martín, and Luis Camacho*

1. INTRODUCTION

The advance in nanotechnology is mainly determined by the development of novel functionalized materials and the use of new principles of device functioning. The biomimetic approach may provide new insights in the design, development, assembly and functionalization of new intelligent materials and systems at the molecular level. The physical principles which drive the interactions leading to formation of self-assembled and self-organized molecular and nanoscopic systems have been widely investigated during the last years in order to establish a relation between chemical composition, structure and organization of these materials and systems with desired physical properties and functions.

In this context, the Langmuir-Blodgett (LB) method is considered one of the most versatile techniques for fabricating organic thin films with well-controlled composition, structure and thickness.[1-2] Due to these features, the LB technique has been widely used to handle and assemble different functional molecules in a predefined manner with the aim of, e.g., fabricating molecular devices, or investigating physicochemical processes occurring in the monolayer at the gas-substrate interface.[3] The present chapter tries to describe the latest developments in the use of this technique to fabricate functional nanoassemblies.

Typical Langmuir films consist of amphiphilic molecules with long alkyl chains that form organized assemblies at the air-water interface (or gas-liquid interface in general). When amphiphilic molecules are spread on a trough containing an aqueous subphase, they form a monolayer where the polar head group is immersed into the water and the hydrocarbon chain oriented toward the air, as depicted in Figure 1. The trough has a moving barrier controlled mechanically over the air-water interface that serves to reduce the surface area. As the monolayer is compressed, it will undergo several phase transitions that can be identified by monitoring the surface pressure (π) as a function of the area occupied by the film (A). A typical π-A isotherm can be observed in Figure 1.

* Inmaculada Prieto, Universidad de Vigo, Vigo, Spain E-36200. María Teresa Martín and Luis Camacho, Universidad de Córdoba, Córdoba, Spain, E-14014

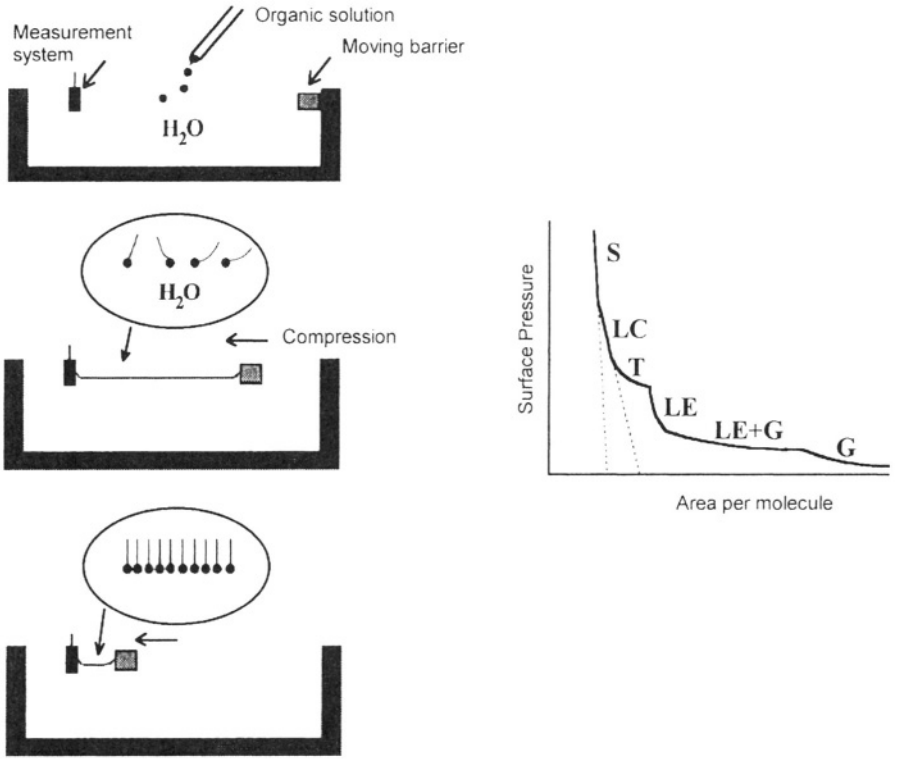

Figure 1. Schematic setup of Langmuir monolayer formation (left); Idealized representation of surface pressure (π)-surface area (A) isotherm (right).

Therefore, in the "gaseous state", noted as G, amphiphilic molecules are far enough apart and they do not interact. As the surface area of the monolayer is reduced, the hydrocarbon chains will start to interact, and the "liquid state" or expanded monolayer phase (LE) is reached, after undergoing a transition where gaseous and expanded phases coexist. When the molecular area is further reduced, condensed phases (LC and S) appear in which the molecules become oriented nearly vertical with their hydrocarbon chains closely packed, and their polar groups immersed in the water surface.

Generally, molecules without long alkyl chains are unable to form well-organized monolayers at the air-water interface. However, new techniques have been developed and reviewed[3] allowing monolayer organization and manipulation of such non-amphiphilic molecules. The incorporation of molecules without long alkyl chains in monolayers of selected amphiphilic molecules, like fatty acids, by adsorption from the aqueous subphase[4-6] or by the cospreading technique[7-8] facilitates the preparation of well-defined organized monolayers of those molecules. Another way of obtaining monomolecular films of hydrophobic non-amphiphilic compounds is including them into host monolayers.[9]

Once the monolayer has reached a selected π at the air-water interface, which involves a specific molecular orientation, it could be transferred onto a solid substrate to fabricate mono- or multilayered Langmuir-Blodgett films (LB films). When the substrate moves through the monolayer at the air-water interface, the monolayer is deposited onto the solid substrate as shown in Figure 2.

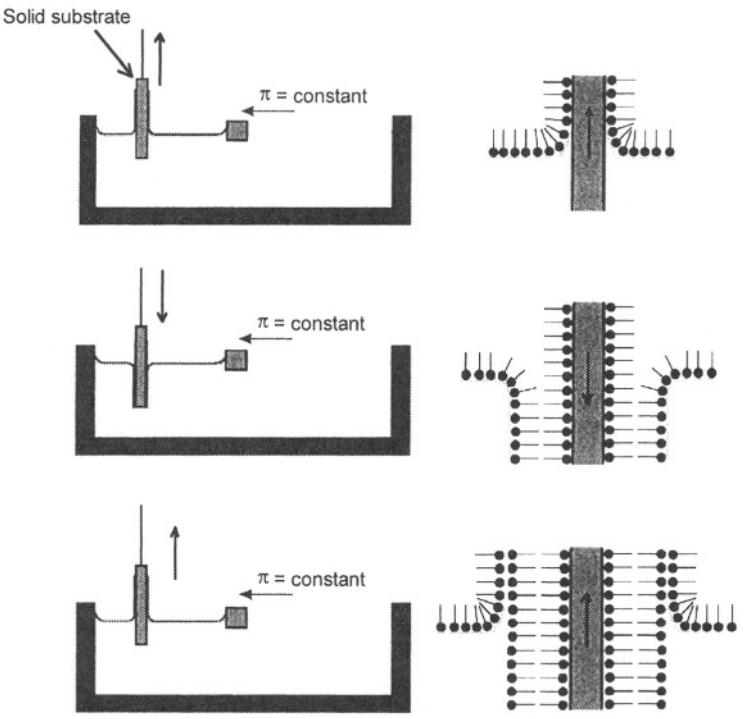

Figure 2. Schematic setup of a multilayer Langmuir-Blodgett film deposition process.

At this point, it is necessary to define the transfer ratio (TR) as the ratio between the decrease of area occupied by the monolayer at the air-water interface, at constant pressure, and the area of the solid substrate coated with the monolayer. Ideally, TR should be one; in practice, it may be greater (when the molecules are slowly dissolving into the subphase) or smaller (when incomplete coverage of the solid substrate is achieved).

The form of LB film deposition determines different types of ordered LB films that can be distinguished:

X type film: it is obtained when the floating monolayer is only transferred to the substrate as it is inserted into the subphase (downstroke process).

Y type film: layers are deposited on the substrate during both up- and downstroke processes. When the substrate surface is hydrophilic, for instance, the first monolayer is transferred as it is raised through the air-water interface. Subsequent monolayers are deposited on each traversal of the interface. As shown in Figure 3, either a head-to-head or a tail-to-tail film pattern is obtained.

Z type film: it is obtained when the monolayer is only transferred to the substrate as it is removed from the subphase (upstroke process).

Thus, *Y type* LB film gives rise to a centrosymmetric multilayer arrangement, whereas *X*- and *Z- type* LB films result in a non-centrosymmetric arrangement. As described above, the LB method permits the construction of complex monolayer assemblies consisting of supramolecular structures, where monolayer components are organized by external control, taking into account specific intermolecular interactions existing in each system.

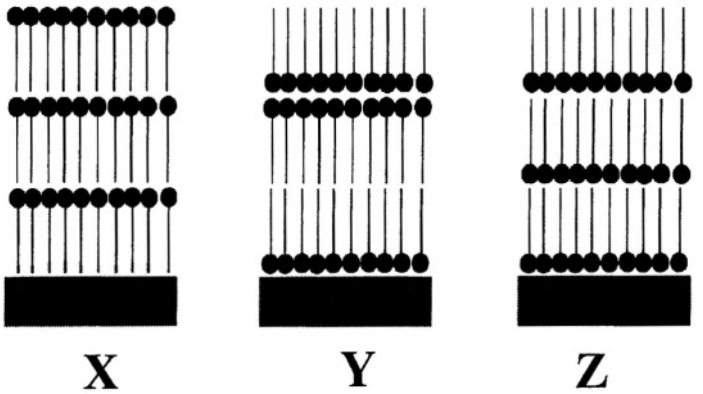

Figure 3. Types of Langmuir-Blodgett films.

The main interest of LB systems relies on the great number of properties that they can exhibit, based on the molecular material used for their construction and on the molecular organization. Indeed, the attachment of a functional group molecule to the polar hydrophilic group or long chain hydrocarbon tail leads to a functionalized molecule which can be manipulated and assembled in supramolecular devices with a specific molecular architecture and diverse properties as described in the following sections.

2. LIQUID CRYSTALS

Liquid crystals (LCs) are structurally intermediate between liquids and solids, i.e. LCs can be defined as fluids where a certain order in the arrangement of the molecules exists. LCs are formed by anisotropic molecules and exhibit thermodynamically stable phases between the liquid and solid states, which result from their anisotropic interactions, and are called liquid crystalline phases or mesophases.

Liquid crystals can initially be classified into *thermotropic,* where the transition between phases is driven by temperature changes, and *lyotropic* type, in which the transition is caused by the concentration of the components.

The most usual *thermotropic* LCs are composed of organic molecules with rod-shaped backbones joined to flexible aliphatic tails. Nematic and smectic LCs phases can be observed at temperatures intermediate between that corresponding to isotropic liquid and that of the crystalline phase(s). The nematic crystalline phase is the least ordered LC phase, in which the molecules have no positional order, but long-range orientational order, that is, they are oriented with their long molecular axis in a preferred direction around which the molecules fluctuate (Scheme 1). This average molecule orientation is described by an unit vector, *n,* called the director of the liquid crystal.

On the other hand, smectic LCs possess a higher degree of order because, in addition to the orientational order of the director, they also have one-dimensional positional order into layers, i.e. they are ordered in layers. Several smectic phases that differ from one another in the tilt angle the director forms with respect to the layer normal, and in the molecular arrangement of molecules within each layer, can be distinguished (see Scheme 1).

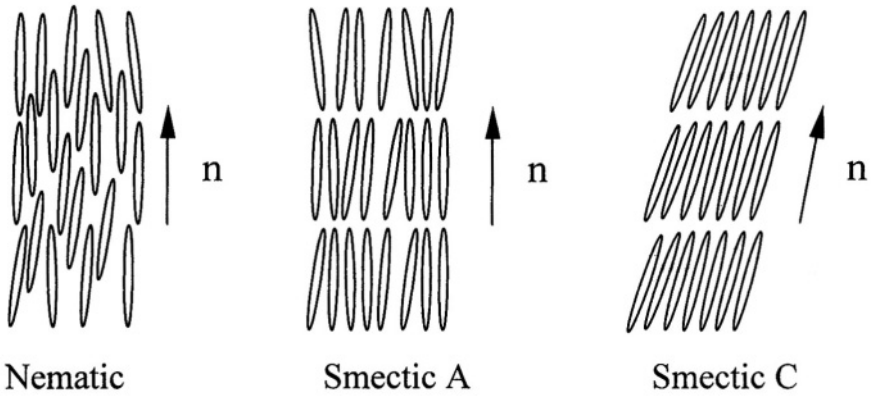

Scheme 1. Depicting of different liquid crystal phases.

The simplest is the smectic A phase, characterized by a director oriented parallel to the layer normal and random positional order within the plane. In the smectic C phase, the director makes a tilt angle relative to the layer normal and has the same random order within layers. Substances which present the smectic A phase also often exhibit the smectic C phase at a lower temperature since the tilt angle normally increases with decreasing temperature. Moreover, other smectic phases with some positional order within the layers (e.g. hexagonal packing) can be found.

In addition, molecules with a disk-like core attached to a number of aliphatic tails give rise to LCs, named discotic liquid crystals. Discogenic molecules can form either discotic nematic phases (ND) or columnar phases with long-range intercolumnar order or only short-range intracolumnar order, depending on the temperature and molecular geometry.

As mentioned above, liquid crystals may also be *lyotropic.* Such liquid crystals, although sharing some basic features with the *thermotropic* liquid crystals, differ from these in structure, properties and applications. Their organization is normally based on the interaction between two, or more, molecules in solution. Thus, the observed phases depend on the concentration of the different components added to the mixture rather than on temperature. These types of liquid crystal are very common in cell membranes, where both, thermotropic and lyotropic, forms of liquid crystals exist.

During recent years, LC field has attracted a considerable attention because of their potential applications as sensors, anisotropic conductors, and electrooptic devices such as flat screen panels, modulators, calculators..., due to their capability for organization in highly anisotropic structures at the air-solid interface. Besides, the operation of such LC displays and devices (LCDs) requires an uniform orientational alignment over large areas in LC cells. Therefore, the orientation of LCs induced by a solid surface is crucial in the production of LCDs in the absence of an external electric or magnetic field. The techniques used to obtain a preferred orientation, called anchoring direction, lie on inducing physical or chemical interactions between a substrate and the LC molecules. In this context, an important issue concerning the LCs is to relate the observed anchoring conditions with the structure of interfaces, and to find out the microscopic interactions that are responsible for a preferred orientation in LCDs. On the other hand, the interfacial ordering and interactions between LC molecules could be also investigated by using the

ordered mono- or multilayer formation of molecules induced by the application of a surface pressure at the air–water interface. For that reason, the LB technique represents a convenient method to systematically study and handle LC systems. However, it is beyond the aim of this chapter to cover in great detail the self-organized assemblies, Langmuir and LB films of LCs which could constitute a separate work by themselves. The reader is referred to the review published by Janietz.[10]

2.1. Alignment Properties of Langmuir-Blodgett Films in Liquid Crystal Cells

The first report about LC alignment using LB films was given in 1994 by Hiltrop and Stegemeyer,[11] who used lecithin films. Since then, it has been well-established that the deposition of LB films with predefined thickness and order on LC cells induces the alignment of liquid crystals at the macroscopic level. The surface density of molecules on LB layers is suitable to allow the homeotropic anchoring of nematic LC molecules, that is, their insertion into the hydrophobic region of the surfactant. In following years, a great number of molecules have been tested as aligning materials.

The typical liquid crystal cell is a sandwich construction where the LC substance is encapsulated between two substrates. These are covered on the inside with a conductive layer and an aligning material, both of them transparent. The conductive layer, for instance indium tin oxide (ITO), is needed to apply an electric field over the cell, and the aligning layer is used to control the orientation of LC molecules next to the substrates. Such layer could be prepared by covalent bonding (self-assembled monolayers, SAMs), LB deposition or spin coating onto solid substrates.

Systematic studies about alignment dynamics and properties of typical amphiphilic molecules, such as fatty acids, as aligning materials have been performed using nematic LC cyanobiphenyl derivatives (CB) or N-(4-methoxybenzylidene)-4-butylaniline (MBBA).[12-13] With that purpose, monolayers of fatty acids at molecular surface densities corresponding to the liquid condensed phase were transferred onto ITO plates. After that, the cells were filled with the nematic liquid crystal MBBA at room temperature. An LC alignment process takes place during and after cell filling and it has been studied by polarization microscopy, electro-optics and non-linear optics. When looking at liquid crystals under a microscope, the LC cell is inserted between crossed polarizers. The first, often called as the *polarizer,* makes sure that the incident light is linearly polarized in one specific direction. Since the polarizers are crossed, no light would emerge through the second polarizer, named *analyzer,* if the LC was absent. However, as the light passes through the anisotropic sample, its polarization state is altered, and thus some of it may pass through the *analyzer*. The LC sample now appears in bright colors, because the effect is wavelength dependent, and the LC alignment process is then easily observed.

Therefore, while the LC cell was filled, a colored image was obtained because of the birefringence of LC. This behavior indicated that the molecules were parallel to the polarizers, i.e. the orientation of nematic LC molecules was quasi-planar with preferred orientation along the filling flow direction (Figure 4, left). Once the cell was filled, an alteration on the LC alignment took place until the whole cell surface adopted a surface induced homeotropic orientation, where the long axes of the LC molecules were oriented perpendicular to the planes of the polarizers or substrate (Figure 4, right). On the homeotropic state, the LC cell appeared completely dark.

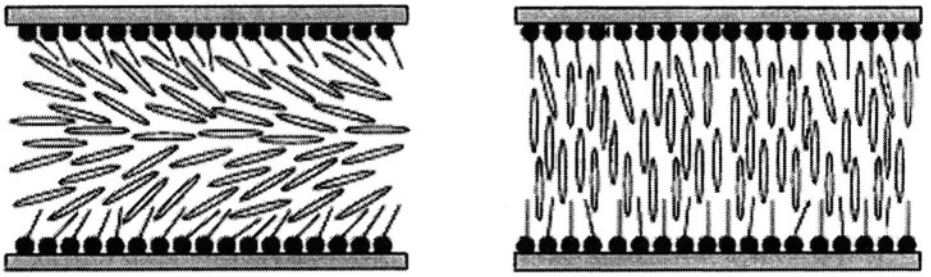

Figure 4. Quasi-planar (left) and homeotropic (right) alignment of LC molecules in a liquid crystal cell.

The aligning properties of nematic LC in cells modified by pure and mixed LB films were observed with each of the fatty acids used in this study, although the LC ordering quality was quite different depending on the type and composition of the monolayers. Thus, stearic acid was found to be very good for aligning nematic LC in the homeotropic state, while behenic acid does not yield a well-defined LC alignment.

Likewise, the speed of expansion of homeotropic domains in LC cells was also clearly sensitive to the surfactant layer, being proportional to the anchoring strength of the liquid crystal. This fact suggested the capability of tuning the anchoring strength by selecting the appropriate composition of the aligning monolayer. To explain it, a model was proposed assuming the mobility of the alkyl chains of amphiphilic molecules and the possibility of being deformed by the LC flow. According to this, when the flow ceases, the chains tend to relax to their equilibrium state with a speed depending on the monolayer composition. In the equilibrium state, the chains are in the upright position and their movement is only due to thermal fluctuations. At room temperature, these fluctuations do not disturb the homeotropic LC alignment. However, in the case of mixed monolayers, on lowering the temperature from the isotropic phase, they prevent the transition from the isotropic to the nematic-homeotropic phase. This behavior could be explained because the different chain length of surfactant molecules induces that the upper segments of the longest chains undergo strong fluctuations, not allowing then the insertion of LC molecules.

In addition to the type of pure and mixed surfactant monolayers, other experimental factors have to be considered on the homeotropic LC alignment process, such as cell thickness, The speed of expansion of the homeotropic LC alignment clearly decreased as the cell thickness increased. This fact is in agreement with the model above described, which involved the elastic relaxation of the liquid crystal splay-bend deformation and the relaxation of the deformed alkyl chains on the LB. The speed of expansion of the homeotropic domains as a function of the cell thickness, *d,* for different aligning materials is given by the equation:

$$\nu = \nu_s + Bd^{-2} \tag{1}$$

where ν_s, called surface relaxation speed, is a constant which depends on the LB aligning monolayer, and B is a proportionality factor which depends on the characteristic elastic constant of the splay-bend deformation of the LC (K) and on the bulk LC viscosity (γ).

On the other hand, the use of chromophores like azobencene molecules and derivatives (noted as Az) has been the basis of a method for photochemical and reversible orientational regulation of LC alignment, through the deposition of monolayers onto solid substrates. The layer of photoreactive azobencene derivative molecules could be prepared by covalent bond [14-15] or by deposition of LB films[16] on quartz substrates. As previously described, the LC cells were constructed by inserting the LC molecules between two Az-modified surface plates.

The LC alignment change was proved by looking at LC in a polarization microscope. As soon as the LC cell was constructed, it appeared bright between crossed polarizers, becoming completely dark with time. The alteration mechanism was clearly driven by light since, when the cells were exposed to UV light, they became bright between the two crossed polarizers, indicating the appearance of birefringence of the LC layer. Also, the alignment change was corroborated by monitoring the transmitted light intensity of a polarized He-Ne laser beam through the LC cell and a crossed polarizer placed behind the cell. The photoresponse showed a discontinuous increase and decrease in the transmittance upon alternate exposure to UV and visible light. This phenomenon was attributed to the LC alignment changes from homeotropic to planar alignment, where the long axis of the nematic LC molecules has been reoriented from perpendicular to an almost parallel way with the substrate surface. The changes were induced by the reversible cis/trans photoisomerization of Az derivative molecules on the substrate upon UV illumination. The reversible alignment switching of LC molecules can be described then in terms of collective host (azobencene)-guest (LC molecules) recognition in the proximity of the interface.

The efficiency of the photoinduced LC alignment could be affected by a number of experimental conditions which has to be controlled in order to enhance the process.[15-16] The first concerns the molecular structure, since the hydrophobic nature of the substituent at the azobenzene moiety holds an important role in the alignment regulation. When the Az is covalently bound to the solid substrate, it has to be considered the mode of silylation and the length of the spacer unit between the Az moiety and the silylating group as key factors in regulating the LC alignment. Furthermore, there is a critical area occupied by an Az molecule for the photoregulation of LC alignment, then a molecular area larger than critical area value results in no photoregulation. Finally, the cell thickness and the light exposure cycles also influence on the observed photoresponse.

The dynamic and reversibility of photoswitching alignment process taking place between the Az layer and LC molecules has been modeled using an interface system.[17-18] This approach involved the use of Langmuir films composed of mixtures of an amphiphilic polymer containing Az side chain and a nematic LC molecule, 4'-pentyl-4-cyanobiphenyl (5CB). Only when the cospreading technique was used, both components of the mixed monolayer were found to be oriented perpendicular to the air-water interface. The orienting interaction, induced by the interpenetration of the rod-shaped components, was characterized under different experimental conditions.[17] After deposition, the obtained LB films were a convenient interface model of the command surface that promotes the LC alignment alteration, although some discrepancies in dynamic properties, attributed to difference in the dimensionality of LC molecules, were found.[18]

Many nematic LCs are not able to form stable monolayers at the air-water interface because of the lack of a polar group. However, its incorporation into a host monolayer of amphiphilic compounds, such as macrocycles with suitable cavities (e.g. calixarenes)[19] or

polymers, opens a way to obtain a monomolecular layer with these compounds, and its alignment as well.

2.2. Studies of Liquid Crystalline Phase Rheology in Langmuir Films

The liquid crystalline behavior is a typical feature of two-dimensional molecular layers, however, in bulk solution it is limited to few specially designed substances. Likewise, the nature and molecular arrangement of the liquid condensed monolayer phases are similar to mesophases found in the smectic LCs above described.[20] Also the optical textures are comparable to those obtained in liquid crystal by polarization microscopy. Then, the Langmuir technique could be considered as an useful tool to infer LC properties which later would be extrapolated to bulk LCs.

The coupling of molecular orientation to flow is well understood for bulk nematic LC phase and the mechanism can be extended to 2D systems. However, there is no understanding of the coupling of structure to flow in the hexatic liquid crystalline phase, often exhibited by molecular monolayers. This constituted the purpose of an interesting work performed by Schwartz′s group. They determined the correlation of the flow and the structure of several crystalline phases in a Langmuir monolayer, based on a microscopic interpretation of the observed phenomena. The investigation combined simultaneously the Langmuir technique and Brewster Angle Microscopy (BAM), allowing the observation of interfacial thermodynamics and rheology of crystalline phases of molecular films at the air-water interface.[21-25] Thus, a monolayer of docosanoic acid, $CH_3(CH_2)_{20}COOH$, was studied in three different hexatic liquid crystalline mesophases, denoted as L_2, L_2' and Ov. The behavior of the interfacial flow of the Langmuir monolayer through a channel, was systematically studied throughout the different condensed monolayer phases as a function of flow rate, temperature, and alkyl chain length.[21-22]

The application of a shear flow to the hexatic condensed phase of the monolayer was also investigated. Previous works showed that L_2' phase monolayers of $CH_3(CH_2)_{20}COOH$, composed by a mosaic of domains with different reflectivities, evolved toward larger domains with only two highly contrasted reflectivities under flow conditions.[26-27] In analogy to the behavior of a 2D nematic phase under flow conditions, docosanoic acid molecules can become aligned at a certain angle with the flow (flow alignment) or describe periodic orbital movements around an axis perpendicular to the air-water interface (tumbling). In the case of the hexatic phase, this fact was interpreted as molecular alignment with the flow, although it was not clear whether the origin of the flow effects comes from distortions in the underlying lattice or from a direct coupling with the tilted alkyl tails. The latter situation would be in agreement with the nematic phase, where the average orientation of the molecules is governed by the flow.

However, the application of a shear flow presents significant differences on the structure of Langmuir monolayers of docosanoic acid in the hexatic phases L_2, L_2' and Ov.[23-25] Thus, continuous changes in domain reflectivity and propagating fronts are observed in the L_2 and L_2' phases, while only propagating fronts are observed in Ov-phase monolayers. The application of consecutive shear-reversal cycles results in an increase in domain size in the L_2 phase, and in fragmentation of the domain structure in the Ov phase. The analysis and understanding of the effects of flow have to take into account the structure of the monolayers, including the ordering of the underlying lattice and the ordering of the alkane tails (polar tilt, azimuth angle, lattice-bond coupling, and

herringbone order). Therefore, the quantitative analysis of the observed transformations leads to propose a mechanism involving a reorganization of the structure of the underlying lattice, followed by the realignment of the alkane tails. The suggested mechanism differs from that expected for 2D nematic liquid crystals. The main difference is that flow acts directly on the preferred molecular orientation in a nematic phase, whereas the behavior in a hexatic monolayer is governed by the local unit cell orientation.

3. LUMINESCENCE PROPERTIES: ORGANIC LIGHT-EMITTING DIODES

The environment and orientation of functional molecules may be controlled by incorporating them in molecular assemblies. Handling and assembling ordered ultrathin films containing different molecules with various functions and well-defined architecture (composition, structure, and thickness) is a promising way for constructing molecular devices. In this sense, the LB method has been used for fabricating organic light emitting diodes (OLEDs).

3.1. The Light Emission Phenomenon and Devices

Electroluminescence (EL) is a non-thermal generation of light resulting from the application of an electric field to a substrate, being the light emission from an active material as a consequence of optical absorption and relaxation by radiative decay of an excited state.[28] The excitation is accomplished by recombination of charge carriers of opposite sign (electron and hole) injected into an inorganic or organic semiconductor beyond a specific threshold voltage depending on the material applied. In the presence of an electric field the charge carriers move through the active layer and are non-radiatively discharged when they reach the oppositely charged electrode. However, if a hole and an electron encounter one another while drifting through the organic layer, excited singlet and triplet states, so-called excitons, are formed. The singlet state may relax by emission of radiation.

OLEDs represent a promising technology for large, flexible, lightweight, flat-panel displays. Such devices consist of one or several semiconductor organic layer(s) sandwiched between two electrodes. When an electric field is applied, electrons are injected by the cathode into the lowest unoccupied molecular orbital (LUMO) of the adjacent molecules, and simultaneously holes are injected by the anode into the highest occupied molecular orbital (HOMO).

The two types of carriers migrate towards each other and a fraction of them recombine to form excitons, some of which decay radiatively to the ground state by spontaneous emission. The simplest emitting diode consists of just one layer located between the hole and the electron injecting electrodes. The active organic material has in this case to provide several functions simultaneously.[29-32] It has to act as transport layer for holes as well as for electrons and, also, it has to control the recombination process giving rise to emission of light (Figure 5). Optimization procedures aimed at increasing the quantum efficiency and at reducing the onset field for emission have been severely limited in such one-layer devices, therefore multilayer devices have been considered as a possible solution and, for instance, three-layer devices consisting of one hole and one electron transport layer separated by an emission layer have been fabricated.[33-34]

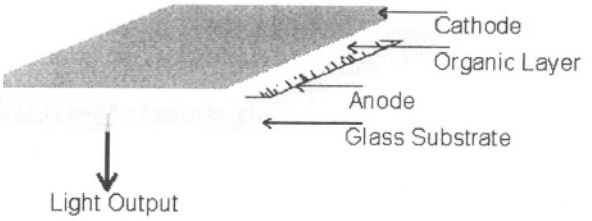

Figure 5. The simplest OLED device structure (Anode/Organic Layer/Cathode).

An optimized OLED device has a thin film multilayer structure, where a specific function has been assigned to each layer. Thus, the hole injection, hole transport, the emissive and electron transport layers are organic thin films sandwiched between two electrodes, the anode (for example, ITO) and the cathode (usually a reflective thin film of a low work function metal). These types of devices emit photons as a result of the following processes: (1) Charge injection of electrons through the cathode and holes through the anode (ITO); (2) Charge transport of the electrons to the lowest unoccupied molecular orbital (LUMO) of the organic electron transport layer (ETL), and holes to the highest occupied molecular orbital (HOMO) of the organic hole transport layer (HTL); (3) Charge injection (and blocking) at the organic-organic interface; (4) Production of excited singlets via charge recombination; (5) Migration of excited singlets; (6) Light emission from some of the excited singlets (see Figure 6). Several parameters are used to test the efficiency of these types of devices:

Internal EL quantum efficiency of an OLED, η_{int}, is defined as the ratio of the number of photons emitted per electrons injected and it can be calculated from the measured *external EL quantum efficiency,* η_{ext}, by using

$$\eta_{int} = 2n^2 \eta_{ext} \tag{2}$$

where n is the refractive index of the organic layer. Likewise, the *internal EL quantum efficiency* has been defined[35] as the ratio of the number of photons produced within the device to the number of electrons flowing in the external circuit,

$$\eta_{int} = \gamma r_{st} q \tag{3}$$

where γ is the ratio of the number of exciton formation events within the device to the number of electrons flowing in the external circuit, r_{st} is the fraction of excitons which are formed as singlets, and q is the efficiency of radiative decay of these singlet excitons. The efficiency of radiative decay depends on the device structure, being strongly affected by the photonic structure of the device, e.g., the proximity of metallic mirrors. In order to achieve efficient luminescence, it is therefore necessary to have good balancing of electron and hole currents, efficient coupling capture of electrons and holes within the emissive layer, strong radiation transitions for singlet excitons, and efficient coupling of these excitons to photon states allowed in the device structure.

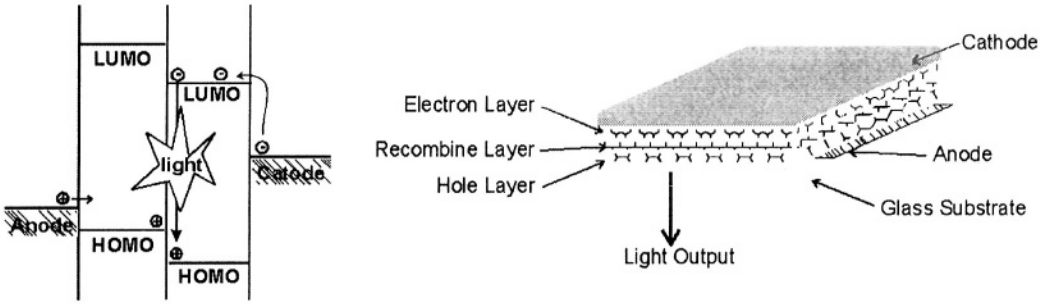

Figure 6. Schematic energy band diagram of a multilayer (hole and electron transport layers) molecular LED (left), and a sample of OLED device structure consisting of three layers (Anode/Hole layer/Recombine layer/Electron layer/Cathode) (right).

Power efficiency, η_{pow}, is the ratio of output light power to input electric power, and can be determined from η_{ext} using the known values of the applied voltage U and the average energy of the emitting photons E_p asfollows

$$\eta_{pow} = \eta_{ext} E_p U^{-1} \tag{3}$$

Luminous efficiency, η_{lum}, is determined by multiplication of η_{pow} by the eye sensitivity curve S as defined by the Commission Internationale de L'Eclairage (CIE). This function pays regard to the fact that the human eye possesses distinct sensitivities with respect to different colors

$$\eta_{lum} = \eta_{pow} S \tag{4}$$

Finally, the *brightness* of an OLED (given in $cd \cdot m^{-2}$) is also used by several authors to estimate the efficiency of their device.

3.2. Background of LED Formation by Using Organic Materials

The light emission by this type of devices was first discovered for inorganic materials in 1936, observing high field electroluminescence from a ZnS phosphor powder dispersed in an isolator and sandwiched between two electrodes.[36]

However, since materials used to fabricate LEDs are complex, more difficult to produce and to process, the evolution of an analogous technology was needed in order to improve automation, cost reduction, size of crystals grown, defect densities and volumes of devices.

Because of the high photoluminescence (PL) quantum yields common in organic molecular semiconductors, there has long been interest in the possibility of light emission by these organic semiconductors through charge injection under an applied high field (electroluminescence). Light emitting devices based on organic materials have advantages compared with conventional semiconductor devices.

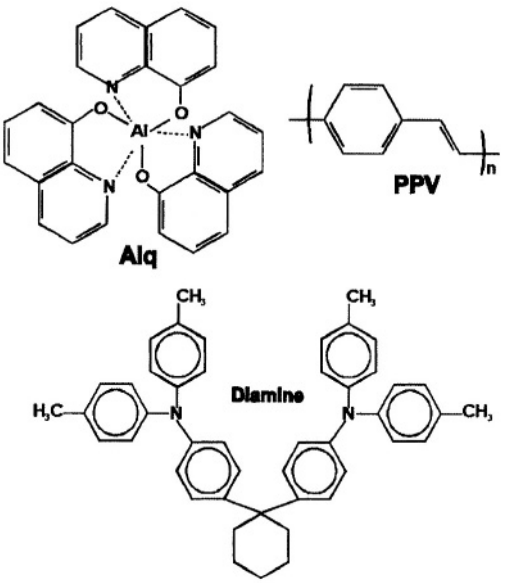

Scheme 2. The molecular structures of some former active organic materials for LEDs.

They can be easily tailored with respect to characteristic electronic properties such as the magnitude of the band gap or the photoluminescence yield, for instance to produce a polarized emission (the tunability of their emissive color can be adjusted by structural modifications), and they can be optimized with respect to their mechanical properties. The performance of such devices, the diode characteristics, the onset voltage for emission or the long-term stability as well as the quantum efficiency will depend not only on the electronic properties of the films and electrodes, but also on the thickness of the films and their smoothness, on the internal morphology of the films and on possible orientations of chromophores within the film.[37] Organic materials are much cheaper to produce than their inorganic counterparts and they can be processed even as very thin films in the range of 100 nm thickness. OLEDs can be operated with low DC voltage and use significantly less power than comparable inorganic LEDs or backlit liquid crystal displays (LCDs). Another improvement is their capability to be illuminated uniformly over a large area and the possibility of making complex character patterns.

Electroluminescence from organic crystals was first observed for anthracene in 1963.[38-39] However, the development of a new generation of light-emitting diodes with organic thin-film electroluminescence was spurred on in the 1980s through the work of Tang and VanSlyke,[33] who demonstrated efficient electroluminescence in two-layer sublimed molecular film devices. These devices consisted of a hole-transporting layer of an aromatic diamine (Scheme 2) and an emissive layer of 8-hydroxyquinoline aluminum (Alq_3) (Scheme 2)- ITO, as the hole-injecting electrode, and a magnesium-silver alloy as the electron-injecting electrode.

In 1990, Burroughes at al.[29] overcame the drawback of expensive and technologically inconvenient vapor deposition of fluorescent dyes and inorganic semiconductors by using a highly fluorescent conjugated polymer (poly-*p*-phenylene-vinylene, PPV, Scheme 2) as a thin film of the active organic material (30-500 nm), which is sandwiched between two electrodes (ITO/PPV/A1). Their greatest merit was that

they indicated for the first time the possibility of producing large area displays by simple coating techniques.

Conjugated polymers have drawn intense research interest as active materials for such devices, due to their unusual electrical and optical properties, reasonable chemical stability, and easy processability.

3.3. Lifetime, Efficiency, and Thickness of OLEDs

The initial works mentioned above have stimulated huge industrial and academic research interest all over the world. Main targets are the improvement of device characteristics such as lifetime and efficiency, and the development of new materials for electrooptical applications. Thus, the preparation of more device structures involving multiple emissive or transport layers, the employment of flexible and transparent electrodes, the optimization of device manufacture techniques, and the development of models in order to obtain an insight into the basic processes of charge generation, transport and recombination are investigated. Likewise, the synthesis of a great variety of polymeric, oligomeric, and low molecular weight materials with different color emissions, electron affinities, ionization potentials, and fluorescence efficiencies is encouraged.

Some strategies have been used to achieve the aims described above.[40] For instance, by shifting the recombination zone towards the center of the organic layer and introducing multilayer OLEDs in which electron and hole transport are performed in different materials and layers, can provide a balanced charge injection, and in turn, the electron and hole injection rates can be better controlled by creating barriers for the charge transport at the heterojunction between semiconducting layers.

On the other hand, the synthesis of oligomers and polymers with higher electron affinity in order to guarantee balanced charge injection can enhance the lifetimes and efficiencies of the corresponding diodes. One way to improve the structural stability of these organic layers is to move from molecular to macromolecular materials, and conjugated polymers are a good choice in that they can, in principle, provide both good charge transport and also high quantum efficiency for the luminescence. Much of the interest on conjugated polymers has been devoted to their properties as conducting materials, usually achieved at high levels of chemical doping.[29]

Doped π-conjugated polymer layers improve the injection of holes in OLED devices; this is thought to result from the more favorable work function of these injection layers compared with the more commonly used layer material (ITO). By increasing the doping level of such polymers, the barrier to hole injection can be continuously reduced. This concept is applied in OLED devices with the hole-limited electroluminescence, finding that it is possible to significantly reduce the operating voltage while improving the light output and efficiency.[41]

The effects of incorporating fatty acid layers into single layer and dual layer organic light emitting structures have been studied. The insertion of arachidic acid (AA) layers between a poly-(2-methoxy,5-(2´ethylhexyloxy)-*p*-phenylenevinylene) (MEH-PPV) film and an aluminum cathode was found to decrease the turn-on voltage for electroluminescence and to double the quantum efficiency. In contrast, depositing the fatty acid layer between the polymer and the ITO anode produced little change in the device efficiency. Dual layer structures using MEH-PPV as the light emissive layer and poly-(*p*-(3-hexyl pyridylene)) (HPPPy) as an electron transport layer were also tested and

an increase in device efficiency could be obtained by placing the AA layers immediately beneath the aluminum.[42] The anode electrode can also be treated, for example, with a copper phthalocyanine as hole injecting layer in order to reduce the driving voltage and increase the device performance.[43-44]

Also, the performance of the device could be improved with some changes in the electrodes (anode or/and cathode). The possible effects of introducing an insulating layer into a metal-insulator-semiconductor structure can: (i) control transport; (ii) shape the electric field in the devices; or (iii) introduce fixed charge, and therefore modify the work function of the metal electrode. By choosing low work function metals such as Ca and Mg to reduce the energy barrier to electrons, high efficiencies can be achieved, although these metals are usually reactive in an air atmosphere. Another approach is to insert an inorganic insulating layer such as CaO, SiO_2 and LiF beneath the cathode electrode. This has been found to improve the electron injection. The anode electrode, usually ITO, can be treated, e.g. with an oxygen plasma, to reduce the turn-on voltage and increase the device performance.

Finally, the preparation methods of the OLED layers seem to be important in order to increase the molecular order and consequently the efficiency of the corresponding devices. In this way, the organic layers can be generated by procedures such as layer-by-layer processes taking advantage of self-assembling,[45-47] or Langmuir-Blodgett (LB) techniques.[48-50]

3.3.1. Layers of OLED Prepared by the Langmuir-Blodgett Technique

The Langmuir-Blodgett technique offers an alternative method of depositing ultrathin, ordered and thickness-controllable layers which are relatively defect-free. As for the light emitting diodes (LEDs), a tradeoff exists in developing techniques to achieve a precise molecular organization of the active moieties in order to control transport and emission properties. In this respect, the LB technique is a way for the achievement of improved self-organized systems of active electroluminescent molecules. Indeed this technique allows a good molecular order and a molecular alignment needed in the case of polarized light emission. Moreover, the use of LB or absorbing layers improves the charge injection at the ITO electrode, i.e., the operating voltage could be drastically reduced, and as a result the lifetime of LEDs can be increased.

The most often used technique for the preparation of thin films with polymeric materials is spin-coating. However, the LB technique, with the advantage of precise control of the thickness down to the molecular scale, together with the self-assembly (SA) technique, allow to study and model polymeric devices with approaching molecular thickness. On the other hand, the degree of order and the type of supramolecular organization obtained with spin-coating and LB techniques are very different. By comparing the properties of films prepared with these techniques, it is possible to study the behavior of LEDs as a function of film thickness and to investigate the properties of the metal/polymer interface during device operation. By varying the supramolecular organization in the films, some information on the role of the structural order can be inferred.

The challenge of fabricating thin film devices by LB techniques is to transfer films with vertical deposition while preserving their good photoluminescence and electroluminescence properties. Thus, vertical depositions can be realized by doping polymers with long chain fatty acids. But, as mentioned earlier, defects in films, in the

form of either impurities or cavities, are detrimental to electrical properties, left alone the fact that the films made are usually unstable and the polymer chains are randomly oriented. A better approach is perhaps to modify the molecular structure of such polymers to render them amphiphilic. The overall structure of such a polymer could have one-half of the side chains staying in the water while the other half stay in the air, thus providing a suitable amphiphilicity, preserving at the same time a high degree of conjugation that is essential for electrical and optical quality.

The use of amphiphile as an extractable agent for delivering the polymer succeeds in preventing premature aggregation and providing effective molecular lubrication. However, as a disadvantage the charge carrier transporting ability of these types of films can be reduced because of the presence of pinholes within the film. The formation of those defects could be due to some local phase separation processes, and consequently to reduce or eliminate the phase separation, water soluble amphiphiles with better miscibility with the polymer may be used. For example, the hydrophobic part of the soluble surfactant may be modified to increase the compatibility with the active component, and the hydrophilic part can also be modified to adjust the solubility, for example, by pH control. The subphase and the temperature are also tunable for optimal conditions. Since the dissolution of amphiphiles is a function of time and surface pressure, both are also influential parameters. Overall, the spreading-then-extracting method provides a flexible alternative to manipulate polymer films which have little or no amphiphilicity. The macroscopic homogeneity and the optical isotropy of films prepared by this method may also be useful for constructing thin film photonic devices.

The flexibility and thickness control offered by the LB technique has been used to fabricate LEDs of a porphyrin derivative deposited at two different surface pressures, and the effect of molecular packing of the active layer on LED characteristics has been studied. The molecule is known to form a monomolecular layer (1.5 nm/layer) at lower surface pressure (L) and stacked multilayer LB films at higher surface pressure (H). The I-V characteristics of (H) and (L) devices could be different due to the packing of emitting layers. The closely packed porphyrin macrocycles in POR(H) film form p-type semiconducting layer and thus the I-V curves show asymmetric nature. In (L) structure on the other hand, larger contribution of alkyl chains (non-semiconducting contribution) reduces the overall hole contribution. The (L) layer thus might act as an intrinsic semiconductor resulting in symmetric I-V curves for the devices.[51]

On the other hand, this technique can help to solve some problems related to the use of organic materials for fabricating OLED as commented below. Conventional organic photoconductor materials have low mobility. In general, the low mobilities of such polymeric materials are due to a trap-dominated hopping transport between photoconductive groups, giving rise to a certain localization of charge carriers. The electronic charge-carrier mobilities of organic systems are mainly determined by the supramolecular arrangement and packing of the molecular units involved.

The overlap of molecular wavefunctions is often more important than the molecular structure itself. Thus is not surprising that organic single crystals are the only organic systems known so far to show electronic charge-carrier mobilities comparable to the amorphous inorganic semiconductors which are the mainstream of the microelectronics industry.

It is now widely accepted that the π-overlap between the electronically active transport units is probably the most important parameter for the charge-carrier transport process in organic systems.

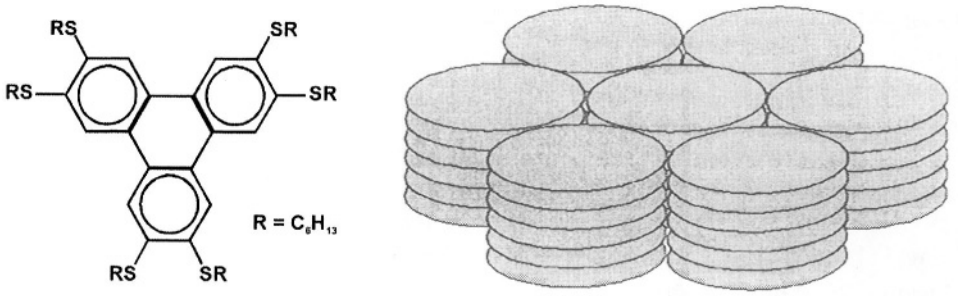

Scheme 3. Molecular structure of a hexahexylthioriphenylene and schematic drawing of the discotic hexagonal phase.

Therefore, order phenomena, on both an energetic and a geometric scale, are strongly correlated with the charge-carrier transport properties. Since order is often dominated by the supramolecular assembly of the molecular transport sites, the approach towards high-mobility organic systems could involve the use of materials like discotic liquid crystals in columnar arrangement (Scheme 3). The molecular units in these materials (e.g. hexahexylthiotriphenylene) self-organized into columnar stacks, providing a favorable face-to-face orientation of the aromatic cores; this leads to a large π-overlap between the adjacent molecular units. This precise molecular organization can be achieved by using the Langmuir–Blodgett method.[52-53]

The handling of the material forming the OLED can sometimes constitute a problem. Solution methods such as casting and spin-coating are often used to prepare soluble organic thin films. Although the solution cast procedure has the advantages of easy operation and low cost, it is very difficult to control the thickness, thickness uniformity, smoothness, and molecular orientation. Most of these characteristics can, however, be controlled by the LB technique through the layer-by-layer deposition process. For instance, the thickness of a Langmuir film of a regioregular poly(3-hexylthiophene) is ~ 33 Å. A device that contains 5 to 10 layers will have a thickness of 160-330 Å. Compared with cast films, which are usually 10^3-10^4 Å thick, the LB film is ultrathin.[54]

The fabrication of multilayer structures by casting and spin-coating is often difficult because the solvent used with the upper-layer material should not dissolve or otherwise deteriorate the underlying layer. On the contrary, the LB technique allows one to control the film thickness on a molecular scale and to fabricate multilayer structures with well-defined boundaries between the different material layers. Although the use of additional charge-transporting and insulating layers in organic LEDs is essential for optimizing the operation and quantum efficiency, this has only recently been studied in the case of LB films. As commented before, interesting studies indicate that a multilayer structure where the hole- or electron-transporting material is contained in a separate layer provides a better control of the charge carrier injection properties than a single layer structure containing a blend of the materials. The balance of electrons and holes can also be controlled by introducing an insulating layer between ITO and the emitting layer to block the injection of holes, thus resulting in an increase in quantum efficiency.[50]

The influence of temperature on the photoluminescence and electroluminescence spectra has been observed for poly(3-decylmethoxythiophene) (PDMT) in ITO/PDMT/A1 as a function of the deposition method.[55] Thus, a strong thermochromism is detected in

the PL spectrum of spin-coating films, which is coherently related to a thermal transition of the polymer, while a very weak thermochromism is observed for the LB films indicating that the multilayered arrangement in planes parallel to the substrate makes them very stable to temperature variations. For the thick spin-coating films (~ 400 Å) the EL spectrum reproduces the PL spectrum measured at about 75-80 °C, while for the thin LB films a blue shift of the EL is observed with respect to the PL, which can be accounted for by a shortening of conjugation length of the polymer due to reactions at the polymer/Al interface. This effect, which has been observed only for LB films, is in fact more valuable in the thinner structures.

As briefly described in this section, OLEDs have greatly been improved with respect to reliability, efficiency and tunability. Their performance is now comparable to, and in some cases even better than, that of commercially available light-emitting devices based on inorganic semiconductors. Moreover, they can produce polarized light and any color in the visible region, including white, which is still difficult to achieve with inorganic materials. Scientists have designed and synthesized a great variety of suitable materials (polyfluorens, polyquinoxalines and poly(p-phenylenevinylene) on one hand and multicomponent systems comprising metal chelates (Alq_3), highly fluorescent dopant emitters (rubrene, coumarins, quinacrione), triarylamines (TPD, NPD) and simple oxadiazole compounds (PBD) on the other hand) over the last couple of years.[40] Only a few of them have been investigated thoroughly. Possibly, the best materials are still unknown or the potential of already available materials has not been recognized. Furthermore, techniques like LB or/and SAM for fabricating OLEDs with good properties have to be taken into account.

4. MAGNETIC PROPERTIES

Magnetism arises from the cooperative behavior of a large number of electron spins and it can be examined at the macroscopic or microscopic levels. The macroscopic level deals with the bulk properties of a material. The bulk magnetic properties of a material, such as magnetic susceptibility (χ) or magnetization (M), involve the ensemble of individual atomic or molecular magnetic behaviors. The microscopic level is associated to the magnetic behavior of individual atoms or molecules. The microscopic magnetic moment (i.e. magnetic moment of a molecule or atom) is called the effective magnetic moment (μ_{eff}). Since magnetism is a cooperative phenomenon, μ_{eff} is related to χ. Moreover, it is important to notice that the magnetic behavior at the macroscopic and microscopic levels may not be identical.

Considering this, conventional magnets (e.g. ferromagnetic iron) can be described as materials consisting of magnetic domains that contain a large number of unpaired electrons with strong interactions, resulting in the alignment of the electron spins in one direction. Most organic materials are *diamagnetic* since the electron spins are paired in an anti-parallel way, and their magnetic moments cancelled. A *paramagnetic* material results when interactions between the molecules are absent, or the electron spins are randomly aligned, leading to an overall cancellation of the electron magnetic moments in the absence of an external magnetic field. However, when interactions between the molecules are non-negligible, the electron spins undergo alignment over large domains below a critical temperature. The alignment could take different forms. Therefore, in an

antiferromagnetic material, the electron spins are locked into an antiparallel arrangement and the net magnetic moment is zero. However, in a *ferrimagnetic* material, an antiparallel arrangement between spins of different strength occurs and they do not cancel completely. In contrast, a *ferromagnetic* material shows a parallel alignment of spin magnetic moments of unpaired electrons within small regions below a critical magnetic ordering temperature, called Curie temperature (T_C). Within each domain, all the spin moments point in the same direction, creating a large magnetization in the absence of a external magnetic field. Above T_C, the behavior is that of a regular paramagnetic material. This behavior is explained because the interaction energy between the spins becomes larger than the thermal energy of the spins at T_C and, as a result, an ordering of unpaired electron spins takes place. Since the interaction energies in most organic compounds are rather small, low T_C values are common. However, high Curie temperatures are necessary for practical applications.

The magnetic susceptibility of a given material varies upon two factors, temperature and applied magnetic field. The four types of magnetic materials above mentioned show different behavior as the temperature and/or field are changed. This fact provides criteria to study the magnetic properties of molecular films and supramolecular devices as are now described.

4.1. Purely Organic Magnetic Monolayers and Films

These monolayers and films are composed of purely organic materials, that is, of organic radicals consisting only of the elements C, H, O and N. An increasing interest in preparing organic ferromagnets has arisen during the last years because they possess interesting properties such as solubility, flexibility, low density, and ability to form thin and transparent films, that make them very convenient to be used in optomagnetic devices. However, by now these magnets cannot compete with inorganic ones in magnetization values.

Two approaches could be used in the design and synthesis of purely organic ferromagnetic materials: the intramolecular and the intermolecular spin alignment. The intramolecular approach occurs when more than a radical is connected through a conjugated chemical coupler, e.g. through a π-conjugated polymer chain. This strategy results in a high-spin molecule. The intermolecular approach, where an assembly of molecules is considered, leads rise to materials with ferromagnetic behavior. As a disadvantage of this approach, the crystalline molecular structure is difficult to predict, and the interaction between unpaired spins in a crystal lattice is unpredictable.

Several novel organic conjugated molecules bearing nitronylnitroxide or imino-nitroxide radicals (Scheme 4) have been designed to study the 2D magnetic behavior of these compounds. It is obviously necessary to control the molecular packing within molecular materials designed for use as molecular magnets due to the cooperative character of the magnetism. Then, the LB technique could be one of the most useful methods to prepare a 2D magnetic organization of radicals. By comparing the properties of bulk materials and films prepared with the LB technique, it is possible to study the magnetic behavior as a function of molecular organization, and information of the dependence of intermolecular spin–spin interaction on the intermolecular orientation may be inferred.

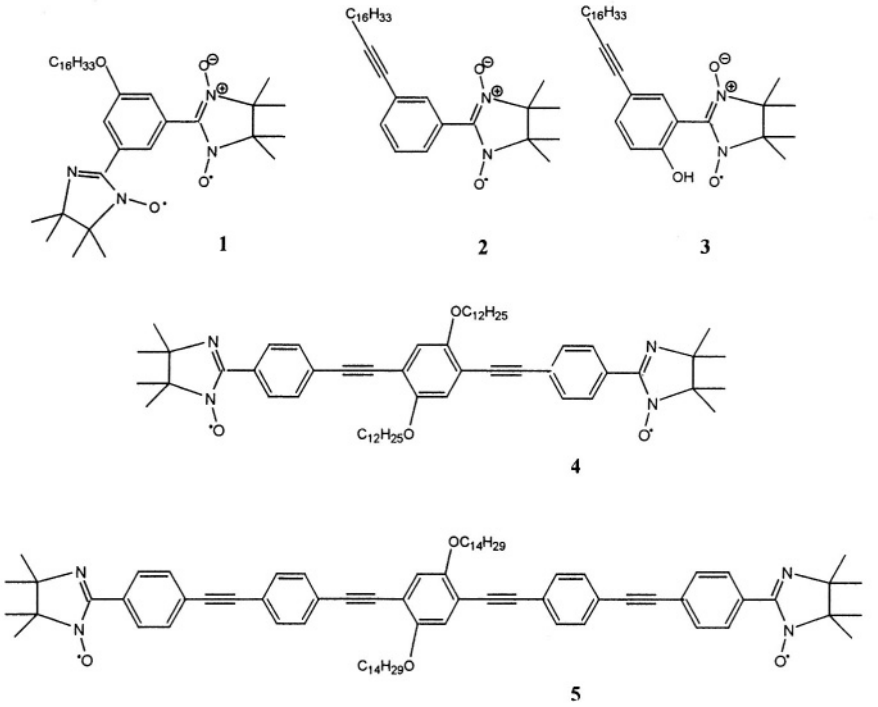

Scheme 4. Molecular structure of some materials for magnetic LB films.

The magnetic behavior of a polycrystalline sample of compound **1**, a benzene ring with nitronyl nitroxide and imino nitroxide radical substituents at the *meta* positions was studied using electron spin resonance (ESR) and superconducting quantum interference device (SQUID) techniques.[56] The integrated intensity of the absorption line of an ESR spectrum is proportional to χ. Hence, the analysis of ESR spectra with temperature is a way of evaluating the existence of magnetic interactions within a bidimensional system. The temperature dependence of magnetic behavior of **1** in bulk solution shows that, above 84 K, the product χT remains almost constant (0.732 emu K mol). Below 84 K, the product increases with decreasing temperature, reaching a maximum at 24 K, and again decreases when lowering the temperature below 24 K. According to that, it could be confirmed an expected intramolecular spin-spin ferromagnetic coupling because of the *meta* positions of the radical substituents in the benzene molecule.

The structure and magnetic properties of Z-type LB films of **1** deposited on quartz glass were also investigated. The first remarkable feature was the dependence of ESR intensity on magnetic field, evidencing the anisotropic character of LB films in their magnetic behavior. This behavior is a typical feature of thin films with magnetic properties. Nevertheless, the most important conclusion of this study came from the analysis of the temperature dependence of the ESR spectra intensity in the LB films. In this case, the product χT remained almost constant above 150 K, and decreased sharply when lowering temperature below 150 K. In this case, the temperature dependence of the magnetic susceptibility clearly does not follow the trend of a ferromagnet, but rather that of an antiferromagnetic material. This fact was later confirmed by SQUID measurements.

Concerning structural studies, X-ray diffraction experiments on Y-type LB films revealed a bilayer structure, where the alkyl chain is tilted approximately 46° with respect to the substrate surface.

In conclusion, the difference in the magnetic behavior of LB films and polycrystalline samples of compound **1** was assigned to the molecular arrangement in both systems. The order and supramolecular organization obtained by LB deposition favored a large intermolecular spin–spin antiferromagnetic interaction over a small intramolecular ferromagnetic coupling contribution to magnetic behavior.

A similar approach was used to prepare high-spin ordered layers of amphiphilic conjugated molecules bearing one nitronylnitroxide radical or two imino-nitroxide magnetically coupled radicals attached at both ends of a rigid rod (compounds **2-5**, Scheme 4).[57-58] It became necessary to know the molecular organization and stability of monomolecular films of these compounds at the air-water interface, where nitronyl nitroxide and imino-nitroxide radicals acted as polar groups. Results obtained by π-A and surface potential-A isotherms, and BAM images, demonstrated a quite different behavior for monoradicals and biradicals.

An exhaustive characterization of the LB films prepared after deposition of mono- or multilayers of compounds on silicon, glass or quartz substrates, showed a property dependence on the substrate type where the films are transferred on, as it was evidenced by optical and diffraction spectra. Results obtained by grazing incidence X-ray analysis (GIXA) on monolayers of **2** and **4** deposited on Si wafers indicated that, for each film, the molecules were oriented almost perpendicular to the substrate.

The electron paramagnetic resonance (EPR) technique has been used to characterize magnetic properties of monolayers of the monoradical **2** and of the biradical **4**, both deposited on hydrophilic quartz plates. A noticeable difference between the EPR spectra of LB films, consisting of a broad single line, as compared to the EPR spectra of radical solutions, well-resolved and with hyperfine splittings, was observed. The fact suggested weak but detectable paramagnetic properties of the LB film. Furthermore, the broadening of the line could be attributed to dipolar interactions and low dimensionality of the LB film.

The molecular structure and magnetic properties of polycrystalline samples and LB films of the monoradical **2** were exhaustively investigated using ESR, SQUID, and X-ray diffraction.[58] For the polycrystalline sample, the layer spacing value was about 29.9±0.2 Å, which is in agreement with a completely extended conformation of the side chain, and a head-to-tail arrangement of amphiphilic molecules. However, the LB monolayer gave a thickness of 22 Å, and consequently, the rigid rod molecules are tilted with respect to the substrate surface.

The ESR spectra of LB films were fully symmetrical, and it was fitted with a Lorentzian derivative, confirming that spins undergo an exchange interaction. In addition, the temperature dependence of the ESR signal was recorded in order to assess the existence of magnetic interactions within the LB films. Again, a discrepancy of magnetic susceptibility measurements of both types of samples as the temperature changes, was appreciated. In the polycrystalline powder of **2**, the temperature dependence of χT in the range from 2 to 300 K was fitted to Curie-Weiss law, from which a negative Weis constant value was calculated. Below 2 K, the product decreases with decreasing temperature. According to those results, the negative value of Weiss constant and χT

decrease at the lowest T reached, the molecular interactions in the bulk material were undoubtedly antiferromagnetic.

On the contrary, the magnetic susceptibility analysis of LB film with temperature gave a perfect fit with the Curie-Weiss law. However, the Weiss constant value was positive pointing toward the existence of ferromagnetic interactions within the film. Again, the LB technique, with the advantage of precise control on the molecular interactions, gave rise to 2D magnetic molecular device starting from a material with antiferromagnetic interactions in the bulk.

4.2. Hybrid Organic-Inorganic Materials

Magnetoelectronics is a rich field to explore, given the intrinsic lamellar structure of devices such as spin valves, magnetoresistive sensors, or magnetic tunneling. Therefore, new lamellar systems with selected magnetic properties, based on a sequential organization of organic and inorganic layers, have been developed. Indeed the Langmuir-Blodgett technique has been extended to create organic-inorganic LB films containing well-organized layers of polyoxometalates (POMs), leading to hybrid materials containing high-spin clusters.[59-62]

POM structures can be described as molecular clusters of close-packed metal oxides of formula $X_aM_bO_c^{n-}$, where M=Mo, W, V... and X= P, Si, B, Co, Fe... Their most important properties are the ability to accept various numbers of electrons giving rise to mixed valence species, and the possibility of accepting d-transition metals at specific sites. These abilities make them very useful to build new materials with electronic, magnetic, and optical properties. Such practical applications rely mostly on the fabrication of POM-based organic-inorganic films, and in consequence several strategies have been developed to prepare lamellar films. The fabrication of lamellar organized materials by using LB technique greatly improves the order and properties of films.

The hybrid organic-inorganic films have been prepared by using a strategy based on the adsorption properties of the polyanion $XW_{12}O_{40}^{n-}$, where X= P^{5+}, Si^{4+}, B^{3+}, Co^{2+}, along a monolayer of a positively charged lipid, as dimethyldioctadecylammonium cation (DODA).[59] A preliminary study to characterize the interactions and optimal conditions of the formation of the Langmuir films involving the cationic amphiphile DODA and different types of anions was performed. The polyanion concentration, pH and ionic strength of the subphase, lipid surface density and the global monolayer charge were experimental conditions that could be modified to optimize the adsorption process at the air-water interface.[60] For instance, by mixing DODA with a negatively charged lipid (or a zwitterionic compound), which modifies the global charge of the Langmuir film, the POM amount in the multilayer LB film was controlled. Furthermore, it resulted to be proportional to the charge of the film. Moreover, no adsorption of polyanions along the gas-water interface could be achieved with neutral or negatively charged monolayers. Hence, the electrostatic nature of the interactions between adsorbed anions and the cationic lipid has opened the possibility of controlling the amount of POMs in the organized LB films, by changing the global charge of the monolayer used for the transfer.

The choice of appropriate polyoxometalate and lipid molecule would allow the construction of LB films having magnetic, optical, or electrochemical properties. Thus, LB films formed by alternating layers of magnetic polyoxometalate clusters and organic donor molecules gives rise to functional molecular materials with magnetic properties. As example, $DODA/CoW_{12}O_{40}$ LB films exhibit magnetic behavior that follow the Curie law

down to about 20 K, as expected for an isolated Co^{II} in a tetrahedral environment.[59] Below this temperature, the magnetic susceptibility decreased because of the zero-field splitting of the S = 3/2 Co^{II} ion, similar to the bulk behavior observed for the potassium salt of this anion. This fact demonstrated that the magnetic site of the polyanion inserted in the LB film is not sensitive to the surrounding charge of the DODA molecules.

Other hybrid systems containing POM molecules, such as $K_6[SiMn(H_2O)W_{11}O_{39}]$ or $K_{10}[Co_4(H_2O)_2(PW_9O_{34})_2]$,[61] and mixed-valence cyanide compounds have been object of later investigations.[62-63]

The promising results obtained in the construction of LB films containing large metal oxide clusters with magnetic properties led to extend this technique as a way of fabricating organized films of single-molecule magnets.[64] In this case, the formation of stable Langmuir films with metal clusters at the air-water interface requires the use of a fatty acid as amphiphilic matrix. This approach implies a mixed acetate (or benzoate) derivative of Mn_{12} clusters and behenic acid Langmuir films. The structure of the LB films was investigated by IR spectroscopy and X-ray diffraction. The obtained results suggested that metal clusters did not modify the matrix organization, and the cluster organization within the films depended on the cluster/behenic acid ratio. Thus, lamellar structures with the clusters organized in well-defined monolayers were observed.

The magnetic susceptibility data provided complementary information on the composition of the LB films, as the amount of Mn_{12} clusters trapped within the LB film. On the other hand, the magnetization data of Mn_{12} cluster films as a function of the applied magnetic field were obtained below and above the blocking temperature of the metal cluster (4 K). The benzoate cluster derivative LB film showed at 2 K a marked and reproducible hysteresis loop with a coercive field of about 0.1 T (0.06 T for the acetate film), which disappeared as the temperature increased to 4 K. The shape of the loop depended on the orientation of the film with respect to the applied magnetic field, corroborating the preferential orientation of the clusters within the layers, with the magnetic axis of the cluster perpendicular to the monolayer.

4.3. Magnetic Nanoparticles

The LB technique has been used to produce bidimensional arrangements of organically functionalized nanoparticles of various types. The potential of this technique lies in the possibility to produce uniform 2D magnetic nanoparticles arrays, while other methods like the evaporation of suspension drops on solid substrates, cannot achieve an uniform nanoparticle arrangement.

The construction of a magnetic nanoparticle Langmuir monolayer involves two important requisites. First, the synthesis of nanoparticles generally leads to polydisperse samples, which makes quite difficult to obtain a homogeneous layer. Consequently, a size-selection procedure has to be performed in order to obtain fractions of almost monodisperse particles. Second, the formation of a nanoparticle monomolecular layer at the air-water interface requires to some extent the hydrophobic character of particles, which could be obtained by coating procedures involving chemical bonding, electrostatic interactions or hydrogen bonds, for instance, thiol ligands chemically bound to the metal surface of gold and silver nanoparticles, or fatty acid molecules weakly bound to the metal-oxide particle surface.

The importance of controlling such factors was demonstrated in the work done by Lefebure et al.[65] This group managed to obtain stable monolayers of hydrophobic

monodisperse magnetic nanoparticles of Fe_2O_3 at the air-water interface. It was shown that iron oxide particles of different sizes, coated with lauric acid, led to non-uniform Langmuir films since the nanoparticles formed dense aggregates whose structure strongly depend on the particle size. Thus, it was possible to observe by transmission electron microscopy (TEM) that, at low pressure, the larger particles (diameter ≈ 15.5 nm) originated interdigitated aggregates, while upon compression they became more compact. However, the smaller particles (diameter ≈ 7.5 nm) formed dense circular nanoparticle assemblies at both low and high surface pressures. This behavior was explained based on the size-dependent balance between van der Waals and magnetic dipole-dipole interactions of molecules. The interactions with an external magnetic field are discussed in the same terms.

The LB technique has been often used to prepare uniform two-dimensional arrays of organically passivated nanocrystal colloids, such as magnetite (Fe_3O_4) and Co-ferrite ($CoFe_2O_4$), under optimized experimental conditions.[66] The magnetite nanoparticles underwent a size-selective precipitation in order to obtain uniform particle suspensions, and, after that, they were coated with oleic acid. The experimental conditions concerning particle concentration in the spreading solution, type of solvent and subphase pH were found to be crucial to obtain a bidimensional and homogeneous arrangement of size-selected nanoparticles.

The magnetic properties of the films were recorded as a function of temperature. Thus, the magnetization curves of Co-ferrite films exhibited hysteresis below 200 K, and the magnetite films below 100 K. Also, the Co-ferrite films had larger coercivity below the blocking temperature than magnetite. The control over the formation of uniform colloidal solutions of magnetite nanocrystals and of 2D arrays on solid substrates could therefore allow the study of interparticle forces between magnetic particles in a well-defined system.

A different approach like adsorption of soluble Fe_2O_3 and Fe_3O_4 magnetic nanocrystallites from an aqueous subphase along an interfacial monolayer of surfactant has also been reported.[67]

5. NONLINEAR OPTICAL PROPERTIES

5.1. Scope and Phenomenon

As light travels trough a material, a variety of nonlinear optical effects (second-order and third order NLO) may occur, and its oscillating electric field interacts with charges in the material.

These interactions can cause the original optical beam to have its frequency, phase, polarization or path significantly changed. The ability to manipulate light in this manner has many important technology ramifications in optical signal processing, generation of variable frequency laser light, tunable filters and optical data storage. These significant technological discoveries are a powerful driving force for research in this area. In order to control light, an appropriate design and synthesis of optimal media within which the modulation or combination of photons can take place, and in which the optical processes can be controlled, is being investigated.

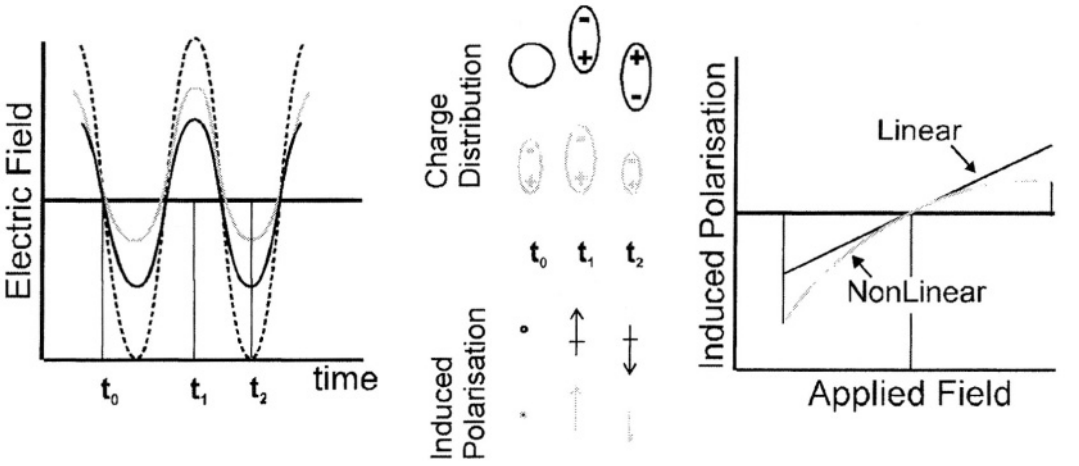

Figure 7. Plots of the electric field of the applied light wave (dashed line) and the induced polarization waves (solid lines) as a function of time, for a linear (black) and a nonlinear material (gray); Scheme of the polarization of the material as a function of time; plots of induced polarization versus applied field for both linear and nonlinear materials.

When electric fields of $\sim 2 \times 10^8$ V m^{-1} are applied, for instance by means of a laser, to an optically excited substance, higher energy vibrational quanta can be excited that extend into the anharmonic (nonlinear) portion of the potential energy vs. charge displacement relationship. These nonlinear displacements are the origin of the NLO phenomena. From a microscopic point of view, when a material is subjected to very high intensity electric fields, the material can become sufficiently polarized and as consequence its polarizability can change. Thus, the induced polarization is a nonlinear function of the field strength. This nonlinear polarization gives rise to nonlinear optical effects (Figure T).[68-69]

In the condensed phase, the nonlinearities depend both on the nonlinear optical properties of the individual molecules and on the arrangement of molecules in this phase. In this sense, the LB method can be used to control the molecular architecture of the material, as discussed in previous sections. LB is a potential method in the field of nonlinear optics.[70] Since the films are deposited layer by layer, films of the order of a wavelength of light can be fashioned with high accuracy. Since the wave vector of a propagating wave in a waveguide depends on the thickness of the film, phase relationships between modes can be maintained over considerable distances. Also, NLO optical properties are phase dependent, so this degree of control offered by LB films is almost unique.[69]

5.2. Properties of Organic Materials for NLO Devices

The study and characterization of organic NLO materials is relatively new compared to investigations of traditional inorganic materials. Most commercial NLO materials are still inorganic, although as a result of difficulties in crystal growth and sample preparation, inorganic materials present problems in their utilization as NLO devices and this constitutes one of the main reasons for pursuing the development of organic photorefractive materials.[69] Thus, since the 1980s, considerable research interest has been

focused on organic materials for nonlinear optical applications[71-72] because they possess several advantages over inorganic materials, such as high optical nonlinearities, ultrafast response times, easy processability, and low cost. Moreover, the desirable NLO properties can be optimized by chemical modification of their structure.

Prerequisites for the appearance of a significant macroscopic second-order NLO susceptibility, χ^2, in the active material are a sufficient molecular second-order hyperpolarizability, β, and the presence of a non-centrosymmetric internal structure both on the molecular and the supramolecular level. Chromophores with high second-order hyperpolarizability are usually linear conjugated chromophores which bear a strong donor and a strong acceptor in p–p′ position, and which have a long, undistorted π-electron system. In this group, for instance, phthalocyanine and related compounds, with their extended two-dimensional π-electron delocalization, are key targets in the study of nonlinear processes and are very promising candidates for optical switching and optical limiting devices. Most studies on phthalocyanines and related macrocycles have been performed on spin-coated or evaporated thin films, where the structure and order parameters are not well controlled, so that microscopic NLO response cannot be reliably correlated with the macroscopic one. On the contrary, by using the LB technique controlled well-ordered multilayers (non-centrosymmetric by X- and Z- type deposition modes,[73] or centrosymmetric by Y mode[74]) can be built up. Also, azobenzene chromophores are known to represent a good compromise between high nonlinear response, and other technologically important properties like sufficient solubility in common solvents and good photochemical stability.[75] Likewise, films consisting of alternating layers of a merocyanine dye and ϖ-tricosenoic acid have been studied.[76] Modeling the films as being uniform, axially isotropic dielectric media, gives a value for β_z for the dye in the monolayer of 10^{-2} C^3 m^3 J^{-2} (2.42×10^{-27} esu), an extraordinarily large value.

On the other hand, many photonic devices are based on the principle of optical waveguiding. A typical waveguide thickness reaches values around one or a few micrometers, and by means of LB technique the structures of waveguides can be controlled on a molecular scale. For instance, a gradient of refractive index can easily be introduced through layer-by-layer deposition of suitable amphiphilic polymers. The control of molecular orientation and of supramolecular arrangement is crucial for two aspects –the kind of molecular packing perpendicular to the layer plane is important to obtain non-centrosymmetric or centrosymmetric structures, while the molecular orientation with respect to the substrate plane is important to obtain an anisotropic refractive index.

The formation of multiple LB layers creates a waveguide structure. In addition to the advantages of a high χ^2, it is also necessary that the final waveguide formed by the multiple layers permit good phase matching between the first and second harmonics. This problem is caused by the difference in the phase velocity of the first and second harmonics as they travel through a dispersive medium. Thus, if uncorrected, there will be interferences between the fundamental and the second harmonic, with power being transferred back to the fundamental. Fortunately, by adjusting the thickness of the waveguides, mismatch can be minimized.[69]

Another practical problem is to attach optical devices (such as prisms or gratings) to the LB film in order to direct the fundamental into the length of the film, and to obtain the second harmonic at the other end of the film. An example of such a system is

provided by an amphiphilic structure made by placing an alkyl chain on one end of a polydiacetylene molecule and a carboxyl group on the other end.[77]

Furthermore, molecules consisting of a donor (D) moiety linked to an acceptor (A) moiety by a conjugated bridge have become the subject of intensive study due to their potential in NLO applications. The development of advanced materials for photonic applications based on second harmonic generation (SHG) requires solution of several major problems. The first is the design of donor–(π-bridge)–acceptor chromophores with maximized hyperpolarizabilities that retain reasonable thermal and photostability. Such D–(π-bridge)–A materials may be optimized by varying the donor–acceptor strength and the length of the π-electron bridge. Although significant progress in deriving the structure–properties relationship has been made, full guidelines for the design of SHG chromophores have not yet been established. The second problem is the assembly of these chromophores in non-centrosymmetric arrangements in miniaturized nanoscale systems. This can be realized by fabricating LB or self-assembled films which incorporate a compatible inert spacer material.[78]

In addition, there are applications of organic semiconductors (OSC), such as in electroluminescent devices, for which there are advantages in having a large current flow. In view of the low mobility of carriers in most organic semiconductors, large field strengths would then be required for this purpose. For practical reasons it is desirable that these large fields be achieved with the application of small applied voltages. The exploitation of the nonlinear optical properties of organic semiconductors is also best accomplished by the high field-low applied voltage configuration. This configuration can only be achieved if the OCS is in the form of a thin film. The Langmuir-Blodgett technique is a successful method for preparing uniform thin films with a total thickness that can range from 4 nm for two monolayers (e.g. of stearic acid) to ~ 1μm, with an uniformity of thickness of ± 4 nm. Some reviews on LB films related to this subject have been published by Roberts,[79] Bosshard et al.[80] and Petty.[20]

Finally, it should be pointed out that the second-harmonic generation (SHG) measurements carried out in order to determine second-order NLO susceptibility of LB multilayers, do not only provide χ^2 values but also information about chromophore orientation and about the internal structure of LB multilayers. For example, in most cases, the LB deposition is sensitive to the temperature dependence of the surface pressure (π, mN/m) of the floating monolayer, to the composition of the subphase, and to the surface properties of the substrate. In order to reduce the number of unknown parameters, the LB deposition should always be carried out under the same conditions, therefore, the change in the deposition behavior with increasing the number of layers should have its origin in material inherent properties. With increasing number of monolayers, the influence of the substrate decreases, which leads to a loss of molecular order especially in the upper layers. It is, therefore, not possible to deposit oriented multilayers from that kind of organic material (e.g. arachidic acid) alone, because the deposition is, in this case, sensitive to the surface energy, which depends on thickness. For azobenzene-containing polymer Z-type multilayers, the chromophores of the first 10 monolayers are oriented almost perpendicular to the substrate plane, but they become more and more tilted as the number of monolayers increases (same consequences as before). The reason could be that the polar groups of the polymer main chain cannot compensate the large dipole moments of the chromophores when the interaction with the substrate loses its influence. As a result, disorder in the upper layers increases in comparison to the lower layers. The

investigation of molecular order by SHG led to the same result. The reflected SHG intensity can be given as a sum of contributions from substrate nonlinear susceptibility χ_s^2 and from the susceptibility of deposited multilayers χ_m^2:

$$I_{2\omega} \propto \left|\chi_s^2 + \chi_m^2\right|^2 I_m^2 \tag{5}$$

For perfectly aligned LB multilayers, χ_m^2 is proportional to the number of deposited layers N and as a result, a dependence according to $I_{2\omega} \propto N^2$ should be observable as a linear increase in a plot of $\sqrt{I_{2\omega}}$ vs. N (that happened only for the first 30 monolayers). Likewise, the SHG results together with ellipsometric measurements, orientation and ordering of chromophores were increasingly reduced for Z-type multilayers above a thickness of 30 monolayers. The detected SH signal in s- and p-polarization depending on the polarization angle of the incident fundamental beam allowed to determine the tilt angle of the chromophore.[75]

6. REFERENCES

1. G. L. Gaines, Jr. *Insoluble Monolayers At Liquid-Gas Interfaces,* (Interscience Publishers, 1966).
2. G. G. Roberts, *Langmuir-Blodgett Films* (Plenum Publ. Co., New York, 1990).
3. H. Kuhn and D. Möbius, in *Investigations of Surfaces and Interfaces,* 2nd Ed., edited by B. W. Rossiter, R. C. Baetzold (John Wiley & Sons, Inc., New York, 1993) Vol. IXB, p. 375.
4. H. Kuhn, Functionalized monolayer assembly manipulation, *Thin Solid Films* **99**, 1-16 (1983).
5. H. Grüniger, D. Möbius, and H. Meyer, Enhanced light reflection by dye monolayers at the air-water interface, *J. Chem. Phys.* **79**, 3701-3710 (1983).
6. U. Lehmann, Aggregation of cyanine dyes at Langmuir-Blodgett monolayers, *Thin Solid Films* **160**, 257-269 (1988).
7. H. Hada, R. Hanawa, A. Haraguchi, and Y. Yonezawa, Preparation of the J-aggregate of cyanine dyes by means of the Langmuir-Blodgett technique, *J. Phys.Chem.* **89**, 560-562 (1985).
8. Y. Yonezawa, D. Möbius, and H. Kuhn, Scheibe-aggregate monolayers of cyanine dyes without long alkyl chains, *Ber. Bunsenges. Phys. Chem.* **90**, 1183-1188 (1986).
9. W. Cordroch, and D. Möbius, Incorporation of non-amphiphilic compounds into host monolayers, *Thin Solid Films* **210/211**, 135-137 (1992).
10. D. Janietz in: *Handbook of Surfaces and Interfaces of Materials,* edited by H. S. Nalwa (Academic Press, San Diego, 2001), Vol. 1, pp. 423–445
11. K. Hiltrop, J. Hasse, and H. Stegemeyer, On the alignment of thermotropic nematic and smectic liquid crystals on lecithin coated surfaces, *Ber. Bunsen-Ges. Phys. Chem.* **98**, 209-213 (1994).
12. V. S. U. Fazio, L. Komitov, and S. T. Lagerwall, Alignment and alignment dynamics of nematic liquid crystals on Langmuir-Blodgett monolayers, *Liq. Cryst.* **24**, 427-433 (1998).
13. V. S. U. Fazio, L. Komitov, and S. T. Lagerwall, Alignment of nematic liquid crystals on mixed Langmuir-Blodgett monolayers, *Thin Solid Films* **327-329**, 681-685 (1998).
14. K. Ichimura, Y. Suzuki, T. Seki, A.Hosoki, and K. Aoki, Reversible Change in Alignment Mode of Nematic Liquid crystals regulated photochemically by "command surfaces" modified with an azobenzene monolayer, *Langmuir* **4**, 1214-1216 (1988).
15. K. Aoki, T. Seki, Y. Suzuki, T. Tamaki, A. Hosoki, and K. Ichimura, Factors affecting photoinduced alignment regulation of cyclohexanecarboxylate-type nematic liquid crystals by azobenzene molecular films, *Langmuir* **8**, 1007-1013(1992).
16. T. Seki, M. Sakuragi, Y. Kawanishi, Y. Suzuki, T. Tamaki, R. Fukuda, and K. Ichimura, "Command surfaces" of Langmuir-Blodgett films. Photoregulations of liquid crystal alignment by molecularly tailored surface azobenzene layers, *Langmuir* **9**, 211-218 (1993).
17. T. Ubukata, T. Seki, and K. Ichimura, Modeling the interface region of command surface 1. Structural evaluations of azobenzene/liquid crystal hybrid Langmuir monolayers, *J. Phys. Chem. B* **104**, 4141-4147 (2000).

18. T. Ubukata, T. Seki, S. Morino, and K. Ichimura, Modeling the interface region of command surface 2. Spectroscopic evaluations of azobenzene/liquid crystal hybrid Langmuir-Blodgett films under illumination, *J. Phys. Chem. B* **104**, 4148-4154 (2000)
19. V. S. U. Fazio, L. Komitov, S.T. Lagerwall, and D. Mobius, D. Incorporation of a non-amphiphilic nematic liquid crystal into a host monolayer, *Mol. Cryst. Liq. Cryst. Sci. Technol., Sect. A* **351**, 403-410 (2000).
20. M. Petty, *Langmuir-Blodgett Films* (Cambridge University Press, Cambridge, UK, 1996).
21. A. T. Ivanova, M. L. Kurnaz, and D. K. Schwartz , Temperature and flow rate dependence of the velocity profile during channel flow of a Langmuir monolayer, *Langmuir* **15**, 4622-4624 (1999).
22. A. T. Ivanova and D. K. Schwartz , Transient behavior of the velocity profile in channel flow of a Langmuir monolayer, *Langmuir* **16**, 9433-9438 (2000).
23. J. Ignés-Mullol and D. K. Schwartz, Alignment of hexatic Langmuir monolayer under shear. *Phys. Rev. Lett.* **85**, 1476- 1479(2000).
24. J. Ignés-Mullol and D. K. Schwartz, Molecular orientation in Langmuir monolayers under shear, *Langmuir* **17**, 3017-3029 (2001).
25. J. Ignés-Mullol and D. K. Schwartz, Shear induced molecular precession in a hexatic Langmuir monolayer, *Nature* **410**, 348-351 (2001).
26. T. Maruyama, G. Fuller, C. Frank, and C. Robertson, Flow-induced molecular orientation of a Langmuir films, *Science* **274**, 233-235 (1996).
27. T. Maruyama, J. Lauger, G. G. Fuller, C.W. Frank, and C. R. Robertson, Orientation of a Fatty Acid Monolayer: Effect of Flow Type, *Langmuir* **14**, 1836-1845 (1998).
28. Y. A. Ono, in: *Electroluminescence in Encyclopedia of Applied Physics,* edited by G. L. Trigg (VCH, Weinheim, 1993), vol. 5, p. 295.
29. J. H. Burroughes, D. D. C. Bradley, A. R. Brown, R. N. Marks, K. Mackay, R. H. Friend, P. L. Burns, and A. B. Holmes, Light-emitting diodes based on conjugated polymers, *Nature* **347**, 539–541 (1990).
30. D. Braun and A. J. Heeger, *Appl. Phys. Lett.* **58**, 1982– (1991).
31. C. Hosokawa, N. Kawasaki, S. Sakamoto, and T. Kusumoto, Bright blue electroluminescence from hole transporting polycarbonate, *Appl. Phys. Lett.* **61**, 2503–2505 (1992).
32. H. Vestweber, A. Greiner, U. Lemmer, R. F. Mahrt, R. Richert, W. Heitz, and H. Bässler, Progress towards processible materials for light-emitting devices using poly(p-phenylphenylenevinylene, *Adv. Mater.* **4**, 661–662 (1992).
33. C. W. Tang and S. A. VanSlyke, Organic electroluminescent diodes, *Appl. Phys. Lett.* **51**, 913–915 (1987).
34. C. Adachi, T. Tsutsui, and S. Saito, Organic electroluminescent device having a hole conductor as an emitting layer, *Appl. Phys. Lett,* **55**, 1489–1491 (1989).
35. R. H. Friend, R. W. Gymer, A. B. Holmes, J. H. Burroughes, R. N. Marks, C. Taliani, D. D. C. Bradley, D. A. Dos Santos, J. L. Brédas, M. Lögdlund, and W. R. Salaneck, Electroluminescence in conjugated polymers, *Nature* **397**, 121–128 (1999).
36. G. Destriau, Scintillations of zinc sulfides with α-rays, *J. Chim. Phys.* **33**, 587-625 (1936).
37. T. Christ, F. Geffart, B. Glüsen, A. Kettnre, G. Lüssem, O. Schäfer, V. Stümpflen, J. H. Wendorff, and V. V. Tsukruk, Analysis of light emitting diodes by X-ray reflectivity measurements, *Thin Solid Films* **302**, 214–222(1997).
38. M. Pope, H. P. Kallmann, and P. Magnante, Electroluminescence in organic crystals, *J. Chem. Phys.* **38**, 2042–2043 (1963)
39. W. Helfrich and W. G. Schneider, Recombination radiation in anthracene crystals, *Phys. Rev. Lett.* **14**, 229–231 (1965).
40. U. Mitschke and P. Bäuerle, The electroluminiscence of organic materials, *J. Mater. Chem.* **10**, 1471–1507 (2000).
41. M. Gross, D. C. Müller, H. G. Nothofer, U. Scherf, D. Neher, C. Bräuchle, and K. Meerholz, Improving the performance of doped π-conjugated polymers for use in organic light-emitting diodes, *Nature* **405**, 661–665 (2000).
42. G. Y. Jung, C. Pearson, L. E. Horsburgh, I. D. W. Samuel, A. P. Monkman, and M. C. Petty, The effect of insulating spacer layers on the electrical properties of polymeric Langmuir-Blodgett film light emitting devices, *J. Phys. D: Appl. Phys.* **33**, 1029–1035 (2000).
43. J. Kido, and Y. lizumi, Fabrication of highly efficient organic electroluminescent devices, *Appl. Phys. Lett.* **73**, 2721–2723 (1998).
44. J. Kido, and T. Matsumoto, Organic electroluminescence devices having a metal-doped electron-injecting layer, *Appl. Phys. Lett.* **73**, 2866–2868 (1998).
45. J. D. Hong, D. Kim, K. Cha, and J. I. Jin, Spectroscopic studies on ultrathin poly(p-phenylenevinylene) film deposited by self-assembly and spin-coating methods, *Synth. Met.* **84**, 815–816 (1997).

46. M. Gao, B. Richter, S. Kirstein, and H. Möhwald, Electroluminescence studies on self-assembly films of PPV and CdSe nanoparticles, *J. Phys. Chem. B* **102**, 4096–4103 (1998).
47. I. Benjamin, H. Hong, Y. Avny, D. Davidov, and R. Neumann, Poly(phenylenevinylene) analogs with ring-substituted polar side-chains and their use in the formation of hydrogen-bonding based self-assembled multilayers, *J. Mater. Chem.* **8**, 919-924 (1998).
48. A. Wu, and M. Kakimoto, LEDs based on poly(p-phenylenevinylene) and polyimide Langmuir-Blodgett (LB) films, *Adv. Mater.* 7, 812-814 (1995).
49. Y. Liu, Q. Li, Y. Xu, X. Jiang, and D. Zhu, Light emitting diodes based on high electron affinity polymer Langmuir-Blodgett films, *Synth. Met.* **85**, 1279–1280 (1997).
50. T. Östergard, J. Paloheimo, A. J. Pal, and H. Stubb, Langmuir-Blodgett light-emitting diodes of poly(3-hexylthiophene): electro-optical characteristics related to structure, *Synt. Metals* **88**, 171-177 (1997).
51. A. Chowdhury, J. Chowdhury, P. Pal, and A. J. Pal, Light-emitting diodes from molecularly thin porphyrin derivative effect of molecular packing, *Solid State Commun.* **107**, 725-729 (1998).
52. J. Simmeer, B. Glüsen, W. Paulus, A. Kettner, P. Schuhmacher, D. Adam. K. H. Etzbach, K. Siemensmeyer, J. H. Wendorff, H. Ringsdorf, and D. Haarer, Transient photoconductivity in a discotic hexagonal plastic crystal, *Adv. Mater.* **8**, 815-819 (1996).
53. I. H. Stapff, V. Stümpflen, J. H. Wendorff, D. B. Spohn, and D. Möbius, Multilayer light emitting diodes based on columnar discotics, *Liquid Cryst.* **23**, 613-617 (1997).
54. G. Xu, Z. Bao, and J. T. Groves, Langmuir-Blodgett films of regioregular poly(3-hexylthiophene) as field-effect transistors, *Lanmguir* **16**, 1834–1841 (2000).
55. A. Bolognesi, C. Botta, G. Bajo, R. Österbacka, T. Östergård, and H. Stubb, Photoluminesence and electroluminescence in Langmuir-Blodgett films of poly(3-decylmethoxythiophene), *Synt. Metals* **98**, 123-127 (1998).
56. D. Zhang, Y. Xu, L. Ding; Y. Liui, and D. Zhu, Magnetic LB films of bis-radicals (nitronyl nitroxide and imino nitroxide) substituted benzene with long alkyl chain, *Chem. Phys. Lett.* **304**, 236-240 (1999).
57. J. Le Moigne, J. L. Gallani, P. Wautelet, M. Moroni, L. Oswald, C. Cruz, Y. Galerne, J. C. Arnault, R. Duran, and M. Garrett, Nitronyl nitroxide and imino nitroxide mono- and biradicals in Langmuir and Langmuir-Blodgett films, *Langmuir* **14** , 7484-7492 (1998).
58. J. L. Gallani, J. Le Moigne, L. Oswald, M. Bernard, and P. Turek, Induced ferromagnetic interactions in Langmuir-Blodgett films of an organic radical, *Langmuir* **17**, 1104-1109 (2001).
59. M. Clemente-León, C. Mingotaud, B. Agricole, C. J. Gómez-Garcia, E. Coronado, and P. Delhaes, Application of the Langmuir-Blodgett technique to polyoxometalates: towards new magnetic films, *Angew. Chem., Int. Ed. Engl.* **36**, 1114-1116 (1997).
60. M. Clemente-León, C. Mingotaud, B. Agricole, C. J. Gómez-Garcia, E. Coronado, and P. Delhaes, Toward New organic/inorgnaic superlattices: Keggin polyoxometalates in Langmuir and Langmuir-Blodgett films, *Langmuir* **13**, 2340-2347 (1997).
61. M. Clemente-León, C. Mingotaud, C. J. Gómez-Garcia, E. Coronado, and P. Delhaes, Polyoxometalates in Langmuir-Blodgett films: toward new magnetic materials, *Thin Solid Films,* **327-329**, 439-442 (1998).
62. C. Mingotaud, C. Lafuente, J. Amiell, and P. Delhaes, Ferromagnetic Langmuir-Blodgett film based on Prussian blue, *Langmuir,* **15**, 289-292 (1999).
63. C. Lafuente, C. Mingotaud, and P. Delhaes, A Langmuir-Blodgett film presenting ferromagnetic state below 25 K, *Chem. Phys. Lett.* **302**, 523-527 (1999).
64. Clemente-León, H. Soyer, E. Coronado, C. Mingotaud, C. J. Gómez-Garcia, and P. Delhaes, Langmuir-Blodgett films of single-molecule nanomagnets, *Angew. Chem., Int. Ed. Engl.* **37**, 2842-2845 (1998).
65. S. Lefebure, C. Menager, V. Cabuil, M. Assenheimer, F. Gallet, and C. Flament, Monolayers of monodispersed magnetic nanoparticles coated with a surfactant, *J. Phys. Chem. B* **102**, 2733-2738 (1998).
66. T. Fried, G. Shemer, and G. Markovich, Ordered two-dimensional arrays of ferrite nanoparticles, *Adv. Mater.* **13**, 1158-1161 (2001).
67. S. A. Iakovenko, A. S. Trifonov, M. Giersig, A. Mamedov, D. K. Nagesha, V. V. Hanin, E. C. Soldatov, and N. A. Kotov, One- and two-dimensional arrays of magnetic nanoparticles by the Langmuir-Blodgett technique, *Adv. Mater.* **11,** 388-391 (1999).
68. S. R. Marder, in: *Inorganic Materials* 2nd Edition, edited by D. W. Bruce and D. O´Hare (John Wiley & Sons, New York, 1996), pp 122–169.
69. M. Pope and C. E. Swenberg, *Electronic Processes in Organic Crystals and Polymers* (Oxford Science Pub., 1999), pp. 1136–1180.
70. M. Matsumoto, H. Tachibana, and T. Nakamura in *Organic Conductors,* edited by J.-P. Farges (Marcel Dekker, New York, 1994), pp. 759–790.
71. J. Zyss, *Molecular Nonlinear Optics* (Academic Press, New York, 1993).

72. H. S. Nalwa and S. Miyata, *Nonlinear Optics of Organic Molecules and Polymers* (CRC Press, Boca Raton, Fl, 1997).
73. Y. Liu and D. Zhu, in: *Handbook of Surfaces and Interfaces of Materials,* edited by H. S. Nalwa (Academic Press, San Diego, 2001), pp. 425–429.
74. F. Fernández.Lázaro, M. A. Díaz-García, A. Sastre, P. Delhaes, C. Mingotaud, F. Agullo-López, and T. Torres, Síntesis and third-order NLO properties in LB films of triazolehemiporphyrazines, *Synt. Metals* **93**, 213–218 (1998).
75. S. Schrader, V. Zauls, B. Dietzel, C. Flueraru, D. Prescher, J. Reiche, H. Motschmann, and L. Brehmer, Linear and nonlinear optical properties of Langmuir–Blodgett multilayers from chromophores-containing maleic acid anhydride polymers, *Materials Science and Engineering C* **8–9**, 527–537 (1999).
76. P. N. Prasad and D. J. Williams, *Introduction to Nonliner Optical Effects in Molecules and Polymers* (John Wiley, New York, 1991).
77. R. H. Tredgold, Ordered organic multilayers, *J. Mater. Chem.* **5**, 1095–1106 (1995).
78. H. Schwartz, R. Mazor, V. Khodorkovsky, L. Shapiro, J. T. Klug, E. Kovalev, G. Meshulam, G. Berkovic, Z. Kloter, and S. Efrima, Langmuir and Langmuir-Blodgett films of NLO active 2-(p-N-alkyl-N-methylamino)benzylidene-l,3-indandione—π–A curves, UV–Visible spectra, and SHG behaviour, *J. Phys. Chem. B* **105**, 5914–5921 (2001).
79. G. G. Roberts, *Electronic and Photonic Applications of Polymers* (ACS Publishers, Washington, DC, 1988).
80. C. Bosshard, K. Shutter, P. Pretre, J. Hulliger, M. Flörsheimer, P. Kaatz, and P. Günter, *Organic Nonlinear Optical Materials* (Gordon and Breach, New York, 1995).

This page intentionally left blank

15
ASSEMBLIES OF MAGNETIC PARTICLES
Synthesis and production

Michael Hilgendorff and Michael Giersig*

1. INTRODUCTION

Because of its promise to provide solutions to the many technological demands of the next century, nanotechnology has in recent years become one of the most active areas of research and development. The preparation of inorganic materials with diameters below 20 nm via colloidal wet chemistry is of great interest to nanotechnology. Colloidal chemistry allows for the preparation of nanosized crystalline or amorphous particles which can be used in liquid or dry form on various substrates as the building blocks for development of new materials. Such research is of great interest for industry since one can exploit the novel properties of such particles to reduce the size of devices, and to develop newer and cheaper preparation techniques. Furthermore, the investigation of nanoparticles is a challenge for ground state scientists who observe exciting new properties that differ from bulk materials. According to the quantum size effect, if the size of condensed matter becomes smaller than the bulk delocalization length, the electronic states of nanoparticles become discrete. As a result, nanosized matter shows unusual properties such as nonlinear optical effects.[1]

Theoretical calculations on the structures and properties of clusters consisting of some hundred atoms have been done in principle. The properties of nanoparticles consisting of several thousand atoms (e.g. a spherical close packed Co nanoparticle, l0 nm in diameter, consists of about 47000 atoms) cannot be theoretically calculated because of the unavailability of sufficient computing power. This can be solved in part by the development of "bits" of reduced size. Let us assume that a magnetic particle of 10 nm in diameter can act as a spin up/spin down 1/0 binary code element. A close packed monolayer of these crystals will then have a data storage capacity in the $Tbit/inch^2$ range, which is several orders of magnitude higher than what is currently possible. Thus, and in accordance with Moore's law, it is no surprise that colloidal chemical preparations of magnetic particles (ferrofluids) have enjoyed increased attention over the past few years.[2] Ferrofluids have received much attention in the past several decades for their interesting properties which can be exploited to develop new

* M. Hilgendorff and M.Giersig. Hahn-Meitner-Institute Berlin, Glienicker Str. 100, 14109 Berlin, Germany.

technologies,[3] such as new refrigerators which employ the magneto caloric effect,[4] new inks for inkjet printers,[5] novel spin valves,[6] or for new cancer therapies, such as hyperthermia[7] and apherese.[8] Therefore, the colloidal chemical synthesis of ferrofluids is of great interest. Many well documented references and patents have described successful syntheses of magnetic nanoparticles and the investigation of their properties and applications. A nearly complete list can be found in the magnetic fluids bibliography.[9]

For the design of novel storage media and bio-sensor arrays one needs a technique for preparing on an industrial scale highly symmetric periodic particle arrays (PPA) within the range of several microns. Different routes have been investigated in the past to assemble small particles with large areas of high symmetry. One can develop PPA with particles having a standard size distribution $\leq 5\%$ by simply drying a drop of solution on suitable substrates. This self assembly technique has been improved through use of different coating techniques (e.g. spin coating, dip coating, or spraying) in combination with applied external forces. The origin of these external forces is either mechanical, as used for the preparation of Langmuir-Blodgett (LB) films,[10] or electrostatic, which is then used for layer by layer (LbL) assembly.[11] For more details see chapters 13 and 14 of this book. The use of external electric and magnetic fields to improve the self assembly of charged and magnetic nanoparticles respectively has also been reported.[12,13] The pioneering work on the self assembly of small particles using sub micron latex and silica particles along with noble metal assemblies has recently been reviewed.[14]

Although noble metals are often used as model systems in many chemical fields this is unfortunately not possible for non-noble materials like Fe_3O_4, Fe, Co, or Ni, which are sensitive to oxidation and complexation reactions in many cases. This is particularly the case in the field of colloid chemistry, where the enhanced dispersivity of the surface-to-volume ratio of nanoparticles implies an enhancement of reactivity compared to bulk materials. Many successful methods developed for noble metal nanoparticles could not be transferred to ferrofluids. Thus, many researchers dealt with Fe_3O_4 and Co as model systems for ferrofluids and their assembly into large PPA. Fe_3O_4 ferrofluids can easily be prepared in water and have been therefore investigated as a model system for assembly methods using electrostatic forces (LbL). Co ferrofluids which are usually prepared in organic solvents because of the necessity to use bulky (i.e. hydrophobic) stabilizers to prevent oxidation and to overcome the magnetic dipole-dipole interaction, have been investigated as a model system for self assembly. Furthermore, Co is more stable towards oxidation than Fe and less expensive than Ni.

Most of the possible applications of ferrofluids require high remanent magnetization and high anisotropy at room temperature. High remanent magnetization is a characteristic feature of soft ferromagnetic materials with diameters above a critical minimum dependent on the material (> 10 nm for Co). On the other hand, hard ferromagnetic materials, which often exist as alloys, exhibit high anisotropies. Soft ferromagnetic materials embedded in a noble metallic matrix show a technologically important effect called the giant magneto resistance (GMR). The ability to prepare air-stable ferromagnetic/noble metal bimetallic particles is therefore a challenge. Well-known ferromagnetic alloys consist of ferromagnetic 3d- and noble metal elements of the platinum group. They are known to have large magnetic moments and large magnetic anisotropies.[15] Accordingly, the synthesis of monodisperse ferromagnetic/noble metal bimetallic particle alloys (especially Fe/Pt) or core-shell particles and their assembly into PPA has been investigated intensely in recent years.[16]

One purpose of this chapter is to give an overview of the existing state of the art wet

chemical syntheses of ferrofluids, which are suitable for assembling experiments. Different preparation methods for the assembly of layers of nanoscale magnetic particles will be discussed.

A second purpose is to update the current knowledge about the principles of assembly methods in the challenging field of magnetic particles science, which this chapter was designed to cover. Actual results of experiments and theoretical calculations concerning particle-particle interactions in the ferrofluids, particle-substrate interactions combined with the theory of drying and the phenomenon of "self assembly" will be discussed. In consideration of the limited space of this chapter, the theoretical background will be given only qualitatively. Moreover, since some chapters presented in this book do overlap, and since a large number of review articles have already discussed theoretical aspects in detail, we will only present a (hopefully) helpful list of important review articles and advanced articles giving rise to a more complete understanding.

Discussion of the assembly of small magnetic clusters consisting of some hundred atoms and of magnetic particles produced using methods different from wet chemical methods is covered in chapter 16. Details of methods applied to investigate magnetic properties of nanoscale materials will be discussed in chapter 17.

2. THEORY

Discussion of the assembly of colloidal magnetic particles requires the discussion of some major items, most notably the theoretical description of nanoparticle interactions in a colloidal suspension. Equations describing the interacting behavior of colloidal nanoparticles were in principle developed by integrating equations describing atomic, ionic, or molecular interactions over the sum of all atoms in a nanoparticle.

The first item of interest is the origin of colloid stability which involves the control of repulsive (F_R) and attractive (F_A) forces acting on colloidal particles as a function of the temperature (Brownian motion). Repulsive electrostatic- (F_{RES}) and steric forces (F_{RS}) in aqueous media and mainly steric repulsion in hydrophobic media must be in equilibrium with attractive van der Waals- (F_{AW}) and magnetic dipole-dipole interactions (F_{AM}). The total interaction force F_T can be written as

$$F_T = F_A + F_R = (F_{AW} + F_{AM}) + (F_{RES} + F_{RS}) \quad (1)$$

The total energy V_T plotted against the separation distance D is commonly comparable to the well-known Lennard-Jones potential which is valid in the absence of applied external fields.

Actually, the most popular preparations concerning self assembled two- and three-dimensional layers of magnetic particles deal with the synthesis of ferrofluids in apolar solvents. In apolar media of low dielectric constant, electrostatic repulsion can be neglected (as well as magnetic dipole-dipole interaction assuming superparamagnetic particles at room temperature and the absence of an external magnetic field), but it is considered that attractive van der Waals forces between the particles are omnipresent. The steric repulsion of adsorbed layers on the particle surface is therefore necessary to overcome this attraction.[17]

A second issue is concerned with the control of crystal growth during the synthesis via the kinetic and thermodynamic control of particle size and particle size distribution.[18]

Moreover, the availability of crystal structures not found in bulk materials has been well established using colloidal chemistry methods.[13b,19] The phenomenon of self assembly was first investigated using submicron spheres of polystyrene (PS)-latex or SiO_2 dispersed in water. This work concluded that self assembly is conditional on the narrow size distribution of the particles (standard deviation ~ 5 %), i.e. a narrow distribution of the sum of repulsive and attractive forces between particles in a colloidal solution. Thus, this conclusion is not limited to well separated single particles. It holds also for aggregates of particles often found in aqueous systems, assuming that equal forces interact between aggregates of similar size.

Finally, in discussing the theory of drying, we must establish a theory to explain the interactions that take place between colloidal solutions and different substrates as well as the forces between all interfaces in the system under observation.

2.1. Forces Influencing the Colloid Stability

2.1.1. van der Wads attraction (assuming a core-shell structure of colloidal particles)

One of the most important attractive forces in the field of colloid chemistry is the London-van der Waals attraction. Expressions for London-van der Waals interactions have been developed about 70 years ago. Due to the instantaneous motion of electron distributions around the atomic nucleus, temporary electric dipoles have been assumed (and did fit experimental observations) to arise and to induce dipoles in neighboring atoms resulting in an attractive energy V_{AW}, inversely proportional to the sixth power of the separation distance D. With the London constant B, describing the (electrostatic) atomic-atomic pair potential, the attractive energy is:

$$V_{AW} = -B/D^6 \tag{2}$$

Eq. (2) is also valid for colloidal particles consisting of thousands of atoms since integration of Eq. (2) over the sum of the attractive energies of all atoms includes both neighboring nanoparticles each of which induces an electric dipole in the opposite particle. Assuming that both particles behave like a large flat plate, the attractive energy per unit volume can be described using Eq. (3).

$$V_{AW} = -A/12\pi D^2 \tag{3}$$

$A = \pi^2\rho^2B$, is the Hamaker constant and ρ the material's molecular density. The integration of Eq. (2) has been applied for different geometries of interacting bodies in the past.[20] Improved theoretical calculations have since been published. Tadmor developed expressions for two-body van der Waals attractions assuming a shell around a spherical particle interacting with another particle or with a semi-infinite wall.[21] This is important in the field of colloid chemistry where the successful preparation of stable fluids always requires the stabilization of the particles with a protecting shell.

Two results of this work are summarized in Figure 1. While Figure 1a describes the situation in a colloidal solution, Figure 1b illustrates the wetting behavior of colloidal particles on substrates (e.g. the interaction of particles with the wall of a beaker used for synthesis).

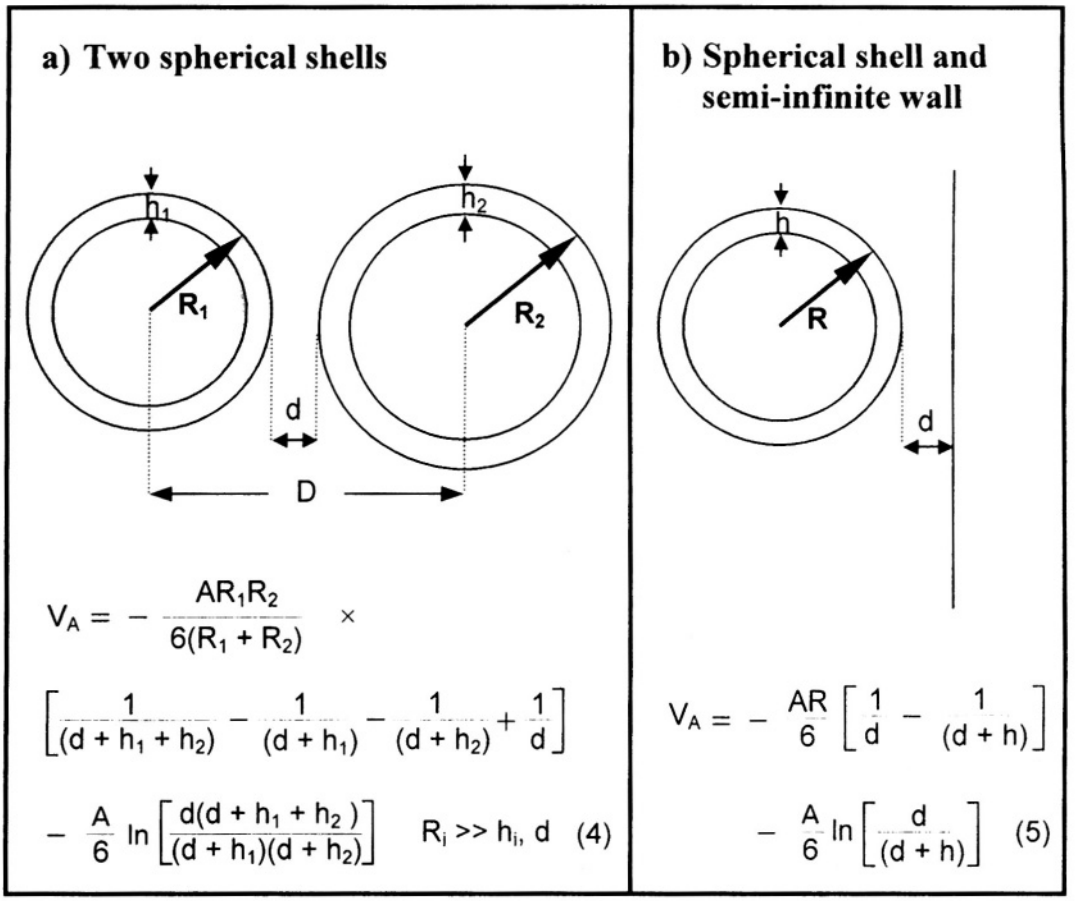

Figure 1. Calculation of the van der Waals interaction of colloidal particles taking into account the presence of a protecting shell. a) Interaction between particles dispersed in solution; b) wetting behavior of a particle on a substrate. Adapted with permission from ref. 21, copyright 2001, IOP Publishing.

It is necessary to point out that for $R_i >> h_i$, d, the attractive energy is described by the interaction of shells. Colloidal systems deal with such parameters as the core material of the particles, their protecting shell, and the dispersion medium having different Hamaker constants A_0, A_1, and A_2, respectively. Therefore, the effective Hamaker constant A is usually approximated by combining laws.

The colloid chemical synthesis of non noble metal colloids often results in materials with an oxidized surface, irrespective of the protective materials used. Thus, magnetic particles, synthesized by colloid chemistry methods consist of particles having a core of the desired material and a double surface layer. While the inner surface layer consists of oxidation products of the core material, the outer layer is built out of stabilizers. A sketch of such a particle is presented in Figure 2.

The binding type and strength of stabilizers is determined by the chemical reactivity of the surface such as the oxidation layer whose chemical properties may differ from the chemical properties of the core material. Further refinements of van der Waals expressions concerning core particles covered with a double layered shell are not to out-knowledge available.

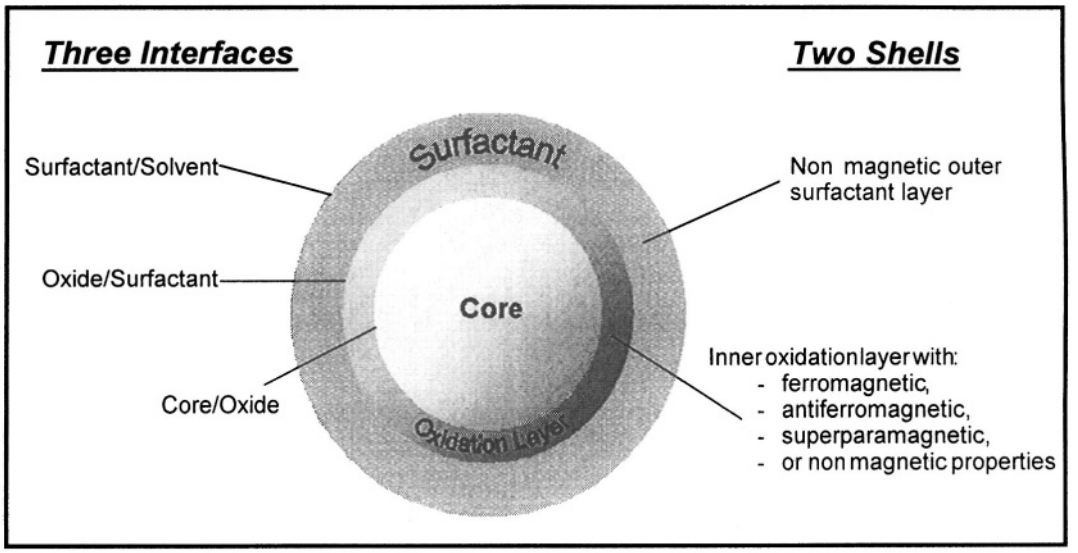

Figure 2. Sketch of a magnetic nanoparticle representing the usual result of colloid chemical synthesis. The desired core material is covered with an inner oxidation layer of the core material and an outer surfactant layer necessary to overcome attractive forces. As a result, three interfaces are present, which determine the nanoparticle properties.

2.1.2. Magnetic dipole-dipole interaction

The description of the magnetic dipole-dipole interaction between magnetic particles in a ferrofluid follows in principle from the description of the electric dipole-dipole van der Waals interaction. Consider a magnetic particle which is completely magnetized in one direction, and thus possesses a magnetic dipole moment which induces a magnetic dipole moment in neighboring particles. This results in an attractive energy V_{AM} which is maximum for parallel dipoles in a head-to-tail configuration. The latter situation holds if a strong external magnetic field is applied, or if the small particle distances, where the magnetic attractions are much stronger than the thermal energy kT, can be described by Eq. (6), with the saturation magnetization of the particles M, and the vacuum permeability μ_0:[22]

$$V_{AM} = V_{AM}^{max} = -[8\pi (R - h)^3 M^2]/9\mu_0 D^3 \qquad D \geq R \tag{6}$$

Single magnetic domain particles are the common result of colloid chemical preparations of ferrofluids. Single domain refers to the case where the spins of all atoms within these particles are aligned in the same direction thus forming a collective super spin. The behavior of these super spins in an applied external magnetic field can be in principle described by rules used for the description of paramagnetic materials, assuming that the super spin of each particle behaves like the spin of an electron. In the absence of applied external magnetic fields and in diluted systems, magnetic colloids above an energy kT are influenced by Brownian motion. As a result rotating super dipoles are observable, which show no collective behavior. In this context the attractive potential can be given as:[22]

$$V_{AM} = -(V_{AM}^{max})^2 / 6kT \qquad V << kT \tag{7}$$

Applying Eq. (7) in light of Eq. (6), the attractive potential of the magnetic dipole-dipole interaction, V_{AM}, follows the same law as the attractive electric dipole-dipole interaction. It is also inversely proportional to the sixth power of the separation distance D.[22]

Ordering phenomena in ferrofluids placed in an external magnetic field have been observed and theoretically calculated in literature. More recently, the formation of ordered stripes and hexagonal sheets has been experimentally observed while drying a thin liquid film of a ferrofluid on a substrate in an applied external magnetic field. Assuming a lattice gas model and the Carnahan-Starling model, theoretical calculations have shown, for a given film thickness and a given applied external magnetic field normal to plane of the thin film, that the ordering parameters are a function of magnetization and concentration of particles having a size distribution close to zero.[23] These calculations result in an $h = f(\phi)$ phase diagram, with the dimensionless magnetic field h and the average volume fraction ϕ, showing isotropic (I), hexagonal (H), and stripe (S) phases, separated in general by first-order phase boundaries. The final picture is qualitatively presented in Figure 3.

One major conclusion of this work is that the shape of ordered structures, which are obtainable by drying a thin layer of ferrofluid under the influence of an external magnetic field applied in an identical plane to the liquid layer, can be completely different. Stripes as well as hexagonal sheets are available and can be made to coexist simply by changing the strength of the applied magnetic field and/or the concentration of the particles.

Nevertheless, the authors themselves pointed out that their model needs further refinements to describe real ferrofluids, especially concerning polydispersity and a non-dipolar part of interaction due to the interaction of stabilizing layers. Moreover, the theory summarized here does not take into account drying-forces acting on particles in ferrofluids during their deposition, as well as the presence of an interaction between an antiferromagnetic oxidation layer and a ferromagnetic core. Some important principles concerning drying forces will be given in section 2.3.

2.1.3. Electrostatic repulsion (aqueous media)

The simplest model of an electric double layer at the interface of two phases was first modeled by Helmholtz in 1879. Assuming that the surface of a solid is charged, this surface in contact with a liquid gives rise to the formation of a static layer of counter ions of the liquid close to the surface of the solid. This electric double layer can be described from first principles as a condenser with parallel plates.

The difference of the inner electric potentials $\Delta\varphi$, corresponding to the voltage U, is then given by

$$\Delta\varphi = Q/C = DQ/\varepsilon_0\varepsilon_r a \tag{8}$$

where D is the distance between layers, a is the plane of the surface, Q is the charge, and C is the capacitance. ε_0 is the vacuum permittivity and ε_r the permittivity of the liquid medium.

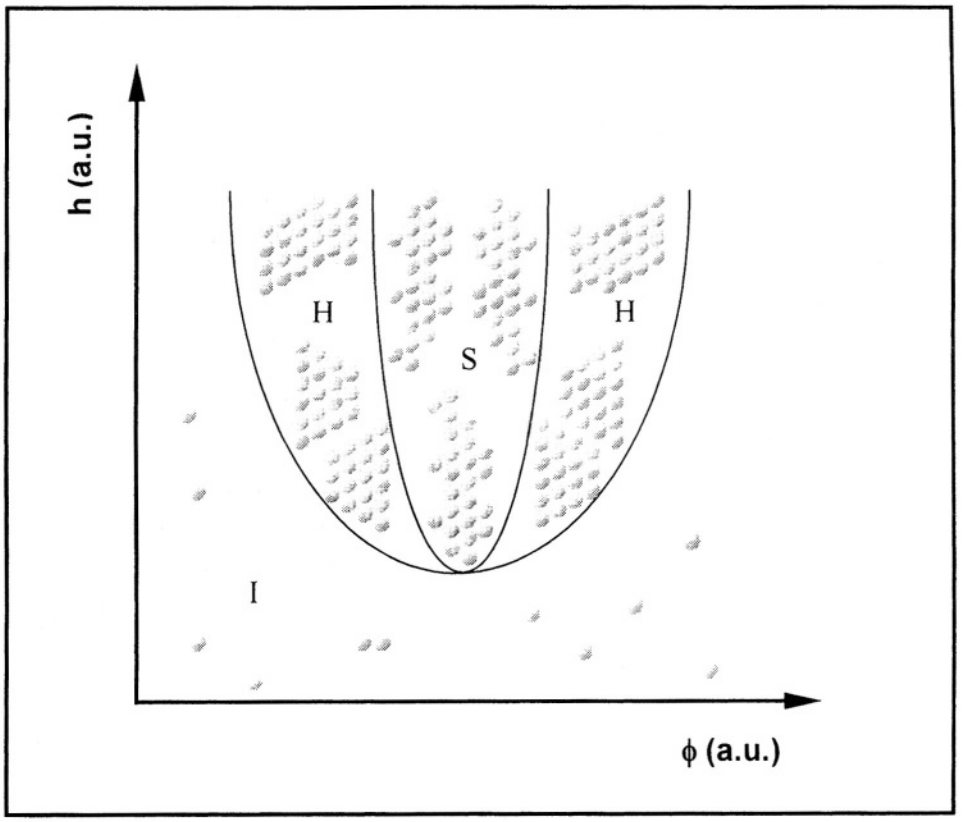

Figure 3. Qualitative sketch of a phase diagram in the (h, ϕ) plane with the dimensionless magnetic field h and the average volume fraction of the particles ϕ. The isotropic phase, the hexagonal phases, and the stripe phase are signed as I, H, and S respectively. The solid lines represent regions of coexistence. Adapted with permission from ref 23, copyright 2001, APS.

The electric double layer model was later modified by Gouy and Chapman in 1913, and again by Stern resulting in a three layer model which is presented in Figure 4. This three layer model, still accurate for the description of colloidal particles, consists of a static inner Helmholtz layer and an outer Helmholtz layer which overlap with a third diffuse layer.

The potential difference across the latter diffuse layers is measurable and known as the zeta potential ζ, and is an important property of colloids prepared in aqueous solutions. The ζ-potential can be either positive or negative according to the nature of the ions in the diffuse layer.

Electrostatic repulsion, often used to stabilize aqueous colloidal dispersions, requires the existence of a ζ-potential which is only present if the surface of the dispersed solid is charged. For a material dependent isoelectric point (pH_{pzc}) the surface of these materials has no charge and therefore no ζ-potential in solution. Preparing colloid particles in acidic media ($pH < pH_{pzc}$) ensures the availability of positively charged particles, while negatively charged particles are present in alkaline solutions ($pH > pH_{pzc}$).

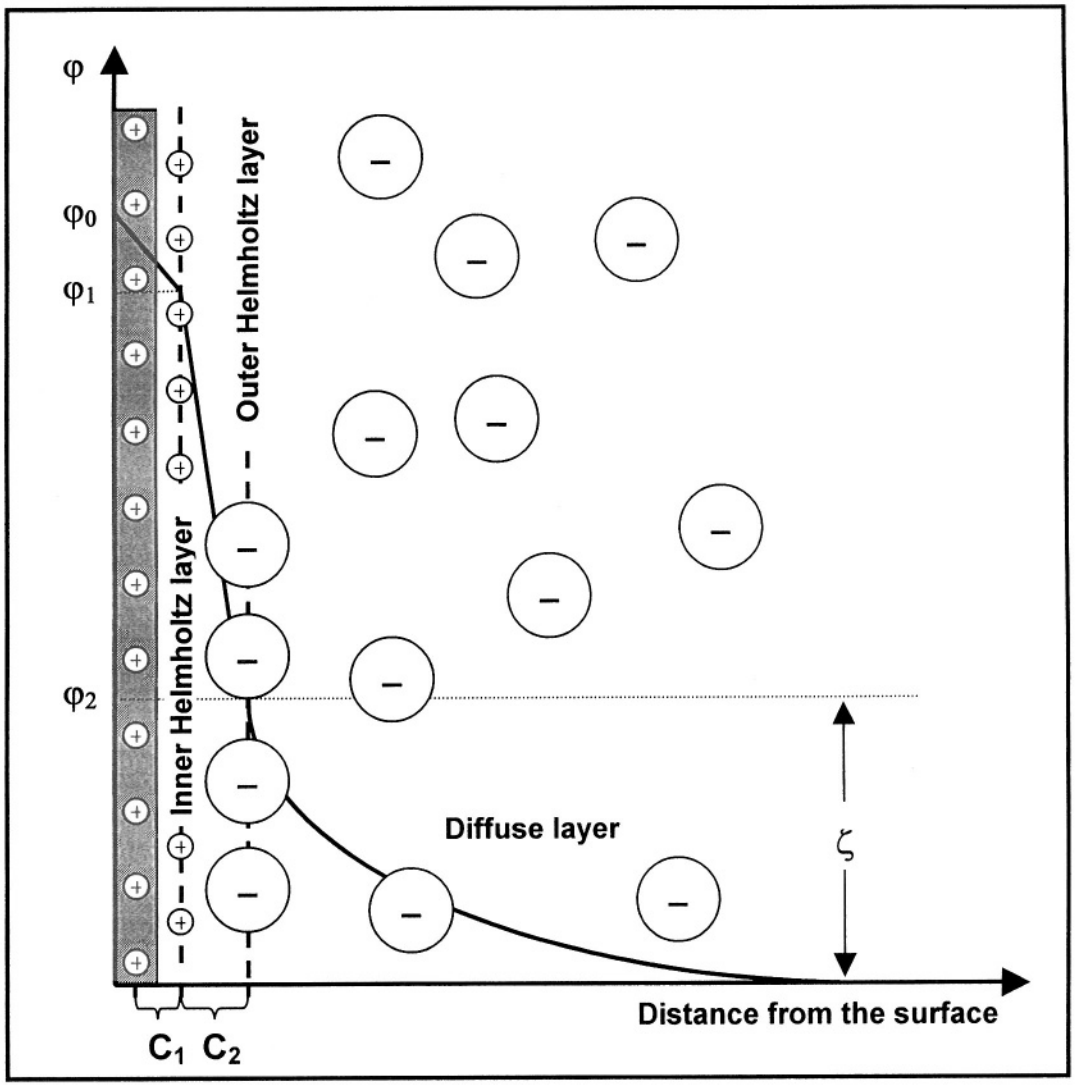

Figure 4. Sketch representing the situation in a three layer model of the Helmholtz layer. φ_x are the electric potentials of the different zones, C_1 and C_2 are the capacitances of the inner and outer Helmholtz layers, respectively, and ζ is the zeta-potential.

In accordance with the theory of Debye-Hückel-Onsager which describes the dimensions and interactions of ionic clouds in strong electrolytes, knowledge of the ζ-potential allows one to make judgments concerning the stability of colloidal dispersions in aqueous media. Usually, successfully stabilized colloids are available if the ζ-potential is $\geq |30\ \text{mV}|$. Moreover the fact that the dimension of ionic clouds increases with decreasing concentration, a consequence of Debye-Hückel-Onsager theory,[24] can explain experimental observations such as the decreasing stability of colloidal dispersions through dilution.

A further refinement of the three layer model, still dealing with homogeneous distributed point charges on flat surfaces, has been developed in recent years by Charmas.[25] Assuming a heterogeneity of the solid surface, his conclusions lead to a four

layer model, dividing the outer Helmholtz layer into two different parts. However, these refinements do not actually affect the description of the behavior of colloidal particles in aqueous solutions. For such systems, the solution of the Poisson equation is

$$\nabla^2 \varphi = -\rho_c / \varepsilon_0 \varepsilon_r \tag{9}$$

with the net density of charge, ρ_c per unit volume at φ, assuming the three layer model and taking into account a small electric double layer overlap (i.e. $\varphi = \varphi_0 \exp(-\kappa D)$), results in an expression (10) which was recently mentioned to be the most appropriate equation for nanosized particles.[26]

$$V_{RES} = 2\pi\varepsilon_0\varepsilon_r R\varphi_0^2 \exp(-\kappa D) \tag{10}$$

$$\kappa = (2N_A e^2 c z^2 / \varepsilon_0 \varepsilon_r kT)^{1/2} \tag{11}$$

2.1.4. Steric repulsion (hydrophobic media)

As explained earlier, the steric repulsion of stabilizers adsorbed on the surface of colloidal particles is necessary to overcome attractive forces. It is no surprise that increased attractive interaction of materials requires increased steric repulsion, which can be satisfied through addition of long chain organic molecules as stabilizing agents. Long chained hydrocarbons are usually hydrophobic and consequently increase the possibility for preparation of stable colloidal dispersions in aqueous media – a flexibility often required for many applications.

Buske et al. showed that the difference in the Hamaker constant between the adsorbed protecting layer (A_1) and the solvent (A_2) is the main criterion for achieving stability and for defining the properties of magnetic fluids.[17] Furthermore, chemisorption (beyond physisorption) of the surfactants is required to prevent instabilities that may occur from adsorption/desorption equilibrium reactions. It is well known in the field of colloid chemistry that the synthesis of stable dispersions of nanosized inorganic materials in liquids requires amounts of stabilizers several orders of magnitude higher than the available space on the surface of nanoparticles can accommodate.

Moreover, the maximum number of molecules that can be adsorbed (accounting for the space) is extremely small as compared to the number of free valences awaiting saturation. Figure 5 presents the calculations of the dimensions for two different geometries of Co particles having the same diameter of 10 nm.

The successful preparation of stable colloidal dispersions using a minimum amount of stabilizers, which is necessary for complete coverage of the nanoparticle surface with respect to the calculations presented in Figure 5, has not been carried out. It is also no surprise that colloidal solutions often become unstable through dilution, specifically through dilution of the excess stabilizer concentration. Unfortunately, unsuccessful results, regardless of their importance to the scientific community, are frequently not published in the literature.

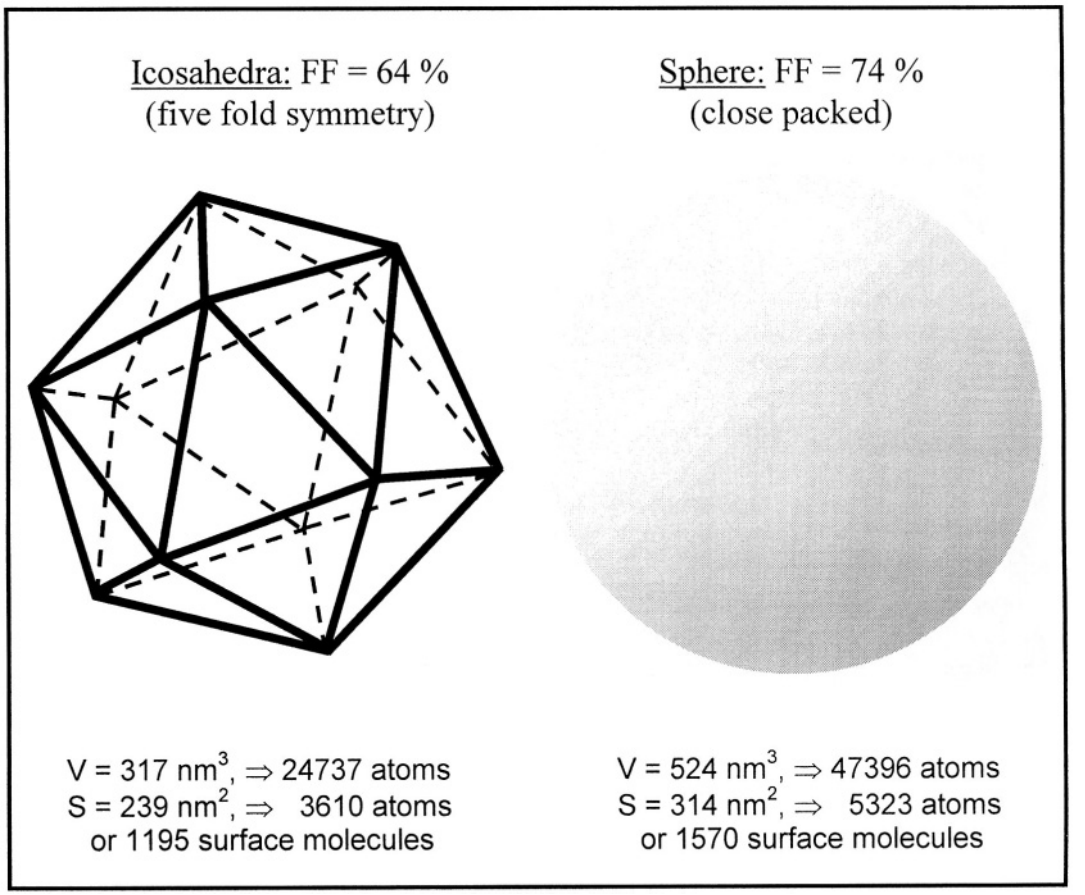

Figure 5. Calculation of the surface-to-volume ratio and the surface area of Co nanoparticles, 10 nm in diameter, for two different geometries; with the filling-factor FF.

2.2. Evolution of nanoparticles in a colloidal solution

As mentioned in the introduction, self assembly of colloidal particles into highly symmetric layers requires a narrow size distribution (standard deviation ~ 5 %). Such a narrow size distribution can be obtained either by size selective precipitation of the particles after preparation or by adjustment of the synthesis parameters in accordance to all interacting forces so as to provide controlled crystal growth (see section 3 for more details). As the latter method is more elegant from a scientific point of view, it is no wonder that several mechanisms have been proposed and theoretically calculated[27] since the earliest growth mechanism suggested by Ostwald ninety years ago.[28]

Proposed models of colloidal crystal growth assume that a small nucleus of a colloidal particle initially forms in a so-called precursor solution containing an ensemble of "colloid-particle-forming" molecules. This nucleus can form time dependency[29] or spontaneously as it does in hot injection technique.[30] This nucleus, which may be a pseudospherical cluster consisting of a "magic number" of atoms will then grow further. Different mechanisms have been suggested to describe this further growth in light of the final particle's properties.

While one growth mechanism is Ostwald ripening, i.e. larger nuclei will growth while smaller nuclei decompose, a second one deals simply with the precipitation of excess precursor molecules on the particle surface, well known as seed mediated growth,[31] and a third mechanism suggested by Henglein[32] proposes crystal growth as a consequence of the aggregation of preformed clusters of magic size followed by coalescence. The latter model has been further developed by Spanhel[33] assuming a fractal growth mechanism for the evolution of the final particles.

Recently, a Monte-Carlo simulation describing the growth of fine particles, when applying either the hot injection technique or the Ostwald ripening for initial nucleus formation, as well as a further Ostwald-driven crystal growth have been published by Talapin et al.[18] Their development, based on experimental results on II-VI and III-V semiconductor colloids, was mentioned to be valid for every kind of nanoparticles. As a result of this work, the synthesis of colloidal particles with a standard particle size deviation of ~ 5 % should be possible through an increase in the surface tension of the solvent-colloid interface through proper choice of surfactants.

The thermodynamic and kinetic control of the colloids synthesis determines not only their size (distribution) but also their shape (distribution). The shape control of nanoparticles has been published to be mainly determined by the choice and the concentration of the stabilizers which is directly contributed to the large surface-to-volume ratio of smart materials.[34]

2.3. The Theory of Drying

Discussion of the assembly of particles requires a description of the theory of drying. Ferrofluids can be dried on substrates using different methods such as spin- or dip-coating. The simplest method involves the drying of a drop of solution on a substrate. This method is commonly used to prepare samples for transmission electron microscopy (TEM) investigations, which is the most favorable technique for the investigation of colloids. Contrary to the investigation of bulk materials, TEM investigations of colloids are extremely fast because it is only necessary to dry a drop of solution on a grid which can then be viewed and analyzed immediately.

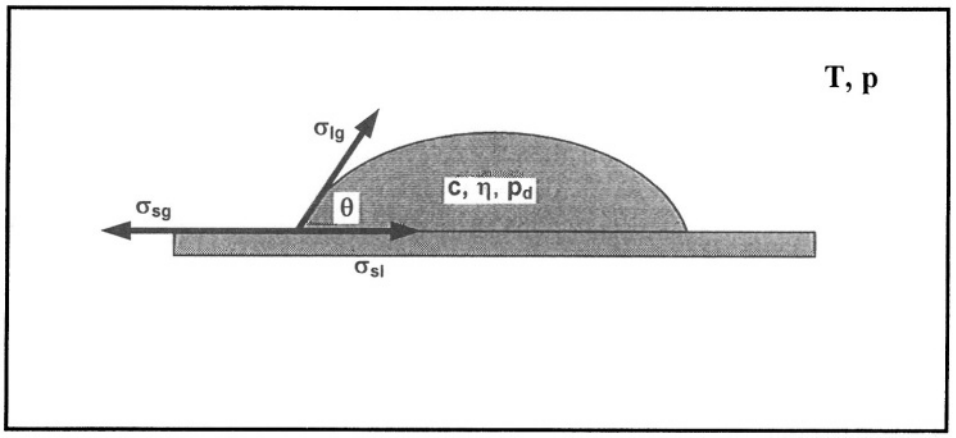

Figure 6. Sketch showing all parameters important for the description of a drop of a colloidal solution during its drying on a substrate. Optionally, external fields can be applied to complicate the description of the system.

Figure 6 shows all parameters necessary to describe the drying situation of a drop of ferrofluid deposited on a substrate. A drop of solution with a concentration c (or the volume fraction ϕ of colloidal particles, may be coated with a layer of surfactants), dynamic viscosity η, vapor pressure p_d, and surface tension σ_{lg} between the drop and atmosphere will have a contact angle θ on a substrate. This angle is related to the interface tensions σ_{sl} acting between the solution and the substrate, and σ_{sg} acting between the substrate and the atmosphere The relationship of these forces with the contact angle θ can be described by Eq. (12)[35]

$$(\sigma_{sg} - \sigma_{sl})/\sigma_{lg} = \cos\theta \tag{12}$$

The drying of colloidal solutions in an environment with a given temperature T and a pressure p is naturally a time dependent process, not reflected by the theoretical calculations described above. Forces that induce ordering phenomena in colloids dried on substrates need a minimum time t_0 to fulfill final conditions. Thus, the choice of solvents evaporating in a time $t < t_0$, will give different results compared to solvents evaporating in a time $t > t_0$.

3. WET CHEMICAL SYNTHESIS OF MAGNETIC NANOPARTICLES

Iron oxide ferrofluids are usually prepared in aqueous solutions by hydrolysis and condensation,[36] well-known in the field of sol-gel chemistry.[1a] Due to the enhanced reactivity of non-noble 3-d transition elements and the large magnetic dipole-dipole interactions of Fe, Co, and Ni ferrofluids of those elements, they are usually synthesized using the water-in-oil (reverse micelles) microemulsion technique.[37] In addition one can perform the reduction or thermal decomposition of metal precursors in organic solvents in the presence of bulky stabilizers such as fatty acids.[13a,b,29,30,38]

As a result, Fe-,[39] Co-,[13a,b,29,30,37,38] Ni-,[40] and FeN_x[41] ferrofluids, as well as their alloys with noble metals of the platinum group, e.g. Fe/Pt,[16b] Co/Pt,[16c] or Co/Rh,[16f] are formed with enhanced anisotropy and stability against oxidation. Use of ferrofluids as the building blocks for GMR devices, the preparation of ferromagnetic particles covered with a noble metal shell, e.g. Co@Ag,[16a] Co@Pt,[16c] or Co@Au,[16e] and vice versa, e.g. Ag@Co,[16g] or Fe@Co[16d] have been published.

As pointed out in our introduction, the synthesis of ferrofluids suitable for the preparation of large areas of highly symmetric magnetic nanoparticles on surfaces has become of increased interest in recent years, because of its possible application in high density data storage media. In addition to the reverse micelle technique (discussed in Chapter 6), the thermal decomposition of Fe-, Co-, and Ni-carbonyls, and the reduction of metal salts in organic solvents in the presence of bulky stabilizers has been reported.

A narrow particle size distribution is required for the self assembly of colloids dried on a substrate. Two principal methods have shown, after intense investigation, to produce the best results. The first method involves a size selective precipitation which exploits the size dependence of nanoparticle stability to separate out monodisperse fractions of particles. Upon adding a solvent having a larger Hamaker constant, larger particles aggregate and precipitate faster than smaller particles.

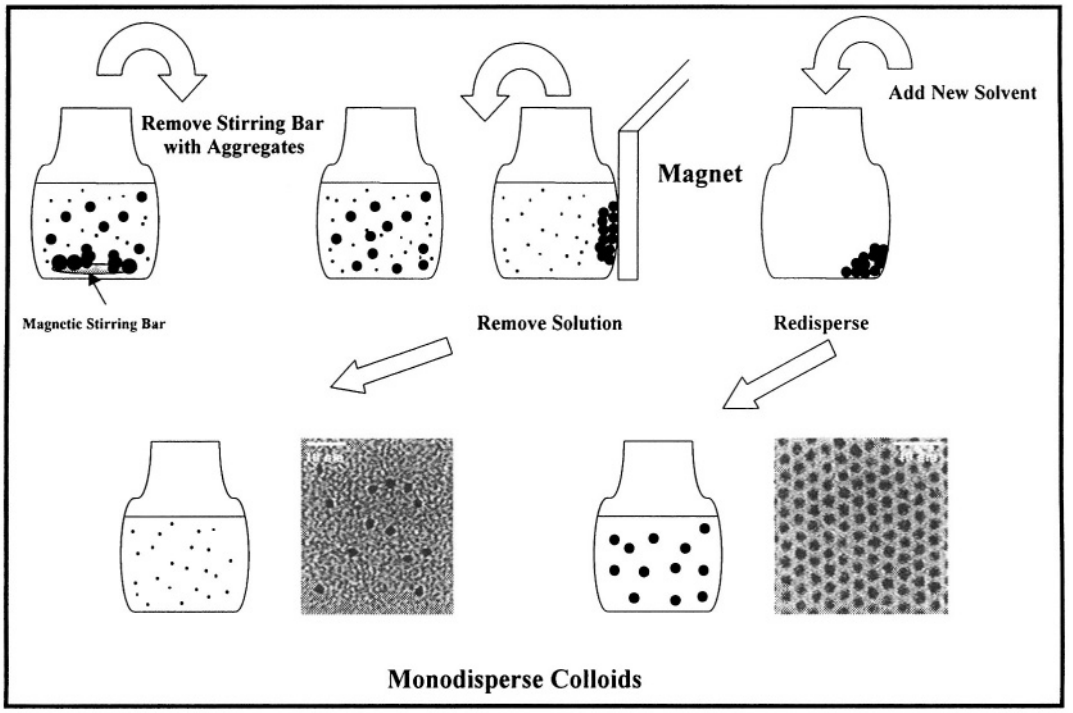

Figure 7. Sketch of the size selective precipitation of magnetic nanoparticles to obtain a standard deviation of the size distribution << 5 %. The TEM images show Co particles having a diameter of 3 nm and 11 nm respectively.

The precipitate can then be separated from the solution by centrifugation or, in the case of magnetic particles, by application of an external magnetic field.[42] A sketch of this method is shown in Figure 7.

The second method is based on the optimization of nucleation and crystal growth during the synthesis. The latter method is of course preferred as it would allow for the direct *in situ* control of nanoparticle formation, but it is usually more expensive as it often requires non-commercial or expensive precursors and an increased expense. So, there is little wonder why many scientists, especially industrial scientists, deal with size selective precipitation, which reliably allows for preparation of colloids having a standard size distribution << 5 %.

Nevertheless, there are application requirements that may favor the second method. These requirements are concerned with anisotropies, often found in alloys or rod-like particles. Rod-like Ni particles have already been prepared successfully using nickel dicyclo-l,5-octadiene as a precursor.[40b] Indeed, the preparation of alloys may even be favored by the use of "exotic" stabilizers. The synthesis of nanoparticles in reverse micelles is the scope of chapter 6 of this book and will be therefore not discussed here.

The colloid chemical synthesis of stable ferrofluids of ternary magnetic particles such as garnets or hexaferrites have not been published to our knowledge. Thus, we will offer an overview about optimizing the preparation of magnetite in aqueous solutions, as well as a review of new advances of the colloid chemical preparation of metallic magnetic particles in organic solutions, further developed in accordance to the requirements of new applications.[43]

3.1. Iron oxide

The most common preparation of magnetite (Fe_3O_4) ferrofluids has been described in detail by Massart in 1987.[36] The synthesis was based on the coprecipitation of Fe(II) and Fe(III) salts in aqueous solutions stabilized by repulsive electrostatic forces. This can be either done in acidic media, giving positively charged particles, or in alkaline media, giving negatively charged particles. Stable ferrofluids are available if the pH of the final solution is far from the pH_{PZC} which is the case if a ζ-potential large enough to overcome attractive van der Waals forces is present, as pointed out in section 2.1.3. As a typical result, particles with a standard size deviation of ~ 25 % are formed. TEM investigations show typically aggregated particles, as presented in Figure 8a, consisting usually of a mixture of ferromagnetic magnetite, and maghemite (γ-Fe_2O_3), and paramagnetic hematite (α-Fe_2O_3). The ratio of the different iron oxide phases is directly compared to the expense associated with performing the synthesis under oxygen free conditions, because γ-Fe_2O_3 and α-Fe_2O_3 are oxidation products of Fe_3O_4.

Since these reports, several optimizations have been discovered to produce ferrofluids useful for new applications. One of them was concerned with the possibility of changing the magnetic properties of the inverse Fe_3O_4 spinell by replacing Fe (II) with Co (II), Ni (II), Mn (II), or Zn (II) ions.[44] A second one dealt with the decrease of the size distribution of the aggregates, which could be achieved by separating the hydrolysis of Fe (II) and Fe (III) salts, and using the bulkier stabilizer tetrabutylammoniumhydroxide, instead of the tetramethylammoniumhydroxide used by Massart.[11c,d,43]

Additionally, many reports dealt with solving the classic problem of nanoparticle aggregation in aqueous solutions. To overcome such aggregation, new preparations have involved micellar solutions (see chapter 6) as well as the transfer of iron oxide particles from aqueous to non-polar solvents by hydrophobizing the surface by adsorbing bulky stabilizers such as fatty acids.[10b,45] Figure 8b shows impressively the difference in iron oxide ferrofluid prepared in aqueous solution (Figure 8a) after its transfer to toluene using oleic acid molecules adsorbed on the surface of the particles as a hydrophobizing agent.

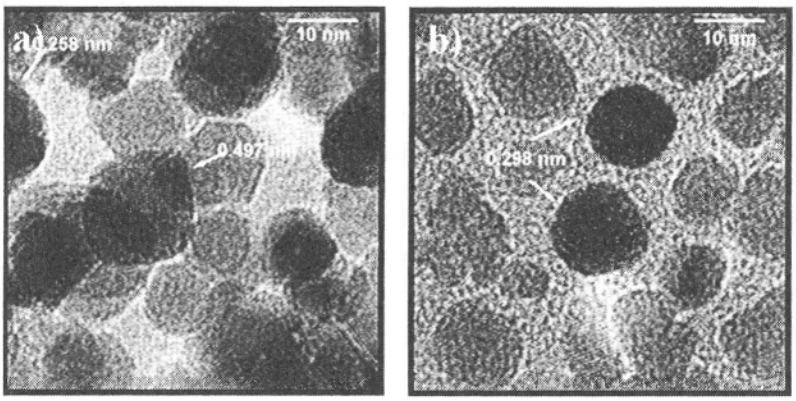

Figure 8. Typical TEM images of iron oxide particles; a) prepared in aqueous solution via Massart method and b) the same particles dried from a toluene solution after adsorbing oleic acid on their surface. The distances shown in the images are the result of fast Fourier analysis, indicating typical lattice planes of magnetite.

Finally, different methods have been applied to decrease particle size distribution. One method that has been successfully applied involves synthesis of iron oxides in reverse micelles. A second method dealt with a size selective precipitation induced by adding agents which cause flocculation and/or the application of external forces. Particle size distributions of < 10 % have been available for magnetite ferrofluids.

In the following section, the size selective precipitation scheme for production of extremely narrow size distributions with a standard deviation of << 5 % for Co particles in a ferrofluid will be presented. The reason for this difference in the obtained standard deviation of the particle size distribution between Co- and FeO_x particles is mainly the coexistence of different iron oxide phases.

3.2. Metals

The synthesis of colloidal solutions of non-noble metal nanoparticles has been the topic of intense research in the past several decades. During this time, methods have been designed and optimized to obtain colloids suitable as building blocks for new applications. Various synthetic routes have been investigated to develop smart ferromagnetic particles with novel and application specific properties. As a partial consequence of this research, stable fluids of non-noble metallic nanoparticles are now available in hydrophobic solvents. Models have argued that either electrostatic forces between particles and their stabilizers (tetraoctylammonium (TOA) salts)[46] or strong chemisorption, as demanded by Buske,[17] are responsible for the physical nature of the surfactant-particle interface in organic solvents.

Colloidal particles enjoyed a warm reception in the field of catalysis. Since catalysis requires extremely small particles possessing a large surface-to-volume ratio and an amorphous, active shell of metal compound, it came as no surprise that they would find increased use as highly reactive and efficient catalysts.

Bönnemann et al. developed a method for the preparation of noble metal, as well as non-noble metal particles, via the reduction of metal salts, dissolved in tetrahydrofuran, with a non commercial, TOA modified, strongly reducing super hydride.[46a] The authors explained that the binding between particles and their stabilizers is electrostatic in nature.

While a summary of Bönnemann's work has recently been published,[16e] the authors did not discuss the varying chemical reactivities, during redox and complexation reactions, of transition elements towards stabilizers. Completely different particle-surfactant models have been published by Bönnemann and Schiffrin.[46] Bönnemann assumed positively charged metal particles surrounded by a negatively charged electron cloud, where the positive TOA ion is located at the particles surface. In contrast, Schiffrin assumed positively charged noble metal particles surrounded by negatively charged ions. Moreover, Schiffrin pointed out that it is important to note that the charge of the surfactant ions points away from the particles. The different models are shown in Figure 9. However, both ionic models describe the physisorption of stabilizers. Physisorption, as opposed to chemisorption, allows for exchange of stabilizers which enables the transfer of particles from non-aqueous to aqueous systems. This method has been recently studied by Gittins et al.[47] As mentioned earlier, chemisorption, more than physisorption, is required to obtain stable non-noble metal particles of larger size.

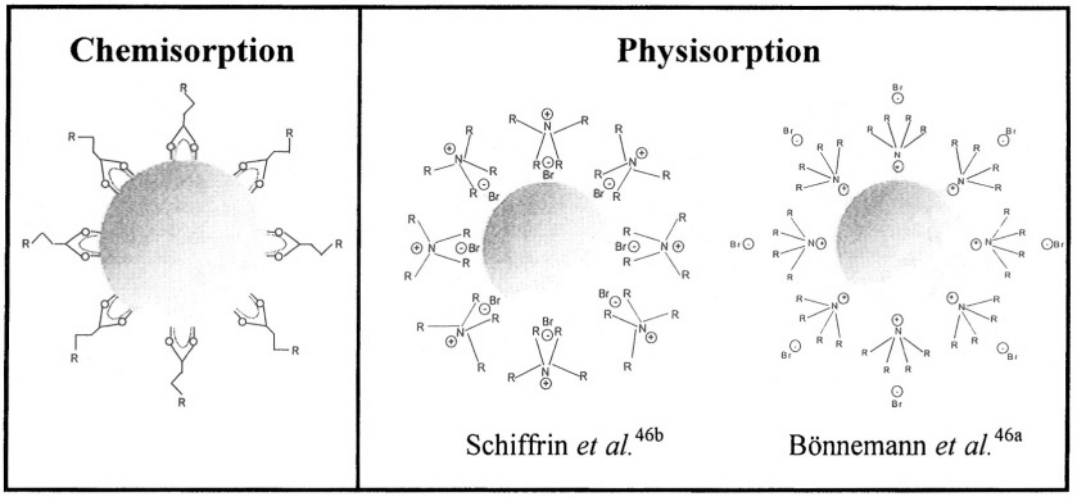

Figure 9. Sketches of different models describing the particle surfactant interface.

Figure 10 presents TEM images of self assembled layers of monodisperse 11 nm Co particles, which were stabilized by a chemisorbed shell of oleic acid molecules obtained after size selective precipitation. Due to chemisorption, no further ligand exchange is possible meaning that the particles can no longer be transferred to polar solvents. As a consequence, such colloids would not be suitable for biological applications and LbL experiments.

The compounds used for a preparation determine not only the shape but also the stability of the final particles. Small changes in preparation conditions can give completely different crystalline phases. Moreover, it is well known in the field of colloid chemistry that crystal structures different from bulk materials are available. Figure 11 shows Co nanoparticles with different crystal structures. While the hcp phase of the particles in Figure 11a[38b,48] is a typical phase of bulk Co, the bcc- (Figure 11b)[13a,19b] and ε-phase (Figure 11c)[13b,19c,49] have been only found in nanoparticles.

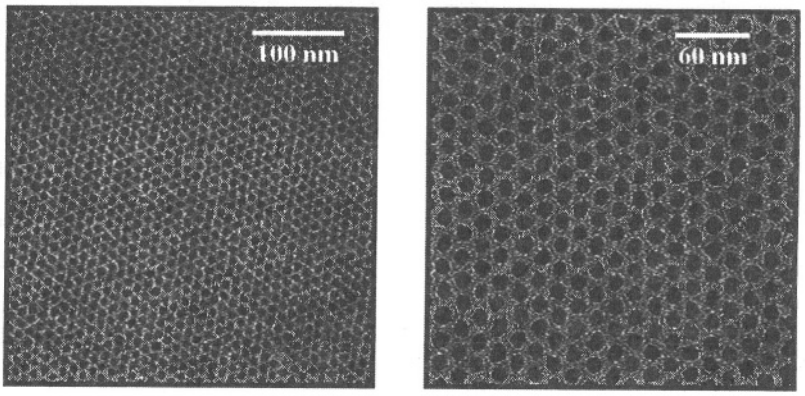

Figure 10. TEM images at different magnifications of monodisperse 11 nm Co particles stabilized by oleic acid, obtained after size selective precipitation, and self assembly on a carbon coated Cu grid.

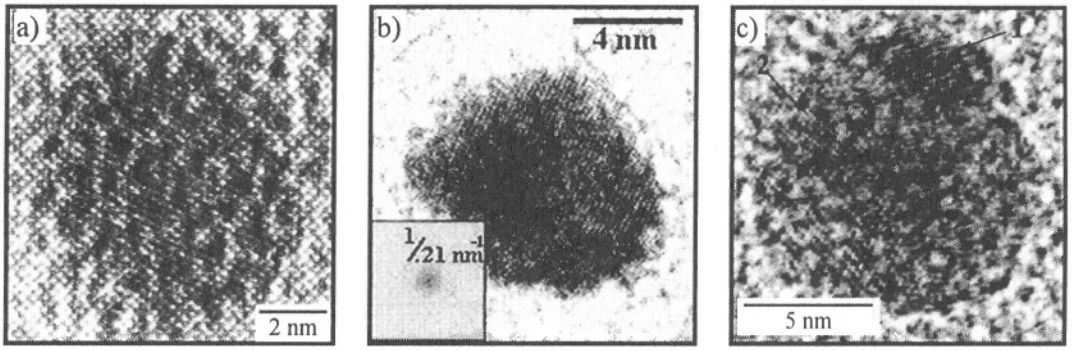

Figure 11. TEM images of Co nanoparticles with different crystal structures. a) hcp, reproduced with permission from [38b], copyright 2001, MRS Publishing; b) bcc, reproduced with permission from [13a], copyright 1999, IOP Publishing; and c) ε-fcc, reproduced with permission from [13b], copyright CSIRO Publishing.

Different crystal structures possess unique properties and anisotropies, which must be considered before the application of such particles for memory devices. It has been simulated that if 10% of a monolayer of magnetic crystals were to consist of crystals of a different structure (a lower anisotropy will cause the percolation of distorted spins), then this fact alone would be the main reason for media noise and an unknown loss of stored data.[50]

It must be summarized that the methods described above have been published to facilitate the preparation of iron oxide and metal ferrofluids as well as the synthesis of colloidal alloys and core-shell particles. The use of these colloids in assembly experiments will be described in the following section.

4. ASSEMBLING MAGNETIC PARTICLES

Two dimensional systems are of much interest from a scientific point of view, and are of great importance technologically. The magnetic behavior of ferromagnetic structures can be manipulated by changing their size and geometry.[51] Specifically, we will show this by using a magnetophoretic deposition method with which it is possible to create one-, two- and three-dimensional structures, based on nanosized magnetic Co particles.[38a,b] We will also show that by using the sphere lithography method it is possible to create two dimensional areas of magnetic particles having different compositions and geometries which possess potential for many applications.[52] One additional method of deposition of magnetic nanoparticles on polystyrene (PS) submicrometer-sized spheres permits the creation of hollow magnetic balloons.[11c]

4.1. Magnetophoretic Deposition Technique (MDT)

The monodisperse solution of Co described in section 3.2, was diluted to a Co concentration of 0.1 mM in toluene or o–xylene. The different substrates like silicon, carbon coated copper grids and glass used for the disposition were positioned between

two of the permanent magnets in parallel and perpendicular positions to the magnetic field lines. 10 μL of the diluted Co solution was deposited onto the substrate and residual solvent was allowed to evaporate. The strength of the magnetic field was varied by changing the distance between the two magnets. Through the variation of external magnetic fields in the range of up to 1 T, it was possible to get information about the formation process of two dimensional structures, depending on the strength and orientation of the applied external magnetic fields during the drying process.[13b]

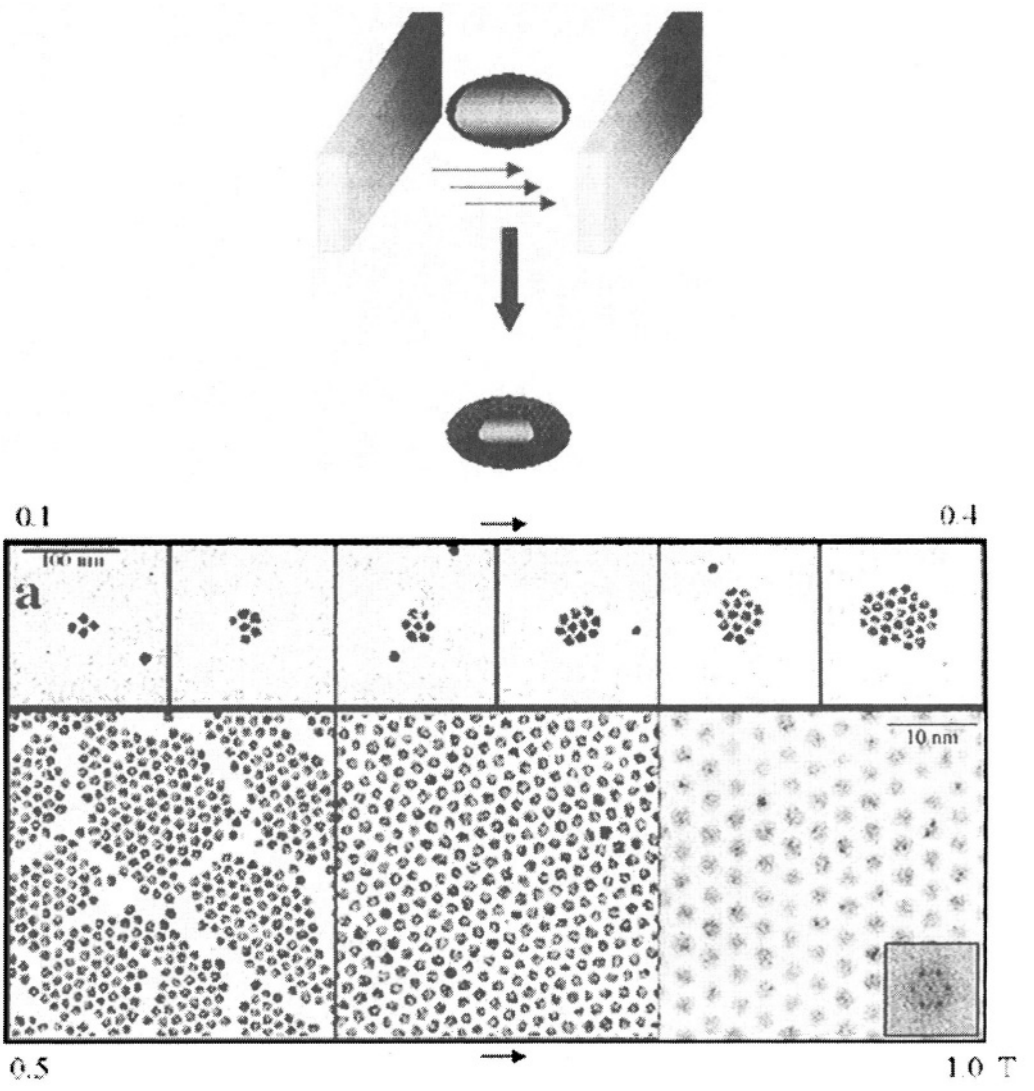

Figure 12. TEM images of ordered domains of 12 nm diameter Co particles deposited on carbon coated copper grids using MDT with magnetic fields between 0.1 and 1 T parallel to the plane of the grid. The size of the domains increases with increasing applied magnetic fields. Adapted with permission from ref. 13b.Copyright 2001. CSIRO Publishing.

The typical result of the MDT in parallel position is shown in Figure 12. The TEM micrographs were recorded after careful deposition of a drop of the solution onto a carbon covered Cu-grid, while applying a magnetic field between 0.2 and 0.8 T parallel to the plane of the grid (see the schematic drawing within this figure).

Under low magnetic fields up to 0.3 T, the MDT experiments resulted in the formation of di- to pentameric structures. Surprisingly, in comparison with self-assembled layers, the distance between the islands was enlarged but the interparticle distance was decreased, thus demonstrating an influence of the magnetic field. Above 0.4 T, larger organized units are created, and these higher field strengths lead to relatively large 2-D structures (ca 0.5 μm^2) even at just 0.8 T. The quality of the 2-D ordering of the cobalt particles, resulting from different magnetic field strengths is evident.

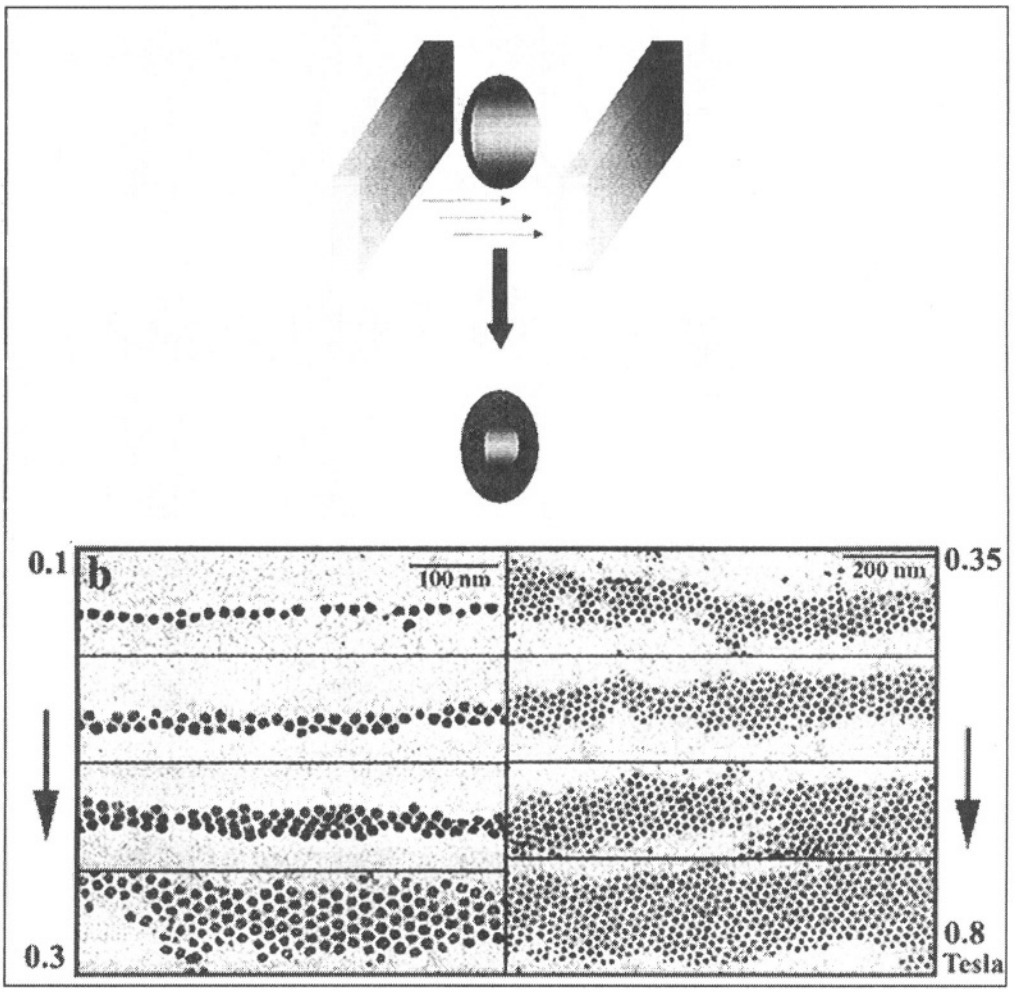

Figure 13. TEM images of ordered domains of 12 nm diameter Co particles deposited on carbon coated copper grids using MDT with magnetic fields between 0.1 and 0.8 T perpendicular to the plane of the grid. The additional force of gravitation leads to the formation of chains. The width of the chains increases with increasing applied magnetic fields. Adapted with permission from ref. 13b.Copyright 2001. CSIRO Publishing.

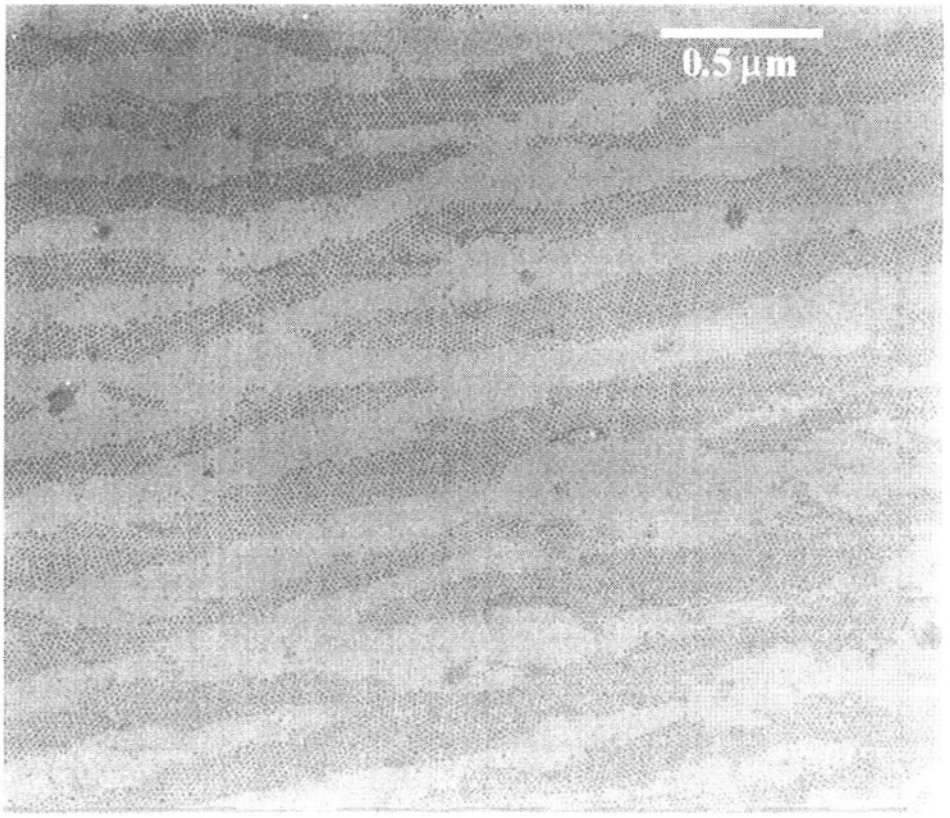

Figure 14. TEM image at low magnification shows a large-area of chains deposited at 0.8 T in perpendicular arrangement. Adapted with permission from ref. 13b.Copyright 2001, CSIRO Publishing.

The power spectrum insert in Figure 12 (with a field strength of 0.8 T) shows that the magnetic Co-particles crystallize into a hexagonal close-packed lattice with an average interparticle separation (core-to-core) of 12.2 nm. The absence of higher order reflections in the power spectrum means that the orientation of the crystallographic axes of the individual particles is random. No differences were found using dispersions containing bcc or ε- Co particles.

With the change of the direction of magnetic fields, (shown schematically in Figure 13), we obtained completely different structures. 2-D chains were observed as a result of the interaction between an external magnetic field perpendicular to the plane of the substrate and the force of gravitation. The width of these chains increases with the increasing magnetic field strength (see Figure 13).

For clarity, the formation of chains in a magnetic field with a strength of 0.8 T is presented in Figure 14 at low magnification. In this image, it can be seen that all chains within this large area have the same orientation.

Through the use of higher magnetic fields in a parallel arrangement, it was possible to create 3-D crystals. A typical result of 3-D deposition is shown in Figure 15 a-c. The TEM micrographs were recorded after MDT, using magnetic fields in parallel arrangement. With a magnetic field strength of 0.7 T, only 2-D ordering was obtained (Figure 15a).

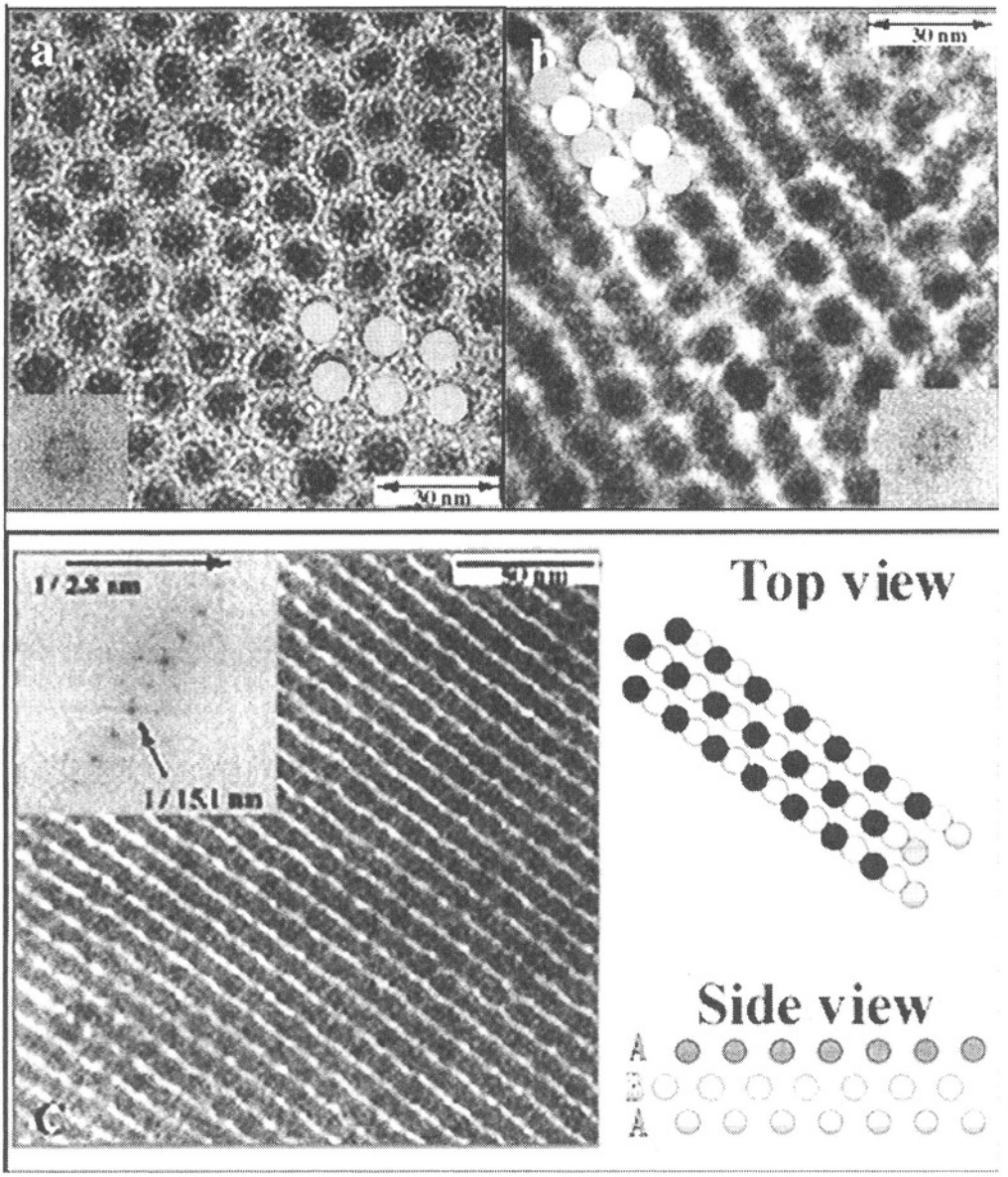

Figure 15. TEM images of the creation of multi-dimensional ordered Co-particles using MDT with external applied magnetic fields of a: 0.8 T, b: 1.5 T, and c: 6 T. The drawings are mentioned as a guide to understand the structure of the presented crystal images (see text for more information). Adapted with permission from ref. 13b.Copyright 2001. CSIRO Publishing

At a magnetic field strength of 1.5 T, the formation of double layers was observed (Figure 15b). With increasing magnetic field strength, the particles became more closely packed and began to assemble into three dimensions, where the minimum interparticle distance was limited by the stabilizing organic layers. Crystal growth was influenced by a further increase in magnetic field strength. The final 3-D structure, consisting of a triple layer, was created with a magnetic field strength of ca. 6 T (see Figure 15c). To aid in the interpretation of the 3-D crystal structures in Figure15c, schematic representations of the

top and side view are provided. Magnetic studies on these structures, in particular their angle-dependent ferromagnetic resonance at room temperature, showed that 12 nm diameter Co particles are magnetically stable.[53]

The resultant crystal structures depend on the angular alignment of the applied external magnetic fields during solvent evaporation. Application of high magnetic field strengths leads to the creation of multidimensional structures. Assuming that each Co-particle could be addressed as a magnetic read/write "bit," this approach in theory offers a simple and cost-effective way to produce large scale magnetic recording media with a memory density of the order of terabits per square inch. Nevertheless, it should be pointed out that the MDT is only a refined self-assembly technique. Thus, colloidal dispersions of particles possessing a narrow distribution of interacting properties are required in order to achieve useful results from MDT.

The MDT of magnetic colloids is influenced by the many parameters that are associated with drying (e.g. concentration, vapor pressure, viscosity, and variation in surface tension of the solution due to variations in the temperature and pressure of the environment, the properties of the substrate which influence the substrate/solution and substrate/environment interface tension and thus the contact angle of the drop). All these parameters are discussed in the theory section.

4.2. Nano Sphere Lithography (NSL)

The formation of monolayers of self-assembled colloidal particles (mainly polystyrene submicron-sized, monodisperse spheres) is well-established and is widely used in various fields of research.[54] Well-ordered latex particle films are used, among others, as masks which allow the production of regularly arranged triangular-shaped structures on almost arbitrary substrates. Through the evaporation of different metals through the mask, it is possible to prepare nanosized particles with diverse optical[54.55] or magnetic properties.[55] These particles can be used in many potential applications such as in optics,[55,56] data storage or even nanotube growth.[57,58] There are many different fabrication methods based on electrophoresis,[12,59] electrostatic deposition,[60,61] the Langmuir-Blodgett technique, spin-coating,[62] the controlled evaporation of solvent from a solution containing latex particles on a hydrophilic substrate[63] or non-photolithographic methods.[64,65] Many authors use Micheletto's method,[63a] or other drying-based methods and point out that a hydrophilic surface is crucial for monolayer deposition.[66] To deposit PS-latex particles onto hydrophobic substrates it is necessary to use an alternative method that involves assembly onto a liquid-gas or a liquid-liquid interface.

To overcome this, one can also use the monolayer transfer technique shown by F. Burmeister et al.[66] Unfortunately, this causes generation of new structure defects. Because of this, we searched for a new solution to cover hydrophobic silicon substrates with latex monolayers. To achieve this effect, we developed a novel preparation technique based on deposition of PS particles similar to a Langmuir-Blodgett film on water. Our preparation method, involving self-assembly on a liquid-gas interface, allows us to apply large (a few cm^2) monolayers directly onto various surfaces. In addition to short preparation times, (in comparison to drying-based methods), one can achieve a high level of hexagonal structure orientation as will be shown below.

The main problem with the formation of 2D latex monolayers is the occurrence of a high number of different structural defects which include point defects (vacancies), line defects (dislocations), and disordered areas or grain boundaries.

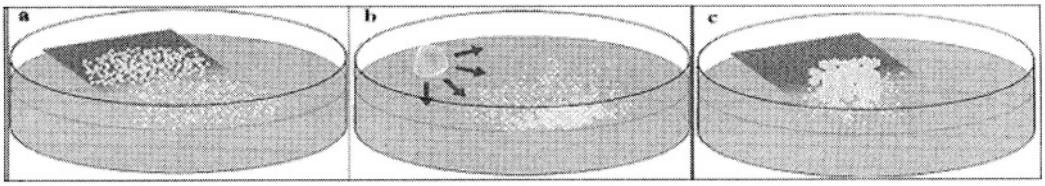

Figure 16. The preparation process for monolayer masks consisting of PS-latex particles: application of latex particles onto a water surface (a), consolidation of particles (b), liftoff of ordered monolayer (c).

In our method we lowered the volume of structural defects through the increase of average grain size and monolayer condensation. Using this simple fabrication technique, it was possible to prepare monolayers as large as a few cm^2 with grain sizes of 5×5 mm^2 and larger (using 1040 and 496 nm latex particles), and areas of even 50 μm^2 without structural defects. The quality of an NSL mask is outstanding when larger 1040, 925 and 496 nm PS-Latex particles are used. However, due to stronger interactions between smaller and lighter particles, (217 or 127 nm), it is much more complicated to obtain uniform monolayers.

The monolayer preparation recipe is schematically shown in Figure 16. More details about preparation parameters can be found in the work by Rybczynski et al.[52]

In Figure 17 typical examples of PS-latex particle depositions are presented. The second step in the preparation involves electron beam evaporation of metal. Details of the experimental procedure have been recently published.[52] Examples of 2-D ordered structures of magnetic materials via deposition through different PS-latex masks and different thicknesses of deposited magnetic materials are shown in Figure 18.

A very good correlation between previously investigated hexagonal latex particle arrays and evaporated metal structures was observed. The presented pictures show well-ordered, triangular-shaped nickel particles, defined by dense hexagonal packing of latex spheres. We also noticed the presence of rings in the middle of round sites left after a liftoff of latex spheres. These small structures surrounding the original contact area of the particles were observed by J. Boneberg et al.[63d] who proposed that these rings came from residue of the dissolved latex particles, a fact which fully corresponds to our investigations. Due to the high adhesion of evaporated nickel to the silicon substrate, it was possible to remove the rings quickly by an additional ultrasonication in THF, without damage to the evaporated particle array.

Figure 19 shows the result of annealed 10 nm nickel particles after evaporation through a 496 nm PS-latex particle mask. The obtained structure exhibits a very high homogeneity of nickel particles. Their mean size is approximately 65 nm. Thus, we can be sure that annealing allows for the fabrication of perfectly round and highly ordered magnetic particle arrays. In the above case, the particle density is, on average, 11 particles/μm^2 which corresponds to 7.1 billion per in^2. Theoretically, that means 7.1 Gbit/in^2 (1 particle = 1 bit). However, when using smaller 217 nm PS-latex particles, this value increases to 10.2 Gbit/in^2.

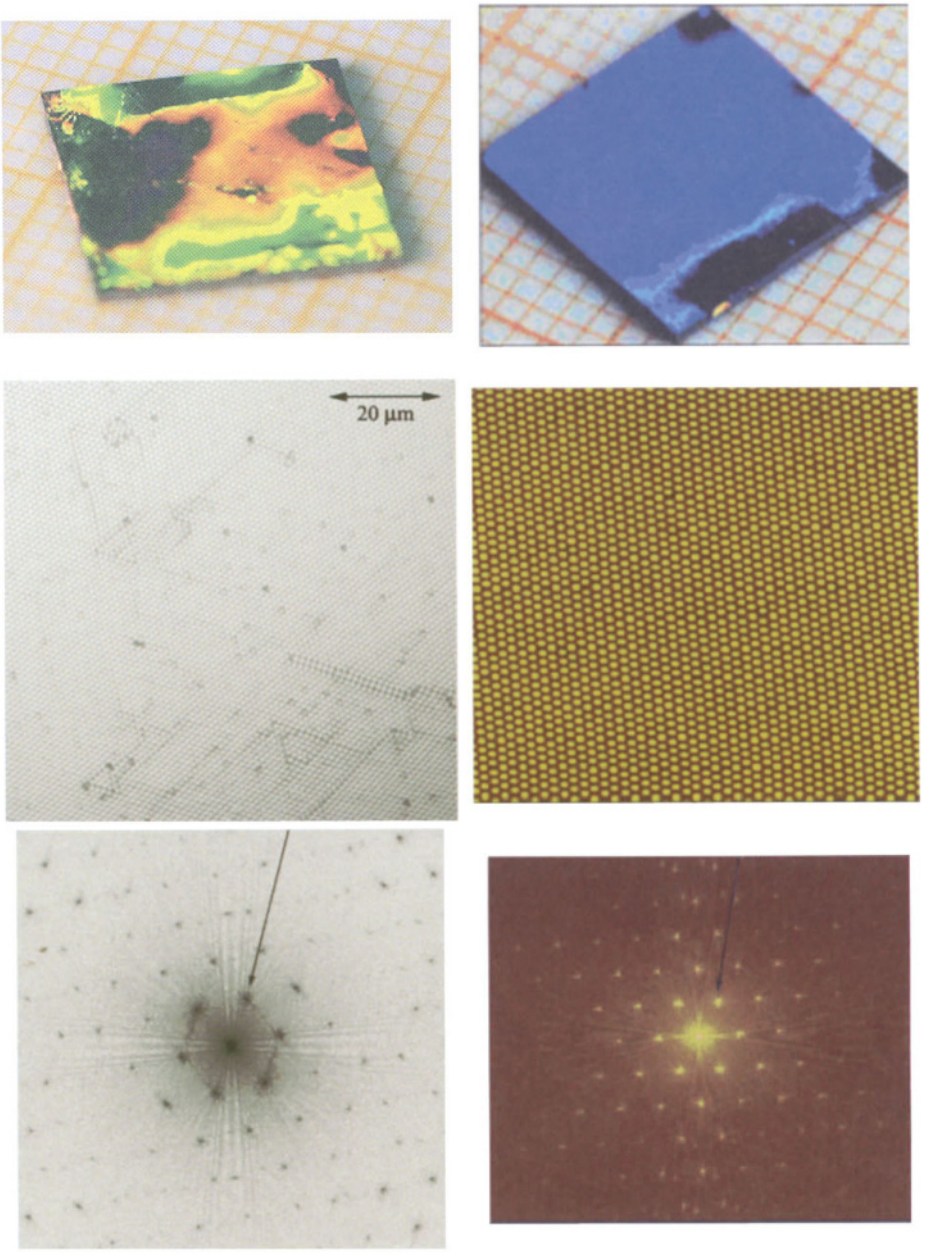

Figure 17. The 1×1 cm^2 silicon wafers covered with 496 nm PS-latex particles deposited as a monolayer. In contrast to the sample at the left side, most of the surface of the right side does not contain any grain boundaries, which are represented as a monochrome light interference (blue) color of the surface (right). In the second row, atomic force microscopy images are shown as representative examples for both samples. Additionally, quantitative information about the structures was obtained from a power spectrum of the pictures. Typical reflections for a polycrystalline structure are shown on the left side, in contrast to the right one which shows a power spectrum of perfectly ordered PS-latex particles.

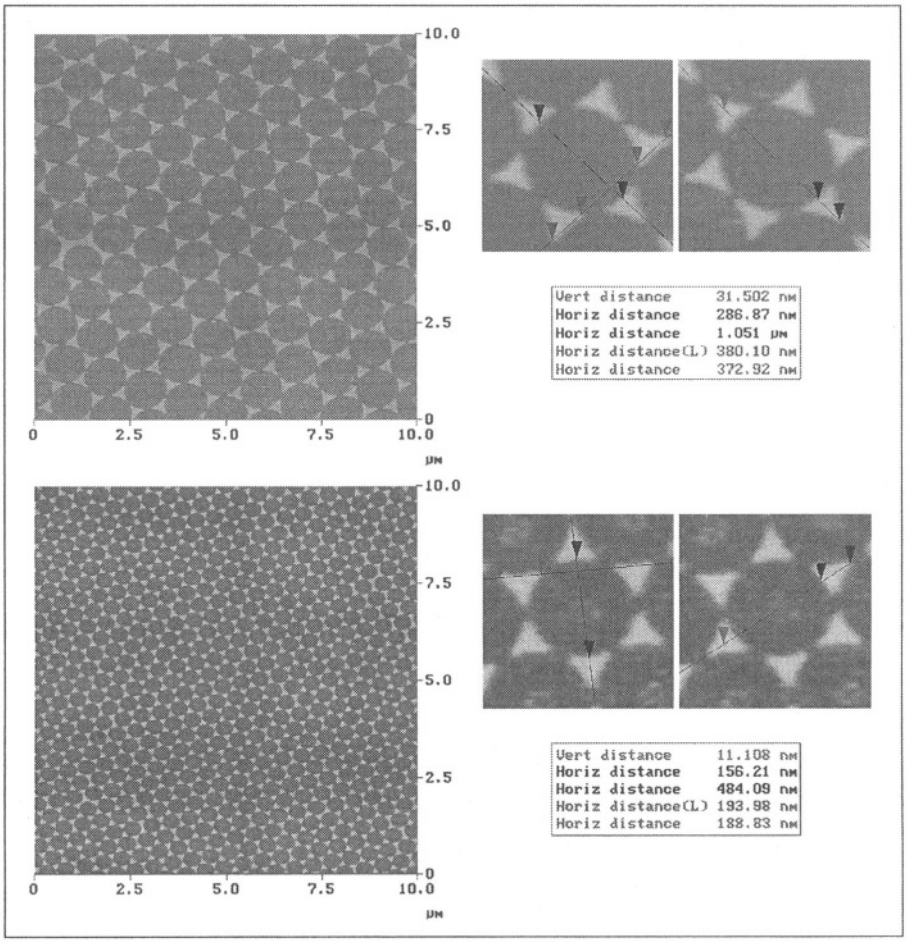

Figure 18. AFM-image gallery showing 2-D magnetic Ni-nanostructures created via deposition through different PS-Latex masks.

A more complicated sandwich-like structure could be obtained by evaporating layers of metal one after another such as in the order Au, Ni, Au. Therefore it is possible to produce core-shell particles containing nickel cores encapsulated within a gold shell, which could protect the core from oxidation and aggressive environmental influence, and could enhance the magnetic properties (see Figure 20).

To prove the presence of nickel and gold and to measure the volume of these elements in a three-layered sample, we additionally performed energy dispersive X-ray analysis (EDXA) investigations. In the case of three-layered samples, qualitative as well as quantitative analysis was performed. The presented EDXA spectra show unequivocally high gold and nickel content. The quantitative measurements exhibit good conformity with assumed theoretical values.

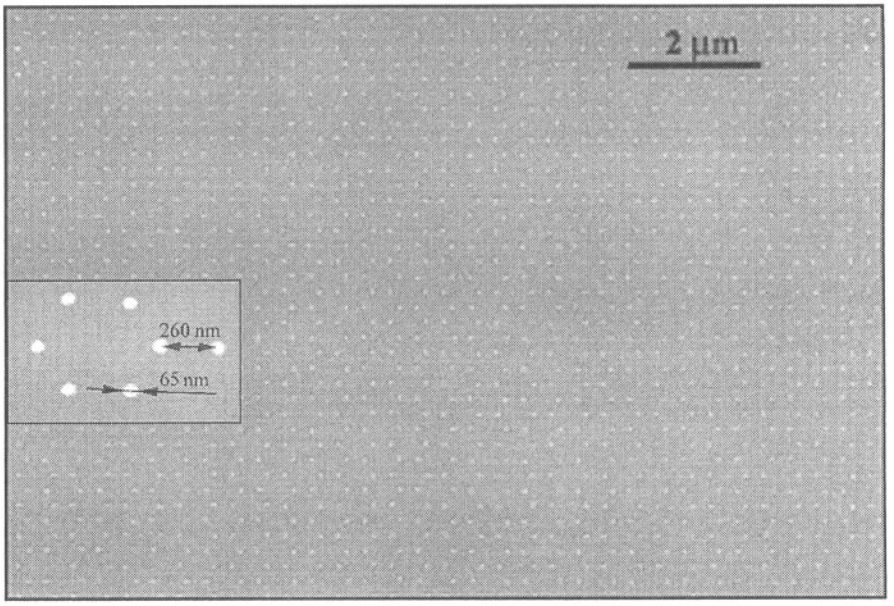

Figure 19. SEM image showing nickel nanostructures after annealing at 900°C for 40 min.

To obtain a periodic array with an increased distance between each evaporated particle, double layered masks were prepared. Evaporation of nickel onto such fabricated surfaces theoretically leads to the formation of round nickel structures with $\sqrt{3}$ times enlarged spacing between them. Since in the case of double layer masks the probability for the appearance of structural defects is twice as high as when using monolayers, such prepared samples most often exhibit a different structure than theory would indicate. During our experiments, we obtained two interesting structures (Figures 21a and 22a).

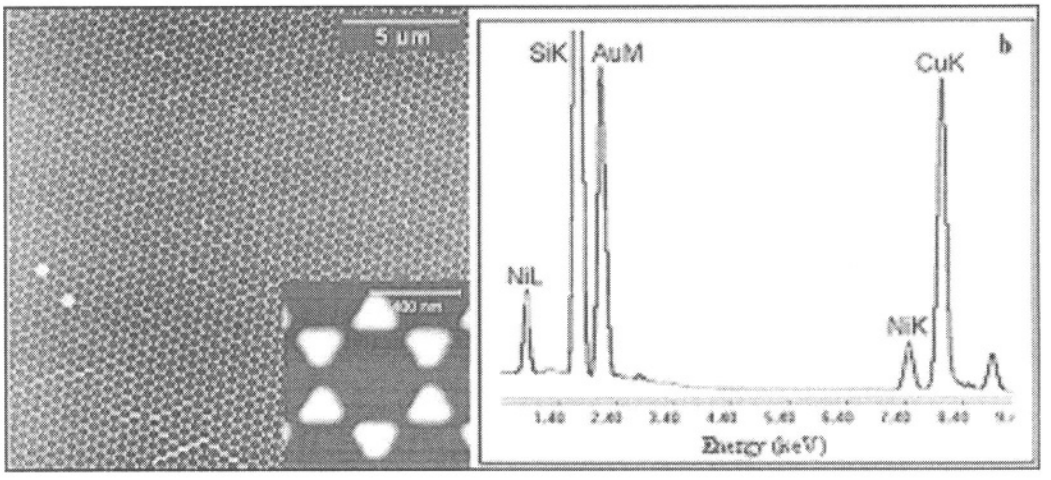

Figure 20. The structure of sandwich-like 10 nm Au – 5 nm Ni – 10 nm Au particles made by evaporation of metals through 496 nm PS-latex spheres (a). A typical EDX spectra of Au-Ni-Au structure. The strongest peaks correspond to Si substrate and the copper microscope grid (b).

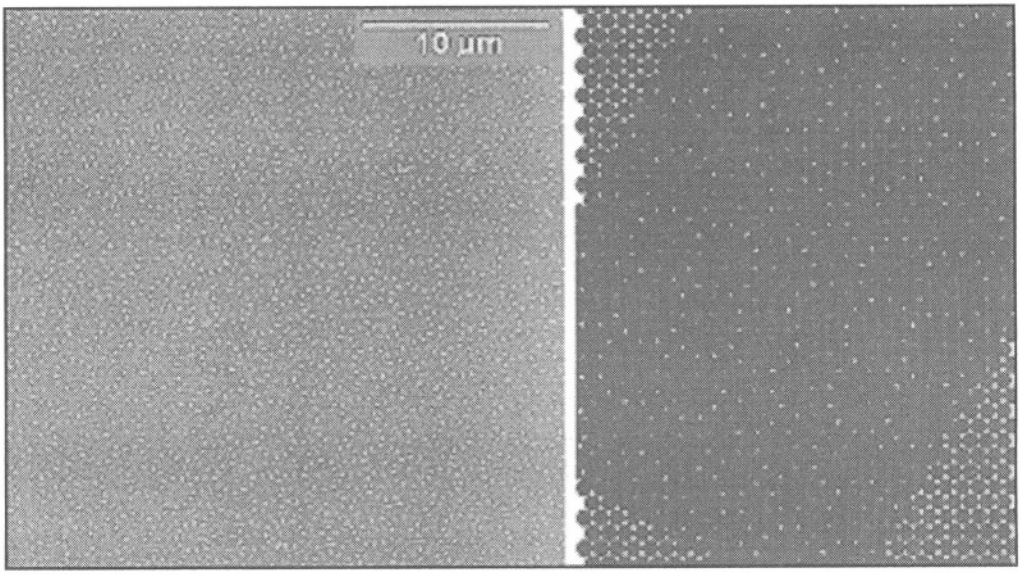

Figure 21. The result of evaporation of 20 nm nickel through a two-layer 496 nm PS-latex particles mask. The angle between both latex layers is about 30° (a). Simulation performed to prove the experimental results (b).

According to AFM measurements these particles are considerably smaller than triangular-shaped ones. The average distance between them is also larger. Since the ordering of these small structures does not correspond to theory, one can explain that there is a different orientation between both layers than in the case of 3D-hexagonal close packing.

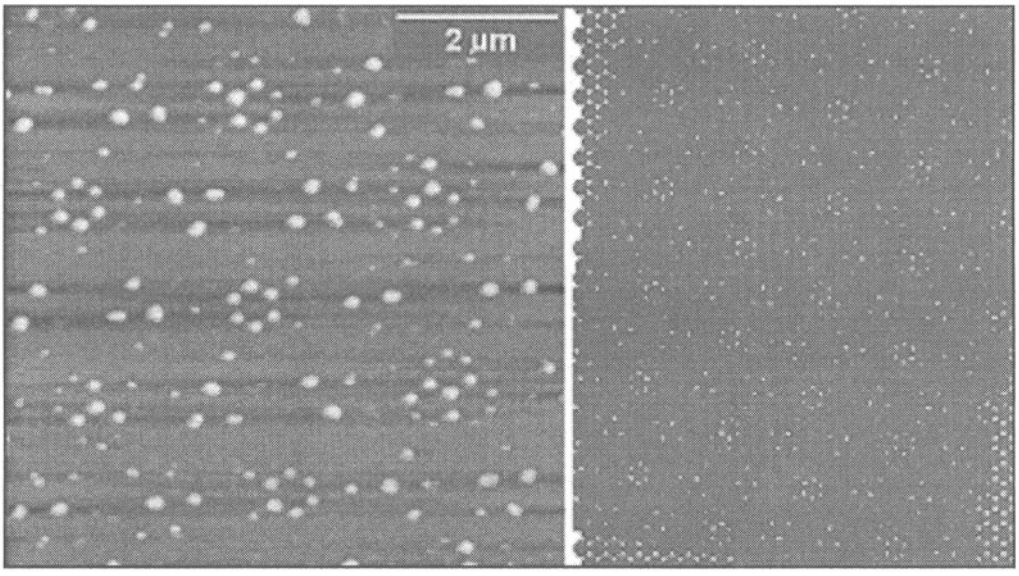

Figure 22. The result of evaporation of 15 nm nickel through double layer 496 nm PS-latex particles mask. The angle between both latex layers is about 10° (a). Simulation performed to prove the experimental results (b).

To investigate this orientation we performed a simple computer simulation, which indicates that the angle between both layers is about 30° (Figure 21b) or 10° (Figure 22b). It is very clear that the NSL technique can be applied to a whole host of applications because of short preparation times, low production costs, and the possibility for production of 2-D nanostructures of different geometries in the scale range of up to $1 cm^2$. Further improvement of evaporated structures could be carried out through annealing, which would ensure a high unification of particle size and particle homogeneity. Fabrication of sandwich-like multilayers of particles by the evaporation of three layers of metal was also presented as a possible method to enhance the magnetic properties of evaporated metal particles.

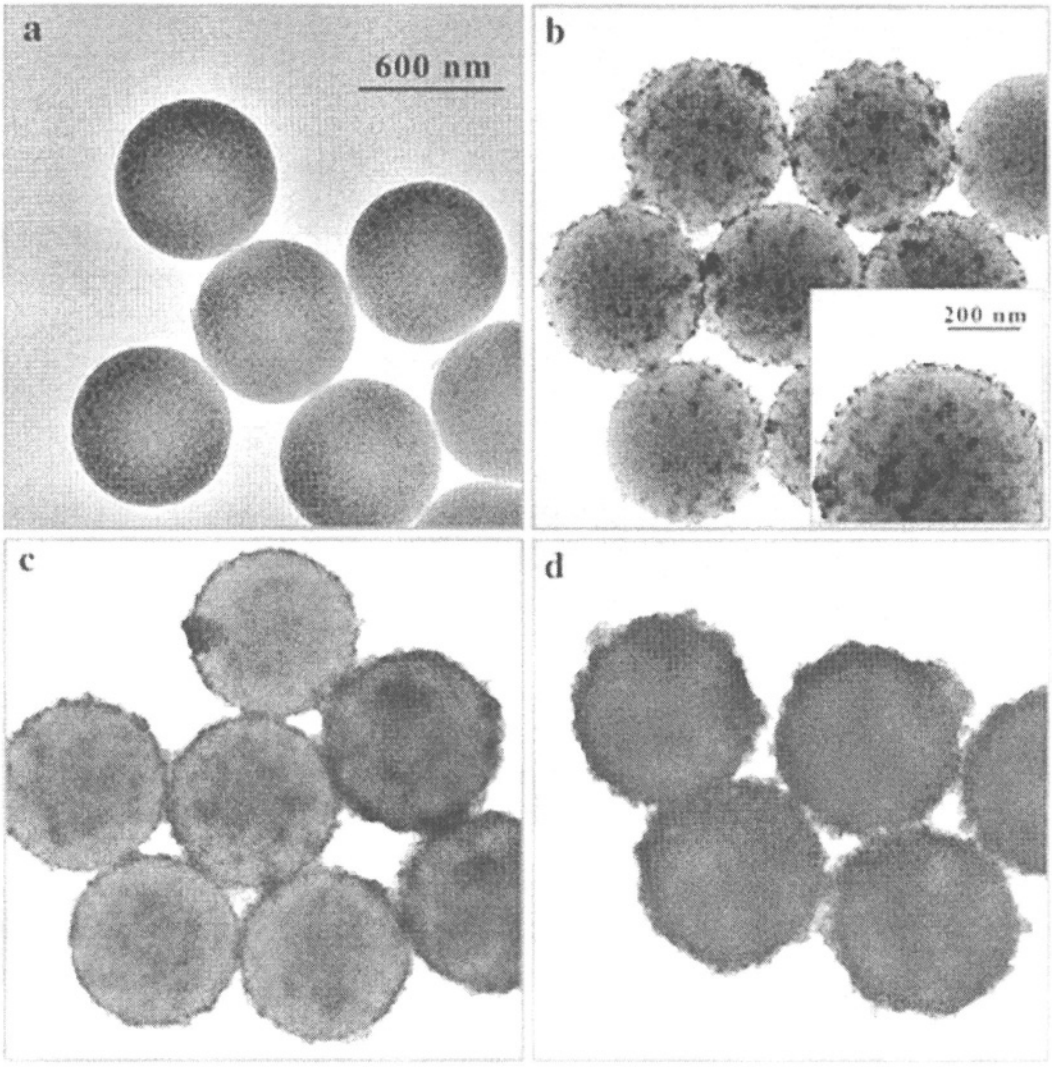

Figure 23. TEM micrographs of uncoated PS particles (a), and polyelectrolyte–modified PS particles with (b) one, (c) two, (d) three Fe_3O_4 nanoparticles/polyelectrolyte layers. The average diameters of the composite particles are respectively : 650, 770, and 960 nm. The insert pictures in (b) shown clearly Fe_3O_4 particles on the PS-particles many of them existing as aggregates. Adapted with permission from ref. 69c. Copyright 1999 Wiley-VCH.

4.3. Electrostatic Self-Assembly (ESA)

The last method we will discuss is based on the work of F. Caruso for the creation of multidimensional structures based on sequential electrostatic adsorption of Fe_3O_4 and poly(diallyldimethylammonium chloride) (PDADMAC) on submicrometer-sized anionic polystyrene (PS) particles. The thickness of the deposited multilayers can be tuned by the number of times the polyelectrolyte and Fe_3O_4 layers are applied onto PS-Latex particles. Novel efforts to produce uniformly coated colloidal particles in solution have relied on a number of different approaches.[67] By following such a scheme it has been possible to coat colloidal particles with polyelectrolytes,[68] nanoparticles,[69] and proteins.[70]

In this special case, 8-12 nm diameter Fe_3O_4 magnetite particles are synthesized according to the prescription in section 3.1, while the ESA is performed as follows. In the first step, 640nm diameter PS-latex particles are coated with a polyelectrolyte multilayer film (polydiallyldimethylammonium chloride, PDADMAC) which provides a uniformly charged surface that facilitates subsequent nanoparticle adsorption.[69c] In this case, the polyelectrolyte creates positive charge on the film surface permitting electrostatic interaction between the negatively charged nanoparticles and the film itself.

Once any excess of PDADMAC has been removed from solution via centrifugation, negatively charged Fe_3O_4 particles are added. Any excess iron particles are also removed by centrifugation, leaving a PS-latex particle with bound iron particles. This process can be repeated many times until the desired thickness of the magnetic layer is achieved (see Figure 23).

In Figure 23, the spherical uncoated particles show a smooth surface (a). It is clear that the diameter of the PS particles regularly increases with the number of Fe_3O_4 nanoparticle/polyelectrolyte multilayers deposited, reflecting the increased magnetic nanoparticle content in the shell structure with each deposition cycle. This coverage is equivalent to 2-3 monolayers (on average) of Fe_3O_4 nanoparticles per deposition.

Magnetic hollow spheres were produced by drying the coated PS particles on quartz substrates at room temperature, and by then calcining at 500°C under N_2 for several hours, followed by gentle redispersion through sonication in water.

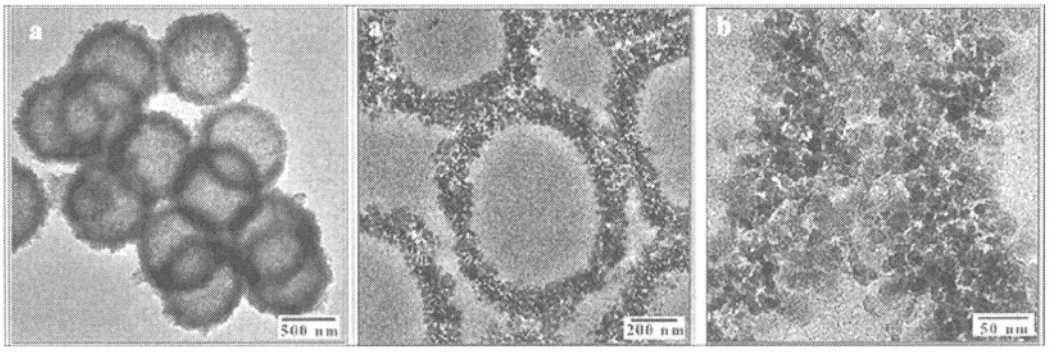

Figure 24. TEM micrographs of (a) magnetic hollow spheres prepared by calcination (500°C) of polyelectrolyte modified PS-particles coated with four Fe_3O_4 nanoparticle layers, (b) cross section of the same magnetic hollow spheres and (c) image (b) by higher magnification showing single magnetic particles deposed in layers. Adapted with permission from ref. 11c. Copyright 2001 Chem. Mater.

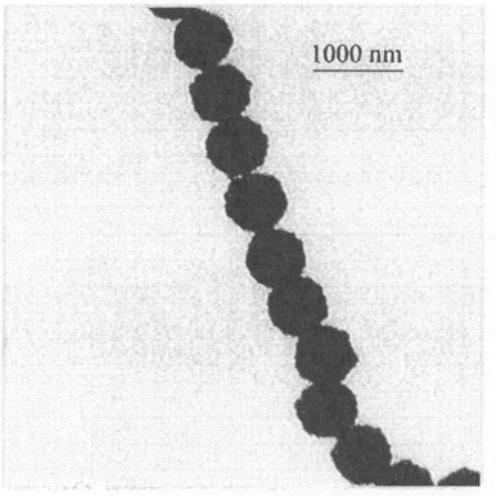

Figure 25. TEM image of composite magnetic particles aligned by using MDT. The core is polystyrene and the shell consists of polyelectrolyte and magnetic particles. Adapted with permission from ref. 69c. Copyright 1999 Wiley-VCH.

As a result of this high temperature treatment, one is left with a hollow shell from dissolution of the latex particles and a variety of iron species such as Fe_3O_4, Fe_2O_3, and FeO.[70] This is presented in Figure 24.

Results similar to those achieved by using the MDT process on cobalt particles can also be obtained on Fe_3O_4 covered PS-latex. For example, ordered chains of the modified PS particles have been observed.[69c] A typical image is shown in Figure 25. From the large body of experimental evidence it is clear that application of ESA and MDT opens up new possibilities for the technological application of colloids.

5. CONCLUSIONS

In this chapter, we have presented both the key theoretical principles behind magnetic assembly as well as some experimental data proving the validity of the methods discussed. The MDT, ESA and NSL methods are inherently more advantageous in comparison to self assembly methods, because they offer better control over the assembly process and greater reproducibility of results. In particular, while the ESA technique can generate large amounts of nanostructures and the NSL technique can produce large arrays of two-dimensional nanostructures, both schemes benefit from ease of sample handling. Of course, all the methods have great promise in aiding the development of technologies relevant to the electronics, pharmaceutical, and biosciences industries.

6. ACKNOWLEDGEMENT

The authors kindly acknowledge the support from their fellow colleagues J. Rybczynski, N. Sobal, U. Bloeck, and T. Kempa. This work was supported by the German Research Community (DFG) and Deutsche Chemische Indrustrie

7. REFERENCES

1. For reviews see e.g. a) C. J. Brinker and G. W. Scherer, *Sol-Gel Science* (Academic Press Inc., San Diego, 1990); b) H.-D. Dörfler, *Grenzflächen- und Kolloidchemie* (VCH, Weinheim, 1994), (in German); c) *Clusters and Colloids,* edited by G. Schmid (VCH, Weinheim, 1994); d) *Nanoparticles and Nanostructured Films,* edited by J. H. Fendler (Wiley-VCH, Weinheim, 1998); e) *Handbook of Surfaces and Interfaces of Materials,* edited by H. S. Nalwa (Academic Press, San Diego, 2001); f) P. Moriarty, Nanostructured materials, *Rep. Prog. Phys.* **64**, 297-381 (2001); g) Special issue on New Aspects of Nanocrystal Research, *MRS Bull.* **26**(12) (2001).
2. a) D. Weller and A. Moser, Thermal effect limits in ultra-high density magnetic recording, *IEEE Trans. Magn.* **35**, 4423-4439 (1999); b) D. J. Sellmyer, M. Yu, and M. D. Kirby, Nanostructured magnetic films for extremely high density recording, *Nanostruct. Mater.* **12**, 1021-1026(1999).
3. R. E. Rosensweig, *Ferrohydrodynamics* (Dover Publishing, New York, 1998).
4. a) Y. Z. Shao, J. K. L. Lai, and C. H. Shek, Preparation of nanocomposite working substances for room-temperature magnetic refrigeration, *J. Magn. Magn. Mater.* **163**, 103-108 (1996); b) V. K. Pecharsky and K. A. Gschneidner Jr., Magnetocaloric effect and magnetic refrigeration, *J. Magn. Magn. Mater.* **200**, 44-56 (1999); c) T. A. Yamamoto, M. Tanaka, Y. Misaka, T. Nakagawa, T. Nakayama, K. Niihara, and T. Numazawa, Dependence of the magnetocaloric effect in superparamagnetic nanocomposites on the distribution of magnetic moment size, *Scripta Materialia* **46**, 89-94 (2002).
5. a) M. Ronay, Preparation of magnetic particles and magnetic fluids by chemical reaction in a magnetic field, *IBM Technol. Discl. Bull.* **19**, 2753-2763 (1976); b) C. Kormann, E. Schwab, F.-W. Raulfs, and K. H. Beck, Magnetic ink concentrate, U.S. Patent 5,500,141 (1996).
6. J. C. Lodder, D. J. Monsma, R. Vlutters, and T. Shimatsu, The spin-valve transistor: technologies and progress, *J. Magn. Magn. Mater.* **198-199**, 119-124 (1999).
7. A. Jordan, R. Scholz, P. Wust, H. Schirra, T. Schiestel, H. Schmidt, and R. Felix, Endocytosis of dextran and silan-coated magnetite nanoparticles and the effect of intracellular hyperthermia on human mammary carcinoma cells in vitro, *J. Magn. Magn. Mater.* **194**, 185-196 (1999).
8. M. Y. Mapra, I. J. Körner, M. Hildebrandt, R. Bargou, D. Krahl, P. Reichardt, and B. Dörken, Monitoring of tumor cell purging after highly efficient immunomagnetic selection of CD34 cells from leukapheresis products in breast cancer patients: comparison of immunocytochemical tumor cell staining and reverse transcriptase-polymerase chain reaction, *Blood* **89**(1), 337-344 (1997).
9. a) S. W. Charles and R.E. Rosensweig, Magnetic fluids bibliography, *J. Magn. Magn. Mater.* **39**, 192-220 (1983); b) S. Kamiyama and R. E. Rosensweig, Magnetic fluids bibliography, *J. Magn. Magn. Mater.* **65**, 403-439 (1987); c) E. Blum, R. Osols, and R. E. Rosensweig, Magnetic fluids bibliography, *J. Magn. Magn. Mater.* **85**, 305-378 (1990); d) V. Cabuil, S. Neveu, and R. E. Rosensweig, Magnetic fluids bibliography, *J. Magn. Magn. Mater.* **122**, 439-482 (1993); e) S. P. Bhatnagar and R. E. Rosensweig, Magnetic fluids bibliography, *J. Magn. Magn. Mater.* **149**, 199-232 (1995); f) L. Vékás, V. Sofonea, and O. Balau, Magnetic fluids bibliography, *J. Magn. Magn. Mater.* **201**, 454-489 (1999).
10. a) S. A. lakovenko, A. S. Trifonov, M. Giersig, A. Mamedov, D. K. Nagesha, V. V. Hanin, E. C. Soldatov, and N. A. Kotov , One- and two-dimensional arrays of magnetic nanoparticles by the Langmuir-Blodgett technique, *Adv. Mater.* **11**, 388-392 (1999); b) T. Fried, G. Shemer, and G. Markovich, Ordered two-dimensional arrays of ferrite nanoparticles, *Adv. Mater.* **13**, 1158-1161 (2001).
11. a) M. A. Correa-Duarte, M. Giersig, N. A. Kotov, and L. M. Liz-Marzán, Control of packing order of self-assembled monolayers of magnetite nanoparticles with and without SiO_2 coating by microwave irradiation, Langmuir **14**, 6430-6435; b) F. G. Aliev, M. A. Correa-Duarte, A. Mamedov, J. W. Ostrander, M. Giersig, L. M. Liz-Marzán, and N. A. Kotov, Layer-by-layer assembly of core-shell magnetite nanoparticles: effect of silica coating on interparticle interactions and magnetic properties, *Adv. Mater.* **11**, 1006-1010 (1999); c) F. Caruso, M. Spasova, A. Susha, M. Giersig, and R. A. Caruso, Magnetic nanocomposite particles and hollow spheres constructed by a sequential layering approach, *Chem. Mater.* **13**, 109-116 (2001); d) E. L. Bizdoaca, M. Spasova, M. Farle, M. Hilgendorff, and F. Caruso, Magnetically directed self-assembly of submicron spheres with a Fe_3O_4 nanoparticle shell, *J. Magn. Magn. Mater.* **240**, 44-46 (2002).
12. M. Giersig and P. Mulvaney, Ordered two-dimensional gold colloid lattices by electrophoretic deposition, *J. Phys. Chem* **97**, 6334-6336 (1993).
13. a) M. Giersig and M. Hilgendorff, The preparation of ordered colloidal magnetic particles by magnetophoretic deposition, *J. Phys. D: Appl. Phys.* **32**, L111-L113 (1999); b) M. Hilgendorff, B. Tesche and M. Giersig, Creation of 3-d crystals from cobalt nanoparticles in external magnetic fields, *Aust. J. Chem.* **54**, 497-501 (2001).

14. *Handbook of Surfaces and Interfaces of* Materials, edited by H. S. Nalwa (Academic Press, San Diego, 2001) vol. 3.
15. a) R. D. Shull and L. H. Bennet, Nanocomposite magnetic materials, *Nanostruct. Mater.* **1**, 83-88 (1992); b) G. R Harp, S. S. P. Parkin, W. L. O'Brian, and B. P. Tonner, Induced Rh magnetic moments in Fe-Rh and Co-Rh alloys using X-ray magnetic circular dicroism, *Phys. Rev. B* **51**, 12037-12040 (1995); c) G. Moraïtis, H. Dreyssé, and M. A. Khan, Band theory of induced magnetic moments in CoM (M = Rh, Ru) alloys, *Phys. Rev. B* **54**, 7140-7142 (1996).
16. a) J. Rivas, R. D. Sánchez, A. Fondado, C. Izco, A. J. García-Bastida, J. García-Otero, J. Mira, D. Baldomir, A. Gonzáles, I. Lado, M. A. López-Quintela, and S. B. Oseroff, Structural and magnetic characterization of Co particles coated with Ag, *J. Appl. Phys.* **76**, 6564-6566 (1994); b) S. Sun, C. D. Murray, D. Weller, L. Folks, and A. Moser, Monodisperse FePt nanoparticles and ferromagnetic FePt nanocrystal superlattices, *Science* **287**, 1989-1992 (2000); c) J.-I. Park, and J. Cheon, Synthesis of "solid solution" and "core-shell" type cobalt-platinum magnetic nanoparticles via transmetallation reaction, *J. Am. Chem. Soc.* **123,** 5743-5746 (2001); d) C. J. O'Conner, V. Kolesnichenko, E. Carpenter, C. Sangregorio, W. Zhou, A. Kumbhar, J. Sims, and F. Agnoli, Fabrication and properties of magnetic particles with nanometer dimensions, *Synth. Met.* **122**, 547-557 (2001); e) H. Bönnemann, Nanostructured metal colloids – chemistry and potential applications, in *Handbook of Surfaces and Interfaces of Materials,* edited by H. S. Nalwa (Academic Press, San Diego 2001), vol. **3**, pp. 41-64; f) M. C. Fromen, A. Serres, D. Zitoun, M. Respaud, C. Amiens, B. Chaudret, P. Lecante, and M. J. Casanove, Structural and magnetic study of bimetallic $Co_{1-x}Rh_x$ particles, *J. Magn. Magn. Mater.* **242-245**, 610-612 (2001); g) N. S. Sobal, M. Hilgendorff, H. Möhwald, M. Giersig, M. Spasova, T. Radetic, and M. Farle, Synthesis and structure of colloidal bimetallic nanocrystals: the non-alloying system Ag/Co, *Nano Lett.* **2**, 621-624 (2002).
17. N. Buske, H. Sonntag, and T. Götze, Magnetic fluids- their preparation, stabilization and applications in colloid science, *Colloids Surf. A* **12**, 195-202 (1984).
18. D. V. Talapin, A. L. Rogach, M. Haase, and H. Weller, Evolution of an ensemble of nanoparticles in a colloidal solution: Theoretical study, *J. Phys. Chem. B* **105**, 12278-12285 (2001).
19. a) L. Katsikas, A. Eichmüller, M. Giersig, and H. Weller, Discrete exitonic transitions in quantum-sized CdS particles, *Chem. Phys. Lett.* **172**, 201-204 (1990); b) M. Respaud, J. M. Broto, H. Rakoto, A. R. Fert, L. Thomas, B. Barbara, M. Verelst, E. Snoeck, P. Lecante, A. Mosset, J. Osuna, T. Quid Ely, C. Amiens, and B. Chaudret, Surface effects on the magnetic properties of ultrafine cobalt particles, *Phys. Rev. B* **57**, 2925-2935 (1998); c) D. P. Dinega and M. G. Bawendi, Eine aus der Lösung zugängliche neue Kristallstruktur von Cobalt, *Angew. Chem.* **111**, 1906-1909; A solution –phase chemical approach to a new crystal structure of cobalt, *Angew. Chem. Int. Ed.* **38**, 1788-1791 (1999); d) I. G. Dance, R. G. Garbutt, and T. D. Bailey, Aggregated structures of the compounds $Cd(SC_6H_4X\text{-}4)_2$ in DMF solution, *Inorg. Chem.* **29**, 603-608 (1990).
20. J. N. Israelachvili, *Intermolecular and Surface Forces* (Academic Press, San Diego, 1992).
21. R. Tadmor, The London-van der Waals interaction energy between objects of various geometries, *J. Phys.: Condens. Matter* **13**, L195-L202 (2001).
22. a) D. Y. C. Chan, D. Henderson, J. Barojas, and A. M. Homola, The stability of a colloidal suspension of coated magnetic particles in an aqueous solution, *J. Res. Develop.* 29, 11-17 (1985); b) A. P. Philipse, M. P. B. van Bruggen, and C. Pathmamanoharan, Magnetic silica dispersions: preparation and stability of surface-modified silica particles with a magnetic core, *Langmuir* **10**, 92-99 (1994).
23. D. Lacoste and T. C. Lubensky, Phase transition in a ferrofluid at magnetic-field induced microphase separation, *Phys. Rev. E* **64**, 41506(8) (2001).
24. D. R. Crow, *Principles and Applications of Electrochemistry* (Chapman and Hall, London, 1979).
25. R. Charmas, Four-layer complexation model for ion adsorption at energetically heterogeneous metal oxide/electrolyte interfaces, *Langmuir* **15**, 5635-5648 (1999).
26. L. M. Liz-Marzán, M. A. Correa-Duarte, Isabel Pastoriza-Santos, P. Mulvaney, T. Ung, M. Giersig, and N. A. Kotov, Core-shell nanoparticles and assemblies thereof, in *Handbook of Surfaces and Interfaces of Materials,* edited by H. S. Nalwa (Academic Press, San Diego 2001), vol. **3**, pp. 189-237.
27. a) A. Henglein, Small-particle research: physicochemical properties of extremely small colloidal metal and semiconductor particles, *Chem. Rev.* **89**, 1861-1873 (1989); b) L. Spanhel and M. A. Anderson, Semiconductor clusters in the sol-gel process: quatized aggregation, gelation, and crystal growth in concentrated ZnO colloids, *J. Am. Chem. Soc.* **113**, 2826-2833 (1991); c) H. Weller, Kolloidale Halbleiter-Q-Teilchen: Chemie im Übergangsbereich zwischen Festkörper und Molekül, *Angew. Chem.* **105**, 43-55 (1993), *Angew. Chem. Int. Ed.* **32**, 41-53 (1993); d) C. B. Murray, C. R. Kagan, and M. G. Bawendi, Synthesis and characterization of monodisperse nanocrystals and close packed nanocrystal assemblies, *Annu. Rev. Mater. Sci.* **30**, 545-610 (2000).
28. W. Ostwald, *Die Welt der vernachlässigten Dimensionen* (Steinkopf, Dresden, 1915).

29. E. Papirer, P. Horny, H. Balard, R. Anthore, C. Petipas, and A. Martinet, The preparation of a ferrofluid by decomposition of dicobalt octacarbonyl, *J. Colloid Interface Sci.* **94**, 207-228 (1993).
30. S. Sun and C. B. Murray, Synthesis of monodisperse cobalt nanocrystals and their assembly into magnetic superlattices, *J. Appl. Phys.* **85**, 4325-4330 (1999).
31. a) K. R. Brown and M. J. Natan, Hydroxylamine seeding of colloidal Au nanoparticles in solution and on surfaces, *Langmuir* **14**, 726-728 (1998); b) N. R. Jana, L. Gearheart, and C. J. Murphy, Evidence for seed-mediated nucleation in the chemical reduction of gold salts to gold nanoparticles, *Chem. Mater.* **13**, 2313-2322 (2001); c) H. Yu, P. C. Gibbons, K. F. Kelton, and W. E. Buhro, Heterogeneous seeded growth: a potentially general synthesis of monodisperse metallic nanoparticles, *J. Am. Chem. Soc.* **123,** 9198-9199 (2001).
32. A. Fojtik, H. Weller, U. Koch, and A. Henglein, Photo-chemistry of colloidal metal sulfides 8. photo-physics of extremely small cds particles: Q-state CdS and magic agglomeration numbers, *Ber. Bunsenges. Phys. Chem.* **88**, 969-977 (1984).
33. a) V. Ptatschek, T. Schmidt, M. Lerch, G. Müller, L. Spanhel, A. Emmerling, J. Fricke, A. H. Foitzik, and E. Langer, Quatized aggregation phenomena in II-VI-semiconductor colloids, *Ber. Bunsenges. Phys. Chem.* **102**, 85-95 (1998); b) C. Lorenz, A. Emmerling, J. Fricke, T. Schmidt, M. Hilgendorff, L. Spanhel, and G. Müller, Aerogels containing strongly photoluminescing zinc oxide nanocrystals, *J. Non-Cryst. Solids.* **238**, 1-5 (1998).
34. a) A. Henglein and M. Giersig, Formation of colloidal silver nanoparticles: capping action of citrate, *J. Phys. Chem. B* **103**, 9533-9539 (1999); b) Z. A. Peng and X. Peng, Mechanisms of the shape evolution of CdS nanocrystals, *J. Am. Chem. Soc.* **123**, 1389-1395 (2001).
35. G. Wedler, *Lehrbuch der Physicalischen Chemie* (VCH, Weinheim, 1987).
36. R. Massart and V. Cabuil, Synthèse en milieu alcalin de magnétite colloïdale: contrôle du rendement et de la taille des particules, *J. Chim. Phys.* **84**, 967-973 (1987).
37. a) J. P. Chen, C. M. Sørensen, and K. J. Klabunde,. Enhanced magnetization of nanoscale colloidal nanoparticles, *Phys. Rev. B* **51**, 11527-11532 (1995); b) M.-P. Pileni, Magnetic fluids: fabrication, magnetic properties, and organization of nanocrystals, *Adv. Funct. Mater.* **11**, 323-336 (2001).
38. a) M. Giersig and M. Hilgendorff, Ordered colloidal magnetic particles by magnetophoretic deposition, in *Cluster and Nanostructure Interfaces,* edited by P. Jena, S. N. Khanna, and B. K. Rao (World Scientific, Singapore, 2000), pp. 203-208; b) C. B. Murray, S. Sun, H. Doyle, and T. Betley, Monodisperse 3d transition-metal (Co, Ni, Fe) nanoparticles, *MRS Bull.* **26**, 985-991 (2001); c) J. Osuna, D. de Caro, C. Amiens, B. Chaudret, E. Snoeck, M. Respaud, J.-M. Broto, and A. Frert, Synthesis, characterization, and magnetic properties of cobalt nanoparticles from an organometallic precursor, *J. Phys. Chem.* **100**, 14571 - 14574 (1996).
39. a) T. W. Smith and D. Wychick, Colloidal iron dispersions prepared via the polymer-catalyzed decomposition of iron pentacarbonyl, *J. Phys. Chem.* **84**, 1621-1629 (1980); b) K. S. Suslick, M. Fang, and T. Hyeon, Sonochemical Synthesis of iron colloids, *J. Am. Chem. Soc.* **118**, 11960-11961 (1996).
40. a) S. R. Hoon, M. Kilner, G. J. Russel, and B. K. Tanner, Preparation and properties of nickel ferrofluids, *J. Magn. Magn. Mater.* **39**, 107-110 (1983); b) N. Cordente, M. Respaud, F. Senocq, M.-J. Casanove, C. Amiens, and B. Chaudret, Synthesis and magnetic properties of nickel rods, *Nano Lett.* **1**, 565-568 (2001).
41. I. Nakatani, M. Hijikata, and K. Ozawa, Iron-nitride magnetic fluids prepared by vapour-liquid reaction and their magnetic properties, *J. Magn. Magn. Mater.* **122**, 10-14 (1993).
42. M. Giersig and M. Hilgendorff, On the road from single, nanosized, magnetic clusters to multi-dimensional nanostructures, *Colloids Surf. A* **202**, 207-213 (2002).
43. M. Hilgendorff and M. Giersig, Synthesis of colloidal magnetic nanoparticles: properties and applications, *NATO ASI Series,* in press.
44. a) R. V. Upadhyay, K. J. Davies, S. Wells, and S. W. Charles, Preparation and characterization of ultra-fine $MnFe_2O_4$ and $Mn_xFe_{1-x}O_4$ spinel systems: II. Magnetic fluids, *J. Magn. Magn. Mater.* **139**, 249-254 (1995); b) K. J. Davies, S. Wells, R. V. Upadhyay, S. W. Charles, K. O'Grady, M. El Hilo, T. Meaz, and S. Mørup, The observation of multi-axial anisotropy in ultrafine cobalt ferrite particles used in magnetic fluids, *J. Magn. Magn. Mater.* **149**, 14-18 (1995); c) P. C. Fannin, S. W. Charles, and J. L. Dormann, Field dependence of the dynamic properties o f colloidal suspensions of $Mn_{0.66}Zn_{0.34}Fe_2O_4$ and $Ni_{0.5}Zn_{0.5}Fe_2O_4$ particles, *J. Magn. Magn. Mater.* **201,** 98-101 (1999).
45. a) K. J. Davies, S. Wells, and S. W. Charles, The effect of temperature and oleate adsorption on the growth of maghemite particles, *J. Magn. Magn. Mater.* **122**, 24-28; (1993) b) I. Mălăescu, L. Gabor, F. Claici, and N. Ştefu, Study of some magnetic properties of ferrofluids filtered in magnetic field gradient, *J. Magn. Magn. Mater.* **222**, 8-12 (2000).
46. a) H. Bönnemann, W. Brijoux, R. Brinkmann, E. Dijius, T. Joußen, and B. Korall, Erzeugung von kolloidalen Übergangsmetallen in organischer Phase und ihre Anwendung in der Katalyse, *Angew. Chem.*

103, 1344-1346 (1991), *Angew. Chem. Int. Ed.* **30**, 1344-1346 (1991); b) J. Fink, C. J. Kiely, D. Bethell, and D. J. Schiffrin, Self-organization of nanosized gold particles, *Chem. Mater.* **10**, 922-926 (1998).

47. D. I. Gittins. and F. Caruso, Spontaneous phase transfer of nanoparticulate metals from organic to aqueous media, *Angew. Chem. Int. Ed.* **40**, 3001-3004 (2001).
48. C. B. Murray, S. Sun, W. Gaschler, H. Doyle, T. A. Betley, C. R. and Kagan, Colloidal synthesis of nanocrystals and nanocrystal superlattices, *IBM J. Res. Dev.* **45**, 47-56. (2001).
49. V. F. Puntes, K. M. Krishnan, and P. Alivisatos, Synthesis, self-assembly, and magnetic behavior of a two-dimensional superlattice of single-crystal ε-Co nanoparticles, *Appl. Phys. Lett.* **78**, 2187-2189 (2001).
50. H. Laidler and K. O' Grady, Crystallographic effects in Co alloy media, *http://www.datatech-online.com* **1,** 93-97 (1998).
51. O. Adeyeye, J.A.C. Bland, and C. Daboo, Magnetic properties of arrays of "holes" in $Ni_{80}Fe_{20}$ films, *Appl. Phys. Lett.* **70**, 3164-3166, (1977).
52. a) J. Rybczynski, M. Giersig, Nanosphere litography: fabrication of large periodic magnetic particles arrays using nanosphere mask, submitted (2002). b) J. Rybczynski, M. Giersig, Nanosphere lithography – Fabrication of various periodic magnetic particle arrays using versatile nanosphere masks, in: Low-Dimensional Systems: Theory, Preparation and Some Applications, edited by L. M. Liz-Marzán and M. Giersig, *NATO ASI Series* 2003, in press.
53. a) U. Wiedwald, M. Spasowa, M. Farle, M Hilgendorff, M. Giersig, Ferromagnetic resonance of monodisperse Co particles, *J.Vac.Sci. Technol. A ,* **19**, 1773-1776, (2001), b) M. Spasova, U. Wiedwald, R. Ramchal, M. Farle, M. Hilgendorff, M. Giersig, *J. Magn. Magn. Mater.,* **240**, 40-43, (2002).
54. S. H. Park, B. Gates, Y. Xia, A three-dimensional photonic crystal operating in the visible region, *Adv. Mat.* **11**, 462-466 (1999).
55. B. Gates, Y. Xia, Photonic crystals that can be addressed with an external magnetic field, *Adv Mat.* **13**, 1605-1608(2001).
56. Y. Xia, B. Gates, Y. Yin, Current chemistry. Building complex structures from monodisperse spherical colloids, *Aust J. Chem.* **54**, 287-290 (2001).
57. J. G. Wen, Z. P. Huang, D. Z. Wang, J. H. Chen, S. X. Yang, Z. F. Ren, J. H. Wang, L. E. Calvet, J. Chen, J. F. Klemic, M. A. Reed, Growth and characterization of aligned carbon nanotubes from patterned nickel nanodots and uniform thin films, *J. Mater. Res.* **16,** 3246-3253 (2001).
58. M. E. Read, W. G. Schwarz, M. J. Kremer, J. D. Lennhoff, D. L. Carnahan, K. Kempa, Z. F. Ren, Carbon nanotube-based cathodes for microwave tubes, *Proc 2001 Part. Accelerator Conf., Chicago* 1026-1028 (2001).
59. M. Giersig, P. Mulvaney, Formation of ordered two-dimensional gold colloid lattices by electrophoretic deposition, J. Phys. *Chem.* **97**(24), 6334-6336 (1993).
60. A. Rogach, A. Susha, F. Caruso, G. Sukhorukov, A. Kornowski, S. Kershaw, H. Möhwald, A. Eychmüller, and H. Weller, Nano- and microengineering: 3-D colloidal photonic crystals prepared from sub-μm-sized polystyrene latex spheres pre-coated with luminiscent polyelectrolyte/nanocrystal shells, *Adv. Mat.* **12** 333-337 (2000).
61. H. W. Deckman and J. H. Dunsmuir, Natural lithography, *Appl. Phys. Lett.* **41**, 377-379 (1982).
62. a) J. C. Hulteen and P. R. Van Duyne, Nanosphere lithography: A materials general fabrication process for periodic particle array surfaces, *J. Vac. Sci. Techn. A ,* **13**, 1553-1558 (1995); b) J. C. Hulteen, D. A. Treichel, M. T. Smith, M. L. Duval, T. R. Jensen, and R. P. Van Duyne, Nanosphere lithography: size-tunable silver nanoparticle and surface cluster arrays, *J. Phys. Chem.* **103**, 3854-3863 (1999); c) M. Winzer, M. Kleiber, N. Dix, and R. Wiesendanger, Fabrication of nano-dot and nano-ring-arrays by nanosphere lithography, *Appl. Phys. A* **63**, 617-619 (1996).
63. a) R. Micheletto, H. Fukuda, and M. Ohtsu, A simple method for the production of a two-dimensional, ordered array of small particles, *Langmuir* **11**, 3333-3336 (1995); b) J. Boneberg, F. Burmeister, C. Schäfle, and P. Leiderer, The formation of nano-dot and nano-ring structures in colloidal monolayer lithography, *Langmuir* **13**, 7080-7084 (1997); c) F. Burmeister, W. Badowsky, T. Braun, S. Wieprich, J. Boneberg, and P. Leiderer, Colloid monolayer lithography – a flexible approach for nanostructuring of surfaces, *App. Surf. Sci.* **144-145**, 461-466 (1999); d) F. Burmeister, C. Schäfle, B. Keilhofer, K. M. Bechinger, J. Boneberg, and P. Leiderer, From mesoscopic to nanoscopic surface structures: Lithography with colloid monolayers, *Adv. Mat.* **10**, 495-497 (1998); e) N. D. Denkov, O. D. Velev, P. A. Kralchevsky, I. B. Ivanov, H. Yoshimura, and K. Nagayama, Mechanism of formation of two-dimensional crystals from latex particles on substrates, *Langmuir* **8,** 3183-3190 (1992); f) S. Rakers, L. F. Chi, and H. Fuchs, Influence of the evaporation rate on the packing order of polydisperse latex monofilms, *Langmuir* **13**, 7121-7124 (1997); g) E. Adachi, A. S. Dimitrov, and K. Nagayama, Stripe patterns formed on a glass surface during droplet evaporation, *Langmuir* **11**, 1057-1060 (1995).
64. Y. Lu, Y. Yin, B. Gates, and Y. Xia, Growth of large crystals of monodispersed spherical colloids in fluidic cells fabricated using non-photolithographic method, *Langmuir* **17**, 6344-6350 (2001).

65. S. H. Park and Y. Xia, Assembly of mesoscale particles over large areas and its application in fabricating tunable optical filters, *Langmuir* **15**, 266-273 (1999).
66. F. Burmeister, C. Schäfle, T. Matthes, M. Böhmisch, J. Boneberg, and P. Leiderer, Colloid monolayer as versative lithographic masks, *Langmuir* **13**, 2983-2987 (1997).
67. F. Caruso, Nanoengineering of particle surfaces, *Adv. Mater.* **13**, 11-22, (2001).
68. a) F. Caruso, E. Donath, and H. Möhwald, Influence of polyelectrolyte multilayer coatings on Förster resonance energy transfer between 6-carboxyfluorescein and rhodamine B-labeled particles in aqueous solution, *J. Phys. Chem. B* **102**, 2011-2016, (1998); b) E. Donath, G. B. Sukhorukov, F. Caruso, S.A. Davis, and H. Möhwald, Novel hollow polymer shells by colloid-templated assembly of polyelectrolytes, *Angew. Chem., Intl. Ed.* **37**,2201-2205, (1998).
69. a) F. Caruso, R.A. Caruso and H. Möhwald, Nanoengineering of inorganic and hybrid hollow spheres by colloidal templating, *Science,* **282**, 1111-1114, (1998); b) A. Susha, F. Caruso, A.L. Rogach, G. B. Sukhorukov, A. Kronowski, H. Möhwald, M. Giersig, A. Eichmülller, and H. Weller, Formation of luminescent spherical core-shell particles by the consecutive absorption of polyelectrolyte and CdTe(S) nanocrystals on latex colloids, *Colloids Surf. A,* **163**(1), 39-44, (2000); c) F. Caruso, A. S. Susha, M. Giersig, and H. Möhwald, Magnetic core-shell particles: preparation of magnetite multilayers on polymer latex microspheres, *Adv. Mater.* **11**, 950 (1999).
70. a) F. Caruso and H. Möhwald, Protein multilayer formation on colloids through a stepwise self-assembly technique, *J. Am. Chem. Soc.* **121**, 6039-6046 (1999); b) F.Caruso, H.Fidler, and K. Haage, Assembly of β-glucosidase multilayers on spherical colloidal particles and their use as active catalysts, *Colloids Surf. A,* **169**, 287-293 (2000).

16
MAGNETIC NANOSTRUCTURES FROM CLUSTERS

A. Perez, V. Dupuis, J. Tuaillon-Combes, L. Bardotti, B. Prével, P. Mélinon, M. Jamet, W. Wernsdorfer, and B. Barbara*

1. INTRODUCTION

The design and fabrication of magnetic nanostructures and the study of their specific properties are playing an increasingly important role directly related with the large number of potential applications in various fields such as information storage and magnetoelectronic devices.[1-5] From the fundamental point of view, the magnetic behaviour of individual, isolated nanoscale systems was mainly theoretically approached while experimental investigations concerned essentially nanoparticles assemblies because of the sensitivity limitation of the magnetic characterization techniques. On the theoretical side**, *ab-initio* calculations within the now standard Local Spin Density (LSD) approximation to the Density Functional Theory (DFT) have proven to be a valuable tool to study the structure and electronic properties of systems up to some few hundreds of atoms. In particular, the spin order of nanosize systems (atomic monolayers, small clusters, etc) is now within reach of such calculations. In the last few years, the appearance of non-colinear spin functionnals[6] combined with attempts to provide a framework for molecular dynamics on the spin degrees of freedom[7,8] allowed to extend the field of application of such approaches. It remains nevertheless that the energy range at which e.g. spin-orbit effects occur (i.e. a few meV) is still a challenge for *ab-initio* calculations aiming at calculating for example the barrier (the anisotropy) for spin flip in nanosize systems. On the experimental side, the recent development of novel original magnetometers with sensitivity approaching 10^{-17} emu which are capable to detect the magnetization reversal of one single nanoparticle (i.e. a few cubic nanometers of cobalt)[9]

---

* A. Perez, V. Dupuis, J. Tuaillon-Combes, L. Bardotti, B. Prével, P. Mélinon and M. Jamet, Département de Physique des Matériaux, Université Claude Bernard Lyon 1 and CNRS (UMR 5586), 69622 Villeurbanne cedex, France. W. Wernsdorfer and B. Barbara, Laboratoire de Magnétisme Louis Néel, CNRS, BP 166, 38042 Grenoble cedex, France.

** The authors are indebted to Dr. X. Blase from the Département de Physique des Matériaux, University Claude Bernard Lyon 1 and CNRS, for helpful discussions on the theoretical treatments of magnetic nanostructures.

has opened a promising window in this field of "experimental nanomagnetism". For example, in bulk magnetic materials (3D), magnetostatic and bulk magnetocrystalline energies are the main sources of anisotropy, whereas in lower dimensionality systems such as thin films (2D), wires (1D) or clusters (0D), strong surface effects are expected emphasizing the necessity of studying one single nano-object to provide information on the different contributions to the magnetic anisotropy. Investigations on the sources of magnetic anisotropy in nanoscale systems are of particular importance for future applications with regard to the superparamagnetic limit characteristic of such small systems.[5] In fact, when decreasing the size of the particle down to the nanometric range, the anisotropy energy K_uV (where K_u is the anisotropy constant and V the volume of the particle) which acts to fix the magnetization along an easy axis is counterbalanced by the thermal energy kT responsible for magnetization fluctuations between easy axis. For isolated nanosize particles of conventional magnetic materials, the blocking temperature T_B indicating the upper limit above which the particles behave as superparamagnetic is of the order of 10 K to a few tens of K. Consequently, a first challenge prior to applications consists of developing novel magnetic materials in the form of nanosize particles with a rather high anisotropy in order to remain magnetically oriented up to room temperature or above.[5,10] In the particular case of recording at high area-densities, based on the simple extrapolation of the continuous density increase in the last two decades directly connected with bit dimension decrease, one can expect that fundamental physics limitations and especially those related with the superparamagnetic limit will begin to predominate typically around 2005.[5] Thus, in this general context of quite fast evolution, the effort to understand the physics of ever smaller structures has been paralleled by attempts to synthesize magnetic nanoparticles with controlled size and morphology, structure and composition, to reach optimum values of various key-parameters: coercivity Hc, remanent magnetization Mr, blocking temperature T_B, etc. In this field, solution phase chemical synthesis has been successfully used to prepare monodisperse pure or alloyed metal particles[1,11] as well as physical methods such as vacuum atomic or molecular deposition techniques or thin film nanoengraving techniques.[12,14] As for the chemical syntheses, they generally offer the unique advantage to prepare large quantities of nanostructured matter while the physical ones mentioned above are very often limited to the preparation of thin films. However, these last methods seem still promising in terms of specificity of the nanoparticle structures and properties related with their non equilibrium preparation conditions generally characterized by relatively high cooling rates. Among various vacuum deposition techniques, a special attention is drawn in this paper to the low energy cluster beam deposition (LECBD) which has been successfully developed during the past ten years to prepare original nanostructured materials of different types (metallic, covalent).[2,15-17] This technique consists of the deposition on various substrates in ultra high vacuum (UHV) of supersonic nanosize clusters preformed in the gas phase using combined vaporization-inert gas condensation sources. In this case, cooling rates as large as 10^{10} K/s (i.e. when using a laser vaporization source) can be at the origin of the formation of clusters with non conventional structures and properties. Moreover, in the low energy deposition regime (i.e. kinetic energy per atom of the cluster lower than 1 eV), clusters are not fragmented upon impact on the substrate leading to the formation of supported nanostructures which retain the memory of the structure and properties of the free incident clusters.

In this chapter we describe the synthesis of magnetic nanostructures using the low energy cluster beam deposition technique as well as their structural and magnetic

properties. Pure transition metal clusters (i.e. Co), and mixed transition metal-rare earth clusters (i.e. Co-Sm) or other mixed transition metal-metal clusters (i.e. Co-Ag, Co-Pt), in the size range from a few hundreds to a few thousands of atoms (diameters ≈ 2-5 nm), were prepared in the gas phase inside a laser vaporisation source associated with a high pressure inert gas condensation and subsequently deposited on various substrates in UHV. Depending on the deposition rate, films of isolated dispersed clusters supported on the surface of the substrate (coverage rate lower than 50 % corresponding to the 2D-percolation threshold), or embedded in non magnetic matrices (volume-fraction lower than about 20 % corresponding to the 3D-percolation threshold) have been prepared. Structural characterizations using high resolution transmission electron microscopy (HRTEM) associated with X-ray diffraction (GISAXS) and absorption (EXAFS) were performed prior to the study of their corresponding magnetic properties. In this last case, various complementary techniques were combined in order to investigate the magnetic behaviour from an isolated individual cluster (using an original microSQUID-magnetometry technique) to an assembly of non-interacting or interacting clusters (using conventional SQUID or VSM-magnetometry techniques). Complementary X-ray magnetic circular dichroism (XMCD) measurements were performed to probe the magnetism of clusters at a local scale. On the basis of the relatively large and synthetic view of the behaviour of magnetic nanostructured systems as deduced from these studies, new routes for the realization of cluster based high area-density devices were tested and the preliminary results are also presented.

2. MAGNETIC NANOSTRUCTURE PREPARATION BY LECBD

Cluster assembled films are prepared by deposition of low energy clusters preformed in the gas phase (LECBD) using a specially designed equipment schematically represented in Figure 1. For that purpose, a cluster generator based on a combined laser vaporisation-gas condensation source has been developed to produce intense supersonic jets of nanoclusters with sizes ranging from a few tens to a few thousands of atoms (diameter ≈ 1 to a few nm), typically. Briefly, a YAG laser (λ = 532 nm, pulse duration ≈ a few ns, frequency ≤ 30 Hz), or a Ti-Sapphire laser (λ = 790 nm, pulse duration ≈ a few μs, frequency ≤ 30 Hz) are used to vaporize the target rod mounted in the source chamber (Figure 1). Combined with the laser-pulse, a high pressure gas-pulse (He, 3 to 6 bars, pulse duration 200 to 500 μs) is injected in the source to rapidly cool the plasma generated at the target surface and to nucleate clusters which are subsequently completely cooled and stabilized in the supersonic expansion taking place at the exit nozzle of the source. The main feature of this type of cluster source compared to others currently used (thermal, sputtering) is the very high cooling rate up to about 10^{10} K/s which governs the formation of the original nanoscale systems in non-equilibrium conditions. From the key parameters of the source (laser pulses, gas pulses/continuous gas flow, delay between both pulses, and geometries of the nucleation chamber in the source and the nozzle), it is possible to control the cluster size distributions measured in the high resolution time of flight (TOF) mass spectrometer mounted immediately after the skimmer (Figure 1). In this case, neutral clusters are photo-ionized using a tunable excimer-dye laser, then deviated and accelerated at the entrance of the TOF-line.

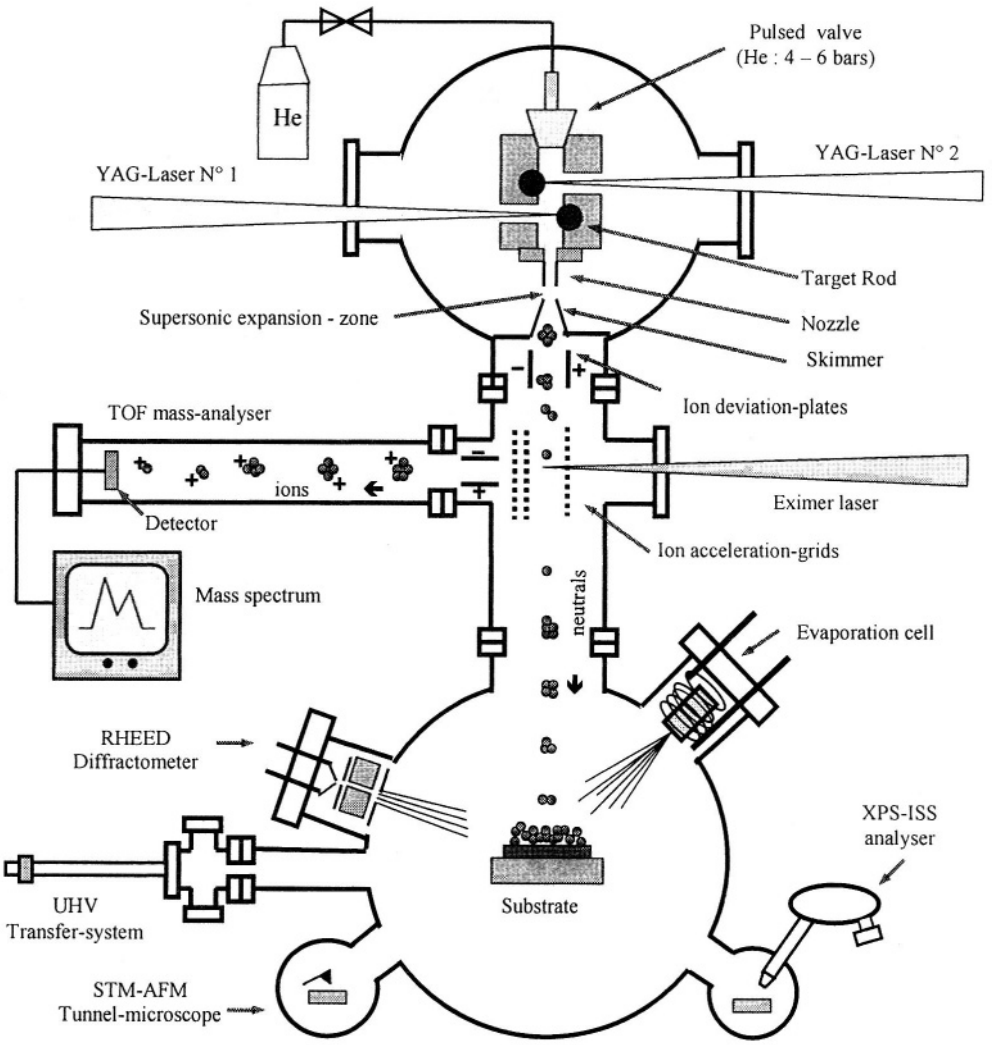

Figure 1. Schematic view of the cluster generator based on a combined laser vaporisation/inert gas condensation source, associated to a time of flight mass spectrometer for the studies of free clusters and a UHV-deposition chamber for cluster assembled film preparations. The source can operate with one or two independent laser/target arrangements for the production of pure clusters as well as mixed clusters. Some characterization techniques of the films are available in situ in UHV : RHEED diffractometry, STM-AFM near field microscopy, XPS-ISS spectrometry. A UHV-transfer system is used for sample transfers to ex-situ equipment. An electron-beam evaporator in situ in UHV is used for co-deposition experiments to produce films of clusters embedded in various media.

At this stage, photo-ionization near threshold and photo-fragmentation experiments are performed on free clusters to characterize their structures and properties. In the particular case of Co and Ni free-clusters, icosahedral structures are clearly observed in a size range up to a few thousands of atoms,[18] while for Fe-clusters the situation seems more complicated probably because of the competition between different structures.[18] For mixed-cluster production (i.e. bimetallic), two methods have been developed, based on the use of a compound target directly mounted in the source or a special source with two

independent targets simultaneously vaporized by two independent lasers (Figure 1). When using the technique with a compound target, it has been verified for various bimetallic systems studied (Pt-Pd,[19] Au-Ni,[20] Au-Ag,[21] Co-Sm[10]) that the clusters exhibit the same compositions as those from target rods. However, depending on some specific effects such as segregation, atoms can be inhomogeneously distributed within the clusters.

After the first stage of free cluster studies in flight, deposition experiments to grow nanostructured films from clusters are performed. In LECBD-experiments, only neutral clusters having the very low energy gained in the supersonic expansion at the exit of the source ($\leq$ a few 10^{-2} eV per atom) are deposited on substrates in the UHV-deposition chamber mounted on line with the cluster generator-TOF arrangement (Figure 1). In this case, the complete distributions of neutral clusters (nearly Gaussian in shape and rather narrow when using the laser vaporization generator) are directly deposited on the substrates to grow films, which allows us to reach relatively high deposition rates (0.1 nm/minute to 0.1 nm/second) for all kinds of clusters. Moreover, by co-depositing on the same substrate an atomic beam emitted by the e-beam evaporator mounted in the deposition chamber (Figure 1), it is possible to produce films of clusters embedded in various matrices (metallic, transparent oxides). In this last case, since both cluster and atomic beams are independent, this technique allows the preparation of any kind of cluster/matrix system, even with miscible elements, in a wide range of cluster concentrations.

3. STRUCTURES AND MORPHOLOGIES OF CLUSTER-ASSEMBLED FILMS

A very simple way to study the characteristic nucleation and growth process of LECBD-metallic films consists of measuring the electrical conductivity of the films in situ during depositions on insulating substrates (i.e. silica glass) with pre-deposited conducting electrodes.[22] As shown in Figure 2, the diagrams representing the conductivity as a function of the equivalent thickness of metal deposited measured using a quartz balance exhibit three zones: a first zone in the form of a plateau at a nearly zero-conductivity for deposited thicknesses lower than the 2D-percolation threshold, followed by a second zone represented by an abrupt increase of several orders of magnitude of the conductivity at a thickness corresponding to the 2D-percolation threshold, and a third zone above with a plateau of conductivity characteristic of a continuous thin metallic film. The equivalent thickness of metal corresponding to the 2D-percolation threshold deduced from these experimental diagrams is of the order of 1.5 to 2 nm when depositing clusters with a size distribution centred around 2 - 3 nm on substrates at room temperature or lower (80 K). This corresponds to a coverage of the surface of the substrate by nanoclusters of about 50 %, in agreement with a model assuming a random deposition of clusters which do not fragment upon impact on the substrate. From the observations of the morphology of the deposits at different stages up to the 2D-percolation threshold this process of a random pavement of the substrate by the incident free clusters is confirmed in the case of Fe, Co, and Ni-clusters deposited on silica glass substrates, or on amorphous carbon films, at 300 K and 80 K.[23]

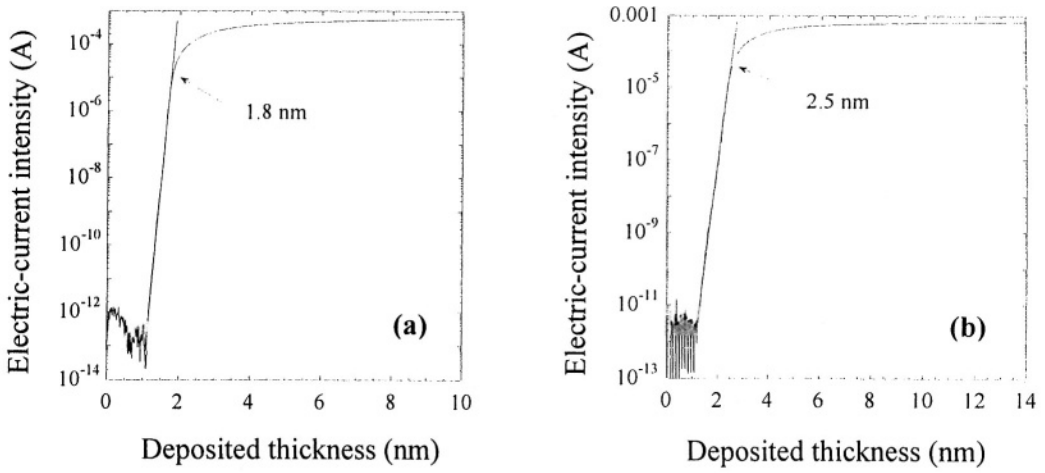

Figure 2. In situ measurements of the electric-current intensity during depositions of Co-clusters (a) or Ni-clusters (b) between two predeposited chromium electrodes on silica-glass substrates at temperatures T = 80 K (a) and T = 300 K (b). The equivalent metal thicknesses deposited in the form of clusters measured using a quartz-balance are reported on the horizontal axes.

The characteristic nanostructured morphologies of cluster assembled films as a function of the deposition parameters (nature, mean size, and flux of the incident free clusters, nature and temperature of the substrate) are observed in-situ using the STM-AFM near field microscope mounted in the UHV-deposition chamber[24] (Figure 3). Complementary high resolution transmission electron microscopy (HRTEM) observations were performed ex-situ to characterize the atomic structure of isolated supported clusters and cluster assembled nanostructures.[23] In this case, deposits below the 2D-percolation threshold (coverage rate < 50 %) were performed on amorphous carbon coated grids and subsequently protected by a thin amorphous carbon layer on top before removing in air. Structural characterizations on collections of clusters by X-ray techniques (diffraction and absorption (EXAFS))[23,25] are generally performed in addition to HRTEM-observations. From both these experimental and theoretical studies it is clearly shown that in the LECBD-regime, clusters are not fragmented upon impact on the surface of the substrate. Deposited clusters as large as a few thousands of atoms can diffuse quite fast on the substrate and a key parameter to control this process is the misfit between both lattices at the cluster/substrate interface, in addition to the substrate temperature.[26-30] Moreover, up to room temperature, experimental observations as well as molecular dynamics simulations show that the coalescence between two adjacent clusters to form a larger nanostructure is limited leading to a characteristic two dimensional growth process of the cluster film.[2,26-31] Such effect is particularly justified for clusters of rather high melting temperature materials which are the cases of the magnetic systems under considerations in our experiments. Finally, depending on the above mentioned cluster/substrate characteristic parameters which are well controlled during deposition experiments, specific nanostructure morphologies can be stabilized on the substrate between the two extreme cases: (i) isolated supported clusters randomly distributed on the substrate when the diffusion process is very limited[24] (Figure 3), and (ii) ramified islands formed by cluster aggregation when diffusion is taking place[24,30] (Figure 4a).

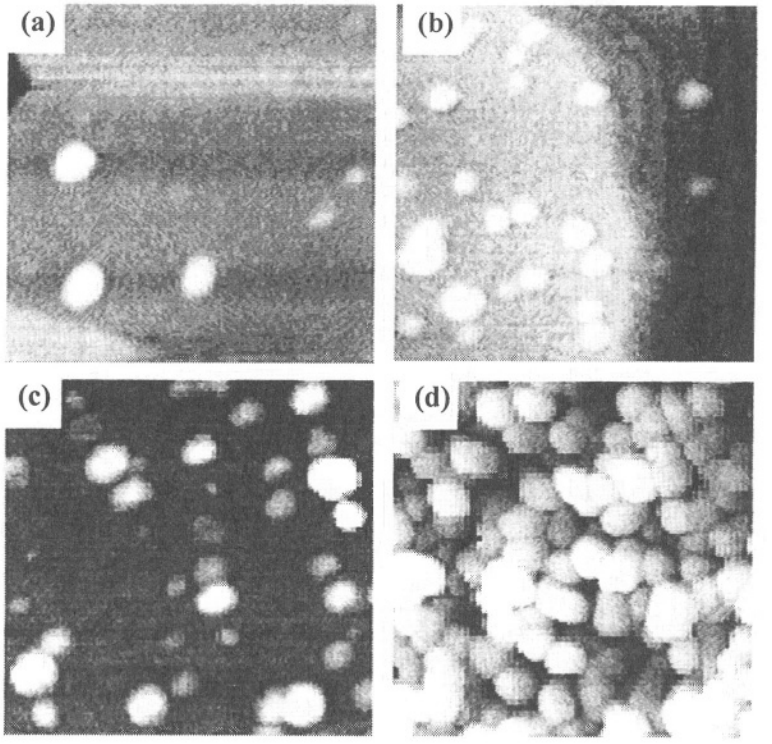

Figure 3. STM-images (100 nm × 100 nm) of gold thin films produced by $Au_{<750>}$-cluster depositions on Au(111) at room temperature with a flux $F=10^{-3}$ nm s^{-1}, for different equivalent thicknesses (e_q): (a) $e_q = 0.01$ nm; (b) $e_q = 0.03$ nm; (c) $e_q = 0.08$ nm; and (d) $e_q = 3.4$ nm.

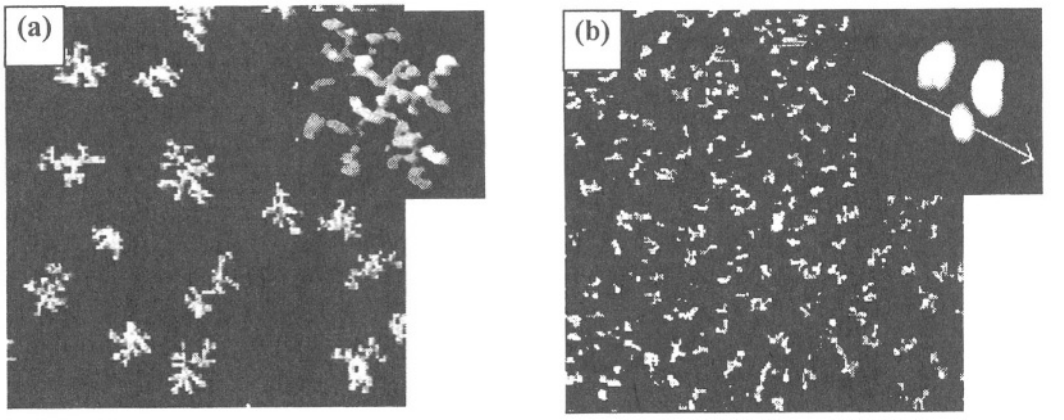

Figure 4. AFM-images (1000 nm × 1000 nm) of 0.5 nm thick gold-films prepared by Au_{750} cluster depositions on HOPG-graphite substrates at room temperature. (a) Virgin substrate, (b) Ion-irradiated substrate (2 keV Ar^+-ions). The characteristic ramified-island morphologies formed by juxtaposition of deposited clusters which easily diffuse on HOPG at room temperature, is clearly observed in the inset of Figure a (100 nm × 100 nm). Different island morphologies are observed in Figure b due to the trapping of the diffusing clusters by radiation defects. Three gold clusters trapped at the border of a nano-hole created by Ar^+-ion impact are shown in the inset of Figure b (25 nm × 25 nm).

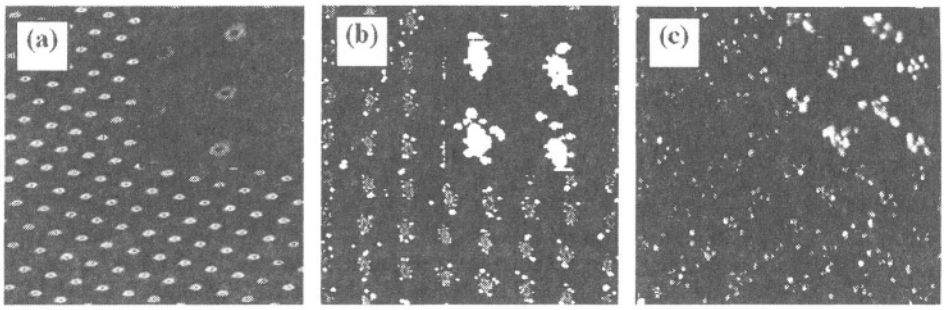

Figure 5. AFM images of a FIB-functionalised HOPG substrate (3.4 μm × 3.4 μm) (a) and 2D-organized arrays of clusters (2 μm × 2 μm) obtained by deposition of Au_{750}-clusters (10^{-2} ML) on FIB-functionalized HOPG substrates at 373 K (b, c). Using the FIB-nanoengraving technique with 30 keV Ga^+-ions, depending on the ion-fluence per point, various types of 2D-organized arrays of nanosized defects are created on HOPG substrates (i.e. array of nanosized holes with a lattice parameter of 300 nm as shown in the inset of image (a) (500 nm × 500 nm). Gold clusters subsequently deposited on these substrates are trapped on the defects (see insets (500 nm × 500 nm) of images (b) and (c)) to form organized arrays. In the case of image c, the FIB fluence per point was 10 times lower than in the cases of images a and b. For such a low FIB-fluence, the defects consist on nanosized bumps which seem quite efficient to trap the diffusing gold-clusters as observed in the inset of image c. The preparation of magnetic cluster arrays (i.e. Co-clusters) is in progress.

In this last case, various defects on the surface of the substrate act as traps for the diffusing clusters leading to the creation of nucleation-centres for the formation of cluster-islands. Surface-defects to trap clusters can be natural (e.g. atomic steps) or artificially created. This is well illustrated in Figure 4b, showing the morphology of a cluster film deposited on an ion-irradiated HOPG-substrate (Highly Oriented Pyrolitic Graphite) compared to the morphology of the film deposited under the same conditions on the non-irradiated HOPG-substrate (Figure 4a). Randomly distributed defects in the form of nano-holes resulting from energetic heavy-ion impacts are at the origin of the trapping process of the diffusing clusters as shown in the inset of Figure 4b. Finally, the capability of surface defects to influence the nucleation and growth processes of cluster assembled films could be efficiently used in a near future to produce 2D-organized arrays of nanoclusters on functionalised substrates for applications in the fields of high density magnetic-memory devices, spin electronics, and more generally quantum devices. In this context, preliminary experiments to deposit clusters on HOPG-substrates exhibiting a 2D-organized array of nanosized defects obtained by the FIB-nanoengraving technique (Focussed Ion Beam) have been carried out[32] (Figure 5). Clusters concentrated around the nano-defects as shown in Figures 5b,c is a promising result prefiguring future experiments under improved conditions to reach the ultimate stage of a 2D-organized array with one dot per site.

The atomic structures of isolated nickel and cobalt deposited-clusters have been observed by HRTEM (Figure 6). Supported nanoparticles with a mean diameter around 3-4 nm well crystallized in the fcc-structure having the shape of truncated octahedrons are systematically observed.[20] In the case of Ni-clusters the fcc-structure is comparable to the one of bulk-Ni, whereas the bulk-Co structure is hcp. Moreover, as mentioned in section 2, free Co and Ni clusters in the gas phase exhibit icosahedral structures while fcc-structure is more likely after deposition on various substrates. In the case of iron, supported clusters well crystallized in the bcc-structure are generally observed.[2,33-35]

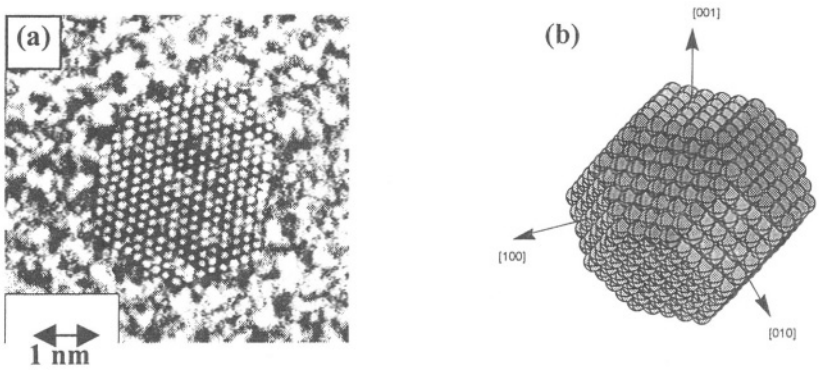

Figure 6. HRTEM-image of an isolated cobalt cluster preformed in the gas phase using a laser vaporisation source and subsequently deposited under UHV on an amorphous carbon coated grid at room temperature (a). This cluster well crystallized in the fcc-structure having the shape of a truncated octahedron is schematically represented in (b).

Grazing incidence X-ray diffraction experiments using the synchrotron radiation facilities at LURE-Orsay were performed on thick cluster assembled films[23] (thicknesses >> 2D-percolation threshold). The spectra presented in Figure 7 for cobalt and nickel films confirm the granular character due to the random stacking process of incident free clusters characteristic of LECBD. Comparable granular morphology observed by STM was previously shown in Figure 3d. The fcc-structure of the grains is confirmed in both Co and Ni cases as well as the bcc-structure in the particular case of iron cluster films. From the widths of the lines in the diffraction spectra we can deduce the mean sizes of the grains which are in good agreement with those obtained from HRTEM on collections of isolated clusters in films with thicknesses lower than the 2D-percolation threshold. The results for Co cluster films deposited on various substrates at room temperature or liquid nitrogen temperature are summarized in Table 1. We observe a variation in the mean supported grain size, while the mean size of the incident free cluster is the same in all cases (≈ 2-3 mn in diameter). Such results are probably related with coalescence effects between adjacent clusters which cannot be completely ruled out depending on the deposition parameters.

Complementary X-ray absorption measurements on films of isolated cobalt-clusters embedded in non–magnetic matrices (i.e. Ag, Pt, Nb)[36-38] prepared by the co-deposition technique described in section 2 have been performed. The fcc atomic structure of Co clusters is also observed in this case. However, in films with a rather low concentration of clusters (volume fraction << 3D percolation threshold ≈ 20%), since cluster-cluster coalescence is significantly reduced in the solid matrix, the cluster-size distribution measured is relatively narrow and comparable to the incident free-cluster one.

Table 1. Mean sizes D of the supported particles measured after deposition of cobalt clusters preformed in the gas phase using a laser vaporisation source (mean diameter ~ 2 nm ~ 300 atoms) on various substrates at different temperatures[22].

Substrate	Silicon wafer		Sapphire	Silica-glass		Amorphous carbon
Temperature (K)	300	80	80	300	80	300
D (nm)	7	6.5	5	4	3	3

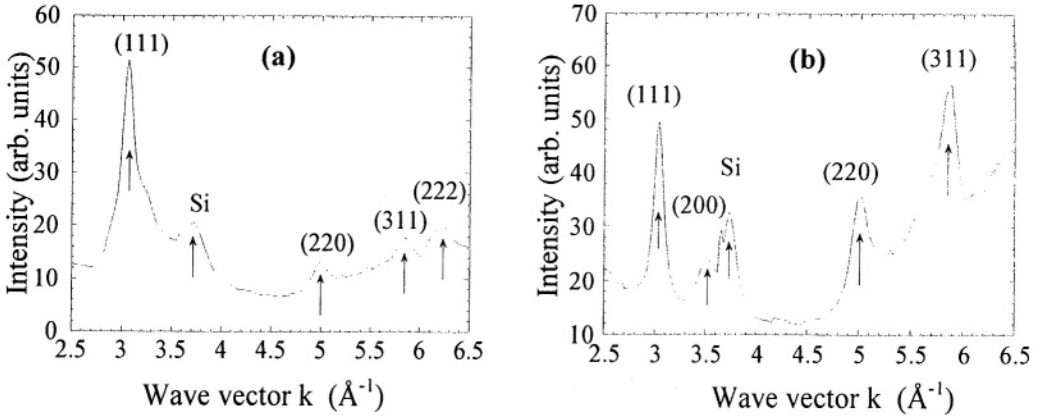

Figure 7. X-ray diffraction spectra at grazing incidence (0.4 °) measured on a Co-cluster assembled film (a) and a Ni-cluster assembled film (b) deposited on Si-substrates at room temperature with thicknesses of 80 nm. The main peaks of the fcc-structure ((111), (220), and (311)) clearly appear in both spectra as well as the peak corresponding to the Si-substrate.

In the nanosize range concerned by clusters, the number of atoms located at the cluster surface is not negligible with respect to the number of atoms in the core (i.e. ≈ 40 % in a fcc Co-cluster of 3 nm in diameter ~ 1200 atoms as in the example of Figure 6b). In this case, magnetic properties combining surface and core effects are expected which justify the characterization of different sites of atoms in the clusters using additional X-ray absorption measurements (EXAFS). Pure Co and Ni-cluster assembled films[23] and films of Co-clusters embedded in matrices (Ag, Pt, Nb)[36-38] have been studied by this technique using the synchrotron radiation facilities at LURE-Orsay. The EXAFS-spectra were recorded in the electron detection mode at 300 K. By considering only the simple scattering of the photoelectron by the neighbours and neglecting the multiple scattering, the radial distributions derived from the EXAFS-signal at the Co or Ni K-edges have been analysed by fitting (Figure 8) using adapted computer codes. Assuming that Co or Ni-clusters are crystallized in the fcc-structure with truncated octahedron shape, three specific local environments are considered for the atoms to fit the EXAFS spectra: (i) atoms in the core of the grains surrounded by 12 first neighbours, (ii) atoms at the surface of the grains surrounded by 9 first metallic neighbours on one side, and (iii) oxygen atoms on the other side. A limited oxygen pollution in the form of some oxygen atoms bounded at the cluster surface cannot be ruled out since it is observed on free clusters in the gas phase (satellite peaks in the TOF-mass spectra) before deposition in the UHV-chamber. Moreover, the thin amorphous carbon layer deposited on top of the cluster films before removing in air, which is convenient for the EXAFS measurements in the electron detection-mode, is not fully efficient to protect against pollution. The results of the fits of the EXAFS spectra for Co and Ni-cluster films deposited on various substrates at 300 and 80 K are reported in Table 2. The number of metallic neighbours is found between 10.1 - 10.9, and 10.5 - 11.1, for Ni and Co-films respectively, indicating grain sizes around 3 - 4 nm in a rather good agreement with HRTEM and X-ray diffraction measurements. One has also to remark that the surface atomic-layer in both Co and Ni fcc-clusters exhibits a slightly dilated lattice parameter (≈ 0.27 nm) compared to the distance of atoms in the core of the clusters (≈ 0.25 nm), and a Debye-Waller coefficient ($\sigma = 0.05$) in agreement with the induced disorder.

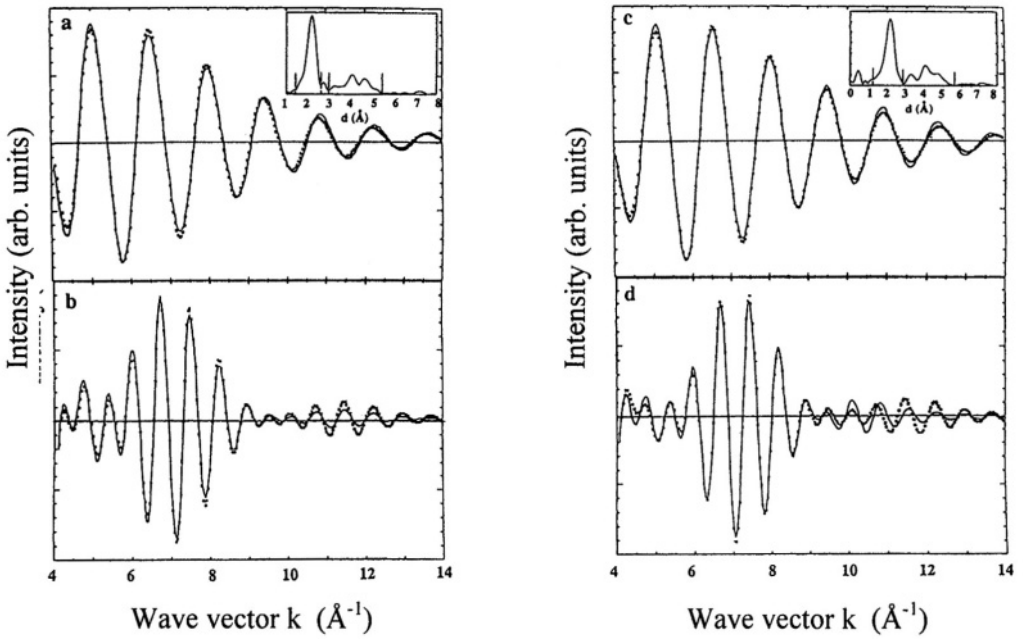

Figure 8. Moduli of Fourier transform of the absorption curves (••• measured) and corresponding simulated EXAFS spectra (—) for Ni-cluster films (a and b) and Co-cluster films (c and d) deposited on kapton. (a) and (c) correspond to the first neighbours and (b) and (d) to the second, third and fourth neighbours. Insets in (a) and (c) show the experimental spectra with selected peaks related to these neighbours.

Table 2. Results deduced from the fits of the EXAFS-spectra of Ni and Co-cluster films deposited on various substrates at different temperatures. nNi_{11} and dNi_{11} are the number of first neighbours in the first shell and the corresponding Ni-Ni distance in nm, respectively. nNi_{12} and dNi_{12} are the number of first neighbours in the second shell and the corresponding Ni-Ni distance in nm, respectively. nO and dNiO are the number of O-neighbours and the corresponding Ni-O distance in nm, respectively. The same notation is used for the Co-results. The three specific local environments of Co-atoms in a cluster so called first shell, second shell and O-polluted surface-shell are defined above in section 3.

Substrate	Temp. (K)	nNi_{11} dNi_{11}	nNi_{12} dNi_{12}	$nNi_{11}+nNi_{12}$	nO dNiO	nCo_{11} dCo_{11}	nCo_{12} dCo_{12}	$nCo_{11}+nCo_{12}$	nO dCoO
Silicon	300	6.5	3.9	10.4	2	9.4	0.4	11.1	5.5
		0.253	0.278		0.216	0.25	0.267		0.22
Silica-glass	300					9	1.6	10.6	1.6
						0.251	0.271		0.21
Silica-glass	80	7.6	2.8	10.2	1.6	9	1.5	10.5	1.5
		0.25	0.27		0.222	0.252	0.271		0.201
a-carbon	300	6	4.1	10.1	1.9	7.9	3	10.9	2
		0.256	0.27		0.214	0.252	0.27		0.233
a-carbon	80					7.4	3.7	11.1	2.2
						0.251	0.285		0.203
Sapphire	80	6.9	4	10.9	3.3	8.9	1.9	10.9	0.7
		0.254	0.272		0.212	0.252	0.274		2.1
Kapton	300	6.8	3.5	10.3	21.1	9.2	1.85	11.1	2
		0.253	0.269		0.23	0.251	0.271		2.21

Lattice parameter expansion is not expected in such small particles since for a low number of nearest neighbours (i.e. 10) a contraction at a value of about 0.245 nm is rather predicted by J. Tuaillon[22] on the basis of the formalism developed by P. Joyes.[39] In our case, the observed dilatation effect could be attributed to the intercalation of oxygen-atoms in the surface layer of the grains.

In the case of Co-clusters embedded in non-magnetic matrices (i.e. Ag, Pt, Nb),[36-38] EXAFS measurements complemented by XPS-analyses confirm that a pure Co-core (fcc) is still conserved in all cases, even when cobalt is miscible with the matrix-element, (i.e. Nb, Pt). However, an alloying effect limited to one or two atomic layers at the cluster/matrix interface takes place depending on the miscibility of elements. In the case of immiscible cluster/matrix elements (i.e. Co/Ag) quite abrupt interfaces are observed. Finally, the cluster/matrix co-deposition technique seems promising for the preparation of specific nanostructured systems since it is not limited by the choice of elements and the cluster concentration range to be investigated. Especially in the field of magnetic nanostructures, the samples with pure magnetic nanoparticles embedded in non magnetic matrices are of great interest for fundamental studies as well as applications. In this last case, the opportunity to control the alloying effect at the cluster/matrix interface offers some attractive prospects to adjust the magnetic properties for specific applications.

4. MAGNETIC PROPERTIES OF INDIVIDUAL CLUSTERS AND CLUSTER ASSEMBLED FILMS

Magnetic nanostructures from pure transition metal clusters (i.e. Fe, Co, Ni) or mixed transition metal-rare earth clusters (i.e. Co-Sm) are studied using various complementary techniques in order to investigate on the magnetic behaviour from an isolated individual cluster to an assembly of non-interacting or interacting clusters. For that purpose, a ultrahigh sensitivity magnetometry technique based on microSQUID devices has been developed[40] to detect for the first time the magnetic signal of one single nanoparticle with size as low as 1000 atoms (i.e. one Co-cluster of $\approx$ 3 nm in diameter)[9]. Such a challenge is achieved by embedding the Co-clusters directly in the metal (niobium) constituting the superconducting microSQUID loop at low temperature (≤ 7 K) to considerably improve the cluster-microSQUID coupling. As for the magnetic measurements on cluster assemblies, conventional SQUID or VSM magnetometry techniques are used complemented by X-ray magnetic circular dichroism (XMCD) measurements[2,34,35] to probe the magnetism of clusters at a local scale.

4.1. MicroSQUID Magnetometry Studies of Individual Magnetic Nanoclusters

The development of novel magnetometers based on microSQUID devices[40,41] with sensitivity approaching 10^{-20} Am^2 (10^3 Bohr-magneton) which are capable to detect the magnetization reversal of individual nanoparticles[6] has allowed to investigate in this field of "experimental nanomagnetism". For that purpose, 20 nm Nb-films with embedded Co-clusters (~ 3 nm fcc-truncated octahedron, see Figure 6) were prepared using the co-deposition technique described in section 2 and subsequently e-beam micro-lithographed to pattern a large number of micro-SQUID loops (Figure 1a). The concentration of Co-clusters was low enough (< 0.1 %) to avoid any interaction between them.

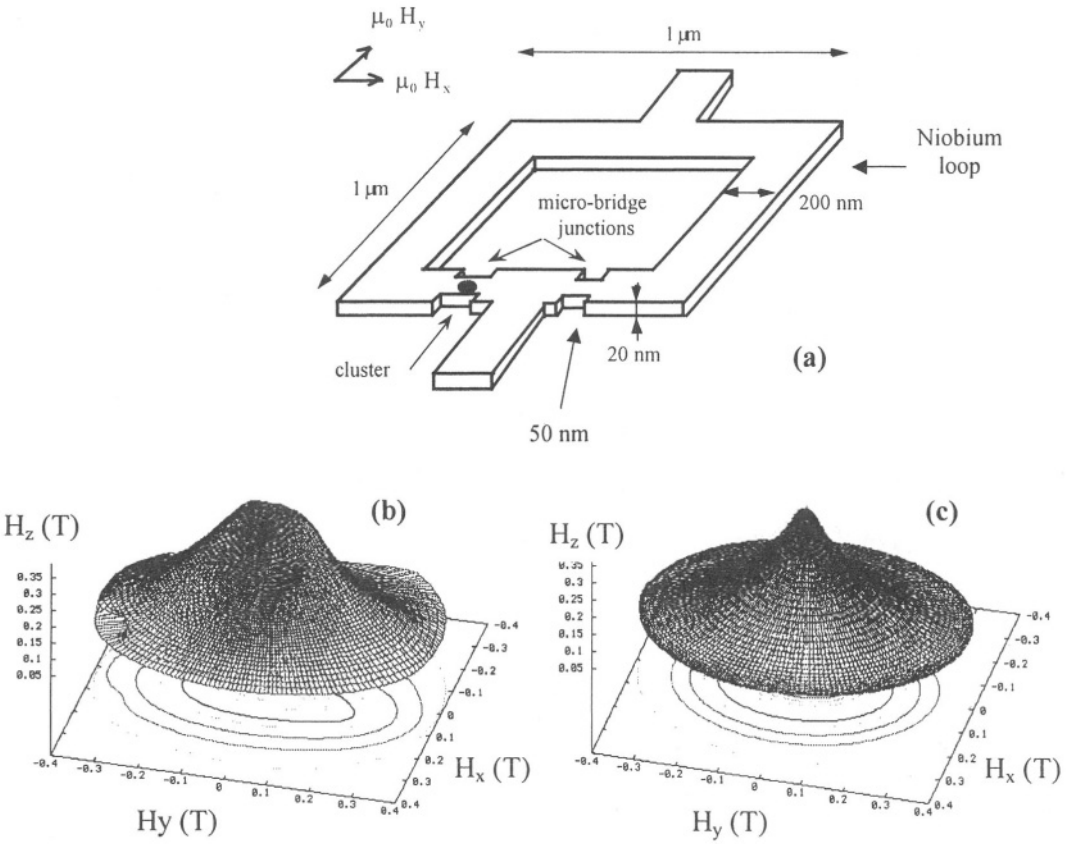

Figure 9. (a) Schematic view of a microSQUID loop patterned out of a 20 nm thick Co-clusters/Nb-matrix film by electron beam lithography. The highest detection sensitivity is obtained for nanoclusters located in the micro-bridges as shown in the Figure. (b) 3D-distribution of the switching field as measured at a temperature of 35 mK for an individual Co-cluster (diameter ≈ 3 nm ≈ 1000 Co-atoms, see Figure 6) embedded in the micro-bridge. (c) Calculated 3D switching field distribution using the Stoner-Wohlfarth model generalized in three dimensions as explained above in section 4.1.

Moreover, only the magnetic flux coupling of a cluster located in a micro-bridge (Figure 9a) is high enough to allow the detection of its individual magnetization reversal and the measurement of the corresponding spatial switching field distribution while other clusters located in other parts of the loop are not detected. 3D-angular dependence of the switching field was measured by rotating the external magnetic field in and out of the microSQUID plane (Figure 9b). This last diagram evidences one easy magnetization direction along the H_z axis and one hard magnetization direction along the H_y axis. Assuming that T = 0 K (the experimental temperature being 35 mK), and a uniform rotation process of the particle magnetization, the Stoner-Wohlfarth model generalized in three dimensions[42] is used to perform a rather good fit of this spatial distribution (Figure 9c). We deduce a second order anisotropy energy : $E(\mathbf{m})/v = - K_1 m_z^2 + K_2 m_y^2$, where v is the magnetic volume of the particle, **m** a unit vector in the magnetization direction, and $K_1 = 2.1 \cdot 10^5$ J/m^3, $K_2 = 0.5 \cdot 10^5$ J/m^3 the anisotropy constants along the easy and hard axes, respectively.

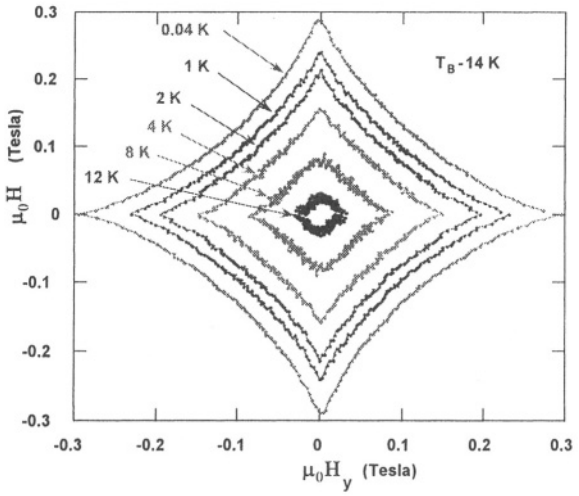

Figure 10. 2D-switching field distributiuons for a nanosize Co-cluster (see Figure 6) measured using the microSQUID technique in the yz-plane (see Figure 9a) at different temperatures up to the blocking temperature of the corresponding cluster $T_B \approx 14$ K.

Finally, we can conclude that a Co-nanoparticle embedded in a niobium matrix mainly behaves as a macrospin with a bi-axial anisotropy corresponding to a second order anisotropy energy term. Let us discuss the physical origin of such an anisotropy. First of all, we can rule out the usual cubic magnetocrystalline anisotropy for fcc-cobalt (Figure 6) since this fourth order term would lead to a completely different 3D-angular dependence of switching fields. Secondly, by considering the nearly spherical shape of the Co-clusters, the shape anisotropy term can also be neglected. Moreover, because the elastic constants of the bcc-niobium are smaller than the fcc-cobalt ones, the contribution of the magneto-elastic anisotropy energy resulting from the matrix induced isotropic stresses on the particle should be small. Consequently, the experimental anisotropy measured for an individual Co-clusters is probably related to an interface anisotropy resulting from the symmetry breaking at the cluster surface. This clearly emphasizes the dominant role of surface/interface effects in the magnetic properties of nanosize systems.

The temperature dependence of the switching field distribution of one individual cobalt nanocluster has been measured using the microSQUID technique. The 2D-distributions measured in the yz – plane at different temperatures are represented in Figure 10. The characteristic shape of the 2D-diagrams so-called "astroid" continuously decreases in size with the increasing temperature allowing to determine the blocking temperature of the corresponding cluster. In the particular case presented in Figure 10, a blocking temperature of the order of $T_B = 14$ K is clearly deduced.

For a better understanding of the role of the Co-Nb interface on the magnetic properties of an individual cluster as reported above, thick samples consisting on Co-cluster assemblies diluted in a niobium matrix (Co-volumic concentration ≤ 5 %) were prepared in view to perform complementary structural and magnetic characterizations. Structural studies[23,38] using HRTEM, X-ray diffraction and absorption indicate that the deposited Co-clusters in the bcc Nb-matrix can be described as fcc-truncated octahedrons containing about one thousand atoms (diameter $\approx$ 3 nm, see Figure 6) distributed as follows: 36% are in the pure Co-core of the grain, 27% participate to a Co_4Nb-phase in

the sub-surface layer, and 37% participate to a Co_6Nb_7-phase in the surface layer. Moreover, from VSM-measurements on the same Co-clusters/Nb-matrix films (Figure 11) we can conclude that the Co-Nb alloyed interface is a "magnetically dead" layer which is probably at the origin of the reduced "magnetic size" distribution observed with respect to the TEM–one[38] (Figure 12).

Additional X-Ray Magnetic Circular Dichroism (XMCD)* experiments were performed at the European Synchrotron Radiation Facilities Grenoble-France). XMCD is used in our case as a local magnetometry technique operating in the low temperature range (i.e. T < 8 K), where the superconducting fluctuations due to the Nb-matrix prevent any conventional magnetization measurements. Finally, from the hysteresis loops measured in the temperature range 5 - 50K, we deduce the remanent magnetization (Figure 13) and an effective anisotropy constant $K_{eff} = 2 \cdot 10^5$ J/m^3 for the Co-clusters.[43] Note that K_{eff} is of the same order of magnitude as K_1 previously found from the micro-SQUID measurements on individual Co-nanoparticles. The Co-clusters/Pt-matrix system which is also a miscible couple has been studied in the same conditions[23,24] to verify the validity of the core-shell model suggested above to account for the magnetic properties in such nanogranular films. Finally, from both Co/Nb and Co/Pt samples we found that cluster magnetization can be written in the form : $M_s(T) = x\, M_s^{core}(T) + (1-x)\, M_s^{shell}(T)$. For Co/Pt, one atomic layer is expected to diffuse at the interface giving x = 0.63. In addition, we assume that $M_s^{core}(T) = M_s^{bulk}(T)$ leading to a magnetization enhancement at the interface $M_s^{shell}(0) = 1900$ kAm^{-1} (to compare with $M_s^{core}(0) = 1430$ kAm^{-1}). On the contrary, in the Co/Nb case $M_s^{shell}(0)$ is found to be equal to zero and x = 0.36, because of the presence of two "magnetically dead" alloyed-monolayers at the cluster-matrix interface, leading to the very low experimental value observed $M_s(0) = 515$ kAm^{-1}.

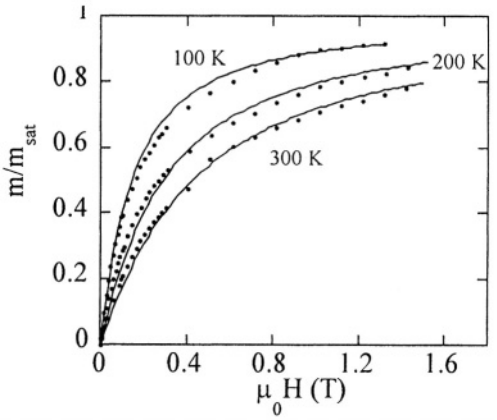

Figure 11. Magnetization curves measured using the VSM-technique (•) on Co-clusters (2% vol.)/Nb-matrix films at different températures (100, 200, and 300 K) in the superparamagnetic domain. A classical Langevin function is used to fit the experimental curves (solid line) in order to deduce the magnetic size distributions reported in Figure 12, considering log-normal size distributions for Co-clusters embedded in niobium.

* The authors are indebted to Professor C. Binns from the university of Leicester, UK, for fruitfull collaboration in the framework of XMCD measurements at ESRF-Grenoble.

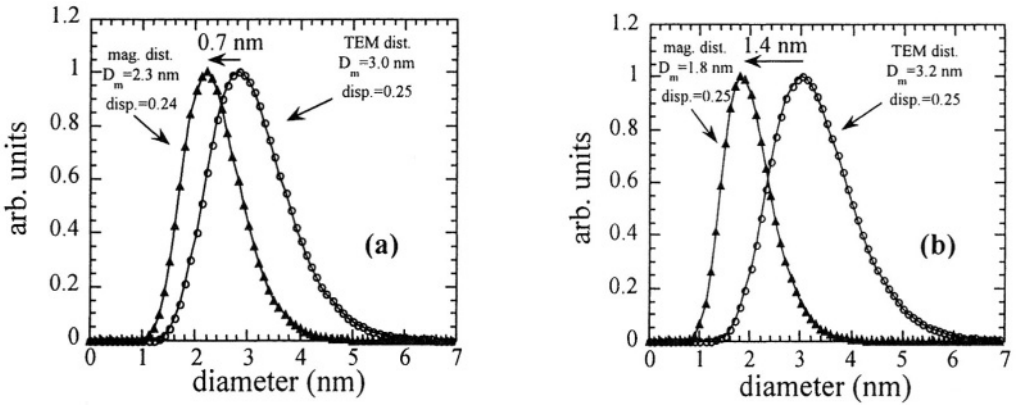

Figure 12. Comparison of the Size distributions of Co-clusters embedded in niobium matrix as deduced from direct observations by TEM (TEM-dist.) and by fitting of the VSM-magnetization measurements reported in Figure 11 (mag. dist.). (a) and (b) correspond to two different deposition rates of niobium during the film preparations : 0.3 nm/s and 0.5 nm/s, respectively. We observe that the mean diameter of the Co-clusters (D) is systematically lower for the magnetic size distributions compared to the TEM-ones while the dispersions of the distributions (disp.) are comparable. This emphasizes the presence of a Co-Nb alloyed interface which acts as a magnetically dead layer. Moreover, the alloying effect at the cluster matrix interface seems to significantly depend on the preparation conditions of the Co/Nb films since this effect increases with the deposition rate of niobium when comparing Figures (a) and (b).

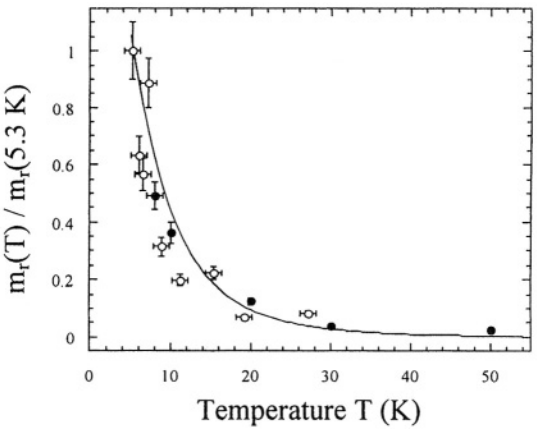

Figure 13. Remanent magnetic moment plotted versus temperature for Co-clusters/Nb films. The signal is first normalized taking : $m_r(8K)_{VSM} = m_r(8K)_{XMCD}$. One can see that the continuous line curve fits both VSM (full dots) and XMCD (open dots) measurements. From this fit, one can deduce the anisotropy constant $K_{eff} = 2.0 \pm 0.3.10^5$ J/m^3 (see details on this procedure in Ref. 25).

4.2. MicroSQUID Magnetometry Studies of 2D Clusters Assemblies, Below the 2D-Percolation Threshold

Magnetization measurements on 2D-disordered arrays of Co-nanoclusters were performed as a function of the deposition rate below the 2D-percolation threshold of the deposit using the microQUID technique. Such a study on intermediate states between an isolated individual cluster and a continuous film of clusters allows to evidence the interactions between clusters for a better understanding of the evolution of the magnetic

behaviour characteristic of a nanogranular system. In the particular case of microSQUID measurements on cluster assemblies, the amount of magnetic matter is larger than in the case of the measurements on one single cluster as reported in section 4.1. Consequently, the sensitivity is high enough to use the simple technique consisting on a direct deposition of clusters in a window patterned on a branch of the microSQUID loop[40] (Figure 14). Figures 15 a and b show typical hysteresis loops of a small number of Co-clusters which are deposited inside two different deposition windows, as seen in the insets, but with the same equivalent film thickness of about 0.2 nm. This thickness is much smaller than the 2D-percolation film-thickness ($\approx$ 2 nm, see section 3). Nevertheless there is still a ferromagnetic coupling between clusters as the observed magnetization jumps are larger than those expected for individual clusters of 2 – 5 nm. The overall amplitude of the magnetization change is 10 times bigger for the sample with the square window (Figure 15a). This is in agreement with the geometry as its surface is 10 times the surface of the elliptic window in Figure 15b. The insets of Figures 15a and b show the largest magnetization jumps corresponding to spin flips of about $5 \cdot 10^5$ μ_B in Figure 15a and $5 \cdot 10^4$ μ_B in Figure 15b. As one round Co-cluster of 5 nm in diameter corresponds to about 10^4 μ_B, we can estimate that there are at least 50 clusters which flip together in Figure 15a, and 5 clusters in Figure 15b. We can mention that the shape of these curves is typical for a material with a huge random anisotropy as encountered in rare-earth based particles.[44] But in our case, the origin of the random anisotropy comes from the random stacking of the nanocrystalline Co-particles on the substrate as discussed in section 3. Near the 2D-percolation threshold, the ferromagnetic correlation length is between 1 and 10 nm. The switching field is independent of the window area. The hysteresis loops show very small and not reproducible magnetization jumps corresponding to the relaxation of a few nanometric particles. In summary, for thicknesses below the 2D-percolation thickness the particles have no macroscopic shape dependence.

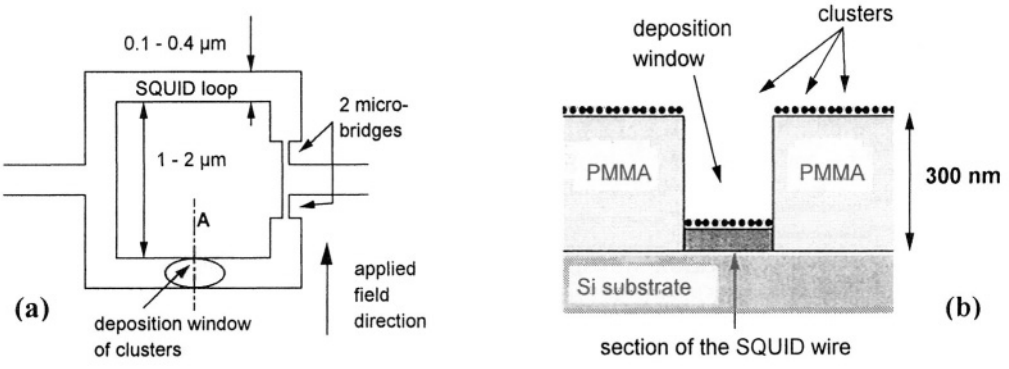

Figure 14. (a) Schematic drawing of the SQUID loop with the two micro-bridge junctions. Cluster deposition is made on the SQUID loop (good flux coupling) using a PMMA masque. The direction of the in-plane applied magnetic field is indicated. (b) Cross section of the deposition window following the line A in Figure a. Note that only the clusters directly supported on the SQUID niobium-wire at the bottom of the deposition window are detected while those supported on top of the PMMA film are two far to be coupled with the SQUID and are not detected.

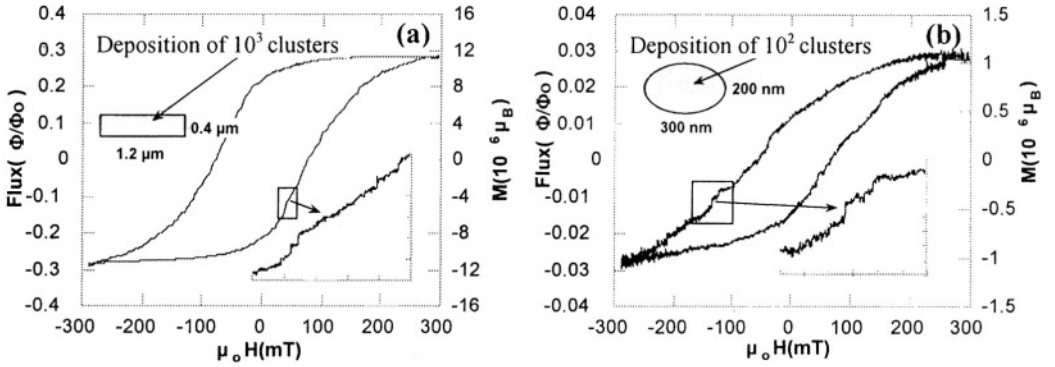

Figure 15. Hysteresis loops measured at a temperatture T = 0.2 K of about (a) 10^3 and (b) 10^2 Co-clusters which are deposited on the SQUID wire as described in Figure 14. The equivalent film-thickness of the deposited clusters is about 0.2 nm in both cases. The measured flux change is given in units of Φ_0 (Φ_0 = h/2e = 2.10^{-15} Wb) and approximately in unites of μ_B. The insets, presenting a zoom of parts of the hysteresis loops, reveal small magnetization jumps coming from several clusters which are strongly coupled.

4.3. MicroSQUID Magnetometry Studies of 2D Clusters Assemblies, Above the 2D-Percolation Threshold

Figures 16a and b show the hysteresis loops of Co-cluster films with equivalent thicknesses of 5 and 15 nm, thus thicker than the 2D-percolation thickness (≈ 2 nm, see section 3). In this case the clusters form a nanocrystallized film. They are strongly coupled by dipole and exchange interactions and the hysteresis loop becomes dependent on the shape of the window. These hysteresis loops are very similar to those obtained on submicron Co-particles patterned by electron beam lithography out of sputtered Co-films.[44,45] First the switching field decreases as the thickness increases (from 0.2 to 5 nm equivalent thicknesses) and the hysteresis loop tends to a rectangular shape as in single-domain Co-particles (Figure 16a). Then, for thicker samples (15 nm equivalent thickness, Figure 16b), the hysteresis loop is similar to hysteresis loops of multi-domain particles. However in the case of nanocrystallized films, the switching field distributions of the magnetization jumps are about 10 times broader (see inset of Figure 16b). This probably comes from the fact that nanocrystallized films are porous and slightly oxidized at cluster boundaries. This leads to a distribution of reduced cluster-to-cluster exchange couplings (with respect to a bulk film[33]) which increases the switching field distribution.

Since in this case the cluster to cluster coupling is much stronger than in the previous one (below the 2D-percolation threshold, see section 4.2), one expects much larger avalanches. This is effectively observed in Figures 16a and b. The magnetization reverses mainly in two or three big avalanches whereas for smaller equivalent film thicknesses (Figures 15a and b) we observe a large number of small avalanches.

4.4. Magnetic properties of thick cluster assembled films

The magnetic behaviour of thick cluster assembled films (≈ 100 nm) were studied using conventional SQUID-magnetometry,[46] ferromagnetic resonance (FMR),[47] and conversion electron Mössbauer spectroscopy (CEMS) in the particular case of Fe-samples.[48]

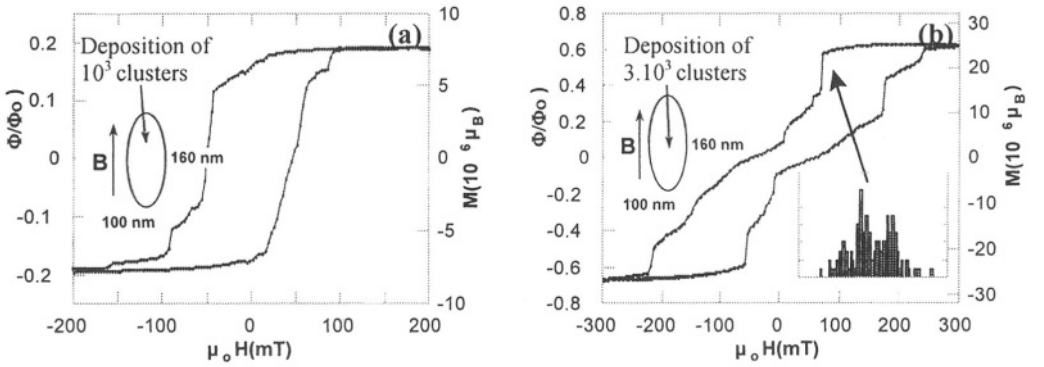

Figure 16. Hysteresis loops measured at a temperature T = 0.2 K of two elliptic nanostructured Co-particles composed of thick layers of Co-clusters forming nanocrystallized films with equivalent film-thicknesses of (a) 5 nm and (b) 15 nm. The measured flux change is given in units of Φ_0 ($\Phi_0 = h/2e = 2 \cdot 10^{-15}$ Wb) and approximately in unites of μ_B. Insets on the left present the shape of the deposition window. The inset on the right in Figure b shows a switching field histogram for the first avalanche drawn from 130 hysteresis loops which were measured at a constant field sweeping rate of 20 mT/s.

Thick cluster-films grow by random stacking of incident free clusters as described in section 3 and the corresponding morphology is well illustrated in Figure 3d. In this case, clusters interact by direct contact and the magnetic behaviour of such films is rather well described in the framework of the random anisotropy model previously proposed by E. Chudnowsky[49] for amorphous materials. However, in the cluster assembled films, the characteristic parameter R_a (correlation length of local anisotropy axes) corresponds to the mean radius of the grains (typically 2 - 3 nm), contrary to amorphous materials in which it represents the characteristic length of the local order ($\approx$ a few Å). The radius of the ferromagnetic domain R_f corresponds to few grains (i.e. $R_f \approx 8$ nm for Fe-cluster films).[46] Finally, at zero magnetic field, the behaviour of the films is comparable to a correlated spin glass. Under magnetic field, depending on the competition between the grain anisotropy and the exchange interaction, two regimes separated by a cross-over field $H_{co} = 2\ A/M_s\ R_a^2$ (where A and Ms are the exchange constant and the saturation magnetization, respectively) are observed: in the low applied magnetic-field regime ($H < H_{co}$), the total grain anisotropy dominates and the magnetization ($\Delta M/M_s$) is proportional to $1/\sqrt{H}$, while above H_{co}, particle-particle exchange interaction dominates leading to a magnetization regime $\Delta M/M_s$ proportional to $1/H^2$. In amorphous materials, since R_a is small, H_{co} is large (several hundreds kOe), and the high field regime is difficult to observe. In the cluster films, R_a is of the order of the grain size as mentioned above, thus H_{co} becomes attainable (i.e. $H_{co} \approx 3$ kOe for Fe-cluster films),[46] and both magnetization regimes described above have been observed and interpreted.[50]

As mentioned previously, in the cluster assembled films produced by direct deposition of clusters on the substrate in the LECBD-regime, adjacent clusters interact by direct contact. Consequently, from the competition between the intrinsic magnetic properties of individual clusters and the interactions between adjacent clusters defined magnetic behaviours are observed as a function of the external magnetic field applied. In order to control the interactions between clusters and then to modify the magnetization regime, films of clusters embedded in matrices have been prepared (see section 2). In this case, since cluster-cluster coalescence effects are limited, homogeneous dispersions of

clusters in the co-deposited matrix exhibiting a rather sharp size-distribution centred on a mean size close to the incident free cluster-size are stabilized. Moreover, the cluster size-distribution in such samples does not dependent on the cluster concentration as in the case of sample produced by precipitation of a magnetic material in a non-miscible non-magnetic matrix. This allows producing films in a wide range of cluster concentration with a constant mean cluster-size. The control of the interactions between particles arises from the mean distance between them directly related to their concentration and the nature of the non-magnetic matrix (insulating, conducting). In this context, large choice of cluster-matrix couples including miscible or non-miscible elements is available using this LECBD-cluster/matrix co-deposition technique. This is well illustrated in the case of films (~ 100 nm thick) of cobalt clusters (diameter ≈ 3 nm) embedded in silver matrix for which transport measurements reveal a nice dependence of the giant magneto-resistance effect (GMR) on the Co cluster concentration[51] (Figure 17). Coupling of Co particles via the conduction electrons of the matrix could be invoked in this case. The maximum GMR value is obtained for a Co-concentration close to the 3D-percolation threshold (~ 20 % vol.) as shown in Figure 17. For Co concentrations lower than this last value, a magnetization regime in 1/T characteristic of a superparamagnetic behaviour is observed, while for concentrations above the percolation threshold, a Block-magnetization regime in $T^{3/2}$ is evidenced.[22] Let us mention that in the case of clusters embedded in transparent non-magnetic matrices, the field of magneto-optic systems can be investigated.

5. FUNCTIONALIZED MAGNETIC NANOSTRUCTURES FROM MIXED CLUSTERS

Pure magnetic transition metal nanostructures extensively studied up to now have significantly contributed to a better understanding on the structure-properties relationship in the case of isolated individual clusters with a particular light on the dominant role of surface/interface effects in the nanosize range. Unfortunately, the superparamagnetic limit leading to very low magnetic blocking temperatures (see Figure 10) prevents the use of pure transition metal particles with sizes lower than about 10 nm for applications (e.g. high density storage media).[5]

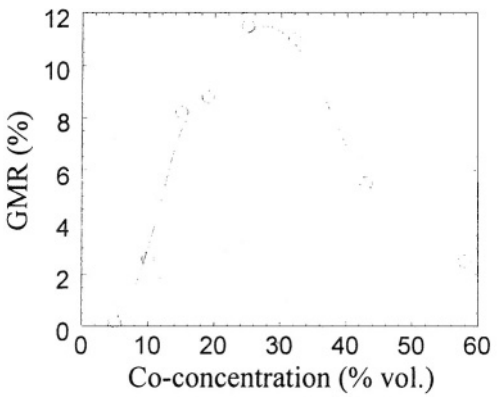

Figure 17. Giant magnetoresistance measured at 4.2 K on films of Co-clusters embedded in a silver matrix as a function of the Co volume concentration. The solid line is just to guide the eyes.

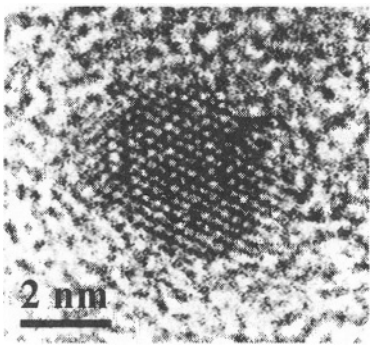

Figure 18. HRTEM image of a Co-Sm mixed cluster deposited on an amorphous carbon coated grid at room temperature and subsequently annealed at 840 K in UHV. However, It was difficult to determine the nature of the crystalline phase of annealed clusters since the symmetry and lattice parameters differ from the well known bulk phases.

A challenge in this field of magnetic nanostructures applications will consist of synthesizing stable nanosized magnetic objects with blocking temperatures around or above room temperature. In this context, various types of mixed clusters, especially clusters of intermetallic compounds with strong magnetocrystalline anisotropy such as rare earth-transition metal alloys have been tested. In particular, $SmCo_5$ - nanoclusters (mean diameter $\approx$ 3 to 4 nm) prepared from a bulk $SmCo_5$-target mounted in the laser vaporization source (see section 2) have been deposited/embedded in the LECBD regime on various substrates/matrices for structural and magnetic studies.[10,52] As previously mentioned in section 2, mixed clusters prepared by this technique exhibit the same composition as the target one, however a poor crystallinity as revealed by TEM observations and a segregation of samarium atoms at the cluster surface are at the origin of a loss of magnetization in the as deposited cluster films compared to the bulk $SmCo_5$ phase. Post annealing treatments in UHV up to 840 K on films of isolated clusters embedded in niobium (cluster concentration $\leq$ 5 % vol.) lead to an improvement of the crystallinity of the Sm-Co nanoparticles (Figure 18), and consequently to a significant increase of their magnetic anisotropy at the origin of a blocking temperature T_B larger than 300 K.

This is illustrated in the Figure 19 showing the characteristic evolution of the magnetization loops with a significant increase of the coercive field upon annealing for a Sm-Co clusters/Nb-matrix film. Note that the choice of a niobium matrix for the annealing experiments is directed by the non-miscible character of this element with samarium. Since in the as deposited samples samarium atoms are segregated at the cluster/matrix interface one can imagine that during thermal treatments they prefer to redistribute inside the clusters rather than to diffuse in the surrounding Nb-matrix. At the same time, the mean size of the embedded Sm-Co clusters slightly increases up to about 6 nm,[52] which cannot explain the T_B-increase up to room temperature or more. Finally, only the efficient role of samarium atoms in the Co lattice of the clusters can be considered in this case to explain such a large magnetic anisotropy/blocking temperature increase.

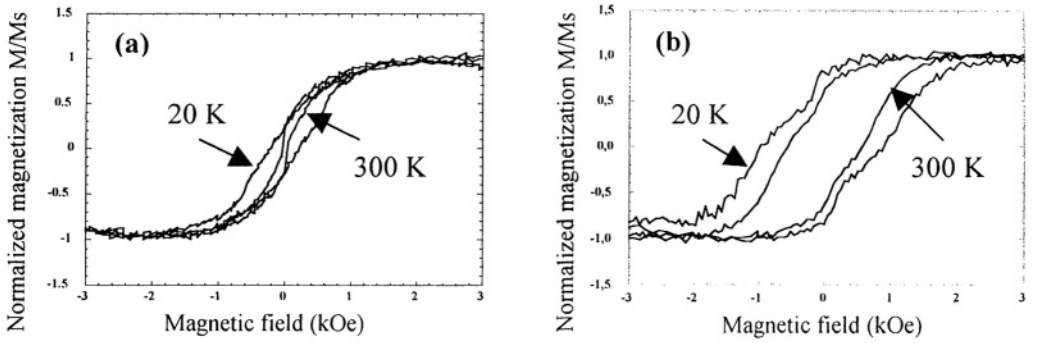

Figure 19. SQUID-magnetization loops measured on (a) an as deposited film of Co-Sm clusters embedded in niobium (concentration ≤ 5 % vol.), and (b) the same film subsequently annealed in UHV at 840 K for 30 min.

6. CONCLUSIONS

Magnetic nanostructures from clusters preformed in the gas phase constitute a fascinating field of research both from the fundamental point of view to understand the key parameters which govern the properties of nanosized magnetic systems, and for applications in various fields of interest (ultrahigh density storage, spin electronics, sensors, magneto-optics systems). In this context the LECBD-technique specially developed for the preparation of original nanostructures, offers some unique potentialities directly related with the non-equilibrium conditions which prevail to the formation of clusters in the gas phase independently of the deposition and stabilization conditions on the substrate. The studies of the magnetic properties of an individual isolated nanocluster and of cluster assemblies emphasize the dominant role of the surface/interface effects on the intrinsic properties of nanoscale systems and the competition with the interactions in the case of assemblies leading to characteristic magnetic behaviours. A further step in these fundamental studies will concern the dynamic aspects of the phenomena. In parallel to the studies of simple and well controlled systems, generally based on pure transition metal clusters, more complex systems such as bimetallic clusters are prepared and studied in view of applications. In this field, the final association of functionalised clusters (i.e. high magnetic anisotropy cluster blocked at room temperature) on functionalised substrates (i.e. 2D-ordered cluster arrays) will be the ultimate stage prior to the realization of novel nanomagnetic devices in the Tbit range.

7. REFERENCES

1. S. Sun and C.B. Murray, *J. Appl. Phys.* **85**, 4325-4330 (1999).
2. C. Binns, Nanoclusters deposited on surfaces, *Surf. Sci. Rep.* **44**(1-2), 1-49 (2001).
3. S. Sun, C.B. Murray, D. Weller, L. Folks, and A. Moser, *Science* **287**, 1989-1992 (2000).
4. W. Wernsdorfer, in : *Metal Clusters at Surfaces : Structure, Quantum Properties, Physical Chemistry,* edited by K. H. Meiwes-Broer (Springer Series in Cluster Physics, Springer-Verlag, Berlin, 2000) pp. 211-236.
5. D. J. Sellmyer, M. Yu, and R. D. Kirby, *Nanostruct. Mat.* **12**, 1021-1026 (1999).
6. L.M.Sandratskii, Non-collinear magnetism in itinerant-electron systems: theory and applications, *Advances in Physics* **47**, 91-160 (1998).

7. V.P.Antropov, M.I. Katsnelson, M. Van Schilfgaarde, and B.N. Harmon, Ab initio spin dynamics in magnets, *Phys. Rev. Lett.* **75**, 729-732 (1995).
8. V.P.Antropov, M.I. Katsnelson, B.N. Harmon, M. Van Schilfgaarde, and D. Kusnezov, Spin-dynamics in magnets - Equation of motion and finite temperature effects, *Phys. Rev. B* **54**, 1019-1035 (1996).
9. M. Jamet, W. Wernsdorfer, C. Thirion, D. Mailly, V. Dupuis, P. Mélinon, and A. Perez, Magnetic anisotropy of a single cobalt nanocluster, *Phys, Rev. Lett.* **86**, 4676-4679 (2001).
10. M. Négrier, J. Tuaillon-Combes, V. Dupuis, A. Perez, M. Pellarin, and M. Broyer, Magnetic nanostructures of mixed cobalt-samarium clusters, *Eur. Phys. J.* **9**, 475-478 (1999).
11. M. P. Pileni, Nanosized particles made in colloidal assemblies, *Langmuir* **13**, 3266-3276 (1997).
12. J. Gierak, D. Mailly, G. Faini, J.L. Pelouard, P. Denk, F. Pardo, J.Y. Marzin, A. Septier, G. Schmid, J. Ferre, R. Hydman, C. Chappert, J. flicstein, B. Gayral, and J.M. Gerard, Nanofabrication With Focused Ion Beam, *in proc. 26th Int. Conf. on Micro and Nano-Engineering* , (Microelectronic Engineering, Elsevier, Amsterdam, 2001).
13. C. Marrian and E. Snaow, Proximal probe lithography and surface modification, *Microelectronic Engineering* **32**, 173-189 (1996).
14. C. Lebreton and Z.Z. Wang, Nano-hole formation on gold surface using scanning tunneling microscope, *Appl. Phys. A* **66**, 777-781 (1998).
15. P. Milani and S. Iannota, *Cluster beam synthesis of nano-structured materials* (Springer Verlag, Berlin, 1999).
16. A. Perez, P. Mélinon, V. Dupuis, P. Jensen, B. Prével, J. Tuaillon, L. Bardotti, C. Martet, M. Treilleux, M. Broyer, M. Pellarin, J.L. Vialle, B. Palpant, and J. Lermé, Cluster assembled materials : a novel class of nanostructured solids with original structures and properties, *J. Phys. D, Appl. Phys.* **30**, 709-721 (1997).
17. A. Perez, P. Mélinon, V. Dupuis, B. Prevel, L. Bardotti, J. Tuaillon-Combes, B. Masenelli, M. Treilleux, M. Pellarin, Jean Lermé, E. Cottancin, M. Broyer, M. Jamet, M. Negrier, F. Tournus, and M. Gaudry, Nanostructured materials from clusters : synthesis and properties, *Materials Transactions, Special Issue on Nano-metals 1,* **42** (8), 1460-1470 (2001).
18. M. Pellarin, B. Baguenard, J. L. Vialle, J. Lermé, M. Broyer, J. Miller, and A. Perez, Evidence for icosahedral atomic shell structure in nickel and cobalt clusters. Comparison with iron clusters, *Chem. Phys. Lett.* **217**, 349-356 (1994).
19. J. L. Rousset, A.M. Cadrot, F. Santos Aires, P. Mélinon, A. Perez, M. Pellarin, J.L. Vialle, and M. Broyer, Preparation of bimetallic Pd_NPt_M supported clusters with well defined stochiometry, *Surf. Rev. Lett.* **1**, 1171-1176 (1996).
20. J.L. Rousset, F.J. Cadette, F. Santos Aires, B.R. Sekhar, P. Mélinon, B. Prevel, and M. Pellarin, Comparative XPS study of Au, Ni, and AuNi clusters produced by laser vaporisation of bulk metals, *J. Phys. Chem. B* **104**, 5430-5435 (2000).
21. B. Prevel, J. Lermé, M. Gaudry, E. Cottancin, M. Pellarin, M. Treilleux, P. Mélinon, A. Perez, J.L. Vialle, and M. Broyer, Optical properties of nanostructured thin films containing noble metal clusters : Au_N, $(Au_{0.5}Ag_{0.5})_N$, and Ag_N, *Scripta Materiala* **44**, 1235-1238 (2001).
22. J. Tuaillon, PhD thesis, Synthèse et propriétés de nanostructures magnétiques obtenues par dépôts d'agrégats de cobalt et de nickel, *University Claude bernard Lyon 1, France* (1995).
23. J. Tuaillon, V. Dupuis, P. Mélinon, B. Prevel, M. Treilleux, and A. Perez, Cobalt and Nickel cluster-assembled thin films obtained by low-energy cluster beam deposition, *Phil. Mag. A.* **76**(3), 493-507 (1997).
24. L. Bardotti, B. Prevel, M. Treilleux, P. Mélinon, and A. Perez, Deposition of preformed gold clusters on HOPG and gold substrates : influence of the substrate on the thin film morphology, *Appl. Surf. Sci.* **164**, 52-59 (2000).
25. M. Jamet, V. Dupuis, P. Mélinon, G. Guiraud, A. Perez, W. Wernsdorfer, A. Traverse, and B. Baguenard, Structure and magnetism of well defined cobalt nanoparticles embedded in a niobium matrix, *Phys. Rev. B* **62**, 493-499 (2000).
26. P. Jensen, Growth of nanostructures by cluster deposition : experiments and simple models, *Rev., Mod. Phys.* **71**(5), 1695-1735 (1999).
27. Q. Hou, M. Hou, L. Bardotti, B. Prevel, P. Mélinon, and A. Perez, Deposition of Au_N clusters on Au(111) surfaces. I. Atomic scale modeling, *Phys. Rev. B* **62**, 2825-2834 (2000).
28. L. Bardotti, B. Prevel, P. Mélinon, A. Perez, Q. Hou, and M. Hou, Deposition of Au_N clusters on Au(111) surfaces. II. Expermental results and comparison with simulations, *Phys. Rev. B* **62**, 2835-2842 (2000).
29. P. Deltour, P. Jensen, and J. L. Barrat, Fast diffusion of a Lennard Jones cluster on a crystalline surface, *Phys. Rev. Lett.* **78**, 4597-4600 (1997).
30. C. Brechignac. P. Cahuzac, F. Carlier, M. De Fructos, A. Masson, C. Mory, C. Colliex, and B. Yoon, Size effect in nucleation and growthy processes from preformed soft landed clusters, *Phys. Rev. B,* **57**, 2084-2087 (1998).

31. H. Haberland, Z. Insepov, and M. Moseler, Molecular dynamis simulation of thin film growth by energetic cluster impact, *Phys, Rev. B* **51**, 11061-11067 (1995).
32. L. Bardotti, B. Prevel, P. Jensen, M. Treilleux, P. Mélinon, A. Perez, J. Gierak, G. Faini, and D. Mailly, Organizing nanoclusters on functionalized surfaces, *Appl. Surf. Sci,,* in press (2002).
33. J.P. Perez, V. Dupuis, J. Tuaillon, A. Perez, V. Paillard, P. Mélinon, M. Treilleux, L. Thomas, B. Barbara, and B. Bouchet-Fabre, Magnetic properties of nanostructured iron films obtained by low energy neutral cluster beam deposition, *J. Magn. Magn. Mat.* **145**, 74-80 (1995).
34. C. Binns, S.H. Baker, and M.J. Maher, Synchrotron radiation studies of mass-selected Fe nanoclusters deposited in situ, *Eur. Phys. J. D* **16**(1-3), 189-192 (2001).
35. C. Binns, S.H. Baker, and M.J. Maher, Magnetism in Fe nanoclusters – From isolated particles to nanostructured materials, *Phys. Stat. Sol. A* **189**(2), 339-350 (2002).
36. M. Négrier, J. Tuaillon-Combes, V. Dupuis, P. Mélinon, and A. Perez, Nanostructured Co-Ag and Co-Pt thin films from clusters, *Phil. Mag. A* **81**(12), 2855-2863 (2001).
37. M. Jamet, M. Négrier, V. Dupuis, J. Tuaillon-Combes, P. Mélinon, A. Perez, W. Wernsdorfer, B. Barbara, and B. Baguenard, Interface magnetic anisotropy in cobalt clusters embedded in a platinum matrix, *J. Magn. Magn. Mat.* **237**, 293-301 (2001).
38. M. Jamet, V. Dupuis, P. Mélinon, G. Guiraud, A. Perez, W. Wernsdorfer, A. Traverse, and B. Baguenard, Structure and magnetism of well defined cobalt nanoparticles embedded in a niobium matrix, *Phys. Rev. B* **62**, 493-499 (2000).
39. P. Joyes, *Les agrégats inorganiques élémentaires* (Les Editions de Physique, Les Ulis, France, 1990).
40. W. Wernsdorfer, K. Hasselbach, A. Benoit, B. Barbara, D. Mailly, J. Tuaillon, J.P. Perez, V. Dupuis, J.P. Dupin, G. Guiraud, and A. Perez, High sensitivity magnetization measurements of nanoscale cobalt clusters, *J. Appl. Phys.* **78**(12), 7192-7195 (1995).
41. W. Wernsdorfer, Classical and quantum magnetization reversal studied in nanometer-sized particles and clusters, *Adv. Chem. Phys.* **118**, 99-190 (2001).
42. A. Thiaville, Coherent rotation of magnetization in three dimension : a geometrical approach, *Phys. Rev. B* **61**, 12221-12232 (2000).
43. M. Jamet, C.Dupuis, C. Thirion, W. Wernsdorfer, P. Mélinon, and A. Perez, Magnetic propertie of an individual Co-nanoparticle, *Scipta Materiala* **44**, 1371-1374 (2001).
44. W. Wernsdorfer, K. Hasselbach, D. Mailly, B. Barbara, L. Thomas, and S. Suran, DC-Squid magnetization measurements of single magnetic particles, *J. Magn. Magn. Mater.* **145**, 33-39 (1995).
45. W. Wernsdorfer, K. Hasselbach, A. Benoit, G. Cernicchiaro, D. Mailly, B. Barbara, and L. Thomas, measurements of the dynamics of the magnetization reversal in in,dividual single domain Co-particles, *J. Magn. Magn. Mater.* **151**, 38-44 (1995).
46. V. Dupuis, J..P. Perez, J. Tuaillon, V. Paillard, P. Mélinon, A. Perez, B. Barbara, L. Thomas, S. Fayeulle, and J.M. Gay, Magnetic properties of nanostructured thin films of transition metal obtained by low energy cluster beam deposition, *J. Appl. Phys.,* **76**(10), 6676-6678 (1994).
47. V. Dupuis, J. Tuaillon, J..P. Perez, V. Paillard, A. Perez , P. Mélinon, L. thomas, B. Barbara, and B. Bouchet, New nanocrystallized thin films of transition metal obtained by low energy cluster beam deposition, *J. Magn. Magn. Mater.* **148**, 1-3 (1995).
48. V. Dupuis, J.P. Perez, J. Tuaillon, V. Paillard, P. Mélinon, G. Guiraud, J.P. Dupin, A. Perez, L. Thomas, B. Barbara, and B. Bouchet, Nanocrystallized thin films of transition metal obtained by low energy cluster beam deposition, *Scripta Metall, Mater.* **33**(11), 1563-1568 (1995).
49. E. M. Chudnovski and M. Eugene, Magnetic properties of amorphous ferromagnets, *J. Appl. Phys.* **64**, 5770-5775 (1988).
50. L. Thomas, PhD thesis, Contribution à l'étude de nanostructures magnétiques : du matériau nanocristallisé à l'agrégat, *University Joseph Fourier, Grenoble, France* (1997).
51. F. Parent, J. Tuaillon, L.B. Stiren, V. Dupuis, B. Prevel, A. Perez, P. Mélinon, G. Guiraud, R. Morel, A. Barthelemi, and A. Fert, Giant magnetoresistance in Co-Ag granular films prepared by low-energy cluster beam deposition, *Phys. Rev B* **55**(6), 3683-3687 (1997).
52. A. Perez, V. Dupuis, J. Tuaillon-Combes, M. Jamet, MP. Négrier, P. Mélinon, W. Wernsdorfer, B. Barbara, and C. Thirion, Magnetic nanostructures from clusters, *IPAP Conf. Ser.* **3**, 34-38 (2001).

17
MAGNETIC THIN FILMS

Michael Farle *

1. INTRODUCTION

Magnetic thin films have provided a highly successful test ground for understanding the microscopic mechanisms which determine macroscopically observable quantitities like the magnetization vector, different types of magnetic order (ferro- , ferri- and antiferromagnetism), magnetic anisotropy and ordering temperatures (Curie, Néel temperature). The success has been based on the simultaneous development of the following techniques: a) the preparation of single crystalline mono- and multilayers on different types of substrates in ultrahigh vacuum systems, b) the development of vacuum compatible, monolayer-sensitive magnetic analysis techniques, c) the advance in computing power to provide first-principles calculations of magnetic ground state properties. Aside from these basic research orientated investigations the technological exploitation of thin film magnetism has lead to huge increases in the hard disk's magnetic data storage capacities and new types of magneto-resistive angle and position sensitive sensors in the automotive industry , for example.

The purpose of this chapter is threefold: a) An introductory level overview about basic physics in thin film magnetism will be given, b) characteristic examples of current research using synchrotron radiation , SQUID and magnetic resonance techniques will be discussed.

Various aspects of ultrathin film magnetism have been discussed in extensive reviews and book chapters over the last few years (see for example refs. 1-9) There is no way to summarize all these issues in such limited space and the reader is referred to the reviews mentioned before. The examples which I will discuss here are strictly restricted to the thickness and temperature dependent magnetic ground state properties of single element ferromagnetic metallic monolayers on metallic single crystalline substrates. This excludes epitaxially grown films comprised of two or more elements and it excludes ferromagnetic layers on semiconducting or insulating substrates. Also, the technological important aspects of exchange biased,[10] spin- valve,[11] or exchange-coupled multilayer[12] structures will not be reviewed here. In general, one should wish to understand the magnetic ground state properties of the simplest low- dimensional magnets first, before

* Michael Farle, Gerhard-Mercator-Universität Duisburg, Experimentelle Tieftemperaturphysik, Lotharstr. 1, ME, 47048 Duisburg, Germany.

turning to more complex systems. It will be shown that epitaxial films consisting of few atomic layers provide an interesting playground for artificially controlling magnetic properties and hence improving the understanding of the underlying physical mechanisms.

This chapter is divided into four sections in which I will present aspects of the film growth and resulting strains, the magnetic anisotropy and the magnetic moment per atom at 0 Kelvin, and finally some of the temperature dependent phenomena observed in magnetic monolayers.

2. FILM GROWTH

Neglecting kinetic principles in film growth one can classify three different growth modes based on the superposition $\Delta\gamma = \gamma_f + \gamma_i - \gamma_s$, of the surface energies of the substrate γ_s, of the interface γ_i, and of the growing film γ_f. For $\Delta\gamma < 0$ the film wets the surface and a monolayer forms. Three-dimensional clusters form immediately on the substrate when $\Delta\gamma > 0$ (*Volmer – Weber mode*). Layer-by-layer growth (*van der Merwe mode*) is achieved, if the subsequent layer wets the previous one, otherwise three-dimensional islands agglomerate (*Stranski-Krastanov mode*). Based on these simple arguments one would conclude that monolayers of the three ferromagnetic 3d metals Fe, Co, and Ni will form a monolayer only on the high melting, high surface energy substrates of Mo, Re, Ta or W and not on Cu, Ag or Au for example. Values for the surface energies and heats of adsorption for the most common materials have been tabulated by Gradmann.[3] However, experimental results have demonstrated that kinetic aspects, strain, anisotropy and temperature dependence modify this simple rule of thumb.[13-19] Using special deposition conditions like ultrahigh deposition rates (laser ablation) or surfactants excellent layer-by-layer deposition have been achieved for systems like Fe on Cu(001).[20]

Another important parameter is the lattice mismatch between the growing film and the substrate. In Figure 1 the case of fcc Ni growing on the (001) face of fcc Cu is sketched. The lattice mismatch $(a_{Cu} - a_{Ni})/a_{Cu} = 2.5\ \%$, with the nearest neighbor distances $a_{Cu} = 0.255$ nm and $a_{Ni} = 0.249$ nm, results in a vertical compression of the growing film of -3.2 %. The crystal structure of the Ni film becomes face centered tetragonal which is stable at least up to 10 monolayer (ML) thickness.

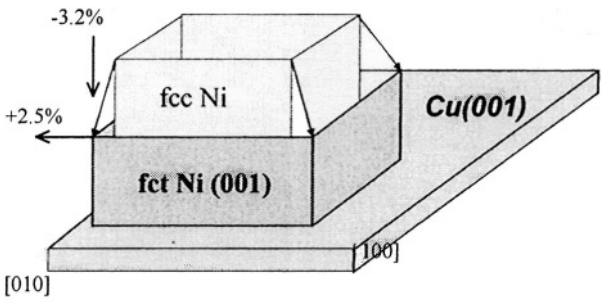

Figure 1. Illustration of the tetragonal distortion of a fcc Ni crystal when grown on Cu(001).

Another interesting case is the growth of Co on Cu(111). The nearest-neighbors distances of Co in its hcp phase (α-Co) (a_{hcp}^{Co} = 2.507 Å, c = 4.070 Å) and its fcc modification (β-Co) ($a_{fcc}^{Co} = 3.544/\sqrt{2}$ = 2.506 Å) match very closely the in-plane lattice parameters of the (111) oriented fcc Cu surface ($a_p^{Cu} = 3.615Å/\sqrt{2}$ = 2.556 Å). This results in a lattice mismatch $\eta = (a_i^{Co} - a_p^{Cu})/a_p^{Cu}$ = -1.9 % which is the same for hcp(0001) or fcc(111) Co. Consequently, there have been controversial results on the type of crystal structure which is stabilized on Cu(111). The difficulty results from the the fact that the staple sequence ABA (hcp) versus ABC (fcc) is already important for the second Co layer, when the outermost Cu layer is counted as layer A. Monoatomic steps at the interface will have a dramatic effect on the sequence resulting in mixtures of both phases in the ultrathin limit.

The lateral mismatch results in a vertical compression or dilation. This vertical distortion $\varepsilon_\perp$ can be calculated by either minimizing the elastic free energy or by assuming that the volume of the unit cell does not change due to the lateral distortion.

By minimizing the elastic free energy density E_{el} for the (111) geometry

$$E_{el} = \tfrac{1}{2}c_{11}(\varepsilon_{11}^2 + \varepsilon_{22}^2) + c_{12}\varepsilon_{11}\varepsilon_{22} + \tfrac{1}{2}c_{33}\varepsilon_{33}^2 + c_{13}(\varepsilon_{11} + \varepsilon_{22})\,\varepsilon_{33} \qquad (1)$$

one calculates $\varepsilon_\perp$ = -0.28 % using $\varepsilon_{33} = \varepsilon_\perp = [(-c_{11}c_{13} + c_{12}c_{13}) / (c_{11}c_{33} - c_{13}^2)]\,\varepsilon_\parallel$. The isotropic in-plane strain $\varepsilon_\parallel = \varepsilon_{11} = \varepsilon_{22}$ = 1.9%. The elastic constants $c_{11} = 30.7\times10^{10}$ Nm^{-2}, $c_{12} = 16.5\times10^{10}$ Nm^{-2}, $c_{13} = 10.3\times10^{10}$ Nm^{-2}, $c_{33} = 35.8\times10^{10}$ Nm^{-2} have been used in this calculation. The use of continuum linear elasticity theory for thin films with in-plane strains on the order of 2% may be questionable. However, studies on hcp(001) Co/W(110)[21] found quantitative agreement between measured and calculated strains up to 3 %.

If one calculates $\varepsilon_\perp$ assuming constant volume one finds a large $\varepsilon_\perp$ = -3.7 % which corresponds to an interlayer spacing d_{ij} = 0.197 nm (bulk 0.205 nm). This is less than the average hcp spacing d_{ave} = 0.200 nm determined by I(E)-LEED studies. Hence, it seems more reasonable to use the vertical compression retrieved by minimizing the elastic energy.

Another tutorial example is the case of Ni on bcc W(110). The lattice misfit between fcc Ni(111) and bcc W(110) planes is along the W[001], i.e. Ni $[\bar{1}10]$ direction $f_{[001]} = (a_{Ni} - a_W)/a_W$ = -21.3% (a_{Ni}=2.492Å, a_W=3.165Å) and along the W $[1\bar{1}0]$, i.e. Ni $[\bar{1}\bar{1}2]$, direction $f_{[1\text{-}10]} = (\sqrt{3}\,a_{Ni} - \sqrt{2}\,a_W)/\sqrt{2}\,a_W$ = -3.6%. Despite this large anisotropy in the lattice mismatch, Ni on W(110) has been found to grow nearly undistorted fcc (111), since the distortion is already accommodated in the first 2 layers.

In the discussion above one had to assume that the substrate is perfectly flat and contamination free. To obtain these perfect surfaces very special procedures have been developed which depend on the type of crystal and its orientation. These procedures require ultrahigh vacuum (UHV) conditions (10^{-8} Pa) and usually involve ion-etching and heating cycles which have to be repeated several times. It is generally accepted that "perfectly flat" means: substrate surfaces with smooth terraces of several hundred nm^2 area separated by mono-atomic steps. To verify the quality of such substrates the only available technique is scanning tunneling microscopy. Another technique with lateral

resolution on the order of 10 nm and monolayer vertical sensitivity is low energy electron microscopy (LEEM).[22] More common - because less expensive – UHV techniques based on electron diffraction – e.g. low energy electron diffraction (LEED) - cannot provide this information.

3. MAGNETIC MOMENT (T = 0K)

The total magnetic moment is given by

$$m_{tot}=g_J\mu_B[J(J+1)]^{1/2}, \tag{2}$$

where J is the total angular momentum determined by the Hund's rule and g_J is the Landé's g factor:

$$g_j = 1+\frac{J(J+1)+S(S+1)-L(L+1)}{2\cdot J(J+1)} \tag{3}$$

Accordingly, a free Fe^{2+} ion , for example, has a magnetic moment $m = 6.70\ \mu_B$ (g_J = 3.5, J = 4) unless the orbital moment is quenched in the solid. In the metallic bulk state with cubic symmetry the orbital magnetic moment μ_L is almost completely quenched, and a magnetic moment $m = 2.22\mu_B$ is measured. The magnetic moments of the four metallic ferromagnets are listed in Table 1. One should note the huge difference of the magnetic moment in the free (spherical potential) atomic and the bulk (cubic or hexagonal crystal potential) state. The free atom and the metallic bulk state represent the limiting cases for the evolution of the magnetic moment as a bulk crystal is built from single atoms, atomic lines and planes. The calculated values of the magnetic moment per atom of Co in the respective 0D, 1D, 2D, and 3D environments are given in Figure 2. One needs to note that in a strict sense only a free-standing monolayer represents a truely 2D system. In real experiments , however, "2D" layers require a substrate, which will influence the electronic structure of the monolayer. This substrate may be the same or a different material as the monolayer under investigation, resulting in different interface and surface magnetic moments (Figure 2).

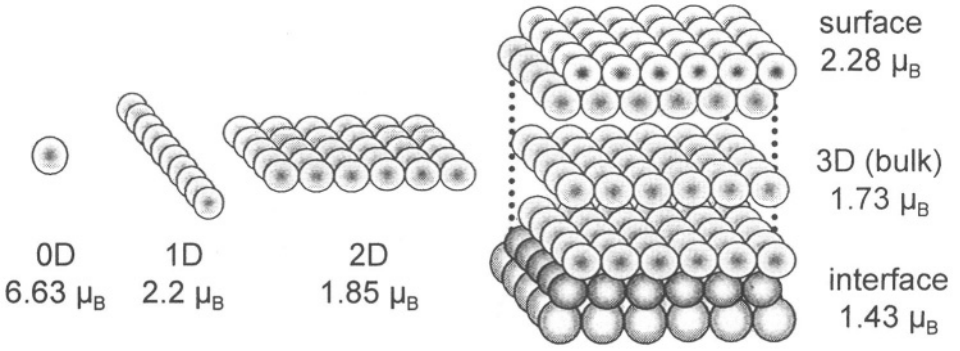

Figure 2. Evolution of the Co magnetic moment per atom from a single atom (0D) to a bulk fcc crystal (3D) adapted from ref. 23 and references therein.

Table 1. The magnetic moment per atom of the four metallic ferromagnets.

	atom					Metal bulk	
		S	L	g_J	m (μ_B)	m(μ_B)	m_L (μ_B)
Fe	$3d^6\,4s^2$	4/2	2	1.5	6.71	2.22	0.14
Co	$3d^7\,4s^2$	3/2	3	1.33	6.62	1.72	0.13
Ni	$3d^8\,4s^2$	1	3	1.25	5.59	0.62	0.06
Gd	$4f^7$	7/2	0	2	7.94	7.63	-

Interestingly, the magnetic moments at the surface, interface, in the 2D and 1D structure do change at most by 30 % in a somewhat unexpected way. For example, based on the simple arguments of lower coordination = higher magnetic moment one would have expected that the surface moments are smaller that the moments in the 1D structure. It is evident that details of the crystal and electronic structure play an important role.

The experimental determination of magnetic moments in ultrathin films represents a challenge in terms of required sensitivity of the apparatus and the film homogeneity and morphology. As discussed in the previous section the issues of film growth have been satisfactorily solved in many cases. When determining magnetic moments quantitatively one needs to acknowledge that the error bar of the magnetic moment per atom is given by the inaccuracy of the determination of the number of atoms carrying the respective moment. In thin film systems the number of atoms is generally determined by dividing the volume of the deposited layers by the number of unit cells. This will always result in an error bar of a few percent. As becomes clear from Figure 2 the challenge is also to discriminate a surface or interface moment from the interior moment, a problem which no technique to date is able to solve.[24] Even the best experimental setups, which will be discussed below, average over all magnetic moments within the monolayer film. The attempts to discriminate interface moments by using different substrate and capping layers are questionable. This approach presumes that the magnetic layer can be grown on different substrates in an identical crystal structure and strain state, which is not realistic. The same material (e.g. Fe) will assume a different crystal distortion and hence a different electronic structure on different substrates.

Table 2 summarizes the experimental methods which are available to determine the magnetization quantitatively[25] in situ in UHV. The sensitivities of the respective techniques are also given: torsion oscillation magnetometry (TOM),[26,27] alternating gradient magnetometry (AGM),[28] X-ray magnetic circular dichroism (XMCD),[29,30] and polarized neutron reflectometry (PNR).[31] All of these techniques have their specific advantages and disadvantages. To determine the magnetic moment per atom the technique must either be capable of measurement the susceptibility or the magnetization as a function of temperature. In the first case, the sensitivity requirements are even more stringent, since the magnetic moment can only be deduced from the Curie-Weiss law in the paramagnetic regime. Up to now no technique has been capable of measuring the susceptibility of monolayers in UHV more than 20 % above the Curie temperature.[32] In the second case magnetization data must be extrapolated to zero Kelvin (as discussed below) from temperature dependent measurements. The simple approach to use a theoretical $T^{3/2}$ dependence has been demonstrated not to be valid in general.

Table 2. Comparison of experimental techniques with sub-monolayer sensitivity for quantitative determinations of the magnetization as a function of temperature M(T) or as a function of magnetic field M(H) in situ in UHV.

Method	Sensitivity/ Accuracy	M(T)	M(H)	Reference
XMCD	$\pm 0.07 \mu_B$/atom	yes	yes	29,30
TOM	0.01 ML Co	>130 K	yes	26,27
AGM	0.4 ML Co	no (*in situ*)	yes	28
PNR	$\pm 0.05 \mu_B$/atom	yes	yes	31
high T_C SQUID	0.3 ML Co	yes	no	33

Furthermore, the effect of magnetic domain formation must be accounted for, which in general involves the characterization of the monolayer by a hysteresis loop.

The method of choice seems to be the x-ray magnetic circular dichroism. This technique is element-specific, can be used in-situ in UHV with large magnetic fields and determines the spin and orbital contribution of the magnetic moment. In an XMCD experiment, an x-ray absorption edge spectrum is measured with the incident photon spin aligned parallel and anti-parallel to the sample magnetization direction. From the difference of these spectra, the orbital and spin magnetic moments of the optically excited electrons (or, equivalently, of the core holes) may be determined through the application of sum rules for the orbital[34] and spin[35] part of the magnetic moment. One should note that the spin sum rule includes a so called dipole term $\langle T_z \rangle$ which is the expectation value of the intra-atomic magnetic dipole moment along the direction of magnetization. This term vanishes for a cubic symmetry, but can become as large as 30% of the total moment in monolayers and at surfaces. This complicates the quantitative analysis of the magnetic moment. However, angular dependent measurements can be used to determine the dipole term, since its angular average is zero. It will vanish for polycrystalline samples, and for crystalline samples it vanishes at the magic angle of 55° between the magnetization direction and the surface normal.[36]

Due to its element-specifity one can –in principle– investigate the effects of spin polarization in dia- or paramagnetic substrates which may be induced by deposition of a ferromagnetically ordered film. This has been successfully demonstrated for example for Co/Cu, Fe/Cu,[37] Ni/Pt,[38] Fe/W, and Fe/Ir [39] multilayers. Quite considerable induced interface magnetic moments of up to 0.2 μ_B were found in the W and Ir layers, which surprisingly showed opposite directions, i.e. antiferromagnetic and ferromagnetic coupling to the Fe layer. One notes that induced interface moments have been measured in the cases of multilayers only. The reason is simply, that for a single Co layer on a Cu single crystal substrate the number of Cu atoms that are influenced by the ferromagnetic layer is much too small in comparison to the overwhelming signal from the undisturbed Cu atoms within the sampling depth. Since the physics of multilayers is not the topic of this chapter, I will discuss an example for XMCD measurements for uncapped Co films deposited on Cu(001) and measured in situ.[40] Co on Cu(001) grows in a tetragonally distorted crystal structure layer-by-layer. The first Co layer is known to contain at least 25 % Cu.[41] The analysis of XMCD–difference spectra requires a careful normalization of the original spectra obtained with the photon spin parallel and anti-parallel to the magnetization direction. Self-absorption effects have to be taken into account. Small changes

on the order of 10^{-3} of the background intensity will cause a big error in the absolute determination of spin and orbital magnetic moments. Usually the safest method is the determination of the ratio of the orbital-to-spin magnetic moments (m_L/m_S), since the background is effectively divided out. In Figure 3 the ratio $(m_L/m_S)_{exp}$ is shown as a function of film thickness.[40] By comparison with theory (Table 3) one finds that the increase of the ratio for thinner films is due to a stronger increase of the orbital magnetic moment while the spin moment increases only slightly. The lowering of the symmetry lifts the quenching of orbital momentum.

The experimental analysis requires that one considers three different ratios corresponding to the interface (A), the surface (C) and the remaining Co layers (d-2) in between (B). Furthermore, the effective electron escape depth $\lambda = 2.3$ nm has to be taken into account, when averaging the signal over all detected Co layers according to

$$\left(\frac{m_L}{m_S}\right)_{exp} = \frac{A\,e^{-D(d-1)/\lambda} + B\sum_{n=3}^{d} e^{-D(n-2)/\lambda} + C}{\sum_{n=0}^{d-1} e^{-nD/\lambda}} \tag{4}$$

This reflects the fact that in the thin film limit relatively more surface and interface Co atoms are detected which sit in a non-cubic environment. The parameters A, B, and C that is the $(m_L/m_S)_{exp}$ of the interface, bulk and surface regions are obtained by fitting Eq. (4) to the experimental ratio. They are in excellent agreement with the calculated ones (Table 3).

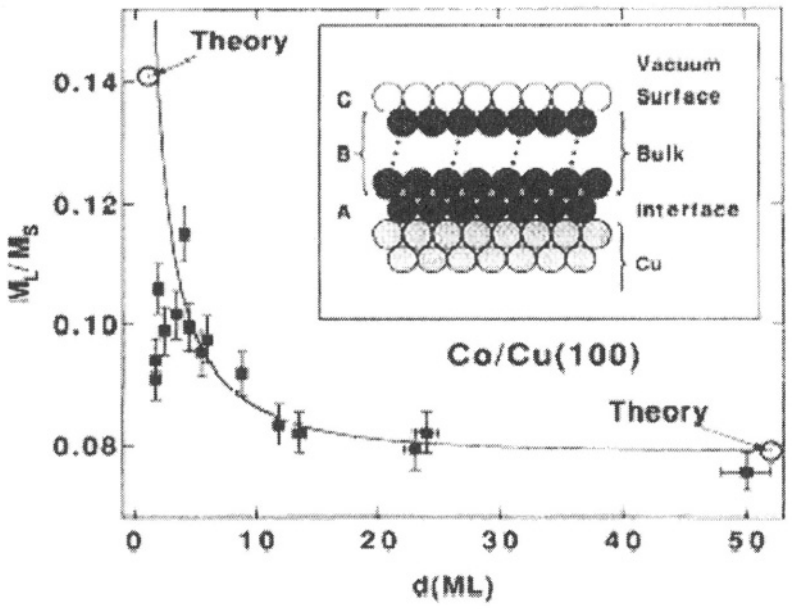

Figure 3. The ratio of orbital-to-spin moment m_L/m_S as a function of film thickness d for experiment (■) and theory (○). The solid line is a fit according to Eq. (4) with the parameters A,B, and C given in the bottom row of Table 3. The experimental data were fitted only for $d \geq 3$ ML, where alloying and interface roughness is negligible. The inset shows the interface, bulk, and surface components. From ref. 40.

Table 3. Calculated values for m_L, m_S and their ratio for fcc Co with the Cu lattice constant. The experimental ratios are given in terms of the weighting factors as discussed in the text.

Quantity	*1 ML Co/Cu(001)*	*Co(fcc, bulk)*	*Co(fcc,surface)*
$m_L\ (\mu_B)$	0.261	0.134	0.234
$m_S\ (\mu_B)$	1.850	1.724	1.921
$(m_L/m_S)_{theo}$	0.141	0.078	0.122
$(m_L/m_S)_{exp}$	A=0.19(5)	B=0.078	C=0.11(3)

Another more recently developed technique[42] uses a commercially available High-T_c-SQUID sensor to measure the magnetic stray field emanating from a fully magnetized ultrathin film. In the analysis one considers the magnetic film to be in a single domain state consisting of elementary magnetic dipoles d**m**, which produce a magnetic field d**B** in a distance **R** given by

$$d\mathbf{B} = \frac{\mu_0}{4\pi} \cdot \left(\frac{(3\mathbf{n} \cdot \mathrm{dm}) \cdot \mathbf{n} - \mathrm{dm}}{R^3} \right) \tag{5}$$

where **n** = **R**/R is a unit vector. The total perpendicular component B_z at position (u,v,h) for an in-plane magnetized film of length and width a in a distance h, with a homogeneous in-plane magnetization M along the x-axis and a thickness d is given by:

$$B_z^{tot}(u,v,h) = \frac{\mu_0}{4\pi} \cdot 3 \cdot M \cdot h \cdot d \int_{-a/2}^{a/2} \int_{-a/2}^{a/2} \frac{u-x}{R^5} \cdot dx \cdot dy \tag{6}$$

where R is the distance between the elementary dipole d**m** at $(x,y,0)$ and the measuring point (u,v,h). As the stray-field is measured only along the x-axis keeping the film centered (i.e. v = 0) Eq. (6) simplifies, and one derives a characteristic field distribution with a positive and a negative peak as it can be seen in Figure 4. The only free parameter is the magnetization M of the film which scales linearly with the peak height. The error of the fitting procedure is 1 to 2%. Together with the distance uncertainty this sums up to a maximum error of 5% for Co which is a remarkably small value for determining directly the total magnetization.

The measured magnetizations at T = 300 K for all films are plotted in Figure 5a versus the inverse thickness (open triangles). Films with d > 8 ML exhibit a magnetization M = (1458 ± 50) kA/m which is in excellent agreement with the well known bulk magnetization of 1447 kA/m at 296 K. The films with thicknesses down to 2.0 ML exhibit a thickness-dependent reduced magnetization down to 1225 kA/m. At first glance one might think that the reduction is due to a reduced magnetization at the interface. However, this interpretation is misleading as the magnetization data of thinner films recorded at T = 590 and 65 K (open circles) show. Their magnetization is considerably higher than at room temperature since the reduced temperature $t = T/T_C$ changes from about 0.5 to 0.2.

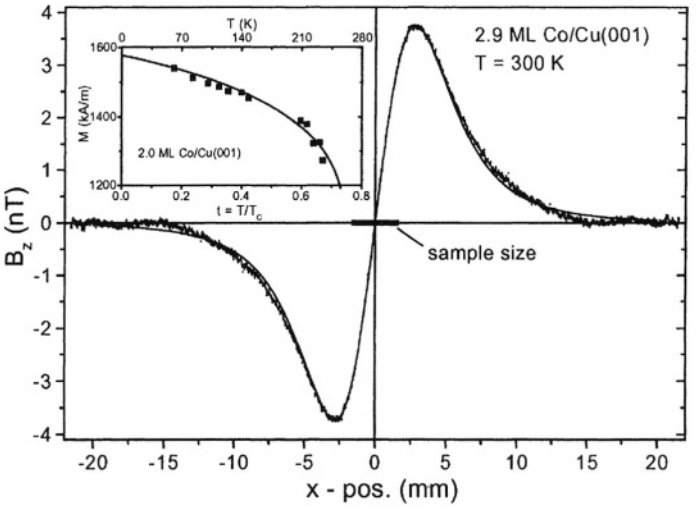

Figure 4. Z-component of the magnetic field of a 2.9 ML Co/Cu(001) film (squares) and a fit according to Eq. (6) (solid line) for h = 5.0 mm and M = 1360 kA/m. Data were recorded within 5 min, no further smoothing was performed. The inset shows temperature dependent measurements for 2.0 ML Co/Cu (001) with the novel setup (T_C=350 K). From ref. 33.

To obtain the true ground state magnetic moment, we correct the low temperature measurements to T = 0 K using the $T^{3/2}$ law which is valid for t < 0.3. Moreover, one has to take into account that the spin-wave parameter is thickness dependent. The corrected results of all measurements are represented by the solid squares in Figure 5a.

One can see that 2.0 ML Co/Cu(001) exhibit a magnetization of (1600±60) kA/m at T = 0 K, which is increased by 11% as compared to the bulk. In Figure 5b the data are given in magnetic moment per atom (full squares). A linear regression gives a bulk Co magnetic moment of 1.69(1) μ_B /atom. Up to this point we have determined the magnetization $\boldsymbol{M}$ and the total moment m_{tot} of our films absolutely. By comparison with XMCD and PND results values for m_L and m_S are derived separately. Both spin and orbital contributions increase with decreasing thickness. The extrapolation to the bulk shows a perfect agreement with PND measurements for bulk cobalt. The enhancement of the total moment is mainly governed by an orbital contribution increased by a factor of 2 which is attributed to an unquenching due to reduced cubic symmetry. The spin-like contribution for a 2 ML film is increased by 0.14 μ_B /atom compared to the bulk. From bulk down to 2 ML of Co/Cu(001) the total moment increases from a bulk like value of 1.69(1) μ_B /atom to 1.87(3) μ_B /atom. This behavior determines a volume contribution which fits both, the theoretical prediction and previous measurements, and an enhanced surface/interface contribution. The orbital contribution increases by a factor of 2 following a 1/d law. The spin contribution increases by 4% at 2 ML.

The total magnetic moment m_{tot} is not layer–resolved and represents the average over all step edge, interface, surface and bulk contributions of the Co magnetic moments. Interestingly, it shows a linear 1/d dependence for films thinner than 5 ML which has been exploited[23] to determine the surface and interface moments. It should be remembered that the separation of interface and surface moment is only possible by capping the co film thus creating "identical" interfaces.

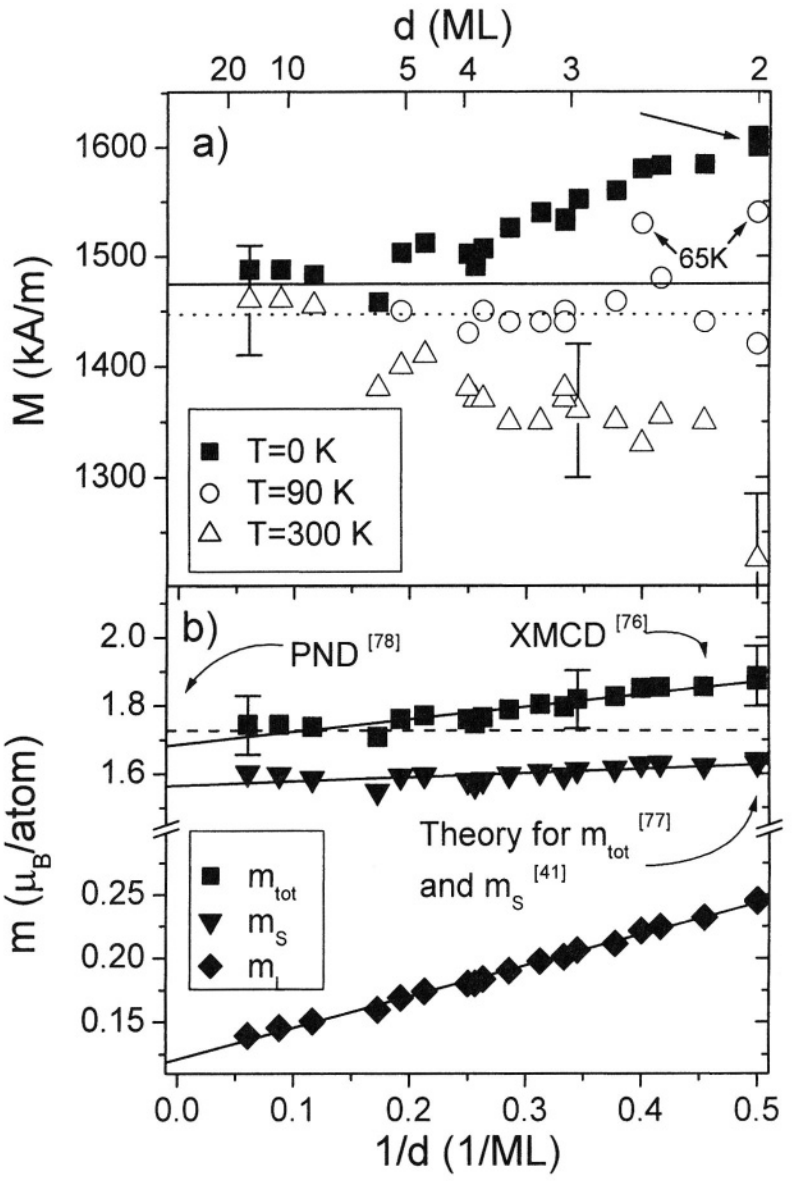

Figure 5. a) Magnetization for different thicknesses of Co/Cu(001) at 300 K and at 90 K. M_{bulk} for 300 (dotted line) and 4 K (solid line) is taken from ref 43. The full squares are extrapolated values to 0 K (see text). The arrow indicates the film from the inset of Figure 4. b) Magnetic moment at T= 0 K vs. inverse thickness. The dashed line indicates the bulk value of the total moment. The measured total moment (squares) separated into spin (down triangles) and orbital contribution (diamonds). Full lines are the results of least square fitting. From ref. 33. PND stands for polarized neutron diffraction.

Using this hypothesis of identical Co on Cu and Cu on Co interfaces one can calculate the interface moment $m_{tot,int}$ and the surface magnetic moment $m_{tot,surf}$ from the experimentally determined $m_{tot}^{uncapped}(d)$ and $m_{tot}^{capped}(d)$ using the simple Ansatz:

$$m_{tot}^{uncapped}(d) = m_{bulk} + (m_{tot,int}+m_{tot,surf}) / d \quad (7)$$

$$m_{tot}^{capped}(d) = m_{bulk} + 2\, m_{tot,int} / d \quad (8)$$

As discussed in ref. 23 in more detail, the strong reduction of the Curie temperature of the different Co films after capping and the different degrees of intermixing at the interfaces have to be taken into account. The impressive result of such an involved – but necessary – analysis is the determination of the surface, interface and bulk moments as shown in Figure 2. Similar studies have been performed for Ni films on Cu(001).[44] A bulk –like magnetization (Table 1) was determined for a 4 ML thickness which is reduced by 22% when the tetragonal distorted Ni film is capped by Cu. For a Ni thickness of 8 ML no reduction is found. These new results obtained by a technique which measures truly the total magnetic moment in its ground state unambiguously show that previous determinations of "dead layers" or dramatically reduced magnetic moments were due to sample imperfections or improper analyses, for example not considering the reduced Curie temperature $T_C(d)$ of ultrathin films.

These new techniques may provide the necessary tests for theoretical predictions that monolayers of 4d and 5d elements develop a net magnetic moment per atom.[45,46]

4. MAGNETIC ANISOTROPY ENERGY DENSITY (T = 0 K)

It is experimentally observed that a ferromagnet can be magnetized more easily along certain crystallographic directions than in others. One finds so called easy, intermediate and hard axes of magnetization, e.g. for bcc Fe these are <100>, <110>, <111> and for fcc Ni <111>, <110>, <100> at room temperature.

The energy difference associated with different directions of M , that is the magnetic anisotropy energy MAE, is a small contribution the order of a few μeV/atom to the total energy (several eV/atom) of a bulk crystal (Table 4). For applications of ferromagnetic materials and for the principal understanding of the microscopic origin of magnetism it is however *the all important quantity,* which determines for example the direction of magnetization coercive fields and domain sizes.

Table 4. Characteristic energies of a metallic ferromagnet. Energies below the double line are for magnetic properties as discussed in the text.

binding energy	1-10 eV/atom
exchange energy	$10 - 10^3$ meV/atom
structure, fcc -bcc	$10 - 10^3$ meV/atom
interface energy	200 meV/atom
stress	100 meV/atom
cubic MAE (e.g. Ni)	2 μeV/atom
uniaxial MAE (e.g. Co)	70 μeV/atom
1 ML Ni (001) MAE (	0.1 meV/atom
$½\mu_0 M^2$(T=0K) for Ni, Co, Fe	11, 90, 140 μeV/atom
step MAE K^{step}	0.1 - 1 meV/atom

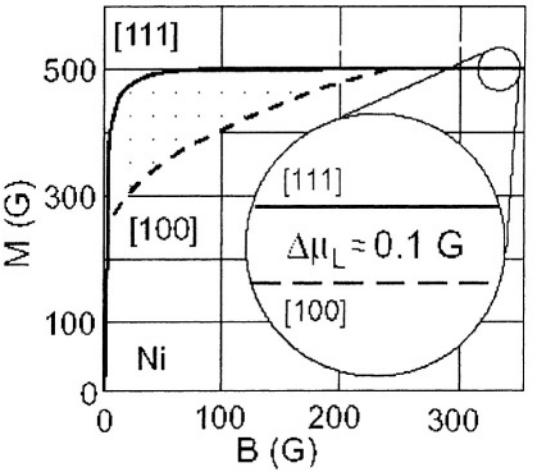

Figure 6. Magnetization curves or the easy [111] and hard [100] axes of bulk Ni. The shaded area between both curves is the magnetic anisotropy energy. The saturation magnetization values along the different directions are slightly different (inset). From ref. 9.

Before discussing the aspects of the MAE of magnetic monolayers it is worthwhile to have a look at experimental results for bulk ferromagnets. In Figure 6 the magnetization curves of a bulk Ni single crystal are shown which were recorded with the magnetic field B applied along the [100] and [111] direction. The area in between these curves has the units of energy and yields directly the magnetic anisotropy energy density (MAE). The saturation magnetizations along the different directions which are the easy and hard axes are different! The effect is very small as the inset shows, but measurable, and well documented (see for example ref. 47). This means in other words that the magnetization vector changes its length, it is "longer" in the easy direction. Since the spin moment is usually assumed isotropic, the MAE arises from the anisotropy of the orbital moment.

The anisotropy $\Delta\mu/\mu_{tot}$ of the moment is correlated with the magnitude of MAE. Both are larger for the lower symmetry of bulk hcp Co and smaller for cubic fcc Co, fcc Ni and bcc Fe. The same observation holds for Rare Earth elements. Even for the S-state ion Gd which crystallizes in the hep structure an anisotropic moment $(\mu_c-\mu_a)/\mu_c = 10^{-3}$ ($\mu_{c,a}$: moment parallel to c, a-axis) has been measured.[49] For Tb with its large orbital moment (L=3) a much larger difference is found.[50] One should also note, that the easy axis can deviate from crystallographic directions as for example in the case of Gd whose easy axis is temperature dependent and lies between the c-axis and the basal plane at T = 0 K.

In the phenomenological Ansatz used in experimental work the crystallographic easy direction of the magnetization is determined by the minimum of the free energy density F, which in an external magnetic field can be expressed as the sum:

$$F = F_{ex} + F_{an} + F_{el} + F_{mag.el.} + F_{\sigma} + F_{d} + F_{zee} \qquad (9)$$

with F_{ex}, the energy of exchange interaction; F_{an}, the energy of crystallographic magnetic anisotropy; F_{el}, the internal elastic energy of the crystal; $F_{mag.el.}$, the energy of magnetoelastic interaction; F_{σ}, the energy of external stresses associated with magneto-

striction; F_d the energy of the demagnetizing field of the sample; and F_{zee} the energy of the magnetized sample with the external magnetic field.

For the moment we will regard the free energy density Eq. (9) for the case of zero applied magnetic field, zero externally applied stress and for a spherical sample shape. Furthermore, we will consider only the single domain state. The exchange energy and the demagnetizing energy for a sphere are isotropic. The easy axis of the spontaneous magnetization is determined by the minimum of the sum $F_{an} + F_{el} + F_{mag.el.}$. One should note that a gain in magneto-elastic energy depends linearly on the elastic deformations while F_{el} is a quadratic function of the deformations. Hence in general, the crystal will spontaneously deform, if a magnetization develops at the para- to ferromagnetic phase transition. The equilibrium lattice constant is determined by the minimum of $F_{an} + F_{el} + F_{mag.el.}$. For a cubic crystal F_{an} is written in the form:[51]

$$E_{an} = K_0 + K_4' (\alpha_x^2\alpha_y^2 + \alpha_y^2\alpha_z^2 + \alpha_z^2\alpha_x^2) + K_6' \alpha_x^2\alpha_y^2\alpha_z^2 + \ldots\ldots \qquad (10)$$

This represents the anisotropic energy at constant volume. If one allows the crystal to deform, the anisotropy parameters K_i' are replaced by coefficients K_i given by $K_i = K_i' + f_i(c_{ij}, a_{ij})$ where c_{ij} are the elastic moduli, and a_i the magnetoelastic coupling constants.

One has to distinguish between anisotropy parameters at constant volume (K_i') and the ones at constant stresses (K_i). The latter case always occurs in practice in bulk crystals. In bulk systems the differences between K_i and K_i' are very small and can be neglected in most cases.

A new situation arises when the ferromagnet is clamped to a substrate and large elastic strains ε on the order of a few percent are present. This is comparable to the application of an external stress to the crystal. Depending on the direction of stress (N/m^2) with respect to the crystallographic axes anisotropic strains develop which modify the intrinsic anisotropy by inverse magnetostriction. The strain anisotropy F_σ can be orders of magnitude larger than the one of the undistorted lattice. An excellent overview on magnetostriction effects in monolayers has been given by D. Sander.[4]

Table 5. Comparison of the difference in total magnetic moments along the easy and hard directions $\Delta\mu = \mu^{easy} - \mu^{hard}$ and the MAE in bulk ferromagnets.

	$\Delta\mu/\mu_{tot}$	Easy axis	MAE (0 K) (μeV/atom)
Fe	$1.7\ 10^{-4}$	[100] bcc	+1.4
Co	$4.5\ 10^{-4}$	[0001] hcp	+65
Co		[111] fcc	1.8
Ni	$1.8\ 10^{-4}$	[111] fcc	-2.7
Gd	10^{-3}	hcp	+50

Magnetostriction contributions to the free energy of hexagonal, tetragonal, and orthorhombic crystals have been derived for example by Mason[52] and Bozorth.[53] Since the free energy is temperature dependent also the anisotropy, magnetostriction and elastic constants must be temperature dependent. This is well-known in bulk physics and will be discussed below.

Note, that a different choice of angles with respect to the crystallographic axes gives different expressions for the free energy of the same crystal. Care must be taken to compare the experimental anisotropy constants used by different groups. Also, one must not confuse these "experimental" K_i with the coefficients k_i [6] appearing in front of the spherical harmonics used in theory. There are also different nomenclatures for the experimental coefficients used in the literature. For example, in hexagonal systems the "first" order coefficients K_1 are the ones for the quadratic angular dependence while for cubic systems the first order coefficients K_1^{cub} are used for the fourth-order angular dependence.

4.1. Microscopic Origin

There are *only two microscopic sources* of MAE !:

a) the dipole - dipole interaction :

$$\hat{H}_{dd} = \frac{1}{4\pi\varepsilon_0}\frac{1}{R_{ij}^3}\left[\vec{S}_i \bullet \vec{S}_j - \frac{3}{R_{ij}^2}\left(\vec{S}_i \bullet \vec{R}_{ij}\right)\left(\vec{S}_j \bullet \vec{R}_{ij}\right)\right] \tag{11}$$

b) the spin - orbit coupling :

$$\hat{H}_{LS} = -\lambda \vec{L}_i \bullet \vec{S}_i = -\frac{e}{2m^2c^2}\left(\frac{1}{r}\frac{dV}{dr}\right)\vec{L}_i \bullet \vec{S}_i \tag{12}$$

Both interactions couple the spin vector to the lattice $\vec{R}$. Different orientations of the spin with respect to the lattice vector yield different interaction energies. The exchange interaction

$$\hat{H}_{ex} = \sum_{i \neq j} J_{ij}\vec{S}_i \bullet \vec{S}_j = \sum_{i \neq j} J_{ij}\left(S_i^x S_j^x + S_i^y S_j^y + S_i^z S_j^z\right) \tag{13}$$

does not contribute to MAE since the scalar product of the spin vectors is independent of the angles with respect to the crystal axes.

The long range dipolar interaction is the source of the so-called shape anisotropy, which senses the outer shape of the sample. For homogeneously magnetized samples the dipolar anisotropy is given by $F_d = 1/2\ \mu_0\ (N_x M_x^2 + N_y M_y^2 + N_z M_z^2)$ with the components of the demagnetization tensor $N_x + N_y + N_z = 1$. One should note that the dipolar interaction in the near field (only nearest neighbors) is sometimes called the pseudo-dipolar or anisotropic exchange energy. This name is misleading , since exchange interaction is isotropic. This contribution vanishes for a cubic crystal. Allowing a spontaneous magnetostrictive deformation of the lattice yields only a slight dipolar anisotropy which is 1/1000 of the MAE measured in Ni or Fe. Also, in bulk hcp Co this

contribution is negligible, since the c/a ratio deviates only by 0.67 % from the ideal ratio $\sqrt{8/3}$.

The more important interaction is the spin-orbit coupling, which couples the spin to the charge (orbital) density distribution in the crystal. Thus, the spontaneous magnetization "gets the feel" of the crystal via the orbital motion of the magnetic electrons. The orbital motion is coupled to the lattice by the ligand field which reflects the symmetry of the lattice. The ligand field $K = \sum_i^N e \cdot \phi(|\vec{r}_i|)$ is given by the sum of the electrostatic potentials $\phi(r_i)$ over the nearest neighbors at sites r_i. For example, in cubic symmetry this yields in cartesian coordinates (x,y,z):

$$K = \frac{35}{4}\frac{q_{ion}}{a^5}\left(x^2 + y^2 + z^2 - \frac{3}{5}r^4\right) \tag{14}$$

Two kinds of microscopic energies may be produced as a result of this mechanism:

a) spin-orbit coupling which depends on the spin states of two or more ionic carriers of magnetic moment (*pair model of magnetic anisotropy*).
b) coupling which depends on the effective spin state of individual ions (*single-ion model of magnetic anisotropy*).

The latter mechanism corresponds closer to the situation in nonmetallic magnets where the moment carrying ion is surrounded by magnetically neutral ions. The ligand (crystal) field whose symmetry is determined by the type of lattice causes a splitting of the atomic levels. For different lattices one obtains different levels (orbital states) corresponding to the ground state (Figure 7). With the ligand field approach it is straight forward to understand why the MAE in cubic lattices is in general much smaller than in distorted cubic or hexagonal structures. The orbital moment in cubic systems is completely quenched.

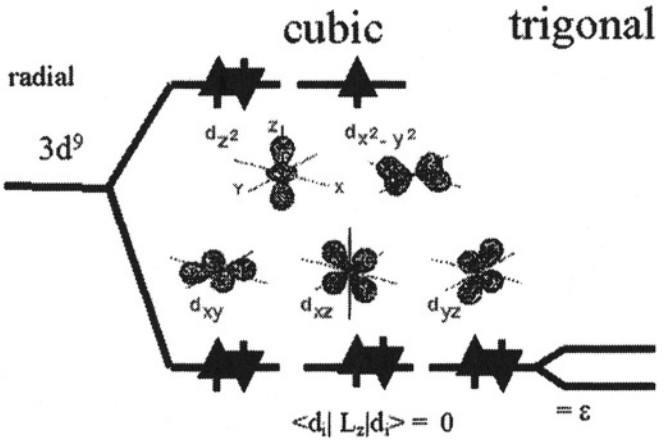

Figure 7. Crystal field splitting of a $3d^9$ state in cubic and trigonal environment. In cubic symmetry the expectation value of the z-component of the orbital momentum is quenched. Any deviation as for example in trigonal symmetry lifts the degeneracy of the ground state yielding a small orbital magnetic moment ε.

Hence in second order one does not expect an orbital contribution to MAE in a cubic crystal. Only with fourth order perturbation a small anisotropic contribution μ_l isobtained (Table 4). In the ligand - field - theory this partial unquenching of orbital moment is due to the combined effect of spin-orbit interaction and trigonal distortion which leads to a small decrease of the ground state energy as schematically depicted in Figure 7.

In metallic ferromagnets the explanation is also based on the spin-orbit mechanism. The correct order of magnitude for MAE can be obtained by taking the spin-orbit interaction (coupling constant λ) and the width of the 3d band ΔW into account.[54] In second order perturbation one finds a vanishing MAE for a cubic system and for an uniaxial system $K_2 \approx \lambda^2/\Delta W$, fourth order perturbation yields an anisotropy for a cubic system $K_4 \approx \lambda^4/\Delta W^3$. With a typical bandwidth of 5 eV and $\lambda \approx 70$ meV for 3d elements one finds $K_2 \approx 1$ meV and $K_4 \approx 0.2$ μeV. Although the quantitative agreement to the experimental data is not satisfactory, the simple perturbative approach reveals again the importance of the symmetry of the crystal for the magnitude of MAE.

Recently *ab initio* calculations of MAE using a self-consistent full-potential method including orbital polarization (the analogue to Hund´s second rule in atomic physics) have become available. The calculation[55] shows that by compressing fee Ni (c/a = 1) the MAE (that is the total energy difference between M ∥ [001] and M ∥ [110]) is tremendously enhanced (Figure 8). The easy axis is parallel to the direction of compression. The largest MAE of about 500 μeV/atom is reached at a ratio $c/a \approx 0.85$. Upon further compression while keeping the volume constant the bcc lattice structure is reached at $c/a = 1/\sqrt{2}$ (Bain path), and the MAE decreases to a value of few μeV/atom characteristic for a cubic system. On the other hand an expansion (c/a > 1) leads to an easy axis perpendicular to the strain axis.

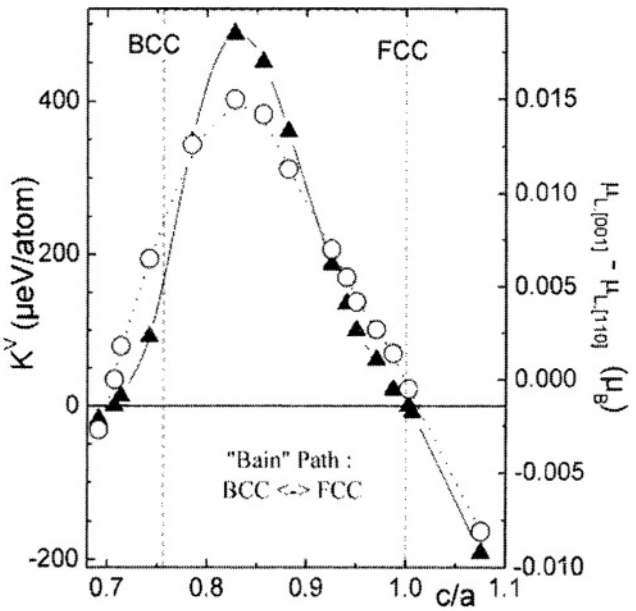

Figure 8. From ref. 55: Volume MAE (▲) and difference of orbital magnetic moment (o) as a function of the vertical compression of a fcc lattice into a bcc lattice.

The increase of K is related to an increase of the difference in the orbital moment between the easy direction [001] and the hard direction. From this the following conclusions on the correlation of MAE and orbital moment are manifested:

- The orbital magnetic moment is anisotropic.
- The larger orbital moment is parallel to the easy axis of magnetization.
- The magnitude of MAE is related to the *difference* of the orbital moments parallel and perpendicular to the easy axis.
- The anisotropy of the orbital moment increases for lower symmetries, e.g. fcc -> fct

Bruno did also show that in a perturbation theory approach the energy difference between easy and hard direction ΔE is linked to the anisotropy of the orbital moment, and for a more than half-filled d-shell he calculates

$$\Delta E = -\alpha \frac{\lambda}{\mu_B}(\mu_L^{easy} - \mu_L^{hard}) \tag{15}$$

where the proportionality factor α ($\approx$0.05 for Co) depends on the details of the band structure. However, a simple proportionality between MAE and orbital moment anisotropy does not exist as demonstrated by the first principles calculation[55] shown in Figure 9.

How can one compare the phenomenological anisotropy coefficients $K_i(T\neq 0K)$ from Eq. (10) to first principles calculations K(T=0 K)? The difference in the free energy for different directions of M along [001], [110] or [100] is given in a tetragonal system with spherical sample shape by:

$$\begin{aligned} E_{[001]} - E_{[110]} &= -K_2 - 1/2\, K_{4\perp} + K_{4\parallel} \\ \text{and}\quad E_{[001]} - E_{[100]} &= -K_2 - 1/2\, K_{4\perp} + 2\, K_{4\parallel} \end{aligned} \tag{16}$$

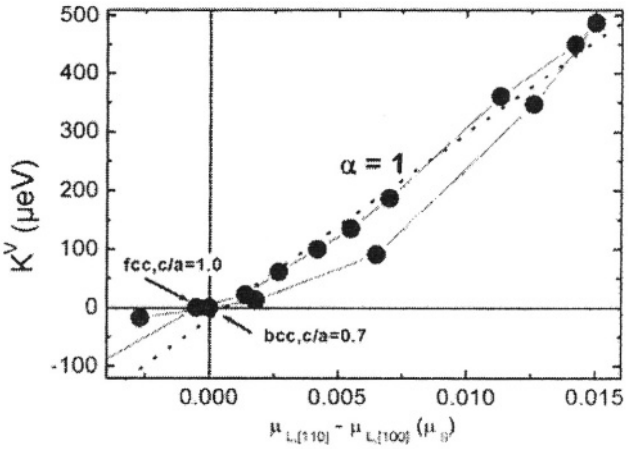

Figure 9. Ab-initio calculation[55] for the volume MAE and the difference of orbital moments along different crystallographic axes function of the ratio c/a. There is no simple proportionality (α=1) between $\Delta\mu_L$ and K^V, see also in ref. 9.

Only if the coefficients K_i are known at T = 0 K, experiment and calculation can be compared. Experimental K_i must be either measured at 4 K or at least extrapolated down to T=0 K from the temperature dependence at higher T. It is worthwhile to stress that in the literature experimental data at 300 K have been compared to ground-state calculations, which is wrong. All K_i are strongly temperature dependent.

4.2. Surface and Interface Anisotropy

The free energy F of systems of reduced dimensions, that is samples with a large surface S to volume V ratio is usually written as the sum of a volume and a surface term.

$$F = f^V(\theta,\varphi)\cdot V + f^S(\theta,\varphi)\cdot S \tag{17}$$

The energy per volume of a thin film becomes:

$$\frac{1}{V}F(\theta,\varphi) \equiv E(\theta,\varphi) = f^V(\theta,\varphi) + \frac{1}{d} f^S(\theta,\varphi) \tag{18}$$

with the film thickness d. In analogy the anisotropic part of the free energy can be written[56,57]

$$K_i = K_i^V + (K_i^{surf} + K_i^{int}) / d \tag{19}$$

where the index i refers to the second and fourth order anisotropy coefficients. The superscripts "surf" and "int" refer to the "surface" contributions of the vacuum/film and film / substrate interface (Figure 1). Since most measurements average over both contributions, $K_i^{surf} + K_i^{int}$ is replaced by the average over both interfaces $2\,K_i^S$. In most experimental studies the K_i appearing in Eq. (19) have been analyzed in second order only, that is K_2^V and K_2^S is determined from a plot of K_2 as a function of 1/d or by plotting $K_2 \cdot d$ versus d. Both effectively contain contributions of dipolar (shape) and spin-orbit (intrinsic) origin as summarized below.

Changes in symmetry (lattice structure) and lattice distortions can lead to a tremendous enhancement of the MAE (Figure 8). This effect is due to spin-orbit interaction and can be orders of magnitude larger than the shape anisotropy (Table 1). Any epitaxially grown film on a non-magnetic single crystal substrate is strained. Depending on the lattice mismatch between substrate and film different thickness regimes must be distinguished: the thickness range of coherency strain and for strain relaxation by incorporation of misfit dislocations. Both regions are connected at the critical thickness d_{cs} which is given by the energetic minimum of the sum of elastic energy, which increases proportional to the strain volume, and the energy to form a dislocation. For a lattice mismatch $\eta < 3\%$ a critical thickness $d_{cs} \approx 10$-20 ML is calculated. For larger η d_{cs} can be as small as 1-2 ML (e.g. Gd or Ni or Co/W(110), Ni/Re(0001)). This thickness dependence has important consequences for the MAE. In the coherent growth regime the lattice constants are assumed thickness independent and different from the bulk structure, i.e. the film assumes the lateral lattice constant of the substrate and relaxes vertically according to the Poisson ratio.

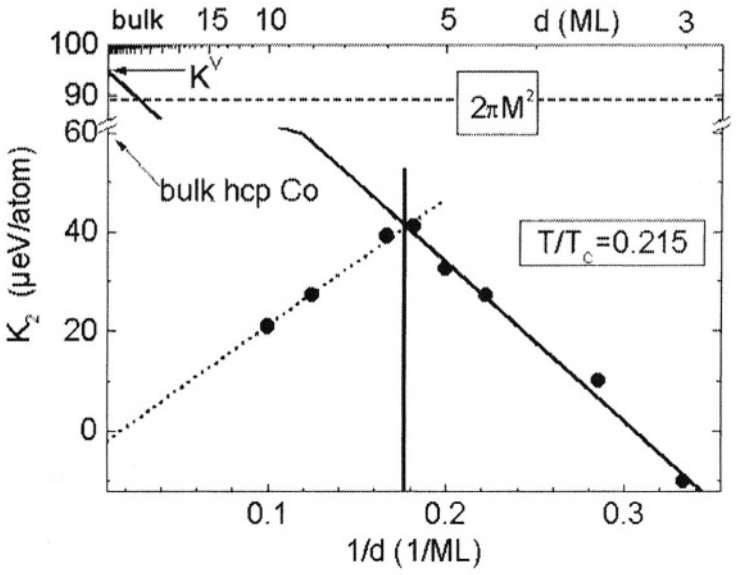

Figure 10. Thickness dependence of second order MAE in Co/Cu(111) from ref. 60.

The total intrinsic MAE consists of a thickness independent ("volume") part K^V and the "surface" contributions K^{surf} and K^{int}. K^V corresponds to the MAE of an artificial crystal with infinite dimensions ($d \rightarrow \infty$). For a (001) oriented fcc film the strain contribution K_ε to MAE is estimated from

$$K_\varepsilon(T) = 3/2\ \lambda_{001}(c_{11}-c_{12})(\varepsilon_\perp-\varepsilon_{II}),\quad \varepsilon_\parallel = -\frac{\nu_{100}-1}{2\nu_{100}}\varepsilon_\perp,\ \nu_{100} = \frac{c_{12}}{c_{11}+c_{12}} \qquad (20)$$

with $\varepsilon_{\perp,\parallel}$ the out-of-plane, in-plane strain, and c_{ij} elastic constants. Expressions for K_ε have been given in refs. 4, 6, and 58.

K^{surf} can be estimated by Néel's model, which considers the pair interaction at the surface of a ferromagnet. Even for an ideally flat interface the contribution K_i^{surf} is not the same as K_i^{int} because of the change in the band structure due to hybridization with the substrate. In general, the thickness dependent contributions $(K_i^{Surf} + K_i^{Int})/d$ dominates for small d. However, opposite signs of K_i^{surf} and K_i^{int} can compensate this effect.

In the incoherent growth regime the thickness dependent accommodation of misfit (η) strains leads to an effective 1/d contribution which does not originate from the interface.[54] Thus, a separate interpretation of the MAE must be made in the regions above and below the critical thickness d_c.[59]

A nice example is shown in Figure 10 and Figure 11. In Figure 10 surface and volume contributions to the MAE are separated by plotting K_2 as a function of reciprocal thickness at constant reduced temperature T/T_C which is the correct thermodynamic parameter. The two different growth regimes discussed above can be identified (above and below 5.5 ML). Below 5.5 ML one sees a linear increase according to Eq. (19) with an intersect and slope corresponding to K_2^V = 98 μeV/atom and K_2^S = -0.16 meV/atom, respectively. Above 5.5 ML the signs are reversed and K_2 decreases linearly with a

positive slope K_2^S = +0.13 meV/atom and negative intersect K_2^V = -3 μeV/atom (10<d<5 ML). This reflects the fact that below 5.5 ML a strong trigonal distortion dominates, while above 5.5 ML the accommodation of misfit dislocation and stacking faults cause a nearly strain free cubic crystal structure. The critical thickness of 5.5 ML agrees well with the nominal 4.5 ML at which stacking faults are known to form and the structural change begins.[60] At first glance the observation of a linear 1/d dependence is surprising, since it is known that thermally deposited Co/Cu(lll) grows in the form of bilayer islands and not layer-by- layer. However the mean roughness of the film surface stays constant after evaporation of about 1 ML as MEED measurements and scanning-tunneling-microscopy (STM) studies revealed. Therefore the same dependence as described by Eq. (9) is expected.

Another example is the case of tetragonal distorted (fct) Ni/Cu(001), which represents one of the most carefully examined systems in magnetic monolayer research (see for example refs. 6, 9, 48, and references therein). The free energy density for a tetragonal lattice which is appropriate for Ni on Cu(001), is given by:

$$E = 2\pi (N_\perp - N_{||}) M^2 \cos^2\theta - K_2 \cos^2\theta - \tfrac{1}{2} K_{4\perp} \cos^4\theta - \tfrac{1}{2} K_{4||} \tfrac{1}{4} (3+\cos 4\varphi) \sin^4\theta \qquad (21)$$

All the anisotropy constants have been experimentally determined by ferromagnetic resonance as function of Ni thickness (Figure 11). One observes the analogous growth dependence of the MAE. Above a critical thickness of about 15 ML the slope changes its sign revealing the relaxation of the crystal structure. One may conclude that the careful determination of MAE yields very sensitive information on structural deformations which may be too small to detect by other methods. For completeness one should note that for negative $K_{4||}$ the easy axis of magnetization is along the [110] direction, for positive $K_{4||}$ along [100].

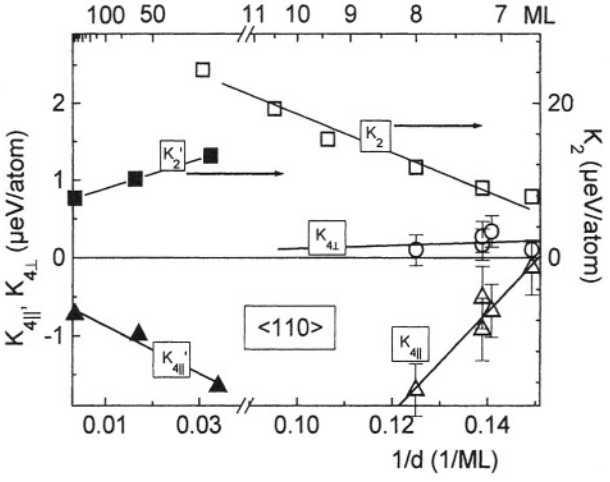

Figure 11. Magnetic anisotropy constants of Ni/Cu(001) determined by ferromagnetic resonance.[6] Fourth- and second order anisotropy constants are shown. Above 11 ML the lattice relaxation begins which is seen by the change of the slope. Again as in the case of Co/Cu(111) the relaxed film (d > 11 ML) has a nearly vanishing cubic volume anisotropy.

Any real surface or interface contains steps and defect sites. This causes an additional reduction of the symmetry and of nearest neighbor coordination. Following the rule of thumb that lower symmetry corresponds to larger MAE one expects a large contribution to the surface and interface anisotropy which was also confirmed in the cases of Ni on Cu(001)[61] and Fe on Ag(001).[62] Preferentially oriented step edges lead to an uniaxial in-plane anisotropy on the order of 1 meV/atom ($\approx 5 \times 10^{-8}$ erg/cm) which increases quadratically with the step density. In principle two different step induced contributions arise at the substrate and the vacuum interface. The substrate step density does not change with film thickness. The step density at the vacuum interface changes with thickness resulting in an unpredictable thickness dependent contribution to $(K_i^{surf} + K_i^{int})/d$.[63] Gradmann et al. showed that step anisotropies at Fe(110) and Fe/Pd interfaces are on the order of -0.39 and -0.16 meV/atom favoring perpendicular magnetization. Their finding contradicts the theoretical prediction by the Néel model[64] that roughness always reduces perpendicular anisotropy. Note that dipolar and spin-orbit induced roughness give contributions of opposite sign to MAE.

The experimental determination of thin film anisotropy was pioneered by Gradmann and coworkers and subsequently studied also by many other groups. Values of K_2^S and K_2^V have been tabulated for the 3d elements in several reviews (for example [1,6,7,57,59]). The thickness independent part K_2^V is in general one order of magnitude larger than the bulk value. K_2^V of fcc Co films on various substrates has the same magnitude as K_2 of bulk hep Co. This is no contradiction to the previous statement, since bulk fcc Co has a much lower cubic K_4. In general, the averaged K_2^S of Co is positive (favoring perpendicular magnetization) and K_2^V is negative. For the hcp Co(0001) and for the fcc Co(100) surface/vacuum interface one finds a negative K_2^S. It must be concluded that strong hybridization with the substrate and defects/steps at the interfaces cause the positive K_2^S leading to a strong perpendicular anisotropy in most ultrathin Co layers. All Fe faces show a similar trend, that is negative K_2^V and positive K_2^S. Exceptions ($K_2^S<0$) are the W/Fe(110), Fe/Pt(100) interfaces. The behavior of Ni interfaces is in general opposite, $K_2^V > 0$ and $K_2^S < 0$. The origin of the differences between Ni and Fe or Co is the opposite sign of the magnetostriction constants. In the monolayer limit the bulk magnetostriction constants have been found to change sign compared to bulk.[4] In some systems good quantitative agreement between measured and calculated Néel-type surface anisotropies is obtained, in most cases however, the sign and magnitude differ.

Also four-fold anisotropies depend strongly on film thickness. Fourth order surface and volume contributions have been determined for Fe (for example [65]) and Co (for example [7,21]). $K_{4\parallel}^S$ of Fe(001) favors the <110> crystallographic direction, while the volume anisotropy favors the [100] direction (= easy bulk).

From the above discussion it should have become clear that a naive analysis according to Eq. (19) assuming an averaged $2K_2^S/d$ and a thickness independent K_2^V is questionable for real films. Nevertheless, numerous experiments have confirmed that this phenomenological approach provides a reasonable description of the MAE in a thin film. An apparent agreement between a calculated and the experimental anisotropy contribution K^S, however, may be coincidental.

Usually the anisotropy is given as energy per volume, e.g. J/m^3. The surface and step anisotropy have the dimensions of energy per area (J/m^2) and energy per line (J/m) which makes numbers hard to compare. A better way is to give the anisotropy in energy per atom, which means that the atomic volume in a sample consisting of N atoms must be estimated. The different faces ((111) versus (100)) contain a different number of

atoms per unit area. This gives a different surface anisotropy in eV/atom, when K^S in J/m^2 is the same for both. A dimension of energy/atom allows a convenient comparison of volume-, surface-, and step-type anisotropy. Also the correlation to calculated values is much more straightforward.

The dipolar interaction which senses the shape of the sample has for magnetic moments located on a two-dimensional sheet the lowest energy when all the moments are aligned in the film (x,y) plane. The magnetization of a thin film lies in the plane along a crystallographic direction determined by in-plane anisotropies. To produce a perpendicular magnetization the shape anisotropy $F_d = \frac{1}{2}\mu_0(N_\perp - N_\parallel)M^2$ must be compensated. $F_d(T=0K)$ for Ni, Co, and Fe layers is on the order of 11, 90 and 140 $\mu eV/atom$ $(N_\perp - N_\parallel = 1)$. These values are much larger than the intrinsic anisotropy K due to spin-orbit coupling of bulk 3d elements. One can estimate the critical thickness d_c for a disk of diameter D above which a perpendicular magnetization is found by $d_c/D = 1/(3\pi^3)(1 - K/F_d)$. $N_\parallel$ of a thin disk is approximately given by $N_\parallel \approx \pi/4\ d/D$. For a 10 mm diameter disk of Co at T=0 K one calculates $d_c \approx 20\mu$. d_c is temperature dependent due to the different temperature dependencies of F_d and K.[66]

In the limit of a few atomic layers it was argued that a film should not be considered as a magnetic continuum. The discreteness of the lattice becomes important. Calculations of the sum of the dipolar interaction for a discrete assembly of magnetic point dipoles have shown that the average demagnetization factor $N_\perp$ for a film containing n atomic layers is reduced to $N_\perp = 1 - A/n$ with A = 0.4245 $(n \geq 2)$ for bcc(001) layers, A= 0.2338 $(n \geq 2)$ for fcc(00l) layers and 0.15 $(n \geq 3)$ for hcp (0001). The deviation is largest for the most open structure, a "bcc" film. On the other hand, susceptibility measurements[67] indicate that the discrete summation of point dipole fields may give questionable demagnetization factors. The classical continuous thin disk approach seems to agree better with the experiment, but a satisfactory conclusion has not been reached yet.

The shape anisotropy contributes in second order only. Some groups include the shape anisotropy in K_{2eff}, that is they use $K_{2eff} = K_2 - \frac{1}{2}\mu_0 M^2 + 2K_2^S/d$. In our work the shape anisotropy is always subtracted, before the intrinsic (spin-orbit) anisotropy (K_2 or K_4) is discussed.

The dipolar anisotropy of the outer layers was calculated[68] to be lower than the one of the inner layers. However, this interface contribution of dipolar origin is negligible in comparison to spin-orbit induced effects discussed below. Roughness of the surface or interface changes the effective dipolar contribution considerably. Bruno[54] calculates a dipolar roughness contribution ΔF_d which is positive (favoring perpendicular magnetization) and decreases effectively as 1/d. The degree of roughness is defined by two statistical parameters, the amplitude, which is the mean square deviation from the ideally flat surface and the correlation length ξ, i.e. the average lateral size of terraces. In the case of a Co film with $\xi \cong 200$ Å and $\sigma \cong 3$Å Bruno obtains a value of $\approx 0.03\ erg/cm^2$ (10 μeV/ML-atom).

The energetic balance of all the anisotropy energies due to spin-orbit effects and dipole-dipole coupling determine the easy axis of magnetization. While the dipolar interaction favors always an easy in-plane axis in monolayers the intrinsic spin-orbit related anisotropy may favor either in-plane or out-of-plane orientations. It has been summarized in several reports (see for example ref. 6) that the thickness dependent interplay of volume, surface, and roughness contributions can cause the reorientation of the easy axis as a function of film thickness as schematically shown in figure 12.

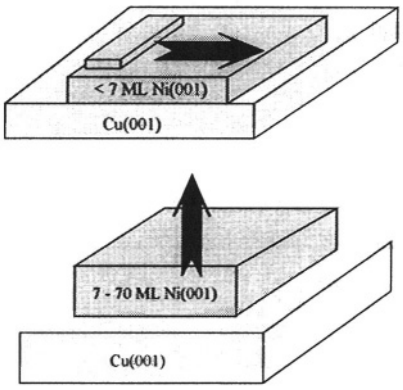

Figure 12. Schematic representation of the easy axis of the magnetization in Ni films on Cu(001). Due to the negative sign of the surface anisotropy the easy axis is in the film plane for films thinner than 7-9 ML. In thicker films the positive volume anisotropy dominates and the easy axis is perpendicular. Note, that in Fe and Co layers one finds for thinner films the perpendicular easy axis and for thicker ones the in-plane easy axis. Gas adsorption can severely influence the reorientation transition.[69]

5. TEMPERATURE DEPENDENT PHENOMENA

In the discussion of temperature dependent phenomena in magnetism one has to distinguish macroscopically observable quantities like the magnetization and magnetic anisotropy energy density from microscopic quantities like the magnetic moment per atom and the anisotropy of the orbital magnetic moment. Let's start the discussion with the macroscopically measured quantities, that is the magnetization and the magnetic anisotropy energy.

The remanent magnetization M_r, which is defined as the magnetization measured in zero external magnetic field, is given by the sum of all magnetic moments in the sample.[70] In general, it decreases with increasing temperature according to Bloch's $T^{3/2}$ law. This law arises from the excitation of spin waves. These small angle deviations cost less exchange energy than flipping an individual magnetic moment. Above the Curie temperature T_C the magnetic moments fluctuate so quickly that no remanent magnetization is present above T_C. Nevertheless the magnetic moment per atom persists as experimental data for the temperature dependent susceptibility show, which follows the well – known Curie Weiss law for all the ferromagnets – also the itinerant ones. The later fact is often forgotten, when the temperature dependence of itinerant ferromagnetism is discussed. In itinerant ferromagnets like Ni the conduction-band electrons which carry the resulting magnetic moment per atom can be divided into two "classes" below $T_C = 631$ K: "spin-up" electrons, which have their magnetic moment aligned parallel to the given magnetization direction, and "spin-down" electrons with their magnetic moment antiparallel. Due to the exchange interaction the kinetic energy of the "spin-up" electrons is raised with respect to the "spin-down" electrons. This results in an exchange split band structure. The exchange splitting $\Delta E_{ex}(E,\mathbf{k},T)$ depends on the energy, wave vector and the temperature. In the case of Ni the contributing electronic bands, the 3d and hybriddized 4sp states, are split by 275 ±20 meV and 204 ±8 meV at room temperature (roughly $0.5\ T/T_C$).[71]

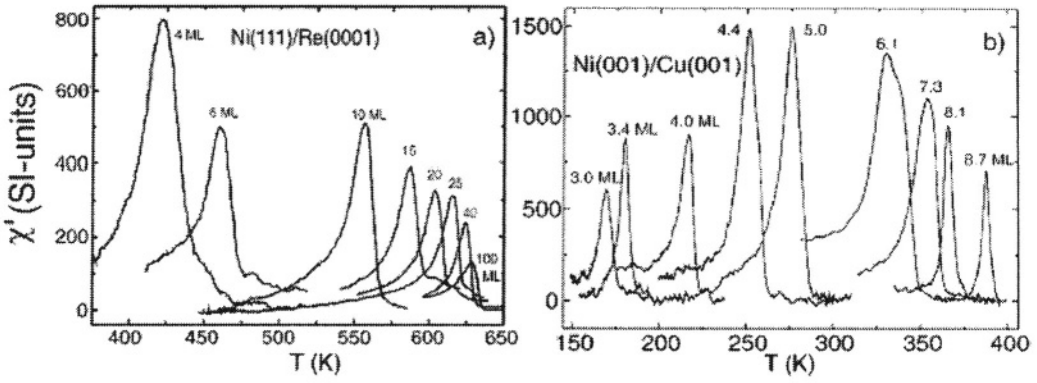

Figure 13. ac-susceptibility (in-phase signal) as a function of temperature for different thicknesses of a) Ni/Re(0001) and b) Ni/Cu(001). The peaks indicate the Curie temperature, which depends on the film thickness. From ref. 9.

The magnetic moment per atom and the orbital moment anisotropy are *not* a function of the temperature. It is defined by Eq. (2) and exists in the magnetically ordered and in the paramagnetic state which sometimes is called "non-magnetic". This is immediately verified when one measures the Curie-Weiss law.

In general, the thermodynamically relevant temperature parameter is the "reduced temperature" T/T_C. Especially in low-dimensional systems magnetic quantities like the magnetization and magnetic anisotropy must be compared at the same reduced temperature. The Curie temperature as a function of film thickness must be known. One of the best techniques to determine T_C is the measurement of the initial susceptibility which diverges at T_C yielding in principle infinite sensitivity. An example of in-situ UHV measurements by K. Baberschke[9] and coworkers[72] is shown in Figure 13. The in-phase signal of a mutual inductance bridge measurement is recorded as a function of temperature for different films, One observes the classical Curie-Weiss susceptibility which diverges at T_C. Below T_C the signal decreases again, since the small oscillating field (mG) which is applied in the measurement is not large enough to overcome the coercive field in the ferromagnetic state. To be more accurate one should remember that the experimentally detected susceptibility is not the true initial susceptibility. Demagnetization effects have to be taken into account. As a rule of thumb one can note that the calibrated amplitude of the ac-signal is inversely proportional to the demagnetization factor of the thin film. In other words this technique is capable of distinguishing changes of the demagnetization factor on the order of 10^{-4} quite easily.

The conventional method to determine T_C is the detection of the remanent magnetization which vanishes at T_C by torque or Kerr magnetometry in UHV. However, care must be taken not to mistake the vanishing of the remanent magnetization M, due to the formation of domains for the Curie temperature.[74,75] In Figure 14 T_C is shown for different Ni films as a function of film thickness d. The T_C of the (111) oriented films is much larger than the one of the (100) oriented film. This shows that the coordination number or in other words the missing nearest neighbors on the vacuum and interface sides – 4 for (001) and 3 for (111) – out of 12 in the bulk is a dominating factor for T_C.

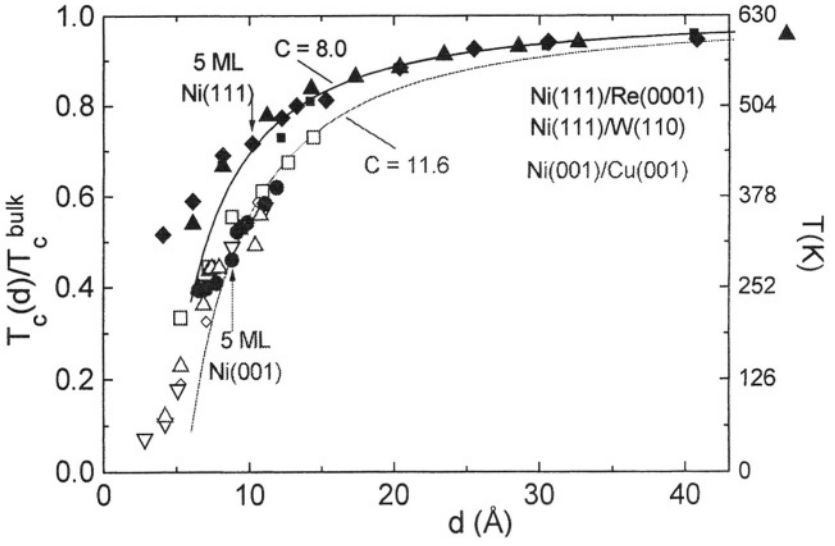

Figure 14. The Curie temperature as a function of film thickness for Ni films of different crystallographic orientations on different substrates.[73] One should note that the plane spacings in <111> and <100> orientation are different, yielding a slightly different number of atomic layers for the same thickness in Å.

The solid lines represent best fits according to 3D finite-size scaling. Deviation from the expected theoretical behavior below 5 ML indicate the onset of two-dimensional behavior for which 3D finite-size scaling is not valid anymore.

The other temperature dependent quantity is the magnetic anisotropy. It has been demonstrated and discussed in detail in refs. 6,9,73 that a thickness dependent analysis in terms of volume and surface anisotropies requires measurements at the same reduced temperature. Since T_C varies strongly in the ultrathin film limit, these types of measurements can be quite tedious.

6. CONCLUSION

Magnetic monolayers offer a huge playground for the basic understanding of magnetic interactions. To obtain reliable data it is all-important to consider the temperature and thickness dependence of the magnetic quantities which are investigated. Magnetic monolayers –when prepared under proper conditions– are magnetically alive! There are no non-magnetic monolayers. The experiment has to be capable of detecting the remanent magnetic state of low dimensional systems in situ in UHV at low temperatures which remains a challenging task.

7. ACKNOWLEDGEMENT

The fruitful cooperation and many discussions with K. Baberschke, his group and so many other colleagues working in the field of thin film magnetism is thankfully acknowledged.

7. REFERENCES

1. J. A. C. Bland, B. Heinrich (eds.), *Ultrathin magnetic structures* I & II (Springer Verlag, Berlin Heidelberg, 1994).
2. H.-J. Elmers, Ferromagnetic monolayers, *Int. J. Mod. Phys.* B **9**, 3115-3180 (1995).
3. U. Gradmann, Magnetism in ultrathin transition metal films, in: *Handbook of Magnetic Materials, Vol.7 (Elsevier Science Publishers B. V., 1993)* pp. 1-96.
4. D. Sander, The correlation between mechanical stress and magnetic anisotropy in ultrathin films, *Rep. Prog. Phys.* **62**, 1-50(1999).
5. C. M. Schneider and J. Kirschner, Magnetism at surfaces and in ultrathin films, in *Handbook of Surface Science, Vol. 2 (Elsevier Science B. V., 2000)* pp. 511 -668.
6. M. Farle, Ferromagnetic resonance of ultrathin metallic layers, *Rep. Prog. Phys.* **61**, 755-826 (1998).
7. B. Hillebrands, Brillouin light scattering from layered magnetic structures, in *Topics in Applied Physics, Vol. 75 (Springer-Verlag Berlin Heidelberg 2000)* pp. 175 – 289.
8. K. De'Bell, A. B. Maclsaac, and J. P. Whitehead, Dipolar effects in magnetic thin films and quasi-two-dimensional systems, *Rev. Mod. Phys.* **72**, 225 -257 (2000).
9. P Poulopoulos and K Baberschke, Magnetism in thin films, J. *Phys.: Condens. Matter* **11**, 9495–9515 (1999).
10. J. Nogués and I. K. Schuller, Exchange bias, *J. Magn. Magn. Mater.* **192**, 203-232 (1999).
11. V. S. Speriosu, D. A. Herman, Jr., I. L. Sanders, and T. Yogi, Magnetic thin films in recording technology, *IBMJ. Res. Develop.* **44**, 186-204 (2000).
12. I. K. Schuller, S. Kim, and C. Leighton, Magnetic superlattices and multilayers, *J.Magn. Magn. Mater.* **200**, 571-582 (1999).
13. H. Brune, Microscopic view of epitaxial metal growth: nucleation and aggregation, *Surf. Sci.* Rep. **31**, 121-229 (1998).
14. B. A. Joyce, Molecular beam epitaxy, *Rep. Prog. Phys.* **48**, 1637-1697 (1985).
15. W. Weiss and W. Ranke, Surface chemistry and catalysis on well-defined epitaxial iron-oxide layers, *Progr. Surf. Sci.* **70**, 1-151 (2002).
16. J. A. Venables, G. D. T. Spiller, and M. Hanbucken, Nucleation and growth of thin films , *Rep. Prog. Phys.* **47**, 399-459 (1984).
17. P. Politi, G. Grenet, A. Marty, A. Ponchet and J. Villain, Instabilities in crystal growth by atomic or molecular beams, *Phys. Rep.* **324**, 271-404 (2000).
18. M. Bäumer and H.-J. Freund, Metal deposits on well-ordered oxide films, *Progr. Surf. Sci.* **61**, 127-198 (1999).
19. H. Ibach, The role of surface stress in reconstruction, epitaxial growth and stabilization of mesoscopic structures, *Surf. Sci. Rep.* **29**, 193-263 (1997), and Erratum *Surf. Sci. Rep.* **35**, 71-73 (1999).
20. P. Ohresser, J. Shen, J. Barthel, M. Zheng, Ch. V. Mohan, M. Klaua, and J. Kirschner, Growth, structure, and magnetism of fcc Fe ultrathin films on Cu(l 11) by pulsed laser deposition, *Phys. Rev. B 59* 3696-3706 (1999).
21. H. Fritzsche, J. Kohlhepp, and U. Gradmann, Epitaxial strain and magnetic anisotropy in ultrathin Co films on W(110),phys. *Rev. B 51,* 15933-15941 (1995).
22. E. Bauer, Low energy electron microscopy, *Rep. Prog. Phys.* **57**, 895 – 938 (1994).
23. A. Ney, P. Poulopoulos, and K. Baberschke, Surface and interface magnetic moments of Co/Cu(001), *Europhys. Lett.* **54**, 820-825 (2001).
24. One might argue that conversion Mössbauer spectroscopy is the answer to this challenge, since it allows the selective positioning of radioactive atoms at the interface, interior, or surface. However, the technique measures the hyperfine field which is no correlated with the magnetic moment in a simple way.
25. Various techniques measure only a quantity proportional to the magnetization such as the magnetooptic Kerr effect (MOKE).
26. H. Fritzsche, H. J. Elmers, and U. Gradmann, Magnetic anisotropies of Fe(110) interfaces, *J. Magn. Magn. Mater.* **135**, 343-354 (1994); H. J. Elmers and U. Gradmann, Magnetic anisotropies in iron(110) films on tungsten(110), *Appl. Phys. A: Solids Surf.* **51,** 255-263 (1990).
27. K. Wagner, N. Weber, H. J. Elmers, and U, Gradmann, Magnetization of free Fe(110) surfaces from thin film magnetometry, *J. Magn. Magn. Mater.* **167**, 21-26(1997).
28. C. Turtur and G. Bayreuther, Magnetic moments in ultrathin Cr. films on Fe (100) *Phys. Rev. Lett.* **72**, 1557-1560 (1994); P. J. Flanders, An alternating gradient magnetometer, *J. Appl. Phys.* **63**, 3940-3945 (1988).

29 P. Srivastava, F. Wilhelm, A. Ney, M. Farle, H. Wende, N. Haack, G. Ceballos, and K. Baberschke, Magnetic moments and Curie temperatures on Ni and Co thin films and coupled trilayers, *Phys, Rev. B* **58**, 5701-5706(1998).

30 C.T. Chen, Y.U. Idzerda, H.-J. Lin, N.V. Smith, G. Meigs, E. Chaban, G.H. Ho, E. Pellegrin, and F. Sette, Experimental confirmation of the X-ray magnetic circular dichroism sum rules for iron and cobalt, *Phys. Rev. Lett.* **75**, 152-155(1995).

31. K. Nawrath, H. Fritzsche, F. Klose, J. Nowikow, and H. Maletta, In situ magnetometry with polarized neutrons on thin magnetic films, *Phys. Rev. B* **60**, 9525-9531 (1999).

32. One should note that in-situ susceptibility measurements near the Curie temperature are available and have been discussed by K. Babersche, The magnetism of Nickel monolayers, *Appl. Phys. A* **62,** 417-427 (1996).

33. A. Ney, P. Poulopoulos, M. Farle, and K.Baberschke, Absolute determination of Co magnetic moments: ultrahigh-vacuum high-Tc SQUID magnetometry, *Phys. Rev. B* **62,** 11336-11339 (2000).

34. B. T. Thole, P. Carra, F. Sette, and G. van der Laan, X-ray circular dichroism as a probe of orbital magnetization, *Phys. Rev. Lett.* **68**, 1943-1946 (1992).

35. P. Carra, B. T. Thole, M. Altarelli, and X. Wang, X-ray circular dichroism and local magnetic fields, *Phys. Rev. Lett.* **70**, 694-697 (1993).

36. C. Binns, K. W. Edmonds, S. H. Baker, M. J. Maher, S. C. Thornton, O. Tjernberg, and N. B. Brookes, Magnetism in nanoscale Fe clusters studied by dichroism in x-ray absorption and photoemission, *Lecture Notes in Physics* **565**, 355-360 (Springer 2001).

37. G. A. Held, M. G. Samant, J. Stöhr, S. S. P. Parkin, B. D. Hermsmeier, M. van Schilfgaarde, and R. Nakajima, X-ray magnetic circular dichroism study of the induced spin polarization of Cu in Co/Cu and Fe/Cu multilayers, Z *Phys. B* **100,** 335–341 (1996).

38. F. Wilhelm, P. Poulopoulos, G. Ceballos, H. Wende, K. Baberschke, P. Srivastava, D. Benea, H. Ebert, M. Angelakeris, N. K. Flevaris, D. Niarchos, A. Rogalev, and N. B. Brookes, Layer-resolved magnetic moments in Ni/Pt multilayers, *Phys. Rev. Lett.* **85,**413-416 (2000).

39. F. Wilhelm, P. Poulopoulos, H. Wende, A. Scherz, K. Baberschke, M. Angelakeris, N. K. Flevaris, and A. Rogalev, Systematics of the induced magnetic moments in *5d* layers and the violation of the third Hund's rule, *Phys. Rev. Lett.* **87**, 207202/1-207202/4 (2001).

40. M. Tischer, O. Hjortstam, D. Arvanitis, J. Hunter Dunn, F. May, K. Baberschke, J. Trygg, J. M. Wills, B. Johansson, and O. Eriksson , Enhancement of orbital magnetism at surfaces: Co on Cu(l00), *Phys. Rev. Lett.* **75,** 1602-1605 (1995), erratum: *Phys. Rev. Lett.* **76**, 1403 (1996).

41. R. Pentcheva and M. Scheffler, Initial adsorption of Co on Cu(001): A first-principles investigation, *Phys. Rev. B* **65,** 155418 (2002); F. Nouvertné, U. May, M. Bamming, A. Rampe, U. Korte, G. Güntherodt, R. Pentcheva, and M. Scheffler, Atomic exchange processes and bimodal initial growth of Co/Cu(001) *Phys. Rev. B* **60,** 14382-14386(1999).

42. D. P. Pappas, G. A. Prinz, and M. B. Ketchen, Superconducting quantum interference device magnetometry during ultrahigh vacuum growth, *Appl. Phys. Lett.* **65**, 3401-3403 (1994).

43. M. B. Stearns, in *Magnetic Properties of Metals,* Landolt-Bornstein, New Series, Group III, Vol. 19, Pt. a ~Springer, Berlin, 1986, pp. 37, 53.

44. A. Ney, K. Lenz, P. Poulopoulos, and K. Baberschke, Absolute magnetometry on ultrathin 3d-metal films by UHV-SQUID, *J. Magn. Magn. Mater.* **240**, 343 -345 (2002).

45. A. E. Garcia, V. Gonzáles-Robles, and R. Baquero, Ferromagnetism in 4*d* (Tc, Ru, Rh, Pd) and 5*d* (Ir, Pt) transition-metal monolayers on a Cu(00l) substrate, *Phys. Rev. B* **59,** 9392-9401 (1999).

46. R. Pfandzelter, G. Steierl, and C. Rau, Evidence for 4*d* ferromagnetism in 2D systems: Ru monolayers on C(0001) substrates, *Phys. Rev. Lett.* 74, 3467-3470 (1995).

47. H. P. J. Wijn, Magnetic Properties of Metals,Subvolume a: 3d, 4d and 5d Elements, Alloys and Compounds, Landolt-Börnstein, Vol III/19a, (Springer, Berlin, Heidelberg, 1986).

48. K. Baberschke, Anisotropy in magnetism, *Lecture Notes in Physics* **580**, pp. 27-45 (Springer Verlag, 2001).

49. H.-E. Nigh, S. Legvold, and F.-H. Spedding, Magnetization and electrical resistivity of gadolinium single crystals, *Phys. Rev.* **132** , 1092-1097 (1963).

50. B. Coqblin, *The Electronic Structure of Rare-Earth Metals and Alloys: the Magnetic Heavy Rare-Earths* (Academic, London, 1977).

51. S.-V. Vonsovskii, *Magnetism* (John Wiley & Sons, New York, 1974).

52. W.-P. Mason, Derivation of magnetostriction and anisotropic energies for hexagonal, tetragonal, and orthorombic crystals, *Phys. Rev.* **96,** 302-310 (1954).

53. R. M. Bozorth, Magnetostriction and crystal anisotropy of single crystals of hexagonal cobalt, *Phys.Rev.* **96** 311-316 (1954).

54. P. Bruno, Tight-binding approach to the orbital magnetic moment and magnetocrystalline anisotropy of transition-metal monolayers *Phys. Rev. B* **39,** 865 (1989).

55. O. Hjorstam, K. Baberschke, J. M. Wills, B. Johanson, and O. Eriksson, Magnetic anisotropy and magnetostriction in tetragonal and cubic Ni, *Phys. Rev.* ***B*** **55**, 15026-15032 (1997).
56. L. Néel, Aniotropie de la surface *J. Phys. Rad.* **15**, 225 and 376 (1954).
57. U. Gradmann, T. Dürkop, and H. J. Elmers, Magnetic moments and anisotropies in smooth and rough surfaces and interfaces, *J. Magn. Magn. Mater.* **165**, 56-61 (1997).
58. P. Krams, B. Hillebrands, G. Güntherodt, and H. P. Oepen, Magnetic anisotropies of ultrathin Co films on Cu(1113) substrates, *Phys. Rev. B* **49**, 3633-3636 (1994).
59. M. T. Johnson, P. J. H. Bloemen, F. J. A. den Broeder, and J. J. de Vries, Magnetic anisotropy in metallic multilayers, *Rep. Prog. Phys.* **59**, 1409-1458 (1996).
60. M. Farle, W. Platow, E. Kosubek, and K, Baberschke, Magnetic anisotropy of Co/Cu(111) ultrathin films, *Surf. Sci.* **439** (1999) 146-152.
61. U. Bovensiepen, Hyuk J. Choi, and Z. Q. Qui, Step-induced magnetic anisotropy in vicinal Ni/Cu(001) and its effect on the spin-reorientation transition, *Phys. Rev. B* **61**, 3235-3238 (2000).
62. R. K. Kawakami, E. J. Escorcia-Aparicio, and Z. Q. Qiu, Symmetry-induced magnetic anisotropy in Fe films grown on stepped Ag(001), *Phys. Rev. Lett* **77** 2570-2573 (1996).
63. J. Chen, and J. L. Erskine, Surface-step-induced magnetic anisotropy in thin epitaxial iron films on tungsten(001), *Phys. Rev. Lett.* **68**, 1212-1215 (1992).
64. P. Bruno, Magnetic surface anisotropy of cobalt and surface roughness effects within Neel's model, *J. Phys. F* **18**, 1291-1298 (1988).
65. H. Fritsche, J. Kohlhepp, H. J. Elmers, and U. Gradmann, Angular dependence of perpendicular magnetic surface anisotropy and the spin-reorientation transition, *Phys. Rev.* B 49, 15665-15668 (1994).
66. D. P. Pappas, Temperature dependent magnetic surface anisotropy in ultrathin Fe films, *J. Vac. Sci. Technol. B* **14**, 3203-3206 (1996).
67. A. Aspelmeier, M. Tischer, M. Farle, M. Russo, K. Baberschke, and D. Arvanitis, ac susceptibility measurements of magnetic monolayers: MCXD, MOKE, and mutual inductance, *J. Magn. Magn. Mater.* **146**, 256-266 (1995), and references therein.
68. H. J. G. Draaisma and W. J. M. de Jonge, Surface and volume anisotropy from dipole-dipole interactions in ultrathin ferromagnetic films, *J. Appl. Phys.* **64** 3610-3613 (1988).
69. R. Vollmer, Th. Gutjahr-Löser, J. Kirschner, S. van Dijken, and B. Poelsema, Spin-reorientation transition in Ni films on Cu(001): The influence of H_2 adsorption, *Phys. Rev. B* **60**, 6277-6280 (1999).
70. This statement is correct, if the sample is in a single domain magnetic state. In the experiment, domain formation may reduce M_r artificially.
71. T. J. Kreutz, T. Greber, P. Aebi, and J. Osterwalder, Temperature dependent electronic structure of Nickel metal, *Phys. Rev. B* **58**, 1300 – 1317 (1998).
72. U. Bovensiepen, C. Rüdt, P. Poulopoulos, and K. Baberschke, AC-susceptibility of Ni/W(110) ultrathin magnetic films: determination of the Curie temperature and critical behaviour, *J. Magn. Magn. Mater.* **231**, 65-73 (2001).
73. K. Baberschke, The magnetism of nickel monolayers, *Appl. Phys. A* **62**, 417-427 (1996).
74. J. Kohlhepp, H. J. Elmers, S. Cordes, and U. Gradmann, Power laws of magnetization in ferromagnetic monolayers and the two-dimensional Ising model, *Phys. Rev. B* **45**, 12 287-12 291 (1992).
75. P. Poulopoulos, M. Farle, U. Bovensiepen, and K. Baberschke, Evidence for domain formation near the Curie temperature in ultrathin Ni/Cu (001) films with perpendicular anisotropy, *Phys. Rev. B* **55**, R1 1961-R11964 (1997).
76. The x-ray magnetic circular dichroism data shown here are the ones from ref. 29 when all types of contributions to the magnetic moment, i.e. m_S, m_L, and the dipolarer Term $\langle T_z \rangle$, and sp are included.
77. L. Szunyogh , B. Ujfalussy, C. Blaas ,U. Pustogowa ,C. Sommers,,P. Weinberger, Oscillatory behavior of the magnetic anisotropy energy in $Cu(100)/Co_n$ multilayer systems, *Phys. Rev. B 56, 14036–14044 (1997)*
78. R. M. Moon, Distribution of Magnetic Moment in Hexagonal Cobalt, *Phys. Rev. 136, A195–A202 (1964)*

18
THREE-DIMENSIONAL PHOTONIC CRYSTALS MADE FROM COLLOIDS

Arnout Imhof*

1. INTRODUCTION

One of the most fascinating properties of monodisperse colloids is that they can form ordered phases. These phases can be thermodynamically stable if the volume fraction of particles is high enough, or they can form under the influence of an external field such as gravity or an electric field. The particles are small enough to exhibit Brownian motion, which causes them to move around randomly until the collective has found a state of minimal free energy. In a colloidal crystal the (almost always spherical) particles stack regularly to form a long-range, three-dimensional array. Particles shaped like rods or plates form additional liquid crystalline phases with nematic or smectic order. The spontaneous formation of such phases is nowadays often called self-assembly or self-organization. Colloidal crystallization has been studied intensively ever since the time that methods became available to synthesize sufficiently monodisperse colloids, i.e. those with particles having sizes that are uniform to better than about 8%.[1-3] Apart from being interesting for their statistical mechanical behaviour colloidal crystals have special and useful optical properties.

The best-known colloidal crystal with special optical properties is almost certainly the opal. It consists of a three-dimensional array of submicrometer silica spheres, which must have formed naturally in a sediment and then cemented together.[4-6] Visible light diffracts from the lattice planes, just like Bragg diffraction of X-rays from molecular crystals. The result is a beautiful iridescence, earning opals the qualification gemstones. Opals can also be made artificially by sedimenting monodisperse silica spheres in the laboratory, after which they are dried and sintered together.

Diffraction by colloidal crystals has also been recognized as a useful optical property. Thus, Asher and co-workers have put these crystals to use as narrow-band filters, that efficiently reject Rayleigh scattered incident light in Raman spectroscopy,[7] as nanosecond optical switches,[8] and as chemical sensors.[9]

In an independent development certain periodic dielectric structures have been proposed as materials which would not permit the propagation of electromagnetic waves

* Arnout Imhof, Debye Institute, Utrecht University, Postbus 80000, 3508 TA Utrecht, The Netherlands.

in a range of frequencies called the photonic band gap.[10,11] In this respect they are to light what semiconductors are to electrons. Such materials are called photonic crystals. Photonic crystals would inhibit spontaneous emission by excited atoms or molecules embedded inside and would localize light to a small volume around impurities. The first photonic crystal was made by Yablonovitch by drilling three sets of cylindrical holes in a block of dielectric in a periodic arrangement.[12] The periodicity was on the order of a millimeter so that the photonic band gap appeared at microwave frequencies.

Photonic crystals offer unique ways to control the propagation of electromagnetic waves.[13] Crystals possessing a band gap will behave like semiconductors for light, offering the possibility that light may be manipulated in ways similar to the way electrons are controlled by semiconductors. If light is forbidden to propagate through the crystal it would remain trapped at defect sites. Such a defect can be shaped in the form of a tiny cavity or as a sharply-curved waveguide, allowing one to manipulate light in ways that have not been possible before. Thus, photonic crystals have been proposed for a large number of applications such as efficient microwave antennas, zero-threshold lasers, low-loss resonators, optical switches, and miniature optoelectronic components such as microlasers and waveguides. The most useful applications would occur at near-infrared or visible wavelengths. This makes it necessary to fabricate photonic crystals with feature sizes of less than a micrometer. Furthermore, the refractive index contrast of the crystal must exceed 2 or 3, depending on the lattice, placing restrictions on the materials used.

A number of different methods is used for the fabrication of photonic crystals. Many of these apply a variety of lithographic techniques used in the semiconductor industry for patterning substrates such as silicon. Two-dimensional photonic crystals have been made this way, which operate at wavelengths down to the visible.[13] Good control over the introduction of defects has also been demonstrated. A number of attempts has been made to create three-dimensional photonic crystals using these techniques.[14-16] However, it has so far proved too difficult to achieve submicron periodicities of much more than one unit cell thickness.

On the other hand, colloidal particles naturally possess the desired sizes and can form periodic structures spontaneously. Moreover, the optical properties of the individual spheres can easily be tuned, or they can be used as templates to make inverted structures. Colloids have therefore been proposed as an easy and inexpensive way to fabricate three-dimensional photonic crystals, and as a suitable system in which to investigate their optical properties.[17,18] Until this realization colloidal crystals had been prepared with only a modest refractive index contrast, in order for them to remain relatively transparent and not opaque due to multiple scattering. They can thus be said to reject light propagating in certain directions, which satisfy the Bragg condition:

$$2d \sin\theta = m\lambda \,. \tag{1}$$

Here, λ is the wavelength of the light in the crystal, d the lattice spacing, θ the angle between the incident ray and the lattice planes, and the integer m is the order of the diffraction. If the dielectric contrast between the spheres and the suspending medium is made larger the range of angles for which waves of a given frequency diffract increases due to multiple scattering. At sufficiently high contrast and for certain crystal types propagation should become impossible in all directions and for both polarizations.

In this chapter, I will describe the fabrication and optical properties of photonic crystals. I will concentrate on the work using colloidal suspensions; however, not without making comparisons with other methods where necessary. Fabrication of photonic crystals is guided by numerical calculation of their optical properties. Therefore, I will start in section 2 with a description of the most important optical properties of photonic crystals, as well as the theories used to describe them and experimental techniques used to probe them. In section 3 methods for the fabrication of photonic crystals are discussed with an emphasis on methods using colloidal self-assembly. Section 4 describes recent work using composite colloids such as core-shell or metallo-dielectric particles.

2. OPTICAL PROPERTIES OF PHOTONIC CRYSTALS

Propagation of electromagnetic waves in periodic media displays many interesting and useful effects. It was already described in the theory of X-ray diffraction by solids in the early 20^{th} century by Ewald and von Laue, see e.g. refs. 19,20. Materials with a layered structure ('stratified media') are used as high reflectance dielectric mirrors,[21] but also as diffraction gratings, distributed feedback lasers, and acousto-optic filters. Materials with a periodicity in only one dimension are not usually called photonic crystals, nor is this the case for materials in which the variation in refractive index is very small, such as in X-ray diffraction where it is at most $\sim 10^{-4}$.

2.1. Propagation of Light in Photonic Crystals

Electromagnetic waves propagating in a photonic crystal experience a periodic variation of the refractive index. At every interface part of the incident wave is reflected (or scattered) and the rest is transmitted. Interference between reflected and transmitted waves determines the wave form in the crystal. This wave form has a periodicity corresponding to that of the crystal lattice and can be determined from the Maxwell equations. For a given angular frequency ω the solutions of the fields have a periodic wave form and are called Bloch modes:

$$\exp(i\mathbf{k}\cdot\mathbf{r})\mathbf{u}_{\mathbf{k}}(\mathbf{r}). \tag{2}$$

Here, $\mathbf{u}_{\mathbf{k}}(\mathbf{r})$ is a function with the same periodicity as the crystal. It is labeled with the Bloch wave vector $\mathbf{k}$, describing the period and direction of propagation of the wave. The frequencies of the allowed modes $\omega(\mathbf{k})$ form the so-called dispersion relation. There will in general be frequencies for which solutions exist only in some directions but not in others. These waves cannot propagate in the excluded directions. Physically, this means that destructive interference cancels the wave in those directions. Instead, the wave is reflected. This is analogous to Bragg diffraction as described by Eq. (1). There may even be one or more ranges of frequencies for which there exists no wave form for $\mathbf{k}$'s in any direction. Such waves are forbidden to propagate in the crystal. Their frequencies are said to be in the photonic band gap.

In Figure 1 the frequencies of the allowed modes are plotted versus wave vectors in the Brillouin zone of a face-centered cubic lattice of spheres consisting of air in a

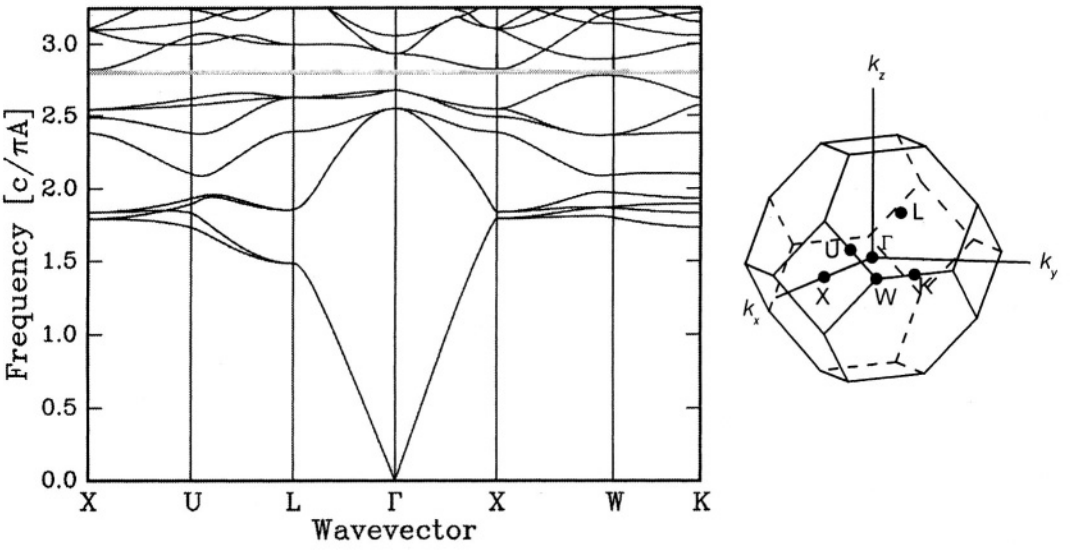

Figure 1. (a) Band structure of an 'inverse' fcc lattice of spheres of refractive index 1 in a background with index 3 calculated with the KKR method.[22] The horizontal gray band outlines the complete band gap. The letters indicate wave vectors corresponding to the special points of the fcc Brillouin zone shown in (b).

background material of refractive index 3. The allowed modes form the photonic band structure of this crystal. There is a narrow band gap at a frequency of $\nu = 2.8c/\pi A$, where c is the speed of light and A the size of the cubic unit cell. The 'inverted' crystal structure is shown here because the 'direct' structure, i.e. spheres of high refractive index in air, does not possess a band gap. If the refractive index contrast (the ratio of the refractive index of the spheres and their background) is increased the band gap widens. Below a contrast of 2.85 the gap is closed.[22]

The band gap in Figure 1 is located between the 8^{th} and 9^{th} bands. This corresponds to the region where, in weakly scattering crystals, the second order Bragg diffraction is located. The first order Bragg diffraction occurs at a lower frequency, around $\nu = 1.7c/\pi A$ for the direction corresponding to the L point. At this point the waves travel perpendicularly to the (111) planes of the crystal. There is a sizeable range of frequencies for which these waves cannot propagate in the crystal and thus are reflected. This frequency range is called a stopgap. Since propagation is still possible in other directions one usually speaks of a partial or incomplete band gap. If the direction is moved away from the L or X points the bands are seen to split in two. These are the different polarization states which are then no longer degenerate.

There is a close analogy with electron waves traveling in the periodic potential of atomic crystals. There, too, the allowed modes are arranged into energy bands separated by energy gaps. That is why much of the terminology in the photonic crystal literature is borrowed from solid state physics. There are also important differences, however, most importantly the fact that electrons are described by scalar wave fields, whereas electromagnetic waves are vectorial in nature, describing the two polarizations, which are not independent.

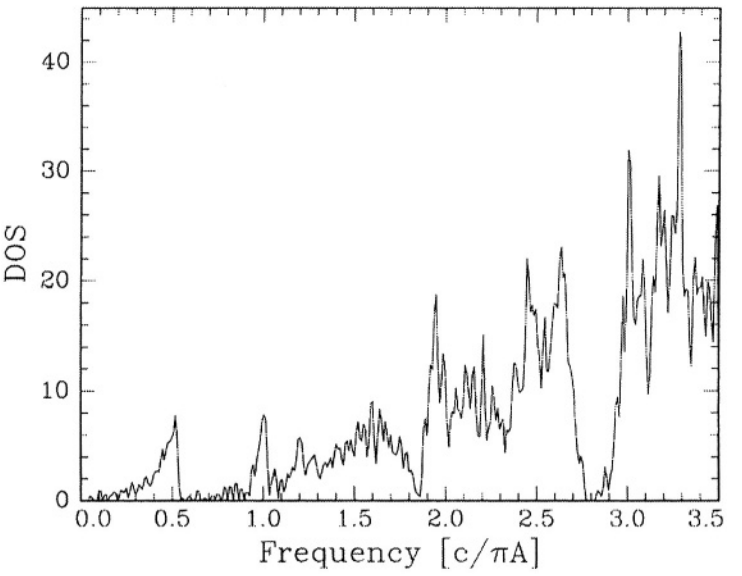

Figure 2. Photonic density of states of the inverse fcc crystal of Figure 1.

Due to the photonic band structure the number of allowed modes varies with frequency. This is described by the density of states (DOS), which is the number of photon modes per unit of frequency. This function is shown in Figure 2 for the fcc crystal of Figure 1. The DOS vanishes for frequencies in the photonic band gap. Around $\nu = 1.8c/\pi A$ the DOS is strongly depleted, but nonvanishing. This region is usually referred to as a pseudogap. The density of states is important for the emission of an excited atom or molecule, because the decay rate of the latter is proportional to the local density of states (LDOS). The LDOS depends strongly on the position within the unit cell.[23,24] In a complete photonic band gap the excited atom cannot decay radiatively, wherever it is sitting. Ideally, it will remain in its excited state until it decays nonradiatively.

Several techniques exist for calculating photonic band structures numerically. The most common method at the moment is the plane wave method (PWM).[25-27] In this method one of the fields, for example **H**, as well as the dielectric constant are expanded in plane waves:

$$\mathbf{H}(\mathbf{r}) = \sum_{\mathbf{G}} \mathbf{H}_{\mathbf{G}} e^{i(\mathbf{k}+\mathbf{G})\cdot\mathbf{r}}$$
$$\varepsilon^{-1}(\mathbf{r}) = \sum_{\mathbf{G}} \varepsilon_{\mathbf{G}}^{-1} e^{i\mathbf{G}\cdot\mathbf{r}} \qquad (3)$$

Here, the **G** run over all reciprocal lattice vectors. The expansions are then substituted into the Maxwell equations and a cutoff is made. Increasing the number of plane waves (i.e. the number of **G**'s) will yield an increasingly accurate band structure. Thus, it was shown that there is no complete band gap between the 2nd and 3rd bands for any fcc lattice of spheres. On the other hand, the diamond lattice, consisting of an fcc lattice with two spheres per unit cell, does have a complete band gap.[27] It occurs for the direct crystal structure at a refractive index contrast above 2.0. Some time later, however, it was shown

that also the fcc structure has a complete gap, but between the 8^{th} and 9^{th} bands and only for the inverted crystal.[28] This work also pointed out some convergence problems with the PWM and provided an extrapolation method to handle these problems. This has led to improvements in the accuracy of the calculated gap widths. An experimental problem of interest is to insert lattice defects into the crystal. These may lead to donor or acceptor states, or allow wave guiding. Numerical calculation of such defect structures is possible in the plane wave framework using the supercell method.[29,30]

For comparison with experiments a calculation is needed of the transmission or reflection spectrum of a finite-sized photonic crystal. These are not easily obtained with the PWM, which only yields the band structure of an infinite crystal. This problem can be circumvented using the transfer matrix method (TMM).[31,32] The system is then divided into small cells and the fields in each cell are related to those in the previous by a transfer matrix. On the incident side the fields are coupled to a set of plane waves. This method also uses less computer time and memory than the PWM, and can be applied more easily to crystals with defects or crystals in which the dielectric constant is frequency dependent or has an imaginary part.

Another efficient method is the photonic version of the Korringa-Kohn-Rostoker (KKR) method, which was originally developed to describe multiple scattering of electrons in crystals. The scattered field of individual scatterers is expanded in spherical harmonics and the band structure is obtained from a secular equation.[22,33] This method converges much more quickly than the PWM and can easily be used with frequency-dependent or complex dielectric constants. If transmission and reflection spectra of finite crystals are required then the scattering matrices of individual layers of scatterers are determined.[34-36] The method is then referred to as the layer KKR (or LKKR) method.

Finally, especially if the time dependence of the fields inside photonic crystals is of interest finite difference time domain (FDTD) techniques are often used.[37]

Two approximate theories must be also mentioned here, which are often used for comparison with experimental data because they yield simpler, analytical results. These are the dynamical diffraction theory (DDT) of X-ray diffraction,[19,20] which has been quite successful in describing optical diffraction by colloidal crystals.[38-40] The other is now called the scalar wave approximation (SWA), and similarly describes this diffraction well.[41,42] In essence, these two approximate theories are very similar. The starting points are the wave equation for the displacement field $\mathbf{D}$ in the DDT or the scalar wave equation for the electric field E in the SWA. In both cases the field in the crystal is expanded in plane waves, as in the PWM, but only the two strongest ones are kept (corresponding to the incident wave and a diffracted wave). Both theories perform reasonably well for wave vectors close to a reciprocal lattice point (where one diffracted wave is much stronger than the others) and become exact in the limit of small refractive index contrast. Experiments suggest that the SWA performs better for larger index contrast,[43] but it has the disadvantage that it cannot describe polarization effects unlike the DDT.[39,40,44] (For completeness it should be remarked that the name scalar wave approximation was originally used for the full plane wave method, but starting from the scalar wave equation.[45,46] These calculations were quickly superseded by the PWM starting from Maxwell's vector wave equation when it became clear that the former predicted the existence of complete band gaps, where in fact there were none due to the polarization of the field.)

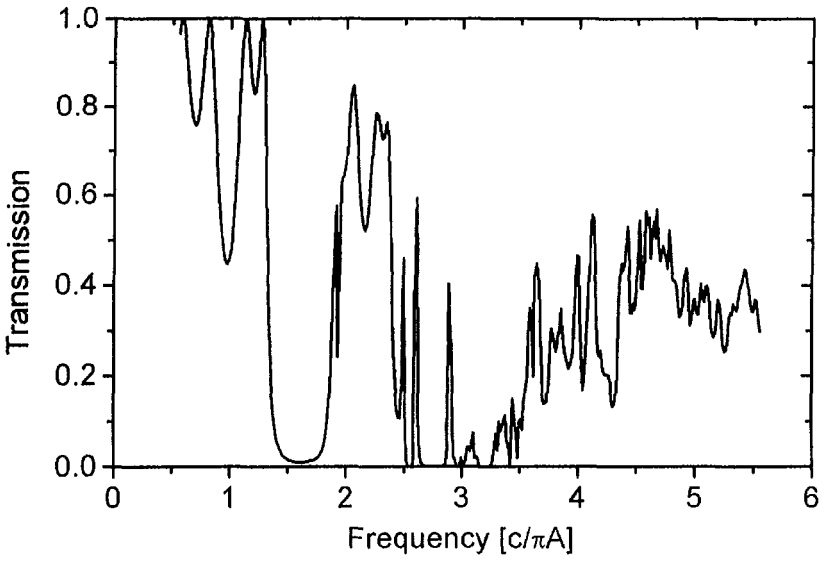

Figure 3. Transmission spectrum of a crystal of air spheres in a material with refractive index 3 calculated with the layer KKR method. The crystal is two unit cells thick and the transmission is measured perpendicular to the (111) planes, i.e. the direction of the L point.

2.2. Experimental Probes of Photonic Crystals

As mentioned above, an infinitely large, perfect photonic crystal would reflect 100% of the incident light at wavelengths in the band gap and would transmit 100% (apart from a few percent ordinary specular reflection) of the light at other wavelengths. At any given angle of incidence there will be such gaps. In the case of a complete band gap the reflected wavelength bands would overlap at every incident angle. This is the reason that one usually searches for photonic band gaps by measuring transmission of reflection spectra at varying angles of incidence. Ideally, the wavelengths at which the transmission goes from 0 to 1 or from 1 to 0 should correspond to the band edges. This approach was taken in the microwave experiments of Yablonovitch demonstrating that certain crystals made by drilling holes in a dielectric possessed a complete band gap.[12] Similar measurements of the positions and widths of optical stop gaps have become by far the most popular method in the literature.

In practice, however, a number of experimental complications arise. First of all, real photonic crystals are never perfect nor infinite. Due to their finiteness the transmission is rarely close to 0 or 1. In fact, numerical calculations of transmission and reflection spectra often show a lot of structure. This is seen in Figure 3. The extra structure arises when, the external wave is coupled to the internal wave using the proper boundary conditions. A considerable part of the wave may be reflected even outside a band gap. Conversely, the transmission inside a band gap does not always drop entirely to zero because, especially near the edges of the gap, the wave may decay with a characteristic length of many unit cells. (Because the wave vector becomes imaginary in the band gap the wave amplitude decays exponentially with distance.) Especially in thin crystals it may therefore not be easy to determine the band edges. This problem is made worse by a

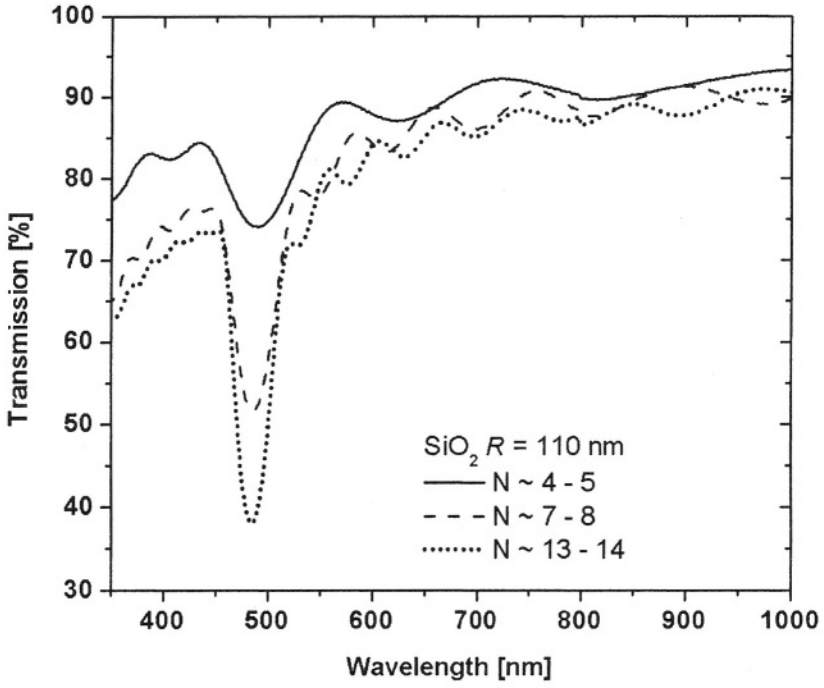

Figure 4. Transmission spectra of colloidal crystals of silica spheres (radius 110 nm) with different numbers of layers *N*. The crystals were prepared by controlled drying (section 3.4), courtesy of Krassimir Velikov.

certain degree of disorder or the presence of defects, which cause the dip in the transmission to broaden and its edges to become less well defined. Another, but related problem is polycrystallinity of the sample, which often occurs in self-assembled crystals. This will result in a large broadening of the transmitted and reflected bands, because changing the wavelength will successively probe different crystallites having different orientations. In all these cases, simply taking the full width at half maximum is therefore not necessarily the best way to proceed.

These difficulties should be minimized by making sure one is observing a single crystal with as few defects as possible. Polycrystallinity is not normally a problem in crystals made with lithographic techniques, but may be a limitation in self-assembled crystals. It has been shown that gap widths extracted from reflection spectra are much more reliable than those obtained from transmission spectra, because reflected light probes only a small number of lattice planes lying close to the surface[47] (thus containing fewer domains with fewer defects). One should therefore reduce the probe beam to a size smaller than a single crystalline domain. Reducing the beam size even further to much less than the domain size will further reduce the influence of defects and surface roughness. This was beautifully demonstrated in reflection and luminescence spectra measured with the use of an optical microscope.[48] Alternatively, polycrystallinity can be avoided by growing large single crystals, which are not too thick (see section 3.4), so that transmission spectra also produce accurate gap widths.[49,50] An example of a transmission measurement done on such a sample is shown in Figure 4. The transmission minimum becomes deeper and narrower as the number of layers is increased. The ripples are Fabry-

Perot fringes caused by interference of light reflected from the top and bottom surfaces of the crystal. The transmission of the crystals decreases gradually at shorter wavelengths due to diffuse scattering by defects.

In studying the band structure and determining the presence of a complete band gap by transmission/reflection measurements one needs to vary the angle of incident light in order to study all directions in the irreducible part of the Brillouin zone. Due to refraction at the crystal surface the direction of the wave inside the crystal will differ from that outside. Although often used, Snell's law is no longer adequate to convert external angles into internal ones, because the effective refractive index changes significantly close to a band gap. Instead, one should use the fact that the component of the wave vector parallel to the surface, $k_{\|} = (\omega / c) \sin \alpha$, is conserved.[21] It should be realized that this component is different for frequencies corresponding to the lower and upper band edge. In other words: at nonzero angle of incidence the transmission/reflection spectra probe varying crystal directions as a function of wavelength. Especially at higher order band gaps this complicates the interpretation.[51] A related difficulty is that, due to refraction, not all internal directions can be reached with an external beam. Moreover, some wave vectors are reflected by the crystal not because they are in a band gap but because they do not couple to an internal mode for symmetry reasons.[52,53] It is therefore necessary to prepare samples with different lattice planes exposed. Furthermore, complementary band structure calculations, as well as calculations of transmission or reflection spectra are required to confirm the presence of a band gap. This was recently performed with inverted silicon crystals, providing strong indications for the presence of a complete band gap around 1300 nm.[54]

A related technique to investigate photonic crystals is the use of Kossel lines,[55,56] which can be interpreted in terms of the band structure of colloidal crystals.[17,57,58] The crystal is illuminated with a laser beam resulting in dark rings on a diffusely lit background, both in reflection and transmission. The diffuse background originates from scattering by defects or, alternatively, from scattering by an external diffuser. In the directions of the stop gaps the scattered light is attenuated producing dark rings.

Although I have so far focused on transmission and reflection spectra, an alternative approach makes use of internal sources. These may be fluorescent dyes, luminescent ions, or quantum dots. The effect of the crystal upon their emission is twofold. First, emitted radiation is Bragg diffracted leading to a dip in the measured emission spectrum that depends on the direction of observation, similar to Kossel lines. This effect is present in every photonic crystal and does not require a high dielectric contrast. Second, the spontaneous emission rate can be modified if the photonic crystal alters the local photonic density of states. This effect has been one of the earliest promises of photonic crystals.[10] For an atom with a transition frequency in a complete photonic band gap the spontaneous emission should be inhibited and a quantum electrodynamic photon state bound to the atom is formed.[59,60] A reduction of the LDOS should be measurable as an increase in the radiative lifetime (in a time dependent measurement) or as an overall reduction of the total amount of emitted light (in a stationary state experiment). This effect is often regarded as one of the most important goals in photonic crystal research. Nevertheless, the filtering effect is still very useful as a probe to investigate the band structure of the crystal.[61-69]

It can be safely said that the distinction between the two effects of a photonic crystal on emission has not always been very clear in the literature so far. This has been caused in part by chemical effects of the environment of dye molecules on the radiative lifetime (for example when they are absorbed to particle surfaces). Secondly, the LDOS may already be modified strongly by a microcavity effect due to scattering resonances in microdroplets or colloidal spheres[70-73] or close to surfaces.[74,75] Although this is also a quantum electrodynamic effect it is not due to the photonic crystal. In colloidal crystals of polystyrene spheres suspended in water containing a dye a change in lifetime by a factor of 1.8 was found,[76] but it has been suggested that this could have been caused by chemical interactions and dye adsorption.[71,77,78] A change to nonexponential fluorescence decay has been observed in dye-doped polymer-filled opals.[79] In both these examples the density of states is expected to have changed only a few percent due to the low refractive index contrast.[80] Such a small change was demonstrated experimentally for silica spheres in which the dye had been incorporated deep inside the spheres to avoid chemical interactions with the solvent or particle surfaces.[81,82] A wavelength resolved demonstration of changes in lifetime as the wavelength is scanned through the band gap is still lacking. Instead of a change in lifetime one may also search for an overall reduction in emitted intensity due to a lower density of states and compare it to a suitable reference sample.[83-86] In three-dimensional titania "air-sphere" crystals, in which propagation of light is restricted to 45% of all available directions such inhibition of spontaneous emission was recently seen.[86]

Other optical probes of photonic band gaps rely on the fact that close to a band gap the photon dispersion relation ω vs. k deviates from linearity. This means that the refractive index $n=ck/\omega$ associated with a band becomes frequency dependent. This index change can be determined by measuring the phase change $\Delta\phi(\omega)$ of a transmitted laser beam in an interferometer as the frequency is tuned through the gap.[87,88] Close to the lower band edge the index decreases by an amount depending on the gap width, while it increases near the upper band edge. The dispersion relation can be determined from $k(\omega) = \omega / c + \Delta\phi / L$, where L is the sample thickness.

A stronger effect can be seen in the group velocity $v_g = d\omega / dk$ which vanishes at the edges of the Brillouin zone, where the bands are horizontal. Short laser pulses should thus slow down if their frequency is tuned to the band edges, an effect which was measured in colloidal crystals and artificial opals.[89,90] The effect on the travel time of a pulse is shown in Figure 5. The largest time delay corresponds to a pulse velocity of about 80% of that far from the gap. Such a pulse experiences an increased effective path length due to multiple reflections in the crystal. Because ultrashort laser pulses consist of a finite frequency bandwidth their different frequency components suffer different delays, resulting in a "chirped" pulse. Using ultrashort pulse interferometry the relative phase shift of these frequency components can be measured.[89] This is expressed in a quantity called the group velocity dispersion (GVD) $\beta_2 = d^2k / d\omega^2$, also shown in Figure 5. It is further seen that when such a measurement is done in reflection the GVD is near zero inside the gap, but very large just outside. Thus, the GVD naturally locates the edges of the stop gaps without further interpretation being necessary.

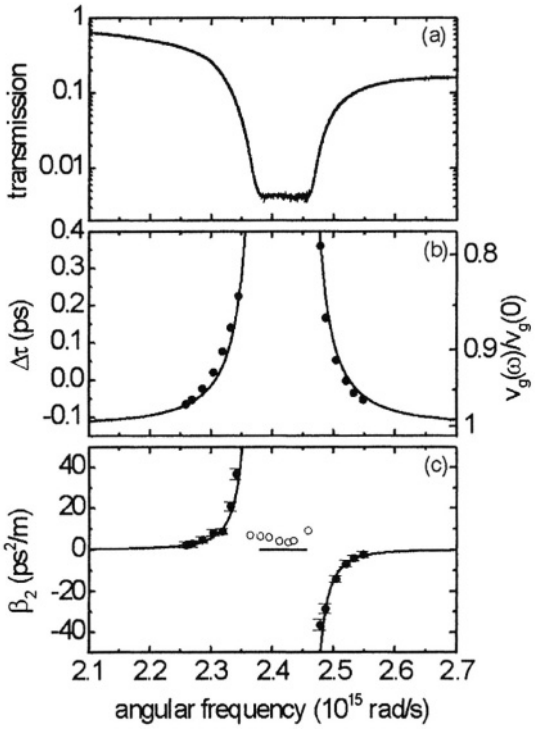

Figure 5. (a) Transmission spectrum of a colloidal crystal of polystyrene spheres in water. (b) Measured pulse delay times near the L gap versus angular frequency. The right axis shows the pulse velocity relative to the velocity away from the gap. (c) Measured group velocity dispersion. Solid symbols are transmission, open symbols reflection measurements. The lines in (b) and (c) are the dynamical diffraction theory.

3. FABRICATION OF PHOTONIC CRYSTALS

Numerical calculations have led to the identification of a number of three-dimensional crystal structures that should have a complete photonic band gap. Fabrication of these structures on a submicrometer length scale is still a challenge, especially because materials with a sufficiently high refractive index and negligible absorption have to be used. Suitable materials are often semiconductors such as TiO_2, Si, or GaAs. The structures must also have a very high porosity, typically containing ~80% air. A number of strategies has been developed. I will first briefly discuss nanofabrication techniques that use lithography and etching, or holography. Then, I will treat methods that use colloidal self-assembly to fabricate the desired structures, as well as templating methods to obtain inverse colloidal crystals. Then a number of methods will be described that use an external field or a surface template for directing self assembly to produce better ordered or more favorable structures. In the last subsection the effects of disorder and lattice defects will be discussed.

3.1. Nanofabrication

Compared to their success in the fabrication of two-dimensional photonic crystals modern semiconductor processing techniques have so far had relatively limited success in

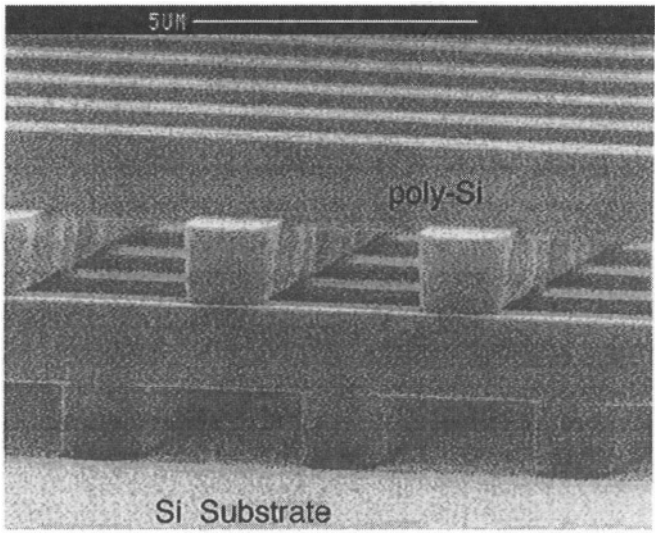

Figure 6. Scanning electron micrograph of the silicon woodpile structure. The width of the rods is 1.2 μm. Courtesy of Sandia National Laboratories. Reprinted by permission from Nature,[14] copyright (1998) Macmillan Publishers Ltd.

producing three-dimensional structures. A promising approach is the layer-by-layer preparation of the so-called woodpile structure (Figure 6), which is known to have a complete band gap.[91,92] Each layer consists of a number of parallel silicon rods with a square cross section. These are made by depositing a layer of SiO_2, etching out rectangular grooves and filling them with polycrystalline silicon. Then a subsequent layer is deposited and the process is repeated with the grooves rotated 90°. Finally, the SiO_2 is removed completely. While the original structures exhibited a band gap at a wavelength of about 11 μm,[14] sizes were later reduced to produce a band gap around 1.5 μm.[15] However, it is a very time-consuming method and has been carried out to only 5 layers, or 1.25 unit cells. Instead of depositing layers one by one it is also possible to fabricate this structure from III-V semiconductors by successively stacking and bonding patterned wafers after careful alignment.[16] This way the number of layers can be increased more quickly and a total of 8 layers has been achieved.

An alternative method is the use of chemically assisted ion beam etching to drill narrow channels into a GaAs or GaAsP wafer[93,94] in a manner similar to that used by Yablonovitch, but on a much smaller length scale. The depth reached was only 1.5 μm, or 4 crystal layers. Using focused-ion-beam etching the same structure with a band gap at 3 μm could be made in silicon up to a depth of 5 unit cells.[95]

Photo-assisted electrochemical etching of pre-patterned silicon has been used to produce a two-dimensional array of very deep (~100 μm) cylindrical holes.[96] By modulating the light intensity in time it is possible to induce a periodicity of up to 25 periods in the vertical direction.[97] So far, this periodicity is relatively large compared to that in the horizontal directions, so that the structure does not yet possess a complete photonic band gap.

A final method mentioned here uses three-dimensionally periodic patterns of light created by interfering up to four laser beams,[98,99] similar to holographic recording. The

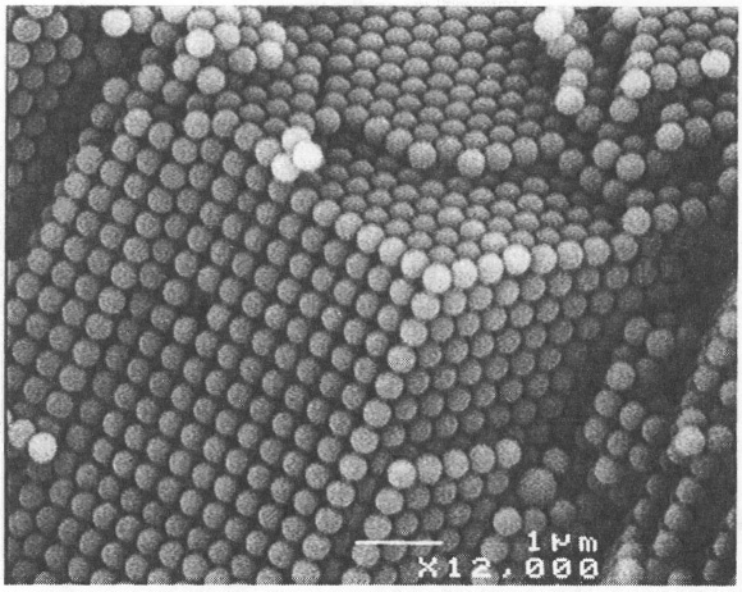

Figure 7. Scanning electron micrograph of a polystyrene colloidal crystal. Planes with hexagonal and square symmetry can be seen indicating that the lattice is fcc.

pattern is recorded in a film of photoresist. Unpolymerized resin is then removed by washing. The method is suitable for quickly producing large-area crystals with any desired structure, as long as the polymerized regions are interconnected. Absorption of the light by the photoresin limits the maximum thickness of the crystals to several tens of μm's, corresponding to several tens of lattice planes. Since photoresists have a relatively low refractive index additional steps (such as templating, section 3.3) must be used to increase the dielectric contrast.

3.2. Self-Assembly Methods

Monodisperse colloidal particles can spontaneously organize into three-dimensionally periodic crystals with a macroscopic size (Figure 7). Their lattice periodicity is easily adjusted from the nanometer to the micrometer range by varying the size of the particles. Colloidal crystals form spontaneously if there is a thermodynamic driving force, for example a sufficiently high particle concentration, making it favorable for the particles to order into a lattice, thus using the limited space more efficiently. When left undisturbed most colloidal particles settle to the bottom of their container where their concentration becomes high enough for crystallization. This process is sometimes accelerated by centrifugation or by filtration of the liquid through a porous membrane. Alternatively, ion exchange resin can be added to the suspensions to increase the range of repulsion between the particles, which leads to crystallization. Typical crystal sizes are from tens to thousands of micrometers. The crystal structure formed in most cases is face centered cubic (fcc), although low volume fraction body centered cubic (bcc) crystals form if the particles interact repulsively over distances much longer than their sizes.[100] Particles which interact nearly as hard spheres show a tendency to form randomly stacked hexagonal layers. In this structure the stacking order of the hexagonally

packed (111) planes is not ABCABC... as in fcc, nor ABAB... as in hcp, but close to random.[101,102]

Their self-organizing properties make spherical colloids suitable candidates for fabricating photonic crystals. There are only a few materials from which colloids can be made with sufficient monodispersity to crystallize, namely silica, ZnS, and a number of polymers, most notably polystyrene and polymethylmethacrylate. Colloidal crystals of most of these materials have a relatively modest refractive index contrast, even when dried. A lot of work has been done on the fabrication and photonic properties of both suspended and dried colloidal crystals, often called artificial opals, and even natural opals.[17,18,61,62,103-108] In this work, the influence of photonic band structures on diffraction was investigated, mostly using angle-dependent transmission and reflection measurements. The influence of the dielectric contrast was established by infiltrating the opals with various liquids or semiconductors (such as CdS or InP), and the sphere filling fraction was varied by gradual sintering of the spheres. The influence of sintering has also been investigated theoretically with the PWM[24] and the TMM.[109] As already discussed in section 2.2 self-assembled crystals have also been filled with luminescent materials in order to study their influence on emission.[61-69]

3.3. Colloidal Crystal Templating

Despite this progress the early calculations had already shown that the prevailing fcc structure possesses a complete photonic band gap only for the inverted crystal structure, in which the spheres have a lower index than their environment.[28] Furthermore, the refractive index contrast needs to be very large (>2.85). Although the diamond structure has a complete band gap for the direct crystal structure[27] it is never formed in colloidal self-assembly. More detailed calculations of the photonic properties of crystals formed by self-assembling systems determined that the optimal air filling fraction was around 80%,[24,110,111] but did not identify structures that are easier to fabricate. These facts quickly led to the development of chemical means by which the interstitial pores of a colloidal crystal can be filled with a high index solid, after which the colloidal particles can be removed.[112-118] These approaches are known collectively as templating methods. In that way, the air filling fraction of such an "inverse opal" is automatically close to the maximum sphere packing fraction of 74% and a larger variety of materials can be used. A general schematic of colloidal crystal templating is shown in Figure 8. First, a colloidal crystal is assembled from a monodisperse colloid. Then the fluid in the interstitial pores is either gelled directly through a sol-gel process or by a polymerization reaction, or it is removed first by drying and then replaced by infiltration of the pores with a solid or a solidifying liquid. In the third step the colloidal template is removed from its solidified environment by dissolution, evaporation, or firing at temperatures of up to 400 °C. This final step often also involves calcination of the material at elevated temperatures in order for the resulting porous framework to densify and crystallize. The uncalcined material is often amorphous and contains micro- and mesopores that lower its refractive index. Calcination frequently results in shrinkage of the porous material by up to 20%. Examples of some resulting materials are shown in Figure 9.

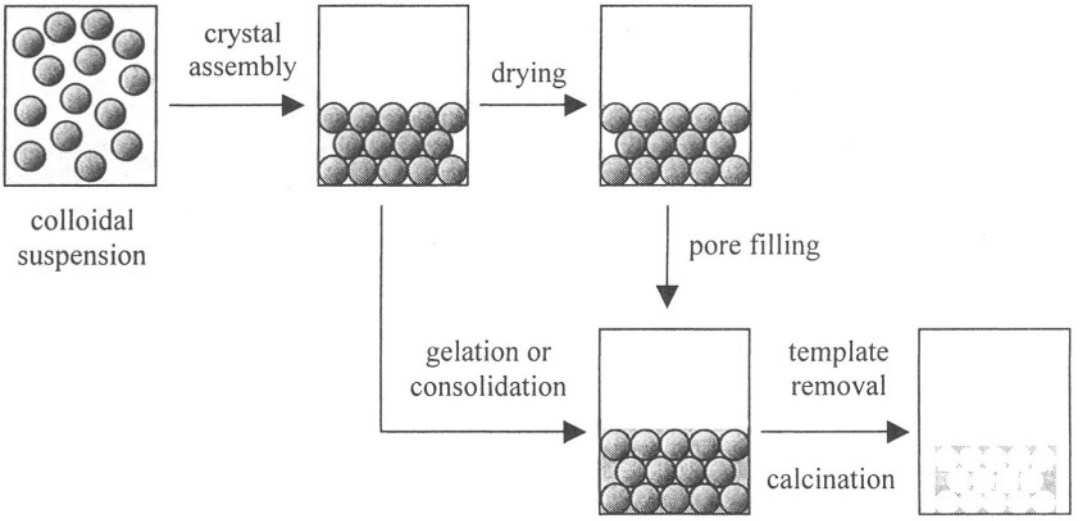

Figure 8. Schematic of colloidal crystal templating.

They form a faithful replica of the original colloidal crystal, including lattice defects such as vacancies. The spherical voids left behind by the spheres are usually connected by windows where the spheres touched, allowing material to be transported during template removal.

The initial templating methods used emulsion droplets[112] or polystyrene spheres[114,116,118] as the colloidal template, and sol-gel chemistry to fill the interstitial space. Using emulsion droplets ordered porous materials of titania (TiO_2), zirconia (ZrO_2), silica, and polyacrylamide were made.[112,113] The emulsion oil droplets are not easy to make monodisperse, but they are easy to remove by dissolution or evaporation. A calcination step then converted the titania gel into the desirable high refractive index titania phases anatase (n=2.5, above 400°C) or rutile (n=2.8, above 900°C).[120] In independent work polystyrene latex spheres and a sol-gel reaction were used to produce inverted crystals of amorphous silica.[114, 115] Because polystyrene spheres are easy to obtain with high monodispersity and because they self-assemble with great ease they have been used in many subsequent templating studies.[116,117,121-124] These particles are removed either by calcination or by dissolution in, for example, toluene. Monodisperse polymethylmethacrylate spheres may be used similarly.[125] Silica spheres can be made equally monodisperse as polymer colloids, but must be removed by etching with a hydrogen fluoride (HF) solution.[54,126-130] All these approaches have resulted in materials containing large domains of well-ordered spherical pores.

The type of material that is desired often limits the methods available for pore filling. For photonic crystals the desired material is obviously one with a high refractive index and a low absorption. For this purpose titania and silicon have so far been the most successful; broad stop gaps have been measured in inverted opals made of these materials.[47,54,123,130] But inverted opals have also been made for many other applications, such as catalyst supports, filtration and separation materials, and thermal insulators. This explains the large variety of different materials that have been used in colloidal crystal templating. This work will now be reviewed briefly. In all cases, it is important that the

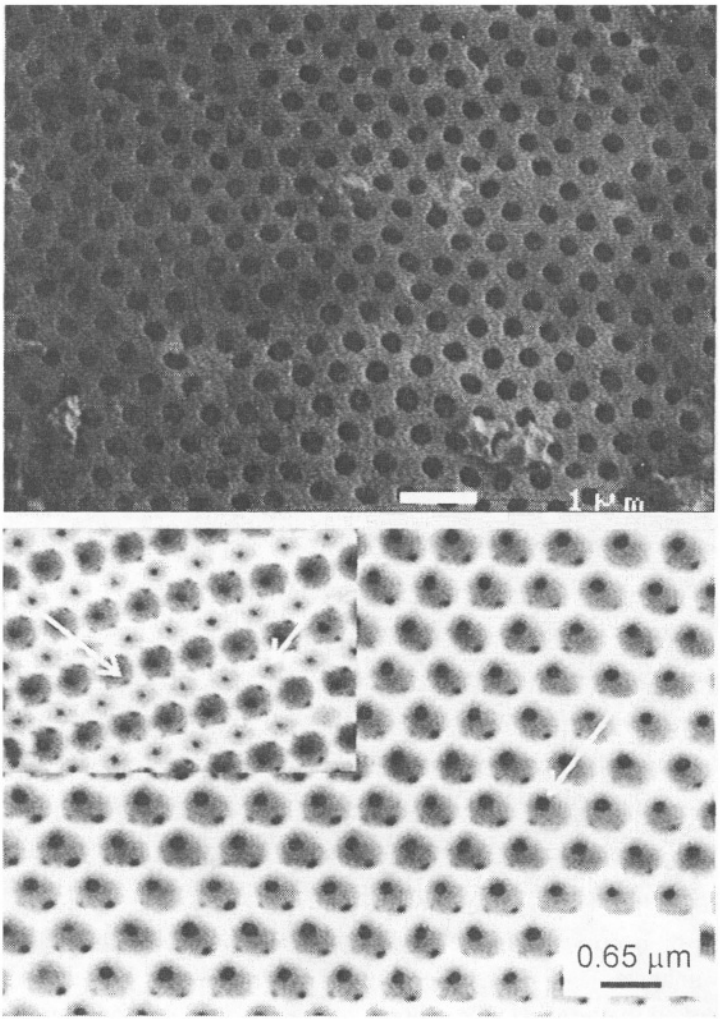

Figure 9. *(Top)* Titania inverse crystal prepared by emulsion templating. *(Bottom)* Titania inverse crystal made by templating polystyrene spheres, with (111) and (110) faces (inset) exposed, courtesy of Willem Vos.

interstitial space of the crystal be sufficiently filled and contiguous, or else the structure will collapse during template removal.

Many metal oxides (titania, silica, zirconia, alumina, yttria, etc.) are produced by hydrolysis of the corresponding liquid metal alkoxide, which is infused into the pores by capillary action, sometimes aided by suction.[116-118,122-124] The alkoxides may be diluted in alcohol to lower their viscosity. After hydrolysis, the process is repeated several more times to increase the degree of filling. In some cases small openings in the center of the interstitial sites are left open when the channels connecting them have become blocked.[118] Calcination of materials prepared in this way sometimes leads to excessive grain growth so that the periodic pore structure may be lost. For this reason, rutile titania could not be prepared this way, unlike the case with emulsion templating.[112] An alternative approach is to use ultrafine powders of silica or nanocrystalline rutile, which are added to a monodisperse polystyrene latex. The mixed suspension is then dried slowly to produce an ordered macroporous material in one step.[131-134] Similar approaches using 4 nm CdSe

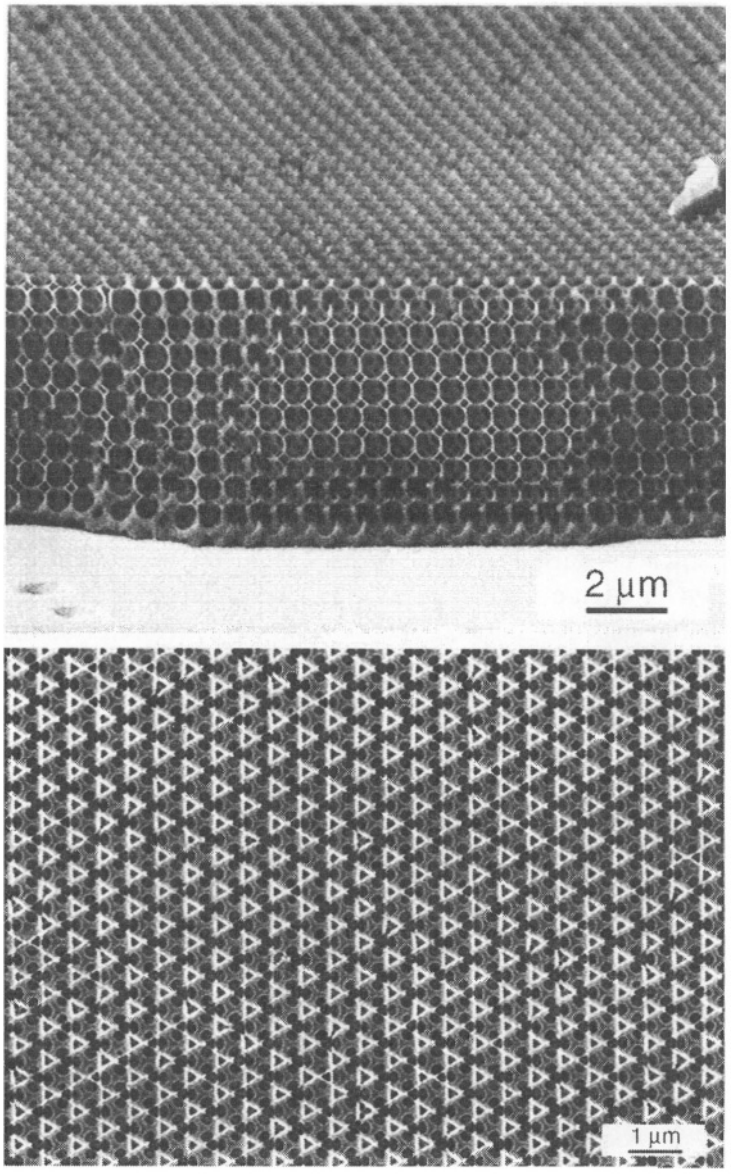

Figure 10. Porous silicon by templating of silica spheres using CVD. Top picture shows a sample edge with a (100) surface. Bottom picture is a (111) surface exposed by reactive ion etching. Courtesy of David Norris, reprinted by permission from Nature,[54] copyright (2001) Macmillan Publishers Ltd.

quantum dots[128] and gold nanocrystals[135,136] have also been used. Due to the small size of the particles efficient pore filling is achieved.

Polymeric inverted opals have been made of polyacrylamide, polystyrene, polymethylmethacrylate, and polyurethane by infiltrating colloidal crystals with a liquid monomer followed by heating or exposure to UV light to initiate the polymerization.[83,113,126,129,137-139]

Precipitation reactions of salts followed by chemical conversion have been applied to expand the variety of accessible materials to a large number of carbonates and oxides of

metals which cannot by prepared by sol-gel chemistry.[140] Subsequent reduction with hydrogen gas has produced ordered macroporous Ni.[141] Similarly, reduction of sol-gel derived germanium oxide has been used to make macroporous germanium, which is transparent in the infrared (λ>1900nm) where the refractive index is as high as 4.

Electrochemical deposition can also be used to template colloidal crystals that have been deposited on an electrode. This way ordered macroporous CdS, CdSe[142,143] and Au[144,145] have been prepared. A variety of porous metals has been made by electroless deposition in silica crystals functionalized with gold nanocrystals.[146] Alternatively, opals can be infiltrated with molten metals at increased pressure.[147]

A final templating method is chemical vapor deposition (CVD), with which the degree of filling can be accurately controlled. Thus, CVD was used to fill silica crystals with graphite and diamond,[127] silicon, which has a refractive index of 3.5 and is transparent a wavelengths above 1100 nm,[130] and germanium.[148] A difficulty was the obstruction with material of the outermost channels which provide access to the innermost channels. Using low-pressure CVD, which prevented channel obstruction, and highly ordered silica crystals, inverted crystals of silicon were made.[54] The resulting material is shown in Figure 10. By measuring two different crystal orientations and comparing reflection and transmission spectra with numerical calculations the authors were able to show that their crystals probably possess a complete photonic band gap around 1300 nm.

3.4. Directed Self-Assembly: More Order and Different Lattices

Although colloidal self-assembly has distinct advantages in the fabrication of three-dimensional photonic crystals it also has a number of drawbacks. Without gentle persuasion the material formed is polycrystalline, contains lattice defects and stacking errors, and can only form a limited number of crystal structures, which have a random orientation. A number of strategies have been developed to overcome these limitations. Methods in which an external influence is used to direct particles to preferred lattice positions will be called directed self-assembly techniques.

A relatively simple technique that already produces well-ordered crystals is called convective self-assembly or controlled drying. It was originally developed for the fabrication of two-dimensional crystals from colloidal spheres,[149,150] but has been extended to allow the formation of three-dimensional crystal films of up to 50 layers in one step.[151] The process is shown schematically in Figure 11. A clean and flat substrate such as microscope slide is placed vertically in a colloidal suspension. As the solvent evaporates from the meniscus more particles are transported to the growing film by fluid flow. Capillary forces in the drying film pull the spheres into a regular close packing. The number of layers can be controlled accurately by the particle volume fraction. The resulting crystal has a uniform orientation over centimeter distances, making it essentially single-domain. Although vacancies exist their number is relatively small. Cracks often form during drying but the crystal orientation is preserved across cracks. Sedimentation of particles larger than about 0.5 μm prevents their deposition in this way. However, this problem can be overcome by applying a temperature gradient which causes a convective flow counteracting sedimentation.[54] Controlled drying has produced some of the best

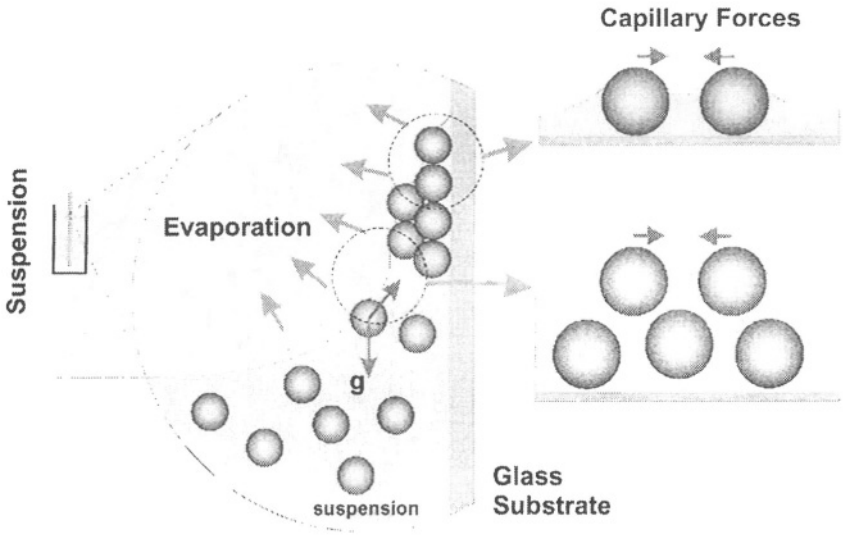

Figure 11. Schematic of controlled drying. See text for explanation.

ordered colloidal crystals, which are suitable for investigating the optical properties of photonic crystals (see Figure 4), both the direct and inverted structures.[49,50,54,151,152]

Another approach to assembly of well-ordered, large-area crystals of close-packed spheres is to filter colloidal spheres into a thin slit between two parallel plates.[153-155] The crystal thickness can be controlled from a monolayer to several hundreds of layers through the plate separation. Fabrication of the filter cells uses photolithography and cleanroom facilities, but an easier method has been developed using replica molding against an elastomeric mold.[156]

Long-range fcc order has also been induced by applying shear flow to a concentrated colloidal suspension enclosed between parallel plates.[157]

Although electrophoretic deposition is widely used for the deposition of particulate films of many different materials it can also be used to prepare ordered three-dimensional sphere packings.[158-161] The quality of the crystals formed appears to be comparable to that obtained by sedimentation, but is somewhat lower than that in crystals formed by controlled drying. It is much faster, however.

The methods to direct colloidal self-assembly mentioned thus far produce (nearly) close packed crystals of the fcc type. Their (111) planes are always arranged parallel to the substrate. Other directed self-assembly methods try to overcome these limitations.

In colloidal epitaxy the colloidal particles sediment onto a substrate that has been patterned lithographically with a regular pattern of pits roughly half a particle deep.[162-163] The first particles fall into the pits, providing a template for other particles. When the first layer was forced to be a (100) or (110) lattice plane of fcc this orientation of the growing crystal was preserved over thousands of layers with relatively few defects. Crystals prepared in this way have recently been templated with selenium.[164] By providing a surface template with a pattern that is unique to the hcp structure a hexagonal close packed crystal grew for tens of layers.[165] Defect lines in the template are reproduced in the successive layers, opening the possibility to construct waveguide structures.[162]

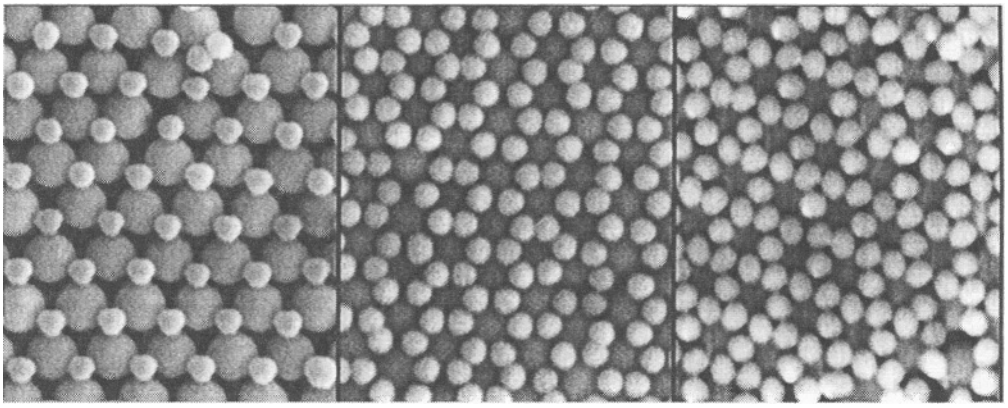

Figure 12. Binary crystal structures AB, AB_2, and AB_3 fabricated using controlled drying, courtesy of Krassimir Velikov.

Another possibility of this method is to make surface templates with a lattice mismatch, which could produce non-close-packed crystals. In an extension of this work (100)-oriented fcc crystals have also been made by patterning the surface with much larger pyramidal pits.[166]

Colloidal crystals can also form binary crystals if the size ratio between the two types of spheres is carefully adjusted. The binary structures AB, AB_2, AB_4, and AB_{13} have been observed.[167,168] Binary crystal structures also occur in natural opals.[6] At present, no band structure calculations of such lattices have been reported. Binary crystal AB, AB_2, and AB_3 can be made layer-by-layer by controlled drying.[169] This is shown in Figure 12. If the two types of particle are made of different material then new crystal structures can be made by selectively removing one of the two types. This was demonstrated for a crystal of silica and polystyrene spheres from which the latter were removed by calcination,[169] leading to a stack of hexagonal planes in an AAA... sequence.

Different crystal structures can also be made by making the interaction potential between the colloidal spheres anisotropic. For example, dipolar interactions can be induced by applying a high-frequency electric field. This results in self-assembly of a body-centered tetragonal crystal structure.[170]

Using optical tweezers or other more advanced techniques of single-particle manipulation it should be possible to build many more crystal structures. Although these techniques are better called 'direct assembly' rather than directed self-assembly we mention them because they may lead to the fabrication of any desired crystal structure. The most interesting structure is the diamond lattice because it has a complete band gap at an index contrast larger than 2.0. Since the gap appears in the first order Bragg region it would also be less vulnerable to lattice disorder. A recent paper proposed building a diamond lattice from two types of spheres, one of which should eventually be removed,[171] using a technique called robot-aided micromanipulation.[172]

3.5. The Effects of Disorder

A certain amount of disorder will be present in all real photonic crystals. Although especially relevant for materials formed by self-assembly disorder also occurs in those

made by nanofabrication. Nevertheless, the effects of disorder on light propagation in photonic crystals has received only modest attention, although John already discussed disorder in periodic lattices in terms of Anderson localization.[11] Effects on transmission and reflection spectra were already briefly mentioned in section 2.2. The length scale that characterizes the degree of disorder as seen by the light used to probe the material is the transport mean free path l. This quantity is the distance over which light propagates before its direction is randomized by random scattering. If the sample thickness L is greater than l the transmission gaps will be broadened by disorder. Broadening was seen in colloidal crystals in which a small number of spheres with different size was deliberately added, as well as impurity modes in the stop gap.[88,173] In reflection measurements only a small depth is probed, determined by the attenuation length of the light, but this depth depends strongly on the wavelength close to the gap. The transport mean free path can be obtained by measuring the total transmission (sum over all angles) as a function of L, or from enhanced backscattering. There exist only a few reports in which photonic crystals have been characterized this way.[174-177] In all cases the crystals had been made by self-assembly without the use of any of the directed self-assembly methods of section 3.4. The value of l found was in the range of 10-20 μm.

On the theoretical side it has been shown that disorder narrows the width of the band gap in fcc inverse opals, making it disappear already at a modest amount of disorder.[178,179] Disorder was modeled as a variation in sphere sizes and positions. The relatively large effect was attributed to the fact that the gap occurs between high-frequency bands: Photonic crystals with their gap in the first-order Bragg region, as made by lithographic methods,[180,181] or for a diamond lattice of spheres,[182] have been found to be much more robust to disorder. For self-assembled crystals one should therefore aim for an extra wide band gap to leave sufficient margin. The effect of stacking faults, which occur in some self-assembled systems forming randomly-stacked hexagonal lattices, has also been considered. It was found that gaps will in general appear wider in these systems[183] and that higher order gaps should become very difficult to observe.[111]

4. ENGINEERING OF COLLOIDAL PARTICLES: CORE-SHELL, METALLO-DIELECTRIC, AND ANISOTROPIC COLLOIDS

A great advantage of colloidal self-assembly over other methods of fabricating photonic crystals is that the single particle properties can be engineered. The possibilities of such approaches have only just begun to be explored. The most common way is to use composite particles with a core-shell structure, where core and shell consist of different materials. Other approaches use anisotropic particles.

Core-shell colloids are prepared chemically by the successive deposition of layers of different materials around a starting particle (called the 'seed'). A very wide variety of core-shell colloids has been prepared for many different applications.[184] A special type of core-shell particle is the hollow shell particle, made by removing the core by dissolution or calcination. An important advantage of the core-shell approach is that one could make the core consist of a quantum-size nanocrystal, or a shell to contain a fluorescent dye.[185] In this way, the active material could be accurately positioned inside the unit cell, where the local density of states may have a lower or higher value than the total density of

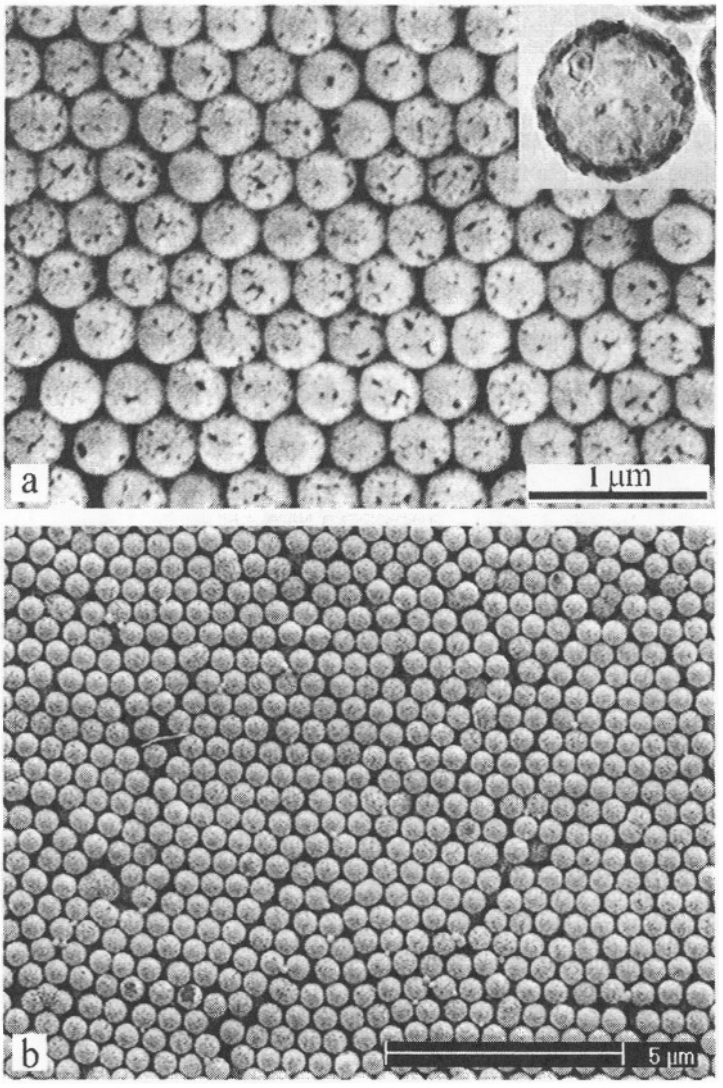

Figure 13. (a) Crystal of hollow titania (anatase) spheres. (b) Metallo-dielectric particles consisting of a silica core coated with 32 nm of gold and 10 nm of silica, courtesy of Christina Graf.

states. Another advantage is that defects could be introduced more effectively into a crystal by, for example, substituting some core-shell particles with normal particles of the same size, or vice versa.

Only recently have core-shell colloids been developed for the purpose of making photonic crystals. Crystals made of these colloids are often aimed at producing a wider, and if possible complete, band gap. Thus, fcc crystals of ZnS spheres coated with silica were shown to have a wider L-stopgap than spheres made of pure ZnS or pure silica.[50] The maximum width was reached when the ratio of the core radius to the total radius was about 0.65. Polystyrene spheres coated with a layer of polymer containing CdTe nanocrystals have also been self-assembled into crystals.[186] An apparent widening of the bandgap was, at least in part, due to absorption by the nanocrystals. Hollow shell

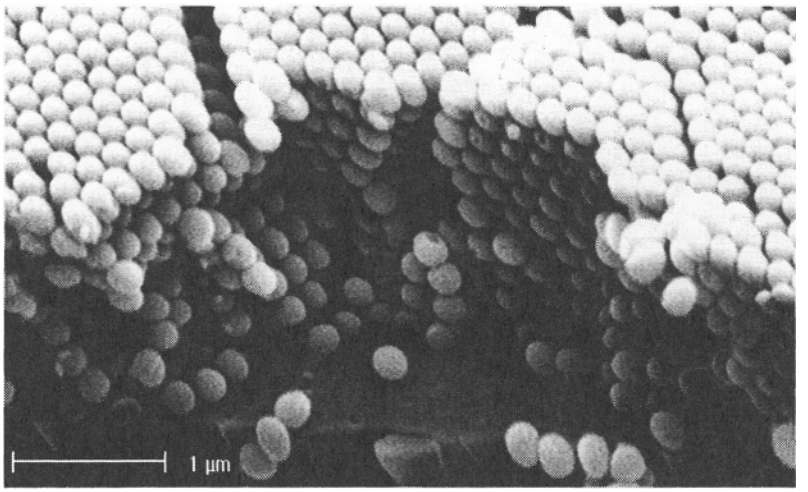

Figure 14. A colloidal crystal of ellipsoidal particles made ion irradiation of silica spheres, courtesy of Krassimir Velikov.

particles offer a much higher refractive index contrast and titania has been the favorite shell material.[187-189] An example is shown in Figure 13a. The resulting material is similar to that obtained by colloidal crystal templating, but the spherical voids are now not connected. The core-shell ratio can be varied at will, which is not the case in the templating method.

A complete band gap is not expected for the materials just mentioned, because the refractive index contrast is still too low.[190] This may no longer be the case, however, if metallic or metallo-dielectric particles are used. Theoretical calculations show that fcc crystals of metal spheres, or metal spheres with a dielectric coating, have wide photonic band gaps, originating from the large, negative value of the real part of the dielectric constant.[191-194] However, absorption, due to the imaginary part of the dielectric constant of the metal, could destroy the band gap. Calculations of the transmission, reflection, and absorption spectra of such crystals show that for the noble metals the absorption will be small enough to make such photonic crystals useful at frequencies in the visible and near infrared, with silver performing the best.[194]

A practical consideration is that metal colloids in the required size range can, at present, not be made sufficiently monodisperse. Luckily, the penetration depth of electromagnetic fields into a metal, or skin depth, is on the order of 10nm at visible wavelengths. One therefore only needs particles with a metal coating that is several tens of nanometers thick. Gold-coated silica spheres have recently been synthesized by depositing gold nanoparticles onto silica spheres.[195,196] A similar approach has been taken for coating silver onto silica[197] or latex[198] spheres. The optical properties of the individual metal shells have been studied,[199-201] showing that they should be useful in optical filters and Raman enhancers. Photonic properties of the crystal have not yet been studied, however. Crystals of gold shell particles were made only recently by coating the metal shells with an extra layer of silica.[196] A dried crystal of these particles is shown in Figure 13b. A further advantage of such silica-gold-silica colloids is that the metal can be accurately positioned at a desired radial position.

As mentioned before, the fcc lattice of dielectric spheres does not have a complete photonic band gap. This can be attributed to a symmetry-induced degeneracy at the W-point of the Brillouin zone. This degeneracy could be lifted by using particles that are anisotropic in shape[202] or in their dielectric properties.[203] This way a complete band gap can open up between the 2^{nd} and 3^{rd} bands if the anisotropy has the proper size and orientation. There have not been many attempts to construct a colloidal crystal of anisotropic particles experimentally. This is, of course, because there are only a few methods to synthesize these particles with a sufficiently uniform size and shape.[204] Such particles then have to be assembled into three-dimensional colloidal crystals with control over the orientation. This has not yet been achieved, although a few strategies have been suggested by means of external fields and surface templates.[205] An alternative approach is to deform the spheres only after crystal assembly. This has been demonstrated for silica and ZnS spheres by irradiation with high-energy Xe^{4+} ions, which deforms the spheres into ellipsoids[206,207] (see Figure 14). The orientation of the ellipsoids can be conveniently controlled through the direction of the bombarding ions. A complication is that not only the spheres are deformed but the fcc lattice as well.

5. CONCLUSIONS

In this chapter the fabrication and optical properties of three-dimensional photonic crystals made from colloids has been described. Recent progress has led to the preparation of photonic crystals with a high degree of order and a low defect density. Combination with templating methods has made it possible to achieve the high refractive index contrasts needed for useful photonic applications. The use of core-shell type composite particles or anisotropic particles to tune and improve photonic properties holds great promise for future research. In order to build actual photonic devices with colloidal crystals it will be necessary to insert lattice defects with a high degree of control. This is a much more challenging task in crystals formed by self-assembly than in those made by lithographic techniques. One way of reaching this goal was recently demonstrated by writing waveguide structures into a self-assembled crystal using multi-photon polymerization in a confocal microscope.[208] External control is another important requirement. Indeed, switching of photonic crystals with electric fields has been achieved by filling colloidal crystals with liquid crystals.[209] These examples show that self-assembly of colloidal particles is a powerful way of fabricating three-dimensional photonic crystals.

6. ACKNOWLEDGMENTS

The author is grateful to Alexander Moroz for performing the numerical calculations the results of which are presented in Figures 1-3. He, Krassimir Velikov and Alfons van Blaaderen are thanked for useful discussions.

7. REFERENCES

1. S. Hachisu, Y. Kobayashi, and A. Kose, Phase separation in monodisperse latices, *J. Colloid Interface Sci.* **42**, 342-348 (1973).
2. S. Hachisu and Y. Kobayashi, Kirkwood-Alder transition in monodisperse latexes. II. Aqueous latexes of high electrolyte concentration, *J. Colloid Interface Sci.* **46**, 470-476 (1974).
3. P. N. Pusey and W. van Megen, Phase behaviour of concentrated suspensions of nearly hard colloidal spheres, *Nature* **320**, 340-342 (1986).
4. J. V. Sanders, Colour of precious opal, *Nature* **204**, 1151-1153 (1964).
5. J. B. Jones, J. V. Sanders, and E. R. Segnit, Structure of opal, *Nature* **204**, 990-991 (1964).
6. J. V. Sanders and M. J. Murray, Ordered arrangements of spheres of two different sizes in opal, *Nature* **275**, 201-202 (1978).
7. P. L. Flaugh, S. E. O'Donnell, and S. A. Asher, Development of a new optical wavelength rejection filter: demonstration of its utility in Raman spectroscopy, *Appl. Spectrosc.* **38**, 847-850 (1984).
8. G. S. Pan, R. Kesavamoorthy, and S. A. Asher, Optically nonlinear Bragg diffracting nanosecond optical switches, *Phys. Rev. Lett.* **78**, 3860-3863 (1997).
9. J. H. Holtz and S. A. Asher, Polymerized colloidal crystal hydrogel films as intelligent chemical sensing materials, *Nature* **389**, 829-832 (1997).
10. E. Yablonovitch, Inhibited spontaneous emission in solid-state physics and electronics, *Phys. Rev. Lett.* **58**, 2059-2062 (1987).
11. S. John, Strong localization of photons in certain disordered dielectric superlattices, *Phys. Rev. Lett.* **58**, 2486-2489 (1987),
12. E. Yablonovitch, T. J. Gmitter, and K. M. Leung, Photonic band-structure - the face-fentered-fubic fase employing nonspherical atoms, *Phys. Rev. Lett.* **67**, 2295-2298 (1991).
13. C. M. Soukoulis (Ed.), *Photonic Crystals and Light Localization in the 21st Century* (Kluwer Academic, Dordrecht, The Netherlands, 2001).
14. S. Y. Lin, J. G. Fleming, D. L. Hetherington, B. K. Smith, R. Biswas, K. M. Ho, M. M. Sigalas, W. Zubrzycki, S. R. Kurtz, and J. Bur, A three-dimensional photonic crystal operating at infrared wavelengths, *Nature* **394**, 251-253 (1998).
15. J. G. Fleming and S. Y. Lin, Three-dimensional photonic crystal with a stop band from 1.35 to 1.95 μm, *Opt. Lett.* **24**, 49-51 (1999).
16. S. Noda, K. Tomoda, N. Yamamoto, and A. Chutinan, Full three-dimensional photonic bandgap crystals at near- infrared wavelengths, *Science* **289**, 604-606 (2000).
17. I. I. Tarhan and G. H. Watson, Photonic band structure of fcc colloidal crystals, *Phys. Rev. Lett.* **76**, 315-318 (1996).
18. W. L. Vos, R. Sprik, A. van Blaaderen, A. Imhof, A. Lagendijk, and G. H. Wegdam, Strong effects of photonic band structures on the diffraction of colloidal crystals, *Phys. Rev. B* **53**, 16231-16235 (1996).
19. W. H. Zachariasen, *Theory of X-Ray Diffraction in Crystals* (Wiley, New York, 1945).
20. R. W. James, *The Optical Principles of the Diffraction of X-Rays (*G. Bell & Sons, London, 1948).
21. M. Born and E. Wolf, *Principles of Optics* (Cambridge University Press, Cambridge, 1999).
22. A. Moroz and C. Sommers, Photonic band gaps of three-dimensional face-centred cubic lattices, *J. Phys. Cond. Matter* **11**, 997-1008 (1999).
23. R. Sprik, B. A. VanTiggelen, and A. Lagendijk, Optical emission in periodic dielectrics, *Europhys. Lett.* **35**, 265-270 (1996).
24. K. Busch and S. John, Photonic band gap formation in certain self-organizing systems, *Phys. Rev. E* **58**, 3896-3908 (1998).
25. K. M. Leung and Y. F. Liu, Full vector wave calculation of photonic band structures in face-centered-cubic dielectric media, *Phys. Rev. Lett.* **65**, 2646-2649 (1990).
26. Z. Zhang and S. Satpathy, Electromagnetic wave propagation in periodic structures - Bloch wave solution of Maxwell equations, *Phys. Rev. Lett.* **65**, 2650-2653 (1990).
27. K. M. Ho, C. T. Chan, and C. M. Soukoulis, Existence of a photonic gap in periodic dielectric structures, *Phys. Rev. Lett.* **65**, 3152-3155 (1990).
28. H. S. Sozuer, J. W. Haus, and R. Inguva, Photonic bands - Convergence problems with the plane-wave method, *Phys. Rev. B* **45**, 13962-13972 (1992).
29. E. Yablonovitch, T. J. Gmitter, R. D. Meade, A. M. Rappe, K. D. Brommer, and J. D. Joannopoulos, Donor and acceptor modes in photonic band-structure, *Phys. Rev. Lett.* **67**, 3380-3383 (1991).
30. R. D. Meade, K. D. Brommer, A. M. Rappe, and J. D. Joannopoulos, Photonic bound-states in periodic dielectric materials, *Phys. Rev. B* **44**, 13772-13774 (1991).

31. J. B. Pendry and A. Mackinnon, Calculation of photon dispersion-relations, *Phys. Rev. Lett.* **69**, 2772-2775 (1992).
32. J. B. Pendry, Calculating photonic band structure, *J. Phys. Cond. Matt.* **8**, 1085-1108 (1996),
33. A. Moroz, Density-of-states calculations and multiple-scattering theory for photons, *Phys. Rev. B* **51**, 2068-2081 (1995).
34. N. Stefanou, V. Karathanos, and A. Modinos, Scattering of electromagnetic-waves by periodic structures, *J. Phys. Cond. Matt.* **4**, 7389-7400 (1992).
35. V. Yannopapas, N. Stefanou, and A. Modinos, Theoretical analysis of the photonic band structure of face-centred cubic colloidal crystals, *J. Phys. Cond. Matt.* **9**, 10261-10270 (1997).
36. N. Stefanou, V. Yannopapas, and A. Modinos, MULTEM 2: A new version of the program for transmission and band-structure calculations of photonic crystals, *Comput. Phys. Commun.* **132**, 189-196 (2000).
37. A. Taflove, *Computational Electrodynamics. The Finite-Difference Time-Domain Method* (Artech House, Boston, 1995).
38. P. A. Rundquist, P. Photinos, S. Jagannathan, and S. A. Asher, Dynamical Bragg-diffraction from crystalline colloidal arrays, *J. Chem. Phys.* **91**, 4932-4941 (1989).
39. Y. Monovoukas, G. G. Fuller, and A. P. Gast, Optical anisotropy in colloidal crystals. *J. Chem. Phys.* **93**, 8294-8299 (1990).
40. Y. Monovoukas and A. P. Gast, A study of colloidal crystal morphology and orientation via polarizing microscopy, *Langmuir* **7**, 460-468 (1991).
41. K. W. K. Shung and Y. C. Tsai, Surface effects and band measurements in photonic crystals, *Phys. Rev. B* **48**, 11265-11269 (1993).
42. I. I. Tarhan and G. H. Watson, Analytical expression for the optimized stop bands of fcc photonic crystals in the scalar-wave approximation, *Phys. Rev. B* **54**, 7593-7597 (1996).
43. D. M. Mittleman, J. F. Bertone, P. Jiang, K. S. Hwang, and V. L. Colvin, Optical properties of planar colloidal crystals: Dynamical diffraction and the scalar wave approximation, *J. Chem. Phys.* **111**, 345-354 (1999).
44. G. S. Pan, A. K. Sood, and S. A. Asher, Polarization dependence of crystalline colloidal array diffraction, *J. Appl. Phys.* **84**, 83-86 (1998).
45. S. Satpathy, Z. Zhang, and M. R. Salehpour, Theory of photon bands in 3-dimensional periodic dielectric structures, *Phys. Rev. Lett.* **64**, 1239-1242 (1990).
46. K. M. Leung and Y. F. Liu, Photon band structures - The plane-wave method, *Phys. Rev. B* **41**, 10188-10190 (1990).
47. M. S. Thijssen, R. Sprik, J. Wijnhoven, M. Megens, T. Narayanan, A. Lagendijk, and W. L. Vos, Inhibited light propagation and broadband reflection in photonic air-sphere crystals, *Phys. Rev. Lett.* **83**, 2730-2733 (1999).
48. Y. A. Vlasov, M. Deutsch, and D. J. Norris, Single-domain spectroscopy of self-assembled photonic crystals, *Appl. Phys. Lett.* **76**, 1627-1629 (2000).
49. J. F. Bertone, P. Jiang, K. S. Hwang, D. M. Mittleman, and V. L. Colvin, Thickness dependence of the optical properties of ordered silica-air and air-polymer photonic crystals, *Phys. Rev. Lett.* **83**, 300-303 (1999).
50. K. P. Velikov, A. Moroz, and A. van Blaaderen, Photonic crystals of core-shell colloidal particles, *Appl. Phys. Lett.* **80**, 49-51 (2002).
51. W. L. Vos and H. M. van Driel, Higher order Bragg diffraction by strongly photonic fcc crystals: onset of a photonic bandgap, *Phys. Lett. A* **272**, 101-106 (2000).
52. W. M. Robertson, G. Arjavalingam, R. D. Meade, K. D. Brommer, A. M. Rappe, and J. D. Joannopoulos, Measurement of photonic band-structure in a 2-dimensional periodic dielectric array, *Phys. Rev. Lett.* **68**, 2023-2026 (1992).
53. K. Sakoda, Group-theoretical classification of eigenmodes in three-dimensional photonic lattices, *Phys. Rev. B* **55**, 15345-15348 (1997).
54. Y. A. Vlasov, X. Z. Bo, J. C. Sturm, and D. J. Norris, On-chip natural assembly of silicon photonic bandgap crystals, *Nature* **414**, 289-293 (2001).
55. P. Pieranski, Colloidal crystals, *Contemp. Phys.* **24**, 25-73 (1983).
56. T. Yoshiyama, I. Sogami, and N. Ise, Kossel line analysis on colloidal crystals in semidilute aqueous solutions, *Phys. Rev. Lett.* **53**, 2153-2156 (1984).
57. T. Yoshiyama and I. S. Sogami, Kossel images as direct manifestations of the gap structure of the dispersion surface for colloidal crystals, *Phys. Rev. Lett.* **56**, 1609-1612 (1986).
58. R. D. Pradhan, J. A. Bloodgood, and G. H. Watson, Photonic band structure of bcc colloidal crystals, *Phys. Rev. B* **55**, 9503-9507 (1997).

59. S. John and J. Wang, Quantum electrodynamics near a photonic band-gap - Photon bound-states and dressed atoms, *Phys. Rev. Lett.* **64**, 2418-2421 (1990).
60. S. John and J. Wang, Quantum optics of localized light in a photonic band-gap, *Phys. Rev. B* **43**, 12772-12789 (1991).
61. Y. A. Vlasov, V. N. Astratov, O. Z. Karimov, A. A. Kaplyanskii, V. N. Bogomolov, and A. V. Prokofiev, Existence of a photonic pseudogap for visible light in synthetic opals, *Phys. Rev. B* **55**, 13357-13360 (1997).
62. V. N. Bogomolov, S. V. Gaponenko, I. N. Germanenko, A. M. Kapitonov, E. P. Petrov, N. V. Gaponenko, A. V. Prokofiev, A. N. Ponyavina, N. I. Silvanovich, and S. M. Samoilovich, Photonic band gap phenomenon and optical properties of artificial opals, *Phys. Rev. E* **55**, 7619-7625 (1997).
63. S. G. Romanov, A. V. Fokin, V. I. Alperovich, N. P. Johnson, and R. M. De La Rue, The effect of the photonic stop-band upon the photoluminescence of CdS in opal, *Phys. Status Solidi A-Appl. Res.* **164**, 169-173(1997).
64. S. G. Romanov, A. V. Fokin, and R. M. De La Rue, Anisotropic photoluminescence in incomplete three-dimensional photonic band-gap environments, *Appl. Phys. Lett.* **74**, 1821-1823 (1999).
65. T. Yamasaki and T. Tsutsui, Spontaneous emission from fluorescent molecules embedded in photonic crystals consisting of polystyrene microspheres, *Appl. Phys. Lett.* **72**, 1957-1959 (1998).
66. A. Blanco, C. Lopez, R. Mayoral, H. Miguez, F. Meseguer, A. Mifsud, and J. Herrero, CdS photoluminescence inhibition by a photonic structure, *Appl. Phys. Lett.* **73**, 1781-1783 (1998).
67. M. Megens, J. Wijnhoven, A. Lagendijk, and W. L. Vos, Light sources inside photonic crystals, *J. Opt. Soc. Am. B* **16**, 1403-1408 (1999).
68. S. G. Romanov, A. V. Fokin, and R. M. De La Rue, Eu^{3+} emission in an anisotropic photonic band gap environment, *Appl. Phys. Lett.* **76**, 1656-1658 (2000).
69. K. Sumioka, H. Nagahama, and T. Tsutsui, Strong coupling of exciton and photon modes in photonic crystal infiltrated with organic-inorganic layered perovskite, *Appl. Phys. Lett.* **78**, 1328-1330 (2001).
70. A. J. Campillo, J. D. Eversole, and H. B. Lin, Cavity quantum electrodynamic enhancement of stimulated-emission in microdroplets, *Phys. Rev. Lett.* **67**, 437-440 (1991).
71. B. Y. Tong, P. K. John, Y. T. Zhu, Y. S. Liu, S. K. Wong, and W. R. Ware, Fluorescence-lifetime measurements in monodispersed suspensions of polystyrene particles, *J. Opt. Soc. Am. B* **10**, 356-359 (1993).
72. M. J. A. de Dood, L. H. Slooff, A. Polman, A. Moroz, and A. van Blaaderen, Local optical density of states in SiO_2 spherical microcavities: Theory and experiment, *Phys. Rev. A* **64**, 033807 (2001).
73. M. J. A. de Dood, L. H. Slooff, A. Polman, A. Moroz, and A. van Blaaderen, Modified spontaneous emission in erbium-doped SiO_2 spherical colloids, *Appl. Phys. Lett.* **79**, 3585-3587 (2001).
74. K. H. Drexhage, Influence of a dielectric interface on fluorescence decay time, *J. Lumines.* **1,2**, 693 (1970).
75. E. Snoeks, A. Lagendijk, and A. Polman, Measuring and modifying the spontaneous emission rate of Erbium near an interface, *Phys. Rev. Lett.* **74**, 2459-2462 (1995).
76. J. Martorell and N. M. Lawandy, Observation of inhibited spontaneous emission in a periodic dielectric structure, *Phys. Rev. Lett.* **65**, 1877-1880 (1990).
77. N. M. Lawandy, Fluorescence-lifetime measurements in monodispersed suspensions of polystyrene particles - Comment, *J. Opt. Soc. Am. B* **10**, 2144-2146 (1993).
78. M. Tomita, K. Ohosumi, and H. Ikari, Enhancement of molecular interactions in strongly scattering dielectric composite optical media, *Phys. Rev. B* **50**, 10369-10372 (1994).
79. E. P. Petrov, V. N. Bogomolov, Kalosha, II, and S. V. Gaponenko, Spontaneous emission of organic molecules embedded in a photonic crystal, *Phys. Rev. Lett.* **81**, 77-80 (1998).
80. Z. Y. Li and Z. Q. Zhang, Weak photonic band gap effect on the fluorescence lifetime in three-dimensional colloidal photonic crystals, *Phys. Rev. B* **63**, 125106 (2001).
81. M. Megens, H. P. Schriemer, A. Lagendijk, and W. L. Vos, Comment on "Spontaneous emission of organic molecules embedded in a photonic crystal", *Phys. Rev. Lett.* **83**, 5401-5401 (1999).
82. E. P. Petrov, V. N. Bogomolov, Kalosha, II, and S. V. Gaponenko, Comment on "Spontaneous emission of organic molecules embedded in a photonic crystal" - Reply, *Phys. Rev. Lett.* **83**, 5402-5402 (1999).
83. K. Yoshino, S. B. Lee, S. Tatsuhara, Y. Kawagishi, M. Ozaki, and A. A. Zakhidov, Observation of inhibited spontaneous emission and stimulated emission of rhodamine 6G in polymer replica of synthetic opal, *Appl. Phys. Lett.* **73**, 3506-3508 (1998).
84. S. Y. Lin, J. G. Fleming, E. Chow, J. Bur, K. K. Choi, and A. Goldberg, Enhancement and suppression of thermal emission by a three- dimensional photonic crystal, *Phys. Rev. B* **62**, R2243-R2246 (2000).
85. H. P. Schriemer, H. M. van Driel, A. F. Koenderink, and W. L. Vos, Modified spontaneous emission spectra of laser dye in inverse opal photonic crystals, *Phys. Rev. A* **63**, 011801 (2001).

86. A. F. Koenderink, L. Bechger, H. P. Schriemer, A. Lagendijk, and W. L. Vos, Broadband fivefold reduction of vacuum fluctuations probed by dyes in photonic crystals, *Phys. Rev. Lett.* **88**, 143903 (2002).
87. I. I. Tarhan, M. P. Zinkin, and G. H. Watson, Interferometric technique for the measurement of photonic band structure in colloidal crystals, *Opt. Lett.* **20**, 1571-1573 (1995).
88. B. T. Rosner, G. J. Schneider, and G. H. Watson, Interferometric investigation of photonic band-structure effects in pure and doped colloidal crystals, *J. Opt. Soc. Am. B* **15**, 2654-2659 (1998).
89. A. Imhof, W. L. Vos, R. Sprik, and A. Lagendijk, Large dispersive effects near the band edges of photonic crystals, *Phys. Rev. Lett.* **83**, 2942-2945 (1999).
90. Y. A. Vlasov, S. Petit, G. Klein, B. Honerlage, and C. Hirlimann, Femtosecond measurements of the time of flight of photons in a three-dimensional photonic crystal, *Phys. Rev. E* **60**, 1030-1035 (1999).
91. K. M. Ho, C. T. Chan, C. M. Soukoulis, R. Biswas, and M. Sigalas, Photonic band-gaps in 3-dimensions - New layer-by-layer periodic structures, *Solid State Commun.* **89**, 413-416 (1994).
92. E. Ozbay, A. Abeyta, G. Tuttle, M. Tringides, R. Biswas, C. T. Chan, C. M. Soukoulis, and K. M. Ho, Measurement of a 3-dimensional photonic band-gap in a crystal-structure made of dielectric rods, *Phys. Rev. B* **50**, 1945-1948 (1994).
93. C. C. Cheng and A. Scherer, Fabrication of photonic band-gap crystals, *J. Vac. Sci. Technol, B* **13**, 2696-2700 (1995).
94. C. C. Cheng, A. Scherer, V. Arbet-Engels, and E. Yablonovitch, Lithographic band gap tuning in photonic band gap crystals, *J. Vac. Sci. Technol. B* **14**, 4110-4114 (1996).
95. A. Chelnokov, K. Wang, S. Rowson, P. Garoche, and J. M. Lourtioz, Near-infrared Yablonovite-like photonic crystals by focused- ion-beam etching of macroporous silicon, *Appl. Phys. Lett.* **77**, 2943-2945 (2000).
96. A. Birner, R. B. Wehrspohn, U. M. Gosele, and K. Busch, Silicon-based photonic crystals, *Adv. Mater.* **13**, 377-388 (2001).
97. J. Schilling, F. Muller, S. Matthias, R. B. Wehrspohn, U. Gosele, and K. Busch, Three-dimensional photonic crystals based on macroporous silicon with modulated pore diameter, *Appl. Phys. Lett* .**78**, 1180-1182 (2001).
98. S. Shoji and S. Kawata, Photofabrication of three-dimensional photonic crystals by multibeam laser interference into a photopolymerizable resin, *Appl. Phys. Lett.* **76**, 2668-2670 (2000).
99. M. Campbell, D. N. Sharp, M. T. Harrison, R. G. Denning, and A. J. Turberfield, Fabrication of photonic crystals for the visible spectrum by holographic lithography, *Nature* **404**, 53-56 (2000).
100. Y. Monovoukas and A. P. Cast, The experimental phase-diagram of charged colloidal suspensions, *J. Colloid Interface Sci.* **128**, 533-548 (1989).
101. P. N. Pusey, W. van Megen, P. Bartlett, B. J. Ackerson, J. G. Rarity, and S. M. Underwood, Structure of crystals of hard colloidal spheres, *Phys. Rev. Lett.* **63**, 2753-2756 (1989).
102. N. A. M. Verhaegh, J. S. van Duijneveldt, A. van Blaaderen, and H. N. W. Lekkerkerker, Direct observation of stacking disorder in a colloidal crystal, *J. Chem. Phys.* **102**, 1416-1421 (1995).
103. V. N. Astratov, Y. A. Vlasov, O. Z. Karimov, A. A. Kaplyanskii, Y. G. Musikhin, N. A. Bert, V. N. Bogomolov, and A. V. Prokofiev, Photonic band gaps in 3D ordered fcc silica matrices. *Phys. Lett. A* **222**, 349-353 (1996).
104. S. G. Romanov, N. P. Johnson, A. V. Fokin, V. Y. Butko, H. M. Yates, M. E. Pemble, and C. M. S. Torres, Enhancement of the photonic gap of opal-based three-dimensional gratings, *Appl. Phys. Lett.* **70**, 2091-2093 (1997).
105. H. Miguez, C. Lopez, F. Meseguer, A. Blanco, L. Vazquez, R. Mayoral, M. Ocana, V. Fornes, and A. Mifsud, Photonic crystal properties of packed submicrometric SiO_2 spheres, *Appl. Phys. Lett.* **71**, 1148-1150 (1997).
106. H. Miguez, F. Meseguer, C. Lopez, A. Blanco, J. S. Moya, J. Requena, A. Mifsud, and V. Fornes, Control of the photonic crystal properties of fcc-packed submicrometer SiO_2 spheres by sintering, *Adv. Mater.* **10**, 480-483 (1998).
107. H. Miguez, A. Blanco, F. Meseguer, C. Lopez, H. M. Yates, M. E. Pemble, V. Fornes, and A. Mifsud, Bragg diffraction from indium phosphide infilled fcc silica colloidal crystals, *Phys. Rev. B* **59**, 1563-1566 (1999).
108. S. G. Romanov, T. Maka, C. M. S. Torres, M. Muller, R. Zentel, D. Cassagne, J. Manzanares-Martinez, and C. Jouanin, Diffraction of light from thin-film polymethylmethacrylate opaline photonic crystals, *Phys. Rev. E* **63**, 056603 (2001).
109. A. Reynolds, F. Lopez-Tejeira, D. Cassagne, F. J. Garcia-Vidal, C. Jouanin, and J. Sanchez-Dehesa, Spectral properties of opal-based photonic crystals having a silica matrix, *Phys. Rev. B* **60**, 1142211426 (1999).
110. R. Biswas, M. M. Sigalas, G. Subramania, and K. M. Ho, Photonic band gaps in colloidal systems, *Phys. Rev. B* **57**, 3701-3705 (1998).

111. R. Biswas, M. M. Sigalas, G. Subramania, C. M. Soukoulis, and K. M. Ho, Photonic band gaps of porous solids, *Phys. Rev. B* **61**, 4549-4553 (2000).
112. A. Imhof and D. J. Pine, Ordered macroporous materials by emulsion templating, *Nature* **389**, 948-951 (1997).
113. A. Imhof and D. J. Pine, Uniform macroporous ceramics and plastics by emulsion templating, *Adv. Mater.* **10**, 697-700 (1998).
114. O. D. Velev, T. A. Jede, R. F. Lobo, and A. M. Lenhoff, Porous silica via colloidal crystallization, *Nature* **389**, 447-448 (1997).
115. O. D. Velev, T. A. Jede, R. F. Lobo, and A. M. Lenhoff, Microstructured porous silica obtained via colloidal crystal templates, *Chem. Mater.* **10**, 3597-3602 (1998).
116. B. T. Holland, C. F. Blanford, and A. Stein, Synthesis of macroporous minerals with highly ordered three-dimensional arrays of spheroidal voids, *Science* **281**, 538-540 (1998).
117. B. T. Holland, C. F. Blanford, T. Do, and A. Stein, Synthesis of highly ordered, three-dimensional, macroporous structures of amorphous or crystalline inorganic oxides, phosphates, and hybrid composites, *Chem. Mater.* **11**, 795-805 (1999).
118. J. E. G. J. Wijnhoven and W. L. Vos, Preparation of photonic crystals made of air spheres in titania, *Science* **281**, 802-804 (1998).
119. C. J. Brinker and G. W. Scherer, *Sol-Gel Science* (Academic, San Diego, 1990).
120. A. Imhof and D. J. Pine, in *Recent Advances in Catalytic Materials,* edited by N. M. Rodriguez, S. L. Soled and J. Hrbek (Materials Research Society, Boston, 1997), Vol. 497, p. 167-172.
121. M. Antonietti, B. Berton, C. Goeltner, and H. P. Hentze, Synthesis of mesoporous silica with large pores and bimodal size distribution by templating of polymer latices, *Adv. Mater.* **10**, 154-159 (1998).
122. J. S. Yin and Z. L. Wang, Template-assisted self-assembly and cobalt doping of ordered mesoporous titania nanostructures, *Adv. Mater.* **11**, 469-472 (1999).
123. A. Richel, N. P. Johnson, and D. W. McComb, Observation of Bragg reflection in photonic crystals synthesized from air spheres in a titania matrix, *Appl. Phys. Lett.* **76**, 1816-1818 (2000).
124. J. Wijnhoven, L. Bechger, and W. L. Vos, Fabrication and characterization of large macroporous photonic crystals in titania, *Chem. Mater.* **13**, 4486-4499 (2001).
125. M. Muller, R. Zentel, T. Maka, S. G. Romanov, and C. M. Sotomayor Torres, Photonic crystal films with high refractive index contrast, *Adv. Mater.* **12**, 1499-1503 (2000).
126. S. A. Johnson, P. J. Ollivier, and T. E. Mallouk, Ordered mesoporous polymers of tunable pore size from colloidal silica templates, *Science* **283**, 963-965 (1999).
127. A. A. Zakhidov, R. H. Baughman, Z. Iqbal, C. Cui, I. Khayrullin, S. O. Dantas, J. Marti, and V. G. Ralchenko, Carbon structures with three-dimensional periodicity at optical wavelengths, *Science* **282**, 897-901 (1998).
128. Y. A. Vlasov, N. Yao, and D. J. Norris, Synthesis of photonic crystals for optical wavelengths from semiconductor quantum dots, *Adv. Mater.* **11**, 165-169 (1999).
129. P. Jiang, K. S. Hwang, D. M. Mittleman, J. F. Bertone, and V. L. Colvin, Template-directed preparation of macroporous polymers with oriented and crystalline arrays of voids, *J. Am. Chem. Soc.* **121**, 11630-11637 (1999).
130. A. Blanco, E. Chomski, S. Grabtchak, M. Ibisate, S. John, S. W. Leonard, C. López, F. Meseguer, H. Míguez, J. P. Mondía, G. A. Ozin, O. Toader, H. M. van Driel, Large-scale synthesis of a silicon photonic crystal with a complete three-dimensional bandgap near 1.5 micrometers, *Nature* **405**, 437-440 (2000).
131. G. Subramanian, V. N. Manoharan, J. D. Thorne, and D. J. Pine, Ordered macroporous materials by colloidal assembly: A possible route to photonic bandgap materials, *Adv. Mater.* **11**, 1261-1265 (1999).
132. G. Subramania, K. Constant, R. Biswas, M. M. Sigalas, and K. M. Ho, Optical photonic crystals fabricated from colloidal systems, *Appl. Phys. Lett.* **74**, 3933-3935 (1999).
133. G. Subramania, R. Biswas, K. Constant, M. M. Sigalas, and K. M. Ho, Structural characterization of thin film photonic crystals, *Phys. Rev. B* **63**, 235111 (2001).
134. Q. B. Meng, Z. Z. Gu, O. Sato, and A. Fujishima, Fabrication of highly ordered porous structures, *Appl. Phys. Lett.* **77**, 4313-4315 (2000).
135. O. D. Velev, P. M. Tessier, A. M. Lenhoff, and E. W. Kaler, A class of porous metallic nanostructures, *Nature* **401**, 548-548 (1999).
136. P. Tessier, O. D. Velev, A. T. Kalambur, A. M. Lenhoff, J. F. Rabolt, and E. W. Kaler, Structured metallic films for optical and spectroscopic applications via colloidal crystal templating, *Adv. Mater.* **13**, 396-400 (2001).
137. S. H. Park and Y. Xia, Fabrication of three-dimensional macroporous membranes with assemblies of microspheres as templates, *Chem. Mater.* **10**, 1745-1747 (1998).
138. M. Deutsch, Y. A. Vlasov, and D. J. Norris, Conjugated-polymer photonic crystals, *Adv. Mater.* **12**, 1176-1180(2000).

139. H. Miguez, F. Meseguer, C. Lopez-Tejeira, and J. Sanchez-Dehesa, Synthesis and photonic bandgap characterization of polymer inverse opals, *Adv. Mater.* **13**, 393-396 (2001).
140. H. W. Yan, C. F. Blanford, B. T. Holland, W. H. Smyrl, and A. Stein, General synthesis of periodic macroporous solids by templated salt precipitation and chemical conversion, *Chem. Mater.* **12**, 1134-1141 (2000).
141. H. Yan, C. F. Blanford, B. T. Holland, M. Parent, W. H. Smyrl, and A. Stein, A chemical synthesis of periodic macroporous NiO and metallic Ni, *Adv. Mater.* **11**, 1003-1006 (1999).
142. P. V. Braun and P. Wiltzius, Electrochemically grown photonic crystals, *Nature* **402**, 603-604 (1999).
143. P. V. Braun and P. Wiltzius, Electrochemical fabrication of 3D microperiodic porous materials, *Adv. Mater.* **13**, 482-485 (2001).
144. J. Wijnhoven, S. J. M. Zevenhuizen, M. A, Hendriks, D. Vanmaekelbergh, J. J. Kelly, and W. L. Vos, Electrochemical assembly of ordered macropores in gold, *Adv. Mater.* **12**, 888-890 (2000).
145. M. C. Netti, S. Coyle, J. J. Baumberg, M. A. Ghanem, P. R. Birkin, P. N. Bartlett, and D. M. Whittaker, Confined surface plasmons in gold photonic nanocavities, *Adv. Mater.* **13**, 1368-1370 (2001).
146. P. Jiang, J. Cizeron, J. F. Bertone, and V. L. Colvin, Preparation of macroporous metal films from colloidal crystals, *J. Am. Chem. Soc.* **121**, 7957-7958 (1999).
147. N. Eradat, J. D. Huang, Z. V. Vardeny, A. A. Zakhidov, I. Khayrullin, I. Udod, and R. H. Baughman, Optical studies of metal-infiltrated opal photonic crystals, *Synthetic Metals* **116**, 501-504 (2001).
148. H. Miguez, E. Chomski, F. Garcia-Santamaria, M. Ibisate, S. John, C. Lopez, F. Meseguer, J. P. Mondia, G. A. Ozin, O. Toader, and H. M. van Driel, Photonic bandgap engineering in germanium inverse opals by chemical vapor deposition, *Adv. Mater.* **13**, 1634-1637 (2001).
149. N. D. Denkov, O. D. Velev, P. A. Kralchevsky, 1. B. Ivanov, H. Yoshimura, and K. Nagayama, Mechanism of formation of 2-dimensional crystals from latex particles on substrates, *Langmuir* **8**, 3183-3190 (1992).
150. N. D. Denkov, O. D. Velev, P. A. Kralchevsky, I. B. Ivanov, H. Yoshimura, and K. Nagayama, 2-Dimensional crystallization, *Nature* **361**, 26-26 (1993).
151. P. Jiang, J. F. Bertone, K. S. Hwang, and V. L. Colvin, Single-crystal colloidal multilayers of controlled thickness, *Chem. Mater.* **11**, 2132-2140 (1999).
152. M. E. Turner, T. J. Trentler, and V. L. Colvin, Thin films of macroporous metal oxides, *Adv. Mater.* **13**, 180-183 (2001).
153. S. H. Park, D. Qin, and Y. Xia, Crystallization of mesoscale particles over large areas, *Adv. Mater.* **10**, 1028-1032 (1998).
154. S. H. Park and Y. Xia, Assembly of mesoscale particles over large areas and its application in fabricating tunable optical filters, *Langmuir* **15**, 266-273 (1999).
155. B. Gates, D. Qin, and Y. Xia, Assembly of nanoparticles into opaline structures over large areas, *Adv. Mater.* **11**, 466-469 (1999).
156. B. T. Mayers, B. Gates, and Y. Xia, Crystallization of mesoscopic colloids into 3D opaline lattices in packing cells fabricated by replica molding, *Adv. Mater.* **12**, 1629-1632 (2000).
157. R. M. Amos, J. G. Rarity, P. R. Tapster, T. J. Shepherd, and S. C. Kitson, Fabrication of large-area face-centered-cubic hard-sphere colloidal crystals by shear alignment, *Phys. Rev. E* **61**, 2929-2935 (2000).
158. M. Trau, D. A. Saville, and I. A. Aksay, Field-induced layering of colloidal crystals, *Science* **272**, 706-709 (1996).
159. M. Holgado, *et al.,* Electrophoretic deposition to control artificial opal growth, *Langmuir* **15**, 4701-4704 (1999).
160. R. C. Hayward, D. A. Saville, and I. A. Aksay, Electrophoretic assembly of colloidal crystals with optically tunable micropatterns, *Nature* **404**, 56-59 (2000).
161. A. L. Rogach, N. A. Kotov, D. S. Koktysh, J. W. Ostrander, and G. A. Ragoisha, Electrophoretic deposition of latex-based 3D colloidal photonic crystals: A technique for rapid production of high-quality opals, *Chem. Mater.* **12**, 2721-2726 (2000).
162. A. van Blaaderen, R. Ruel, and P. Wiltzius, Template-directed colloidal crystallization, *Nature* **385**, 321-324 (1997).
163. A. van Blaaderen and P. Wiltzius, Growing large, well-oriented colloidal crystals, *Adv. Mater.* **9**, 833 (1997).
164. P. V. Braun, R. W. Zehner, C. A. White, M. K. Weldon, C. Kloc, S. S. Patel, and P. Wiltzius, Epitaxial growth of high dielectric contrast three-dimensional photonic crystals, *Adv. Mater.* **13**, 721-724 (2001).
165. A. van Blaaderen et al., in *Photonic Crystals and Light Localization in the 21st Century,* edited by C. M. Soukoulis (Kluwer Academic, Dordrecht, 2001).
166. Y. D. Yin and Y. N. Xia, Growth of large colloidal crystals with their (100) planes orientated parallel to the surfaces of supporting substrates, *Adv. Mater.* **14**, 605-608 (2002).
167. S. Hachisu and S. Yoshimura, *Nature* **283**, 188 (1980).

168. P. Bartlett, R. H. Ottewill, and P. N. Pusey, Superlattice formation in binary mixtures of hard-sphere colloids, *Phys. Rev. Lett.* **68**, 3801-3804 (1992).
169. K. P. Velikov, C. G. Christova, R. P. A. Dullens, and A. van Blaaderen, Layer-by-layer growth of binary colloidal crystals, *Science* **296**, 106-109 (2002).
170. U. Dassanayake, S. Fraden, and A. van Blaaderen, Structure of electrorheological fluids, *J. Chem. Phys.* **112**, 3851-3858 (2000).
171. F. García-Santamaría, C. López, F. Meseguer, F. López-Tejeira, J. Sánchez-Dehesa, and H. T. Miyazaki, Opal-like photonic crystal with diamond lattice, *Appl. Phys. Lett.* **79**, 2309–2311 (2001).
172. H. T. Miyazaki, H. Miyazaki, K. Ohtaka, and T. Sato, Photonic band in two-dimensional lattices of micrometer-sized spheres mechanically arranged under a scanning electron microscope, *J. Appl. Phys.* **87**, 7152-7158 (2000).
173. R. D. Pradhan, Tarhan, II, and G. H. Watson, Impurity modes in the optical stop bands of doped colloidal crystals, *Phys. Rev. B* **54**, 13721-13726 (1996).
174. Y. A. Vlasov, M. A. Kaliteevski, and V. V. Nikolaev, Different regimes of light localization in a disordered photonic crystal, *Phys. Rev. B* **60**, 1555-1562 (1999).
175. Y. A. Vlasov, V. N. Astratov, A. V. Baryshev, A. A. Kaplyanskii, O. Z. Karimov, and M. F. Limonov, Manifestation of intrinic defects in optical properties of self-organized opal photonic crystals, *Phys. Rev. E* **61**, 5784-5793 (2000).
176. A. F. Koenderink, M. Megens, G. van Soest, W. L. Vos, and A. Lagendijk, Enhanced backscattering from photonic crystals, *Phys. Lett. A* **268**, 104-111 (2000).
177. J. Huang, N. Eradat, M. E. Raikh, Z. V. Vardeny, A. A. Zakhidov, and R. H. Baughman, Anomalous coherent backscattering of light from opal photonic crystals, *Phys. Rev. Lett.* **86**, 4815-4818 (2001).
178. Z. Y. Li and Z. Q. Zhang, Fragility of photonic band gaps in inverse-opal photonic crystals, *Phys. Rev. B* **62**, 1516-1519 (2000).
179. Z. Y. Li and Z. Q. Zhang, Photonic bandgaps in disordered inverse-opal photonic crystals, *Adv. Mater.* **13**, 433-436(2001).
180. S. H. Fan, P. R. Villeneuve, and J. D. Joannopoulos, Theoretical Investigation of Fabrication-Related Disorder On the Properties of Photonic Crystals, *J. Appl. Phys.* **78**, 1415-1418 (1995).
181. A. Chutinan and S. Noda, Effects of structural fluctuations on the photonic bandgap during fabrication of a photonic crystal, *J. Opt. Soc. Am. B* **16**, 240-244 (1999).
182. M. M. Sigalas, C. M. Soukoulis, C. T. Chan, R. Biswas, and K. M. Ho, Effect of disorder on photonic band gaps, *Phys. Rev. B* **59**, 12767-12770 (1999).
183. V. Yannopapas, N. Stefanou, and A. Modinos, Effect of stacking faults on the optical properties of inverted opals, *Phys. Rev. Lett.* **86**, 4811-4814 (2001).
184. F. Caruso, Nanoengineering of particle surfaces, *Adv. Mater.* **13**, 11 -22 (2001).
185. A. van Blaaderen and A. Vrij, Synthesis and characterization of colloidal dispersions of fluorescent, monodisperse silica spheres, *Langmuir* **8**, 2921-2931 (1992).
186. A. Rogach, A. Susha, F. Caruso, G. Sukhorukov, A. Kornowski, S. Kershaw, H. Mohwald, A. Eychmuller, and H. Weller, Nano- and microengineering: Three-dimensional colloidal photonic crystals prepared from submicrometer-sized polystyrene latex spheres pre-coated with luminescent polyelectrolyte/nanocrystal shells, *Adv. Mater.* **12**, 333-337 (2000).
187. P. Jiang, J. F. Bertone, and V. L. Colvin, A lost-wax approach to monodisperse colloids and their crystals, *Science* **291**, 453-457 (2001).
188. R. Rengarajan, P. Jiang, D. C. Larrabee, V. L. Colvin, and D. M. Mittleman, Colloidal photonic superlattices, *Phys. Rev. B* **64**, 205103 (2001).
189. A. Imhof, Preparation and characterization of titania-coated polystyrene spheres and hollow titania shells. *Langmuir* **17**, 3579-3585 (2001).
190. G. R. Yi and S. M. Yang, Bandgap engineering of face-centered cubic photonic crystals made of hollow spheres, *J. Opt. Soc. Am. B* **18**, 1156-1160 (2001).
191. A. Moroz, Three-dimensional complete photonic-band-gap structures in the visible, *Phys. Rev. Lett.* **83**, 5274-5277 (1999).
192. A. Moroz, Photonic crystals of coated metallic spheres, *Europhys. Lett.* **50**, 466-472 (2000).
193. W. Y. Zhang, X. Y. Lei, Z. L. Wang, D. G. Zheng, W. Y. Tam, C. T. Chan, and P. Sheng, Robust photonic band gap from tunable scatterers, *Phys. Rev. Lett.* **84**, 2853-2856 (2000).
194. Z. L. Wang, C. T. Chan, W. Y. Zhang, N. B. Ming, and P. Sheng, Three-dimensional self-assembly of metal nanoparticles: Possible photonic crystal with a complete gap below the plasma frequency, *Phys. Rev. B* **64**, 113108 (2001).
195. S. J. Oldenburg, R. D. Averitt, S. L. Westcott, and N. J. Halas, Nanoengineering of optical resonances, *Chem. Phys. Lett.* **288**, 243-247 (1998).

196. C. Graf and A. van Blaaderen, Metallodielectric colloidal core-shell particles for photonic applications, *Langmuir* **18**, 524-534 (2002).
197. J. B. Jackson and N. J. Halas, Silver nanoshells: Variations in morphologies and optical properties, *J. Phys. Chem. B* **105**, 2743-2746 (2001).
198. A. B. R. Mayer, W. Grebner, and R. Wannemacher, Preparation of silver-latex composites, *J. Phys. Chem. B* **104**, 7278-7285 (2000).
199. S. J. Oldenburg, G. D. Hale, J. B. Jackson, and N. J. Halas, Light scattering from dipole and quadrupole nanoshell antennas, *Appl. Phys. Lett.* **75**, 1063-1065 (1999).
200. S. J. Oldenburg, S. L. Westcott, R. D. Averitt, and N. J. Halas, Surface enhanced Raman scattering in the near infrared using metal nanoshell substrates, *J. Chem. Phys.* **111**, 4729-4735 (1999).
201. M. V. Artemyev, U. Woggon, R. Wannemacher, H. Jaschinski, and W. Langbein, Light trapped in a photonic dot: Microspheres act as a cavity for quantum dot emission, *Nano Letters* **1**, 309-314 (2001).
202. J. W. Haus, H. S. Sozuer, and R. Inguva, Photonic bands - Ellipsoidal dielectric atoms in an f.c.c. lattice, *J. Mod. Opt.* **39**, 1991-2005 (1992).
203. Z. Y. Li, J. Wang, and B. Y. Gu, Creation of partial band gaps in anisotropic photonic-band-gap structures, *Phys. Rev. B* **58**, 3721-3729 (1998).
204. E. Matijevic, Preparation and properties of uniform size colloids, *Chem. Mater.* **5**, 412-426 (1993).
205. Y. Lu, Y. D. Yin, and Y. N, Xia, Three-dimensional photonic crystals with non-spherical colloids as building blocks, *Adv. Mater.* **13**, 415-420 (2001).
206. E. Snoeks, A. van Blaaderen, T. van Dillen, C. M. van Kats, M. L. Brongersma, and A. Polman, Colloidal ellipsoids with continuously variable shape, *Adv. Mater.* **12**, 1511-1514 (2000).
207. E. Snoeks, A. van Blaaderen, T. van Dillen, C. M. van Kats, K. Velikov, M. L. Brongersma, and A. Polman, Colloidal assemblies modified by ion irradiation, *Nuclear Instruments & Methods in Physics Research Section B* **178**, 62-68 (2001).
208. W. M. Lee, S. A. Pruzinsky, and P. V. Braun, Multi-photon polymerization of waveguide structures within three-dimensional photonic crystals, *Adv. Mater.* **14**, 271-274 (2002).
209. K. Yoshino, Y. Shimoda, Y. Kawagishi, K. Nakayama, and M. Ozaki, Temperature tuning of the stop band in transmission spectra of liquid-crystal infiltrated synthetic opal as tunable photonic crystal, *Appl. Phys. Lett.* **75**, 932-934 (1999).

19

FUNDAMENTALS AND TECHNOLOGICAL ASPECTS OF CARBON NANOTUBES

Shekhar Subramoney *

1. INTRODUCTION

Since their initial discovery as a by-product of fullerene-synthesis in the arc-discharge process, carbon nanotubes have attracted a very significant amount of attention from the scientific community the world over. The existence of tubular forms of carbon has been known by scientists and engineers working in the fields of chemical reactors and thermal management systems for at least half a century.[1,2] These tubes of carbon, typically several tens of nanometers in diameter and several hundreds of micrometers in length, were formed due to the catalytic decomposition of either hydrocarbons or carbon monoxide by nanometer-sized particles of transition metals typically found inside the reactors. Analysis of these tubular forms of carbon showed that they were multi-walled in structure, and the individual sheets of graphite (graphene) that constituted the walls of these tubes were found to be extremely defect laden.

Scientific and technical interest in carbon nanotubes was very significantly revived by the discovery in 1991 by Sumio Iijima[4] at NEC of multi-walled nanotubes (MWNT) grown in the plasma of the arc-discharge apparatus used for the synthesis of fullerenes or buckyballs. Similar to the whiskers discovered by Roger Bacon[3] at GE in 1960, these MWNT were grown without the aid of a catalyst and formed in the plasma of the arc, where the temperature is estimated to range anywhere from 3000 to 5000 °C. Subsequent work by other reserchers at NEC[5] demonstrated that the MWNT formed at significantly higher pressures on inert gas (such as helium or argon) than needed for conventional fullerene synthesis. A very significant number of scientific papers and books have been published over the last decade on studies related to the structure, properties, and applications of MWNT, as will be detailed later in this chapter. However, the almost simultaneous discovery in 1993 at NEC[6] and IBM[7] of the single-walled variants of carbon nanotubes (SWNT) has considerably overshadowed the scientific excitement associated with MWNT. SWNT can be considered as unique materials for several reasons: they are prototype one-dimensional quantum wires that are made up of one element (carbon) that are one atom in wall thickness and tens of atoms in circumference

* Shekhar Subramoney, DuPont Co. Laboratory Experimental Station P.O. Box 80228 Wilmington, DE 19880-02288, USA.

with every atom on the surface of the tube. The theoretical as well as experimentally measured values of the mechanical properties of SWNT, with elastic modulus and tensile strength calculated to be near 1000 and several tens of gigapascals (GPa), respectively, are comparable to those predicted for single sheets of graphene. Perhaps the most exciting characteristics of SWNT are their electronic properties, which depend exclusively on their diameter and chirality (the manner in which the single sheet of carbon atoms is wound). Their electronic properties, in combination with their mechanical properties, render SWNT as a very exciting class of materials for research and for several current and potential applications.

The predecessor to what the scientific community now refers to as carbon nanotubes was discovered in the late 1950s.[3] It was referred to as a graphite whisker and it was synthesized in a graphite arc in an argon atmosphere under high pressure and temperature conditions. These whiskers were large enough to allow the direct measurement of physical properties, and based on structural and mechanical property analyses, it was determined that each whisker consisted of one or more concentric tubes, with each tube being in the form of a scroll extending continuously along the length of the whisker, with the graphitic c-axis being normal to the axis of the whisker. Mechanical property measurements indicated that the tensile strength and elastic modulus of these whiskers were 20 gigapascal (GPa) and 800 GPa, respectively – which are very close to the theoretical values calculated for single crystal graphite.

2. SYNTHESIS OF CARBON NANOTUBES

The discovery of both variants of carbon nanotubes[4,6,7] was achieved using the same process used for fullerene synthesis – the evaporation of graphitic electrodes in an arc-discharge set-up. A schematic of an arc-discharge unit is shown in Figure 1.

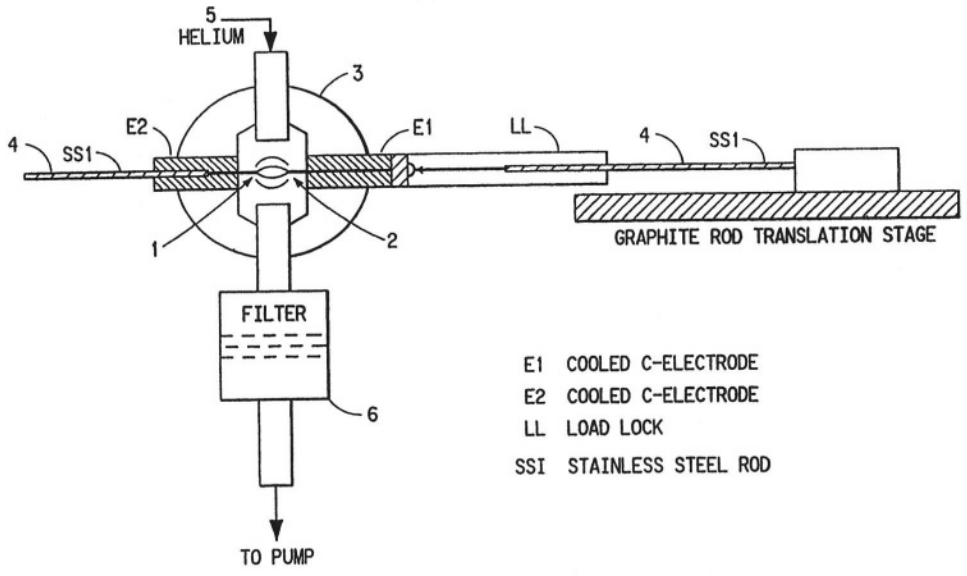

Figure 1. Schematic of the arc-discharge apparatus used for the synthesis of fullerenes and carbon nanotubes.

In this process, the positive electrode (anode) is consumed while a growth (which is sometimes referred to as a boule) occurs on the face of the negative electrode. The atmosphere inside the arc-discharge chamber is typically an inert gas such as helium or argon. The gap between the anode and the cathode is maintained by controlling the speed of the linear motion feedthrough. Conventional fullerenes such as C_{60} and C_{70} are formed in the vapor-phase and deposit on the cold chamber walls along with amorphous carbon, from which they can be solvent-extracted using organic solvents such as benzene, toluene, or carbon tetrachloride. The optimum pressure inside the chamber for maximum yields of conventional fullerenes is typically in the order of 100 torr of helium.[8] MWNT are formed in the high-temperature regime of the plasma of the arc and are found in the boule that grows on the face of the cathode, and yields of MWNT are maximized by increasing the inert-gas pressure inside the arc-discharge chamber to about 500 torr.[5] Typical low-resolution and high-resolution transmission electron microscope (TEM) images of MWNT are shown in Figure 2. The tubular structure and the number of graphene layer planes constituting each wall are clearly visible in Figure 2(b).

The incorporation of small amounts of transition metals into the anode leads to the formation of a felt-like deposit on the cold chamber walls, and TEM was initially used to demonstrate that this soot contained significant quantities of SWNT. Figure 3 is a conventional TEM image of a soot (which was produced with iron and nickel incorporated into the anode as a catalyst in the arc-discharge process) with a significant amount of SWNT in it. A well-designed subsequent study by Seraphin clearly demonstrated that mixtures of transition metals are clearly superior to individual transition metals when incorporated into the anode during the arc-discharge process for the catalysis of large quantities of SWNT.[9]

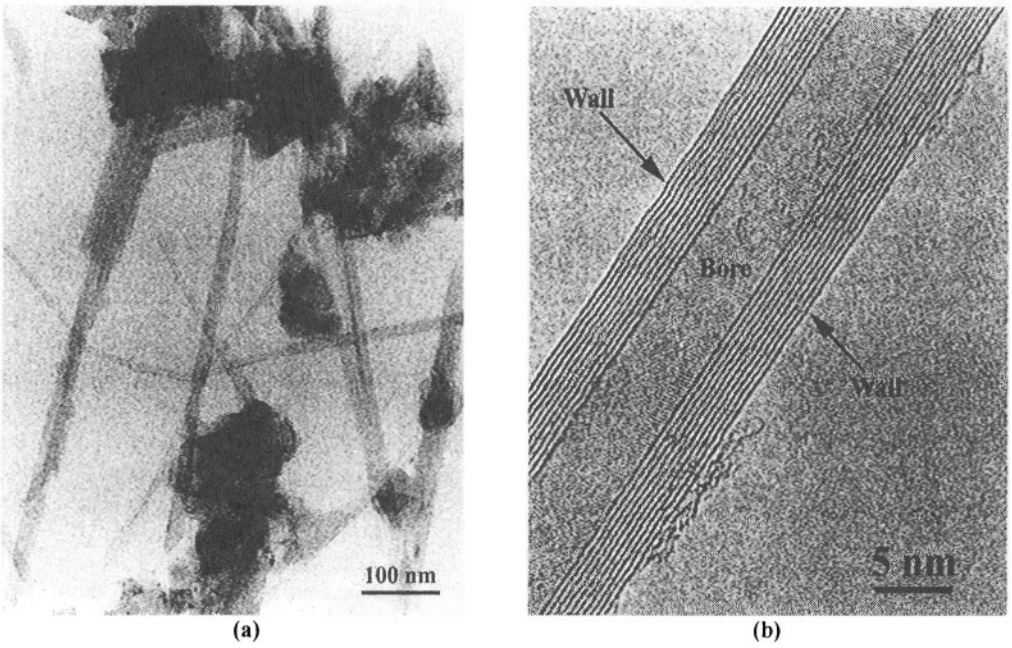

Figure 2. TEM (a) bright-field (low magnification) and (b) high-resolution images of MWNT.

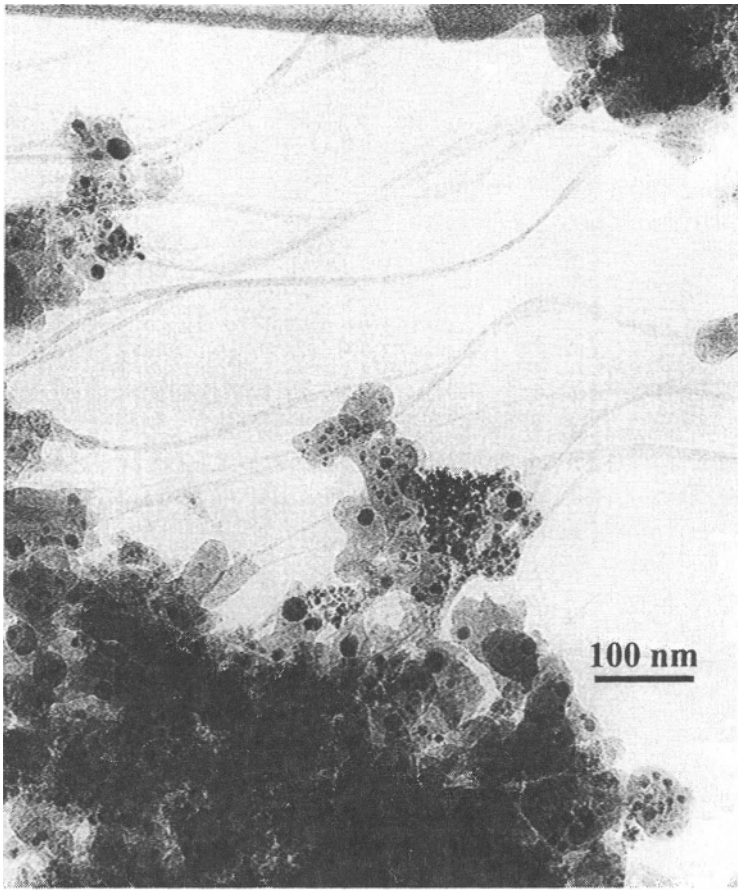

Figure 3. TEM bright-field image of ropes of SWNT grown by the arc-discharge process using a Ni-Fe catalyst.

One of the major breakthroughs in the synthesis of SWNT came about in 1996 when Richard Smalley's group at Rice University reported a development for the synthesis of SWNT in high yields using lasers as the energy source.[10] This technique, where a composite catalyst metal-graphite (nickel-cobalt-carbon) target that was heated under flowing argon at 1200 °C was bombarded with a Nd-YAG double-laser pulse, yielded single-walled tubes with rather uniform diameters of about 1.38 nm each, as calculated from X-ray diffraction studies. The uniformity of diameters of individual tubes leads to a greater tendency for the SWNT produced by laser ablation to self-organize as ropes or aligned bundles. Figure 4 is a unique high-resolution TEM image recorded at Rice University of a rope of SWNT at a near-normal projection to the plane of the paper, clearly illustrating that the individual tubes organize in a hexagonal close-packed array within the rope.

The double-laser based vaporization and condensation of catalyst-graphite targets typically yielded SWNT in the 70 to 90% range. However, similar yields were also obtained by the arc-discharge process using mixtures of rare-earth and transition metals (such as Y and Ni) as catalysts within the graphite electrode.

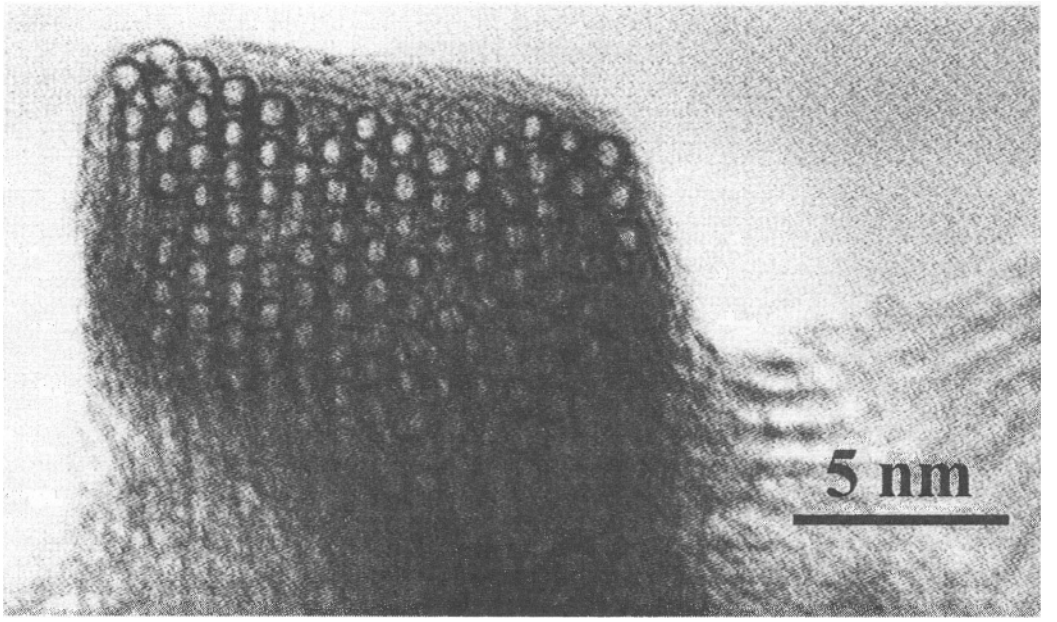

Figure 4. *High-resolution TEM image of a rope of SWNT synthesized in the laser ablation process. Observe the uniformity of individual tube diameter and their hexagonal close-packed configuration. Reprinted from Science (Reference 10) with permission from the American Association for the Advancement of Science.*

These high yields of SWNT, which also manifested themselves as ropes, were found in a "collar"-like growth around the cylindrical boule that occurs on the face of the cathode during the arc-discharge process.[11] The laser ablation and modified arc-discharge processes described by the groups of Smalley[10] and Bernier[11] demonstrated that it was possible to produce gram quantities of well-defined SWNT in the form of highly organized ropes during every day of operation, opening avenues for research and development into the unique properties of these novel nano-scaled materials as well as for exploring commercial applications.

The major drawback of the processes described above for the synthesis of SWNT is that none of them could be scaled into a continuous process for production of significantly higher quantities. This led to the work by various groups to explore chemical vapor deposition (CVD) processes for SWNT synthesis using various precursor and catalyst combinations. The group of Hongjie Dai[12,13] at Stanford University has been one of the pioneers in exploring the field of CVD for SWNT synthesis. By systematically optimizing the process conditions as well as the chemistry and physics associated with both the catalyst system and the support for the catalyst, they were able to demonstrate that materials that contain over 40 weight percent SWNT (the rest being catalysts and support) can be synthesized in a CVD process. The CVD-grown SWNT produced from the decomposition of methane over oxide-supported metal catalysts were found to consist of both individual and roped tubes; structural analysis indicated that the tubes were not over-coated by amorphous carbon and were fairly defect-free. Subsequent work at Rice University[14] using a gas-phase catalytic process involving the thermal decomposition of iron pentacarbonyl by carbon monoxide precursor under high pressures and temperatures demonstrated that even larger volumes of SWNT could be produced that were not

associated with an oxide support. This process, where the carbon SWNT are formed by the disproportionation of CO, is termed as high-pressure CO (HiPCO) and produces SWNT with diameters as small as 7Å. A high-resolution image of SWNT by the HiPCO process is shown in Figure 5, and it is evident that carbon-encapsulated Fe nanoparticles responsible for the catalysis of individual tubes are interwoven into the SWNT ropes and account for a large fraction of the weight of the material obtained from the reactor. Being a continuous-flow process rather than a batch process, the HiPCO method offers the advantage of being able to be scaled up to produce SWNT in kilogram quantities per day.

3. STRUCTURE OF CARBON NANOTUBES

The structure of carbon nanotubes has been a fascinating topic to researchers the world over even prior to Iijima's discovery of MWNT in 1991.[4] In fact, a theoretical study from a group of researchers at the Naval Research Laboratory[15] in Bethesda, Maryland, USA early in 1991 predicted that a tubular structure composed of a graphene sheet would have a charge carrier density similar to that of metals with no Peierls distortion at room temperature. This paper was deemed as being too speculative at the time of submission and therefore was not published until 1992. The experimental discoveries in 1991 and 1993 of MWNT and SWNT, respectively, by the arc-discharge evaporation of graphitic targets led to numerous studies aimed at delineating the structure of carbon nanotubes at the highest resolutions possible.

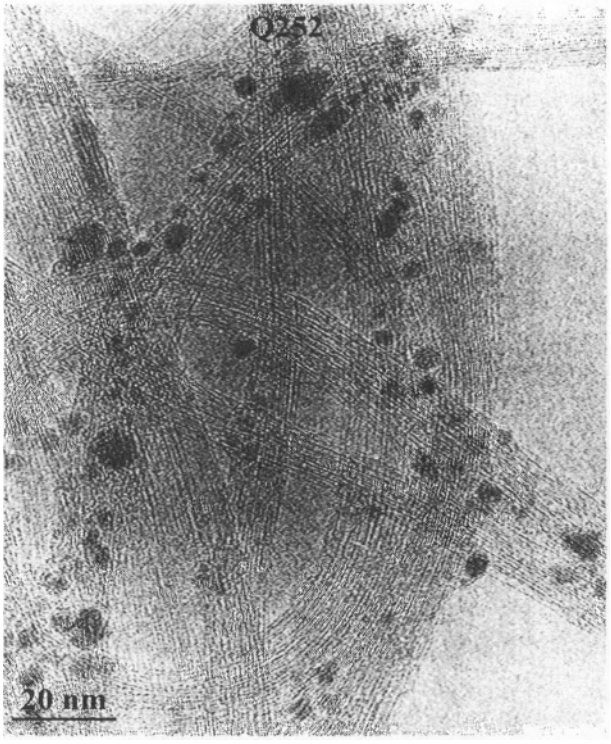

Figure 5. High-resolution TEM image of ropes of SWNT synthesized by the HiPCO process. Observe the iron catalyst nanoparticles woven into the structure of the SWNT ropes.

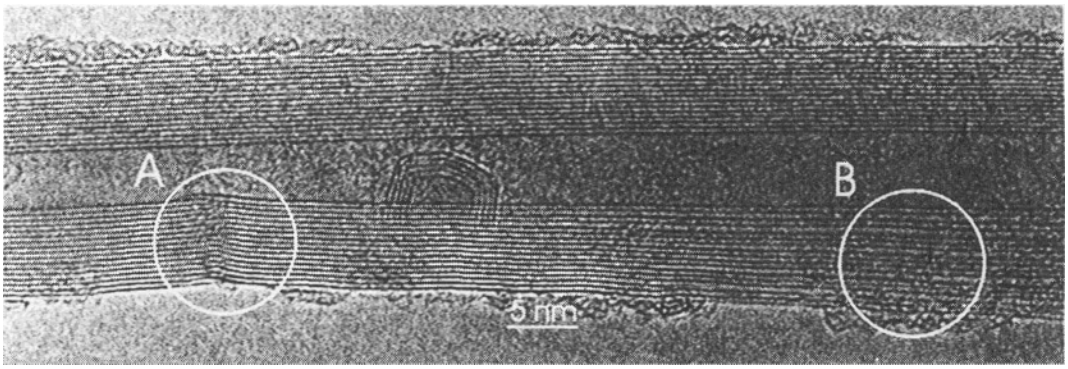

Figure 6. High-resolution TEM image of anomalously large layer spacings (B) associated with defect structures on walls of MWNT (A). Reprinted from Carbon (Reference 17) with permission from Elsevier Science.

MWNT have been characterized by various analytical tools such as X-ray diffraction, electron diffraction, and scanning probe microscopy. However, high-resolution TEM has undoubtedly been the most widely used analytical technique in the characterization of individual MWNT structure. As shown in Figure 2(b), high-resolution TEM images of MWNT show evenly spaced lattice fringes (typically about 3.4 Å apart from the neighboring layers) with an equal number of fringes on either side of the core of the tube. There have been numerous studies to determine the answer to one of the basic questions involving MWNT – whether the layer structure observed in high-resolution TEM images corresponds to a "Russian doll" arrangement of discrete tubes one within the next[4] or whether it corresponds to a scroll-like structure.[16] In some cases, it has been observed that the fringes on one side of the core contain anomalously large spacings, as shown in the high-resolution TEM image in Figure 6.

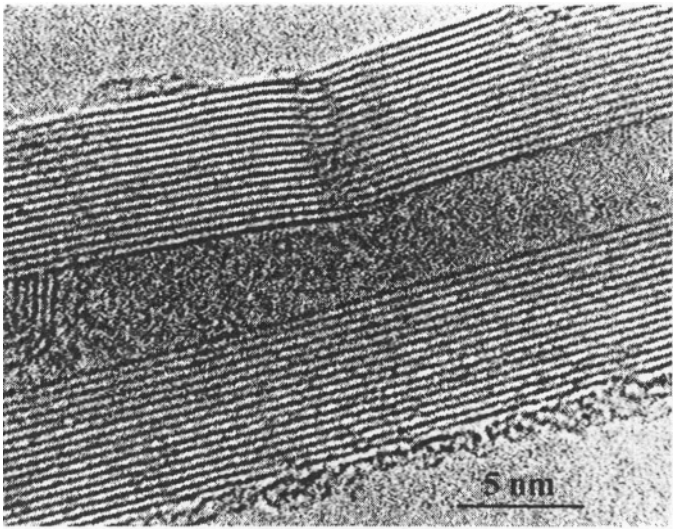

Figure 7. High-magnification image of the defect structure (A) on MWNT shown in Figure 6. Observe an extra layer plane in the vicinity of the defect compared to the number of planes visible on the "defect-free" side. Reprinted from Carbon (Reference 17) with permission from Elsevier Science.

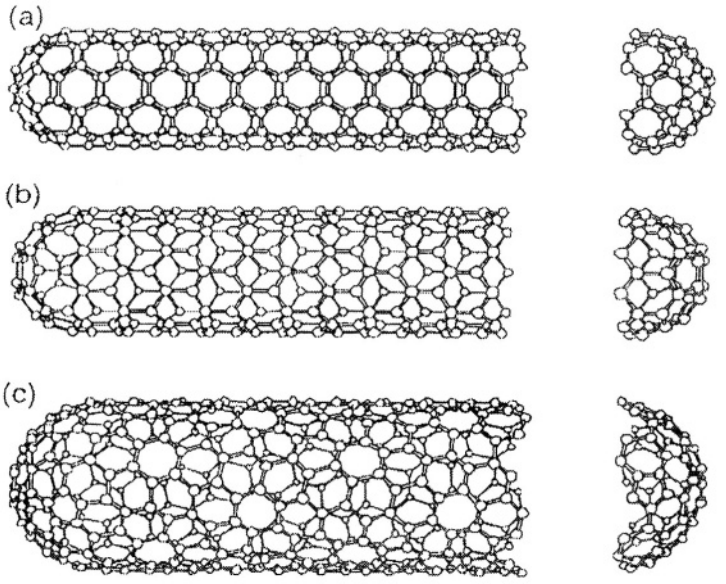

Figure 8. Schematic representation of different conformations of SWNT: (a) arm-chair, (b) zig-zag, and (c) chiral. Reprinted from Carbon (Reference 18) with permission from Elsevier Science.

Structural studies of such tubes reveal that such changes in layer spacing (marked as "B" in Figure 6) are typically in the vicinity of defects (marked as "A" in Figure 6) that are analogous to edge dislocations in a crystal, as illustrated in the significantly higher magnification image shown in Figure 7. These defects are believed to mark the transition from scrolls on one side to nested tubes on the other. Analysis of the helicity of the tubes shows a strong correlation between diameter and helicity. This suggests that the organizing principle for the tubes is not van der Waals forces, as in the case of graphite or turbostratic carbon, but preservation of helicity.[17]

The structure of SWNT is a significantly more exciting research topic due to the fact that it can be defined uniquely in terms of two parameters – its diameter and chirality. The structure of SWNT can be broadly classified into three groups, namely the armchair, zig-zag, and chiral, and these three types of tubes are schematically represented in Figure 8.[18]

This simple structure, in combination with other factors such as every atom being on the surface and all of the atoms being composed of only one element (carbon) renders the SWNT as a unique class of nano-structured materials with extremely fascinating properties and current and potential applications. The diameter and chirality of a SWNT can be characterized by a vector $\mathbf{c} = n\mathbf{a}_1 + m\mathbf{a}_2$ or (n, m) that connects crystallographically equivalent sites on a two-dimensional graphene sheet. In the above nomenclature, $\mathbf{a}_1$ and $\mathbf{a}_2$ are the graphene lattice vectors and n and m are integers. Based on electronic band structure calculations, it has been predicted that the integer set (n, m) determine whether the individual SWNT would be metallic or semi-conducting.

As illustrated earlier, high-resolution TEM can be used to determine how SWNT are configured in the reaction product from a particular synthesis route, whether the SWNT tend to form ropes or not, and how the catalysts may be dispersed within the reaction product. TEM can also be used to evaluate the efficacy of various cleaning processes to

remove catalyst particles and/or glassy carbon as well as to determine the diameter and possibly the length of individual SWNT. Electron nano-diffraction[19] techniques have been used on bundles of SWNT to analyze the helicity distribution and packing characteristics of the ropes, In SWNT structural analysis, diameter-selective Raman scattering from vibrational modes[20] in SWNT has been employed to obtain spectra that are indicative of the chirality of the tubes within individual ropes. Probably the highest resolution technique currently available to characterize the structure of SWNT is the group of scanning tunneling microscopy (STM) measurements. The group of Charles Lieber[21] at Harvard University has been successfully able to characterize the electronic properties of atomically resolved individual SWNT by STM and measure current versus voltage at specific locations along the length of the tubes to yield normalized conductance. Normalized conductance has been known to be a good measure of the main features in the local density of states (LDOS) for both metals and semiconductors. The STM-based analysis has been the major force in the development of carbon nanotube-based molecular electronics, as will be detailed later in this chapter.

4. PHYSICAL PROPERTIES AND APPLICATIONS OF CARBON NANOTUBES

4.1 Mechanical Properties

The sp^2 carbon-carbon bond in the basal plane of a graphene sheet is the strongest known of all chemical bonds, and the elastic modulus of a graphene sheet (based on measurements from single crystals of graphite) is 1060 GPa. These values would suggest that an SWNT whose axis is parallel to the basal plane of a graphene sheet should possess exceptional mechanical properties. As described in the Introduction to this chapter, early work on graphite whiskers grown in a DC arc under pressures over 90-atmosphere inert gas (argon) and temperatures over 3600 °C indicated that they had tensile strengths of over 20 GPa and elastic modulus values of over 800 Gpa.[3] Scanning electron microscopic (SEM) observations indicated that these whiskers were scroll-like in structure and appeared more perfectly formed that vapor-phase produced carbon fibers. Since the discovery of SWNT in 1993,[6,7] based on the assumption that the in-plane elastic modulus of a graphene sheet being 1060 GPa, it was natural for researchers the world over to conclude that these materials would have extremely remarkable mechanical properties. Considering that these SWNT had hollow cores, it was also natural to assume that the mechanical property-to-weight ratio would be very impressive as well. However, it is fairly apparent that nanotubes are too small to be tested by conventional mechanical test apparatus, and too strong when pulled by “optical tweezers” in the laboratory. These conditions place rather stringent restrictions on how one might go about measuring the mechanical properties of carbon nanotubes. Some attempts at these “alternate” techniques have been made, and they include studies such as computer-based simulations, inferences based on configurations of nanotubes observed in electron microscopes, and most recently, some clever experimental techniques were nanotubes were mechanically tested *in-situ* inside the SEM.

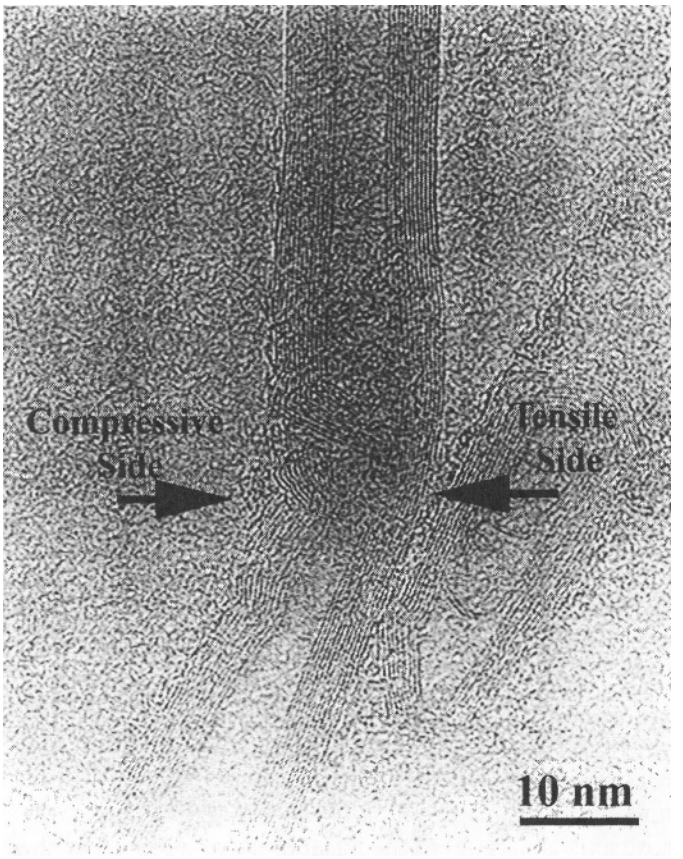

Figure 9. High-resolution TEM image of a MWNT that was subjected to mechanical stress by adhering it to a formvar film on a copper TEM grid which was subsequently deformed by heating the grid. Observe the damage on the wall subjected to the compressive load compared to the wall subjected to the tensile load.

While graphite is by itself a very brittle material, serendipitous observations of both MWNT and SWNT in the TEM appear to indicate that they are extremely resilient, capable of high levels of bending and torsional strains prior to fracture. MWNT that were bent either accidentally or intentionally (but under undetermined stress conditions) during sample preparation exhibited more damage on the compressive side than on the tensional side, as shown in Figure 9.

On other occasions, observations that the walls of MWNT are deformed by van der Waals forces generated by a second tube lying side-by-side have been observed.[22] The amplitude of vibration of the free-standing ends of MWNT that were anchored at the opposite end and subjected to thermal vibrations was analyzed to predict exceptionally high elastic moduli for carbon MWNT, of the order of several thousands of GPa.[23] In molecular-dynamic simulations by Yakobson and co-workers,[24] carbon nanotubes have been shown to elongate to very high strains and they do not fracture easily, with chains of carbon forming that are supplemented by carbon atoms "popping in" from the adjoining locations to retard the fracture process, as illustrated in Figure 10.

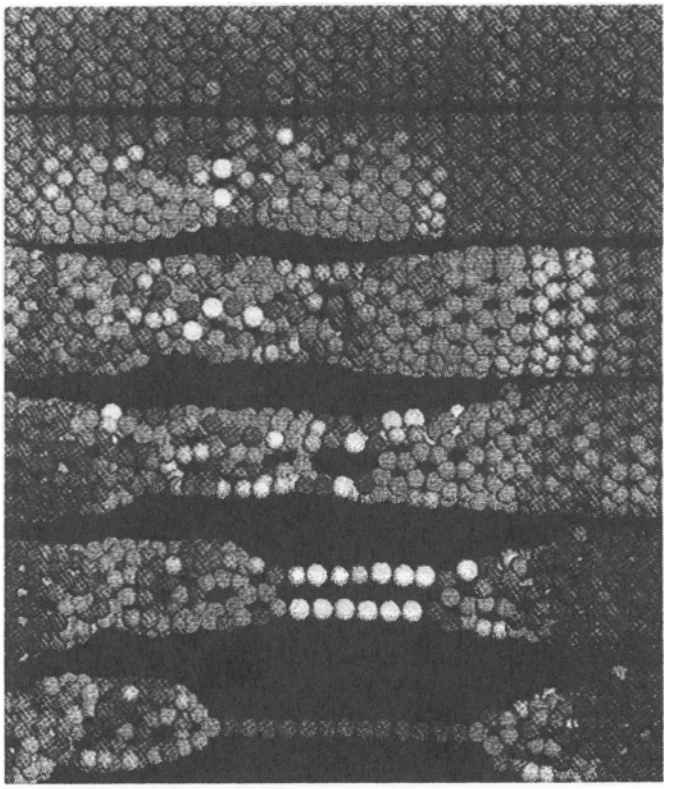

Figure 10. Molecular-dynamic simulations have shown that carbon nanotubes elongate to very high strains and do not fracture easily, with chains of carbon forming that are supplemented by carbon atoms "popping in" from the adjoining locations to retard the fracture process. Reprinted from Computational Materials Science (Reference 24) with permission from Elsevier Science.

While direct measurement of the mechanical properties is by no means an easy and straightforward experiment, the mechanical properties of MWNT were experimentally measured in tension under *in-situ* conditions inside an SEM equipped with a custom designed tensile stage.[25] While the degree of control in such experiments is far from ideal, this work demonstrates that the multi-walled tubes typically fail by a "sword-in-sheath"-type fracture mechanism, similar to that observed in some carbon fibers. While the scattering in the data was rather significant, the experimental observations suggest that the tensile strength of MWNT be typically on the order of several tens of GPa and that the Young's modulus is typically on the order of several hundreds of GPa. Recently, the same group has extended their experimental treatment to ropes of single-walled nanotubes stressed under *in-situ* conditions inside a scanning electron microscope equipped with a custom designed tensile stage.[26] Although the scattering in the data was once again fairly significant, they concluded that most single-walled tubes failed at strain values of 5.3% or lower, and correspondingly their tensile strength was on the order of tens of GPa, with an average value of about 30 GPa. Their experiments also indicated that the Young's modulus of the single-walled tubes was typically on the order of several hundred GPa, with an average value of about 1000 GPa.

4.2 Electronic Properties

The field of electronic properties of carbon nanotubes has perhaps been the most active area of research since their discovery in the early 1990s. Theoretical studies on the electronic properties of carbon nanotubes have been made using band structure calculations similar to those for planar sheets of graphene.[15,27] Considering the one-dimensional structural characteristics of nanotubes, number of allowed electron states in the axial direction will be large, whereas it would be significantly limited in the circumferential direction. In these studies using conventional indices (*n, m*) to represent the chirality of the individual tubes, the electronic structure of the nanotube can be calculated on an analogous basis to that of graphene, with the additional imposition of the necessary boundary conditions due to the limits on the nanotube circumference. Calculations of the electronic density of states near the Fermi level can be graphically depicted as shown in Figure 11.

In terms of their electronic properties, carbon nanotubes can therefore be classified into two major groups – those with a moderate band-gap where $n - m \neq 3p$ (where n and m are the tube indices and p is an integer) that are electrically semi-conducting and those with a small band gap that satisfy the relation $n - m = 3p$ that are electrically metallic in nature.

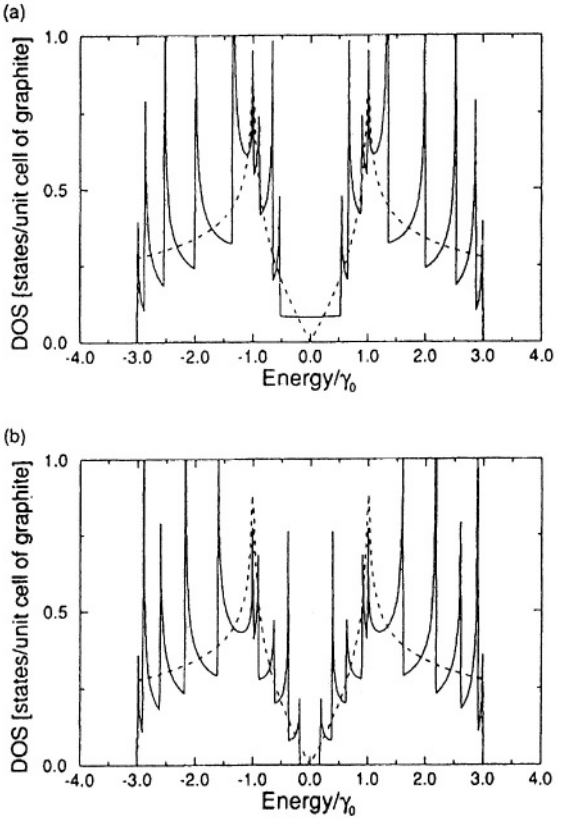

Figure 11. The electronic density of states (DOS) for two zig-zag tubes (a) (9, 0) metallic tube and (b) (10. 0) semi-conducting tube. The dotted line shows the DOS for a two-dimensional graphene sheet. Reprinted from Applied Physics Letters (Reference 27) with permission from the American Institute of Physics.

These findings suggest that arm-chair (*n, n*) tubes would be metallic under all circumstances and that zig-zag (*n,* 0) and chiral (*n, m*) tubes would be metallic in one-third of the cases and semi-conducting in the other two-thirds. It is also important to note that several other theoretical studies have demonstrated that "defect" structures on the tubes would lead to metal-semiconductor, semiconductor-semiconductor, and metal-metal junctions at the defect sites, which might themselves behave as nanoscale device elements.[28-31] Topological defects and atomic impurities in the tubes alter the local electronic density of states near the Fermi level, leading to localized variations in the dominant conductivity associated with the individual tube.

Recently, several research groups have attempted to measure the electrical properties of carbon nanotubes experimentally. The development of scanning tunneling microscopy (STM) and spectroscopy-based techniques has been particularly helpful in these experimental developments. The initial step of the experimental approach involves the dispersing of dilute suspensions of nanotubes onto patterned electrical contacts with the intention of contacting single nanotubes to two adjacent electrodes for electrical transport measurements. Considering that electrons in π-state control the electrical transport in nanotubes, the low-bias resistance of the nanotube for ballistic transport would be $h/4e^2$, which is about 6 kΩ. However, the two-point resistance of single nanotube samples draped over platinum-electrodes (or gold electrodes in other cases), which is shown in Figure 12, was initially measured to be closer to 1 MΩ at room temperature.[32]

The key learning from this initial experiment was that the contact resistance between the carbon nanotube and metal electrode was a major factor in determining resistivity numbers and this was an issue that needed further consideration in future experiments.

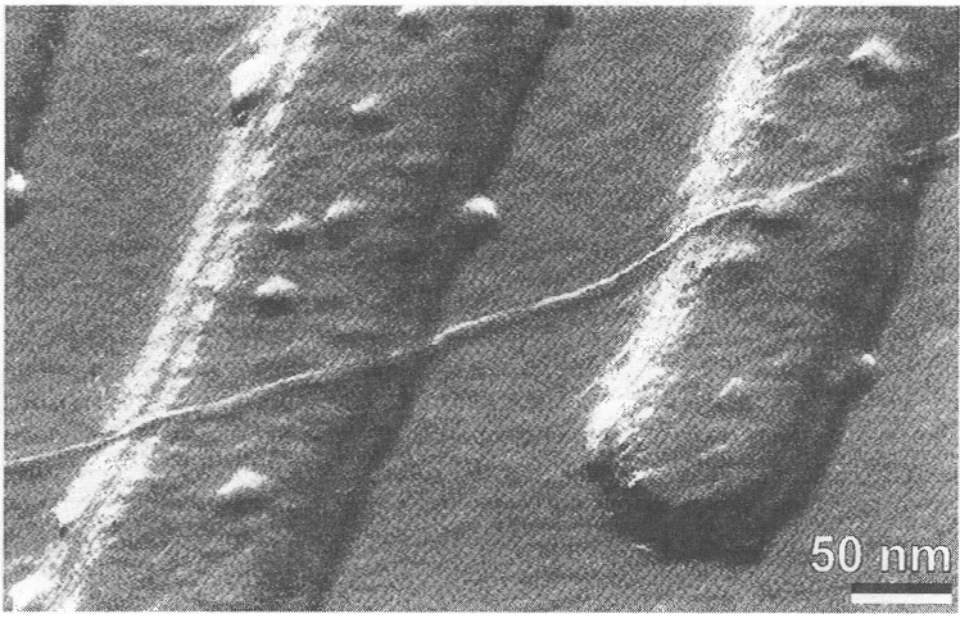

Figure 12. Atomic force microscope (AFM) tapping mode image of a single SWNT draped over two Pt-electrodes on a Si/SiO_2 substrate. Reprinted from Nature (Reference 32) with permission from Nature.

Also, the localized changing of the bond-structure of the carbon atoms from sp^2-like to sp^3-like when the nanotube was "draped" over the metal electrodes led to significant resistivity enhancement and it was another serious technical issue to be addressed. But it was apparent from the initial experimental analysis of electronic properties that carbon nanotubes behaved as coherent quantum wires and that the structure (chirality) was indeed a major factor in determining whether individual tubes were metallic or semiconducting.[33] Recent experiments have also demonstrated that the conductivity of individual SWNT depends significantly on adsorbed gases such as oxygen, making pure SWNT extremely sensitive detectors for oxygen.[34] These elegant experiments clearly confirmed the theoretical work on electronic properties of carbon nanotubes, as did other experiments that confirmed that defects structures led to substantial enhancement in the resistivity of carbon nanotubes.[35]

5. APPLICATIONS INVOLVING CARBON NANOTUBES

5.1. Carbon Nanotube-Based Field Emitters

The unique combination of the physical structure (high aspect ratio and nanometer-scale radius of curvature of the tip), mechanical properties such as stiffness and strength, and the chemical stability of the graphene plane that constitutes its surface makes the carbon nanotube the consummate field-emitting device. The group at Rice University[36] initially demonstrated this for MWNT, using an isolated single multi-walled nanotube. Subsequently, several research groups have demonstrated that thin ropes of single-walled nanotubes are superb field-emitting sources that show higher emission properties (lower turn-on voltage and higher emissivity) than their multi-walled counterparts. The heart of such devices is the cathode, where the nanotubes serve as emission sources following appropriate fabrication techniques.

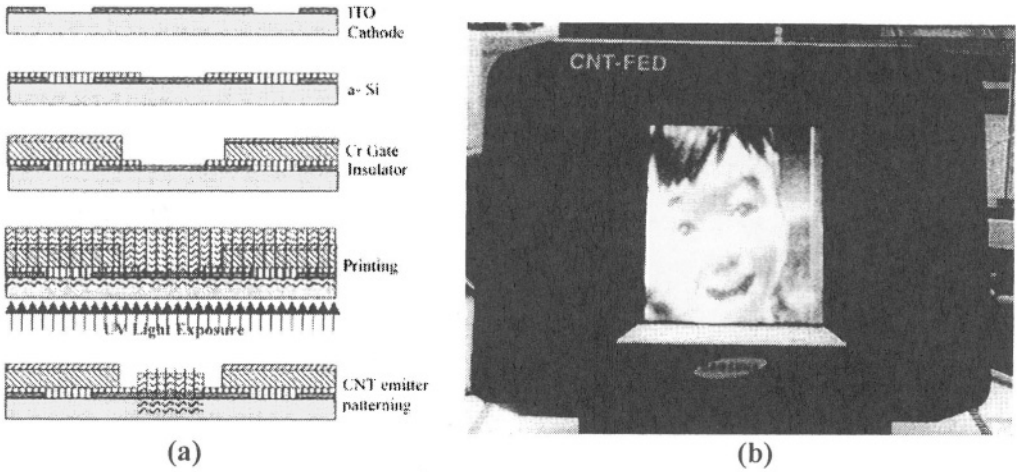

Figure 13. (a) Schematic of the field emitting display with a gated structure developed at Samsung Corporation with SWNT as the emission source and (b) video running image with a 5-inch diagonal active display area (original figure in color). Adapted from Applied Physics Letters (Reference 38) with permission from the American Institute of Physics.

Typically, single-walled tubes show better emission uniformity than multi-walled tubes. In prototype demonstrations using a 4.5-inch diode-based flat panel display with ropes of single-walled tubes serving as emitting sources, researchers in the field emitting display program at Samsung have demonstrated that the device can be turned on at low voltages (less than 1 volt per micrometer), and the brightness measured on the green phosphor (ZnS:Cu, Al) of the screen was of the order of 1800 candelas per square meter at 4 volts per micrometer.[37] This development appears to be well on its way to commercialization, with the recent demonstration of SWNT-based field emitters with gated structures, which allow the addressing of individual pixels and the subsequent development of video running image displays. The schematic of the field emitting display with SWNT as the emission sources with a gated structure and the flat panel display video image obtained from it are shown in Figure 13.[38]

5.2. Single-Electron Field Effect Transistors

Of the various existing and potential applications involving carbon nanotubes, none appears to evoke the level of interest or excitement as the use of single nanotubes, particularly single semi-conducting SWNT, as field effect transistors (FET) at room temperature. What is driving this particular application/technology? Conventional semiconductor lithographic techniques are reaching their theoretical, practical, and possibly economic limits. The demand/value for continuing shrinkage of scale will probably continue to grow even after conventional structures have reached these limits. The major technical challenge would be identify suitable molecular-level materials capable of effectively performing as FET at room temperatures.

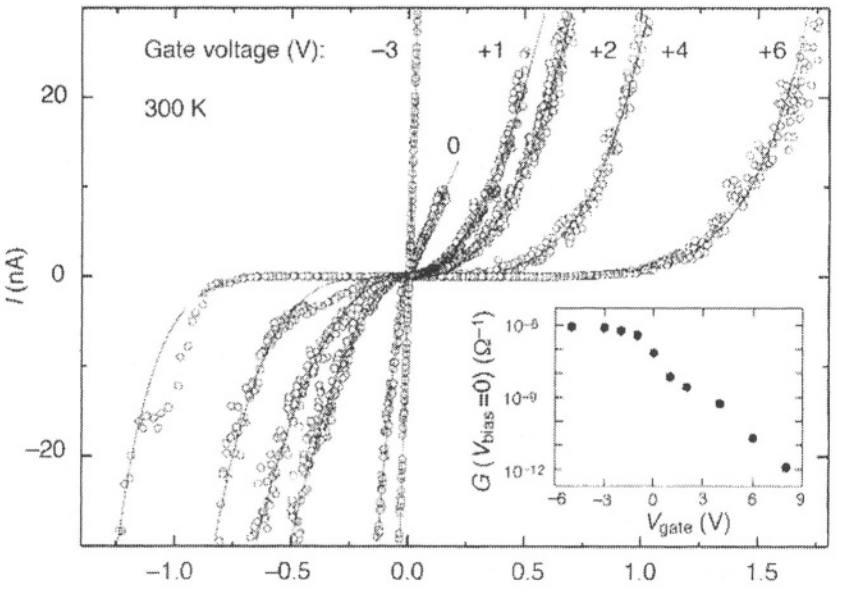

Figure 14. Two-probe I-V bias curves for a single semi-conducting SWNT measured at room temperature in a vacuum of about 10^{-4} mbar for various gate voltages. Reprinted from Nature (Reference 39) with permission from Nature.

This chapter has dealt with the unique and exciting properties of carbon nanotubes, which have been shown to be quasi one-dimensional nanostructures with unique electronic properties that render them to be ideal candidates for applications in microelectronics. In 1998, the group at Delft University led by Cees Dekker[39] reported for the first time the fabrication of an FET where one semi-conducting SWNT connected to two metal electrodes, whose current-voltage (I-V) characteristics are shown in Figure 14.

Subsequent work by the group led by Phaedon Avouris[40] at IBM confirmed this finding and also showed that the transport through the semi-conducting SWNT is dominated by holes and not by electrons, suggesting that the semi-conductivity was of the *p*- and not the *n*-type. From a technological standpoint, the need for *n*-type FET is critical, as it allows the fabrication of nanotube-based complementary logic devices and circuits. This can be achieved by converting the predominantly p-type SWNT to n-type SWNT by either alkali-metal (such as potassium) doping or by annealing the device either in vacuum or in an inert atmosphere, which results in oxygen removal which subsequently alters the line-up of the valence bands at the electrode-nanotube junction.[41] Besides the effect of carbon nanotube doping to alter the transport properties of individual SWNT, lowering the contact resistance of the nanotube-electrode junction by "end-bonding" the nanotube to metals such as titanium,[42] and altering the configuration of the gate electrodes[43] to improve the overall electrical characteristics have been the latest developments in the field of molecular-level electronics. Although the technological field of using carbon nanotubes in molecular-level electronics is still in its infancy, the promising results from the various related experiments appear to suggest that the potential for this field is indeed very promising, especially for intermolecular and intra-molecular inverters and logic circuits.[44,45]

Besides the applications discussed earlier, a whole host of other applications have been envisaged from carbon nanotubes, some of which are in the early stages of research/development. These applications, to name a few, include the use of either MWNT or SWNT as scanning probe microscopy tips,[46] electromechanical actuators,[47] sensing devices for chemical or biological molecules,[48] and hydrogen storage devices.[49] Which of these applications pan out into commercial successes should probably become apparent before the end of the current decade.

6. THE FUTURE OF CARBON NANOTUBES

While a variety of topics ranging from the structure to the properties to potential applications of carbon nanotubes have been discussed hitherto, very little has been touched upon in terms of manipulating carbon nanotubes to render them "controllable" for specific purposes. These manipulations have been the focus of several studies in both academic and industrial laboratories the world over. Examples of such endeavors include the synthesis of large arrays of well-aligned MWNT on glass or silica substrates[50] to the synthesis of extremely small quantities (preferably individual tubes) to bridge patterned islands to directly synthesize molecular-scale devices.[51] Both chemical and mechanical means have been exploited to "cut" ropes of SWNT into lengths that might render them more useful for many of the devices that are being contemplated.[52,53] While it has been demonstrated that naked carbon nanotubes can effectively serve as sensors for particular gases,[48] non-covalent side-wall functionalization can be utilized to suitably alter the

properties of the SWNT for other specific purposes. Observations by high-resolution TEM clearly demonstrates that even the acid/oxidizing treatment to remove amorphous carbon and catalyst particles from freshly prepared SWNT samples functionalizes the surfaces of individual nanotubes with chemical groups such as –COOH. Other examples include the functionalization of the side-walls of SWNT with species such as amine-rich polymers converts semi-conducting *p-type* SWNT into the desirable *n-type* species.[54] Other fimctionalizing species such as succinimidyl ester groups can be used to effectively provide anchoring sites for immobilizing specific bio-molecules on the side-walls of SWNT for biosensor applications.[54] In fact, a large number of studies have reported the chemical alteration of tubes to render them soluble in various solvents.[56-58] In fact, covalent functionalization of carbon nanotubes has currently become a very significant topic of research,[59-62] and recent developments in this field suggest that it might be possible to develop an entirely new field of organic chemistry based on these functionalized nanotubes. The development of optimum functionalization chemistries for carbon nanotubes is likely to lead to the development of very interesting and exciting properties that might lead to very significant commercial applications in the not-too-distant future.

In summary, this chapter has provided a brief insight into the novel world of carbon nanotubes. The references that are cited at the end of this chapter have been carefully chosen and represent some of the outstanding work that has been documented over the last decade. They do not, however, do entire justice to the hundreds of other excellent publications (journal articles, textbooks, and conference proceedings) that are dedicated to this very exciting field of carbon nanotubes. The reader is encouraged to follow the trail of publications cited in this chapter and elsewhere to probe deeper into any particular topic of interest related to carbon nanotubes.

7. REFERENCES

1. W. R. Davis, R. J. Slawson, and G. R. Rigby, An unusual form of carbon, *Nature* **171**, 756 (1953).
2. L. J. E. Hofer, E. Sterling, and J. T. MacCartney, Structure of the carbon deposited from carbon monoxide on iron, cobalt and nickel, *J. Phys. Chem.* **59**, 1153 – 1155 (1955).
3. R. Bacon, Growth, structure, and properties of graphite whiskers, *J. Appl. Phys.* **31**, 283 – 290 (1960).
4. S. Iijima, Helical microtubules of graphitic carbon, *Nature* **354**, 56 – 58 (1991).
5. T. W. Ebbesen and P. M. Ajayan, Large-scale synthesis of carbon nanotubes, *Nature* **358**, 220 – 222 (1992).
6. S. Iijima and T. Ichihashi, Single-shell carbon nanotubes of 1-nm diameter, *Nature* **363**, 603 – 605 (1993).
7. D. S. Bethune, C. H. Kiang, M. S. de Vries, G. Gorman, R. Savoy, J. Vazquez, and R. Beyers, Cobalt-catalyzed growth of carbon nanotubes with single-atomic-layer walls, *Nature* **363**, 605 – 607 (1993).
8. W. Krätschmer, L. D. Lamb, K. Fostiropoulos, and D. R. Huffman, Solid C_{60}: a new form of carbon, *Nature* **347**, 354 –358 (1990).
9. S. Seraphin, Single-walled tubes and encapsulation of nanocrystals into carbon clusters, *J. Elecirochem. Soc.* **142**, 290–297 (1995).
10. A. Thess, R. Lee, P. Nikolaev, H. Dai, P. Petit, J. Robert, C. Xu, Y. H. Lee, S. G. Kim, A. G. Rinzler, D. T. Colbert, G. E. Scuseria, D. Tománek, J. E. Fischer, and R. E. Smalley, Crystalline ropes of metallic carbon nanotubes, *Science* **273**, 483 – 487 (1996).
11. C. Journet, W. K. Maser, P. Bernier, A. Loiseau, M. L. de la Chapelle, S. Lefrant, P. Denoard, R. Lee, and J. E. Fischer, Large-scale production of single-walled carbon nanotubes by the electric-arc technique, *Nature* **388**, 756–758 (1997).
12. J. Kong, A. M. Cassell, and H. Dai, Chemical vapor deposition of methane for single-walled carbon nanotubes, *Chem. Phys. Lett.* **292**, 567 – 574 (1998).
13. A. M. Cassell, J. A. Raymakers, J. Kong, and H. Dai, Large scale CVD synthesis of single-walled carbon nanotubes, *J. Phys Chem. B* **103**, 6484 – 6492 (1999).

14. P. Nikolaev, M. J. Bronikowski, R. K. Bradley, F. Rohmund, D. T. Colbert, K. A. Smith, and R. E. Smalley, Gas-phase catalytic growth of single-walled carbon nanotubes from carbon monoxide, *Chem. Phys. Lett.* **313**, 91 – 97 (1999).
15. J. W. Mintmire, B. I. Dunlap, and C. T. White, Are fullerene tubules metallic?, *Phys. Rev. Lett.* **68**, 631 – 634 (1992).
16. O. Zhou, R. M. Fleming, D. W. Murphy, C. H. Chen, R. C. Haddon, A. P. Ramirez, and S. H. Glarum, Defects in carbon nanostructures, *Science* **263**, 1744 – 1747 (1994).
17. J. G. Lavin, S. Subramoney, R. Ruoff, S. Berber, and D. Tománek, Scrolls and nested tubes in multiwall carbon nanotubes, *Carbon* **40**, 1123 - 1130 (2002).
18. M. S. Dresselhaus, G. Dresselhaus, and R. Saito, Physics of carbon nanotubes, *Carbon* **33**, 883 – 891 (1995).
19. L. –C. Qin, S. Iijima, H. Kataura, Y. Maniwa, S. Suzuki, and Y. Achiba, Helicity and packing of single-walled carbon nanotubes studied by electron nanodiffraction, *Chem. Phys. Lett.* **268**, 101 – 106 (1997).
20. A. M. Rao, E. Richter, S. Bandow, B. Chase, P. C. Eklund, K. A. Williams, S. Fang, K. R. Subbuswamy, M. Menon, A. Thess, R. E. Smallye, G. Dresselhaus, and M. S. Dresselhaus, Diameter-Selective Raman Scattering from Vibrational Modes in Carbon Nanotubes, *Science* **275**, (1997).
21. T. W. Odom, J. –L. Huang, P. Kim, and C. M Lieber, Atomic structure and electronic properties of single-walled carbon nanotubes, *Nature* **391**, 62 - 64 (1998).
22. R. S. Ruoff, J. Tersoff, D. C. Lorents, S. Subramoney, and B. Chan, Radial deformation of carbon nanotubes by van der Waals forces, *Nature* **364**, 514 - 516 (1993).
23. M. M. J. Treacy, T. W. Ebbesen, and J. M. Gibson, Exceptionally high Young's modulus observed for individual carbon nanotubes, *Nature* **381**, 678 – 680 (1996).
24. B. I. Yakobson, M. P. Campbell, C. J. Brabec, and J. Bernholc, High strain rate fracture and C-chain unraveling in carbon nanotubes, *Comput. Mater. Sci.* **8**, 341- 348 (1997).
25. M. –F. Yu, O. Lourie, M. J. Dyer, K. Moloni, T. F. Kelly, and R. S. Ruoff, Strength and breaking mechanism of multiwalled carbon nanotubes under tensile load, *Science* **287**, 637 – 640 (2000).
26. M. –F. Yu, B. S. Files, S. Arepalli, and R. S. Ruoff, Tensile loading of ropes of single wall carbon nanotubes and their mechanical properties, *Phys. Rev. Lett.* **84**, 5552 – 5555 (2000).
27. R. Saito, M. Fujita, G. Dresselhaus, and M. S. Dresselhaus, Electronic structure of chiral graphene tubules, *Appl. Phys. Lett.* **60**, 2204 - 2206 (1992).
28. L. Chico, V. H. Crespi, L. X. Benedict, S. G. Louie, M. L. Cohen, Pure carbon nanoscale devices: nanotube heterojunctions, *Phys. Rev. Lett.* **76**, 971 – 974 (1996).
29. R. Saito, G. Dresselhaus, and M. S. Dresselhaus, Tunneling conductance of connected carbon nanotubes, *Phys. Rev. B* **53**, 2044 – 2050 (1996).
30. H. J. Choi, J. Ihm, S. G. Louie, and M. L. Cohen, Defects, quasibound states, and quantum conductance in metallic carbon nanotubes, *Phys. Rev. Lett* **84**, 2917 - 2920 (2000).
31. M. S. Fuhrer, J. Nygard, L. Shih, M. Forero, Y. G. Yoon, M. S. C. Mazzone, H. J. Choi, J. Ihm, S. G. Louie, A. Zettl, and P. L. McEuen, Crossed nanotube junctions, *Science* **288**, 494 – 497 (2000).
32. S. J. Tans, M. H. Devoret, H. Dai, A. Thess, R. E. Smalley, L. J. Geerligs, and C. Dekker, Individual single-wall carbon nanotubes as quantum wires, *Nature* **386**, 474 – 477 (1997).
33. J. W. G. Wildöer, L. C. Venema, A. G. Rinzler, R. E. Smalley, and C. Dekker, Electronic structure of atomically resolved carbon nanotubes, *Nature* **391**, 59 – 64 (1998).
34. P. G. Collins, K. Bradley, M. Ishigami, and A. Zettl, Extreme oxygen sensitivity of electronic properties of carbon nanotubes, *Science* **287**, 1801 – 1804 (2000).
35. H. Dai, E. W. Wong, and C. M. Lieber, Probing electrical transport in nanomaterials: conductivity of individual carbon nanotubes, *Science 272,* 523 – 526 (1996).
36. A. G. Rinzler, J. H. Hafner, P. Nikolaev, L. Lou, S. G. Kim, D. Tománek, P. Nordlander, D. T. Colbert, and R. E. Smalley, Unraveling nanotubes: field emission from an atomic wire, *Science* **269**, 1550 – 1553 (1995).
37. W. B. Choi, D. S. Chung, J. H. Kang, H. Y. Kim, Y. W. Jin, I. T. Han, Y. H. Lee, J. E. Jung, N. S. Lee, G. S. Park, and J. M. Kim, Fully sealed, high-brightness carbon nanotube field emission display, *Appl. Phys. Lett.* **75**, 3129–3131 (1999).
38. D. –S. Chung, S. H. Park, H. W. Lee, J. H. Choi, S. N. Cha, J. W. Kim, J. E. Jang, K. W. Min, S. H. Cho, M. J. Yoon, J. S. Lee, C. K. Lee, J. H. Yoo, J. –M. Kim, J. E. Jung, Y. W. Jin, Y. J. Park, and J. B. You, Carbon nanotube electron emitters with a gated structure using backside exposure processes, *Appl. Phys. Lett* **80**, 4045 – 4047 (2002).
39. S. J. Tans, A. R. M. Verschueren, and C. Dekker, Room-temperature transistor based on a single carbon nanotube, *Nature* **393**, 49 – 52 (1998).
40. R. Mattel, T. Schmidt, H. R. Shea, T. Hertel, and Ph. Avouris, Single- and multi-wall carbon nanotube field effect transistors, *Appl. Phys. Lett.* **73**, 2447 – 2449 (1998).

41. V. Derycke, R. Martel, J. Appenzeller, and Ph. Avouris, Controlling doping and carrier injection in carbon nanotube transistors, *Appl. Phys.Lett.* **80**, 2773 – 2775 (2002).
42. R. Martel, V. Derycke, C. Lavoie, J. Appenzeller, K. K. Chan, J. Tersoff, and Ph. Avouris, Ambipolar electrical transport in semiconducting single-wall carbon nanotubes, *Phys. Rev. Lett.* **87**, 256805-1 - -4 (2001).
43. S. J. Wind, J. Appenzeller, R. Martel, V. Derycke, and Ph. Avouris, Vertical scaling of carbon nanotube field effect transistors using top gate electrodes, *Appl. Phys. Lett.* **80**, 3817 – 3819 (2002).
44. V. Derycke, R. Martel, J. Appenzeller, and Ph. Avouris, Carbon nanotube inter- and intramolecular logic gates, *Nano Lett.* **1**, 453 – 456 (2001).
45. A. Bachtold, P. Hadley, T. Nakanishi, and C. Dekker, Logic circuits with carbon nanotube transistors, *Science* **294**, 1317-1320 (2001).
46. H. Dai, J. H. Hafner, A. G. Rinzler, D. T. Colbert, and R. E. Smalley, Nanotubes as nanoprobes in scanning probe microscopy, *Nature* **384**, 147 – 150, (1996).
47. R. H. Baughman, C. Cui, A. A. Zakhidov, Z. Iqbal, J. N. Barisci, G. M. Spinks, G. G. Wallace, A. Mazzoldi, D. De Rossi, A. G. Rinzler, O. Jaschinski, S. Roth, and M. Kertesz, Carbon Nanotube Actuators, *Science* **284**, 1340 – 1344 (1999).
48. J. Kong, N. R. Franklin, C. Zhou, M. G. Chapline, S. Peng, K. Cho, and H. Dai, Nanotube molecular wires as chemical sensors, *Science* **287**, 622 – 625 (2000).
49. A. C. Dillon, K. M. Jones, T. A. Bekkedahl, C. H. Kiang, D. S. Bethune, and M. J. Heben, Storage of hydrogen in single-walled carbon nanotubes, *Nature* **386**, 377 – 379 (1997).
50. Z. F. Ren, Z. P. Huang, J. W. Xu, J. H. Wang, P. Bush, M. P. Siegal, and P. N. Provencio, Synthesis of large arrays of well-aligned carbon nanotubes on glass, *Science* **282**, 1105 – 1107 (1998).
51. J. Kong, H. T. Soh, A. M. Cassell, C. F. Quate, and H. Dai, Synthesis of individual single-walled carbon nanotubes on patterned silicon wafers, *Nature* **395**, 878–881 (1998).
52. J. Liu, A. G. Rinzler, H. Dai, J. H. Hafner, P. K. Bradley, P. J. Boul, A. Lu, T. Iverson, K. Shelimov, C. B. Huffman, F. Rodriguez-Macias, Y. –S. Shon, T. R. Lee, D. T. Colbert, and R. E. Smalley, Fullerene pipes, *Science* **280**, 1253 – 1256 (1998).
53. I. Stepanek, G. Maurin, P. Bernier, J. Gavillet, A. Loiseau, R. Edwards, and O. Jaschinski, Nano-mechanical cutting and opening of single wall carbon nanotubes, *Chem. Phys. Lett.* **331**, 125 – 131 (2000).
54. M. Shim, A. Javey, N. W. S. Kam, and H. Dai, Polymer functionalization of air-stable n-type carbon nanotube field-effect transistors, *J. Am. Chem. Soc.* **123**, 11512–11513 (2001).
55. R. J. Chen, Y. Zhang, D. Wang, and H. Dai, Noncovalent sidewall functionalization of single-walled carbon nanotubes for protein immobilization, *J. Am. Chem. Soc.* **123**, 3838 – 3839 (2001).
56. J. Chen, M. A. Hamon, H. Hu, Y. Chen, A. M. Rao, P. C. Eklund, and R. C. Haddon, Solution properties of single-walled carbon nanotubes, *Science* **282**, 95 – 98 (1998).
57. J. Chen, A. M. Rao, S. Luksyutov, M. E. Itkis, M. A. Hamon, H. Hu, R. W. Cohn, P. C. Eklund, D. T. Colbert, R. E. Smalley, and R. C. Haddon, Dissolution of full-length single-walled carbon nanotubes, *J. Phys. Chem. B* **105**, 2525 – 2528 (2001).
58. W. Huang, Y. Lin, S. Taylor, J. Gaillard, A. M. Rao, and Y. –P. Sun, Sonication-assisted functionalization and solubilization of carbon nanotubes, *Nano Lett.* **2**, 231 – 234 (2002).
59. P. J. Boul, J. Liu, E. T. Mickelson, C. B. Huffman, L. M. Ericson, I. W. Chiang, K. A. Smith, D. T. Colbert, R. H. Hauge, J. L. Margrave, and R. E. Smalley, Reversible sidewall functionalization of buckytubes, *Chem. Phys. Lett.* **310**, 367 – 372 (1999).
60. J. L. Bahr, J. Yang, D. Y. Kosynkin, M. J. Bronikowski, R. E. Smalley, and J. M. Tour, Functionalization of carbon nanotubes by electrochemical reduction of aryl diazonium salts: a bucky paper electrode, *J. Am. Chem. Soc.* **123**, 6536 – 6542 (2001).
61. J. L. Bahr and J. M. Tour, Covalent chemistry of single-wall carbon nanotubes, *J. Mater. Chem.* **12**, 1952 – 1958 (2002).
62. A. Hirsch, Functionalization of single-walled carbon nanotubes, *Angew. Chem. Int. Ed.* **41**, 1853 – 1859 (2002).

This page intentionally left blank

20

MOLECULAR ASSEMBLY OF FULLERENES AS NANOCLUSTERS AND NANOSTRUCTURED FILMS

K. George Thomas and Prashant V. Kamat*

1. INTRODUCTION

Design of molecular systems, which can spontaneously self-assemble and generate three dimensionally extended structures such as clusters is of interest in "chemical nanotechnology".[1-3] Of particular interest is the utilization of fullerene materials for developing next generation nanodevices. Recent studies on molecular systems based on C_{60},[4,5] particularly the dyads and triads,[6-15] have renewed the interest towards building photovoltaic systems[16-21] and mimicking photosynthesis.[6-15] Organizing molecules as nanoclusters or binding them to inorganic nanoparticles serve as important building blocks in developing new generation nanodevices. Assembly of such nanostructures in an orderly fashion would assist in designing optoelectronic nanodevices that can perform specific functions such as light induced energy and electron transfer processes. Thus, designing strategies to obtain robust films of carbon nanostructures on desired electrode surfaces with a well-controlled morphology remains a major challenge.

Fullerenes and their derivatives readily form self-assembled molecular clusters in mixed solvents.[22-27] These molecular clusters are optically transparent and thermodynamically stable. Recent studies have demonstrated interesting photochemical and photoelectrochemical properties of fullerene-based cluster systems.[12,15,22,25,28-31] Furthermore, one can dope these spherical fullerene assemblies with electron donors such as ferrocene, amines, phenothiazine.[30,32] The local concentration of electron donors is much higher in these clusters. Formation of long lived electron transfer products, following the photoexcitation of the fullerene cluster and various electron donors were confirmed through flash photolysis studies.[25,30] The size and shape of these clusters can be altered with structural modifications. These clusters can be readily assembled as 3-dimensional arrays on a conducting glass electrode.[12,29,31,33] An efficient method has also been reported to fabricate almost perfect and uniformly shaped nanotubular crystals, which order spontaneously by self-assembly of derivatized fullerenes.[34] These interesting fullerene nanostructures show unusual electrochemical sensing and light energy

* Prashant V. Kamat, Notre Dame Radiation Laboratory, Notre Dame, Indiana 46556-0579, USA. K. George Thomas, Photochemistry Research Unit, Regional Research Laboratory (CSIR), Trivandrum 695 019, India

conversion properties. Salient features of 3-D molecular assemblies of fullerene derivatives as nanostructures are presented here.

2. PREPARATION OF FULLERENE NANOCLUSTERS AND NANOSTRUCTURED FILMS

By manipulating the solubility of fullerenes in nonpolar solvents and insolubility in polar solvents one can prepare 100-300 nm diameter molecular clusters in mixed solvents. The structures of various fullerene derivatives chosen for the present study are given in Chart 1. A *fast injection method*[24,25] can be successfully employed to prepare stable cluster suspensions of various fullerene derivatives. In a typical procedure, one prepares concentrated solution of C_{60} (or its derivatives) in toluene. Cluster suspension is then prepared by quickly injecting concentrated toluene solution of fullerene in a pool of acetonitrile using a microsyringe (the final solvent ratio of mixed solvent is in the range of 9:1 to 3:1 corresponding to (v/v) acetonitrile/toluene). An instant yellow-brown coloration of the suspension confirms the formation of fullerene clusters. These optically transparent clusters are quite stable at room temperature and can be reverted back to the monomeric form by diluting with toluene. The ratio of polar/nonpolar solvents that is necessary to achieve aggregation, in each case, depends on the nature of fullerene functionalization. Additionally one can incorporate electron donor such as N-methyl phenothiazine or ferrocene into the clusters by incorporating it into acetonitrile solution before the injection of fullerene solution. This simple process allows incorporation of electron donor or electroactive species into the molecular clusters.

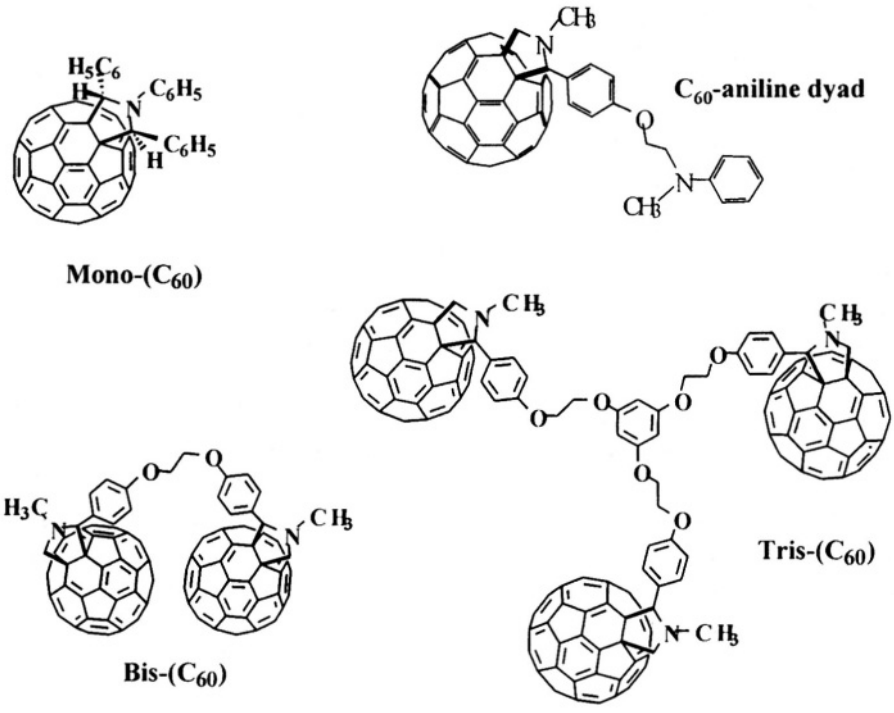

Chart 1. Structures of various fullerene derivatives.

Upon subjecting the cluster suspension to a low electric (dc) field (<5 V) it is possible to increase the size of clusters. A known amount (~2 mL) of cluster solution (0.11 mM of C_{60}) was transferred to a 1 cm cuvette in which two optically transparent electrodes (OTE) were kept at a distance of ~6 mm using Teflon spacer. The cell design employed for electrophoresis experiment is shown in Figure 1. A dc voltage (5-200V) can be applied using a Fluke 415 high voltage dc power supply. This cell configuration allows one to carry out spectroelectrochemical measurements and monitor the absorption changes during the electrodeposition process. An example of cluster growth in an electric field involves fullerene-aniline dyad system.[12] An increase in the absorption throughout the visible region was observed as clusters grew from 160 to 200 nm in diameter. By maintaining the electrode parallel to the probe beam it was possible to monitor the changes in the absorption spectrum of the cluster suspension during the application of dc voltage. Such a growth in cluster size arises from the charging of clusters during the application of electric field, which is succeeded by the association of smaller clusters to form larger ones (Eq. 1).

$$(C_{60}\text{-aniline})_m + (C_{60}\text{-aniline})_n \xrightarrow{(<5\text{V dc})} (C_{60}\text{-aniline})_{m+n} \quad (1)$$

At higher dc voltages (>20 V) we observe a different behavior from these clusters systems, namely, deposition on the electrode surface. Within 30-60 seconds of dc voltage (50 V) application, the cluster suspension in the spectroelectrochemical cell turns colorless and all the fullerene clusters get deposited as a brown film on the positive electrode.

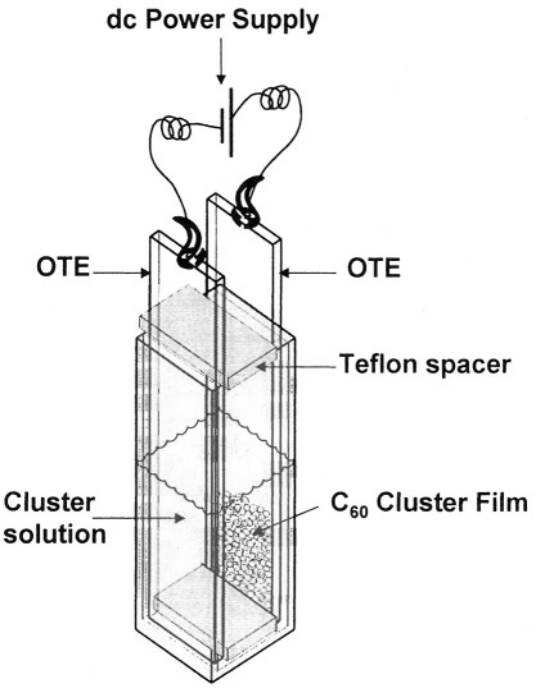

Figure 1. Electrophoretic assembly for the deposition of cluster films on conducting glass electrodes.

A similar method can be employed to cast films of a variety of fullerene derivatives as well as ferrocene incorporated C_{60} clusters ($Fc@C_{60}$) on other electrode surfaces such as glassy carbon electrode. It should be noted that prior to electrodeposition it is necessary to form the clusters of C_{60} in the mixed solvents since C_{60} films cannot be deposited directly from pristine C_{60} solution under similar experimental conditions. It is likely that in the presence of a polar solvent such as acetonitrile the clusters become charged, thus facilitating their deposition on the electrode surface.

3. PROPERTIES OF FULLERENE CLUSTERS

3.1. Absorption and Emission Characteristics

Fullerenes being strongly hydrophobic in nature prefer to form clusters so as to minimize its nonpolar surface exposed to the polar surrounding in mixed solvents. Compared to monomer absorption spectrum in a nonpolar solvent, the clusters show a broad featureless spectrum, with a significant increase in molar extinction coefficient.[22] Examples of absorption and emission spectra of bis-(C_{60}) are shown in Figure 2 A&B (trace b).[32] Intermolecular interactions lead to increased absorption in the cluster systems. The spectral features are quite broad as compared to those of well defined aggregates (H–, J– or Herring bone type molecular aggregates based upon the nature of interacting molecules and the nature of the medium.[35-38] Interestingly the clusters of fullerenes are highly photoactive and show singlet and triplet excited state properties that are in close resemblance of corresponding monomer forms. The spectral properties of various fullerene clusters are summarized in Table 1.

Table 1. Photophysical properties of monomers and clusters of bis- and tris-(C_{60}) derivatives.

Fullerene Derivative		Extinction Coeff. at 470 nm (10^4 M^{-1} cm^{-1})	Emission Max. (nm)
Mono-(C_{60})[c]	Monomer[a]	0.37	715
	Cluster[b]	2.12	730
Bis-(C_{60})[d]	Monomer[a]	0.56	715, 776
	Cluster[b]	2.71	750
Tris-(C_{60})[d]	Monomer[a]	0.33	715
	Cluster[b]	5.17	735, 780
C_{60}-aniline dyad[e]	Monomer[a]	0.24	713
	Cluster[f]	1.86	738

[a] in toluene; [b] in 19:1 acetonitrile:toluene mixed solvent; [c] from reference 30; [d] from reference 32; [e] from reference 12; [f] in 3:1 acetonitrile:toluene mixed solvent.

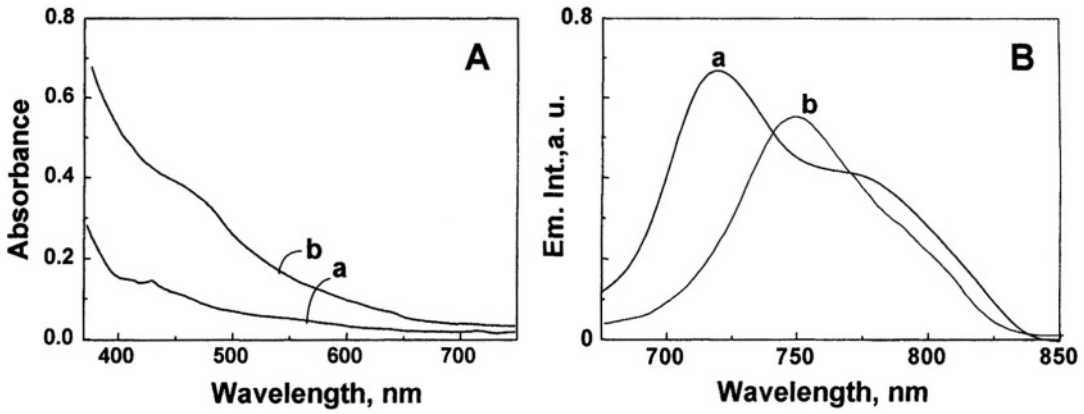

Figure 2. Absorption (A) and emission spectra (B) of bis-(C_{60}) (12 μM) in (a) monomer form in toluene and (b) cluster form in 12.5% (v/v) toluene-acetonitrile. (From reference 32. Reprinted with permission from the American Chemical Society.)

3.2. Size and Shape of Clusters

TEM images of the clusters prepared from bis-(C_{60}) and tris-(C_{60}) derivatives in acetonitrile/toluene mixed solvents, recorded at two different magnifications, are shown in Figures 3A & 3B respectively. Tris-(C_{60}) clusters are spherical in shape with diameter ranging from 100 nm to 400 nm (Figure 3). What is noticeable from Figure 3 is the self-assembled clusters of tris-(C_{60}) molecules in a globular form that are further entangled to form a network of clusters.

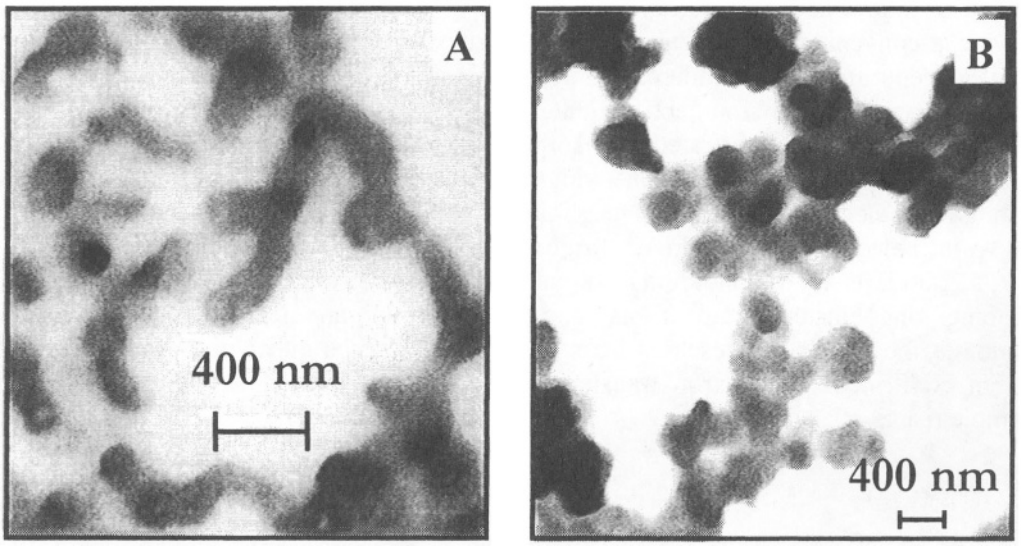

Figure 3. TEM image of A. bis-(C_{60}) and B. tris-(C_{60}) derivatives. (From reference 32. Reprinted with permission from the American Chemical Society.)

Interestingly, a different type of clustering phenomenon is seen for bis-(C_{60}) clusters prepared in acetonitrile/toluene mixture (Figure 3A). The clusters deposited on a carbon grid show elongated structures with varying lengths (200 nm to 1 μm). The tubular structures, seen in Figure 3B represent self-assembled fullerene molecules that are flexible enough to template themselves into nonspherical shapes. If linear stacking is the dominant pathway for bis-C_{60} molecules to aggregate, one would expect the clusters to grow preferentially in one direction. Elongated structure observed in Figure 3A gives the credence to such an argument. Aggregation of tris-C_{60} on the other hand, has a geometric possibility to from clusters in a three dimensional fashion. It is clear from the TEM pictures that the tris-C_{60} derivative aggregates uniformly in all directions via hydrophobic interactions to give spherical structures (Figures 3B). In both these cases, the linker groups containing polar nitrogen as well as oxygen atoms may preferably be exposed to the polar solvent environment. The selection of the linker is also important in the formation of such supramolecular self-assembly. This type of aggregation mimics a dendrimeric type molecular growth to produce spherical shaped clusters. In the present case we have been able to achieve similar cluster growth through simple hydrophobic interactions. The two examples illustrated above demonstrate the possibility of designing different carbon nanostructures by simply modifying the fullerene functionalization. A template driven clustering can further aid in designing well-defined shape and size for these clusters.

3.3. Photoinduced Electron Transfer between Fullerene Clusters and Electron Donors

For light energy harvesting applications, it is desirable to develop cluster systems that undergo charge separation under excitation of photoactive molecules. Donor-acceptor dyad molecules using C_{60} as the electron acceptor moiety have been extensively studied to induce such charge separations.[6,16,25,39,40] The fullerene based cluster systems provide a convenient way to incorporate electron donors into the cluster network. The local concentration of the fullerene molecules is much higher in these clusters and the microheterogeneous environment facilitates trapping of donor molecules. The feasibility of this concept was demonstrated by incorporating a series of electron donors of different oxidation potentials into 1,2,5-triphenylpyrrolidinofullerene (TPPF) clusters.[30] Formation of long lived electron transfer products, following the photoexcitation of the TPPF cluster and various electron donors were confirmed through flash photolysis studies.

A comparison of photoinduced intermolecular electron transfer between the monomer and cluster forms of bis- and tris-(C_{60}) and an electron donor, N-methyl phenothiazine (NMP) is presented here.[32] The fluorescence quenching observed in this system confirmed the electron transfer to occur in the excited singlet state (see for example reaction 2).

$$^1\text{Tris-}(C_{60})^* + \text{NMP} \longrightarrow \text{Tris-}(C_{60})^{-\bullet} + \text{NMP}^{+\bullet} \quad (2)$$

The difference absorption spectrum recorded in a laser flash photolysis experiment shows the formation of $NMP^{+\bullet}$ species with absorption maximum at 520 nm (Figure 4). The formation of the transient at 1000 nm confirmed the formation of fullerene anion as expected from reaction 2 (Figure 4 inset).

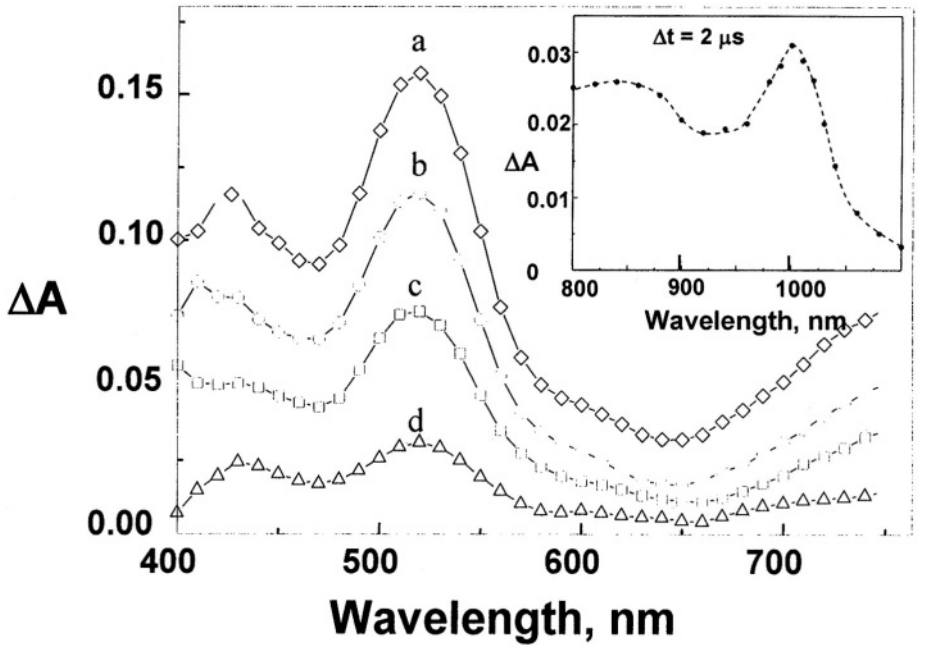

Figure 4. Time-resolved transient absorption spectra recorded (a) 2; (b) 10; (c) 20 and (d) 60 μs after 337 nm laser pulse excitation of deaerated toluene (15%)-acetonitrile (85%) (v/v) solution of 10 μM tris-(C_{60}) and 0.1 M NMP. The inset shows the difference absorption spectrum corresponding to the fullerene anion in the infrared region. (From reference 32. Reprinted with permission from the American Chemical Society.)

For pristine C_{60}, this absorption band lies around 1060 nm. However, the absorption of fullerene anion is sensitive to the nature of functionalization as it exhibits a blue-shifted absorption. The strong absorption of the fullerene anion at 1000 nm enabled us to evaluate the fate of electron transfer products and their stabilization by comparing the absorption decay in monomer and cluster systems. The decay of fullerene anion is dependent on the number of fullerene units in monomer and cluster forms. The decay of the monomer form of fullerene anions was fitted to single exponential decay whereas biexponential kinetics was necessary to fit the decay of cluster anions. The lifetimes measured from the kinetic analysis of the decay of the monomer anion and cluster anion, for mono-, bis- as well as tris-(C_{60}) derivatives, are summarized in Table 2. An increase in the lifetime of 18 to 34 μs was observed, for monomer systems, by increasing the fullerene unit from one to three. These observations further support an earlier argument that stabilization of charge can be achieved by bringing together several fullerene units in close proximity. It is evident from these results that the fullerene anion lifetime increases with increasing number of fullerene moieties. Indeed, clusters of all these molecules showed a long-lived component with a lifetime greater than 100 μs. Once the electron is transferred to a fullerene moiety it can quickly hop around the adjacent fullerene moieties, thus allowing the electron transfer product to stabilize.[25]

Table 2. Charge Separation and Charge Stabilization in Fullerene Clusters.[32]

Fullerene Derivative		Anion Lifetime[c]/μs τ_1	τ_2	Charge Transfer Quantum Yield[d]
Mono-C_{60}	Monomer[a]	18	-	0.11
	Cluster[b]	16.6 (64%)	109 (36%)	0.13
Bis-C_{60}	Monomer[a]	20	-	0.09
	Cluster[b]	11.8 (70%)	134 (25%)	0.07
Tris-C_{60}	Monomer[a]	34.0	-	0.11
	Cluster[b]	12.0 (85%)	146 (15%)	0.06
C_{60}-aniline dyad	Monomer[a]	-	<10	-
	Cluster[b]	-	60	-

[a]in toluene; [b]in 19:1 acetonitrile:toluene mixed solvent; [c]numbers in bracket indicate the fractional contribution to the overall decay; [d]measured from the fullerene anion yield (ε(1000 nm) = 16250 M^{-1} cm^{-1}) and benzophenone triplet as the actinometry reference (ε(530 nm) = 7600 M^{-1} cm^{-1}).

In the example discussed above, the electron donor (NMP) was incorporated into the cluster. An orderly way to achieve such a donor-acceptor assembly would be to use a dyad molecule (e.g., C_{60}-aniline dyad) and then achieve charge stabilization by forming clusters.[25] By comparing the photochemical behavior of aniline-C_{60} dyad in neat solvents and toluene:acetonitrile mixtures (1:3), it was possible to infer two major conclusions: (i) The aniline-fullerene dyad molecules undergo fast intramolecular photoinduced electron transfer in polar solvents and (ii) charge stabilization is observed only in solvent mixtures that favor aggregation or clustering of dyad molecules. The dyad molecules undergo a spontaneous self-assembly in mixed solvents in such a way that the hydrophobic fullerene moieties come together leaving the polar aniline moiety away.[12] The self-assembled geometry of cluster framework helps the initially transferred electron to leave the parent fullerene molecule and hops on to the adjacent fullerene moiety in the cluster. Subsequent hopping of the electron from one fullerene moiety into the other increases the distance of separation of radical ion pair and this in turn retards the charge recombination. The transferred electrons, thus get fully delocalized within the fullerene cluster network, while the positive charges may be localized at the aniline functions. The ultimate goal of the research in this area is to generate long lived charge separated intermediates and the example discussed here demonstrates a novel method for charge stabilization, by taking advantage of the clustering behavior of the C_{60}.

4. NANOSTRUCTURED FULLERENE FILMS

Earlier efforts to cast fullerene films using solvent evaporation,[18,41] Langmuir-Blodgett technique,[42,43] self assembled monolayer[44,45] or layer-by-layer assembly,[46,47] have produced polymorphous films. However, a high degree of molecular order has been achieved with the films formed on pyrolytic graphite (HOPG).[48] These C_{60} films deposited on HOPG surface exhibit aggregation. Nanoscopic formation of aggregates of

C_{60} on various surfaces has also been modeled via experimental[49] and numerical simulations.[50] Electrophoretically deposited fullerene films on the other hand exhibit unique nanostructure features. The electrophoretically deposited C_{60} film is highly porous and consists of C_{60} clusters that are assembled in a fairly orderly fashion. The absorption spectrum of the electrophoretically deposited fullerene cluster films showed broad spectral features similar to those observed in cluster suspensions. The electrophoretically deposited films are photochemically and electrochemically active and are capable of undergoing multielectron reductions similar to those observed for C_{60} molecules in different solvents.

4.1. Electrophoretic Deposition

Figure 5 shows the AFM images of electrophoretically deposited C_{60} cluster films. Several C_{60} clusters coalesce to form larger aggregates of spherical shape (diameter ~500 nm). The AFM image scanned at higher resolution shows the ordering of C_{60} clusters as nanoballs thus giving a fine nanostructure to the fullerene film. Each of these aggregated nanoballs consists of 100-200 nm diameter C_{60} clusters of varying shapes. Since these clusters are expected to be hollow,[51] it is no surprise that close packing of these C_{60} clusters would alter the shape of individual clusters in the film. A schematic illustration of the electrodeposition process is presented in Figure 6.

The magnitude of the applied dc voltage had a pronounced effect on the morphology of the electrophoretically deposited C_{60} cluster films. At higher deposition voltages the packing of the C_{60} clusters becomes denser and we observe relatively less void spaces in the film. Thus, we can conclude that the porosity of the nanostructured C_{60} film diminishes with increasing the deposition voltage. Controlling the morphology of the nanostructured fullerene films by means of applied deposition voltage would prove to be useful in any device oriented applications.

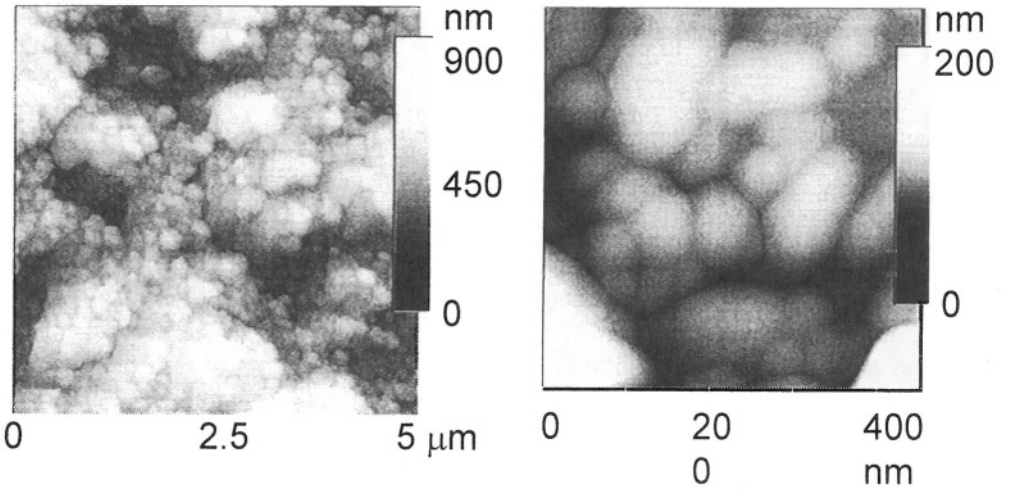

Figure 5. AFM image of C_{60} cluster film deposited on OTE electrode at a deposition voltage of 50 V dc. The image was recorded in the tapping mode using etched Silicon tip as a probe. Images A and B were recorded at different magnifications. (From reference 31. Reprinted with permission from Wiley-VCH.)

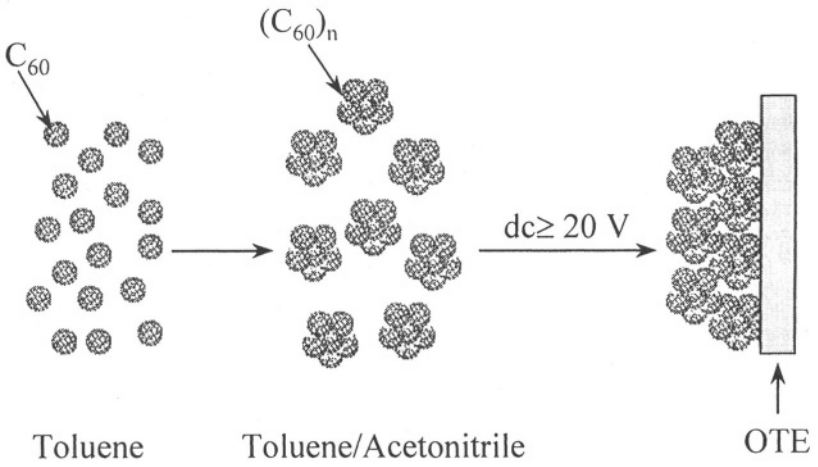

Figure 6. Schematic illustration of assembling fullerene clusters as nanostructured films on an electrode surface. (From reference 31. Reprinted with permission from Wiley-VCH.)

4.2. Fullerene Functionalized Gold Clusters And Films

Another approach of designing fullerene clusters is to use a metal nanocore as the template on which several fullerene moieties can be anchored.[53,54] One such example involves self-assembled photoactive antenna systems containing gold nanoparticles as central nanocores and appended fullerene moieties as the photoreceptive hydrophobic shells (Figure 7). Such molecular-gold nanoassemblies can serve as important building blocks in the design of light harvesting systems.

The preparation and characterization of fullerene functionalized gold nanoparticles are described elsewhere.[52] A dilute solution of Au-S-C_{60}, when dried on a carbon grid, shows relatively large clusters of varying size. The TEM image shows large cluster aggregates of ~30 nm diameter (Figure 8). This is in contrast to well dispersed thiol stabilized gold nanoparticles with diameter of 3-5 nm. Up to ninety C_{60} units can be linked to a single gold nanoparticle. Because of the high concentration of C_{60} around Au nanoparticle we can observe secondary clustering effects. What we observe in the TEM picture are large clusters, which are preferably formed as a result of interparticle clustering. The formation of such cluster assemblies is a further indication that these fullerene-gold nanoassemblies prefer to form larger aggregates even in nonpolar solvents. Strong affinity between fullerenes and gold nanoparticles as reported in an earlier study[55] is likely to cause interparticle aggregation effects.

The gold nanocore in the Au-S-C_{60} system is redox active and is capable of altering deactivation pathways of surface bound fullerene. In the absence of gold nanoparticles, the emission spectrum of fullerene thiol in toluene shows a maximum at 710 nm, which corresponds to its singlet-excited state. Interestingly, the fullerene thiol emission is totally quenched when it is anchored on the gold nanocore. Low yields of singlet and triplet of fullerene moiety in excited Au-S-C_{60} assembly and the absence of any charge separated products confirm that the excited energy of the fullerene moiety is quickly dissipated via energy transfer to gold nanoparticles.

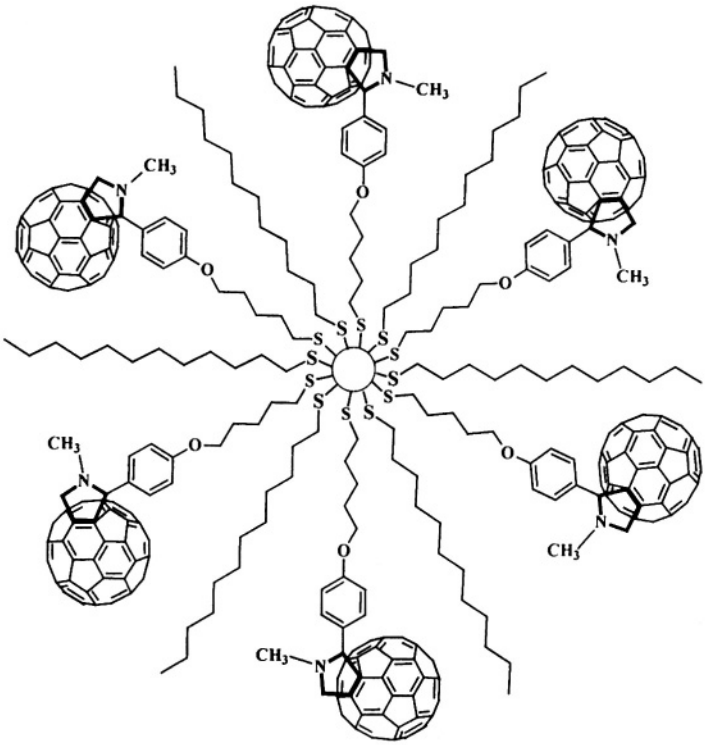

Figure 7. Fullerene functionalized gold nanoparticles. (From reference 52. Reprinted with permission from the American Chemical Society.)

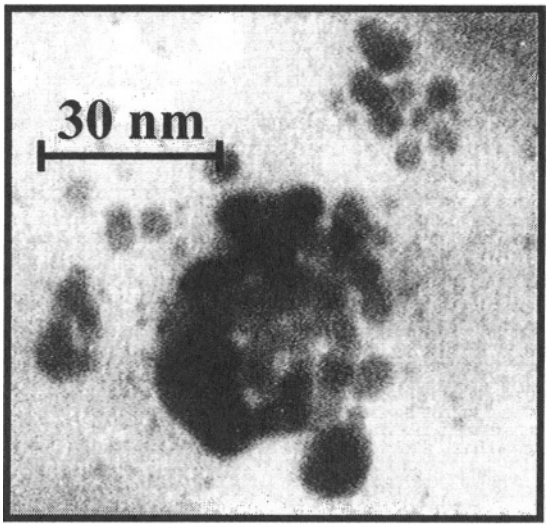

Figure 8. Transmission electron micrograph images of fullerene thiol/dodecanethiol (1/19 mole fraction) bound gold nanoparticles. (From reference 52. Reprinted with permission from the American Chemical Society.)

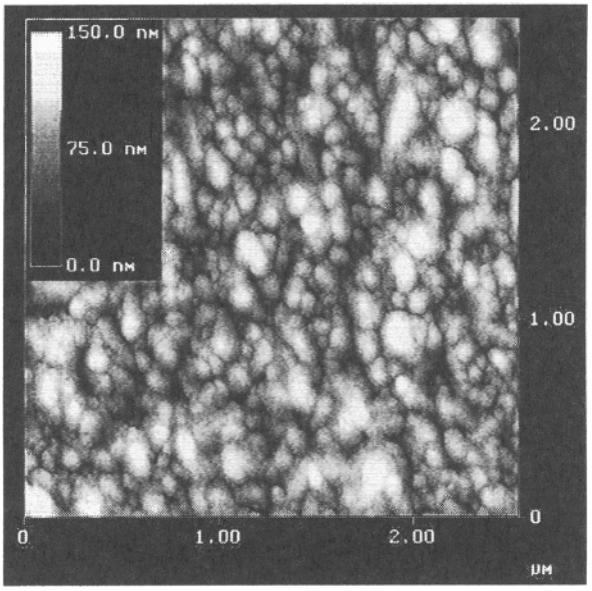

Figure 9. AFM image of Au-S-C_{60} deposited on OTE electrode using an electrophoretic approach (applied dc voltage was 50V). (From reference 52. Reprinted with permission from the American Chemical Society.)

4.3. Nanostructured Films of Au-S-C_{60}

One of the convenient ways to utilize a fluorophore-gold nanoassembly in light harvesting applications is to assemble them in an orderly fashion on an electrode surface. We employed an electrophoretic method to deposit Au-S-C_{60} nanoassemblies on an optically transparent electrode (OTE) surface. Under the application of a dc electric field Au-S-C_{60} clusters become charged in toluene solution and get deposited on the positively charged electrode surface. The film cast by electrophoretic approach produces a robust coverage of the fullerene functionalized gold assemblies on the optically transparent electrode (OTE).

The AFM image presented in Figure 9 shows a 3-D assembly of Au-S-C_{60} clusters that renders a nonporous morphology to the film. Upon close examination of the AFM image (Figure 6) it is evident that the nanostructured Au-S-C_{60} film consists of 50-100 nm diameter clusters and these clusters are larger than those present in solution. These films are quite robust and can be washed with organic solvents to remove any loosely bound Au-S-C_{60} nanoassemblies. Because of the high coverage, these films are useful for electrocatalytic and sensor applications.

5. APPLICATIONS

Fullerene nanostructures have a wide range of applications. Its ability to absorb light throughout the visible region, capture and store electrons and ease of synthesizing hybrid structures has opened up newer ways to develop diverse optoelectronic devices (sensors, photonic systems etc.) to light harvesting systems. Photovoltaic devices containing blends of poly (paraphenylenevinylene, PPV) derivatives as donor materials with various C_{60}

derivatives as acceptors have been developed.[16,56,57] Nanocomposite resists for sub-100 run features have been developed by incorporating C_{60} in a commercial resist ZEP520.[58] The specific examples discussed below highlight some of the unique features of fullerene nanostructures.

5.1 Electrocatalytic Aspects

C_{60} films constitute a new class of *carbon* electrodes with properties that differ from graphite and diamond electrodes. These films are quite stable to oxidative potentials, but show unusual electrochemical dependence on the method of preparation and the electrolyte medium.[59] For example, the one- and two-electron-reduced forms of C_{60} undergo complexation with the cation (for example, tetrabutyl ammonium ion in acetonitrile medium) and exhibit a hysteresis in the cyclic voltammograms. The variation in the film morphology also affects the rate of ion transport within the C_{60} film.[60] By incorporating a redox couple (e.g., ferrocene), in C_{60} clusters before assembling them as thin films on an electrode surface it is possible to modulate the electrochemical properties of fullerene films.[61] Layer-by-layer (LBL) assembled films of a fulleropyrrolidinium-androstane-ferrocene dyad have revealed a surprisingly high level of intermolecular organization producing linear nanowire superstructures.[62]

The C_{60} cluster films that were deposited without incorporating ferrocene, do not exhibit any oxidation peaks (inset in Figure 10), thereby confirming the stability of C_{60} to electrochemical oxidation at potentials below 1 V.[61] The Fc@ C_{60} films on the other hand showed an oxidation peak corresponding to ferrocene oxidation. At negative potentials one observes a broad cathodic peak around –590 mV, which corresponds to the reduction of C_{60}. The two scans (#1 & 2) in Figure 10 exhibit a normal electrochemical behavior that one would anticipate from the cyclic voltammograms of two electroactive species, viz. Fc^0/Fc^+ and C_{60}/C_{60}^-. Upon reversal of the scan following the reduction of C_{60} (scan #3) we observe a different behavior. A significant enhancement is seen for the oxidation peak at the potential corresponding to ferrocene oxidation. This enhanced oxidation peak represents increased oxidation events that involve Fc^0.

The unusual electrochemical behavior observed in the anodic scan can be attributed to the catalytic process mediated by C_{60} anions in the cluster films (reactions 3-6).[61]

$$\text{At } -0.6 \text{ V:} \qquad (C_{60})_n \longrightarrow (C_{60})_n^- \xrightarrow{TBA^+} \{(C_{60})_n^- \text{-} TBA^+\} \tag{3}$$

$$\text{At } +0.43 \text{ V:} \qquad Fc^0 \longrightarrow Fc^+ \tag{4}$$

$$\text{Catalytic reaction:} \qquad Fc^+ + \{(C_{60})_n^- \text{-} TBA^+\} \longrightarrow Fc^0 + (C_{60})_n + TBA^+ \tag{5}$$

$$\text{At } +0.36\text{V:} \qquad Fc^+ \longrightarrow Fc^0 \tag{6}$$

Once the C_{60} in the cluster film undergoes reduction (reaction 1), the anion gets stabilized in the cluster film. As discussed in an earlier work,[60] the complexation between C_{60} anion and tetrabutyl ammonium cation (TBA^+) is responsible for the stabilization of reduced species in the cluster film. Szucs et al.[63,64] have demonstrated that the cation

stabilized reduced films of C_{60} remain stable even when exposed to air. As evident from the cyclic voltammograms in Figure 10, the stabilized $\{(C_{60})_n^{-}\text{-}TBA^{+}\}$ species are not directly accessible for reoxidation at the electrode surface. The stabilized $\{(C_{60})_n^{-}\text{-}TBA^{+}\}$ species is retained in the film undisturbed until the electrochemical scan reaches a potential around +300 mV. At this potential, the Fc^0 in the film starts getting oxidized (reaction 4). As soon as ferrocene gets oxidized, it extracts the electron from $\{(C_{60})_n^{-}\text{-}TBA^{+}\}$ and regenerates the ferrocene in the cluster film (reaction 5). Continuous oxidation and regeneration events (reactions 4 and 5) at this ferrocene oxidation potential (E^0= 395 mV) render the anodic peak current to rise sharply. Once all the $\{(C_{60})_n^{-}\text{-}TBA^{+}\}$ in the film is consumed, a saturation in anodic current is reached (E_{pa}=430 mV). At this point all the ferrocene in the film gets converted into its oxidized form. In the reverse scan (scan #4) we observe usual reduction wave of Fc^{+} (reaction 6). An important aspect of the electrocatalytic reaction is to improve the sensitivity of electrochemical detection by increasing the oxidation-reduction turn over events at the detection potential. For example, in the experiment discussed above a reduced C_{60} film can yield more than 5 times higher anodic current than the unreduced C_{60} film during the oxidation of ferrocene.

5.2 Photoelectrochemical Conversion of Light Energy

The broad absorption of nanostructured fullerene films in the visible and in the near IR region as well as higher molar absorptivity compared to the pristine C_{60} (makes these films suitable for harvesting solar energy. By employing the C_{60} film cast on an optically transparent electrode (OTE) as a photoanode in a photoelectrochemical cell, it is possible to evaluate their potential application in light energy conversion processes.[12,15,29]

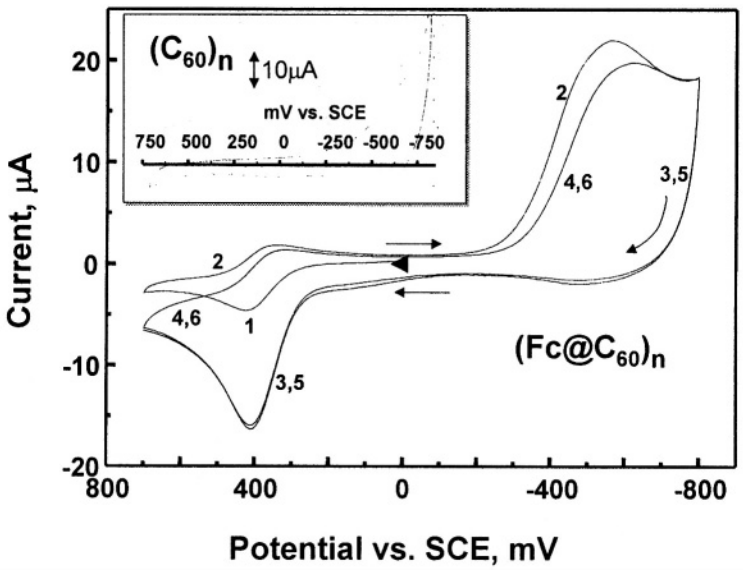

Figure 10. Cyclic voltammogram of (a) $(C_{60})_n$ cluster film and (b)$(Fc@C_{60})_n$ cluster films deposited on a glassy carbon electrode. (Electrolyte .1 M TBAP in acetonitrile). (From reference 61. Reprinted with permission from the Royal Chemical Society.)

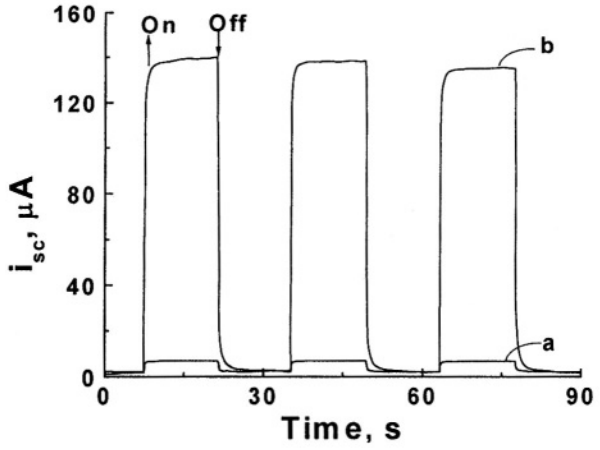

Figure 11. (a) Absorption spectrum of OTE/SnO_2/$(C_{60})_n$ and (b) photocurrent action spectrum of OTE/SnO_2/$(C_{60})_n$. The photocurrent action spectra of (c) OTE/SnO_2; (d) OTE/TiO_2/$(C_{60})_n$ and (e) OTE/$(C_{60})_n$ films are also shown. The IPCE values were calculated by normalizing the photocurrent values for incident light energy and intensity. Electrolyte: 0.5 M LiI in acetonitrile, Counter Electrode:Pt gauze. (From reference 29. Reprinted with permission from the American Chemical Society.)

Figure 11 shows photocurrent generation in photoelectrochemical cell using $(C_{60})_n$ films cast on SnO_2 nanostructured film electrodes as a photoanode. The photocurrent generation was prompt, steady and reproducible during several on/off cycles of white light (λ>425 nm) illumination.

The applications of such systems are not only restricted to the area of photonic materials, but can be also found in catalysis.[60] Due to the connecting windows between neighboring air bubbles, the metal nanoparticles can be easily accessed when the porous solid is placed within the medium where the reaction to be catalyzed is to take place. Various modifications of this process can also be envisaged for the fabrication of materials with different and interesting properties.

Under visible light irradiation (λ>425 nm, 130 mW/cm^2) and using I_3^-/I^- as redox couple, the photoelectrochemical cell delivered a stable photocurrent of ~0.14 mA/cm^2 and an open circuit voltage of ~200 mV. At an applied bias of 0.15 V we obtained photocurrent as high as 0.2 mA/cm^2 (λ>425 nm, 130 mW/cm^2). Blank SnO_2 films yielded < 5 μA/cm^2 under similar illumination conditions. The photocurrents observed using C_{60} cluster films are 2-3 orders of magnitude greater than recently reported values using functionalized fullerenes as photosensitizers[44] and an order of magnitude greater than the C_{60}-oligophenylenevinylene-based photovoltaic cell.[19,65]

The photocurrent action spectrum of $(C_{60})_n$ film cast on a nanostructured SnO_2 electrode showed a broad response in the visible with photoconversion efficiencies decreasing with increasing wavelength (Figure 12). The photoelectrochemical response follows the broad spectral feature observed in the absorption spectrum of C_{60} clusters, thus confirming the excitation of C_{60}–cluster film as the origin of photocurrent generation. It is interesting to note however, that these electrodes show enhanced photoresponse in the red region. A maximum IPCE (Incident Photon to Charge carrier generation Efficiency) of ~4% was observed in the wavelength region of 420 nm.

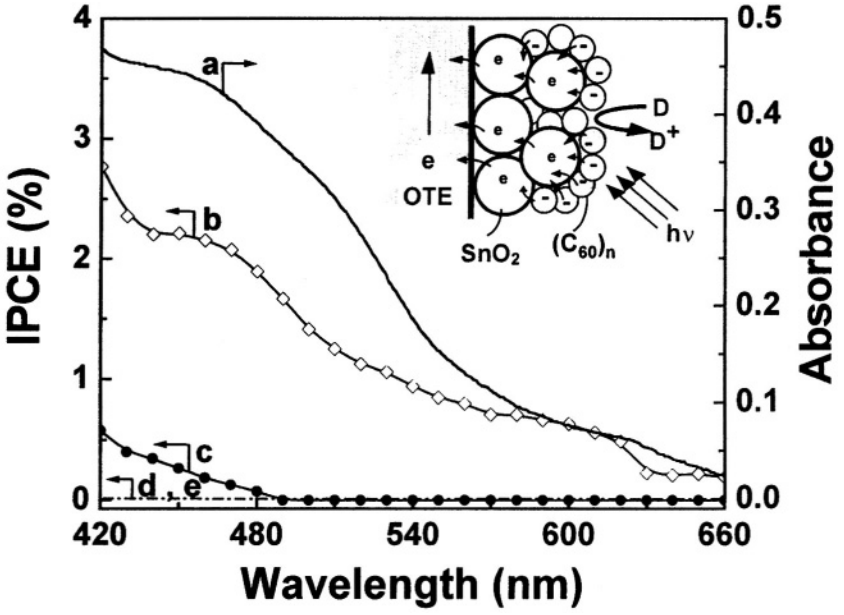

Figure 12. Generation of photocurrent at (a) OTE/SnO_2 and (b) OTE/SnO_2/C_{60} film electrodes under visible light excitation (λ>425 nm) in the absence of any applied bias. (Electrolyte: 0.5 M LiI, 1 mM I_2 in acetonitrile, Counter Electrode:Pt gauze) (From reference 29. Reprinted with permission from the American Chemical Society.)

The net power conversion efficiency obtained under low intensity visible excitation (~1 mW/cm^2) remained about 0.1%. The photocurrent generation in the C_{60} cluster film involves a photogalvanic type behavior that involves photoinduced electron transfer between excited C_{60} and the redox couple to generate C_{60} anion and the C_{60} anion in turn transfers electron to SnO_2 or TiO_2 nanoparticles.

It is important to note that C_{60} readily undergoes one electron reduction ($(E(C_{60}/C_{60}^-) \approx -0.2$ V vs. NHE) in the presence of electron donors. In the example discussed here photoinduced electron transfer between $(C_{60})_n$ and I^- is considered to be the primary step in the photocurrent generation process (Reactions 1-3).[29]

$$(C_{60})_n + h\nu \longrightarrow (C_{60})_n^* \quad (7)$$

$$2(C_{60})_n^* + 3I^- \longrightarrow 2(C_{60})_n^- + I_3^- \quad (8)$$

$$(C_{60})_n^- + SnO_2 \longrightarrow (C_{60})_n + SnO_2\,(e) \quad (9)$$

Evidence for the formation of C_{60}^- species can be obtained from the laser flash photolysis experiment. The transient absorption spectrum recorded immediately after 337-nm laser pulse excitation confirmed the formation of C_{60} anion with its characteristic absorption at 1010 nm. The electrons transferred to the SnO_2 nanocrystallites are driven to the counter electrode *via* external circuit to regenerate the redox couple. The transfer of electrons from C_{60} anion to the conduction band of SnO_2 is energetically feasible and

thus, we expect a flow of electrons towards the conducting surface of OTE. On the other hand, C_{60} films cast on nanostructured TiO_2 films failed to show any photocurrent generation. Since the reduced anion of C_{60} is unable to transfer the electrons to TiO_2 (E_{CB}= –0.5 V vs. NHE) it was not possible to observe any significant photocurrent generation using OTE/TiO_2 electrodes modified with C_{60} cluster films.

Another effective way to build photosensitive electrodes is to employ donor-bridge-acceptor molecules as the light harvesting units.[15,66] The photoinduced charge separation in these units can then be effectively harvested to generate photocurrent. Since fullerene-aniline dyad clusters show long-lived charge separation it is possible to utilize them for photoelectrochemical conversion of light energy.[25] The clusters of fullerene-aniline dyad[25] and fullerene–porphyrin dyad[15] have been deposited on nanostructured SnO_2 film and used as photoanodes in the photoelectrochemical cell. For example, fullerene-aniline dyad cluster films under visible light irradiation (λ>425 nm) deliver a stable photocurrent of ~0.2 mA/cm^2 and an open circuit voltage of ~170 mV. Under visible light illumination, the OTE/SnO_2/(C_{60}-aniline)$_m$ electrode shows remarkable rectification behavior in the potential range of –300 to 200 mV vs. Ag/AgCl. The electron flow towards the collecting electrode can be controlled by the application of an electrochemical bias. The charge-separated pair in fullerene-aniline dyad cluster is stabilized as the electrons hop away to the neighboring fullerene moieties. Both the photoinduced charge transfer within the C_{60}-aniline dyad cluster and the electron transfer from reduced fullerene moiety ($E(C_{60}/C_{60}^-) \approx -0.2$ V vs. NHE) into SnO_2 nanocrystallites (E_{CB} (SnO_2)= 0.0 V vs. NHE) are thermodynamically favored processes. While the reduced anion moiety of the dyad cluster injects electrons into the SnO_2 nanocrystallites, the oxidized aniline counterpart undergoes charge transfer with the iodide in the electrolyte. The electrons transferred to the semiconductor nanocrystallites are collected at the OTE surface and are driven to the counter electrode via external circuit to regenerate the redox couple. The examples discussed here showed the potential use of fullerene clusters for light energy harvesting applications. The improved performance of these fullerene electrodes can be attributed to the increased molar absorptivity in the visible region, long-lived charge separation, and production of electroactive C_{60} anion moieties that are capable of delivering charges to SnO_2 nanocrystallites.

6. ACKNOWLEDGMENT

We would like to acknowledge the support of the Office of Basic Energy Science of the Department of the Energy (USA) and the Council of Scientific and Industrial Research, Government of India (KGT) . This is contribution No NDRL 4404 from the Notre Dame Radiation Laboratory and No RRLT-PRU 158 from RRL, Trivandrum .

7. REFERENCES

1. C. A. Mirkin and W. B. Caldwell, Thin film, fullerene-based materials, *Tetrahedron* **52**, 5113-5130 (1996).
2. M. Antonietti and C. Göltner, Superstructures of functional colloids: chemistry on the nanometer scale, *Angew. Chem. Int. Ed. Engl.* 36, 911-928 (1997).

3. A. N. Shipway, E. Katz, and I. Willner, Nanoparticle arrays on surfaces for electronic, optical, and sensor applications, *Phys. Chem. Phys* **1,** 18-52 (2000).
4. H. Imahori and Y. Sakata, Donor-linked fullerenes. Photoinduced electron transfer and its potential application, *Adv. Mater.* 9, 537-546 (1997).
5. D. M. Guldi, Fullerenes: Three dimensional electron acceptor materials, *Chem. Commun.,* 321-327 (2000).
6. D. Gust, T. A. Moore, and A. L. Moore, Fullerenes linked to photosynthetic pigments, *Res. Chem. Intermed.* **120**, 4398-4405 (1997).
7. D. M. Guldi, M. Maggini, G. Scorrano, and M. Prato, Intramolecular electron transfer in fullerene/ferrocene based donor-bridge-acceptor dyads, *J. Am. Chem. Soc.* **119**, 974-980 (1997).
8. F. Diederich and M. Gómez-López, Supramolecular fullerene chemistry, *Chem. Soc. Rev.,* 263-277 (1999).
9. N. Martin, B. Sanchez, B. Illescas and I. Perez, C_{60}-based electroactive organofullerenes, *Chem. Rev.* **98,** 2527-2547(1998).
10. K. George Thomas, Functionalized fullerenes as photosynthetic mimics, *Interface* **8**, 30-33 (1999).
11. D. M. Guldi, C. Luo, T. Da Ros, M. Prato, E. Dietel, and A. Hirsch, Photoinduced electron transfer in multicomponent arrays of a -stacked fullerene porphyrin dyad and diazabicyclooctane or a fulleropyrrolidine ligand, *Chem. Commun.,* 375-376 (2000).
12. P. V. Kamat, S. Barazzouk, S. Hotchandani, and K. George Thomas, Nanostructured thin films of C_{60}-aniline dyad clusters. Electrodeposition, charge separation and photoelectrochemistry, *Chem., Eur. J.* **6**, 3914-3921 (2000).
13. V. Biju, K. George Thomas, M. V. George, D. M. Guldi, and P. V. Kamat, Photoinduced charge separation in fullerene-aniline dyads, in *Fullerenes* (eds. Kamat, P. V., Guldi, D. M. & Kadish, K.) 296-303 (The Electrochemical Society, Pennington, N. J., 1999).
14. H. Imahori, K. Tamaki, D. M. Guldi, C. Luo, M. Fujitsuka, O. Ito, Y. Sakata, and S. Fukuzumi, Modulating charge separation and charge recombination dynamics in porphyrin-fullerene linked dyads and triads: Marcus-normal versus inverted region, *J. Am. Chem. Soc.* **123**, 6617-6628 (2001).
15. H. Imahori, T. Hasobe, H. Yamada, P. V. Kamat, S. Barazzouk, M. Fujitsuka, O. Ito, and S. Fukuzumi, Spectroscopy and photocurrent generation in nanostructured thin films of porphyrin-fullerene dyad clusters, *Chem. Lett.,* 784-785 (2001).
16. G. Yu, J. Gao, J. C. Hummelen, F. Wudl, and A. J. Heeger, Polymer photovoltaic cells: Enhanced efficiencies via a network of internal donor-acceptor heterojunctions, *Science* **270,** 1789-1791 (1995).
17. G. Yu and A. J. Heeger, Charge separation and photovoltaic conversion in polymer composites with internal donor/acceptor heterojunctions, *J. Appl. Phys.* **78**, 4510-4515 (1995).
18. S. Licht, O. Khaselev, P. A. Ramakrishnan, D. Faiman, E. A. Katz, A. Shames, and S. Goren, Fullerene photoelectrochemical solar cells, *Solar Energy Mater. Solar Cells* **51**, 9-19 (1998).
19. J.-F. Nierengarten, J.-F. Eckert, J.-F. Nicoud, L. Ouali, V. Krasnikov, and G. Hadziioannou, Synthesis of a C60-oligophenylenevinylene hybrid and its incorporation in a photovoltaic device, *Chem. Commun.,* 617-618 (1999).
20. E. Peeters, P. A. van Hal, J. Knol, C. J. Brabec, N. S. Sariciftci, J. C. Hummelen, A. René, and R. A. J. Janssen, Synthesis, photophysical properties, and photovoltaic devices of oligo(p-phenylene vinylene)-fullerene dyads, *J. Phys. Chem. B* **104**, 10174-10190 (2000).
21. M. F. Durstock, B. Taylor, R. J. Spry, L. Chiang, S. Reulbach, K. Heitfeld, and J. W. Baur, Electrostatic self-assembly as a means to create organic photovoltaic devices, *Synth. Met.* **116**, 373-377 (2001).
22. Y. M. Wang, P. V. Kamat, and L. K. Patterson, Aggregates of C_{60} and C_{70} formed at the gas-water interface and in DMSO/water mixed solvents. A spectral study, *J. Phys. Chem.* **97**, 8793-7 (1993).
23. M. Sundahl, T. Andersson, K. Nilsson, O. Wennerstrom, and G. Westman, Clusters of C60-fullerene in a water solution containing γ- cyclodextrin: A photophysical study, *Synth. Met.* **55**, 3252-7 (1993).
24. Y.-P. Sun, B. Ma, C. E. Bunker, and B. Liu, All-carbon polymers(polyfullerenes) from photochemical reactions of fullerene clusters inroom-temperature solvent mixtures, *J. Am. Chem. Soc.* **117**, 12705-12711 (1995).
25. K. George Thomas, V. Biju, M. V. George, D. M. Guldi, and P. V. Kamat, Photoinduced charge separation and stabilization in clusters of a fullerene-aniline dyad, *J. Phys. Chem. B* **103**, 8864-8869 (1999).
26. S. Nath, H. Pal, D. K. Palit, A. V. Sapre, and J. P. Mittal, Aggregation of fullerene, C-60, in benzonitrile, *J. Phys. Chem. B* **102**, 10158-10164 (1998).
27. Y.-P. Sun, J. E. Riggs, and B. Liu, Optical limiting properties of [60]fullerene derivatives, *Chem. Mater.* **9**, 1268-1272(1997).
28. P. V. Kamat, I. Bedja, and S. Hotchandani, Photoinduced charge transfer between carbon and semiconductor clusters. One-electron reduction of C_{60} in colloidal TiO_2 semiconductor suspensions, *J. Phys. Chem.* **98**, 9137-9142 (1994).

29. P. V. Kamat, S. Barazzouk, K. George Thomas, and S, Hotchandani, Electrodeposition of C60 clusters on nanostructured SnO_2 films for enhanced photocurrent generation, *J. Phys. Chetn. B* **104**, 4014-4017 (2000).
30. V. Biju, S. Barazzouk, K. George Thomas, M. V. George, and P. V. Kamat, Photoinduced electron transfer between 1,2,5-triphenylpyrrolidinofullerene cluster aggregates and electron donors, *Langmuir* **17**, 2930-2936 (2001).
31. P. V. Kamat, S. Barazzouk, and S. Hotchandani, Electrochemical aspects of C60-ferrocene cluster films, in *Fullerenes-2001* (eds. Kamat, P. V., Guldi, D. M. & Kadish, K.) (The Electrochemical Society, Pennigton, NJ, 2001).
32. V. Biju, P. K. Sudeep, K. George Thomas, M. V. George, S. Barazzouk, and P. V. Kamat, Clusters of bis- and tris-fullerenes, *Langmuir* **18**, 1831-1839 (2002).
33. P. V. Kamat, S. Barazzouk, and S. Hotchandani, Nanostructured fullerene films, *Adv. Mater.* **13**, 1614-1617 (2001).
34. V. Georgakilas, F. Pellarini, M. Prato, D. M. Guldi, M. Melle-Franco, and F. Zerbetto, Supramolecular self-assembled fullerene nanostructures, *Proc. Natl. Acad. Sci. USA* **99**, 5075-5080 (2002).
35. V. I. Yuzhakov, Association of dye molecules and its spectroscopic manifestation, *Russ. Chem. Rev.* **48**, 1076-1091 (1979).
36. V. E. Korobov and A. K. Chibisov, Primary photoprocesses in colorant molecules, *Russ. Chem. Rev.* **52**, 27-42 (1983).
37. O. Valdes-Aguilera and D. C. Neckers, Aggregation phenomena in xanthene dyes, *Acc. Chem. Res.* **22**, 171-177 (1989).
38. S. Barazzouk, H. Lee, S. Hotchandani, and P. V. Kamat, Excited pinacyanol H-aggregates and their interaction with SiO_2 and SnO_2 nanoparticles, *J. Phys. Chem. B* **104**, 3616-3623 (2000).
39. H. Imahori, H. Norieda, H. Yamada, Y. Nishimura, I. Yamazaki, Y. Sakata, and S. Fukuzumi, Light-harvesting and photocurrent generation by gold electrodes modified with mixed self-assembled monolayers of boron-dipyrrin and ferrocene-porphyrin-fullerene triad, *J. Am. Chem. Soc.* **123**, 100-110 (2001).
40. D. M. Guldi, Fullerene-porphyrin architectures; photosynthetic antenna and reaction center models, *Chem. Soc. Rev.* **31**, 22-36 (2002).
41. B. Miller, J. M. Rosamilia, G. Dabbagh, R. Tycko, R. C. Haddon, A. J. Muller, W. Wilson, D. W. Murphy, and A. F. Hebard, Photoelectrochemical behavior of C60 films, *J. Am. Chem. Soc.* **113**, 6291-3 (1991).
42. C. P. Luo, C. H. Huang, L. B. Gan, D. J. Zhou, W. S. Xia, Q. K. Zhuang, Y. L. Zhao, and Y. Y. Huang, Investigation of the photoelectrochemistry of C-60 and its pyrrolidine derivatives by monolayer-modified SnO_2 electrodes, *J. Phys. Chem. B* **100**, 16685-16689 (1996).
43. W. Zhang, Y. Shi, L. Gan, C. Huang, H. Luo, D. Wu, and N. Li, pH-Dependent photoinduced electron transfer at C60-EDTA Langmuir-Blodgett film modified ITO electrode, *J. Phys. Chem. B* **103**, 675-681 (1999).
44. H. Imahori, T. Azuma, A. Ajavakom, H. Norieda, H. Yamada, and Y. Sakata, An investigation of photocurrent generation by gold electrodes modified with self-assembled monolayers of C_{60}, *J. Phys. Chem. B* **103**, 7233-7237 (1999).
45. O. Enger, F. Nuesch, M. Fibbioli, L. Echegoyen, E. Pretsch, and F. Diederich, Photocurrent generation at a fullerene self-assembled monolayer-modified gold electrode cast with a polyurethane membrane, *J. Mater. Chem.* **10**, 2231-2233 (2000).
46. C. P. Luo, D. M. Guldi, M. Maggini, E. Menna, S. Mondini, N. A. Kotov, and M. Prato. Stepwise assembled photoactive films containing donor-linked fullerenes, *Angew. Chem. Int. Ed.* **39**, 3905-3909 (2000).
47. M. F. Durstock, B. Taylor, R. J. Spry, L. Chiang, S. Reulbach, K. Heitfeld, and J. W. Baur, Electrostatic self-assembly as a means to create organic photovoltaic devices, *Synth. Met.* **116**, 373-377 (2001).
48. P. Janda, T. Krieg, and L Dunsch, Nanostructuring of highly ordered C_{60} films by charge transfer, *Adv. Mater.* **10**, 1434-1438(1998).
49. K. Yase, N. Ara-Kato, T. Hanada, H. Takiguchi, Y. Yoshida, G. Back, K. Abe, and N. Tanigaki, Aggregation mechanism in fullerene thin films on several substrates. *Thin Solid Films* **331**, 131-40 (1998).
50. H. Rafii-Tabar and K. Ghafoori-Tabrizi, Modeling nanoscopic formations of C-60 on supporting substrates, *Progr. Surf. Sci.* **67**, 217-233 (2001).
51. S. Zhou, C. Burger, B. Chu, M. Sawamura, N. Nagahama, M. Toganoh, U. E. Hackler, H. Isobe, and E. Nakamura, Spherical bilayer vesicles of fullerene based surfactants in water: A laser light scattering study, *Science* **291**, 1944-1947 (2001).
52. P. K. Sudeep, B. I. Ipe, K. George Thomas, M. V. George, S. Barazzouk, S. Hotchandani, and P. V. Kamat, Fullerene Functionalized Gold Nanoparticles. A self assembled photoactive antenna-metal nanocore assembly, *Nano Lett.* **2**, 29-35 (2002).

53. J. G. Hou, X. Li, Y. Q. Li, and H. Q. Wang, Synthesis and characterization of metal-C-60 nanostructured films, *Adv. Mater.* **11,** 1124-1126 (1999).
54. T. Akiyama, H. Imahori, A. Ajawakom, and Y. Sakata, Synthesis and self assembly of porphoryn-linked Fullerene on gold surface using S-Au linkage, *Chem. Lett.,* 907-908 (1996).
55. M. Brust, C. J. Kiely, D. Bethell, and D. J. Schiffrin, C-60 mediated aggregation of gold nanoparticles, *J. Am. Chem. Soc.* **120,** 12367-12368 (1998).
56. C. J. Brabec, N. S. Sariciftci, and J. C. Hummelen, Plastic solar cells, *Adv. Funct. Mater.* **11,** 15-26 (2001).
57. F. Padinger, C. J. Brabec, T. Fromherz, J. C. Hummelen, and N. S. Sariciftci, Fabrication of large area photovoltaic devices containing various blends of polymer and fullerene derivatives by using the doctor blade technique, *Opto-Electronics Review* **8,** 280-283 (2000).
58. K. E. Gonsalves, L. Merhari, H. P. Wu, and Y. Q. Hu, Organic-inorganic nanocomposites: Unique resists for nanolithography, *Adv. Mater.* **13,** 703-714 (2001).
59. J. Chlistunoff, D. Cliffel, and A. J. Bard, Electrochemistry of fullerene films, *Thin Solid Films* **257,** 166-184 (1995).
60. J. F. Carlisle, C. A. Wijayawardhana, T. A. Evans, P. R. Melaragno, and I. B. Alin-Pyzik, Ion transport and ferrocene incorporation in electroactive fullerene films, *J. Phys. Chem.* **100,** 15532-15538 (1996).
61. S. Barazzouk, S. Hotchandani, and P. V. Kamat, Unusual electrocatalytic behavior of ferrocene bound fullerene cluster films, *J. Mater. Chem.* **12,** 2021-2025 (2002).
62. D. M. Guldi, C. P. Luo, D. Koktysh, N. A. Kotov, T. Da Ros, S. Bosi, and M. Prato, Photoactive nanowires in fullerene-ferrocene dyad polyelectrolyte multilayers, *Nano Lett.* **2**, 775-780 (2002).
63. A. Szucs, A. Loix, J. B. Nagy, and L. Lamberts, Fullerene film electrodes in aqueous solutions. 1. Preparation and electrochemical characterization, *J. Electroanal. Chem.* **397,** 191-203 (1995).
64. A. Szucs, A. Loix, J. B. Nagy, and L. Lamberts, Fullerene film electroodes in aqueous solutions. 2. Effects of doping cations, *J. Electroanal. Chem.* **402,** 137-48 (1996).
65. J.-F. Eckert, J.-F. Nierengarten, S. G. Liu, L. Echegoyen, F. Barigelletti, N. Armaroli, L. Ouali, V. Krasnikov, and G. Hadziioannou, Fullerene-oligophenylenevinylene hybrids: Synthesis, electronic properties, and incorporation in photovoltaic devices, *J. Am. Chem. Soc.* **122,** 7467-7479 (2000).
66. H. Imahori, M. Arimura, T. Hanada, Y, Nishimura, I. Yamazaki, Y. Sakata, and S. Fukuzumi, Photoactive three-dimensional monolayers: porphyrin-alkanethiolate-stabilized gold clusters, *J. Am. Chem. Soc.* **122,** 335-336 (2000).

INDEX